PROCEEDINGS OF THE NINTH INTERNATIONAL SEMINAR

on

FIRE AND EXPLOSION HAZARDS

21-26 April 2019, Saint Petersburg, Russia

VOLUME 2

Edited by
Snegirev A.
Tamanini F.
Bradley D.
Liu N.
Molkov V.
Chaumeix N.

Saint Petersburg
Peter the Great St. Petersburg Polytechnic University
2019

Proceedings of the Ninth International Seminar on Fire and Explosion Hazards

21-26 April 2019, St. Petersburg, Russia

Edited by A. Snegirev, N. Liu, F. Tamanini, D. Bradley, V. Molkov, and N. Chaumeix

Volume 2

Copyright and Disclaimer

The papers published in the ISFEH9 Proceedings are protected by the copyright, which allows for subsequent publication elsewhere, but only in modified and extended form and with the full reference to the ISFEH9 Proceedings.

All articles in the Proceedings have been peer reviewed. However, the Editors assume no responsibility for the accuracy of the information provided. No responsibility is assumed by the Editors and the Publisher for any use or operation of any data, methods, instructions or ideas contained herein.

ISBN 978-5-7422-6498-9 (Vol. 2)
978-5-7422-6497-2

Saint Petersburg
Peter the Great St. Petersburg Polytechnic University
2019

Seminar Committees

International Organizing Committee

Chair: A. Snegirev (Russia)

Co-Chairs: D. Bradley (UK), D. Drysdale (UK), V. Molkov (UK), F. Tamanini (USA)

Members: N. Chaumeix (France), R. Dobashi (Japan), N.A. Liu (China), B. Merci (Belgium), E. Oran (USA), A. Pękalski (UK), J.G. Quintiere (USA), J. Torero (USA), K. Vågsæther (Norway)

Scientific Advisory Board

Chair: N.A. Liu (China)

Co-Chairs: D. Bradley (UK), N. Chaumeix (France), V. Molkov (UK), A. Snegirev (Russia), F. Tamanini (USA)

Paper selection and assignment

Track Chairs: J.G. Quintiere (USA), N. Chaumeix (France), N.A. Liu (China), G. Rein (UK), F. Tamanini (USA), V. Molkov (UK), A. Pekalski (UK), K. Boyce (UK), R. Dobashi (Japan), A. Snegirev (Russia)

Track Members: B. Merci (Belgium), D. Bradley (UK), E. Oran (US), K. Vaagsaether (Norway), Y. Nakamura (Japan), S. Stoliarov (US), J. Torero (US), P. Chatterjee (US), C. Fleischmann (New Zealand), H. Phylaktou (UK), A. Marshall (US), V. Novozhilov (Australia), Y. Wang (US)

Reviewers: G. Agarwal (US), G. Andrews (UK), R. Alpert (US), G. Atkinson (UK), A. Bartlett (UK), C.R. Bauwens (US), M. Beach (US), T. Beji (Belgium), J. Bergthorson (Canada), G. Bernard-Michel (France), C. Beyler (US), S. Bhattacharjee (US), D. Bjerketvedt (Norway), L. Boeck (US), P. Boulet (France), P. Bowen (UK), S. Brennan (UK), A. Brown (US), D. Brzezińska (Poland), G. Chamberlain (UK), M. Chaos (US), H. Chen (China), W.K. Chow (Hong Kong), D. Cirrone (UK), A. Coppalle (France), R. Cracknell (UK), M. Delichatsios (US), S. Dembele (UK), J. Deschamps (France), Y. Ding (US), B. Ditch (US), S. Dorofeev (US), R. Fahy (US), J. Fang (China), N. Fernandez Anez (Norway), C. Fernandez-Pello (US), K. Frank (New Zealand), O. Fujita (Japan), A. Gaathaug (Norway), A. Gajek (Poland), C. Gardner (UK), A. Gavrikov (Russia), M. Ghiji (Australia), K.E.T. Giljarhus (Norway), M. Gollner (US), S. Golovastov (Russia), Y. Gopala (US), R. Grosseuvres (France), H. Guo (US), A. Hamins (US), N. Hashimoto (Japan), P. Van Hees (Sweden), J. Hewson, J. Hidalgo (Australia), S. Hostikka (Finland), L. Hu (China), X. Huang (Hong Kong), B. Husted (Sweden), M. Idir (France), S. Jackson (US), W. Jahn (Chile), S. Jallais (France), J. Ji (China), S. Kashkarov (UK), D. Kasymov (Russia), W. Kim (Japan), M. Kinsey (UK), O. Korobeinichev (Russia), U. Krause (Germany), A. Krisman (US), A. Kronenburg (Germany), S. Kudriakov (France), A. Kumar (India), K. Kuwana (Japan), M. Kuznetsov (Germany), C. Lautenberger (US), J. Lei (China), I. Leventon (US), Y.-T. Liao (US), Y.C. Liu (China), J. Lundberg (Norway), K. Luo (UK), U. Maas (Germany), D. Makarov (UK), E. Markus (Russia), O. Mathieu (US), T. Matsuoka (Japan), S. McAllister (US), R. McDermott (US), K. McGrattan (US), M. McKinnon (US), B. Meacham (US), J. Melguizo-Gavilanes (France), R. Mevel (China), R. Mikalsen (Norway), T. Mogi (Japan), V. Molkov (UK), A. Morgan (US), E. Mueller (UK), D. Nilsson (Sweden), , J. Oijen (Netherlands), O. Oluwole (US), A. Palacios (Mexico), P. Panda (India), D. Pau (New Zealand), D. Purser (UK), A. Rangwala (US), F. Restuccia

(UK), E. Richardson (UK), F. Richter (UK), T. Rogaume (France), E. Ronchi (Sweden), Z. Rozanski (Poland), W. Rudy (Poland), P. Russo (Italy), N. Ryder (US), S. Sazhin (UK), M. Schmidt (Germany), Y. Shebeko (Russia), L. Shi (Australia), A. Simeoni , T. Skjold (Norway), I. Sochet (France), P.-C. Su (US), P. Sunderland (US), M. Suzuki (Japan), F. Takahashi (US), S. Takahashi (Japan), F. Tanaka (Japan), A. Tchouvelev (Canada), P. Tofilo (Poland), H. Torikai (Japan), A. Trouve (US), T. Tsuruda (Japan), D. Valiev (China), A. Venetsanos (UK), K. Verfondern (Germany), E. Vyazmina (France), K. Wakatsuki (Japan), B. Wang (China), X. Wang (Australia), J. Wen (UK), J. White (USA), T. Wu (US), S. Yakush (Russia), L. Yang (China), Y.-H. Yoo (South Korea), M. Zammarano (US), D. Zeng (US), H. Zhang (Singapore), R. Zitoun (France), O. Zybina (Russia), and the Track Chairs and Members listed above.

Local Organizing Committee

Chair: A. Snegirev

Co-Chair: L. Tanklevskiy

Members: K. Snegireva, E. Markus, E. Kuznetsov, O. Zybina

Preface

The Ninth International Seminar on Fire and Explosion Hazards (ISFEH9) inherits the long-term traditions established by the past successful events in Hefei, China (2016), Providence, USA (2013), Leeds, UK (2010), Edinburgh, UK (2007), Londonderry, UK (2003), Lake Windermere, UK (2000), and Moscow, Russia (1995, 1997). During its more than 20-year history, the Seminar has become one of the important international events in fire and explosion science and engineering, bringing together professionals from the leading universities, research institutions, industrial and insurance companies operating worldwide. Being organized in St. Petersburg, Russia, from 21 to 26 April 2019 by the Autonomous Non-Profit Organization "Fire and Explosion Safety", with the support of Peter the Great St. Petersburg Polytechnic University and the Gefest Group, the 9th ISFEH includes broad areas of research in fires and explosions, as well as the studies in its prevention, mitigation, and suppression. These are reflected in 135 papers included in the Proceedings after careful evaluation and selection by the Scientific Advisory Board with the help of the Track Chairs, Track Members, and Reviewers from 246 initially submitted extended abstracts, of which 204 were selected for inviting the authors to submit full papers. The papers in these Proceedings are co-authored by 391 authors from 30 countries. Among these are six plenary papers, authored by the recognized international authorities: Geoffrey Chamberlain (Waverton Consultancy Ltd., the University of Loughborough, and Shell Research Ltd., UK), Brian Lattimer (Jensen Hughes, USA), Mikhail Tyurin (Gagarin Research and Test Cosmonaut Training Center, Russia), Christophe Proust (INERIS, France), James Quintiere (the University of Maryland, USA), and Karl Meredith (FM Global, USA).

The Organizers and Editors express sincere thanks to all who contributed to the Seminar and made this conference possible, including but not limited to the institutions and companies listed below:

Autonomous Non-Profit Organization "Fire and Explosion Safety", St. Petersburg, Russia

Peter the Great St. Petersburg Polytechnic University, St. Petersburg, Russia

Gefest Enterprise Group, St. Petersburg, Russia

FM Global, USA

OZM Research, Czech Republic

State Hermitage Museum, St. Petersburg, Russia

Sincere gratitude and appreciation are extended to numerous professionals for their tangible involvement in evaluation and selection of the submissions. Enthusiasm and dedication of the Local Organizing Committee were remarkable and this is gratefully acknowledged.

The Editors
April 2019
St. Petersburg, Russia

Table of Contents

Part 5. Fire Dynamics

Flame spread

Upward-Concurrent Flame Spread over a Thin Cotton Fabric: The Effect of Ambient Pressure

Thomsen M.[1], **Fernandez-Pello C.**[1, *], **Ruff G.**[2], **Urban D.**[2]

[1]*Department of Mechanical Engineering, University of California, Berkeley, CA, 94720, USA*
[2]*NASA Glenn Research Center, 21000 Brookpark Rd., Cleveland, OH, 44135, USA*
* *Corresponding author's email: ferpello@me.berkeley.edu*

ABSTRACT

Understanding the flammability of combustible materials at various ambient conditions is important for fire safety applications because fires may occur in environments different from standard atmosphere. In high altitude locations or in an aircraft, for example, the ambient pressure will be lower than at sea level. In the case of a spacecraft such as the International Space Station the cabin environment may be quite different, although the ambient pressure is approximately that of standard Earth, it includes microgravity, low velocity flows induced by the spacecraft ventilation. These low velocity flows (~20 cm/s) cannot be attained in normal gravity because flame induced buoyancy flows (~40 to 60 cm/s) would mask microgravity flows. Ambient pressure affects the buoyant flow induced by the flame and consequently also affects the way that flames spread. Thus, fire testing of materials may require different environments depending on the potential application of the material. The objective of this work is to provide further information of the effect of ambient pressure, and in turn buoyancy, on the upward concurrent spread of flames over a thin cotton fabric in low velocity air flows. The cotton material has been selected because it is common clothing material, and also because it will be one of the materials that will be tested in the microgravity experiments to be conducted during NASA's Spacecraft Fire Experiment (Saffire), on board of the Orbital Corporation Cygnus spacecraft.

KEYWORDS: Concurrent flame spread, thin fuel, ambient pressure, buoyancy.

INTRODUCTION

The flammability of solid combustible materials is typically characterized by their ignitability, flame spread rate, heat release rate, and toxicity. Although, the most effective fire safety strategy is to prevent ignition altogether, if ignition occurs the fire must spread to present a risk. For this reason, flame spread is one of the fire processes utilized to determine the flammability of solid combustible materials [1, 2]. A flame spreads over a solid fuel surface by first preheating the virgin fuel to its pyrolysis temperature, pyrolyzing it, and igniting the resulting flammable mixture of pyrolyzate and oxygen. Thus, the flame propagates in a creeping fashion as a series of ignition steps where the flame acts both as the source of solid heating and flammable gas ignition [1–4]. Thus, the spread of flames over the surface of a solid combustible material is a complex phenomenon resulting from a number of processes occurring in both the solid phase (heat transfer, thermal decomposition, gasification) and the gas phase (transport, mixing, combustion) which are very much affected by external environmental conditions such as oxidizer flow velocity, pressure, oxygen concentration, buoyancy (gravity level) or external heating. Thus, there is an interest in studying the effect of environmental conditions on flame spread.

Concurrent, or flow assisted, flame spread occurs when the spread of the flame and the gas flow are in the same direction (upward spread in buoyant flow and downstream spread in a forced flow).

Proceedings of the Ninth International Seminar on Fire and Explosion Hazards (ISFEH9), pp. 731-740
Edited by Snegirev A., Liu N.A., Tamanini F., Bradley D., Molkov V., and Chaumeix N.
Published by Saint-Petersburg Polytechnic University Press
ISBN: 978-5-7422-6498-9 DOI: 10.18720/spbpu/2/k19-7

Because the gas flow assists the spread of the flame this mode of flame spread is generally fast and consequently hazardous. It is for this reason that some material flammability tests use this mode of flame spread to characterize the fire hazard of combustible materials. In this flame spread configuration, the solid preheating and pyrolysis rates are dominated by convection and flame radiation, and the external flow velocity will therefore influence both the flame length and the heat flux from the flame to the solid surface [3, 5–15]. Since there are marked differences in the velocity distributions in flame induced buoyant flows at different pressure [16], it is expected that there will be also notable differences in the spread of flames. The ambient pressure affects, through the density, the thickness of the boundary layer, and consequently the position of the flame respect to the solid surface (Fig. 1). As the pressure is reduced the boundary layer thickens, the flame moves away from the surface, and the heat transferred from the flame to the solid surface is reduced. Consequently, the rate of flame spread is reduced, both because the reduced heat flux on the surface and a reduction in the flame length [7]. Thus, the effect on the flame characteristics and the spread rate, of reducing the ambient pressure is similar to that of reducing the flow velocity. This is relevant because in a high-altitude location or in an aircraft, for example, the ambient pressure will be lower than at sea level. In the case of a spacecraft such as the International Space Station the cabin environment may be quite different, although the ambient pressure is approximately that of standard Earth, it includes microgravity, low velocity flows induced by the spacecraft ventilation.

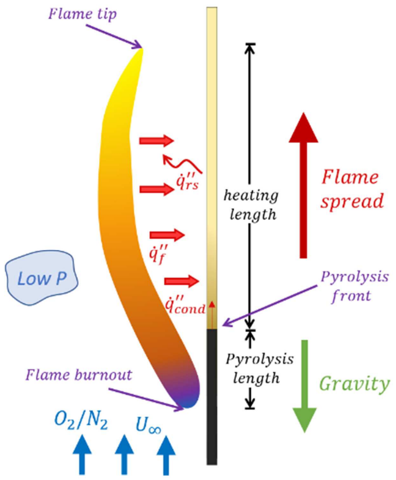

Fig. 1. Upward/Concurrent flame spread diagram.

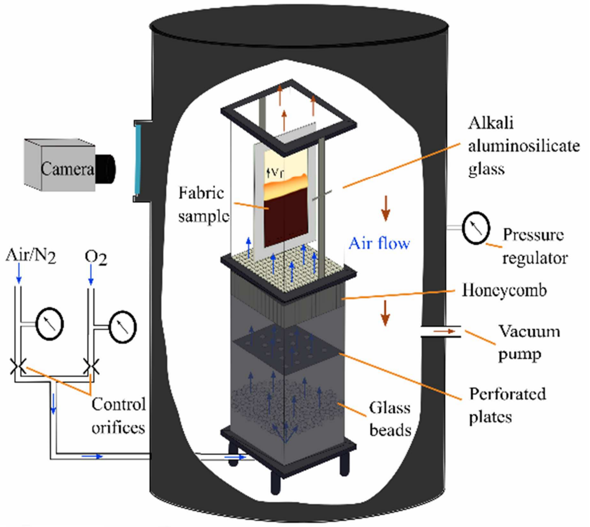

Fig. 2. Schematic of experimental apparatus.

Several studies have been conducted on the spread of flames over solid fuels under reduced pressure to observe the effect of buoyancy on flame spread in reduced gravity [17–21], flame spread in a high-altitude location [22–25], and limiting condition for flame spread [26, 27]. However, there is still a need to systematically study the effect of pressure, and consequently buoyancy, on the spread of flame over different solid combustible materials. The objective of this work is to determine the effect of ambient pressure on the upward concurrent spread of flames over a thin cotton fabric in low velocity air flows. The material has been selected because it is common clothing material, and also it will be one of the materials that will be tested in the microgravity experiments to be conducted during NASA's Spacecraft Fire Experiment (Saffire), on board of the Orbital Corporation Cygnus spacecraft [28]. The ambient pressures have been selected to cover a wide range of environments and buoyantly induced gas flow velocities.

EXPERIMENTAL SETUP

The normal gravity experiments were conducted in an apparatus previously developed to study the flammability of solid combustible materials under varied ambient conditions [27]. The apparatus is basically the same as that used in the studies of Ref. [21], although modified to accept the cotton samples. A brief description of the apparatus is given here for completeness. The apparatus consists of a laboratory scale combustion tunnel that has a 125 mm by 125 mm cross section and is 600 mm in total length. The first 350 mm section of the duct serves as a flow straightener, the other 250 mm segment of the duct is used as the test section. The tunnel is inserted in a pressure chamber as shown in Fig. 2. The side walls of the test section (normal to the plane of the samples) are made of clear polycarbonate. The walls parallel to the sample are 0.56 mm thick alkali-aluminosilicate glass. The sample is placed vertically at the midplane of the test section with both sides exposed to the flow. The fabric sample is made out of pure cotton and has an overall area density of 21.8 mg/cm^2. The sample material and configuration was selected to match one of the materials that will be used in future Saffire microgravity experiments [28]. The cotton samples were 150 mm long by 50 mm wide. The sample was held in between two identical stainless-steel frames of 200 mm by 125 mm and 0.4 mm thick. Each frame had an identical rectangular opening the size of the sample to serve as the test area. Sample ignition is induced with a 29-gage Kanthal wire braided along the upstream edge of the fabric as shown in Fig. 3. The igniter is energized using a controlled current power supply (BK Precision 1785) set to deliver 40 W, the time required to assure ignition changed depending on the ambient pressure tested but was between 3 to 10 seconds.

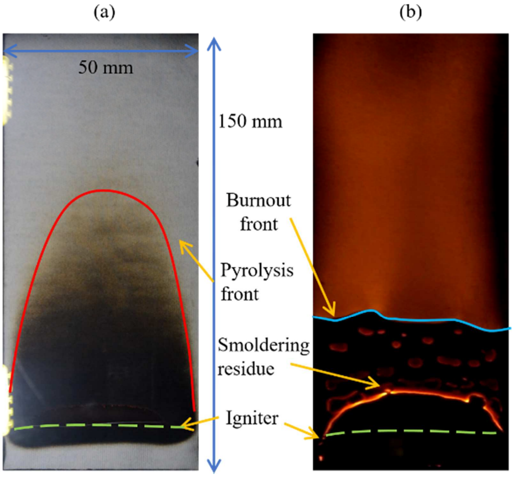

Fig. 3. Front view showing two representative frames of a video of the flame spread over the cotton surface (a) pyrolysis front, and (b) flame burnout front.

The tests were conducted in air under pressures of 100, 80, 70, 50, and 30 ± 2 kPa. Compressed house air was supplied through critical nozzles (O'Keefe Controls) while constantly evacuating to maintain constant the pressure inside the chamber. The chamber pressure was controlled by a high-capacity vacuum generator (Vaccon JS-300) and a mechanical vacuum regulator. The chamber pressure was monitored constantly with an electronic pressure transducer (Omega Engineering, Inc. PX303-015A5V). The forced flow velocity was fixed to 20 cm/s in all the tests. The direction of the flow was upward so that the spread of the flame was in the concurrent configuration. The forced flow velocity was selected to match that to be tested in the microgravity Saffire experiments. Once the sample was in position, the chamber was sealed to adjust the system to the desired conditions. Two 9000 lumen LED were installed with an operating electronic circuit to act as a strobe light to visualize and measure during the same experiment flame spread rates and the flame appearance. The ignition and subsequent flame spread were video recorded with a resolution of 1280 by 720 at 59 frames per second using a Nikon D3200 camera to track the pyrolysis front. A second camera (Sony RX10-III) was used to record videos of visible flame length with a resolution of 1280 by 720 at 59 frames per second. For each test condition, at least five experiments were conducted to address the experimental uncertainty.

RESULTS

Concurrent flame spread over cotton was investigated under different ambient pressures. The primary data collected were the evolution of the pyrolysis front and burnout front positions over time (Fig. 1). The flame tip was not recorded because it was difficult to determine accurately its location with time. Representative frames with the flame spreading over the cotton sample are shown in Fig. 3. Figure 3a presents a frame with the strobe light on and shows the pyrolysis front. Here, the position of the pyrolysis front was defined as the point where the fabric is first visibly blackened as it propagates over the material. Figure 3b presents a frame with the light off and shows the flame burnout front as well some cotton residue smoldering after the passing of the flame. Here, the burnout front position was defined as the upstream edge of the flame, which coincides with where the flame begins receding. During each test, after ignition is achieved, the flame spreads uniformly along the surface of the sample. The pyrolysis front had an inverted "U" shape in all tests, while the flame burnout front had a flatter, more unstable shape. Usually, after ignition of the sample, as the flame spreads over the fabric it consumes most of the cotton, leaving behind some smoldering cotton residue (bottom of Fig. 3b) that eventually burns out most of the fabric. As ambient pressure was reduced, ignition of the sample was more difficult, and, in occasions, part of the cotton fabric would be left unburnt.

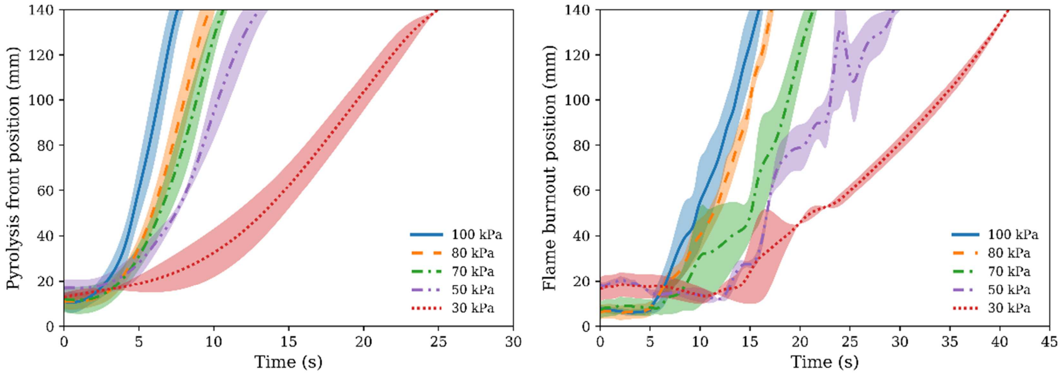

(a) Pyrolysis front (b) Burnout front

Fig. 4. Time evolution of the (a) pyrolysis front position and (b) flame burnout position for different ambient pressures.

Some characteristic results of the time evolution of the pyrolysis front and burnout front are presented in Fig. 4 for ambient pressures ranging from 100 to 30 kPa. Figure 4a shows the progress of the pyrolysis front as a function of time. It is seen that as ambient pressure is reduced the spread of the flame is slower. During most of the tests, the flame is still accelerating as it spreads over the solid. The work of Markstein and De Ris [5] indicates that this is due to the sample not being long enough to reach steady state. Similar results to those presented in this work were presented by the authors using a different material, a composite cotton/fiber glass fabric (Sibal) [21]. When comparing the characteristics of the flame spread of Thomsen et al. [21] with a longer Sibal sample reported by Olson et al. [20] (samples of 0.15 m vs. 1 m) it showed that despite the similitudes in the pyrolysis front and burnout front profiles, the sample size was not long enough for the flame spread to reach steady state. However, as pressure was reduced, the pyrolysis front and flame burnout front begin to stabilize faster. From Fig. 4 is seen that the average total burn time for an initial pressure of 100 kPa was 16 s, significantly smaller when compared to the average 41 s obtained at an ambient pressure of 30 kPa.

The evolution of the pyrolysis front as a function of time is commonly used to determine flame spread rate. The data of Fig. 4 is then used to obtain average flame spread rate values as a function of ambient pressure, as shown in Fig. 5. Because of the acceleratory characteristics of the upward flame spread, an averaged spread rate over the last 50 mm of the sample is presented in the figure so that transient effects are minimized. It is seen that the flame spread rate decreases from 30.7 to 10.0 mm/s as the ambient pressure is decreased from 100 to 30 kPa.

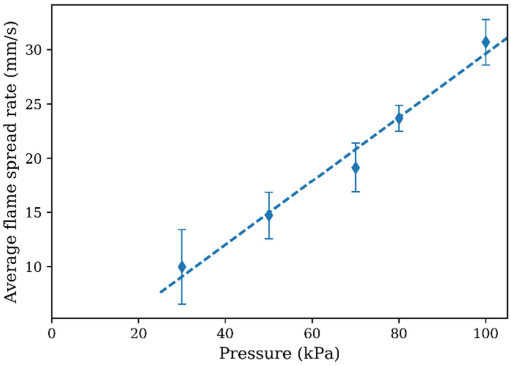

Fig. 5. Average flame spread rate as a function of ambient pressure obtained from the pyrolysis front.

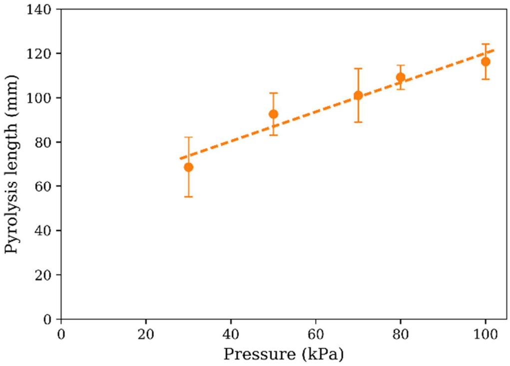

Fig. 6. Pyrolysis length as a function of ambient pressure.

Another important parameter for concurrent flame spread is the pyrolysis length because it determines the flame length and consequently the heat that can be transferred from the flame to the solid. In this work, this length is obtained by subtracting the burnout front position from the pyrolysis front position, and the results are presented in Fig. 6. Because of the accelerative characteristic of the spread process, the pyrolysis length is obtained toward the end of the test when it approaches steady state. From Fig. 6 it is seen that the pyrolysis length decreases from 116.4 to 68.7 mm with decreasing ambient pressure from 100 to 30 kPa. This indicates that ambient pressure affects more the rate of spread of the pyrolysis front than the mass burning, since it determines the rate of spread of the burnout front.

The visible flame characteristics also change with decreasing ambient pressure, although changes are less noticeable when compared with the flames generated by the burning of other materials [21]. Figure 7 shows still photographs of the material burning under different pressure environments. As pressure is reduced the flame becomes less turbulent and its intensity is reduced. As pressure is reduced, visible flame height is also affected, becoming shorter at lower pressures.

DATA CORRELATION

The above data can be used to verify the predictive capabilities of flame spread models on the effect of pressure, or buoyancy, on the concurrent spread of flames over a thin combustible fuel. This was done in Ref. [21] by correlating the data of the dependence on pressure of the concurrent flame spread rate over a composite cotton/fiberglass fabric (Sibal) using the simplified analysis of Ref.

[3]. Here a similar approach is followed to correlate the cotton data presented in Figs. 5 and 6. Since the development of the data correlation was presented in [21], only a summary is presented here.

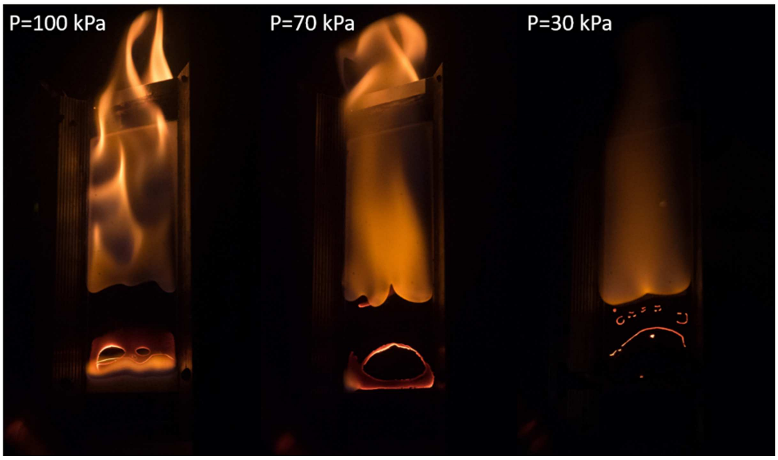

Fig. 7. Visible flame as a function of ambient pressure.

The flame spread analysis is based on the main controlling mechanisms for concurrent flame spread over a thin solid and treats the spread process as a sequence of ignitions where the flame acts as a source of heat to the solid and the pilot for ignition [1–4]. The analysis provides an analytical equation for concurrent flame spread over a thin solid as [3, 21]:

$$V_f = l_h \left[\frac{\rho_s c_s s (T_p - T_o)}{h\left(T_f - T_p\right) + \dot{q}''_{fr} - \dot{q}''_{rs}} - \frac{Cx}{U_m} \varphi(t_{chem}) \right]^{-1} \tag{1}$$

Where l_h is the heated length (Fig. 1), $h\left(T_f - T_p\right)$ represents the convective heat flux at the solid surface, $\dot{q}''_{fr}$ is the flame radiant flux, $\dot{q}''_{rs}$ the re-radiation from the solid. U_m is the mixed flow velocity and $\varphi(t_{chem})$ is a function of the chemical time, t_{chem}. ρ_s and c_s are the solid density and specific heat and s is the solid thickness. T_f is the flame temperature, and T_p and T_o are the pyrolysis and initial temperatures of the solid. The first term inside the parenthesis in Eq. (1) describes the heat transfer mechanisms of the flame spread process and the second term represents the gas phase chemical kinetics. Although reducing pressure will eventually affect the chemical kinetic process [21], it will be assumed here that for the present experimental conditions the spread rate is controlled by heat transport effects only. It is also assumed that the radiant flux from the flame to the solid is approximately balanced by the surface re-radiation, and that there is not an external heat flux. The heated length is approximately related to the pyrolysis length that $l_h \sim C_1 l_p^c$, where C_1 is a constant and the exponent c is one or less than one [29]. The flame temperature is directly proportional to the ambient oxygen concentration but is not strongly dependent on ambient pressure until the pressure is relatively low and the chemical time starts to become larger than the physical time. Because the oxygen concentration is that of air for all the experiments, the flame temperature is assumed constant in the range of pressures of the present experiments. This is a simplification in the analysis that should be reasonable for not too low ambient pressures. Under these conditions the flame spread rate becomes:

$$V_f \approx l_p \left[\frac{h(T_f - T_p)}{\rho_s c_s s (T_p - T_o)} \right] \tag{2}$$

From Eq. (2) it is seen that the flame spread rate is proportional to the convective heat transfer coefficient at the solid surface, which in turn is directly related to the boundary layer thickness through $h = k/\delta$, where k is the gas thermal conductivity and δ the boundary layer thickness. For a mixed flow, forced and free, as that of the present experiments, the average convective heat transfer coefficient can be expressed in terms of the Reynolds Number (*Re*) and the Grashof number (*Gr*) as [30]:

$$h = C\frac{k}{l_p}Gr^{1/4}\left(\frac{Re^4}{Gr^2}+1\right)^{1/8}Pr^{1/3} \tag{3}$$

Where C is a generic constant related to the type of flow and the pyrolysis length, l_p, has been selected as the characteristic length of the problem. Then, $Re = \rho U_f l_p/\mu$, $Gr = g\beta\Delta T l_p^3\rho^2/\mu^2$, and Pr is the Prandtl number. U_f represents the forced flow velocity component of the mixed flow, μ is the dynamic viscosity, ρ is gas phase density, β is the coefficient of thermal expansion and g is gravity level.

Since the flame spread rate is determined primarily by the heat flux on the fuel surface, the normal gravity and the microgravity data could be related by defining a mixed flow gas velocity such that when applied to a purely forced flow, like in the microgravity experiments, would produce a boundary layer of the same thickness as that encountered by the flame in the mixed flow condition in normal gravity. Since the boundary layer thickness is directly related to the heat transfer coefficient through $h = k/\delta$, then the heat transfer coefficients would be the same and thus the flame spread rate would also be the same. This mixed flow velocity can be obtained by equating the heat transfer coefficient for a mixed flow as in Eq. (3) and that of a pure forced flow obtained from Eq. (3) with g=0, and solving for the flow velocity in the forced flow boundary layer. Then, the following mixed convection velocity, U_m, is obtained in terms of pressure, forced flow velocity in the mixed flow, and gravity.

$$U_m = U_f\left(\frac{P}{P_0}\right)\left[\frac{g^2 l_p^2}{U_f^4}+1\right]^{\frac{1}{4}} \tag{4}$$

where P_0 is a reference ambient pressure (standard Earth ambient pressure) and U_f is the forced flow velocity at this reference pressure P_0. From Eq. (4) it is seen that for zero gravity or large flow velocity the mixed flow velocity is that of a pure forced flow at a given test pressure, $U_m = \frac{\mathrm{P}}{\mathrm{P_0}}U_f$. For elevated gravity and/or zero forced velocity, the mixed flow velocity becomes that of natural convection at a given test pressure, $U_m = \frac{\mathrm{P}}{\mathrm{P_0}}\left(gl_p\right)^{1/2}$. With the mixed flow velocity as given in Eq. (4), the convective heat transfer coefficient for the forced flow, based on the mixed flow velocity, would be

$$h = C\frac{k}{l_p}\left(\frac{U_m P l_p}{\mu}\right)^{\frac{1}{2}}Pr^{\frac{1}{3}} \tag{5}$$

And the flame spread would be given by

$$V_f \approx l_h\frac{\left(\frac{Ck}{l_p}\left(\frac{U_m P l_p}{\mu}\right)^{\frac{1}{2}}Pr^{\frac{1}{3}}\right)(T_f - T_p)}{\rho_s c_s s(T_p - T_o)} \approx \frac{C_1 k\left(\frac{U_m P l_p}{\mu}\right)^{\frac{1}{2}}Pr^{\frac{1}{3}}(T_f - T_p)}{\rho_s c_s s(T_p - T_o)} \tag{6}$$

The flame spread data of Fig. 5 can be correlated in terms of the mixed convective flow velocity, U_m, given by Eq. (4), as shown in Fig. 8. It is seen that Eq. (4) correlates well the variation of the flame spread rate with pressure. As ambient pressure is decreased, the calculated mixed flow velocity is also reduced, and this is reflected in slower flame spread rates. A similar analysis can also be done with the experimental data presented in Fig. 6 for the pyrolysis length as shown in Fig. 9.

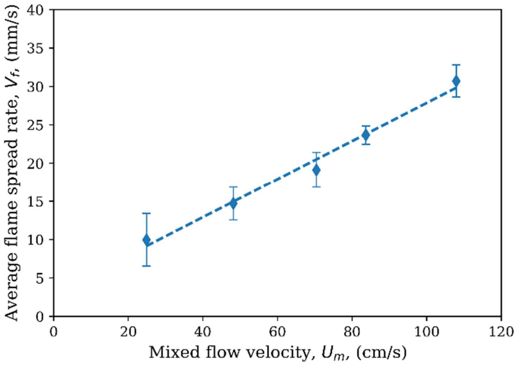

Fig. 8. Average flame spread rate as a function the mixed flow velocity.

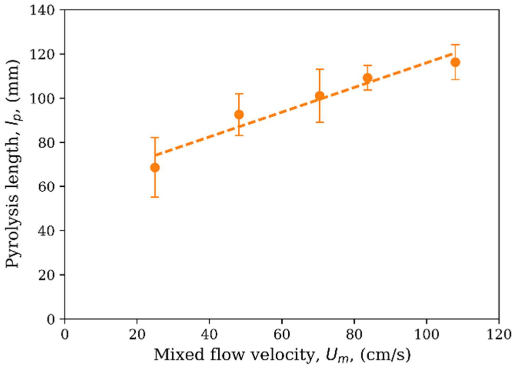

Fig. 9. Pyrolysis length as a function the mixed flow velocity.

Table 1. Cotton properties [31]

Property	Value	Units
Solid density, ρ_s	417	kg/m^3
Solid specific heat, c_s	1.380	kJ/(kg·K)
Material thickness, s	5.08×10^{-4}	m
Pyrolysis temperature, T_p	629	K
Flame temperature, T_f	2500	K

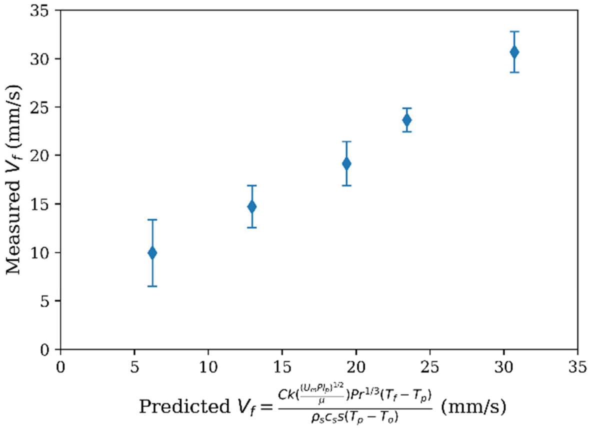

Fig. 10. Measured average flame spread rate as a function the predicted flame spread rate obtained from Eq. (6).

Additionally, the experimental results of Fig. 5 can be used to compare with the predictions obtained from Eq. (6). This is shown in Fig. 10 where the measured average flame spread rate is presented as a function of the predicted flame spread rate of Eq. (6). For the calculations, the cotton properties were taken as those of thin cellulose paper [31] and are presented in Table 1, the flame temperature is taken as the paper adiabatic flame temperature [31]. The value of the constant C_1 was set to match the experimental flame spread rate measured at normal ambient pressure (100 kPa). From Fig. 10 it is seen that Eq. (6) predicts fairly well the experimental flame spread rates obtained in lower pressure environments. However, the flame spread results are slightly underpredicted and the differences seem to get bigger at lower pressures.

CONCLUSIONS

The concurrent flame spread rate over a thin cotton fabric has been study under reduced ambient pressure to determine the effect of buoyancy on the flame spread process. It has been found that as pressure is reduced, the flame spread rate over the cotton fabric is also reduced, as observed with other thin fuels [21, 32]. Flame intensity is also weakened resulting in dimmer flames. The measured flame spread rate is correlated well in terms of a simple flame spread formula and a mixed convection heat transfer coefficient. The correlation of the flame spread rate data in terms of a mixed flow velocity parameter that includes gravity and pressure suggests that reduced pressure can be used to simulate the effect of buoyancy on the concurrent spread of flames.

ACKNOWLEDGMENTS

This research is supported by NASA Grant NNX12AN67A. The authors would like to thank Saul Pacheco, Grace Mendoza, Runbiao Wei, Ryan So, Mina Fanaian, and Madison Hales for their contributions conducting the experiments.

REFERENCES

[1] F.A. Williams, Mechanisms of fire spread, Symp. Combust. 16 (1976) 1281–1294..

[2] J. Quintiere, A simplified theory for generalizing results from a radiant panel rate of flame spread apparatus, Fire Mater. 5 (1981) 52–60.

[3] C. Fernandez-Pello, The solid phase, in: G. Cox (Ed.), Combustion Fundamentals of Fire, Academic Press Limited, 1994, pp. 31–100.

[4] M.A. Delichatsios, Creeping flame spread: energy balance and application to practical materials, Symp. Combust. 26 (1996) 1495–1503.

[5] G.H. Markstein, J. De Ris, Upward fire spread over textiles, Proc. Combust. Inst. 14 (1973) 1085–1097.

[6] M. Sibulkin, J. Kim, The dependence of flame propagation on surface heat transfer II. upward burning, Combust. Sci. Technol. 17 (1977) 39–49.

[7] A.C. Fernandez-Pello, A theoretical model for the upward laminar spread of flames over vertical fuel surfaces, Combust. Flame 31 (1978) 135–148.

[8] A.C. Fernandez-Pello, Flame spread in a forward forced flow, Combust. Flame 36 (1979) 63–78.

[9] L. Chu, C.H. Chen, J.S. T'ien, Upward propagation over paper samples, in: Proc. ASME Pap. 81-WA/HT-42, 1981.

[10] H.T. Loh, C. Fernandez-Pello, A study of the controlling mechanisms of flow assisted flame spread, Proc. Combust. Inst. 20 (1984) 1575–1582.

[11] K. Saito, J.G. Quintiere, F.A. Williams, Upward turbulent flame spread, Fire Safety Science – Proceedings of the First International Symposium, pp, 75–86 (1986).

[12] H.T. Loh, A.C. Fernandez-Pello, Flow Assisted Flame Spread over Thermally Thin Fuels, Fire Saf. Sci. 1 (1986) 65–74.

[13] L.K. Honda, P.D. Ronney, Mechanisms of concurrent-flow flame spread over solid fuel beds, Proc. Combust. Inst. 28 (2000) 2793–2801.

[14] M.J. Gollner, X. Huang, J. Cobian, A.S. Rangwala, F.A. Williams, Experimental study of upward flame spread of an inclined fuel surface, Proc. Combust. Inst. 34 (2013) 2531–2538.

[15] M.J. Gollner, C.H. Miller, W. Tang, A.V. Singh, The effect of flow and geometry on concurrent flame spread, Fire Saf. J. 91 (2017) 68–78.

[16] C.K. Law, S.H. Chung, N. Srinivasan, Gas-phase quasi-steadiness and fuel vapor accumulation effects in droplet burning, Combust. Flame 38 (1980) 173–198.

[17] P. V. Ferkul, J.S. T'ien, A model of low-speed concurrent flow flame spread over a thin fuel, Combust. Sci. Technol. 99 (1994) 345–370.

[18] J. Kleinhenz, I.I. Feier, S.Y. Hsu, J.S. T'ien, P. V. Ferkul, K.R. Sacksteder, Pressure modeling of upward flame spread and burning rates over solids in partial gravity, Combust. Flame 154 (2008) 637–643.

[19] Y. Nakamura, N. Yoshimura, H. Ito, K. Azumaya, O. Fujita, Flame spread over electric wire in sub-atmospheric pressure, Proc. Combust. Inst. 32 (2009) 2559–2566.

[20] S.L. Olson, S.A. Gokoglu, D.L. Urban, G.A. Ruff, P. V. Ferkul, Upward flame spread in large enclosures: Flame growth and pressure rise, Proc. Combust. Inst. 35 (2015) 2623–2630.

[21] M. Thomsen, C. Fernandez-pello, D.L. Urban, G.A. Ruff, S.L. Olson, On simulating concurrent flame spread in reduced gravity by reducing ambient pressure, Proc. Combust. Inst. 37 (2019) 3793-3800.

[22] Y. Zhang, X. Huang, Q. Wang, J. Ji, J. Sun, Y. Yin, Experimental study on the characteristics of horizontal flame spread over XPS surface on plateau, J. Hazard. Mater. 189 (2011) 34–39.

[23] Y. Zhang, J. Ji, J. Li, J. Sun, Q. Wang, X. Huang, Effects of altitude and sample width on the characteristics of horizontal flame spread over wood sheets, Fire Saf. J. 51 (2012) 120–125.

[24] J. Gong, L. Yang, X. Zhou, Z. Deng, G. Lei, W. Wang, Effects of low atmospheric pressure on combustion characteristics of polyethylene and polymethyl methacrylate, J. Fire Sci. 30 (2012) 224–239.

[25] J. Gong, X. Zhou, Z. Deng, L. Yang, Influences of low atmospheric pressure on downward flame spread over thick PMMA slabs at different altitudes, Int. J. Heat Mass Transf. 61 (2013) 191–200.

[26] A.F. Osorio, C. Fernandez-Pello, D.L. Urban, G.A. Ruff, Limiting conditions for flame spread in fire resistant fabrics, Proc. Combust. Inst. 34 (2013) 2691–2697.

[27] M. Thomsen, D.C. Murphy, C. Fernandez-pello, D.L. Urban, G.A. Ruff, Flame spread limits (LOC) of fire resistant fabrics, Fire Saf. J. 91 (2017) 259–265.

[28] G. Jomaas, J.L. Torero, C. Eigenbrod, J. Niehaus, S.L. Olson, P.V. Ferkul, G. Legros, A.C. Fernandez-Pello, A.J. Cowlard, S. Rouvreau, N. Smirnov, O. Fujita, J.S. T 'ien, G.A. Ruff, D.L. Urban, Fire safety in space – beyond flammability testing of small samples, Acta Astronaut. 109 (2015) 208–216.

[29] K. Tu, J.G. Quintiere, Wall Flame Heights with External Radiation, Fire Technol. 27 (1991) 195–203.

[30] C.-P. Mao, A.C. Fernandez-Pello, P.J. Pagni, Mixed convective burning of a fuel surface with arbitrary inclination, J. Heat Transf. 106 (1984) 304–309.

[31] Y.T.T. Liao, J.S. T'ien, A numerical simulation of transient ignition and ignition limit of a composite solid by a localized radiant source, Combust. Theory Model. 17 (2013) 1096–1124.

[32] M. Thomsen, X. Huang, C. Fernandez-Pello, D.L. Urban, G.A. Ruff, Concurrent flame spread over externally heated Nomex under mixed convection flow, Proc. Combust. Inst. 37 (2019) 3801-3808.

Calculation Analysis on the Fuel Preheating Mechanisms in Surface Fire Spread over a Horizontal Fuel Bed

Xie X.[1,2], Liu N.[2,]*, Yuan X.[2], Li H.[2], Zhang L.[2]

[1]*State Key Laboratory of Disaster Prevention and Reduction for Power Grid Transmission and Distribution Equipment, Changsha, China*
[2]*State Key Laboratory of Fire Science, University of Science and Technology of China, Hefei, Anhui, China*
**Corresponding author's email: liunai@ustc.edu.cn*

ABSTRACT

This work aims to investigate the effects of heat radiation and convection in the near field and far field of a spreading flame front over a horizontal fuel bed. Model calculations are made to examine different fuel preheating mechanisms that affect the fire spread. The results indicate that the convective cooling effect is important and could not be ignored. For the fuel elements in the near field, the radiation from the flame front and the combustion zone is not sufficient for fuel preheating, and the mechanism of convective heating should be considered. The convective cooling of the fuel bed has a considerable long influence range ahead of the flame front, while the influence range of convective heating is in a shorter length scale. The flame radiation on fuel preheating takes effect in the whole field. There is a sharp increase of the temperature when fuel elements get closer to the flame front in the near field due to the combined effects of three heating mechanisms. The contributions of the flame radiation, the combustion zone radiation and the convective heating to fuel preheating are of the same magnitude in the near field. The combustion cooling takes effect in the far field, while the convective cooling coefficient affects both far field and near field.

KEYWORDS: Fire spread, flame radiation, convective cooling, convective heating.

NOMENCLATURE

ρ	fuel density (kg m^{-3})
c	specific heat capacity (J·kg^{-1}·K^{-1})
T_s	fuel surface temperature (K)
X	distance away from flame front (m)
α	absorptivity of the medium (m^{-1})
ε_f	flame emissivity
ε_c	emissivity of fuel bed
σ	Stefan-Boltzmann constant
T_f	flame temperature (K)
T_a	ambient temperature (K)
T_{fm}	film temperature (K)
h	convective heat transfer coefficient (W·m^{-2}·K^{-1})
R	rate of fire spread (m·s^{-1})
T_c	radiative temperature of fuel bed (K)
ρ_b	dry fuel bed density (kg·m^{-3})
c_f	specific heat of dry fuel (J·kg^{-1}·K^{-1})
ρ_w	density of moisture within the fuel (kg·m^{-3})
c_w	specific heat of water (J·kg^{-1}·K^{-1})
l	heat of vaporization of water at 373 K (J·kg^{-1}·K^{-1})
T_i	ignition temperature (K)
T_g	hot gas temperature (K)

Proceedings of the Ninth International Seminar on Fire and Explosion Hazards (ISFEH9), pp. 741-747
Edited by Snegirev A., Liu N.A., Tamanini F., Bradley D., Molkov V., and Chaumeix N.
Published by Saint-Petersburg Polytechnic University Press
ISBN: 978-5-7422-6498-9 DOI: 10.18720/spbpu/2/k19-91

INTRODUCTION

Prediction of rate of spread (ROS) is a fundamental problem in wildland fire research. The heat transfer mechanisms for preheating of unburnt fuels is the major focus for physical modelling of fire spread. In early works, a physical model was proposed to predict the rate of spread (ROS) over a horizontal fuel bed in still air by de Mestre et al. [1]. It was indicated that when only radiative heat transfer was considered, the predicted ROS was thirteen times the measured value, while when natural convective cooling was introduced in the model, a good agreement was achieved. Baines [2] calculated the temperature of the fuel bed surface based on the model of de Mestre et al. [1]. It was found that the surface temperature immediately ahead of the flame front was much lower than ignition temperature. One possible explanation is that besides radiative heat transfer, there is an additional short-range convective heating effect for fuel elements close to the flame front. Natural convection was found to take effect in the far field, while the flame-induced convection exists only in the near field of the flame (close to the flame) [3]. Considerable efforts [4-8] have been devoted to explaining fuel preheating mechanisms for linear fire line in a horizontal fuel bed in still air, however, the quantitative comparison between heat radiation and heat convection are not fully understood.

This paper aims to investigate the effects of heat transfer mechanisms on fuel preheating in both near field and far field of the flame front. Specifically, the considered fuel preheating mechanisms include flame radiation, combustion zone radiation, convective heating and cooling.

FIRE SPREAD MODEL

In the model calculation, the considered fuel preheating mechanisms include flame radiation, the radiation from combustion zone, radiation loss and the convective cooling to the ambient. The heat conduction through the fuel bed is ignored. The governing equation (refer to [2]) for fuel surface temperature along the fuel bed centerline is expressed as

$$-R\rho c\frac{dT_s}{dX}=\alpha\varepsilon_f\sigma\left(T_f{}^4-T_a^4\right)W(X)+\alpha\varepsilon_c\sigma\left(T_c{}^4-T_a^4\right)U(X)-\alpha\sigma\left(T_s{}^4-T_a^4\right)-4h\alpha\left(T_s-T_a\right), \tag{1}$$

where X denotes the distance away from the flame front, ρc is given by

$$\rho c=\begin{cases}\rho_b c_f+\rho_w c_w+\dfrac{\rho_w l}{373-T_a}, & T_s<373\,\mathrm{K}\\ \rho_b c_f, \quad T_s>373\,\mathrm{K}\end{cases}, \tag{2}$$

$W(X)$ and $U(X)$ are the view factors respectively from the flame front and combustion zone to the fuel elements. Here R 0.0049 m/s, T_f = 1093 K, T_a = 296 K, T_c = 1139 K. For other parameters, refer to Refs. [1-2].

The impact of combustion zone radiation is limited by the large absorptivity of the fuel bed, and usually the effective influence range is confined to a distance of about 2 cm or less [2]. Therefore, the combustion zone radiation is mainly near field radiation, and $U(X)$ is negligible if X > 0.02 m.

The boundary conditions for the temperature field are

$$T_s\big|_{X=0}=T_i = 593\text{ K},\; T_s\big|_{X\to\infty}=T_a = 296\text{ K}. \tag{3}$$

For free convection, the convective heat transfer coefficient h is expressed as [9]

$$Nu = \frac{hD}{\lambda} = CRa^n , \tag{4}$$

where Nu is the Nusselt number, Ra is the Rayleigh number, D is the characteristic length, λ is the thermal conductivity of air, C and n are the constants. The convective heat transfer coefficient h in Eq. (1) is thus calculated to be $h = 1.02\lambda Ra^{0.148}/D$ = 44.4 $\mathrm{W \cdot m^{-2} \cdot K^{-1}}$. The coefficient h = 44 $\mathrm{W \cdot m^{-2} \cdot K^{-1}}$ was used in Baines' work [2], and the fitting to the experimental data was better than that of h = 23.2 $\mathrm{W \cdot m^{-2} \cdot K^{-1}}$ [1]. Thus, h = 44 $\mathrm{W \cdot m^{-2} \cdot K^{-1}}$ is employed in this study.

This model is used to calculate the effects of convective cooling, convection heating, flame radiation, combustion zone radiation and radiation loss on fuel surface temperature.

RESULTS AND DISCUSSION

Convective cooling

We first calculate the fuel surface temperature with no consideration of the convective cooling, i.e. the convection term $4h\alpha(T_s - T_a)$ in Eq. (1) is ignored. The results are presented in Fig. 1. As shown, the fuel temperature T_s decreases almost linearly with distance away from the flame front. The results significantly deviate from the experimental data, and in particular, the fuel temperature immediate ahead of the flame front $T_s|_{X\to 0}$ = 867 K is much higher than the ignition temperature T_i of 593 K. Therefore, the mechanism of convective cooling could not be ignored. This implies that convective cooling plays an important part in the heat balance during fire spread.

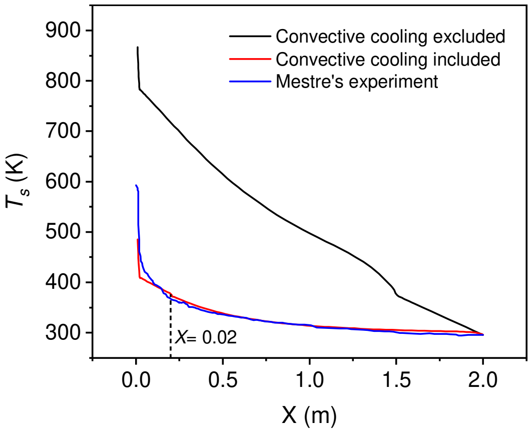

Fig. 1. Fuel surface temperature with or without convective cooling.

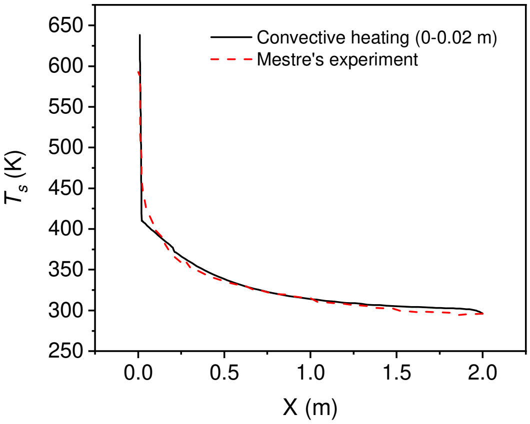

Fig. 2. Considering convective heating in the near field.

We then include the convective cooling for calculating the fuel surface temperature. As shown in Fig. 1, the calculated data agree well with the experimental data in the far field of the flame front (0.02 m X < 2 m) , where the fuel surface temperature T_s increases slowly with decreasing X. In the near field of the flame front (0 < X < 0.02 m), the fuel surface temperature T_s increases rapidly with decreasing X. This indicates that the preheating mechanism in the near field plays a major role in raising T_s to the ignition temperature. However, the fuel surface temperature immediately ahead of the flame front $T_s|_{X\to 0}$ = 485 K is much lower than the ignition temperature. Therefore for fuel elements in the near field, the radiation from the flame front and that from the combustion zone are not sufficient for fuel preheating, and a kind of convective heating induced by hot gas puffing over the fuel bed should also be considered.

We now examine the contribution of radiative heating in the near field, for which, the radiation from the flame front and that from the combustion zone are discussed separately. We found that when both radiative heating mechanisms are considered, the fuel surface temperature immediately ahead of the flame front is $T_s|_{X\to 0}$ = 485 K. When only flame radiation is considered, the fuel surface temperature is $T_s|_{X\to 0}$ = 412 K. When only combustion zone radiation is considered, Eq. (1) is changed as

$$\begin{cases} -R\rho c\dfrac{dT_s}{dX} = \alpha\varepsilon_f\sigma\left(T_f^{\,4}-T_a^{\,4}\right)W(X)-\alpha\sigma\left(T_s^{\,4}-T_a^{\,4}\right)-4h\alpha\left(T_s-T_a\right), & 0.02 < X < 2\text{ m} \\ -R\rho c\dfrac{dT_s}{dX} = \alpha\varepsilon_c\sigma\left(T_c^{\,4}-T_a^{\,4}\right)U(X)-\alpha\sigma\left(T_s^{\,4}-T_a^{\,4}\right)-4h\alpha\left(T_s-T_g\right), & 0 < X < 0.02\text{ m} \end{cases}, \tag{5}$$

then the fuel surface temperature $T_s|_{X\to 0}$ = 418 K. The results indicate that the contributions of flame radiation and combustion zone radiation to fuel preheating are of almost same importance.

Near-field convective heating

As discussed above, the convective cooling of the fuel bed is very important in a considerably long influence distance ahead of the flame front. Comparatively, when the convective heating is considered, it is important on a shorter length scale, since it depends on hot gases puffing over the fuel bed and the gases rise rapidly because of buoyancy [2]. Thus convective heating is assumed in the near field ($0 < X < 0.02$ m). For fuel preheating in the near field, the model includes flame radiation, radiation from combustion zone, radiation loss and convective heating by hot gases. For fuel preheating in the far field, the model includes flame radiation, radiation from combustion zone, radiation loss and convective cooling to the environment. The governing equation is expressed as

$$\begin{cases} -R\rho c\dfrac{dT_s}{dX} = \alpha\varepsilon_f\sigma\left(T_f^{\,4}-T_a^{\,4}\right)W(X)+\alpha\varepsilon_c\sigma\left(T_c^{\,4}-T_a^{\,4}\right)U(X) \\ \qquad\qquad -\alpha\sigma\left(T_s^{\,4}-T_a^{\,4}\right)-4h\alpha\left(T_s-T_a\right), \quad 0.02 < X < 2\text{ m} \\ -R\rho c\dfrac{dT_s}{dX} = \alpha\varepsilon_f\sigma\left(T_f^{\,4}-T_a^{\,4}\right)W(X)+\alpha\varepsilon_c\sigma\left(T_c^{\,4}-T_a^{\,4}\right)U(X) \\ \qquad\qquad -\alpha\sigma\left(T_s^{\,4}-T_a^{\,4}\right)-4h\alpha\left(T_s-T_g\right), \quad 0 < X < 0.02\text{ m} \end{cases}, \tag{6}$$

The calculated fuel surface temperature for convective heating in the near field is presented in Fig. 2. The results have a better agreement with the experimental data. There is a sharp increase of the temperature when fuel elements get close to the flame front. The fuel temperature immediately ahead of the flame front $T_s|_{X\to 0}$ = 638 K is slightly higher than the ignition temperature, which may be due to the overestimate of flame temperature, emissivity, or hot gas temperature.

For the convective heat transfer mechanism in the near field, when the convective cooling effect is changed to convective heating, the calculations show that the fuel surface temperature $T_s|_{X\to 0}$ increases from 485 K to 638 K, with a temperature difference of 153 K. This indicates the convective heating is very important for fuel preheating in the near field. It is also suggested that the convective heating is more reasonable than convective cooling as a convection term in the near field.

To examine the contribution of various heating mechanisms to fuel surface temperature in the near field, only one heating mechanism was considered each time. The calculated results are presented in Fig. 3. When the flame radiation, the combustion zone radiation and the convective heating are considered separately, the fuel surface temperature $T_s|_{X\to 0}$ is obtained as 503, 501, and 505 K respectively, and the curves of $T_s \sim X$ are very close to each other. The results indicate that the contributions of the flame radiation, the combustion zone radiation and the convective heating to fuel preheating are of the same magnitude. It also reveals that radiative heating is the dominant mechanism for fuel pre-heating, while the combined effects of three heating mechanisms control the fuel surface temperature increasing to ignition temperature in the near field.

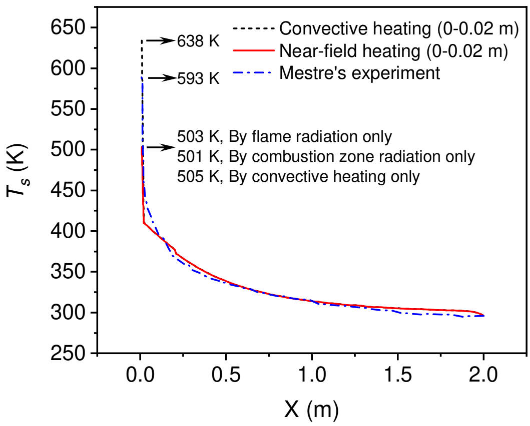

Fig. 3. Fuel surface temperature under various heating mechanisms in the near field.

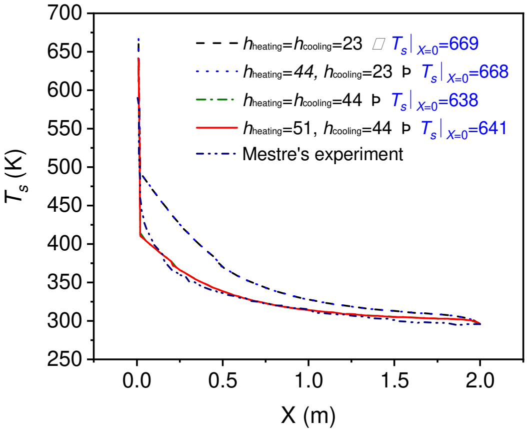

Fig. 4. Fuel surface temperature *v.* convective heat transfer coefficient.

The flame radiation on fuel preheating takes effect in the whole field. Comparatively, the combustion zone radiation and convective heating take effects in the near field, with fewer effects in the far field. These are the main cause that the fuel surface temperature T_s increases slowly with decreasing X in the far field then increases rapidly in the near field.

Convective heat transfer coefficient

The convective heat transfer coefficient is the key parameter in calculating both convective heating and cooling. The coefficient is related to film temperature, external flow, turbulence status, etc. The value h = 23.2 W·m^{-2}·K^{-1} [1] and h = 44 W·m^{-2}·K^{-1} [2] are used for calculating the convective cooling. In the above discussion, $h_{cooling}$ = 44 W·m^{-2}·K^{-1} and $h_{heating}$ = 44 W·m^{-2}·K^{-1} are employed to calculate the convective cooling and heating, respectively. The film temperature is higher in the near field than that in the far field. When the film temperature T_{fm} = 600 K, the coefficient could be obtained by Eq. (4), then we have $h_{heating}$ = 51 W·m^{-2}·K^{-1}.

To examine the effects of coefficient h on the fuel surface temperature, different values of $h_{cooling}$ and $h_{heating}$ are used, and the results are shown in Fig. 4. When $h_{cooling}$ = 23 W·m^{-2}·K^{-1}, the calculated results are higher than the experimental data in both far field and near field. When $h_{cooling}$ = 44 W·m^{-2}·K^{-1}, the calculated results fit better to the experimental data. The results indicate that convective cooling coefficient affects both far field and near field, while the effect of convective heating coefficient is only in near field. It is obvious that the fuel surface temperature increases with decreasing $h_{cooling}$ both in the near field and far field, while it increases with increasing $h_{cooling}$ in the near field.

Flame temperature

When $h_{heating}$ = 51 W·m^{-2}·K^{-1} and $h_{cooling}$ = 44 W·m^{-2}·K^{-1}, the fuel surface temperature $T_s|_{X\to 0}$ = 641 K is higher than ignition temperature, maybe due to overestimate of flame temperature, emissivity, convective heating. Since the flame radiation takes effect on fuel preheating is in both near field and far field, the variation of flame temperature also affects the whole field. The calculated fuel surface temperature for different flame temperatures is shown in Fig. 6. It is obvious that the fuel surface temperature increases with increasing flame temperature. When T_f = 1093 K, the calculated values agree better with the experimental data. Since the flame temperature T_f = 1093 K is used in the model, the overestimate of $T_s|_{X\to 0}$ is not caused by using higher flame temperature.

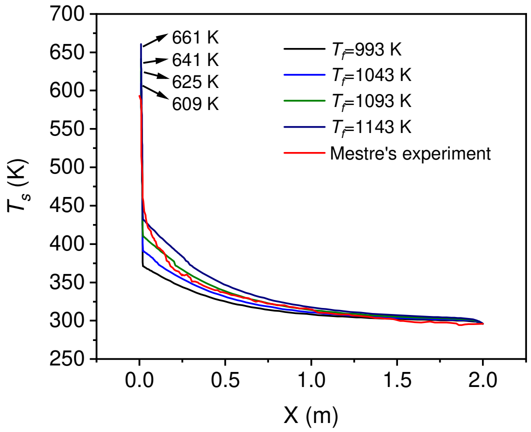

Fig. 5. Fuel surface temperature *v.* flame temperature.

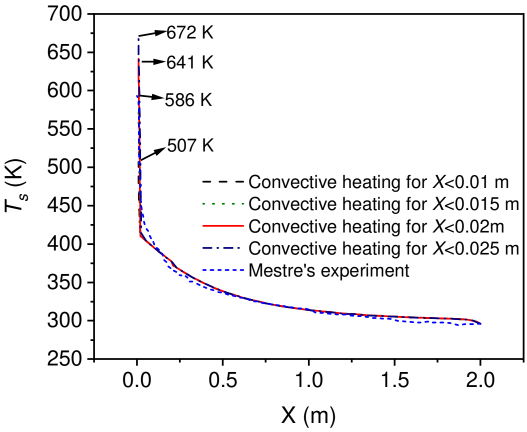

Fig. 6. Fuel surface temperature *v.* convective heating influence range.

Convective heating influence range

The convective heating influence range is assumed in the near field for $X < 0.02$ m. For various influence range, the calculated fuel surface temperature is presented in Fig. 6. The results indicate that fuel surface temperature $T_s|_{X\to 0}$ increases with increasing influence range. For influence range $X < 0.015$ m, the fuel surface temperature $T_s|_{X\to 0}$ is lower than the ignition temperature. For the influence range $X < 0.025$ m, the fuel surface temperature $T_s|_{X\to 0}$ is much higher than the ignition temperature. Therefore, the influence range $X < 0.02$ m is more reasonable. It is demonstrated that the convective heating mainly affects the near field.

In summary, the parameters used in the model are reasonable, including convective cooling coefficient $h_{cooling}$ = 44 W·m^{-2}·K^{-1}, flame temperature T_f = 1093 K, the convective heating influence range $X < 0.02$ m.

CONCLUSION

This paper presents a calculation analysis on surface fire spread. Heat radiation and convection are quantitatively analyzed. The major results are summarized as follows.

(1) For fuel preheating mechanism, the convective heating and the combustion zone radiation take effect in the near field, the convective cooling affects in the far field, while the flame radiation and the radiation loss affect in both near field and far field.

(2) For fuel elements closer to the flame front, the fuel surface temperature increases slowly in the far field then increases rapidly in the near field. The contributions of flame radiation, combustion zone radiation and convective heating to fuel preheating are of the same magnitude in the near field. Radiative heating is the dominant mechanism for fuel pre-heating. Fuel surface temperature increases to ignition temperature in the near field due to the combined effects of three heating mechanisms.

(3) Convective heating coefficient only affects near field, while convective cooling coefficient affects both far field and near field.

ACKNOWLEDGEMENTS

This research is funded by the National Key R&D Program of China (No. 2016YFC0800100), the National Natural Science Foundation of China (No. 51625602), and the Fundamental Research Funds for the Central Universities under Grants (No.WK2320000038).

REFERENCES

[1] N.J. de Mestre, E.A. Catchpole, D.H. Anderson, R.C. Rothermel, Uniform Propagation of a Planar Fire Front Without Wind, Combust. Sci. Technol. 65 (1989) 231-244.

[2] P.G. Baines, Physical Mechanisms for the Propagation of Surface Fires, Math. Comput. Model. 13 (1990) 83-94.

[3] N. Liu, J. Wu, H. Chen, L. Zhang, Z. Deng, K. Satoh, D.X. Viegas, J.R. Raposo, Upslope Spread of a Linear Flame Front Over a Pine Needle Fuel Bed: The Role of convection Cooling, Proc. Combust. Inst. 35 (2015) 2691-2698.

[4] R.O. Weber, Modelling Fire Spread Through Fuel Beds, Prog. Energ. Combust. Sci. 17 (1991) 67-82.

[5] J.L. Dupuy. Testing Two Radiative Physical Models for Fire Spread Through Porous Forest Fuel Beds, Combust. Sci. Technol. 155 (2000) 149-180.

[6] F. Morandini, P.A. Santoni, J.H. Balbi, Validation Study of a Two-Dimensional Model of Fire Spread Across a Fuel Bed, Combust. Sci. Technol. 157 (2000) 141-165.

[7] G.C. Vaz, J.C.S. Andre, D.X. Viegas, Fire Spread Model for a Linear Front in a Horizontal Solid Porous Fuel Bed in Still Air, Combust. Sci. Technol. 176 (2004) 135-182.

[8] D. Morvan, Numerical Study of the Effect of Fuel Moisture Content (FMC) Upon the Propagation of a Surface Fire on a Flat Terrain, Fire Safety J. 58 (2013) 121-131.

[9] V.T. Morgan, The Overall Convective Heat Transfer From Smooth Circular Cylinders, Advances in Heat Transfer 11 (1975) 199-264.

An Experimental Study of Horizontal Fame Spread over Polyoxymethylene in Still Air

Korobeinichev O.[1,] *, **Glaznev R.**[1,2], **Shmakov A.**[1,2], **Paletsky A.**[1], **Hu Y.**[3], **Wang X.**[3], **Hu W.**[3]

[1] *Voevodsky Institute of Chemical Kinetics and Combustion, Novosibirsk, Russia*
[2] *Novosibirsk State University, Novosibirsk, Russia*
[3] *University of Science and Technology of China, State Key Laboratory of Fire Science, Hefei, China*
**Corresponding author's email: korobein@kinetics.nsc.ru*

ABSTRACT

Polyoxymethylene (POM) is one of the most important polymer materials. There are only a few studies devoted to ignition and combustion of POM in counterflow with oxidant. The paper presents an experimental study of flame spread over horizontally placed slabs of polyoxymethylene (POM) in still air. The flame spread rate over the polymer surface was measured. Temperature distributions in the gas phase near the solid fuel surface and in the condensed phase were measured using microthermocouples. Spatial variation of the species (CH_2O, H_2, CO, CO_2, O_2, H_2O, and N_2) concentration in the flame near the solid fuel surface was measured using probing mass spectrometry. Analysis of these data showed that pyrolysis of CH_2O took place near the burning surface in the absence of oxygen, to form CO, which was later oxidized to CO_2. The data obtained indicate that it is necessary to use a two-step global reaction mechanism of oxidation of volatile pyrolysis products in the gas phase in the POM combustion model, instead of a one-step global reaction mechanism used in the modern models of polymer combustion. The data obtained can be used to develop a coupled numerical model of flame spread over POM.

KEYWORDS: flame spread, heat fluxes, polymer, polyoxymethylene, temperature field.

INTRODUCTION

Polyoxymethylene (POM) is a widespread structural material, the thermal properties of which are of special interest. A number of papers devoted to its thermal decomposition and combustion are indicated in the literature [1-10]. Depending on the method of manufacture, POM differs significantly for its physicochemical properties, which affect the melting point, the kinetics of thermal decomposition, and the burning rate. There are data on the kinetics of the thermal decomposition of a homopolymer of POM (Delrin) and copolymers of POM, which decompose at temperature ~ 350-450 °C [1, 3, 8, 9]. The POM copolymer [1] has a low oxygen index (LOI) (15.5 %). The maximum rate of thermal decomposition of technical POM is observed at temperature ~ 380 °C, while complete decomposition occurs at temperature 400-430 °C [1, 3, 8, 9]. The activation energy of thermal decomposition of various POM modifications assuming the first-order reaction is significantly different: 121, 159, 381 kJ/mol according to the data [9], [8] and [10], respectively. POM is a convenient model object for studying the burning mechanism of polymers, since the main product of its decomposition is formaldehyde, a monomer with low molecular weight [11]. However, despite the wide use of POM, there are insufficient data relating to its combustion [5-7]. In the work [5] POM combustion in opposed-flow diffusion flame was studied. Candle-like combustion of POM was studied in [6]. The opposed-flow diffusion flame system was

Proceedings of the Ninth International Seminar on Fire and Explosion Hazards (ISFEH9), pp. 748-754
Edited by Snegirev A., Liu N.A., Tamanini F., Bradley D., Molkov V., and Chaumeix N.
Published by Saint-Petersburg Polytechnic University Press
ISBN: 978-5-7422-6498-9   DOI: 10.18720/spbpu/2/k19-37

used to study POM ignition in [7]. However, there are no works devoted to the study of the flame spread over POM in the literature. This research is devoted to the experimental study of flame spread over POM and to determining its combustion characteristics, such as the mass loss rates, the flame spread rate, the length of the pyrolysis zone, the temperature profile in the condensed phase, temperature and species concentration fields in the flame over the burning POM, and conductive heat fluxes from the flame to the polymer burning surface. The results obtained will be used for developing and validating a numerical model for this process, which is important for better understanding of polymer combustion and hence for raising the fire safety of polymers and predicting the hazard of real fires.

EXPERIMENTAL

Material

POM used in this study was manufactured by DuPont (Delrin 100T). The POM slabs 100 mm wide, 5 mm thick and 200 mm long were produced by hot pressing of granules at pressure 100 atm and temperature 170 °C. The sample density, ρ_s was 1380 kg/m^3.

Experimental

The study of POM slab combustion was performed using the experimental setup, the configuration of which is shown in Fig. 1. The slabs were inserted into a thin metal frame, which served to prevent flame spread along the slab sides, and were placed on an incombustible heat insulating board 10 mm thick, which was positioned on an electronic balance. A balance was placed on a movable platform, which moved at a speed equal to the rate of flame propagation over the polymer, but in the opposite direction. In this way, the flame stabilization relative to the laboratory frame of reference was carried out.

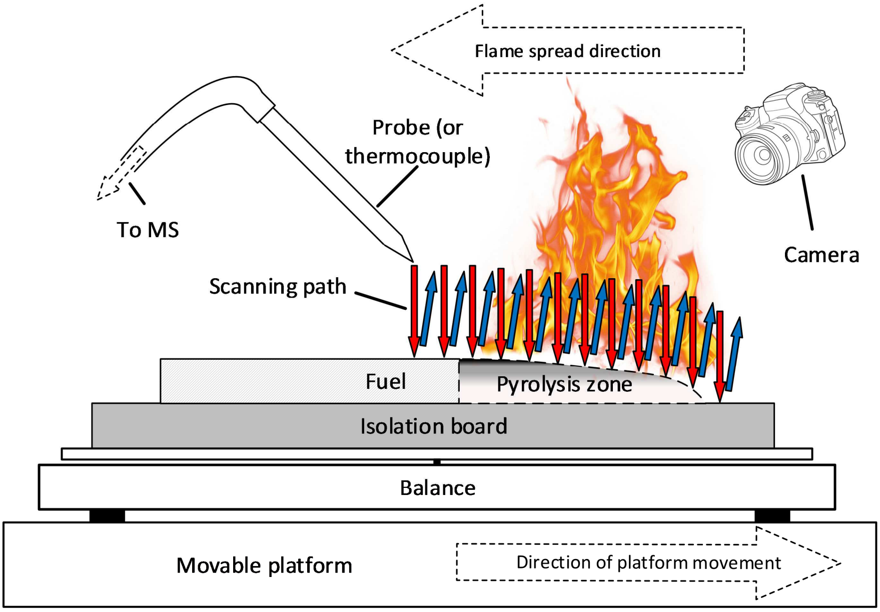

Fig. 1. Configuration of the experimental setup.

The slab was ignited from its edge by the flame of a propane-butane burner. During ignition, the upper surface of the slab was protected from flame with an incombustible heat insulating plate, which was removed after the slab was ignited. The scanning of the flame began after a steady-state mode of burning was reached. To measure the temperature profiles in the fuel, two thermocouples made from Pt and Pt+10%Rh wire 50 μm in diameter were used. One thermocouple was mounted on the upper surface of the slab at a distance of 50 mm from the frontal edge of the slab. The other thermocouple was fixated on the lower surface of the slab at the same distance from the frontal edge of the slab. The thermocouples junctions were installed at the distance of 50 mm from the leading edge of the POM slab and 50 mm from the side edge in grooves (0.2-0.3 mm deep, 0.3-0.4 mm wide and 10 mm long) made on the slab surfaces. To fill the remaining volume of the groove, a strip of POM ($1\times5\times10$ mm^3) was placed onto it, heated with a gas burner until starting to melt; thus, the thermocouple was fixated on the slab surface. To measure the flame temperature, one more thermocouple was used, which was made from Pt and Pt+10% Rh wires with a diameter of 50 μm. The diameter of the junction was 70 ± 10 μm, and the thermocouple shoulders were 5.5 mm long. The thermocouple was covered with a layer of SiO_2 to prevent catalytic reactions on the surface.

The chemical structure of the flame was measured using a quartz microprobe with the orifice diameter of 55 ± 7 μm connected with a Hiden HPR 60 mass-spectrometer. The internal angle of the probe's opening at the cone base was 20 degrees. The thickness of the probe walls near the opening was 0.14 mm. The probe and thermocouple were installed on a three-dimensional positioning system with three stepping motors, allowing the thermocouple and probe to be moved in three coordinates. It was operated with a computer. A quartz microprobe, connected with a quadrupole mass-spectrometer, was used for sampling the flame gases. Gas samples were introduced into the ion source of the Hiden HPR 60 mass-spectrometer as molecular flow, allowing species to be identified in the flame and their concentration profiles to be determined. The energy of the ionizing electrons in the ion source was 70 eV. Thus, the chemical structure of the flame was determined. The mole fractions of CH_2O, H_2, CO, CO_2, O_2, H_2O, and N_2 in the flame were measured. In measuring the temperature profiles, the signals from the thermocouples and from the electronic balance were recorded with a 14-bit AD converter E14-140-M. The probe (or thermocouple) moved along the pathway indicated in Fig. 1. The motion code for the thermocouple and the probe was written in such a way as to allow them to approach the burning surface of the slab as its position in space varied due to burnout of the slab, i.e. at different distances from the flame front, the probe was additionally lowered to the distance close to the burning surface. The cross section of the pyrolysis zone used for writing the motion code was obtained from the experiment in which the burning specimen was extinguished and its cross section was measured.

RESULTS AND DISCUSSION

The flame spread rate and the mass loss rate were measured as functions of time. In Fig. 2, the time dependences of the flame spread rate and the mass loss rate are shown. It is shown in Fig. 2 that the flame spread rate became stationary at the 6-th minute of combustion, and the mass loss rate became steady 13 minutes after the beginning of the specimen's burning. After the steady-state combustion mode was achieved, the flame spread rate and the mass loss rate were 0.077 mm/s and 0.053 g/s, respectively. The width of the pyrolysis zone was 65 mm.

Figure 3 shows the dependences of the temperature of the upper surface and the lower surface of the slab from the distance from the flame front. The surface temperature of the sample in the flame front and at a distance of 10 mm from the front was 450 °C, then, with the increasing distance from 10 to 30 mm from the flame front as the sample burnt out, the temperature decreased to 350-370 °C.

Figure 4 shows a two-dimensional temperature field of the POM flame and cross section of the burning fuel sample. The maximum flame temperature was 1650 °C, taking into account the radiation correction calculated by the Kaskan formula [12]. Analysis of the temperature field showed that the distance from the burning surface to the maximum temperature position increased from 1 to 6-8 mm, as the distance from the flame front grew.

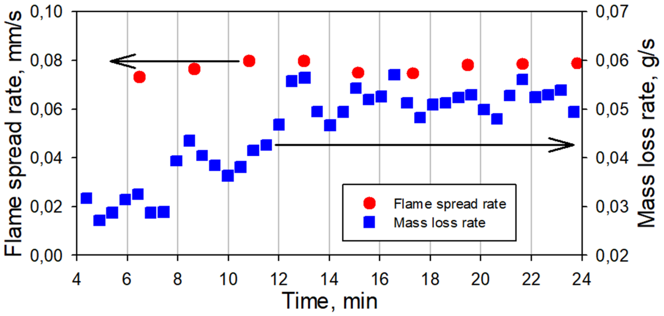

Fig. 2. The flame spread rate (red circles and left axis) and the mass loss rate (blue squares and right axis) as functions of time.

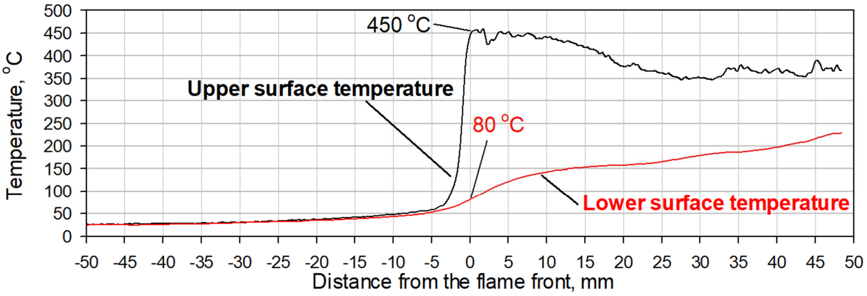

Fig. 3. Temperature profiles in the condensed phase of the polymer.

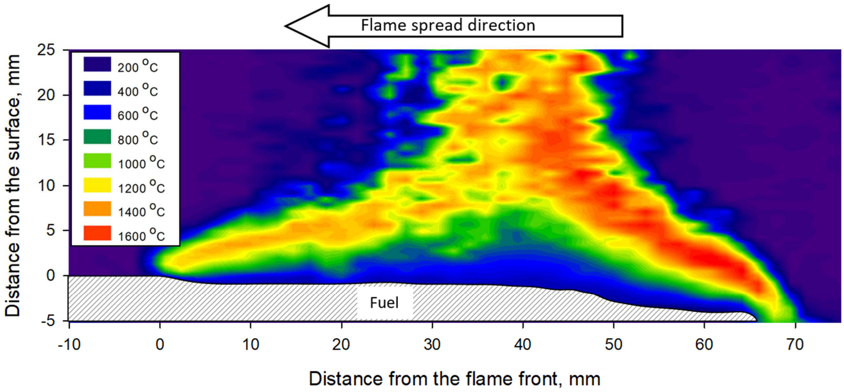

Fig. 4. Two-dimensional temperature field of the POM slab flame.

Based on these data, the temperature gradients near the fuel surface were calculated, which served as a basis for calculating the conductive heat fluxes from the flame to the fuel, shown in Fig 5.

The maximum heat flux of 70 kW/m^2 was observed near the flame front. Then the heat flux gradually decreased to 20 kW/m^2. The following species were identified in the flame: CH_2O, H_2, CO, CO_2, O_2, H_2O, and N_2; their concentrations and the fields of their concentration above the fuel were measured. Two-dimensional distribution of concentrations (mole fractions) of the major species of the POM flame is shown in Fig. 6.

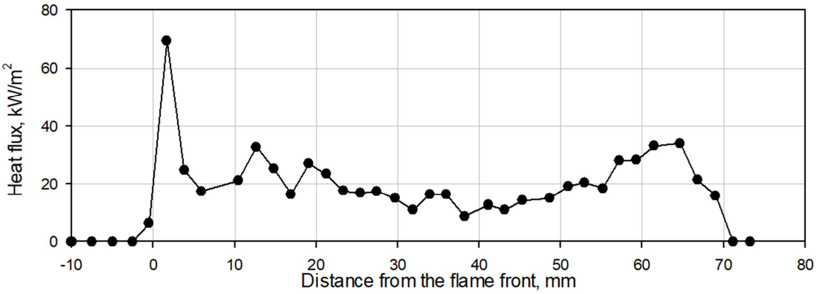

Fig. 5. The conductive heat flux versus the distance from the POM flame front.

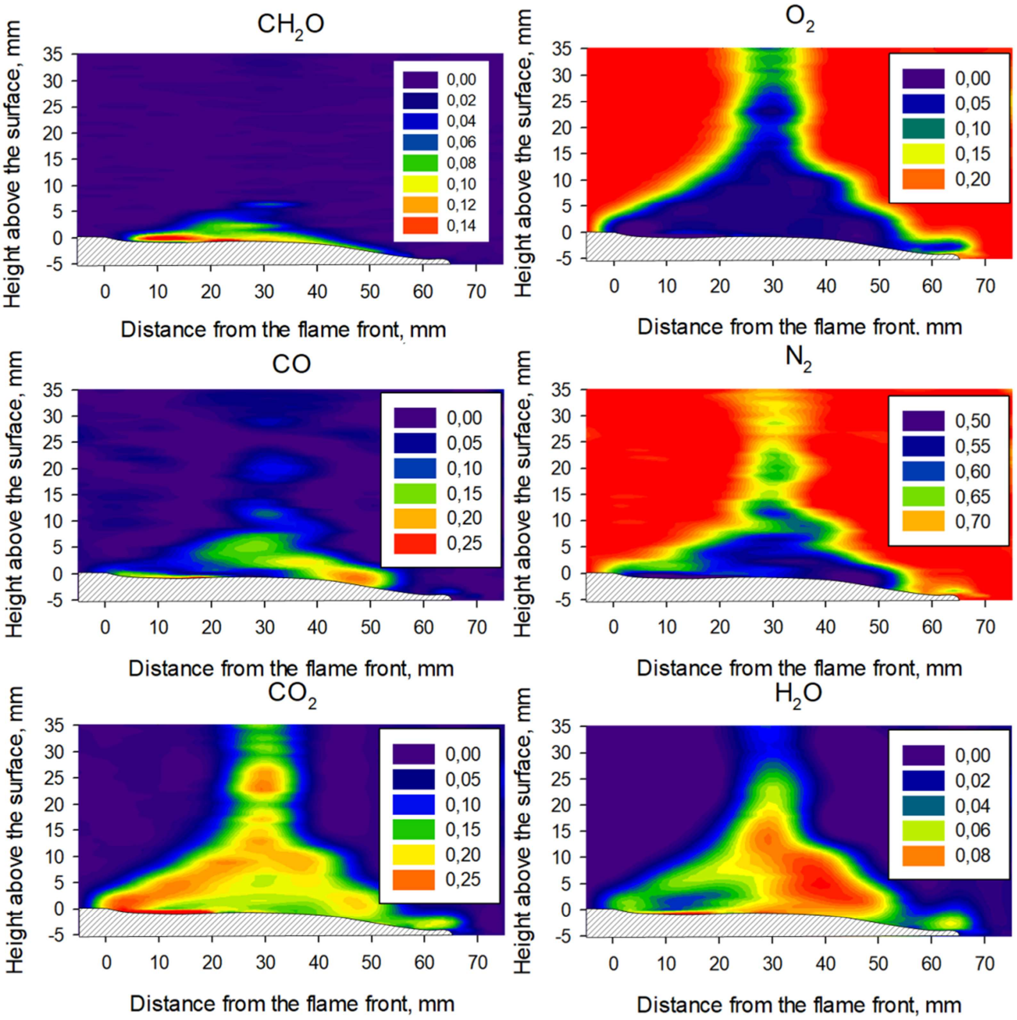

Fig. 6. Two-dimensional concentration fields of the major species of the POM slab flame.

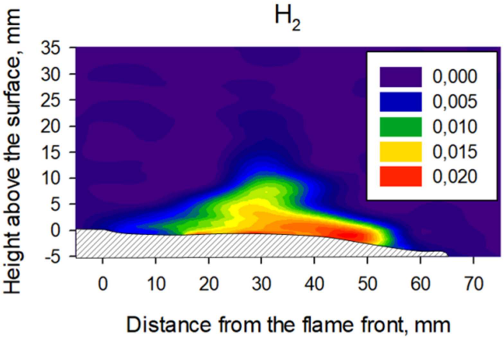

Fig. 6 (cont.). Two-dimensional concentration fields of the major species of the POM slab flame.

Near the burning surface of the polymer oxygen was not found at a distance of 5 to 50 mm from the front of the flame. Based on this, it can be stated that the thermal decomposition of POM in this area occurs in an inert medium. The maximum mole fraction of formaldehyde was observed near the surface of the sample at a distance of 10-40 mm from the flame front. In this area, the concentration of formaldehyde dropped to 0 at a distance of 5-8 mm from the burning surface, while the mole fraction of CO reached 0.15-0.2 and then decreased. Thus, analysis of these data showed that pyrolysis of CH_2O took place, to form CO, which was later oxidized to CO_2. In the polymer combustion model, a one-step global reaction mechanism in the gas phase is usually used. The data obtained indicate that it is necessary to use a two-step global reaction mechanism of oxidation of volatile pyrolysis products in the gas phase in the POM combustion model to make this model more precise.

CONCLUSIONS

A comprehensive experimental study of flame spread over the POM slab in still air has been performed. The following combustion characteristics have been first measured in the steady-state mode: the mass loss rates, the flame spread rate, the cross section of burning polymer, the length of the pyrolysis zone, the temperature profile in the condensed phase, temperature and species concentration fields in flame over burning POM, and conductive heat fluxes from the flame to the polymer burning surface at different distances from the flame front. It has been established that conductive heat fluxes from the flame into solid fuel depend on the distance from the flame front; the maximum conductive heat flux is observed in the flame front and decreases as the specimen burns out. The following main flame species CH_2O (formaldehyde), H_2, O_2, CO, CO_2, H_2O, N_2, have been identified, and spatial variations of their mole fractions have been measured. Their analysis showed that the combustion reaction of formaldehyde includes at least two global steps: the first step consists in pyrolysis of formaldehyde in the absence of oxygen, with CO formed, and the second step is the oxidation of CO to CO_2 by oxygen of air. This result must be taken into account in numerical modeling of the flame spread over POM, which is traditionally done for polymers by using one global reaction. The data obtained are valuable for understanding the mechanism of polymer combustion and will be further used for developing and validating a numerical model of flame spread over POM.

ACKNOWLEGMENTS

This work was supported by the RFBR under Grant #16-58-53128 and by the NNSF of China under Grant # 51120165001.

REFERENCES

[1] S. Sun, Y. He, X. Wang, D. Wu, Flammability characteristics and performance of halogen-free flame-retarded polyoxymethylene based on phosphorus–nitrogen synergistic effects, Journal of Applied Polymer Science 118.1 (2010) 611-622.

[2] M. Day, J.D. Cooney, C. Touchette-Barrette, S.E. Sheehan, Pyrolysis of mixed plastics used in the electronics industry, Journal of Analytical and Applied Pyrolysis 52.2 (1999) 199-224.

[3] S. Igarashi, I. Mita, H. Kambe, Thermogravimetric analysis of polyoxymethylene, Bulletin of the Chemical Society of Japan 37.8 (1964) 1160-1165.

[4] L.A. Dudina, L.V. Karmilova, E.N. Tryapitsyna, N.S. Enikolopyan, The kinetics and mechanism of thermal and thermal-oxidative degradation of formaldehyde polymers, Journal of Polymer Science Part C: Polymer Symposia 16.4 (1967) 2277-2288.

[5] D.J. Holve, R.F. Sawyer, Diffusion controlled combustion of polymers, Proc. Combust. Inst. 15 (1975) 351-361.

[6] T.B. Zhubanov, K.M. Gibov, Oxygen index and minimum limiting rates of polymer combustion, Fire and Materials 12.4 (1988) 169-172.

[7] S.A. Beckel, R.D. Matthews, Ignition of polyoxymethylene, Combustion and Flame 57 (1984) 71-86.

[8] G. Kumar, L. Mahesh, N.R. Neelakantan, N. Subramanian, Studies on thermal stability and behaviour of polyacetal and thermoplastic polyurethane elastomer blends, Polymer International 31.3 (1993) 283-289.

[9] M. Mucha, Isothermal thermogravimetric studies of molten diacetate terminated polyoxymethylene in nitrogen and air, Colloid and Polymer Science 262.11 (1984) 851-855.

[10] J. Shi, B. Jing, X. Zou, H. Luo, W. Dai, Investigation on thermo-stabilization effect and nonisothermal degradation kinetics of the new compound additives on polyoxymethylene, Journal of Materials Science 44.5 (2009) 1251-1257.

[11] J. Troitzsch, International Plastics Flammability Handbook, second ed., Hanser, Munich, 1990.

[12] W.E. Kaskan, The dependence of flame temperature on mass burning velocity, Proc. Combust. Inst. 6 (1957) 134-143.

Flame Spread in Laminated Bamboo Structures

Solarte A.[1, *], **Numapo J.**[1], **Hidalgo J.P.**[1], **Torero J.L.**[2]

[1] *The University of Queensland, Brisbane, Australia*
[2] *University of Maryland, Maryland, USA*
**Corresponding author's email: a.solartecastaneda@uq.edu.au*

ABSTRACT

Flame spread behaviour of laminated bamboo produced from the species Phyllostachys pubescens (Moso) is characterised herein by determining relevant properties such as thermal conductivity and thermal inertia, which ultimately are correlated with the flame spread rate of the material. A description of the variance of thermal conductivity at temperatures ranging from ambient to 350°C is provided in order to accurately account for possible charring and heat transfer processes taking place at the surface of the samples. Testing for those thermal properties was carried out for both parallel and perpendicular positions of the fibre relative to the heat source. For the actual flame spread characterisation, the theory and methodology associated with the Lateral Ignition and Flame Spread Test (LIFT) apparatus was followed. Piloted ignition and opposed flame spread in lateral configuration framework are used for analysis, making possible to obtain the parameters of the progressed distance of the flame, maximum travelled distance, effective spread and time for extinction. In the same manner, the Flame Spread Parameter, a value that can be used for material classification, is calculated using the thermal inertia of the material at ambient and elevated temperatures. The values obtained for flame spread velocity did not adhere to a specific trend; this condition is possibly due to the formation of cracks and a charring front in the sample surface during preheating.

KEYWORDS: Flame spread, thermal inertia, thermal conductivity, flame spread parameter.

NOMENCLATURE

V_f	spread rate (m/s)
k	thermal conductivity (W/mK)
C_P	specific heat capacity (J/kgK)
T_{ig}	Temperature for igniton (°C)
T_s	Surface temperature (°C)
q''_e	esternal heat flux (W/m^2)
q''_s	heat transfer through the solid (W/m^2)
q''_g	heat transfer through gas (W/m^2)
$q''_{o,ig}$	critical heat flux for igntion (W/m^2)
h_T	heat transfer coefficient (W/m^{2}K)

Greek

ϕ	flame spread parameter (kW^2/m^3)

Subscripts

∞	ambient

INTRODUCTION

Today's society is competing to build the tallest buildings with the latest technological designs, all in the most sustainable way. This reality drives us to pick the most innovating materials that would allow to design and construct those structures. Engineered-bamboo products are novel construction materials currently being used by engineers and architects in buildings [1]. Its favourable qualities include features such as great aesthetics, environmentally renewable and sustainable nature [2, 3],

Proceedings of the Ninth International Seminar on Fire and Explosion Hazards (ISFEH9), pp. 755-766
Edited by Snegirev A., Liu N.A., Tamanini F., Bradley D., Molkov V., and Chaumeix N.
Published by Saint-Petersburg Polytechnic University Press
ISBN: 978-5-7422-6498-9 DOI: 10.18720/spbpu/2/k19-125

excellent mechanical properties [4] with favourable structural behaviour that has shown to be equal to or greater than timber, and because of this it is being used in many regions of the world [5]. All of these characteristics contribute to place bamboo as an innovative construction material with a great potential to be used in structural elements, internal lining and external façade for modern multi-story buildings.

RESEARCH SIGNIFICANCE

Despite the positive qualities described above, the fire hazard is an important matter that needs to be addressed. Currently, there is limited knowledge related to the flame spread behaviour of this material. Recent events like the fires in the Grenfell Tower in London and Sao Paulo's high-rise building collapse are a consequence of the little information available on the characterisation of the flame spread behaviour in novel materials and complex systems.

To date, previous research has provided information on flame spread modelling of PMMA and other ideal materials from the point of view of pyrolysis and combustion. However, the existing models addressing cellulosic, charring and composites materials are much more limited and generally difficult to implement in practice [6].

The understanding of the fire spread phenomena needs to be looked in a holistic way, and the ability to tackle the problem from its basic principles is fundamental. Only once this knowledge is obtained, a trained professional will be able to assess and design fire-safe structures that take in consideration the full–scale fire scenario, which is key to create solutions to the problem thoroughly. The use of experiments like the Lateral Ignition and Flame Spread Test (LIFT) provides flammability parameters that describe the heat transfer mechanism from the flame to the fuel, which can be incorporated into mathematical correlations that will characterise the velocity of the flame spread [7]. The information from these fundamental studies provides input data for assessing risks in a real fire scenario. It is important to understand that the parameters obtained by these tests are not material properties, but a combination of the specific conditions and configurations by which the samples are tested [8]. For example, changes in natural convection, atmospheric conditions, or moisture content, among others, can cause particular behaviours. Therefore, the extrapolation to different scenarios needs to be done with caution.

This work is part of an ongoing project that intends to characterise the fire performance of laminated bamboo by exploring the flame spread parameter. The characterisation of how the flame spreads will provide an understanding on how the fire will grow and its contribution to the production of the smoke and heat influencing the occurrence of flashover in a compartment, or the external flame spread in a façade system. This information constitutes a tool for performance-based design approach that is necessary to build future fire-safe bamboo buildings.

METHODOLOGY

Materials and Methods

The present study will provide the flame spread characterisation of three different samples of laminated bamboo Phyllostachys pubescens (Moso). This experimental programme consists of two main steps of testing. The first step comprises bench-scale tests of laminated bamboo samples to determine their thermal conductivity and obtain the thermal inertia. The second step aims to provide information about the flame spread parameters of the same material. For this work, three different types of laminated bamboo were tested. Table 1 describes each of the samples.

Thermal properties

The thermal inertia is the resistance of a material to change its temperature, and it is a key parameter to characterise the flame spread. It is the product of the thermal conductivity, k (W/(m·K)), the density ρ (kg/m^3) and the specific heat capacity, C_p (J/(kg·K)). The thermal conductivity is a parameter that drives a material's ability to conduct heat, and determines the rate at which energy is transported. The thermal conductivity will depend and change according to its physical structure, as well as its atomic and molecular characteristics [9].

Table 1. Types of laminated bamboo "*Moso*" tested

Laminates bamboo	Adhesive	Treatment	Use	Density, kg/m^3	Moisture Content, %
Sample A	Polyurethane	Not Steamed	Interior	540	7.17%±0.06
Sample B	Resorcinol Formaldehyde	Steamed	Interior	730	6.08%±0.40
Sample C	Formaldehyde Prefere	Steamed	Intended for structural applications	745	8.12%±0.02

Due to the process of fabrication of the laminated bamboo (hot-pressing, bleaching, caramelising, type of adhesive, etc.) [10], some physical characteristics could be changed and different values of thermal conductivity might be obtained from different manufacturing process. According to Fernandez-Pello et al. [11], the difference in thermal conductivity can affect the way that heat is transferred in the solid, and a sample comprised by high conductive materials would result in a high rate for the flame spread. This property is also key to characterise the mechanical behaviour in fire conditions due to the way in which heat transfer will take place.

The thermal conductivity was measured experimentally with the use of the Hot Disk Thermal Constants Analyser, which uses the transient plane source (TPS) method. This process is based on the use of a transiently heated plane sensor, that conducts electrical impulses in a double spiral pattern [12]. This sensor was fitted in between two sample pieces and through the application of an electrical current, the temperature of the sensor was increased and the resistance temperature was recorded as a function of time [13].

Three types of samples mentioned in Table 1, were analysed. Samples B and C were tested at the three surface sides of a cubic sample. As shown in Fig. 1, side PP1 and PP2 is the nomenclature used for the surface that is exposed perpendicularly to the fibre and side PLL refers to the surface that has been exposed parallel to the fibre. The difference between PP1 and PP2 is that PP1 has the long side of the strip (around 6 mm) placed horizontally, and PP2 has the long side of the strip placed vertically. These tests were conducted for ambient conditions (20°C -25°C) as well as for elevated temperatures (50°C - 350°C). For ambient tests, the sensor spiral was sandwiched between two sheets of Kapton, and for the elevated temperatures two sheets of Mica was used.

Fig. 1. Nomenclature of the surface tested on the laminated bamboo samples.

Flame spread

Flame spread is a mechanism in which a flame moves forward in the proximity of a pyrolysing region of the surface fuel [6]. When studying flame spread behaviour, it is important to assess the governing mechanisms of the material that can influence the phenomenon such as configuration, thickness and intrinsically material characteristics such as thermal inertia, thermal conductivity, melting, charring, delamination, among others [11]. Previous studies have analysed the different behaviour of flame spread, however, two principle modes have been established: (1) opposed-flow flame spread and (2) concurrent flow flame spread [11].

From Fig. 2a, it can be seen that for opposed-flow flame spread, the flame front is moving forward, preheating the unburned fuel. However, there is a flow coming from the opposite direction which may or may not slow down the movement of the flame, according to the de Ris regime [14], or Fernandez-Pello regime [11] . From Fig. 2b, it can be seen how the flow is pushing in the same direction as the flame, effectively "driving" it forward and enabling propagation.

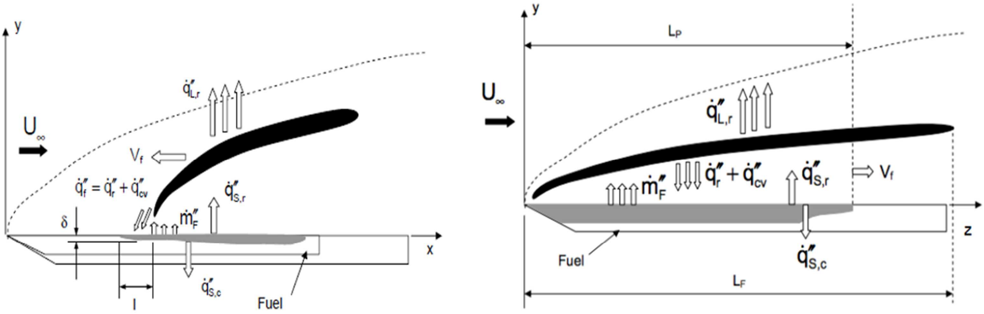

Fig. 2. (a) Opposed flow flame spread (b) concurrent flow flame spread
(from Jose L. Torero class notes, University of Edinburgh, 2011).

This work will focus on the analysis of opposed flame spread in a lateral configuration, as the first step to understand the problem and classify the product. Future steps will study the vertical configuration for concurrent flow flame spread, to understand the hazards of putting this material in walls and façades. From Quintiere [15] Eq. (1) was used for the fundamentals of this study. This expression correlates the spread rate, V_f (m/s), with the thermal conductivity, k (W/(m·K)), the density ρ (kg/m^3), the specific heat C_P (J/(kg·K)), the temperature for ignition T_{ig} (°K), and the surface temperature T_s (°K), and introduces the flame spread parameter, ϕ (W^2/m^3). The flame spread parameter is the product of heat flux from the flame onto the sample in the gas phase, and the heated length, it can be calculated experimentally with the use of the Lateral Ignition and Flame Test (LIFT).

$$V_f = \frac{\phi}{k\rho C_P \left(T_{ig} - T_s\right)^2}, \tag{1}$$

Nevertheless, to use this simplified equation, some assumptions need to be stated [8, 16, 17]:

1. The solid is considered inert until ignition.
2. T_{ig} can be used as the temperature for pyrolysis T_p.
3. Samples are thermally thick.

4. The flame is driven by three sources of heat: (1) external heat transfer ($\dot{q}_e''$), (2) heat transfer through the solid ($\dot{q}_s''$), and (3) the heat is transferred from the flame through the gas phase ($\dot{q}_g''$), mainly through conduction.
5. As the flame moves forward the "virgin material" reaches ignition temperature, and the flame acts as a pilot ignitor that enables the spread.
6. The flame is not close to extinction, so the heat produced is bigger than the heat needed to increase the temperature of the new air allowing the flame to spread with the thermal wave.

If the sample is preheated and achieves thermal equilibrium, the total losses of the sample are equivalent to the heat input. With this, Eq. (2), (3) and (4) are introduced to simplify Eq. (1)

$$T_{ig} = T_\infty + \frac{\dot{q}_{0,ig}''}{h_T},\ T_s = T_\infty + \frac{\dot{q}_e''}{h_T} \tag{2, 3}$$

and

$$T_{ig} - T_s = \frac{\dot{q}_{0,ig}'' - \dot{q}_e''}{h_T}, \tag{4}$$

where $\dot{q}_{0,ig}''$ (W/m^2) is the critical heat flux for ignition, and Eq. (5) becomes the correlation of the flame spread parameter in terms of the critical heat flux for ignition and the external heat flux applied.

$$V_f = \frac{h_T{}^2 \phi}{k\rho C_P \left(q_{0,ig}'' - q_e''\right)^2}. \tag{5}$$

Samples of *Phyllostachys pubescens* (Moso) of 600 x100 x 40 mm were studied under the Lateral Ignition and Flame Test (LIFT) based on ASTM-E-1321-13 [18]. To reduce the heat loses from the back of the sample, the sides and back of each specimen were covered by two layers of ceramic insulation material 2.5 mm thick and a final layer of aluminium foil 0.2 mm thick. The samples were placed in a holder frame angled at 15 degrees to the centreline of the radiant panel. Each sample was marked every 25 mm for tracking the movement of the flame and a video camera was placed perpendicular to the sample, to record all tests. To guarantee that the tests would start under steady thermal conditions, eight thermocouples were placed in the sample, 2 mm from the surface to follow and measure the increase of the temperature due to the heating of the surface during the arrival of the flame front.

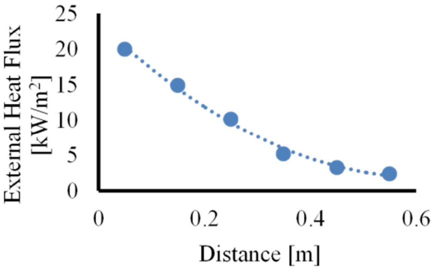

Fig. 3. Heat flux mapping distribution

Before these tests were carried out, it was mapped the external heat flux imposed from the radiant panel on the whole surface of the samples. A non-combustible fibre block was placed and the mapping was performed starting from the leading edge at 50, 150, 250, 350, 450, and 550 mm. A water-cooled heat flux gauge was used to record the surface heat flux of each location; this it was placed around 5 mm offset of the insulation surface to avoid convection effects. A heat flux distribution is shown in Fig. 3, which was obtained by recording measurements in different locations and interpolating the values in between.

The external heat flux imposed at the leading edge was chosen to be 20 kW/m^2, around 5 kW/m^2 above the critical heat flux for ignition, which was found to be 14 kW/m^2 in previous experiments [19]. In order to guarantee thermal equilibrium, each sample was preheated for at least 1,000 seconds. When the temperature measured by the thermocouples reached a plateau, the sample was deemed to be reach a steady state. Once the thermal equilibrium of the specimen was reached, a pilot flame was introduced in the leading edge to mark the onset of ignition. However, given the charring nature of the material, this preheating time led to the creation of an initial charred surface in the first 150 mm of the sample before ignition occurred. Once ignition started, visual observations recorded the flame front position as a function of time. The rate at which the flame spreads will depend on the chemical decomposition and pyrolysis front that will start to progress with the ignition of the sample.

RESULTS AND DISCUSSION

Thermal inertia

To experimentally obtain the value of the thermal inertia, the thermal conductivity was measured by testing 35 samples with the Hot Disk, for ambient temperature. Sample types A, were tested for face PP1, and B and C were tested for each face PP1, PP2, PLL, the sides described in the previous section. Table 2 shows the results obtained for the thermal inertia at ambient conditions.

Table 2. Thermal conductivity and thermal inertia results of laminated bamboo "*Moso*" tested

Laminates bamboo at 20°C	Thermal Conductivity, W/(m·K)	Thermal Inertia, $W^2 \cdot s/(m^4 \cdot K^2)$
Sample A: perpendicular to the fibre Side PP1	0.201±0.01	$2.56 \times 10^5 \pm 6.95 \times 10^3$
Sample B: perpendicular to the fibre Side PP1	0.24±0.01	$3.94 \times 10^5 \pm 9.50 \times 10^3$
Sample B: perpendicular to the fibre Side PP2	0.26±0.01	$4.27 \times 10^5 \pm 6.01 \times 10^3$
Sample B: parallel to the fibre Side PLL	0.29±0.01	$4.71 \times 10^5 \pm 1.47 \times 10^4$
Sample C: perpendicular to the fibre Side PP1	0.25±0.01	$4.13 \times 10^5 \pm 2.09 \times 10^4$
Sample C: perpendicular to the fibre Side PP2	0.24±0.01	$4.10 \times 10^5 \pm 2.07 \times 10^4$
Sample C: parallel to the fibre Side PLL	0.27±0.01	$4.44 \times 10^5 \pm 1.22 \times 10^4$

The results show that the thermal conductivity tested in face PP1 for sample A is lower than for samples B and C, this can be explained due to the lower density associated with a higher porous media found for samples type A. Sample B and C show higher values for the side where the heat is transferred parallel to the grain (PLL). Sample B depicts the highest values for the sides PP2 and PLL. To obtain the thermal inertia, the values of the experimental thermal conductivity, density and specific heat were multiplied. The value of the specific heat was used as 2260 J/(kg·K), which was obtained by Bartlett et al. [20]. The highest value of the thermal inertia was found to be 4.71×10^5 $W^2 \cdot s/(m^4 \cdot K^2)$ for sample B followed by 4.44×10^5 $W^2 \cdot s/(m^4 \cdot K^2)$ by sample C, both for parallel to the grain (PLL) configuration. From Table 2 it can be seen that the values of the thermal inertia for sample A are almost 50% less than the highest value. The difference in the values obtained for sample B and C is up to 16%.

For temperatures above 30 °C test were conducted in a furnace and the thermal conductivity was measured. Sample type A, B and C were tested for two surfaces PP1 and PLL. Figure 4 shows the thermal conductivity results at elevated temperatures. For all three cases, the thermal conductivity shows higher results than those measured at ambient temperature. As for ambient temperatures, the values of sample B and C are higher than the ones obtained for Sample A. For the tests conducted perpendicular to the grain (PP1), the thermal conductivity shows a steady tendency up to around 225 °C, however, starts to decrease after the samples were heated beyond 225 °C. Samples A and B show a clear rise in the values for the tests performed parallel to the grain (PLL) in comparison to the ones perpendicular to the grain (PP1), and show higher values than the results obtained for sample C. The reduction of the thermal conductivity after 225 °C can be due to the fact that, at these temperatures, the degradation reactions trigger mass loss and charring processes which create gaps of air within the sample, resulting in a porous media and therefore lower values of thermal inertia.

For the test run perpendicular to the grain (PP1), the results from 30 to 225 °C were averaged to obtain a bulk value for this range of temperatures. The thermal conductivity for samples A, B and C were 0.26±0.01, 0.34±0.01 and 0.36±0.01 W/(m·K) respectively. Measurements of thermal conductivity parallel to the grain yielded the highest value of 0.38 W/mK for sample A at 84 °C, 0.47 W/(m·K) for sample B at 120 °C , and 0.43 W/(m·K) for sample C at 220 °C.

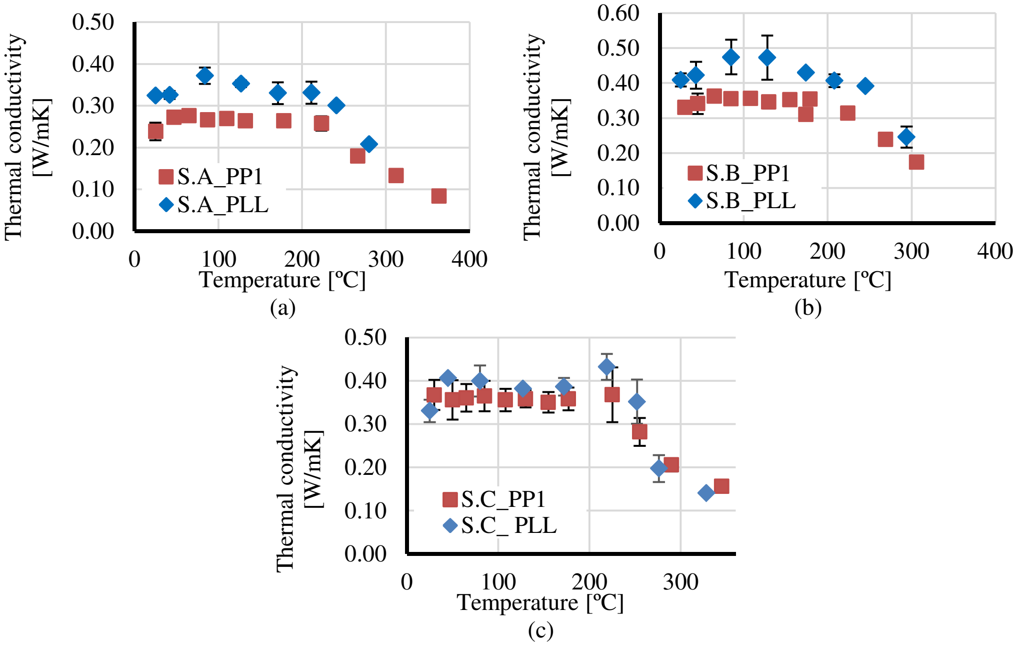

(a) (b)

(c)

Fig. 4. Thermal conductivity at elevated temperatures (a) Sample A, (b) Sample B, (c) Sample C.

Shah et al. [21] tested samples of engineered bamboo at ambient temperatures and obtained a thermal conductivity of 0.2±0.07 W/(m·K) for laminated bamboo (Moso). Compared to engineered timber, which has a thermal conductivity of 0.14 W/(m·K) [20], laminated bamboo has a higher value. To the knowledge of the authors, there was no information available to compare for this parameter at elevated temperatures.

Flame spread

Tests were carried out in the LIFT to study the flame spread behaviour of laminated bamboo. Three test were conducted for sample type B and sample type C, all exposed to the PP1 side. As shown in

Fig. 5a, the preheating caused degradation and charring of the surface of the sample for approximately 250 mm from the leading edge, therefore the readings of the flame spread started around the 250 mm mark. Figures 5b and 5c show the evolution of the travelling flame, and Fig. 5d show extinction of the flame at around 400-415 mm.

The nomenclature in the following figures indicates the sample type by S.B or S.C (sample type B or C) and the test number by T1, T2, and T3.

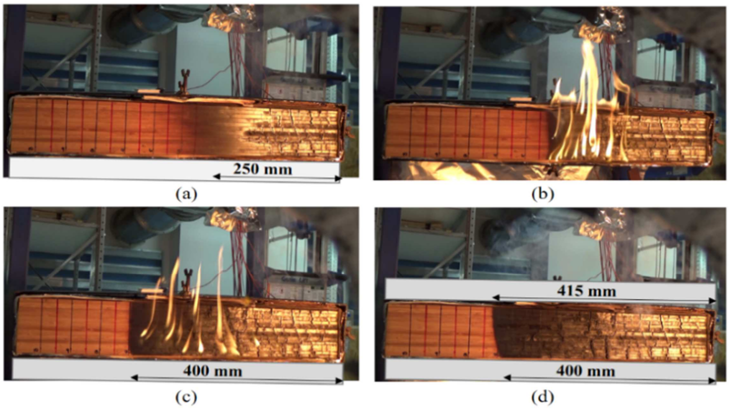

Fig. 5. Flame spread test (a) before ignition, (b) flame travelling, (c) before extinction, (d) at extinction.

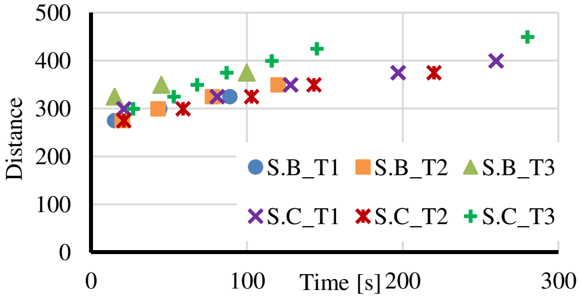

Fig. 6. Flame spread test distance travelled in time.

From Fig. 3 we can derive that the critical heat flux for flame spread was around 5 kW/m^2. Figure 7 shows the velocity of the spread in time. Sample type B depicts a decreasing tendency with a polynomial fit. For Sample C, shown in Fig. 7b, the velocities show that they tend to decrease, slightly increase and decrease again. All samples have a similar behaviour between them but from 60 – 90 s the spread velocities of S.C_T3, increase abruptly. This could be explained because during this part of the test, it was seen an incoming flow current, possible by an open door in the lab, and seemed to have been changing the flow creating a faster and more turbulent flame. During the tests, it was possible to notice the role that the cracks and the char layer had on the spread, stopping the movement forward until the flame was able to advance. Because of this condition, no steady spread was observed.

For each sample, the flame spread parameter was calculated with the values of thermal inertia by multiplying the density, specific heat and the thermal conductivity. Two values of the thermal inertia were obtained with the results of the thermal conductivity found in the previous section for side PP1, at ambient (20 °C) and at elevated temperatures (averaging results obtained for 30 to 225 °C).

Table 3 shows the results of the flame spread parameter associated to each thermal conductivity. The value used for total heat transfer was 37 W/m^{2}K following the regression proposed by Hidalgo [22]. The average value of the flame spread parameter (ϕ) for sample type B was found to be 5.41 ± 5.45 kW^2/m^3, and 9.83±9.89 kW^2/m^3 for ambient and elevated temperatures, respectively. The average value of the flame spread parameter for sample type C was found to be 7.68±0.30 kW^2/m^3 and 13.57±0.53 kW^2/m^3 for the thermal conductivity at ambient and at the higher temperatures, respectively.

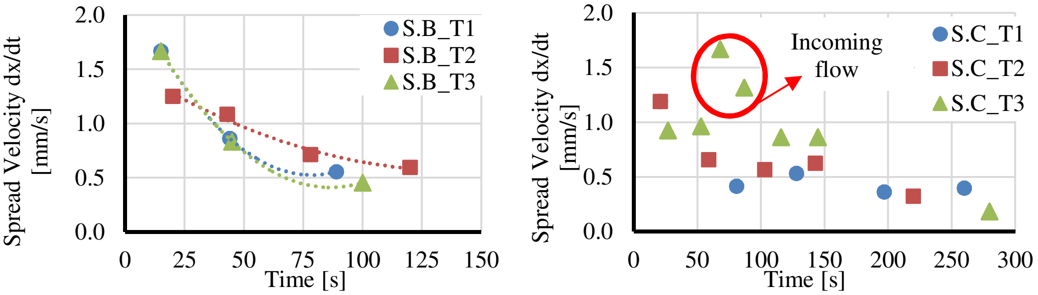

(a) (b)

Fig. 7. Flame spread test spread velocity in time (a) sample type B (b) sample type C.

A linear regression representing Eq. (5) was used to obtain the flame spread parameter for each sample (Fig. 8).

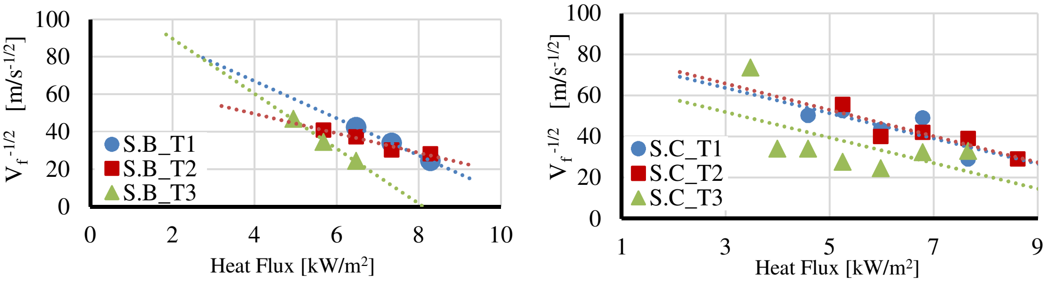

(a) (b)

Fig. 8 Correlating plot for flame spread parameter (a) sample type B (b) sample type C.

It can be observed the high variability for sample type B, however eliminating sample S.B_T2 from the average the results obtained are 2.31±1.27 kW^2/m^3, and 4.196±2.21 kW^2/m^3 for the thermal inertia calculated with the thermal conductivity at ambient and at higher temperatures, respectively. More experiments need to be carried out to be able to validate these data.

Table 3. Flame spread parameter results of laminated bamboo "*Moso*" tested

Sample	ϕ with $k_{Ambient}$, kW^2/m^3	ϕ with $k_{Elevated\ Temp}$, kW^2/m^3
S.B_T1	3.17	5.76
S.B_T2	11.62	21.10
S.B_T3	1.45	2.63
S.C_T1	7.94	14.04
S.C_T2	7.35	13.00
S.C_T3	7.74	13.68

To the best knowledge of the authors, there is no available flame spread parameter data to compare with laminated bamboo on this subject. For charring materials, there is also limited data to compare for flame spread. According to Di Blasi [23], these types of fuels create a complex problem because of the strong interaction between the chemical processes. Atreya [24] mentioned that many of the experiments that have been made on wood are not very reproducible, due to the characteristics of wood, such as evaporation of moisture, grain direction, degradation of wood, among others.

The flame spread parameter was found for various materials by Merryweather et al. [25]. Some of the charring materials tested in this group were plywood, medium density fibreboard. Results yielded a flame spread parameter of 28.0 kW^2/m^3, and 17.1 kW^2/m^3, respectively. Both of these results show higher values to the ones obtained for laminated bamboo. However, the authors want to clarify that this is a work in progress and any comparison made to this point is to give some initial perspective on how this material stands. Nevertheless, further analysis needs to be done to completely understand the flame spread behaviour on laminated bamboo.

SUMMARY AND CONCLUSIONS

Tests have been undertaken to determine the risk of flame spread in laminated bamboo samples. For these tests, an experimental calculation of the thermal inertia was provided with the actual test measurement of the thermal conductivity.

Two different sensors were used to measure the thermal conductivity: a Kapton sensor used at ambient temperature and a Mica sensor used at elevated temperatures. Thermal conductivities provided by both sensors around ambient temperature were slightly different. Further tests will be performed to determine if the type of sensor affected the measurement at ambient temperature.

The thermal conductivity was tested at ambient temperatures (20-25 °C) as well as for higher temperatures (30-350 °C). The samples were tested perpendicular to the grain (PP1 and PP2) as well as parallel to the grain (PPL).

The sample type with the lower density (Sample A) had the lower thermal conductivity for ambient temperatures yielding a value of 0.2094 ± 0.0057 W/mK. The results for Sample B and C were similar among them for the configuration perpendicular to the grain; however, the samples tested parallel to the grain depicted a slightly higher thermal conductivity.

The tests carried out at elevated temperatures and done perpendicular to the grain (PP1) showed to have a higher value than those at ambient. The results also show that the thermal conductivity displays a steady tendency up to around 225°C. Nevertheless, it starts to decrease after the samples were heated beyond 225 °C.

Experiments were carried out to find the behaviour of the spread of the flame. Samples B and C were tested perpendicular to the grain (PP1). During the preheating time, the first 250 mm of the sample degraded and charred. Once ignition started, the flame travelled around 200 mm and then quenched, at the distance where the radiative incident heat flux was around 5 kW/m^2.

It was observed that the maximum travelled distance recorded was around 450mm, after this extinction always occurred which resulted in a critical heat flux for flame spread of around 5kW/m^2.

The average value of the flame spread parameter for sample type C was found to be 7.68 ± 0.30 kW^2/m^3 and 13.57 ± 0.53 kW^2/m^3 associated with the thermal conductivity at ambient and at the higher temperatures.

The flame spread parameter results for sample B showed that test S.B_T2 was out of the trend observed for the other two tests. However eliminating sample S.B_T2 from the average the results obtained are 2.31 ± 1.27 kW^2/m^3, and 4.196± 2.21 kW^2/m^3 for the thermal conductivity at ambient and higher temperatures, respectively.

It can be observed the high variability for sample type B, so more experiments need to be carried out to be able to validate these data, and further analysis needs to be considered to completely understand this condition.

ACKNOWLEDGEMENTS

Non-financial support to this research was provided by several individuals and companies and we would like to highlight in particular Moso International and Yes Bamboo. The authors gratefully acknowledge The University of Queensland's Centre for Future Timber Structures for its support throughout this research; as well as Dr Andres Osorio, Jeronimo Carrascal, Dr Cristian Maluk, Mateo Gutierrez, Ian Pope, Aaron Bolanos, Tam Do, and the rest of the UQ Fire Research Team for their feedback and motivation.

REFERENCES

[1] X. Liu, et al., Nomenclature for Engineered Bamboo, BioResources, 11 (2016) 1141-1161.

[2] L. Yiping, et al., Bamboo and climate change mitigation. Technical Report-International Network for Bamboo and Rattan (INBAR), Vol. 32, 2010.

[3] P. Van der Lugt, A.A.J.F. Van den Dobbelsteen, J.J.A. Janssen, An environmental, economic and practical assessment of bamboo as a building material for supporting structures, Construct. Build. Mater. 20(9) (2006) 648-656.

[4] B. Sharma, et al., Engineered bamboo for structural applications, Construct. Build. Mater. 81 (2015) 66-73.

[5] A. Gatóo, et al. Sustainable structures: bamboo standards and building codes, In: Proceedings of the Institution of Civil Engineers-Engineering Sustainability, Thomas Telford Ltd., 2014.

[6] Y. Hasemi, Surface flame spread, In: SFPE Handbook of Fire Protection Engineering, Springer, 2016, pp. 705-723.

[7] J.L. Torero, Scaling-up fire, Proc. Combust. Inst. 34 (2013) 99-124.

[8] J. Torero, Flaming ignition of solid fuels, In: SFPE Handbook of Fire Protection Engineering, Springer, 2016, pp. 633-661.

[9] T.L. Bergman, A.S. Lavine, F.P. Incropera, D.P. DeWitt, Fundamentals of heat and mass transfer, John Wiley & Sons, 2011.

[10] B. Sharma, et al., Engineered bamboo: state of the art, Proc. Inst. Civil Eng. – Construct. Mater. 168(2) (2015) 57-67.

[11] C. Fernandez-Pello, T. Hirano, Controlling mechanisms of flame spread, Combust. Sci. Technol. 32 (1983) 1-31.

[12] H.D. AB, Hot Disk Thermal Constants Analyser Instruction Manual, 2015.

[13] M. Gustavsson, E. Karawacki, S.E. Gustafsson, Thermal conductivity, thermal diffusivity, and specific heat of thin samples from transient measurements with hot disk sensors, Rev. Sci. Instr. 65 (1994) 3856-3859.

[14] J. De Ris, Spread of a laminar diffusion flame, Proc. Combust. Inst., 12 (1969) 241-252.

[15] J. Quintiere, The application of flame spread theory to predict material performance, J. Res. National Bureau of Standards 93 (1988) 61-70.

[16] D. Drysdale, An introduction to fire dynamics, John Wiley & Sons, 2011.

[17] J. Quintiere, A simplified theory for generalizing results from a radiant panel rate of flame spread apparatus, Fire Mater 5 (1981) 52-60.

[18] ASTM E1321-13 Standard Test Method for Determining Material Ignition and Flame Spread Properties, E.F. Standards, ASTM, 2009.

[19] A. Solarte, J.P. Hidalgo, J.L. Torero, Flammability Studies for the Design of Fire-Safe Bamboo Structures, In: World Conference on Timber Engineering, Seoul, Republic of Korea, 2018.

[20] A.I. Bartlett, et al., Thermal and Flexural behaviour of Laminated Bamboo exposed to sever radiant heating, In: World Conference on Timber Engineering, Seoul, Republic of Korea, 2018.

[21] D.U. Shah, et al., Thermal conductivity of engineered bamboo composites, J. Mater. Sci. 51 (2016) 2991-3002.

[22] J.P. Hidalgo, Performance-based methodology for the fire safe design of insulation materials in energy efficient buildings, the University of Edinburgh, 2015.

[23] C. Di Blasi, Processes of flames spreading over the surface of charring fuels: effects of the solid thickness, Combust. Flame 97 (1994) 225-239.

[24] A. Atreya, Fire growth on horizontal surfaces of wood, Combust. Sci. Technol. 39 (1984) 163-194.

[25] G. Merryweather, M. Spearpoint, Flame spread measurements on wood products using the ASTM E 1321 LIFT apparatus and a reduced scale adaptation of the cone calorimeter, Fire Mater 34(3) (2010) 109-136.

The Impact of DOPO and TPP Flame Retardants on Flame Spread over the Surface of Cast PMMA Slabs

Trubachev S.[1,2], Korobeinichev O.[1,]*, Gonchikzhapov M.[1], Paletsky A.[1], Shmakov A.[1,2], Tereshchenko A.[1], Karpov A.[3], Hu Y.[4], Wang X.[4], Hu W.[4]

[1] Institute of Chemical Kinetics and Combustion, SB RAS, Nobosibirsk, Russia
[2] Novosibirsk State University, Novosibirsk, Russia
[3] UdmFRC, UrB RAS, Izhevsk, Russia
[4] State Key Laboratory of Fire Science, University of Science and Technology of China,
96 Jinzhai Road, Hefei, Anhui 230026, China
**Corresponding author's email: korobein@kinetics.nsc.ru*

ABSTRACT

The effect of flame retardants DOPO and TPP on combustion of PMMA and on its thermal decomposition has been investigated. It was suggested that the presence of an oxidizer in the pyrolysis zone affects the flame propagation rate in the case of PMMA-TPP and has no effect in the case of PMMA-DOPO. With the addition of TPP and DOPO a reduction of the total heat flux from the flame to the surface was detected. Before the flame front, diffusion of the oxidant takes place in the longitudinal direction to the flame zone. local increase of the heat flux near the flame front in the case of PMMA-TPP was found, as opposed to in PMMA without additives. From the data of the species concentrations in the flame zone of a PMMA-TPP slab, the presence of oxygen at the flame front (up to 10%) was detected. PMMA-TPP decomposes more rapidly than PMMA and PMMA-DOPO in the oxidizing medium. Farther from the flame front, where there is no oxygen, addition of TPP does not affect the decomposition rate of PMMA in an inert medium. The DOPO additive, in turn, affects the kinetics of thermal decomposition and reduces the heat flux from the flame. An oxidant does not affect PMMA-DOPO decomposition. Thus, it was concluded that the presence of oxygen near the pyrolysis surface affects the flame propagation velocity in the case of PMMA-TPP and has no effect in the case of PMMA-DOPO.

KEYWORDS: Flame retardants, PMMA, TPP, DOPO, flame spread, pyrolysis.

INTRODUCTION

Reducing the combustibility of polymers is a vital problem, as they are used in various areas of the human activity. One of the ways to reduce the flammability of polymers is to ad flame retardants to their composition. Flame retardants can reduce the flammability of polymeric materials by increasing the ignition delay time, reducing the rate of burning, and reducing flame spread velocity. The problem of determining the location of the flame retardant' action - the condensed phase or the gas phase, is one of the key issues regarding the mechanism of flame retardancy. A flame retardant may affect the thermal decomposition of a polymer, as well inhibit the oxidation of volatile gaseous products [1]. Phosphorus-containing flame retardants may reduce flammability of a polymer both by forming a carbonaceous frame (char) in the condensed phase and by inhibiting gas-phase reactions. There are three mechanisms by which the formation of char reduces the combustibility of solid fuel:

1. Part of the carbon (and hydrogen) remains in the condensed phase, thus reducing the yield of gaseous products upon decomposition;

Proceedings of the Ninth International Seminar on Fire and Explosion Hazards (ISFEH9), pp. 767-775
Edited by Snegirev A., Liu N.A., Tamanini F., Bradley D., Molkov V., and Chaumeix N.
Published by Saint-Petersburg Polytechnic University Press
ISBN: 978-5-7422-6498-9 DOI: 10.18720/spbpu/2/k19-38

2. The char layer of low thermal conductivity serves as a thermal insulator for the polymer, and
3. The dense char acts as a physical barrier for the yield of gaseous fuel degradation products [2].

In the literature, there are practically no studies of flame propagation over polymers with additives of flame retardants, including investigation of the thermal and chemical structure of their flame. In this paper, non-charring cast PMMA was chosen as the object of the study. Its mechanism of thermal decomposition and combustion was widely studied [3-7]. Cast PMMA is widely used as a polymeric material. The purpose of this work was to explore the mechanism of action of flame retardants DOPO and TPP on reducing the flammability of cast PMMA on the basis of comprehensive physical and chemical studies, primarily the studies of flame propagation along the PMMA surface with additives of TPP and DOPO, including investigation of its flame structure and thermal decomposition.

EXPERIMENTAL

Cast PMMA slabs with a width of 100 mm wide, 5 mm thick and 200 mm long were investigated. The samples were prepared as follows. The cast PMMA was prepared by polymerization of MMA monomer at 60 ^{o}C for 30 min in the presence of Dibenzoyl Peroxide. The prepolymer was heated at 90 ^{o}C for 3 h in the oven to get the cast PMMA. Then, the cast PMMA was crushed, and dried at 100 ^{o}C overnight to remove the unreacted monomers. The cast PMMA pellets were then hot pressed at 190 ^{o}C under 10 MPa for 3 min. To obtain PMMA+10%TPP the following technique was provided. The pellets of cast PMMA were crushed and mixed with TPP flame retardant. Then the mixture was heated and extruded into special molds in the extruder and hot pressed at a pressure of 100 bar. The cast PMMA-DOPO was prepared by polymerization of MMA monomer with 10 wt% DOPO. DOPO was dissolved with MMA at room temperature under stirring, and then heated to 60 ^{o}C for 30 min in the presence of Dibenzoyl Peroxide (1.5 g). The prepolymer was heated at 90 ^{o}C for 3 h in the oven to get the cast PMMA-DOPO. Then, the cast PMMA-DOPO was crushed, and dried at 100 ^{o}C overnight to remove the unreacted monomers. The cast PMMA-DOPO pellets were then hot pressed at 190 ^{o}C under 10 MPa for 3 min. The slabs were inserted into a metal frame, which served to prevent flame spread along the slab sides. The samples were placed on a thermally insulating board with thermal conductivity of 0.15 W/(m$\cdot$K) and specific heat of 950 J/(kg$\cdot$m$\cdot$K). The board with the specimen was mounted on an electronic balance. To determine the flame spread rate, horizontal lines were drawn on the upper surface of the sample every 10 mm. On the upper surface of the slabs, at a distance of 1 cm from the edge, an incombustible heat insulating plate was installed to protect the sample from the flame. After ignition with a propane-butane burner, the plate was removed. To measure the flame temperature, a thermocouple was used, which was made from Pt and Pt + 10% Rh wires with a diameter of 50 μm. The diameter of the junction was 70±10 μm, and the thermocouple shoulders were 5.5 mm long. The thermocouple was covered with a layer of SiO_2 to prevent catalytic reactions on the surface. It was installed on a three-dimensional positioning system with three stepping motors, allowing the thermocouple to be moved in three coordinates. In the paper, the coordinate along the sample width was fixed at the position of the middle of the samples. The thermocouple and the electronic weights were recorded using an E14-140-M ADC. The correction of the thermocouple measurements due to radiation was calculated by using the formula proposed in [8]. Temperature measurements were carried out by continuous scanning, moving the thermocouple from top to bottom to the surface of the burning plate. The temperature profiles were recorded every 5, 2, 1 mm for PMMA, PMMA-DOPO and PMMA-TPP correspondingly during the flame propagation over the surface. The pre-installed program was used to fix the position of the flame front with respect to the thermocouple along X axis (Fig. 1) during scanning. Obtained temperature profiles were used to determine the temperature gradients in the gas phase near the surface of the slab. Based on the obtained gradients, the conductive heat flux from the flame to the surface was calculated. A quartz microprobe, connected with a quadrupole mass-spectrometer, was used for sampling the flame online, allowing species to be identified in the flame and their concentration profiles. Thus, the chemical structure of the flame was determined. The mole fractions of methyl methacrylate (MMA), TPP, DOPO, O_2, N_2, CO, CO_2, H_2O in the flame for the test samples were determined. The microprobe and the thermocouple were moved with the speed of 2 mm/s along the height (Y axis). To fix the position of the flame front during the species sampling procedure a movable platform was used. It moved the sample during the combustion with the same velocity as the flame spreading velocity but in opposed direction. All the measurements have been conducted after a stationary flame to be established. The schematic of the setup used is shown in Fig 1.

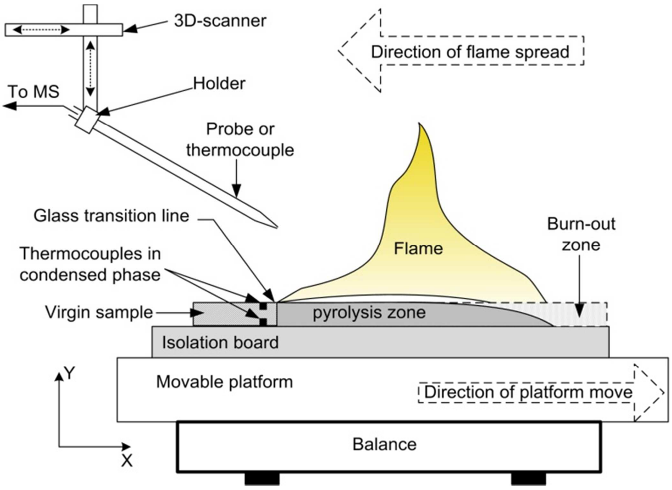

Fig. 1. The experimental apparatus for studying horizontal flame spread over solid fuel and for measuring of temperature and species concentration profiles.

RESULTS AND DISCUSSION

Table 1 presents the burning characteristics of cast PMMA slabs without addition of flame retardants and with 10% TPP and 10% DOPO additives.

The velocity of flame propagation along the cast PMMA surface, measured in this study was found to be close to that obtained for cast PMMA in other works [9-10]. We have also investigated the cast PMMA-DOPO*, prepared as follows. The cast PMMA-DOPO* was prepared by polymerization of MMA monomer with 10 wt% DOPO. DOPO was dissolved with MMA at room temperature under stirring, and then heated to 60 ^oC for 30 min in the presence of Dibenzoyl Peroxide (1.5 g). Afterwards, the mixture was cooled down to room temperature in the water bathing and then poured into a glass mould. The mould was put in the oven and then heated to 60 ^oC for 12 hours and 90 ^oC for another 2 hours. Then the PMMA samples were taken out from the glass mould. After this plate 5 mm thick were cut them into plates 200x100 mm. Comparison of the combustion characteristics of the cast PMMA-DOPO* and the cast PMMA-DOPO (the flame spread rate, the width of the pyrolysis zone, etc.) has demonstrated their identity.

Table 1. Combustion characteristics for slabs with various additives

	L^a, cm	$v_m{}^b$, g/s	v^c, mm/s	h^d, cm	$H_p{}^e$, J/g	Q^f, MJ/m^2	P^g, W	$T_{\max,\,in}{}^h$, °C	$T_{\max,\,ox}{}^i$, °C	$T_{surf}{}^j$, °C
cast PMMA	10	0.078	0.12	20	1040	100	54	372	277	410
cast PMMA +10% TPP	4	0.054	0.075	9	802	82	31	372	305	430
cast PMMA +10% DOPO	1	0.021	0.033	3	897	75	13	382	369	430

[a] L – length of the pyrolisis zone; [b] v_m – mass loss rate; [c] v – flame spread rate; [d] h – the flame height; [e] H_p – heat of pyrolysis; [f] Q – total heat release determined in cone calorimeter tests; [g] P – the total conductive heat flux from the flame to the polymer burning surface; [h] $T_{\max,\,in}$ – the temperature of the DTG curve maximum pyrolisis rate in inert medium (Fig. 8); [i] $T_{\max,\,ox}$ – the temperature of the DTG curve maximum pyrolisis rate in oxidative medium (Fig. 8); [j] T_{surf} – the burning surface temperature.

Addition of flame retardants led to a decrease in the flame propagation rate, the mass burning rate of the samples, the length of the pyrolisis zone, and the flame height. It can be seen from Table 1 that for the same percentage of the additive, the flame retardant DOPO has a greater retardancy effect than TPP. It follows from Fig. 2 that for samples with and without additives a steady state is reached almost simultaneously - after about 800 seconds of combustion.

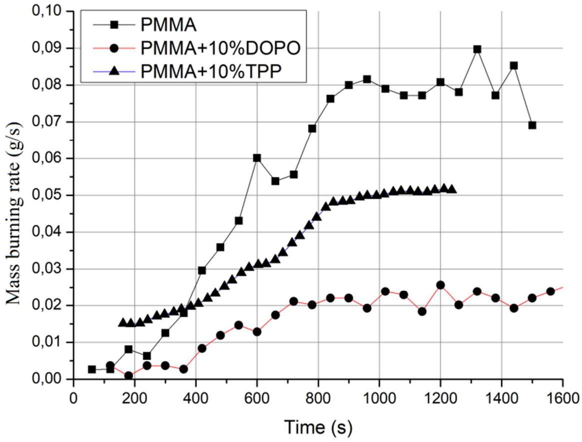

Fig. 2. The dependence of mass burning rate on time for cast PMMA and cast PMMA with TPP and DOPO additives.

Figure 3 shows the temperature profiles for PMMA, PMMA-TPP and PMMA-DOPO samples as a function of the distance from the flame front (the flame front is taken to be 0). Negative X values refer to the non-flame zone, and positive values refer to the flame zone. It can be noted that only in the case of PMMA + 10% TPP, high temperature is observed ahead of the flame front, which leads to a large heat flux (Fig. 4).

The total conductive heat flux from the flame, marked as *P* in Table 1, has been obtained by integrating the conductive heat flux over the combustion zone. With the addition of fire retardants, *P* decreases, and in the case of DOPO, the decrease is more noticeable than in the case of TPP. However, it can be seen from the Fig. 4 that at the flame front the conductive heat flux on the burning surface from the flame of PMMA-TPP is higher than that of PMMA and much higher than that of PMMA-DOPO. The heat flux for PMMA-TPP decreases to 10 kW/m^2 at a distance of 5 mm from the flame front, whereas for PMMA it remains at the level of 10 kW/m^2 almost to the end of the pyrolysis zone. In the case of PMMA-DOPO, the heat flux decreases to zero at a distance of 13 mm from the flame front. Figure 5 shows mole fractions of oxygen in the flame front during combustion of PMMA, PMMA + 10% TPP and PMMA + 10% DOPO.

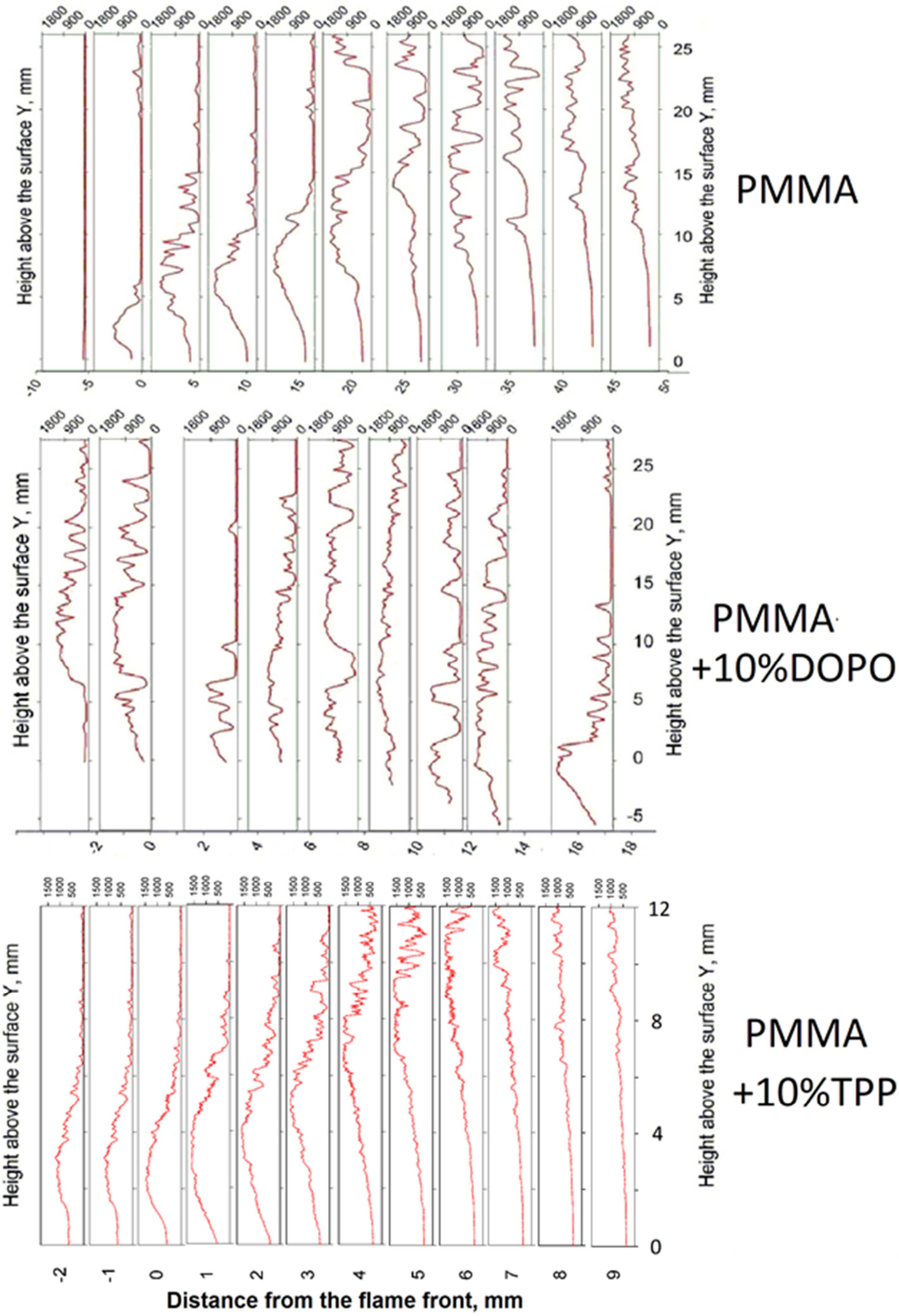

Fig. 3. Vertical temperature profiles of cast PMMA, cast PMMA + 10% TPP and cast PMMA + 10% DOPO at different distances from the flame front. The initial surface level is taken to be 0 along Y axis.

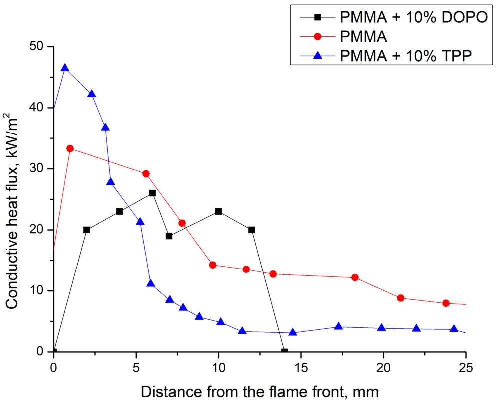

Fig. 4. Conductive heat fluxes for PMMA, PMMA-TPP and PMMA-DOPO.

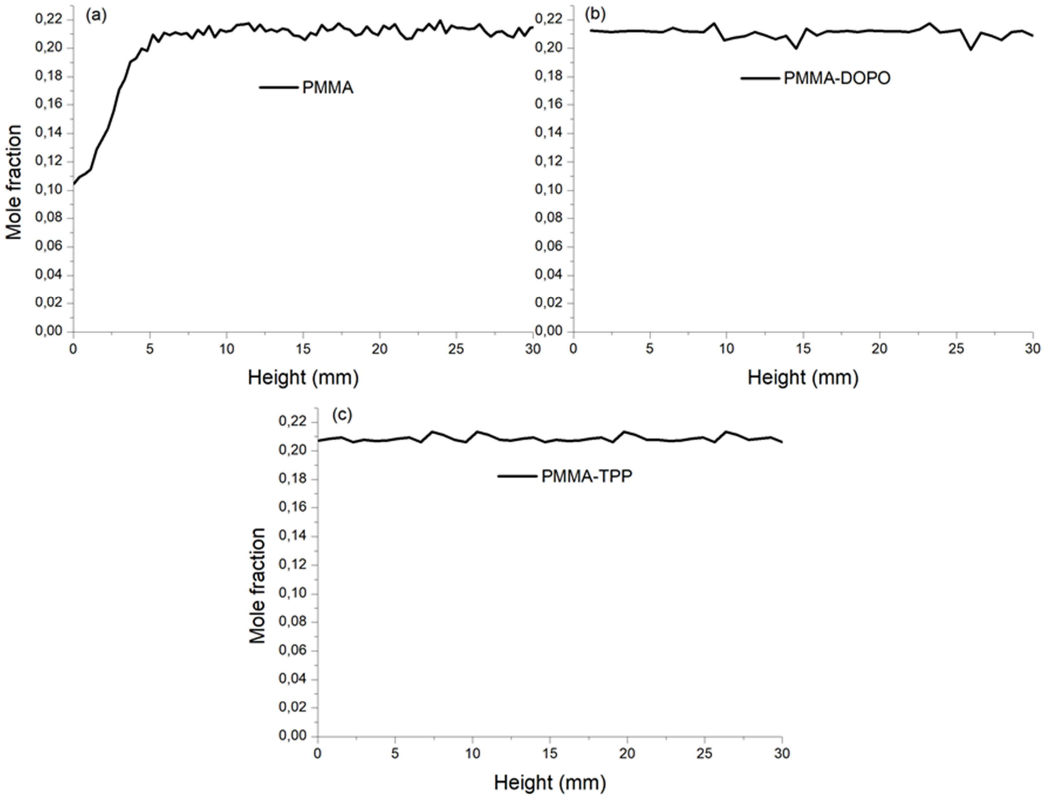

Fig. 5. Vertical profiles of mole fractions of oxygen at the flame front (a) for PMMA, (b) PMMA-DOPO and (c) for PMMA-TPP.

Figures 7 and 8 present thermogravimetric (TG) data for PMMA, PMMA-TPP and PMMA-DOPO samples in inert and oxidizing environment. The influence of the medium can be seen from the graphs: in the N_2 atmosphere, the maximum thermal decomposition rate of PMMA and PMMATPP coincide, and in air, PMMA decomposes more rapidly. In the oxidizing environment, the decomposition of PMMA takes place in two stages, whereas in the inert one there are only one. In the case of PMMA with additives in the oxidizing environment, the decomposition also becomes more complicated - there are several (2 or 3) stages of thermal decomposition. The temperatures at which the pyrolisis rate reaches its maximum are presented in Table 1.

Addition of DOPO reduces the pyrolysis rate of PMMA in an inert medium, whereas the TPP additive does not have this effect. In the presence of oxygen, the pyrolysis rate increases significantly for PMMA and PMMA-TPP, while for PMMA-DOPO it is insignificant. In the case of PMMA-TPP, greater heat flux near the flame front is observed than in the case of PMMA. This can be explained by the fact that there is a greater amount of oxygen near the surface in the flame front of PMMA-TPP than in the front of the PMMA flame. At the same time, in the oxidizing environment, according to the thermal analysis data, the degradation rate of PMMA-TPP (the maximum pyrolysis rate is 305 °C) is greater than for PMMA in an inert medium (maximum pyrolysis rate is 372 °C).

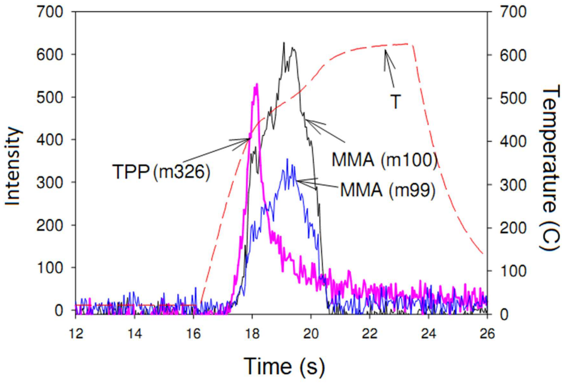

Fig. 6. Differential mass spectrometric thermal analysis (DMSTA) data for PMMA-TPP slab. TPP and MMA peaks were recorded. The heating rate – 150 K/s.

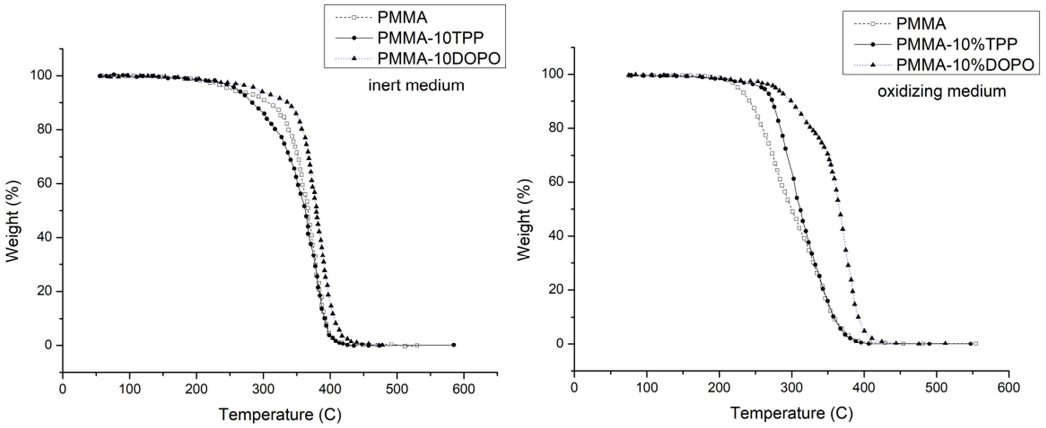

(a) (b)

Fig. 7. TG curves for PMMA, PMMA-TPP and PMMA-DOPO. (a) inert media; (b) oxidizing meda.

We estimated flame propagation rate over the cast PMMA, PMMA-TPP, and PMMA-DOPO slabs using the heat transfer equation [12],

$$\int_0^l q\,dx = v\rho h[H_p + C_p(T_s - T_o)]\,, \tag{1}$$

where q is the total conductive heat flux to the surface (W/m^2), v is the flame spread rate (m/sec), ρ is the density of the solid (kg/m^3), $h = h_0 - h_b$ is the burned sample thickness (m), h_0 is the initial thickness and h_b is the thickness after burnout, l is the pyrolysis length along the burning surface (m), H_p is the heat of pyrolysis (J/kg), C_p is the heat capacity (J/(kg·K)), T_s is .he averaged surface temperature (K) and T_0 is the ambient temperature (K). Measurements of the surface temperature showed that it did not change with addition of the flame retardants within the error of the experiment, being equal to about 400 °C. Equation (1) includes radiant, conductive, and convective heat fluxes to the surface of the polymer, as well as a heat flux carried away by radiation from the surface. Since in this paper only conductive heat fluxes to the surface were measured, the estimation of the combustion rate was based on these quantities. According to the calculation, the flame propagation rate decreased by 2.7 times with addition of DOPO and by 1.7 times with addition of TPP, whereas according to the experimental data these values were 3.6 and 1.6 times, respectively.

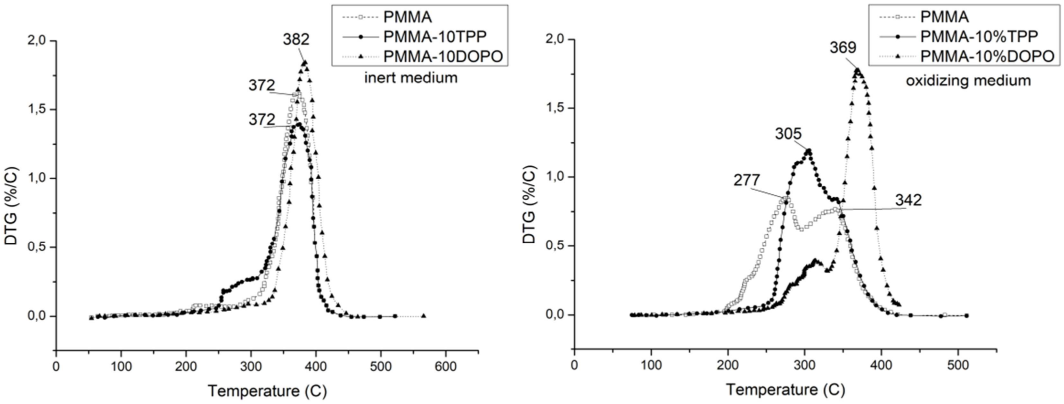

(a) (b)

Fig. 8. DTG curves for PMMA, PMMA-TPP and PMMA-DOPO. (a) inert media; (b) oxidizing media.

CONCLUSIONS

A comprehensive experimental study of the effect of flame retardants DOPO and TPP on the flammability of cast PMMA slabs was carried out. It was found that addition of flame retardants leads to a decrease in the heat flux from the flame to the fuel, the width of the pyrolysis zone, the mass burning rate, the flame propagation velocity, the flame height, and the total heat release. It was found that in the flame front, the heat flux for samples with TPP additive is higher than for samples without additives and samples with DOPO. Due to the presence of oxygen near the flame front, it affects the rate of polymer degradation and thus the heat flux from the flame to the surface in the flame front. Moreover, for PMMA-TPP this effect is greater than for PMMA and much greater than for PMMA-DOPO Far from the flame front, oxygen is absent, and addition of DOPO leads to decrease of the degradation rate of PMMA, whereas addition of TPP does not affect the decomposition rate of the polymer, according to TG data obtained in inert medium. This explains the dependence of the heat fluxes on the distance to the flame front for the investigated samples. Thus, it was found that TPP and DOPO affect the flammability of cast PMMA both in the gas and condensed phases.

ACKNOWLEDGEMENTS

This work was supported by the RFBR under Grants #16-58-53128 and by the NNSF of China under Grant 51120165001.

REFERENCES

[1] C.P. Fenimore, G.W. Jones, Phosphorus in Burnt Gas from Fuel-Rich Hydrogen-Oxygen Flames, Combust. Flame 8 (1964) 133–137.

[2] T. Kashiwagi, Polymer combustion and flammability role of the condensed phase, Proc. Combust. Inst. (1994) 1423-1437.

[3] A. Ito, T. Kashiwagi, Temperature measurements in PMMA during downward flame spread in air using holographic interferometry, Proc. Combust. Inst. (1988) 65-74

[4] M. Zarzecki, J.G. Quintiere, R.E. Lyon, T. Rossmann, F.J. Diez, The effect of pressure and oxygen concentration on the combustion of PMMA, Combust. Flame 160 (2013) 1519–1530.

[5] T. Delzeit, L. Carmignani, T. Matsuoka, S. Bhattacharjee, Influence of edge propagation on downward flame spread over three-dimensional PMMA samples, Proc. Combust. Inst. 37 (2019) 3203-3209.

[6] T.-Y. Tsai, M.-J. Lin, C.-W. Chang, C.-C. Li, Morphology and properties of poly(methyl methacrylate)/clay nanocomposites by in-situ solution polymerization, J. Phys. Chem. Solids 71 (2010) 590–594.

[7] O.P. Korobeinichev, M.B. Gonchikzhapov, A.G. Tereshchenko, I.E. Gerasimov, A.G. Shmakov, A.A. Paletsky, A.I. Karpov, An experimental study of horizontal flame spread over PMMA surface in still air. Combust. Flame 188 (2018) 388-398.

[8] A.V. Singh, M.J. Gollner, Local Burning Rates and Heat Flux for Forced Flow Boundary-Layer Diffusion Flames, AIAA J. 54 (2016) 408-418.

[9] A.C. Fernandez-Pello, F.A. Williams. Laminar flame spread over PMMA surfaces, Proc. Combust. Inst. (1975) 217-231.

[10] A. Ito, T. Kashiwagi, Characterization of flame spread over PMMA using holographic interferometry sample orientation effects, Combust. Flame 71 (1988) 189-204.

[11] O.P. Korobeinichev, L.V. Kuibida, A.A. Paletsky, A.G. Shmakov, Molecular-beam mass-spectrometry to ammonium dinitramide combustion chemistry studies, J. Prop. Power 14 (1998) 991-1000.

[12] L. Jiang, C.H. Miller, M.J. Gollner, J. Sun, Sample width and thickness effects on horizontal flame spread over a thin PMMA surface, Proc. Comb. Inst. (2016) 1-8.

Measurement of Thermal Structure inside Flame Front with a Melting Layer for Downward Flame Spread of XPS Foam

Luo S.F., Xie Q.Y.*, Da L.J.

State Key Laboratory of Fire Science, University of Science and Technology of China,
Hefei, 230027, China
**Corresponding author's email: xqy@ustc.edu.cn*

ABSTRACT

Thermal structure of flame front during downward flame spread was experimentally measured with the help of the coordinate transformation method for XPS foam with a thickness of 1.6 cm. Temperature and temperature gradient in the condensed phase, the shape of the molten liquid of XPS fuel, and heat flux through the solid, were obtained. The results show that temperature and temperature gradient gradually decrease from the surface to the inner XPS foam. The temperature distribution also illustrates the shape of the interface between melting liquid and solid. It shows that the interface between the solid and the liquid is flatter in the initial stage than that in the later stage, and the slopes of the solid-liquid interface are in the range about 30-50 degrees. The results also show that the melting layer is thinnest near the flame front and it is thicker for the location farther away from the flame front in the burning area. The molten liquid adheres to the back wall with the downward burning of the XPS sample, which increases the area of the burning surface at the top of the melting layer, and consequently, increases the flame height. In addition, the vertical heat conduction from the melting layer to the unburned zone is calculated by the integration of heat flux along the solid-liquid interface, and the result shows that the average heat flux through solid here is about 580 W/m^2.

KEYWORDS: XPS foam, downward flame spread, melting layer, thermal structure.

NOMENCLATURE

C	The curve of solid-liquid interface
k_s	heat conduction coefficient (W/(m·K))
q''_s	heat conduction through solid phase(W/m^2)
T_m	melting temperature (K)
T_0	initial temperature (K)
t	time (s)
w	width of the XPS sample (m)
x	x axis of static coordinate system
x'	x axis of moving coordinate system
x_c	x position of thermocouple tip on static coordinate system
x_f	x position of flame front on static coordinate system
y	y axis of static coordinate system
y'	y axis of moving coordinate system
y_c	y position of thermocouple tip on static coordinate system
y'_c	y position of thermocouple tip on moving coordinate system

Greek

δ	thickness of XPS sample (m)

Subscripts

0	ambient
c	thermocouple
f	fire
m	melting

Proceedings of the Ninth International Seminar on Fire and Explosion Hazards (ISFEH9), pp. 776-785
Edited by Snegirev A., Liu N.A., Tamanini F., Bradley D., Molkov V., and Chaumeix N.
Published by Saint-Petersburg Polytechnic University Press
ISBN: 978-5-7422-6498-9 DOI: 10.18720/spbpu/2/k19-119

INTRODUCTION

Extruded polystyrene (XPS) foams have been widely used as thermal insulation layers in the building wall and roof, refrigeration house and duct of air condition. The fire hazard of XPS foams is a big threat for not only the residents in the buildings but also the firefighters. The Beijing TVCC fire in 2009 is considered as one of the terrible fire accidents with the fastest spread velocity, which is induced by the XPS burning [1]. There are shrinkage, melting, dripping and flowing behaviors during the burning and flame spread of XPS foams. As a typical thermoplastic foam, its burning behavior and flame spread controlling mechanism of vertical or horizontal XPS sheet is obviously different with those traditional solid fuels, such as wood, paper and even PMMA [2-5]. As suggested in previous works, the downward burning of XPS foam is not a conceptually surface flame spread but a downward moving pool fire [1, 6].

The heat transfer, mass transfer and chemical reaction mechanisms in the local region of the flame front play a key role in the flame spread modeling of solid materials. Most of previous experimental works for the controlling mechanism of flame spread of various solid materials mainly focused on the heating of the unburnt surface by flame front, as well as the thermal and flow parameters measurement in the adjacent gas region [7-11]. Recently, Rakesh Ranga and Vasudevan Raghavan investigate the structure and spread rate of flames over PMMA slabs and analyzed flame structure and the temperature field in the gas phase with a 3D-scanning device [12]. For the detailed heat and mass transfer inside the solid materials, especially in the local region of flame front, rare experimental data are available because of the inner measuring difficulty for opaque thick solids and moving behavior of the flame front. However, it is not difficult to inserting thermocouples into the porous polymers. They are good sensors for measuring the temperatures in the burning XPS foam sample. On the other hand, more thermocouples in the XPS foam would be certainly helpful to measure more detailed inner temperatures but also make more disturbance to the sample burning behaviors at the same time. In this work, a method was developed to measure the inner temperatures near the flame front with only a few thermocouples. The detailed temperature field in the condensed phase and the heat transfer mechanism were analyzed for the flame front of XPS foam downward burning based on this method.

EXPERIMENT AND RESULTS

Method for inner thermal structure measurement

The main idea for continuous temperature measurement is based on the relative motion principle. The principle of the method is that the downward movement of the flame relative to the thermocouples can be transformed as the upward movement of the thermocouples relative to the flame. Figure 1 gives the sectional side view for the downward flame spread of XPS foam and two coordinate systems, namely, a static one and a moving one. The origin of the static coordinate system is on the top of XPS foam. The other coordinate system is moving together with the flame front with its origin always on the moving flame front position, which is continuously monitored by a camera. Thermocouples are inserted into the XPS foam. As shown in Fig. 1(a), in the static coordinate system (x, y), the flame front will pass the thermocouple as the downward burning of XPS foam continues. However, in the moving coordinate system (x', y'), the downward burning is transferred as another behavior as shown in Fig. 1(b). That is, the flame is considered as static, the thermocouple scans to the flame region from the preheat zone and monitors the time-dependent temperature. In this case, the measured time-dependent temperatures by a fixed thermocouple are transformed as space-dependent temperatures in the flame front region by coordinate system transformation with the help of the camera. Therefore, the temperature along the flame spreading direction near the flame front can be measured. This is the main idea for the inner temperature measurement in this work. In this way, a vertical temperature distribution of the flame front region can be measured by one thermocouple. As shown in Fig. 1(a), for a thermocouple in XPS foam, whose location is (x_{c-i}, y_{c-i}) in the static coordinate system, the measured temperatures can be described as

$$T(x_{c-i}, y_{c-i}) = T(t), \tag{1}$$

where T is the measured temperature by the thermocouple, K, and t is a moment during the XPS foam downward burning, s.

At the moment t, as shown in Fig. 1(a), the location of flame front in the static coordinate system can be addressed as $(x_{f(t)}, 0)$, which is the origin of the moving coordinate and can be continuously measured by a camera. Therefore, the temperatures along the locations with $y = y_{c-i}$ in the flame front region can be achieved.

$$T'(x', y'_{c-i}) = T_{x_{c-i}, y_{c-i}}(t),\ x' = x_{c-i} - x_{f(t)},\ y'_{c-i} = y_{c-i}, \tag{2}$$

where T' is the transformed temperature at location (x', y'_{c-i}) in moving coordinate system, K. $T_{x_{c-i}, y_{c-i}}(t)$ is the measured temperature by the thermocouple at location (x_{c-i}, y_{c-i}) at the moment *t*. $x_{f(t)}$ is the x-coordinate of flame front at the moment t. The constant x_{c-i} and y_{c-i} are the x-coordinate and y-coordinate of the thermocouple in the static coordinate system.

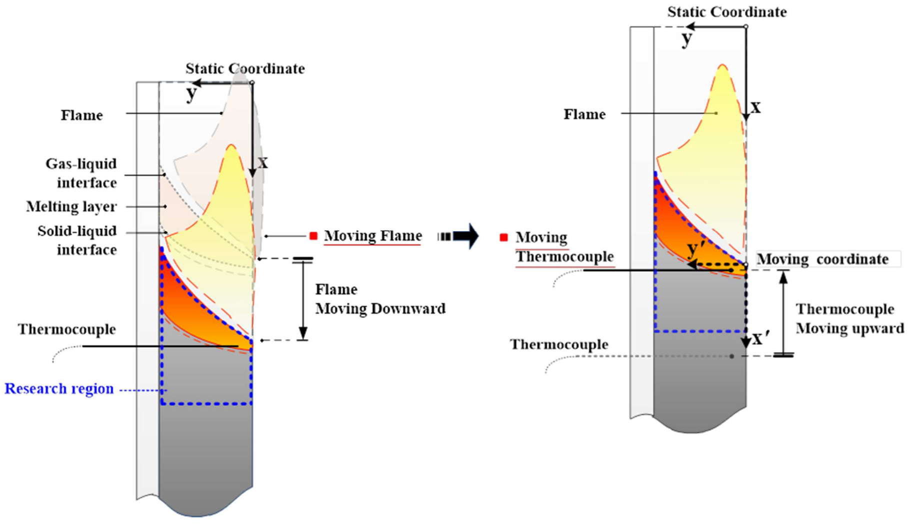

Flame spread downward pass through the thermocouple
(a)

Thermocouple upward scan throughout the flame region
(b)

Fig. 1. Schematic of time-space transforming principle in different coordinate system. (a) Downward moving of flame front in a static coordinate system; (b) Upward scanning of thermocouple in moving coordinate system.

Equation (2) shows the method for measuring the vertical temperatures along the flame front through just one thermocouple in the XPS foam by continuously recording the time-dependent temperature. It is suggested that the camera for monitoring the flame front plays a key role in the “time-space” coordinate transformation. Here several thermocouples at different *y*-coordinates in the XPS foam are used to measure the temperatures at varied distances to the vertical XPS foam surface. It should be noted that the method developed here is based on the hypothesis of the stable thermal structure of flame spread. As the downward burning of XPS foam is a downward moving pool fire, the temperature distribution in the flame zone varies greatly with time because of the turbulence burning and flame pulsation of the pool fire. Therefore, the temperature there cannot be accurate measured in this way. However, during a short downward flame spread stage, the temperature distribution in the preheated solid and the melting region, as shown in the blue frame in Fig. 1, can be reasonably considered to be stable. Therefore, the temperatures in the XPS foam with condensed phases are the mainly measured here. More details about this method will be shown in the following experimental design and results.

EXPERIMENT

Figure 2 gives the schematic of the experimental setup for the inner temperature measurement during the downward burning of XPS foam. The XPS foam, which is 80cm long and 20cm wide, is vertically adhered to gypsum boards on its back and two sides. The gypsum board is a kind of good thermal insulation material, so the heat loss from the XPS sample to the steel frame is not considered in the heat transfer calculation here.

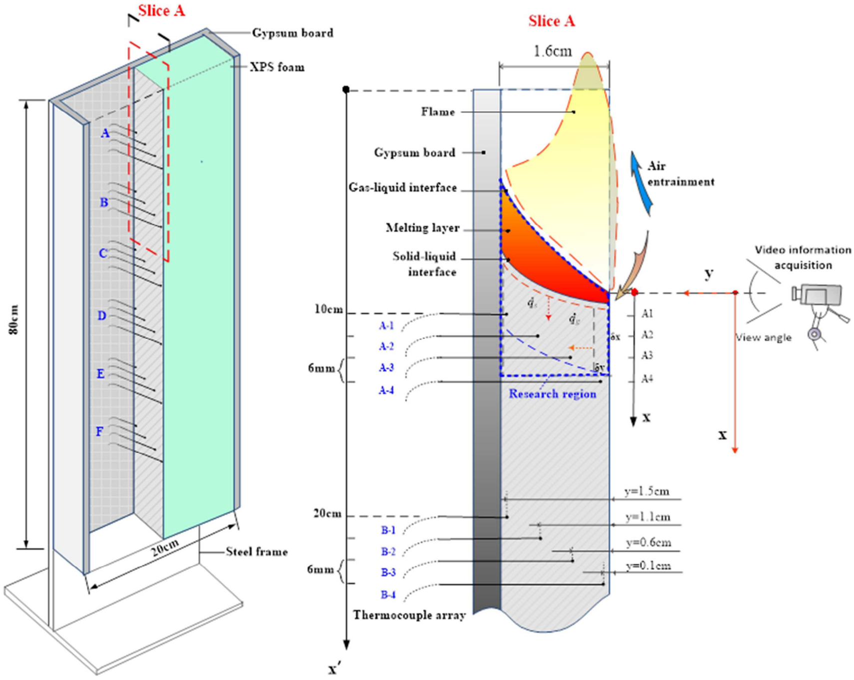

(a) (b)

Fig. 2. (a) Schematic of the experimental setup for downward burning of XPS foam with thickness of 1.6 cm; (b) The detailed locations for the six groups of thermocouples.

As shown in Fig. 2(a), 24 thermocouples are located in the central section of the XPS foam. They are divided into six groups for measuring the temperature distribution ahead of the flame front at six stages, respectively. They are Group A, B, C, D, E and F. Fig. 2(b) gives more details about the thermocouples locations in the top two groups, namely, Group A and Group B. As shown in Group

A, four thermocouples were inserted into the XPS foam from the backside with different depths. The distances of the four thermocouple tips with the front surface of XPS foam are respectively 1, 6, 1.1, and 1.5 mm. On the other hand, the vertical distance between the adjacent two thermocouples is 6 mm. The K-type thermocouples with the diameter of 1 mm were used in our research. It is well known that there are less thermal inertia and physical disturbance for thermocouples with a smaller diameter. However, due to the insufficient hardness of the smaller diameter thermocouples, it is not easy to fix the positions of thermocouples when the thermocouples are inserted into the XPS sheets. On the other hand, since the research region of this study is mainly concentrated on the condensed phase with slowly changing temperature, the disturbance of thermocouples to the thermal behavior of fuel is not that much here. According to the tilted shape of the melted layer which will be shown in the section of result and discussion, the inserting depth of the thermocouples at lower positions in Group A is larger. In this way, the interference of the thermocouples on the downward burning of XPS foam is reduced. As shown in Fig. 2(b), the distance between the first thermocouple in Group A and the top of the XPS foam sample is 10 cm. The distance between the two groups of thermocouples is also 10 cm. In this work, experiments were done for XPS foam with thicknesses of 1.6 cm. As shown in Fig. 2(b), the inserting depths of the four thermocouples in each group are 0.1, 0.6, 1.1, and 1.5cm, respectively. Namely, the thermocouples tips are set at 4 positions of $y = 1.5$, 0.9, 0.5, 0.1 cm, where y is the distance from the front surface of the XPS sheet.

As addressed above, a HD camera in front of the XPS foam is used to monitor the downward burning behavior, especially the location of the flame front at the vertical center line. Table 1 gives the physical properties of the XPS foam, which is the typical product commercially available in China. The downward flame spread of XPS foam is ignited with a line of ignition flame on the top.

Table 1. Physical properties of XPS foam

Density of solid foam, kg/m^3	Conductivity, W/(m·K)	Specific heat, J/(kg·K)	Melting temperature, K	Evaporation temperature, K
29.03	0.028	1500	394	503

RESULTS AND DISCUSSIONS

Several runs were carried out for the downward flame spread of XPS foam for repeatability. Here, the main focus will be the temperature processed by coordinate transformation. As discussed in the previous section, the temperature in the flame zone is just the trend of temperature. In this research, the research region is mainly the condensed phase. During a short downward flame spread distance from the beginning preheated solid to the end of the melting region, the temperature in the condensed phase is approximately considered to be relatively stable. As shown in Fig. 2, the 6 thermocouple groups were arranged along the flame spread direction to obtain the temperature distribution at 6 different flame spread stages.

Figure 3 shows a serial of photos of flame near the 6 thermocouple groups in the plane perpendicular to the XPS sample. The thermocouple groups are just under the leading edge of the central flame. The flame leading edge is approximately one-dimensional throughout the experiment, and variation is probably due to surface irregularities and other random factors. It shows that the flame height increase with the downward burning from group A to F, which will be discussed later. Additionally, since the thermocouples were inserted along the vertical symmetrical centerline of the XPS sample, the video camera was used to monitor only the leading edge position of the central flame for the coordinate transformation.

The thermocouples may have some interferences with the heat transfer and the shape of the melting layer. To estimate the disturbances introduced by thermocouples, Fig. 4 gives leading edge position and flame spread rate of the central flame. The positions of the 6 thermocouple groups are also marked on the curve of the leading edge position of the central flame, and the positions of the 6 thermocouple groups are 10, 20, 30, 40, 50, 60 cm, respectively. The flame spread rate over XPS sample is found to be about 0.18cm/s. Although the instantaneous spread rate fluctuates slightly, the averaged spread rate remains relatively steady near the positions with thermocouples or without thermocouples. Therefore, the disturbances introduced by the thermocouples are reasonably not considered in this study.

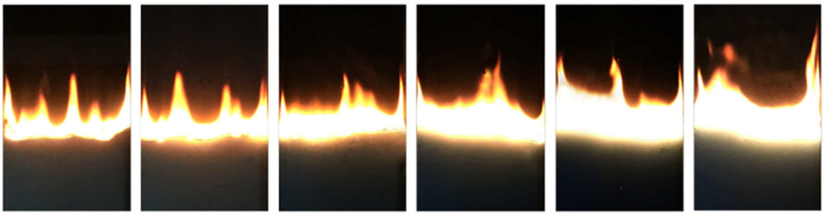
Group A Group B Group C Group D Group E Group F

Fig. 3. Photos of flame near the thermocouple groups.

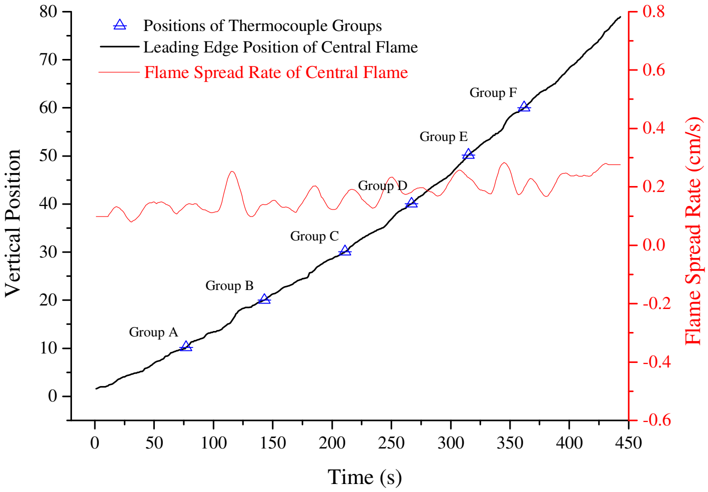

Fig. 4. Downward flame spread Distance and the flame spread rate of the central flame of XPS sample.

Figure 5(a) gives a typical result of the temperature profile measured by the thermocouples of Group D. Note that the x coordinate is not the time, but the difference of vertical position of the thermocouple and the flame front point (see Eq.(2)). The $x = 0$ represents the flame front location based on the video measurement, $x > 0$ defines the preheated zone, and the burning zone is located at $x < 0$. It is seen that the temperature increases quickly when the thermocouple cross the flame zone. The result shows that the temperature of the condensed phase decreases from the surface to the inner solid. Moreover, near $x = 0$, the temperature near the surface starts to rise before the flame front, while the temperature near the backside of solid rises after the flame front. This indicates that the preheat front in the solid phase is tilted outwards. Fig. 5(b) gives the vertical temperature gradient derived by the temperature difference of adjacent nodes in the x-axis direction in Fig. 5(a). It shows that the temperature gradient decrease from the surface to the interior of the XPS fuel, which means that the downward heat transfer in the condensed phase is concentrated in the area close to the solid surface. It can be explained as the effect of the air entrainment of flame and the difference in oxygen distribution. That is, oxygen in the entrainment air firstly contacts the outer surface of the flame and reacts with the combustible gas generated by the pyrolysis. From the incoming surface to the inner dense material, the oxygen gradually depletes as the oxygen reacts with the pyrolysis gas. Correspondingly, the downward heat transfer through the gas is weakened. Therefore, the temperature gradient at the outer surface of the material is higher than the temperature gradient of the inner side.

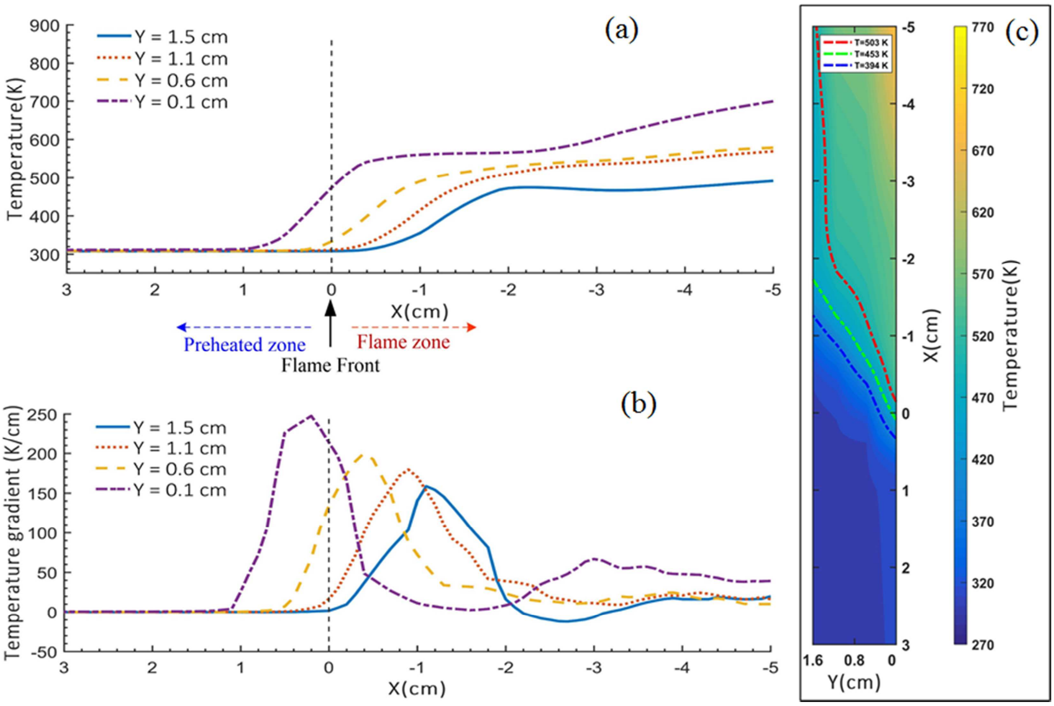

Fig. 5. (a) Temperature profiles in condensed phase at different depth Y; (b) Vertical temperature gradient derived by the temperature difference of adjacent node; (c) Temperature distribution obtained by two-dimensional interpolation.

The temperature distribution of the gas phase and solid for solid PMMA has been analyzed by Ito [13] and Hirano [14] with holographic interferometry. However, It may not easy to obtain the temperature distribution inside XPS solid. Here, the two-dimensional interpolation method is used to construct the inner temperature field of solid. Fig. 5(c) shows the temperature distribution which is obtained by two-dimensional interpolation of the data in Fig. 5(a). It should be noted that the evaporation temperature is about 503 K, above which is the flame region. The temperature above 503 K is not the accurate value because of flame pulsation and the limitation of the thermocouple response time, and it just represents the trend of temperature in the flame area. Three temperature level lines, melting temperature(394 K), evaporation temperature (503 K) and a middle temperature(453 K), are redrawn in the temperature distribution field. According to the vertical distance between the melting temperature line (394 K) and evaporation temperature line (503 K), the melting layer is thinnest near the flame front and it is thicker for the location farther away from the flame front in the burning area.

In addition, there is a clear inclination along the interface between the solid and liquid phases. As discussed in the experimental section, the connection of the four thermocouple tips is an obliquely downward straight line. Therefore, it allows the thermocouple tips to contact the molten interface almost simultaneously. This improves the measurement accuracy of the molten fuel temperature.

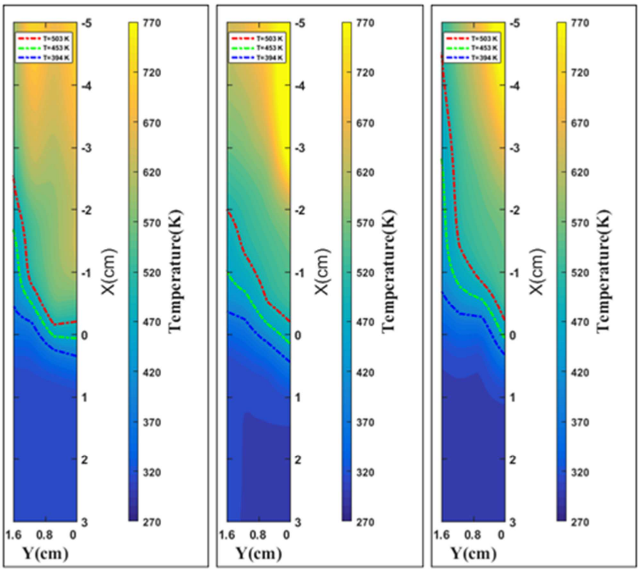

Group A Group B Group C

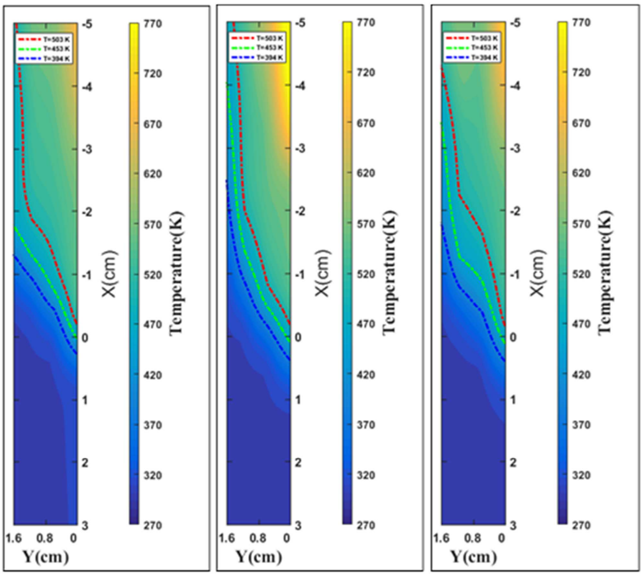

Group D Group E Group F

Fig. 6. Contour of temperature distribution at the flame front region on downward flame spread of XPS sample (Group A-F)

Figure 6 gives the all the results of temperature distribution at the flame front region from Group A to F. The results show that the interface between the solid and the liquid is flatter in the initial stage (Group A-C) than that in the later stage(Group D-F), and the slopes of the solid-liquid interface are in the range about 30-50 degrees. The evaporation temperature lines are getting more inclined after Group D, especially the line segment near the back side. This means that molten liquid adheres to the back wall with the downward burning of XPS sample, which increases the area of the burning surface at the top of the melting layer, and consequently, the flame height, as shown in Fig. 3, increases with the downward burning.

Jiang [15] measured the heat conduction through the solid phase by Fourier's law of heat conduction $q''_{s,c} = k_c \, \partial T/\partial x$, using one thermocouple in solid phase. However, the results of this study show that the temperature and temperature gradient varies greatly from the surface of the sample to the inner solid. Therefore, it cannot be simplified as a one-dimensional heat conduction model. In the case of this research, solid heat conduction into the preheated solid from melting layer through solid $q''_{s,c}$ (W/m^2) can be calculated by the integration of heat flux along the solid-liquid interface

$$q''_s = \int_C w k_s \left(dT(x, y)/dx \right)_{T=T_m} dy \, , \tag{3}$$

where k_s, W/(m·K), is the heat conduction coefficient, w (m) is the width of XPS sample, x (m) and y (m) represent the downward and horizontal direction respectively, T_m (K) and C represent the melting temperature and melting interface curve inside the condensed phase, and $\left(dT(x, y)/dx \right)_{T=T_m}$ means the vertical temperature gradient along the melting interface.

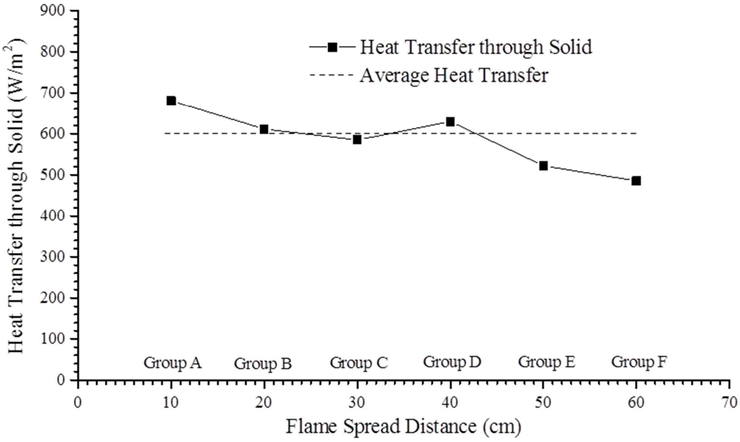

Fig. 7. Heat transfer through solid on downward flame spread of XPS sample.

The temperature profile in Eq. (3) can be obtained from the results of temperature distribution shown in Fig. 6(A-F). Fig. 7 shows the heat fluxes at the solid-liquid interface near the flame front measured by 6 thermocouple groups. As the 6 thermocouple groups are placed at 6 different positions along downward flame spread, the temperature distributions from Group A to F represent the temperature profile at 6 different flame spread distance. In this experimental configuration, the Groups from A to F are corresponding to the flame spread distances from 10 to 60 cm. The result shows that the average heat flux through solid is about 580 W/m^2.

CONCLUSIONS

In this work, a method is developed to measure the detailed inner thermal structure ahead of the flame front for vertically downward burning XPS sample. The time-dependent temperatures directly measured by the thermocouples in the XPS sample were transformed to the space-dependent temperatures along the flame spread direction based on the method. Following characteristics of thermal structure in the condensed phase have been analyzed. Firstly, the temperature distribution in the condensed phase gives the shape of the molten layer, which shows that the interface between the solid and the liquid is flatter in the initial stage than that in the later stage, and the slopes of the solid-liquid interface are in the range about 30-50 degrees. Secondly, the results also show that the melting layer is thinnest near the flame front, and it is thicker for the location farther away from the flame front in the burning area. Moreover, the molten liquid adheres to the back wall of the XPS sample with the downward burning, which increases the area of the burning surface at the top of the melting layer, and consequently increases the flame height. In addition, the vertical heat transfer from the condensed phase to the unburned solid zone is calculated by the integration of heat flux along the solid-liquid interface, and the result shows that the average heat flux through the solid is about 580 W/m^2.

ACKNOWLEDGEMENT

This work was supported by National Natural Science Foundation of China (51476157) and National Key R&D Program of China (2017YFC0805901). The authors appreciate all these supports.

REFERENCES

[1] S.F. Luo, Q.Y. Xie, X.Y. Tang, R. Qiu and Y. Yang, A quantitative model and the experimental evaluation of the liquid fuel layer for the downward flame spread of XPS foam, J. Hazard. Mater. 329 (2017) 30-38.

[2] A.C. Fernandez-Pello, T. Hirano, Controlling Mechanisms of Flame Spread, Combust. Sci. Technol. 32 (2007) 1-31.

[3] A.C. Fernandez-Pello, Flame Spread Modeling, Combust. Sci. Technol. 39 (2007) 119-134.

[4] A.C Fernandez-Pello, F.A. Williams, Laminar flame spread over PMMA surfaces, Proc. Combust. Inst. 15 (1975) 217-231.

[5] I.S. Wichman, Theory of opposed-flow flame spread, Progr. Energy Combust. Sci. 18 (1992) 553-593.

[6] W.G. An, H.H. Xiao, J.H. Sun, K.M. Liew, W. Yan, Y. Zhou, Effects of Sample Width and Sidewalls on Downward Flame Spread over XPS Slabs, Fire Saf. Sci. 11 (2014) 234-247.

[7] B. Comas, T. Pujol, Energy Balance Models of Downward Combustion of Parallel Thin Solid Fuels and Comparison to Experiments, Combust. Sci. Technol. 85 (2013) 1820-1837.

[8] S.Y. Hsu, J.S. T'ien, Flame spread over solids in buoyant and forced concurrent flows Model computations and comparison with experiments, Proc. Combust. Inst. 33 (2011) 2433-2440.

[9] W.C. Park, A. Atreya, H.R. Baum, Experimental and theoretical investigation of heat and mass transfer processes during wood pyrolysis, Combust. Flame. 157 (2010) 481-494.

[10] G.L. Juste, L. Contat-Rodrigo, Temperature field reconstruction from phase-map obtained with moiré deflectometry in diffusion flame on solids, Combust. Sci. Technol. 179 (2007) 1287-1302.

[11] S. Bhattacharjee, A. Simsek, F. Miller, S. Olson, P. Ferkul, Radiative, thermal, and kinetic regimes of opposed-flow flame spread A comparison between experiment and theory, Proc. Combust. Inst. 36 (2017) 2963-2969.

[12] H.R. Ranga, O.P. Korobeinichev, A. Harish, V. Raghavan, A. Kumar, I.E. Gerasimov, A.G. Shmakov, Investigation of the structure and spread rate of flames over PMMA slabs. Appl. Thermal Eng., 130 (2018) 477-491.

[13] A. Ito, T. Kashiwagi, Temperature measurements in PMMA during downward flame spread in air using holographic interferometry, Proc. Combust. Inst. 21 (1988) 65-74.

[14] T. Hirano, K. Sato, Effects of radiation and convection on gas velocity and temperature profiles of flames spreading over paper, Proc. Combust. Inst. 15 (1975) 233-241.

[15] L. Jiang, C.H. Miller, M.J. Gollner, J.H. Sun, Sample width and thickness effects on horizontal flame spread over a thin PMMA surface, Proc. Combust. Inst. 36 (2017) 2987-2994.

Effects of Electric Current and Sample Orientation on Flame Spread over Electrical Wires

Zhao L.Y.[1], Zhang Q.X.[1], Tu R.[2], Fang J.[1], Wang J.J.[1], Zhang Y.M.[1,]*

[1] State Key Laboratory of Fire Science, University of Science and Technology of China,
Hefei, Anhui 230026, China
[2] College of Mechanical Engineering and Automation, Huaqiao University,
Xiamen, Fujian 361021, China
**Corresponding author's email: zhangym@ustc.edu.cn*

ABSTRACT

Experiments were performed to study the effects of electric current and sample orientation on flame spread along the polyethylene (PE) insulation on copper wires. The flame spread rate vs. inclination angle showed a non-monotonic trend i.e., flame spread rate first decreased and then increased as the inclination angle increased. The molten polymer coating flew along the wire during the spread if the wire was inclined. For upward flame spread, a periodic flame spread phenomenon was observed due to the flowing of molten polymer. A sub-flame was observed to spread in the opposite direction to the primary flame. The flowing of molten insulation has little influence on upward flame spread rate. With the increase of the electric current, both the amount of molten insulation and the flame spread rate increased. The downward spread was shown to be more susceptible to the electric current in this study. For downward flame spread, the flowing molten polymer brought heat from the burning region to the preheat region and promoted the flame spread. A flame spread model concerning with both the orientation angle and electric current was developed in this study.

KEYWORDS: Flame spread, electric wire, orientation effect, molten insulation.

NOMENCLATURE

c	constant pressure specific heat (J/(kg·K))
$\bar{h}$	average convection coefficient (W/(m^2·K))
ΔH	latent heat of pyrolysis (J/kg)
I	constant electric current (A)
L_f	flame length (cm)
L_h	flame preheat length (cm)
L_p	pyrolysis length (cm)
Nu	Nusselt number (-)
Q	heat flux (W)
q''	heat flux per unit area (W/m^2)
r	radius (cm)
Ra	Rayleigh number
T	temperature (K)

ρ'	electrical resistivity (Ω·m)
α	thermal diffusivity (m^2/s)
β	volumeric thermal expansion coefficient (K^{-1})
λ	thermal conductivity (W/(m·K))
ε	emissivity (-)
ν	kinematic viscosity (m^2/s)
σ	Stefan-Boltzmann constant (W/(m^2·K^4))
ϕ	inclination angle (grad)
Φ	Joule heat (W)

Subscripts

a	ambient
c	core
f	flame

Proceedings of the Ninth International Seminar on Fire and Explosion Hazards (ISFEH9), pp. 786-795
Edited by Snegirev A., Liu N.A., Tamanini F., Bradley D., Molkov V., and Chaumeix N.
Published by Saint-Petersburg Polytechnic University Press
ISBN: 978-5-7422-6498-9 DOI: 10.18720/spbpu/2/k19-54

t	time (s)
V_f	flame spread rate (cm/s)

Greek

ρ	density (kg/m^3)

g	gas
p	polymer coating or pyrolysis
0	Original

INTRODUCTION

Flame spread along the polymeric coatings on electrical wires is of interest for fire prevention and has been widely studied in recent years [1-3]. Fujita et al. performed a series of experiments to study the effects of external flow velocity [1], wire size [2], ambient pressure [3] and oxygen concentration [4] on flame spread over polyethylene (PE) wires in microgravity. Takahashi et al. [5] studied the influence of external flow velocity on the volume change of the melted insulation in microgravity. Huang et al. [6] developed a model to explain the ignition and ignition-to-spread phenomenon of electrical wires.

Previous studies usually considered the burning of horizontal wires, and limited studies were on the orientation effect. However, in practical application, flame spread over wires occurs at many different orientation angles. Hu et al. [7] studied the limiting oxygen concentration for extinction of upward spreading flames over inclined wires with opposed-flow. Lu et al. [8] studied the interaction between the wire inclination and horizontal wind. Hu et al. [9] found that as the inclination angle ϕ varies from – 90° to + 75° (relative to the horizontal plane, '–' means downward spread and '+' means upward spread), the flame spread rate (FSR) of electrical wires first decreases then increases ('U' shape), which is quite different from low thermal conductivity materials such as paper [10] or wood [11]. Explanations of this phenomenon are that for electrical wires with high thermal conductivity metal cores (such as Cu), heat conduction through the metal core from the burning zone to pyrolysis zone dominates the flame spread process, while for low thermal conductivity materials, heat conduction through the solid media could be neglected.

However, it has been found by Yoshinari et al. [12, 13] that for vertical wires, the downward FSR is dominated by the downward dripping of the molten insulation, but is comparatively not sensitive to the core material. During the flame spread process, the polymeric coating first melts, and then decomposes to release combustible gases for burning. If the polymeric coating melts faster than its burning, the molten insulation begins to accumulate and flows along the wire (if the wire is inclined) or drip down (if the wire is horizontal).The phase change process has been numerically analyzed by Kim et al. [14, 15]. Wang et al. [16] found that the accumulation rate of molten insulation increases with the increasing current. Therefore, the effects of flowing molten insulation on wire fire should be concerned especially for cases with large current. When predicting the FSR, Hu et al. [9] neglected the heat flux from the flame to the preheat region ahead of the pyrolysis front in the energy balance equation of wire burning. However, surface heat flux in the preheat zone is very important for flame spread, especially for upward flame spread. In addition, the orientation angle was not included in the model of Hu et al. [9].

In this study, the effects of direct current I (0 ~ 7 A) and inclination angle ϕ, (–90° ~ +60°) on flame spread over PE insulated copper wires were studied. A periodic spread phenomenon was observed in upward flame spread due to the flowing of molten insulation. A flame spread model concerning with electric current and orientation angle was developed.

EXPERIMENTAL

A schematic drawing of the experimental apparatus is shown in Fig. 1, which mainly consists of a rotary stand, a sample holder, an ignition part and two constant current sources (CCS). PE insulated copper wires (inner diameter: d_c = 0.5 mm and outer diameter: d_p = 0.8 mm) were used as samples in the tests. The copper wires were applied with constant currents from 0 to 7 A by CCS 1 with a precision of 0.1 A. And a coil heater (NiCr) located at one end of the sample wire was charged with 6 A current by CCS 2 for ignition. A weight coupled with a pulley fixed on the sample holder was used to keep the sample straight during the experiments. A protractor was used to accurately set the angle of wire ϕ (relative to the horizontal plane, '–' means downward spread and '+' means upward spread) ranging from –90° to +60°. During the experiments, a side-view video camera (SONY NEX-5R, 30fps) was used to record the flame spread process. The characteristic parameters of flame shape and propagation velocity were obtained by image processing algorithm.

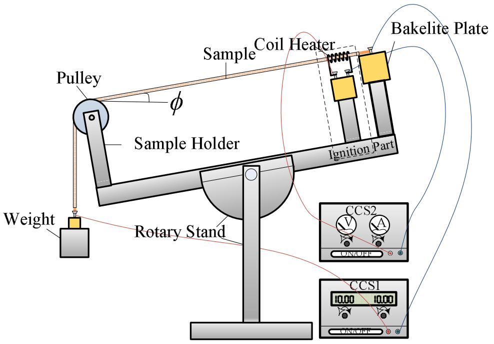

Fig. 1. Flame spread apparatus.

In the tests, the sample wire was ignited after being energized for 3 minutes (to make the sample wire reach a relative thermal equilibrium). Once ignition occurred, the ignition current was cut off immediately, while the electric current in the sample wire was still on. Effective length of the sample wire was 25 cm (distance from the ignition point to the pulley). Each test condition was repeated at least three times to ensure reproducible results. All experiments were performed under laboratory conditions of approximately 20 ± ℃ and 30 ± 5 % relative humidity.

RESULTS AND DISCUSSION

Periodic flame spread phenomenon

During the flame spread, the insulation melts, flows into the burning region and accumulates into a ball. When the ball is large enough, part of it flows down along the inclined wire. For downward flame spread ($\phi < 0$), part of the molten ball flows down from the burning zone to the preheat zone, losing heat to the preheat fuel and is not burnt. However, for upward flame spread ($\phi > 0$), a periodic spread phenomenon is observed. In Fig. 2, variations of the flame shape with time in one cycle of the periodic spread phenomenon for $\phi = +15°$ are shown. As the molten ball flows along the wire, it remains burning and consumes gradually, which results in the appearance of a subflame downstream. Height of the primary flame decreases first because of the flowing down of molten liquid, and then recovers itself as the flame continues to melt the unburnt fuel. The sub-flame moves in the opposite direction to the primary one. It decreases in size with time as the molten ball consumes gradually. In Fig. 2b, it is seen that the flame even breaks off (1.40s) with I = 3 A.

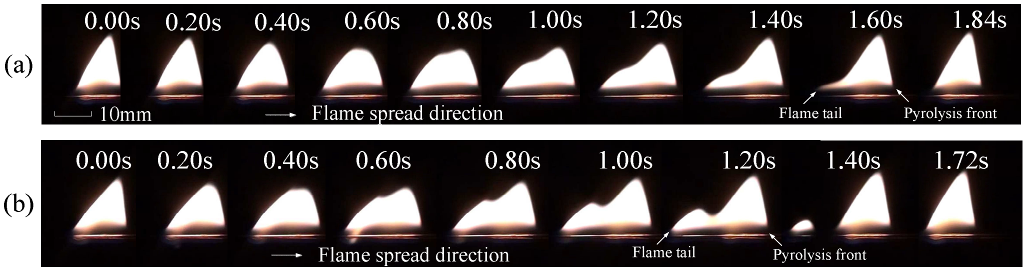

Fig. 2. Variations of flame shape with time at $\phi = +15°$ with (a) $I = 0$ A and (b) $I = 3$ A.

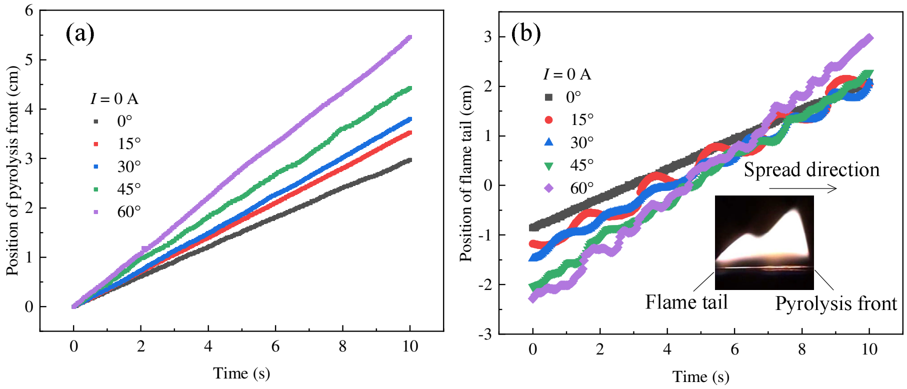

Fig. 3. Propagation of (a) pyrolysis front and (b) flame tail with time at $I = 0$ A in upward spread.

Figs. 3a and 3b illustrate the propagation of pyrolysis front and flame tail as a function of time with different orientation angle at $I = 0$ A in upward flame spread. The flame tail moves periodically with time and the cycle is shorter for the larger orientation angle. The pyrolysis front moves linearly with time and is shown not to be affected by the flame tail. In this study, the average movement rate of pyrolysis front is taken as flame spread rate (FSR). Note that for upward flame spread, though the flame shape varies periodically, structure of the primary flame just before the sub-flame appears is used for model prediction of flame spread hereinafter.

Flame shape and flame spread rate

Figure 4 shows the variations of flame length L_f and pyrolysis length L_p with inclination angles. Definitions of flame length and pyrolysis length are given in Fig. 4a. Length of the wire surrounded by the flame is defined as pyrolysis length. One can see that both L_f and L_p first decrease and then increase as the inclination angle increases from –90° to +60°, which shows a "U" trend as is described in the work of Hu et al [9]. The smallest values of L_f and L_p appear at $\phi = 0$. As the current increases, both the flame length and pyrolysis length increase. In Fig. 4a, as the electric current increases, the flame length data of downward spread are more scattered than that of the upward case, which indicates that the electric current has a stronger effect on flame length in downward spread.

Flame spread rate as a function of inclination angle is plotted in Fig. 5. The dependences of FSR on inclination angle and electrical current are similar to that of the flame length. The FSR varies with the inclination angle as a "U" trend. The FSR data of different currents are more scattered for downward spread indicating that the electric current has a stronger effect on downward FSR than upward FSR. The primary reasons are explained as follows. As the electrical current increases, the polymeric coating melts faster and more molten insulation flows along the wire if the wire is inclined. The FSR depends more strongly on the heat flux to the surface in the preheat zone than on the surface heat flux in the burning zone [17]. For upward flame spread, the molten insulation brings heat to the burning zone, while for downward spread, the molten insulation brings heat to the preheat zone and makes greater contributions to flame spread.

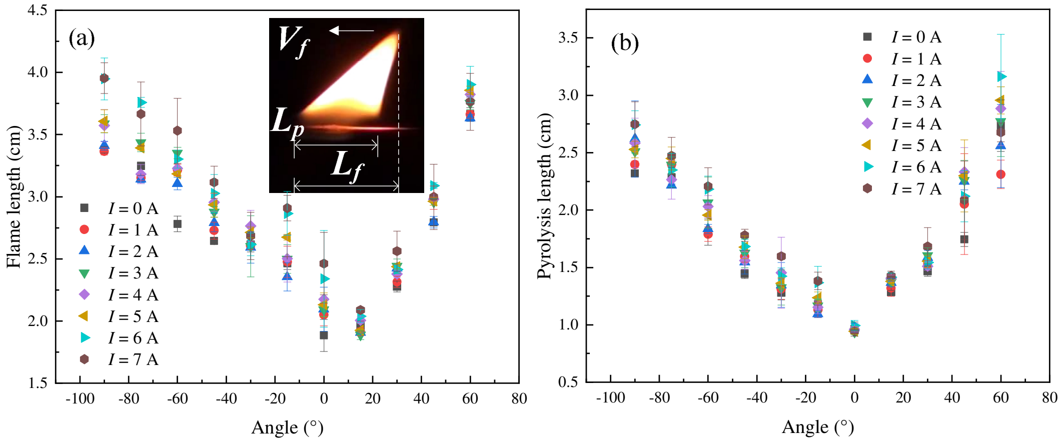

Fig. 4. Variations of (a) flame length and (b) pyrolysis length with inclination angle.

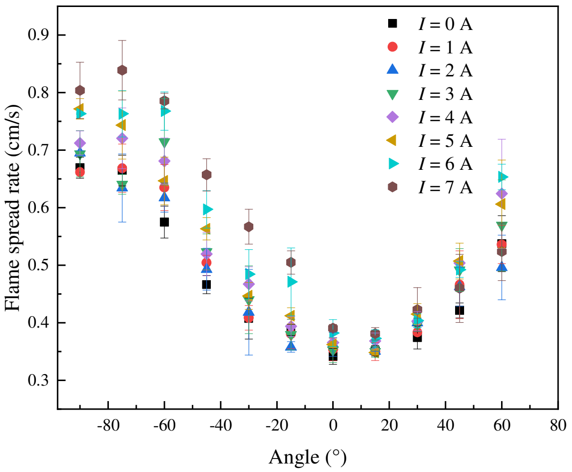

Fig. 5. Flame spread rate as a function of the inclination angle.

Both flame length and pyrolysis length are characteristic lengths that are related to the heat transfer process from the flame to the wire. Heat balance analyses concerning with the two characteristic lengths, orientation angle and electric current are conducted in the next section to predict the FSR.

Flame spread model

A simplified description of steady-state flame spread over a thin electrical wire at a constant velocity of V_f is illustrated in Fig. 6. Several assumptions are adopted here: (1) the coordinate system is fixed to the location of the flame; (2) both the PE insulation and core wire are thermally thin so that temperature profile across the cross-section of PE or metal core is uniform; (3) heat conduction through the PE insulation is ignored; (4) the complex shape change of polymer during the melting process is ignored; (5) flame radiation heat feedback is ignored; (6) heat flux from the molten insulation to the wire is ignored.

After being energized for 3 min before ignition, temperature of the wire reaches steady state, which gives:

$$I^2 \frac{\rho'}{\pi r_c^2} - 2\pi r_p \bar{h}_1 (T_0 - T_a) = 0\,, \tag{1}$$

where r is radius, with the subscript c for core and p for polymer coating, ρ' is the electrical resistivity, T_a is the ambient temperature, T_0 is the thermal equilibrium temperature of the wire before ignition and $\bar{h}$ is the average convection coefficient over the wire surface. Then we obtain

$$T_0 = T_a + \frac{\rho' I^2}{(2\pi r_p)\bar{h}_1 (\pi r_c^2)}\,. \tag{2}$$

$\bar{h}$ can be calculated as follow [18]:

$$\begin{gathered} \bar{h} = \bar{N}u_d \lambda_g / d = \left(CRa_d^n\right)\lambda_g / d\,, \\ Ra_d = Gr_d Pr = \frac{g\beta\left(T - T_a\right) d^3 \left|\sin\phi\right|}{\nu^2}\,, \end{gathered} \tag{3}$$

where λ_g is the thermal conductivity of gas, β is the volumetric thermal expansion coefficient, v is the kinematic viscosity, $C = 1.02$, and $n = 0.148$.

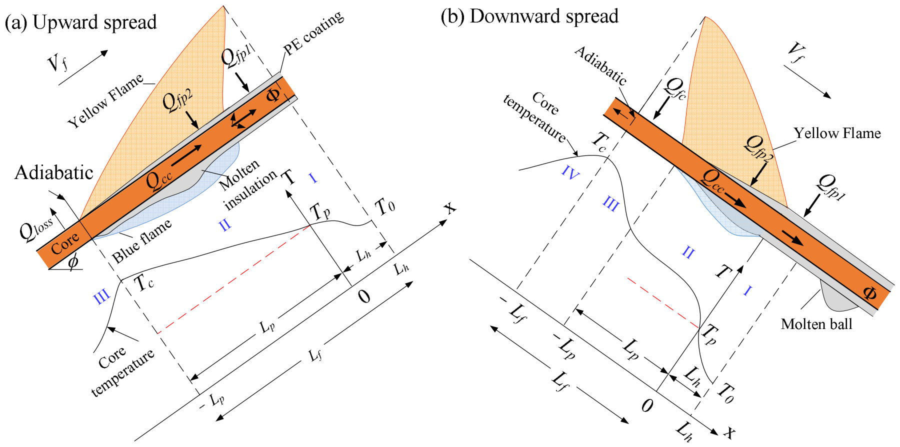

Fig. 6. Illustration of the flame structure and temperature profile of wire during steady-state spread: (a) upward spread, and (b) downward spread.

Equations of heat transfer between flame and wire can be expressed as:

$$Q_{in} + \Phi = \pi\left(r_p^2 - r_c^2\right)\rho_p V_f \left[c_p\left(T_p - T_0\right) + \Delta H\right] + \pi r_c^2 \rho_c c_c V_f \left(T_c - T_0\right), \tag{4}$$

where Q_{in} is the incident heat flux from flame to wire, c is the heat capacity, T_c is the temperature of copper wire at the flame tail, ΔH is the latent heat of pyrolysis of the polymer coating (254 kJ/kg for PE [9]), and Φ is the Joule heat produced in the control volume expressed as:

$$\Phi = I^2 \frac{\rho'}{\pi r_c^2} L_{ch} , \tag{5}$$

where L_{ch} is the length of the control volume. Then the FSR can be obtained from Eq. (4) as:

$$V_f = \frac{Q_{in} + \Phi}{\pi\left(r_p^2 - r_c^2\right)\rho_p\left[c_p\left(T_p - T_0\right) + \Delta H\right] + \pi r_c^2 \rho_c c_c\left(T_c - T_0\right)} , \tag{6}$$

Upward flame spread

For upward spread (as shown in Fig. 6a), the incident heat flux from flame to wire is:

$$Q_{in} = Q_{fp1} + Q_{fp2} , \tag{7}$$

where Q_{fp1}, Q_{fp2} are the heat convection between flame and polymer coating in the preheat zone (Region I in Fig. 6a) and the pyrolysis zone (Region II in Fig. 6a), respectively

The heat flux per unit area from flame to wire can be expressed as [19]:

$$\dot{q}''(x) = \begin{cases} \dot{q}''(0)\exp(-x/L_h), & x > 0 \\ \dot{q}''(0), & -L_p < x < 0 \end{cases} , \tag{8}$$

where L_h is the flame preheat length expressed as $L_h = L_f - L_{ba}$, and $\dot{q}''(0)$ is the surface heat flux per unit area at $x = 0$, which can be estimated as:

$$\dot{q}''(0) \approx \bar{h}_2\left(T_f - T_p\right) , \tag{9}$$

where $\bar{h}_2$ is the average heat transfer coefficient over the wire surface in Region II. We can see from Eqs. (3) and (9) that as the inclination angle increases, $\bar{h}$ increases and therefore $\dot{q}''(0)$ increases.

In the preheat region, Q_{fp1} can be expressed as:

$$Q_{fp1} = 2\pi r_p \int_0^\infty \dot{q}''(0)\exp(-x/L_h)dx = 2\pi r_p L_h \dot{q}''(0) . \tag{10}$$

In Region II,

$$Q_{fp2} = 2\pi r_p L_p \dot{q}''(0) . \tag{11}$$

At the flame tail, thickness of the molten insulation reduces to zero and the wire core is exposed to the flame. In Region III (as shown in Fig. 6a), heat flux from the flame is negligible and temperature of the wire core decreases rapidly due to heat loss to the environment. Therefore, it's reasonable to assume that temperature of the wire reaches the maximum at the flame tail, and then T_c can be determined by

$$\dot{q}''(0) + I^2\rho'/\pi r_c^2\left(2\pi r_c\right) = \varepsilon\sigma\left(T_c^4 - T_a^4\right) + \bar{h}_3\left(T_c - T_a\right) \tag{12}$$

By substituting Eqs. (5), (10) and (11) in Eq. (6), upward FSR can be predicted as:

$$V_f = \frac{\left(2\pi r_p \dot{q}''(0) + I^2 \rho' / \pi r_c^2\right) L_f}{\pi\left(r_p^2 - r_c^2\right)\rho_p \left[c_p \left(T_P - T_0\right) + \Delta H\right] + \pi r_c^2 \rho_c c_c \left(T_c - T_0\right)} . \tag{13}$$

Downward flame spread

For downward flame spread (Fig. 6b), the incident heat flux from flame to wire Q_{in} is:

$$Q_{in} = Q_{fp1} + Q_{fp2} + Q_{fc} , \tag{14}$$

where Q_{fc} is the heat flux from flame to exposed wire in Region III (in Fig. 6b). The heat flux per unit area from flame to wire can be expressed as:

$$\dot{q}''(x) = \dot{q}''(0) \begin{cases} \exp\left(-x/L_h\right), & x > 0 \\ 1, & -L_p < x < 0 , \\ \exp\left(-\left(x + L_p\right)/L_p\right), & x < -L_p \end{cases} \tag{15}$$

where L_h is the flame preheat length approximated as [20]:

$$L_h \approx \sqrt{2}\alpha_g / u_\infty \approx \sqrt{2}\alpha_g \Big/ \left(\alpha_g g \sin|\phi|\right)^{1/3} , \tag{16}$$

where α_g is the thermal diffusivity of gas.

Heat fluxes from flame to wire are:

Region I:

$$Q_{fp1} = 2\pi r_p \int_0^\infty \dot{q}''(0) \exp\left(-x / L_h\right) dx = 2\pi r_p L_h \dot{q}''(0) , \tag{17}$$

Region II:

$$Q_{fp2} = 2\pi r_p L_p \dot{q}''(0) , \tag{18}$$

Region III:

$$Q_{fc} = 2\pi r_c \int_{-L_f}^{-L_P} \dot{q}''(0) \exp\left(\left(x + L_p\right) / L_p\right) dx = 2\pi r_c L_p \dot{q}''(0) \left(1 - \exp\left(1 - L_f / L_p\right)\right) \tag{19}$$

Temperature of the copper core reaches the maximum at $x = -L_f$, and T_c can be determined by:

$$\dot{q}''(0) \exp\left(\left(-L_f + L_p\right) / L_p\right) + I^2 \rho' / \pi r_c^2 \left(2\pi r_c\right) = \varepsilon\sigma\left(T_c^4 - T_a^4\right) + \bar{h}_3 \left(T_c - T_a\right) \tag{20}$$

By substituting Eqs. (14) and (17)-(19) into Eq. (6), the downward FSR can be predicted by:

$$V_f = \frac{2\pi r_p \left(L_p + L_h\right) \dot{q}''(0) + 2\pi r_c L_p \left(1 - \exp\left(1 - L_f / L_p\right)\right) \dot{q}''(0) + I^2 \rho' \left(L_f + L_h\right) \Big/ \pi r_c^2}{\pi\left(r_p^2 - r_c^2\right)\rho_p \left[c_p \left(T_p - T_0\right) + \Delta H\right] + \pi r_c^2 \rho_c c_c \left(T_c - T_0\right)} \tag{21}$$

The predicted flame spread rates under various conditions are obtained by deriving characteristic lengths into Eq. (13) or (21), which are plotted in Fig. 7. Gas phase properties are all evaluated at the film temperature. It is observed that for opposed-flow flame spread, the predicted values are much smaller than the experimental ones, which is primarily attributed to that flame radiation feedback and heat flux from the molten material (liquid-phase Marangoni convection and dripping heating) are ignored in the model. For upward flame spread, our model achieves a good accuracy. As ϕ increases, the flame sheet moves closer to the sample wire, the flame length elongates and results in a larger heat flux from flame to fuel, which finally leads to a larger FSR as suggested by Eq. (13).

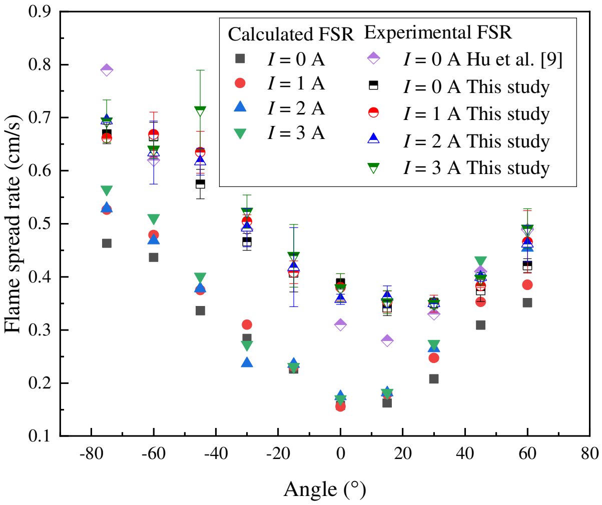

Fig. 7. Comparison of calculated flame spread rate with experimental values.

CONCLUSIONS

Effects of constant electric current and orientation angle on flame spread over PE insulated copper wires were studied in this paper. The flame spread rate was shown to increase with the increasing electric current. The current had a larger influence on downward flame spread compared with upward spread. For downward spread, the flowing molten liquid brought heat from the burning zone to preheat zone and promoted the spread. For upward flame spread, a periodic flame spread phenomenon was observed due to the flowing of molten polymer. A flame spread model concerning with both the orientation angle and electric current was developed. Good accuracy was observed between the calculated and experimental flame spread rate.

ACKNOWLEDGMENTS

This work was supported by the National Key Research and Development Plan under Grant No. 2017YFC0805100, the National Natural Science Foundation of China under Grant No. U1733126 and 41675024, and the Fundamental Research Funds for the Central Universities under Grant No. WK2320000035. The authors gratefully acknowledge all of these supports.

REFERENCES

[1] O. Fujita, K. Nishizawa, K. Ito, Effect of Low External Flow on Flame Spread over Polyethylene-Insulated Wire in Microgravity, Proc. Combust. Inst. 29 (2002) 2545-2552.

[2] O. Fujita, M. Kikuchi, K. Ito, K. Nishizawa, Effective Mechanisms to Determine Flame Spread Rate over Ethylene-Tetrafluoroethylene Wire Insulation: Discussion on Dilution Gas Effect Based on Temperature Measurements, Proc. Combust. Inst. 28 (2000) 2905-2911.

[3] Y. Nakamura, N. Yoshimura, H. Ito, K. Azumaya, O. Fujita, Flame Spread over Electric Wire in Sub-Atmospheric Pressure, Proc. Combust. Inst. 32 (2009) 2559-2566.

[4] M. Kikuchi, O. Fujita, K. Ito, A. Sato, T. Sakuraya, Experimental Study on Flame Spread over Wire Insulation in Microgravity, Proc. Combust. Inst. 27 (1998) 2507-2514.

[5] S. Takahashi, H. Takeuchi, H. Ito, Y. Nakamura, O. Fujita, Study on Unsteady Molten Insulation Volume Change During Flame Spreading over Wire Insulation in Microgravity, Proc. Combust. Inst. 34 (2013) 2657-2664.

[6] X. Huang, Y. Nakamura, F.A. Williams, Ignition-to-Spread Transition of Externally Heated Electrical Wire, Proc. Combust. Inst. 34 (2013) 2505-2512.

[7] L. Hu, Y. Lu, K. Yoshioka, Y. Zhang, C. Fernandez-Pello, S.H. Chung, O. Fujita, Limiting Oxygen Concentration for Extinction of Upward Spreading Flames over Inclined Thin Polyethylene-Insulated Nicr Electrical Wires with Opposed-Flow under Normal-and Micro-Gravity, Proc. Combust. Inst. 36 (2017) 3045-3053.

[8] Y. Lu, X. Huang, L. Hu, C. Fernandez-Pello, The Interaction between Fuel Inclination and Horizontal Wind: Experimental Study Using Thin Wire, Proc. Combust. Inst. (2018).

[9] L. Hu, Y. Zhang, K. Yoshioka, H. Izumo, O. Fujita, Flame Spread over Electric Wire with High Thermal Conductivity Metal Core at Different Inclinations, Proc. Combust. Inst. 35 (2015) 2607-2614.

[10] J.G. Quintiere, The Effects of Angular Orientation on Flame Spread over Thin Materials, Fire Safety J. 36 (2001) 291-312.

[11] Y. Zhang, J. Ji, Q. Wang, X. Huang, Q. Wang, J. Sun, Prediction of the Critical Condition for Flame Acceleration over Wood Surface with Different Sample Orientations, Combust. Flame 159 (2012) 2999-3002.

[12] Y. Kobayashi, Y. Konno, X. Huang, S. Nakaya, M. Tsue, N. Hashimoto, O. Fujita, C. Fernandez-Pello, Effect of Insulation Melting and Dripping on Opposed Flame Spread over Laboratory Simulated Electrical Wires, Fire Saf. J. 95 (2018) 1-10.

[13] Y. Kobayashi, X. Huang, S. Nakaya, M. Tsue, C. Fernandez-Pello, Flame Spread over Horizontal and Vertical Wires: The Role of Dripping and Core, Fire Saf. J. 91 (2017) 112-122.

[14] Y. Kim, A. Hossain, Y. Nakamura, Numerical Study of Melting of a Phase Change Material (Pcm) Enhanced by Deformation of a Liquid–Gas Interface, Int. J. Heat Mass Transfer 63 (2013) 101-112.

[15] Y. Kim, A. Hossain, Y. Nakamura, Numerical Modeling of Melting and Dripping Process of Polymeric Material Subjected to Moving Heat Flux: Prediction of Drop Time, Proc. Combust. Inst. 35 (2015) 2555-2562.

[16] H. He, Q. Zhang, R. Tu, L. Zhao, J. Liu, Y. Zhang, Molten Thermoplastic Dripping Behavior Induced by Flame Spread over Wire Insulation under Overload Currents, J. Hazard. Mater. 320 (2016) 628-634.

[17] M. Sibulkin, J. Kim, J.V. Creeden Jr., The Dependence of Flame Propagation on Surface Heat Transfer I. Downward Burning, Combust. Sci. Technol. 14 (1976) 43-56.

[18] V.T. Morgan. The Overall Convective Heat Transfer from Smooth Circular Cylinders, In: Advances in Heat Transfer, Elsevier, 1975, pp. 199-264.

[19] M. Sibulkin, J. Kim, The Dependence of Flame Propagation on Surface Heat Transfer II. Upward Burning, Combust. Sci. Technol. 17 (1977) 39-49.

[20] J.G. Quintiere, Fundamentals of Fire Phenomena. John Wiley, Chichester, 2006, pp. 210-211.

Fire Growth in a High-rack Storage

Markus E.[1,] *, Snegirev A.[1], Kuznetsov E.[1], Tanklevskiy L.[1,2]

[1] *Peter the Great St.-Petersburg Polytechnic University, St. Petersburg, Russia*
[2] *Gefest Enterprise Group, St. Petersburg, Russia*
**Corresponding author's email: eksmarkus@gmail.com*

ABSTRACT

The mechanisms controlling the heat release growth rate and its dependency on time are studied in this work for cases of a high-rack storage facility and a single large-scale vertical PMMA slab. The latter case is considered to be a simplified set-up to get a deeper understanding of transient dynamics of the HRR growth rate and studied both theoretically and numerically. First, we modify and apply the simplified analytical model based on the classical approach, in which combustible surface is divided into the inert heating zone and the pyrolysis zone. The relationship for the flame spread is based on empirical correlations for turbulent flame length and HRR. In this work we set the turbulent flame height to be equal to the inert heating zone height and, thus, an accelerating flame spread can be predicted. Assuming that a pyrolysis front is flat and normal to the direction of propagation, the HRR growth rate for this scenario can be described using the t^3 dependence, which over-predicts the published measured values. Overall, a reasonable agreement is achieved.

Secondly, we address the same scenario with CFD simulations using FDS with finite-rate pyrolysis model. The transient HRR rate is predicted and favourably agrees the published measured data. This and and the predicted distribution of the burning rate over the burning surface justify that the pyrolysis front is in fact curviliniar.

Finally, the simplified approach is applied to predict the fire growth in the rack storage configuration. We show that a dramatically fast HRR growth rate can be observed for a large-scale scenario. A t-cube dependency of HRR growth rate is in a better agreement with FDS results than a conventional t-squared fire curve for the fast and ultrafast growth rate recommended by NFPA 204, etc. The predicted fire dynamics is analysed and the influence of the ignitor position is found to be substantial only for the initial stages of fire growth.

KEYWORDS: Flame spread, ignition, heat release rate, pyrolysis, CFD, rack storage fire, t-squared fire.

INTRODUCTION

High-rack storage fires are extremely destructive due to the very rapid growth and enormous heat release rate. An exceptionally high fire growth rate is determined by the fuel load geometry with densely packed combustible items; intense radiative exchange between the items causing its rapid ignition; the chimney-like effect generating the intensive in-rack flows and suction of fresh air into the burning region.

A designed-fire approach and the t-squared curve for the HRR rate routinely used by engineers (NFPA 72, 92B, 204, etc.) fail to reproduce the actual HRR growth rate occurring in the rack storages. Indeed, the t-squared dependence replicates the ideal scenario of symmetric expansion of the burning surface at a constant spread rate (if the burning rate is also constant). When either of the assumptions fails, the t-squared dependence becomes invalid. Clearly, if the burning zone expands

Proceedings of the Ninth International Seminar on Fire and Explosion Hazards (ISFEH9), pp. 796-807
Edited by Snegirev A., Liu N.A., Tamanini F., Bradley D., Molkov V., and Chaumeix N.
Published by Saint-Petersburg Polytechnic University Press
ISBN: 978-5-7422-6498-9 DOI: 10.18720/spbpu/2/k19-70

at an accelerating rate and/or the burning rate per unit surface area increases in time, then a higher exponent becomes appropriate in the power law to approximate the actual HRR dynamics.

The examples are the large-scale tests undertaken by Yu et al. in Refs. [1, 2], where the t^3 dependence was observed. More recent large-scale tests and simulations by Ren et al. [3] and Wang et al., Ref [4] are also consistent with this observation. To replicate the transient dynamics of the heat release rates observed in the warehouse containing high-rack storage, the exponential function was used by Alvares et al. in Ref. [5]. Even stronger dependence of the convective heat release rate on time, $\alpha\exp(\beta t)(a+bt)$, was derived by Ignason in Refs. [6, 7, 8], where the effect of a vertical flue size on the high-rack storage fire was examined.

The objective of this work is to get a deeper insight into the mechanisms controlling the HRR growth rate in the rack storage facilities. We focus on the initial stage of the fire development before the fire suppression systems are activated.

Fire growth rate in a rack storage is governed by the flame spread over the combustible surfaces. In its turn, the acceleration of the HRR growth is mainly determined by the upward flame spread over the vertical combustible surfaces. This scenario, therefore, needs to be considered in detail, both analytically and numerically. Indeed, the dynamics of the HRR growth occurring in this simplified scenario will also explain the transient fire growth rate in a realistic rack storage. Also, accelerating burning of the vertical combustible surface is an important benchmark to validate the CFD code.

In the first part of this work, we show that the t^3 dependence represents the growth rate in an upward turbulent flame spread over a vertical combustible surface, provided the pyrolysis front is flat and normal to the direction of propagation. This is done by utilising a modified version of the classical flame spread model, which is based on the simplified (thermal) pyrolysis model.

Based on the extensive CFD study, we then show that the fire growth rate in the rack storage is so fast that its approximation may require even higher order transient dependence.

UPWARD FLAME SPREAD OVER THE VERTICAL COMBUSTIBLE SURFACE

Approximate analytical model

Objective of the approximate analytical model is to provide simple relations for the transient flame spread velocity and the heat release rate when the flame propagates upwards over a vertical combustible surface. Following the classical approach [9, 10 etc.], the combustible surface is divided into two parts: the inert heating zone (where the surface temperature rises from the initial value to the ignition temperature), and the pyrolysis zone (where the surface temperature and the volatiles mass flux are assumed to be constant). The extent of the inert heating zone is set equal to the flame height, L_f, while the location of the pyrolysis front, x_p, is defined as the height at which the heating time just exceeds the time to ignition (estimated according to the thermal theory for thermally thick or thermally thin layer). Flame spread rate is then evaluated as the rate at which the pyrolysis front propagates upwards:

$$V_p = \frac{dx_p}{dt} = \frac{L_f}{\tau_{ign}}. \tag{1}$$

The turbulent flame height is evaluated using the empirical correlation proposed in Ref. [11]:

$$\frac{L_f}{W} = CQ^{*2/3}, \tag{2}$$

where W is the width of the combustible surface, C is the empirical constant, and Q^* is the non-dimensional heat release rate,

$$Q^* = \frac{\dot{Q}}{\rho_0 c_P T_0 \sqrt{g} W^{5/2}} . \tag{3}$$

In Eq. (3), ρ_0, c_P, T_0 are the density, heat capacity, and temperature of ambient air, and g is the gravity acceleration. Total heat release rate, $\dot{Q}$, is evaluated assuming the flat shape of the pyrolysis front and uniform distribution of the burning rate, m'', over the pyrolysis zone:

$$\dot{Q} = x_p W m'' f_c \Delta h_c , \tag{4}$$

where Δh_c is the heat of combustion of volatiles, and f_c is the combustion efficiency.

Substituting Eqs. (3) and (4) to Eq. (2) yields the relation for the flame length:

$$L_f = C\left(\frac{x_p m'' f_c \Delta h_c}{\rho_0 c_P T_0 \sqrt{g}}\right)^{2/3} = x_*^{1/3} x_p^{2/3} , \tag{5}$$

where

$$x_* = C^3 \left(\frac{m'' f_c \Delta h_c}{\rho_0 c_P T_0 \sqrt{g}}\right)^2 . \tag{6}$$

According to Eq. (5), the flame height does not depend on the surface width, W. Using Eqs. (5) and (1), we arrive at the differential equation for the coordinate of the pyrolysis front:

$$\frac{dx_p}{dt} = \frac{x_*^{1/3} x_p^{2/3}}{\tau_{ign}} . \tag{7}$$

It is worthy of note, that in Refs. [9, 10], among others, Eq. (2) is written as $x_f / W = C Q^{*2/3}$, where $x_f = x_p + L_f$. This is equivalent to replacing Eq. (7) by

$$\frac{dx_p}{dt} = \frac{x_*^{1/3} x_p^{2/3} - x_p}{\tau_{ign}} . \tag{8}$$

Consider Eq. (8) in more details. Solving Eq. (8) with the initial condition, $x_p(0) = 0$, yields:

$$x_p = x_* \left(1 - \exp\left(-\frac{t}{3\tau_{ign}}\right)\right)^3 , \text{ and } V_p = \frac{x_*}{\tau_{ign}} \exp\left(-\frac{t}{3\tau_{ign}}\right)\left(1 - \exp\left(-\frac{t}{3\tau_{ign}}\right)\right)^2 . \tag{9}$$

This solution shows that the size of the pyrolysis zone asymptotically approaches a constant value of x_*, while the flame spread velocity reaches its maximum at $t = (3\ln 3)\tau_{ign}$ and decreases afterwards. Clearly, such a behavior contradicts the experimental observations, which firmly indicate accelerating flame propagation [12]. This artefact is attributed to the continuously reduced size of the heating zone due to x_f increasing slower than x_p. It will be shown below that this inconsistency is avoided by using Eqs. (2) and (7).

For the velocity of steady flame spread over a sufficiently thick material layer (no burnout), the experimental correlation was suggested (for example, see [9]):

$$V_p = Ax_p^n, \tag{10}$$

which implies that Eq. (1) yields finite accelerating solution, $x_p(t)$, only if $n < 1$. This is consistent with Eqs. (2) and (7), which imply $n = 2/3$. Using Eq. (10), it can be shown that $x_p = \left((1-n)At\right)^{1/(1-n)}$, $V_p = A\left((1-n)At\right)^{n/(1-n)} \sim t^{n/(1-n)}$, and

$$x_p = (1-n)V_p t\ . \tag{11}$$

Using Eqs. (7) and (10), the following relations are obtained for $n = 2/3$:

$$V_p = \frac{x_*}{\tau_{ign}}\left(\frac{t}{3\tau_{ign}}\right)^2, \tag{12}$$

$$x_p = x_*\left(\frac{t}{3\tau_{ign}}\right)^3. \tag{13}$$

Time to ignition, τ_{ign}, can be estimated using the assumption that the ignition occurs once the surface temperature attains the value of T_{ign} being exposed to a constant net heat flux, q''_{net}:

$$\tau_{ign} = \min\left(\frac{\pi}{4}\frac{kc\rho\left(T_{ign}-T_0\right)^2}{q''^2_{net}}, \frac{\delta c\rho\left(T_{ign}-T_0\right)}{q''_{net}} - \frac{1}{\pi}\frac{\delta^2}{a}\right), \tag{14}$$

where k, c, ρ are the thermal conductivity, heat capacity, and density of the material, and δ is the layer thickness. Two arguments in Eq. (14) correspond to the thermally thick and the thermally thin limits, respectively (a more accurate analytical solution is proposed in Ref. [13]).

The net heat flux allows for the incident (radiative and convective) heat flux, q''_{inc}, and the re-radiation:

$$q''_{net} = q''_{inc} - \varepsilon\sigma T_{ign}^4, \tag{15}$$

where ε is the surface emissivity.

The relations given by Eqs. (12), (13), and (14) constitute the simplified analytical model of the upward spread of a turbulent flame over a vertical combustible surface. According to Eq. (4), we obtain $\dot{Q} \sim t^3$ for the transient heat release rate. According to Eq. (13), time required for the pyrolysis zone to reach the top of the surface is $t_H = 3\tau_{ign}\left(H/x_*\right)^{1/3}$, where H is the height of the combustible surface.

To validate the model, we consider the large-scale experiment [12], in which upward flame spread over the 5 m high vertical PMMA slab (0.58 m wide, 2.5 cm thick) was studied. The lower part of the slab was exposed to the heat flux produced by the radiative panel (igniter). In the experiments [12], transient dynamics of total heat release rate, spatial distributions of surface heat fluxes, height of the pyrolysis region were recorded. Table 1 summarizes the thermal properties of the combustible material and ambient air used in the simulations to replicate the experimental conditions. Data in

Table 1 imply that the heat release rate per unit area of a burning surface is equal to $Q'' = m'' f_c \Delta h_c$ = 419 kW/m^2.

Table 1. Material properties

Material	Property	Value
PMMA	Conductivity, W/(m·K)	0.21
	Specific heat, J/(kg·K)	1500
	Density, kg/m^3	1190
	Critical mass flux, kg/(m^2·s)	0.02
	Ignition temperature, K	640
	Heat of combustion, kJ/kg	25600
	Heat of gasification, kJ/kg	700
	Combustion efficiency, –	0.82
	Emissivity, –	0.85
Ambient air	Specific heat, J/(kg·K)	1000
	Density, kg/m^3	1.1
	Temperature, K	300

To allow for the heat of gasification, Δh_g, the specific heat in Eq. (14) is multiplied by $1+\Delta h_g \big/ \left(c\left(T_{ign}-T_0\right)\right)$. Based on the literature data [9, 11] for the flame heat flux with no external heating, the incident heat flux is set q''_{inc} = 30 kW/m^2. With the model constant C = 2, Eqs. (6) and (14) yield x_* = 1.32 m, τ_{ign} = 266 s (thermally-thick limit), and Eq. (13) becomes $x_p = \alpha t^3$, where $\alpha = x_* \big/ \left(3\tau_{ign}\right)^3$ = 2.59·10^{-9} m/s^3. This dependency is shown in Fig. 2, a, by the dashed line; it can be seen that the analytical model with the selected value of the model constant replicates the transient propagation of the pyrolysis front in good agreement with the experiment.

For a flat shape of the pyrolysis front (normal to the direction of spread), Eq. (4) yields the dependence, $\dot{Q} = W m'' f_c \Delta h_c \alpha t^3$, which is depicted by the dashed line in Fig. 2, b. The heat release rate predicted by the approximate analytical model exceeds that observed in the experiment [12] (the latter can be approximated by $\dot{Q}_{exp} = 2.233 \cdot 10^{-12} t^{4.7}$, kW). Such a discrepancy can be attributed to the curvilinear shape of the pyrolysis front (pyrolysis front at the periphery of the surface propagates slower than that at the central line), and, possibly, to both spatial and temporal variation of the burning rate per unit surface area.

Assuming the burning rate to be constant, the ratio of the actual pyrolysis area to that in case of the flat pyrolysis front can be estimated as $\dot{Q}_{exp} \big/ \dot{Q} = 3.62 \cdot 10^{-6} t^{1.7}$. Thus, at the time instant of t_H = 1245 s (when the pyrolysis front at the central line reaches the top of the combustible surface), only 66% of the surface area is engulfed in flame in the experiment. This conclusion was also supported by the FDS simulations [14] with the finite-rate pyrolysis model. These simulations predicted curvilinear pyrolysis front, and, depending on the shape of the front, three different regimes of the flame spread were identified (see Ref. [14] for more details).

CFD MODELING

We also use the FDS software [15] to perform the simulations, in which the gaseous flame is coupled with the ignition and burning of the solid material. We apply the finite-rate single-step pyrolysis reaction, the kinetic parameters for which as well as other model settings are listed in Ref. [14]. Computational grid consists of 368640 cubic cells (2.5^3 cm^3) covering the domain (see Fig. 1, a) with the dimensions 1.2 x 0.6 x 8 m (length x width x height). The thermal properties are the same as in the previous section (see Table 1).

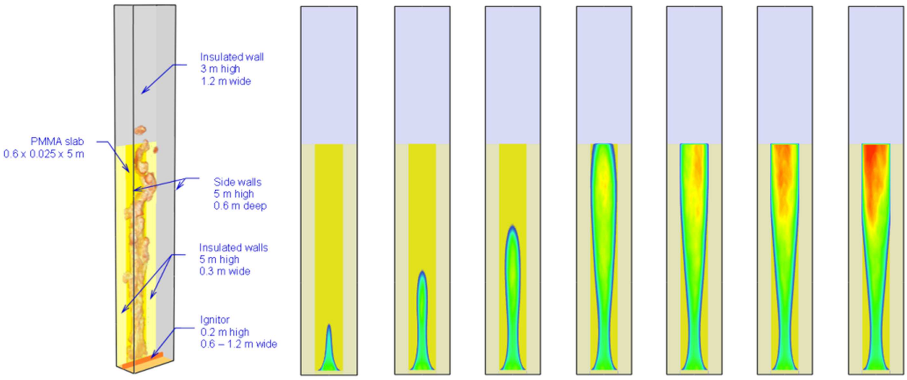

(a) (b)

Fig. 1. Predicting upward flame spread over the vertical PMMA slab by FDS. (a) Computational domain and boundary conditions. (b) Instantaneous surface distributions of the burning rate at time instants 600, 900, 1047, 1197, 1224, 1254, and 1284 s (ignitor width 1.2 m, temperature 825 °C). Finite-rate pyrolysis model.

This computational mesh is expected to resolve the controlling length scales. In case of upward flame spread these scales are the flame height (which determines the heated area of the slab prior to ignition), and the flame thickness normal to the wall (which determines the heat flux from flame). In our previous work [14], several fine meshes (cubic cells with the dimensions of 2, 3, 5, 10, and 15 mm) were used to perform grid sensitivity analysis for the vertical porous burner (0.38 m wide, 0.792 m high) and to assess mesh resolution in the vicinity of the burner surface. As shown in Ref. [14], total (convective and radiative) heat flux from the flame can still be predicted with a reasonable accuracy if the cell size is of order of 1^3 cm^3.

In this work, three computational meshes with cubic cells of 2.5^3 cm^3 (referred as basic), 1.6^3 cm^3, and 1.25^3 cm^3 were used to conduct a grid sensitivity analysis. The total heat release rate is not affected by the grid refinement, although the computational cost increases dramatically. It takes 340 hours of the wall clock time to compute 600 s of simulation time using 24 CPU cores with the finest mesh (2 CPU Intel Xeon E5-2697 v3), which is at least four times higher than with the basic mesh. This cell size is sufficient to predict turbulent flame dynamics and flame height since the characteristic length scale, $D^* = \left(\dot{Q}/\rho_0 c_{P,0} T_0 \sqrt{g}\right)^{2/5}$, is spanned by more than 10 cells, which obeys the recommendations provided in Ref. [15].

The solid phase resolution was not specifically studied in this work as the default FDS procedure for treatment of solid phase gridding issues is considered to be reliable. The size of the first cell is automatically chosen to resolve the thickness of the heated layer in the solid material, and the mesh is stretched in the outward direction from the surface to the middle of the slab. Only a 1D heat conduction mode is used in this study. To ensure adequate coupling between gas and solid phases, the wall temperature is updated at every time step.

To initiate flame propagation, bottom part of the slab is exposed to external heat flux produced by the ignitor (hot brick) located as shown in Fig. 1, a. The hot surface of the ignitor is faced towards the slab and located at a distance of 0.2 m away from the slab surface. Two scenarios were considered in the simulations, with the ignitor width and temperature set to 0.6 m, 900 °C, and 1.2 m, 825 °C. As shown in Fig. 2, the finite-rate pyrolysis model replicates the experimental dynamics of flame spread and HRR growth to a good accuracy. More information on the influence of the ignitor parameters on the fire dynamics is provided in Ref. [14].

Furthermore, dissimilar to the approximate analytical model, the CFD model predicts transient dynamics of the heat release rate, which is in favorable agreement with the measurement data reported in Ref. [12]. This is consistent with the observation that predicted shape of the pyrolysis zone is curvilinear, and the distribution of the burning rate over the burning surface is non-uniform as shown in Fig. 1, b (note also that the peak value increases in time as the flame size is growing).

It can therefore be concluded that the growth rate of the fire driven by the upward flame spread is higher than that corresponding to the t-squared fire. The best fit to the experimental data [12] yields $n = 4.7$, while the approximate analytical model predicts $n = 3$.

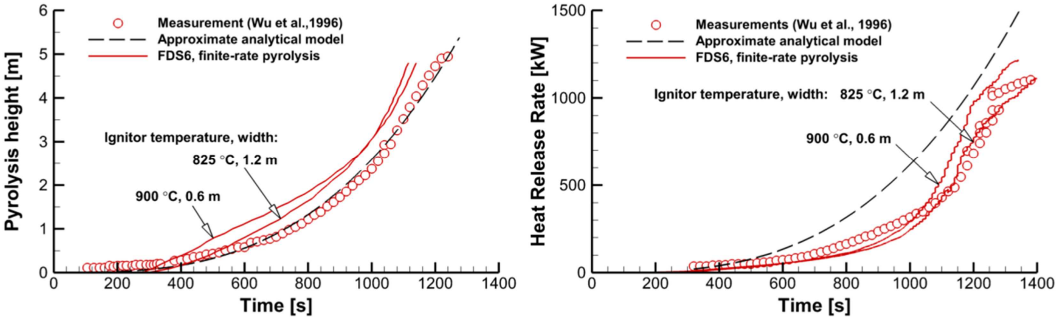

(a) (b)

Fig. 2. Upward flame spread over the vertical PMMA slab: elevation of the pyrolysis front at the axis (a) and the heat release rate (b) as a function of time (FDS data is smoothed).

HIGH RACK STORAGE FIRE SIMULATIONS

Model setup

The above analysis shows good ability of the FDS software in predicting upward spread of the turbulent flame over the vertical combustible surface. It is expected that the simplified (thermal) pyrolysis model (consistent with the assumptions made in the approximate analytical model described in the previous section) should also be capable of predicting the experimental dynamics of flame spread, provided the model parameters are properly calibrated. Indeed, in Ref. [16] we demonstrate it for the fire growth in the rack with 2x4x3 combustible boxes and show that the predicted heat release rate is in reasonable agreement with that measured in the full-scale tests [3, 4]. The guidance on how to select to select the model parameters to fit the measurement data on the transient heat release rate is also provided in Ref. [16].

Here we apply this approach to predict the fire growth rate in the high-rack storage facility if the fire suppression system is not activated. We consider three double rows racks, 6 boxes wide array with 11-tier height each (see Fig. 3). Each box has dimensions of 0.8x1.2x1.0 m, horizontal and vertical flues are 0.1 and 0.4 m, respectively, the distance between the rows in one rack is 0.5 m, and the distance between the racks is 3.54 m. For simplicity, we do not take into account wooden pallets, which are often used in practice. Each box is treated as a solid obstruction, and the thermal pyrolysis model is applied as the boundary condition at the box sides.

Model input parameters are retained the same as those in Ref. [16] and summarized in Table 2. These model parameters were selected in the iterative procedure which includes (i) evaluation of the literature data on material thermal properties and ignition temperature, (ii) estimation of HRRPUA and burnout time based on the HRR measurements, and (iii) calibration of the heat of gasification. With these model parameters, the measured heat release rate produced by burning of the corrugated cardboard boxes in the validation experiments [4] was reasonably replicated in FDS simulations with the simplified (thermal) pyrolysis model [16].

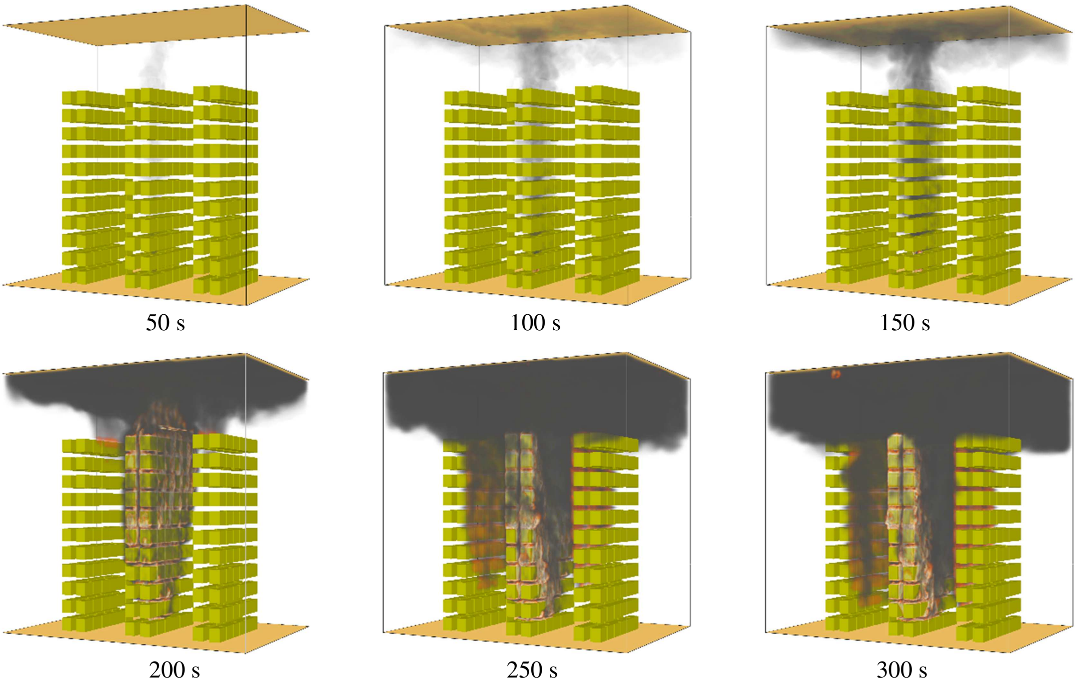
50 s 100 s 150 s

200 s 250 s 300 s

Fig. 3. FDS predictions of the fire development in the high-rack storage: instantaneous iso-surfaces of 200 kW/m^3 heat release rate and soot mass fraction at 50-300 s.

Table 2. Model parameters for the high-rack storage fire simulations

Material	Property	Value
Corrugated double wall cardboard	Conductivity, W/(m·K)	0.1
	Specific heat, J/(kg·K)	2700
	Density, kg/m^3	184
	Ignition temperature, K	633
	Heat of combustion, kJ/kg	14200
	Heat of gasification, kJ/kg	1000
	Emissivity, –	0.9
	HRRPUA, kW/m^2	200
	Burnout time, s	290
	Layer thickness, m	0.022

The fire is initiated by the ignitor, which is represented by the rectangular box with the dimensions of 0.4x0.6x0.3 m^3, located at the bottom of the central rack. The ignitor heat release rate rises from 0 to $\dot{Q}_{0,\max}$ = 1 MW according to the expression $\dot{Q}_0 = \min\left(\alpha_0 t^2, \dot{Q}_{0,\max}\right)$, where α_0 = 0.011 kW/s^2. Three ignitor positions are considered as illustrated in the inset in Fig. 4 and referred hereafter as cases 1, 2, and 3.

The computational domain is unconfined (side boundaries are open) and has the dimensions of 20x14x20 m^3. The central rack area is spanned with 5^3 cm^3 cubic cells. A coarser grid with 10^3 cm^3 cubic cells is used in the space between the racks and above the central rack (which corresponds to the main plume). The coarsest grid with 20^3 cm^3 cubic cells is used around the side racks. In spite of the rather large grid cells, the total number of cells is considerable (5145600), which is due to the large sizes of the domain. Simulation of 200 s physical time took 20 hours of CPU time with 84 cores of 2 Intel Xeon E5-2697 v3, 2.60 GHz processors.

Due to the large size of the domain compared to the length scales of horizontal and vertical flues, it is extremely expensive to conduct a comprehensive grid sensitivity analysis, which requires meshes with tens of millions of grid cells. However, our previous work, see Ref. [16], have shown that a quantitative agreement of the predicted dynamics of the heat release rate with that measured in the FM Global rack storage fire scenario ((2x4x3 boxes in the rack, horizontal flue 15 cm, vertical flue 46 cm, see Refs. [3, 4]) can still be obtained with the comparable grid resolution (2.5^3 cm^3 cubic cells in the central rack area). For the high-rack storage facilities, validation data is not available, and the predictions made in this work should be regarded as qualitative.

Simulation results

As shown in Fig. 4, the ignitor position greatly affects the overall HRR dynamics which is determined by the ventilation conditions and the distances between the combustible surfaces. The fastest fire development is observed when the ignitor is placed below and between two boxes, just below the narrow vertical flue (see case 2 in the inset in Fig. 4). In this case, a small distance between the boxes leads to intensive radiative exchange between and rapid ignition of the adjacent surfaces, while the vertical flue above the ignitor promotes fast upward flame spread over the vertical side surfaces of the boxes, jointly with the intensive air entrainment due to the chimney-like effect.

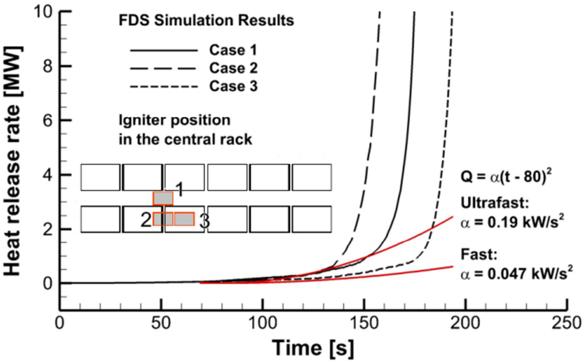

Fig. 4. Predicted heat release rate time dependences (cases 1, 2, 3 – ignitor locations).

In contrast, the longest delay of the HRR growth rate is observed if the ignitor is located centrally beneath the box, away from the vertical flues (see case 3 in Fig. 4). In this case, the upward flame spread is delayed for the time needed for the flame to engulf the bottom of the adjacent box just above the ignitor.

In case 1 the igniter is located in the centre of the rack between the rows, i.e. in the wide vertical flue (see the inset in Fig. 4). In this case, the ventilation and geometrical conditions are favourable for upward flame spread, but, on the other hand, the larger distance between the combustible surface implies less intensive radiative exchange than that in case 2, and this explains the longer times to ignition and the longer delay in the HRR runaway.

A typical predicted fire dynamics is illustrated by the instantaneous flame shapes and smoke concentrations shown in Fig. 3 for case 1. Similar to Refs. [3, 4, 16], the following stages of fire development can be identified. First, at time instant 80 s the vertical surfaces of the boxes of the first tier are ignited. Then the flame propagates upward over the vertical surfaces of the boxes facing inside the rack. At 160 s, the plume starts to widen and the flame spreads over the horizontal surfaces of the 2nd to 6th tiers. At 180 s, the flame spreads over the vertical surfaces of the boxes in 5th and 6th tiers. At about 190 s, all the surfaces of the 7th to 10th tiers are engulfed in fire. High irradiation leads to ignition of vertical surfaces of the 11th tier of the side racks, the flame then starts to spread downwards. At 250 s, all the boxes of the central rack at the level of 5th to 11th tiers burn. At 300 s flame spreads over the horizontal surfaces at the side racks.

Thus, the time periods of primarily vertical flame spread are followed by the time periods when the flame also propagates horizontally over the box surfaces. In the catastrophic case when the fire suppression system is not activated, radiative ignition of the upper tiers of the side racks occurs eventually. This is followed by the downward flame propagation, which is slower than the upward flame spread in the central rack.

As the fire develops, the effect of the ignitor location ceases, and the above listed stages of the fire growth remain to be almost the same, as well as the rate at which the HRR grows. Thus, for the three ignitor locations considered in this work, the difference is mainly in the initial delay of the HRR runaway.

It is worthy of note, that the predicted HRR rises extremely rapidly. Clearly, the t-squared fire curves shown by the red solid lines for the fast and ultrafast growth rate (as classified by NFPA 204) fail to replicate the HRR growth rates characteristic of the rack-storage fires. The predicted HRR growth rates can still be approximated by the power-law, $\dot{Q} \sim (t-t_0)^n$, where the value of n is in the range from 3 to 6 depending on the selected value of the incubation period, t_0. In particular, if the incubation period of t_0 = 130 s is assumed, then the good fit is provided by n = 3.

CONCLUSIONS

Fire growth for two scenarios of practical importance is considered in this work and particular attention is given to high-rack storage fires and the mechanisms controlling the heat release growth rate and its dependency on time, which is found to be stronger than the conventional t-squared fire curves recommended by NFPA 204, etc. Provided that the fire growth during initial stages, i.e. before the suppression system is activated, is governed mainly by the upward flame spread propagation we first examine a simplified scenario addressing the upward flame spread over a continuous 5 m high PMMA slab both numerically and theoretically. Indeed, the dynamics of the HRR growth occurring in this simplified scenario also explains the transient fire growth rate in a realistic rack storage.

First, we modify and apply the simplified analytical model, in which combustible surface is divided into the inert heating zone and the pyrolysis zone. The relationship for the flame spread is based on empirical correlations for turbulent flame length and HRR. In this work we set the turbulent flame height to be equal to the inert heating zone height and, thus, an accelerating flame spread can be predicted. Assuming that a pyrolysis front is flat and normal to the direction of propagation, the

HRR growth rate for this scenario can be described using the t^3 dependence, which exceeds the published measured values [12].

Secondly, we address the same scenario with CFD simulations using FDS with finite-rate pyrolysis model. The transient HRR rate is predicted and favourably agrees the published measured data. This and the predicted distribution of the burning rate over the burning surface, which found to be non-uniform and transient in time, justify that the pyrolysis front is in fact curviliniar, which explains why the analytical model over-predicts the HRR growth rate for the same scenario. The growth rate of the fire driven by the upward flame spread in this case is higher than that corresponding to the t-squared fire. The best fit to the experimental data [12] yields $n = 4.7$, while the approximate analytical model predicts $n = 3$. Regimes and mechanisms of flame spread are also examined and found to be depended on the igniter properties and size, the analysis of which can be found elsewhere [14].

Finally, the simplified approach is applied here to predict the fire growth in the rack storage configuration. The predicted fire dynamics is analysed and the influence of the ignitor position is found to be substantial only for the initial stages of fire growth. The time periods of primarily vertical flame spread are followed by the time periods when the flame also propagates horizontally over the box surfaces. In the catastrophic case when the fire suppression system is not activated, radiative ignition of the upper tiers of the side racks occurs eventually. This is followed by the downward flame propagation, which is slower than the upward flame spread in the central rack. We show that a dramatically fast HRR growth rate can be observed for this large-scale scenario, which, however, still can be described using the power-law function $\dot{Q} \sim (t - t_0)^n$. In particular, if the incubation period of 130 s is assumed, a t-cube curve is in a better agreement with FDS results than a conventional t-squared fire curve for the fast and ultrafast growth rate (as classified by NFPA 204).

ACKNOWLEDGEMENT

This work is supported by RSF (project 16-49-02017). Simulations were performed at the supercomputer center “Polytechnic” (SPbPU).

REFERENCES

[1] H.-Z. Yu. Transient Plume Influence in Measurement of Convective Heat Release Rates of Fast-Growing Fires Using a Large-Scale Fire Products Collector, J. Heat Transfer 112 (1990) 186-191.

[2] H.-Z. Yu, P. Stavrianidis. The Transient Ceiling Flows of Growing Rack Storage Fires. In: Cox G., Langford B. (Ed.), Fire Safety Science – Proceedings of the Third International Symposium, pp. 281-290, 1991.

[3] N. Ren, J. de Vries, X. Zhou, M. Chaos, K. V. Meredith, Y. Wang, Y. Large-Scale Fire Suppression Modeling of Corrugated Cardboard Boxes on Wood Pallets in Rack-Storage Configurations, Fire Safety J. 91 (2017) 695–704.

[4] Y. Wang, K. V. Meredith, X. Zhou, P. Chatterjee, Y. Xin, M. Chaos, N. Ren and S. B. Dorofeev. Numerical Simulation of Sprinkler Suppression of Rack Storage Fires. In: Nilsson D., van Hees P., Jansson R. (Ed.), Fire Safety Science – Proceedings of the Eleventh International Symposium, IAFSS, pp. 1170–1193, 2014.

[5] N. J. Alvares, H. K. Hasegawa, K. Hout, A. C. Fernandez-Pello, J. White, Analysis of a Run-Away High Rack Storage Fire. In: Kashiwagi T. (Ed.), Fire Safety Science – Proceedings of the Fourth International Symposium, IAFSS, pp. 1267-1278, 1994.

[6] H. Ingason, Heat Release Rate of Rack Storage Fires, Proceedings of 9th Interflam 2001 Fire Science & Engineering Conference, p. 731-740, 2001.

[7] H. Ingason, In-Rack Fire Plumes. In: Evans D. D. (Ed.), Fire Safety Science – Proceedings of the Fifth International Symposium, IAFSS, pp. 333–344, 2003.

[8] H. Ingason. Effects of Flue Spaces on the Initial In-Rack Plume Flow. In: Evans D. D. (Ed.), Fire Safety Science – Proceedings of the Seventh International Symposium, IAFSS, pp. 235-246, 2003.

[9] J.G. Quintiere. Surface Flame Spread. In: SFPE Handbook of Fire Protection Engineering, 2nd Ed. NFPA, 2002. p. 2-246 – 2-257.

[10] Y. Hasemi, Surface Flame Spread, in: M.J. Hurley (Ed.), SFPE Handbook of Fire Protection Engineering, Springer, New York, NY, 2016, pp. 705-723.

[11] J. G. Quintiere, T. G. Cleary, Heat Flux from Flames to Vertical Surfaces, Fire Technol. 30 (1994) 209–231.

[12] P.K. Wu, L. Orloff, A. Tewarson. Assessment of Material Flammability with the FSG Propagation Model and Laboratory Test Methods, 13th Joint Panel Meeting of the UJNR Panel on Fire Research and Safety, NIST Report NISTIR 6030, Gaithersburg, MD, USA, 1996.

[13] A. Snegirev, E. Kuznetsov, E. Markus. Coupled Analytical Approach to Predict Piloted Flaming Ignition of Non-Charring Polymers. Fire Safety Journal 93 (2017) 74-83.

[14] E. S. Markus, E. A. Kuznetsov, A. Yu. Snegirev. Buoyant Turbulent Diffusion Flame near a Vertical Surface Combustion, Explosion, and Shock Waves. 54 (2018) 284-293.

[15] K. McGrattan, S. Hostikka, R. McDermott, J. Floyd, M. Vanella. Fire Dynamics Simulator, Technical User’s Guide. NIST Spec. Publ. 1019, 6th ed., 2018.

[16] E. Markus, A. Snegirev, E. Kuznetsov, L. Tanklevskiy. Application of a Simplified Pyrolysis Model to Predict fire Development in Rack Storage Facilities. J. Physics: Conf. Series 1107 042012– Proceedings of the Third European Symposium on Fire Safety, 2018.

Jet fires

Fires, Explosions, and Venting in Nuclear Reactors

Palacios A.[1,]*, Bradley D.[2]

[1] *Universidad de las Americas, Puebla, Department of Chemical, Food and Environmental Engineering, Puebla, Mexico*
[2] *University of Leeds, School of Mechanical Engineering, Leeds, UK*
**Corresponding author's email: adriana.palacios@udlap.mx*

ABSTRACT

A brief historical review covers salient reactor fires and explosions, principally centred around the use of graphite as a neutron moderator, and the high temperature generation of hydrogen in reactions of steam and zirconium. An alternative to uncontrolled, excessive, build-up of pressure, followed by uncontrolled explosion, is the provision of a buffer vessel, in which there is separation of hydrogen from radioactive products in permeable membrane separators. The hydrogen is then flared. Possible rates of production of hydrogen are compared, along with the rates at which it can be separated and flared in lifted jet flames, which give the highest burn rates. Cross winds can result in a transition to rim attached, downwash and wake-attached flames, all with a significantly reduced burn rate, or complete flame extinction. The performance of lifted jet flames of C_3H_8, CH_4 and C_2H_4, when exposed to increasing air cross winds velocities, are presented. These provide a basis for synthesising the performance of H_2 flames, also in cross flows. The H_2 relationship is rather different from that of the hydrocarbons, on account of the higher chemical reactivity of hydrogen, its small laminar flame thickness, reduced air requirement, higher acoustic velocity, and minimal flame lift-off distance. Destruction of hydrogen lifted jet flames by the cross flow of atmospheric air is significantly less likely than it is for propane jet flames. Flaring with micro-tubes might be advantageous for integrating flaring with membrane hydrogen separation, whilst high mass flow rates can be achieved with large diameter flares in the lifted flame, supersonic regime.

KEYWORDS: Hydrogen, jet flames, reactor venting, cross flow.

NOMENCLATURE

B	molar fuel/cross flow air rate ratio
C	molar fraction of air in combined molar flows of fuel and air into lift-off volume
C_c	critical value of C for reduction in U_b* by cross flow
C_p	constant pressure specific heat (J/kg·K)
C_{SL}	values of C, at the equivalence ratio for maximum laminar burning velocity, S_L
D	pipe diameter (m)
D_o	pipe external diameter (m)
f	ratio of fuel to air moles in fuel-air mixture for S_L
k	thermal conductivity (W/m·K)
L	flame lift-off distance (m)
u_j	mean fuel flow velocity at the exit plane of pipe for subsonic flow. For ratios of atmospheric pressure to P_i equal to, or less than the critical pressure ratio, or choked sonic velocity after isentropic expansion from P_i (m/s)
$U*$	dimensionless flow number for choked and unchoked flow, $(u_j/S_L)(\delta_k/D)^{0.4}(P_i/P_a)$
$U_\delta*$	Value in Eq. (1) with $\delta = \nu/S_L$ in expression for $U*$

Greek

δ_k	laminar flame thickness, (m) $(k/C_p)_{To}/\rho_j S_L$
φ_{SL}	equivalence ratio for maximum laminar

Proceedings of the Ninth International Seminar on Fire and Explosion Hazards (ISFEH9), pp. 809-818
Edited by Snegirev A., Liu N.A., Tamanini F., Bradley D., Molkov V., and Chaumeix N.
Published by Saint-Petersburg Polytechnic University Press
ISBN: 978-5-7422-6498-9 DOI: 10.18720/spbpu/2/k19-9

$\bar{m}_c$	cross flow air mole density, (moles/m^3)
$\bar{m}_j$	fuel mole density, (moles/m^3)
P_a	atmospheric pressure (Pa)
P_i	initial stagnation pressure (Pa)
Re_c	air cross flow Reynolds number, u_cD_o/ν_{air}
S_L	maximum laminar burning velocity of the fuel-air mixture in ambient atmosphere (m/s)
To	temperature at inner layer of laminar flame (K), see [17]
u_c	cross wind velocity (m/s)
	burning velocity
ν	kinematic viscosity, under conditions of ambient atmosphere (m^2/s)
ρ	density (kg/m^3)

Subscripts

a	ambient conditions
air	air
b	value at blow-off
c	cross flow air
i	initial stagnation conditions
j	jet fuel

INTRODUCTION

Four key reactor combustion incidents are briefly summarised in Table 1. This is followed by more detailed considerations, which identify key problems, particularly the rapid formation rate of undesirable products at high temperature, their inadequate containment, and the feasibility of venting at an adequate rate to the atmosphere.

Table 1. Some key nuclear reactor fires and explosions

Incident	Problem	Remedy
1957 Windscale. Plutonium production. Graphite moderated, air cooling, graphite fire.	Temp. > 380 °C during Wigner release. Metal melted. Fire increased by increased air flow.	Fire further increased by CO_2. Water risked H_2 generation, but “If it goes up we go with it”.
1979 Three Mile Island. Pressurised Water Reactors (PWR), loss of coolant.	Core melted. Zircalloy and steam generated H_2 bubbles at top of reactor.	Hydrogen bubbles, at top released in stages, then mixed with air.
1986 Chernobyl. Boiling Water Reactors (BWR). Graphite moderator cooling by He/N_2. Uncontrolled rising temperature. Steam bubble increases reactivity.	Zirconium/steam generated H_2. Steam explosion probably followed by hydrogen explosion.	Excessive overpressure destroyed reactor. Extensive fires combatted with water.
2011 Fukushima. BWR. Coolant failure due to earthquake and tsunami.	Hot zirconium cladding reacted with steam after water level dropped, producing H_2. 3 reactors had meltdowns and 1 building destroyed.	All 4 reactors had H_2 explosions. Injection of water, including seawater. Concerns about H_2 explosions.

GENERAL CONSIDERATIONS

The 1957 Windscale fire arose from the use of graphite to moderate neutron energies in the course of plutonium production. Associated Calder Hall power reactors used CO2 as a coolant which, at high temperatures could react with the graphite. The Windscale fire was caused by overheating of the coolant air above 380 °C during Wigner energy release. This caused the graphite to burn in the coolant air. During the fire CO_2, was used as an attempted coolant, but it increased the combustion rate. At some risk of excessive H_2 generation, H_2O was successfully employed [1]. Graphite moderation was employed at Chernobyl and in the subsequent fire, after loss of control of the reactors, the graphite became incandescent, with the formation of CO. This burned, along with the fuel cladding. Additional difficulties are created in reactors by neutron-induced material degradation [2]. A problem with graphite in such reactors as the Advanced Gas Cooled Reactor, is the neutron displacement damage to the graphite structure. It is difficult to replace the damaged graphite, during the reactor lifetime, although this was achieved with the St. Petersburg reactor. Containment prior to the Chernobyl incident was inadequate.

At Three Mile Island, through loss of coolant, about half the reactor core melted. Radio-nuclides remained inside the reactor or dissolved in water. Reaction of steam with the zirconium cladding of the fuel rods generated H_2. Corrosion rates of zirconium become 10 times greater inside a reactor [2]. There was no major breach of the containment. Power failure prevented venting of the primary containment up the 100 m high stack. Some of the gases seeped into reactor buildings, accidently exploded, and removed parts of the structure. The widespread dispersal of H_2 would weaken the mixture, reducing its laminar burning velocity and whilst, initially, turbulence would enhance the burn rate, ultimately it could extinguish it. It has been estimated that a rather lean, near-homogeneous mixture of 8% H_2/air burned, creating an overpressure of 190 kPa [3], and reducing the overall damage. Figure 1, from research sponsored by the UK Atomic Energy Authority at the time, shows the development of flame quenching with increasing turbulence in weak mixtures of 6, 8, and 10% hydrogen (stoichiometric % = 29.6) [4].

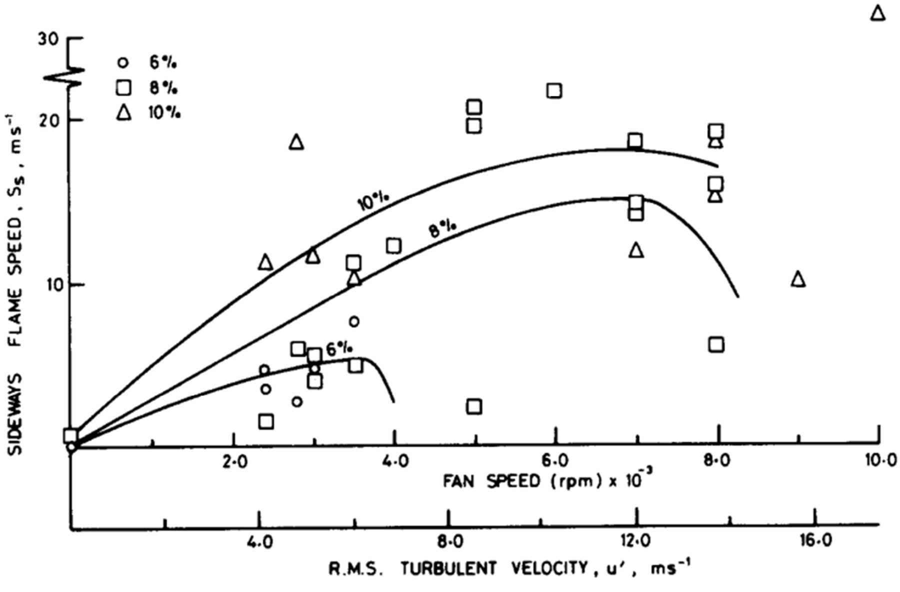

Fig. 1. Quenching effect of the rms turbulent velocity on hydrogen-air flame speed, taken from [4].

After this incident, reactor owners were required to strengthen venting systems to prevent leakage of H_2 into secondary containment buildings. Most of the H_2 was generated from Zircalloy cladding reacting with steam. It has been estimated that 1,200 kg of H_2 would be created, were all the cladding to be be oxidised by steam, and that complete combustion of the zirconium in a 1,000 MW(e) reactor would release $198{\cdot}10^{9}$ Joules [2].

Hydrogen and O_2 can also be formed in light water cooled nuclear reactors by the radiolytic decomposition of water [5]. If significant amounts of H_2 and O_2 were to be created by radiolysis in stoichiometric proportions, this would be very serious because of the very high reactivity of such a mixture [6]. However, Gordon et al. [7] found this not to be so, with no more than 0.7% H_2 created by radiolysis, and this was removed by recombination. To avoid explosive recombination with O_2, many reactors have been retrofitted with passive hydrogen recombiners within the containment. One approach, implemented in a few Boiling Water Reactors, has been to burn the H_2 inside the containment using distributed glow plugs [8]. Other remedial action has involved injection of N_2 into the reactor. At Fukushima, reactors survived the earthquake, less so the tsunami. There was no reactor cooling an hour after shut down. At both Three Mile Island and Fukushima there was a failure to remove the radioactive decay heat from the fuel [9].

At Fukushima all the fuel in Unit 1 melted, much of it leaking out. Seawater with neutron absorbing boron were used as coolant, but reactors overheated for many days. The reactors were GE/Toshiba/Hitachi Boiling Water Reactors, operational since 1971-75, with powers ranging from 460 to 1,784 MW(e). Pressure built up in Units 1 to 3, with most of the fuel melting [9]. Venting was designed to be through an external stack, but, in the absence of power, most of it back-flowed into the top floor of the reactor building. Venting began almost 24 hours into the emergency [10]. Containments were vented to atmosphere. Hydrogen leaked into reactor buildings and caused large explosions in Units 1, 3 and 4. Each Unit is estimated to have produced 800-1,000 kg of H_2. Hydrogen explosions caused tremendous damage. Even when fissioning had ceased, significant heat was generated through radioactive decay.

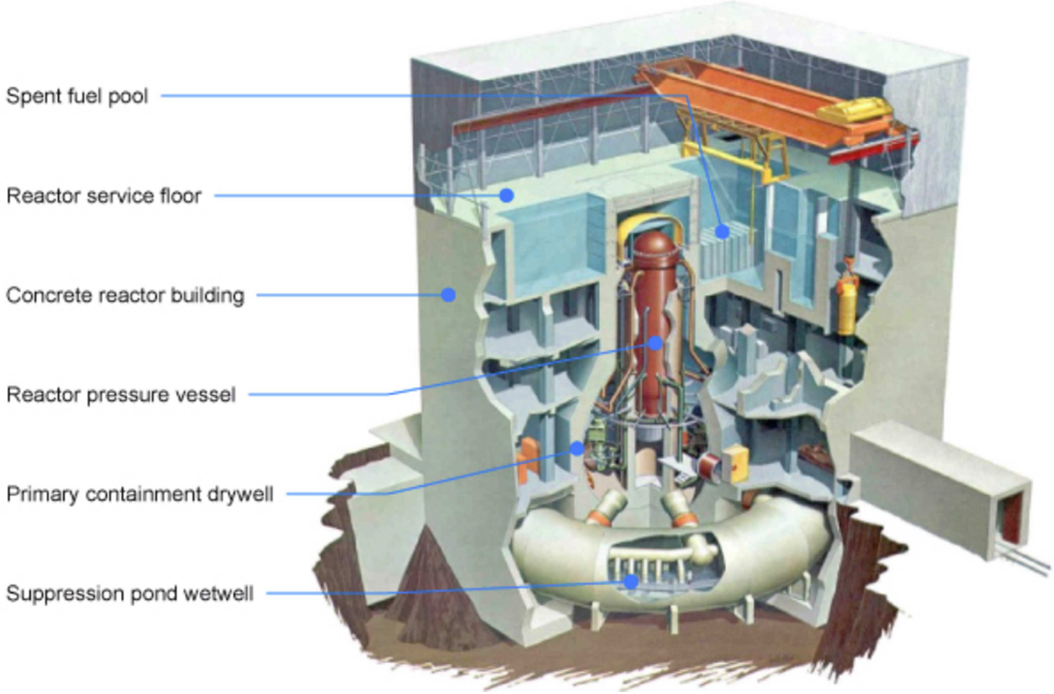

Fig. 2. Containment of Reactor Pressure Vessel, taken from [9].

As a consequence, the three Fukushima reactor cores, see Fig. 2, melted in the first two or three days of the emergency. There were considerable releases of radio nuclides and cooling water, with a total of ten core melts. The rate of formation of H_2 was controlled by the rate of oxidation of the zirconium fuel cladding by steam, at about 1,300 °C [5]. This rate of reaction was far beyond the capability of H_2 recombiners, N_2 inerting, and the time required to ensure the requisite purity of vented gases. This poses the current major challenge.

THE CHALLENGE

In a loss of coolant, or similar crisis, the reactor and its immediate containment are of inadequate volume to contain all the hydrogen that might be produced, as is evident from the relatively small Primary Reactor Containment shown in Fig. 2. Boiling Water Reactors operate at pressures of about 8 MPa, while Pressurised Water Reactors, with a secondary circuit, operate at about 16 MPa. Were venting to be long delayed a worse situation would arise from failure of the reactor/containment. Unless it is well controlled, allowing emergency venting to atmosphere too early will disperse undesirable radio-nuclides and increase the probability of uncontrolled hydrogen explosions. This perspective leads to the necessity of a large buffer vessel into which the primary products are vented. Ultimately, large amounts of H_2 must be vented, preferably free of undesirable radio-active products. This might be achieved by separating and containing such products, while the hydrogen would be contained and flared in a controlled manner.

Hydrogen separation has been proposed, through the use of hydrogen gas permeable membrane separators in a stream rich in H_2. This could be passed through a charcoal adsorber to adsorb radio-active particles and then flared in a gas burner [11, 12]. Inability to control the build-up of the high temperature reaction products, inadequate venting rates, particularly of hydrogen, and crisis management have been characteristic features of the described malfunctions. An essential requirement is a large buffering volume to contain the products during their initial high rates of formation. It is also desirable to separate and contain the most damaging products, whilst flaring hydrogen as soon as possible, in order to prevent its build up. A safe balance must be sought between rates of H_2 production, separation, and flaring. Although flaring of H_2 is not essential, if the release is large, it is a safeguard against its hazardous accumulation elsewhere. The hydrogen flaring process is now briefly considered, in terms of its feasibility for achieving adequate burn rates, the practicality of flaring, and the ability of flares to withstand cross winds.

CONTROL OF HYDROGEN FLARING

Limitations due to blow-off

Jet flames exhibit a variety of structures, ranging from lifted flames with high burn rates, in which the fuel jet flow is dominant, to rim and turbulent wake flames, the latter stabilised by the wake of a strong air flow across the fuel pipe. Flame blow-off and extinctions in the former case occur at sufficiently high values of the flow number, U^*. In the latter, they occur when the Reynolds numbers Re_c, based upon the pipe outer diameter and cross flow air velocity becomes sufficiently high [13]. Between these limits are a variety of other structures ranging from rim-stabilised to downwash flames. Because of the importance of their higher burn rate, lifted flames will be considered in detail, together with the effects of an increasing cross flow of air. The parameter U_b^* was formulated on the bases of both stretched laminar flamelet mathematical modelling [14] and the experimental derivation, correlation, and validation of appropriate dimensionless groups. Data were drawn from a vast experimental data bank [15]. This covered jet velocities, burning velocities, emitting plume heights, flame lift-off distances, and flame heights, involving six different fuels.

Flaring consists of the burning of a jet of excess fuel in the atmosphere. The highest burn rate within the reaction zone is achieved at the leading edge if the lifted flame, with flamelets burning at the maximum laminar burning velocity, S_L. The lift-off distance, L, is the distance between the exit plane of the pipe and this leading edge. If the ratio of fuel pipe diameter, D, to laminar flame thickness, δ_k, [14] is too small, there is difficulty in maintaining combustion, and the flame is soon quenched by excessive air entrainment.

Figure 3 shows experimentally-based correlations of the dimensionless flow number, U_b*, at blow-off, for different values of δ_k/D_b [16]. There is no cross flow and data are shown for four fuels. The flow number on the x axis, is defined as U_b*, = $(u_j/S_L)(\delta_k/D_b)^{0.4}(P_i/P_a)$, where u_j is the mean fuel exit velocity, D_b is the pipe diameter for blow-off, and (P_i/P_a) is the ratio of upstream stagnation to atmospheric pressure. Uniquely, in H_2 flames, the high diffusivity of H atoms induces significant heat release earlier in the flame [17]. This necessitates a different approach in the use of flame thickness in generalised correlations [18]. This thickness is given by $\delta_k = (k/C_p)_{To}/\rho_j S_L$ [18] for the leading maximum laminar burning velocity. The data in Fig. 3 are experimentally based, from [16], except for C_2H_4 from [19], and are overwhelmingly from the subsonic pre-choked regime.

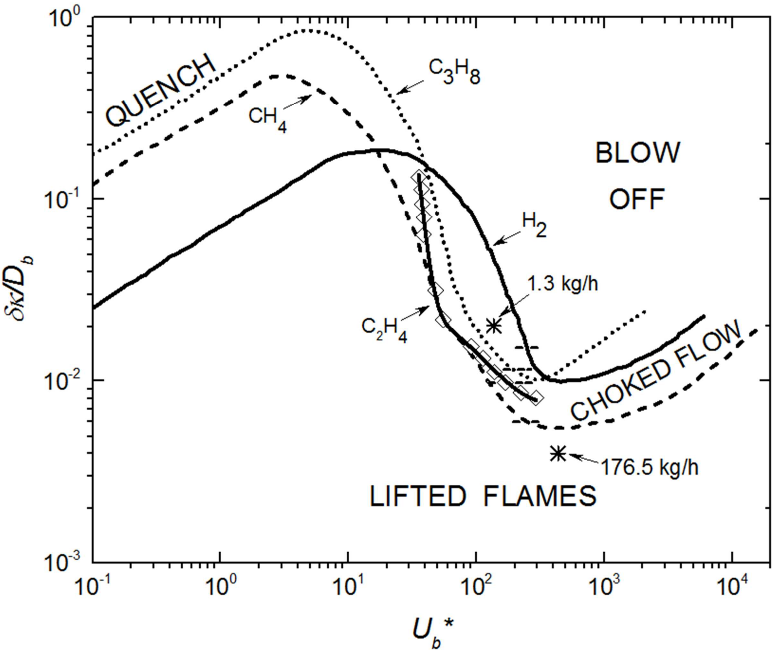

Fig. 3. Sonic and subsonic lifted jet flame blow-off and quench boundaries, for C_3H_8, CH_4, C_2H_4, and H_2. Short dashed horizontal lines show critical pressure ratio condition.

Locations at which the critical pressure ratio is attained on each blow-off curve in Fig. 3 were found from the compatibility of δ_k/D_b and U_b* at this pressure ratio. These are indicated by the short horizontal broken lines, below which flow is choked at blow-off. Below the blow-off curve, U_b*, for a given fuel, towards the lower values of δ_k/D_b, is the regime of lifted flames, with larger pipe diameters, above which stable lifted flames can be maintained. Above the curve, is the regime of decreasing pipe diameters, below which blow-off occurs.

Hydrogen flaring, with S_L = 3.03 m/s, is analysed, in terms of these generalised characteristics of lifted jet flames. First, in Fig. 3 the use of a micro-tube, D = 2.0 mm, δ_k = 0.03985 mm [16, 18], δ_k/D_b = 0.02, is considered. The initial/atmospheric pressure ratio is P_i/P_a = 1.8, just within the subsonic regime, before choked flow develops. Because of the high acoustic velocity of H_2, arising from the low molecular mass, the exit velocity, u_j, is also high, at 1,159 m/s, and U_b* = 144. These conditions give a micro-tube mass flow rate of H_2 of 1.3 kg/hour, indicated by the upper asterisk in Fig. 3.

Now consider blow-off in the choked flow regime, with P_i/P_a increased to 10 and D = 10 mm. In this regime, the reaction rate is enhanced by shocks and supersonic flows, at high U_b*. Now δ_k/D_b = 0.004, and u_j is equal to the acoustic velocity of 1,202 m/s, with an associated density of 0.51924 kg/m^3. These conditions yield U_b* = 436, a mass flow rate of 176.5 kg/hour, indicated by the lower asterisk, and a jet flame heat release rate of 6.9 MW. The generalised data in [15] suggest the jet flame height would be 4.8 m.

Hydrogen has a number of characteristics contributing to high jet velocity flames: a high laminar burning velocity, small flame thickness, small air requirement, and a high acoustic velocity. In contrast, its high reactivity makes it more prone to flame flashback from premixed flames.

LIMITATIONS DUE TO AIR CROSS FLOW

A further desirable characteristic in the flared venting of jet flames is an ability to survive the cross winds that might occur in the atmosphere. Available experimental data, on the effect of cross wind on U_b* have been re-expressed, but for pre-choked flow only, in terms of a parameter *C*. This is the mole fraction of cross flow air in the mixture that is created with the jet fuel, within the lift off distance, *L*. This has a volume $(\pi D^2/4)L$, with measured steady fuel jet and air cross flows into it. The resulting experimental data for U_b*, processed in this way for C_3H_8, and CH_4, from [19], are plotted against values of *C* for different D/δ_k, in Fig. 4. Stable, smaller diameter, jet flames exist within the peninsula. At the upper, lifted flame, limit, blow-off occurs, and at the lower limit slower burning flames are no longer lifted, but are attached to the burner.

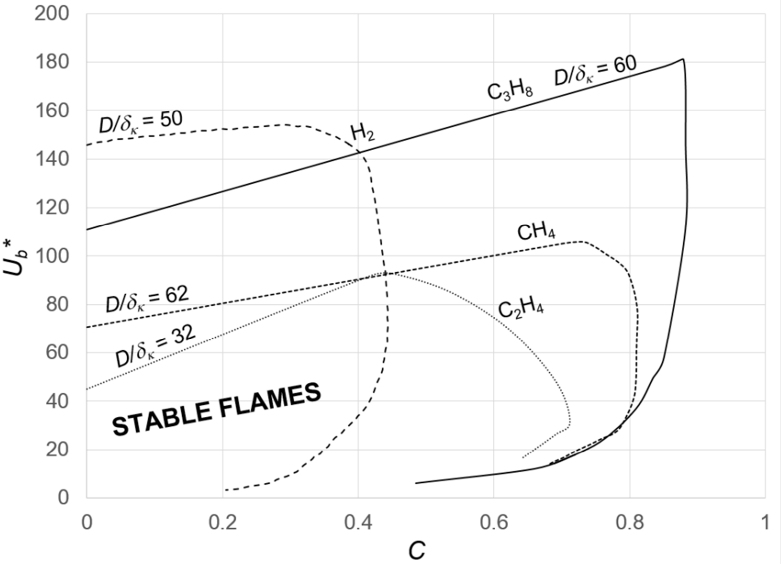

Fig. 4. Blow-off limits of stable CH_4, C_2H_4 and C_3H_8, lifted flames with air cross flows, in terms of U_b* versus *C*, for different values of D/δ_k. The dashed curve for H_2 is synthesised from the data of the other fuels.

Initially, as the air cross flow velocity, u_c, and *C* increase from zero, the mixture within the lift-off volume becomes more reactive. This causes the blow-off velocity and U_b* to increase. Other similar stability peninsulas for these gases, at different values of D/δ_k, can be constructed from the data in [19]. The experiments show that eventually increasing the cross flow necessitated significant reductions in the fuel flow rates and the values of U_b* that could be sustained, at a critical value of *C*, = C_c. This occurs before *C* has attained a value, C_{SL}, = $(1 + \varphi_{SL})^{-1}$, at which the associated equivalence ratio in the lift-off volume is that for S_L, namely, φ_{SL}. Both of these values of *C* are given in Table 2 for the different fuels. Of course, additional air is still entrained by the jet downstream beyond the lift-off distance. At C_c, the flow number U_b* must decrease in order to sustain the flame. Ultimately there is a transition to the lower limb of the peninsula and u_c is much reduced. For smaller values of D/δ_k, values of C_c, become less clearly defined. An example of this is indicated by the dotted curve for C_2H_4 in Fig. 4.

For the C_3H_8 peninsula in Fig. 4, at C_c the experimental data show quenching to begin at u_j = 242 m/s, with u_c = 5 m/s, as U_b* begins to fall sharply. For the CH_4 peninsula comparable values are u_j = 192 m/s and u_c = 3 m/s. These low values of u_c suggest that quite moderate cross flows can jeopardise the stability of lifted flames.

No cross wind data could be found for H_2, but from the experimental cross wind data available for the other three gases, it was possible to estimate the performance of hydrogen lifted jet flames in air cross flow. Another important factor controlling lifted jet flames in the presence of cross flows, is the ratio, f, of fuel to air moles at φ_{SL}. Values of f also are given in Table 2. Hydrogen requires significantly less air than hydrocarbons, and the value of f for H_2 is more than ten times higher than that for C_3H_8. As can be seen from Table 2, its C_{SL} value of 0.569, is significantly lower than those for the hydrocarbons. It was found that, for the same value of D/δ_k, C_c tends to decrease with C_{SL}. Consequently, the value of C_c also will be low. Guidance about the extent of this deficit below C_{SL} for H_2 was obtained from consideration of that occurring for other gases. This led to the tentative assignment of a value of C_c = 0.44 for H_2, with a value of U_b* of 144 at C = 0, and D/δ_k = 50, taken from Fig. 3. These considerations enabled the tentative, dashed, characteristic peninsula for H_2, shown in Fig. 4, to be constructed.

From the material balance of jet and cross flows in the lift-off volume, it follows that that $C = 1/(B + 1)$. Here $B = (u_j\overline{m}_j/u_c\overline{m}_c)\pi/4(D/L)$, in which the first bracketed term is the ratio of fuel to air molar fluxes into the lift-off volume. Evaluation of u_j/u_c requires the normalised lift-off distance for H_2 lifted flames, and this was found from the expression given for L/D, based on a different expression for flame thickness in U_δ* [24]:

$$(L/D)f = -0.0002U_\delta^{*2} + 0.19U_\delta^{*} - 3.3. \quad (1)$$

This remains valid as the cross flow develops, but it becomes increasingly unreliable beyond C_c. The expression for B yields values of u_j/u_c, at the onset of the rapid decline in U_b*. The value of U_b* then gives that of u_j.

Table 2. Property values and references for characterising Fig. 4

Fuel	D/δ_k	Ref. S_L	φ_{SL}	S_L, m/s	f	C_{SL}	C_c
C_3H_8	60	[20]	1.1	0.43	0.046	0.956	0.93
C_2H_4	32	[21]	1.2	0.72	0.084	0.923	0.65
CH_4	62	[22]	1.02	0.39	0.107	0.903	0.81
H_2	50	[23]	1.8	3.03	0.756	0.569	(0.44)

These various considerations suggest that for H_2, with U_b* = 144 and u_j = 1159 m/s, with C_c = 0.44, D/δ_k = 50, and f = 0.756, then u_c = 62 m/s. A natural atmospheric cross wind as high as this is uncommon. It is therefore unlikely that a lifted, venting hydrogen flame could be significantly disturbed by atmospheric conditions, and make the transition to a slower burning attached flame. This behaviour contrasts with that for C_3H_8 and CH_4. The high value of f for hydrogen reduces the air requirement and lift-off distance, while the high acoustic velocity is associated with high jet velocities at a given Mach number. These can be subsonic and in excess of 1,000 m/s.

CONCLUSIONS

1. Loss of coolant and other malfunctions can result in reactors over-heating and creating a variety of chemical reactions and heat releases. This must also be viewed in the context of improving operational efficiencies by operating reactors at higher temperatures. The least acceptable consequence of these is uncontrolled reactor failures, with the release of radioactive products and explosive gases into the atmosphere. Ideally, such a release could be avoided by early venting of the reactor, without any release of noxious products and flammable gases, and no external explosion. This might be achieved by venting the reactor into a much larger buffer vessel, in which the hydrogen might be wholly or partially separated and then flared.

2. In normal operation, H_2 recombiners can process about 195 kg/h of H_2, but in the case of an accident, the required rate would increase 100 to 400 fold [11], beyond the capabilities of this technique. In this situation, it has been proposed that, after removal of the water from the gaseous mixture, the H_2 should be separated, using a gas permeable membrane separator [11]. The H_2 stream would then pass through a charcoal adsorber to remove radioactive products, before being finally flared. If choked flow flaring on a 10 mm pipe, as demonstrated in Fig. 3 at a rate of 176.5 kg/h, were to be employed, the accumulated approximate estimate of 3,000 kg of H_2 at Fukushima would be flared on three such burners in just under 6 hours. There are many ways in which H_2 membrane separation can be implemented, covering a rich variety of materials, and structures [25].

3. With hydrogen permeable membrane separation, it is suggested in [11] that the differential pressure across the membranes should not exceed 1.724 MPa. If the H_2 were to be stored at 2 MPa and 300 K, 1,000 kg of H_2 would occupy a volume of 1,638 m^3, a cube with a 11.8 m side. This is a practically convenient size, which might combine storage and separation. The present analyses of the subsequent flaring have shown that the characteristics of H_2 are particularly well suited to a flexible approach to storage, separation and flaring, albeit with some possible delay for H_2 separation if dispersal of harmful radio-active products is to be avoided.

4. Flaring of H_2 is favoured by its low air requirements which leads to compact lifted flames. Its high acoustic velocities, arising from its low molecular mass, combined with its high burning velocity, lead to high values of fuel jet velocity. Although the analysis of air cross flow on H_2 lifted flames provides only an estimate of velocities, rather than accurate predictions, it nevertheless clearly shows that the extinction of lifted flames due to atmospheric cross winds is unlikely. The same cannot be said of C_3H_8 and CH_4 flames. There is clearly a need for experimental data on H_2 lifted jet flames in cross flows.

5. A unique aspect of H_2 jet flames is their ability to support micro-jet flames, a consequence of their low δ_k values. This could be relevant also in the separation process. Another possibility is for vented gas from the reactor to be immediately flared in micro-jets, followed by removal of radio-nuclides.

ACKNOWLEDGEMENTS

A.P. gratefully acknowledges the financial support of the Royal Society in the form of a Postdoctoral Newton International Fellowship.

REFERENCES

[1] The Windscale Inquiry, The National Archives, 1978.

[2] S.J. Zinkle, G.S. Was, Materials Challenges in Nuclear Energy, Acta Mater. 61 (2013) 735–758.

[3] H.A. Postma, Analysis of Three Mile Island (TMI-2) Hydrogen Burn, Thermal Hydraulics of Nuclear Reactors, 1983.

[4] D. Bradley, K.J. Al-Khishali, S.F. Hall, Turbulent Combustion in Near-Limit Hydrogen-Air Mixtures, Combust. Flame 54 (1983) 61–70.

[5] Safety of Nuclear Reactors, World Nuclear Association, Updated May 2016.

[6] D. Bradley, M. Shehata, Acceleration of Laminar Hydrogen/Oxygen Flames in a Tube and the Possible Onset of Detonation, Int. J. Hydrogen Energ. 43 (2018) 6734–6744.

[7] S. Gordon, K.H. Schmidt, J.R. Honekamp, An Analysis of the Hydrogen Bubble Concerns in the Three Mile Island Unit-2 Reactor Vessel, Radiat. Phys. Chem. 21 (1983) 247–258.

[8] F. Tamanini, E.A.Ural, J.L. Chaffee, Hydrogen Combustion Experiments in a 1/4 Scale Model of a Nuclear Power Plant Containment, Proc. Combust. Inst. 22 (1988) 1715–1722.

[9] Fukushima Accident, World Nuclear Association, Updated October 2017.

[10] M. Holt, R.J. Campbell, M.B. Nikitin, Fukushima Nuclear Disaster, Congressional Research Service Report for Congress., 7–5700, 2012.

[11] V.M. Callaghan, E.P. Flynn, B.M. Pokora, Containment Hydrogen Removal System for a Nuclear Power Plant, United States Patent 4430293 (1984).

[12] Lei Wang, Cheng Shao, Hai Wang, Hong Wu, Radial Basis Function Neural Networks-Based Modeling of the Membrane Separation Process: Hydrogen Recovery from Refinery Gases, Jour. Nat. Gas Chem. 15 (2006) 230–234.

[13] M.R. Johnson, L.W, Kostiuk, Efficiencies of Low-Momentum Jet Diffusion Flames in Crosswinds, Combust. Flame 123 (2000) 189–200.

[14] D. Bradley, P.H. Gaskell, Xiao-Jun Gu, The Mathematical Modeling of Liftoff and Blowoff of Turbulent Non-Premixed Methane Jet Flames at High Strain Rates, Proc. Combust. Inst. 27 (1998) 1199–1206.

[15] D. Bradley, P.H. Gaskell, X.-J. Gu, A. Palacios, Jet Flame Heights, Lift-Off Distances and Mean Flame Surface Density for Extensive Ranges of Fuels and Flow Rates, Combust. Flame 164 (2016) 400–409.

[16] A. Palacios, D. Bradley, Generalised Correlations of Blow-Off and Flame Quenching for Sub-Sonic and Choked Jet Flames, Combust. Flame 185 (2017) 309–318.

[17] D. Bradley, S.E-D. Habik, S.A. El-Sherif, A Generalisation of Laminar Burning Velocities and Volumetric Heat Release Rates, Combust. Flame 87 (1991) 336–345.

[18] J. Göttgens, F. Mauss, N. Peters, Analytic Approximations of Burning Velocities and Flame Thicknesses of Lean Hydrogen, Methane, Ethylene, Ethane, Acetylene and Propane Flames, Proc. Combust. Inst. 24 (1992) 129–135.

[19] G.T. Kalghatgi, Blow-Out Stability of Gaseous Jet Diffusion Flames Part I: In Still Air, Combust. Sci. Tech. 26 (1981) 233–239.

[20] A. Vanmaaren, L.P.H. DeGoey, Stretch and the Adiabatic Burning Velocity of Methane- and Propane-Air Flames, Combust. Sci. and Tech. 102 (1994) 309–314.

[21] T. Hirasawa, C.J. Sung, A. Joshi, Z. Yang, H. Wang, C.K. Law, Determination of Laminar Flame Speeds using Digital Particle Image Velocimetry: Binary Fuel Blends of Ethylene, Proc. Combust. Inst. 29 (2002) 1427–1434.

[22] Xiao-Jun Gu, M.Z. Haq, M. Lawes, R. Wooley, Laminar Burning Velocity and Markstein Lengths of Methane–Air Mixtures, Combust. Flame 121 (2000) 41–58.

[23] C.J. Sun, C.J. Sung, L. He, C.K. Law, Dynamics of Weakly Stretched Flames: Quantitative Description and Extraction of Global Flame Parameters, Combust. Flame 118 (1999) 108–128.

[24] A. Palacios, J. Casal, D. Bradley, Prediction of Lift-Off Distance in Choked and Subsonic Hydrogen Jet Fires, Catal. Today (2017) https:doi.org10.1016j.cattod.2017.11.024.

[25] N.W. Ockwig, T.M. Nenoff, Membranes for Hydrogen Separation, Chem. Rev. 107 (2007) 4078–4110.

CFD Modelling of Vertical Sonic Jet Fires

Rengel B.[1], Mata C.[1], Palacios A.[2], Pastor E.[1], Casal J.[1], Planas E.[1], *

[1] Universitat Politècnica de Catalunya, Barcelona, Spain
[2]Universidad de las Americas Puebla, Puebla, Mexico
**Corresponding author's email: eulalia.planas@upc.edu*

ABSTRACT

The use of Computational Fluid Dynamics (CFD) models can contribute to prevent jet fire accidents in facilities. Despite their great potential, validation analysis must be performed before their use in real applications to examine the accuracy of the results obtained. The paper examines the predictive capabilities of the FDS, FireFOAM and FLACS-Fire codes when modelling the expanded regions of vertical sonic jet fires of propane in an open environment. To comply with the low Mach number limitation of the CFD codes used, the pseudo-diameter approach has been applied to simulate the equivalent exit conditions of the jet after the expansion. Predictions of the flame temperatures, the emitted radiative heat fluxes, and the flame-geometry descriptors are compared with experimental data. The promising results indicate the suitability of the technique used to predict the hazardous effects of sonic flows, especially in FDS and FLACS-Fire.

KEYWORDS: CFD, fire modelling, jet fires, sonic flow.

NOMENCLATURE

A	flame area (m^2)
c	speed of sound (m/s)
D	diameter (m)
k	turbulent kinetic energy (m^2/s^2)
L	flame length (m)
$\dot{m}$	mass flow rate (kg/s)
M_a	Mach Number
M_w	molecular mass of fuel (g/mol)
R	constant of ideal gases
Re	Reynolds number
S	lift-off distance (m)
T	temperature (K)
u	gas velocity (m/s)
Greek	
ε	dissipation rate (m^2/s^3)
ρ	density (kg/m^3)
Subscripts	
eq	equivalent exit conditions
F	flame
or	orifice
∞	ambient conditions

INTRODUCTION

Onshore and offshore facilities, involving chemical process industries or refineries, are continuously exposed to the risk of industrial accidents (fires, explosions and toxic releases) [1]. In particular, explosions and toxic releases may injure people within a large damage radius. However, fires are the most common events (41.5%) as reported from a MHIDAS (Major Hazard Incident Data Service) survey involving 6,099 accidents [2]. Most hydrocarbon fires originate from a loss of containment. However, the final type of fire can be different, depending on the fuel properties and their state [3]. When a pipe is broken, when a hole forms in a tank, when gas leaks from a flange, or

Proceedings of the Ninth International Seminar on Fire and Explosion Hazards (ISFEH9), pp. 819-830
Edited by Snegirev A., Liu N.A., Tamanini F., Bradley D., Molkov V., and Chaumeix N.
Published by Saint-Petersburg Polytechnic University Press
ISBN: 978-5-7422-6498-9 DOI: 10.18720/spbpu/2/k19-36

when a safety valve is opened, a high-velocity leak of gas, or two-phase flow, can be immediately ignited creating a jet fire [4]. For most gases, the sonic velocity is reached if the source pressure exceeds 1.9 bar, which is common in many storage tanks and pipelines [5].

In general, sonic jet fires are smaller than other accidental fires; nevertheless, the high probability of flame engulfment and the high heat flux can in turn affect other equipment within a very short period of time, leading to a significant escalation of the accident, known as the domino effect [6]. In this context, active protection systems as well as inherently safer design measures are commonly applied, such as effective separation distances, in order to prevent the chain of accidents possibly caused by jet fires [7]. Specifically, international standards provide safe distances that should be attained between potential ignition sources and flammable materials, to restrict the occurrence of jet fires. However, these are based on empirical and statistical data, and do not cover the overall characteristics of the fire behaviour, and are restricted to certain fire scenarios [8]. In addition, the continuous developments of the processes performed in these facilitates may affect the geometrical distribution of the plant, the fuel inventory, and the location of the ignition sources. Therefore, separation distances could be unfeasible due to the high costs involved and the operability restrictions.

Given the difficulties in establishing reliable separation distances by traditional methods, alternative techniques should be used, such as Computational Fluid Dynamics (CFD) modelling. CFD codes solve the fundamental conservation equations governing fluid dynamics coupled with additional sub-models (i.e. turbulence, combustion, radiation) to describe the processes occurring during a fire. By this, an in-depth understanding of the phenomena associated with accidental jet fires can be attained, combined with the implementation of reliable safety distances. Despite the great potential of CFD codes, validation analysis must be performed before their use in real applications to examine the accuracy of the results obtained. The fundamental strategy is to compare computational estimations with experimental data.

This paper assesses the predictive capabilities of the Fire Dynamics Simulator v6.6.0 (FDS), the fire solver of OpenFOAM v6.0 (FireFOAM 2.2.x) and the Flame Accelerator Simulator Fire v10.7 (FLACS-Fire) when modelling the expanded regions of experimental vertical sonic jet fires. The pseudo-diameter approach is used to convert the sonic flow compressible conditions to subsonic expanded conditions as function of different Mach numbers. Predictions of the mean flame temperatures, mean heat fluxes, mean flame lengths, and mean flame areas are qualitatively and quantitatively compared against experimental data.

EXPERIMENTAL DATASET

CFD simulations are aimed at reproducing five vertical sonic experimental propane jet fires in an open environment, designated D10_0.09, D12.75_0.13, D15_0.18, D20_0.27 and D25.5_0.34 [9]. The first figure corresponds to the diameter of the jet orifice in mm and the second figure the mean mass flow rate of the gas through the exit orifice in kg/s. During the experiments, a wide-angle radiometer was located at 5 m distance from the fire origin and 1 m above the exit orifice to record the heat flux. Also, a B-type (0.35 mm-diameter) uncoated thermocouple was located 3.2 m above the orifice to register the flame axis temperature. Moreover, jet fires were filmed using a VHS camera, which registered visible images, and a thermographic IR camera, which indicated the apparent temperature distributions of the flames, defining the jet flame contour by the isotherm of 525 ºC [9] (Fig. 1).

For each test, the recorded IR images corresponding to the stationary state of the fires were subsequently treated with an in-house MATLAB® algorithm [10]. The stationary state is that of a fully developed flame, stabilized with a lift-off distance from the jet exit. The main goal of the image treatment was to separate the flame region from the background of the IR images, by comparing the temperature at each pixel element. Pixels with greater apparent temperatures than 525 ºC were considered as flame, while the rest were considered as background. Mean values of the flame-geometry descriptors were obtained by averaging the segmented images. The flame length was defined as the orthogonal distance between the fire base and the highest pixel element; and the flame area was determined by multiplying the number of pixel elements by the area occupied for each one.

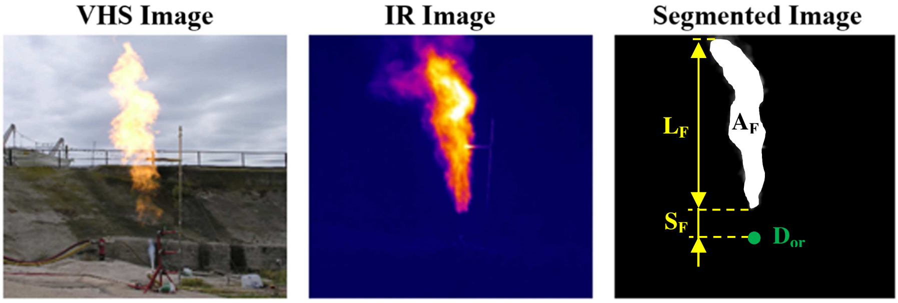

Fig. 1. Example of images recorded from the D25.5_0.34 sonic jet fire experiment by means of a VHS camera, an IR camera, and the corresponding segmented image.

NUMERICAL MODELLING

CFD codes

FDS is an open source code developed by the National Institute of Standards and Technology (NIST) that numerically solves a form of the Navier-Stokes equations appropriate for low-speed, thermally-driven flow. FireFOAM is another open code developed between CFD Direct and FM Global, based on a set of object-orientated CFD toolboxes written in C++. FLACS-Fire is a commercial CFD code especially designed for fire hazard applications in the process industry.

Due to the high-turbulent flows occurring in sonic jet fires, the exact solution of the governing equations is beyond the capabilities of the most powerful computers. Alternatively, numerous turbulent models are available to figure out the flow structures in a sub-grid scale stress accounting for the important small-processes that cannot be directly resolved. In particular, the $k-\varepsilon$ two-equation eddy viscosity model is implemented in FLACS-Fire to ensure the closure the Reynolds-averaged Navier–Stokes equations (RANS). It is one of the least computational expensive turbulence models as it solves the Navier-Stokes equations for the mean flow variables. On the other hand, FDS and FireFOAM represent the flow motion via Large Eddy Simulations (LES). Additional equations are not required and a more realistic flow field is rendered; however, LES are more computationally expensive than RANS. In both codes the sub-grid scale turbulent viscosity is dynamically solved as a function of the sub-grid kinetic energy, the LES filter size, and a model constant.

The chemical reaction of fuel and oxidant is computed in the codes used by means of the Eddy Dissipation Concept (EDC), which simplifies the chemistry and neglects the kinetic effects derived. Specifically, the differences between codes lie in the way of solving the mixing time scales between fuel and oxidizer. For example, in FLACS-Fire, these depend on the mass fractions and the reacting fractions of fine structures. Differently, the mixing scale times in FireFOAM are calculated as a function of two model constants, the LES filter size, and the sub-grid kinetic energy. Otherwise, FDS uses a more detailed reaction time scale model, based on the fastest physical process of the local state of the flow field.

Moreover, the Discrete Transfer Model approach is used to compute the radiation transport equation in FLACS-Fire, whose spatial discretization notably depends on the number of solid angles, and the ambient emissivity. Particularly, 100 solid angles were set-up to solve the radiation field in FLACS-Fire. On the other hand, FDS and FireFOAM use the Discrete Ordinate Model to estimate the radiation heat transfer. The main difference between both codes is that FDS incorporates a correction factor. A total of 48 solid angles have been proven sufficient for an accurate angular discretization for the solution of the radiative transport equation in FireFOAM [11], whereas 100 were set-up for FDS, as defined by default. More technical details about the sub-models solved and the model's constants can be found in [12] for FDS, in [13] for FireFOAM, and in [14] for FLACS-Fire.

Measuring devices

Different virtual sensors were located, as described in the experimental dataset within the computational domain for each jet fire simulation, to estimate the flame temperatures and heat fluxes. The flame-geometry descriptors were calculated by means of a 2D slice file (SF) that recorded the temperatures evolution on the centreline axis of the jet. Then, different post-processors were used to convert the slice files into spreadsheets containing the mean temperatures gathered at each cell for the different simulated times: fds2ascii for FDS, ParaView v5.4 for FireFOAM and Flowvis v5 for FLACS-Fire. As performed with the IR segmented images, the flame regions for each simulation were separated from the background by applying the defined threshold temperature.

Mach number constraint

Sonic jet fires are usually divided into three zones, which are related to different Mach numbers: (i) the nearfield or under-expanded zone ($M_a \geq 1.0$); (ii) the transition zone ($0.3 \leq M_a \leq 1.0$); and (iii) the farfield or expanded zone ($M_a \leq 0.3$) [15]. Within the nearfield zone, the sonic velocity is established at the nozzle exit ($M_a = 1.0$) with a gas pressure greater than the ambient. Then, the released flow undergoes rapid expansion and quickly accelerates to supersonic expansion ($M_a >> 1.0$) with the decrease in pressure and density. Consequently, the outflowing gas is governed by compressible and viscous effects, which avoids its mixture with the ambient flow. As the supersonic flow crosses the Mach disk, better mixing occurs in the transition zone, due to an abrupt decrease in velocity to subsonic speeds and increases in pressure and density. Both flameless zones are surrounded by a supersonic flow and coincide with the lift-off distance, defined as the distance between the outlet orifice and the base of the flame. Figure 2 shows the schematic representation of the under-expanded structure of sonic jet fires and the Mach number distribution [16]. As the distance from the gas release orifice increases, the velocity of the flow and the Mach number decrease progressively, until the air-fuel mixing is completed and the jet flame occurs. At this point, at the farfield zone, the jet is totally expanded, the subsonic regime is achieved and the flow becomes incompressible.

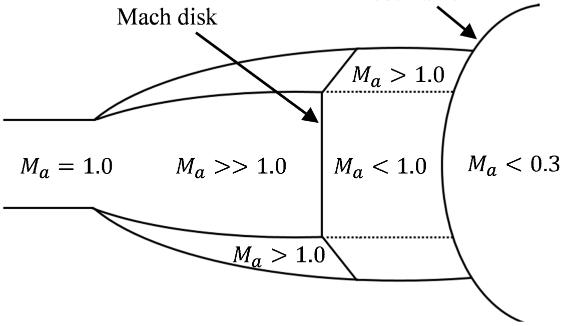

Fig. 2. Schematic representation of the under-expanded structure of sonic jet fires [16].

The CFD tools used consider the low Mach number formulation of the Navier-Stokes equations to reduce the number of equations solved, hence improving the numerical stability and reducing the computational times. Therefore, these CFD codes are only able to simulate the farfield zones, where the jet is in pressure equilibrium with the ambient fluid. In this context, the pseudo-diameter approach is used to scale the compressible initial conditions of the sonic jet at the exit orifice (i.e. temperature, velocity, diameter and velocity) to the expanded zone (Fig. 3) [17]. The method relies on mass conservation, and prevents air entrainment within the compressible region. Also, the equivalent pressure and temperature are assumed to be the same as the ambient fluid: (i) $\dot{m}_{eq} = \dot{m}_{or}$; (ii) $T_{eq} = T_{\infty}$; (iii) $P_{eq} = P_{\infty}$. Given that $u_{eq} = M_a c$, the equivalent diameter of the sonic jet fire can be determined as a function of M_a as follows: $D_{eq} = \sqrt{4\dot{m}_{eq}/\pi\rho_{eq}M_a c}$.

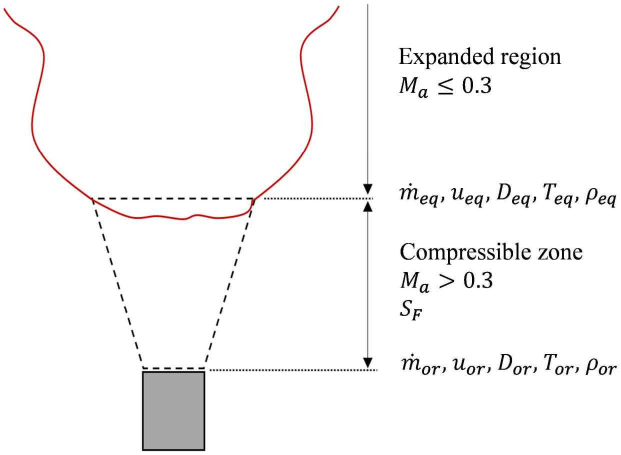

Fig. 3. Sketch of the pseudo-diameter approach used to scale the initial conditions of the sonic jet fires [17].

Table 1. Equivalent diameters of the jet fire experiments as a function of the Mach number

Mach number	-	0.01	0.025	0.05	0.10	0.20
Experiment	d_{or} (mm)	d_{eq} (mm)				
D10_0.09	10	140	90	60	40	30
D12.75_0.13	12.75	160	100	70	50	40
D15_0.18	15	190	120	90	60	40
D20_0.27	20	240	150	110	70	50
D25.5_0.34	25.5	260	170	120	80	60

The equivalent diameter approach proposed for this analysis neglects some of the real physical effects. First, the amount of ambient air entrained into the base of the flame that mixes with the fuel is not accounted. Also, the flameless distance between the exit orifice and the flame base is not estimated. Instead, an equivalent diameter of the flame base is directly assumed as a function of a Mach number, whose value is unknown. In this sense, five different Mach numbers have been considered for the analysis, to identify the most appropriate one: 0.01, 0.025, 0.05, 0.10 and 0.20 (Table 1). As observed, the greater the Mach number, the smaller the equivalent diameter of the jet after the expanded region. Even if $M_a = 0.3$ typically represents the threshold accounting for flow compressibility, this value has not been considered due to the very small diameters that would imply. Indeed, the equivalent diameter values would be very similar to the experimental ones, hence significantly increasing the computational times due to the very thin cell sizes required.

Mesh resolution

The size of the cells modelled may probably represent the most important numerical parameter defined by the user in CFD simulations. The grid sizes, coupled with the numerical methods, often determine the accuracy of the results reached and the computational times: the thinner the cell size, the better the computational resolution and the greater the simulation time. Consequently, it is necessary to provide a good balance between low grid resolution and reasonable computational costs. Cell sizes of buoyant plume simulations are commonly based on the characteristic diameter of the fire [18]. However, this approach cannot be used in sonic jet fires due to its momentum-dominated nature and the high flow velocities achieved. Furthermore, the equivalent diameters of the jets are the only geometrical constraints that define the minimum cell size. Consequently, the cell size of each jet fire scenario (in m^3) has been defined as the cubic root of its equivalent diameter (in m). For example, the D10_0.09 ($M_a = 0.01$) scenario has been modelled with a cell size of 0.14 x 0.14 x 0.14 m^3, and the D12.75_0.13 ($M_a = 0.05$) with a cell size of 0.07 x 0.07 x 0.07 m^3.

Simulations were run for 60 s to achieve long-duration steady states. The mass loss rates were prescribed according to the experimental data. A soot fraction of 0.09 kg/kg was assumed for the combustion of propane [19]. Apart from that of the ground, the rest of the boundaries were open.

RESULTS AND DISCUSSION

Experimental results

Figure 4 depicts the scatter plots of the variables experimentally measured for the different sonic jet fires as function of the Reynolds number: the flame temperature obtained with the thermocouple, the heat flux, the flame length, and the flame area. These values correspond to the mean values obtained by averaging the variables evolutions over 30 s during the steady state. Also, vertical bars are added to represent the standard deviation around their mean values.

The mean flame temperatures oscillate considerably between 1100 and 1600 ºC due to the continuous thermocouple reading fluctuations along the jet axis, as a result of the high-velocity flow driven forces. Also, some temperatures measuring errors could be induced due to the type of thermocouple used. So, discrepancies between simulated and measured temperatures may be found, given the difficulties of reaching stable values of the mean flame temperature. On the other hand, the measured heat fluxes slightly increase with Reynolds number, i.e. higher flow velocities lead to greater heat fluxes received at a certain distance from the jet flame. Then, the dimensionless flame-geometry descriptors behave similarly: their mean values decrease as the Reynolds number increases. In particular, the non-dimensional flame areas constantly decrease, while the dimensionless flame length variations become more evident when $Re > 3 \cdot 10^6$. Consequently, it is deduced that sonic jet flames become thinner and longer as the Re increases until achieving maximum lengths at a certain experimental conditions.

CFD modelling results

Figure 5 qualitatively compares the previous experimental measurements against the mean predictions obtained with the CFD codes used by averaging the steady evolutions computed during 30 s. The solid diagonal line indicates perfect agreement between predictions and measurements, while dotted lines and long-dashed lines represent the ± 25% and ± 50% prediction error, respectively, compared to the experimental measurement. All graphs include vertical and horizontal bars that represent the standard deviation of the simulation results and the experiments, respectively.

Prior to the analysis, it is worth noting that FLACS-Fire could not perform simulations with cell sizes smaller than 0.06 m, which occurred in those tests with Mach numbers of 0.10 and 0.20. The use of very thin grids under RANS turbulence model creates convergence problems in the near boundary surfaces of the domain leading to numerical instabilities. On the other hand, when FireFOAM simulations were run with cell sizes greater than 0.15 m (Mach numbers of 0.01 and 0.025), jet flames are represented as "columns of fire" ranging from their bases to the upper boundary layer. In that case, the coarse grids cannot accurately resolve the rate of fuel/oxidant mixing.

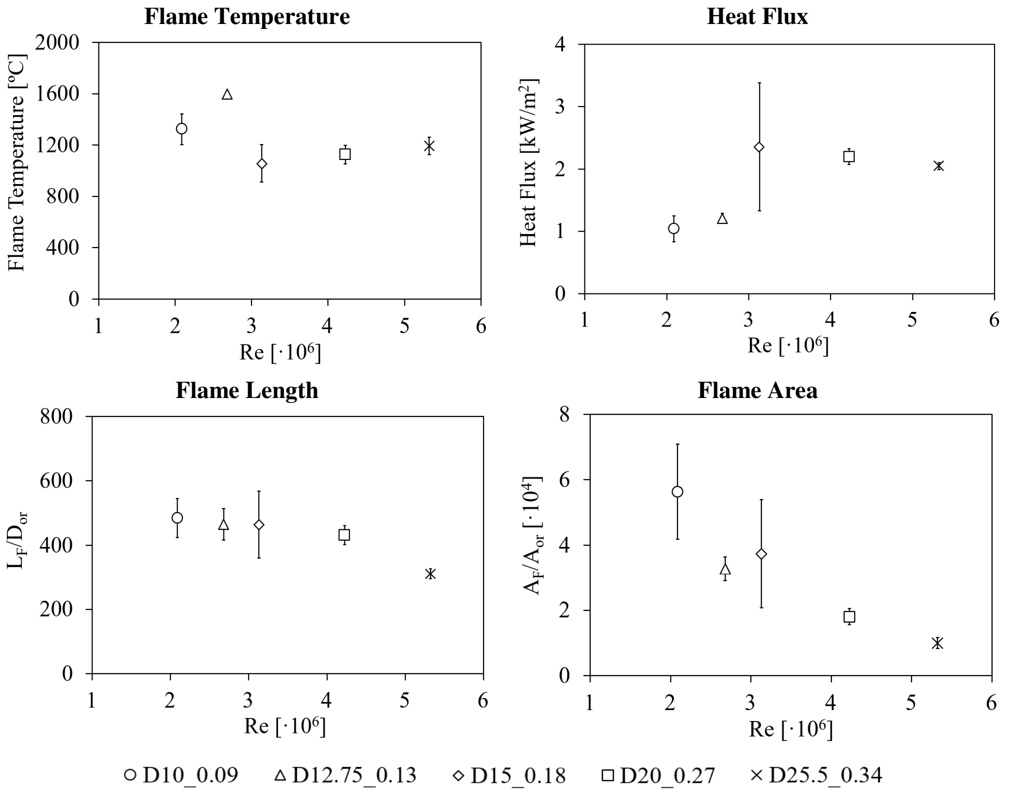

Fig. 4. Flame temperatures, heat fluxes, flame lengths, and flame area measurements obtained for the different sonic jet fires analysed.

In general, flame temperatures are often under-predicted in the CFD codes used. FDS estimations lead to an error estimation that ranged between 25% and 50%, where better agreement is often found when jet fires are modelled at smaller Mach numbers. In the case of FireFOAM, a lack of agreement is clearly observed, as an error estimation higher than 50% is reached in most cases. The maximum simulated temperatures are 650 ºC, while the measured values notably exceeded 1000 ºC. The lower accuracy obtained in this code could be mainly due to the model constants implemented within the combustion approach, as well as the simplicity of the mixing scale time calculation method. On the other hand, FLACS-Fire appears to be the most precise CFD model to predict the temperatures of the flame, as most of the values lead to an error estimation lower than 35%. This highlights the suitability of the $k - \varepsilon$ turbulence model, and the methodology used to compute the mixing scale times within the EDC approach.

Concerning the heat flux predictions, each code behaves differently. For example, over/under estimations are obtained in FDS, with an error estimation often lower than 50%. In contrast, heat fluxes are largely over-estimated in FireFOAM, with an averaged error estimation greater than 50%. The implementation of a model constant able to correct the emission term in the DOM equation, such as this applied in FDS, could improve agreement. Also, a better agreement may be reached in both codes by increasing the number of solid angles. Furthermore, the FLACS-Fire results reasonably match the experimental measurements, as occurs with the predicted flame temperatures. The promising results obtained in FDS and in FLACS-Fire could be also used in further analysis to determine the surface emissive power of the jets by considering the atmospheric transmissivity (often assumed to be 1) and the corresponding view factor.

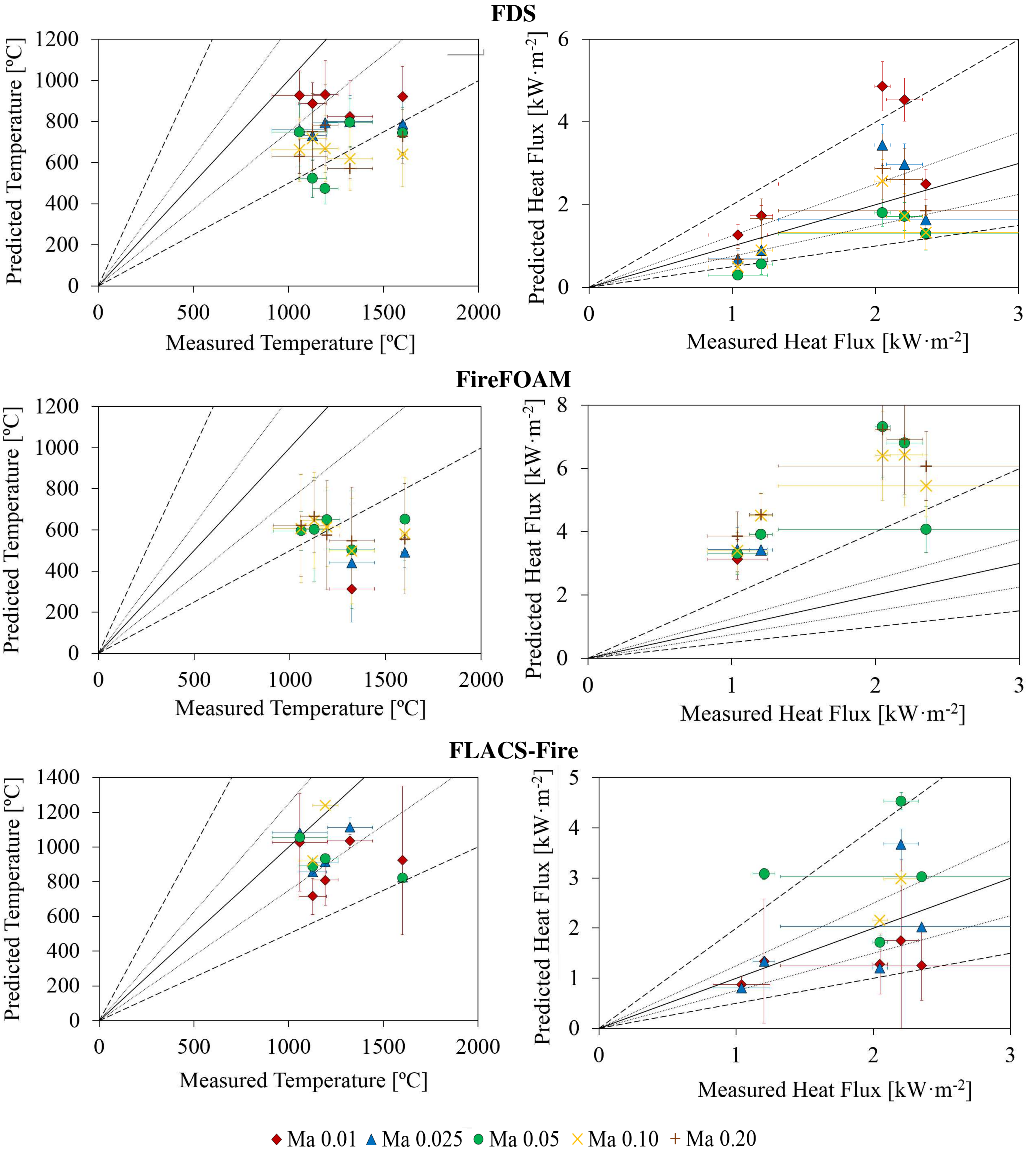

Fig. 5. Predicted values of the mean flame temperatures (left) and the mean radiative heat fluxes (right) estimated in FDS, FireFOAM and FLACS-Fire.

Furthermore, very good agreement is reached in FDS when calculating the mean flame lengths, with error estimations always lower than 25%, whereas less accurate predictions are obtained in FireFOAM and FLACS-Fire (Fig. 6). In general, the lower the Mach number, the more precise the estimations found in FLACS-Fire. On the other hand, flame areas are reasonably predicted in FDS, with better agreement reached under smaller cells. Contrarily, these are remarkably under-estimated in FireFOAM and in FLACS-Fire, regardless of the cell size. Therefore, both codes simulate very thin flames, hence demonstrating that the air entrained into the domain mixes with the released fuel much faster than in reality.

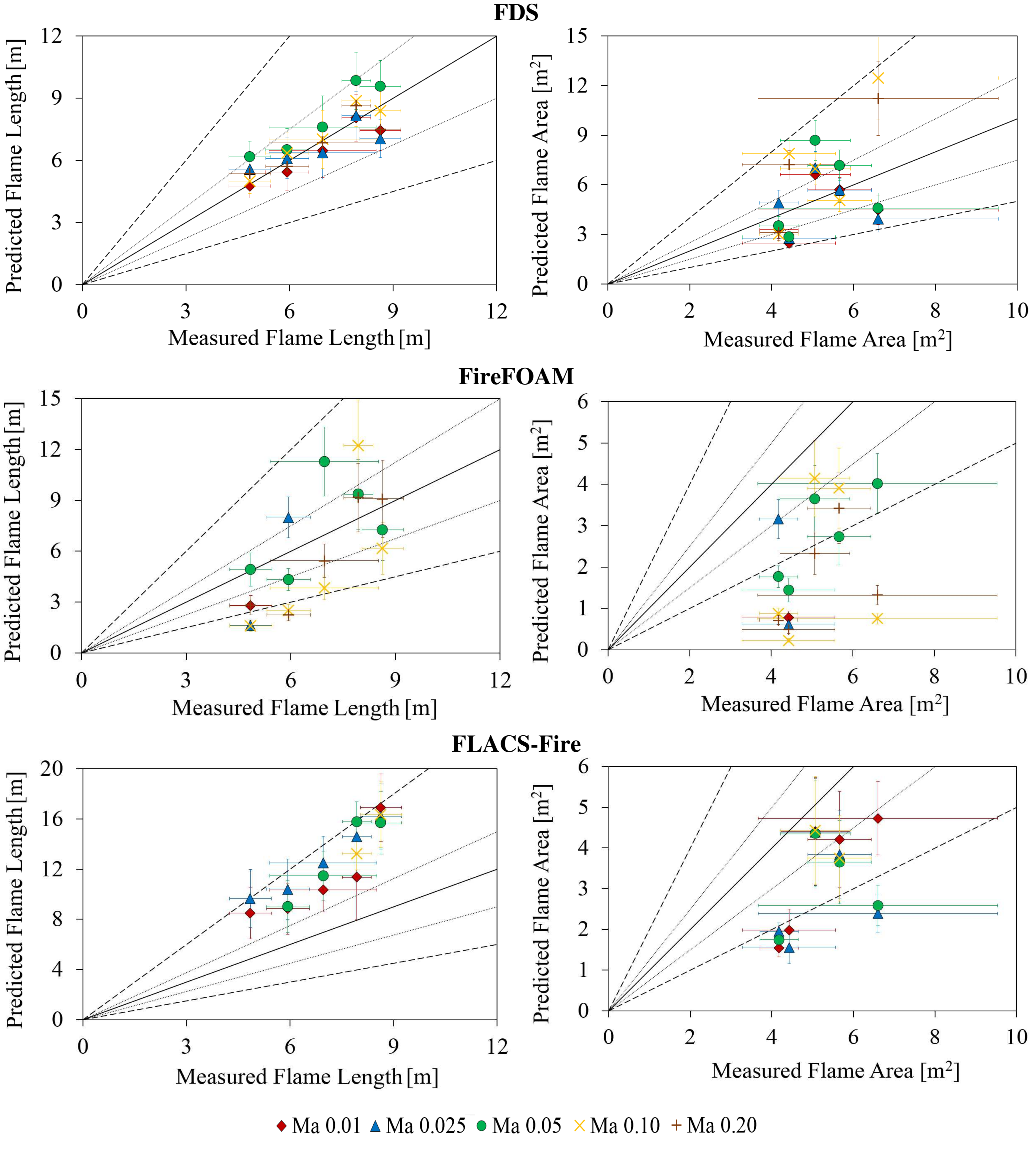

Fig. 6. Predicted values of the mean flame lengths (left) and the mean flame areas (right) estimated in FDS, FireFOAM and FLACS-Fire.

Quantitative error estimation

Qualitative comparisons are of high interest to quickly determine the suitability of a code to predict a variable of interest. However, when using this approach, there is no quantification of either the computational uncertainties or the agreement reached over time. Alternatively, the fractional bias

(FB) and the normalized mean square error (NMSE) quantitative performance measures have been calculated (Table 2) [20]. Although a perfect model would have FB and NMSE values of 0, it is to be noted that for research-grade field experiments, "acceptable" performing models must be within the performance criteria (PC): $\text{NMSE} \leq 0.5$ and $-0.3 \leq \text{FB} \leq 0.3$ [21].

Table 2. FB and NMSE values for the main variables of interest obtained with the different CFD codes as a function of the Mach number. Bold italic values indicate that the metric is within the established PC

CFD	Mach Number	Temperature		Heat Flux		Flame Length		Flame Area	
		FB	NMSE	FB	NMSE	FB	NMSE	FB	NMSE
FDS	0.01	0.32	***0.14***	-0.42	***0.30***	***0.06***	***0.01***	***0.18***	***0.13***
	0.025	0.47	***0.25***	***0.05***	***0.15***	***0.02***	***0.01***	***0.10***	***0.13***
	0.05	0.63	***0.49***	***0.26***	***0.39***	***-0.15***	***0.03***	***0.04***	***0.14***
	0.10	0.61	***0.46***	***0.30***	***0.23***	***-0.04***	***0.00***	***-0.21***	***0.20***
	0.20	0.57	***0.40***	***-0.03***	***0.10***	***0.00***	***0.01***	-0.63	1.09
FireFOAM	0.05	0.70	0.60	-0.96	1.33	***-0.03***	***0.08***	0.67	0.62
	0.10	0.71	0.65	-1.01	1.44	0.32	***0.47***	1.05	5.56
	0.20	0.71	0.64	-1.07	1.65	0.36	***0.28***	1.12	3.06
FLACS-Fire	0.01	0.33	0.62	***0.27***	0.38	-0.47	***0.26***	0.49	1.02
	0.025	***0.27***	***0.13***	***0.06***	***0.13***	-0.60	***0.39***	0.63	0.62
	0.05	***0.28***	***0.14***	***-0.28***	***0.40***	-0.65	***0.32***	0.57	0.51

Concerning the FDS estimations, it is observed that most of these are within the criteria established. Nevertheless, the notable under-predictions of the flame temperatures lead to fractional bias values greater than 0.30 for all the Mach numbers modelled. Also, non-acceptable values of the statistical metrics are obtained for flame areas and for heat fluxes when simulations are performed with very thin and coarse cell sizes, respectively. Apart from the predictions of the flame temperatures, whose deviations may be caused for multiple reasons (i.e. sub-models implemented, models constants, numerical schemes, etc.), the rest of the variables are reasonably well estimated. In particular, the sonic jet fire simulations performed in the current study are recommended to be run with equivalent diameters obtained with Mach number ranged between 0.025 and 0.10 in FDS. The numerous Mach numbers suggested for FDS allows simulations with multiple cell sizes, which could be of great interest when modelling complex geometries. Moreover, the favourable predictions of the heat fluxes and the flame lengths, make FDS a suitable candidate for determining hazardous effects of sonic jet fires.

Differently, notorious errors are found in the FireFOAM predictions, hence highlighting the need for further improvement before its application when modelling real sonic jet fires. Specifically, a sensitivity analysis of the modelling parameters previously discussed (i.e. model's constants, mixing scale times, number of solid angles, etc.) could be performed to determine the most suitable ones. Furthermore, FLACS-Fire is revealed as the most suitable among the CFD codes used to determine the flame temperatures of expanded jet fires. Also, the heat fluxes found are in accordance with the performance criteria. However, neither the flame lengths nor the flame surfaces are accurately calculated. Despite this, reliable results can be obtained in FLACS-Fire when the equivalent diameter of the jets is obtained with a Mach number ranged between 0.025 and 0.05.

According to the different levels of agreement in the CFD codes when varying the Mach number, it is deduced that the unconventional boundary condition at inflow have a strong impact on the final results. Despite the highlighted discrepancies when comparing simulation results with experimental measurements, promising results were often found under very low Mach numbers (≤ 0.05), especially in FDS and in FLACS-Fire. In consequence, reasonable estimations of the main hazardous effects of sonic jet fires can be obtained under cell sizes and equivalent diameters of at least 5 times higher than the exit orifice. In short, the pseudo-diameter approach is noted as a worthwhile technique for modelling sonic flows in CFD.

CONCLUSIONS

1. FDS, FireFOAM and FLACS-Fire codes were used to predict the flame temperatures, the heat fluxes and the flame-geometry descriptors of five propane jet fire experiments in an open environment. Due to the low Mach number formulation of the CFD codes used, the pseudo-diameter approach was used to determine the conditions of the jets after the expansion of the released gas. The equivalent properties of these (temperature, velocity and diameter) were simulated as a function of five Mach numbers proposed for analysis for each jet fire experiment.
2. Simulations and measurements were qualitatively and quantitatively compared in order to reveal the level of agreement reached in each CFD code. Temperatures were only accurately estimated in FLACS-Fire, while FDS and FireFOAM provided notable under-estimations. On the other hand, the radiative heat fluxes were reasonably calculated in FLACS-Fire and in FDS, whereas important over-estimations were achieved in FireFOAM. Also, acceptable predictions of the flame-geometry descriptors were obtained in FDS, while significant discrepancies were achieved in FLACS-Fire and FireFOAM. Indeed, these two codes predicted very thin flames as the air entrained into the domain mixed with the released fuel much faster than in reality.
3. The notorious discrepancies found in FireFOAM suggest that further improvement of the constants, as well as the mixing scale times calculation method within the combustion sub-model should be re-examined. Also, a higher number of solid angles, and the implementation of a correction factor to solve the DOM equation could deliver more accurate radiative heat fluxes predictions. Otherwise, FDS and FLACS-Fire are able to predict reasonably the hazardous effects of sonic jet fires under cell sizes of at least 5 times higher than the exit orifices.
4. This paper has demonstrated the capabilities of CFD tools to predict sonic jet fires by considering the equivalent conditions after expansion. Given the promising results found, especially in FDS and in FLACS-Fire, the pseudo-diameter approach may be used when modelling sonic flows in further analyses. In particular, additional sonic jet fire experiments could be simulated and compared with the main findings highlighted in the present paper.

ACKNOWLEDGMENTS

This research was partially funded by the Spanish Ministry of Economy and Competitiveness (project CTM2014-57448-R and CTQ2017-85990-R, co-financed with FEDER funds), Spanish Ministry of Education, Culture and Sport (FPI Program) and Autonomous Government of Catalonia (Project No. 2014-SGR-413). A.P. gratefully acknowledges the financial support of the Royal Society in the form of a Postdoctoral Newton International Fellowship.

REFERENCES

[1] R. Benintendi, A. Deisy, S. Marsh, A risk-based approach to safety distance determination in the process industry, in: 24th Inst. Chem. Eng. Symp. Hazards, 2014.

[2] E. Palazzi, B. Fabiano, Analytical modelling of hydrocarbon pool fires: Conservative evaluation of flame temperature and thermal power, Process Saf. Environ. Prot. 90 (2012) 121–128.

doi:10.1016/j.psep.2011.06.009.

[3] J. Casal, Evaluation of the Effects and Consequences of Major Accidents in Industrial Plants, 2nd ed. Elsevier, Amsterdam, 2017.

[4] M. Gómez-Mares, M. Muñoz, J. Casal, Axial temperature distribution in vertical jet fires., J. Hazard. Mater. 172 (2009) 54–60. doi:10.1016/j.jhazmat.2009.06.136.

[5] A. Palacios, A. Muñoz, J. Casal, Jet fires: An experimental Study of the Main Geometrical Features of the Flame in Subsonic and Sonic Regimes, AlChE J. 55 (2008) 256–263. doi:10.1002/aic.

[6] M. Masum, A. Rahman, S. Ahmed, F. Khan, LNG pool fire simulation for domino effect analysis, Reliab. Eng. Syst. Saf. 143 (2015) 19–29. doi:10.1016/j.ress.2015.02.010.

[7] M. Tanabe, A. Miyake, Effective implementation of inherently safer design during design phase of modularized onshore LNG projects, Chem. Eng. Trans. 48 (2016) 535–540. doi:10.3303/CET1648090.

[8] C. Azzi, L. Rogstadkjenet, Use of CFD in the Performance-Based Design for Fire Safety in the Oil and Gas Sector, in: 11th Conf. Performance-Based Codes Fire Saf. Des. Methods, 2016.

[9] A. Palacios, M. Muñoz, R.M. Darbra, J. Casal, Thermal radiation from vertical jet fires, Fire Saf. J. 51 (2012) 93–101. doi:10.1016/j.firesaf.2012.03.006.

[10] C. Mata, E. Pastor, B. Rengel, M. Valero, E. Planas, A. Palacios, J. Casal, Infrared Imaging Software for Jet Fire Analysis, Chem. Eng. Trans. 67 (2018) 877–882. doi:10.3303/CET1867147.

[11] P. Chatterjee, Y. Wang, K. V. Meredith, S.B. Dorofeev, Application of a subgrid soot-radiation model in the numerical simulation of a heptane pool fire, Proc. Combust. Inst. 35 (2015) 2573–2580. doi:10.1016/j.proci.2014.05.045.

[12] K. McGrattan, S. Hostikka, R. McDermott, J. Floyd, C. Weinschenk, K. Overholt, Fire Dynamics Simulator User's Guide, 2017. doi:10.6028/NIST.SP.1019.

[13] Y.Z. Li, C. Huang, J. Anderson, R. Svensson, H. Ingason, B. Husted, M. Runefors, J. Wahlqvist, Verification , validation and evaluation of FireFOAM as a tool for performance design, (2017) 84.

[14] G. AS, FLACS v10.7 User's Manual, 2017.

[15] E. Franquet, V. Perrier, S. Gibout, P. Bruel, Free underexpanded jets in a quiescent medium: A review, Prog. Aerosp. Sci. 77 (2015) 25–53. doi:10.1016/j.paerosci.2015.06.006.

[16] V.G. Dulov, G.A. Lukyanov, Gas Dynamics of the Outflow Processes, Novosibirsk (Russia), 1984.

[17] A.D. Birch, D.R. Brown, M.G. Dodson, The Structure and Concentration Decay of High Pressure Jets of Natural Gas, Combust. Sci. Technol. 5 (1984) 249–261.

[18] C. Lin, Y. Ferng, W. Hsu, N.T. Hua, Investigations on the Characteristics of Radiative Heat Transfer in Liquid Pool Fires, Fire Technol. 46 (2010) 321–345. doi:10.1007/s10694-008-0071-7.

[19] J.H. Kent, A quantitative relationship between soot yield and smoke point measurements, Combust. Flame. 63 (1986) 349–358.

[20] P. Rew, D. Deaves, The validation and application of pool fire models, in: Saf. Eng. Risk Anal., 1995: pp. 57–65.

[21] S.R. Hanna, O.R. Hansen, S. Dharmavaram, FLACS CFD air quality model performance evaluation with Kit Fox, MUST, Prairie Grass, and EMU observations, Atmos. Environ. 38 (2004) 4675–4687. doi:10.1016/j.atmosenv.2004.05.041.

Lift-off Behavior of Horizontal Subsonic Jet Flames Impinging on a Cylindrical Surface

Wang Z.[1], **Zhou K.**[1,]* , **Liu M.**[1], **Wang Y.**[1], **Qin X.**[1], **Jiang J.**[2,]**

[1] *College of Safety Science and Engineering, Nanjing Tech University,*
Nanjing, Jiangsu, 211816, China
[2] *Jiangsu Key Laboratory of Hazardous Chemicals Safety and Control,*
Nanjing Tech University, Nanjing, Jiangsu, 211816, China
**Corresponding author's emails: kbzhou@njtech.edu.cn and jcjiang@njtech.edu.cn*

ABSTRACT

This paper presents a systematic experimental study on the lift-off behavior of jet flames impinging on a cylindrical surface by conducting horizontal jet fire experiments. In the tests, the fuel exit velocity was varied between 8.5 and 73.1 m/s, while the internal diameter of the nozzle was 2.0, 3.0, and 4.2 mm. The nozzle-to-surface spacing was set to be infinite (corresponding to free jet flame), 15, 20, and 25 cm. The flame lift-off distance was observed to be between 0.46 and 20.97 cm. This distance was accurately calculated by using an image visualization technique to reconstruct the image frames of a camera. It was found that the lift-off distance depends on not only the exit velocity but also on the nozzle diameter of the free jet flame. The proportionality of lift-off distance to exit velocity increases as the nozzle diameter increases. It is also indicated that the exit velocity, nozzle diameter and nozzle-to-surface spacing have a complex coupled effect on the jet flame lift-off behavior. For the 2.0 mm diameter nozzle, the lift-off distance of a jet flame impinging on a cylinder increases more remarkably than that of free jet flame. The lift-off distance first increases and then remains the same as the exit velocity increases for all nozzle-to-surface spacings. For the 3.0 mm diameter nozzle, the lift-off distance is only affected at a nozzle-to-surface spacing of 15 cm. For the 4.2 mm diameter nozzle, the cylinder has no effect on the lift-off distance regardless of the nozzle-to-surface spacing. The dimensionless flow number expression for the lift-off distance of free and impinging jet flames in the subsonic regime provides the best fit, after consideration of four different available correlations that are evaluated against the experimental measurement in this paper.

KEYWORDS: Lift-off distance, jet flame, impinging jet, subsonic.

INTRODUCTION

Jet fires caused by accidental fuel gas leakage can increase the scale of an accident by impinging on such structural elements as pipes and tanks. This process, known as the domino effect, has been reported to be responsible for some disastrous events, e.g. the San Juanico disaster of 1984 [1]. In such events, the most common scenario involved jet flames impinging on a cylindrical surface. Even though impinging flames have been applied in different fields of metal heating and melting, chemical vapor deposition, and even aerospace, most researchers only focused on the heat transfer aspect of the process [2], and neglected the flame geometric shapes and flame instabilities. However, the flame instabilities consisting of lift-off and blow-off are important phenomena in combustion and in the fire safety field [3, 4].

In general, a free jet diffusion flame lifts off away from the burner nozzle and forms a stable lifted flame, as the exit velocity increases beyond the lift-off stability limit [3]. Although there are several

Proceedings of the Ninth International Seminar on Fire and Explosion Hazards (ISFEH9), pp. 831-842
Edited by Snegirev A., Liu N.A., Tamanini F., Bradley D., Molkov V., and Chaumeix N.
Published by Saint-Petersburg Polytechnic University Press
ISBN: 978-5-7422-6498-9 DOI: 10.18720/spbpu/2/k19-79

competing theories for explaining the behavior of lifted diffusion flames, none of them is entirely satisfactory. These theories may roughly be classified into four main categories. They include theories based on (i) the premixed flame propagation model [3, 5, 6], (ii) the extinction of laminar diffusion flamelets [7, 8], (iii) the large-scale turbulent structures [9, 10], and (iv) the concept of triple flames [11]. Even though all the theories seem to include the correct mechanisms, their application is strictly limited to vertical jet flames. In particular, some empirical correlations are developed for the lift-off distance by fitting experimental data of vertical jet flames.

However, the available lift-off distance correlations need further evaluation as they are used for horizontal jet flames. Peters and Göttgens [12] proposed an approximate solution to calculate the flame trajectory of large buoyant jet diffusion flames with the jet direction from vertical to horizontal. Similar work has also been done by Kim et al. [13] for hydrogen jet flames with the jet Reynolds number of 2400. Johnson et al. [14] investigated the flame shape and external thermal radiation of large-scale horizontal natural gas jet fire. Siebers et al. [15] focused on the effects of in-cylinder gas oxygen concentration on the flame lift-off of a horizontal direct-injection diesel fuel jet fire. Smith et al. [16] experimentally explored the effects of buoyancy and momentum on the global characteristics of horizontal propane jet flames, such as flame dimensions, centerline trajectory, emission indices, radiative fraction. Gopalaswami et al. [17] and Zhang et al. [18] investigated the flame length, lift-off distance, and flame area of horizontal propane jet flames. The exit velocities varied from 25 m/s to 210 m/s, and the flame lengths from 1 to 6 m. Zhou et al. [19] reviewed correlations of jet flame lift-off distance, flame length, and radiative fraction, and proposed a line source model to predict the heat flux of horizontal jet flame. Additionally, there are some limited research studies on the flame structure of impinging jet flames. For example, Johnson et al. [20] simulated an open air sonic propane flame and a subsonic natural gas flame impinging on a 2 m diameter cylindrical target by using computational fluid dynamics. Patej et al. [21] investigated the thermal load and the thermal response of the pipes directly impinged by different hydrocarbon jet flames. But neither study addressed the question of a new lift-off distance correlation nor evaluated the available correlation for horizontal jet flames.

In view of the limitation of the available lift-off distance correlation for horizontal jet flame, this paper attempts to study the flame lift-off distance of horizontal jet flames impinging on a cylindrical surface. First, propane jet fire experiments are conducted with different exit diameters and velocities, and nozzle-to-surface spacings. Comparisons are then made of lift-off distances, to explore the difference between vertical, horizontal, free, and impinging jet flames. Finally, four different available lift-off distance correlations are evaluated against the experimental measurements of free and impinging horizontal jet flames, with the aim of developing a lift-off distance correlation for horizontal jet flames.

EXPERIMENTAL

Figure 1 depicts the experimental facility and measurement setup. It consists of a fuel supply system and a jet nozzle of stainless steel. The nozzle diameter was varied from 2.0 mm, 3.0 mm to 4.2 mm, with a length of 15 cm. Commercially pure propane was used as fuel and its supply rate was recorded by an Alicat® mass flow controller with an accuracy of ±0.2% of reading + 0.8% of full scale. With the mass flow controller, the fuel exit velocity was set to be 8.51 m/s to 73.10 m/s, with subsonic flow in all tests. A hollow steel cylinder with outer and inner diameters of 8.9 cm and 8.6 cm, was used as target. The horizontal jet flame was set to be normal to cylindrical surface in the test. The spacing between the burner nozzle and the cylindrical surface was 15, 20 and 25 cm, and a free horizontal jet flame was also studied. The spacing was selected to ensure that the size of free jet flame would be at least comparable to that of the impinging jet flame for most of the experimental conditions, and the specific geometrical features could be easily extracted, using an image processing technique. A Digital Video of sensor size 1/2.5 inch with 3840×2160 pixels was used to record the flame at 25 frame per second. The flame video was decompressed into flame images (40 s, nearly 1000 frames), and these images were further processed by the Otsu method [22] to obtain the flame presence probability contours as shown in Fig. 2. The maximum flame lift-off was obtained by measuring the distance from the nozzle outlet to the starting tip of the flame contour line of 50% probability, shown in Fig. 2.

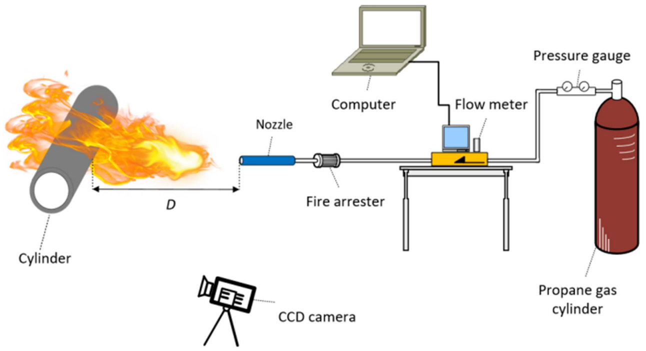

Fig. 1. Schematic diagram of experimental setup.

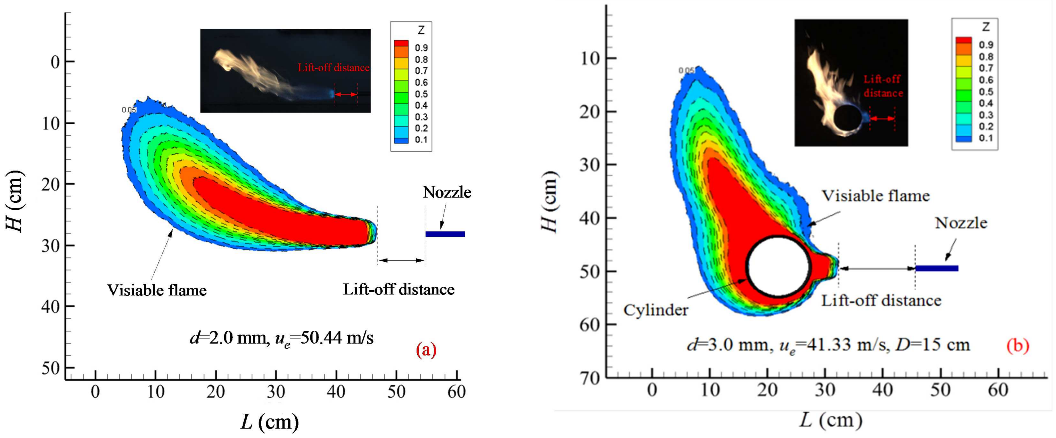

Fig. 2. Flame lift-off quantification according to flame appearance intermittency contour. (a) Free jet flame; (b) Impinging jet flame.

RESULTS AND DISCUSSION

Lift-off of horizontal free jet flames

Several researchers [23, 24] have proposed that the lift-off distance can be related to the global strain rate defined as the ratio of the exit velocity to the nozzle diameter. Figure 3 shows a comparison of the dimensionless lift-off distance with the global strain for horizontal jet flames. Given the limited research on horizontal jet flames, the lift-off behavior has lacked attention. The data provided by Gopalaswami et al. [17] and Zhang et al. [18] are amongst the few available. Data analysis reveals that the lift-off distance of the horizontal propane jet flame is also proportional to the exit velocity, but that the nozzle diameter also has a significant effect on the lift-off behavior. As shown, the proportionality of lift-off distance to exit velocity increases as the nozzle diameter increases. By contrast, using the lift-off data from Kalghatgi et al. [3], Santos et al. [24], and

Palacios et al. [25], with nozzle diameters of 4.06 mm to 43.1 mm, Zhou et al. [19] found that the nozzle diameter has no effect on the lift-off distance versus the exit velocity for vertical propane jet flames. A universal correlation was proposed, with a proportionality of factor of 2.13×10^{-3}.

Vanquickenborne and Van Tiggelen [5], in their early work employed a premixed flame propagation model to explain the stabilization mechanism of lifted diffusion flames. They considered that the premixed nature of the fuel-air mixture controls the flame base location where a stoichiometric composition is achieved. In such a region, the turbulent burning velocity equals the mean flow velocity. Later, assuming a turbulent flame propagating through a premixed fuel-air mixture, Kalghatgi [3] further proposed a scaling law to fit the lift-off distance of vertical jet flames with a wide range of exit velocity (u_e), nozzle diameter (d) and fuel type. With such scaling law, the lift-off distance (l_f) can be described by:

$$Re_{lf} \equiv l_f S_L / \nu_e \sim \left(u_e / S_L\right)\left(\rho_e / \rho_\infty\right)^{1.5}, \tag{1}$$

where Re_{lf} is the local turbulence Reynolds number based on the integral length scale, ν_e is the fuel gas kinematic viscosity, S_L is the maximum laminar burning velocity of the fuel-air mixture, and ρ_e, ρ_∞ are the densities of fuel gas and ambient air, respectively.

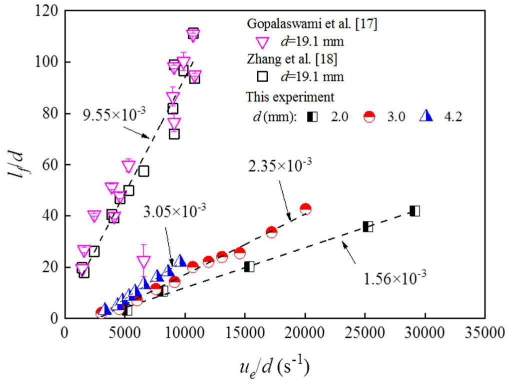

Fig. 3. Dimensionless lift-off distance versus global strain rate for horizontal propane jet flames of different nozzle diameters.

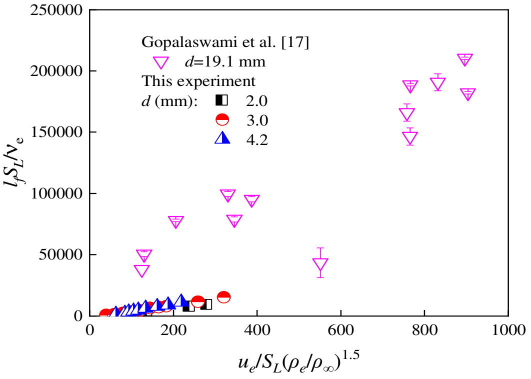

Fig. 4. Lift-off distance fitted by the correlation of Kalghatgi et al. [3] for horizontal jet flames.

As shown in Fig. 4, Eq. (1) correlates the lift-off distance of horizontal jet flames with different nozzle diameters. The scatter becomes apparent as the nozzle diameter reaches 19.1 mm. Kumar et al. [26] also found the deviation when using Eq. (1) to correlate the lift-off of vertical jet flames, especially for large $\left(u_e/S_L\right)\left(\rho_e/\rho_\infty\right)^{1.5}$. Kalghatgi's dimensionless analysis is unable to explain the effect of nozzle diameter on lift-off distance. Since the same image processing technique for flame base location was applied by this work and Gopalaswami et al. [17], the reason for the major discrepancy between different nozzle diameters was considered to be the inherent inadequacy of Eq. (1). Note that Eq. (1) is based on the premixedness model, which assumes that the lifted flame stabilization is controlled by relatively small turbulent structures. Also note that this model does not incorporate the intermittency of turbulent flow [6].

Broadwell et al. [9] proposed another correlation that successfully attempts to correlate the lift-off distance of a vertical jet flame. This model is based on the idea of large-scale motions in the turbulent jet that can maintain the lifted flame stabilization. In detail, the hot reaction products that are expelled to the edges of the jet by large turbulent vortices are re-entrained to ignite the fresh fuel-air mixture in the lift-off region. His correlation for lift-off distance can be written as:

$$l_f \sim \left[u_e d\left(\rho_e/\rho_\infty\right)^{1/2} \kappa/S_L^2\right]^{1/2}, \tag{2}$$

in which κ is the thermal diffusivity. Equation (2) can be revised in the dimensionless form of $l_f/d\sqrt{\rho_e/\rho_\infty} \sim \sqrt{\left(\kappa/S_L^2\right)/\left(d\sqrt{\rho_e/\rho_\infty}/u_e\right)}$ in which the two terms, κ/S_L^2 and $d\sqrt{\rho_e/\rho_\infty}/u_e$, provide the measure of two characteristic times. The first one is the characteristic chemical reaction time, while the other is the mixing time of re-entrained hot products with fresh reactants.

As shown in Fig. 5, Eq. (2) correlates well the lift-off distance of horizontal jet flames with different nozzle diameters. The equations shows how the nozzle diameter affects the lift-off distance in detail. However, it is stressed that the mixing time of re-entrained hot products into fresh reactants is hard to determine. It is controversial to use the expression $d\sqrt{\rho_e/\rho_\infty}/u_e$, in Eq. (2), to accurately calculate the mixing time. Pitts [6] suggested a stricter approach, treating the mixing time as that for re-entrainment of hot products at the upstream edges of large-scale vortices. Note that the large-scale inviscid motions, rather than the small-scale turbulent structures, are the source of lift-off stabilization. Figure 6 presents the comparison in the lift-off distance fitted by Eq. (2) between the horizontal and vertical propane jet flames. As shown, Eq. (2) can fit both well, but the horizontal jet flame shows a trend that is different from that of the vertical flame data. The lift-off distance of vertical jet flames shows a linear relationship, while such a relationship is complex for horizontal jet flames.

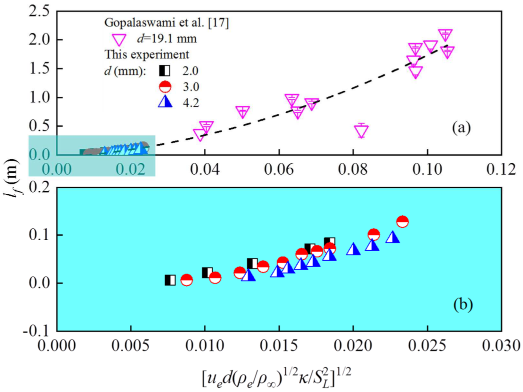

Fig. 5. Lift-off distance fitted by the correlation of Broadwell et al. [9] for horizontal jet flames. Bottom is an enlarged view of the rectangular shaded area.

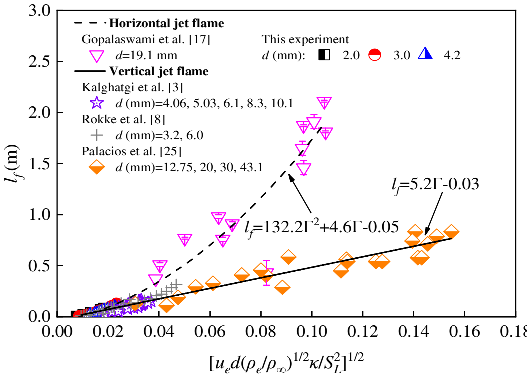

Fig. 6. Lift-off distance fitted by the correlation of Broadwell et al. [9] used for both vertical and horizontal propane jet flames.

Miake-Lye and Hammer [10] also obtained a linear relationship of lift-off distance for vertical jet flames. It is based on the idea that large-scale coherent motions dominates the turbulent jet. By reasoning similar to that by Broadwell et al. [9], the stability criterion is expressed in terms of the critical strain rate that equals the inverse of the chemical reaction time:

$$l_f \sim \left(\kappa/S_L^2\right)\left(Z_{st}/Y_f\right)u_e, \tag{3}$$

where Z_{st} is the mass fraction of pure fuel in air at stoichiometric conditions, and Y_f is the mass fraction of fuel in the jet fluid. Figure 7 presents the lift-off distance correlated by Eq. (3) for both vertical and horizontal jet flames. As shown, the inferred linear relationship is difficult to reproduce. In particular, a significant deviation is observed in the case of large nozzle diameters. The effect of flame speed and thermal diffusivity should be excluded, given the somewhat different values of S_L and κ used in [3, 27, 28]. Thus, such deviation can be mainly attributed to the overly simple chemistry used in the strain-out condition. In addition, Upatnieks et al. [29] used cine-particle imaging velocimetry to measure the lift-off distance of vertical jet flames and assessed the poor validity of Eq. (3), for the correlation between flame propagation and passage of large eddies, not considered by Miake-Lye and Hammer [10]. However, the interaction between the large-scale structure and the flame zone is shown by Schefer et al. [30], who performed planar imaging measurements of CH_4, CH, and temperature of a jet flame. Later, a study by Lyons [31] concluded that the impact of large-scale structures is significant as the turbulent/reaction zone interaction increases and strengthens.

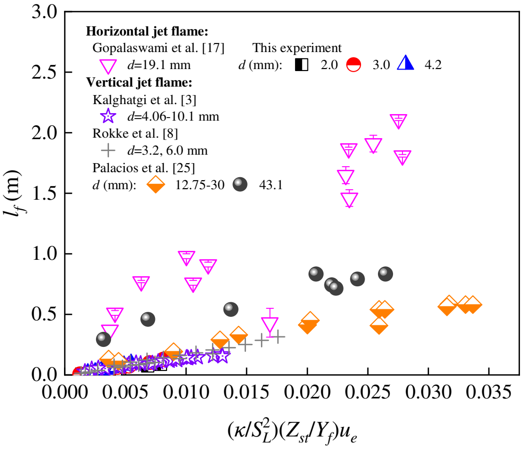

Fig. 7. Lift-off distance fitted by the correlation of Miake-Lye and Hammer [10] used for both vertical and horizontal propane jet flames.

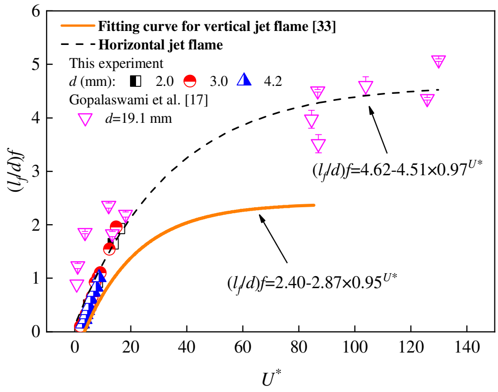

Fig. 8. Lift-off distance fitted by the correlation of Bradley et al. [32] used for both vertical and horizontal jet flames.

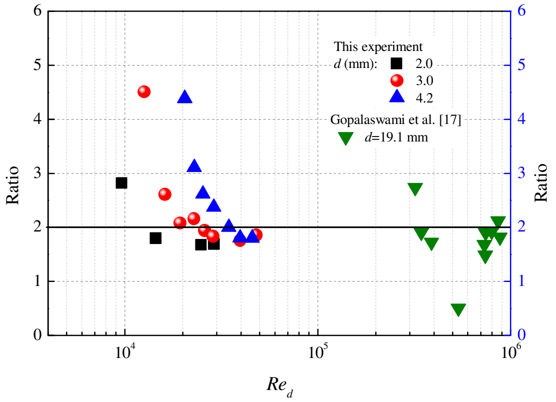

Fig. 9. Lift-off distance ratio of horizontal to vertical jet flames versus Reynold number.

Recently, Bradley et al. [32] made some progress in more practical, generalized correlations for the extensive experimental data of flame dimensions of vertical jet flames in both subsonic and sonic regimes. Their main innovation involves a dimensionless flow number that related to the Karlovitz stretch factor in premixed turbulent combustion. The dimensionless flow number (U^*) is:

$$U^{*}=\left(u_e/S_L\right)\left(\delta/d\right)^{0.4}\left(P_i/P_\infty\right), \tag{4}$$

in which δ is the laminar flame thickness, given by $\delta=\nu_e/S_L$ at the ambient air conditions, and P_i, P_a are the initial stagnation and atmospheric pressures, respectively. The dimensionless flow number was used to fully correlate the lift-off distance for vertical jet flames of different fuel gases, by introducing the ratio of fuel to air moles (f) in fuel–air mixture for maximum burning velocity [32]. Figure 8 presents the dimensionless lift-off distance versus dimensionless flow number for horizontal propane jet flame, as well as the fitting curve of vertical jet flame in [33]. As shown, the horizontal jet flame holds a larger lift-off distance as the dimensionless flow number is the same.

Figure 9 shows the ratio of lift-off distance between horizontal to vertical jet flames versus the exit Reynolds number ($Re_d = u_e d/\nu_e$). As shown, the ratio approaches nearly two as the exit Reynolds number increases. Nevertheless, such a ratio can help to assess the hazardous scope and consequence of large horizontal jet fires with the available behaviors of vertical jet fires.

LIFT-OFF OF HORIZONTAL JET FLAMES IMPINGING ON A CYLINDER

In order to quantify the effect of the cylindrical surface, near the nozzle, on lift-off distance, as mentioned in the section describing the experiments, the spacing between the nozzle exit and the cylindrical surface, *D*, varies from 15 to 25 cm. Figure 10 demonstrates the effect of the spacing on the normalized lift-off distance versus the global strain rate, for three different nozzle diameters, as well as typical flame photos, with increasing exit velocity for *D* = 15 cm and *d* = 3.0 mm.

As indicated in Fig. 10 (a), the lift-off distance of a jet flame impinging on a cylindrical surface increases more remarkably than that of a free jet flame for the nozzle of 2.0 mm in diameter. It is of interest to observe that the lift-off distance of impinging flame first increases, and then remains stable as the exit velocity increases. In particular, the lift-off distance will reach the nozzle-to-surface spacing as the exit velocity approaches the blow-out limit (see the data in the dashed circles of Figs. 10 (a) and 10 (b) and the last flame image in Fig. 10 (d)). A plausible reason for this phenomenon might result from the complex interaction between the high-temperature jet flame and the cylindrical surface characteristic. It is known that propane fuel flow undergoes a conversion from a gas-liquid mixture to pure gas with the increase in release pressure or exit velocity. Gómez-Mares et al. [34] concluded that flames fed by a two-phase flow mixture are luminous and yellow, while those fed by gas are nearly transparent and blue. As shown in Fig. 10 (d), the impinging flame was also observed to turn from yellow to blue, as the exit velocity increased.

There seem to be two different mechanisms for interpreting the lift-off behaviors of impinging jet flame in such a geometric configuration. In the range of low exit velocity, the soot indicated by bright yellow color plays an important role in heat radiated by jet flames [17], and as seen in Fig. 11 (a), the soot deposits on the contact surface after the jet flame impingement, due to the thermophoresis [35]. These opaque particles escape from the hot flame zone and move towards the cold pipe wall surface where a sharp temperature gradient exists [21]. In this case, the downstream lift-off behavior was not affected, and the lift-off distance still fits the linear law. On the other hand, in the range of high exit velocities, the transparent jet flame causes an oxidation of the steel pipe, resulting from high temperature, as indicted in Fig. 11 (b). So the upstream high temperature oxidation of the alloy, accompanied by intense thermochemical heat release [2], dominates the maximum limitation of downstream lift-off distance of the impinging jet flame. In Fig. 10 (b), the lift-off distance of the impinging jet flame is still affected by the cylindrical surface, as the spacing is 15 cm. However, when the spacing increases further, the cylindrical surface has no effect on lift-off distance, and the same situation was also observed in all test conditions for *d* = 4.2 mm.

Obviously, the spacing should be also a main factor that affects the lift-off distance of the impinging jet flame. Overall, the exit velocity, nozzle diameter and nozzle-to-surface spacing hold a complex, coupled effect on the lift-off behavior of impinging jet flames. It seems that the effect of cylinder on impinging jet flame would appear at the high exit velocity as the nozzle diameter and nozzle-to-surface spacing decrease.

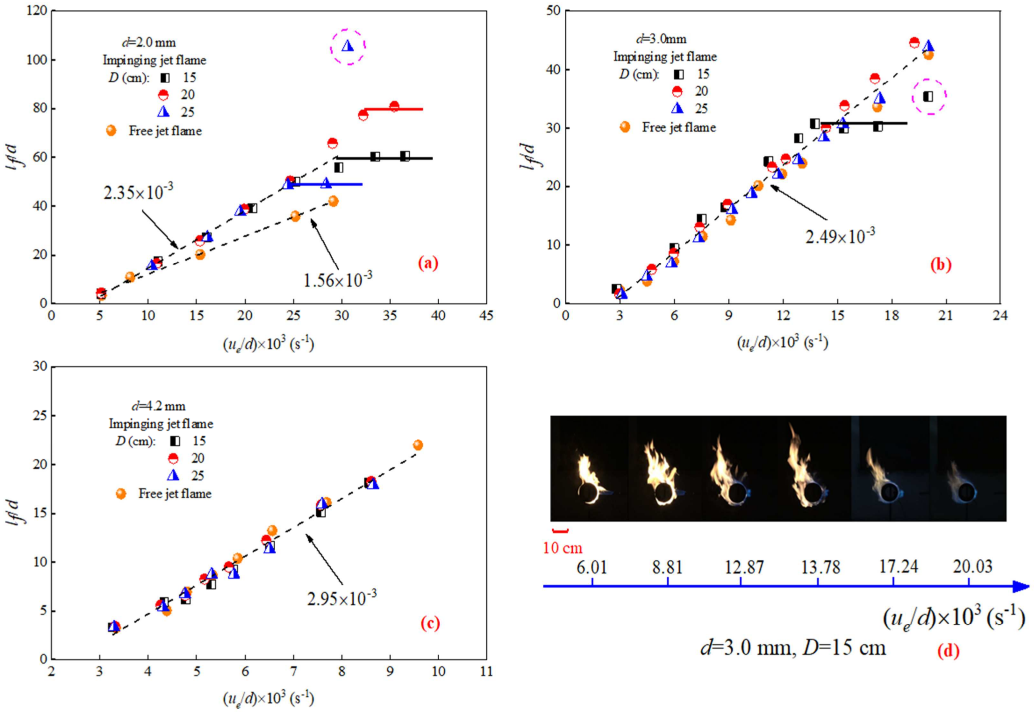

Fig. 10. Dimensionless lift-off distance versus global strain rate for horizontal propane jet flames impinging on a cylindrical surface for d = 2.0 mm (a), 3.0 mm (b), and 4.2 mm (c), and typical flame images versus exit velocity for D = 15 cm and d = 3.0 mm.

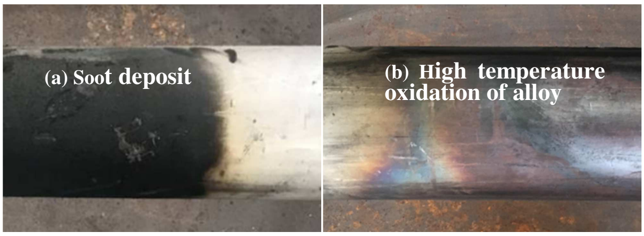

Fig. 11. Evolution of the pipe wall surface due to jet flame impingement. (a) soot deposit; (b) high temperature oxidation of alloy.

Figure 12 presents the lift-off distance fits for impinging jet flames with different available correlations. These attempted correlations for lift-off distance proposal are those from Kalghatgi et al. [3], Broadwell et al. [9], Miake-Lye's and Hammer [10] and Bradley et al. [32], which are shown in Figs. 12 (a), (b), (c) and (d), respectively. As can be seen, the correlations of Kalghatgi, Miake-Lye and Bradley are found to fit well the lift-off distance of impinging jet flames. In contrast, there is large scatter resulting from different nozzle diameters for Broadwell's method. This method seems to be not optimal for the lift-off distance correlation of impinging jet flames. Note the disadvantage of Kalghatgi's and Miake-Lye's methods for free jet flames as stressed in the previous discussion. In short, only the methodology of [32] can give a better fit for the lift-off distance of both free and impinging jet flames. As shown in Fig. 13, the method of Bradley et al. can fully characterize the lift-off behavior of free and impinging jet flames. More experimental data on jet flame lift-off are needed to validate Bradley's method, involving a wide range of exit velocity, nozzle diameter, nozzle-to-surface spacing, and target shape and size.

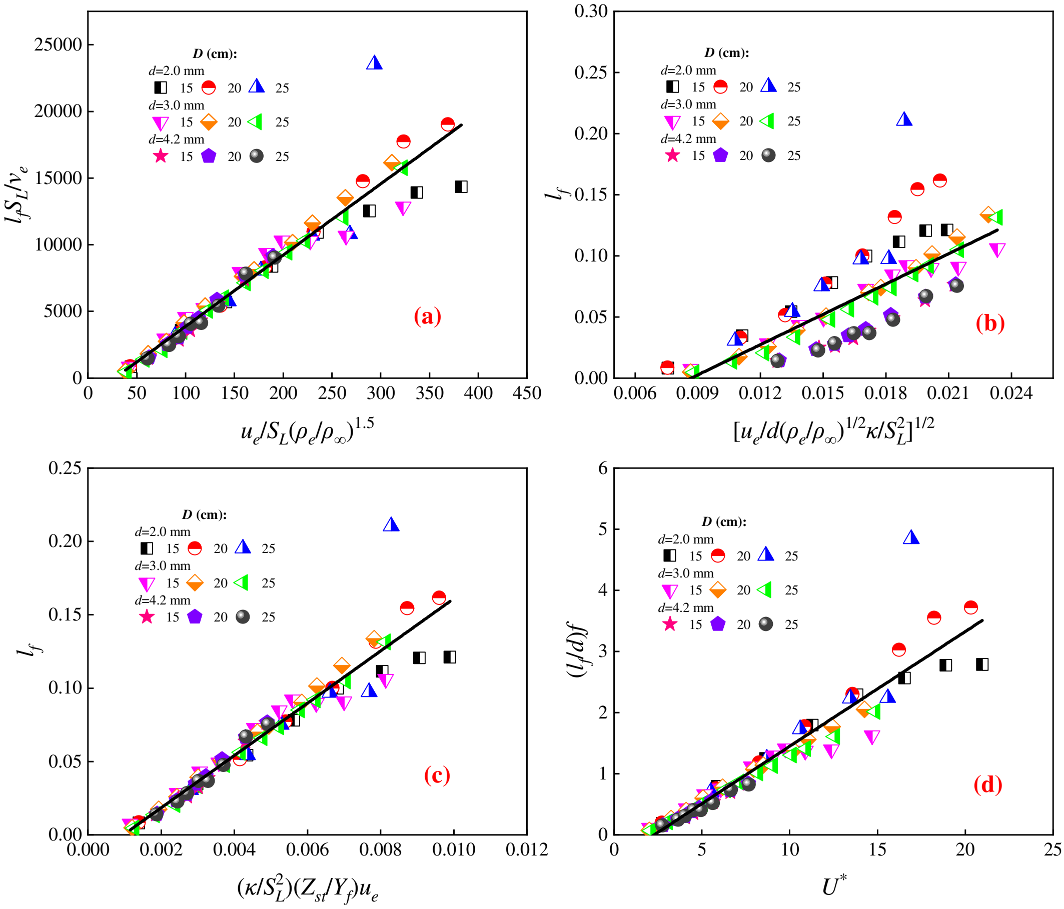

Fig. 12. Comparisons between lift-off distance fittings using different available correlations: (a) Kalghatgi's method [3], (b) Broadwell's method [9], (c) Miake-Lye's method [10] and (d) Bradley et al. [32].

CONCLUSIONS

This paper has reported a systematic experimental investigation on the lift-off behavior of free and impinging horizontal jet flames in the subsonic regime. Comparison in the lift-off distance is conducted between vertical and horizontal jet flames. Four different available correlations of lift-off distance are evaluated against the experimental measurement of free and impinging horizontal jet flames in the subsonic regime. The major findings are as follows:

(1) The lift-off distance is linearly proportional to the exit velocity for vertical jet flames for all nozzle diameters, while the slope of the linear variation of lift-off distance with exit velocity significantly increases as the nozzle diameter increases.

(2) For small nozzle diameter and nozzle-to-surface spacing, the lift-off distance increases linearly,

and then remains constant, finally reaching the nozzle-to-surface spacing as the exit velocity increases. As the nozzle diameter and nozzle-to-surface spacing increase to be large enough, the lift-off distance only becomes a linear function of the exit velocity.

(3) In comparison with correlations of Kalghatgi, Broadwell and Miake-Lye, the dimensionless flow number proposed by Bradley et al. can be used to fit the lift-off distances of free and impinging horizontal jet flames in the subsonic regime.

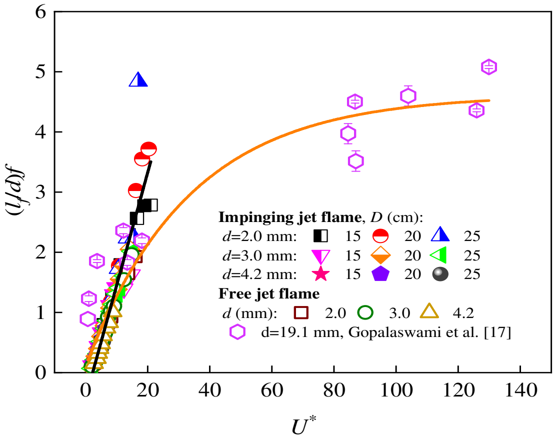

Fig. 13. Lift-off distance fitted by the correlation of Bradley et al. [32] for both free and impinging jet flames.

ACKNOWLEDGEMENTS

This work was financially supported by the National Key R&D Program of China (No. 2016YFC0800100), and the National Natural Science Foundation of China under Grant Nos. 51876088 and 51834007.

REFERENCES

[1] G. Reniers, W. Dullaert, S. Karel, Domino effects within a chemical cluster: a game-theoretical modeling approach by using Nash-equilibrium, J. Hazard. Mater. 167 (2009) 289-293.

[2] C.E. Baukal Jr, B. Gebhart, A review of empirical flame impingement heat transfer correlations, Int. J. Heat Fluid Flow 17 (1996) 386-396.

[3] G.T. Kalghatgi, Lift-off Heights and Visible Lengths of Vertical Turbulent Jet Diffusion Flames in Still Air, Combust. Sci. Technol. 41 (1984) 17-29.

[4] Q. Wang, L. Hu, S.H. Chung, Blow-out of nonpremixed turbulent jet flames at sub-atmospheric pressures, Combust. Flame 176 (2017) 358-360.

[5] L. Vanquickenborne, A. van Tiggelen, The stabilization mechanism of lifted diffusion flames, Combust. Flame 10 (1966) 59-69.

[6] W.M. Pitts, Assessment of theories for the behavior and blowout of lifted turbulent jet diffusion flames, Proc. Combust. Inst. 22 (1989) 809-816.

[7] N. Peters, F.A. Williams, Liftoff characteristics of turbulent jet diffusion flames, AIAA journal. 21 (1983) 423-429.

[8] N.A. Røkke, J.E. Hustad, O.K. Sønju, A study of partially premixed unconfined propane flames, Combust. Flame 97 (1994) 88-106.

[9] J.E. Broadwell, W.J.A. Dahm, M.G. Mungal, Blowout of turbulent diffusion flames, Proc. Combust. Inst. 20 (1985) 303-310.

[10] R.C. Miake-Lye, J.A. Hammer, Lifted turbulent jet flames: a stability criterion based on the jet large-scale structure, Proc. Combust. Inst. 22 (1989) 817-824.

[11] C.M. Müller, H. Breitbach, N. Peters, Partially premixed turbulent flame propagation in jet flames, Proc. Combust. Inst. 25 (1994) 1099-1106.

[12] N. Peters, J. Göttgens, Scaling of buoyant turbulent jet diffusion flames, Combust. Flame 85 (1991) 206-214.

[13] J.S. Kim, W. Yang, Y. Kim, S.H. Won. Behavior of buoyancy and momentum controlled hydrogen jets and flames emitted into the quiescent atmosphere, J. Loss Prev. Process Ind. 22 (2009) 943-949.

[14] A.D. Johnson, H.M. Brightwell, A.J. Carsley. A model for predicting the thermal radiation hazards from large-scale horizontally released natural gas jet fires, Process Saf. Environ. Prot. 72 (1994) 157-66.

[15] D.L. Siebers, B. Higgins, L. Pickett, Flame lift-off on direct-injection diesel fuel jets: oxygen concentration effects, Report No. 2002-01-0890, SAE Technical Paper, 2002.

[16] T. Smith, C. Periasamy, B. Baird, S.R. Gollahalli, Trajectory and characteristics of buoyancy and momentum dominated horizontal jet flames from circular and elliptic burners, J. Energy Resources Technol. 128 (2006) 300-310.

[17] N. Gopalaswami, Y. Liu, D.M. Laboureur, B. Zhang, M.S. Mannan, Experimental study on propane jet fire hazards: Comparison of main geometrical features with empirical models, J. Loss Prev. Process Ind. 41 (2016) 365-375.

[18] B. Zhang, Y. Liu, D. Laboureur, M.S. Mannan, Experimental study on propane jet fire hazards: thermal radiation, Ind. Eng. Chem. Res. 54 (2015) 9251-9256.

[19] K.B. Zhou, J.Y. Liu, J.C. Jiang, Prediction of radiant heat flux from horizontal propane jet fire, Appl. Thermal Eng. 106 (2016) 634-639.

[20] A.D. Johnson, A. Ebbinghaus, T. Imanari, S.P. Lennon, N. Marie, Large-scale free and impinging turbulent jet flames: numerical modelling and experiments, Process Saf. Environ. Prot. 75 (1997) 145-151.

[21] S. Patej, T. Durussel, Experimental analysis of jet fire impingement on industrial pipe, 11th Int. Conference Interflam, Interscience comm., 2007, pp. 1389-1395.

[22] N. Otsu, A threshold selection method from gray-level histograms, IEEE Trans. Systems, Man, Cybernetics 9 (1979) 62-66.

[23] M.S. Cha, S.H. Chung, Characteristics of lifted flames in nonpremixed turbulent confined jets, Proc. Combust. Inst. 26 (1996) 121-128.

[24] A. Santos, M. Costa, Reexamination of the scaling laws for NOx emissions from hydrocarbon turbulent jet diffusion flames, Combust. Flame 142 (2005) 160-169.

[25] A. Palacios, M. Muñoz, J. Casal, Jet fires: an experimental study of the main geometrical features of the flame in subsonic and sonic regimes, AIChE J. 55 (2009) 256-263.

[26] S. Kumar, P.J. Paul, H.S. Mukunda, Prediction of flame liftoff height of diffusion/partially premixed jet flames and modeling of mild combustion burners, Combust. Sci. Technol. 179 (2007) 2219-2253.

[27] K.J. Bosschaart, L.P.H. De Goey, The laminar burning velocity of flames propagating in mixtures of hydrocarbons and air measured with the heat flux method, Combust. Flame 136 (2004) 261-269.

[28] R.C. Reid, J.M. Prausnitz, B.E. Poling, Diffusion Coefficients, in: B. Sun, G.H. Fleck (Eds.), The properties of gases and liquids, Fourth ed., McGraw-Hill, New York, 1987, pp. 577-631.

[29] A. Upatnieks, J.F. Driscoll, C.C. Rasmussen, S.L. Ceccio, Liftoff of turbulent jet flames—assessment of edge flame and other concepts using cinema-PIV, Combust. Flame 138 (2004) 259-272.

[30] R.W. Schefer, M. Namazian, J. Kelly, Stabilization of lifted turbulent-jet flames, Combust. Flame 99 (1994) 75-86.

[31] K.M. Lyons, Toward an understanding of the stabilization mechanisms of lifted turbulent jet flames: experiments, Progr. Energy Combust. Sci. 33 (2007) 211-231.

[32] D. Bradley, P.H. Gaskell, X. Gu, A. Palacios, Jet flame heights, lift-off distances, and mean flame surface density for extensive ranges of fuels and flow rates, Combust. Flame 164 (2016) 400-409.

[33] A. Palacios, D. Bradley, L. Hu, Lift-off and blow-off of methane and propane subsonic vertical jet flames, with and without diluent air, Fuel 183 (2016) 414-419.

[34] M. Gómez-Mares, M. Muñoz, J. Casal, Radiant heat from propane jet fires, Exp. Thermal Fluid Sci. 34 (2010) 323-329.

[35] C.S. McEnally, Ü.Ö. Köylü, L.D. Pfefferle, D.E. Rosner, Soot volume fraction and temperature measurements in laminar nonpremixed flames using thermocouples, Combust. Flame 109 (1997) 701-720.

Investigation on the Flame Tilt Characteristics of Hydrogen/Propane Mixture Diffusion Jets in Cross Flow: Parameter Analysis Based on the Hydrogen Blending Fraction

Chen X.[1,] *, Wang Q.[2], Lu S.X.[1], Wang J.W.[1]

[1] State Key Laboratory of Fire Science, University of Science and Technology of China,
Hefei, Anhui, China
[2] School of Transportation Engineering, Hefei University of Technology,
Hefei, Anhui, China
**Corresponding author's email: summercx@mail.ustc.edu.cn*

ABSTRACT

An experimental study of hydrogen/propane mixture diffusion jets in cross flow has been performed to obtain the jet flame tilt characteristics when considering the combined effect of the cross flow and hydrogen blending fraction. The pipe nozzle with an inner diameter of 4 mm was employed in the experiments, using hydrogen and propane as the fuel jet velocity in the range of 11.06-49.76 m/s. The cross wind speed changed from 0.5 to 1.5 m/s. The experimental results showed that the hydrogen/propane mixed jet flame evolution was affected by the hydrogen blending fraction and cross flow wind. The flame trajectory length decreases with increasing the hydrogen fraction. The flame tilt angle decreases with the hydrogen blending fraction for a given mean jet velocity. Moreover, a simplified theoretical analysis was adopted to discuss the flame height and hydrogen blending fraction.

KEYWORDS: Jet diffusion flame, hydrogen/propane mixture, hydrogen blending fraction, flame tilt angle, cross wind.

NOMENCLATURE

A	area (m^2)
C	concentration of jet (-)
D	inner nozzle diameter (m)
d	diameter of nozzle (mm)
H	flame height (m)
K	stoichiometric ratio
L	flame length (m)
$\dot{m}$	mass flow rate (-)
R	momentum ratio
Q	heat release rate (kW)
u	velocity (m/s)
V	volume flow rate (m^3/s)
X	volume fraction (-)

Greek

α	flame tilt angle (-)
ρ	density (kg/m^3)

Subscripts

f	flame
j	jet
∞	air
v	velocity

INTRODUCTION

Jets in cross-flow (JICF) are an important problem with the rapid development of energy and petrochemical industry, and they have a wide variety of combustion applications, such as flares, air-

Proceedings of the Ninth International Seminar on Fire and Explosion Hazards (ISFEH9), pp. 842-850
Edited by Snegirev A., Liu N.A., Tamanini F., Bradley D., Molkov V., and Chaumeix N.
Published by Saint-Petersburg Polytechnic University Press
ISBN: 978-5-7422-6498-9 DOI: 10.18720/spbpu/2/k19-121

breathing gas turbine engines, quench devices in RQL combustors, and fluidic flame stabilization[1]. Combustion in a flare or jet fire occurring in the form of a strong turbulent flame might be dominated by buoyancy or momentum. Such a flame presents a number of challenging phenomena for study, including the effect of crosswind on flame shape and size, radiation and formation, and dispersion of smoke and other gaseous pollutants [2].

Much work has been done on the characteristics of a jet flame in cross flow, and theoretical or empirical equations have been established to predict the shape, length, and tilt characteristics of such jets in cross flow [3-9]. Brzustoski [3] and Gollahalli [4] conducted a series of experiments and found that the initial effect of cross flow was to shorten the flame, after which increases in a cross-flow velocity caused increases in the flame height. Huang and Wang [5] made a division of the jet flame mode based on the flow field of wake-stabilized jet flames (R_M). Kalghatgi [6] developed correlations to determine the flame length scales based on experiments on the turbulent jet diffusion flames in cross winds. Majeski [7] pointed out that diluting the fuel only changed the timescale for the fuel to mix with the required amount of air and burn. Wang [8] investigated the evolution characteristics of turbulent jet diffusion flame, considering the effect of cross flow and sub-atmospheric pressures. Wang [9] investigated the tilt angle of turbulent jet diffusion flames in crossflow and proposed a global correlation with momentum flux ratio.

Hydrogen syngas is expected as the next generation of fuels for the engines and other power sources, with the rising global demand for stringent energy and emission regulations. Many researchers have studied the effect of the addition of hydrogen into natural gas on engine performances and emissions in recent years [10-12]. Practical studies of internal combustion engines and gas turbines combustors indicated that a blended fuel with a mixture of hydrocarbon and hydrogen syngas could improve the performance of the combustors [13]. However, relatively less work has been focused on the characteristics of mixed jet diffusion flames, especially the mixture of hydrocarbon and hydrogen fuel. In the present study, experiments were conducted in a wind tunnel with the hydrogen/propane diffusion jet flames to discover the flame tilt characteristics of the mixed jet diffusion flames in a cross wind. The effect of hydrogen blending fraction on the mixed jet flame lengths and tilt angles is discussed. Moreover, a simplified theoretical analysis was adopted to explain the flame tilt characteristics.

EXPERIMENTAL APPARATUS

A 20.2 m total length wind tunnel with the cross sectional dimensions of 1.8 m height and 1.8 m width was employed for the experiments (Fig. 1). The detailed tunnel facility has been described in [14]. The cross flow speed changed in the range of 0.5-1.5m/s and was monitored by the vertically installed hot-wire anemometer (the fluctuation is under 2%). A 4.0 mm diameter nozzle was mounted at a height of 30 cm above the tunnel floor level. The stable hydrogen/propane mixture fuel was supplied from the mixing chamber with a 3m long gas pipe with a gas flow rate meter for each test. The volumetric flow rates of hydrogen and propane were in the range of 0.25-1.50 m^3/h and 0.25-0.75 m^3/h, respectively. Hence, the hydrogen blending fraction $X_{j,\mathrm{H_2}}$ in the experiments ranged from 0.25 to 0.86. The heat release rate was in the range of 6.61-21.29 kW. The experimental scenarios are listed in Table 1. All the tests were repeated three times to reduce the random errors.

We defined the hydrogen blending fraction, $X_{j,\mathrm{H_2}}$, of the mixed jet diffusion flames, as $X_{j,\mathrm{H_2}} = V_{j,\mathrm{H_2}} \big/ \left(V_{j,\mathrm{C_3H_8}} + V_{j,\mathrm{H_2}} \right)$, where $V_{j,\mathrm{H_2}}$ and $V_{j,\mathrm{C_3H_8}}$ are hydrogen and propane volumetric flow rates, respectively. Moreover, $u_{j,\mathrm{H_2}} = V_{j,\mathrm{H_2}} \big/ A_{nozzle}$ and $u_{j,\mathrm{C_3H_8}} = V_{j,\mathrm{C_3H_8}} \big/ A_{nozzle}$.

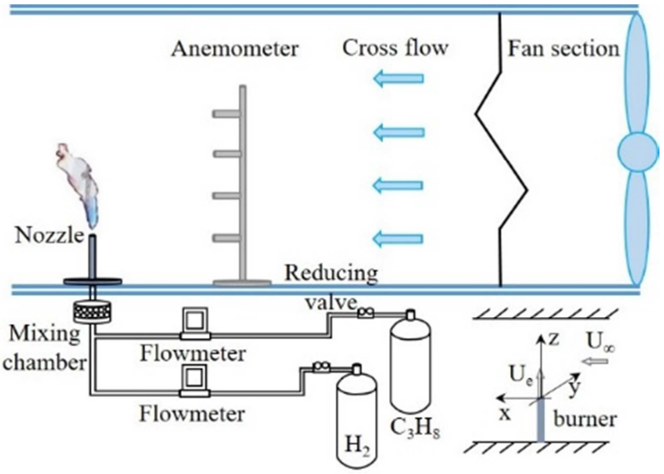

Fig. 1. Schematic diagram of experimental apparatus.

Table 1. Summary of experimental scenarios

u_∞ (m/s)	$u_{j,\ C_3H_8}$ = 5.53 m/s				$u_{j,\ C_3H_8}$ = 11.06 m/s				$u_{j,\ C_3H_8}$ = 16.59 m/s			
	$u_{j,\ H_2}$ (m/s)	u_j (m/s)	$X_{j,\ H_2}$ (-)	Q (kW)	$u_{j,\ H_2}$ (m/s)	u_j (m/s)	$X_{j,\ H_2}$ (-)	Q (kW)	$u_{j,\ H_2}$ (m/s)	u_j (m/s)	$X_{j,\ H_2}$ (-)	Q (kW)
0.5	5.53	11.06	0.50	6.61	5.53	16.59	0.33	12.53	5.53	22.12	0.25	18.46
	11.06	16.59	0.67	7.30	11.06	22.12	0.50	13.22	11.06	27.65	0.40	19.15
	16.59	22.12	0.75	7.99	16.59	27.65	0.60	13.91	16.59	33.18	0.50	19.83
	22.12	27.65	0.80	8.68	22.12	33.18	0.67	14.60	22.12	38.71	0.57	20.52
	27.65	33.18	0.83	9.37	27.65	38.71	0.71	15.29	27.65	44.24	0.63	21.21
	33.17	38.7	0.86	10.06	33.17	44.23	0.75	15.98	33.17	49.76	0.67	21.90
1.0	5.53	11.06	0.50	6.61	5.53	16.59	0.33	12.53	5.53	22.12	0.25	18.46
	11.06	16.59	0.67	7.30	11.06	22.12	0.50	13.22	11.06	27.65	0.40	19.15
	16.59	22.12	0.75	7.99	16.59	27.65	0.60	13.91	16.59	33.18	0.50	19.83
	22.12	27.65	0.80	8.68	22.12	33.18	0.67	14.60	22.12	38.71	0.57	20.52
	27.65	33.18	0.83	9.37	27.65	38.71	0.71	15.29	27.65	44.24	0.63	21.21
	33.17	38.7	0.86	10.06	33.17	44.23	0.75	15.98	33.17	49.76	0.67	21.90
1.5	5.53	11.06	0.50	6.61	5.53	16.59	0.33	12.53	5.53	22.12	0.25	18.46
	11.06	16.59	0.67	7.30	11.06	22.12	0.50	13.22	11.06	27.65	0.40	19.15
	16.59	22.12	0.75	7.99	16.59	27.65	0.60	13.91	16.59	33.18	0.50	19.83
	22.12	27.65	0.80	8.68	22.12	33.18	0.67	14.60	22.12	38.71	0.57	20.52
	27.65	33.18	0.83	9.37	27.65	38.71	0.71	15.29	27.65	44.24	0.63	21.21
	33.17	38.7	0.86	10.06	33.17	44.23	0.75	15.98	33.17	49.76	0.67	21.90

RESULTS AND DISCUSSION

Flame configurations

The hydrogen/propane flame evolution in the cross wind, under increasing hydrogen flow is illustrated in Fig. 2, with a propane flow velocity of 5.53 m/s and a cross wind speed and hydrogen flow velocity in the range of 0.5-1.5 m/s and 5.53-33.17 m/s, respectively. It can be seen from the figures that the flame trajectory length increases with the cross wind speed, as well as the flame tilt characteristics. Previous work [2] had found that the initial effect of cross flow was to shorten the flame, after which an increase in cross-flow velocity increased the flame length. The tails of the jet flame body become smooth and an axisymmetric tail flame can be observed as the cross wind speed increases. It may be suppressed by the vorticity circulation at the flame edge, and the counter-rotating vortex pair exits in the flame edge [15-16]. The similar qualitative trend of the diffusion jet flame has been discussed by the previous studies [8, 15]. It also can be seen that with the fuel jet velocity increasing, the jet flame tilt becomes less pronounced and both the flame height in the cross wind direction and flame trajectory length become shorter. In addition, as the hydrogen flow velocity increases, the jet flame body becomes less luminance and the blue flame area at the base becomes enlarged. The flame body area becomes smaller and the tail of the jet flame presents much less wrinkled as the hydrogen blending fraction increases.

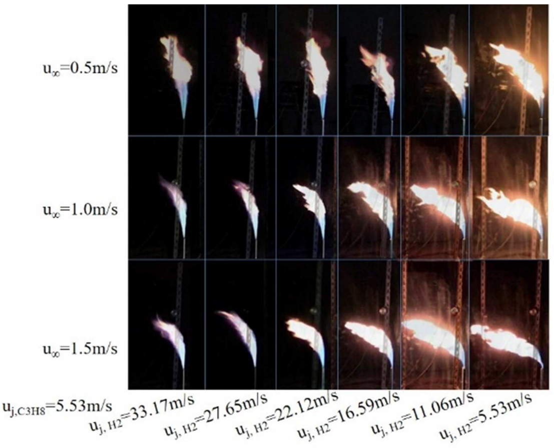

Fig. 2. Flame evolution in the cross wind with increasing hydrogen flow velocity.

Flame length and flame tilt angle

Each recorded image of the hydrogen/propane mixture jet flame was converted to binary images by the Otsu method [17], and the flame intermittency distribution was obtained by averaging the values of these consecutive binary images in each pixel position. Fig. 3 illustrates the determination of flame trajectory-line length, L_f, flame height, H_f, and flame tilt angle, α and α_B, from the recorded flame images. As can be seen, the flame trajectory-line length L_f is the distance between the nozzle exit and flame tip along the flame tilt trajectory, and the flame height H_f is the perpendicular distance from the flame tip to the nozzle exit. The flame tilt angle α_B is the angle between the jet exit axis and the line joining the flame tip to the nozzle tip, while α is the included angle between the tangent line of the flame trajectory line and the jet exit axis.

The variations of flame trajectory lengths with the hydrogen blending fraction at different cross wind speeds are illustrated in Fig. 4. The flame trajectory lengths for the different cross wind speeds have a decreasing trend with increasing hydrogen blending fraction. The flame trajectory lengths range from 46.7 to 61.7 cm under a cross wind of 0.5 m/s, the values range from 30.9 to 60.4 cm under across wind of 1.0 m/s, and from 31.27 to 57.9 cm under the cross wind of 1.5 m/s. The flame trajectory length could decrease with an increase in air entrainment and mixing with fuel due to the strong vorticity circulation. However, as the cross flow becomes stronger, the vorticity circulation may be suppressed at the flame edge, which presents the smooth flame edge as shown in Fig. 2.

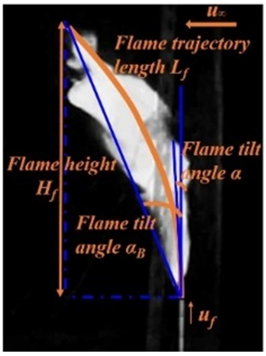

Fig. 3. Determination of flame trajectory-line length L_f, flame height H_f, and flame tilt angles α and α_B from flame images (d = 4 mm, u_j = 38.70 m/s, u_∞ = 1.0 m/s).

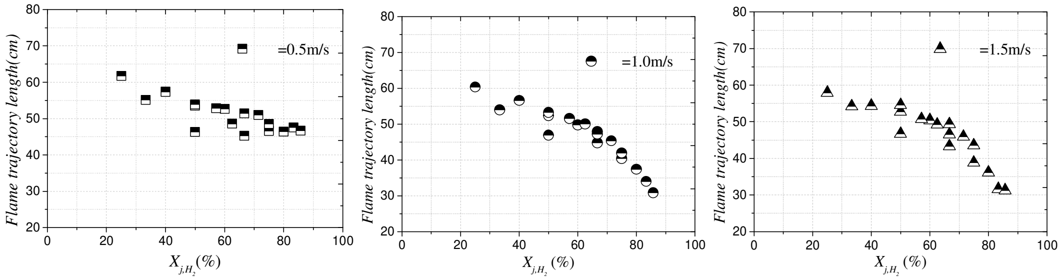

Fig. 4. Flame trajectory length versus hydrogen blending fraction at different cross wind speeds.

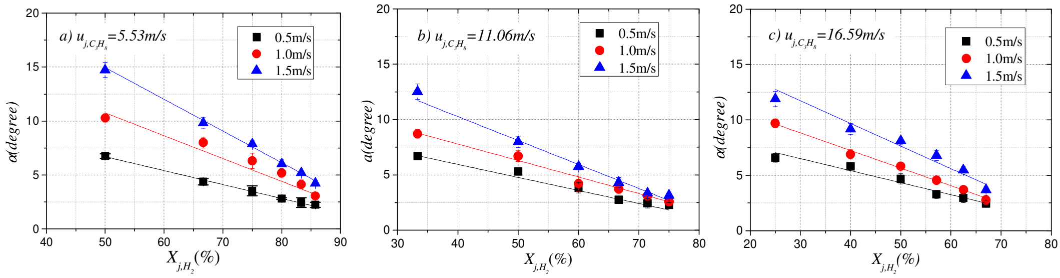

Fig. 5. Variation of flame tilt angle (α) with hydrogen blending fraction under different cross wind speeds (where α is the including angle between the tangent line of the flame trajectory line and the jet exit axis).

Figure 5 illustrates the flame tilt angles α for the propane jet flow velocity of 5.53 m/s (a), 11.06 m/s (b) and 15.59 m/s (c) with increasing the hydrogen fraction under different cross wind speeds where α is the angle between the tangent line of the flame trajectory line and the jet exit axis. A significant trend observed in Fig. 5 is that the flame tilt angle α becomes smaller with increasing hydrogen addition. For the same hydrogen blending fraction, α becomes smaller as the cross wind speed increases. It is evident from Fig. 5 (a), (b) and (c) that the flame tilt angle α for the propane jet flow of 5.53 m/s varies from 2.1 to 14.95, whereas the variations in the flame tilt angle α for the greater propane jet flow of 11.06 m/s and 16.59 m/s are 2.28-12.51 and 2.49-11.89, respectively. The linear curves of α fit well with the hydrogen blending fraction. We can see that the flame tilt angles α_B also linearly correlate with the hydrogen blending fraction for the different propane jet flow velocities (Fig. 6) where α_B is the angle between the burner axis and the connecting line of the flame tip and the burner exit. It can also be seen from Fig.6 (a), (b) and (c) that the flame tilt angles α_B present a decreasing trend, with the hydrogen blending fraction increasing for the different cross wind speeds. It can be seen that the flame tilt angle α_B of 0.5 m/s cross wind speed is smaller than that of the 1.0 and 1.5 m/s cases.

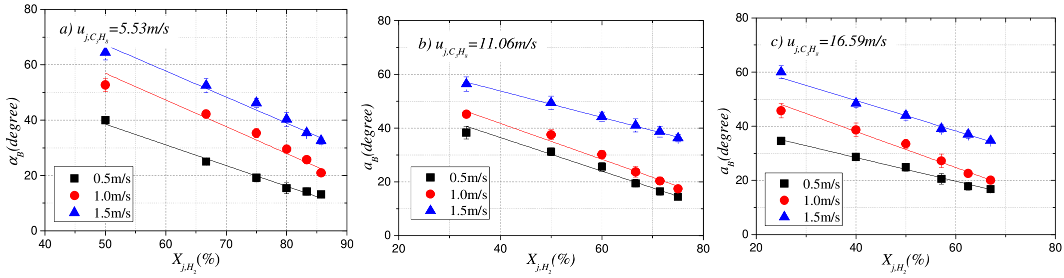

Fig. 6. Variation of flame tilt angle (α_B) with hydrogen blending fraction. (α_B is the angle between the jet exit axis and the line joining the flame tip to the nozzle tip).

Simplified theoretical analysis

Kalghatgi [6] developed correlations to determine the flame height scales based on experiments on the turbulent jet diffusion flames in the cross wind. The expression for flame height is:

$$\frac{H_f}{D_s} = 6 + \frac{2.35}{R_v} + 20R_v . \tag{1}$$

Here H_f is the flame tip from the plane of the burner (m), $D_s = D\left(\rho_j/\rho_\infty\right)^{0.5}$ is the effective source diameter, and $R_v = u_\infty/u_j$ is the non-dimensional velocity, where D is the inner nozzle diameter(m), ρ_j is the density of the mixed jet fuel (kg/m^3), $\rho_j = X_{j,\mathrm{H_2}}\rho_{j,\mathrm{H_2}} + \left(1 - X_{j,\mathrm{H_2}}\right)\rho_{j,\mathrm{C_3H_8}}$, ρ_∞ is the density of the cross wind (kg/m^3), u_∞ is the cross wind speed (m/s), u_j is the jet fuel velocity (m/s).

The comparison between the predicted and measured flame height is shown in Fig 7. The theoretical values calculated in Kalghatgi's model are lower than the measured values. Kalghatgi [6] also pointed out that the range of validity of these correlations is for values of R_v greater than 0.02 and less than 0.25, while for $R_v < 0.02$, the wind-free data may be used to determine the flame heights and the tilt may be assumed to be zero. However, for the hydrogen/propane mixture diffusion jet flame in this experiment, the measured values of H_f/D_s under the cross flow of 0.5m/s are almost concentrated in the range of $R_v < 0.02$.

A relationship is presented in the normalized form of flame height and velocity in Fig.8, and the experimental results are well fitted with the related coefficient being greater than 0.90 in the following:

$$\frac{H_f}{D_s}=\exp\left(5.2-10.4R_v\right). \tag{2}$$

Substituting $D_s=D\left(\rho_j/\rho_\infty\right)^{0.5}$ in Eq.(2) yields

$$\frac{H_f}{\exp\left(5.2-10.4R_v\right)D}=\left(\frac{\rho_j}{\rho_\infty}\right)^{0.5}. \tag{3}$$

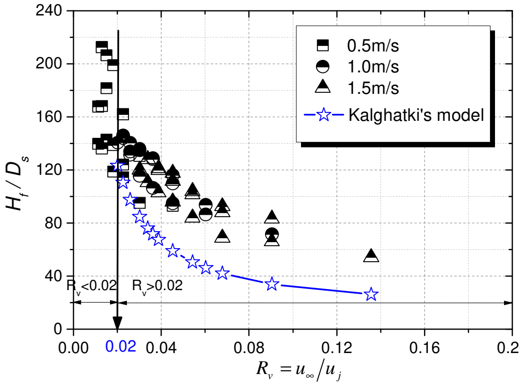

Fig. 7. Variation of between predicted and measured flame height with velocity ratio

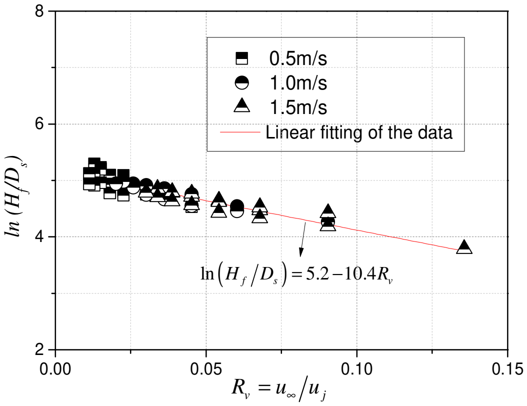

Fig. 8. Normalized flame height versus non-dimensional velocity ratio

Majeski [7] introduced the stoichiometric ratio K_s to discuss the mean flame height when considering the effect of fuel dilution,

$$H_f\propto K_s^{1/2}, \tag{4}$$

where $K_s=\dot{m}_{O_2}/C_f\dot{m}_j$, $\dot{m}_{O_2}$ is the total supply of oxygen to the flame, and $\dot{m}_j$ is the total mass flow rate of the jet, and C_f is the concentration of fuel in the jet, $C_f=\rho_f V_{j,f}/\rho_j V_j$, $V_{j,f}$ and V_j are the volume flow rate of the jet and fuel component, respectively. Hence, Eq. (3) could be revised as

$$\frac{H_f}{\exp\left(5.2-10.4R_v\right)D}\sim K_s^{1/2}\left(\frac{\rho_j}{\rho_\infty}\right)^{0.5}, \tag{5}$$

Using

$$\rho_j=X_{j,\,\mathrm{H_2}}\rho_{j,\,\mathrm{H_2}}+\left(1-X_{j,\,\mathrm{H_2}}\right)\rho_{j,\,\mathrm{C_3H_8}} \text{ and } K_s=\frac{X_{j,\,\mathrm{H_2}}\rho_{j,\,\mathrm{H_2}}\dfrac{32}{4}+\left(1-X_{j,\,\mathrm{H_2}}\right)\rho_{j,\,\mathrm{C_3H_8}}\dfrac{160}{44}}{X_{j,\,\mathrm{H_2}}\rho_{j,\,\mathrm{H_2}}+\left(1-X_{j,\,\mathrm{H_2}}\right)\rho_{j,\,\mathrm{C_3H_8}}},$$

calculated for the mixture of hydrogen and propane, in Eq. (5). Eq. (5) can be represented as:

$$\frac{H_f}{\exp\left(5.2-10.4R_v\right)D}\sim\left(\frac{X_{j,\,\mathrm{H_2}}\rho_{j,\,\mathrm{H_2}}\dfrac{32}{4}+\left(1-X_{j,\,\mathrm{H_2}}\right)\rho_{j,\,\mathrm{C_3H_8}}\dfrac{160}{44}}{\rho_\infty}\right)^{1/2}. \tag{6}$$

Substituting $\rho_{j,C_3H_8} = 1.84$ kg/m^3, $\rho_{j,\mathrm{H}_2} = 0.09$ kg/m^3, $\rho_\infty = 1.189$ kg/m^3 at normal temperature and pressure and $D = 0.004$ m into Eq. (6), gives the correlation in Fig. 9. This illustrates the flame height versus the hydrogen blending fraction in the modified model. As can be seen in Fig. 9, the flame height presents the linear correlation with hydrogen blending fraction for the different cross flow velocities.

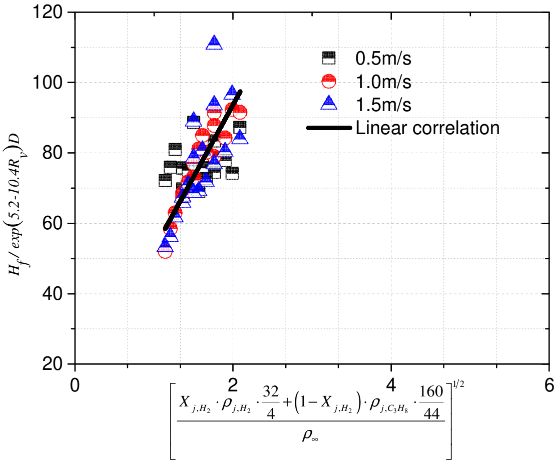

Fig. 9. Comparison of simplified model (Eq.(6)) with experimental results of flame height and hydrogen blending fraction for different cross flow velocity.

CONCLUSION

This paper experimentally investigates the hydrogen/propane mixture diffusion jets in cross flow. The cross wind speed and fuel jet velocity range from 11.06 to 49.76 m/s and from 0.5 to 1.5 m/s. Several flame tilt characteristic parameters were obtained considering the combined effect of the cross flow and hydrogen blending fraction. Major findings include:

(1) The flame trajectory length presented a decreasing trend with increasing hydrogen blending fraction and was approximately in the range of 30 cm – 60 cm for the different cross wind speeds.

(2) The flame tilt angle (α and α_B) decreased with the hydrogen blending fraction and ranged from 2-15 degree for a given mean jet velocity.

(3) A simplified theoretical analysis on the basis of stoichiometric ratio K_s proposed by Majeski, was adopted to discuss the flame height and the hydrogen blending fraction.

ACKNOWLEDGEMENT

This paper was supported by National Nature Foundation of China under Grant (No.51704268) and China Postdoctoral Science Foundation funded project (2018M632549).

REFERENCES

[1] A.R. Karagozian, The jet in crossflow, Phys. Fluids 26(10) (2014) 1-47.

[2] C.L. Beyler, Fire hazard calculations for large, open hydrocarbon fires. In The SFPE Handbook of Fire Protection Engineering, (5th Edn), J.H. Morgan, M.J. Hurley (Eds). National Fire Protection Association, Quincy MA, 2016.

[3] T.A. Brzustowski, A new criterion for the length of a gaseous turbulent diffusion flame, Combust. Sci. Technol. 6 (1973) 313-319.

[4] T.A. Brzustowski, S.R. Gollahalli, H.F. Sullivan, The turbulent hydrogen diffusion flame in a cross-wind, Combust. Sci. Technol. 11 (1975) 29-33.

[5] R.F. Huang, S.M. Wang, Characteristic flow modes of wake-stabilized jet flames in a transverse air stream, Combust. Flame 117 (1999) 59-77.

[6] G.T. Kalghatgi, The visible shape and size of a turbulent hydrocarbon jet diffusion flame in a cross-wind, Combust. Flame 52 (1983) 91-106.

[7] A.J. Majeski, D.J. Wilson, L.W. Kostiuk, Predicting the length of low-momentum jet diffusion flames in crossflow, Combust. Sci. Technol. 176 (2004) 2001-2025.

[8] Q. Wang, L.H. Hu, X.C. Zhang, et al., Turbulent jet diffusion flame length evolution with cross flows in a sub -pressure atmosphere, Energy Conv. Manag. 106 (2015) 703-708.

[9] J. Wang, J. Fang, S. Lin, et al., Tilt angle of turbulent jet diffusion flame in crossflow and a global correlation with momentum flux ratio, Proc. Combust. Inst. 36 (2017) 2979-2986.

[10] H. Ozcan,. Hydrogen enrichment effects on the second law analysis of a lean burn natural gas engine, int. J. Hydrogen Energy 35 (2010) 1443-1452.

[11] E. Porpatham, A. Ramesh, B. Nagalingam, Effect of hydrogen addition on the performance of a biogas fuelled spark ignition engine, Int. J. Hydrogen Energy 32 (2007) 2057-2065.

[12] C. Ji, S. Wang, Effect of hydrogen addition on combustion and emissions performance of a spark ignition gasoline engine at lean conditions, Int. J. Hydrogen Energy 34 (2009) 7823-7834.

[13] L. Pan, E. Hu, F. Deng, et al., Effect of pressure and equivalence ratio on the ignition characteristics of dimethyl ether-hydrogen mixtures, Int. J. Hydrogen Energy 39 (2014) 19212-19223.

[14] X. Chen, Q. Wang, S. Lu, et al., Investigation on the size and trajectory of mixed jet diffusion flames in cross wind, Energy Procedia 142 (2017) 1516-1521.

[15] A.R. Karagozian, Transverse jets and their control, Progr. Energy Combust. Sci. 36 (2010) 531-553.

[16] M.S. Lawal, M. Fairweather, P. Gogolek, S.R. Gubba, D.B. Ingham, L. Ma, M. Pourkashanian, A. Williams, Large eddy simulations of wake-stabilised flares, Fuel Proc. Technol. 112 (2013) 35-47.

[17] N. Otsu, A threshold selection method from gray-level histograms, IEEE Transactions on Systems, Man, and Cybernetics 9 (1979) 62-66.

A Phenomenological Model of a Reacting Fuel Jet Tilted in Crossflow Employing Air Entrainment

Wang K.[1], Fang J.[1,]*, Wang J.W.[1], Zheng S.M.[1], Shah H.R.[1], Guan J.F.[2], Lin S.B.[1], Zhang Y.M.[1]

[1] *University of Science and Technology of China, State Key Laboratory of Fire Science, Hefei, Anhui, China*
[2] *Tsinghua University, Hefei Institute for Public Safety Research, Hefei, Anhui, China*
**Corresponding author's email: fangjun@ustc.edu.cn*

ABSTRACT

Jet flame combustion in cross-flow is meaningful to promote reaction in many industrial combustion devices. Previous research about the tilt angle has limited predictive capability in a large range of the jet-to-crossflow momentum flux ratio (R_M). In this work, a new tilt angle model was provided by employing the air entrainment. The study showed that: the air entrainment ratio, defined as the mass flow rate ratio of the hot gas in the whole flame region to stoichiometric gases, was neversely proportional to the jet flame Froude number (Fr). Additionally, two regimes of the tilt angles were identified as $1 < Fr < 10^3$, $0.1 < R_M < 100$ for medium turbulent jet flames, and $10^3 < Fr < 10^6$, $100 < R_M < 3000$ for highly turbulent jet flames, respectively. For a fixed Fr, with the increasing R_M, the tilt angle decreased. For highly turbulent jet flames, the contributions of air entrainment to the tilt angle could be ignored; with the same R_M value, the flame deflected more than the low momentum jet flames.

KEYWORDS: Turbulent diffusion flame, cross-flow, tilt angle, momentum flux ratio, air entrainment.

NOMENCLATURE

b	Flame half-width
C_f	Drag coefficient
d_n	Nozzle diameter
Fr	Froude number $Fr = u_j^2/(gd_n)$
L	Length
$\dot{m}_{air}$, $\dot{m}_j$	Mass flow rate of entrained air or fuel jet
$\dot{m}_H$, $\dot{m}_V$	Mass flow rate in the horizontal or vertical direction
MW	Molecular weight
r	Radial direction
Re	Renolds number $\mathrm{Re} = \rho_j u_j d_n/\mu_j$
Ri	Richardson number $\mathrm{Ri} = (\rho_\infty - \rho_f) g d_n / (\rho_f u_j^2)$
x, z	Cartesian coordinates

Greek

$\alpha_{e(\dot{m})}$	Mass flow rate ratio of hot gases in the whole flame region to stoichiometric gases
θ	Flame tilt angle
μ	Dynamic viscosity
ξ	Axial ordinate in x, z plane
ρ	Density
σ	Standard deviation

Subscripts

ad	Adiabatic condition
air	Air
j	Fuel jet
f	Flame

Proceedings of the Ninth International Seminar on Fire and Explosion Hazards (ISFEH9), pp. 851-859
Edited by Snegirev A., Liu N.A., Tamanini F., Bradley D., Molkov V., and Chaumeix N.
Published by Saint-Petersburg Polytechnic University Press
ISBN: 978-5-7422-6498-9 DOI: 10.18720/spbpu/2/k19-93

R_M Jet-to-crossflow momentum flux ratio

$R_M = (\rho_j u_j^2)/(\rho_\infty u_w^2)$

S Air-to-fuel mass stoichiometric ratio

T Temperature

u Velocity

H, V Horizontal or vertical direction

N_2 Nitrogen

st Stoichiometric condition

w Wind

∞ Ambient condition

INTRODUCTION

The jet in cross-flow or transverse jet has been studied extensively because of its relevance to a wide variety of flows in technological systems, including fuel or dilution air injection in gas turbine engines, thrust vector control for high speed air breathing and rocket vehicles, and exhaust plumes from power plants [1, 2]. In practical engineering, researches relating to the tilt behavior of the momentum controlled jet flame in cross-flow are very important combustion design.

Escudier [3] presented a theoretical treatment for the motion of a turbulent gas jet burning in an oxidizing crossflow. Brzustowski [4] described a simple model of a hydrocarbon turbulent diffusion flame in a horizontal subsonic cross-flow of air and modeled the flame as a bent-over initially vertical and non-buoyant circular jet. Kostiuk et al. [5] changed the traverse air velocity and diameter of the burner tube to consider the scaling of the flame length, the cross-stream dimension of the plume of combustion products, and the overall combustion efficiency of wake-stabilized jet diffusion flames. Zhao et al. [6] gave a correlation for the stoichiometric flame length in crosswind as a function of the fuel source Froude number and the velocity ratio of wind to fuel based on the numerical results. Huang et al. [7] found that there are four ranges of flame pulsation intensities: slight, medium, strong, and over excitations. Besides, Hu and his co-workers have produced a series of experiments to study the flame tilt angle [8, 9], horizontal extents [10], flame length evolution [11] etc of diffusion flames under cross-wind. Recently, Tang et al. [12] studied the flame base drag length of diffusion flames with different aspect ratios under crossflow.

For the flame tilt angle, Pipkin et al. [13] deduced a classical model, in which cylindrical flame shape was assumed, the fuel velocity was expected to be uniform in the visible flame region. Flame width has the same size with the pool diameter, and the wind was assumed to have a 'drag force' with a drag coefficient C_f. When the momentum balance due to the cross-wind, initial inertia and buoyancy was applied in the direction normal to the surface of the flame body (positive upward), the tilt angle θ was:

$$f(\theta) = \frac{\tan\theta}{\cos\theta} = \frac{2C_f}{\pi} \frac{1}{1+Ri\left(\rho_f/\rho_j\right)\cos\theta} \frac{\rho_\infty u_w^2 L_f}{\rho_j u_j^2 d_n}, \tag{1}$$

where the Richardson number is $\mathrm{Ri} = (\rho_\infty - \rho_f) g d_n / (\rho_f u_j^2)$, ρ is the density, u is the velocity, L is the length, d_n is the nozzle diameter. The subscripts f, j, w, ∞, 0 represent flame, fuel jet, cross-flow, ambient condition, and initial condition, respectively. It can be seen that, the title angle is dependent on the flame length, the drag coefficient C_f depends on multiple factors and is very complicated to be interpreted and obtained. Moreover, the effects of entrained air have been ignored.

In the previous work, the tilt angle mainly depends on the flame length and other unpredictable parameters [13], or the air entrainment was assumed to be of a value that only supports complete combustion [14]. However, in the cross-wind condition, a large amount of air was entrained into the flame convection zone and the flame upper edge by coherent structures with large vortices, leading to great variation in the flame tilt angle [15]. Therefore, the variation of air entrainment can greatly affect the flame inclination, which cannot be neglected, or assumed to be of fixed valued.

In the present work, the tilt angle of momentum-controlled highly turbulent jet flames was modelled by employing air entrainment, which was different from the model of Eq. (1) that depends on unpredicatable parameters, and previous work [14] in which the air entrainment ratio was assumed to be unity. Experiments of momentum-controlled propane jet flames with values of R_M of 0.1–10, Fr of 1–100 were carried out in a open-loop wind tunnel, in order to verify the tilt angle model.

THEORETICAL ANALYSIS

Assumption made in building the model are: the diffusion flame is axisymmetric [4], steady and isothermal; the cross-flow is steady and non-turbulent; the cylindrical flame has an average flame width [16]; self-similarity of the jet flame is retained in cross-flow; stoichiometric and fast chemical reaction prevails; and the burning efficiency of the propane is assumed to be 100% [5].

Additionally, the buoyancy was neglected in this model. One might expect the vertical velocity to decrease by entrainment but increase by buoyancy simultaneously. Escudier [3] has pointed out that, buoyancy forces generated by the release of thermal energy during the combustion process have a negligible effect on the motion until far downstream. For highly turbulent jet flow, $Ri\left(\rho_f/\rho_j\right)\cos\theta$ in Eq. (1) is generally far smaller than unity, indicating that buoyancy momentum is small compared with inertia momentum. Furthermore, the solution of the effects of scaling on the relative influence of initial momentum and buoyancy showed that, due to the decrease of the vertical velocity, the flame bends over near the nozzle. Buoyancy has little influence near the nozzle, while it has a large influence in the downstream to curve up the flame [4].

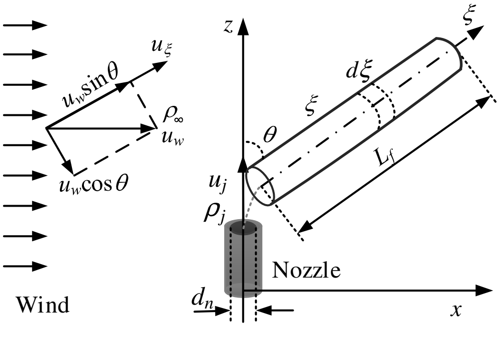

Fig. 1. Configurations of a tilted jet flame in cross-flow in x, z coordinates. (The gas jet discharges at a velocity u_j with density ρ_j from a nozzle of diameter d_n into a cross-flow of density ρ_∞ at horizontal velocity u_w; ξ is the axial ordinate in x, z plane; $d\xi$ is the flame element; $u_w\sin\theta$ and $u_w\cos\theta$ are the components of the cross-flow velocity, parallel and normal to the axial velocity u_ξ, respectively).

The definitions of the configuration of a tilted flame in cross-flow are shown in Fig. 1. When the momentum balance is applied in the direction of the main flow motion:

$$\tan\theta = \left(\dot{m}_H u_w\right)/\left(\dot{m}_V u_V\right). \tag{2}$$

Based on the assumption of a cylindrical flame shape, in the horizontal direction, the cross-flow mass flow rate through the cylindrical flame surface is:

$$\dot{m}_H = \rho_\infty u_w 2bL_f \cos\theta\,, \tag{3}$$

where b is the half-width of the flame.

For stoichiometric reaction, the air entrainment ratio $\alpha_{e(\dot{m})}$, i.e., the mass flow rate ratio of the hot gas in the whole flame region to stoichiometric gases, is:

$$\alpha_{e(\dot{m})} = \dot{m}_{air} \big/ \left((S+1)\dot{m}_j \right). \tag{4}$$

Here S is the air-to-fuel mass stoichiometric ratio, $\dot{m}_{air}$ and $\dot{m}_j$ are the mass flow rates of entrained air and fuel jet, respectively. $\alpha_{e(\dot{m})}$ is related to the air entrainment coefficient [17], but not the same.

The mass flow rate of the mixture of stoichiometric gas and entrained air is $\dot{m}_V = \alpha_{e(\dot{m})}(S+1)\dot{m}_j$. Eq. (2) then becomes:

$$\tan\theta = \frac{\rho_\infty u_w^2 2bL_f \cos\theta}{\overline{\alpha}_{e(\dot{m})}(S+1)\dot{m}_j u_V}. \tag{5}$$

For a cylindrical flame, its tilt angle is constant. Here in the whole flame length L_f, there are three characteristic parameters are assumed: the air entrainment ratio $\overline{\alpha}_{e(\dot{m})}$, flame mean half-width $\overline{b}$, and vertical velocity $\overline{u}_V$. Altering the form of Eq. (5), gives:

$$\frac{\tan\theta}{\cos\theta} = \frac{\rho_\infty u_w^2 2\overline{b}L_f}{\overline{\alpha}_{e(\dot{m})}(S+1)\dot{m}_f \overline{u}_V}. \tag{6}$$

The solutions of $\overline{b}$ and $\overline{u}_V$ are now addressed.

The similarity solution for the flame half-width, b, relates to the axial coordinate by [18]:

$$b(\xi) = 0.23\xi\left(\rho_{st}/\rho_j\right)^{1/2}, \tag{7}$$

where $\rho_{st}/\rho_j = \left(MW_{\mathrm{N}_2}/MW_j\right)\left(T_j/T_{st}\right)$, MW are the molecular weights, T is the temperature, the subscripts N_2 and st stand for the nitrogen gas and stoichiometric condition, respectively. For the case of a one-step irreversible reaction with infinitely fast chemistry, with assumed, infinitely fast, reversible, reactions are assumed, all species are in chemical equilibrium at each value of mixture fraction. If the enthalpy equation takes the same form as the mixture fraction, the enthalpy becomes a linear function of the mixture fraction. The stoichiometric temperature T_{st} calculated under these conditions is the adiabatic flame temperature T_{ad} [19]. With $T_{st} = T_{ad} = 1554$ K [20].

In the isothermal flame, the mean half-width in the flame region is:

$$\overline{b} = \frac{1}{L_f}\int_0^{L_f} b(\xi)d\xi = \frac{1}{2}b(L_f) = 0.115L_f\left(\rho_{st}/\rho_j\right)^{1/2}. \tag{8}$$

In still air, the axial velocity ($\xi = z$) can be obtained, based on Spalding's entrainment theory, [4]:

$$\frac{u_\xi(\xi)}{u_j(\xi)} = \left(1 + 0.32(\xi/d_n)\left(\rho_\infty/\rho_j\right)^{1/2}\right)^{-1}. \tag{9}$$

Here $u_\xi(\xi)$ is the axial velocity at ξ height and $u_j(\xi{=}0) = u_j$. With cross-flow, $u_\xi(\xi)$ is the axial velocity at ξ along ξ direction, $u_j(\xi)$ is the initial coupling velocity of jet and cross-flow in ξ direction.

The average velocity over the flame length $\bar{u}_\xi$ is then defined by assuming the same residence time is retained, as:

$$\frac{L_f}{\bar{u}_\xi} = \int_0^{L_f} \frac{1}{u_\xi(\xi)} d\xi . \tag{10}$$

Substituting Eq. (9) in Eq. (10), the flame axial velocity, averaged in the axial direction, $\bar{u}_{\xi(axial)}$ is:

$$\bar{u}_{\xi(axial)} = u_j(\xi)\left(1+0.16\left(L_f/d_n\right)\left(\rho_\infty/\rho_j\right)^{1/2}\right)^{-1} . \tag{11}$$

In the radial direction *r* of the flame, the vertical velocity distribution has the following form:

$$u_\xi(\xi,r) = u_\xi(\xi)\exp\left(-r^2/\left(2\sigma^2\right)\right), \tag{12}$$

where σ is the standard deviation related to the spread of the profile across the centerline. Since 4σ is the width of the distribution that encompasses 95% of the area under the profile from statistics, one can assume 4σ = 2*b*. Thus the average vertical velocity across the radial direction is:

$$\bar{u}_{\xi(radial)} = \frac{1}{\pi b^2}\int_0^\infty 2\pi r u dr = \frac{u_\xi(\xi)}{2} . \tag{13}$$

Combining Eqs. (11) and (13), the average fuel velocity in still air is:

$$\bar{u}_{\xi(axial,radial)} = \frac{1}{2}u_j(\xi)\left(1+0.16\left(L_f/d_n\right)\left(\rho_\infty/\rho_j\right)^{1/2}\right)^{-1} . \tag{14}$$

When there is cross-flow, as shown in Fig. 1, ξ becomes the flame tilt coordinate, $\xi\cos\theta = z$. The scalars of the vectors in ξ and $\xi\cos\theta$ (z) coordinates have the following mapping relationships:

$$\xi \to \xi\cos\theta = z ,\ r \to r\cos\theta ,\ \sigma \to \sigma\cos\theta ,\ u_j(z) = u_j(\xi)\cos\theta = u_j ,\ u_\xi(z) = u_\xi(\xi)\cos\theta . \tag{15}$$

Based on Eq. (15), the average vertical velocity at $L_f \cos\theta$ height in cross-flow is:

$$\bar{u}_V \approx \frac{1}{2}u_j\left(1+0.16\cos\theta\left(L_f/d_n\right)\left(\rho_\infty/\rho_j\right)^{1/2}\right)^{-1} . \tag{16}$$

Substituting Eqs. (8), (16) and $R_M = (\rho_j u_j^2)/(\rho_\infty u_w^2)$ into Eq. (6) gives:

$$\frac{\tan\theta}{\cos\theta}\left(1+0.16\cos\theta\left(L_f/d_n\right)\left(\rho_\infty/\rho_j\right)^{1/2}\right) = \frac{2}{\pi}\frac{1}{\bar{\alpha}_{e(\dot{m})}(S+1)R_M}\left(L_f/d_n\right)^2\left(\rho_{st}/\rho_j\right)^{1/2} . \tag{17}$$

In still air, experiments have shown that the length of a momentum-controlled turbulent diffusion flame is about $100d_n$. The value of L_f/d_n is very large and Eq. (17) can be simplified:

$$\frac{\tan\theta}{\cos\theta}\left(0.16\cos\theta\left(L_f/d_n\right)\left(\rho_\infty/\rho_j\right)^{1/2}\right) = \frac{2}{\pi}\frac{1}{\bar{\alpha}_{e(\dot{m})}(S+1)R_M}\left(L_f/d_n\right)^2\left(\rho_{st}/\rho_j\right)^{1/2} . \tag{18}$$

For low Mach number flow jets, *Fr* numbers are generally smaller than 10^5. The inclined flame length ratio L_f/d_n is independent of the momentum ratio [21]. The theoretical and experimental results showed that, the dimensionless heights of turbulent flames are dependent on *Fr* as $L_f/d_n = 27Fr^{1/5}$ [18], With

$\frac{\rho_\infty}{\rho_j} = \frac{MW_{\text{air}}}{MW_j}\frac{T_j}{T_\infty}$, $\frac{\rho_{st}}{\rho_j} = \frac{MW_{\text{N}_2}}{MW_j}\frac{T_j}{T_{st}}$, $T_j = T_\infty$, $MW_{\text{air}} \approx MW_{\text{N}_2}$, Eq. (18) can be further simplified to give:

$$\tan\theta = \frac{337.5}{\pi}\frac{1}{\bar{\alpha}_{e(\dot{m})}(S+1)R_M}\left(T_\infty/T_{st}\right)^{1/2} Fr^{1/5} . \tag{19}$$

According to the definition of $\bar{\alpha}_{e(\dot{m})}$ in Eq. (4), when $\bar{\alpha}_{e(\dot{m})} \le 1$, the amount of entrained air is less than required for stoichiometric combustion, which is very common for the high speed, strong jet flame. When $\bar{\alpha}_{e(\dot{m})} > 1$, it implies that a large amount of air, sufficient to cause oxygen-rich combustion, is entrained into the flame, which occurs for low speed jet flames.

EXPERIMENTAL SETUP

Propane was used as the fuel and all experiments were carried out in a wind tunnel with a test section 6 m long, 1.8 m wide and 1.8 m high. The facility can simulate cross-flow between 0.5 and 15 m/s with turbulence fluctuation intensity of less than 2%. The transient cross-flow is measured by four hot-wire anemometers, with an accuracy of 0.01 m/s.

Four nozzle sizes were used with inside diameters from 8 to 14 mm, and the nozzle, in the middle of the test section, at a height of 50 cm, to reduce the influence of the floor boundary layer. The vertical jet flow was measured and controlled by an Alicat mass flow meter, with a precision of ±(0.8% of reading + 0.2% of full scale).

The jet-to-crossflow momentum flux ratio R_M for this work was in the range of 0.1~10, where the Reynolds number ($\text{Re} = \rho_j u_j d_n/\mu_j$, and Froude number $Fr = u_j^2/(gd_n)$ of the jet fuel gas are approximately $2100 < Re < 4000$ and $1 < Fr < 100$.

A high speed camera (2000 frames per second) was used in the front perspective of the tilted flames to record video images through the glass observation window on the side of the wind tunnel [14].

RESULTS AND DISCUSSION

Imaging analysis

Figure 2 shows typical flame images recorded by the high speed camera (a) and the contours of flame intermittent rate (b). In Fig. 2, the flickering flame length was obtained by image processing and the flame tilt angle by the vector of the mean flame length. The slant length was defined as the distance between the center of the nozzle exit and the “peak” of the contour of fifty percent of flame occurrence probability. With increasing wind velocity, the flame was increasingly inclined from the nozzle axis.

Tilt angle regime

The tilt angle with different Froude numbers, air entrainment ratio, and various momentum flux ratios, over a large range is shown in Fig. 3.

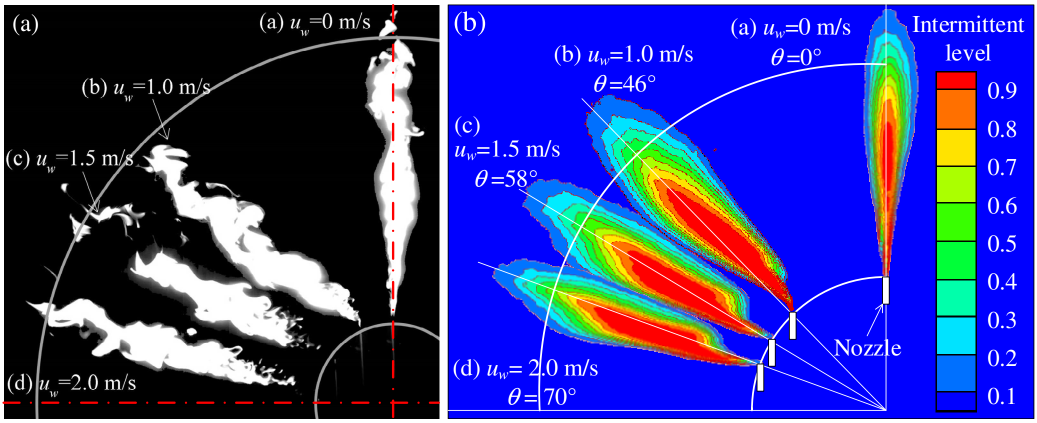

Fig. 2. Flame images (a) and the contours of the flame intermittent rate (d_n = 8 mm, u_j = 2.65 m/s).

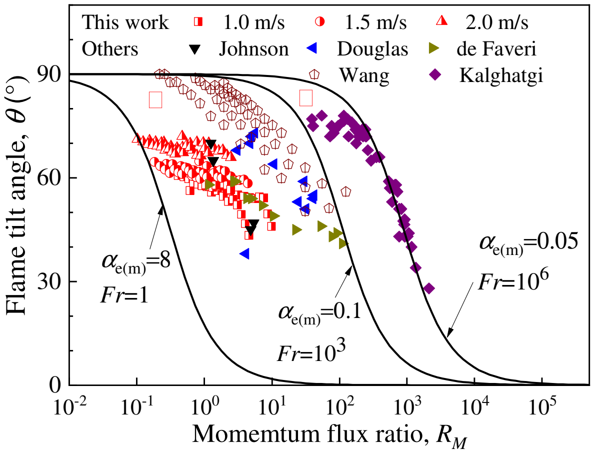

Fig. 3. Tilt angle with momentum flux ratio. The solid line is based on Eq. (19). Johnson [22]: propane, methane, 18.8 < Fr < 20.3; Douglas [23]: flare stack, 25 < Fr < 59; de Faveri [24]: diesel oil, 0.085 < Fr < 1.36; Kalghatgi [25]: propane, 1022 < Fr < 6.7×10^5; Wang [26]: propane, 47 < Fr < 756.

Escudier [3] postulated that the air is entrained into the jet at rates proportional to the magnitudes of these two characteristic velocities by using Morton entrainment theory, which can be expressed as:

$$d\dot{m}_{air}/d\xi = 2\pi\rho_\infty b\left(\alpha_{e(u)}\left|u_\xi - u_w\sin\theta\right| + \beta_{e(u)}u_w\cos\theta\right), \tag{20}$$

where $\alpha_{e(u)}, \beta_{e(u)}$ are the air entrainment coefficients related to the components of the cross-flow velocity parallel and normal to the flame axis. Ricou and Spalding [27] showed that for large ξ/d_n, $\alpha_{e(\dot{m})} = \dot{m}_{air}/(S+1)\dot{m}_j \propto \xi$, and $\alpha_{e(\dot{m})} = 0$ at ξ = 0. After dividing Eq. (20) by the fuel mass flow rate $\dot{m}_j = \pi d_n^2 u_j \rho_j/4$, the universal excess air entrainment ratio in the flame region is:

$$\bar{\alpha}_{e(\dot{m})} = \frac{d\alpha_{e(\dot{m})}}{d\xi}L_f = 8\frac{1}{S+1}\frac{L_f b}{d_n^2}\left(\frac{\rho_\infty}{\rho_j}\right)\left[\bar{\alpha}_{e(u)}\left(\frac{\left|\bar{u}_\xi - u_w\sin\theta\right|}{u_j}\right) + \bar{\beta}_{e(u)}\frac{u_w\cos\theta}{u_j}\right]. \tag{21}$$

As $Fr = u_j^2 / (gd_n)$, $\overline{\alpha}_{e(\dot{m})} \sim 1/Fr$. Therefore, the values of $\overline{\alpha}_{e(\dot{m})}$ and Fr in the calculation of the solid line in Fig. 3 were negatively correlated with each other.

There are two regimes (regime I: $1 < Fr < 10^3$, $0.1 < R_M < 100$; regime II: $10^3 < Fr < 10^6$, $100 < R_M < 3000$) for the medium and highly turbulent jet flames, respectively. For fixed Froude numbers, with increasing R_M, the tilt angles decreases. For highly turbulent jet flames in regime II, as the jet-flow Froude number is very large, the contributions of air entrainment to the tilt angle is negligible, so with the same R_M, the tilt angle is bigger than the low momentum jet flames in regime I.

CONCLUSIONS

Motivated by improving the understanding of the behaviors of jet flame in cross-flows, the work has provided a new tilt angle equation for air entrainment. The air entrainment ratio, defined as the mass flow rate ratio of the hot gas in the whole flame region to stoichiometric gases, was proportional to the jet flame Fr.

Experiments with propane jet diffusion flames analyzed and verified the angle equation. Based on the experimental results and tilt angle equation, two regimes of tilt angles were identified for the medium and highly turbulent jet flames: regime I: $1 < Fr < 10^3$, $0.1 < R_M < 100$; regime II: $10^3 < Fr < 10^6$, $100 < R_M < 3000$. For fixed Froude numbers, with increasing R_M, the tilt angle decreased. For highly turbulent jet flames, the contributions of air entrainment to the tilt angle can be ignored, so with the same R_M value, the flame deflected more than in low momentum jet flames.

ACKNOWLEDGMENTS

This work was sponsored by the National Natural Science Foundation of China (Nos. 51636008, 51576186, and 51323010), Key Research Program of the Chinese Academy of Sciences (No. QYZDB-SSW-JSC029), National Key R&D Program (No. 2016YFC0801500), Fundamental Research Funds for the Central Universities (No. WK2320000036) and China Postdoctoral Science Foundation funded project (No. 2018M632549). Fang Jun expresses sincere appreciation to Prof. Forman A. Williams for his valuable suggestions during the visit to UCSD.

References

[1] A.R. Karagozian, Transverse jets and their control, Prog. Energy Combust. Sci. 36 (2010) 531-553.

[2] L. Hu, A review of physics and correlations of pool fire behaviour in wind and future challenges, Fire Saf. J. 91 (2017) 41-55.

[3] M.P. Escudier, Aerodynamics of a burning turbulent gas jet in a crossflow, Combust. Sci. Technol. 4 (1971) 293-301.

[4] T.A. Brzustowski, The hydrocarbon turbulent diffusion flame in subsonic cross-flow, In. The hydrocarbon turbulent diffusion flame in subsonic cross-flow. Los Angeles, California, 1977, pp. 24-26.

[5] L.W. Kostiuk, A.J. Mejeski, P. Poudenx, M.R. Johnson, and D.J. Wilson, Scaling of wake-stabilized jet diffusion flames in a transverse air stream, Proc. Combust. Inst. 28 (2000) 553-559.

[6] Y. Zhao, L. Jianbo, and L. Lu, Numerical modeling of fires on gas pipelines, Appl. Therm. Eng. 31 (2011) 1347-1351.

[7] R.F. Huang, R.K. Kimilu, and C.M. Hsu, Effects of jet pulsation intensity on a wake-stabilized non-premixed jet flame in crossflow, Exp. Therm. Fluid Sci. 78 (2016) 153-166.

[8] X. Zhang, W. Xu, L. Hu, X. Liu, X. Zhang, and W. Xu, A new mathematical method for quantifying trajectory of buoyant line-source gaseous fuel jet diffusion flames in cross air flows, Fuel 177 (2016) 107-112.

[9] F. Tang, L. Hu, X. Zhang, X. Zhang, and M. Dong, Burning rate and flame tilt characteristics of radiation-controlled rectangular hydrocarbon pool fires with cross air flows in a reduced pressure, Fuel 139 (2015) 18-25.

[10] Y. Lin, X. Zhang, and L. Hu, An experimental study and analysis on maximum horizontal extents of buoyant turbulent diffusion flames subject to relative strong cross flows, Fuel 234 (2018) 508-515.

[11] Q. Wang, L.H. Hu, X. Zhang, X. Zhang, S. Lu, and H. Ding, Turbulent jet diffusion flame length evolution with cross flows in a sub-pressure atmosphere, Energy Convers. Manage. 106 (2015) 703-708.

[12] F. Tang, Q. He, and J. Wen, Effects of crosswind and burner aspect ratio on flame characteristics and flame base drag length of diffusion flames, Combust. Flame 200 (2019) 265-275.

[13] O.A. Pipkin, and C.M. Sliepcevich, Effect of Wind on Buoyant Diffusion Flames. Initial Correlation, Ind. Eng. Chem. Fund. 3 (1964) 147-154.

[14] J.W. Wang, J. Fang, S.B. Lin, J.F. Guan, Y.M. Zhang, and J.J. Wang, Tilt angle of turbulent jet diffusion flame in crossflow and a global correlation with momentum flux ratio, Proc. Combust. Inst. 36 (2017) 2979-2986.

[15] M. Tsue, T. Kadota, and M. Kono, Temperature and velocity fluctuations of a jet diffusion flame in a cross-flow, Proc. Combust. Inst. 29 (2002) 1937-1942.

[16] A.J. Majeski, D.J. Wilson, and L.W. Kostiuk, Predicting the Length of Low-Momentum Jet Diffusion Flames in Crossflow, Combust. Sci. Technol. 176 (2004) 2001-2025.

[17] B. Karlsson, J. Quintiere, Enclosure Fire Dynamics, CRC Press, 2000.

[18] N. Peters, Turbulent Combustion, Cambridge University Press, Cambridge, U.K., 2004.

[19] N. Peters, Turbulent Combustion, Cambridge University Press, Cambridge, U.K., 2004.

[20] M.J. Hurley, D.T. Gottuk, J.R. Hall Jr, K. Harada, E.D. Kuligowski, M. Puchovsky, J.M. Watts Jr, and C.J. Wieczorek, SFPE Handbook of Fire Protection Engineering, (5th ed), Springer, 2015.

[21] P.J. DiNenno, SFPE Handbook of Fire Protection Engineering, (3rd ed), National Fire Protection Association, Quincy, MA, 2002.

[22] M.R. Johnson, and L.W. Kostiuk, Efficiencies of low-momentum jet diffusion flames in crosswinds, Combust. Flame 123 (2000) 189-200.

[23] D.M. Leahey, and M.B. Schroeder, Observations and predictions of jet diffusion flame behaviour, Atmos. Environ. 21 (1987) 777-784.

[24] D.M. de Faveri, A. Vidili, R. Pastorino, and G. Ferraiolo, wind effects on diffusion flames of fires of high source momentum, J. Hazard. Mater. 22 (1989) 85-100.

[25] G.T. Kalghatgi, The visible shape and size of a turbulent hydrocarbon jet diffusion flame in a cross-wind, Combust. Flame 52 (1983) 91-106.

[26] J. Wang, J. Fang, J. Guan, Y. Zhang, and J. Sun, Effect of crossflow on the air entrainment of propane jet diffusion flames and a modified Froude number, Fuel 233 (2018) 454-460.

[27] F.P. Ricou, and D.B. Spalding, Measurements of entrainment by axisymentrical turbulent jets, J. Fluid Mech. 11 (1961) 21-32.

Thermal Radiation Hazards from Gas Pipeline Rupture Fireballs

Cowling N.[1,2,]*, Phylaktou H.[2,]*, Allason D.[1], Andrews G.E.[2]

[1] GL Industrial Services UK Ltd (DNV GL), Loughborough, Leicestershire, LE11 3GR, UK
[2] University of Leeds, Leeds, LS2 9JT, UK
**Corresponding author emails: nick.cowling@dnvgl.com, h.n.phylaktou@leeds.ac.uk*

ABSTRACT

Increasing world-wide demand for gas is resulting in an increased network of gas piping which poses potential hazards to the natural and man-made environment in proximity to the pipelines. In this work we report experimental measurements of the thermal radiation levels generated by fireballs from two full-scale, below-ground, natural-gas pipeline ruptures. The tests were carried out at the DNV GL's Spadeadam Test Site simulating the rupture of a 1219 mm diameter pipe carrying high pressure natural gas (at 13.4 MPa -nominal gauge pressure). The duration of the fireball and the maximum heat fluxes (as high as 70 kW/m^2 at 200 m downwind) were well predicted by current simple mathematical models when a reasonable radiative fraction of the total energy release was assumed. The empirical radiant fraction equation adopted by OGP was shown to overpredict the incident heat flux in these tests. In the second test the grass surrounding the test location was ignited and other vegetation showed significant thermal damage. To interpret such data correctly and to evaluate the hazards, to natural and man-made environments, more information is needed on the effects of short exposure times (of the order of a few seconds) to high transient heat fluxes.

KEYWORDS: Thermal radiation, fireball, gas pipeline.

INTRODUCTION

With worldwide demand for gas is set to rise until 2034 [1]. This will inevitably lead to environmental receptors being located closer to gas transmission installations and pipelines. In the 3 years from 2013 there were 60 gas pipeline releases within the EU [2, 3]. To assess the environmental risks from a pipeline release, credible scenarios need to be considered for each site which can include unignited or ignited releases the magnitude of which will depend on the size and rate of the release and the timing of ignition after the initiation of the release. Of the potential scenarios and consequences, the full-bore rupture of an onshore pipeline and a resulting fireball represents a worst-case scenario for pipeline operators.

In the event of a rupture of an onshore natural gas transmission pipeline, high pressure gas will be instantaneously released, leading to the formation of a crater. The initial phase will be highly transient, with the formation highly turbulent jet with a mushroom cap. This initial phase typically lasts 30 seconds. The gas cloud will increase in height due to the momentum of the release and the entrained air, gradually dispersing until an almost steady state plume is developed [4].

If ignited shortly after the rupture event, combustion of the turbulent gas cloud will lead to the generation of a fireball and crater fire. Whilst missile and overpressure hazards are also generated, experience has shown that from experiments by DNV GL, the hazard ranges associated with these are smaller than thermal radiation hazards [5].

Proceedings of the Ninth International Seminar on Fire and Explosion Hazards (ISFEH9), pp. 860-868
Edited by Snegirev A., Liu N.A., Tamanini F., Bradley D., Molkov V., and Chaumeix N.
Published by Saint-Petersburg Polytechnic University Press
ISBN: 978-5-7422-6498-9 DOI: 10.18720/spbpu/2/k19-131

In the case of immediate ignition, the radiant heat flux emitted will vary significantly from the combustion of a steady state release. There are a variety of simple models for estimating thermal radiation heat flux levels from gas jet fires [6, 7] i.e. the steady state fire which develops after a fireball event. Such models have been extensively validated and refined. Publicly available data on thermal radiation data from fireballs following a large scale gas pipeline ruptures with immediate ignition are limited to few sources [8, 9]. There are however, several simple correlations for the estimation of fireball diameters and durations which have been validated for BLEVE's [7]. The International Association of Oil and Gas producers (OGP) recommend the use of one these models-discussed in detail later - to predict the thermal radiation levels for fireballs from pipelines [10].

The main aim of the present work is to provide experimental measurements of the thermal radiation levels generated following the ignition of flammable gas from a full-scale, below-ground, natural-gas pipeline rupture and to understand the implications this has for current models used in assessing the environmental risks. Evidence of thermal damage to surrounding and strategically placed vegetation will also be obtained, and this will be compared to the measured radiative fluxes and used to build up a library of vegetation damage evidence that could also be useful for investigation of pipeline fireball incidents or other thermal radiation incidents.

METHODOLODGY

The fracture propagation facility at DNV GL's Spadeadam Test Site was used to accommodate the 48-inch (1219 mm) diameter test pipes. The test layout consisted of two 48-inch (1219 mm) diameter pipe reservoirs each with a length of approximately 165 m, at a nominal test pressure of 13.5. The reservoirs were spaced with a gap between the reservoir ends of approximately 130 m where the test section comprising of eleven pipe lengths could be installed. The length of the reservoir on each end of the test section was such that it simulated an infinitely long pipeline, thus enabling that gas decompression from the test section to replicate actual pipeline conditions (at an initial 13.4 MPa gauge pressure) without experiencing any pressure reflections during the fracture event. The outer end of each of the reservoirs was terminated with a dome end and fitted with connections to a 12-inch nominal bore (323 mm) diameter gas recirculation loop through full bore isolation ball valves.

The recirculation loop incorporated a set of fan units providing a circulation velocity of nominally 0.5 m s^{-1} in the 48-inch (1219 mm) diameter test pipe to ensure that a homogeneous gas mixture was achieved throughout the test rig. A heat exchanger supplied with an ethylene glycol/water mixture and circulated through two refrigeration units was used to control the temperature of the gas. To reduce any heat loss or heat gain throughout the system, the flow loop, reservoirs and test section were insulated with spray applied polyurethane foam.

The circulating loop incorporated injection points with meters to measure both the natural gas content (injection was from an LNG source) and the volume of gas in the test rig.

To prevent reservoir movement during a test, both reservoirs were installed within large concrete anchors. Four anchors were equally spaced along each reservoir to resist any bending forces applied during the test and one at each end supported by steel piles to resist axial thrust. The reservoirs were also protected at their inner ends by wire wound crack arrestors, in the event that the fracture failed to arrest within the test section.

Prior to carrying out a pneumatic test of the rig, instrument and cable locations were covered with a layer of sand padding and then backfilled with indigenous clay type soil so that the top of the test pipes was 0.9 m below ground level. A photo of the eastern end of the test section before being backfilled is shown in Fig. 1.

The test was initiated using a 1 m long explosive cutting charge in the centre of the initiation pipe. Although there was a high probability that ignition of the test gas on initiation would occur, ignition sources were also deployed at both at high and low level by firing of pyrotechnics into the area of the cloud at the same time as the test initiation.

Fig. 1. Image of the test section prior to being backfilled.

Fig. 2. Radiometer locations**.**

The thermal radiation resulting from the fracture test was measured using an array of Medtherm wide angle radiometers (total field of view of 150^o) distributed around the test area. In the north-south direction (nominally crosswind from the prevailing wind direction), radiometers were placed at distances of 200 m and 500 m north of the initiation point. On the east-west axis, radiometers were placed at 200 m and 500 m west of the initiation point and distances of 200 m, 500 m, 750 m and 1000 m east of the initiation point. A diagram showing the locations and nomenclature for the radiometers is shown in Fig. 2. The radiometers have a response time of 1 s and an accuracy of ±5% and were calibrated prior to testing in a black body furnace over five different heat fluxes. Each Medtherm radiometer is fitted with a calcium fluoride window that transmits light in the wavelength range 0.3 to 11.5μm and employs a Schmidt-Boelter thermopile to measure incident thermal radiation. Incident thermal radiation is absorbed at the sensor surface and transferred to an integral heat sink that remains at a temperature below that of the sensor surface. The difference in temperature between two points along the path of the heat flow from the sensor to the sink is proportional to the heat being transferred, and is, therefore, proportional to the incident thermal radiation. Medtherm radiometers have thermocouple junctions fitted at two such points. These form a differential thermoelectric circuit, providing an EMF between the two output leads which is directly proportional to the incident thermal radiation. The radiometers will be aimed at the nominal predicted centre of the fireball.

Two full scale rupture experiments have been carried out. These tests were identical in the experimental set-up with respect to the purposes of the study presented here. However, due to a malfunction of the data loggers the East and North radiometer recordings were lost in Test 2. Additionally, there were environmental differences between the tests which are summarised in the Table 1.

Table 1. Test conditions

	Date	Ambient Temp (°C)	Atmospheric Pressure (mbar)	Relative Humidity (%)	Wind direction (°)	Wind speed (m/s)
Test 1	28th March	11	967	94	295	7.6
Test 2	6th June	9.7	984	94	253	7

RESULTS AND DISCUSSION

In the first test, a peak thermal radiation level of over 70 kW/m^2 at 200 m was observed (see Fig. 3). It took 6 seconds to reach this thermal radiation level. At 750 m it took over 20 seconds for the thermal radiation level to fall below 1 kW/m^2. The fireball mushroomed from the release point and was observed to be tilted by the prevailing wind direction (295°, 7.6 m/s) as shown in 4. Thus, the peak thermal radiation level was observed on the eastern radiometer. As a peak of 35 kW/m^2 observed on the western radiometer also located 200 m from the release point, the thermal radiation field was found to be asymmetrical.

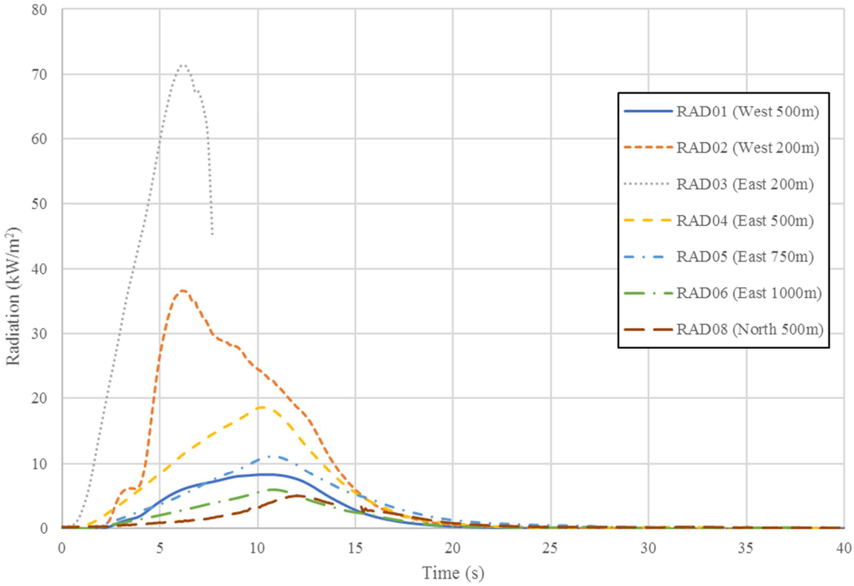

Fig. 3. Thermal Radiation Measurements from Test 1.

Comparison to calculated maximum heat fluxes

Using the same method as Wang [8], which has the same form as the OGP method [10], the peak thermal radiation at a given distance can be calculated using the equations for the maximum diameter, duration and height of the fireball:

$$D_{max} = 6.48M^{0.325} \tag{1}$$

$$H = 4.35M^{0.333} \tag{2}$$

$$t_d = 2.60M^{0.167}, \tag{3}$$

where D_{max} is the maximum diameter of the fireball (m), M the mass of fuel involved (90,000 kg), H (m) the height of the fireball from ground level and t_d (s).

The distance (X) from the fireball to the receiver is:

$$X = \sqrt{l^2 + H^2} \tag{4}$$

where l is the distance to the point on the ground beneath the fireball.

Fig. 4. Fireball from Test 1 (view looking east).

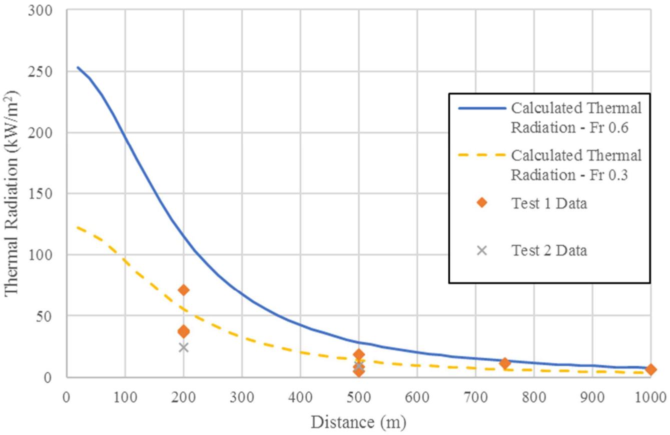

Fig. 5. Maximum thermal radiation (predicted and observed) as a function of the ground level distance from the centre of the release location.

The view factor (v_f), transmissivity (τ) and surface emissive power (E) are given by:

$$v_f = \left(\frac{D_{max}}{2X}\right)^2 \tag{5}$$

$$\tau = 2.02 \times \left[RP_w\left(X - \frac{D_{max}}{2}\right)\right]^{-0.09} \tag{6}$$

$$E = \frac{\Delta H\ M\ F_r}{\pi D_{max}^2 t_d}, \tag{7}$$

where R is the relative humidity (0.94 for Test 1), P_w is the water saturation pressure (1312 Pa) and ΔH is the heat of combustion (52 MJ/kg). The fraction of heat radiated (F_r) is given by Wang as:

$$F_r = 0.27P_b^{0.32} \tag{8}$$

where P_b is the pipe design pressure in MPa (13.4 MPa was used which is pipeline pressure before rupture) .

The radiation (I) received by an observer at distance X is:

$$I = v_f \, \tau \, E \tag{9}$$

The maximum thermal radiation levels predicted using the above model, as a function of distance from the fireball vertical axis, are shown as a solid blue line in Fig. 5, where they are compared with the measured data. Good agreement (within 20%) is shown in the far field, at distances over 700 m and low heat fluxes. In the near field the theoretical calculation overpredicts the measured values by an order of 60%.

Examination of the outputs from each of the above equations indicates that the main source of the difference is the larger than expected radiative fraction (Fr) calculated from Equation (8). The equation gives a value of Fr of 0.61 which is much larger than a generic value of 0.3 for large hydrocarbon fires and fireballs. The radiative fraction is strongly dependent on the soot content and temperature of the flame, but measurements above 0.4 are rare. The rational and origin of the relationship are unclear, but it has been adopted by OGP [10], and therefore it is significant to show that it results in overprediction in this case. Equation (8) is an empirical relationship with no link to the physics of the phenomena. Interestingly Wang and Co-workers [8] used the same expression giving Fr = 0.7, in their case. They also showed good agreement with their data from LNG experiments, which will have different sooting characteristics to the current case. Additionally, a low heat of combustion was used in Wang et al [8], without explanation.

As a comparison Eq. (8) in the above model was replaced with Fr = 0.3 (i.e. the generic value typically used radiative fire hazard calculations). The results are shown as a dashed line in Fig. 5, and clearly demonstrate a much better agreement with the experimental test data from this work.

Worthy of note is the result from Eq. (3), with a duration of the fireball from this release of 17.4 s, which compares well with the duration of the thermal pulse indicated in Fig.3.

Thermal damage to vegetation

During the second test, two types of plants (Laurustinus and Portuguese Laurel) were located at each of the radiometer locations. During the second test the leaves of the Portuguese Laurel at 200 m showed scorching (shown in Fig. 6). However, grass located 150 to 250 m from the release point was ignited.

In fire hazard calculations the minimum heat flux required either for pilot ignition or autoignition of solid material is a very important parameter, as it defines the ignition propensity of the material. As it is the minimum heat flux that is of interest then necessarily the exposure times are long. For example for wood the minimum heat flux required to achieve piloted ignition, is typically quoted as 12.5 kW/m^2,while for autoignition it is 29 kW/m^2 [11]. However, it should be understood that at these heat fluxes it may take several minutes before ignition occurs.

The exposure time to fireballs resulting from pipeline ruptures, or other transient events, is short but the actual incident heat fluxes are large. For this reason, the minimum heat flux data for pilot ignition or autoignition of the material is of little use in establishing the thermal threat level that these events pose to their surroundings. More work is needed in this area to develop a database of ignition propensity to short high intensity heat fluxes.

With respect to the second test, it is possible that hot embers and debris could have fallen onto the grass to cause piloted ignition in patches, as shown in the debris field in Fig. 7. However, it is also likely that the radiative flux was sufficient to ignite the grass in June when most likely it was dryer than in March.

There are many variables which will affect whether vegetation will ignite: Type of solid (thermally thin or thick), ambient conditions, size and orientation of object, heating methods, moisture levels, fuel arrangement, topography. Also, different species will have varying resistance to fire, for example juniper trees have a thin bark and a lack of other defence mechanisms, so will be sensitive to fires [12].

Moisture levels are an important variable for vegetation, as a substance needs to be dry for combustion. to occur and, as water has a high latent heat of vaporisation, considerable thermal radiation is needed to dry out a substance [13].

Fig. 6. Scorching to Portuguese Laurel – Test-2, 200 m.

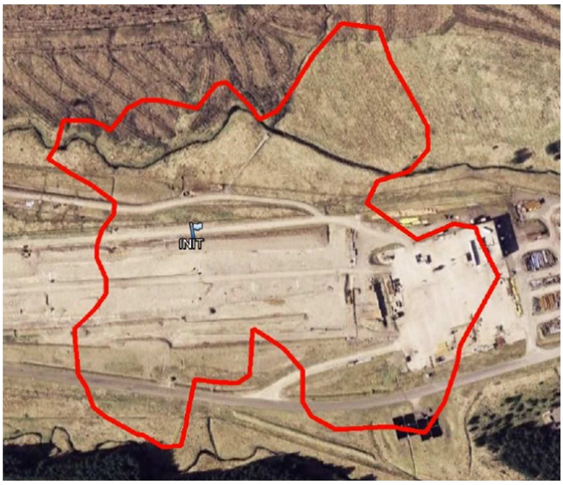

Fig. 7. Debris field.

Ignition of cellulosic materials determined in the laboratory is likely to have been conducted on substances which have been dried out. However, as shown in the second test, the intensity of radiation from the fireball phase is sufficient to dry out a substance and cause combustion to occur.

Weather conditions also play a role, as a long dry period, will make the ecosystem easier to ignite. Damage to grass was limited in the first test, which is likely to be due to significant rain and snow in advance of the test.

In the event of a real release, the fireball phase will be followed by a steady state fire. The duration of this steady state fire will be dependent upon how easily the plant is to isolate. In 2004, an 80 bar, 40-inch gas pipeline ruptured [14]. Thermal damage was caused, extending to a radius of approximately 200 m which is equivalent to 125,000 m^2. Figs. 8 to 10 show damage to trees, grass and timber pallets around the building.

In the UK, environmental risk assessments can be carried in line with the Chemical and Downstream Oil Industries Forum (CDOIF) guidance on environmental risk tolerability [15].

To determine whether there is the potential for a major accident to the environment (MATTE) the following steps can be carried out:

1. Deduce credible scenarios to assess;
2. Determine whether there is pathway to cause harm to a receptor (i.e. thermal radiation);
3. Calculate the hazard distance to determine which receptors would be affected;
4. Assess the area of damage caused for different receptors against the CDOIF guidance;
5. Determine the duration of the harm.

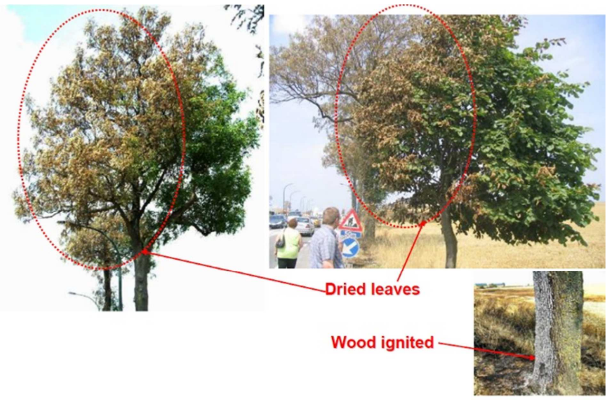

Fig. 8. Damage to trees 210 m from the crater [14].

Fig. 9. Damage to grass. View 400 m from the crater [14].

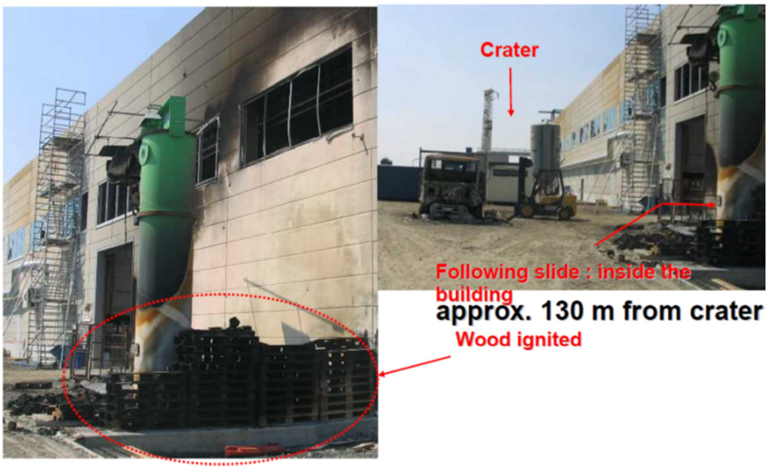

Fig. 10. Damage caused to wooden pallets 130 m from the crater [14].

In the case of a pipeline rupture, Figs. 8 to 10 show that harm can be caused by a pipeline rupture to environmental receptors. Area criteria for assessing damage to environmental receptors start from 0.5 hectares (5,000 m^2) or 10% of the area, if less for sensitive receptors and 10 hectares (100,000 m^2). The experimental data have shown that in the initial fireball phase of a pipeline rupture, visible damage to vegetation is caused to plants within 200 m of the release. Most of the burnt area in this case was grass. Grass has an unusual growth mechanism in that it starts from the stem, rather than the tip [13]. Therefore, unless the soil is badly damaged it is likely for the grass to re-grow. In assessing the possible impacts for grass, it is likely to recover within 3 years and so therefore, it is in accordance with the CDOIF guidelines, such an incident would not be classed as a MATTE.

Other criteria are included with the CDOIF guidelines and further information is required in assessing the consequences more sensitive receptors.

CONCLUSIONS

Two large scale tests of fireballs from full-scale, below-ground, natural-gas pipeline rupture enabled experimental measurements of the thermal radiation levels generated to be made. The duration of the fireball and the maximum heat fluxes were well predicted by current simple mathematical models when a reasonable radiative fraction of the total energy release is assumed. The empirical radiant fraction equation adopted by OGP was shown to overpredict the incident heat flux. In the second test the grass surrounding the test location was ignited and other vegetation showed significant thermal damage. To interpret such data correctly and to evaluate the hazards presented by such pipeline ruptures to natural and man-made environments more information is needed on the effects of short exposure times of the order of a few seconds to high transient heat fluxes.

REFERENCES

[1] Energy Transition Outlook 2018 Oil And Gas, Forecast to 2050, DNV GL, 2018.

[2] Incident Statistics. PHMSA. https://www.phmsa.dot.gov/hazmat-program-management-data-and-statistics/data-operations/incident-statistics, 2018 (accessed 11 May 2018).

[3] Gas Pipeline Incidents, 9th Report of the European Gas Pipeline Incident Data Group 1970-2013, EGIG 14.R.0403, 2015.

[4] R.P. Cleaver, P.S. Cumber, P. Genillon, A Model to Predict the Characteristics of Fires Following the Rupture of Natural Gas Transmission Pipelines, Process Saf. Env. Prot. 79 (2001) 3–12.

[5] R.P. Cleaver, A.R. Halford, A model for the initial stages following the rupture of a natural gas transmission pipeline, Process Saf. Env. Prot. 95 (2015) 202–214.

[6] B.J. Lowesmith, G. Hankinson, M.R. Acton, G. Chamberlain, An Overview of the Nature of Hydrocarbon Jet Fire Hazards in the Oil and Gas Industry and a Simplified Approach to Assessing the Hazards, Process Saf. Env. Prot. 85 (2007) 207–220.

[7] S. Mannan (Ed.), Lees' Loss Prevention in the Process Industries (Fourth Edition), Vol. 1, Ch. 16: Fire, pp. 1075-1366, Elsevier, 2012.

[8] K. Wang, Z. Liu, X. Qian, P. Huang, Long-term consequence and vulnerability assessment of thermal radiation hazard from LNG explosive fireball in open space based on full-scale experiment and PHAST, J. Loss Prev. Process Ind. 46 (2017) 13–22.

[9] M.R. Acton, G. Hankinson, B.P. Ashworth, M. Sanai, J.D. Colton, A Full Scale Experimental Study of Fires Following the Rupture of Natural Gas Transmission Pipelines, p. V001T01A008, 2000.

[10] Consequence Modelling, OGP, 434–07, 2010.

[11] D. Drysdale, An introduction to fire dynamics, 3rd ed, Chichester, Wiley, 2011.

[12] P. Evangelista, T. Stohlgren, D. Guenther, S. Stewart, Vegetation Response To Fire And Postburn Seeding Treatments In Juniper Woodlands Of The Grand Staircase-Escalante National Monument, Utah., Western North American Naturalist 64(3) (2004) 13.

[13] Effect of Fire on Vegetation, R2842, DNV GL, 1999.

[14] Rupture and ignition of a gas pipeline, ARIA, 2009.

[15] Environmental Risk Tolerability for COMAH Establishments, Chemical and Downstream Oil Industries Forum, Version 2.

Battery fires

Measuring the Energetics of a Lithium Ion Battery in Thermal Runaway

Quintiere J.G.

University of Maryland, Department of Fire Protection Engineering, College Park, MD, USA
jimq@umd.edu

ABSTRACT

A calorimetry technique is developed to measure the energetics of an 18650 Li-ion battery in thermal runaway. The technique uses the battery as a calorimeter with temperature and mass loss measurements to analyze the energetics. Runaway is induced by heating of the battery. Only one battery is investigated over a range of heating power and state of charge (SOC). The dynamics of the battery are investigated including time events, temperature, mass lost and energies. The total energy in runaway is manifested by the internal energy stored in the battery and the enthalpy of the ejected mass. Combustion of the ejected gases is not studied here. Here a safety vent first causes the release of gases, then this is followed by the more dominant ejection during runaway. Vent times decrease dramatically with heating power. The duration of runaway decreases with the SOC, and runaway energy increases with the SOC. The total energy measured in runaway is compared to an alternative technical to show its accuracy. The need to assume a specific heat of the ejected mass in the current technique has an effect on accuracy. Also the possibility of melting in runaway is not included in the current technique.

KEYWORDS: Batteries, calorimeter, Li-ion, thermal runaway.

INTRODUCTION

Lithium ion batteries have a high electrical energy density. These batteries are used extensively in commercial products from electronics to powering automobiles. As with any new technology they can cause unanticipated safety issues. It has become well known that such batteries are prone to "thermal runaway" that can lead to fire and explosion hazards [1-3]. In general, thermal runaway is a process that is accelerated due to temperature. It involves a feedback mechanism in which the exothermic energy produces an increase in temperature, and the temperature causes an increase in the rate of energy generated. In runaway of a Li-ion battery, many exothermic decomposition reactions are triggered among its components, and modeling all of the electrical and chemical processes in runaway is very complex [4-6]. The primary hazard from the runaway of a battery is the transfer of this energy to other batteries causing a possible chain reaction, and the transfer of energy to the surrounding materials to cause fire and possible explosion in a confined system. The energy dynamics of runaway are key in the design of safety mitigation systems to prevent the consequences from runaway.

A typical Li-ion battery consists of a cathode of a lithium metal oxide on aluminum and a graphite anode on copper. The electrolyte is an organic solvent and is combustible. A plastic membrane separator, within the electrolyte, limits the ion transfer between the anode and cathode. The separator is a key failure point in the initiation of runaway. Failure can be initiated in several ways: (1) a manufacturing defect that produces dendritic growth breaking the membrane, (2) heating to cause the membrane to melt, (3) direct accidental puncture, and (4) over-charging. Failure of the membrane leads to an internal short circuit and thermal runaway.

Proceedings of the Ninth International Seminar on Fire and Explosion Hazards (ISFEH9), pp. 870-880
Edited by Snegirev A., Liu N.A., Tamanini F., Bradley D., Molkov V., and Chaumeix N.
Published by Saint-Petersburg Polytechnic University Press
ISBN: 978-5-7422-6498-9 DOI: 10.18720/spbpu/2/k19-49

The internal energy generated within the battery in runaway is composed of resistive heating and the sum of several exothermic decomposition reactions involving the cathode, anode and electrolyte [6]. Gases produced in early reactions pressurize the battery and are first intentionally vented by a pressure-relief device. This is followed by a more catastrophic ejection of mass during runaway. The energy output of a battery in thermal runaway is composed of (1) the internal energy from resistive heating and decomposition, (2) the thermal energy of the vented materials, and (3) potentially combustion energy of the vented gases. The vented materials can include gases composed of CO_2, CO, H_2, CH_4, other hydrocarbon and possibly a little oxygen, and solids composed of copper, graphite and molten aluminum [3]. These three energies comprise the potential fire hazard to the surroundings.

Measurement techniques have been used to measure the thermodynamic energy and the rate of energy from batteries during runaway. A commercially available technique is an adiabatic Accelerating Rate Calorimeter (ARC) but it is limited to temperature ranges well below the temperatures after the onset of runaway. In Roth et al [7] an ARC measures energy rates up to about 160 ºC. A novel technique was developed by Walters and Lyon [8] and Lyon and Walters [9] using a standard oxygen bomb device, but with an atmosphere of nitrogen. The “bomb” and ARC methods are closed systems and will measure both the energy internally generated in runaway and the energy vented from the battery. Another technique using the battery itself as a calorimeter was developed by Liu et al [10] and Said et al [11] in which they address runaway rates and energies for several Li-ion batteries. Results will be presented here for a similar battery calorimeter. These results are based on a report by Quintiere et al [12] that also included the combustion energy as measured in a combustion calorimeter [13].

BATTERY CALORIMETER DESIGN

The calorimeter design is based on an energy balance for the battery. An 18650 battery (18 mm in diameter and 65 mm in length) was considered without its plastic covering. Although the battery is a cylinder, its internal battery element consists of a thin rectangular battery pouch wound into a cylindrical shape. A measurement of the battery temperature and its mass over time in runaway is used to compute the various energy components. The battery is heated by a wrapped powered Nichrome wire to induce runaway. An electric arc is used to ignite the escaping gases at the battery’s vented end. A holder for the battery consisted of a tight thin copper sleeve (0.6 mm), covered by thin ceramic paper with a winding of Nichrome heating wire around its outside. Power (*P*) to the wire was measured by current and voltage. The entire battery and holder assembly is continuously weighed; and temperature is measured by a flattened thermocouple sandwiched between the copper sleeve and the outer steel shell of the battery. The entire battery and holder is wrapped in thick low density (48 kg/m^3) ceramic blanket and jacketed by a steel 70 mm diameter cylindrical shell. The components of the assembly are illustrated in Fig. 1. A schematic is shown in Fig. 2.

Fig. 1. Calorimeter components.

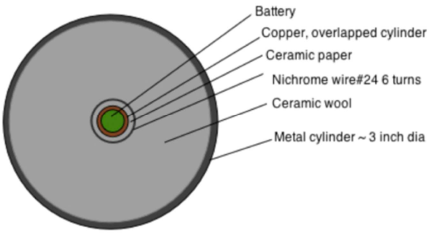

Fig. 2. Schematic of calorimeter.

CALIBRATION OF CALORIMETER

The battery calorimeter is calibrated by using an energy balance with a solid aluminum cylinder identical in size to the 18650 batteries. The specific heat of the aluminum is taken as 1.05 kJ/(kg·K) at 125 ºC. A control volume (CV) is selected to encompass the aluminum cylinder, copper and ceramic paper sleeves, and the nichrome heating wires. Heat is lost from the control volume to surroundings comprising the ceramic blanket wool and the exiting electrical wires for power. The aluminum is inert so the mass of the CV-contents is constant and taken as that of copper (21.5 g) and aluminum (47 g). The masses of the ceramic paper and the 24 AWG (0.5 mm diameter and 46 cm in length) resistance wire are neglected. Applying the conservation of energy to the CV with the following assumptions: (1) the battery and copper cylinder are considered thermally thin at the same homogeneous temperature, and (2) the heat loss rate ($\dot{Q}_{loss}$) is by conduction into a semi-infinite media, gives

$$\left[(mc)_{Cu} + (mc)_{Al}\right]\frac{dT}{dt} = P - \dot{Q}_{loss} \,. \tag{1}$$

The heat loss rate to the ceramic insulation and from the wires is assumed to be of the form

$$\dot{Q}_{loss} = \beta(T - T_i)\big/\sqrt{t} \,. \tag{2}$$

The specific heat of aluminum was derived from the calorimeter analysis and compared to its literature value. The analysis used β =1.4 W·s$^{1/2}$/K and a specific heat for copper of 0.39 kJ/(kg·K) in two repeated tests each with a power input of 26.4 W. Figure 3 shows the computed specific heat for aluminum. For early times and for corresponding low temperatures, the thermally thin assumption is not appropriate. However, as the heat loss is small in this early period, the aluminum calorimeter appears to give a good calculation for its specific heat.

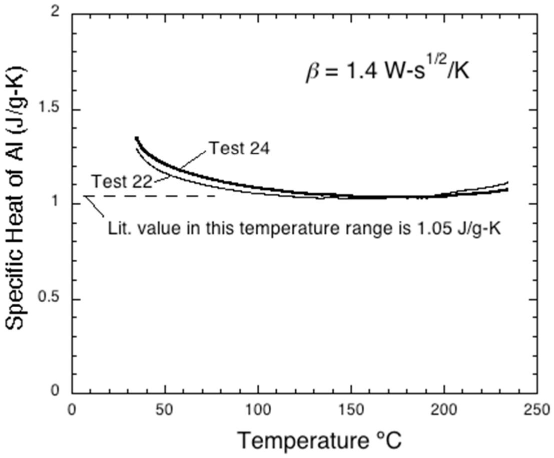

Fig. 3. Calibration of the calorimeter using an aluminum battery surrogate.

BATTERY

In this study only one battery was tested. It was a Li-ion 18650 battery with a $LiCoO_2$ cathode having a nominal 3.7 V and 2600 mA-hr rating. This gives a nominal maximum stored energy of 34.6 kJ. The battery mass was 44.2±0.1 g over the series tested in which the power input to initiate runaway was varied from about 10 to 74 W, and the State of Charge (SOC) was varied from about 0 to 100 %. Here the SOC is found by a discharge of the battery from its rated capacity.

Temperature uniformity of battery

Several tests were made to investigate the assumption of the battery and copper sleeve as thermal thin and uniform in temperature at any time. The internal battery temperature was measured at its axial and lateral center along with the normal calorimeter temperature measured on the outer center of the battery between it and the tight fitting copper sleeve. Figure 4a shows the results. Also Figure 4b shows the results for the outer center and end of the battery in another test. The results indicate that the battery temperature is reasonably homogeneous within about 20 ºC, however there is an anomaly for the center-outer temperature after runaway. From Figure 4a it can be seen that there is a delay in response to the outer battery shell of about 20 s and about 60 s for the interior of the battery. So the thermally thin assumption for the system is reasonable after 60 s.

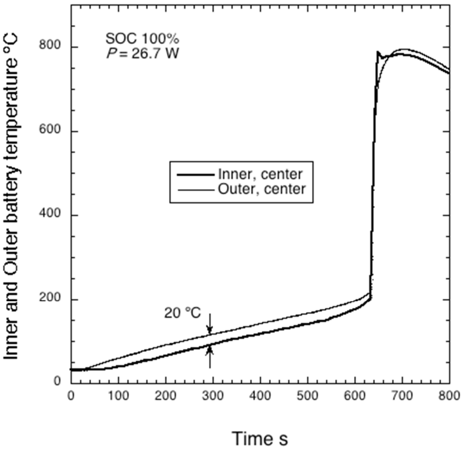

Fig. 4a. Temperature within battery and outer shell.

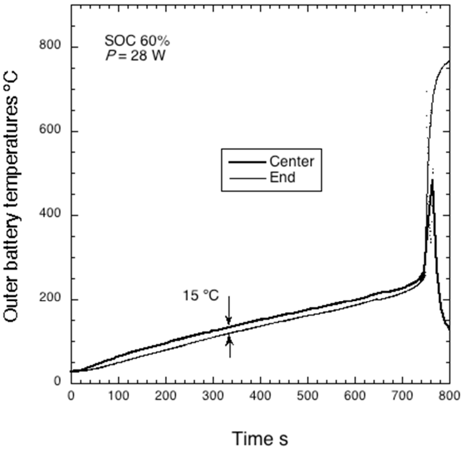

Fig. 4b. Outer center and end temperatures.

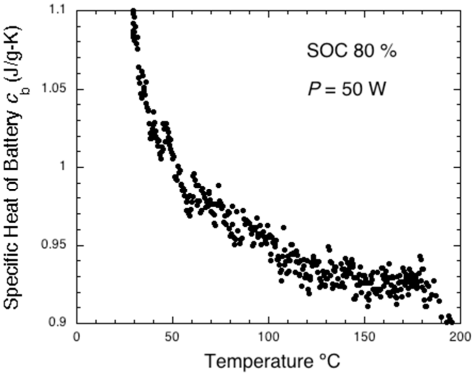

Fig. 5. Typical determination of the battery specific heat before runaway.

Specific heat of battery

The specific heat of the battery was determined for each thermal runaway experiment during the inert battery phase before runaway. This inert period was primarily below 200 ºC for this battery. Equation (1), with the battery substituted for the aluminum, was used to reduce the data. Figure 5 shows a typical determination for the battery specific heat. The inaccuracy below about 100 ºC is due to the delayed temperature response of the battery. The specific heat did not significantly vary over the range of testing this battery and was found to be 0.95±0.03 kJ/(kg·K). This value was taken as constant for all analyses in the tests, in spite of mass lost from the battery during runaway.

MODELING THE DYNAMICS OF BATTERY RUNAWAY

In these tests runaway was induced by heating of the outer battery. The heating power was varied in the tests as well as the SOC of the battery. The heating likely melted of the plastic membrane separator and caused an internal electrical discharge and runaway. This electrical and chemical energy is manifested within the battery as a generation term $\dot{Q}_b$, and outside of the battery by an ejection term of enthalpy from the battery. The conservation of mass for the system CV yields that the rate of mass ejected is equal to the rate of change for the battery mass, *m*. As shown in [14], the conservation of energy states that the rate of internal energy plus the rate of ejected enthalpy is equal to the sum of the heating power (*P*) and the generation term ($\dot{Q}_b$) minus the heat loss into the ceramic wool ($\dot{Q}_{loss}$) given by Eq. (2). Rearranging to solve for the internal generation term gives

$$\dot{Q}_b = (mc)_{Cu} \frac{dT}{dt} + c_b \frac{d(mT)_b}{dt} + \dot{Q}_{loss} - P - c_g T \frac{dm}{dt}. \tag{3}$$

The values for the constants in Eq. (3) are: $(mc)_{Cu}$ = 8.4 J/K, c_b = 950 J/(kg·K), and c_g is assumed as 1050 J/(kg·K). The value of the specific heat for the ejected materials is selected for expedience as their components are not known and can comprise gases of hydrogen, carbon dioxide, methane and others, as well as possibly molten aluminum. At 1000 K, the specific heats of hydrogen, carbon dioxide and methane are respectively, 15000, 1200 and 4500 J/(kg·K). Therefore the uncertainty of the specific heat for the ejected mixture as well as ignoring any possible melting leads to an underestimation for this ejected energy term defined as

$$\dot{Q}_g \equiv c_g T \frac{dm}{dT}. \tag{4}$$

It will be shown that the battery undergoes very rapid changes during runaway. As a consequence the computation of time derivatives from the temperature and mass measurements can be problematic. Moreover the practical manner to assess the hazard of the battery in runaway is not to have the precise rate of energy released, but to have the total energy, realizing this is a potential transfer to the surroundings in a short time. Therefore, Eq. (3) is integrated to obtain the energy released over time

$$\int_0^t \dot{Q}_b dt = Q_b = (mc)_{Cu}(T - T_i) + c_b(mT - m_i T_i) + \int_0^t \dot{Q}_{loss} dt - Pt - c_g \int_{m_i}^{m} T dm, \tag{5}$$

with the ejected energy as $Q_g \equiv c_g \int_{m_i}^{m} T dm$. Equation (5) will be used to reduce the data for a series of tests on the battery varying SOC and *P*. In all the tests the heating power was initiated at the start and kept constant throughout the test. An electric arc was manually initiated at the start of venting to attempt to ignite the gases. This was not always successful due to timing and location, and at times auto ignition could occur before the arc was struck.

TYPICAL DATA AND ANALYSES

Test 17 using a heating power of 25.6 W and a SOC of 100% is examined to show the typical results for this battery. The raw data of battery temperature and mass are shown in Figure 6. There is a nearly linear rise in temperature until about 500 s when the pressure safety vent opens and releases white vapors. In general these vapors could be ignited but ignition was not achieved in this test at the first vent. These vapors continue to vent until about 550 s where thermal runaway occurs. The feedback between battery temperature and decomposition takes place over several seconds.

This is seen as a nearly vertical jump in temperature and drop in battery mass. Runaway is a violent process with a high velocity jet from the pressure safety end of the battery. This ejection is about 35% of the original battery mass. In several seconds the battery temperature jumped from about 200 ºC to 800 ºC. Runaway is a dramatic event.

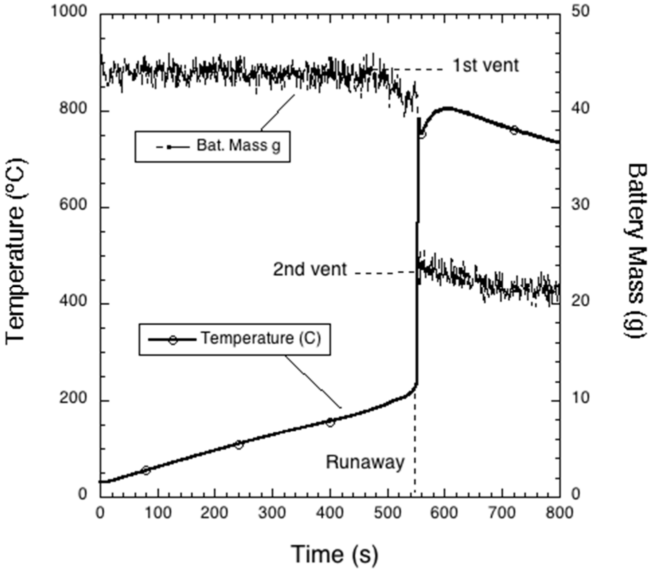

Fig. 6. Battery temperature and mass at 100% SOC and heating power at 25.6 W.

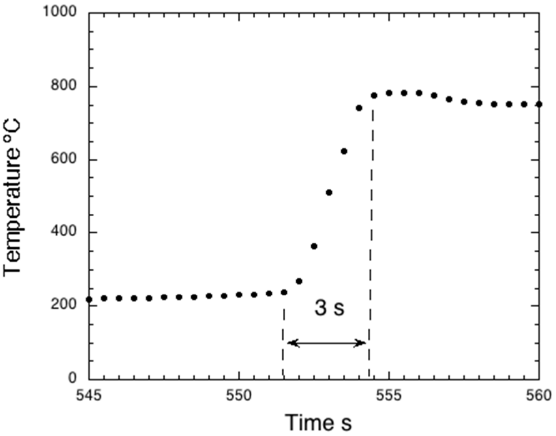

Fig. 7. Temperature at jump.

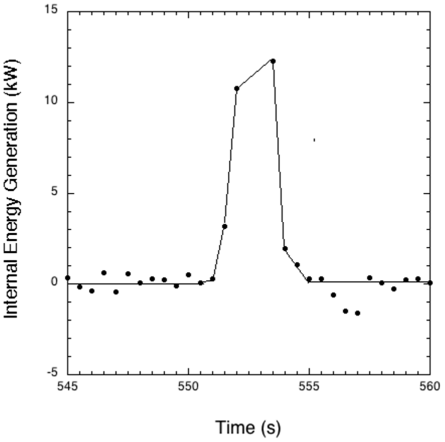

Fig. 8. Internal generation rate of energy.

The runaway event is examined more closely over the jump period (551.5 to 554.5 s). Figure 7 shows the temperature jump and Fig. 8 shows the rate of internal energy computed, $\dot{Q}_b$. The dramatic jump in 3 seconds shows the characteristic of thermal runaway in a battery. While the rate of internal energy generation can be computed, its distribution over time may not be as significant as the total energy dumped in this process. However ejected energy from the battery commenced at the first vent (~ 500 s) at about 190 ºC; then most of this category of energy was released during the jump after the second vent (~ 550 s). Consequently most of the battery energy converted from its original electrochemical energy is primarily transferred in this jump period, and will be represented by Q_b and Q_g over the entire heating period of the battery as given in Eqns. (4) and (5).

Figure 9 shows the specific energy terms in Eq. (5) individually computed for Test 17. As Q_b is computed from the algebraic sum of the RHS terms some inaccuracy can be noted as its value is about −1.5 kJ before the jump instead of zero. However after the jump this internal energy computed is 30 kJ. Q_g reaches about 18 kJ. Therefore the total energy of the battery released during runaway is about 48 kJ, compared to its rated energy at 100 % SOC of 34.6 kJ. Of course this does not include the combustion energy that can be released if the vented gases are ignited.

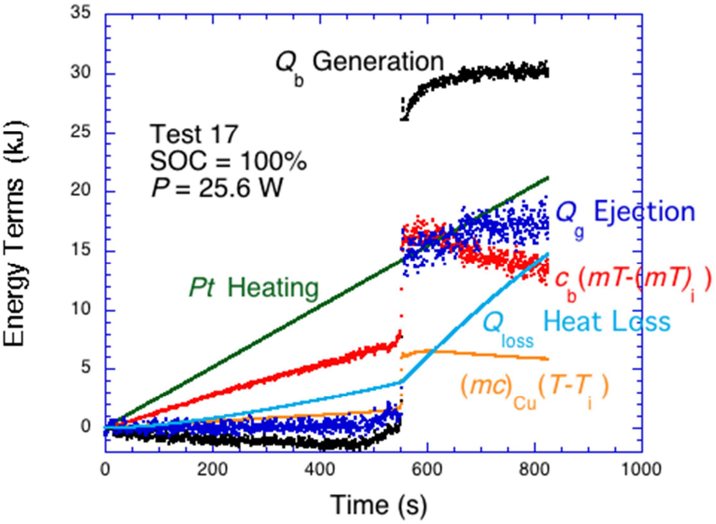

Fig. 9. Battery energy terms over time.

OVERALL RESULTS DEPENDENCE ON SOC AND HEATING POWER

About 25 tests were made with the same battery to assess the effects of the heating power the SOC. It might be expected that energy in runaway would be related to the electrical energy stored, and that the heating power should affect the time to runaway.

EFFECT OF HEATING POWER

In this series the battery SOC was maintained at 80% and the heating power varied from about 10 to 74 W for the duration of each test. The heating power reduces the time for runaway, as the safety vent operation and for the second venting at thermal runaway both decrease with heating (Fig. 10). In the configuration of the battery in the calorimeter, all heating powers were able to initiate runaway. The duration of the runaway event varied from 3 to 12 s without a definite trend with the heating power.

Although the times for venting and runaway varied significantly, the associated temperatures only varied slightly. Figure 11 shows these slight trends where the trigger temperature for runaway is about 220 to 300 ºC. During runaway the temperatures rise to over 750 ºC in 3 to 12 s. This rapid rise is indicative of the battery hazard in thermal runaway. Figure 12 shows the mass loss fractions of the battery after the first safety vent and the runaway vent occur. The mass loss fractions are not significantly dependent on the heat power. About 10% of the original mass is ejected during the safety venting and up to 40% is lost after runaway. This indicates that more hot stuff is ejected following runaway, and much of this is combustible.

Figure 13 shows a slight effect of heating power on the internal energy and on the ejected energy.

The former is about 30 to 35 kJ for this 80% SOC and the latter is about 10 to 18 kJ. Hence heating power significantly effects the time for venting and runaway, but not significantly the vent and runaway temperatures, and mass ejected and energy produced.

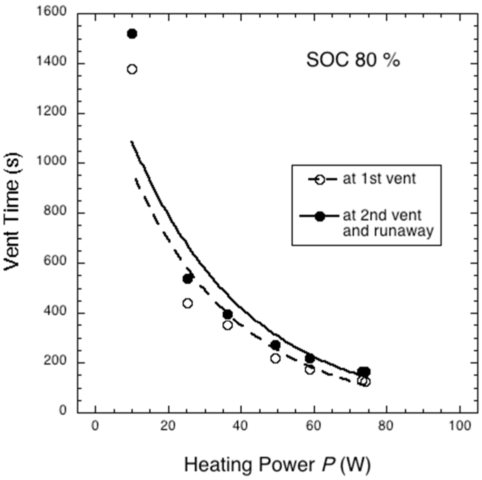

Fig. 10. Vent times as a function of heating.

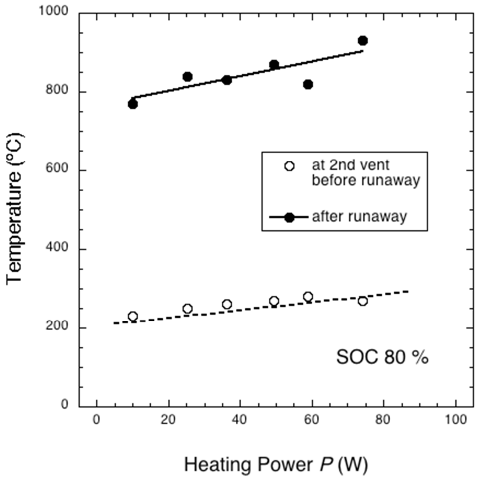

Fig. 11. Temperature at onset and after runaway.

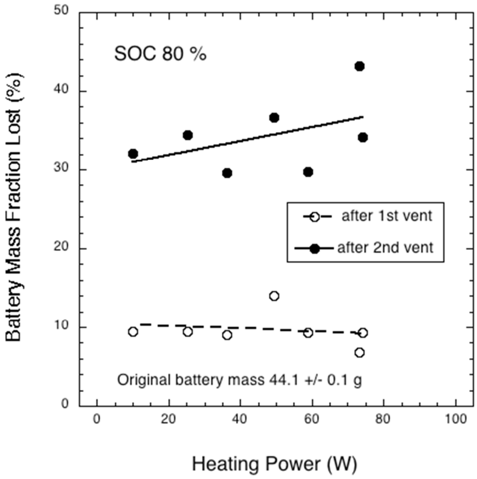

Fig. 12. Battery mass lost at venting.

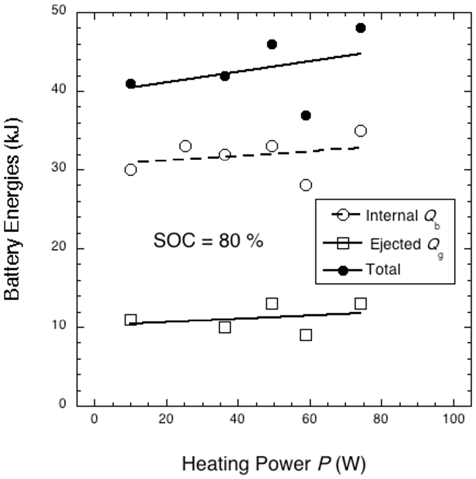

Fig. 13. Battery runaway energies vs heating rate.

EFFECT OF STATE OF CHARGE

The effect of SOC is now examined. Here the heating power is essentially constant for all the tests at about 25±2 W. Figure 14 shows the times to safety vent (1st) and runaway (2nd) are nearly invariant with SOC. The temperatures at of the 1st vent and the onset runaway are also invariant with SOC, but the final temperature of the battery increases with the SOC (Fig. 15). The 1st vent temperature is indicative of the designed pressure relief vent configuration, and is due solely to the heating power. The 2nd vent temperature is indicative of the onset of thermal runaway that depends on the battery and its heat loss environment. The temperature after runaway depends on the internal energy remaining in the battery and its ejected energy.

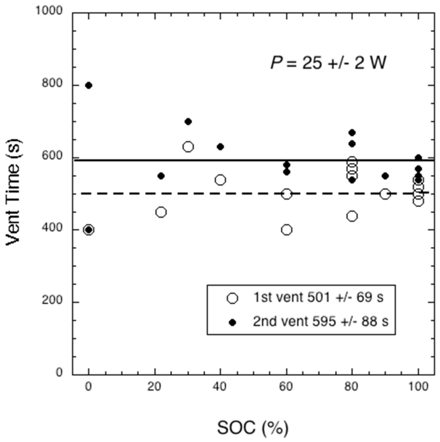

Fig. 14. Vent times vs SOC.

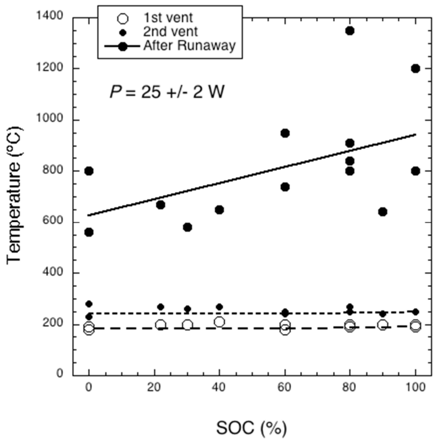

Fig. 15. Temperature vs SOC.

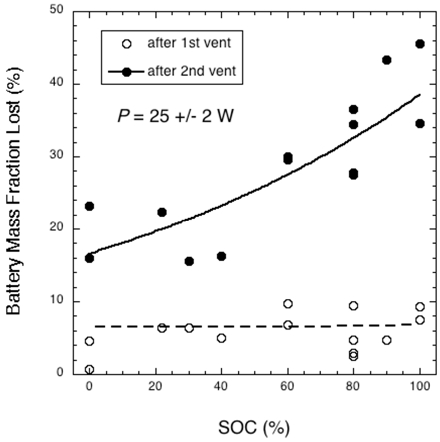

Fig. 16. Battery mass vs SOC.

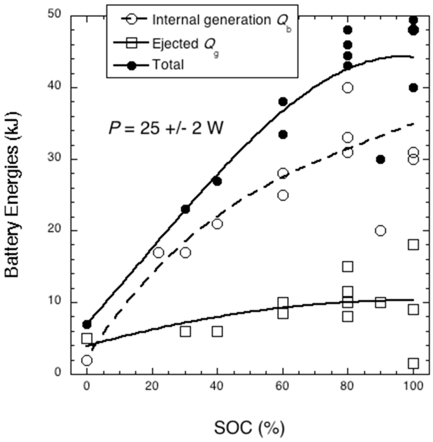

Fig. 17. Battery energies vs SOC.

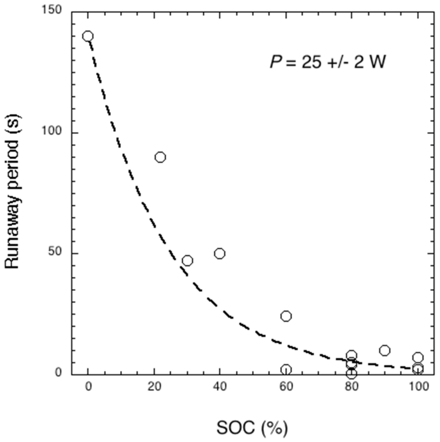

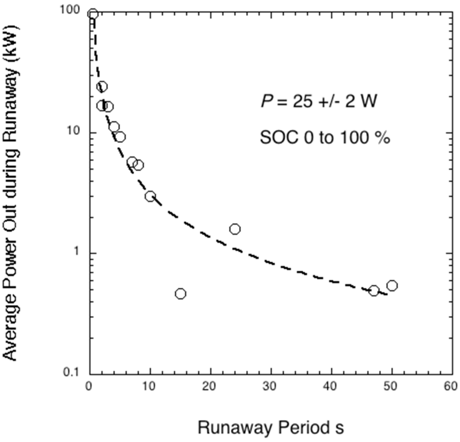

Fig. 18. Runaway time period vs SOC. **Fig. 19.** Average runaway power vs runaway period.

Figures 16 and 17 show that, at runaway, the mass ejected and the energies released (internal and ejected) are directly related to the SOC. If runaway is perceived as an internal short circuit, then a portion of the original battery energy would be represented as resistance heating. As the remaining portion of the energy is due to decomposition dependent on temperature then it too will increase with SOC as Fig. 15 shows the temperature after runaway increases with SOC. As the mass ejected increases after runaway, so does the combustion potential hazard of these gases.

Here the "runaway period" is defined as the time increment from just after the onset of runaway to just before the end of runaway as indicated by battery temperature. The runaway period decreases dramatically with SOC – from nearly 100 s at 20% to as low as 0.5 s at 80% at which the runaway temperature nearly reached 1400 ºC (Figs. 15 and 18). The average runaway power in this period can be computed from the total energy released. Figure 19 shows how this varies with the runaway period. Nearly 100 kW can be released in ½ second!

DISCUSSION OF RESULTS

For this thermally induced runaway in a battery, the SOC has a strong dependence on the battery hazard. Studies have also found this increase in hazard with SOC for other Li-ion batteries [8-12]. Figure 20 shows a comparison of the current results for the same battery with Liu et al [10], along with their combustion energy measured in the Cone [13]. Similar decreases in combustion energy at high SOC were also noted for other batteries [12]. The heat of combustion of the ejected gases was found to range from about 1 to 18 kJ/g for various batteries [12].

The accuracy of the current results can be tested by a technique developed to measure the overall energy [8] that used an Oxygen Bomb apparatus but with an atmosphere of nitrogen. A comparison of their results with the total energy measured here for the same battery is shown in Fig. 20. Recall that a weakness of the current method is the uncertainty of the specific heat of the material ejected, and no consideration in the analysis for melting. The "Nitrogen Bomb" is more accurate in capturing the total energy released, especially above 80% SOC. The total energy is approximately 2 times higher than the corresponding rated energy at the SOC. Also the variation in the results for a given SOC could be attributed to the chaotic nature of runaway.

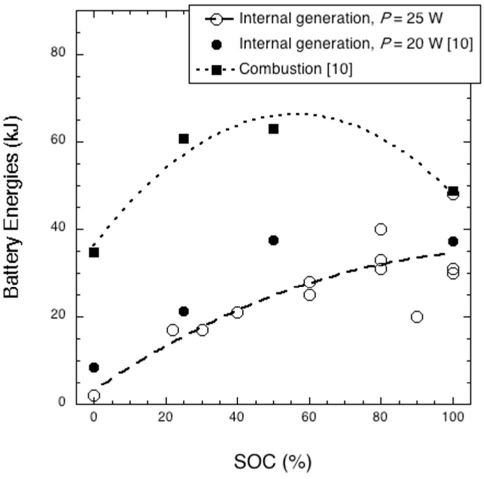

Fig. 20. Current method with Liu et al [10].

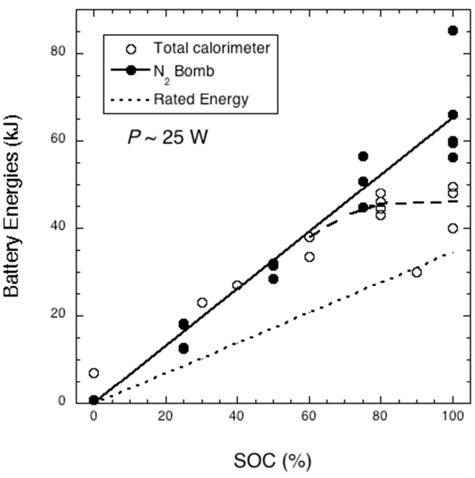

Fig. 21. Current method with nitrogen bomb [8].

CONCLUSIONS

The hazard of a Li-ion battery is shown to increase with the SOC. The hazard as measured here is composed of the sudden release of energy to produce a very hot battery and the ejection of hot material containing combustibles.

ACKNOWLEDGEMENTS

This work was supported by the FAA Technical Center, where the experimental support of Sean Crowley was essential, and discussions with Richard Walters and Richard Lyon were invaluable.

REFERENCES

[1] H. Webster, Flammability Assessment of Bulk-Packed, Rechargeable Lithium-Ion Cells in Transport Category Aircraft, Report No. DOT/FAA/AR-06/38, Federal Aviation Administration, 2006.

[2] H. Webster, Fire Protection for the Shipment of Lithium Batteries in Aircraft Cargo Compartments, Report No. DOT/FAA/AR-10/31, Federal Aviation Administration, 2010.

[3] C. Mikolajczak, M. Kahn, K. White, R.T. Long, Lithium-ion Batteries Hazard and Use Assessment, Report No. 1100034.000/A0F0/0711/CM01, The Fire Protection Research Foundation, 2011.

[4] D.H. Doughty, P.C. Butler, R.G. Jungst, E.P. Roth, Lithium Battery Thermal Models, J. Power Sources 110 (2002) 357-363.

[5] R. Spotnitz, J. Franklin, Abuse Behavior of High-power, Lithium-ion Cells, J. Power Sources 113 (2003) 81-100.

[6] Q. Wang, P. Ping, X. Zhao, G. Chu, J. Sun, C. Chen, Thermal runaway caused fire and explosion of lithium ion battery, J. Power Sources 208 (2012) 210–224.

[7] E.P. Roth, D.H. Doughty, Thermal Abuse of High-power 18650 Li-ion Cells, J. Power Sources 128 (2004) 308-318.

[8] R.N. Walters, R.E. Lyon, Measuring Energy Release of Lithium-ion Battery Failure using a Bomb Calorimeter, Report No. DOT/FAA/TC-TN16/22, Federal Aviation Administration, 2016.

[9] R.E. Lyon, R.N. Walters, Energy Release by Rechargeable Lithium-Ion Batteries in Thermal Runaway, Report No. DOT/FAA/TC-TN15/34, Federal Aviation Administration, 2016.

[10] X. Liu, Z. Wu, S.I. Stoliarov, M. Denlinger, A. Masia, and K. Snyder, Heat Release Rate During Thermally-Induced Failure of a Litium Ion Battery: Impact of Cathode Composition, Fire Saf. J., 85 (2016) 10-22.

[11] A.O. Said, C. Lee, X. Liu, Z. Wu, S.I. Stoliarov, Simultaneous Measurement of Multiple Thermal Hazards Associated with a Failure of Prismatic Lithium Ion Batteries, Combustion, Proc. Combust. Inst. 37 (2018) 4173-4180.

[12] J.G. Quintiere, S. Crowley, R.N. Walters, R.E. Lyon, D. Blake, Fire Hazards of Lithium Batteries, DOT/FAA/TC-TN15/17, Federal Aviation Admin. William J. Hughes Technical Center, Atlantic City Int. Airport, NJ 08405, February 2016.

[13] ASTM E7354-04a, Standard Test Method for Heat and Visible Smoke Release Rates for Materials and Products Using an Oxygen Consumption Calorimeter, ASTM International, West Conshohocken, 2004.

[14] J.G. Quintiere, Fundamentals of Fire Phenomena, John Wiley and Sons, Ltd., Chichester, 2006.

Fire Behaviour of NMC Li-ion Battery Cells

Russo P.[1, *], Longobardo G.[2], Mazzaro M.[2], Di Bari C.[3], Cancelliere P.[2]

[1] *Sapienza University of Rome, Department Chemical Engineering Materials Environment, Rome, Italy*
[2] *Italian National Fire Rescue and Service, DCPST, Rome, Italy*
[3] *ENEA DTE-PCU-STMA, CR Casaccia, Rome, Italy*
**Corresponding author's email: paola.russo@uniroma1.it*

ABSTRACT

The main features of Lithium-ion (Li-ion) batteries are high energy and power density, which make this storage technology suitable for portable electronics, power tools, and hybrid/full electric vehicles. Moreover, during conditions that lead to failure, Li-ion battery cells could undergo into a process called thermal runaway, which has resulted in numerous fire accidents. Thermal runaway implies a rapid increase in battery cells temperature, accompanied by the release of flammable gases. These flammable gases could be easily ignited by the battery's high temperature, resulting in a fire. In addition, the combustion of these gases when venting from the battery poses another safety concern: the accumulation and potential explosion of the gases themselves. Thermal runaway may also be responsible for mechanical effects such as the projection of fragments as well as the release of toxic gases and vapours. This study reports and discusses the results of fire tests performed on single Li-ion cells. Lithium Nickel Manganese Cobalt oxides cells from Panasonic were used in the tests. The tests were carried out in a cone calorimeter changing the state of charge of the cells and the radiant power of the conical heater. In order to assess the ignition and combustion characteristics, ignition time, mass loss, heat release rate and surface cell temperature were measured and recorded. The volatile organic compounds released during the tests were also measured by a photoionization detector. Since the appropriate fire prevention and protection measures have not yet been developed, this paper investigates the effects of thermal abuse conditions on Li-ion cells of battery systems for hybrid/full electric vehicles, in order to develop safe instructions and procedures for a rescue team that is called to respond to accidents involving these vehicles.

KEYWORDS: Li-ion battery, thermal runaway, fire, explosion, cone calorimeter, heat release rate.

INTRODUCTION

Li-ion batteries are characterised by high energy and high power density, which make this technology the most suitable choice for feeding portable electronics, power tools, and hybrid/full electric vehicles [1]. The electrical work performed by Li-ion cells consists of exchanging lithium ions through electrolytes between positive and negative electrodes separated by ion-permeable polymer membranes. Lithium salts dissolved in high purity linear and cyclic organic carbonates are the typical electrolytes used in Li-ion cells and these materials are combustible [2]. In normal use conditions, electrons flow through the terminals and lithium ions pass from the anode to the cathode through the electrolyte in a process that is quasi-reversible, with no significant changes in the chemical structure of the cell components. In case of a Li-ion cell failure due to an internal short circuit, the generated power rapidly surpasses the cell external heat losses, thus the polymer separator and the electrodes melt due to the temperature increase. Subsequently, electrolytes mix, then react and thermally decompose. The thermal decomposition produces both flammable gases

Proceedings of the Ninth International Seminar on Fire and Explosion Hazards (ISFEH9), pp. 881-890
Edited by Snegirev A., Liu N.A., Tamanini F., Bradley D., Molkov V., and Chaumeix N.
Published by Saint-Petersburg Polytechnic University Press
ISBN: 978-5-7422-6498-9 DOI: 10.18720/spbpu/2/k19-126

and oxidants that are generated within the cell, making the ignition and the combustion of batteries quite different compared to the mechanisms of ordinary hydrocarbon fuels, since the fuel is not exposed and no external oxygen is required. The Li-ion battery failure mechanism that could lead to a fire or an explosion (or both) is called thermal runaway [3].

Besides the related thermal hazard (fires, explosions), thermal runaway may also be responsible for mechanical effects such as projection of fragments as well as toxic gases and vapours [3]. The Li-ion cell gases formed during the thermal runaway can establish a variety of exhaust gas concentrations and components. However, the majority of the Li-ion venting gases components is made of carbon, hydrogen, and oxygen. As the temperature increases within a lithium battery cell, the organic compound begins to react with other components of the cell. The reactions lead to the increase in cell temperature and the production of flammable hydrocarbon and hydrogen gases. Thermal cracking, an additional possible mechanism for the conversion of organic compounds into smaller hydrocarbon molecules, occurs when sufficient heat is applied [5].

A special regulation has been issued by the International Air Transport Association Dangerous Goods Regulations for Li-ion battery transport [6]. Moreover, following some major air accident during the transportation of Li-ion batteries, a series of real scale tests was conducted by US Federal Aviation Administration to determine the flammability characteristics of primary lithium batteries, as well as and the dangers associated with shipping them in bulk on cargo aircrafts [7].

Li-ion batteries can be non-rechargeable – also called primary type batteries – or rechargeable. Primary batteries are practical for applications that draw occasional power, but they can get expensive when in continuous use. They are generally more hazardous than secondary ones. Among the rechargeable families, the most spread Li-ion batteries are based on Lithium Cobalt Oxide (LCO), Lithium-Iron Phosphate (LFP), Lithium Manganese Oxide (LMO) and Lithium Nickel Manganese Cobalt Oxide (NMC).

LCO was the first material used for the cathodes in secondary cells. Its major limitations are the high cost, low thermal stability, and fast capacity wane when at high current rates or during deep cycling. Low thermal stability refers to the release of significant amounts of energy, when the cathode break down occurs. The onset of chemical breakdown is at a relatively low temperature (about 200°C). LCO has the lowest thermal stability of any commercial cathode material [8]. Among them, LFP cathodes do not break down with the release of oxygen until much higher temperatures (400-500°C) releasing much less energy [9]. Alternatively, Lithium-polymer batteries have evolved from Li-ion batteries. Lithium-polymer differs from other battery systems in the type of electrolyte used. Instead of using a liquid lithium-salt electrolyte (such as $LiPF_6$) held in an organic solvent, the battery uses a solid polymer electrolyte such as polyethylene oxide, polyacrylonitrile, polymethyl methacrylate or polyvinylidene fluoride.

Recent studies on the safety issues of Li-ion batteries have focused on chemical, electrical and environmental features related to the components materials and battery parts: separators, electrolytes, additives, electrodes [10-13].

Large scale fire tests were also conducted to determine fire protection guidance for warehouse storage of cartoned Li-ion batteries [14]. The fire tests conducted utilizing an external fire as the ignition source showed a rapid fire growth of the carton packaging, causing heating of the stored Li-ion batteries. It could result in the potential involvement of many Li-ion batteries before a sprinkler system operates.

In this study, fire tests were performed on single Li-ion cells. Lithium NMC cells from Panasonic (NCR 18650 BM) were used in the tests. They were carried out in a cone calorimeter by varying the state of charge (SoC) of the cells and the radiant power of the conical heater. The volatile organic compounds (VOC) released during the tests were measured by a photo ionization detector (PID).

The heat flux used in the cone calorimeter simulates the conditions that can occur when a cell is involved in a fire, i.e. when a EV or PHEV catches on fire. The aim of this paper is to investigate the effects of thermal abuse conditions on Li-ion cells of battery systems for hybrid/full electric vehicles, in order to develop safe instructions and procedures for a rescue team in case of accidents.

EXPERIMENTAL SET-UP AND PROCEDURES

The Heat Release Rate (HRR) is a critical parameter for the evaluation of compartment fire growth [15]. The measurement of the HRR is used to quantify the test specimen's ability to ignite and contribute to the fire [16]. It is based on the observation that, generally, the net heat of combustion of a material is directly related to the quantity of oxygen required for its combustion.

During the test, specimens are exposed to ambient air conditions, while being subjected to a certain value of radiant heat (generally 10 to 100 kW/m^2) in the presence of a spark ignition source. The oxygen concentration changes and exhaust gas flow rate are monitored and, from these data, the HRR is calculated. The ignition time and mass-loss rate are also measured.

In the case of batteries the electrochemical energy is released inside the battery for different reasons: a manufacturing defect, mechanical abuse, heating in a fire. The heat flux used in the cone calorimeter simulates the conditions that can occur when a cell is involved in a fire, i.e. when a EV or PHEV catches on fire. Such technique has been directly applied to study the energy release characteristics, during combustion, of energetic material like Li-ion cells. Using these tests, thermal hazard parameters of cells with different chemistries, sizes and state of charge have been compared directly [17-19].

In this study the HRR was calculated following the calculation method proposed by ISO 5660-1:2015 [16]. The methodology to establish the HRR is based on Oxygen Consumption Calorimetry (OC). It was originally based on the observation that HRR is proportional to oxygen consumption during the combustion of most organic liquid and gaseous fuels [20]. The energy released per mass unit of O_2 consumed for a given fuel is assumed constant (13.1 kJ/g O_2). Recently, it was used for combustion analysis conducted for major single organic solvents and their mixtures used in lithium ion battery technology [12]. This methodology allows estimating the HRR directly from measurements; the knowledge of the material chemical composition or the combustion chemistry is not necessary and the HRR can be estimated also for composite and non-homogeneous materials, like Li-ion cell batteries.

Recently, some authors claimed the OC calorimetry is inappropriate for determining HRRs from lithium ion cell venting and combustion, because significant percentages of CO_2 are formed through pyrolysis process rather than combustion [13]. In order to figure out the validity of HRR data obtained by the cone calorimeter for Li-ion cells, the HRR was calculated by employing thermochemistry (TC) technique also, and comparisons of the two HRR results were made [17]. Heat release rate results of the three carbonate solvent mixtures obtained by these two separate methods are found to be in good agreement. Moreover, Ribiere et al. [19] determined total combustion heats and its kinetic of production as a function of the cell state of charge using the method of O_2 consumption. The resulting combustion heat is revealed to be consistent with cumulated contribution values pertaining to each organic part of the cell (polymers and electrolytes) as calculated from thermodynamic data. Thus, oxygen consumption calorimetry is considered to be an appropriate technique to determine the heat release in fires of lithium ion cells.

THE CONE CALORIMETER

The Cone Calorimeter is a suitable tool to measure and quantify critical information such as the heat release rate and total energy released from the combustion of a material. The main components of the cone calorimeter are depicted in Fig. 1.

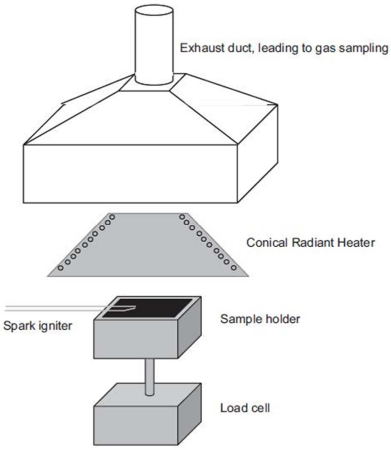

Fig. 1. Main components of the cone calorimeter.

Fig. 2. A picture of a single cell Panasonic NCR 18650 BM.

A horizontal specimen, is exposed to a conical radiator pre-set to 15-50 kW/m^2 in these tests mounted beneath an instrumented hood and duct. A spark ignition is used and the specimen is mounted on a load cell in order to get the mass loss during combustion. The O_2 concentration is determined. The fire model of the cone calorimeter always appears to be well ventilated. The cone calorimeter and test procedure are describe in details in the international standard ISO 5660-1:2015 [16].

LI-ION CELL SPECIMENS DESCRIPTION

The cells used for the tests are the Panasonic Li-ion NMC named NCR 18650 BM. According to the producer datasheet, these NCR 18650 BM Li-ion cells have high energy and voltage. They also show long stable power with flat discharge voltage, therefore they are ideal for application such us portable communication, portable computing, robotics, and electric vehicle, e.g. Tesla. The specification of the NCR 18650 BM batteries is reported in Table 1.

Table 1. Panasonic NCR 18650 BM specifications

Rated Capacity[a]	Min. 2700 mAh
Capacity[b]	Min 2570 type. 2900 mAh
Nominal voltage	3.6 V
Charging	CC-CV[d], Std. 1925 mA 4.20 V, 3.0 hrs
Temperature	Charge 0 to 45°C. Discharge -20 to +60 °C. Storage -20 to + 50 °C
Energy density	Volumetric 577 Wh/l. Gravimetric 214 Wh/kg
Length	65 mm
Width	18 mm

[a]At 20°C; [b]At 25°C; [c]Based on bare cell dimensions.
[a]CC= constant current; CV=costant voltage

The test specimens have a positive electrode made of lithium nickel manganese cobalt oxide and a negative carbon electrode. The electrolyte is organic and mainly composed of alkyl carbonate: a mixture of ethylene carbonate (EC), ethyl methyl carbonate (EMC), or diethyl carbonate (DEC). The cell enclosure is made of plastic. Figure 2 shows a picture of a single cell.

TEST PROCEDURE

The cells were charged at a constant current of 12 A with a maximum limit voltage of 4.2 V to obtain 100% of SoC or a maximum limit voltage of 3.7 V to obtain 50% of SoC. The tests were carried out in a cone calorimeter by varying the SoC of the cells and the radiant power of the conical heater. HRR and surface temperature were recorded during the test as well as VOC released, which were measured by a photo ionization detector (PID). The VOC are expressed as ethyl methyl carbonate concentration (ppm). Each specimen was weighed before and after each test to determine the total mass loss. 10 cells at a given SoC were tested by varying the radiant power from 15 to 50 kW. The tests were also recorded by a videocamera. Table 2 contains the experimental test conditions and the measured parameters.

Table 2. Experimental test conditions and measured parameters

Test Id	SoC (%)	Radiant power (kW/m^2)	HRR max (kW/cell)	T max (°C)	Gas venting time (s)	Explosion time (s)	Mass loss (g)	Total Energy (kJ/cell)
1	100	15	0.9	367	580	810	28.08	184
2	100	25	1.3	703	300	385	24.27	132
3	100	35	1.1	328	274	315	34.14	65
4	100	50	0.8	497	171	226	20.89	28
5	100	35	1.1	735	236	294	43.53	72
6	100	50	11 (0.9)	440	240	272	20.24	304
7	50	25	0.1	726	470	580	10.73	15
8	50	35	1.2	367	246	324	17.33	62
9	50	50	1.0	643	204	230	43.97	40
10	0	50	1.3	487	138	196	8.31	33

The gas venting time was defined by a clearly audible sound, immediately followed by an appearance of aerosol jets emanating from the safety vent ports. The explosion time is the time when the failure of cell was observed. The error of HRR values was calculated to be about 20%.

Figure 3 (a) shows the specimens under constant current charge while Fig. 3 (b) depicts a cell before and after cone calorimeter test.

RESULTS AND DISCUSSION

The tests showed that fire behaviour of cells can be characterized in three major phases: i) the onset of thermal runaway; ii) the venting and accelerating heating with flame and/or smoke; iii) the cell failure with flame. These phases are shown in Fig. 4, as an example, for 50% SoC cell during test at 35 kW/m^2. The results of the tests reported in Table 2 show that the venting time and the explosion time decrease as the radiant power increases up to 35 kW/m^2 than remain almost constant. On the contrary, the HRR increases as the radiant power increases.

a) b)

Fig. 3. Experimental setup: (a) specimens under charge; (b) specimen before and after cone calolimeter test.

(a) 246 s; venting (b) 250 s; flame

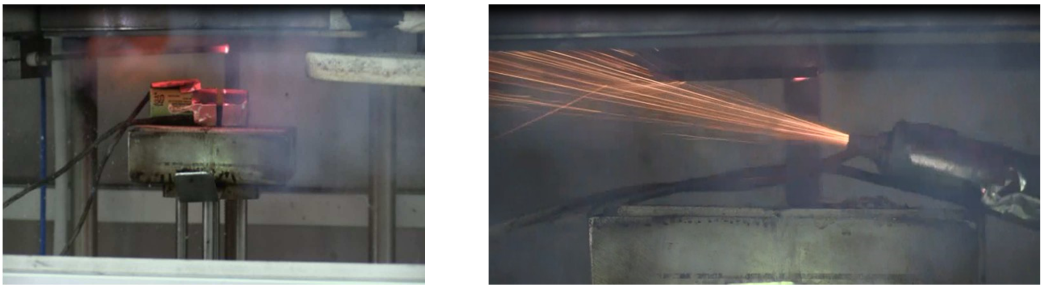

(c) 322s; smoke (d) 324s; cell failure

Fig. 4. Stages of cell thermal runaway of NMC cell at SoC 50% during test at 35 kW/m^2.

The HRR data for single NMC cells as a function of SoC are shown in Fig. 5 for tests at 50 kW/m^2. The dependence on SoC for the onset of heat release is evident. The cell tested at 100% SoC shows a first very rapid HRR onset at 80 s, and a secondary peak when the failure of cell occurs (280 s). This first peak (11 kW) was observed in correspondence of the venting of gases from the cell and their subsequent ignition, the second when the cell failure occurs (0.9 kW). On the contrary the 50 and 0% SoC samples have a similar behaviour with a slower HRR onset and a prolonged period of heat evolution when the cell fails.

In correspondence of the HRR peak due to the cell failure, a peak of VOC concentration is observed, which decreases as the SoC of cell increases. The VOC release is an indication of the incomplete combustion of the cell materials, which is higher as the energetic content of the cell decreases. It can be also argued that for 100% SoC cell the first HRR peak is due to the combustion of the vented electrolyte vapours or flammable gases obtained by the decomposition of the electrolyte and its reaction with other components of the cells.

The results relevant to the tests at 35 kW/m^2 are reported in Fig. 6. In this case one peak of HRR is observed for 50% SoC cell and two peaks for that at 100% SoC. Moreover, the first peak of 100% SoC cell occurs earlier than that at 50% SoC, and is accompanied by a smaller quantity of VOC released.

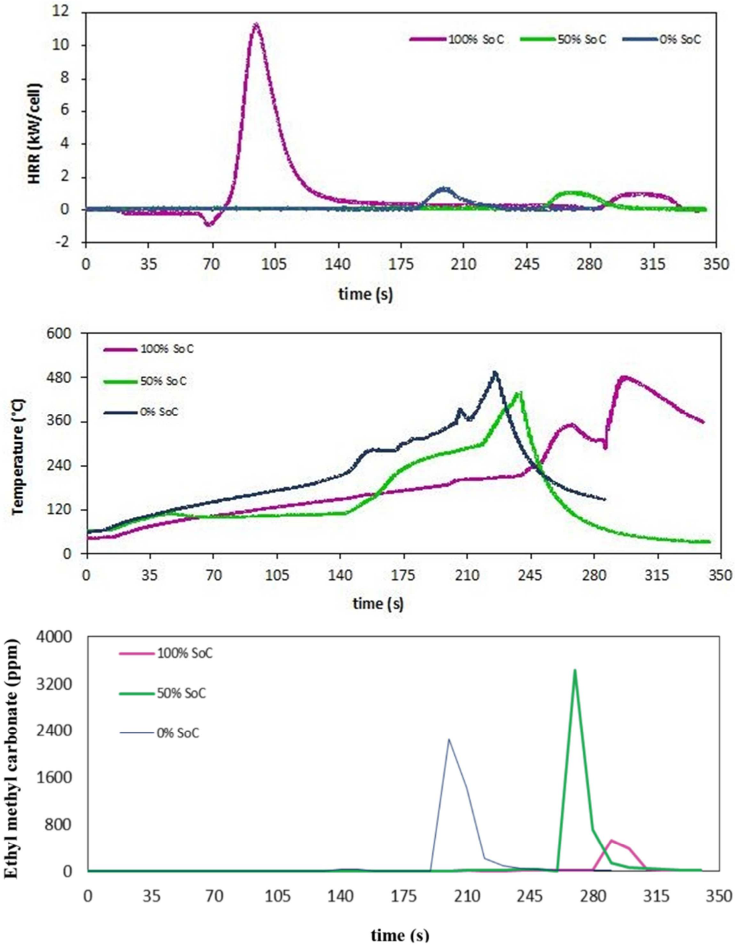

Fig. 5. HRR, surface temperature and VOC concentration (ppm) during tests at 50 kW/m^2.

Finally, comparing the results of tests relevant to cells at the same SoC (50%), but heated up by different power (35 and 50 kW/m^2), the higher radiant power determines a faster increase of temperature cell and an higher HRR, with higher release of VOC (Fig. 7).

The HRR profile integration allows the estimation of the overall dissipated combustion heat. The calculated values were reported in Table 2, corresponding to a maximum total energy released of 6.4 kJ/g of cell. The SOC has the most influence on the total energy released by a cell decreasing from 300 kJ/cell to 60 kJ/cell as SOC decreased from 100% to 50%. The effective heat of combustion of the cell contents is then calculated dividing the total energy release by the weight loss. The values ranged from 1–15 kJ/g.

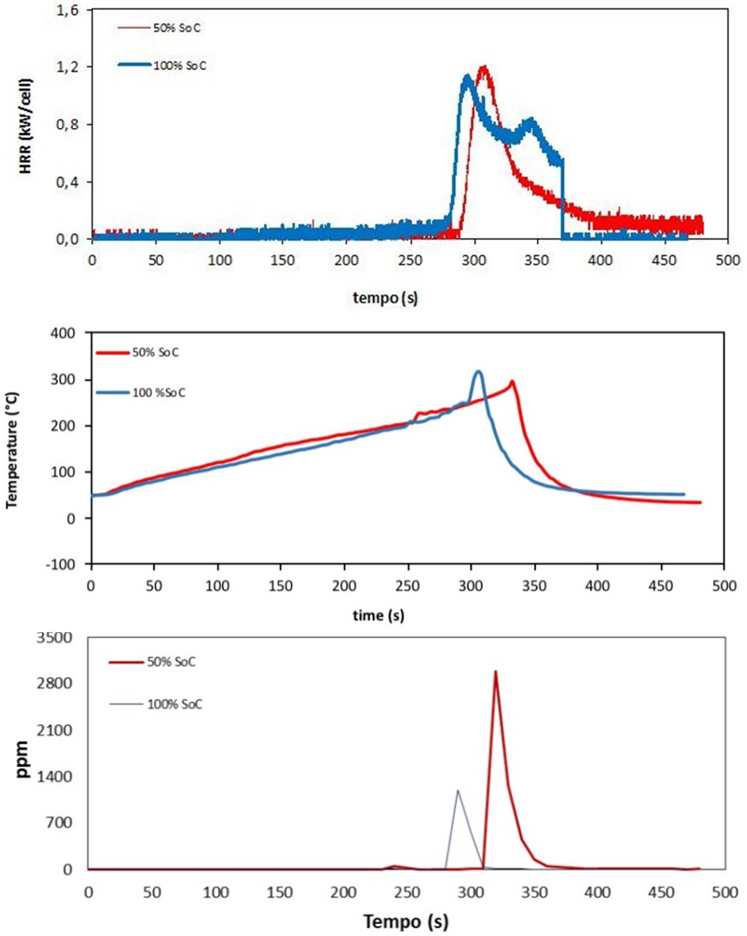

Fig. 6. HRR, surface temperature and VOC concentration (ppm) during tests at 35 kW/m^2.

CONCLUSIONS

This study reports results of a series of fire tests of Li-ion cells performed in a Cone Calorimeter test rig. The tests were conducted varying the SoC of the cell specimens and the radiant power. The tests showed that fire behaviour of cell can be characterized in three major phases: i) the onset of thermal runaway; ii) the venting and accelerating heating with flame and/or smoke; iii) the cell failure with flame. At 100% SoC these phases occur at shorter times and the peak of the HRR and the total energy released are higher compared to the cells with a 50% SoC. The observed behaviour as a function of SoC implies that the onset of the thermal event is related to the electric Li-ion cell energy content which provides the activation energy needed to initiate the thermal runaway or the combustion of electrolyte.

The maximum overall dissipated combustion heat was calculated equal to 6.4 kJ/g of cell, while the effective heat of combustion of the cell contents is in the range 1–15 kJ/g. These values are in agreement with those reported in literature for secondary cells of different chemistries and geometries. It was found that the combustion energy ranged in approximately 1–4 kJ/g of original battery and the effective heat of the combustion ranged in approximately 2–25 kJ/g [18].

The heat flux used in the cone calorimeter simulates the conditions that can occur when a cell is involved in a fire. Therefore, data generated from these tests can be used in the design and implementation of fire risk mitigation strategies for battery modules and packs that are used in EVs and PHEVs. This information can also be used in developing safe practices and priorities when responding to accidents involving E-vehicles.

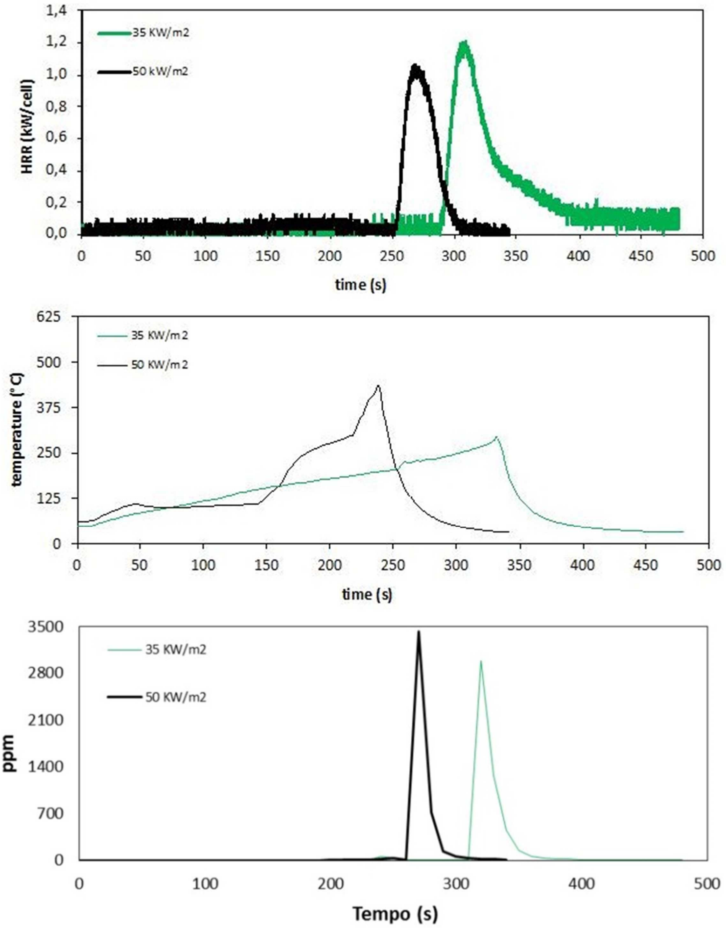

Fig. 7. HRR, surface temperature and VOC concentration (ppm) during tests at 50% SoC.

AKNOWLEDGEMENTS

This work has been financed by the Italian Ministry of Economic Development, RSE PAR 2017 in the frame of a Cooperation Agreement between ENEA and Sapienza Università di Roma.

REFERENCES

[1] J.M. Tarascon, M. Armand, Issues and challenges facing rechargeable lithium batteries, Nature 414 (2001) 359-367.

[2] Lithium Batteries: Science and Technology, G.A. Nazri and G. Pistoia, Eds., Springer Publishers, New York, 2003.

[3] Q. Wang, P. Ping, X. Zhao, G. Chu, J. Sun, C. Chen, Thermal runaway caused fire and explosion of lithium ion battery, J. Power Sources 208 (2012) 210–224.

[4] FAA. Lithium batteries & Lithium battery-powered devices. www.faa.gov/about/office_org/headquarters_offices/ash/ash_programs/hazmat/aircarrier_info/media/battery_incident_chart.pdf (accessed 10 June 2018).

[5] T. Maloney, Lithium Battery Thermal Runaway Vent Gas Analysis, Report No. DOT/FAA/TC-15/59, U.S. Department of Transportation William J. Hughes Technical Center Aviation Research Division, 2016.

[6] International Air Transport Association, Lithium Battery Guidance Document, Revised for the 2014 Regulations, 2013.

[7] H. Webster, Flammability Assessment of Bulk-Packed, Report No. DOT/FAA/AR-04/26, Federal Aviation Administration, US Department of Transportation, 2004.

[8] N. Nitta, F. Wu, J.T. Lee, G. Yushin, Li-ion battery materials: present and future, Mater. Today 18 (2015) 252-264.

[9] B. Wu, Y. Ren, N. Li, LiFePO4 Cathode Material, In: S. Soylu (ed.), Electric Vehicles The Benefits and Barriers, InTech Publisher, Shangai, 2011, pp. 199-216. Available from: http://www.intechopen.com/books/electric-vehicles-the-benefits-and-barriers/lifepo4-cathode-material

[10] M.D. Farrington, Safety of lithium batteries in transportation, J. Power Sources 96 (2001) 260–265.

[11] D. Lisbona, T. Snee, A review of hazards associated with primary lithium and lithium-ion batteries, Process. Saf. Environ. 89 (2011) 434–442 4.

[12] G.G. Eshetu, S. Grugeon, S. Laruelle, S. Boyanov, A Lecocq, J.P. Bertrand, G. Marlair, In-depth safety-focused analysis of solvents used in electrolytes for large scale lithium ion batteries, Phys. Chem. Chem. Phys. 15 (2013) 9145-9155.

[13] W. Zhang, X. Chen, Q. Chen, C. Ding, J. Liu, M. Chen, J. Wang, Combustion calorimetry of carbonate electrolytes used in lithium ion batteries, J. Fire Sciences 33 (2015) 22–36.

[14] B. Ditch, J. de Vries, Flammability Characterization of Lithium-ion Batteries in Bulk Storage, FM Global Report, 2013.

[15] H. Biteau, T. Steinhaus, C. Schemel, A. Simeoni, G. Marlair, N. Bal, J.L. Torero, Calculation Methods for the Heat Release Rate of Materials of Unknown Composition, Fire Saf. Sci. 9 (2008) 1165-1176.

[16] ISO 5660-1:2015 Reaction to fire tests - Heat release, smoke production and mass loss rate - Part 1: Heat release rate (cone calorimeter method) and smoke production rate (dynamic measurement).

[17] Y. Fu, S. Lu, K. Li, C. Liu, X. Cheng, H. Zhang, An experimental study on burning behaviors of 18650 lithium ion batteries using a cone calorimeter, J Power Sources 273 (2015) 216-222.

[18] J.G. Quintiere, S.B. Crowley, R.N. Walters, R.E. Lyon, D. Blake, Fire Hazards of Lithium Batteries, Report No. DOT/FAA/TC-TN15/17, U.S. Department of Transportation Federal Aviation Administration, 2016.

[19] P. Ribière, S. Grugeon, M. Morcrette, S. Boyanov, S. Laruelle, G. Marlair, Investigation on the fire-induced hazards of Li-ion battery cells by fire calorimetry, Energy Environ. Sci. 5 (2012) 5271-5280.

[20] W. Thornton, The Relation of Oxygen to the Heat of Combustion of Organic Compounds, Phil. Mag. 33 (1917) 196 – 203.

Thermal Explosion Hazards Investigation on 18650 Lithium-ion Battery Using Extend Volume Accelerating Rate Calorimeter

Zhao C.P.[1], **Sun J.H.**[1], **Wang Q.S.**[1,2,*]

[1] *State Key Laboratory of Fire Science, University of Science and Technology of China, Hefei, China*
[2] *Key Laboratory of Materials for Energy Conversion, Chinese Academy of Sciences (CAS), University of Science and Technology of China, China*
**Corresponding author's email: pinew@ustc.edu.cn*

ABSTRACT

With the increase of lithium-ion batteries energy density and capacity, the thermal explosion is becoming a significant issue that can't be ignored. In this work, one kind of commercial 18650 lithium-ion battery with different states of charge (SOCs) and cycling times is used to evaluate the thermal explosion hazards by a ramp heating method in an extend volume accelerating rate calorimeter (EV-ARC). Some thermal characteristic parameters are selected and analyzed from the experiment trails, such as the cell surface temperature, temperature raise rate, canister internal pressure and average canister temperature. The experiment results show that the maximum surface temperature of the battery and the maximum canister internal pressure increase with the increase of SOC when the thermal explosion occurs. The thermal energy released from the battery under different SOCs during thermal explosion is calculated using the initial and the maximum temperature on the battery and the canister surface. A fully charged fresh battery can release 61.7 kJ energy when it gets into thermal explosion, which could be converted to an explosion TNT-equivalent of 5.57 g. Compared with fresh batteries, aging batteries are more prone to get into thermal explosion and the thermal explosion hazards increase.

KEYWORDS: Lithium-ion battery, EV-ARC, thermal explosion, thermal runaway.

INSTRUCTION

As a new type of clean energy, lithium-ion battery has been widely used in electric vehicles filled for its high energy density and long-life span, but thermal runaway (TR) with fire or even explosion will occur under some abuse conditions such as overheating, overcharging, crush and short circuit [1-3]. Nowadays, with the decreasing numbers of basic units in the battery pack and the increasing vehicle energy density, the new generation lithium-ion batteries would have higher energy density and specific capacity. Once the battery with higher specific energy got into thermal explosion (TE), it would certainly cause more severe damage. Hence, it is very vital to conduct the study on the TE hazards of high specific energy lithium-ion battery.

The safety behaviors of lithium-ion battery is affected by electrode materials, SOCs, cycling times, etc. [4-14]. The safety rank of cathode materials is $LiFePO_4$ (LFP) > $LiMnO_4$ (LMO) > $LiNi_xCo_yMn_zO_2$ (NCM) > $LiCoO_2$ (LCO) [4-7]. Furthermore, the charged cells are more dangerous than discharged cells [8, 9], meanwhile the cells at high SOCs would release more energy when it gets into TR [10-12]. Aging also play an important role in lithium-ion battery safety, the cell which cycled many times at specific temperatures usually has a reduced thermal stability [13], e.g. the aging cells create an additional decomposition reaction before the fresh cells under the same abuse conditions [14]. Liu et al. [11] investigated the thermally-induced failure of 18650 cells with a

Proceedings of the Ninth International Seminar on Fire and Explosion Hazards (ISFEH9), pp. 891-901
Edited by Snegirev A., Liu N.A., Tamanini F., Bradley D., Molkov V., and Chaumeix N.
Published by Saint-Petersburg Polytechnic University Press
ISBN: 978-5-7422-6498-9 DOI: 10.18720/spbpu/2/k19-22

Copper Slug Battery Calorimetry, the results showed that for LCO, LFP and NCM cells, the LCO cells released the highest energy of 37 kJ/cell at 100% SOC. Besides, the combustible materials released from failure cells would translate into another fire and/or explosion if the ventilation was poor. Lu et al. [10] also calculated the energy released by 18650 LCO cell at 4.2 V. The released energy measured by vent size packet 2 (VSP2) with a customized stainless steel canister was converted to 1.77 g TNT-equivalent. Chen et al. [9] improved the TNT-equivalent method [10] for the conversion of battery TE energy, and they found that the TNT-equivalent mass for one 18650 LCO cell at 100% SOC was 1.9 g. However, in research [9] and [10] the thermal energy absorbed by the air and canister were ignored, and these two parts of energy were also ignored in our previous work [15]. Yayathi et al. [12] analyzed the energy distributions exhibited for runaway lithium-ion batteries by extend volume accelerating rate calorimeter (EV-ARC) with a sealed canister, and the energy absorbed by the canister was 45-55% of the total energy. Christopher et al. [16], explored the influence of cell sizes on thermal runaway energetics on cells from 3 to 50 Ah, and the results showed that the normalized total heat released is relatively constant over that cell size range and the normalized heating rate increased with the increase of cell sizes.

In this paper, one kind of 18650 NCM battery was tested by the EV-ARC with a sealed canister. The total energy released form the cells was calculated and the value was converted to a TNT-equivalent. The cell surface temperature (T_{surf}) and the canister internal pressure (P_{inter}) during the whole test were recorded. The effects of SOCs and cycling times on TE hazards of sample cells were also discussed.

EXPERIMENTAL SETUP

A series of tests were carried out by the EV-ARC (THT Inc. England) [17] with a sealed stainless canister. The canister mass is 0.7 kg with a specific heat capacity of 0.5 kJ/(kg·K). There are 6 ports on the canister and the internal volume is 292 ml. One port is designed for the introduction of the thermocouple into the canister and one 1/16" port is to connect the pressure measurement line, the other 4 1/8" ports could be used for voltage monitoring wires, gas flushing, nitrogen inerting or for additional thermocouples. In our tests these four ports were tightened with plugs and the canister is initially filled with air [18]. To ensure the canister with leakage during the tests, the thermocouple port was sealed with epoxy (Araldite 2014-1) and the hole in the middle of the canister was sealed with a viton O-ring. Three thermocouples were set at different positions on the canister surface to get an average temperature.

A ramp heating method was used to induce the sample cells to get into TE. Compared with common EV-ARC tests, in this mode the "Start Temperature" value was set to 300 °C and the EV-ARC would overheat the sample until it got into TE. The advantage of this "ramp heating method" is that it can greatly reduce the duration time of the test (about 70-90 min for per test) and at the same time the TE onset temperature (T_0), the max cell surface temperature (T_{max}), the max canister internal pressure (P_{max}) and the average canister temperature (T_{avg}) could be picked up from the experiment trails. The battery explosion heat could be calculated using these data. However, the experiment results couldn't be used to estimate the exothermic onset temperature and the apparent kinetic parameters of the sample cells.

Figure 1a shows the picture of the sample cell located in the canister before tightening the lid and Fig. 1b shows the final test apparatus in the EV-ARC. In order to ensure reproducibility, at least 2 tests were conducted under each operating condition.

Figure 2 shows the picture of pre- and post-tests sample cell. The jelly roll was ejected from the can when the cell got into TE. The test sample is a commercial 18650 lithium-ion cell with 2000 mAh capacity, the cathode and anode materials are Li ($Ni_{0.5}Mn_{0.2}Co_{0.3}$) O_2 and graphite, respectively. The operating voltage range is from 2.75 V to 4.2 V. In this work, the SOCs of fresh cells were 25, 35, 50, 65, 75, 85, and 100%. And before being charged to the special SOC with a rate of 0.5 C, the fresh cells were cycled 3 times with 0.5 C at ambient temperature (25 °C). For the aging cells, they were cycled with 1 C at ambient temperature with 100, 200, 300 and 400 times and were finally fully charged with 0.5 C.

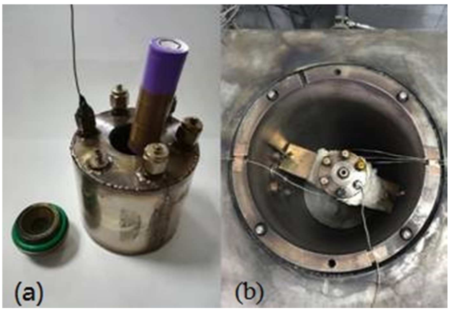

Fig. 1. The illustration of the canister (a) [15] and the final test apparatus in the EV-ARC (b).

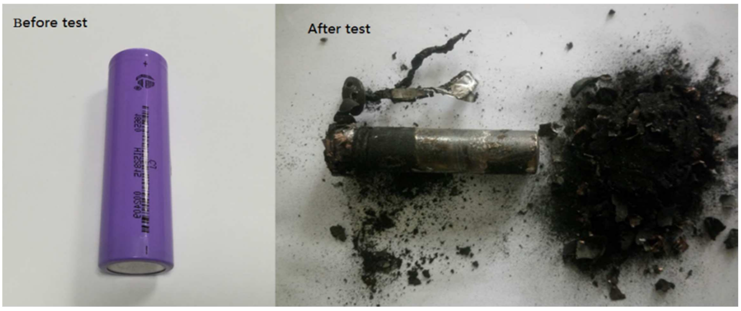

Fig. 2. The picture of the sample cells before and after the EV-ARC test. After the test the cell can ruptured and some broken electrodes ejected from the cell.

RESULTS AND DISCUSSION

The initial temperature of thermal explosion

According to Fig. 3a, the whole experimental progress could be divided into 3 stages with 2 critical temperatures (T_{vent} and T_0) [19, 20].

Stage 1: The T_{surf} and the T_{avg} rises slowly, as shown in Fig. 4. The rise rate of T_{surf} is also relatively moderate. In stage 1, the battery capacity starts to fade that is caused by the fact that lithium-ion deintercalated from anode [21, 22]. Then the solid electrolyte interface (SEI) starts to decompose. Without the protection of SEI the anode begins to react with the electrolyte to release some heat [23, 24]. When the temperature continues to get higher, the separator starts to melt, thus making some micro short circuit points appear. Although the separator melting reduces the temperature rise rate, soon an accelerating process appears because of the micro internal short circuit [25].

Stage 2: When the cell surface temperature gets to T_{vent} = 176 °C, a temperature rise rate reduce and a small pressure rise can be observed as shown in Fig. 3. At T_{vent}, the cell safety valve opens and some gas leak from the cell to reduce the cell internal pressure. In stage 2, the internal short circuit continues and the cathode begins to react with the electrolyte [2, 3]. Besides, the temperature rise rate is significantly higher than that in stage 1.

Stage 3: When the cell surface temperature gets to T_0=234 °C, the temperature growth rate increases rapidly and a significant pressure rise can be observed as shown in Fig. 3b. In Fig. 4, the cell surface temperature begins to rise exponentially, thus meaning the sample gets into TE. So, T_0 was defined as the initial temperature of TE in this paper.

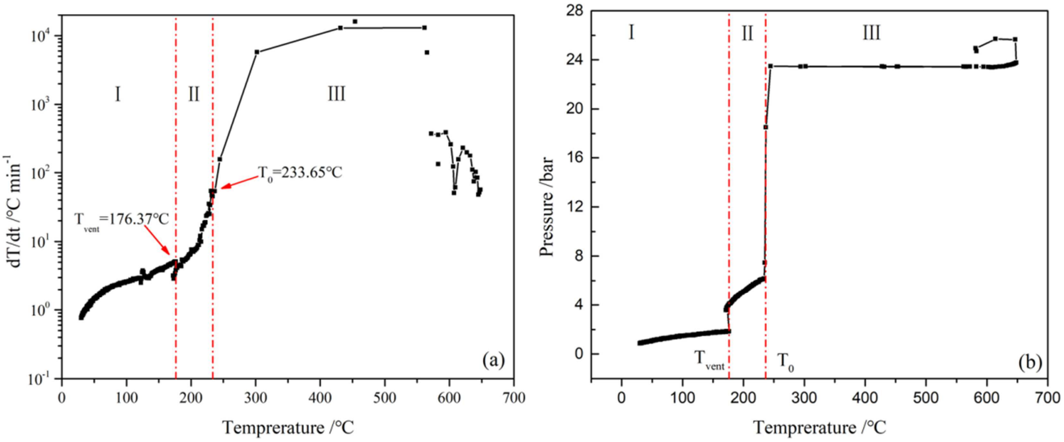

Fig. 3. The test data profiles of fresh cell at 75% SOC: (a) cell surface temperature rise rate versus cell surface temperature; (b) canister internal pressure versus cell surface temperature.

INFLUENCE OF THE SOC ON THERMAL EXPLOSION HAZARD OF FRESH CELLS

Transient data was collected throughout each test for T_{surf}, T_{avg} and P_{inter}. All tests were conducted when the T_{surf} reached 30 °C. Figure 4 shows the temperature (both T_{surf} and T_{avg}) and P_{inter} profiles for 4 picked tests. Noting that the O-ring would get damaged when the pressure exceeds about 24 bar, so the peak pressure for high SOC (75, 85, and 100%) samples got down in several minutes rather than maintained for stable value, as shown in Fig. 4. All peak temperatures and pressures are marked in each figure. The trend of three curves of each test is consistent as shown in Fig. 4; T_{surf} is lower than T_{avg} until the sample gets T_0, then T_{surf} goes up exponentially and there is also a rapid increase for P_{inter}. T_0 is a critical point between T_{surf} and T_{avg}. Before this point, the canister is heated directly by the EV-ARC and then the cell is heated by the hot canister, so the T_{avg} is higher than the T_{surf}. After this point, there is a series of violent exothermic reactions happening in the cell [2, 3], which release amount of energy to make the cell and canister temperature rise instantly. The P_{inter} has two jumps during the entire experiment: (1) The cell safety valve opens to release a bit of gas and energy, which makes the pressure rise slightly by about 1.46 bar (an average value for 15 tests). This slight ejection also causes the cell surface temperature to decrease slightly, but it rebounds quickly; (2) The cell gets into TE, a large amount of gas, tiny solids and energy are ejected from the cell to make the pressure increase significantly. Besides, some energy is absorbed by the canister, causing a sharp temperature jump of the canister.

Figure 5 shows the change curves of T_{surf} and P_{inter} with time under different SOCs. It can be observed that, overall, the time from cell started to be heated to TE (t_{TE}) increases as its SOC decreasing, and 100% SOC is about 13 min earlier than 25% SOC. Meanwhile, when a cell gets into TE, the higher the SOC is, the higher the maximum cell surface temperature and the canister internal pressure is. In Fig. 5, the maximum pressure is 36.2 bar at 682 °C of 100% SOC, while for 25% SOC it's 14.2 bar at 476 °C.

The critical statistics of fresh cells is summarized in Table 1. When the battery gets into TE, overall, the maximum temperature and the maximum pressure increase with the increase of SOC, but the initial temperature/pressure of vent and TE varied little from 25 to 100% SOC, while in high SOCs (75, 85, and 100%) these values get a little lower. It’s probably caused by the experimental errors. The mass loss at 100 and 85% SOC are higher than other conditions, the quality of the loss includes electrolyte solution and some electrode materials. $T_{\max}$ increases with the increase of SOC as shown in Fig. 6, and the value between 25 and 35% SOC is very close as well as for 75 and 85% SOC.

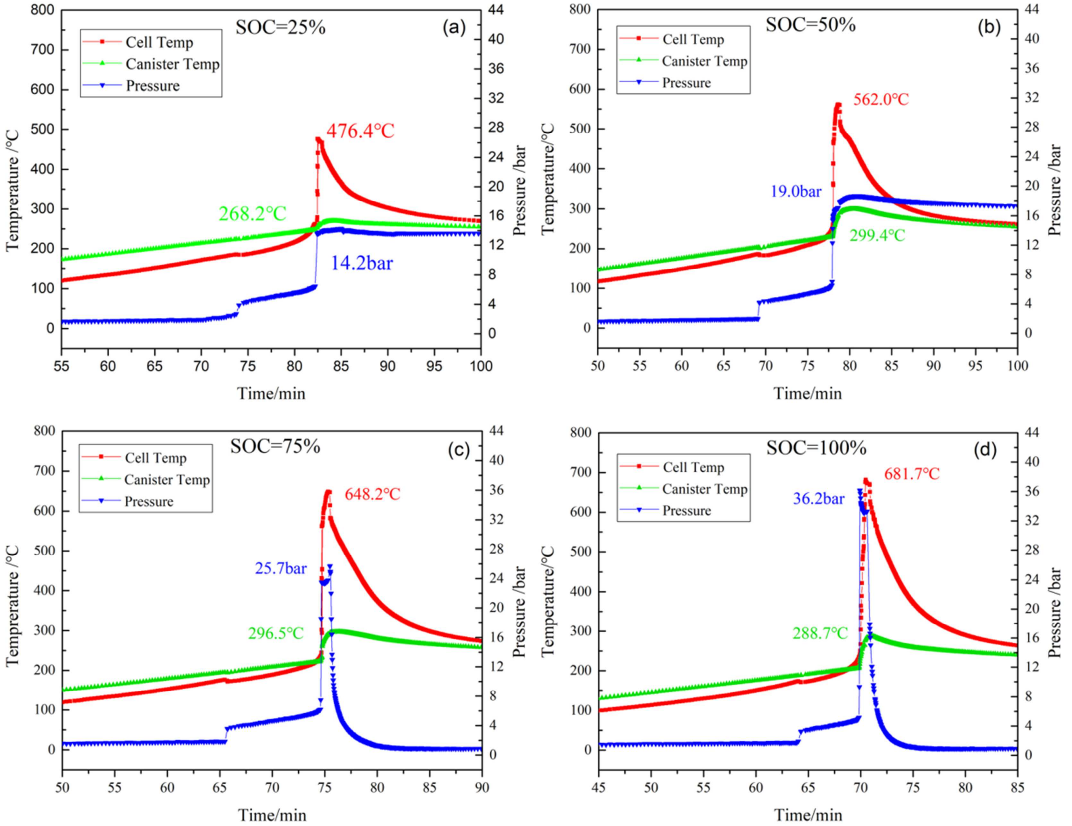

Fig. 4. The sample data of typical operating conditions: fresh cell at 25, 50, 75, and 100% SOC.

The pressure increase trend is more obvious and regular. As shown in Fig. 6, the pressure values could be approximated as an arithmetic progression with a tolerance of 3 from 25 to 85% SOC until it suddenly rises at 100% SOC. The pressure value at 100% SOC is about 1.3 times of the value at 85% SOC, and about 2.5 times of the value at 25% SOC. This may be caused by the violent internal reaction of 100% SOC, which caused more flammable gas releasing and at high SOCs even a gas explosion [26] would occur in the canister. Besides, the cell doesn't go to TE at 0% SOC and some electrolyte solution released from the cell was found on the bottom of the canister, Wu et al. [27] had confirmed this point in their research.

Table 2 shows the state of health (SOH) of these aging cells, the capacity loss is not obvious when cycle times is less than 300. When the cells are cycled 400 times, the capacity decreases to less than 80%, which can be regarded as scrap [24, 28]. Compared with fresh cells (0.5 C, 3 cycles at ambient temperature), the t_{TE} of aging cells are advanced, and the more cycles the cell has, the easier the cells get into TE. In Fig. 7, both the peak temperature and peak pressure of fresh cells and aging cells are close, but the aging cells are more prone to get into TE. For 400-cycles-cell, the t_{TE} is about 15 min ahead of fresh cells. 100, 200 and 300-cycles-cells have similar capacity fade and thermal profiles. Although their capacity fade is not obvious, the t_{TE} is still shorter than fresh cells. This may be caused by some irreversible changes, including active material loss, electrolyte reduction and lithium deposition [13, 14, 29].

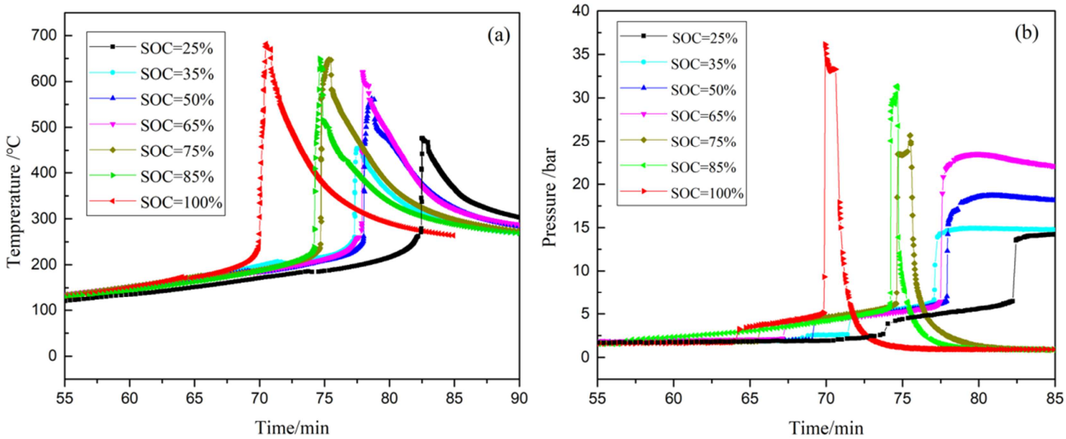

Fig. 5. The test data profiles of fresh cells at different SOCs: (a) the comparison cell surface temperature; (b) the comparison of canister internal pressure.

Table 1. Summary of the experimental data from the fresh cells

SOC, %	Mass, g	Loss mass, g [c]	Vent [b]		Start of TE		Thermal Explosion	
			T_{vent}, °C	P_{vent}, bar	T_0, °C	P_0, bar	$T_{\max}$, °C	$P_{\max}$, bar
25	44.16	6.98	197.0	2.4	265.5	6.8	454.2	14.4
35 [d]	43.62	8.99	191.3	2.0	251.5	6.1	462.8	15.0
50	44.00	6.33	185.5	1.9	246.2	6.2	528.7	18.2
65 [d]	42.98	7.26	184.3	1.9	267.2	5.8	632.9	20.5
75	43.56	7.87	167.1	1.6	248.8	5.6	687.6	23.3
85	43.91	10.45	177.2	1.7	247.5	5.8	689.5	27.0
100	44.05	12.88	169.4	1.5	237.3	4.6	727.6	36.3

[a] All calculations were the average of two tests except 100% SOC, in this condition there were 3 tests.

[b] T is the cell surface temperature, P is the canister internal pressure, 1 bar = 100000 Pa.

[c] Pre-test and post-test mass were measured to determine the overall mass loss of the cells.

[d] These data come from our previous work [15].

Table 2. The state of health (SOH) of ageing cells

Numbers	Initial capacity, mAh	Remained capacity, mAh	SOH
Fresh	-	-	100%
100	2010	2000	99.5%
200	2100	2000	95.2%
300	2040	1972	96.7%
400	1925	1574	79.2%

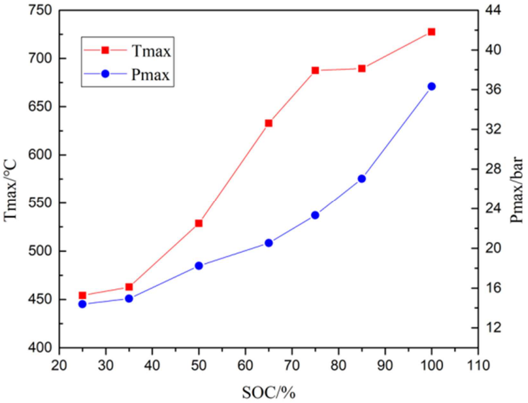

Fig. 6. The maximum battery surface temperature and the pick pressure of fresh cells.

INFLUENCE OF CYCLE TIMES ON THE THERMAL EXPLOSION HAZARD OF CELLS

Table 3 shows the average of the two experiment results. Except for the T_0 and $T_{\max}$, the other key experimental values are very close. The 400-cycles-cell shows the lowest T_0, 205 °C, which is about 32 °C lower than the fresh cells. The fresh cells show the highest $T_{\max}$, 728 °C, while the $T_{\max}$ of 400-cycles-cell is only 552 °C, but still higher than 100-cycles-cell, which has the highest external pressure, 36.9 bar.

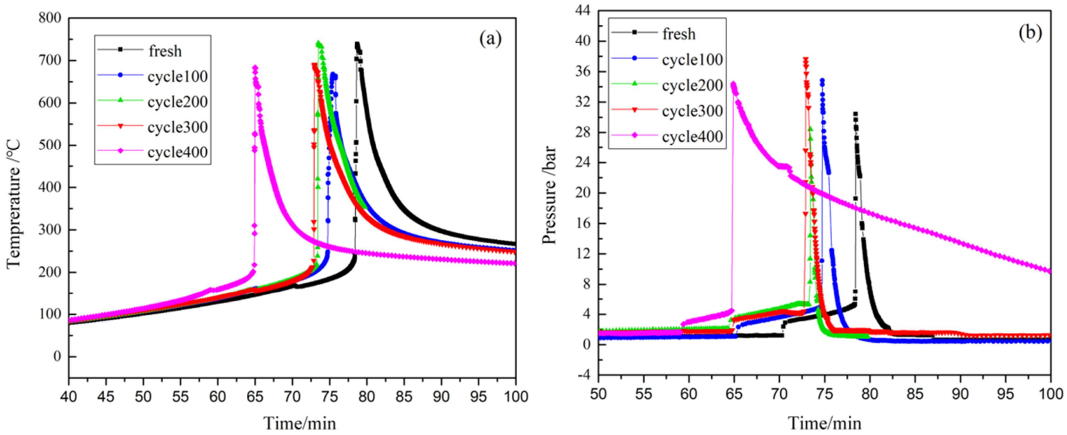

Fig. 7. The test data profiles of aging cells at 100% SOCs: (a) the comparison of cell surface temperature; (b) the comparison of canister internal pressure.

Table 3. Summary of the experimental data from the aging cells

Cycle	Mass, g	Loss mass, g	Vent		Start of TE		Thermal Explosion	
			T_{vent}, °C	P_{vent}, bar	T_0, °C	P_0, bar	$T_{\max}$, °C	$P_{\max}$, bar
Fresh	44.05	12.88	169.4	1.48	237.3	4.51	727.6	36.33
100	44.24	13.11	158.8	1.16	228.1	4.84	534.8	39.31
200	43.69	14.42	161.5	1.98	219.7	5.43	635.8	34.08
300	43.65	15.09	159.0	1.92	220.3	4.65	699.3	35.87
400	43.23	14.20	156.7	1.36	205.0	4.68	551.7	36.63

ENERGY CALCULATION AND CONVERSION

By knowing the mass, the specific heat capacity and the transient temperature profiles, the total energy released from batteries during the TE can be calculated. The total energy is a combination of the energy which raises the cell temperature and the canister temperature, we ignore the energy raising canister internal gas temperature because it is difficult to calculate and the value is very small [8, 12]. The calculation method is shown in Eq. (1)

$$\Delta H = C_P m\left(T_{\max} - T_0\right), \tag{1}$$

where ΔH is the energy (kJ), C_P is the specific heat capacity (kJ/(kg·K)), m is the mass of sample cell or canister (kg), $T_{\max}$ is the maximum temperature of the cell surface and canister surface (the average value) (°C), T_0 is the initial temperature of cell surface and canister surface (°C). Note that the temperature of canister is an average of three data and the C_P of sample cell is measured by the EV-ARC, which is 1.06 kJ/(kg·K), for canister C_P is 0.5 kJ/(kg·K). In order to get a more intuitive interpretation of the energy released from the cells, we use the TNT-equivalent method to convert the thermal energy to TNT-equivalent [10]. The conversion method is shown in Eq. (2) [9]

$$W = \frac{\eta \Delta H}{H_{TNT}^{1/3}}, \tag{2}$$

where W is the TNT-equivalent (g TNT), η is the empirical mass of TNT (1-15 mass%, in general) and in this study we take 15% [9], H_{TNT} is the explosive heat of TNT, for which a typical value is 4.437 kJ/g. The amount of gas produced from the cell is calculated using the ideal gas law and the pressure data, note that we replace the gas temperature with the T_{surf} for there is only one thermocouple port on the canister. The estimate method is shown in Eq. (3) [19, 30]

$$n = \frac{pV}{RT} - n_0 = \frac{pV}{RT} - \frac{p_0 V}{RT_0}, \tag{3}$$

where P is the recorded pressure (Pa), $V = 2.92\times10^{-4}$ m^3 is the canister internal volume, T is the cell surface temperature (K), $R = 8.314$ J/(mol·K) is the ideal gas constant. The calculation results are shown in Table 4. For fresh cells, the total energy released from the cells increases with the increase of SOC, and the average 100% SOC energy release is 61.72 kJ, which is equivalent to 5.57 g TNT. Furthermore, 116.6 mmol gas is released by the cell during the whole test. For aging cells, over all, the total thermal energy is lower than fresh cells at 100% SOC, which is close to fresh cells at 75 and 85% SOC. However, the 400-cycles-cell releases 148 mmol gas and there is only 72.3 mmol and 92.3 mmol for 75 and 85% SOC. The total energy released from 300-cycles-cell is higher than other aging cells, the value is 56.5 kJ which is close to fresh cells at 100% SOC. In this situation the cell is at the junction of capacity fade and thermal stability decreasing. Although the electrochemical energy stored in the cell body is the same as fresh cells, the internal state is similar to 400-cycles-cell. So, the 300-cycles-cell releases much more thermal energy while it still maintains the similar thermal profiles to 100 and 200-cycles-cell.

Figure 8 shows the energy distribution and the normalized θ [12]. The fresh cells at 100% SOC release the highest energy and the thermal energy absorbed by the canister is the 54-69% of the total energy in all experiments. For fresh cells, the normalized θ decreases with the increase of SOC, but for the aging cells it increases with the increase of cycle numbers. This ratio indicates that the thermal energy caused by cell thermal explosion is higher than the electrochemical energy stored in the cell.

Table 4. Characteristic calculated average values in the thermal-explosion experiments

Item	Cell energy, kJ	Canister energy, kJ	Total energy, kJ	Electrochemical Energy[b], kJ	*W*, g TNT	θ[a]	*N*, mmol
Fresh-25%	8.84	12.49	21.33	6.51	1.92	3.28	53.73
Fresh-35%	9.77	14.74	24.51	9.13	2.21	2.69	56.66
Fresh-50%	13.17	18.59	31.76	13.25	2.86	2.40	64.75
Fresh-65%	16.63	22.53	39.16	17.41	3.53	2.25	65.23
Fresh-75%	20.26	28.88	49.15	20.08	4.43	2.45	72.29
Fresh-85%	20.58	25.88	46.45	22.81	4.19	2.04	92.28
Fresh-100%	22.91	38.80	61.72	27.57	5.57	2.24	116.6
Cyc-100	14.36	31.90	46.27	27.59	4.17	1.68	165.0
Cyc-200	19.28	29.74	49.01	27.81	4.42	1.76	122.1
Cyc-300	22.16	34.37	56.53	27.47	5.10	2.06	113.7
Cyc-400	15.77	30.37	46.14	22.24	4.16	2.07	148.2

[a] The dimensionless θ factor is the total calculated energy released to the electrochemical energy ratio.

[b] The cell electrochemical energy was obtained from the battery test system.

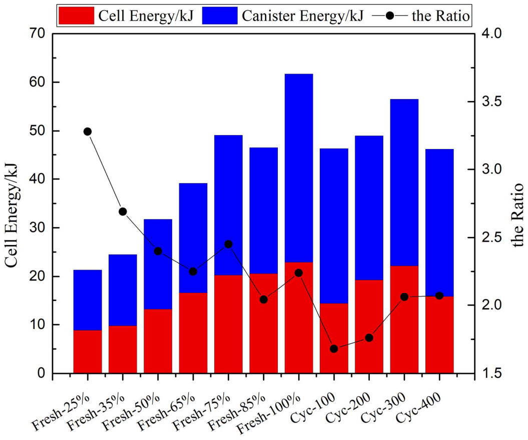

Fig. 8. Comparison of the energy distribution and the ratio (θ).

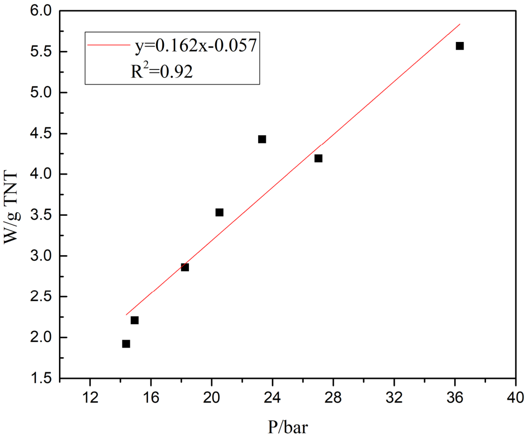

Fig. 9. The explosion equivalent versus the peak canister internal pressure.

According to Table 1 and 4, the total energy increases with the increase of SOC, but the regularity of the maximum surface temperature is not very clear, which is related to the accuracy of the thermocouple and the calorimeter. On the contrary, the peak pressure has the similar variation tendency to the total energy released from the fresh cells. Figure 9 shows the relationship between peak pressure and explosion heat equivalent. It can be seen that the explosion heat equivalent is a linear function of peak pressure, that is, the greater the external pressure, the higher the explosion heat equivalent of the battery, and the higher the thermal explosion hazards, which is more convenient and intuitive than calculating the total energy released from the batteries.

CONCLUSIONS

The thermal explosion hazards of a commercial 18650 NCM cell at various SOCs and cycle numbers were studied by extend volume calorimeter with a ramp heating method. In this study, both fresh cells and aging cells were charged to specific SOCs, and then put into the EV-ARC to be heated until them got into thermal explosion. A sealed canister was designed to measure the external pressure and the considerable energy released from a thermal runaway battery. The experimental results indicated that the thermal explosion hazards of 18650 lithium-ion battery increase with the increase of SOCs and cycle numbers. For fresh cells, the cells at 100% SOC released the highest thermal energy of 61.7 kJ (equivalent to 5.57 g TNT), the highest runaway temperature of 728 °C, the highest peak pressure of 36.3 bar and the most gas of 116.6 mmol. For aging cells, the time from started to be heated to thermal explosion decreased with the increase of cycle numbers, and the time for 400-cycles-cell was about 15 min ahead of fresh cells at 100% SOC, besides, the 400-cycles-cell had the lowest initial temperature at 205 °C, which was 32 °C lower than that of fresh cells with the same SOC. For fresh cells, the peak pressure showed a much more similar tendency to the total energy released from the cells at different SOCs, so it could be used as one of the judge standard of the thermal explosion hazards that the higher the peak pressure, the higher the thermal explosion hazards.

ACKNOWLEDGEMENT

This work was supported by the National Key R&D Program of China (No.2016YFB0100305), the National Natural Science Foundation of China (No. 51674228), the External Cooperation Program of BIC, CAS (No. 211134KYSB20150004) and the Fundamental Research Funds for the Central Universities (No. WK2320000038). Dr. Q.S Wang is supported by Youth Innovation Promotion Association CAS (No.2013286).

REFERENCE

[1] S.-i. Tobishima, J.-i. Yamaki, A Consideration of Lithium Cell Safety, J. Power Sources 81-82 (1999) 882-886.

[2] Q. Wang, P. Ping, X. Zhao, G. Chu, J. Sun, C. Chen, Thermal Runaway Caused Fire and Explosion of Lithium Ion Battery, J. Power Sources 208 (2012) 210-224.

[3] X. Feng, M. Ouyang, X. Liu, L. Lu, Y. Xia, X. He, Thermal Runaway Mechanism of Lithium Ion Battery for Electric Vehicles: A Review, Energy Storage Mater. 10 (2018) 246-267.

[4] J. Jiang, J.R. Dahn, ARC Studies of the Thermal Stability of Three Different Cathode Materials: LiCoO2; Li[Ni0.1Co0.8Mn0.1]O2; and LiFePO4, In LiPF6 and LiBoB EC/DEC Electrolytes, Electrochem. Commun. 6 (2004) 39-43.

[5] Y. Wang, J. Jiang, J.R. Dahn, The Reactivity of Delithiated Li(Ni1/3Co1/3Mn1/3)O2, Li(Ni0.8Co0.15Al0.05)O2 or LiCoO2 with Non-aqueous Electrolyte, Electrochem. Commun. 9 (2007) 2534-2540.

[6] T.M. Bandhauer, S. Garimella, T.F. Fuller, A Critical Review of Thermal Issues in Lithium-Ion Batteries, J. Electrochem. Soc. 158 (2011) R1-R25.

[7] C.-Y. Jhu, Y.-W. Wang, C.-Y. Wen, C.-M. Shu, Thermal Runaway Potential of LiCoO2 and Li(Ni1/3Co1/3Mn1/3)O2 Batteries Determined with Adiabatic Calorimetry Methodology, Appl. Energy 100 (2012) 127-131.

[8] C.Y. Jhu, Y.W. Wang, C.M. Shu, J.C. Chang, H.C. Wu, Thermal Explosion Hazards on 18650 Lithium Ion Batteries with a VSP2 Adiabatic Calorimeter, J. Hazard. Mater. 192 (2011) 99-107.

[9] W.-C. Chen, Y.-W. Wang, C.-M. Shu, Adiabatic Calorimetry Test of the Reaction Kinetics and Self-heating Model for 18650 Li-ion Cells in Various States of Charge, J. Power Sources 318 (2016) 200-209.

[10] T.-Y. Lu, C.-C. Chiang, S.-H. Wu, K.-C. Chen, S.-J. Lin, C.-Y. Wen, C.-M. Shu, Thermal Hazard Evaluations of 18650 Lithium-ion Batteries by an Adiabatic Calorimeter, J. Therm. Anal. Calorim. 114 (2013) 1083-1088.

[11] X. Liu, Z. Wu, S.I. Stoliarov, M. Denlinger, A. Masias, K. Snyder, Heat Release During Thermally-induced Failure of a Lithium Ion Battery: Impact of Cathode Composition, Fire Saf. J. 85 (2016) 10-22.

[12] S. Yayathi, W. Walker, D. Doughty, H. Ardebili, Energy Distributions Exhibited During Thermal Runaway of Commercial Lithium Ion Batteries Used for Human Spaceflight Applications, J. Power Sources 329 (2016) 197-206.

[13] M. Börner, A. Friesen, M. Grützke, Y.P. Stenzel, G. Brunklaus, J. Haetge, S. Nowak, F.M. Schappacher, M. Winter, Correlation of Aging and Thermal Stability of Commercial 18650-type Lithium Ion Batteries, J. Power Sources 342 (2017) 382-392.

[14] A. Friesen, F. Horsthemke, X. Monnighoff, G. Brunklaus, R. Krafft, M. Borner, T. Risthaus, M. Winter, F.M. Schappacher, Impact of Cycling at Low Temperatures on the Safety Behavior of 18650-type Lithium Ion Cells: Combined Study of Mechanical and Thermal Abuse Testing Accompanied by Post-mortem Analysis, J. Power Sources 334 (2016) 1-11.

[15] C. Zhao, Q. Wang, Y. Yu, Thermal Explosion Hazards of Lithium-ion Batteries in Hermetic Space, Energy Storage Sci. Technol. 7 (2018) 424-430.

[16] C. Orendorff, J. Lamb, L.A. Steele, S.W. Spangler, J. Langendorf, Quantification of Lithium-ion Thermal Runaway Energetics, Report No. SAND2016-0486, Sandia National Lab., 2016.

[17] Thermal Hazard Technology. http://www.thermalhazardtechnology.com/downloads.

[18] S. Koch, A. Fill, K.P. Birke, Comprehensive Gas Analysis on Large Scale Automotive Lithium-ion Cells in Thermal Runaway, J. Power Sources, 398 (2018) 106-112.

[19] A.W. Golubkov, D. Fuchs, J. Wagner, H. Wiltsche, C. Stangl, G. Fauler, G. Voitic, A. Thaler, V. Hacker, Thermal-runaway Experiments on Consumer Li-ion Batteries with Metal-oxide and Olivin-type Cathodes, RSC Adv 4 (2014) 3633-3642.

[20] M. Lammer, A. Koenigseder, V. Hacker, Holistic Methodology for Characterisation of the Thermally Induced Failure of Commercially Available 18650 Lithium Ion Cells, Rsc Adv. 7 (2017) 24425-24429.

[21] K. Takei, K. Kumai, Y. Kobayashi, H. Miyashiro, N. Terada, T. IwahoriT, Tanaka, Cycle Life Estimation of Lithium Secondary Battery by Extrapolation Method and Accelerated Aging Test, J. Power Sources 97-98 (2001) 697-701.

[22] X. Han, M. Ouyang, L. Lu, J. Li, Y. Zheng, Z. Li, A Comparative Study of Commercial Lithium Ion Battery Cycle Life in Electrical Vehicle: Aging Mechanism Identification, J. Power Sources 251 (2014) 38-54.

[23] P. Biensan, B. Simon, J.P. Peres, A.d. Guibert, M. Broussely, J.M. Bodet, On Safety of Lithium-ion Cells, J. Power Sources 81-82 (1999) 906-912.

[24] M. Fleischhammer, T. Waldmann, G. Bisle, B.-I. Hogg, M. Wohlfahrt-Mehrens, Interaction of Cyclic Ageing at High-rate and Low Temperatures and Safety in Lithium-ion Batteries, J. Power Sources 274 (2015) 432-439.

[25] X. Feng, M. Fang, X. He, M. Ouyang, L. Lu, H. Wang, M. Zhang, Thermal Runaway Features of Large Format Prismatic Lithium Ion Battery Using Extended Volume Accelerating Rate Calorimetry, J. Power Sources 255 (2014) 294-301.

[26] F. Larsson, S. Bertilsson, M. Furlani, I. Albinsson, B.-E. Mellander, Gas Explosions and Thermal Runaways During External Heating Abuse of Commercial Lithium-ion Graphite-LiCoO2 Cells at Different Levels of Ageing, J. Power Sources 373 (2018) 220-231.

[27] T. Wu, H. Chen, Q. Wang, J. Sun, Comparison Analysis on the Thermal Runaway of Lithium-ion Battery Under Two Heating Modes, J. Hazard Mater. 344 (2017) 733-741.

[28] W. He, N. Williard, M. Osterman, M. Pecht, Prognostics of Lithium-ion Batteries Based on Dempster–Shafer theory and the Bayesian Monte Carlo Method, J. Power Sources 196 (2011) 10314-10321.

[29] T. Waldmann, M. Wilka, M. Kasper, M. Fleischhammer, M. Wohlfahrt-Mehrens, Temperature Dependent Ageing Mechanisms in Lithium-ion Batteries – A Post-Mortem Study, J. Power Sources 262 (2014) 129-135.

[30] P. Huang, P. Ping, K. Li, H. Chen, Q. Wang, J. Wen, J. Sun, Experimental and Modeling Analysis of Thermal Runaway Propagation Over the Large Format Energy Storage Battery Module with Li4Ti5O12 Anode, Appl. Energy 183 (2016) 659-673.

Part 6. Material Behavior in Fires

Flammability testing

Comparison of Large-Scale Façade Fire Test Benches: Methodological Approach

Delcour S.*, Marquis D.M.

Laboratoire National de métrologie et d'Essai (LNE), Fire behavior and fire safety department,
Trappes, France
**Corresponding author's email: simon.delcour@lne.fr*

ABSTRACT

The development of external thermal insulation in buildings has given rise to a risk of fire spread by the façade of buildings, as was demonstrated by the recent Grenfell Tower fire. In order to assess this risk, several countries have enforced mandatory real-scale tests, but these test methods are very different from one country to the next. In these tests, the fire performance assessment is based on different criteria, such as temperature thresholds or propagation. Considering all these differences, comparing the results obtained between different façade fire tests is difficult. The aim of this study is to develop an alternative approach based on a numerical tool (FDS), in order to compare façade fire tests. The analysis focuses on the dynamic evolution of the incident heat flux and its surface distribution. Results indicate that this new approach is able to discriminate between the test benches, and a correlation was exposed between surface impact and heat flux.

KEYWORDS: façade fire, modeling, CFD, thermal stress, comparison methodology, test bench.

INTRODUCTION

Fire is one of the main hazards in high-rise buildings, especially the risk of fire propagation from one floor to the next. For this reason, most building regulations impose fire-protection systems to be implemented in these buildings, especially to prevent the fire to reach the staircases (containment). Another way of fire propagation is via the outside [1], where the fire can make contact with additional fuel, namely the External Thermal Insulation Component Systems (ETICS). These systems are made of a thermal insulation layer (like mineral wool, Polyurethane or Polyisocyanurate), assembled with a wooden or metal structure, sometimes associated with an external cladding (which can be burnable or inert) and an air gap. If the insulation system is not correctly designed, the flame propagation on the façade can be dramatically increased, as it was the case in the Grenfell Tower fire.

These insulation systems often require a specific fire test to be performed to assess their effect on fire spread. Test methods varies considerably from one country to the next, but are often based on full scale test benches, which consider both reaction and resistance to fire. In these tests, a post-flashover room fire scenario is assumed, where the fire destroyed the room's window and is venting through the opening. The ETICS to be tested is fitted on the bench's wall, exposed to the flame.

As these benches are very different from one another (on both geometry and fire source), it is difficult to compare their results and requirements [2,3]. The only common point between these test benches is that they have a compartment fire venting through an opening, with the test wall above the opening. In the literature, experimental data can sometimes be found on reference tests

Proceedings of the Ninth International Seminar on Fire and Explosion Hazards (ISFEH9), pp. 903-912
Edited by Snegirev A., Liu N.A., Tamanini F., Bradley D., Molkov V., and Chaumeix N.
Published by Saint-Petersburg Polytechnic University Press
ISBN: 978-5-7422-6498-9 DOI: 10.18720/spbpu/2/k19-18

performed without an ETICS fitted on the benches. Based on geometrical features, two groups of benches can be identified:

- Corner tests, fitted with a side wall to add a corner effect to the plume. ISO [4], DIN (Germany) [5] and BS (UK) [6] are part of this group.
- Flat wall tests that can include windows (which can be a parameter of the test procedure). LEPIR (France) [7] and SP (Sweden) [8] are example of that group.

A review of the tests' criteria was recently published by Smolka [3], pointing at the diversity of parameters considered during the tests. Most common parameters are visual flame spread and temperature levels at specific height above the fire source. Smolka also pointed the absence of heat exposure measurement in these tests, and named it a crucial parameter in the development of a harmonized test methodology.

A possible way to evaluate the heat exposure is the incident heat flux on the ETICS, and its repartition over the tested surface. This parameter is of utmost importance, as the same amount of fuel can give very different heat exposure given the effect of the geometry, ventilation and wind, as was also pointed out by Smolka [3].

From an experimental standpoint, as the heat flux is distributed on the surface, it would require a prohibitively large amount of heat flux gauges to measure it accurately over the entire exposed surface of a full scale test bench (test surface area is often around 25 square meters). Experimental data exists but was mostly aimed at obtaining a vertical distribution of heat flux above the opening [9, 10].

On the numerical side, simulation studies of different test benches were conducted [11, 12, 13]. However, these studies were mostly concentrating on the gas phase parameters like temperature and velocity profiles inside the plume.

Thus, an alternative approach was developed, using numerical simulations and data treatment to gain insight on the surface distribution of the incident heat flux. Each test bench was simulated, and the data were used to build correlations representing the distribution of the thermal stress imposed by each bench on the ETICS' surface.

NUMERICAL SIMULATIONS

Numerical tool

The modeling tool used in the present work is FDS, v6.5.2 [14]. FDS solves an approximation of the Navier–Stokes equations appropriate for low-Mach number, thermally driven flows. The numerical algorithm employed is an explicit predictor/corrector scheme, second order accurate both in space and time, using a direct Poisson solver. Turbulence is treated using Large Eddy Simulation (LES), via the Deardorff subgrid scale model. A lumped species combustion model assuming a unique, Arrhenius piloted global chemical reaction is used to estimate the heat release and smoke distributions in the computational domain. The radiation transport is treated using a finite volume solver in which grey gas absorption coefficient for soot and gas species is linked to the products fraction.

Modelling of testing facilities

Three dimensional models of the façade fire tests were created by using a Cartesian mesh. The quality of the computational mesh and the resolution of flow field can usually be assessed by non-dimensional ratio $D^*/\Delta d$. Lin et al. [15] recommend $D^*/\Delta d \geq 10$ or more to predict with precision the radiative heat flux. The recent MaCFP workshop report [16] gave more insight on the importance of taking into account other length scales to select the mesh size. According to this requirement, the cells dimensions should be order of 10 cm. Therefore, a uniform numerical grid Δd of 5 cm was chosen, as a result of a compromise between flow resolution and computational time. The computational domain is defined in order to contain the flame as a whole. The domain boundaries are located at a sufficient distance from the building (and the flame) so that they do not incorrectly affect the flame dynamics. Minimal distance between the solid walls and the domain boundaries is 0.5 meters.

The test apparatus was dimensioned according to the experimental test facility. The dimensions of the test benches are adapted to fit within the chosen spatial discretization. The errors induced on the dimension are in the range of 5%.

As initial conditions, the gas in the computation domains was set still with ambient temperature (T_∞ = 23°C). At the domain borders, a zero normal gradient static (Neumann type) was employed. The atmospheric pressure is fixed at 101325 Pa and the humidity is defined at 50%. Thermal properties of the materials were unified between the different benches to focus the analysis on the effects of bench design and fire source. Table 1 details the material properties used in the simulations. Table 2 lists the features of the tests benches, as defined by their respective standards, as well as the dimensions of the computational domain considered.

Table 1. Material properties

Property	Combustion chamber	Test wall
Specific heat, kJ/(kg·K)	0.88	0.88
Thermal conductivity, W/(m·K)	0.92	0.76
Density, kg/m^3	2500	1500

DATA PROCESSING

In order to compare the benches, data from the simulations should be extracted; this is usually done with localized sensors in FDS, measuring the values of a quantity through time at a pre-determined position in space. However, one would need a (very) large amount of sensors to obtain the complete heat flux mapping on the tested wall. In this paper, a new approach is presented, using the boundary files data. Boundary files are often used for qualitative observations, but are scarcely used for quantitative measurements, in no small part due to the fact that these files are encoded for Smokeview and not readily understandable for the user.

The fds2ascii program is a small utility software used to extract data from the boundary files (.bf extension) in a human-understandable format. Using a MATLAB script to perform repeated calls of this software through a loop, the time-resolved incident heat flux data were obtained, using a 10 s time averaging. This 10 s averaging was deemed a good compromise between time resolution and data volume. These data are then converted in stacks of matrix format, whose dimensions are equivalent to the size of the considered wall (3rd dimension is the time). For test benches outfitted with a side wall, main wall and side wall are treated separately then the side wall piece matrix is appended to the main wall matrix.

The matrix dimensions are limited by the mesh size used during the FDS simulations. In order to ensure a better behavior of subsequent image treatment algorithms, a bicubic interpolation scaling [17] was used to increase each dimension by a factor 5.

By considering the heat flux matrices as images, a thresholding algorithm was then applied, converting the values in each cell to a zero or a one whether their values are below or above the considered threshold. Threshold values were chosen from 10 to 70 kW/m^2, with 5 kW/m^2 steps. An example of the original Smokeview visualization and corresponding binary image is presented in Fig. 1.

Table 2. Test benches features

Standard	ISO 13785-2	LEPIR II	SP FIRE 105	DIN E 4102-20	BS 8414-1
Ref.	[4]	[7]	[8]	[5]	[6]
Country	International	France	Sweden	Germany	UK
Configuration	Corner	Flat wall	Flat wall	Corner	Corner
Vertical main test wall	$w \geq 3.0$ m $h \geq 4.0$ m	w = 5.0 m h = 6.5 m	w = 4.0 m h = 6.0 m	$w \geq 2.5$ m $h \geq 5.5$ m	$w \geq 2.6$ m $h \geq 6.0$ m
Vertical return wall (wing at 90°)	$w \geq 1.2$ m	-	-	$w \geq 1.5$ m	$w \geq 1.5$ m
Volume of Combustion chamber	$20 \leq V \leq 100$ m^3	30.3 m^3	6.74 m^3	0.7 m^3	≥ 4.275 m^3
Main opening	2.4 m²	2 x 1.5 m²	2.13 m²	0.7 m²	4 m²
Secondary opening Natural ventilation	-	0.99 m² on rear face by a variable opening	0.94 m²	-	-
Heat source	a/ Propane b/ Liquids c/ Wooden cribs	Wooden cribs (x2)	Heptane fuel	a/ Wooden crib b/ Liquids	a/ Timber crib b/ Liquids
Fuel quantity	a/ Calibration b/ ~ 60 liter (ex: Heptane) c/ ~400 kg	300 kg each	60 liter	a/ 30 kg b/ propane	a/ Nominal total heat output of 4500 MJ (30 min) at a peak rate of 3 ±0.5 MW
Test duration	23 - 27 min	60 min	15-20 min	a/ 20 min b/ 30 min	30 - 60 min
Computational domain dimensions	8.1 x 7.2 x 7.2 m^3	7 x 8 x 7.2 m^3	6 x 6 x 8 m^3	4.5 x 3.2 x 6 m^3	5.4 x 5 x 9 m^3

(h: height above the window opening)

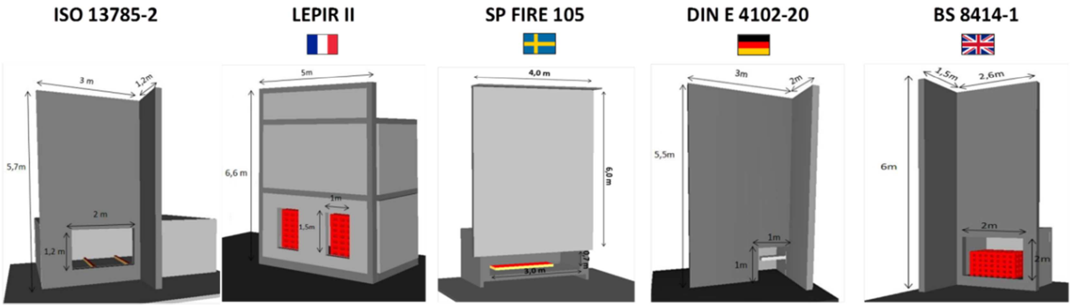

At each time step, each binary matrix is summed, and the result is then divided by the total number of cells in the matrix (minus the cells representing the openings). Thus, the time-resolved fraction of the surface area that received a heat flux superior to the threshold value is obtained. This parameter S/S_0 will be called surface impact (S_0 being the total surface area of the bench, minus the openings).

Using the same binary image, the maximum height reached by the threshold heat flux can also be measured (measurement axis being the centerline of the opening). Normalizing by the height above the opening give the second parameter H/H_0, called height impact. Figure 2 resumes the quantities measured, using the ISO bench as an example.

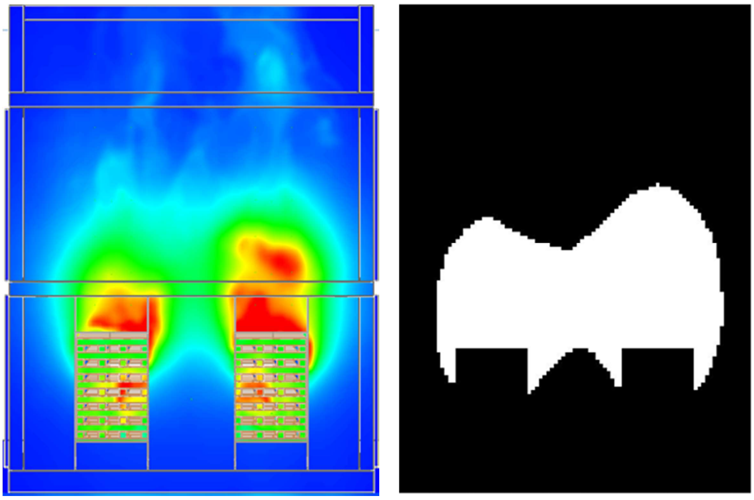

(a) (b)

Fig. 1. LEPIR Bench. (a) Incident heat flux as seen in Smokeview; (b) associated binary image (Threshold 20 kW/m^2).

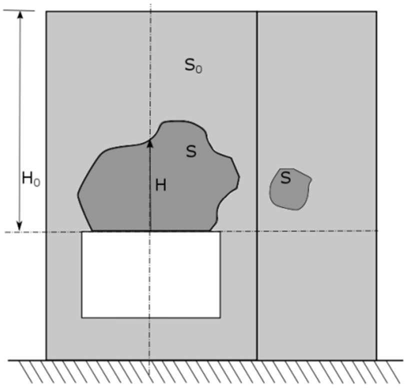

Fig. 2. Measured quantities on the ISO bench.

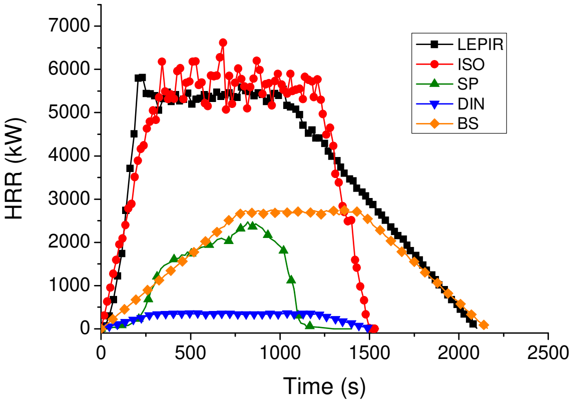

Fig. 3. Heat Release Rate (HRR) used for each simulation.

The use of the opening centerline as an axis for the measurement of H warrants a discussion. One could argue that, due to the corner effect, maximum height will be reached at (or toward) the corner and not on the centerline. However, the available experimental data mostly give centerline measurements [9,10]. Furthermore, in order to maintain comparability between flat and corner benches, a compromise had to be made. In the future, the possibility to consider the tilt angle and length of the plume (instead of raw height) will be investigated.

All the heat release rates (HRR) used in the simulations present a stationary stage (except SP), as described in Fig. 3. Hence, the surface fraction and maximum height associated to each threshold value were averaged on the time window corresponding to this stationary stage. For the SP bench, as an experimental HRR curve was used [18], the averaging window was centered on the maximum HRR and spanned 2 min before and 2 min after the maximum. Table 3 gives the parameter used for the determination of the stationary state.

Table 3. Stationnary state parameters used for each test bench

Test bench	Start time (s)	End time (s)	HRR (kW)
ISO	330	1200	5687
LEPIR	200	1000	5403
SP	710	950	2500
DIN	300	1200	340
BS	135	620	2507

RESULTS AND DISCUSSION

Time-dependent measurement of surface area

Figure 4 represents the obtained results of surface impact associated to thresholds of 20 and 40 kW/m^2, as a function of time. The behavior of the surface impact variable is following the HRR curves, with the exception of the ISO bench showing a general decreasing tendency after the initial increase. This figure also shows that the choice of the incident heat flux threshold value can change the relative position of each bench. For a 20 kW/m^2 threshold, SP and BS are equivalent (considering maximum values), while SP reaches higher than BS for 40 kW/m^2.

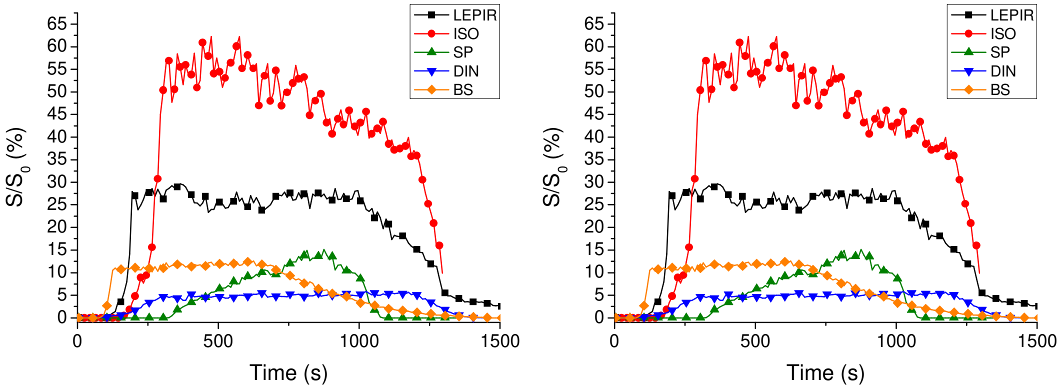

(a)

(b)

Fig. 4. Surface impact as a function of time. (a) Threshold value 20 kW/m^2; (b) Threshold value 40 kW/m^2.

Time-averaged values of surface area

As explained previously, the obtained data were time-averaged on the duration of the stationary stage. This step was necessary to filter out the fluctuation associated with the turbulent fire plume. The results are shown on Fig. 5 as a function of heat flux values, where error bars are the standard deviation on the interval considered for the time-average.

From these results, several conclusions can be drawn. It appears first that the ISO bench is generating the most thermal stress on the wall, being systematically above the other benches, surface-wise, on the entire heat flux range considered. The LEPIR bench, while using a slightly less powerful heat source (5.4 MW vs 5.7 MW for ISO), has less of an impact on the test wall. It is clear that this difference is caused by the geometric features of the benches, especially opening dimensions and side wall.

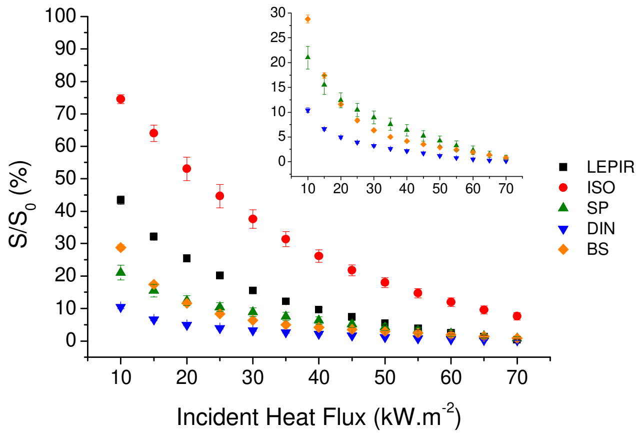

Fig. 5. Surface impact as a function of incident heat flux (in picture: zoom on the SP, BS and DIN values).

Comparing the SP and BS benches (both 2.5 MW) shows a different behavior. Except for 10 kW/m^2, where the BS surface impact is higher, both benches give similar results in terms of surface impact, despite their geometric differences. On the other hand, BS and DIN have very different surface impact, despite having very similar geometric features. This can be explained by the relatively low heat release rate used for the DIN test (340 kW).

Surface impact data correlates extremely well with the incident heat flux q_i’’, following a decreasing exponential law: $s/s_0 = \alpha \exp(-q_i''/\beta)$. Table 4 lists the exponential laws parameters α and β, as well as the correlation coefficients R² for each bench. So far, there is no physical interpretation of this correlation, as it is probably a combination of several parameters of the tests. More than likely, heat release and geometry both contribute to this correlation.

Table 4. Exponential regression parameters for surface impact

Test bench	α	β	R²
ISO	108.4	27.9	0.999
LEPIR	72.4	19.2	0.997
SP	30.6	23.9	0.990
DIN	17.2	17.5	0.983
BS	55.8	13.9	0.977

Time-dependent measurement of height

Figure 6 represents the maximum height obtained for the same thresholds. It is difficult to draws a conclusion when considering the height parameter, as this parameter is very sensitive to the geometrical features of the bench (corner effect, number of openings) as well as the effect of turbulence. It must be noticed that for a 20 kW/m^2 threshold, the maximum height for the ISO bench equals the height of the bench (e.g. the flame reaches higher than the wall). This behavior is a potential source for uncertainties.

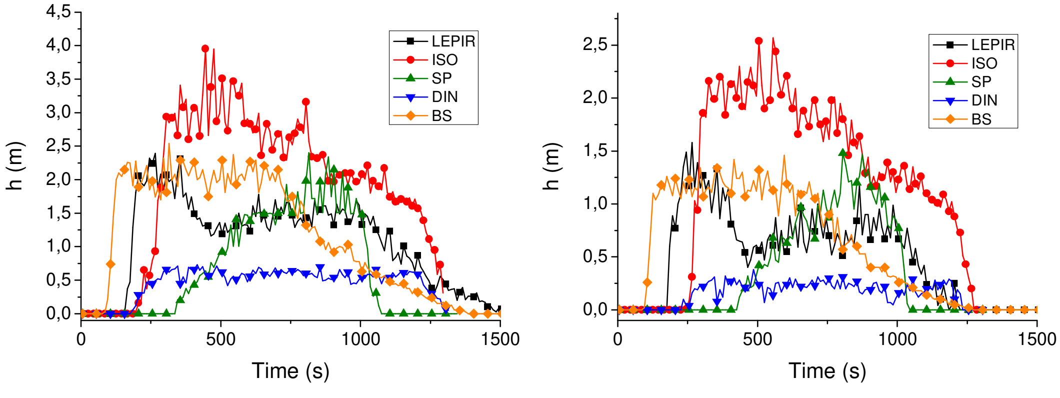

(a) (b)

Fig. 6. Height impact as a function of time. (a) Threshold value 20 kW/m^2; (b) Threshold value 40 kW/m^2.

Time-averaged values of height impact

The treatment used for surface impact was also applied for height data, and presented on Fig. 7. The transition from flaming region to plume region is difficult to identify on these data. Previous experimental work by Lee et al. [10] produced correlations between the external heat release (fuel burning outside of the combustion chamber) and the vertical variation of heat flux received on the wall. These correlations were relying on measurements of the flame height but such a parameter is difficult to access in a numerical simulation, as there are several possible parameters to consider (HRRPUV, temperature, etc.).

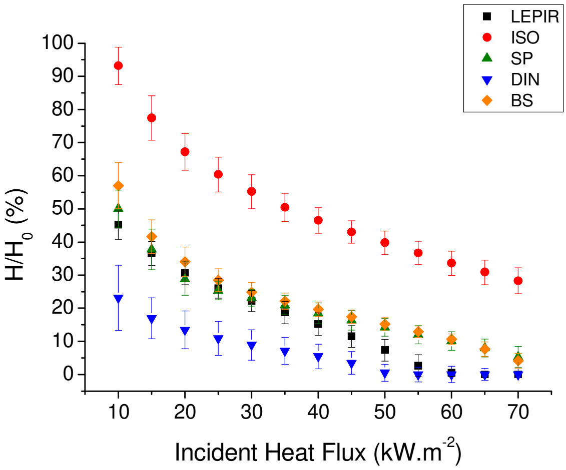

Fig. 7. Normalized height impact as a function of incident heat flux.

Uncertainties and sensibility

The existing literature on numerical simulation of this type of test benches [12, 13] yields uncertainties on numerical values of heat flux in the range of 15%. This means that uncertainties in the present results are to be expected on the higher heat flux values considered, as a constant 5 kW.m^{-2} interval was used in this work. Height impact values appear to be more prone to variations that surface values. This is coherent with the fact that the flame oscillates more on the vertical axis than on the horizontal axis; it is a reasonable assumption to consider that most of the variation in the surface impact values are generated by vertical variations.

CONCLUSION AND FUTURE WORK

In this work, numerical simulations of different façade fire test benches were conducted, and a numerical methodology was proposed for the heat flux data. This methodology is designed for data distributed over a planar surface, so it could also be used for wall temperature, or even accumulated thermal energy (using time integration of net heat flux). The proposed methodology gave access to the time-resolved surface distribution of incident heat flux for the test benches. From this distribution, two time-averaged parameters can be derived, namely surface impact and height impact. These values, being based on the incident heat flux, are representative of the thermal stress imposed by the test procedure on the surface.

The most evident added value of these parameters is that they can be defined independently of the bench geometry (flat wall or corner). It can even be used for smaller test benches like ISO 13785-1 or EN 13823 (Single Burning Item). As these parameters are based on the surface distribution of heat flux, they are less sensitive to local effects and completely independent of sensor positioning as the entire surface is the sensor. Height impact could be associated to flame height measurements, in order to check the available correlation of the literature. This would require a reliable numerical measurement of flame height.

The presence of wind during outside tests (namely LEPIR) can tilt and/or stretch the flame, generating an oblique thermal imprint on the surface. This would likely have no influence on the surface impact values, but the height impact values can be severely affected by this phenomenon, as only the vertical direction was considered in the present work, and the measurement were made on the centerline. Future development will include numerical simulations with variable wind speed and orientation, as well as data treatment modifications to deal with oblique thermal plume. This development will also be used to investigate oblique plume generated by corner effects.

If the façade material could be considered as a single, homogeneous material, a critical heat flux measurement could be used to evaluate immediately the minimal surface that is going to be burned during the test. However, most external insulation systems are assemblies of several different materials (insulation, cladding etc.) with different properties. The way the system is assembled is also a critical parameter, especially for ventilated air gap systems, like the one used on the Grenfell Tower.

Given the scale of the test benches and the costs to run them, it is difficult to obtain validation data to compare the simulations with experiments. Furthermore, in the considered test benches, it is sometimes difficult to obtain an accurate measurement of the actual HRR, especially when using solid (wood cribs) or liquid (hydrocarbon) fuel. Analytical approach currently used to estimate the HRR/MLR of such type of fire source is designed for an open space fire and is not suitable for a semi-confined room fire. It is also difficult to determine the amount of fuel that burns outside of the combustion chamber. This fraction is of critical importance as it is responsible for the most part of the thermal stress imposed on the surface. Hence, it may be difficult to compare the present results with the existing correlations built on intermediate scale tests [1].

In order for the proposed methodology to be relevant, more experimental data will be required, especially on the true heat release rate to be considered. This might be a challenge given the size of the experimental facilities involved, but there is a need for reliable heat release data in order to consolidate this comparison methodology.

ACKNOWLEDGMENTS

The authors would like to thank Ms. Leïla Chlyeh for her work on the original simulations that led to this study, as well as Mr. Cédric Bourdon for his work and insights on the MATLAB script.

REFERENCES

[1] M.A. Delichatsios, Enclosures and Façade Fires: Physics and Applications. Fire Safety Science– Proceedings of the Eleventh Internationnal Symposium pp, 3-27, IAFSS, 2014.

[2] M. Smolka, B. Messerschmidt, J. Scott and B. le Madec, Semi-natural Test Methods to Evaluate Fire Safety of Wall Claddings, MATEC Web of Conferences, Volume 9 (2013) 1st International Seminar for Fire Safety of Façades.

[3] M. Smolka, L. Boström, T. Crimi, V. Dowling, B. Messerschmidt, K.-W. Park and H. Yoshioka. Principles of Testing and Regulating Fire Safety of Façades, Interflam, 2016.

[4] INTERNATIONAL STANDARD ISO 13785-2, Reaction-to-fire Tests for Façades – Part 2: Large-scale Test. First edition 2002-12-15.

[5] DIN 4102-20 Entwurf. Fire Behaviour of Building Materials and Building Components – Part 20: Particular Verification of the Fire Behaviour of Cladding for External Walls. Edition 2016-06-05.

[6] BRITISH STANDARD BS 8414-1 :2002. Fire Performance of External Cladding Systems – Part 1: Test Method for non-Loadbearing External Cladding Systems Applied to the Face of the Building. Edition 2002-12-13.

[7] Protocole Relatif à l'Essai LEPIR II Complémentaire à l'Arrêté du 10 Septembre 1970 Diffusé par la DSC- le 17 juillet 2014 (suite à GT de 3 juin 2014) -Révision en séance IT 249 du 09 septembre 2014 - Révision par GC labo du 3 juillet 2015.

[8] SP Fire 105, External Wall Assemblies and Façade Claddings – Reaction to Fire, Swedish National Testing and Research Institute, Fire Technology, issue no. 5, Edition 1994-09-09.

[9] C. Abecassis Empsis, Analysis of the Compartment Fire Parameters Influencing the Heat Flux Incident on the Structural Façade, PhD Thesis, University of Edinburgh, Scotland, 2004.

[10] Y.-P. Lee, M. Delichatsios and G. Silcock, Heat Fluxes and Flame Heights in Façades from Fires in Enclosures of Varying Geometry, Proc. Combust. Inst. 31 (2007) 2521-2528.

[11] V. Dréan, R. Schillinger and G. Auguin, Fire exposed façades: Numerical Modelling of the LEPIR2 Testing Facility. MATEC Web of Conferences 46 (2016), 2nd International Seminar for Fire Safety of Façades.

[12] S. Hostikka and G. Bytskov, Numerical Simulations of the ISO 13785-2 Façade Fire Tests. MATEC Web of Conferences 46 (2016), 2nd International Seminar for Fire Safety of Façades.

[13] V. Drean , R. Schillinger, H. Leborgne, G. Auguin and E. Guillaume, Numerical Simulation of Fire Exposed Façades using LEPIR II Testing Facility, Fire Technol. 54 (2018) 943-966.

[14] K. Mc Grattan, S. Hostikka, R. McDermott, J. Floyd, M. Vanella, C. Weinschenk and K. Overholt, Fire Dynamics Simulator User's Guide, NIST Special Publication 1019, Sixth Edition, 2017.

[15] C.H. Lin, Y.M. Ferng and W.S. Hsu, Investigating the Effect of Computational Grid Sizes on the Predicted Characteristics of Thermal Radiation for a Fire, Appl. Thermal Eng. 29 (2009) 2243-2250.

[16] A. Brown, M. Bruns, M. Gollner, J. Hewson, G. Maragkos, A. Marshall, R. McDermott, B. Merci, T. Rogaume, S. Stoliarov, J. Torero, A. Trouvé, Y. Wang, E. Weckman, Proceedings of the First Workshop Organized by the IAFSS Working Group on Measurement and Computation of Fire Phenomena (MaCFP), Fire Saf. J. 101 (2018) 1-17.

[17] R. Keys, Cubic Convolution Interpolation for Digital Image Processing. IEEE Transactions on Acoustics, Speech and Signal Processing, 6 (1981) 1153-1160.

[18] J. Anderson and R. Jansson, Façade Fire Tests – Measurements and Modeling, MATEC Web of Conferences, Volume 9 (2013) 1st International Seminar for Fire Safety of Façades.

Effect of Finger Joint Direction on Wood Ignition in Façade Elements

Makovicka Osvaldova L.[1], *, **Olos M.**[2]

[1] *University of Zilina, Zilina, Slovakia*
[2] *Safirs, s.r.o., Ruzomberok, Slovakia*
**Corresponding author's email: linda.makovicka@fbi.uniza.sk*

ABSTRACT

Statistics show that the number of façade fires has been relatively large in the past few years. The surprising fact is that even in modern high-rise buildings, which are covered with non-flammable façade elements and equipped with high-quality fire-fighting equipment, we have recorded a relatively large number of fires spreading along the façades. They do not have disastrous consequences but they damage buildings, endanger people during evacuation and make the situation more difficult for fire-fighters. Many scientific studies refer to cladding and its functions. Besides its aesthetic function, it serves as thermal, acoustic as well as fire insulation. Building façades are threatened in three ways – by a direct flame from a burning element in front of the building itself, by a fire from the interior of the building, or by a heat radiation source coming from a neighboring building on fire. The choice of material and its application onto the building is important for the fire safety of façades. A wooden spruce façade containing two types of finger joints has been chosen for the experiment and the effect of the joint type using the selected evaluation criteria has been observed. Parts of the façade have been used for the experiment. Samples of 20 x 60 x 250 mm have been made, 15 pieces per each section. A thermal radiator of 1000 W, acted as the heat source, simulating the conditions of thermal radiation coming from a neighboring building. Weight loss and burning rate are the evaluation criteria. The experiment results are represented graphically. The experiment shows that the direction of the finger joints has an impact on the evaluation criteria as well as on the penetration of radiation heat into other parts of the structure thus increasing the probability of its ignition from the radiation heat source.

KEYWORDS: Finger joint, wood ignition, façade elements.

INTRODUCTION

Fire, according to the Slovak legislation [5], is each type of undesirable burning damaging a person´s property, the environment or causing the death or injury of a natural person or an animal; fire is also defined as undesirable burning when a person´s property, the environment and the lives or health of natural persons or animals are at risk. Burning and fire are two phenomena which cannot be considered identical.

In general, burning and fire are intentional and desirable processes with a particular use, burning in the desired time and space and using specified materials – fuel. The energy, which is obtained, is utilized. Fire represents unwanted burning, in unwanted space and time. All materials affected by the fire become fuel [3, 7]. Fire is characterized by several chemical and physical phenomena that are related to each other. According to civil engineers and security experts, it is the cladding which is at fault in the case of a fire. Cladding has various functions and it is, in many cases, made from highly flammable materials [2, 8]. The application of flammable materials (e.g. wood) for cladding has lately been preferred by designers and architects [4, 6, 11]. Their projects and designs require

Proceedings of the Ninth International Seminar on Fire and Explosion Hazards (ISFEH9), pp. 913-920
Edited by Snegirev A., Liu N.A., Tamanini F., Bradley D., Molkov V., and Chaumeix N.
Published by Saint-Petersburg Polytechnic University Press
ISBN: 978-5-7422-6498-9 DOI: 10.18720/spbpu/2/k19-21

further measures to be implemented to prevent a fire. These measures aim to prevent the uncontrolled spread of a fire on the surface or in the cavities. If these measures are implemented, wood can be used without lowering any safety levels in terms of fire protection. These measures can be divided into several categories [3]:

- Material solutions;
- Design solutions;
- Certification;
- Legal solutions in the field of fire protection.

The problem arises with the addition of thermal insulation to buildings using flammable material as well as from an increased demand for wood from an aesthetic and functional point of view. In many countries, special attention is paid to wooden cladding of façades and strict criteria and conditions have been set out for such cladding. In general, it is based on fire scenarios of potential ignition and the subsequent fire of a façade which are shown in Fig. 1 [11].

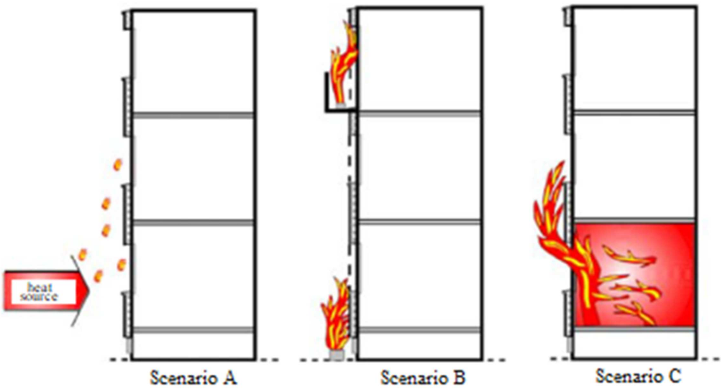

Fig. 1. Fire scenarios for façade fires [11].

Scenario A

The fire spreads from the neighboring buildings onto another building. For a larger cladding the fire risk is limited to an ignition risk assessment when the façade is exposed to a radiant heat source. If the buildings are close to each other, the analysis can be extended - including contact with flame and the flare-up of materials is being observed. This scenario also takes into consideration the spread of the fire from a neighboring building onto other neighboring buildings. For flammable façades, we need to take into consideration the heat from the burning façade - if the façade ignites - as well as radiant heat from cavities and flames coming from the vents on the façade of the neighboring building. Fire protection legislation for this fire scenario also deals with the issue of the distance between the adjacent buildings.

Scenario B

The fire spreads from an external source adjoining the façade (not a neighboring building) e.g. vehicle on fire, litter bin, and so on. A balcony fire might also fall into this category.

Scenario C

A vertical fire spreads through the vents from a fully developed fire inside the building. There is at least one vent on the façade.

Several authors [9, 12] monitored the effect of the construction itself - its surface, smoothness etc. (see Fig. 2), however, the types of joint elements used within the structure have not been monitored yet.

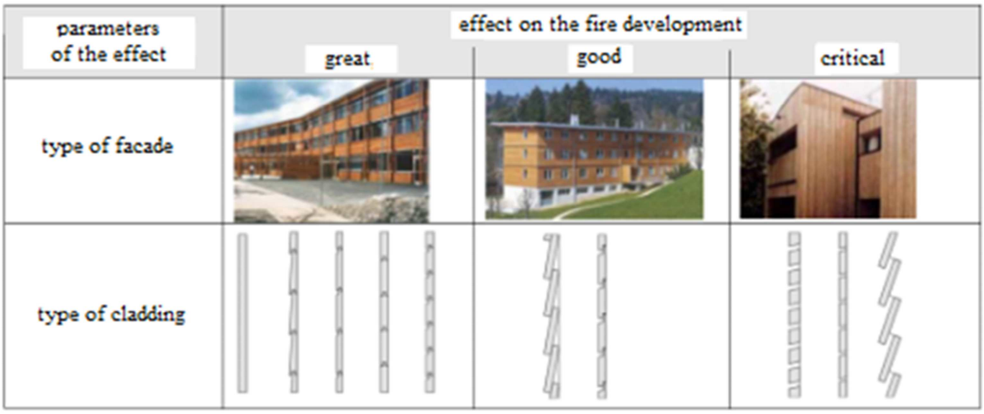

Fig. 2. Examples of parameters affecting fire behavior of multi-story façades [12].

THE EXPERIMENT

The wood of Norway spruce (Picea abies (L) Karst.) was selected for the test. It is the second most widely used wood in Slovakia and the most important one from an economic point of view. Spruce is light, soft, elastic, easy to chop, easy to stain but more difficult to impregnate. The wood is free of defects and typically has symmetric and narrow annual growth rings (1 to 4 mm) with summerwood ratio in the annual ring ranging from 5 to 20 %. Primarily, it is used as construction lumber for above-ground structures. The wood is also used for residential roof structures, farm buildings as well as other special buildings. Spruce lumber is a part of frame constructions of panels for wooden buildings. Spruce wood is easy to dry, it is not prone to shriveling or crinkling [1, 10, 13].

A wooden façade made from spruce and one type of finger joint in two directions were chosen for the experiment. The effect of the finger joint direction in façade elements on the selected evaluation criteria has been observed. The control sample was jointless (compact). The type of joint and its direction is shown in Fig. 3.

Fragments of the façade were used for the experiment - samples of 20 x 60 x 250 mm, 15 pieces per each section (including the control samples). A thermal radiator of 1000 W is used as the heat source simulating the conditions of scenario A – a fire coming from a neighboring building.

The test method is not standard; however, it is flexible and suitable for testing not only different types of finger joints but also different types of wood and wood treatment methods - wood of different age classes, retarding treatment or other aesthetic adjustments of façades and their effect on ignition and the burning process. It is possible to change the delivery of the thermal radiator, or to replace the radiant heat source with a flame heat source. The power output of 1000 W as well as the distance of the sample from the source were, after carrying out some preliminary experiments, set to the values given above to prevent the sample from burning down – partially or completely. Thanks to these parameters, it is possible to observe whether the direction of the finger joint influences the ignition and burning of the sample that constitutes a part of the façade.

The thermal radiator is warmed up, - after reaching the given temperature, the samples are exposed to heat for 10 minutes. Fig. 4 shows the direction of the thermal radiator and the sample. The sample is placed 40 mm below the lower edge of the thermal radiator.

The reason for doing so is a follow-up evaluation of the experiment, which is not the subject of this article. The whole surface of the sample was exposed to the heat of the thermal radiator. The finger joint is located in the center of the sample. The apparatus is shown in Fig. 4.

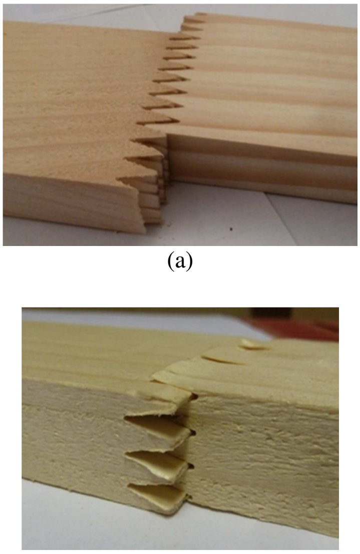
(a)

(b)

Fig. 3. Finger joint: (a) vertical; (b) horizontal.

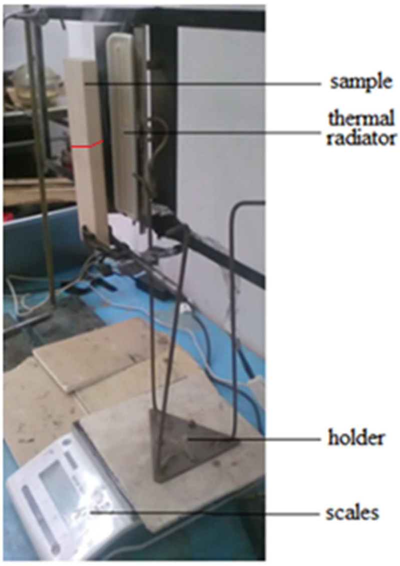

Fig. 4. The apparatus – exposure of samples to radiant heat.

Weight loss and burning rate are the evaluation criteria. Weight loss was calculated according to the following Eq. (1),

$$\delta_m(\tau) = \frac{\Delta m}{m(\tau)} 100 = \frac{m(\tau) - m(\tau + \Delta\tau)}{m(\tau)} 100 \ (\%), \tag{1}$$

where $\delta_m(\tau)$ is the relative weight loss at a time τ, %, $m(\tau)$ is the sample weight at a time τ, g, $m(\tau+\Delta\tau)$ is the sample weight at a time $\tau + \Delta\tau$, g, Δm is the weight difference, g.

Relative burning rate will be determined according to the relation Eq. (2) and Eq. (3),

$$v_r = \left| \frac{\partial \delta_m}{\partial \tau} \right| (\%/\mathrm{s}), \tag{2}$$

or numerically

$$v_r = \frac{|\delta_m(\tau) - \delta_m(\tau + \Delta\tau)|}{\Delta\tau} \ (\%/\mathrm{s}), \tag{3}$$

where v_r is the relative burning rate, %/s, $\delta_m(\tau)$ is the relative weight loss at a time τ, %, $\delta_m(\tau+\Delta\tau)$ is the relative loss of weight at a time $\tau + \Delta\tau$, %, and $\Delta\tau$ is the time interval where the weights are being subtracted, s.

EVALUATION AND DISCUSSION

The experiment confirmed that the finger joint direction has an impact on the evaluation criteria and therefore on the penetration of radiant heat into other parts of the structure. This means that the finger joint direction affects the possibility of ignition from a heat source. When evaluating the experiment, it is necessary to point out that special attention has been paid to the homogeneity of all samples: their density (360 ± 10 kg/m^3), moisture level (12 ± 2 %) and the quality of woodworking. The term homogeneity is understood as a selection of samples according to their density in the given interval, keeping the samples air-conditioned, since the density and moisture level of the samples could influence the experiment results and the finger joint direction does not need to manifest itself if not selected properly. These factors could have had an impact on the experiment results. This is why the samples were homogenized so that the impact of the type of finger joint and its direction would be the most clearly manifested. Photographic documentation was not done throughout the tests. The continuous burning rate and the change in weight were the only parameters recorded during the test, at 10 second intervals.

As we can see from Fig. 5, the effect of the finger joint direction manifests itself from the very first minutes of the experiment. From the very first minute (which is relatively early), an increase in weight loss for the vertical finger joint samples was observed. In the second minute of the experiment, this increase is noticeable, and it is rising throughout the whole experiment.

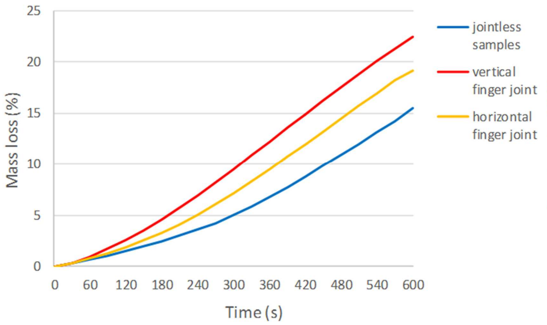

Fig. 5. The course of weight loss for a test sample and the effect of finger joint direction on weight loss.

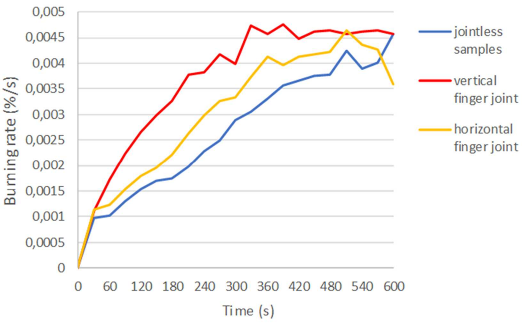

Fig. 6. Burning rate course of a control sample and the effect of finger joint direction on burning rate.

There is a constant difference between the joint-less samples as well as between the finger joint ones. The final weight losses are as follows: jointless samples 15.51 %, horizontal finger joint samples 19.13 % and vertical finger joint samples 22.47 %. For the horizontal finger joint sample, the difference is 3.98 % compared to the control sample, for the vertical finger joint one it is 7.32 %, and there is a difference of 3.34 % when comparing the two types of finger joints.

When assessing the second evaluation criterion (burning rate) we can come to similar conclusions as for weight loss. An increase in the burning rate can be observed immediately after the first minute of the experiment (see Fig. 6). The burning rate (for the control samples as well as the finger joint samples) gradually increases due to the exposure to the heat source. The increase in the burning rate is much more abrupt for the finger joint samples compared to the control samples. As it is obvious from Fig. 6, the burning rate is influenced by the finger joint direction; it is more intense for the vertical finger joints than the horizontal ones. In the case of vertical finger joints, the most intense burning rate was reached at the 330th second of the experiment and at the 510th second of the experiment for the horizontal finger joint. The burning rate for the control samples was recorded at the end of the experiment at the 600th second.

The peak values of the evaluation criteria are stated in Table 1. In addition to the basic ones, it also includes the time necessary to achieve the burning rate peak and the ratio of these two variables (maximum burning rate and the time when this value was reached). This table clearly shows the effect of finger joint direction on the evaluation criteria. The differences in the values were caused by two factors: a weak heat source and a very short time interval. In case of fire (a more intense heat source and a longer time of exposure), these disparities will certainly be higher.

The a/b ratio has been chosen as an auxiliary indicator. It is an indicator that is used during some tests to determine the fire protection properties of wood. If the maximum burning rate is reached in the first "minutes" (at the beginning of the experiment), the material has a negative assessment for fire protection purposes compared to the same burning rate value reached in the middle or at the end of the experiment. (e.g. burning rate of 10 is achieved at the 1st , 5th and 10th minute of the experiment then the ratio is 10, 2, 1. The lower the ratio (a/b) is, the better the assessment of the material (finger joint) is.

Table 1. Peak value of the evaluation criteria

Evaluation criteria (peak value)	Type of construction		
	Jointless samples	Vertical finger joint	Horizontal finger joint
Mass loss (%)	15.51	19.13	22.47
a Burning rate (%/s)	0.004375	0.004638	0.004776
b Time max. burning rate (s)	600	510	420
Ratio **a/b***10^6	7.29	9.09	11.4

The burning rate has decreased/stabilized for the finger joints samples. For the vertical finger joints, this happens in approximately the 420th second of the experiment and approximately in the 540th second of the experiment for the horizontal finger joints. This slowdown in the burning rate can be a result of a charred layer being created directly inside the joint and functioning as an “insulator”.

The charred layer slows down the burning rate, however, the degradation of the finger joint (for both types of joints – see Fig. 7 and Fig. 8) and the material continues even if the process has slowed down.

Fig. 7. Charred layer – vertical finger joints.

Fig. 8. Charred layer – horizontal finger joints.

Carbonization sets in sooner for horizontal finger joint samples - it covers a larger surface but it does not have such an important impact. It just brings about a constant charring rate in a relatively long period of time. In the case of horizontal finger joints, a steeper decrease in the burning rate can be observed as a consequence of a layer of compact wood coming after the charred layer and representing an “obstacle” preventing heat transfer from advancing.

PSPP software was used to calculate the descriptive properties of the statistical data where the group called "finger joints - width" is labeled as VFJ and the group HFJ is short for "finger joints - thickness". Weight loss was the only parameter subject to the statistical evaluation (see Table 2 and Fig. 9).

Table 2. Outputs of descriptive statistics

	N	Mean	S.E. Mean	Std. Dev.	Variance	Kurtosis
VFJ	15	21.44	0.31	1.31	1.72	-1.10
HFJ	15	19.15	0.20	0.77	0.59	-0.19

	S.E. Kurt.	Skewness	S.E. Skew	Range	Min	Max	Sum
VFJ	1.12	0.36	0.58	4.06	19.73	23.78	321.65
HFJ	1.12	0.05	0.58	2.81	17.63	20.44	287.23

Valid cases ′15; cases with missing values (s) = 0

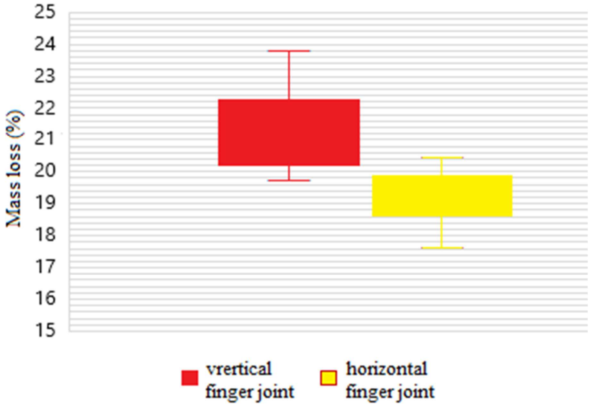

Fig. 9. Box plot for the given groups.

The statistical data show that the weight loss was greater for VFJ samples compared to HFJ samples. VFJ samples showed a larger variability as evidenced by a higher standard deviation (SD) = 1.31 compared to the second group where the SD = 0.77. Maximum and minimum weight losses ranged almost in the same intervals for both groups. In general, they were slightly above and below the median values. Kurtosis for the VHJ group reached -1.10. It indicates that the values in the population deviate from the normal distribution in the population and the minus indicates that the distribution is shallower i.e. the values in the population are lower or higher than the mean. On the other hand, kurtosis for the HFJ group was significantly lower, i.e. -0.19, so most data were close to the mean. As for skewness, both VFJ and HFJ samples reach values very close to 0 (0.36 and 0.05), therefore the data in the population are distributed normally.

CONCLUSION

A relatively simple experiment confirmed that attention needs to be paid not only to façades and cladding material but also to the type of joint used. The evaluation criteria confirmed different behavior patterns of finger joints made from spruce wood and the fact that the finger joint direction affects the test results. In order to evaluate the selected evaluation criteria, a heat source with a lower intensity has been chosen. The wood did not even ignite, which was the aim of the experiment. Despite this fact, the evaluation criteria confirm that the finger joint direction has an impact on the heat transfer through the joint. We should bear this fact in mind in practice. It is recommended that the finger joint made from a flammable material is protected by a fireproof material or coating from the other side to prevent the rapid ignition of the reverse side of the façade where, in the case of a vented type of a façade, it may result in the very rapid spread of the fire along the façade.

The maximum burning rate for the vertical finger joints is achieved since the joint creates a direct heat bridge (free of obstacles) at a length of 220 mm. Although the joint is glued, radiant heat breaks through that length/surface of 4400 mm^2 more easily than in the case of horizontal finger joint creating an obstacle by its own teeth.

It is necessary to pay attention to other types of joints, e.g. metal fasteners, too. Metal fasteners may conduct heat faster than the surrounding material or its joint. As the experiment proved, the form of the joint may influence the spread and the speed of fire. Therefore, we also recommend, by means of a simple test, to test the other types of joints that are commonly applied onto façades. Attention should be paid to glued joints as well as the materials which form the load-bearing structure to which the elements of the façade are fixed.

REFERENCES

[1] C.B. Ong, W.S. Chang, D. Brandon D, M. Sterley, M.P. Ansell, P. Walker, Fire performance of hardwood finger joints. In: WCTE 2016 - World Conference on Timber Engineering. Vienna University of Technology, 2016.

[2] R. Lesko, M. Lopusniak, Regulative and Standard Requirements on Façades in Slovakia and Their Mutual Comparison with Selected European Countries, In: Proceedings of 2nd International Seminar for Fire Safety of Façades, Lund: EDP Sciences, 2013, pp. 1–8.

[3] A. Osvald, Wood Fire Protection, In: Fire protection, safety and security 2017, International scientific conference, Conference Proceedings, Zvolen, Publisher TUZVO in Zvolen, 2017, pp. 193–200.

[4] J.C.F. Walker, Primary Wood Processing, Springer, Dordrecht, 2006, 596 P.

[5] Act No. 314/2001 Coll. on fire protection as amended.

[6] W. Yu, Application of multi-objective genetic algorithm to optimize energy efficiency and thermal comfort in building design, Energy and Buildings 88 (2015) 135–143.

[7] R.S. Williams, Weathering of wood. In: Handbook of Wood Chemistry and Wood Composites, 2005, pp. 139-185, CRC Press.

[8] W. Sonderegger, K. Kranitz, C.T. Bues, P. Niemz, Aging effects on physical and mechanical properties of spruce, fir and oak wood, J. Cultural Heritage 16 (2016) 883–889.

[9] B.L. Östman, Fire safety in timber buildings. First draft comments, 2009.

[10] T. Gabor, Testing of selected wooden joints for heat source reaction, Diploma thesis, University of Zilina, Zilina, Slovakia, 2018.

[11] I.Kotthoff, Brandschutz im Holzbau, 9. DGfH-Brandschutztagung, Würzburg Okt., 2001, http://www.lignum.ch (accessed 15 April 2017).

[12] K.P. Schober, I. Matzinger, Brandschutztechnische Ausführung von Holzfassaden. proHolz Austria (Hrsg.) Arbeitsheft 8/06, 2006 http://www.lignum.ch.

[13] C.B. Ong, W.S. Chang, M.P Ansell, D. Brandon, M. Sterley, P. Walker, Bench-scale fire tests of Dark Red Meranti and Spruce finger joints in tension, Construct. Build. Mater. 168 (2018) 257–265.

Simplified Methodology to Predict Polyurethane Foam Mass Loss Rate in the Cone Calorimeter

Leroy A.[1,2], Erez G.[1,3], Suzanne M.[1,] *, Thiry-Muller A.[1,3], Collin A.[3], Boulet P.[3]

[1] Laboratoire Central de la Préfecture de Police, Paris, France
[2] École Nationale Supérieure de Techniques Avancées Bretagne, Brest, France
[3] Laboratoire Énergies, Mécanique Théorique et Appliquée, Nancy, France
**Corresponding author's email: mathieu.suzanne@interieur.gouv.fr*

ABSTRACT

The work presented here is the first step of a larger study aiming at improving the description of fuel mass loss rate (MLR) in fire simulations, through multi-scale experimentation and model development. The final model, based on cone calorimeter scale measurements and on heat transfer modelling, is developed to predict full-scale fire spread over polyurethane foam slabs. In the present paper, small-scale tests performed in cone calorimeter are described, as well as a model predicting the material mass loss rate as a function of heat flux from the cone heater.

Several irradiance levels were tested (from 20 to 70 kW/m^2), and two simple mathematical functions were chosen to describe experimental curves of mass loss rate. Correlations between the functions parameters and cone calorimeter heat fluxes were computed, thus producing a model able to predict MLR as a function of time and irradiance level. The numerical results are in accordance with experimental data for intermediate heat fluxes (approximately 40 to 70 kW/m^2). For lower heat fluxes, the model fails (by construction) to reproduce the combustion decay. This is not considered to be a problem, as the range of heat fluxes for which the correlations are valid can be easily estimated from the results. In conclusion, the proposed methodology allows to predict MLR results in cone calorimeter conditions (e.g. only for 5 cm-thick samples) for various heat fluxes. After adding other sub-routines, it will be coupled to a heat transfer model in order to predict fire spread over polyurethane foam slabs.

KEYWORDS: Cone calorimeter, fire testing, modelling.

NOMENCLATURE

a	coefficient in the hyperbolic tangent function (s^{-1})
MLR	mass loss rate (kg/s)
t	time (s)

Greek

ϕ	incident heat flux (kW/m^2)
σ	standard deviation (s)

Subscripts

1/3	time when one third of the mass has been burned
end	time of flame out
first	for the first stage of MLR
ign	time of ignition
max	maximum value of MLR

INTRODUCTION

Numerical simulations are now a major tool for fire engineers and investigators. They can produce valuable results, provided appropriate data and models are used. Among these, fuel mass loss rate

Proceedings of the Ninth International Seminar on Fire and Explosion Hazards (ISFEH9), pp. 921-929
Edited by Snegirev A., Liu N.A., Tamanini F., Bradley D., Molkov V., and Chaumeix N.
Published by Saint-Petersburg Polytechnic University Press
ISBN: 978-5-7422-6498-9 DOI: 10.18720/spbpu/2/k19-43

(MLR) is particularly important. This is usually done by prescribing a time dependent MLR (based on full-scale tests or engineering calculations), or by modelling pyrolysis (based on material properties and dedicated matter scale models). The first approach is often used for its simplicity, but is limited by the fact that experimental data may not be fully representative of the scenario being investigated. The second approach is more versatile (MLR is calculated based on the conditions in the simulation), but requires extensive input data, model calibration and computational resources. As long as pyrolysis models are not usable for engineering applications, an alternative seems necessary. The approach proposed here is to adapt fuel mass loss rate to the changes in heat flux during the simulation. This would be done using bench-scale MLR experimental data, thus avoiding the complexity of modelling chemical reactions in the condensed phase. This compromise would thus require a heat transfer model and a MLR model (to predict mass loss based on irradiance level, a so-called "thermal model" [1]). The work presented here focuses on the later, by describing a simplified approach to predict MLR at various heat fluxes at cone calorimeter scale.

The fuel chosen to illustrate this modelling approach is polyurethane (PU) foam, as it is widely used in upholstered furniture, and is involved in many residential fires. Its burning behaviour is thus crucial to understand and model, for fire safety engineering but also for fire investigation. Upholstered furniture and PU foams have long been studied [2–6]. Although numerous models are available [4, 7–10], none of them suited the purpose described earlier. New data were thus acquired through an extensive cone calorimeter experimental campaign, as described in the next section, and used to build a model to predict MLR as a function of time and irradiance level.

EXPERIMENTAL STUDY

Experimental setup

The polyurethane foam used here had a density of 30 kg/m^3 (water blown, 2/3 polyol and 1/3 toluene diisocyanate). Tests were performed in the cone calorimeter according to the ISO 5660 standard [11] (5 cm thick samples), except for the specimen holder. For the latter, three setups from the literature were tested:

1. Aluminium foil with steel frame [11, 12];
2. Aluminium only, on all sides [12];
3. Aluminium only, on the back and bottom centimetre of the sides [6].

The second one was chosen because it showed the highest repeatability, was more convenient to use (compared to the first configuration), and did not allow for side burning (as opposed to the third configuration). In addition to the aluminium foil, samples laid on a 1 cm thick gypsum substrate to protect the load cell.

Heat release rates and mass loss rates were measured, and all the experiments were videotaped. For the tests used here, irradiance levels ranged from 20 to 70 kW/m^2, and experiments were repeated at least three times.

Results

Only mass loss rate measurements will be presented here, as it was chosen to focus on the prediction of MLR (rather than heat release rate [HRR]). Indeed, the objective is to provide a fire spread model based on heat transfers: it seems a reasonable approximation to consider that mass loss mainly depends on heat transfers (and chemistry for material decomposition), whereas it is not for heat release, which can be more strongly affected by oxygen concentration for example. Moreover, mass loss is easier to measure than energy release, especially at larger scales. Similarly, the MLR is calculated with less parameters than the HRR [11]. Consequently, with measuring devices of equivalent precision, the uncertainties on HRR are higher than on MLR.

MLR were post-processed using a low frequency filter defined as

$$MLR_{filtered}(t) = 0.8MLR_{raw}(t-1) + 0.2MLR_{raw}(t) \tag{1}$$

The filter had to be efficient enough to soften the fluctuations of the signal without losing information such as the maximum value of MLR. This post-processing step is illustrated in Fig. 1.

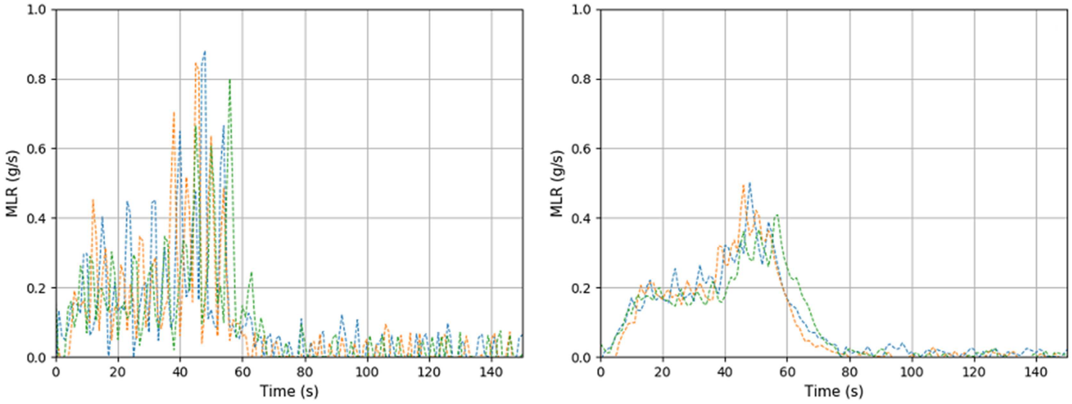

(a)

(b)

Fig. 1. Processing of mass loss rate data using a low frequency filter (irradiance level equal to 70kW/m^2, one dashed curve per repeated test). (a) Raw data; (b) Filtered results.

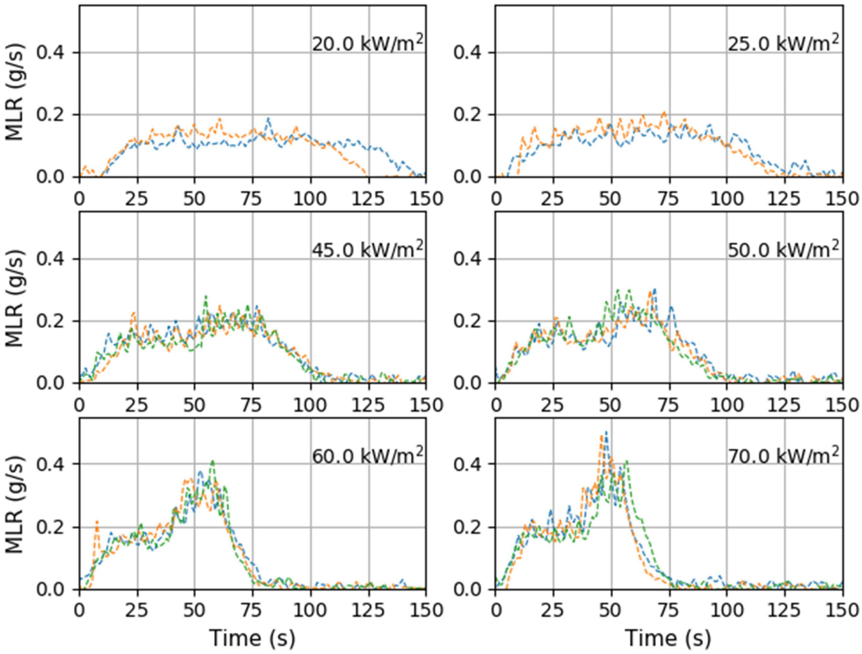

Fig. 2. Mass loss rate for polyurethane foam during cone calorimeter tests at irradiance levels ranging from 20 to 70 kW/m^2 (one dashed curve per repeat).

The results for irradiance levels from 20 to 70 kW/m^2 are shown in Fig. 2. Two stages of MLR can be distinguished for high values of irradiance level (greater than 45 kW/m^2). The first stage corresponds to a steady phase quickly reached after ignition, followed by a second stage where the

MLR grows toward a maximum value. These observations are in accordance with previous results [6] and a proposed decomposition scheme for polyurethane foam [13]. For lower irradiance levels, the MLR curves are quasi-stationary. Figure 2 also shows a good repeatability for the tests.

DATA ANALYSIS

Modelling functions

Figure 3 shows a schematic representation of MLR results observed for irradiance levels higher than 45 kW/m^2. As mentioned before, PU burning in cone calorimeter can be divided in two stages (see solid red and hatched blue fills): a quasi-steady phase (see MLR_{first}) followed by a rapid increase to a maximum MLR ($MLR_{\max}$). The first stage accounts for approximately one third of the mass loss, so its end time is referred to as $t_{1/3}$.

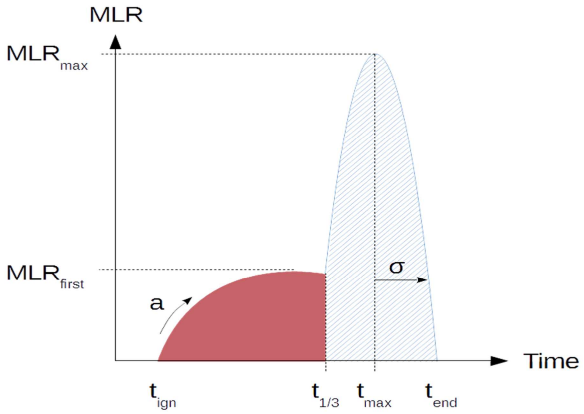

Fig. 3. Schematic view of the mass loss rate results observed for irradiance levels higher than 45 kW/m^2. The parts referred to as first and second stages are represented in red (solid) and blue (hashed) respectively.

In order to describe these two stages, simple mathematical functions were chosen. The first part (see solid red part in Fig. 3) could be approximated by an exponential or a hyperbolic tangent function. Both options were evaluated and the later showed a better agreement with the experimental data. This part of the mass loss rate was thus modelled using

$$MLR(t) = MLR_{first} \tanh(a\,t), \tag{2}$$

where MLR_{first} is the asymptote of the hyperbolic tangent function (i.e. the MLR for the steady phase) and a (s^{-1}) describes the growth of the curve to its asymptote (the higher the value of a, the faster the growth toward MLR_{first}).

The second part of experimental MLR curves (see hatched blue part in Fig. 3) fits well with a Gaussian function given by

$$MLR(t) = MLR_{\max} \exp\left(-\frac{(t - t_{\max})^2}{2\sigma^2}\right), \tag{3}$$

where $MLR_{\max}$ is the maximum MLR value, $t_{\max}$ is the time when it is reached (mean of the Gaussian function), and σ the standard deviation (the width of the curve). The higher the irradiance level, the smaller $t_{\max}$ and σ.

CORRELATIONS WITH HEAT FLUX

In order to build a model predicting MLR based on incident heat flux from the cone heater, correlations between irradiance level and the parameters listed in the previous section (see also Fig. 3) were investigated. The authors note that here irradiance level refers to the radiative heat flux delivered by the cone calorimeter according to the ISO standard [11]: other important factors (e.g. heat flux from the flame) should be accounted for in the future to give more accurate results.

For each parameter, values were extracted from average test results for three irradiance levels (25, 45 and 60 kW/m^2), and correlated to the heat flux. The other test results (i.e. 20, 50 and 70 kW/m^2) will be used to assess the predictive capability of the model.

Times of ignition and flameout, t_{ign} and t_{end} respectively, are based on the observations of the test operator (i.e. when the specimen ignited and when it extinguished). They were correlated to the incident heat flux as shown in Table 1 (where all equations are summarized).

Table 1. Examples of empirical correlations (based on 25, 45 and 60 kW/m^2 test results)

Parameter (unit)	Parameter values based on	Correlation (heat flux ϕ in kW/m^2)	
t_{ign} (s)	User input during the test (from first to last visible flames)	$1/t_{ign} = 0.0159\phi - 0.252$	(4)
t_{end} (s)		$t_{end} = -1.89\phi + 188$	(5)
$t_{1/3}$ (s)	Minimization of Eq. (12)	$t_{1/3} = -0.362\phi + 63.0$	(6)
MLR_{first} (g/s)	Fit of MLR using Eq. (2) (for $t_{ign} < t < t_{1/3}$)	$MLR_{first} = 0.000814\phi + 0.114$	(7)
a (s^{-1})		$a = 2.81\phi + 49.4$	(8)
$MLR_{\max}$ (g/s)	Fit of MLR using Eq. (3) (for $t_{1/3} < t < t_{end}$)	$MLR_{\max} = 0.0812\exp(0.0228\phi)$	(9)
$t_{\max}$ (s)		$t_{\max} = \text{-}0.586\phi + 90.1$	(10)
σ (s)		$\sigma = -0.425\phi + 38.3$	(11)

The time to burn one third of the mass, $t_{1/3}$, corresponds to time t_i which minimizes the following function:

$$\left| \frac{1}{3}\int_0^{t_{end}} MLR(t)dt - \int_0^{t_i} MLR(t)dt \right|. \tag{12}$$

This procedure is illustrated with data from 60 kW/m^2 tests in Fig. 4 (top graph).

MLR for the first stage (MLR_{first}) was computed by fitting the chosen function (see Eq. (2)) on experimental data from t_{ign} to $t_{1/3}$, as illustrated in Fig. 4 (bottom left). This also provided parameter a. Equation (7) (MLR_{first} as a function of the irradiance level) is shown in Fig. 5 (left).

The second stage was also fitted using the function described earlier (see Eq. (3)), to provide values for $MLR_{\max}$, $t_{\max}$ and σ. This is illustrated in Fig. 4 (bottom right graph), and the correlation in

Eq. (9) is shown in Fig. 5 (right plot). Note that the standard deviation σ will be used to adjust the function in the next section (and can thus be modified).

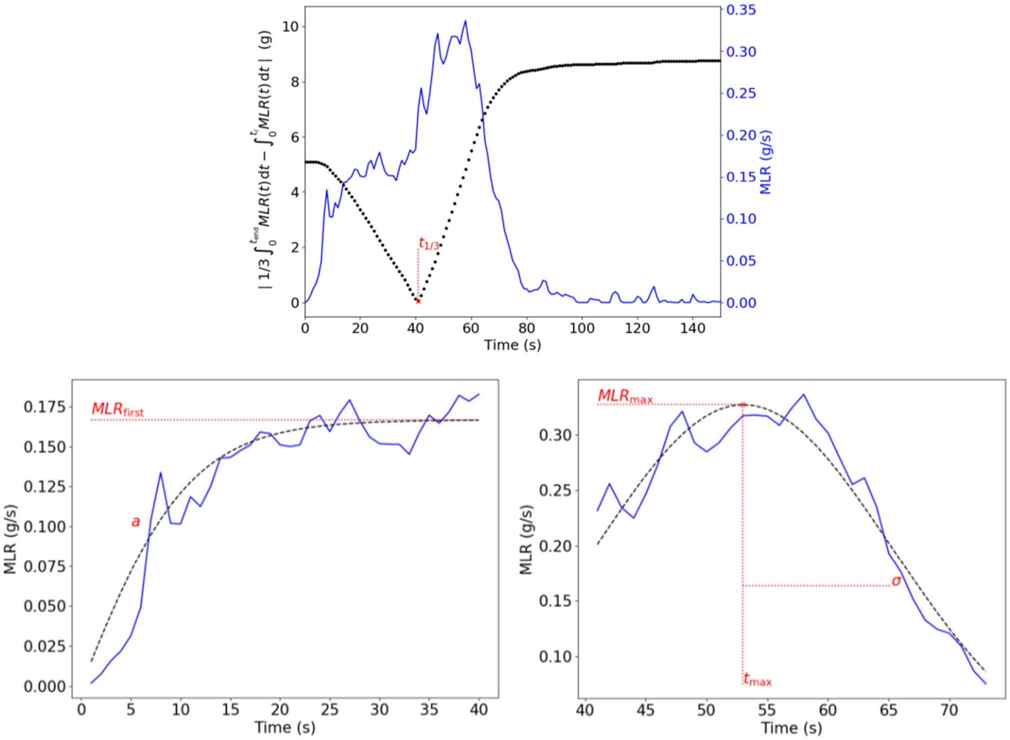

Fig. 4. Examples of how parameters were determined from average data for the 60 kW/m^2 tests. Top: $t_{1/3}$; bottom left: MLR_{first} and a; bottom right: $MLR_{\max}$, $t_{\max}$ and σ.

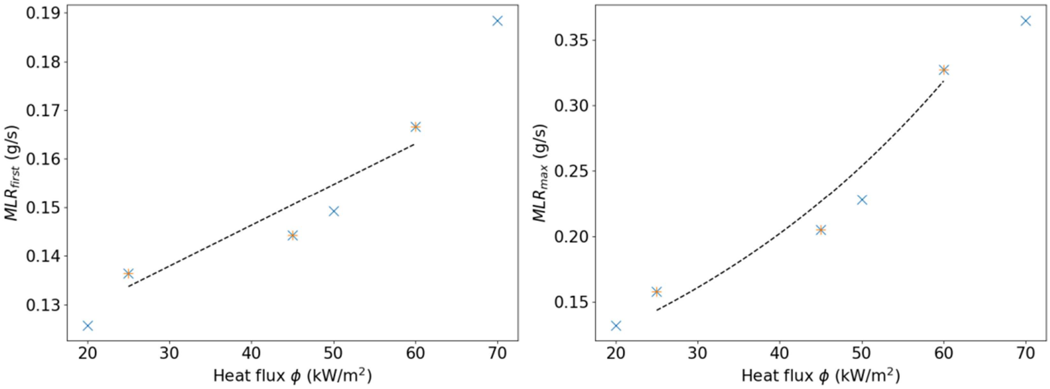

Fig. 5. Values of mass loss rate for the first stage (MLR_{first}) and maximum MLR ($MLR_{\max}$). Dashed line for correlations (see Eq. (7) and (9), respectively), symbols for experimental data (points with a + sign were used to compute the correlations).

MASS LOSS RATE PREDICTION

The previous section showed that key quantities describing the foam burning behaviour correlate well with the incident heat flux (see Table 1). Two modelling functions were also chosen to describe the stages of the foam combustion (see Eq. (2) and (3)). To summarize, the model follows

$$MLR(t,\phi) = \begin{cases} MLR_{first}(\phi)\tanh\left(a(\phi)\,t\right), & t < t_{1/3} \\ MLR_{\max}(\phi)\exp\left(-\dfrac{(t-t_{\max})^2}{2\sigma^2}\right), & t \geq t_{1/3} \end{cases} . \tag{13}$$

The junction at $t_{1/3}$ is made by satisfying

$$MLR_{first}(\phi)\tanh\left(a(\phi)t\right) < MLR_{\max}(\phi)\exp\left(-\frac{(t-t_{\max})^2}{2\sigma^2}\right). \tag{14}$$

If needed, σ is increased until this condition is verified. The resulting standard deviation is shown in Fig. 6, along with the original correlation (see Eq. (11) in Table 1).

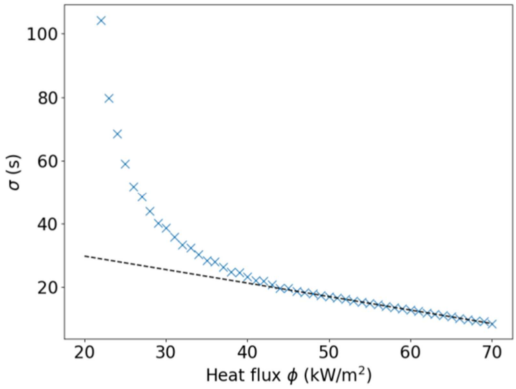

Fig. 6. Standard deviation for the Gaussian function, see Eq. (3). Dashed line: initial correlation, Eq. (11); symbols: corrected values to satisfy Eq. (12).

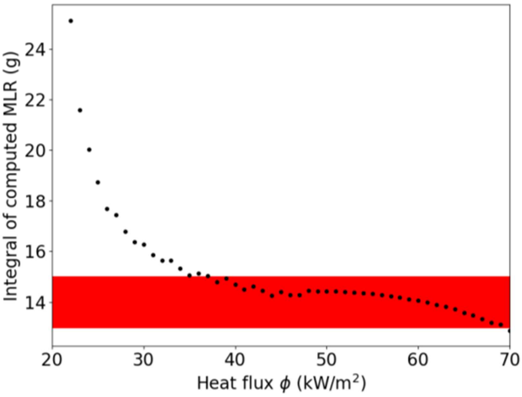

Fig. 7. Burned masses according to the model (black dots). The red rectangle shows the mass of the tested samples (14±1 g).

As can be seen, the correction to satisfy Eq. (12) yields very large σ values for low heat fluxes, which in turn produce unrealistic results. This was expected because the two-stage behaviour (on which the model presented here is based) was not observed at 20 or 25 kW/m^2. However, it is believed that a simple threshold would allow determining the lowest irradiance level beyond which the model is not valid anymore (e.g. here around 40 kW/m^2). This limit is in agreement with the predicted burned mass, shown in Fig. 7, as it is consistent with the sample mass (see red rectangle, 14±1 g) for heat fluxes higher than 40 kW/m^2.

Comparisons with experiments at 20, 50 and 70 kW/m^2 (i.e. that were not used to compute the correlations) are shown in Fig. 8. As expected, prediction at 20 kW/m^2 is poor (combustion decay is not captured). Results at higher heat fluxes (50 and 70 kW/m^2 in Fig. 8, but also 45 and 60 kW/m^2) are far more consistent with cone calorimeter data. This confirms that this simple approach can produce valid MLR predictions at intermediate irradiance levels (i.e. approximately 40 to 70 kW/m^2).

CONCLUSIONS

Numerous tests were performed in cone calorimeter, at irradiance levels ranging from 20 to 70 kW/m^2. The results, and more specifically mass loss rates, were used to determine modelling functions that could describe MLR evolution in time. Two stages were identified for irradiance level greater than 45 kW/m^2 (in accordance with the literature [6,13]). A hyperbolic tangent function (Eq. (2)) and a Gaussian function (Eq. (3)) were chosen to model the first and second part respectively. The parameters for each function were then correlated to the heat flux (see Table 1), using part of the experimental data (25, 45 and 60 kW/m^2). The resulting equations (Eq. (13)) were used to predict MLR from 20 to 70 kW/m^2. As expected, the agreement is poor for low heat fluxes (approximately below 40 kW/m^2) because foam did not display the two-stage behaviour (see data for 20 and 25 kW/m^2 in Fig. 2). For higher irradiance levels, predicted MLR are close to experimental values, even for tests not used when establishing the correlations (i.e. 50 and 70 kW/m^2, see Fig. 8).

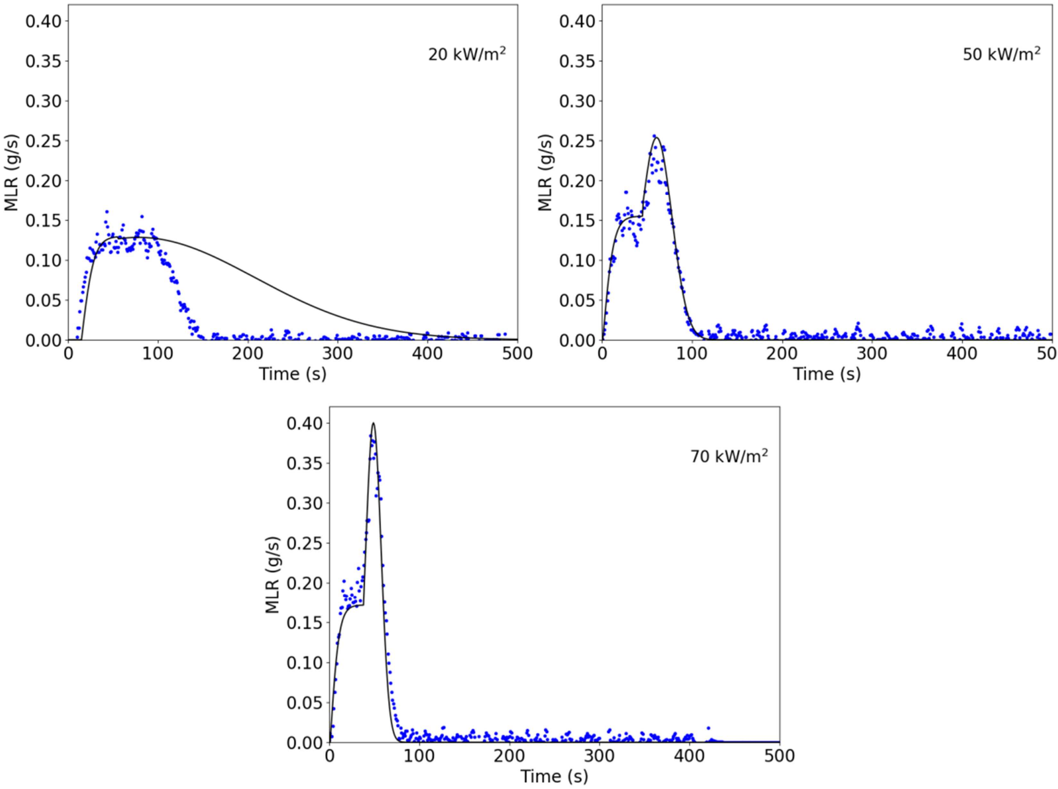

Fig. 8. MLR predictions (solid black lines) compared to experimental data (blue points). Top left: 20 kW/m^2; top right: 50 kW/m^2; bottom: 70 kW/m^2.

The methodology presented here should allow predicting the MLR at cone calorimeter scale for various heat fluxes, based only on a few measurements. The parameters in Table 1 still have to be correlated to the net heat flux experienced by the sample, and not only the incident heat flux from the cone heater (e.g. by accounting for heat flux from the flame [4, 14] or for sample regression during the tests [15]). Application to full-scale foam combustion will require additional models, for thickness scaling for example [4].

When finalized, the proposed modelling approach is meant to be coupled to a heat transfer model predicting the incident heat flux at the fuel surface (based, for example, on flame size/geometry, fuel type, etc.), in order to predict MLR, and consequently flame spread. The same methodology could also be applied to other fuels, by choosing appropriate functions depending on the observed fire behaviour.

ACKNOWLEDGMENTS

The entire staff of the Fire Engineering division at LCPP is greatly acknowledged for their help, especially Ms Delphine Cendra, Sylvie Dupont and Adissa Traoré for their contribution to the experimental part of this work.

REFERENCES

[1] F.V. Lundström, P. van Hees, É. Guillaume, A review on prediction models for full-scale fire behaviour of building products, Fire Mater. 41 (2017) 225–44.

[2] L. Bustamante Valencia, Experimental and numerical investigation of the thermal decomposition of materials at three scales: application to polyether polyurethane foam used in upholstered furniture phdthesis, PhD thesis, École nationale supérieure de mécanique et d'aérotechnique, Poitiers, France, 2009.

[3] M. Ravey, E.M. Pearce, Flexible polyurethane foam. I. Thermal decomposition of a polyether-based, water-blown commercial type of flexible polyurethane foam, J. Appl. Polym. Sci. 63 (1997) 47–74.

[4] B. Sundström, CBUF, Fire Safety of Upholstered Furniture - the final report of the CBUF research programme, 1995.

[5] J.U. Ezinwa, L.D. Robson, M.R. Obach, D.A. Torvi, E.J. Weckman, Evaluating Models for Predicting Full-Scale Fire Behaviour of Polyurethane Foam Using Cone Calorimeter Data, Fire Technol. 50 (2014) 693–719.

[6] L.D. Robson, Scalability of Cone Calorimeter Test Results for the Prediction of Full Scale Fire Behavior of Polyurethane Foam, University of Saskatchewan, Saskatoon, Canada, 2014.

[7] U. Wickström, U. Göransson, Full-scale/Bench-Scale correlations of wall and ceiling linings, Fire Mater. 16 (1992) 15–22.

[8] B. Messerschmidt, P. van Hees, U. Wickström, Prediction of SBI (Single Burning Item) test results by means of cone calorimeter test results, Interflam'99 (Edinburgh, UK: Interscience Communications Ltd), pp 11–22, 1999.

[9] T. Hakkarainen, M. A. Kokkala, Application of a one-dimensional thermal flame spread model on predicting the rate of heat release in the SBI test, Fire Mater. 25 (2001) 61–70.

[10] A.S. Hansen, Prediction of heat release in the single burning item test, Fire Mater. 26 (2002) 87–97

[11] ISO 5660-1 2002 Reaction-to-fire tests – Heat release, smoke production and mass loss rate - Part 1: Heat release rate (cone calorimeter method).

[12] V. Babrauskas, W.H. Twilley, W.J. Parker, The effects of specimen edge conditions on heat release rate, Fire Mater. 17 (1993) 51–63.

[13] W.M. Pitts, Role of two stage pyrolysis in fire growth on flexible polyurethane foam slabs, Fire Mater. 38 (2014) 323–38.

[14] F. Hermouet, Développement d'une approche innovante de modélisation de la cinétique de décomposition thermique des matériaux solides en espaces confinés sous-ventilés. Application aux incendies en tunnel, École nationale supérieure de mécanique et d'aérotechnique, Chasseneuil-du-Poitou, France, 2015.

[15] W. M. Pitts, Applied Heat Flux Distribution and Time Response Effects on Cone Calorimeter Characterization of a Commercial Flexible Polyurethane Foam, Fire Technol. 50 (2014) 635–72.

Smoke Particle Size Distribution in Pine Wood Fires

Mustafa B.G.[1,2], Mat Kiah M.H.[1], Andrews G.E.[1,] *, Phylaktou H.N.[1], Li H.[1]

[1] *School of Chemical and Process Engineering, University of Leeds, Leeds, United Kingdom*
[2] *Chemical Engineering, University of Maiduguri, Maiduguri, Borno State, Nigeria*
**Corresponding author's email: profgeandrews@hotmail.com*

ABSTRACT

There is a growing concern about the impact of ultra- fine particulates released from fires on the health of humans in fires and the related environmental pollution. However, there is no requirement to measure particle mass or number from legislated test fires and hence there is minimum information in the literature on this toxic hazard in fires. This work compares particulates generated from freely ventilated and restricted ventilation pine wood fires using the cone calorimeter. The standard cone calorimeter with freely ventilated combustion was modified by adding a discharge pipe to the cone heater that enabled direct fire product sampling from the cone outlet. The controlled atmosphere cone calorimeter was used for the restricted ventilation fire with metered air fed to the enclosure around the test area. Both tests used a radiant heat flux of 35kW/m^2. Real-time particulate number and size distribution were measured using the Cambustion DMS 500 particle electrical mobility spectrometer. The particulate size distribution showed a peak of ultra-fine aerosol particles of <100 nm in the early stage of the fire development and then changed to the larger size (100-1000 nm) with a peak of 200 nm as the fire progressed. The restricted ventilation fire generated more particles. There were high numbers of 20 nm particles throughout the fire and these have the greatest health risks. Toxic gases were also measured from the raw exhaust gases using a heated Gasmet FTIR gas analyser.

KEYWORDS: Fire Particle size, Fire Toxic gases, Compartment Fires.

INTRODUCTION

Most fire deaths are due to smoke inhalation and associated toxic gases. Currently 'smoke' production is the only aspect of fire toxicity that is included in legislated fire tests of construction products, furniture materials, electrical cables, aircraft cabin materials and polymers. Smoke production in legislated testing is measured by optical obscuration and is related to visibility and impairment of escape through lack of line of sight to escape doors. The smoke regulations are not there because of the toxicity of smoke. The smoke production regulations have no requirement to measure the composition of the smoke either for soot particle size or toxic gases. The victims and some of the survivors of the Grenfell Tower fire in London had black lungs and some of those who survived had to have black particles flushed out of their lungs. The size of particles that reach the alveolar region of the lungs is <50 nm and particles of this size have no effect on light obscuration and so are not measured in the traditional fire smoke tests.

In the mid-1990s, epidemiological data in the USA and UK showed that 1% extra deaths occurred for every 10 μg/m^3 of PM_{10} in ambient air within days of the high particulates in the atmosphere [1-3]. Epidemiological studies have linked fine particulates in air pollution with cardiopulmonary mortality. The only medical explanation of this effect is that particles <50 nm must be present [4] as they cause alveolar inflammation and blood thickening [5], which reduces lung function and places a strain on the heart. This epidemiological data is based on correlations of PM_{10} in the atmosphere and hospital admissions and asthma drug demand. The medical explanation [4] involves the

Proceedings of the Ninth International Seminar on Fire and Explosion Hazards (ISFEH9), pp. 930-939
Edited by Snegirev A., Liu N.A., Tamanini F., Bradley D., Molkov V., and Chaumeix N.
Published by Saint-Petersburg Polytechnic University Press
ISBN: 978-5-7422-6498-9 DOI: 10.18720/spbpu/2/k19-52

presence of solid nano-particles in the alveolar region of the lungs and the composition of these particles is not significant [4]. However, other evidence of health effects of fine particles include allergic reactions, chronic obstruction pulmonary disease (COPD), pulmonary fibrosis and lung cancer [6], indicate that the chemicals absorbed on the particles may also be part of the health effects of ultra-fine particles.

There have been few studies of the ultra-fine particles generated in fires and they are not discussed in the fire literature as a cause of impairment of escape. However, in atmospheric particulate pollution the mass concentration limit is an annual 24 hour average of PM_{10} of 40 µg/m^3. The present work will show that in wood fires huge numbers of particles are generated <100 nm and thus it is likely that breathing nano-particles in fires will be a major cause of impairment of escape and deaths in fires, that is currently not recognised. Gravimetric measurements [7] of particle mass in pine wood fires have shown that concentrations of particles >0.1 g/m^3 occur in compartment fires, which is >10^4 times the atmospheric level of particle concentration where health hazards occur. In a fire, victims can breathe in one minute the equivalent of one day's exposure to contaminated ambient air. Thus it is clear that the breathing of fine particles in fires could be a significant cause of death and impairment of escape. Despite the health hazards and the associated impairment of escape due to fine particulates in fires, very little research has been done on fine particulate exposure in fires.

EXPERIMENTAL TECHNIQUES

Fuel properties

Wood is the most dominant combustible in fires, accounting for approximately 70% of CO_2 emissions and 65% of CO emissions [8]. Construction pine wood was used as fuel with characteristics shown in Table 1. Ultimate and proximate analysis were carried out using the Thermo Flash EA elemental analyser to determine the CHONS and the Shimadzu TGA-50 with a TA60WS processor to determine the water, volatiles, fixed carbon and ash content. The gross calorific value of the pine was determined using a Parr 6200 oxygen bomb calorimeter.

Table 1. Fuel properties

Parameter	Pine Wood Sticks
Proximate Analysis (Wt. %) (daf)	
Volatile Matter	86.54
Fixed Carbon	13.46
Ultimate Analysis (Wt. %) (daf)	
Carbon	53.95
Hydrogen	6.79
Nitrogen	0.11
Sulphur	0.00
Oxygen	39.15
Stoichiometric A/F by carbon balance	5.89
Gross Calorific value (MJ/kg)	18.9
Moisture (as received) (%)	6.18
Ash (as received) (%)	2.27

The cone calorimeter

The cone calorimeter (ISO 5660) is designed to measure the heat release rate and flammability properties of materials. The cone calorimeter reproduces the oxidative pyrolysis stage (class 1b) and well ventilated flaming fires (class 2) classification of ISO 19706 [9]. The authors have adapted the standard cone calorimeter [10] for direct raw gas analysis of the fire products at the outlet from the cone heater and used it with both free ventilation and restricted ventilation fires. The controlled atmosphere enclosure around the 100 mm square test fire in the cone calorimeter was used as a compartment fire with a metered air supply to the enclosure to generate a restricted ventilation fire, 3a classification of ISO 19706 [9]. It was operated with a controlled air supply designed to create rich combustion conditions that occur in air starved compartment fires.

The controlled atmosphere cone calorimeter with associated instrumentation is shown in Fig. 1. It was used for the restricted ventilation experiment to simulate an air starved compartment fire and for comparison with free ventilation, without the controlled atmosphere enclosure. The load cell, sample holder and cone heater were enclosed in the steel box, which had an air supply through the bottom of the air tight box. The airtight box was 38 cm long, 30 cm wide and 33 cm high, with a volume of 0.0376 m^3. In the process of developing this experimental method it was observed that there was excessive heat loss from the metal box which influenced the temperature of the test specimen and hence influenced the heat release rate, HRR. The airtight box design was improved by insulating the inside and the door from the outside, using an insulation board to avoid heat loss. The combustion process was observed through a glass window on the cone calorimeter enclosure which was also insulated when not being used for viewing the flame. An insulation board was also placed in the sample holder underneath the test specimen to prevent heat losses to the supporting metal cylinder leading to the load cell heating.

The airflow introduced to the combustion chamber was from a compressed air supply and was measured using a variable air flow meter with the air flow varying from 6 – 28 L/min. This is 0.12 – 0.56 g/s air mass flow. The air mass flow per exposed surface area of the test specimen (0.01 m^2) was 12 – 56 g/cm^2. The simple assumption that for all fuels there are 3.05 MJ of heat release per kg of air is another way of representing the ventilation conditions. This translates the air mass flow range into fire HRR in kW as 0.37 – 1.71 kW fires and in terms of the exposed surface area of the wood is 37 – 171 kW/m^2. In the present work a single air flow was used of 192 g/cm^2 or 58 kW/m^2 for the restricted ventilation condition. This is the maximum possible heat release rate (HRR) in the primary fire in the enclosed compartment.

Differential mobility spectrometer (DMS 500) particle size analyser

The Cambustion DMS 500 (Differential mobility spectrometer) was used to measure the particle size and concentration in real time. It measures particle sizes ranging from 5-1000 nm based on their electrical mobility. The DMS 500 responds to both liquid and solid aerosols. Liquid aerosols may occur from the volatile release from wood. Solid aerosols would comprise soot and ash particles. The DMS 500 is a transient instrument and can take numerous size distributions per second. In the present work, the size distribution as a function of the fire duration was measured.

Experimental procedure

The pine wood sample was exposed to the conical heater of the cone calorimeter radiating at 35 kW/m^2 for both free ventilation and with 192 g/cm^2 air mass flow in the controlled atmosphere cone calorimeter. 35 kW/m^2 is the standard heat flux for use in material evaluation for performance in fires using the standard cone calorimeter [10]. Also, 35 kW/m^2 was recommended by Flecknoe-Brown et al. [11]. Herzberg [12] noted that 35 kW/m^2 was a "trade-off between a lower value, which possibly would have caused materials to pyrolyse only, and a higher value which might have provoked an unrealistically clean burning behaviour".

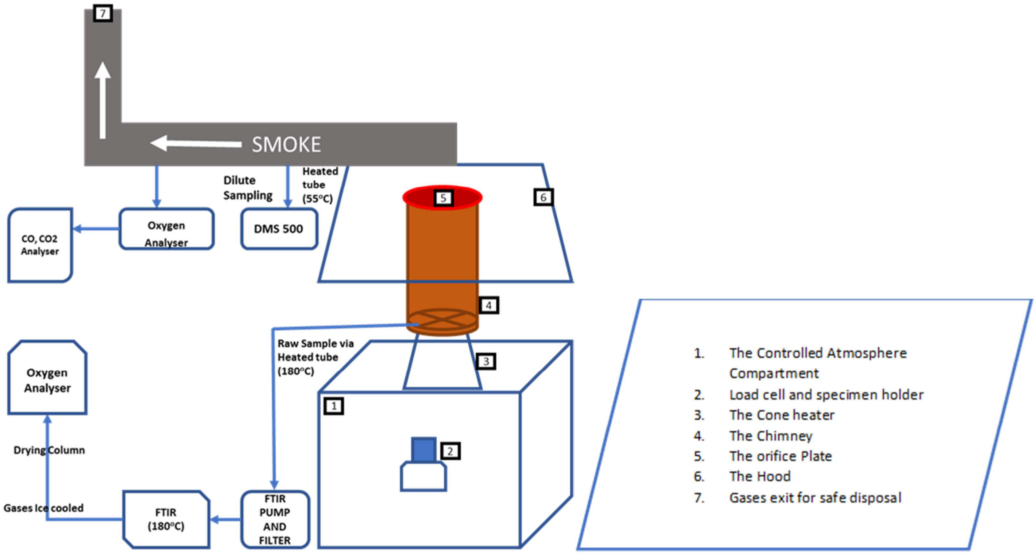

Fig. 1. The controlled atmosphere cone calorimeter.

Five rectangular shaped pine sticks (100 x 20 x 20 mm) were arranged horizontally in a 100 x 100 mm square sample holder of the cone calorimeter, exposing the top surface to the applied radiant heat flux. The initial weight of the wood was determined by the load cell as 127 g and 119 g for the two tests at different ventilations. The load cell was calibrated by checking with reference weights at the start of each test programme and was very stable. The 35 kW/m^2 radiant heat flux caused the thermal decomposition of the samples leading to auto ignition of the evolved gases and the auto ignition delay time was determined in the tests at 29 s for the restricted ventilation test and 192 s for the freely ventilated test. The fire continued until flaming combustion ceased and there was only char burning. It will be shown that this transition from flaming combustion to char smouldering combustion was associated with a change in the particle size distribution.

Sampling and analysis method

Both cone calorimeter experimental setups were modified to enable a raw gas sample to be obtained from the exit of the chamber. A 20 hole X sample probe was mounted on top of the exit plane of the cone heater for the sampling of the mean composition of the raw gases. A single hole probe had been used but was shown to not give a mixed mean sample. The X probe was mounted in a 76 mm diameter duct with flanges to join the cone heater exit to the chimney. This gas sample probe duct was 40 mm long. An 80 mm diameter chimney, the same diameter as the cone outlet, and 210 mm long was mounted on top of the sample probe and the total chimney length was 250 mm. It was found that oxygen was detected in the sample probe with rich mixture combustion, which should not occur. It was concluded that air was back flowing down the chimney, partially because the FTIR sample flow rate was similar to the air flow into the fire compartment. To avoid the air backflow, a grid plate restrictor was placed at the chimney exit to increase the exhaust flow pressure loss, which then prevented back flow of air down to the sample probe. This orifice plate on the chimney outlet had a 90% blockage of the flow and this prevented any oxygen occurring in the gas sample for rich combustion fires.

The schematic diagram showing the sample gas transport system to the gas analysers is shown in Fig. 2. The gases from the exhaust were transported via a heated 180 ^{o}C sample line to a heated pump (2.5-3 lpm) and filter. Another heated line was connected to the pump to transport the gases to the heated Gasmet FTIR. The raw gas sampling was used because it prevented any post oxidation of

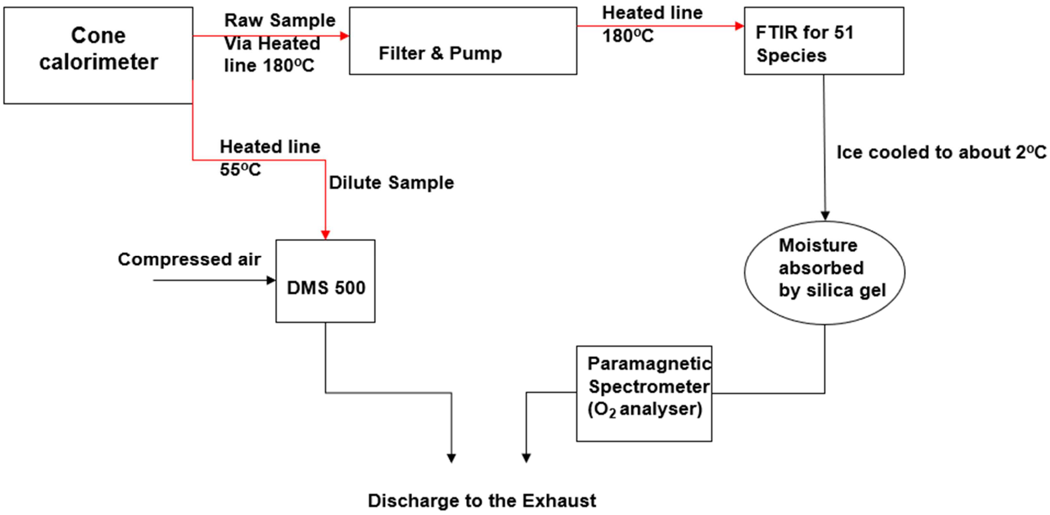

Fig. 2. Schematic of the analysers.

species by dilution of the gases with ambient air, as the gases were entrained into the cone calorimeter diluted flow metering section. It also prevented any losses of condensable gases that would occur if the exhaust was just thermally cooled [13]. The gas sample from the FTIR outlet was transported to a refrigeration cooler of about 2 °C via a PTFE tube and then to a silica gel column for the removal of water vapour before going into a paramagnetic oxygen analyser, after which it was discharged through the cone calorimeter discharge duct.

A dilute sample was used for the particle size analysis, as shown in Fig. 1. The standard dilution on the cone calorimeter was used and this prevents water vapour from the combustion products appearing as droplets, by cooling and reducing the concentration. Another reason for dilution is to reduce particle agglomeration, which affects the size distribution and reduces the number of particles. Kittelson [14] advocated that a dilution ratio of around 100/1 or more should be used. The products of combustion from the cone heater outlet (chimney outlet in the present case) are diluted with ambient laboratory air before entering the exhaust duct of the cone calorimeter. Thus, the gas sample for particle size analysis was taken from the cone calorimeter dilution tunnel.

A 55 °C heated sample line was connected to the dilution tunnel of the cone calorimeter to convey the sample to the Cambustion DMS 500 particle size analyser [15]. A heated line was used to allow dilution of the sample gas which serves to lower the dew point of the air so that condensation does not take place in the instrument. The DMS500 particle size analyser has an internal 10/1 diluter and the particle concentration provided by the instrument as output includes this dilution. The dilution from the chimney to the cone calorimeter was the ratio of the two air flow rates of 24 l/s for the cone calorimeter and between 6 and 28 L/min for the controlled atmosphere box or the air inflow for the standard freely ventilated test. This gave a dilution ratio range of between 240/1 and 51/1 for the controlled atmosphere setup. For the air flow used in the present work the cone calorimeter dilution was 146 for the restricted ventilation experiment and 26 for the freely ventilated experiment. The Cambustion number concentration was multiplied by 146 and 26 to give the concentration in the chimney. The overall dilution including the 10/1 in the DMS500 was 1460 and 260/1, which would ensure no size distribution change in the dilution system.

RESULTS AND DISCUSSION

Mass loss and heat release rates (HRR)

Compartment fires and freely ventilated fires are compared for the same pine wood test specimen at 35 kW/m^2 cone radiant heating and both had a gas sample for toxic gas and oxygen analysis taken as a raw heated mean gas sample from the chimney fitted on the cone exit. The results of the secondary combustion after air dilution beyond the chimney are not presented, apart from for the particle number analysis. Figure 3 shows that the ignition delay was much shorter for the restricted ventilation fire, due to the richer mixtures during the delay period, shown in Fig. 7, which have shorter ignition delays than the lean mixture for freely ventilated fires. Figure 3 shows the mass loss rate and total heat release rate for the primary combustion in the compartment. Both tests showed a mass loss rate at steady state of 0.07 g/s, with a much slower burn rate during the char burn phase from 1200 s. The two peaks in the mass burn rates will be shown to be associated with peaks in toxic gas emissions and in particulate emissions.

The oxygen mass consumption based heat release rate, shown in Fig. 3b, was computed from cone outlet chimney oxygen analysis, downstream of the FTIR. The wet based oxygen analysis (corrected for the water vapour removed based on the FTIR water analysis) is shown in Fig. 4. For the restricted ventilation fire Fig. 3b shows that the HRR peaked immediately after ignition and remained steady at 50 kW/m^2, which was about one third of the freely ventilated fire where the steady state HRR was about 130 kW/m^2. This was due to the low combustion efficiency with high CO, H_2 and HC emissions in the restricted ventilation fire due to the low fire temperature. Figure 4 shows that for free ventilation there was always surplus oxygen in the fire with high oxygen levels in the chimney. For the restricted ventilation fire the oxygen was close to zero for most of the time and combustion was completed in an external flame downstream of the chimney using the entrained oxygen from the dilution air.

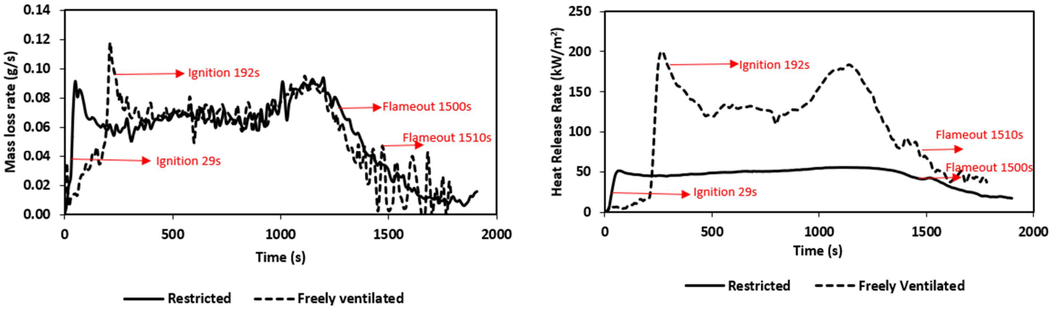

(a) (b)

Fig. 3. Mass loss rate (a) and primary heat release rate (b).

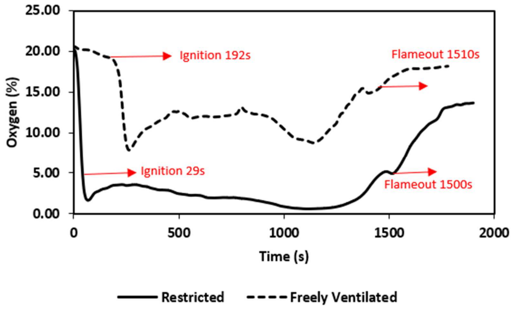

Fig. 4. Oxygen in the cone outlet chimney.

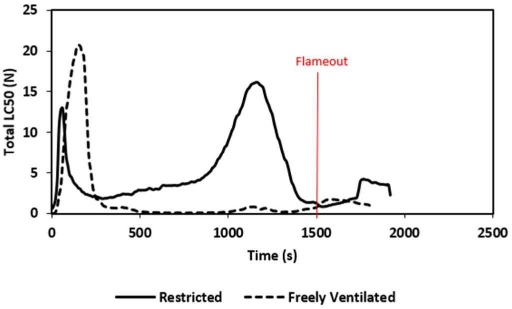

Fig. 5. Total LC_{50} FEC toxicity.

Toxicity, CO, hydrocarbon, fire equivalence ratio and combustion efficiency

All the FTIR measured toxic gases were divided by the LC_{50} limit and then summated to give the FEC total toxicity. This is shown as a function of time in Fig. 5, which shows both ventilations had a peak toxicity in the initial flaming combustion phase, but for restricted ventilation there was a second large toxic peak just before the flame out and a second smaller peak for free ventilation. These two peaks in toxicity occurred at the same time as the two peaks in the mass burn rate in Fig. 3 and the two minimum in oxygen in Fig. 4. The CO and total hydrocarbon (HC) yields are compared for the two fire ventilation conditions in Fig. 6 and they had a similar shape to the total toxicity results. The fire mean equivalence ratio by carbon balance and the combustion efficiency computed from the energy content of CO and HC are shown in Fig. 7. The restricted ventilation fire had rich combustion with an equivalence ratio of 2.0 throughout the flaming period. In the burning period after the ignition delay the CO and HC yields were much higher for the restricted ventilation fire as a result of the rich combustion. The freely ventilated fire burned lean with an equivalence ratio of 0.4 for most of the flaming period. The CO and HC yields were very low once combustion started after the ignition delay, as expected from the lean combustion. During the ignition delay period the CO yield was almost 3 times higher and HC was about 7 times higher in the freely ventilated test. This was due to the long ignition delay period of 192 s compared to 29 s of ignition delay for the restricted fire, where the products of wood decomposition were present but not ignited. The free ventilation dispersed the products of thermal decomposition, reduced their concentration and delayed their auto-ignition.

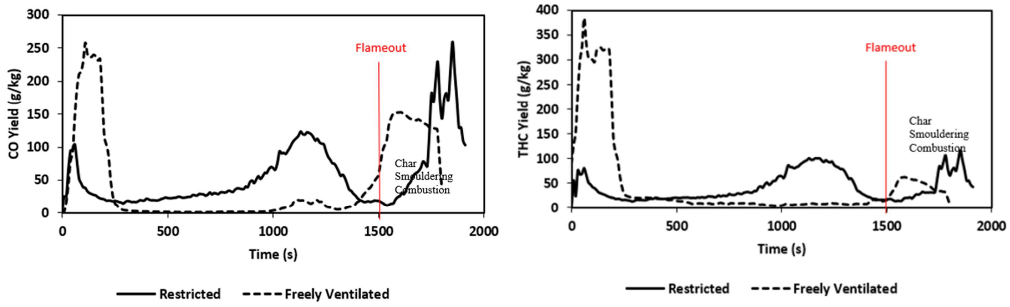

(a) (b)

Fig. 6. CO yield (a) and HC yield (b).

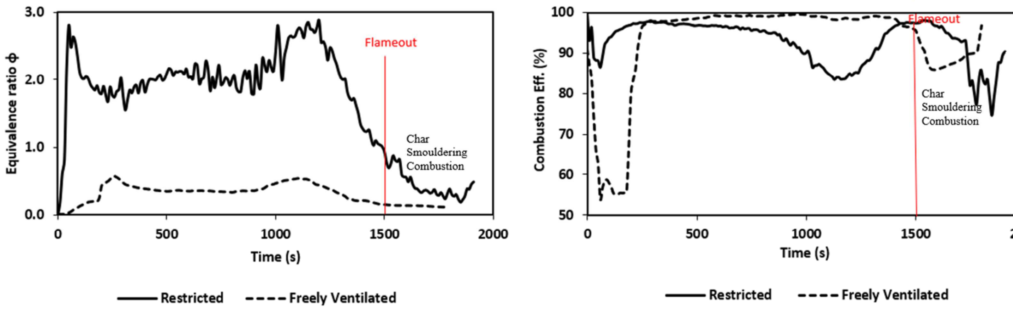

(a) (b)

Fig.7. Equivalence ratio (a) and combustion efficiency (b).

Particle number concentration

The particle number concentration as a function of size and time is shown in Fig. 8. A bimodal distribution of the particle sizes was observed indicating the nucleation mode and accumulation mode of the particle size distribution. The nuclei mode for both ventilation conditions was found to peak at 20 nm and the accumulation mode at 200 nm. The number of particles for the two modes, 20 nm and 200 nm are compared in Fig. 9 as a function of time for both ventilation conditions. The particle concentrations were highest at the peak HRR of 50 and 130 kW/m^2 for the restricted and free ventilated fires. For both ventilations, the 20 nm particle number was 10^4 higher than those at the roadside [16], where the health hazards are known to be high. The effect of restricting the fire ventilation was to increase the ultra-fine particle number, due to the richer mixtures generated, as shown in Fig. 7. However, even for free ventilation with lean combustion the particle number was high at 1000 times roadside levels [16] for 20 nm particles. These results show that ultra-fine particulate emissions in fires from wood burning are a potential serious toxic impairment of escape hazard and materials should be evaluated for their propensity to form ultra-fine particles in fires.

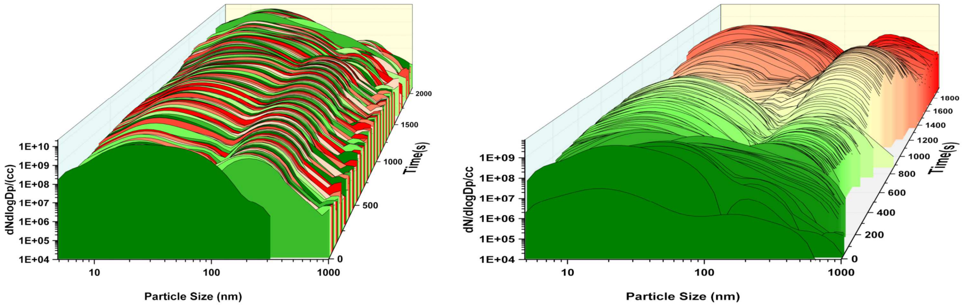

(a) (b)

Fig. 8. Particle number concentration and size distribution; (a) restricted (b) freely ventilated.

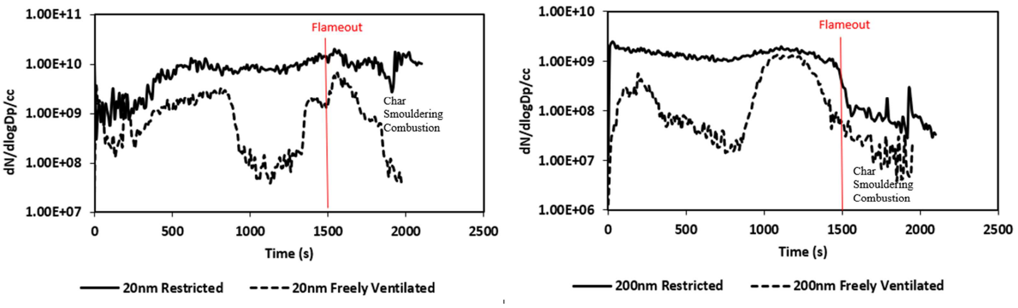

(a) (b)

Fig. 9. 20 nm particle number concentration (a) and 200 nm particle number concentration (b).

Particle number comparison

The particle number size distributions as a function of time in the fire are shown in Fig. 10 for freely and restricted ventilation fires. Both fires showed a nuclei mode with a peak at 20 nm and an accumulation mode at 200 nm. These two size ranges are shown as a function of time in Fig. 9. This shows that for restricted ventilation the particle numbers were higher than for free ventilation. However, the time dependency was different with fairly consistent peak numbers at 20 and 200 nm throughout the restricted ventilation fire. For the free ventilation fire there were two peaks in the particle number of both 20 and 200 nm particles. These peaks in particle number coincide with the two peaks in HRR in Fig. 3b.

Relatively few investigations have been published on the particle size distribution in fires, especially in simulated compartment fires. Hertzberg and Blomqvist [12] used the low pressure impactor particle size analyser, the Dekati ELPI, to measure the particle number from 60 nm to 10 µm size range for different fire materials, using the standard cone calorimeter. Figure 10 shows a comparison between the pine wood test at both ventilation conditions with the unspecified 'wood' measured by Hertzberg and Blomqvist [12]. All their particle size distributions were monomodal. At 200 nm, Hertzberg and Blomqvist [12] measured particle number of 10^6 p/cm^3. In the present pine wood work, at 200 nm there were 10^9 p/cm^3 for the restricted condition and 10^8 – 10^9 p/cm^3 for the free ventilation condition. These higher particle numbers for restricted ventilation were due to the richer mixtures where carbon formation occurs. The 5-60 nm size range of particles, which account for the greatest health risk, was not measured in Hertzberg's work for 'wood' [12]. This size range of particles accumulates in the alveolar regions of the lungs, and such particles penetrate into the blood stream [1-6]. The ELPI particle size analyser does not have the size resolution, below 50nm where the greatest toxic particle hazard occurs and thus is not a good instrument for assessing particle size in fires. It is much better for larger particles >1µm of interest in optical obscuration.

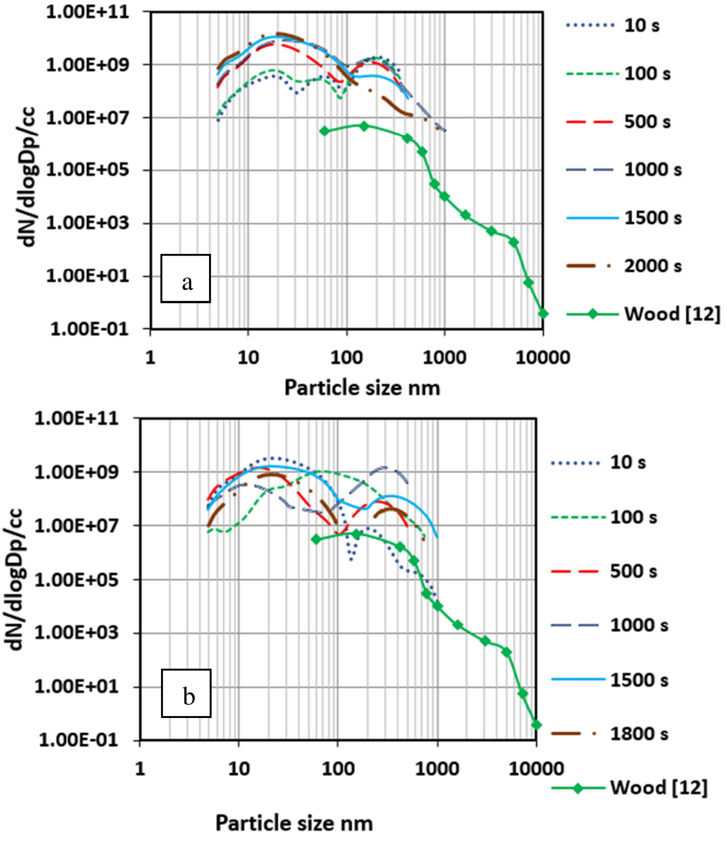

Fig. 10. Comparison of particle number distribution with that of Hertzberg [12] using the ELPI aerodynamic size separation instrument for restricted (a) and freely ventilated (b).

CONCLUSIONS

1. The particle size distribution of pine wood was measured in real time under restricted and free ventilation condition showing a bimodal distribution of nucleation mode and agglomeration mode.

2. The nucleation mode showed a peak of 20 nm on a number basis and a peak of 200 nm in the accumulation mode.
3. More particles were generated in the restricted ventilation fire due to richer combustion.
4. Concentration of ultra-fine particles generated in the pine wood test was much higher than that found in the literature. These ultra-fine particles could be a significant cause of death and impairment of escape in fires.
5. The cone calorimeter with ventilation controlled atmosphere around the combustion zone is good way to study the fire toxicity and particulate emissions of materials.

REFERENCES

[1] A. Violi, Effects of Combustion-Generated Nanoparticles on Cellular Membranes, Combust. Sci. Technol. 188 (2016) 769-775.

[2] C.A. Pope et al., Heart rate variability associated with particulate air pollution, Amer. Heart J. 138 (1999) 890-899.

[3] J.S. Lighty, J.M. Veranth, A.F. Sarofim, Combustion aerosols: factors governing their size and composition and implications to human health. J. Air Waste Management Assoc. 50 (1995) 1565-1618.

[4] A. Seaton et al., Particulate air pollution and acute health effects, The Lancet 345(8943) (1995) 176-178.

[5] A. Peters et al., Respiratory effects are associated with the number of ultrafine particles. Amer. J. Respiratory Crit. Care Medicine 155 (1997) 1376-1383.

[6] A. Kocbach Bølling et al., Health effects of residential wood smoke particles: the importance of combustion conditions and physicochemical particle properties, Particle Fibre Toxicol. 6 (2009) 29.

[7] G.E. Andrews, J. Ledger, H.N. Phylaktou, The Gravimetric Determination of Soot Yields in Enclosed Pool Fires. In: 3rd International Colloquia on Explosions in Reactive Systems, 2000, Windermere, UK.

[8] B. Persson, M. Simonson, Fire Emissions into the Atmosphere, Fire Technol. 34 (1998) 266-279.

[9] 19706:2011, I., BS ISO 19706:2011: Guidelines for assessing the fire threat to people.

[10] 5660-1:2015, B.I., BS ISO 5660-1:2015: Reaction-to-fire tests. Heat release, smoke production and mass loss rate. Heat release rate (cone calorimeter method) and smoke production rate (dynamic measurement), 2015, British Standards Institute.

[11] K.W. Flecknoe-Brown, K. Livkiss, P. Van Hees, Experimental and Numerical Investigation on Fire Behaviour of Foam/Fabric Composites, In: 15th Int. Conf. Fire and Materials, 2017, San Francisco, USA.

[12] T. Hertzberg, P. Blomqvist, Particles from fires – a screening of common materials found in buildings, Fire Mater. 27 (2003) 295-314.

[13] A.A. Alarifi, H.N. Phylaktou, G.E. Andrews, Heated Raw Gas Sampling with Heated FTIR Analysis of Toxic Effluents from Small and Large Scale Fire Tests, In: 10th Asia-Oceania Symposium on Fire Science and Technology, 2015, Tsukuba, Japan, IAFSS.

[14] D. Kittelson, 100/1 Dilution for Particle Number.

[15] Cambustion, DMS500 Fast Particulate Spectrometer with Heated Sample Line High Ratio Diluter User Manual, 2011, Cambridge.

[16] J.J.N. Lingard, E.I. Agus, D.T. Young, G.E. Andrews, A.S. Tomlin, Observations of urban airborne particle number concentrations during rush-hour conditions: analysis of the number based size distributions and modal parameters, J. Environ. Monitor. 8 (2006) 1203-1218.

Study of Ignition and Extinction of Spruce Glulam Exposed to a Radiative Flux

Terrei L.[1,]*, Acem Z.[1], Lardet P.[2], Georges V.[2], Boulet P.[1], Parent G.[1]

[1] *LEMTA, UMR CNRS 7563, Université de Lorraine, France*
[2] *Université Paris-Est, Centre Scientifique et Technique du Bâtiment (CSTB), France*
**Corresponding author's email: lucas.terrei@univ-lorraine.fr*

ABSTRACT

Wood-based materials, which are more and more used in building construction, are often characterized by the normative tests such as cone calorimeter. Measurements of ignition time, mass loss or heat release rate, and temperatures are usually performed. The degradation dynamics of samples depends on a large number of variables (humidity, density, scale sample, experimental conditions), and it can induce flaming ignition. The autoignition phenomenon has already been studied, but opinions concerning the involved physical processes remain controversial. The ability of wood to self-extinguish in case of fire is also an important issue, especially concerning structure mechanical strength. The purpose of the present work is to study thermal degradation of glulam in the cone calorimeter with the dedicated experimental setup. In particular, we focus on ignition, extinction, and re-ignition. The cone calorimeter with vertical sample orientation was modified to study extinction and re-ignition so that the external heat flux can be quickly switched off. The samples were exposed to the heat fluxes at four values in the range from 15 to 75 kW/m^2. For the low heat flux, the transition was observed between pyrolysis and smoldering combustion at the temperature about 400 °C. The ignition only occurred at the heat flux higher than 55 kW/m^2. For 55 kW/m^2, re-ignition was not consistent and random. However, for the highest flux, re-ignition occurred for each new exposure to the external heat flux. Both the ignition and extinction times increased at each exposure. Char layer delays the ignition.

KEYWORDS: Cone calorimeter, extinction, ignition, re-ignition.

INTRODUCTION

Wood is one of the oldest building materials because of its cost effectiveness, mechanical properties and ease to implement. Currently, among available solutions, wood appears to be an interesting material because of its environmental advantages. There is a global rise of wood-based materials in structure as well as in architecture. It now becomes a viable alternative to concrete and steel for modern structures.

Before their usage, building materials are subjected to fire tests at different scales [1]. Cone calorimeter is one of them. It is a standard test (ASTM and ISO) useful for measuring the Mass Loss Rate (MLR), Heat Release Rate (HRR), ignition time and ignition temperature [2].

For fire safety concerns in construction domain, the study of fire behavior and flame propagation in wood structures is important due to its flammability. Nevertheless, some previous studies have shown that wood can exhibit encouraging resistance to fire, especially slow in-depth propagation and ability to self-extinction [3]. This ability is essential particularly for the rescue intervention or the structure resistance.

Proceedings of the Ninth International Seminar on Fire and Explosion Hazards (ISFEH9), pp. 940-949
Edited by Snegirev A., Liu N.A., Tamanini F., Bradley D., Molkov V., and Chaumeix N.
Published by Saint-Petersburg Polytechnic University Press
ISBN: 978-5-7422-6498-9 DOI: 10.18720/spbpu/2/k19-63

The fire behavior of wood has been widely studied for several years, mainly with regard to ignition criteria [4]. The sample exposure to an external heat flux or a flame leads to pyrolysis process within the sample, releasing pyrolysis gases. This process depends on several parameters such as moisture, density, heat flux and experimental conditions. It is consequently very difficult to clearly identify and characterize “the ignition conditions” [5, 6], even if it is well known that ignition occurs when the pyrolysis products, at a sufficient concentration, reach their flash point. The wood degradation by radiative heat flux leads to the formation of a char layer. Many studies have shown that the char layer tends to reduce the degradation process. Indeed, during the sample degradation, the heat release rate and mass loss rate decrease when the char is formed [7, 8]. This phenomenon is attributed to the forming of the char layer protecting the virgin wood from the direct exposure to heat flux. The flaming self-extinction of wood is also a process that generates an increase of interest. Some experiments were realized at the fire compartment and at cone calorimeter scale to estimate heat flux and critical MLR at self-extinction [9, 3]. Bartlett et al. [10] used fire propagation apparatus (FPA), and determined a critical mass loss rate below 3.48 g/(m²·s) and an incident heat flux below 31 kW/m^2 conducting to the auto-extinction of samples (at ambient oxygen concentrations). In similar tests using cone calorimeter, Emberley et al. [11] reported a critical mass flux between 2.65 to 8.28 g/(m²·s) and a critical heat flux between 24.1 to 56.6 kW/m^2 according to wood species. These values are determined after MLR decrease, at steady state.

The material studied here was laminated wood (glulam) of spruce which is a re-composition of solid wood for structural wood of great lengths. This material is composed with laminated wood purged, joined then glued together in the direction of the wood grain. The glulam can be considered like solid wood if the wood layers and the glue are correctly chosen [12, 13].

The aim of this work is the study of the auto-ignition, auto-extinction and re-ignition of the glulam exposed to heat fluxes provided by a vertically oriented cone calorimeter. For that purpose, the cone calorimeter was modified to study sample extinction and re-ignition by suddenly applying or withdrawing the heat flux. This modification was useful for studying samples extinction and re-ignition by suddenly applying or withdrawing the heat flux. A precision scale was used in order to record mass loss and to calculate MLR during the test. In addition, the radiation from the surface of wood samples during thermal degradation was recorded through the cone aperture thanks to a multispectral infrared camera. Infrared images were post-processed, involving a subtraction method between successive images, to withdraw the high incident flux from the cone calorimeter partly reflected by the sample. Then, the increase in intensity between two times steps was used to compute the increase of surface temperature as described in [14]. For each test, time-to-ignition and time-to-extinction was recorded and linked with surface temperature and MLR to determinate the critical MLR of extinction.

EXPERIMENTAL SETUP

Samples and cone calorimeter tests

Figure 1 presents the experimental setup. In addition, to remove suddenly the heat flux, this configuration allows to measure continuously the surface temperature with the infrared camera. The selected glulam material was made of spruce glued with melamine-urea-formaldehyde (MUF). The sample sizes were 100 × 100 mm with a 50 mm thickness. The sample moisture content was 9 % corresponding to an average density of 480 kg/m^3. As specified in the standard ISO 5660-1 [15], the samples were wrapped with two layers of aluminum foil, except the top side exposed to radiative flux. After, the sample is placed in the sample holder with a ceramic plate behind the back side. The distance between the sample and the heater was 25 mm. The samples were exposed vertically to external constant heat fluxes between 15 and 75 kW/m^2. The cone emission could be assumed to be close to those of a blackbody [16]. The sample was considered ignited with the appearance of the flame, recorded by a fast camera to deduct the ignition origin. Once ignited, samples continued to be exposed to heat flux for different times (5, 10, 30 and 60 minutes) in order to observe the impact on the extinction.

The radiative heat flux emitted by the cone was controlled before each test thanks to a Schmidt-Boelter fluxmeter (by Medtherm). The heat flux was considered correct when the value was ± 0.5 kW/m^2 from the desired flux. In the original cone calorimeter device, an insulating screen is used to prevent the sample from being exposed to the radiative flux emitted by the cone, mainly during the initialization step of the test (acquisition of the baseline of the mass cell). When this screen is in front of the cone coil, heat losses are reduced (compared to the heat losses without the screen), and the electrical power required to maintain the cone coil at the temperature setpoint is reduced. When the screen is removed, losses increase, the temperature of the cone decreases, and as result the emitted flux also. So it will take a while for the temperature of the cone to reach the setpoint again. In the proposed modified device, the screen is no longer needed. The cone is simply translated in front of the sample. In this way the desired heat flux is stable from the beginning of the experiment. Figure 2 compares the heat evolution for the two configurations with an exposure of 75 kW/m^2 during 5 minutes.

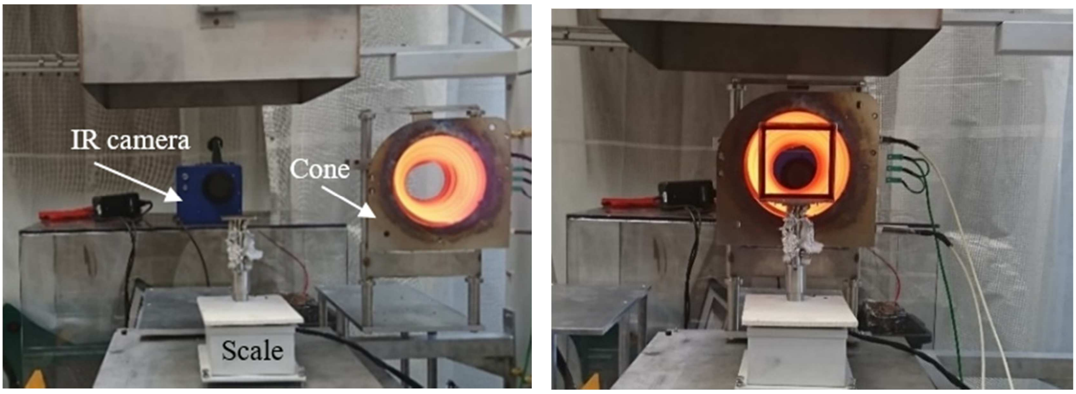

(a) (b)

Fig. 1. Experimental setup: (a) the sample is not exposed to the cone; (b) the sample holder is exposed to the cone (the sample is removed from the sample holder to make the cone aperture visible. The infrared camera looks to the sample through this aperture).

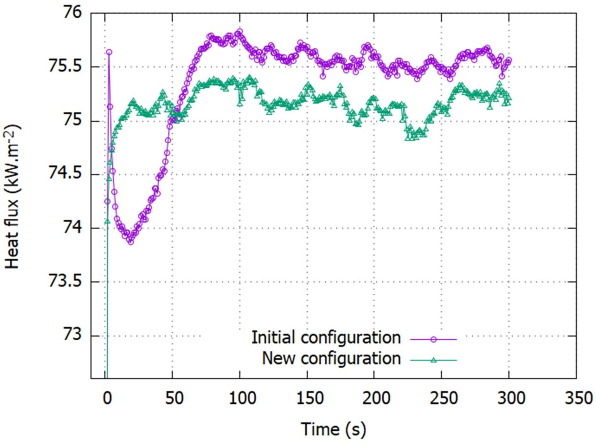

Fig. 2. Heat flux measured for the initial and new configurations (75 kW/m^2).

Variations of heat flux are different during the first hundred seconds. For the new cone configuration, heat flux increases rapidly to the desired value and then remains constant. For the initial configuration, when the shield is removed, heat flux increases before decreasing suddenly due to the increase of heat losses as explained before. The desired heat flux is achieved after 90 s. Thanks to this new setup we can ensure a steady heat flux from the very beginning of tests.

Temperature measurement

Surface or ignition temperatures are usually measured using thermocouples. However, these measurements are punctual and could be inaccurate due to the heat sink along the thermocouple wire, direct exposition to the cone radiation or to poor contact between the thermocouple and the sample. This contact seems all the more difficult for the wood that is degrading, producing char and cracks [17]. In this work, surface temperatures were measured thanks to a multispectral infrared camera (Orion SC7000 by FLIR). This non-intrusive measurement allows studying temperature field evolution on a large surface. The contact problem is also eliminated. In fire safety, this measurement is increasingly used [18, 19], especially owing to its accuracy. During infrared measurements, the flame between the infrared camera and the sample surface may lead to mismeasurement of the temperature. Some studies have shown that the emission by flames is observed to be predominant in specific wavelengths where major combustion gases (CO, CO_2 and H_2O) can emit [20]. Outside these bands, only soot can emit, and since the optical thickness of flames involved in cone calorimeter experiments is very small, the flame can be considered as almost transparent in these specific wavelengths. For the present study, the selected wavelength filter for IR camera is 3.9 µm (2564 cm^{-1}), which is outside the emission bands of combustion gases and corresponds to a wavelength where wood emissivity remains almost constant around 0.9 during degradation [16]. This type of measurement was already successfully performed by our team on other materials. More details are presented in [14].

Figure 3 shows the temperature field for a test at 55 kW/m^2 when ignition occurs. The white circle corresponds to the studied area where the mean surface temperature is calculated. At 0.32 s, field temperature is homogenous and constant. This temperature increases during sample exposure. At 74 s, there is the flame presence and some cracks (in yellow) appear. The field temperature is quite the same even if the cracks temperature is lower than that of the exposed surface.

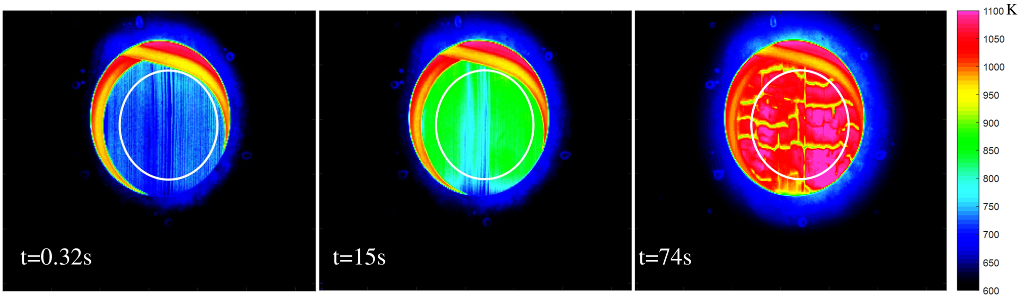

Fig. 3. Temperature field in Kelvin and studied area (white circle) for one test at 55 kW/m^2.

RESULTS

Samples were exposed to three external heat fluxes (15, 55, 75 kW/m^2). Flame ignition was observed only for tests at 55 and 75 kW/m^2. For the test at 15 kW/m^2, only smoldering combustion was observed. In the following, after first showing the benefits of the new setup, regarding the stability of the supplying heat flux, we will first present results regarding smoldering combustion only. Then we will focus on the ignition/extinction/re-ignition studies.

Study of smoldering combustion (no flame)

For tests with a 15 kW/m^2 external heat flux, total exposure time was 3600 s. After this time, the cone was removed. Tests were repeated three times. During these tests, no flame appeared but the smoldering combustion phenomenon was observed as discussed below. Figure 4 shows MLR and surface temperature evolution provided by the IR camera.

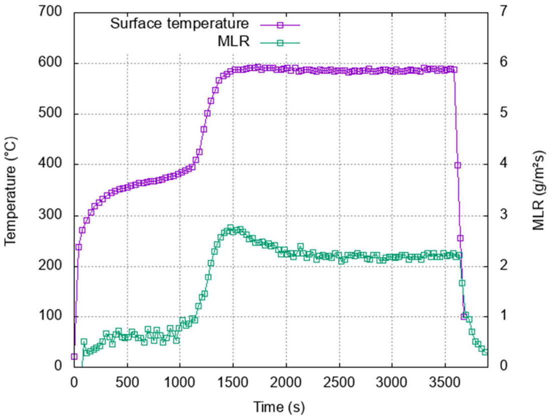

Fig. 4. MLR and surface temperature for tests without ignition

In a general way, MLR first increases to a maximum. Then MLR decreases, as the char plays the role of an insulator layer that reduces heat transfer within the sample, before reaching a plateau. At 1100 s MLR suddenly increases. This increase is also observed for the temperature for which the transition occurs at around 410 °C. This phenomenon corresponds to the beginning of the smoldering combustion of the char that leads to an additional amount of released energy. Finally, the surface temperature reaches a plateau at around 600 °C at 1500 s, corresponding to a constant MLR of 2.1 g/(m²·s).

Study of ignition and extinction

Tests were also carried out with higher radiative heat fluxes for which ignition occurs. After different time of exposure, the cone was slid in order to measure the extinction time of the sample. Figure 5 shows the MLR and the surface temperature of sample evolutions for tests under 55 and 75 kW/m^2 for one hour of exposure.

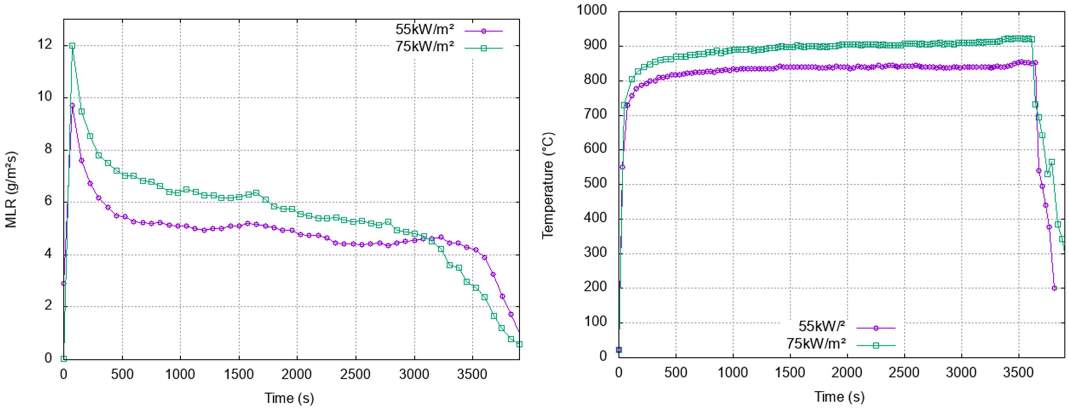

Fig. 5. MLR and surface temperature for tests with sample ignition.

Similar overall trends as previous tests without ignition are observed. The main difference is a drastic increase in MLR and surface temperature when the ignition occurs. Ignition occurs at around 15 s for the test at 75 kW/m^2 and around 35 s for the test at 55 kW/m^2. When ignition occurred, three types of ignition were observed [21]: auto-ignition close to the exposed surface, auto-ignition far from the exposed surface, within pyrolysis gases, and ignition considered piloted by the coil of the cone. These types could influence ignition time if the imposed heat flux is close to the critical heat flux allowing auto-ignition.

The corresponding temperatures at ignition were estimated at 600 °C for 75 kW/m^2 and 618 °C for 55 kW/m^2. The maximum MLR is more important for the highest flux. After ignition, MLR decreases due to the protecting role plays by the char, as discussed previously. As stated by Emberley et al. [11] and Bartlett et al. [9], MLR has two distinct states: transient and steady after 500 s even if MLR slightly decreases all along tests. For the test performed at 75 kW/m^2, a decrease appears at 3000 s before the cone slid. This decrease indicates that the sample is completely degraded, there is no more wood to burn.

After 3600 s of exposure to the external heat flux, the cone was slid. MLR and surface temperature decreased suddenly, and self-extinction occurred rapidly. The sample was considered extinguished when flames disappeared from the exposed surface. For the two heat fluxes where ignition occurred, samples auto-extinguished between 10 to 40 s. These extinction times are in agreement with those measured by Emberley et al. [3]. For most tests performed at 75 kW/m^2 during one hour, auto-extinction occurred before the cone removing because the virgin wood was already completely degraded. Table 1 shows the critical MLR for the test performed at 55 and 75 kW/m^2 for different time expositions.

Table 1. Critical MLR for self extinction for 55 and 75 kW/m^2 exposed at different times

Heat flux, kW/m^2	Critical MLR for self-extinction, g/(m²·s)			
	5 min	10 min	30 min	60 min
75	7.26	4.97	4.94	3
55	5.9	4.94	4.7	3.7

Generally, the critical mass loss rate decreases when the exposure to the heat flux increases. It seems logical with the MLR decreasing in time. Higher values are for the lower time exposures because it was still transient MLR state and the char layer just started to form. For 5 minutes of exposure, critical MLR is higher for 75 kW/m^2 due to thermal aggression. From 10 to 30 minutes, in the steady state, critical MLR is quite the same whatever the imposed heat flux. It was estimated to 4.89 ±0.13 g/(m²·s), in good agreement with Emberley et al. [11]. However, for one hour of exposure at 75 kW/m^2, most tests were already extinguished after the cone removing as explained above. For those where the flame was still present, critical MLR is lower than other exposure times because residual virgin wood is protected by the char layer.

Study of the re-ignition

The new setup allowed to switch on or off the exposed heat flux, which was useful for cycling studies. Therefore, the study of the re-ignition of samples can be performed. The experiment consisted to expose samples to aheat flux during 5 or 10 minutes. After this time, the cone was removed for 2 minutes and the extinction time was recorded. This process was repeated three times for each sample with the same heat flux.Tests were repeated three times with two heat fluxes (55 kW/m^2 and 75 kW/m^2). Figures 7a and 7b show the evolution of the MLRobtained when the sample was exposed for 5 and 10 minutes to a heat flux of 55 kW/m^2.

Figure 7 shows a good repeatability in the evolution of the MLR. Table 1 gathers the ignition and extinction times in seconds. The maximum of MLR is at the first exposure, when the char layer is not yet formed. After the peak, MLR decreases before reaching a constant value. The withdrawal of the cone induces a decrease of MLR. The extinction of the sample happens in a few seconds after the cone removal. A new exposure to the heat flux results again in an increase of MLR. The latter tends towards a constant value close to that of the first exposure.

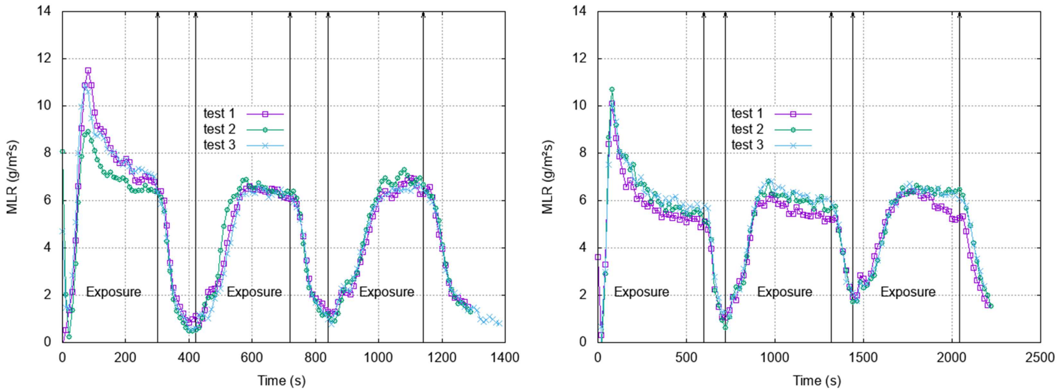

(a) (b)

Fig. 7. MLR of tests with an exposure of 55 kW/m^2 (a) 5 min; (b) 10 min.

Table 2. Ignition time (t_{ig}) and extinction time (t_{ext}) for samples exposed to 55 kW/m^2

Tests	Exposure	5 min		10 min	
		t_{ig}	t_{ext}	t_{ig}	t_{ext}
Test 1	1st	45	15	40	10
	2nd	-[a]	-	180	5
	3rd	-	-	-	-
Test 2	1st	-	-	43	15
	2nd	-	-	-	-
	3rd	-	-	200	11
Test 3	1st	40	13	51	20
	2nd	-	-	-	-
	3rd	240	20	140	15

[a] No Ignition occurs, Consequently there is no extinction time.

According to Table 2, re-ignition did not occur for any exposure. There was no ignition for test 2 with an exposure of 5 minutes. Ignition time increased for the second exposure. When the cone is removed, the presence of a flame does not have an impact on the evolution of MLR. The char layer seems to increase the ignition time. However, when re-ignition occurred after a new exposure to heat flux, critical MLR for self-extinction were quite the same (around 5.9 and 4.9 g/(m²·s) for 5 and 10 minutes, respectively). Figures 8a and 8b show the evolution of MLR obtained when the samples were exposed for 5 and 10 minutes to a heat flux of 75 kW/m^2.

Figure 8 shows the good repeatability of tests. MLR evolution is very close to tests with 55 kW/m^2. The imposed heat flux being more important, the value of MLR peak increases. The second and third exposure lead to an increase of MLR to the same constant value.

Contrary to tests with an exposure of 55 kW/m^2, ignition occurs for each test. Ignition time is between 13 and 20 s for the first exposure. For the second exposure, ignition time increases of about 35 s like the extinguishment time. The re-ignition occurs close to the exposed surface in terms of cracks where the pyrolysis gases get out. Ignition time increases more for the third exposure, about 45 s for an exposure of 5 minutes and between 60 and 100 s for an exposure of 10 minutes. Samples are more degraded for the exposure of 10 minutes and the char layer is thicker. The formation of the char layer protects virgin wood and explains the increase of ignition time. However, explained for tests at 55 kW/m^2, critical MLR for self-extinction does not decreased after a new exposure (7.26 and 4.97 g/(m²·s) for 5 and 10 minutes respectively).

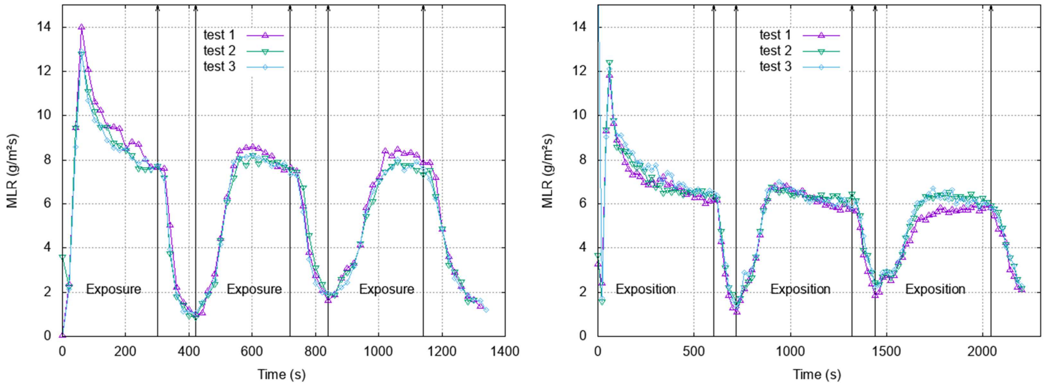

(a) (b)

Fig. 8. MLR of tests with an exposure of 75 kW/m^2 (a) 5 min; (b) 10 min.

Table 2. Ignition time (t_{ig}) and extinction time (t_{ext}) for samples exposed to 75 kW/m^2

Tests	Exposure	5 min		10 min	
		t_{ig}	t_{ext}	t_{ig}	t_{ext}
Test 1	1st	20	14	14	19
	2nd	30	20	31	10
	3rd	40	30	80	16
Test 2	1st	13	13	15	18
	2nd	35	18	64	20
	3rd	45	30	100	35
Test 3	1st	17	18	13	20
	2nd	30	19	40	40
	3rd	47	30	60	50

CONCLUSION

A dedicated experimental setup was used in order to study the thermal degradation of spruce glulam under cone calorimeter. The new configuration allowed the cone to move horizontally for studying sample extinction while measuring continuously mass loss and surface temperature. Cone removal made it possible to get a constant heat flux at the beginning of the test. The auto-ignition and the auto-extinction of the spruce glulam were studied by exposing samples to heat fluxes of 15, 55 and 75 kW/m^2 during different times. A precision scale recorded the mass loss during the test in order to calculate MLR. Surface temperature was also measured with a multispectral infrared camera. This temperature was determined using a filter to overcome the presence of the flame. The calculation was done by inverting Planck's law. The sample extinguishment was characterized by the disappearance of the flame.

The auto-ignition only occurred for heat fluxes beyond 55 kW/m^2. For tests performed at 15 kW/m^2, there was only smoldering combustion. MLR evolutions and surface temperature are linked and highlight well the transition from pyrolysis to smoldering combustion. The withdrawing of the cone led both to a decrease of MLR and surface temperature. The flame disappeared quickly, and the time-to-extinction was lower than one minute. The critical mass loss rate for the extinction depends on the exposure time to heat flux. For the lower exposure time, the degradation is transient and the value of critical MLR value is the highest because the char layer just started to form. This value decreases due to the constant degradation after 500 s of exposure and tends to 4.9 g/(m^2·s). For one hour of exposure, the critical MLR for the self-extinction decreases since the char layer is thicker and thicker.

The new configuration of the cone enabled the study of the glulam re-ignition, too. For 55 kW/m^2, re-ignition was not systematic but the sample degradation seems to be the same even if there was no flame. For 75 kW/m^2, ignition occurred for each new exposure but ignition time and extinction time increased. The char layer plays an important role in the protection of virgin wood.

REFERENCES

[1] V. Babrauskas, R.D. Peacock, Heat release rate: the single most important variable in fire hazard, Fire Saf. J. 18 (1992) 255-272.

[2] V. Babrauskas, Development of the cone calorimeter- a bench-scale heat release rate apparatus based on oxygen consumption, Fire Mater. 8 (1984) 81-95.

[3] R. Emberley, A. Inghelbrecht, Z. Yu, J.L. Torero, Self-extinction of timber, Proc. Combust. Inst. 36 (2017) 3055-3062.

[4] V. Babrauskas, Ignition of wood: a review of the state of the art, J. Fire Prot. Eng. 12 (2002) 163-189.

[5] M. Janssens, Piloted ignition of wood: a review, Fire Mater. 15 (1991) 151-167.

[6] K.L. Friquin, Material properties and external factors influencing the charring rate of solid wood and glue-laminated timber, Fire Mater. 35 (2011) 303-327.

[7] Q. Xu, L. Chen, K.A. Harries, F. Zhang, Q. Liu, J. Feng, Combustion and charring properties of five common constructional wood species from cone calorimeter tests, Construct. Build. Mater. 96 (2015) 416-427.

[8] A. Bartlett, R. Hadden, L. Bisby, A. Law, Analysis of cross-laminated timber charring rates upon exposure to non-standard heating conditions, In: Proc. of the 14th International Conference and Exhibition Fire and Materials 2015, 2015, pp. 667-681.

[9] A.I. Bartlett, R.M. Hadden, J.P. Hidalgo, S. Santamaria, F. Wiesner, L.A. Bisby, S. Deeny, B. Lane, Auto-extinction of engineered timber: Application to compartment fires with exposed timber surfaces, Fire Saf. J. 91 (2017) 407-413.

[10] A.I. Bartlett, R.M. Hadden, L.A. Bisby, B. Lane, Auto-extinction of engineered timber: the application of firepoint theory, In: Proc. of the Fourteenth International Conference and Exhibition on Fire Science and Engineering Interflam, 2016, pp. 1381-1391.

[11] R. Emberley, T. Do, J. Yim, J.L. Torero, Critical heat flux and mass loss rate for extinction of flaming combustion of timber, Fire Saf. J. 91 (2017) 252-258.

[12] O. Grexa, H. Lübke, Flammability parameters of wood tested on a cone calorimeter, Polym. Degrad. Stab. 74 (2001) 427-432.

[13] A. Frangi, M. Fontana, E. Hugi, R. Jübstl, Experimental analysis of cross-laminated timber panels in fire, Fire Saf. J. 44 (2009) 1078-1087.

[14] Z. Acem, D. Brissinger, A. Collin, G. Parent, P. Boulet, T.H.Y. Quach, B. Batiot, F. Richard, T. Rogaume, Surface temperature of carbon composite samples during thermal degradation, Int. J. Thermal Sci. 112 (2017) 427-438.

[15] ISO 5660-1. Reaction-to-fire tests-Heat release, smoke production and mass loss rate-Part 1: heat release rate (cone calorimeter method) (2002).

[16] P. Boulet, G. Parent, Z. Acem, T. Rogaume, T. Fateh, J. Zaida, F. Richard, Characterization of the radiative exchanges when using a cone calorimeter for the study of the plywood pyrolysis, Fire Saf. J. 51 (2012) 53-60.

[17] J. Urbas, W.J. Parker, G.E. Luebbers, Surface temperature measurements on burning materials using an infrared pyrometer: accounting for emissivity and reflection of external radiation, Fire Mater. 28 (2004) 33-53.

[18] M. Chaos, Spectral aspects of bench-scale flammability testing: application to hardwood pyrolysis, Fire Saf. Sci. 11 (2014) 165-178.

[19] J. De Vries, N. Ren, M. Chaos, Temperature measurements on solid surfaces in rack-storage fires using IR thermography. In Thermosense: Thermal Infrared Applications XXXVII. International Society for Optics and Photonics. (2015) p. 94850H.

[20] G. Parent, Z. Acem, S. Lechêne, P. Boulet, Measurement of infrared radiation emitted by the flame of a vegetation fire, Int. J. Thermal Sci. 49 (2010) 555-562.

[21] L. Terrei, Z. Acem, V. Georges, P. Lardet, P. Boulet, G. Parent, Experimental tools applied to the ignition study of spruce wood under cone calorimeter, 3rd European Symposium on Fire Safety Science, 12-14 Sep 2018, Nancy, J. Phys.: Conf. Ser. 1107 (2018) 032022.

Fire Response of a Carbon Epoxy Composite: Comparison of the Degradation Provided with Kerosene or Propane Flames

Chazelle T., Perrier A., Schuhler E., Cabot G., Coppalle A.*

Normandy University, INSA Rouen, CORIA St. Etienne du Rouvray, France
**Corresponding author's email: alexis.coppalle@coria.fr*

ABSTRACT

In the aeronautics, composite materials are widely used. An important issue is that they may be exposed to a flame, during a malfunction of the engines or after a crash. This work is a comparative study, at laboratory scales, of the degradation of carbon epoxy composites with impinging jets of kerosene and propane flames. The propane and kerosene burners have been developed to allow the exposition of small composite samples, of few cm sizes, to heat fluxes greater than 110 kW/m^2. The sample holders were designed to carry out measurement of the mass loss rate and IR temperatures at the rear face during tests. For the two flame tests, the mass loss is nearly complete after 300 s, the resin is almost degraded throughout the sample depth, leaving the fibers naked on the front face, and a small amount of degraded resin on the rear face. However the speed of the degradation is slower with the kerosene flame, with a maximum temperature value reached at the rear face lower than for the propane flame. This is explained by the presence of high amounts of soot in the kerosene flame, while they are nearly non-existent in the propane flame. The high soot content in the kerosene flame induces the built-up of a black carbon layer on the front face, which may reduce the heat transfer between the impinging flame and the sample face.

KEYWORDS: Composites, fire reaction, propane flame, kerosene flame.

NTRODUCTION

In the aeronautics, composite materials are now widely used. Unfortunately under some circumstances, as a malfunction of the engines or after a crash, they may be exposed to a flame. Then the composite is degraded and it losses its mechanical performances. In order to test the fire reaction of the materials, there are several standard tests specific to aeronautical applications [1], in particular some of them use propane or kerosene impinging flames [2-3]. In research at laboratory scales, most of tests are done with a cone calorimeter to apply a radiative flux on the sample [4-5]. Up to now, there are much less studies which have used a flame to induce thermal stress on the material [6-8]. The mains advantages of a flame exposure is that heat fluxes greater than 100 kW/m^2 can be easily reached and a direct flame impact is a more realistic stress for a lot of fire scenarios.

An impinging jet flame induces both convective and radiative fluxes, with different contribution depending on the nature of the fuel. In the case of a non-sooting flame, like the one produced by a burner supplied in stoichiometric conditions, the convective flux is important. With a kerosene flame, the soot production is higher, which increases the contribution of the radiative flux. Another important issue is the soot deposition on the sample, which may be high with kerosene flames, and it can change the heat transfer inside the sample.

The main aim of this work is to compare, at laboratory scales, the degradation of a carbon epoxy composite under the thermal stress provided by a kerosene or propane flame. The burner designs and the flames properties are presented. Details are given on the sample holders and measurement

Proceedings of the Ninth International Seminar on Fire and Explosion Hazards (ISFEH9), pp. 950-958
Edited by Snegirev A., Liu N.A., Tamanini F., Bradley D., Molkov V., and Chaumeix N.
Published by Saint-Petersburg Polytechnic University Press
ISBN: 978-5-7422-6498-9 DOI: 10.18720/spbpu/2/k19-17

systems. The results of mass loss rates and IR temperatures at the rear face, obtained during several tests are shown and discussed.

BURNERS AND FLAME PROPERTIES

The propane burner is similar to the one used in [8], and its design is schematized below on Fig. 1 a. The propane combustion is produced in a small chamber in stoichiometric proportions, and the combustion products are injected inside a long flame-tube (50cm long and 3.5 cm diameter), thus providing at the exit an homogeneous flux of hot gases at the surface of the composite sample. Fig. 1 b shows a picture of the flame impinging one sample during a test. A screen put just above the sample holder can also be seen on the picture, and it avoids the hot gas recirculation on the rear face of the sample. The sample holder itself is placed 17 mm above the burner exit. The design of the sample holder is provided in Fig. 2. An aperture of 45mm diameter is made on both sides of the holder, on the front size to delimit the surface exposed to the flame impact and on the back side to enable the IR temperature measurement. The samples are square shaped with size of 50 mm.

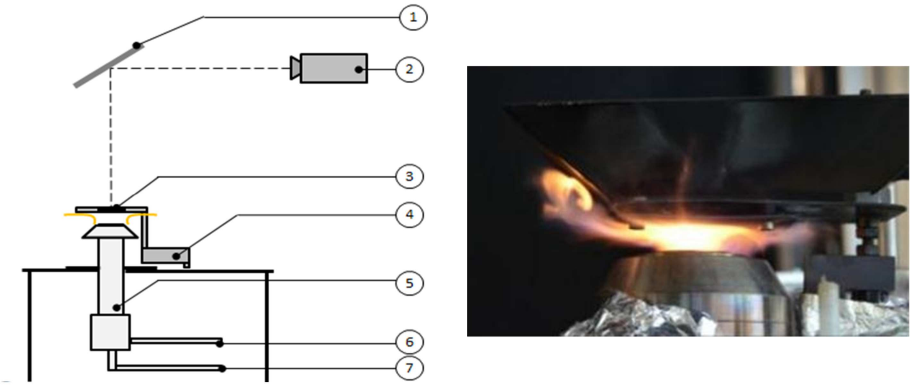

(a) (b)

Fig. 1. (a) Schematic view of the propane burner and the associated measurement setup (1 – mirror, 2 – infrared camera, 3 – sample holder, 4 – load cell, 5 – burner, 6 – air inlet, 7 – propane inlet); (b) picture of the flame impinging one sample during a test

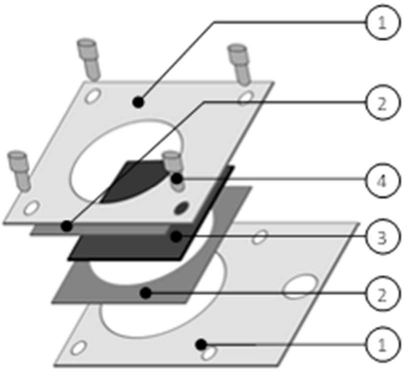

Fig. 2. Schematic of the sample holder for the propane flame case.
1 – sample holder, 2 – insulation sheet, 3 – sample, 4 - screw

The sample degradation by the kerosene flame is based on the same principle. The test bench used for this work is shown in Fig. 3 a. In it, a fuel domestic burner, fed with kerosene and with an air to combustible ratio equals 0.85 of the stoichiometric value, generates a turbulent jet flame. This lower value of the air to combustible ratio for the kerosene burner has been required to obtain the same heat flux and temperatures as with the propane burner A tube is put around the exit of the burner, and it is ended by a flame-tube of 30 cm long and 5 cm diameter (Fig. 3 b). The sample holder is placed 50 mm from the flame-tube exit. A picture of the sample holder for the kerosene tests is provided in Fig. 4. An aperture of 50mm diameter is made alike on both sides of the holder, for delimiting the surface exposed to the flame and to enable the IR temperature measurement on the rear face. The samples are square shaped with a size of 100mm.

Before each test and for both flames, heat flux and flame temperature measurements are carried out with the sample holder removed and at the same location in the free flame. The heat flux is measured using a water cooled heat flux sensor (Captec manufacturer) inserted into a movable steel plate, as shown for example in Fig. 5 for the kerosene flame. Likewise, the temperature is measured using a movable row of 5 type K thermocouples, the spacing between each thermocouple being 7 mm. After the burner ignition, a period of ten minutes is necessary in order to reach steady conditions in temperature and flux. For the propane and kerosene flames, respectively, the mean temperature on the axis is 1110 °C and 1110°C, and the heat flux is 106 kW/m^2 and 116 kW/m^2.

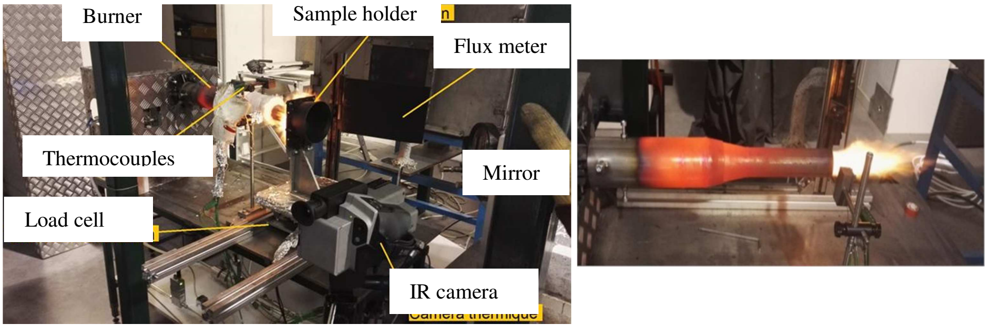

Fig. 3. (a) The kerosene burner and the measurement setup, (b) picture of the flame exiting of the flame-tube (without insulation).

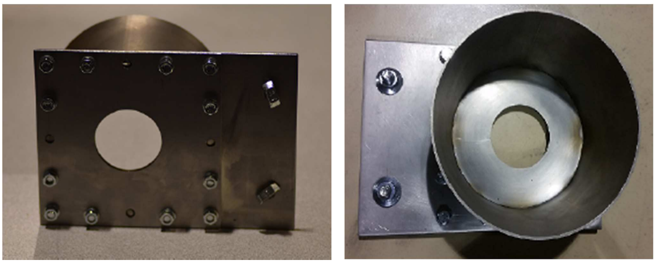

(a) (b)

Fig. 4. Pictures of the sample holder for the kerosene flame case, (a) front face (b) rear face.

MASS LOSS AND IR TEMPERATURE MEASUREMENTS DURING THE TESTS

For the tests with the propane flame, the mass is monitored using a precision load cell, based on resistive foil technology (VPG transducers manufacturer), to which is attached the sample holder. For the tests with the kerosene flame, the sample holder is too heavy to use the same system. So it has been used a weigh scale on which the sample holder has been placed, as seen on Fig. 3 a. The precision of both systems is 0.01g.

The temperature of the rear face of the samples has been observed using an IR camera. The propane and kerosene benches are equipped with a mirror located far away from the sample holder and an infrared camera model ThermaCam PM595 (Fig. 1 a and Fig. 3 a). With this layout, the camera is looking at right angle to the burner axis and it is outside the hot gas flow. The major drawback of the IR measurement method is ignorance, during tests, of the degraded surface emissivity. Therefore we assumed the emissivity to be constant and equal to 0.9, as measured on carbon fibers by Balat-Pichelin et al. [9]. It is also a common value used in the literature for char [10]. However the method allows a temperature measurement of the whole sample surface and so to analyze the temperature homogeneity on the rear surface.

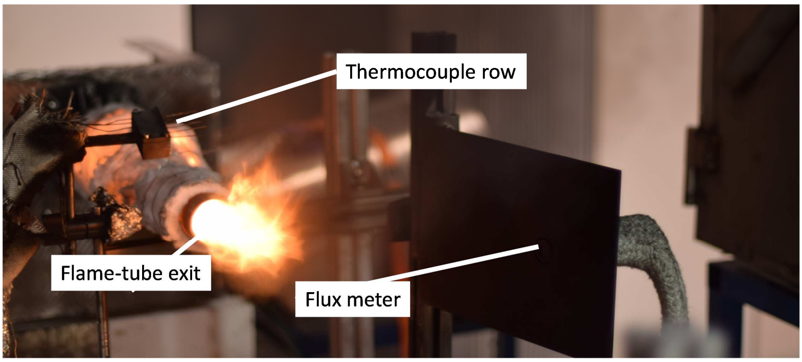

Fig. 5. Picture showing the free kerosene jet flame exiting the flame-tube, the thermocouple row and the flux meter inserted into a steel plate.

COMPOSITE MATERIAL

The samples studied in this work are cut from a 2 mm thick plate, with 50x50 mm² and 100x100 mm² sizes for the propane and kerosene flame respectively. The plate is epoxy-based reinforced with carbon fibers, this composite can be considered as a reference since it has been common CFRP material used in aeronautic structural parts for more than 30 years. The stacking sequence of carbon fiber (T300 3K) is 5-harness satin weave embedded in the polymer matrix. The mass fraction of fiber is 74%. The degradation onset temperature T_d is 320°C and the peak of mass loss rate occurs at temperature T_p equal to 390°C, as shown in Fig. 6.

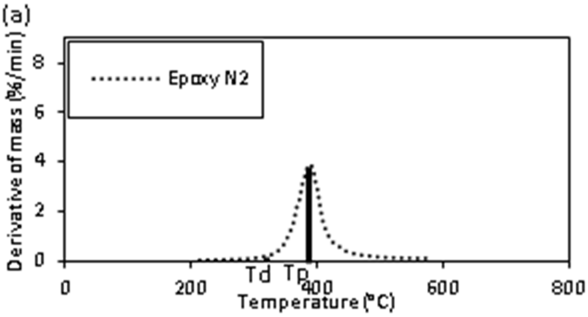

Fig. 6. DTG results for the C/epoxy composite materials in N_2 [8].

RESULTS AND DISCUSSIONS

The samples have been exposed during 300 s to the flame and then the sample holder is removed quickly. For each flame, three tests have been carried out in order to check the reproducibility of the experimental setup as a whole.

Sample appearance after the test

Fig. 7 shows the C/epoxy appearance of one sample, after 300s exposition to the propane flame. On the front side, there is no more matrix residue, the fibers are naked and the surface is slightly curved. A slight deposit has been observed on the front face. On the other side, not exposed to the flame, there is still a small amount of resin residue between the fibers. The back surface has remained more or less flat.

On Fig. 8 is shown the appearance of another sample, after 300s exposition to the kerosene flame. The front side aspect is different, compared to the one obtained with the propane flame. An significant soot layer has been deposed and the surface is not curved. On the other hand, the back face looks like more or less the same as the one observed with the propane flame.

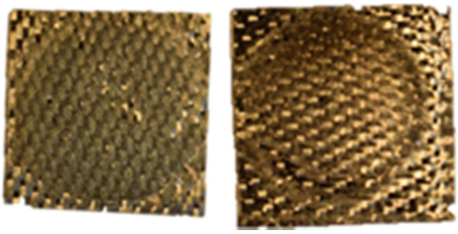

(a) (b)

Fig. 7. View of the C/epoxy sample, after 300s exposition to the propane flame, of the back face (a) and of the front face (b).

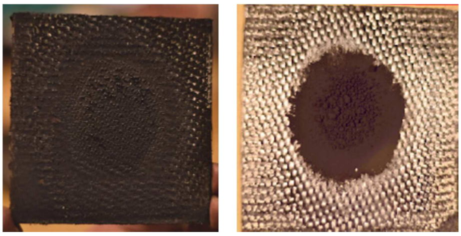

(a) (b)

Fig. 8. View of the C/epoxy sample, after 300s exposition to the kerosene flame, of the back face (a) and of the front face (b).

Mass loss

The mass loss of the C/epoxy samples exposed to the propane or kerosene flames is given in Fig. 9. First of all, one can see that the reproducibility of the measurements is good for the two experimental setups. However, there are important differences in the fire response of the composite. For the kerosene flame, the mass loss is much slower at the beginning and reaches, at 300 s, values that are lower than in the propane flame tests. For this last one, all the mass loss occurs during the first 100 s of the tests. While for the kerosene flame, the mass loss seems not finished at 300 s.

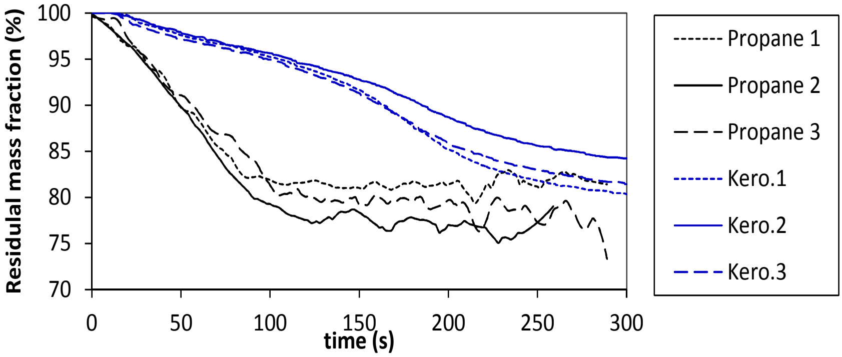

Fig. 9. Mass loss fraction of the C/epoxy samples, exposed to the propane or kerosene flames.

Table 1. Mass before and after the three kerosene tests. All mass in [g]

	Kero 1	Kero 2	Kero 3
Sample mass before the test	29.94	27.78	29.08
Sample holder mass before the test {A}	1879.68	1878.74	1880.61
Sample holder mass with the soot deposit {B}	1873.41	1874.17	1874.89
Sample holder mass without the soot deposit {C}	1873.22	1874.05	1874.78
Total sample mass loss {A-B}	6.27	4.57	5.72
Soot mass deposit {B-C}	0.19	0.12	0.11
Soot mass deposit	3.0%	2.6%	1.9%

Before and after each test, it is easy to measure the mass of the sample and its holder. Table 1 gives these values for the three kerosene tests. The differences between the sample holder mass before {A} and after {B} the tests provide the total sample mass losses. One could suspect that these values may be under estimated because of soot deposit. The mass difference between the sample holder with the soot deposit on the entire surface {B} and without {C} is equal or less than 3%. The exact value of deposited soot mass on the exposed surface of the sample is thus lesser, due to the ratio of the exposed surface exposed to sample holder. So the soot deposit occurs however it represents a small mass compared to the total mass loss.

Temperature at the back face

Figure 10 presents, for test ‘kero 1’, the back face temperature, as measured by the IR camera at 150s. No temperature inhomogeneity is observed on the rear face zone delimited by the aperture of 5cm made in the sample holder. This suggest that most part of the thermal flux applied on the corresponding zone on the front of the sample holder, and also delimited by an aperture of 5cm, is transmitted through the depth of sample, with a low radial flux. For all the other tests with kerosene or propane, pictures and similar temperature homogeneities, as the ones shown on Fig. 1, have been observed.

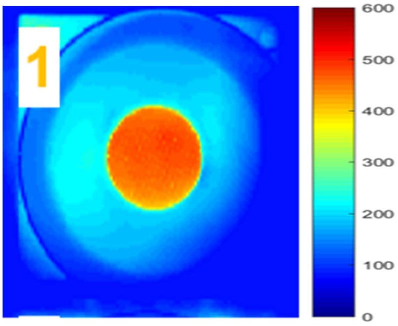

Fig. 10. Back face temperature for test ‘kero 1’ measured by the IR camera at 150s.

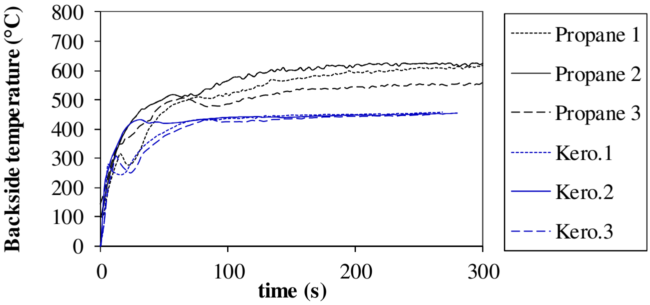

Fig. 11 Back side temperatures at the center of the samples and reported as a function of the exposure time

Backside temperatures measured at the center of the samples and with the infrared camera are reported on Fig. 11 as a function of the exposure time.

During the first 20 s, the temperature increases quickly and in the same way for both flame fluxes, indicating a strong thermal conduction through the sample thickness. The heating rate at the back face approaches 750 K/mn. During this stage, the temperature gradient between the front-face and the back-face is very high, which must lead to high thermally-induced mechanical strains into the material, resulting in micro-cracks formation within the matrix and debonding between plies, as it has been shown in the previous work [8].

At the end of this first period, the temperatures lie between 250–300 °C. This temperature range corresponds to the thermal decomposition of the matrix as shown in Fig. 6. In the second period, the temperature increase slows down. For some tests (propane 1, Kero 1 and 3), the values drop significantly. This observation is associated with the occurrence of thermally induced cracks within the sample [8, 11-12]. It is assumed that the cracks act as a thermal barrier and therefore affect the thermal conduction through the sample. It is important to note that this phenomenon does not occur automatically since it is not observed for half of the tests. Another important question, that would be interesting to answer, is to determine if this cracks occur slowly and later for these tests. One can observe that, even when the cracks do not occur at the beginning, these samples reach the same final temperature as the others.

This final temperature at the back face is lower for tests with kerosene, the difference is quite significant (>100°C). This can be explained by the soot deposit on the front face, which is non negligible for the kerosene flame. At the beginning of the tests, it seems to be low, since no strong differences of the temperature are observed on Fig. 11 during first period up to 20 s. After this period, it becomes bigger. It may act as a thermal barrier, reducing the heat transfer inside the sample, and thus the temperature increase is slowed down which delays also the degradation of the resin. This is observed on the mass loss curves on Fig. 9, which show that the mass loss rate is lower for the kerosene flame from the first moments of the tests. In order to check this assumption, the thermal resistance of a soot layer must be estimated. In a steady-state regime, the temperature variation inside the soot deposit is given by the Fourier law:

$$\Phi = k_{eff} \frac{dT}{dx}, \tag{1}$$

where Φ is the heat flux at the exposed surface, x is the coordinate along the depth and k_{eff} is the effective heat conductivity of the soot layer. At the end of the test, the back face temperature does not vary any more with time, so the assumption of a steady-state heat transfer can be assumed. So the temperature gap inside the soot layer is given by the relation

$$\Delta T = \Phi \frac{l}{k_{eff}}, \tag{2}$$

l being the thickness of the layer. The effective conductivity of the soot deposit layer is a function of the porosity ε of the porous medium, which is defined by $\varepsilon = V_g / V$, where V_g is the volume of gas in the porous medium and V its total volume. Tavman [13] has made an inventory of existing relationships to express the effective thermal conductivities of porous materials. As part of our study, we take the minimum and maximum values given by Tavman [13]:

$$\frac{1}{k_{eff,\perp}} = \frac{\varepsilon}{k_g} + \frac{1-\varepsilon}{k_p} \tag{3}$$

for the series mixing case, and

$$k_{eff,\parallel} = \varepsilon k_g + (1-\varepsilon) k_p \tag{4}$$

for the parallel mixing case. In Eqs. (3) and (4), k_g and k_p are the heat conductivity of the gas and of the particle matter respectively. In order to apply Eq. (2), the soot layer depth is supposed to be equal to 0.5 mm, and different extreme cases have been considered. They are given in Table 2. The heat conductivity of the gas inside the soot layer has been taken equal to that one of air at 600 K, 0.046 W/(m·K), and those of the soot particle matter equal to the one of graphite at ambient temperature, 4.2 W/(m·K).

It is hard to decide which case, series or parallel, is representative of the soot material. On the other side, the exact value of the porosity is certainly between the two extreme ones used in table 2. However some calculated ΔT values in this table may be real and close to difference observed between the kerosene and propane flames, at the end of the test. This crude estimation of the temperature gap shows that the soot deposit layer may act as a thermal barrier, reducing the heat transfer inside the sample. Further studies are necessary to determine more accurately the porosity and depth of the soot deposit, and to perform calculation in an unsteady regime, in order to explain the differences of temperature variations observed between the propane and kerosene flames.

Table 2. For the soot deposit layer: values of the effective heat conductivity and the corresponding temperature gap, considering two different porosity values and using the series or parallel mixing laws

Porosity	$\varepsilon = 0.1$	$\varepsilon = 0.9$
$k_{eff,\perp}$, W/(m·K)	0.42	0.052
ΔT, K[a]	130	1057
$k_{eff,\parallel}$, W/(m·K)	3.78	0.462
ΔT, K[a]	14	119

[a] $\Phi = 110$ kW/m^2.

CONCLUSION

A comparative study, at laboratory scales, of the degradation of carbon epoxy composites with impinging jets of kerosene and propane flames has been carried out. The sample holders were designed to carry out measurement of the mass loss rate and IR temperatures at the rear face during tests. Measurements obtained with three different tests and with the same conditions show that the reproducibility of the two test benches is good, and such systems are well designed to analyze the composite degradation at laboratory scales.

Under a flux of 110 kW/m^2, the mass loss is nearly complete after 300 s for the two cases, the resin is almost degraded throughout the sample depth, leaving the fibers naked on the front face, and a small amount of degraded resin on the rear. However, under the same flux, the speed of the degradation is slower with the kerosene flame, the maximum temperature value reached at the rear face is about 150 °C lower than the one obtained with the propane flame. This is explained by the presence of high amounts of soots in the kerosene flame. This high soot content in the kerosene flame induces the built-up of a black carbon layer on the front face. A rough estimation of the thermal resistance of this soot layer has shown that it may reduce the heat transfer between the impinging flame and the sample face.

Further studies are necessary to determine more accurately the porosity and depth of the soot deposit, and to perform more accurate calculations of the thermal resistance of the soot layer on the front face. Comparison with large scale test results is also important and it will be done in future.

REFERENCES

[1] A.P. Mouritz, A.G. Gibson. Fire Tests for Composites. In: Fire Properties of Polymer Composite Materials. Solid Mechanics and its Applications Vol. 143, 2006, Springer, Dordrecht.

[2] ISO2685:1998(E). Aircraft-environment test procedures for airborne equipment – resistance to fire in designated fire zones.

[3] FAR25.856(b):2003. Title 14 code of Federal – test methods to determine the burnthrough resistance of thermal/acoustic insulation materials (Appendix F, Part VII).

[4] S.I. Stoliarov, S. Crowley. R.E. Lyon, G.T. Linteris. Prediction of the burning rates of non-charring polymers. Combust. Flame 156 (2009) 1068-1083.

[5] N. Grange, K. Chetehouna, N. Gascoin, A. Coppalle, I. Reynaud, S. One-dimensional pyrolysis of carbon based composite materials using FireFOAM, Fire Saf. J. 97 (2018) 66–75.

[6] A.G. Gibson, W.N.B. Wan-Jusoh, G. Kotsikos, A propane burner test for passive fire protection (PFP) formulations containing added halloysite, carbon nanotubes and graphene, Polym. Degrad. Stab. 148 (2018) 86–94.

[7] P. Tranchard et al. Fire behaviour of carbon fibre epoxy composite for aircraft: Novel test bench and experimental study, J. Fire Sci. (2015) 1–20.

[8] E. Schuhler, A. Coppalle, B. Vieille, J. Yon, Y. Carpier, Behaviour of aeronautical polymer composite to flame: A comparative study of thermoset- and thermoplastic-based laminate, Polym. Degrad. Stab. 152 (2018) 105-115.

[9] M. Balat-Pichelin, J.F. Robert, J.L. Sans, Emissivity measurements on carbon–carbon composites at high temperature under high vacuum, Appl. Surf. Sci. 253 (2006) 778-783.

[10] J.B. Henderson, T.E. Wiecek, A Mathematical Model to Predict the Thermal Response of Decomposing, Expanding Polymer Composites. J. Comp. Mat. 21 (1987) 373-393.

[11] A.P. Mouritz, A.G. Gibson, Fire Properties of Polymer Composite Materials. Solid Mechanics and its Applications Vol. 143, 2006, Springer, Dordrecht.

[12] G. Leplat, C. Huchette, V. Biasi, Thermal and damage analysis of laser-induced decomposition within carbon/epoxy composite. J. Fire Sci. 34 (2016) 361-384.

[13] I.H. Tavman, Effective thermal conductivity of granular porous materials, Int. Comm. Heat Mass Transfer 23 (1996) 169-176.

[14] W.C. Hinds, Aerosol technology: properties, behaviour, and measurement of airborne particles (2nd ed.), Wiley Interscience, New York, 1999.

Complexities of the Thermal Boundary Conditions when Testing Timber using the Fire Propagation Apparatus

Cuevas J.I.[1, *], Hidalgo J.P.[1], Torero J.L.[2], Maluk C.[1]

[1] *University of Queensland, Brisbane, Australia*
[2] *University of Maryland, College Park MD, USA*
**Corresponding author's email: j.cuevas@uq.edu.au*

ABSTRACT

The potential for Engineered Timber Products to self-extinguish is the focus of study of numerous researchers worldwide, but regardless of scientific efforts, a relatively high discrepancy still exists on the definition of the critical threshold for self-extinguish. This discrepancy can be attributed to the variability in the test sample material, testing conditions, and/or test methodologies executed. The work presented herein analyses the impact of the thermal boundary conditions imposed by the experimental setup, analysing the divergence of the thermal response from the idealized scenario usually proposed in theoretical frameworks. In particular, the impact of two key assumptions, a semi-infinite solid behaviour and the existence of one-dimensional heat transfer within the solid, are evaluated by means of a case study corresponding to a series of bench-mark experiments conducted in the Fire Propagation Apparatus. By means of a simple one-dimensional heat transfer model, it was found that in order to guarantee a semi-infinite solid behaviour for a thermal exposure of 50kW/m^2 during one hour, a minimum sample thickness of 150 mm is needed. Furthermore, the results of this numerical model have shown that imposing an adiabatic boundary condition in the back face of the sample decreases the time during which this assumption can be sustained, whereas having an exposed or heat sink boundary condition at the back face generates the opposite effect. Following, in order to assess the validity of assuming a one-dimensional heat transfer regime during the tests, the radiative heat transfer between the heating elements and the sample was simulated. The results show the presence of additional heat fluxes through the lateral faces of the sample. The effectiveness of insulating the lateral faces of the sample, to minimize this undesired effect, was analysed by means of a set of experimental tests. The results show that the effect of the lateral incident heat flux over the sample can be minimized, but not discarded. Thus, it is not valid to assume a one-dimensional heat transfer regime within the solid. It is proposed that neglecting these effects can, therefore, cause an inaccurate determination of the thermal conditions imposed during testing.

KEYWORDS: heat transfer, timber, fire propagation apparatus, bench-scale testing.

INTRODUCTION

The timber industry has experienced a renaissance in the built environment. Driven by the increasing need for eco-friendly construction and by the vast potential of engineered timber products, there has been a rapid growth in the design and construction of timber structures. Materials like Cross-laminated Timber (CLT), Laminated Vernier Lumber (LVL), and Glue-laminated Timber (Glulam) stand as comparable alternatives to conventional construction materials such as concrete or steel. The equivalence (and sometimes advantage) of engineered timber is not only associated with load-bearing capacity, but also with a range of other considerations: cost, ease of construction, aesthetics, energy saving, and many others.

Regarding fire safety, a number of regulations incorporate fire safety guidelines for the design of load-bearing timber structures; mainly by means of fire rated encapsulation. Nevertheless, driven by

Proceedings of the Ninth International Seminar on Fire and Explosion Hazards (ISFEH9), pp. 959-969
Edited by Snegirev A., Liu N.A., Tamanini F., Bradley D., Molkov V., and Chaumeix N.
Published by Saint-Petersburg Polytechnic University Press
ISBN: 978-5-7422-6498-9 DOI: 10.18720/spbpu/2/k19-88

the aesthetic aspect of timber, there is an increasing demand for timber to remain exposed; hence, vulnerable to the effects of direct exposure to fire. This presents a challenge that must be addressed before timber can be used with the same confidence we use other building materials and systems [1, 2].

The challenge of achieving fire-safe timber structures is not new; in the early 40s, the work presented by Hottel [3] concluded that a minimum incident radiant heat flux of about 32 kW/m^2 was necessary to sustain flaming combustion of small-scale spruce test samples. Also, Bamford et al. [4] reported that flame extinction of deal panels occurred immediately after the external source of heat was halted and the critical mass loss rate of the sample was approximately 2.5 g/m^{2}s. In the late 70s, Tewarson and Pion [5], and Petrella [6] formally validated the fundamental principle that the heat transferred from the flame impinging on the timber surface is not sufficient to sustain flaming combustion. This led to state that an external source of heat was required to sustain timber combustion.

More recently, Inghelbrecht [7] reported that the occurrence of self-extinguishment is always attained for small-scale Cross-Laminated Timber (CLT) Radiata Pine samples after removing the external source of heat. In this work, the time to self-extinguishment varied because of heat-induced delamination of the lamellae of the CLT samples. For the samples that did not experience delamination, a critical mass loss rate of 4 g/m^{2}s was registered when flame extinction occurred. Considering a more rigorous definition, Crielaard et al. [8] performed a series of bench-scale CLT samples and determined a critical incident radiant heat flux of 5-6 kW/m^2 for the complete stop of combustion (flaming and smouldering). Emberley et al. [9], also testing bench-scale CLT samples, determined a critical mass loss rate of 4.0 g/m^{2}s and critical incident radiant heat flux of 42 kW/m^2, for the cease of flaming combustion. Bartlett et al. [10] tested bench-scale CLT samples and concluded that the conditions for flame extinction occur at approximately 32 kW/m2 and a mass loss rate of 3.5 g/m^{2}s. Based on the numerous studies done to date, a relatively high discrepancy still exists on the definition of self-extinguishment of timber and the critical threshold for its occurrence.

As presented above, the broad range of configurations and methodologies used to study self-extinguishment of timber generates a high degree of discrepancy and uncertainties in the results obtained. As a result, inefficient design criteria are obtained. For example, a difference of a 30% on the critical incident radiant heat flux for self-extinguishment (considering values of 42 and 32 kW/m^2) can be translated into under- or over-sized CLT lamellae, decreasing the level of safety in the first case, and increasing production costs in the second. Furthermore, the inconsistencies among the results obtained at different scales of study prevent the formulation of guidelines that responsibly ensure the fire-safe use of engineered timber in load-bearing structures.

The work described herein aims at tackling the inconsistencies associated with the study of self-extinguishment of timber and the testing methods used for this, by developing a series of testing guidelines that homogenise the analysis of self-extinguishment at a bench-scale, and more specifically when using FM Global's Fire Propagation Apparatus (FPA). The work is divided into two stages: modelling and experimental.

METHODOLOGY

Theoretical Background

When timber is exposed to heat, the exposed surface will gradually heat up and influenced by the thickness of the test sample and the species of the wood, temperature in-depth will increase. Furthermore, a physicochemical degradation process will be triggered because of this temperature increase. This degradation includes moisture evaporation, generation of pyrolysis gases, char formation and oxidation, and as a result of the regression of the exposed surface [11, 12]. Figure 1a presents a schematic of some of the processes involved in the heating and flaming combustion of timber.

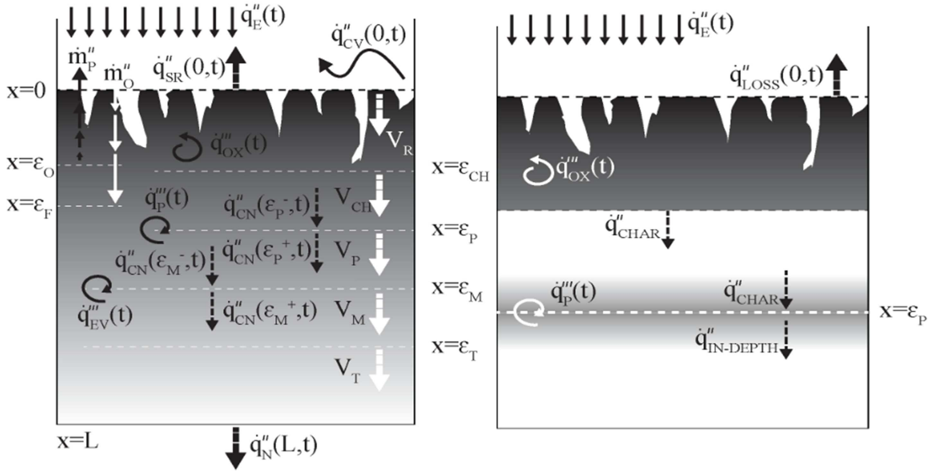

Fig. 1. Different heat fluxes and processes occurring during the burning of timber. (a) Complete scenario, adapted from [11]; (b) Simplified scenario proposed by Emberley et al. [13].

Due to the intrinsic difficulties that arise when dealing with this problem, it is often common to simplify this model by means of the following assumptions:

1. One-dimensional heat transfer is considered.
2. The sample is assumed to behave as a semi-infinite solid.
3. The effects of cracks the material's porosity [14], moisture migration [15], and surface regression at the exposed surface are neglected.
4. Only the material's thermal conductivity is considered as temperature-dependent.
5. Pyrolysis is considered as an isothermal process happening at an infinitely fast rate at a temperature of T_{pyr}. Consequently, the progression of the pyrolysis front can be described by tracking the T_{pyr} isotherm within the solid.

Under these assumptions, Emberley et al. [9] proposed the following energy balance on the charring front:

$$\rho_{char} c_{p\,char} \frac{\partial T}{\partial t} = \dot{q}''_e + \dot{q}''_{oxi} - \dot{q}''_{char} - \dot{q}''_{loss}\,, \tag{1}$$

where $\dot{q}''_e$ is the incident heat flux at the exposed surface of the char layer and it incorporates the heat flux provided by the flame and the one from external sources. The term $\dot{q}''_{oxi}$ represents the energy added due to the exothermic oxidation reaction, and the term $\dot{q}''_{loss}$ represents the energy losses. Following, the rate of energy transferred from the char layer into the pyrolysis front $\dot{q}''_{in-depth}$ is evaluated by means of the following equation,

$$\dot{q}''_{in-depth} - \left(-k \left.\frac{\partial T}{\partial x}\right|_{x=\varepsilon_P} \right) = \Delta H_p \dot{m}''_f\,, \tag{2}$$

where ΔH_p is the heat of pyrolysis and $\dot{m}_f''$ is the mass flow of pyrolysis gases being generated. Thus, combining these two last expressions, the following expression is obtained, that allows relating the mass flow of gases consumed in the flame with the different heat fluxes involved in the process:

$$\dot{m}_f'' = \frac{1}{\Delta H_p}\left(\dot{q}_e'' + \dot{q}_{oxi}'' - \dot{q}_{loss}'' - \left(-k\left.\frac{\partial T}{\partial x}\right|_{x=\varepsilon_P}\right) - \rho_{char} c_{p\,char}\frac{\partial T}{\partial t}\right) \tag{3}$$

From this expression, self-extinguishment can be evaluated through worst-case scenario analysis; the maximum burning rate achievable (that translates into the maximum flow of pyrolysis gases $\dot{m}_f''^{*}$) is obtained when the subtracting terms in the right side are minimized and steady-state conditions are reached. If self-extinguishment is achieved for $\dot{m}_f''^{*}$, it will be achieved for every other mass flow smaller than this one.

PROPOSED APPROACH

From the theoretical formulation presented above, the experimental determination of a $\dot{m}_f''$ only becomes valid if the assumptions used in the theoretical framework are met. The two most powerful and common assumptions made in this study are (1) that test sample exhibits a semi-infinite solid behaviour, and (2) that it experiences a dominant one-dimensional heat transfer in the direction transversal to the exposed surface.

In order to quantify the impact of the first assumption, a one-dimensional transient heat transfer model was implemented. The model considered the heat diffusion equation presented in Eq. 4, with a uniform heat flux boundary condition on the exposed surface (Eq. 5):

$$\frac{\partial k}{\partial T}\left(\frac{\partial T}{\partial x}\right)^2 + k\frac{\partial^2 T}{\partial x^2} = \rho c_p \frac{\partial T}{\partial t}, \tag{4}$$

$$-\left.\frac{\partial T}{\partial x}\right|_{x=0^+} = \dot{q}_e'' - \dot{q}_{loss}'' = \dot{q}_e'' - h_T\left(T_S - T_\infty\right), \tag{5}$$

where $\dot{q}_e''$ is the total incident heat flux over the exposed surface, and the heat losses term $\dot{q}_{loss}''$ is defined by means of a total heat transfer coefficient h_T, evaluated as presented in Eq. 6, according to Hidalgo [16]:

$$h_T = 0.0761\left(T_S\right) + 9.5761 \tag{6}$$

Where T_S is the temperature of the exposed surface, in Celsius. In particular, this model aimed at (1) determining the minimum sample thickness that ensures a semi-infinite behaviour, and (2) due to the spatial limitations of the experimental setup, the determined sample thickness may not be feasible. Thus, the effect of the back-face boundary condition needs to be quantified. This was done by simulating three possible scenarios:

- Insulated (adiabatic) back face, described by a Neumann boundary condition:

$$-k\frac{\partial T\left(L,t\right)}{\partial x} = 0 \tag{7}$$

- Exposed back face, described as

$$-k\frac{\partial T(L,t)}{\partial x}=h\left(T_{\infty}-T(L,t)\right). \tag{8}$$

- Heat sink attached to the back face, described according to Carvel et al. [17] as

$$-k\frac{\partial T(L,t)}{\partial x}=\frac{1}{A}\left(\frac{\partial T}{\partial t}mc_p\right)_{HS} \tag{9}$$

Where m and c_p are the mass and specific heat of the heat sink. For the thermal properties of timber, a moving-boundary model for a non-reacting solid was implemented. This model considered three different phases (wet timber, dry timber, and char) and was implemented following the approach proposed by Lautenberger and Fernandez-Pello [18], in which the solid's density is assumed constant for each phase, while the thermal conductivity and specific heat capacity vary according to the temperature, as presented in the following expressions:

$$k(T)=k^{*}\left(T/T_r\right)^{n_k} \tag{10}$$

$$c_p(T)=c_p^{*}\left(T/T_r\right)^{n_c} \tag{11}$$

Where T_r is a reference temperature, k^{*} and c_p^{*} are referential values of the solid's conductivity and specific heat capacity (evaluated at T_r) and the exponents n_k and n_{cp} describe the variation of these properties according to the element's temperature. The corresponding values used to evaluate these parameters can be found in [19].

Following, a comparison was made in order to determine which one of these scenarios resembles the most to the ideal one (semi-infinite solid). This comparison was based on the in-depth temperature profiles and the progression of the thermal wave for each one of the scenarios.

In order to ensure one-dimensional heat transfer, the thermal boundary conditions under which the samples are tested were characterized and quantified. With this information, the need of additional measures (such as insulating the sides of the sample) was determined, and their effectiveness (based on how much the testing conditions resemble the one-dimensional scenario) analysed.

Experimental setup

The bench-scale experiments were conducted in the Fire Propagation Apparatus (FPA) developed by FM Global, under the specifications of the ASTM E2058-13a standard [20].

Figure 2 presents a schematic of the test apparatus. The upper portion of the calorimeter corresponds to an exhaust system that collects all the combustion-generated products that are driven to the gas analyser. This exhaust system is composed by an intake funnel, a test section where gas temperature and exhaust flow rate are measured, and a high-temperature sampling outlet from where samples of the gases are sent to the gas analyser.

The lower part of the calorimeter corresponds to the combustion chamber which comprises a combustion air distribution chamber, sample holder, weighing cell, ignition device (ethylene pilot flame), and four infrared heaters. In order to evaluate the sample's mass loss, a Tedea Huntleigh Load Cell was used. To characterize the thermal response of the sample, a set of type K thermocouples embedded into the sample and connected to a National Instruments NI-9210 data acquisition system was used.

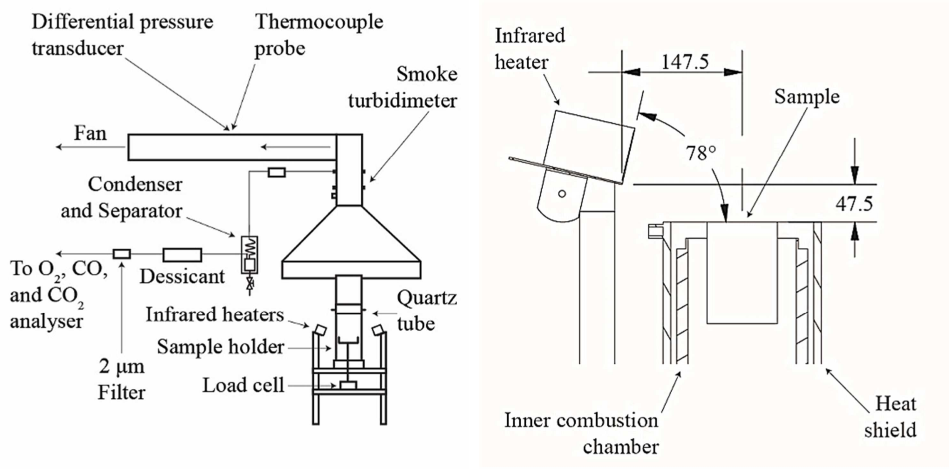

(a) (b)

Fig. 2. Schematic of the experimental apparatus. (a) General schematic of the calorimeter; (b) Geometrical configuration of the infrared heaters (all dimensions in mm).

RESULTS AND DISCUSSION

Semi-infinite solid behaviour assumption

As previously mentioned, to determine the impact of the semi-infinite solid hypothesis, a numerical one-dimensional heat transfer model was implemented under the parameters presented in Table 1, and solved by means of an implicit finite-difference scheme [21, 22] ($O(\Delta t, \Delta x^2)$, and taking Δt = 5 ms, Δx = 0.25 mm). The model was validated by replicating the results presented in [19], were the same material thermal properties were used. A thermal exposure of 50kW/m^2 during one hour was selected. Furthermore, this thermal exposure is imposed in order to match a set of experiments conducted by the author and not reported here.

Table 1. Numerical simulation parameters

Parameter	Value
Thermal exposure	50 kW/m^2 during 3600 s
Material	White pine (*Pinus sp.,* thermal properties from [18])
Dimensions	Rectangular prism with a cross-section of 90x90 mm and variable length

Figure 3a shows the modelled in-depth temperature profiles of a timber, for different times. As it can be seen, the moisture evaporation front (based on the 100 ºC isotherm) reaches a depth of 50 mm after approximately 2650 s, almost 45 minutes. For that same time, the pyrolysis front (based on the 385 ºC isotherm according to [18]) has progressed to approximately 10 mm of depth. Furthermore, if an increase of 0.5 ºC in the original temperature is defined as the criterion to track the progress of the thermal wave (minimal resolution available in the experimental set-up, given by the thermocouple's uncertainty), it was found that the thermal wave has propagated through the sample up to a depth of 150 mm. Therefore, this sample thickness is presented as a candidate for the optimal sample thickness.

Following, the next step was to determine the effect and relevance of the boundary condition at the unexposed face (located at 150 mm from the exposed surface). The results of this stage are presented in Figure 3b. From the figure, it can be seen that the thermal behaviour of the solid is almost independent of the boundary condition considered at the unexposed surface, except for the later portion of it. It was found that the heat sink (in a larger level) and exposed surface (in a lower level) boundary conditions overestimate the arrival of the thermal wave when compared to the semi-infinite wave propagation curve. On the other hand, the adiabatic back boundary condition was found to underestimate the time of arrival of the thermal wave when compared to the same parameter. These results can be explained by the following reasons; an adiabatic boundary has a barrier effect on the propagation of heat, therefore facilitating the storage of it within the element and finally elevating its temperature. For the other two conditions, their effect is the complete opposite; if the element's back face is exposed to the ambient (modelled as air at a constant temperature of 18°C) or to an adjacent heat sink (modelled as a 20 mm thick Aluminium block), there is an additional heat flux at this boundary, evacuating (by means of convection/radiation or conduction, respectively) any amount of heat that reaches this portion of the sample, allowing it to remain cooler for a longer period.

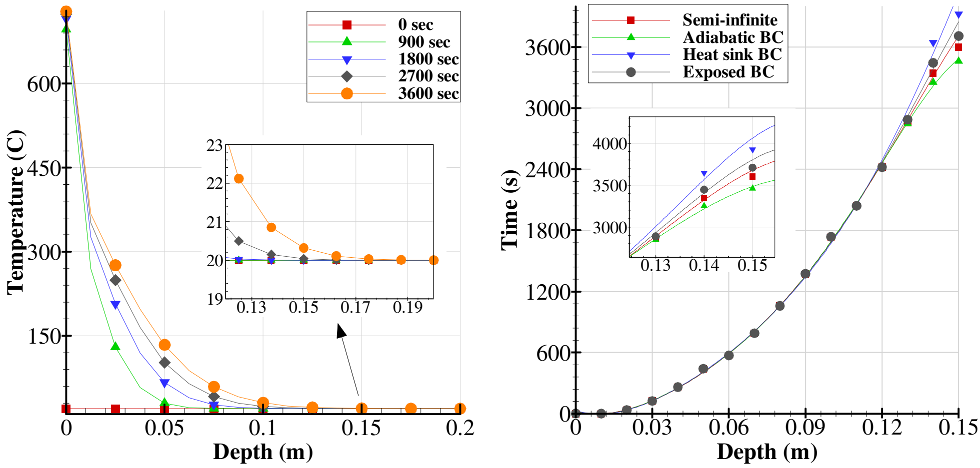

(a) (b)

Fig. 3. Thermal response of the modelled timber element. (a) In-depth temperature profiles for different times; (b) Time needed for the thermal wave to reach a certain depth, for different boundary conditions at the unexposed surface.

From this first part of the study, it can be partially concluded that a timber sample of 150 mm thick with a heat sink element attached to its unexposed face it is expected to show a semi-infinite solid behaviour when exposed to a constant incident heat flux of 50 kW/m^2.

ONE-DIMENSIONAL HEAT TRANSFER ASSUMPTION

For the next part of the present study, a set of experimental tests were conducted to determine the boundary conditions under which the samples are actually tested in the experimental setup described previously. One of the most relevant parameters in this point is to characterize the radiant incident heat flux over the exposed surface of the sample. This characterization was done by means of a numerical model that simulated the radiant incident heat flux over the sample. This model was calibrated using a set of experimental measurements conducted using a Medtherm Schmidt-Boelter-type heat flux gage (model: GTW-10SB-8-36-40-484). The results of the model are presented in Fig. 4.

From Fig. 4a, it can be seen that the heater's configuration imposes over the exposed surface an incident heat flux over sufficiently homogeneous to partially enable the one-dimensional heat transfer assumption, as discussed Boulet et al. [23]. On the other hand, Figure 4b indicates the presence of an unneglectable (approx. 40% of the maximum heat flux) heat flux over the lateral faces of the element. To completely validate the one-dimensional transfer assumption, it is necessary to mitigate the effect of this lateral heating by means of corrective actions. Figure 4c shows the data used to calibrate this model. In the figure, the black dots represent the 17 measurements points considered in the calibration. An overall agreement can be seen between the data collected experimentally (Fig. 4c) and the results obtained by the model (Fig. 4a).

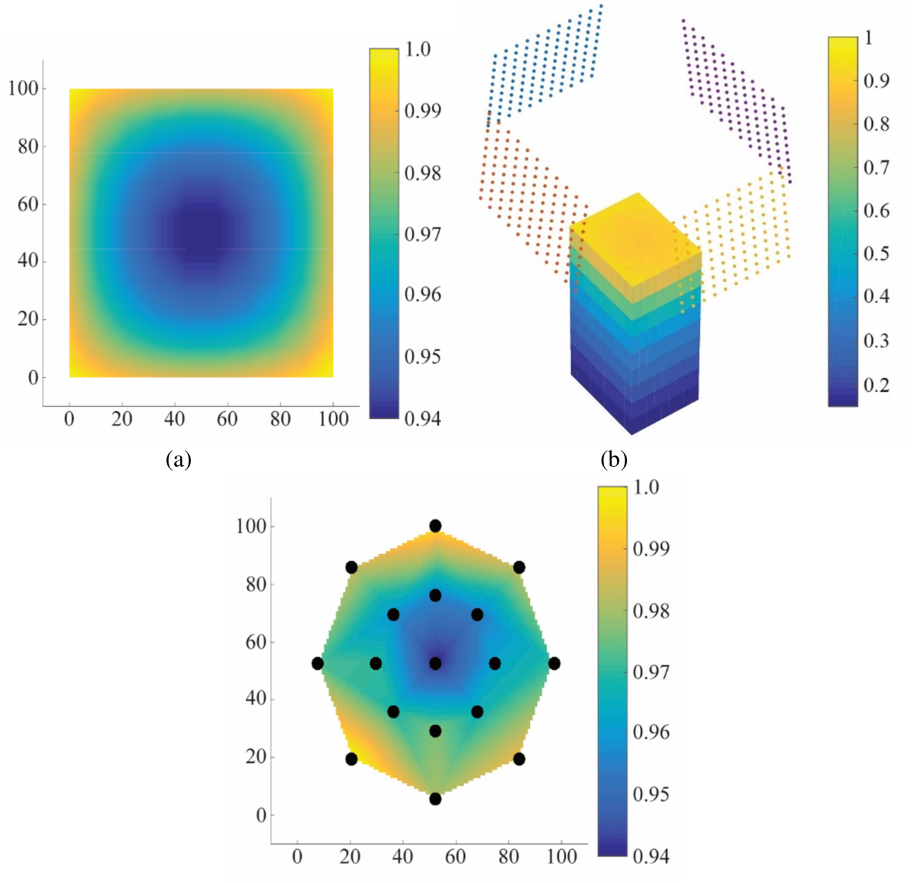

(a) (b)

(c)

Fig. 4. Results of the numerical modelling of the incidental heat flux over the sample (all units in mm). (a) Normalized spatial distribution of the incident heat flux over the complete sample; (b) Normalized spatial distribution of the incident heat flux over the exposed surface. (c) Results of the experimental measurements used to calibrate the numerical model.

The effectiveness of a corrective action consisting on protecting the sides of the sample with an insulating jacket was evaluated by means of an experimental study which compared the thermal degradation of samples (in terms of mass loss and in-depth temperature measurements) with and without insulation. A general description of this experimental campaign is presented in Table 2 and the results in Fig. 5.

From Figs. 5 a and b, the relevance of the presence of lateral insulation is left in evidence; the temperature curves registered by the thermocouples placed at 35 mm from the exposed surface show temperature difference of approximately 150 °C after 900 s. Moreover, the heating profile described by the unprotected sample at a depth of 75 mm is with the range of the one showed at 55 mm by the protected sample for the majority of the exposure time. This radical difference in the thermal behaviour of the sample is also evidenced when looking at the thermal profiles presented in Fig. 5c; after 900 s the unprotected sample has lost approximately 40% of its original mass, while the protected on has lost approximately 10% of it.

Table 2. Parameters for the experimental campaign

Parameter	Value
Thermal exposure	50 kW/m^2 (constant), during 15 min
Sample dimensions	Rectangular prism with an exposed surface of 90x90 mm, 150 mm thick
Material	Cross-laminated Timber (Radiata Pine)
Sample preparation	(1) Inner layer of 9 mm thick Ceramic Paper (SiO_2-Al_2O_3 based material); (2) Outer lining of reflective material
Thermocouples	12 Type K thermocouples (TC) in-depth placed at: 35 mm (4 TCs), 55 mm (2 TCs), 75 mm (2 TCs), 95 mm (1 TC) mm centred about the sample. 3 TCs at a depth of 95mm within the insulation (inner, middle, and outer)

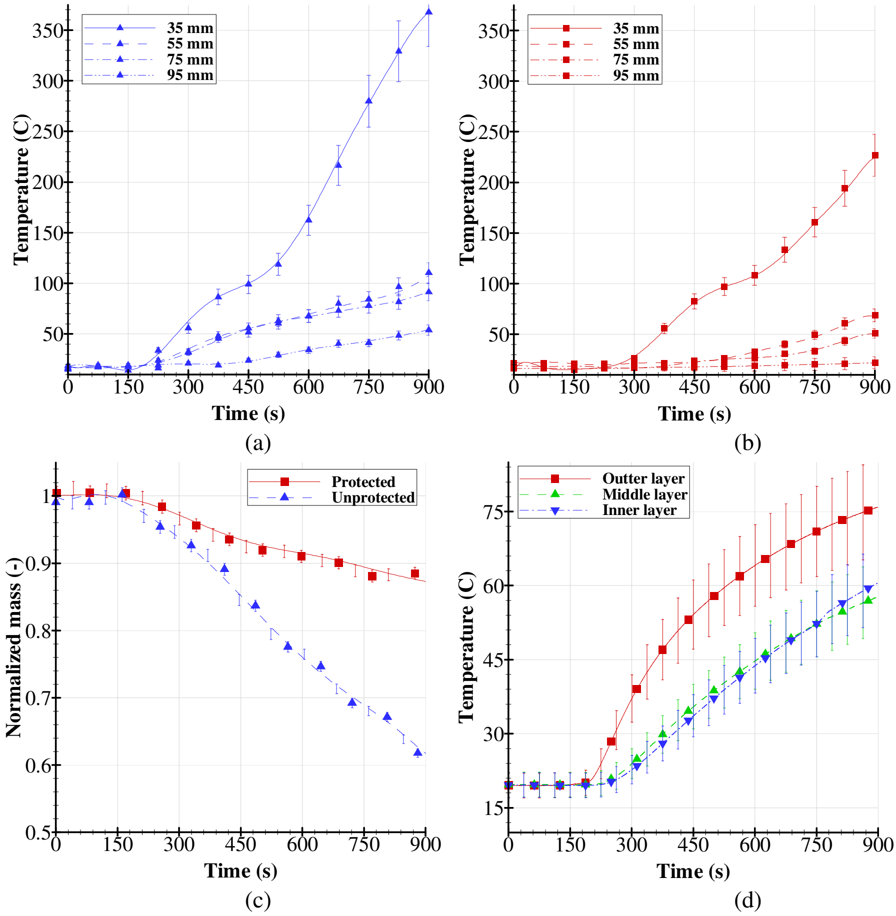

(a) (b)

(c) (d)

Fig. 1: Experimental evaluation of the effectiveness of lateral insulation. (a) In-depth temperature profiles for an unprotected sample; (b) In-depth temperature profiles for a protected sample; (c) Comparison of mass loss measurements; (d) Temperature profiles within the insulation, at a depth of 95 mm from the exposed surface of the test sample.

Regardless of the improvement in the thermal response of the sample due to the presence of lateral insulation, this corrective action is not sufficient to ensure one-dimensional heat transfer, as presented in Fig. 5d. The measurements shown in Fig. 5d correspond to the readings of the thermocouples positioned at a depth of 95 mm from the exposed surface, within the three insulation layers. The inner layer thermocouple was placed between the inner Aluminium lining (place at the sides of the test sample) and the first layer of Ceramic Paper, the middle layer thermocouple was placed in between the first two insulation layers, and the outer layer thermocouple was placed in between the last two insulation layers. From the figure, it can be seen that the temperature that the insulation reaches is higher than the one at the centre of the sample (at the same depth from the exposed surface). The presence of such high temperatures in the inner insulating layer indicates the heating of the sides of the samples during testing.

CONCLUSIONS

The present work has analysed the relevance of two of the most common assumptions used in scientific analysis experimental bench-scale timber fire studies; the semi-infinite solid behaviour and one-dimensional heat transfer within the solid sample. Meeting these assumptions in bench-scale testing is not only relevant to achieve results that are consistent with the theoretical frameworks, but also enables the scaling up of these results in order to predict the full-scale fire behaviour of timber. In an attempt to evaluate the conditions necessary to meet these assumptions, a minimum sample thickness was determined by means of a numerical heat transfer model. Following, the unavoidable presence of lateral heating was also identified by simulating the radiative heat transfer between the infrared heaters and the test sample. Furthermore, experimental results show that for a thermal exposure of 50 kW/m^2, after the first 15 minutes (900 seconds) of heating, an unprotected sample will lose up to 30% more mass than a protected sample. Also, results show that temperatures at a depth of 35 mm from the exposed surface can be more than 100°C higher when comparing unprotected and protected test samples. Regarding this last aspect, even though protecting the sides of the sample shifts the thermal response of the element towards an ideal behaviour (i.e. without lateral heating), the protection used within the scope of this work demonstrated not to be sufficient to achieve one-dimensional heat transfer during the full duration of a test.

The presence of heating at the sides of the test sample is given by the need to use a standardized apparatus to perform standardized tests, using non-standardized test samples [20]. Neglecting this effect can, therefore, cause an inaccurate determination of the thermal conditions imposed during testing. This could explain the apparent discrepancy that exists in the determination of the critical conditions for the self-extinction of timber; especially between Inghelbrecht [7], Crielaard et al. [8], Emberley et al. [9], and Bartlett et al. [10].

Finally, in order to generate valuable scientific outcomes, the common theoretical frameworks must be modified to take into account the abovementioned conditions associated with fire testing of timber using the Fire Propagation Apparatus.

REFERENCES

[1] A. Law, A. Bartlett, R. Hadden, N. Butterworth, The Challenges and Opportunities for Fire Safety in Tall Timber Construction, in: 2nd Int. Tall Build. Fire Saf. Conf. 2014, 2014: pp. 17–19.

[2] R. Gerard, D. Barber, A. Wolski, Fire safety challenges of tall wood buildings, National Fire Protection Research Foundation, 2013.

[3] H.C. Hottel, G. Wilkes, Wood Flammability Under Various Conditions of Irradiation, OSRD Publ. 432 (1942).

[4] C.H. Bamford, J. Crank, D.H. Malan, A.H. Wilson, The combustion of wood. Part I, Math. Proc. Cambridge Philos. Soc. 42 (1945) 166–182.

[5] A. Tewarson, R.F. Pion, Flammability of plastics-I. Burning intensity, Combust. Flame 26 (1976) 85–103.

[6] R. V. Petrella, The Mass Burning Rate and Mass Transfer Number of Selected Polymers, Wood, and Organic Liquids, Polym. Plast. Technol. Eng. 13 (1979) 83–103.

[7] A. Inghelbrecht, Evaluation of the burning behaviour of wood products in the context of structural fire design, International Master of Science in Fire Safety Engineering MSc, The University of Queensland, Ghent University, 2014.

[8] R. Crielaard, J.-W.W.G. van de Kuilen, K.C. Terwel, G.J.P. Ravenshorst, P. Steenbakkers, A. Breunese, A. Breunesse, Self-extinguishment of cross-laminated timber, in: Proc. World Conf. Timber Eng. (WCTE 2016), Vienna, Austria, 2016.

[9] R. Emberley, A. Inghelbrecht, Z. Yu, J.L. Torero, Self-extinction of timber, Proc. Combust. Inst. 36 (2017) 3055–3062.

[10] A. Bartlett, R. Hadden, L. Bisby, B. Lane, Auto-extinction of engineered timber: the application of firepoint theory, in: Interflam, 2016.

[11] J.L. Torero, Flaming Ignition of Solid Fuels, in: SFPE Handb. Fire Prot. Eng., 5th ed., Springer New York, 2016: pp. 633–661.

[12] D. Drysdale, An introduction to fire dynamics : 3rd ed., Wiley, Chichester, West Sussex, 2011.

[13] R. Emberley, T. Do, J. Yim, J.L. Torero, Critical heat flux and mass loss rate for extinction of flaming combustion of timber, Fire Saf. J. 91 (2017) 252–258.

[14] R.K.K. Yuen, G.H. Yeoh, G. de Vahl Davis, E. Leonardi, Modelling the pyrolysis of wet wood – I. Three-dimensional formulation and analysis, Int. J. Heat Mass Transf. 50 (2007) 4371–4386.

[15] R. Aseeva, B. Serkov, A. Sivenkov, Fire Behavior and Fire Protection in Timber Buildings, Springer, 2014.

[16] J.P. Hidalgo-Medina, Performance-based methodology for the fire safe design of insulation materials in energy efficient buildings, The University of Edinburgh, 2015.

[17] R. Carvel, T. Steinhaus, G. Rein, J.L. Torero, Determination of the flammability properties of polymeric materials: A novel method, Polym. Degrad. Stab. 96 (2011) 314–319.

[18] C. Lautenberger, C. Fernandez-Pello, A model for the oxidative pyrolysis of wood, Combust. Flame 156 (2009) 1503–1513.

[19] A.F. Osorio, J.P. Hidalgo, P.D. Evans, Enhancing the fire performance of engineered mass timber and its implications to the fire safety strategy, in: Proc. World Conf. Timber Eng. (WCTE 2018), Seoul, Republic of Korea, 2018.

[20] ASTM International, ASTM E2058-13a Standard Test Methods for Measurement of Material Flammability Using a Fire Propagation Apparatus (FPA), i (2013) 30.

[21] T.L. Bergman, F.P. Incropera, D.P. DeWitt, A.S. Lavine, Fundamentals of Heat and Mass Transfer, 7th ed, John Wiley & Sons, 2011.

[22] R.H. Pletcher, J.C. Tannehill, D.A. Anderson, Computational fluid mechanics and heat transfer, 3rd ed., CRC Press, 2013.

[23] P. Boulet, G. Parent, Z. Acem, A. Collin, M. Försth, N. Bal, G. Rein, J.L. Torero, Radiation emission from a heating coil or a halogen lamp on a semitransparent sample, Int. J. Therm. Sci. 77 (2014) 223–232.

Ignition from High Heat Flux for Flat versus Complex Geometry

Brown A.L.[1,]***, Engerer J.D.**[1]**, Ricks A.J.**[2]**, Christian J.M.**[3]

[1] *Sandia National Labs, Fire Sci. and Tech. Dept., Albuquerque, NM, USA*
[2] *Sandia National Labs, Tech. Anal. Dept., Albuquerque, NM, USA*
[3] *Sandia National Labs, Conc. Solar Tech. Dept., Albuquerque, NM, USA*
**Corresponding author's email: albrown@sandia.gov*

ABSTRACT

Ignition of solid materials from radiative heat flux has been well studied, as it relates to common fire instantiation and propagation. Conventional testing involves a small (~10 cm) flat sample in a test apparatus such as a cone calorimeter exposed to fluxes in the range of 25-100 kW/m^2. Higher heat flux ignition has been less-well studied, and the majority of scientific data come from similarly scaled experiments mostly on flat surfaces. High heat flux ignition is less well studied because it has a more limited application space given that fewer fire scenarios involve high (> 200 kW/m^2) fluxes. We have been performing experimental investigations of the behavior of a variety of materials exposed to concentrated solar power with peak flux in excess of 2 MW/m^2. Dozens of materials at a variety of flux conditions with varying scales and configurations have been tested thus far. While we have found good correlation in our new data to historical data and model constructs, some of our data are not well predicted by existing models and correlations. Present results suggest ignition on flat materials is not necessarily a good predictor of other materials and configurations, and that future testing would benefit from an increased emphasis on the geometry of exposed materials.

KEYWORDS: Ignition, heat flux.

INTRODUCTION

Ignition from an incident radiative flux is well characterized for many materials under flux conditions typical of conventional hydrocarbon fires (25-100 kW/m^2). Standards such as ASTM E1740-15 and ASTM E1354 govern this type of testing. We are focused on ignitions and fire behavior from much higher fluxes (100-10,000,000 kW/m^2), which may be obtained from metal fires, propellants, lightning, directed energy, space exploration, etc.

Historical data on ignition from high heat fluxes are not as plentiful. Notable compilations of data in this flux regime include Glasstone and Dolan (1977) [1] and Martin and collaborators [2-3]. Glasstone and Dolan correlated ignition for a variety of materials to the yield and distance from a nuclear weapon, a construct that is not particularly useful in other applications. Martin et al. represented their ignition data in terms of scaled flux and fluence, a more useful construct for extensibility. The Martin datasets are dominated by cellulose paper data and exposure areas of around 10 cm^2, the primary focus of their efforts. They found various behavioral regimes characterized by different parameters. At low fluxes, the sample thickness and imposed energy were most significant. At higher fluxes, the incident energy was the dominant parameter. At even higher fluxes, the imposed energy and the flux magnitude had comparable significance. Different types of ignition were observed (glowing, sustained flaming, transient flaming). Transient flaming was defined by flaming that occurred only as the heat flux was incident on the object. Sustained flaming lasted beyond the exposure.

Proceedings of the Ninth International Seminar on Fire and Explosion Hazards (ISFEH9), pp. 970-979
Edited by Snegirev A., Liu N.A., Tamanini F., Bradley D., Molkov V., and Chaumeix N.
Published by Saint-Petersburg Polytechnic University Press
ISBN: 978-5-7422-6498-9 DOI: 10.18720/spbpu/2/k19-92

We have been adding to the body of work on high-heat flux ignition by testing materials under high flux (> 200 kW/m^2) conditions using concentrated solar energy. Work began with a focus on flat materials with an objective to reach-back to the majority of the historical data [2-3], but has included enough geometric variation to begin to deduce the important role geometry has in the ignition behavior. Our prior reporting of this work illustrates the significant role of scale in the fire behavior [4], a new approach to the ignition and damage threshold modelling [5], and the effect of wind and gas phase radiation attenuation on the fire response of materials [6].

Evaluations of the recent data suggest an additional significant feature of the materials that appears to affect the outcome of the event. The shape of the samples appears to affect the resultant ignition behavior. The effect of shape is not systematically studied in any of the historical datasets, and consequently is ignored in prior models and inferences derived therefrom. More complex shapes may tend to more easily ignite and sustain ignition. This paper examines the evidence for this statement in the context of the recent concentrated solar ignition tests. The purpose and value of this paper is in the identification of the important role that shape has on the propensity for sustained ignition from high heat flux events. The objective is to help motivate an increased exploration of the shape as an important factor leading to high heat flux ignition to better characterize a broader range of material response.

METHODS

The National Solar Thermal Test Facility at Sandia National Labs in Albuquerque has two main facilities that concentrate solar energy. One is the Solar Tower, that uses a heliostat field (an array of large mirrors with fine motor control that actively track the sun to maintain a relatively constant target location for the rays) to achieve a concentration factor greater than 2000 suns (1 sun is approximately 1 kW/m^2), and a power of 6 MW at length scales of 0.3-1 m. The other is the smaller Solar Furnace that uses a single heliostat and a parabolic dish for smaller length scale testing (5-7 cm). Several hundred high flux ignition tests have been conducted at these facilities including varying material types, thicknesses and shapes, while also varying flux, fluence, length-scale, wind, and ambient temperature.

Tests were conducted in test phases. A Solar Furnace test phase involved approximately 50 test shots, while the solar tower test phase involved about 30 shots. The test matrix for each test was determined by a panel of researchers. Materials were selected from a list of relevant materials. Test and environment conditions were controlled as well as could reasonably be done for the facilities available. Test objectives were manifold, so the test programs were not apparently targeted in their approach to specific objectives. Rather, a wide variety of materials and test conditions were employed with the outcome of the tests being the identification of prospective subsequent tests to explore interesting observations from prior test phases. The three main programmatic objectives were:

1. To produce quality datasets with sufficient repeatability to employ for validating 3D computational models of fire and related phenomena.
2. To explore environmental factors with the intent of reach-back to historical datasets to understand material dynamics under various conditions.
3. To explore practical or unique ignitions that are under-represented in the body of historical testing.

Tests were split roughly evenly between the above three objective areas. The reason for testing in phases while incorporating multiple objectives is because of the uncertainties in funding cycles and the desire to have broad impact rather than narrowly focused program results. A negative consequence of this method is that it may take multiple test phases to achieve sufficient data to quantitatively resolve phenomenology from the tests. An advantage of the method is that a targeted assessment is made after each phase of testing, and the subsequent plans are formulated after gaining insight from the results from prior phases.

Table 1 shows some details of the sample tested. Flat samples were 23×11.5 cm at the solar furnace, and approximately 90×120 cm at the solar tower. L-shaped samples consisted of two chairs, photographs of which are shown in Fig. 1. A polypropylene patio chair and a wood/foam/fabric office chair were used. Chairs were oriented differently during the tests to optimize exposure to the incident flux. The polypropylene chairs were upright with the back of the seat back exposed to the flux, and the fabric chairs were on their side with the front of the seat back in direct exposure.

Table 1. Details regarding the reported Solar Tower (ST) and Solar Furnace (SF) experiments

Material	Geometry	Thickness (mm)	ST	SF
Cellulose	Flat	1.2-5.0		X
Paper	Flat	0.11-0.25	X	X
Fabric	Flat/L	0.7-0.9	X	X
Biomass	Irregular/Flat	Variable	X	X
Polyethylene	Circular/Flat	≈ 3 mm	X	X
Polystyrene (PS)	Flat	0.5-3.2	X	X
Synthetic Rubber	Circular/Flat	Variable	X	X
Polymethyl-methacrylate (PMMA)	Flat	3.2-11.3	X	X
Polypropylene	L/Flat	Variable < 4	X	X
Vinyl	Flat	1.1		X

Fig. 1. Pre-test photographs of the polypropylene (left) and wood/foam/fabric chairs (right).

INSTRUMENTATION

A variety of instrumentation was deployed for the tests, the details of which may be found in the test series documentation. For this paper, highlights of the instrumentation are outlined only. Details on the instrumentation are available in the corresponding test phase documentation [3-6]. Each test included the following:

1. Flux measurements to confirm the imposed thermal environment, and characterization of the day, time, and configuration of the flux source

2. Multiple angle fiducially accurate video imagery from standard, high-speed, and filtered optical cameras
3. Atmospheric data from a weather station to confirm the ambient conditions
4. Pre- and post-test photography
5. A temporal fiducial to allow post-test synchronization of instrumentation results from various sources
6. Controls output containing data on the temporal sequence for each test

Tests mostly included:

7. Pre- and post-test weight of samples

Some tests included:

8. Strategically mounted thermocouples for temperature measurements
9. IR camera imagery for thermal response
10. Witness strings as local air flow indicators
11. Post-test 3D scanning for digital re-construction of the thermal crater

Ignition and burn times are key to the analysis presented in this paper. These were deduced through post-test analysis of the video imagery. Ignition was often discernable through the observed flames in the video output. In some tests, the pyrolysis gases obscured direct views of the ignition. The ignition event usually included a rapid increase in the motion of the pyrolysis gases, in which case the flames were not directly observed but inferred based on the motion of the opaque gases and the presence of flaming later in the video.

Characterization of Environment

Tests were conducted within a few hours of solar noon on clear (cloudless) days. The environment was characterized using pre- and post-test analysis of heat flux instrumentation to verify the test conditions. Because of the response time of the test facility hardware, the imposed flux was a ramp to a constant hold, and a ramp back down to ambient.

Fluence (defined as flux integrated with time) magnitude was a target condition, which explains the regularity of intervals in some of the fluence data. Fluence targets were usually round numbers, however post-analysis sometimes adjusted these away from the target values. For this paper, exposures are simplified to a fluence condition. Solar Furnace fluence was applied over a roughly 4-6 cm diameter spot [7], Solar Tower exposures varied spatially, but spanned the samples. Peak flux and fluence was centered on each sample.

Tests were conducted at different times of the year in an outdoor environment. Ambient temperatures for two Solar Furnace test series conducted in July/August were 20-35ºC. The second Solar Furnace phase was conducted in February/March, and mid-day ambient temperatures were between 5-25ºC. The Solar Tower tests were conducted from August-November, and ambient temperatures varied between 10-30ºC. Post-processing of the data has not suggested a significant effect of the initial ambient temperature on any resultant parameters over the range of variation.

RESULTS AND DISCUSSION

We grouped materials in a few categories for this analysis. The first main grouping is by material type. Cellulosic materials (plant matter, paper, wood, fabrics, etc.) are grouped, as cellulose constitutes a significant fraction of these materials. Synthetic polymers are also grouped. The second grouping consists of the shape of the test objects. Flat objects are primarily surfaces exposed to the flux, and represent the traditional way of assessing ignition at high heat flux. A few of the samples consisted of significant L-shapes, and these are termed L-shaped materials. Some materials were round (tires and trash cans). They differ from the flat materials because there were no significant flat surfaces, and the curves were the dominant shape of the exposed surfaces. These are termed circular. Irregular shapes are generally biomass materials that are characterized by high surface area compared to the volume.

The test series involved more tests than are exhibited here. Tests omitted include ones that defied characterization by the shape parameters (flat, circular, L and irregular), those that did not fit the material type categorization, as well as those that did not achieve flaming ignition.

Combining the duration of burn results with the fluence imposed on the samples, a picture emerges suggesting a significant role that shape plays in the duration of burn. For convenience in plotting, burn durations greater than 1000 seconds have been truncated to 1000, and durations below 1 second have been increased to 1. While this is not a hard rule, it turns out that tests that involved transient flaming all are below 10 s burn time, and the sustained flaming tests all fall at or above 10 seconds. Figure 2 shows a plot of cellulosic materials on the fluence/burn duration plot. There is a very clear stratification between the data by shape. The few L-shaped tests show generally higher burn durations than other tests. The irregular shaped objects tend to have higher burn durations. The flat materials exhibit generally lower burn durations. There were no ‘circular’ samples for the cellulosic materials.

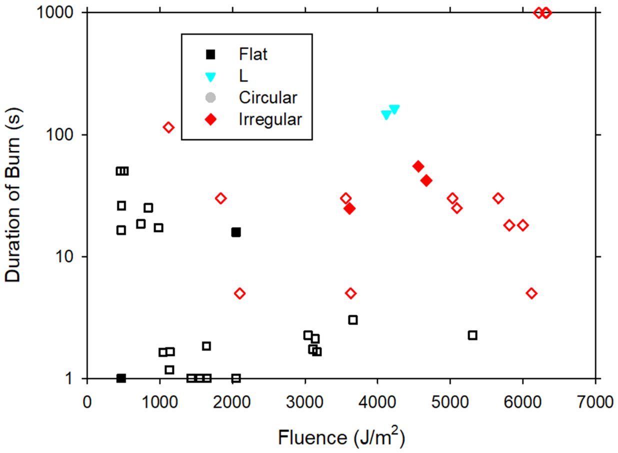

Fig. 2. Duration of burn versus fluence for cellulosic samples. Solar Tower experiments are differentiated from Solar Furnace tests, having closed symbols instead of open.

Because the tests were not systematically varied specifically for this parameterization, there is a need to interpret the meaning of these results in the context of a more representative evaluation including the other variabilities. The flat materials generally did not result in sustained burning. The general exception to this is flat materials that were sufficiently thin that the imposed radiant energy pyrolyzed the sample completely through. Figure 3 illustrates some sustained ignition of thin materials fitting the just described behavior. The fire was initially (post-exposure) localized to edges on the sample, typically a circular ring at the center of the sample. Thicker samples pyrolyzed, but would not sustain flaming if they ignited. The flat materials that sustained flaming were all sufficiently thin to burn in this manner. It is not a particular surprise to see the irregular shaped materials generally exhibiting longer burn times. When burning solid materials, the surface area to volume is widely recognized to be a very significant parameter. The three irregular samples that fall below 10 s burn duration were a mix of green and dry needles. The green needles alone did not ignite, and the dry needles alone generally burned profusely. The large-scale (Solar Tower) and some of the small-scale tests were green plant materials. The trees at the Solar Tower were cut within 30 minutes of their exposure, and were well watered. Even with the high moisture content of a live tree that normally is expected to inhibit flaming, the irregular materials appear to result in much greater burn times than was typical of the flat biomass samples. This suggests a more significant effect of shape as compared to moisture in these tests.

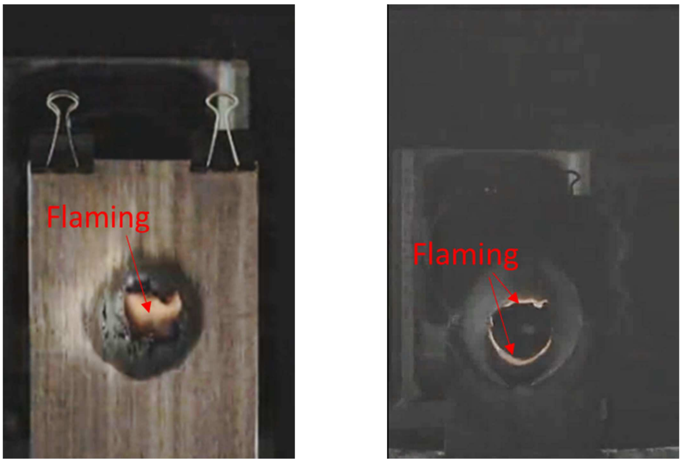

Fig. 3. Two thin rectangular Solar Furnace samples exhibiting sustained flaming at/within the rim of the hole. The left figure is a walnut veneer at 3.5 seconds, and the right figure is black polystyrene at 3.5 seconds. Figures were enhanced with adjustments to brightness and contrast.

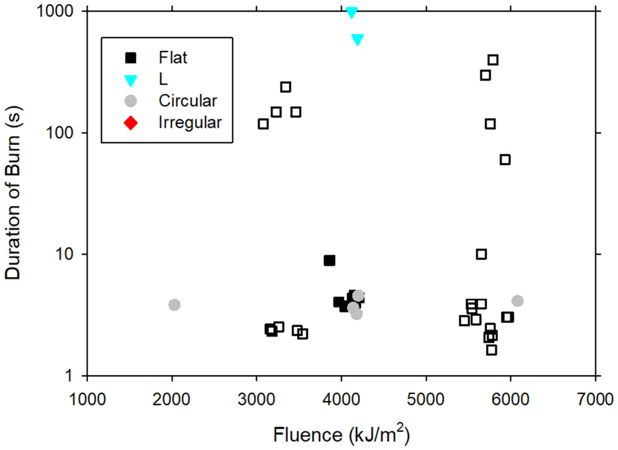

Fig. 4. Duration of burn versus fluence for synthetic polymer samples. Solar Tower experiments are differentiated from Solar Furnace tests, having closed symbols instead of open.

A similar plot of burn duration versus fluence for the synthetic polymer samples is shown in Fig. 4. These data lacked samples that could be considered ‘irregular’, however included a number of samples that could be considered circular. The response of flat synthetic polymer samples was observed to be similar to that of cellulosics in that the tests tended to produce transient flaming results unless the samples were thin and holes were formed in the material at the center of the exposure. The L-shaped chairs exhibited the longest flaming, and this was surprising. The same polypropylene chair seats had been cut and tested at the Solar Furnace as flat panels at higher fluxes. They did not ignite, even with a higher flux/fluence condition. The differing ignition/non-ignition behavior was not particularly surprising, as PMMA flat panels behaved similarly with scale changes. What was surprising was that the flaming was sustained for a very long time without the immediate burn-through that seemed to be the contributing factor for flat materials to exhibit sustained burning. There were multiple L-shapes on the polypropylene chairs. The seat/back formed L's. But the legs and seat also had smaller L-shaped structural members. It was at these that flaming was sustained. The chair back melted and sloughed during the exposure and was not able to maintain the L-shape through to the end of the exposure. The seat was made of thicker and more rigid material, and was oriented less orthogonal to the incident flux. The seat and legs remained mostly rigid during the test (one leg burned through long after the exposure).

The circular materials were only tested at the Solar Tower, and resulted in transient flaming, consistent with flat surfaces. There was postulation ahead of the testing that the trash can with a circular cavity might augment ignition and burn prospects due to the ability of the material to retain more energy by radiating within the cavity. The tests did not suggest that this was a significant effect. The circular materials generally agreed with the flat materials in terms of burn duration.

Because the burn duration relates to the size of the samples in the sense that full burn-out limits the potential for longer burn durations, there is a desire to filter the data to differentiate on this effect. It is also desirable to differentiate the comparatively thick samples that classically are only ignited in the transient mode. The normalization of the fluence is done by Martin et al. by the heat capacity of the material. The resultant parameter is not fully non-dimensionalized, as the scaled parameter retains units of temperature. Martin et al. found for cellulose that sustained flaming was generally attained when the scaled fluence was greater than 1000 K. Below 1000 K there was either no flaming or transient flaming depending on the magnitude of the scaled flux. The relation for the scaled fluence is:

$$Scaled\ Fluence = \frac{\alpha q^{"}}{\rho C_P L} \tag{1}$$

Here α is the absorptivity, $q"$ is the imposed fluence (J/m^2), ρ is the bulk material density (kg/m^3), Cp is the specific heat of the solid (J/(kg·K), and L is the characteristic length (m), which is the primary thickness of the samples. Thermal properties were estimated from measurements (typically density, absorptivity, fluence, and thickness) and common literature sources (specific heat and select others), and are expected to be accurate to within at least 10%. This accuracy is believed adequate for the purposes of this analysis.

We re-cast the burn duration data in terms of the scaled fluence in Figs. 5 and 6, providing a comparison back to the historical sustained flaming threshold. The cellulosic materials in Fig. 5 show a reasonably consistent trend with the expected transition based on the data of Martin et al. to sustained flaming above 1000 K (the green line). Some transient flaming is observed for materials with higher scaled fluence than 1000 K. These flat materials were mostly the wood veneers. The irregular materials that fit this category included the mix of dry and green needles. Transient flaming data below 100 K scaled fluence included a stack of 50 copy paper pages. These ignited in an expected regime because the scaled flux was relatively high (even though scaled fluence was relatively low; the construct of Martin et al. allows for this). Some sustained flaming was observed for samples with lower scaled fluence than 1000 K. This included most notably the solar tower fabric test. The L-shaped chairs had noticeably high burn duration compared to other samples at the same scaled flux, but were in a regime where ignition was not unexpected.

Even though Martin et al. imply that scaled fluence ignition thresholds for different materials might be different, we have generally found the cellulose scaled ignition data to roughly coincide with the data from the common polymer samples we have been testing thus far. The synthetic polymer data in Fig. 6 might also be expected to transition between transient and sustained flaming at about 1000 K on the scaled fluence axis. The L shaped polypropylene chairs are a notable exception. They are moderately below the threshold, yet exhibited the greatest burn duration. This is added evidence for the significance of the L-shape to the ignition and burn duration. A cluster of flat materials had scaled fluence around 2000 K but did not sustain ignition. These are solid vinyl and thicker polystyrene samples. The circular samples that did not sustain ignition all fall below 1000 K, suggesting that they were not necessarily expected to. All flat samples that sustained ignition had scaled fluence above 1000 K. These were mostly burn-through scenarios involving comparatively thin materials.

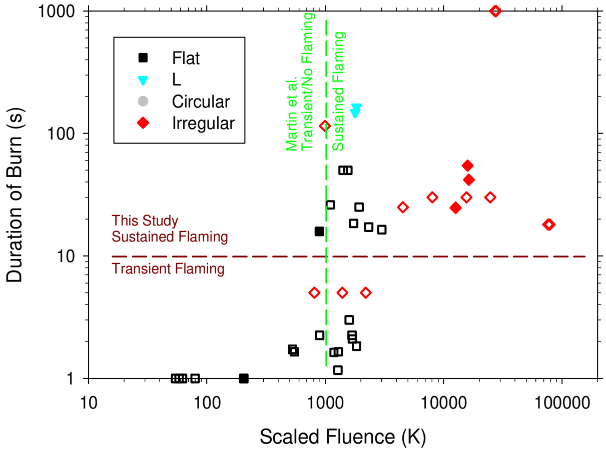

Fig. 5. Duration of burn versus scaled fluence for cellulosic samples. Solar Tower experiments are differentiated from Solar Furnace tests, having closed symbols instead of open.

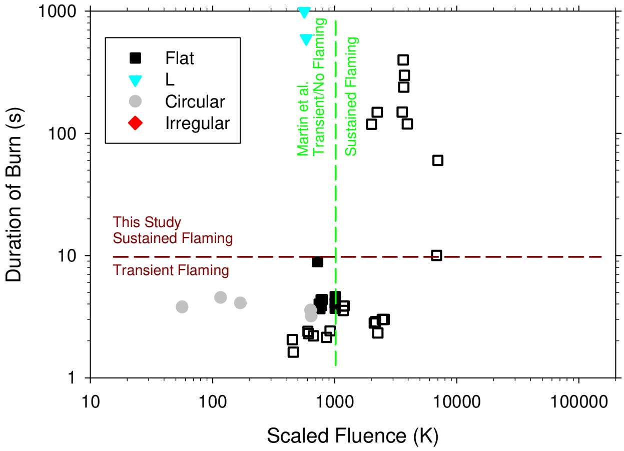

Fig. 6. Duration of burn versus fluence for synthetic polymer samples. Solar Tower experiments are differentiated from Solar Furnace tests, having closed symbols instead of open.

GENERAL DISCUSSION

The results presented herein point to a significant effect of the shape parameter on the burn duration and on the ignition of a variety of materials. The fact that what we have called irregular shaped materials are more prone to longer burn durations is not a particularly surprising or novel conclusion. The basis for this expectation is in conventional fire starting where kindling is often used to initiate larger fires. The surface area compared to the volume is augmented, reducing the thermal sink and augmenting the fraction of energy that results in pyrolysis. One would assume the same behavior and sensitivity might be applicable to high flux conditions as well. The more significant finding is that the chairs that have been characterized as L-shaped are significantly more prone to ignition and sustained burning. The mechanism differentiating L-shaped and flat materials is likely quite different than that between the irregular (high surface area/porous) and flat materials. From a surface area to volume ratio perspective, the L-shaped materials are much more closely related to the flat materials than the irregular materials. L-shaped materials may have two different features that contribute to augmenting the propensity for fire. First, they have the ability of the surfaces to emit or reflect radiation from one to the other, a feature not available to flat surfaces. Second, they create a different flow pattern for the product gases and will interact differently with ambient winds.

Prior to testing these materials, the radiation (first) mechanism was anticipated to be the dominant mechanism that might augment the prospects of burning and ignition. Imposed radiative flux from the concentrated solar panels at these high flux conditions is expected to dwarf any reasonably expected convective heat flux. Post-test, there is reason to attribute greater relative significance to the convective (second) mechanism. Fig. 7 shows images from two chair fire tests. The polypropylene chair illustrated had sustained burning on one of the two symmetrically similar chair legs. Because the radiation flux was relatively symmetric as well, we conjecture that the wind direction was the contributing factor to the continuing burn. The fabric chairs exhibited significant vortical motion in the volume between the seat and seat back. This is best observed in the video results, but the image showing the narrow elongated plume from the chair fire helps illustrate presence of significant vortical flow originating at the fire. The fact that circular geometries with cavities did not sustain ignition also lends to the argument, but the cavity also has the effect of limiting oxygen while the L-shape provides better exhaust pathways for product gases.

Fig. 7. Post-exposure flaming of the polypropylene chair (left) and the fabric chair (right).

There was a noticeable edge effect for flat samples when they experienced burn-through that appears to relate significantly to the sustainability of the fire. Because high flux ignitions involve large energy input, the majority of the historical tests were either similar to the Solar Furnace tests where the samples were much larger than the exposure, or had a mask that eliminated edge effects. This may not be representative of many fire scenarios of interest, in which case there may be reason in the future to examine offset ignitions on samples that contain pre-existing edges in the exposure. On larger-scaled tests, the flames often would originate or be obviously influenced by the sample edges.

Upon evaluating the geometry based ignition performance from these tests, it is recommended that subsequent tests increase the formal study of geometry related parameters. Additional L-shaped tests in particular would be insightful including simplified geometries, scale, wind, and material variations. Flat panel testing is still useful for reach-back to historical tests, validation scenarios, and semi-infinite geometry scenarios, but may significantly under-represent the ignition and burning potential of more complex geometries. Including pre-existing exposed edges might also help better characterize ignition for a broader range of materials.

CONCLUSIONS

Major findings of this study of ignition from high incident heat fluxes include:

- Sustained ignition appears to be augmented for L-shaped and irregular geometries. Two different chairs exhibited long-term sustained burning in the solar tower tests with long-term flames localized to the internal cavity regions and edges. Irregular shapes like plant material (needles, trees, shrubs, grasses) also exhibited prolonged sustained burning.
- Circular geometries (tires and plastic trash cans) were not as prone to sustained ignition as irregular and L-shaped geometries.
- Flat geometries are more heavily tested historically, but may be poorly representative of more practical (complex) geometries with respect to sustained ignition.
- Flat geometries tend not to exhibit sustained ignition unless they develop (via burn-through) or include exposed irradiated edges.

We consequently recommend increasing the experimental focus on non-planar samples and samples with edges in subsequent testing to better capture the ignitability of a broader range of materials and configurations.

ACKNOWLEDGEMENTS

Sandia National Laboratories is a multimission laboratory managed and operated by National Technology and Engineering Solutions of Sandia, LLC., a wholly owned subsidiary of Honeywell International, Inc., for the U.S. Department of Energy's National Nuclear Security Administration under contract DE-NA-0003525.

REFERENCES

[1] S. Glasstone, P.J. Dolan, The effects of nuclear weapons, Department of Defense, Washington DC, 1977.

[2] S.B. Martin, Fire setting by nuclear explosion: A revisit and use in nonnuclear applications. J. Fire Prot. Eng. 14 (2004) 283-297.

[3] S. Martin, Diffusion-controlled ignition of cellulosic materials by intense radiant energy, Proc. Combust. Inst. 10 (1965) 877-896.

[4] A.L. Brown, J.D. Engerer, A.J. Ricks, J.M. Christian, Scale Dependence of Material Response at Extreme Incident Radiative Heat Flux, The 2018 ASME/AIAA Joint Thermophysics and Heat Transfer Conference, Atlanta, Georgia, June 25-29, 2018.

[5] J.D. Engerer, A.L. Brown, J.M. Christian, Ignition and Damage Thresholds of Materials at Extreme Incident Radiative Heat Flux, The 2018 ASME/AIAA Joint Thermophysics and Heat Transfer Conference, Atlanta, Georgia, June 25-29, 2018.

[6] A.J. Ricks, A.L. Brown, J.M. Christian, Flash Ignition Tests at the National Solar Thermal Test Facility, The 2018 ASME/AIAA Joint Thermophysics and Heat Transfer Conference, Atlanta, Georgia, June 25-29, 2018.

[7] C. Ho, S. Khalsa, and N. Siegel, "Analytical methods to evaluate flux distributions from point-focus collectors for solar furnace and dish engine applications," ASME 2010 4th International Conference on Energy Sustainability, American Society of Mechanical Engineers, 2010, pp. 501–509.

Flame retardants

Permanent Flame Retardant Finishing of Textiles by the Photochemical Immobilization of Polyphosphazenes

Opwis K.[1,]*, Mayer-Gall T.[1,2], Gutmann J.S.[1,2]

[1] *Deutsches Textilforschungszentrum Nord-West gGmbH, Adlerstr. 1, Krefeld, Germany*
[2] *University Duisburg-Essen, Universitätsstr. 5, D-45117 Essen, Germany*
**Corresponding author's email: opwis@dtnw.de*

ABSTRACT

UV-based grafting processes are appropriate tools to improve the surface properties of textile materials without changing the bulk. Based on our previous investigations on the photochemical immobilization of vinyl phosphonic acid, here, a new photochemical method for a permanent flame retardant finishing of textiles is described using allyl-modified linear polyphosphazenes and derivatives. Exemplarily, we show results on the flame-retardant finishing of cotton and cotton/PET blends with allyl polyphosphazene. We used the terminal allyl group for the photo-induced coupling of allyl polyphosphazene on textile substrates. Using our UV technology 20 to 40 weight percent of the functionalized polyphosphazenes can be fixed covalently to different textile substrates. We observed a slight decrease of the fixed polyphosphazene amount after the first washing cycle indicating the removal of non-bonded molecules. After this initial washing step the add-on is stable. Even after six laundering cycles the modified material withstands various standardized flammability tests. In summary, photochemical treatments allow the permanent surface modification of natural and synthetic fibers by irradiating with UV light in the presence of reactive media. We have successfully demonstrated that these procedures are appropriate for the fixation of flame retardants as well. Polyphosphazene modified textiles show high levels of flame retardant performance even after several textile laundering cycles.

KEYWORDS: Textiles, cotton, polyester, polyphosphazenes, flame retardant finishing.

INTRODUCTION

Textiles made of natural and synthetic polymers such as cotton (CO), polyester (PET) or polyamide (PA) are omnipresent in our day-to-day life. Besides apparel, typical in-door applications are curtains, carpets, bedding or upholstered furniture. Because of their high flammability, these materials represent a potential hazard for goods and life [1]. To achieve flame retardant textiles, the polymers are usually blended or finished with inorganic salts (e.g. nontoxic aluminum or magnesium hydroxide), organohalogens (e.g. chloroparaffins, bromobiphenylether and bromobisphenols) or formaldehyde-based flame retardants [1-4]. Because of their high toxicity the political pressure is growing steadily to replace halogen- and formaldehyde-based flame retardants [5, 6]. Due to the fact that conventional organohalogen-based flame retardants are getting banned more and more, several halogen-free substitutes have been developed, e.g., polyphosphates, organic phosphates or nitrogen compounds [7]. In this context nitrogen and phosphorus-containing chemicals are especially interesting, because of their P-N synergistic effect in flame retardant applications. However, their low stability with regard to washing and mechanical abrasion is limiting their applicability [8, 9]. Furthermore, an increasing amount of organo-phosphorus derivates from flame retardants are found in the environment and even in human tissue. Some of these substances have a potential hormone like effect. Thus, alternative products that combine safety, high flame retardant properties and the possibility to fix them permanently to the textile

Proceedings of the Ninth International Seminar on Fire and Explosion Hazards (ISFEH9), pp. 981-990
Edited by Snegirev A., Liu N.A., Tamanini F., Bradley D., Molkov V., and Chaumeix N.
Published by Saint-Petersburg Polytechnic University Press
ISBN: 978-5-7422-6498-9 DOI: 10.18720/spbpu/2/k19-105

matrix are still desirable. One new approach to achieve flame retardant textiles is the use of layer-by-layer coatings, e.g., the combination of cationic polyelectrolytes such as polyallylamine, chitosan or polyethylenimine with anionic nano-clays, polyphosphates or DNA. Other strategies are based on sol-gel chemistry, carbon nanotubes, polycarboxylic acid, casein coating and photo- or plasma-grafting. More information on textile flame retardants are given in different reviews [10, 11] and books [2, 6-8].

Now, we have identified polyphosphazenes (PPZ) as another promising group of halogen-free flame retardant materials for textile applications. Polyphosphazenes can be divided into different polymer types: linear polyphosphazenes and polymers with cylcophosphazene units (back bone or side chain) [12]. These materials exhibit high limiting oxygen indices [13, 14] and improve the flame retardant properties of polymer blends significantly [14]. Technically, polyphosphazenes are used, e.g. in hydrocarbon insoluble O-rings, biomedical applications, as bio-inert or bio-compatible coatings or in fuel cell membranes. A small number of textile finishings based on polyphosphazenes are already described. Shukal and Arya showed that poly(fluorophosphazene) in combination with organo-bromine compounds improve the flame retardant properties of PET, while it is still unclear if the effect depends on the bromine-containing compounds or the polyphosphazene [15]. Other textile application for polyphosphazenes as finishing agents, textile polymer blending or in a polyurea coating are described in patents. Even fully inorganic polyphosphazenes such as (poly)aminophosphazene, phospham, phosphorus oxynitride and cylcophosphazenes have been used as flame retardants. While these examples demonstrating the general usefulness of polyphosphazenes as flame retardants, no commercial textile PPZ-based finishing is available. The main reasons for this are the lack of polyphosphazenes with appropriate anchor groups for the durable fixation on the fiber surface and suitable process technologies. Because of our experience in the field of photo-initiated reactions for the surface functionalization of textile substrates [16-19], our goal was to develop a flame retardant linear polyphosphazene with sufficient side-chain functionalities, that allow photochemical covalent bonding to typical textile materials, e.g. cotton and cotton/polyester blends.

Generally, polyphosphazenes can be synthesized by different synthetic routes [20]. The most common route is the high temperature ring opening polymerization of the cyclic trimer hexachlorophosphazene in a sealed glass tube developed by Allcock et al. A solvent-based synthesis was developed by the group of Magill [21] that produces polymers with up to 15,000 monomer units. The substitution of the chlorine atoms by, e.g., alkoxy, phenoxy, amino, fluoroalkoxy groups or even mixtures of them results in chemically and thermally stable species [13, 20]. Due to the huge variety of possible side-chain functionalities, the properties of polyphosphazene derivatives can be varied easily, e.g., from water-soluble to highly hydrophobic polymers [22].

EXPERIMENTAL

Textiles and chemicals

Table 1 summarizes the used textiles. Hexachlorotriphosphazene was obtained from Eurolabs Limited (United Kingdom) and allyl alcohol (≥ 99%) from Merck (Germany). Sulfamic acid (≥ 99.3%), calcium sulfate ($CaSO_4 \times 2\ H_2O$, ≥ 98%) and tetrahydrofuran (THF ≥ 99.9%) were obtained from Carl Roth (Germany). 1,2,4-trichlorobenzene (≥ 99%), sodium hydride (55-65%, moistened with oil) and acetylacetone (≥ 99%) were obtained from Sigma-Aldrich (USA).

Instrumentation

Table 2 summarizes the used instruments.

Table 1. Textiles used

Textile	Composition [%]	Textile construction	Mass per unit area [g/m^2]	Supplier
CO white	100	twill 3/1	230	CHT R. Beitlich GmbH (Germany)
CO/PET orange	50/50	warp satin 4/1	340	Huntsman Textile Effects GmbH (Germany)
CO/PET camouflage	50/50	twill 2/1 core PET/shell CO	170	Bluecher GmbH (Germany)

Table 2. Instruments used

Instrument	Analytical method/method/remarks	Supplier
DSC Q20	differential scanning calorimetry (DSC), under 50 mL/min N_2, heating rate 10 K/min	TA Instruments (USA)
Bruker DMX300	NMR spectroscopy, ^{1}H, ^{13}C, ^{31}P	Bruker (USA)
SEM S-3400 N II	Scanning electron microscopy (SEM)	Hitachi High-Technologies Europe
X-Max 50 mm² SDD Detector	Energy disperse x-ray (EDX)	Oxford Instruments (UK)
HPV-E2, H emitter, Type 100 - 200	Ultraviolet A (UVA) print system lamp with dichroitic reflector for IR reduction, power 200 W/cm	Hoenle UV Technology (Germany)
linitester	Washing test	Atlas Material Testing Technology (Germany)
Nu-Martindale	Abrasion test	James H. Heal & Co. (UK)
Varian 720-ES spectrometer	Inductively coupled plasma optical emission spectra (ICP/OES)	Varian (Germany)
MarsXpress instrument	Microwave digestion	CEM (Germany)

Synthesis and characterization of allyl-oxy-polyphosphazene (PPZ)

Freshly sublimated hexachlorotriphosphazene (40 g), sulfamic acid (170 mg) and $CaSO_4$ x 2 H_2O (150 mg) were dissolved in 32 mL 1,2,4-trichlorobenzene under a nitrogen atmosphere and heated to 210 °C for 45-60 min. At the end of the reaction, a strong increase of the viscosity can be observed. The chloropolyphopshazene was precipitated by the addition of dry petroleum ether and the solids were washed twice with petroleum ether. The obtained polymer was dissolved in 100 mL THF. The concentration of the solution was determined by evaporating an aliquot and weighting of the residue. Afterwards, a freshly prepared sodium allyl alcoholate solution (4 eq. allyl alcohol with 1.25 eq. NaH in 50 ml THF) was added. The reaction mixture was rigorously stirred for 4 h at room temperature (RT), then refluxed for 6 h. The PPZ was precipitated by the addition of water. ^{1}H NMR (300 MHz, THF-d_8): δ 5.93 (ddt, J = 17.2, 10.4, 5.1 Hz, 1H), 5.29 (dd, J = 17.2, 1.8 Hz, 1H), 5.05 (dd, J = 10.4, 1.7 Hz, 1H), 4.48 (d, J = 5.5 Hz, 2H). ^{13}C{^{1}H} NMR (75 MHz, THF-d_8) δ 135.8, 116.0, 30.7. ^{31}P NMR (122 MHz, THF-d_8): δ –7.71. IR (ATR): 802 (P-O-C), 864, 923, 991, 1024 (P-N-backbone), 1101 (P-O-R), 1232 (P=N-backbone), 1423 (P-O-C), 1458 and 1647 (C=C), 2854 (C-H, sp^3), 2924 (C-H, sp^3), 3016 (C-H, sp^2), 3076 (C-H, sp^2) cm^{-1}. DSC (10 K/min, N_2 (50 mL/min)): T_G 180 °C, T_{Decomp} 282 °C.

Fabric UV treatment and characterization of the fixed PPZ

PPZ was dissolved in acetylacetone (25 wt%). The fabrics were wetted with 1 mL/g textile of the PPZ solution. The fabrics were irradiated single-sided for 10 min under an argon atmosphere. The distance between the light source and the sample was 20 cm. Subsequently, each sample was washed once in a textile linitester to remove non-bonded PPZ, afterwards dried at RT and weighed. In order to determine the phosphor content of the textiles quantitatively, 0.4 g were digested with 8.0 mL HNO_3 (65%) in a microwave digester at 180 °C. After digestion, the samples were diluted to 25 mL with water and measured by ICP-OES. The error of the phosphorus determination is less than 5%.

Washing resistance and abrasion test

In order to evaluate the washing fastness of the modified textiles, the materials were washed up to six times in a linitester according to EN ISO 105-C06 (liquor volume 150 ml, liquor ratio 1:80, ECE detergent 4.0 g/l, 30 min, 40 °C). The samples were then dried at room temperature and weighed. To investigate the fastness against mechanical stress, the modified textiles were subjected to 5,000, 10,000 or 50,000 abrasion cycles with a pressure of 9 kPa in a Martindale apparatus (abrasion test). Afterwards the samples were weighted. For the test an inverted Martindale setup has been used to get samples of at least 5 cm × 10 cm for a flammability test. The sample size was 140 mm diameter and the abrasive cloth (Martindale SM 25 (ISO 12947-1)) 40 mm diameter, with an abrasive exposed area of 110 mm diameter.

Evaluation of the flame retarding properties

All flame retardant and LOI measurements were carried out after at least one washing cycle. The flame retardant properties were measured according to DIN EN ISO 15025 (protective clothing - protection against heat and flame - method of test for limited flame spread), with a reduced sample size of 5 cm × 10 cm and a Proxxon lighter (combustion gas butane). In addition, selected samples were tested externally by Staatliches Pruefamt fuer das Textilgewerbe - University of Applied Science Hof (Germany) according to DIN EN ISO 4589-2 (limiting oxygen index, LOI, 0.5% steps), DIN 75200, DIN EN ISO 15025 and EN ISO 11925-2.

RESULTS AND DISCUSSION

Synthesis of allyl-oxy-polyphosphazene (PPZ)

PPZ was successfully synthesized by ring-opening polymerization of cyclic hexachlorotriphosphazene and subsequent nucleophilic substitution of the chlorine atoms by allyl alcoholate as shown in Fig. 1. The material is well soluble in acetylacetone.

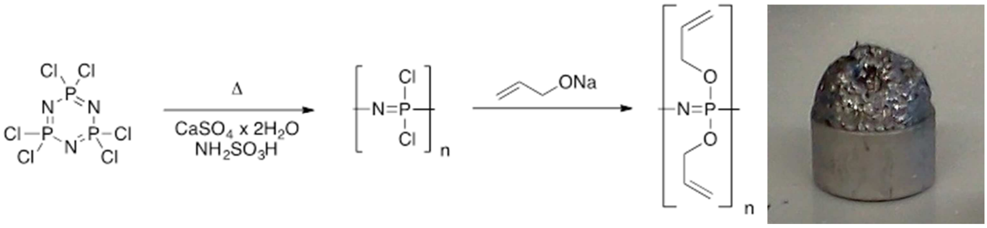

(a) (b)

Fig. 1. Allyl-oxy-polyphosphazene. (a) Synthesis, (b) after heating to 600 °C.

The ^{31}P NMR spectrum exhibits one singulett at -7.61 ppm, which indicates the presence of a non-crosslinked polymer with a typical chemical shift for a polyphosphazene. In addition, the ^{1}H NMR spectrum exhibits the typical signals for an allyl group. This correlates with the IR bands at 1232 cm^{-1} (P=N band) and at 1024 cm^{-1} (P-N band), which are characteristic bands for the polymeric backbone. The band at 1101 cm^{-1} represents the signal for the P-O-C ether. To achieve flame retardant properties, the flame retardant should have a decomposition temperature lower then the textile. Using DSC, we found a sharp exothermic degradation peak at 282 °C. When heating PPZ up to 600 °C the polymeric material shows an intumescent behavior. The foam-formation is shown in Fig. 1. In the case of fire the foam layer can act as a heat barrier.

Photochemical bonding of PPZ to textile materials

For our studies, we chose three different kinds of fabrics, one cotton fabric and two CO/PET blends (both 50/50 mixtures) used in common textile applications (e.g., clothing incl. protective clothing, car interior and furniture), where an improvement of the flame retardant properties is highly desired. The CO/PET blends differ in their fabric construction. The orange fabric is a warp satin woven material with one CO and one PET side. The second fabric (camouflage) consists of a PET core yarn with CO in the shell.

Beside phosphorus and nitrogen, which are responsible for the flame retardant properties of polyphosphazenes, our PPZ contains allyl groups, which are suitable for photo-induced grafting and cross-linking/homopolymerization. After wetting the textiles with a PPZ solution the materials were irradiated by a broadband-UV lamp under an argon atmosphere. Before characterization, the materials were washed once to remove non-bonded compounds. The PPZ-modified textiles were characterized by gravimetric measurements and SEM in combination with EDX for surface morphology and composition. Total phosphorus content was measured by ICP-OES after digestion. Table 3 summarizes the results. After the first washing step a high add-on of PPZ between 20 and 40 wt% was determined by gravimetry. An average weight loss after one washing step in the range of only 2–3% proofs the general efficiency of our photo-induced immobilization method. The phosphorus content found by ICP-OES is close to the calculated P content obtained by gravimetry. The surface P determined by EDX is between 18.5 and 22.5 wt%, which correlates with the mass fraction of P in the PPZ. Therefore, the layer thickness of immobilized PPZ must be higher than the information depth of the used EDX technology - thus at least 1.0 µm. The measured phosphorus contents (about 4 wt%) are higher than the recommended value for flame retardant properties (> 1.5 wt%).

Table 3. Summary of calculated and measured values for the P content of PPZ modified textiles

Textile	Add-on [wt%]	P calculated from add-on [wt%]	P measured[a] [wt%]	P surface[b] [wt%]
CO white	40.8	5.7	4.9	18.8
CO/PET orange	22.3	3.6	3.1	18.5
CO/PET camouflage	32.8	4.8	4.2	22.7

[a] Measured quantitatively by ICP-OES.
[b] Measured qualitatively by EDX.

Accordingly, flame retardant properties for the PPZ finished textiles can be expected. SEM micrographs (Fig. 2) show a film deposition of PPZ on the textile´s surface. As a consequence the corresponding ATR-FT-IR spectra of the textiles (Fig. 3) changes completely to the IR signals of pure PPZ; only the strong substrate signals like the carbonyl band of the PET part of the blends or the OH-signal of CO are weakly left. Taking the high add-on and the corresponding thickness of the

PPZ layer into account we assume that the PPZ is mainly bound by photo-induced homopolymerization between PPZ polymer chains yielding a stable film surrounding the fiber.

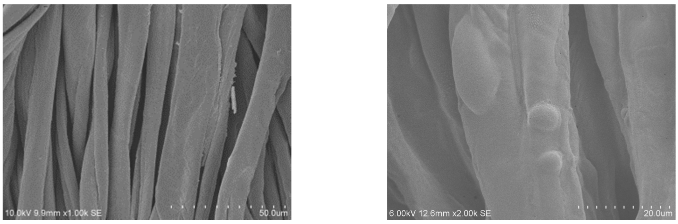

(a) (b)

Fig. 2. SEM micrographs of cotton fibers before (a) and after PPZ finishing (b).

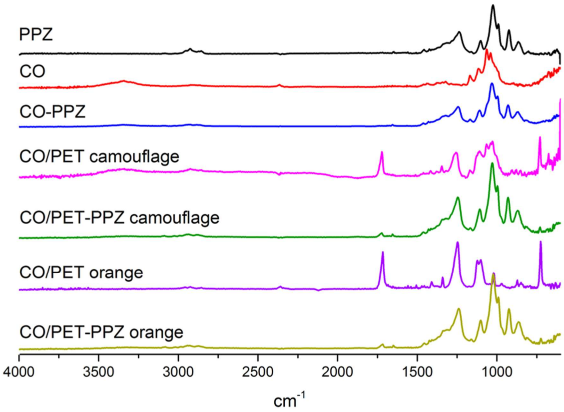

Fig. 3. ATR-IR-spectra of cotton/polyester blends and cotton fabrics before and after PPZ finishing in comparison to pure PPZ.

Flame retardant properties

In order to evaluate the flame retardant properties of the textiles, various methods were used. By measuring the limiting oxygen index (LOI) the minimum amount of oxygen in a mixture of oxygen and nitrogen is determined that is required to keep an ignited polymer burning. Normally, an increased LOI is accompanied by a lower ignitability and, therefore, improved flame retardant properties. For different textile applications different flammability testing standards exist. Here, we choose three methods. In the first test, the burning speed of a horizontal sample is measured, this test is described in DIN 75200 and is essential for textiles used in car interiors. DIN EN ISO 15025 represents a test for protective clothing. In addition, the test EN ISO 11925-2 was carried out to achieve the classification „normal flammability” according to DIN 4102-1 class B2 or EN ISO 13501-1 class E for building materials. Because of the vertical edge ignition applied in this test, the conditions are highly ambitious for textiles.

Table 4 summarizes the results of the various burning tests and the corresponding LOI measurements. Compared to the untreated materials, the LOI of the PPZ-finished textiles increases by 5-8%, which provides a first indication for a reduced flammability. During the horizontal burning test (DIN 75200), the untreated fabrics burn completely down with burn rates of 60-120 mm/min. In contrast, both modified CO/PET blends are self-extinguishing after the removal of the flame. In the case of modified CO, an acceleration of the burning was observed, however, the char yield is raised due to a significant carbonization of the material. By changing to a vertical flame test (DIN EN 15025), with a 10 s flame contact at the surface, the untreated materials burn down again completely. In contrast, the PPZ-modified cotton and the CO/PET orange blend do not keep burning after the removal of the flame and no afterglowing was observed.

Table 4. Results of the LOI measurements and the standardized burning tests on PPZ-modified textiles

Textile	CO white	CO/PET orange	CO/PET camouflage
	LOI		
Untreated	17.5 - 18.0	18.5 - 19.0	16.5 - 17.0
PPZ	23.0 - 23.5	26.5 - 27.0	24.0 - 24.5
	DIN 75200		
Burning rate [mm/min]	142	0	0
Comment	carbonization	-	-
Test passed	no	yes	yes
Burning behavior of untreated material	burns down, 98 mm/min	burns down, 59 mm/min	burns down, 119 mm/min
	DIN EN ISO 15025		
Flame reaches upper or lateral edge	no	no	yes
Afterflame time [s]	0	0	20
Afterglow beyond flame area	no	no	no
Afterglow [s]	0	0	0
Appearance of particles	no	no	no
Burning particles	no	no	no
Hole formation	yes	no	no
Comment	-	-	extinguishes almost
Test passed	yes	yes	no
Burning behavior of untreated material	burns down within 8 s	burns down within 22 s	burns down within 11 s
	EN ISO 11925-2		
Reaching the test mark	7 s	5 s	4 s
Max. flame height	> 25 cm	> 25 cm	> 25 cm
Moment of max. flame height	12 s	12 s	10 s
Self-extinguished	0 s	0 s	5 s
Dripping	no	no	no
Test passed	no	no	no
burning behavior of untreated material	burns down, test mark 5 s	burns down, test mark 6 s	burns down, test mark 4 s

Finally, the three textile materials were subjected to a fire test with a 15 s vertical edge flame impingement test. All PPZ-modified textiles do not pass the test requirements, because the flame reaches the upper test mark during impingement. However, a significant flame retardant behavior was observed. In contrast to the untreated materials, all PPZ-modified samples are self-extinguishing after the removal of the flame. Figure 4 illustrates the strong improvement of the flame retardant properties off PPZ-finished textiles compared to the blank substrates.

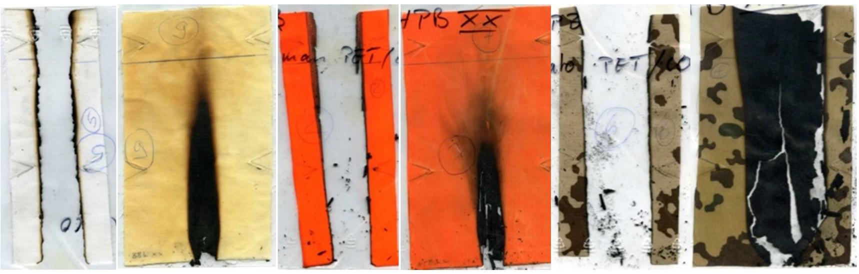

(a1) (a2) (b1) (b2) (c1) (c2)

Fig. 4. Blank (1) and PPZ-finished (2) textiles after the 15 s vertical flame test (EN ISO 11925-2). The test mark of 150 mm is visible as blue line on the fabric. (a) CO white, (b) CO/PET orange, (c) CO/PET camouflage.

Investigations on the permanence of the polyphosphazene finishing towards washing and abrasion

To evaluate the stability (fastness) of the PPZ modification, samples were subjected to several washing cycles and rigorous abrasive tests. Afterwards, the flame retarding properties were investigated according to the modified DIN EN ISO 15025 conditions. Figure 5 summarizes the add-on of the PPZ-layer on the orange CO/PET textile after different washing cycles. After the first washing cycle, non-covalently bonded PPZ was removed, which leads to a significant weight loss of nearly 3%. After the following washing cycles, no further weight loss was observed. Moreover, in all flame retardant tests, the specimens are self-extinguishing accompanied by a formation of a carbonized layer. Although the flame reaches the upper edge after six laundering cycles, a strong permanence of the flame retardant effect against washing can be assigned.

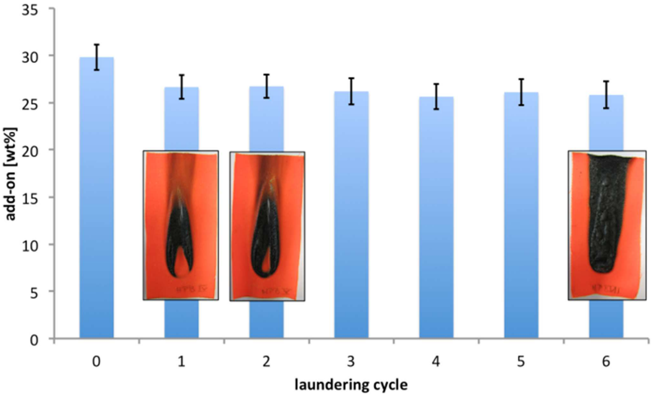

Fig. 5. Washing fastness of PPZ-modified CO/PET blend (PPZ-add-on and flammability behavior after six washing cycles).

In addition, the abrasion fastness of the PPZ-modified CO/PET (camouflage) blend was tested. After subjecting the textiles to 5,000, 10,000 or 50,000 abrasion cycles in a Martindale tester, the flame retardant properties of the materials did not change significantly. All samples are self-extinguishing after the removal of the flame.

CONCLUSIONS

Polyphosphazenes belong to the class of inorganic polymers. Due to their phosphorus and nitrogen backbone, they exhibit excellent flame retardant properties. However, their industrial application in textile finishing was as yet limited by the lack of durable fixation strategies for a permanent flame retardant effect during the product´s lifetime. We succeeded in bonding a non-combustible and strongly foam-forming polyphosphazene derivative by an UV-induced grafting process to cotton and cotton/polyester blends in high add-ons up to 40 wt%. SEM imaging proofs the successful immobilization, and a total phosphorus content between 3-5 wt% was found. The polyphosphazene finishing leads to textiles with higher LOI. The textiles exhibit improved flame retardant properties and pass several standardized flammability tests such as standards for protective clothing and automotive textiles. The charred layer acts as a thermal isolating barrier layer and protects the underlying material. The permanence of the finishing was proven by washing and abrasion tests. The most essential results of PPZ-modified cotton and cotton/polyester blends are summarized in Table 5.

Table 5. Results of the LOI measurements and the standardized burning tests on PPZ-modified textiles (– = failed/no improvement, (+) = failed, but significant flame retardant effect, + = passed/strong improvement)

Test	CO white[a]	CO/PET orange[a]	CO/PET camouflage[a]
LOI[b]	+	+	+
DIN 75200	-	+	+
DIN EN ISO 15025	+	+	(+)
EN ISO 11925-2	(+)	(+)	(+)
Washing fastness[c]	+	+	+
Abrasion fastness[c]	+	+	+

[a] – = failed/no improvement, (+) = failed, but significant flame retardant effect, + = passed/strong improvement.

[b] after one laundering cycle

[c] modified DIN EN ISO 15025 procedure.

In consideration of these excellent results, we state that functional polyphosphazenes could be a new class of permanent and halogen-free flame retardant agents for textile applications in the near future. However, competitive and commercial products for the textile industry have to be water-based (water-soluble or at least water-dispersible). Therefore, a future focus will be the synthesis of innovative polyphosphazenes, which combine functional side groups for a permanent attachment and hydrophilic side groups for an improved solubility in aqueous systems.

ACKNOWLEDGEMENT

The authors wish to acknowledge financial support by the Forschungskuratorium Textil e.V. for the project IGF 16780 N. The support was granted within the program Industrielle Gemeinschaftsforschung (IGF) from resources of the Bundesministerium für Wirtschaft und Energie (BMWi) via a supplementary contribution by the Arbeitsgemeinschaft Industrieller

Forschungsvereinigungen e.V. (AiF). We thank the Staatliches Pruefamt fuer das Textilgewerbe - Hof University of Applied Science (Muenchberg, Germany) for LOI and standardized flammability tests and DTNW Oeffentliche Pruefstelle GmbH for the ICP measurements.

REFERENCES

[1] A.R. Horrocks, D. Price, Fire Retardant Materials, Woodhead Publishing Limited, Cambridge, UK, 2001.

[2] A.R. Horrocks, B.K. Kandola, in: Plastics Flammability Handbook: Principles, Regulations, Testing, and Approval, J. Troitzsch (Ed.;), Hanser, Munich, Germany, 2004, pp. 173–188.

[3] D.J. Guckert, S.L. Lovasic, R.F. Parry, in: Handbook of Building Materials for Fire Protection, C.A. Harper (Ed.), McGraw-Hill Education, New York, 2003, Chapter 5, pp. 5.0–5.51.

[4] J. Troitzsch, Plastics Flammability Handbook: Principles, Regulations, Testing, and Approval, Hanser, Munich, Germany, 2004.

[5] National Research Council (US) Subcommittee on Flame-Retardant Chemicals. Toxicological Risks of Selected Flame-Retardant Chemicals; National Academies Press (US): Washington, DC, 2000.

[6] J. Alongi, A.R. Horrocks, F. Carosio, Update on Flame Retardant Textiles: State of the Art, Environmental Issues and Innovative Solutions; Smithers Rapra Technology, Shropshire, UK, 2013.

[7] A.B. Morgan, C.A. Wilkie, The Non-halogenated Flame Retardant Handbook, Wiley, Chichester, UK, 2014.

[8] A.R. Horrocks, In: Textile Finishing, D. Heywood (Ed.), Society of Dyers and Colourists, Bradford, UK, 2003, pp. 214-250.

[9] W.D. Schindler, P.J. Hauser, In: Chemical Finishing of Textiles, W.D. Schindler, P.J. Hauser (Eds.), Woodhead Publishing, Cambridge, UK, 2003, Chapter 8, pp. 98–116.

[10] A.R. Horrocks, Flame Retardant Challenges for Textiles and Fibres: New Chemistry versus Innovatory Solutions, Polym. Degrad. Stab. 2011, 96, 377–392.

[11] A.R. Horrocks, B.K. Kandola, P.J. Davies, S. Zhang, S.A. Padbury, Developments in Flame Retardant Textiles – a Review, Polym. Degrad. Stab. 88 (2005) 3–12.

[12] H.R. Allcock, Recent Developments in Polyphosphazene Materials Science, Curr. Opin. Solid State Mater. Sci. 10 (2006) 231–240.

[13] M. Gleria, R. De Jaeger, Polyphosphazenes: A Review, Top. Curr. Chem. 250 (2005) 165–251.

[14] C.W. Allen, D. Hernandez-Rubio, in: Applicative Aspects of Poly(organophosphazenes), R. De Jaeger, M. Gleria (Eds.), Nova Science Publishers, Hauppauge, NY, 2004, Chapter 6, pp. 119–137.

[15] L. Shukla, P. Arya, Flame Retardant based on Poly (Flourophosphanzene) and Organo Brominated Compound for the Polyester/Cotton Shirting, Text. Dyer Printer 31 (1998) 16–18.

[16] K. Opwis, A. Wego, T. Bahners, E. Schollmeyer, Permanent Flame Retardant Finishing of Textile Materials by a Photochemical Immobilization of Vinyl Phosphonic Acid, Polym. Degrad. Stab. 96 (2011) 393–395.

[17] D. Praschak, T. Bahners, E. Schollmeyer, Excimer UV Lamp Irradiation induced Grafting on Synthetic Polymers, Appl. Phys. A: Mater. Sci. Proces 71 (2000) 577–581.

[18] K. Opwis, T. Bahners, E. Schollmeyer, Improvement of the Alkali-resistance of Poly(ethylene terephthalate) by a Photo-chemical Modification using Excimer-UV-Lamps, Chem. Fibers Int. 54 (2004) 116–119.

[19] S.L. Gao, R. Haessler, E. Maeder, T. Bahners, K. Opwis, E. Schollmeyer, Photochemical Surface Modification of PET by Excimer UV Lamp Irradiation, Appl. Phys. B: Lasers Opt. 81 (2005) 681–690.

[20] H.R. Allcock, Chemistry and Applications of Polyphosphazenes, Wiley, Hoboken, NJ, 2003.

[21] A.N. Mujumdar, S.G. Young, R.L. Merker, J.H. Magill, A Study of Solution Polymerization of Polyphosphazenes, Macromolecules 23 (1990) 14–21.

[22] R. De Jaeger, M. Gleria, Applicative Aspects of Poly(organophosphazenes), Nova Science Publishers, Hauppauge, NY, 2004.

The Chemical Mechanism of Thermolytic Synthesis in Charring Intumescent Coatings for Passive Fire Protection

Ustinov A.[1], *, **Zybina O.**[1], **Tanklevsky L.**[1,2]

[1] *Peter the Great St. Petersburg Polytechnic University, Saint-Petersburg, Russia*
[2] *"Gefest" Enterprise Group, St. Petersburg, Russia*
**Corresponding author's e-mail: au.spbpu@gmail.com*

ABSTRACT

Fireproofing properties of charring intumescent materials are determined by the formation of the carbonaceous porous layer, which is generated as a result of thermolytic synthesis. The layer has low thermal conductivity, and it shields the construction from the external heat flux. Char-forming coatings have been used for passive fire protection for more than 50 years. However, the existing technologies of creating new intumescent compositions are still fully empirical, and the problem of ensuring optimal combination of material properties has not been resolved yet. This implies the need in an in-depth understanding of the thermolysis mechanism that controls the performance of the coating in fire conditions.

The primary objective of this work is to identify the main chemical reactions occurring in the thermolytic synthesis of the intumescent carbonaceous layer. The intumescent coatings were exposed to annealing in a furnace and thereby produced carbonaceous samples were studied by chromatography-mass spectrometry and IR spectroscopy. TGA-DSC thermal analysis of the virgin samples of the intumescent coatings has also been undertaken. It has been established that in the thermolytic synthesis the melamine forms three-dimensional polymer-oligomeric structures with aldehydes. In its turn, the aldehydes are produced by the pentaerythritol decomposition catalyzed by ammonium polyphosphate and titanium dioxide. It is also shown that the role of the ammonium polyphosphate is two-fold. First, it generates ammonia gas, which facilitates swelling. Second, it serves as a blocking catalyst in hardening of the ammonia-aldehyde porous char produced by the resin. As a result, the heat-resistant layer of graphite-like carbon nitride (g-C_3N_4) forms. It consists of condensed nitrogenous fragments incorporated into a graphene π-linking system inlaid with refractory inorganic compounds such as titanium pyrophosphate. The above mechanism is expected to be useful to enhance the efficiency of porous char formation by new intumescent coatings.

KEYWORDS: fireproofing, intumescent coatings, thermolysis, chromatography, mass spectrometry, IR spectroscopy.

INTRODUCTION

The paper overviews a sequence of physico-chemical transformations of swelling multi-component systems in the process of their annealing and the way how those systems act as fireproofing materials. Experimental data made it possible to establish the concept of thermolytic synthesis of polymer-oligomeric structure of a charred layer and roles of ingredients in an intumescent process.

An intumescent composition must be prepared according to strict recipes in order to maintain its fireproofing efficiency. Intumescent components which perform in the best way have been already established [1-3] and thus intumescent compounds have proven themselves as an effective method of ensuring fire protection. However, there are several studies in which traditional intumescent

Proceedings of the Ninth International Seminar on Fire and Explosion Hazards (ISFEH9), pp. 991-999
Edited by Snegirev A., Liu N.A., Tamanini F., Bradley D., Molkov V., and Chaumeix N.
Published by Saint-Petersburg Polytechnic University Press
ISBN: 978-5-7422-6498-9 DOI: 10.18720/spbpu/2/k19-78

components are replaced by their functional analogs [4-6]. We have conducted the experiment to replace one of the intumescent components by its analog. Coatings formed by such compositions were exposed to annealing (at 600 °C) in a furnace and after that the volumes of the charred layers were compared. Results represented in Table 1 show that pentaerythritol is an indispensable component of intumescent systems since the coating formed from the composition without pentaerythritol loses its fireproofing properties. Also, replacing melamine and ammonium polyphosphate with their «functional analogs» leads to degradation of swelling ability and deterioration of fireproofing properties of the intumescent materials [7].

Table 1. Results of basic intumescent component replacement

№ of sample	The replaced component	The substitutional component	Swelling coefficient
Initial	–	–	47
1	Pentaerythritol	Galactose	–
2	Pentaerythritol	D-Fructose	–
3	Melamine	Urea	13
4	Ammonium polyphosphate	Potassium phosphate	15

According to the theory, an intumescent composition forms ester resins as a result of heating, and these resins get swelled by the gaseous products [8-12]. However, this becomes incorrect at the technology level. That is why we aim to reconsider and clarify the char-forming process.

METHODS

To understand the interactions between the basic components of intumescent compositions during heating, the thermal analysis was conducted of the basic components and the melamine-pentaerythritol binary mixture using Derivatograph Q-1500D (J. Paulik, P. Paulik, I.Erdey, MOM, Hungary). The measurements were performed in air, at the constant heating rate of 20℃/min. The sample mass was 50 mg. Aluminium oxide was used as the reference substance. The thermal analysis included differential thermal analysis (DTA) and thermogravimetric analysis (TG).

To identify the products formed in material decomposition, the charring samples were studied by chromatography-mass spectrometry. The study included two steps, manufacturing and annealing the samples with the compositions shown in Table 2, followed by the chromatography-mass spectrometry of the samples extracted from the carbonaceous residue.

Table 2. Recipe of the intumescent composition

Components	Quantity, mass. particles
Aqueous dispersion of vinyl acetate with ethanol	23
Ammonium polyphosphate	27
Melamine	9
Pentaerythritol	11
Dicyandiamide	2
Titanium dioxide	5
Water	23

Results are represented by chromatograms of mixtures separated from hexane, benzene, methyl chloride, acetone, ethanol and acetic acid fractions of carbonaceous samples formed from intumescent compositions which were exposed to annealing in a furnace for 10 min at 200, 300, 400, and 500 °C.

Chromatography-mass spectrometry was conducted using the gas chromatograph Agilent 6890 and the interface with the high-molecular mass-selective detector Agilent 5973N. Chromatograph included quartz capillary (30 m length, 0.25 mm diameter) column modified by HP-5MS phase. Helium was used as the carrier gas flow at the flow rate of 1 ml/min. The evaporator temperature was 320 °C. The sample temperature increased from 100 to 300 °C at the rate of 6 °C/min. The voltage of the ionizing source was 70 eV. A full ionic current regime was used. The individual substances were identified using the NIST library.

The carbonaceous sample made by annealing the intumescent coating in the furnace at 500 °C was also investigated by IR spectroscopy.

Thermolytic synthesis of swollen resin was conducted using the mixture of melamine and pentaerythritol located at the molten ammonium polyphosphate surface. The melamine and pentaerythritol (in 1:1 proportion) were mixed and adjusted to the mass of ammonium polyphosphate. This mixture was then annealed in the furnace at 350 °C.

RESULTS

Results of thermal analysis of basic intumescent components and of melamine-pentaerythritol binary mixture are presented in Fig. 1.

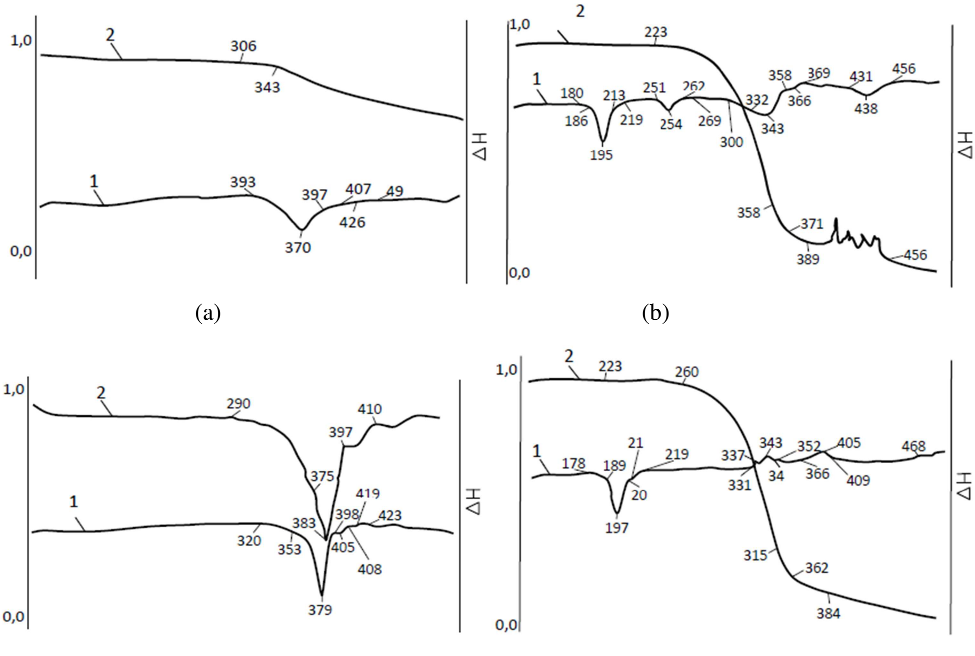

(a) (b)

(c) (d)

Fig. 1. Results of thermal analysis: (a) DTA (1) and TG (2) curves of ammonium polyphophate; (b) DTA (1) and TG (2) curves of pentaerythritol; (c) DTA (1) and TG (2) curves of melamine; (d) DTA (1) and TG (2) curves of melamine-pentaerythritol binary mixture. Horizontal axis is t□mp□r□tur□(̊□), v□rtic□l □□is is Δ□ (kJ)

It is known that intensive pentaerythritol decomposition begins at 190°-220 °C and stops at 265 °C [13]. According to DTA, ammonium polyphosphate reacts with pentaerythritol at 300 °C. However, at that instant pentaerythritol is already decomposed and, at the same time, there is melamine which can «accept» aldehydes formed from pentaerythritol. DTA of binary mixture including melamine and pentaerythritol shows that the mass loss starts at about 240 °C and nearly stops at 360 °C. It should be mentioned that, according to the theory, melamine serves as the gas-forming agent and therefore the mass loss should significantly increase at a temperature above 350 °C [14-16]. However, it does not happen because melamine binds aldehydes thereby forming the polymer-oligomeric resins [17, 18]. At 300 °C, melamine-pentaerythritol mixture mass loss is almost 100%. At that temperature, amino-aldehyde resin and the intumescent material are produced.

Activation energies shown in Table 3 indicate the possible interaction between pentaerythritol and melamine. During the intumescent process, ammonium polyphosphate is expected to preferably react with melamine, rather than with pentaerythritol. Products of these reactions were detected in the intumescent samples as shown below. Results of chromatography-mass spectrometry are presented in Table 4.

Table 3. The results of thermal analysis of intumescent components and their mixtures

Sample	$T_{5\%}$*, °C	$T_{10\%}$, °C	$T_{20\%}$, °C	E_a, kJ/mol
Melamine	320	342	355	129
Ammonium polyphosphate	306	343	416	128
Pentaerythritol	265	285	303	96
Melamine – pentaerythritol	281	296	302	98

*$\mathbf{T_{5\%}}$ – value of temperature related to the percent of weight loss according to TG

Table 4. Substances detected in a carbonaceous sample by chromatography-mass spectrometry

Temperaure of coating thermolysis, °C	200	300	400	500
Products of thermolysis	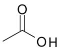	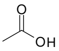	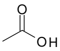	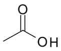
	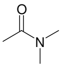	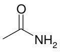	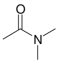	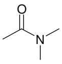
	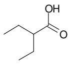	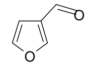	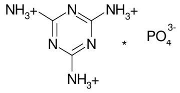	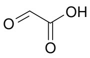
	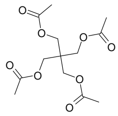	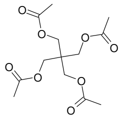	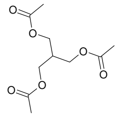	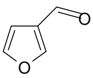
	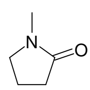	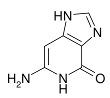	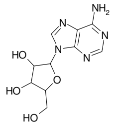	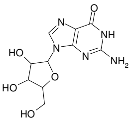
	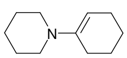	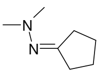	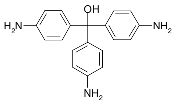	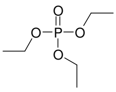

At the annealing temperatures listed above, the acetic acid was detected in hexane. Initially, it forms as a result of binding polymer destructive saponification to 250 °C, and at higher temperatures – when pentaerythritol decays wherein it's an oxidized acetaldehyde. Also another acetaldehyde's form was detected at all temperatures; in particular it's an acetic acid's ammonolysis product – N,N-dimethylacetamide which subsequently can take part in cyclization reactions as a reagent or as a catalyst.

Melamine phosphate (Fig. 2) which was detected in acetic acid extract of a carbonaceous sample made at 400 °C serves as a proof for our hypothesis about the role of melamine: it does not act as a porophore in intumescent process and does not decay with releasing of NH_3, H_2O and CO; instead its structure does not change and it can react and release gases mentioned above as by-products. As soon as phosphoric acids form, as a result of ammonium polyphosphate decay (at 350 °C), they get an ability to react with free melamine's NH_2-groups and form salts.

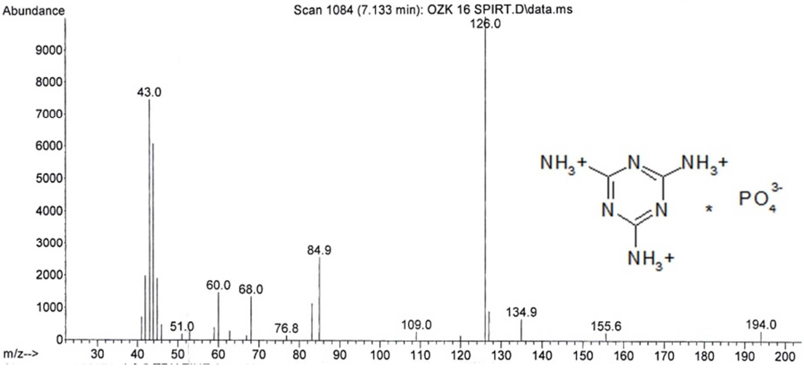

Fig. 2. Mass-fragmetogram of melamine' solid form in acetic acid extract of a sample made at 400°C; *y*-line is abundance (mV), *x*-line is m/z.

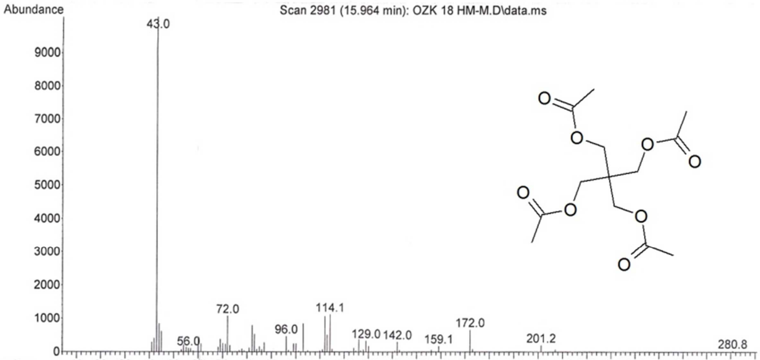

Fig. 3. Mass-fragmetogram of pentaerythritol in acetic acid extract of a sample made at 300 °C; *y*-line is abundance (mV), *x*-line is m/z.

Spectrograms (Fig. 3) show that there is pentaerythritol in its initial form in acetic acid extracts of carbonaceous samples made at 300 °C. It was not detected in samples at higher temperatures, which means that pentaerythritol decayed. Efforts which were made to prove pentaerythritol's ability to form ethers at temperatures below its melting point (215 °C) are inefficient, if a reaction does not occur in a liquid phase. As pentaerythtritol is produced by the method of aldol condensation of formaldehyde with acetaldehyde and alkali as a catalyst, in appropriate topochemical conditions (catalyst and high temperature) there will occur an opposite process – decay with releasing water, initial aldehydes and/or products of their condensation.

Results of IR spectroscopy of carbonaceous sample made at 500 °C are presented on Fig. 4. A group of bands represented on a spectra at the interval 2882-3000 cm^{-1} is caused by C-H bond vibrations in carbonaceous structure; doublet 3164-3120 is caused by –NH2 vibrations. The spectroscopy band at 1631 cm^{-1} is related to C=N bond vibrations which are possibly an azomethine bond typical for products of amines and aldehydes interactions. There are evidences of amide groups existing at 1404 cm^{-1}. Groups –C-N-H are presented by bands at 988 cm^{-1}. A band at 1007 cm^{-1} represents a phosphate ion. An intensive wide band at 1240 cm^{-1} represents P-O bond vibrations; P=O bond is possibly shielded. Also the group O-P-O is detected at 489 cm^{-1}. Thus IR spectroscopy allowed to detect functional groups and molecules of substances which were detected by chromatography-mass spectrometry before.

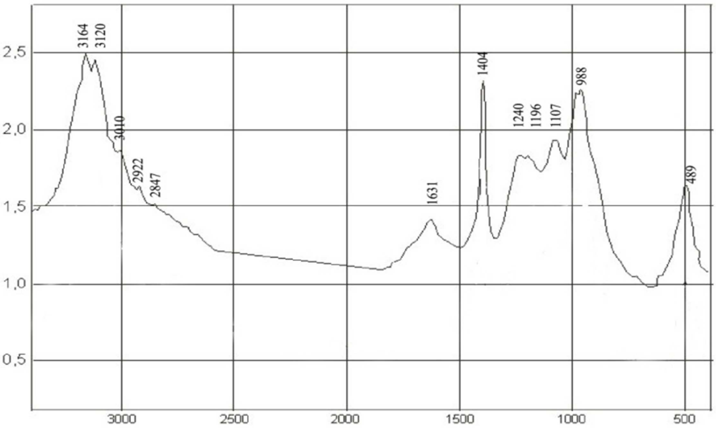

Fig. 4. IR spectra of the carbonaceous sample; *y*-line is absorption, *x*-line is wavenumber (cm^{-1}).

In conclusion, there are results of thermolytic synthesis of swollen resin. As the system was exposed to annealing in a furnace at >350 °C, the forming and swelling of sand-colored resin were detected (Fig. 5, Fig. 6b). A sensitive test of releasing gases by resorcinol dissolved in water has shown the presence of aldehydes in those gases. A swelling coefficient of resin is close to such of a charred layer made from melamine - pentaerythritol - ammonium polyphosphate (3:1:1) mixture whereas a mixture of pentaerythritol and ammonium polyphosphate did not form a resin (Fig. 6a).

DISCUSSION

Previous studies show that melamine resins start decaying at above 350 °C [19, 20]. Melamine phosphate in its turn has higher thermostability and remains the same until 386 °C which was proven above by chromatography-mass spectrometry.

Melamine and its different forms can react with acetic acid and dimethylacetamide forming nitrogenous polycyclic substances. The latter can also be formed in the following way. Acetonitrile and aminoacetonitrile are formed as a result of dehydration of acetamide under the influence of phosphorus oxide and as a result of acetic ammonolysis of acid in excess of ammonia. Acetonitrile and aminoacetonitrile can then react with formamide (at 250 °C) and form 4,5-diaminopyrimidine. The latter cyclizates and forms purine and similar substances such as glycosylamines, adenosine and guanosine which are detected in char samples starting from 300 °C. Its molecules include residue of purine basis tied with residue of ribose by a nitrogen atom. Ribose forms as a result of pentaerythritol restructuring into aldehydes and their self-condensation [21-26].

(a) (b) (c)

Fig. 5. Synthesis of swollen resin from melamine and pentaerythritol located on molten ammonium polyphosphate surface: (a) ammonium polyphosphate melting; (b) adjusting the mixture of melamine and pentaerythritol to molten solid ammonium polyphosphate; (c) a swollen resin formed as a result of heating.

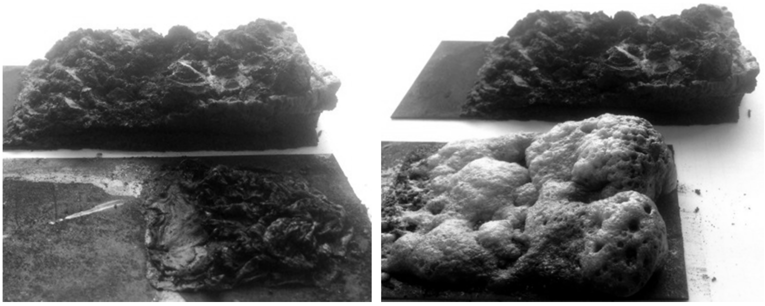

(a) (b)

Fig. 6. Presentation of binary mixtures exposed to annealing in comparison with the primal sample (on the background): (a) pentaerythritol + ammonium polyphosphate (no swelling); (b) pentaerythritol + melamine (thermolytic synthesis of a resin).

Dicyandiamide and urea are known to be the typical ingredients for melamine synthesis [27, 28]. By-products in melamine synthesis are NH_3, H_2O and carbon oxides, just like in intumescent process. For the intumescent compositions, which include dicyandiamide and urea, and do not include melamine, it is possible that formation of char will still follow the synthesis of melamine or another nitrogen-containing heterocyclic substances and their reaction with aldehydes which will result in formation of spatially cross-linked resins.

Our experimental data show that, during an intumescent process, the melamine forms the three-dimensional polymer-oligomeric structures with aldehydes, which, in its turn, form as the pentaerythritol decays. If these structures are not clearly three-dimensional (with NH_2-groups incorporated into melamine-aldehyde resins), then the free amino-groups form the compounds jointly with the ammonium phosphates, thereby completing formation of the spatial structures. On the contrary, previous studies [7, 29] have shown that the ether is formed as a result of heating the intumescent composition, followed by partial thermal decay of the ammonium polyphosphate.

The mechanism of synthesis of carbonaceous layers in thermolysis of intumescent composition including melamine, pentaerythritol and ammonium polyphosphate can now be generalized. The initial stage of heating includes restructuring of pentaerythritol with titanium dioxide and ammonium polyphosphate acting as catalysts. Pentaerythritol decays releasing aldehydes (mainly formaldehyde and acetaldehyde); by that time a polymer binder must be decayed. As aldehydes join the system, the synthesis of polymer-oligomeric resins (mainly melamine-aldehyde resins) starts. A spatial regularity of those resins is maintained by ammonium polyphosphate. Ammonium phosphates play another important role: they catalyze dehydration of the polymer binder and capture generated water. Thus, thermo-oxidative decay of the binder decelerates, whereas both carbonization and graphitation accelerate, and the original material structure remains unchanged. Since the ammonium phosphates act in thermolysis as a source of phosphorous acids, they not only tie the melamine-aldehyde structures, but also increase its chemisorption the substrate surface. This is essential in fireproofing of metals. Lots of by-products (including ammonia, carbon oxides and water) evolve as the resin forms. Gaseous products expand and get the resin swollen and harden. Finally, the heat-resistant graphite-like carbon nitride (g-C_3N_4) forms. It consists of condensed nitrogenous fragments incorporated into the graphene π-linking system inlaid with refractory inorganic compounds such as titanium pyrophosphate [30, 31].

CONCLUSIONS

The experiments conducted in this work enable reconsidering and clarifying the role of basic intumescent compositions ingredients such as melamine, pentaerythritol, and ammonium polyphosphate. A concept of thermolytic synthesis of intumescent coatings is suggested. It is shown that pentaerythritol decays and generates aldehydes. This process is catalyzed by ammonium polyphosphate and titanium dioxide. Melamine and urea react with the aldehydes and form resins wherein the by-product gases induce swelling of the resin. Ammonium polyphosphate acts as a dehydrating agent and as a catalyst of hardening the structure of the charred layer.

REFERENCES

[1] M. Morys, B. Illerhaus, H. Sturm, B. Schartel, Variation of Intumescent Coatings Revealing Different Modes of Action for Good Protection Performance, Fire Technol. 53 (2017) 1569–1587.

[2] L. Calabrese, F. Bozzoli, G. Bochicchio, B. Tessadri , S. Rainieri, G. Pagliarini, Thermal characterization of intumescent fire retardant paints, J. of Phys.: Conf. Ser. 547 (2014).

[3] C. Anderson, D. Ketchum, W. Mountain, Thermal Conductivity of Intumescent Chars, J. Fire Sci. 6 (1988) 390–410.

[4] H. Horacek, Preparation and Fire Test of Intumescent Powder Coatings, Open Access Library J. 1 (2014) 1-15.

[5] L. Xuejun, Q. Jiedong, L. Hongqiang, Z. Xingrong, T. Shuang, C. Ye, C. Zhen, Flame-Retardant and Thermal Degradation Mechanism of Caged Phosphate Charring Agent with Melamine Pyrophosphate for Polypropylene, Int. J. Polymer Sci. (2015) 360274.

[6] F. Xie, Y.-Z. Wang, B. Yang, Y. Liu, A Novel Intumescent Flame-Retardant Polyethylene System, Macromol. Mater. Eng. 291 (2006) 247–253.

[7] A. Pavlovich, A. Drinberg, L. Mashlyakovsky, Fireproofing swelling paintwork coatings, LKM-Press, Moscow, 2018 (in Russian).

[8] M. Thirumaln, Recent developments of intumescent fire protection coatings for structural steel: A review, J. Fire Sci. 34 (2016) 120–163.

[9] R.G. Puri, A.S. Khanna, Intumescent coatings: A review on recent progress, J. Coatings Technol. Res. 14 (2017) 1–20.

[10] R.B.R.S. Olivera, A.L. Moreno Jr., L.C.M. Vieira, Intumescent paint as fire protection coating, Struct. Mater. J. 10 (2017) 220–231.

[11] G. Wang, Y. Huang, X. Hu, Synthesis of a novel phosphorus-containing polymer and its application in amino intumescent fire resistant coating, Progr. Org. Coat. 76 (2013) 188–193.

[12] B. Gardelle, S. Duquesne, V. Rerat, S. Bourbigot, Thermal degradation and fire performance of intumescent silicone-based coatings, Polym. Adv. Technol. 24 (2013) 62–69.

[13] B. Pani, S. Sirohi, D. Singh, Studies on the Effects of Various Flame Retardants on Polypropylene, Amer. J. Polymer Sci. 3(4) (2013) 63–69.

[14] S.C. Gupta, A. Shivhare, D. Singh, S. Gupta, Melamine Polyimide Composite Fire Resistant Intumescent Coatings, Defence Sci. J. 63 (2013) 442–446.

[15] G. Camino, L. Costa, L. Trossarelly, Study of the Mechanism of Intumescence in Fire Retardant Polymers. Part VI: Mechanism of Ester Formation in Ammonium Polyphosphate-Pentaerythritol Mixtures, Polym. Degrad. Stab. 12 (1985) 213-228.

[16] M. Jimenez, S. Duquesne, S. Bourbigot, Intumescent fire protective coating: toward a better understanding of their mechanism of action, Thermochim. Acta 449 (2006) 16–26.

[17] S. Ullah, M. A. Bustam, M. Nadeem, M. Y. Naz, W. L. Tan, A. M. Shariff, Synthesis and Thermal Degradation Studies of Melamine Formaldehyde Resins, Scientific World J. (2014) 940502.

[18] O. Zybina, M. Gravit, A. Pizhurin, The research of influence of polymeric compounds on the effectiveness of intumescent coatings for the fire-protection of construction structures, IOP Conf. Ser.: Earth Environ. Sci. 90 (2017) 012206.

[19] S. Ullah, M. A. Bustam, F. Ahmad, M. Nadeem, M. Y. Naz, M. Sagire, A. M. Shariffa, J. Chin, Synthesis and Characterization of Melamine Formaldehyde Resins for Decorative Paper Applications, Chem. Soc. 62 (2015) 182-190.

[20] L. Costa, G, Camino, Thermal behaviour of melamine, J. Thermal. Anal. 34 (1988) 423-429.

[21] O. Zybina, I. Yakunina, O. Babkin, S. Mnacakanov, E. Voynolovich, Specific reactions of ingredients of fire-protective swelling coatings, Russian Coatings J. 12 (2014) 30-33 (in Russian).

[22] O. Zybina, A. Varlamov, N. Chernova, S. Mnacakanov, On the role and conversions of components of fire-protective compositions in the process of thermolysis, J. Appl. Chem. 4 (2009) 1445-1449 (in Russian).

[23] G. Camino, C. Luigi, R. Trossarelli, Study of the mechanism of intumescence in fire retardant polymers: Part III – Effect of urea on the ammonium polyphosphate-pentaerythritol system, Polym. Degrad. Stab. 7(1984) 221–229.

[24] I.H. Anderson, M. Cawley, W. Steedman, Melamine-formaldehyde resins. II. Thermal degradation of modern compounds and resins, Br. Polym. J. 3 (1971) 86–92.

[25] D.J. Merline, S. Vukusic, A.A. Abdala, Melamine formaldehyde: curing studies and reaction mechanism, Polym. J. 45 (2013) 413–419.

[26] K. Slimer, P. Christjansosn, T. Kaljuvee, T. Pehk, I. Lasn, I. Saks, TG-DTA study of melamine-urea-formaldehyde resins, J. Therm. Anal. 92 (2008) 19–27.

[27] L. Noth, Process for the preparation of melamine, Patent Japan no. 10231. (1984).

[28] W. Haines, Process for production of melamine, Nitrogen 12 (41) (1988) 1438-1439.

[29] H.L. Vandersall, Intumescent Coating Systems. Their Development and Chemistry, J. Fire Flammab. 2 (1971) 97-140.

[30] A. Ustinov, O. Zybina, O. Babkin, Research on the impact of titanium dioxide of different trademarks on the process of thermolysis of intumescent fire-protective coatings, Russian Coatings J. 5 (2018) 32-35 (in Russian).

[31] L. Hongfei, H. Zhongwu, S. Zhang, Q.Zhao, Effects of titanium dioxide on the flammability and char formation of water-based coatings containing intumescent flame retardants, Progr. Organic Coatings. 78 (2015) 318-324.

Investigation of the Effect of Inorganic Smart Fillers and Expanded Graphite on the Flame Retardancy of Polyisocyanurate Insulation Foam

Asimakopoulou E.[1,]*****, **Zhang J.**[1], **McKee M.**[1], **Wieczorek K.**[2], **Krawczyk A.**[2], **Andolfo M.**[2], **Scatto M.**[3], **Sisani M.**[3], **Bastianini M.**[3]

[1] *FireSERT, Belfast School of Architecture and the Built Environment, Ulster University, UK*
[2] *Selena Lab, Poland*
[3] *Prolabin and Tefarm SRL, Italy*
**Corresponding author's email: e.asimakopoulou@ulster.ac.uk*

ABSTRACT

Use of highly insulating polyisocyanurate (PIR) based insulation materials enhanced with eco-friendly lamellar inorganic fillers contributes to meeting energy performance requirements, environmental challenges and cost reduction without undue compromise of the overall building fire safety. This work aims to assess the fire behaviour of PIR foams enhanced with lamellar inorganic smart fillers, namely Layered Double Hydroxides (LDHs), Expandable Graphite (EG) and Ammonium Polyphosphate (APP). The morphology of the foam structure was firstly studied using Optical Microscopy and Field Emission Scanning Electron Microscope and subsequently the fire reaction properties and thermal stability of foam samples enhanced with different types of lamellar inorganic smart fillers were evaluated using cone calorimeter (CC) and thermogravimetric analysis (TGA). TGA results indicated that thermal decomposition of the neat PIR samples occurs in two distinct stages associated with the degradation of the urethane-urea linkages of the hard segment, releasing low calorific capacity products and the degradation of polyol derived products with higher calorific capacity than those derived from isocyanate. The initial degradation temperature of PIR-layered filler samples decreases compared with neat PIR foam, indicating that incorporation of flame retardants decelerates the degradation of PIR foam and as a result decreases the thermal stability of PIR foam. The cone calorimeter data showed that the effects of LDH alone has limited effect on reducing the heat release rate (HRR) or smoke production rate (SPR) as it is only act in the solid phase. With the addition of EG or EG+APP, HRR is further decreased owing to the increased char strength as well as the release of non-combustible gases, and simultaneously effectively suppress smoke and gases during the combustion process.

KEYWORDS: Polyisocyanurate insulation, layer doubled hydroxides, expanded graphite, ammonium polyphosphate, fire performance, thermogravimetric analysis, cone calorimeter.

INTRODUCTION

Modern day energy codes are driving the design and multi-layered configuration of exterior wall systems with significant emphasis on achieving high-performance insulation towards improving energy performance of building envelopes. Insulation in walls may comprise of either non-combustible materials such as fiberglass or mineral wool, or frequently encountered a wide range of highly insulating combustible foam plastic materials. Most commonly used insulation materials include polymers such as extruded polystyrene, expanded polystyrene, polyurethane foam (PUF) and polyisocyanurate (PIR) with or without flame retardants [1]. Appropriate use of the above materials requires that they meet energy performance requirements, environmental challenges and cost reduction without undue compromise of the overall building fire safety. Numerous studies, e.g.

Proceedings of the Ninth International Seminar on Fire and Explosion Hazards (ISFEH9), pp. 1000-1009
Edited by Snegirev A., Liu N.A., Tamanini F., Bradley D., Molkov V., and Chaumeix N.
Published by Saint-Petersburg Polytechnic University Press
ISBN: 978-5-7422-6498-9 DOI: 10.18720/spbpu/2/k19-40

[1-3], have established that thermal decomposition of polymeric foams, in both inert and oxygen atmospheres, is a complex process consisting of numerous decomposition pathways that strongly depend on the reactivity of organic compounds employed in its synthesis. PIR foams are part of the polyurethane (PUR) rigid foam family and their main characteristic is that they contain a high percentage of cyclic isocyanurate chemical linkages and use of polyester polyol instead of the standard polyether polyol used in PURs. PIR are based on the reaction of polycyclotrimerization of diisocyanates or isocyanate terminated prepolymers to form triazine-trione ring structured isocyanurate rings [4] that, from the thermodynamic point of view, are more thermally stable than urethane bonds found in PUR foams as it dissociates at approximately 200 ^{o}C as opposed to 350 ^{o}C for polyisocyanurates [5].

To improve the flammability of polymer-based insulation materials, various fire retardants can be used. The substitution of commonly used halogen-based flame retardants in polymers for eco-friendly second-generation “greener” ones such as mineral fillers like Layered Double Hydroxides (LDHs) or zirconium phosphate nanocomposites [2, 3], is currently of great interest for increasing flame retardancy, thermal stability and smoke suppression by avoiding the release of corrosive and toxic volatile compounds from combustion [6]. LDHs consist of synthetics layered compounds containing positively charged metal hydroxide layers with charge balancing anions located in between. More specifically, LDHs are described by the generic formula $[M^{II}_{1-x}M^{III}_{x}(OH)_2](A^{n-})_{x/n} \cdot yH_2O$, where M^{II} is the divalent cation, M^{III} is the trivalent cation, A is the interlayer anion with n-charge, x is the $[M^{III}/(M^{II}+M^{III})]$ metal molar ratio, generally confined between 0.2-0.4 and y is the mol of water in the interlayer region [7]. LDHs may be formed with all divalent and trivalent metal ions including transition metals, able to do an octahedral coordination with the OH hydroxyl groups and are classified as members of the magnesium aluminum hydroxy carbonate hydrotalcite ($MgAlCO_3$) supergroup [8].

The increased fire retardancy by LDHs is observed in both gaseous and solid phases as they develop non-flammable gases diluting flammable gases and promoting surface charring. Their main mechanism during thermal degradation is the release of water and carbon dioxide, diluting combustion gases, and reducing endothermic decomposition of metal hydroxides. Specifically, this latter inorganic-reinforced carbonaceous residue thermally protects the underlying polymer as the formation of this residue and slows down the combustion process of PUF [2, 6]. At elevated temperatures, LDHs have been shown to release water and go through endothermic decomposition. Different authors have recently studied several types and contents of LDH in polymeric-based insulation materials [2, 3]. Despite their effectiveness, LDHs have until now limited commercial success as fire retardants because of their difficulty to disperse and distribute uniformly in polymers, which limits their effectiveness [2]. Whilst most available studies [2, 3, 6] concern the fire retardancy effects of LDHs in on PUF, a recent study [9] investigated the potential synergistic effect between organically modified nanoclay LDH and flame retardants on PIR nanocomposites.

Recent studies also revealed that (i) the fire behaviour of PIR [10] and PUR [11] foams improve when modified with high Expandable Graphite (EG) contents and (ii) the addition of Ammonium Polyphosphate (APP) can further improve total fire behaviour while enhancing residue formation. EG is a graphite intercalation compound with a special layered structure of graphite that is found to expand when exposed to heat, to up to 100 times, forming a huge insulation layer that enhances the fire resistance of the PIR [10]. This formed char layer is characterised by the presence of “worms” that are derived during its expansion which is attributed to a redox process between H_2SO_4, intercalated between graphite layers and the graphite itself, producing CO_2, H_2O and SO_2 [12,13]. APP has a polyphosphate chain structure and high molecular weight and its efficacy is attributed to the increased char formation by a condensed phase reaction [10]. The phosphoric acid generated from APP has good synergistic effect with EG towards improving the char morphology [12].

The aim of the current work is to assess the fire behaviour and potential synergistic effects of lamellar inorganic smart fillers, including LDH, EG and APP, on the flame retardancy of PIR foams. The morphology of the foam structure was studied using Optical Microscopy and Field Emission Scanning Electron Microscope (FE-SEM) and the fire reaction properties and thermal stability of foam samples enhanced with different types of lamellar inorganic smart fillers were evaluated using cone calorimeter (CC) and thermogravimetric (TGA) analysis.

EXPERIMENTAL INVESTIGATION

Materials

The PIR samples having a constant isocyanate index (NCO/OH) of 3.0 were produced at Selena Lab by high pressure impingement mixing type of foam machinery, operating at constant processing parameters. The initial premixing of the main components of the polyol blend including polyol, catalysts, stabilizer and methylal blowing agent, of all samples was performed for 2-3 min at 1500 rpm. This polyol mix was then mixed with the fillers for 5 min at 2500 rpm. The required amount of isocyanate, methylene diphenyl diisocyanate (MDI), was finally poured into the mixture and stirring was continued for 10 s at the same speed. The average density of the PIR is about 45 kg/m^3.

All the fillers, i.e., Layered Double Hydroxides containing $MgAlCO_3$ (LDH), Expanded Graphite (EG) and Ammonium Polyphosphate (APP) were produced at Prolabin and Tefarm SRL. The final formulations were prepared at Selena Lab. In total, five formulations were examined, namely neat PIR, PIR-2%LDH, PIR-2%LDH+5.1%EG, PIR-2%LDH+5.1%EG+3.6%APP1 (APP with high degree of polymerisation) and PIR-2%LDH+5.1%EG+3.6%APP2 (APP with low degree of polymerisation). The loadings specified are in % wt. The sample sizes in the cone calorimeter tests are 100 mm x 100 mm x 24 mm whereas powders were used in TGA.

Test methods

Optical Microscopy at 500 μm was used for the morphological evaluation of the foam structure. Images and fluorescence photos were collected using the Avio Zoom V16 Zeiss Stereo and Zoom Microscope. Cellular structure of the samples was further evaluated using a LEO 1525 FE-SEM (Field Emission Scanning Electron Microscope) at 100 μm to provide elemental identification and quantitative composition information.

The thermal stability was evaluated under Air (reactive) and N_2 (inert gas) using a Mettler Toledo TGA apparatus. About 10 mg foam sample was placed in an alumina pan with no lid. The heating rate was 20 ^oC/min with a maximum temperature of 1000 ^oC. The gas flow rate is 150 ml/min. The following parameters were determined: initial degradation temperature, $T_{5\%}$ (temperature at 5% weight loss), the weight, W, at the maximum weight loss rate and corresponding maximum temperature, T_{max}, for each degradation step and char residue at 1000 ^oC.

Cone calorimeter (CC) tests were performed with a Dark Star Research Ltd (UK) apparatus according to the ISO 5660-1 [14]. The samples were horizontally placed in a 106 mm x 106 mm x 26 mm stainless steel metal holder. The interior surface was insulated with 2 sheets of 3 mm high temperature vitreous wool Insulfrax® Paper, with a nominal density of 150 kg/m^3 and conductivity 0.098 W/mK at 400 ^oC, coated with 0.07 mm AT502 30 Micron aluminium foil tape, Category 1 according to BS 476 Part 6 and 7 [15, 16]. All samples were conditioned before testing according to ISO 554 [17] at 23 ^oC +/-2 ^oC at 50%+/-5% relative humidity. At least two repeatability tests were performed for each specimen tested. The heat flux used was 50 kW/m^2. For each formulation, at least three tests were conducted to ensure good repeatability. Experimental results include time to ignition (TTI), heat release rate (HRR), total heat released (THR), peak HRR (p-HHR), average heat of combustion (Av-HOC), smoke production rate (SPR), and smoke and CO yield. The unexposed surface temperature was measured using a 1 mm type-K shielded thermocouple.

Additionally, two digital cameras were positioned facing the front or sideway of the test apparatus to record observations regarding specimen burning behaviours and smoke colour. The uncertainty of the measurements complied to ISO 5660 [14]. The holder seemed adequate to support the edges of the samples in the initial burning stages and thus no additional retainer framing has been used to prevent samples deformation. In several samples, a significant glowing was observed after flameout.

RESULTS AND DISCUSSION

Optical microscopy and FE-SEM

A morphological evaluation, in terms of regular and cellular structure, of the tested samples has been performed by optical microscopy and FE-SEM, as depicted in Figs. 1 and 2 respectively for selected formulations. Figure 1 shows that LDH does not significantly alter the morphology of the PIR sample. The FE-SEM results indicate that the average cell diameter of neat PIR, PIR-2%LDH, PIR-2%LDH+5.1%EG, PIR-2%LDH+5.1%EG+3.6%APP1 and PIR-2%LDH+5.1%EG+3.6%APP2 samples is respectively 390, 312, 192, 142 and 271 µm. There is a slight decrease in the average cell diameter with fillers but cellular morphology with the addition of fillers has not been substantially changed in comparison with PIR samples.

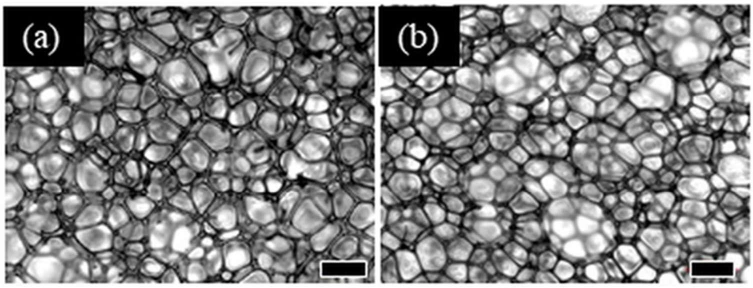

Fig. 1. Morphological evaluation using optical microscopy (black scale bar indicates 500 µm) of pure PIR (a) and PIR-2%LDH (b).

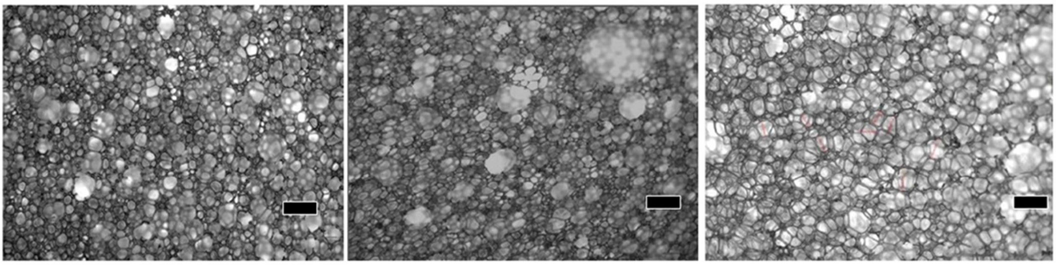

Fig. 2. Morphological evaluation using SEM (black scale bar indicates 500 µm) of PIR-2%LDH+5.1%EG (a), PIR-2%LDH+5.1%EG+3.6%APP1 (b), PIR-2%LDH+5.1%EG+3.6%APP2 (c).

Thermogravimetric analysis (TGA)

Figures 3 and 4 present the weight loss and weight loss rate of all formulations under N_2 and Air atmospheres respectively with the results summarised in Table 1. TGA analysis reveals that the initial degradation temperature of PIR-layered filler samples decreases compared with the neat PIR foam, indicating that incorporation of flame retardants decelerates the degradation of PIR foam and as a result decreases the thermal stability of the PIR foam. It can also be observed that the degradation of all PIR foams without APP in both atmospheres occurs in two steps associated with the degradation of the urethane-urea linkages of the hard segment, releasing low calorific capacity products and the degradation of polyol derived products with higher calorific capacity than those derived from isocyanate. With the addition of APP, an additional degradation step was observed at around 530 °C associated with the degradation of APP.

The initial degradation temperature, $T_{5\%}$, is 258 °C for pure PIR. It can be seen form Table 1 that $T_{5\%}$ decreases with the addition of LDH compared with net PIR foam, indicating that incorporation of flame retardants accelerates the degradation of PIR foam and as a result decreases the thermal stability of PIR foam higher temperature range. But this is not the cases for EG-containing formulations (w/wo APP) indicating that EG degrades at lower temperatures.

The first pyrolysis step takes place from 200 to 400 °C is identified as the main mass loss step in accordance to bibliography [18, 19]. The temperature at the maximum degradation rate, $T_{\max,1}$, is slightly decreased with the LDH filler, whereas it is substantially decreased with the incorporation of EG or EG with APP. This first step is related to the degradation of the urethane-urea linkages of the hard segment [19], releasing low calorific capacity products; residue weight values of this first reaction are denoted as W_1.

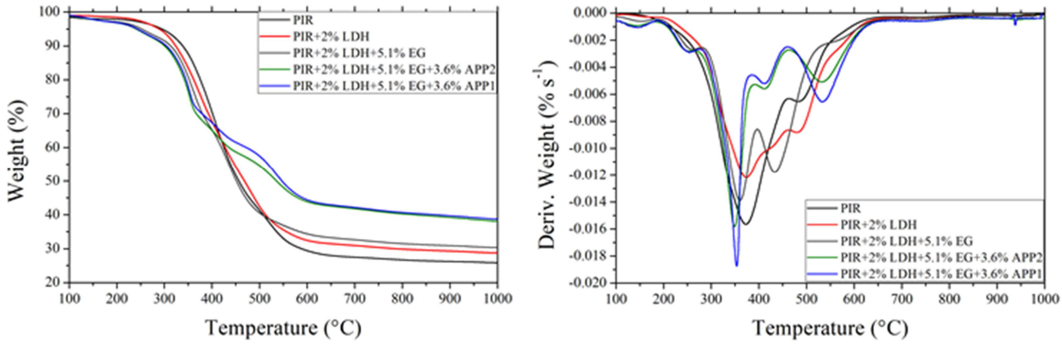

Fig. 3. TG (left) and DTG (right) of all the formulations in N_2 atmosphere.

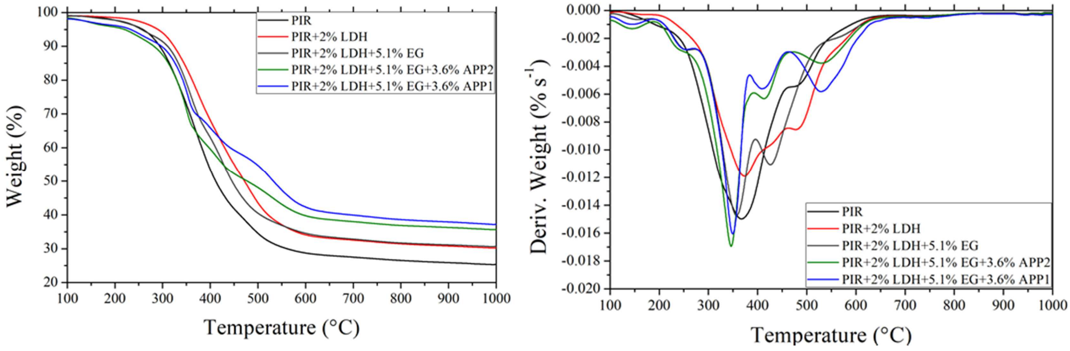

Fig. 4. TG (left) and DTG (right) of all the formulations in air atmosphere.

The second stage of decomposition corresponds to the degradation of polyol derived products with higher calorific capacity than those derived from isocyanate [3] and lower residue weight, W_2. The second degradation step of the pure PIR foam takes place between 400 and 600 °C, and the maximum rate degradation temperature, $T_{\max,2}$, is 457 °C with the final char residue 25.4% of the initial mass. With the addition of EG, the temperatures are generally decreased due to degradation of the fillers at lower temperature. Increasing filler content results in increased char formation.

The former decrease is more substantial with the addition of EG and APP. Samples PIR+2%LDH+5.1%EG+3.6%APP1 and PIR+2%LDH+5.1%EG+3.6%APP2 final residue is above 37% in both atmospheres. All the above results indicate that the addition of APP to PIR decreases the thermal stability of PIR at the first stage and decreases the thermal stability at the second stage. From 500 °C, the amount of residue is always higher than 25% suggesting that the potential synergistic effect of APP on the formation of thermally stable material is better than the incorporation of plain EG and LDH.

Table 1. TG/DTG results of all formulations

Samples	Gas	$T_{5\%}$ [°C]	Stage 1		Stage 2		Stage 3		Residue 1000°C [%]
			$T_{\max,1}$ [°C]	W_1 [%]	$T_{\max,2}$ [°C]	W_2 [%]	$T_{\max,3}$ [°C]	W_3 [%]	
PIR	N_2	295	373	80.8	480	44.7	-	-	25.9
PIR+2%LDH		289	374	76.0	511	40.3	-	-	28.7
PIR+2%LDH+5.1%EG		251	360	76.9	416	61.1	-	-	30.3
PIR+2%LDH+5.1%EG+3.6%APP1		241	349	78.5	435	62.8	534	52.2	38.8
PIR+2%LDH+5.1%EG+3.6%APP2		241	349	77.0	425	61.3	534	50.2	38.2
PIR	Air	258	372	64.1	457	40.7	-	-	25.4
PIR+2%LDH		290	370	77.5	446	55.9	-	-	30.3
PIR+2%LDH+5.1%EG		255	357	76.4	429	54.7	-	-	30.7
PIR+2%LDH+5.1%EG+3.6%APP1		219	349	71.8	421	62.6	538	49.1	37.2
PIR+2%LDH+5.1%EG+3.6%APP2		232	349	77.3	416	56.9	538	44.3	35.7

Cone calorimeter analysis

Figure 5 shows comparisons of the HRR and SPR histories of all formulations. It is worth noting that all formulations ignited almost immediately after being exposed to the heater due to its low density and high flammability. Neat PIR has the highest HRR and SPR as expected. Fissures were observed on the final char residue at the end of the test along with detachment and exfoliation of the upper layer surface as highlighted in Table 6. The trends of SPR are similar to those of HRR, and consequently we will focus our discussions in this section on the HRR.

With the addition of LDH alone, there is a small decrease in the first peak HRR with a more substantial reduction in the second peak HRR. The char also appears stronger than that of the neat PIR. With a further inclusion of EG, the HRR is reduced further, however, it is interesting to note that APP1 has limited effect on the HRR whereas PIR-2%LDH+5.1%EG+3.6%APP2 achieves the lowest HRR and SPR, likely because of the increased strength of the char layer as shown in Table 6, which provides an effective barrier against heat and oxygen, release non-combustible gases, and simultaneously effectively suppress smoke and gases during combustion process.

The present results also demonstrated that the degree of polymerisation has a very important effect on the fire performance of the composites as shown in both Figs. 5, 6 and Table 2. Another important finding is that LDH decreases smoke and CO yields compared to neat PIR. Improved fire behaviour when EG and APP2 fillers are used, is evident as the flame-retardant properties of PIR+2%LDH+5.1%EG+3.6%APP2 sample are improved significantly. Both the p-HRR and Av-

HOC are decreased with additions of fillers. The fact that EG or EG + APP has considerably lower values of heat of combustion than PIR or PIR+2%LDH confirms that they act also in the gaseous phase in suppression combustion. One other important observation is that all the fillers have either similar or lower smoke or CO yields compared to neat PIR, highlighting one of their main advantages of these type of fire retardants in comparison with halogenated fire retardants.

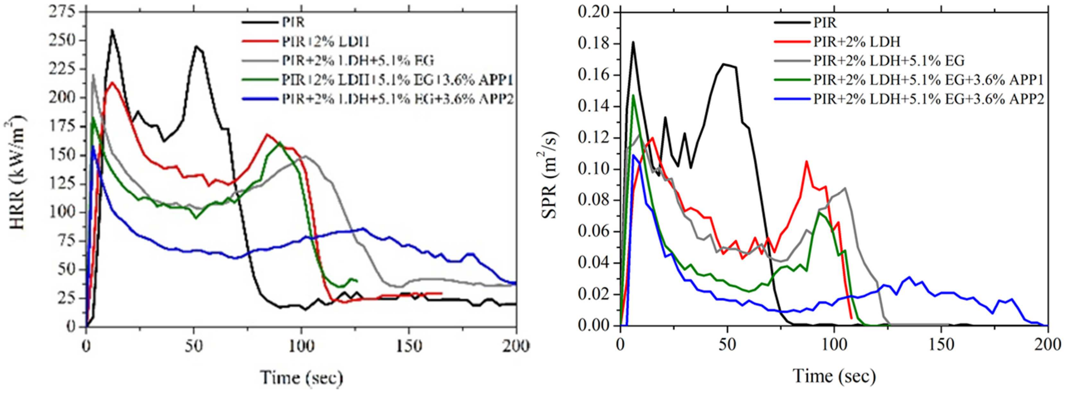

Fig. 5. Comparisons of HRR (left) and SPR (right) of all formulations.

Table 2. Summary of cone calorimeter results at 50 kW/m^2

Samples	THR [MJ/m^2]	p-HRR [kW/m^2]	Av-HOC [MJ/kg]	Smoke yield [-]	CO yield [-]
PIR	17.85	259.1	49.7	0.0980	0.1130
PIR+2%LDH	17.15	213.4	32.1	0.0690	0.0400
PIR+2%LDH+5.1%EG	16.76	207.5	20.9	0.0734	0.0305
PIR+2%LDH+5.1%EG+3.6%APP1	13.66	183.0	22.5	0.0907	0.0553
PIR+2%LDH+5.1%EG+3.6%APP2	15.03	157.9	23.1	0.0484	0.0383

Table 3 presents the char residue of all samples after the tests. As can be seen in the figure, the presence of fillers promotes the formation of a more rigid and hardened residual char layer. For pure PIR sample, the char was brittle and non-uniformly distributed. In addition, detachment and exfoliation of the upper layer surface was also observed.

A very distinction in appearance was observed in the residual char from PIR+2%LDH+5.1%EG+3.6%APP1 and PIR+2%LDH+5.1%EG+3.6%APP2, which were intact and spongy. Clearly, the strength and integrity of the char plays a very important role in reducing the burning rate/heat release rate for mesco- to large-scale samples, in which internal heat and mass transfer becomes important, as opposed to the mg samples used in TGA.

The abovementioned results are verified by the temporal evolution of the unexposed surface temperature of all formulations as depicted in Fig. 6 for all formulations. The unexposed surface temperature rise is slower with the inclusion of LDH and significantly slower with the inclusion of EG and EG +APP. The improved fire behaviour and potential synergistic effect of EG and APP2 is more pronounced in PIR+2%LDH+5.1%EG+3.6%APP2 as the formed char quality is increased. A decreased thermal degradation was observed for samples PIR+2%LDH+5.1%EG+3.6%APP1 and PIR+2%LDH+5.1%EG+3.6%APP2, as the temperature achieved a maximum value at nearly 700 ^{o}C delayed by more than 2 min. The unexposed surface temperature was found strongly dependant on the deformation during combustion as the thermocouple tip is attached to the centre of the sample holder in direct contact with the unexposed surface. Those deformations are more intense in plain PIR and PIR+2%LDH samples, as depicted in Table 3, and though they could be reduced with the use of a grid it was avoided by the authors as that would mean changing the material's properties and fire response.

Table 3. Residual char digital photos of all PIR samples after the CC testing at 50 kW/m^2

Samples	Char Residue	Observations
PIR	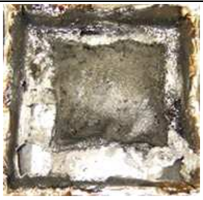	• Fissures at the char • Black smoke during combustion • Detachment and exfoliation of upper layer surface
PIR+2%LDH		• Considerable combustion • White sooty smoke before ignition • Deformation and expansion of the sample
PIR+2%LDH+5.1%EG	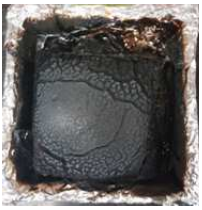	• Considerable combustion • White sooty smoke before ignition • Deformation and expansion of the sample
PIR+2%LDH+5.1%EG +3.6%APP1		• Complete combustion • White sooty smoke before ignition • Deformation and expansion of the sample
PIR+2%LDH+5.1%EG +3.6%APP2		• Complete combustion • White sooty smoke before ignition • Deformation and expansion of the sample

CONCLUSIONS

Fire reaction properties and thermal stability of PIR form with smart fillers including Layered Double Hydroxides (LDHs), Expandable Graphite (EG) and Ammonium Polyphosphate (APP) were evaluated using TGA and cone calorimeter (CC). Optical Microscopy and FE-SEM (Field

Emission Scanning Electron Microscope) measurements were performed for the samples, which verified that the fillers were exfoliated in the PIR samples.

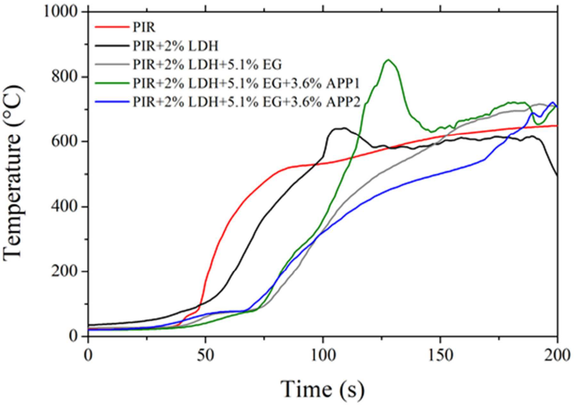

Fig. 6. Unexposed surface temperature of all formulations.

It was found that all fillers promote the formation of a reinforced char layer providing an effective barrier against heat and oxygen. The effects of LDH alone has limited effect on reducing the HRR or SPR as it only acts in the solid phase as the total heat release of PIR+2%LDH is the same as that of the neat PIR. With the addition of EG or EG+APP, the HRR is further decreased owing to the increased char strength as well as the release of non-combustible gases, which effectively suppress smoke and gases during the combustion process. The best performance was achieved by PIR+2%LDH+5.1%EG+3.6%APP2 that resulted in higher char residue, decreased p-HRR values, and decreased smoke generation and CO production. This result also confirms that the degree of polymerisation of fire retardants is also significant in its fire performance.

Further coupled TGA-FTIR analysis at different heating rates under both oxygen and inert atmospheres will be further conducted. Degradation products will be identified, and information will be used to derive a kinetic model to simulate the pyrolysis degradation mechanism of PIR-layered filler foams. Additional combinations of different layered fillers will be investigated in the future to further tune the fire resistance properties of PIR nanocomposites.

ACKNOWLEDGEMENTS

This work is conducted within the EENSULATE project is financially supported by EU H2020 project (EEB-01-2016, Grant No. 723868).

REFERENCES

[1] D. O'Connor, The Building Envelope: Fire Spread, Construction Features and Loss Examples", SFPE Handbook of Fire Protection Engineering (5th ed) Hurley M.J. (ed.), National Fire Protection Association, Quincy, MA 02269, 2016, p 3242/3512.

[2] Y.C. Li, Y.H. Yang, J.R. Shields, R.D. Davis, Layered double hydroxide-based fire-resistant coatings for flexible polyurethane foam, Polymer 56 (2015) 284-292.

[3] S. Gomez-Fernandez, L. Ugarte, C. Pena-Rodriguez, M. Zubitur, M.A. Corceuera, A. Eceiza, Flexible polyurethane foam nanocomposites with modified layered hydroxides, Appl. Clay Sci. 123 (2016) 109-120.

[4] K. Chen, C. Tian, S. Liang, X. Zhao, X. Wang, Effect of stoichiometry on the thermal stability and flame retardation of polyisocyanurate foams modified with epoxy resin, Polym. Degrad. Stab. 150 (2018) 105-113.

[5] M. Kuranska, U. Cabulis, M. Auguscik, A. Prociak, J. Ryszkowaska, M. Kirpluks, Bio-based polyurethane-polyisocyanurate composites with an intumescent flame retardant, Polym. Degrad. Stab. 127 (2016) 11-19.

[6] D.Y. Wang, Novel fire-retardant polymers and composite materials (1st ed) Woodhead Publishing Series in Composite Science and Engineering, Woodhead Publishing, 2016.

[7] P. Nalawade, B. Aware, V.J. Kadam, R.S. Hirlekar, Layer double hydroxides: A review, J. Sc. Res. India. 68 (2009) 267-272.

[8] S.J. Mills, A.G. Christy, J.M.R. Genin, T. Kameda, F. Colombo, Nomenclature of the hydrotalcite supergroup: natural layered hydroxides, Mineral. Magazine 76 (2012) 1289-1336.

[9] L. Gao, G. Zheng, Y. Zhou, L. Hu, G. Feng, Y. Xie, Synergistic effect of expandable graphite, melamine polyphosphate and layered double hydroxide on improving the fire behavior of rosin-based rigid polyurethane foam, Ind. Crop. Prod. 50 (2013) 638-647.

[10] X.M. Hu, D.M. Wang, Enhanced behaviour of rigid polyurethane foam by intumescent flame retardants, J. Appl. Polym. Sci. 129 (2013) 238-246.

[11] X. Meng, L. Ye, X. Zhang, P. Tang, J. Tang, X. Ji, Z. Li, Effects of expandable graphite and ammonium polyphosphate on the flame retardant and mechanical properties of rigid polyurethane foams, J. Appl. Polym. Sc. 114 (2009) 853-863.

[12] M. Modesti, A. Lorenzetti, Flame retardancy of polyisocyanurate–polyurethane foams: use of different charring agents, Polym. Degrad. Stab. 78 (2002) 341-347.

[13] G. Camino, S. Duquesne, R. Delobel, B. Eling, C. Lindsay, T. Roels, In: G.L. Nelson, C.A. Wilkie, editors. Symposium Series No797/ Fires and Polymers. Materials and Solutions for Hazard Prevention. Washington DC: ACS Pub., 2001, p 90/109.

[14] ISO 5660-1, Reaction to fire tests – Heat release, smoke production and mass loss rate – Part 1: Heat release rate (cone calorimeter method), International Organization for Standardization, Geneva, Switzerland, 2002.

[15] British Standards Institution (1989) 476-6: Fire tests on building materials and structures - Method of test for fire propagation for products.

[16] British Standards Institution (1997) 476-7: Fire Tests on Building Materials and Structures - Method of test to determine the classification of the surface spread of flame of products.

[17] ISO 554, Standard atmospheres for conditioning and/or testing specifications, International Organization for Standardization, Geneva, Switzerland, 1974.

[18] J.O. Hidalgo, J.L. Torero, S. Welch, Experimental characterisation of the fire behaviour of thermal insulation materials for a performance-based design methodology, Fire Technol. (2017) 1201-1232.

[19] D.K. Chattopadyay, D.C. Webster, Thermal stability and flame retardancy of polyurethanes, Progr. Polym. Sci. (2009) 1008-1133.

Effects of French Chalk/Hollow Glass Beads on the Flame Retardation of Silicone Foams

Kang F.R.[1,2]**, Deng J.**[1,2,]***, Xiao Y.**[1,2]**, Zhang Y.N.**[1,2]**, Cheng F.M.**[1,2]**, Yi X.**[1,2]

[1] *School of Safety Science and Engineering,*
Xi'an University of Science and Technology, Xi'an, China
[2] *Shaanxi Key Laboratory of Prevention and Control of Coal Fire,*
Xi'an University of Science and Technology, Xi'an, China
**Corresponding author's email: kangfuru@stu.xust.edu.cn*

ABSTRACT

Low-density (0.18–0.31 g/cm^3), flame-retardant closed cell silicone foams (SiFs) were successfully obtained through dehydrogenation at room temperature. Moreover, a flame-retardant system for SiF composites was obtained through a synergistic combination of French chalk (FC)/hollow glass beads (HGB). The mechanical properties, flame retardancy, and thermal stability of SiF composites with FC and HGB were tested using the tension test, limiting oxygen index (LOI), UL-94 test, cone calorimeter, and thermogravimetry. The mechanical properties of SiFs could be significantly improved by interfusing FC. The fire retardancy of the SiFs could be prominently improved by adding FC and HGB. With 50 wt% FC, the SiF achieved the UL-94-V0 rating with the LOI value of 41.6%. Remarkably, the addition of 30 wt% FC and 1 wt% HGB significantly reduced the peak heat release rate by 59.9%, total heat release by 40.9%. TG test showed that FC and HGB can promote the char formation in the degradation process of SiFs. The initial decomposition temperature of SiF with 30 wt% FC and 1 wt% HGB was 445.0 °C and the residue at 900.0 °C was 81.0%, which were noticeably higher than that of pure SiF. Through the analysis of the results of this experiment, it was a promising strategy for preparing flame retardant SiFs with improved mechanical performance and thermal stability by adding FC and HGB.

KEYWORDS: Silicone foams, flame retardancy, thermal stability, mechanical properties.

INTRODUCTION

Flexible silicone foams (SiFs) are a series of cellular polymer materials with –Si–O–Si– comprising their main chains [1]. As a high-performance type of material, SiFs exhibit many outstanding characteristics, including good biological compatibility, nontoxicity, antiaging, strong sound absorption, chemical stability, light weight, ozone resistance, high and low-temperature resistance, electrical insulation, etc. [2–5]. Therefore, they are widely applied in aerospace, national defence, medicine, electrical, transportation, construction industries, etc. [6–9].

However, belonging to the abundant hydrocarbon groups on its side-chain, SiFs can smoulder, combust, and release choking smoke once ignited, which becomes a bottleneck restricting their rapid popularization and application. To improve the flame retardancy and mechanical behavior of SiFs, Deng et al. [10] fabricated SiFs with seven bilayers of chitosan/ammonium polyphosphate coatings; the limiting oxygen index (LOI) increased from 20.2% to 23.8%, the peak heat release rate (PHRR) decreased by 27.6%, and the total smoke production decreased by 42%. Chruściel et al. [11] prepared flame-retarded SiFs whose content was 30% melamine and expanded graphite and whose limiting oxygen index (LOI) was 41–43%. Verdejo et al. [12] examined the fire resistance of silicone-based foams with carbon nanotubes, the limiting oxygen index of the composite increased

Proceedings of the Ninth International Seminar on Fire and Explosion Hazards (ISFEH9), pp. 1010-1018
Edited by Snegirev A., Liu N.A., Tamanini F., Bradley D., Molkov V., and Chaumeix N.
Published by Saint-Petersburg Polytechnic University Press
ISBN: 978-5-7422-6498-9 DOI: 10.18720/spbpu/2/k19-10

as a function of carbon nanotube content, attaining the self-extinguishing grade even at low mass fraction of the carbon nanotubes (0.5 wt%). Additionally, inorganic fillers such as carbon black, asbestos, kaolin, and artificial fibres are widely applied in flame-retardant SiFs [13–19]. Other designs of flame-retardant SiFs have been rarely reported.

Superfine French chalk (FC) is a naturally occurring hydrated magnesium sheet silicate, $3MgO_4SiO_2H_2O$. It can be used as semi-reinforcing and flame retardancy filler for silicone rubber. Moreover, hollow glass beads (HGB) can improve the fire retardancy capabilities and thermal stability of composites effectively. The heat release rate (HRR) of ethylene-vinyl acetate (EVA) composites with 1.0 wt% HGB reduced by 37% and show higher thermal stability at high temperature when compared with EVA composites without HGB [20]. Additionally, the weight of hollow glass beads-filled composites can be effectively decreased compared with the initial composition [21].

In this study, low-density (0.18–0.31 g/cm^3), flame-retardant closed cell SiFs were prepared through condensation dehydrogenation. The flame retardancy, mechanical properties, and thermal stability of SiFs with FC and HGB as flame-retardant filler were tested using the LOI, UL-94 test, cone calorimeter, tension test, and thermogravimetry.

MATERIALS AND METHODS

Materials

The base gum comprised 75 wt% vinyl terminated siloxane (viscosity: 10,000 MPa·s) and 25 wt% fumed silica, which was kindly donated by Salirone New Materials Co. (Huizhou, China). Hydroxy silicone oil (viscosities: 20–30 MPa·s and 1500 MPa·s), hydrogen-containing silicone oil, and Pt compounds (3000 ppm) were produced by Shenzhen Osbang New Materials Co. (Shenzhen, China). The hydrogen content of the hydrogen-containing silicone oil was 0.7 mol%. Methylbutynol was obtained from Shaoguan Koya Fine Chemicals Co. (Shaoguan, China). French chalk was produced by Guangfu Institute of Fine Chemical Engineering (Tianjin, China). Hollow glass beads (particle size: 37.4 μm) was obtained from Sunda Chemical Co. (Dongguan, China).

Preparation of samples

The condensation dehydrogenation method was used to synthesize SiF composites. In detail, a combination of hydroxy silicone oil (viscosities: 20–30 MPa·s and 1500 MPa·s), base gum, methylbutynol, Pt compounds, and flame retardant were placed into a beaker with a mechanical stirrer and stirred for 10 min. Thereafter, hydrogen-containing silicone oil was added, followed by stirring for 3 min. Then poured the mixture carefully into a mould (150 × 150 × 10 mm^3). Afterwards, it foamed and cured at room temperature after approximately 2.0–4.0 min. Finally, the mixture was dried in an oven at 80.0 °C for 3 min. Subsequently, the white closed cell SiFs with smooth surface were finally obtained. The specific formulations are summarized in Table 1.

In this experiment, vinyl terminated siloxane, fumed silica, hydroxy silicone oil, and methylbutynol were used as crosslinking agent, reinforcing filler, vesicant, and inhibitor, respectively. Hydrogen-containing silicone oil was taken as vesicant and crosslinking agent. Pt compounds was used as catalyst, FC and HGB were used as flame-retardant fillers.

Characterisation

The mechanical properties were performed on a HZ-1009C universal tensile testing machine (Shanghai Hengzhun, Shanghai, China) with a drawing speed of 100 mm/min. The specimens were prepared in accordance with the ISO 37-2005. For each sample, five measurements on different surface locations were averaged.

The density of SiFs were measured according to ASTM D1622-2008, and each specimen was 150 × 100 × 10 mm^3. The density of SiFs were calculated by the weight and the volume of the specimen. All specimens were tested three times, and then the average values were reported.

Table 1. Formulation and characteristics of flame retardant SiF composites

Foam	FC/wt%	HGB/wt%	Density (g/cm^3)	LOI (%)	UL-94
SiF0	0	0	0.26	28.8	V1
SiF1	10	0	0.27	31.5	V0
SiF2	20	0	0.28	33.8	V0
SiF3	30	0	0.29	36.6	V0
SiF4	40	0	0.30	39.1	V0
SiF5	50	0	0.31	41.6	V0
SiF6	0	1	0.23	29.2	V1
SiF7	0	2	0.21	29.6	V1
SiF8	0	3	0.20	29.9	V1
SiF9	0	4	0.19	30.4	V1
SiF10	0	5	0.18	30.8	V0
SiF11	30	1	0.26	36.7	V0
SiF12	30	3	0.22	36.9	V0
SiF13	30	5	0.20	37.2	V0

The LOI value was determined using a JF-3 oxygen index instrument (Jiangning, Nanjing, China) in accordance with the ISO4589 standard. The dimensions of all samples were 150 × 10 × 10 mm^3.

The UL-94 vertical flame test was conducted using a CZF-3 horizontal and vertical combustion tester (Jiangning, Nanjing, China) in accordance with the UL-94 test standard. The specimens were 127.0 × 12.7 × 3.0 mm^3 in accordance with the ASTM D3801-2010 test standard.

The experiments were conducted using a cone calorimeter (Fire Testing Technology, London, UK) at an external heat flux of 35 kW/m^2 in accordance with the ISO 5660 standard. All specimens (100 × 100 × 5 mm^3) were tested three times, and the results were reproducible within ±10%.

Thermogravimetry (TG) was performed using a Netzsch TG209F1 (Netzsch, Bavaria, Germany) thermal analyser. At a heating rate of 10 °C/min, 10 mg of the sample was heated from 40 to 900 °C in a nitrogen atmosphere.

RESULTS AND DISCUSSION

Mechanical properties

Mechanical properties are vital factors that affect the performance of polymer materials. To investigated the effects of FC and HGB on the mechanical properties of the SiFs, the tensile strength and elongation at break of SiFs are shown in Fig. 1.

The results for the samples containing only FC indicated that the tensile strength and elongation at break of SiFs first ascended and then descended by increasing FC content from 0 to 50 wt%. When FC content was 30 wt%, the SiFs exhibited highest tensile strength and elongation at break. SiF11 (30 wt% FC, 1 wt% HGB) exhibited higher tensile strength and elongation at break than pure SiF.

Furthermore, the tensile strength and elongation at break of SiF11 (30 wt% FC, 1 wt% HGB), SiF12 (30 wt% FC, 3 wt% HGB), and SiF13 (30 wt% FC, 5 wt% HGB) were higher than the SiFs with the same content of HGB but without FC. Notably, FC can significantly improve the mechanical properties of SiFs, while the tensile strength and elongation at break of SiFs decreased markedly with the increasing content of HGB. For instance, when the HGB content increased from 1 to 5 wt%, the breaking strength and elongation at break of SiFs declined from 80 KPa, 172% to 45 KPa, 125% (i.e., a decrease of approximately 44% and 27%, respectively). This phenomenon may contribute to the unsatisfactory compatibility between HGB and SiFs.

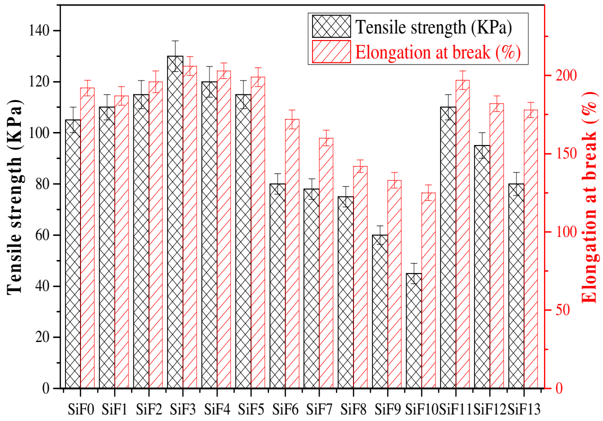

Fig.1. Tensile strength and elongation at break of SiF composites.

Density

As expected, the additon of HGB had a positive effect on the density of the SiF composites. From Table 1, we could plainly see that the density of SiFs increase with the increasing content of FC, while it dramatically decrease with the increasing content of HGB. Compared with SiF0, the density of SiF10 with 5 wt% HGB significantly reduced by 30.8%. In addition, SiF11 (30 wt% FC, 1 wt% HGB) could keep the same density as SiF0.

Flame retardancy

The LOI values and UL-94 tests were used to determine the flammability of the flame-retardant materials. LOI, which is the minimum oxygen concentration by volume required to maintain the burning of a material, is critical for evaluating SiF flame retardancy [22]. The LOI and UL-94 test results for the SiFs were recorded in Table 1. Notably, we could conclude that the LOI values of SiFs rose with the increasing content of FC and HGB. With 50 wt% FC, SiF5 achieved the UL-94-V0 rating with the LOI value of 41.6%. Meanwhile, all the SiFs with no less than 10 wt% FC could achieve the UL-94-V0 rating, which indicated that FC apparently improved the LOI value of SiFs. Moreover, SiFs with only 5 wt% HGB could achieve the UL-94-V0 rating, and the LOI values of SiF11 (30 wt% FC, 1 wt% HGB), SiF12 (30 wt% FC, 3 wt% HGB), and SiF13 (30 wt% FC, 5 wt% HGB) were obviously higher than SiF3 (30 wt% FC) . According to Table 1, SiF0 and SiF11 possessed the same density, however, SiF11 significantly increased the LOI by 27.4% after added 30 wt% FC and 1 wt% HGB. In summary, SiF composites with FC/HGB exhibited excellent flame retardancy.

Fire hazard analysis

The cone calorimeter test is a universal method for investigating the combustion behavior of polymer materials, especially for evaluating the heat release behavior in a real fire [23, 24]. The

HRR and total heat release (THR) of SiF0, SiF1, SiF3, SiF6, SiF10, and SiF11 are delineated in Fig. 2. The main parameters, including time to ignition (TTI), PHRR, and time to PHRR (TPHRR) of the SiF composites, are listed in Table 2. Moreover, the fire growth index (FGI) and the fire performance index (FPI) for SiF composites were shown in Fig. 3.

It could be seen from Fig. 2 (a) and Table 2 that the Pure SiF burned very fast after ignition, and a sharp PHRR of 132.61 kW/m^2 was obtained at 45 s. The PHRR of the SiF composites with FC or HGB was much lower than that of pure SiF, and the PHRR values of SiF1, SiF3, SiF6, SiF10, and SiF11 were as follows: 60.14 kW/m^2, 60.89 kW/m^2, 71.22 kW/m^2, 53.18 kW/m^2, 50.64 kW/m^2. Remarkably, SiF11 with 30 wt% FC and 1 wt% HGB significantly reduced the PHRR by 59.9%. Furthermore, the TTI of pure SiF were only 20 s, while the TTI of SiF11 were 123 s. Compared with SiF3 (30% FC), SiF11 (30 wt% FC, 1 wt% HGB) had a more excellent flame retardant ability.

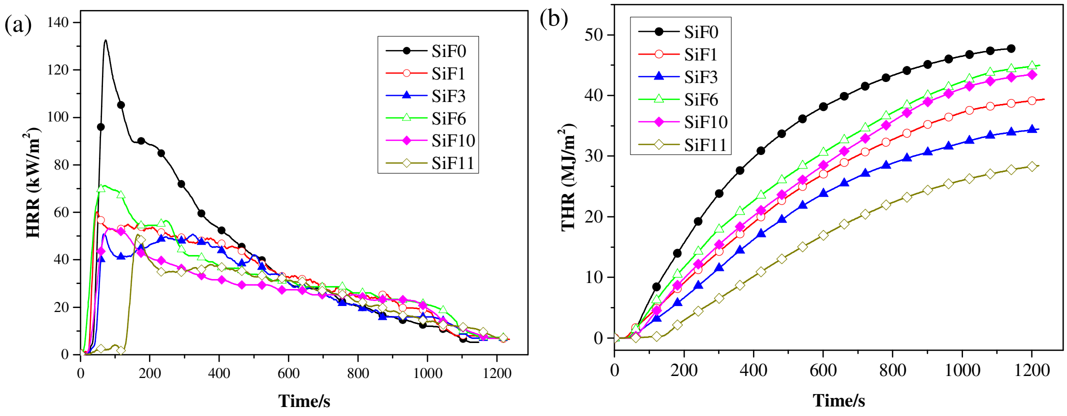

Fig. 2. (a) HRR and (b) THR curves of SiF composites.

Table 2. Cone calorimeter data of SiF composites

Sample	TTI (s)	TPHRR (s)	PHRR (kW/m^2)	THR (MJ/m^2)
SiF0	20	45	132.61	47.79
SiF1	27	49	60.14	39.38
SiF3	40	68	60.89	34.46
SiF6	24	72	71.22	44.98
SiF10	47	87	53.18	43.50
SiF11	123	166	50.64	28.42

Figure 2 (b) presented the THR of SiF composites. It could be seen that the THR value (47.79 MJ/m^2) of pure SiF was obviously higher than that of other SiF composites. The THR of pure SiF was 47.79 MJ/m^2, while the THR of SiF1, SiF3, SiF6, SiF10, and SiF11 were 39.38 MJ/m^2, 34.46 MJ/m^2, 44.98 MJ/m^2, 43.50 MJ/m^2, and 28.42 MJ/m^2, respectively. Compared with SiF0, SiF11 with 30 wt% FC and 1 wt% HGB significantly reduced the THR by 40.9%. It was reported that the gradient of THR curve can be assumed as representative of flame spread [25, 26]. From Fig. 2 (b), we could see that the flame spread rate was considerably reduced. The reason was that there was a much compact char residue forming on the surface of the sample to restrict flames spread.

The FGI was the ratio of PHRR to TPHRR, and the FPI was the ratio of TTI to PHRR. The FGI and FPI are parameters directly reflect the safety rank of samples directly. A lower FGI and higher FPI indicate a greater safety rank. [27, 28] The FGI and FPI of SiF11 were 0.31 kW/(m^2·s) and 2.43 m^2·s/kW, which were the lowest FGI value and highest FPI value among the SiF composites, which indicated that SiF11 possessed relatively higher safety rank than other SiF composites.

The above phenomena can be illustrated in the following. Firstly, after the SiFs is ignited, a lot of heat can be absorbed during the pyrolysis process of FC. Secondly, FC and HGB can form compact char residue on the surface of the SiF composites and improve the weight of char residue. At last, the SiFs with HGB have poor thermal conductivity, which can count against the heat transfer on the surface of the SiF composites.

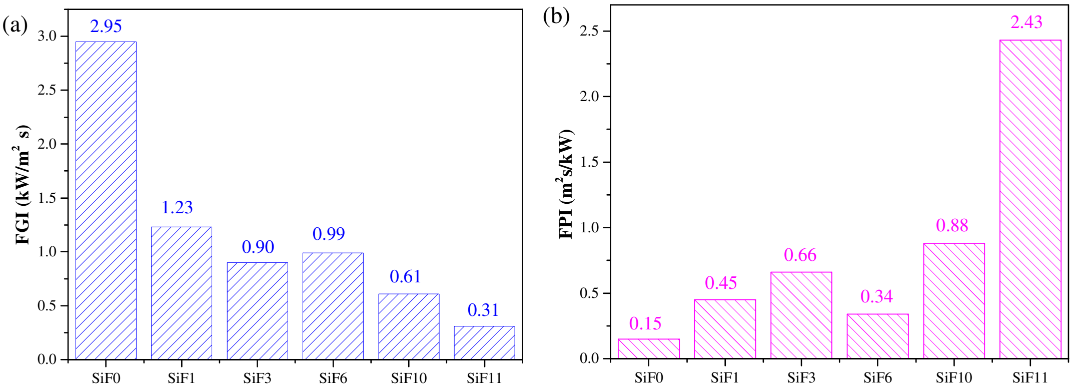

Fig. 3. Cone calorimeter (a) fire growth index and (b) fire performance index for SiF composites.

Thermal stability

The thermal stability of SiF has a bearing on the decomposition products and char formation, which can reveal the flame retardant mechanism [29, 30]. The curves of TG and derivative TG (DTG) for the SiF composites are presented in Fig. 4, and the key parameters are summarized in Table 3. The data clearly indicate that SiF0 started to decompose gradually at 399 °C. Two-stage decomposition of SiF0 was observed from T_{1max} and T_{2max} of 454 and 649 °C, respectively. Ultimately, 63.1% of the char residue remained at 900 °C. The occurrence of the first stage was mainly attributed to the cleavage of Si–C bonds and side organic groups, whereas the occurrence of the second stage was ascribed to the decomposition of the main chains (Si–O–Si).

Compared with pure SiF, the fire retardancy and thermal stability of the SiFs could be prominently improved by adding FC and HGB. The initial decomposition temperatures (T–1 wt%) of SiF1, SiF3, SiF6, SiF10, and SiF11 was 468 °C, 466 °C, 431 °C, 454 °C, and 445 °C, respectively, which were noticeably higher than that of pure SiF. Usually, the thermal degradation of SiF1, SiF3, SiF6, SiF10, and SiF11 comprises three stages, and the extra stage was attributed to the decomposition of FC and HGB. When the temperature was higher than 588 °C, the residual masses of SiF1, SiF3, SiF6, SiF10, and SiF11 were heavier than that of pure SiF. In particular, the residual masses of SiF1, SiF3, SiF6, SiF10, and SiF11 at 900 °C were 80%, 80%, 74.9%, 75%, and 81.0%, respectively, which were significantly higher than that of pure SiF (63.1%).

It was easy to come to a conclusion that the thermal stability of SiF composites were increased by FC and HGB so that they started decomposing later than pure SiF, and the residual masses were higher than that of pure SiF. The decomposition rates of SiF1, SiF3, and SiF11 were generally lower than pure SiF, and the time to reach the peak value of DTG were longer than that of pure SiF. It was obvious that FC contributed more to the char forming progress than HGB. The formed carbon layer delayed the thermal degradation process, and reduced the fire risk of SiF composites.

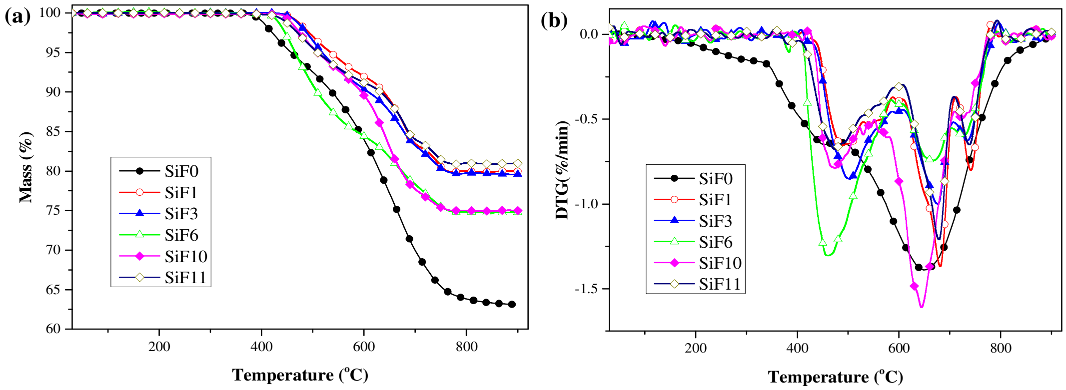

Fig. 4. (a) TG and (b) DTG curves of SiF composites at a heating rate of 10.0 °C/min in N_2.

Table. 3. TG parameters of SiF composites

Sample	$T_{-1wt\%}$ (°C)	T_{1max} (°C)	T_{2max} (°C)	T_{3max} (°C)	Residue at 900 °C (%)
SiF0	399.0	454.0	649.0	–	63.1
SiF1	468.0	489.0	681.0	741.0	80.0
SiF3	466.0	503.0	675.0	733.0	80.0
SiF6	431.0	461.0	668.0	722.0	74.8
SiF10	454.0	474.0	644.0	726.0	75.0
SiF11	445.0	474.0	678.0	738.0	81.0

CONCLUSIONS

In this study, low-density (0.18–0.31 g/cm^3) environmentally friendly flame-retardant closed cell SiFs were successfully prepared at room temperature. The detailed conclusions for the SiF composites tested for mechanical properties, LOI, UL-94, cone calorimeter, and TG were as follows. First, FC could significantly improve the mechanical properties of SiFs. Second, the fire retardancy and thermal stability of the SiFs could be prominently improved by adding FC and HGB. Furthermore, the SiF with 30 wt% FC and 1 wt% FC exhibited optimal flame retardancy, mechanical properties, and thermal stability. In summary, the FC/HGB synergistic flame-retardant system for SiF composites was effective.

REFERENCES

[1] E. Yilgör, I. Yilgör, Silicone containing copolymers: Synthesis, properties and applications, Progr. Polym. Sci. 39 (2014) 1165–1195.

[2] S. Hamdani, C. Longuet, D. Perrin, J. Lopez-Cuesta, F. Ganachaud, Flame retardancy of silicone-based materials, Polym. Degrad. Stab. 94 (2009) 465–495.

[3] S. Fang, Y. Hu, L. Song, J. Zhan, Q.L. He, Mechanical properties, fire performance and thermal stability of magnesium hydroxide sulfate hydrate whiskers flame retardant silicone rubber, J. Mater. Sci. 43 (2009) 1057–1062.

[4] J.A. Rabe, S. Spells, D.M. Rasch, G.R. Homan, C.L. Lee, Evaluation of silicone foam for flat plate solar collector insulation, Sol. Energy Mater. 4 (1981) 159-168.

[5] R. Verdejo, C. Saiz-Arroyo, J. Carretero-Gonzalez, F. BarrosoBujans, M.A. Rodriguez-Perez, M.A. Lopez-Manchado, Eur. Polym. J. 44 (2008) 2790–2797.

[6] P. Liu, D. Liu, H. Zou, P. Fan, W. Xu, Structure and Properties of Closed-Cell Foam Prepared from Irradiation Crosslinked Silicone Rubber, J. Appl. Polym. Sci. 113 (2009) 3590–3595.

[7] E. Stochmal, J. Strzezik, A. Krowiak, Physicochemical and catalytic properties of polysiloxane network–Pt systems, RSC Adv. 7 (2017) 26342–26360.

[8] J.B. Grande, A.S. Fawcett, A.J. McLaughlin, F. Gonzaga, T.P. Bender, M.A. Brook, Anhydrous formation of foamed silicone elastomers using the Pierse-Rubinsztajn reaction, Polymer 53 (2012) 3135–3142.

[9] X. Wang, W. Dou, Preparation of graphite oxide (GO) and the thermal stability of silicone rubber/GO nanocomposites, Thermochim. Acta 529 (2012) 25–28.

[10] S.B. Deng, W. Liao, J.C. Yang, Z.J. Cao, Y.Z. Wang, Flame-retardant and smoke-suppressed silicone foams with chitosan-based nanocoatings, Ind. Eng. Chem. Res. 55 (2016) 7239–7248.

[11] J.J. Chruściel, E. Leśniak, Preparation of flexible, self-extinguishing silicone foams, J. Appl. Polym. Sci. 119 (2010) 1696–1703.

[12] R. Verdejo, F. Barroso-Bujans, M.A. Rodriguez-Perez, J.A. de Saja, M.A. Lopez-Manchado, Functionalized graphene sheet filled silicone foam nanocomposites, J. Mater. Chem. 18 (2008) 2221–2226.

[13] E.S. Kim, H.S. Kim, S.H. Jung, J.S. Yoon, Adhesion properties and thermal degradation of silicone rubber, J. Appl. Polym. Sci. 103 (2007) 2782–2787.

[14] J. Zhang, S. Feng, Q. Ma, Kinetics of the thermal degradation and thermal stability of conductive silicone rubber filled with conductive carbon black, J. Appl. Polym. Sci. 89 (2003) 1548–1554.

[15] C.L. Lee, Method of preparing fire retardant open-cell siloxane foams and foams prepared therefrom. U.S. Patent 4,026,842, 1977.

[16] S.B. Smith, Method of preparing fire retardant siloxane foams and foams prepared therefrom. U.S. Patent 3,923,705, 1975.

[17] J.R. Harper, Method for preparing flame resistant polysiloxane foams and foams prepared thereby. U.S. Patent 4,433,069, 1984.

[18] M. Alexandre, P. Dubois, M. Devalckenaere, M. Claes, Fireproof composition. U.S. Patent 9,290,676, 2016.

[19] W.R. Nicholson, L.J. Rapson, K.L. Shephard, Flame retardant silicone foams. U.S. Patent 6,084,002, 2000.

[20] L. Liu, J. Hu, J.L. Zhuo, C.M. Jiao, X.L. Chen, S.X. Li, Synergistic flame retardant effects between hollow glass microspheres and magnesium hydroxide in ethylene-vinyl acetate composites, Polym. Degrad. Stab. 104 (2014) 87–94.

[21] A. Aruniit, J. Kers, J. Majak, A. Krumme, K. Tall, Influence of hollow glass microspheres on the mechanical and physical properties and cost of particle reinforced polymer composites, Proc. Est. Acad. Sci. 61 (2012) 160–165.

[22] Q. Tang, B. Wang, Y. Shi, L. Song, Y. Hu, Microencapsulated ammonium polyphosphate with glycidyl methacrylate shell: application to flame retardant epoxy resin, Ind. Eng. Chem. Res. 52 (2013) 5640–5647.

[23] H. Li, H. Liu, J. Li, P. Li, Preparation and characterization of magnesium hydroxide-multiwalled carbon nanotubes/poly (ethylene-co-vinyl acetate) nanocomposites, Mater. Focus 3 (2014) 261–266.

[24] B. Schartel, T.R. Hull, Development of fire retarded materials-interpretation of cone calorimeter data, Fire Mater, 31 (2010) 327–354.

[25] X. Almeras, M.L. Bras, P. Hornsby, S. Bourbigot, G. Marosi, S. Keszei, F. Poutch, Effect of fillers on the fire retardancy of intumescent polypropylene compounds, Polym. Degrad. Stab. 82 (2003) 325–331.

[26] C.M. Jiao, X.L. Chen, Flammability and thermal degradation of intumescent flame-retardant polypropylene composites, Polym. Eng. Sci. 10 (2010) 767–772.

[27] X.L Chen, Y.F Jiang, C.M Jiao, Smoke suppression properties of ferrite yellow on flame retardant thermoplastic polyurethane based on ammonium polyphosphate, J. Hazard. Mater. 266 (2014) 114–121.

[28] B. Schartel, T.R. Hull, Development of fire-retarded materials-interpretation of cone calorimeter data, Fire Mater. 31 (2007) 327–354.

[29] X. Chen, C. Jiao, J. Zhang, Thermal and combustion behavior of ethylene-vinyl acetate/ aluminum trihydroxide/Fe-montmorillonite composites, Polym. Eng. Sci. 52 (2012) 414–419.

[30] Y. Wang, J. Zhang, Thermal stabilities of drops of burning thermoplastics under the UL 94 vertical test conditions, J. Hazard. Mater. 246 (2013) 103–109.

Flammability Assessment of an Intumescent Flame Retardant Thermoplastic Polymer

Celiński M.[1], Salasińska K.[1], *, Mirowski J.[2], Kozikowski P.[1], Mizera K.[3], Borucka M.[1], Gajek A.[1]

[1] *Central Institute for Labour Protection – National Research Institute,*
Department of Chemical, Biological and Aerosol Hazards, Warsaw, Mazovia, Poland
[2] *University of Science and Technology in Bydgoszcz, Faculty of Chemical Technology and Engineering, Bydgoszcz, Kuyavian-Pomeranian, Poland*
[3] *Warsaw University of Technology, Faculty of Materials Science and Engineering, Warsaw, Mazovia, Poland*
**Corresponding author's email: macel@ciop.pl, kasal@ciop.pl*

ABSTRACT

Intumescence is a result of synergic effect of three components: charring source, char promoter and foaming agent. Phosphoric acid derivatives, are an object of interest of many researches and flame retardants industry potentates. As an intumescence mechanism component, melamine salts combines two out of three key features, char promotion and gasses generation. As part of the work, a complex compound based on a high nitrogen content substance bis(melamine phosphate)copper (II) phosphate (CUMP) was introduced into high-density polyethylene (PE-HD) and subjected to a flammability and smoke emission tests. The influence of a novel intumescent fire retardant (IFR) addition on the properties of polymer was determined by static tensile test, thermogravimetric analysis (TGA), as well as cone calorimetry (CCT) and single-chamber tests. Moreover, microstructure of the materials and char residue after cone calorimetry test were investigated by scanning electron microscope (SEM). The material containing 20 wt% of CUMP were characterized by ability to form a less combustible char layer inhibiting the decomposition process. The results were compared to those for unmodified polyethylene and a polymer containing 20 wt% of ammonium polyphosphate (APP). New IFR compound has an effect on flame retardancy of polyethylene, comparable to or even greater than commonly used ammonium polyphosphate.

KEYWORDS: Cone calorimeter, flammability, intumescent flame retardant, smoke emission.

INTRODUCTION

Most plastics are carbon-based materials that will burn and give off gases and smoke when subjected to a flame. Plastics are excellent fuels but are generally classified as ordinary combustibles and fall into the same category as wood, pellet and other common materials, which does not reflect their true nature. Most commonly used plastics are polyolefin, carbon/hydrogen-based materials like polyethylene or polypropylene. Polyethylene (PE) is the most widely used plastic in the world. According to the data [1] in 2017 the production of this plastic exceeded 100 million tons, accounting for 34% of the total plastics market. Its primary use is in packaging (plastic bags, plastic films, containers) and cladding (furniture, elevation). Due to the simple chemical structure polyethylene can be very good and effective fuel during fires. It is believed that polyethylene was responsible for such rapid spread of the fire in Grenfell Tower in 2017 where over 70 people died and another 70 were hospitalized [2]. That is why materials have to comply with

Proceedings of the Ninth International Seminar on Fire and Explosion Hazards (ISFEH9), pp. 1019-1028
Edited by Snegirev A., Liu N.A., Tamanini F., Bradley D., Molkov V., and Chaumeix N.
Published by Saint-Petersburg Polytechnic University Press
ISBN: 978-5-7422-6498-9   DOI: 10.18720/spbpu/2/k19-109

very strict, however necessary, fire safety requirements in applications, such as transport, architecture, etc. Usually, in order to comply with these requirements, fire retardants (FR) are added to the polymer during manufacturing processes like extrusion, injection molding, etc. [3-4].

Intumescent flame retardants (IFR) are a mixture of compounds that promote formation of swollen char layer on the surface of the material under the influence of a flame or temperature. Char swelling effect is based on a interactions between individual components of flame retarding system i.e. acid source, carbonizing agent, blowing agent [5-6]. Attractiveness of this phenomenon is the almost unlimited possibilities for the combination to achieve only one goal, to make plastics safer. There are many studies and theories connecting polymer structure with the char formation efficiency and its influence on the flammability of plastics. Currently, it was established that the most promising group of potential IFR are compounds containing aromatic rings, high concentration of nitrogen, e.g. diazol, tiazine combined with phosphoric and boric acids derivatives. Compounds based on phosphoric acid acts as a flame retardants both in the condensed phase (promoting char) and in vapor phase (free-radicals inhibition).

A novel oligomeric phosphorus-containing IFR, poly (2-morpholinyl-4-pentaerythritolphosphate-1,3,5-triazine) (PMPT) was synthesized by Zuo [7]. The incorporation of PMPT into PP improved its thermal stability and flame retardancy, while it had a slight effect on the mechanical properties. Lai et al. [8] synthesized a pentaerythritol phosphate based intumescent flame retardants (PETBP). Incorporation of 25 wt% of PETBP into PP resulted in increase in LOI up to 29.5%, and also allowed to classify it as V-0 in UL-94 test. However, chemical compounds used to synthesize this IFR normally include chlorides or phosphorus oxychloride [9-12], which are highly reactive and toxic to environment.

The role of organic and inorganic salts of transitional metals in flame retardants is also known and widely researched. The most promising transitional metal used as a flame retardant is zinc. As a boric salt zinc shows great smoldering and smoke suppressing properties. Le at al. [12] have shown that addition of 2 wt% of hydrophobic zinc borate caused a noticeable increase in thermal stability of PE. Phosphate salt of zinc was also tested. Muller et al. [13] studied the influence of melamine poly(zinc phosphate) as a IFR in epoxy resin. Although it showed good flame retarding properties, its influence on thermal stability was undesirable. Manzi-Nshuti et al. [14] tested the influence of zinc aluminum oleate on the flammability of PE during cone calorimeter test (CCT) at heat flux of 50 kw/m^2. Based on the obtained results it was concluded that addition of 20 wt% of zinc aluminum oleate to the PE decreased maximum peak of heat release rate (pHRR) from 1800 kW/m^2 to 500 kW/m^2. Nonetheless the modification also decreased ignition time (TTI) and increased the volume of smoke emission (VOS) twofold.

In this paper an impact of novel nitrogen-rich IFR on a combustibility of polyethylene was evaluated. The flame retardancy and smoke emission of the manufactured materials were investigated by cone calorimetry and single-chamber tests. Fire behaviour of novel nitrogen-rich IFR was compared with results gained for APP, commonly used flame retardant with proven ability to generate swollen char during thermal decomposition [15]. Detailed investigation of the decomposition pathways and the morphology of the fire residues via thermogravimetric analysis and cone calorimetry test were also provided. Moreover, structural characteristics along with mechanical properties of the polymers were defined. The research was of a preliminary nature, allowing for the setting of the course of further analysis.

EXPERIMENTAL

Materials and methods

All chemical compounds used in the synthesis process such as phosphoric acid, melamine, 3-amino-triazole etc. were acquired from Sigma-Aldrich, Merck or Alfa Aesar with the declared purity of 95%+. The high-density polyethylene (PE-HD) Tipelin BA 550-13 from MOL Petrochemicals Co. Ltd., with a melt mass-flow index (190 °C/5.0 kg, ISO 1133) of 1.5 g/10 min, was used as polymer. The halogen-free fire retardant ammonium polyphosphate, trade name Addforce FR APP203 (APP), received from Walter Thieme Handel GmbH were applied.

Bis(melamine phosphate)copper (II) phosphate (CUMP) was synthesized by one-pot reaction, and the corresponding synthetic route was illustrated in Fig. 1.

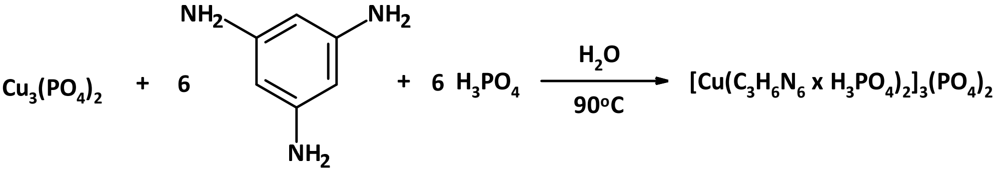

Fig. 1. Synthesis route for CUMP.

In the 1500 ml beaker, 65 grams (0.5 mole) of melamine was partially dissolved in 900 ml of deionized water at 90 °C. Solution of 35 grams (0.09 mole) of copper phosphate in 55 ml (85% solution in water, ~ 0.8 mole) of phosphoric acid was added dropwise. During the addition, a blue solid appeared and temperature raised due to the formation of melamine phosphate and complex salt. Next, the mixture was stirred for 4 hours in 90 °C. After cooling to room temperature solid phase was filtered, poured with heated water (70 °C, 2x100 ml) and dried to steady mass. About 134 grams (92% yield) of CUMP was obtained.

To better mix of polyethylene with fire retardants and to manufacture samples of normalized shapes, two-stage processing was performed. Stage one included mixing of the components using a EHP-2x24M co-rotating twin screw extruder (Zamak Mercator Ltd.) with maximum temperature setting 180 °C. The obtained mixtures were ground by means of a Rapid 150-21 mill (Rapid Granulier-Systeme GmbH & Co.), then the samples were manufactured using hydraulic press PHM-63 (Ponar Żywiec). The temperature, pressure and time of process were 180 °C, 120 kG/cm^2 and 6-10 min, respectively. The amount of CUMP in materials reached 20 wt%. The samples from unmodified polyethylene (PE) and with 20 wt% of ammonium polyphosphate, as reference materials, were also manufactured.

The examinations of the fracture surfaces were conducted with a high-resolution field emission scanning electron microscope (FE SEM) SU8010 (Hitachi High-Technologies Corp.), equipped with a backscattered electron (BSE) detector and energy-dispersive X-ray spectrometer (Utra Dry Silicon Drift). In order to increase the conductivity, samples were coated with gold using Q150T ES (Quorum Technologies Ltd.). Burnt samples were fixed on carbon tape using conductive carbon cement Leit-C.

Mechanical properties of materials were determined in static tensile test in accordance with the document ISO 527, by means of Zwick Roell Z010 testing machine (Zwick GmbH & Co.KG,) with 5 kN nominal force. The assumed length of the measured distance was 30 mm, and tests were realized with 5 mm/min cross speed.

The thermogravimetric analysis was carried out on a TGA Q500 (TA Instruments Ltd.). The samples were tested in an atmosphere of nitrogen with flowing gas at a rate 10 ml/min in the chamber and 90 ml/min in the oven. They were heated from room temperature to 1000 °C at a rate of 10 °C/min.

Horizontal burning rates were measured according to the standard IEC 60695-11-10, which corresponding to the American National Standard UL-94. The specimens with dimensions of 125x10x4mm were subjected to a 50W test flame.

Limiting oxygen index (LOI) was measured in accordance with the procedure described in EN ISO 4589-2. LOI data were determined in an oxygen index instrument with the specimen dimensions of 100×10×4 mm.

The flammability properties were examined by a cone calorimeter device (Fire Testing Technology Ltd.). The specimens (100×100×6 mm) were placed in an aluminum tray and irradiated horizontally at a heat flux of 35 kW/m^2. Spark ignition was used to ignite the pyrolysis products. The procedure of the tests was performed in accordance with the ISO 5660-1.

The smoke emission was determined using a smoke density chamber (Fire Testing Technology Ltd.) and the measurements were conducted in accordance with ISO 5659-2. During the test, the specimens (75×75×6mm) were exposed to an external heat flux of 25 kW/m^2.

RESULTS AND DISCUSSION

Images of sample fracture at 1000× magnification were presented in Fig. 2.The microstructure analysis allowed to observe a random arrangement of fire retardants particles in entire volume of samples. SEM photographs showed that the particles of fillers differed in size, and also agglomerates could be found. In turn, the voids, resulting from the loss of the fire retardants' particle, suggest that the adhesion between the polyethylene and filler was poor.

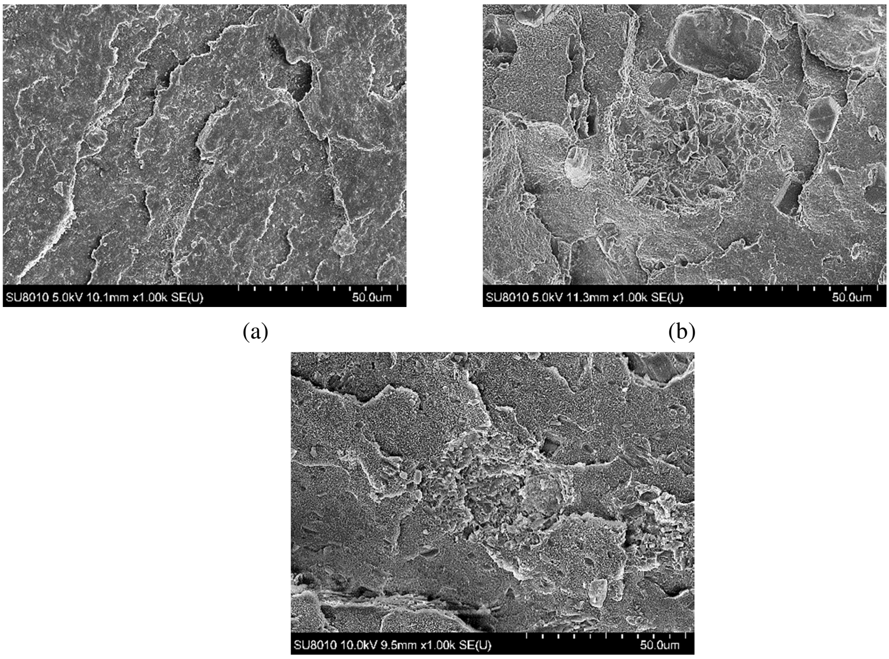

(a) (b)

(c)

Fig. 2. SEM photographs of breakthroughs of polyethylene (a) and polymer modified by fire retardants: APP (b), CUMP (c), mag. 1000.

Tensile strength ($б_{M}$), Young's modulus (Et) and elongation at break (ε) were measured by static tensile test to evaluation the influence of a new fire retardant incorporation on high density polyethylene mechanical properties and summarized in Table 1. The addition of CUMP led to a decrease in tensile strength in comparison to the unmodified polymer, the same as for ammonium polyphosphate. In turn, the values of Et were slightly lower, opposite to the result obtained for polyethylene modified by commercial fire retardant. The use of APP caused a significant increase in stiffness of polymer, which depending on application may be an undesirable phenomenon. It can be observed that the highest differences were achieved in the case of elongation at break. ε values for both polymers modified by fire retardants were about 45 times lower than for the pure polyethylene. Despite a reduction in the mechanical properties it did not exclude using them in most applications.

Table 1. Mechanical properties of unmodified polymer and polyethylene with fire retardants[a]

Sample designation	Tensile strength, MPa	Young's modulus, GPa	Elongation at break, %
PE	26.4 (0.3)[a]	485.4 (45.1)	1136.1 (189.7)
PE/APP	22.0 (0.2)	635.4 (37.3)	25.1 (4.5)
PE/CUMP	20.4 (0.6)	412.4 (41.3)	27.2 (10.3)

[a] The values in parentheses are the standard deviations.

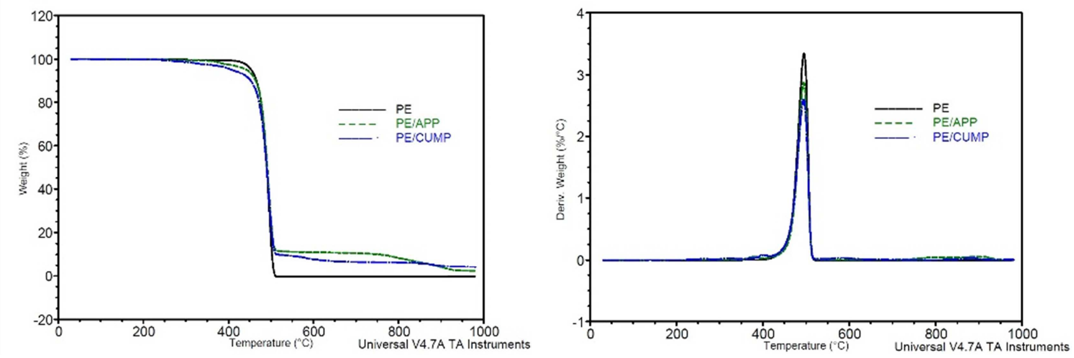

(a) (b)

Fig. 3. TG (a) and DTG (b) curves of reference materials and PE-HD with fire retardants under inert atmosphere.

The thermal stability of the investigated materials was assessed by: the temperature of 5%, 10% and 50% weight loss, the temperature of maximum rates of weight loss and intensity of degradation as well as percentage of char residue at about 1000 °C. Obtained results are presented in Fig. 3 and Table 2.

Table 2. The thermal stability of unmodified polymer and polyethylene with fire retardants

Sample designation	5% mass loss, °C	10% mass loss, °C	50% mass loss, °C	Residual mass, %	DTG, °C; %/°C
PE	454	466	490	0.0	495; 3.341
PE/APP	443	465	492	2.3	495; 2.88
PE/CUMP	409	453	489	4.2	494; 2.59

The initial degradation temperature, defined as 5% mass loss, for unmodified high-density polyethylene reached 454 °C. The polymer had one stage of weight loss, corresponding to a single peak at DTG curve, which appeared at approx. 495 °C. The weight loss at 1000 °C was 100% leaving no char residue. The introduction of fire retardants slightly changed the thermal stability of PE. The onset of degradation occurred earlier compared to neat polymer, especially in the case of CUMP (409 °C), due to the lower decomposition temperature of the used substances. In the literature, it can be found that IFR decomposes at lower temperatures reacting with polymer and forming the protective char layer [16]. However, at a measuring point recorded at 50% mass loss the differences between measured temperature values were negligible. It should be noted that the highest residual mass and the lowest intensity of degradation were recorded for PE/CUMP.

Table 3. The UL-94 and LOI results of PE, PE/APP and PE/CUMP (irradiance 35kW/m^2)

Sample designation	UL-94 horizontal rating	LOI, % V/V
PE	HB	20
PE/APP	HB	21
PE/CUMP	HB	20

The results of fire hazard testing, corresponding to the UL-94 standard, were presented in Table 3. All of the samples were rated at the HB class. However, compared with the unmodified polyethylene and also PE/APP, the PE/CUMP showed the slight inhibition of the dripping and formation of a char (Fig. 4). In turn the limiting oxygen index values, summarized in Table 3, were similar, and 1% higher values in comparison with PE were recorded only in the case of PE/APP.

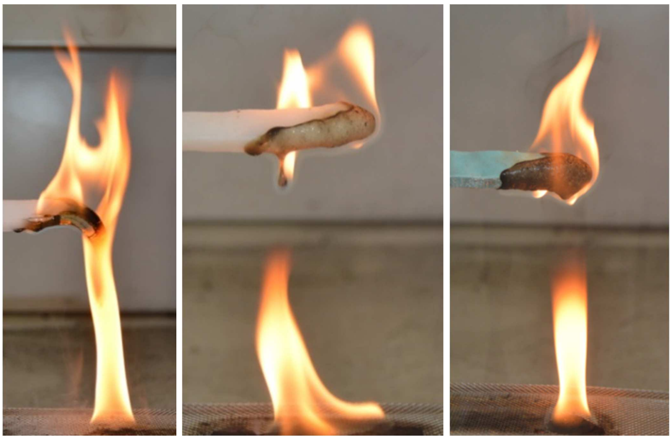

(a) (b) (c)

Fig. 4. Photographs of PE (a), PE/APP (b), PE/CUMP (c) samples during UL-94 tests.

Average values of parameters characterizing the behavior of prepared plastics, under the influence of intense radiant heat, gained during cone calorimeter measurements were summarized in Table 4. Heat release curves for most representative samples were presented in Fig. 5.

Both PE/CUMP and PE/APP show peak of Heat Release Rate (pHRR) below 430 kW/m^2, while for unmodified PE it was 627 kW/m^2 (Fig. 5). CUMP seems to be very promising flame retardant for use in thermoplastic materials. It combines smoke suppressing properties of cooper and foamed char promoting properties of melamine phosphate in one non-soluble complex compound. PE/CUMP shows the longest Time to Ignition (TTI), the lowest heat release both mean and maximum, which results in the lowest Maximum Average Rate of Heat Emission (MARHE) value. It is important to notice that the Total Smoke Release (TSR) and Total Heat release (THR) are much higher for PE/CUMP than for other tested materials. Those values are connected with the duration of the test for individual materials. The long smoldering period near the end of the flaming phase for PE/CUMP caused that the flaming phase to last for 1000 s, when for PE/APP it was in the range of 750-800 s.

Table 4. The cone calorimeter results of PE, PE/APP and PE/CUMP (irradiance 35 kW/m^2)

Sample designation	TTI, s	pHRR, kW/m^2	HRR, kW/m^2	MARHE, kW/m^2	THR, MJ/m^2	TSR, m^2/m^2
PE	117 (1)[a]	627.3 (162)	242 (45)	295.1 (40)	184.9 (25)	1433.4 (93)
PE/APP	114 (3)	423.9 (63)	209 (20)	262.3 (10)	177.5 (32)	1828.4 (636)
PE/CUMP	148 (64)	376.8 (40)	187 (30)	250.9 (22)	229.2 (34)	2233.9 (317)

[a] The values in parentheses are the standard deviations.

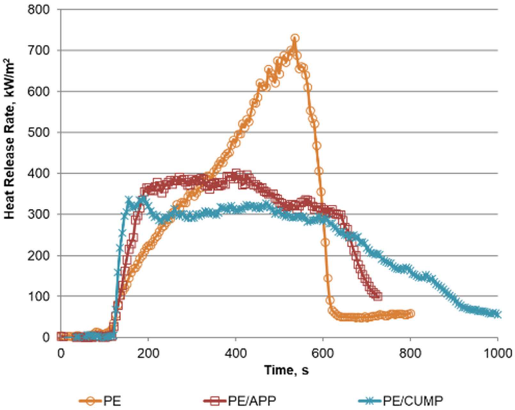

Fig. 5. Representative Heat release rate (HRR) curves of PE and polyethylene with fire retardants.


(a) (b) (c)

Fig. 6. Photographs of PE (a), PE/APP (b), PE/CUMP (c) samples after a cone calorimetry test.

From the visual assessment of char residue of tested samples it can be concluded that PE sample burned out completely (Fig. 6). Such effect is typical for polymers built from short linear hydrocarbon chains. PE/CUMP formed multi-layered char structure that proved to be effectiveness in inhibits the burning process. In turn, PE/APP formed thin yet sustainable char layer that exhibits good fire retarding properties but it shows no signs of homogeneous. For further investigation all residues were examined with use of scanning electron microscope (SEM) and presented in Fig. 6.

As can be seenб both materials formed a char with the smooth outer surface, hindering the gas and matter transfer. However, the char layer of PE/APP was rather thin without cell structure, characteristic to intumescent fire retardants. It is confirmed by the photographs of the inner part of residue, being a reflection of the outer part. In its turn, in the case of CUMP, a porous structure inside the char can be observed. The chemical composition of residue was determined by EDS and is shown in Fig. 7.

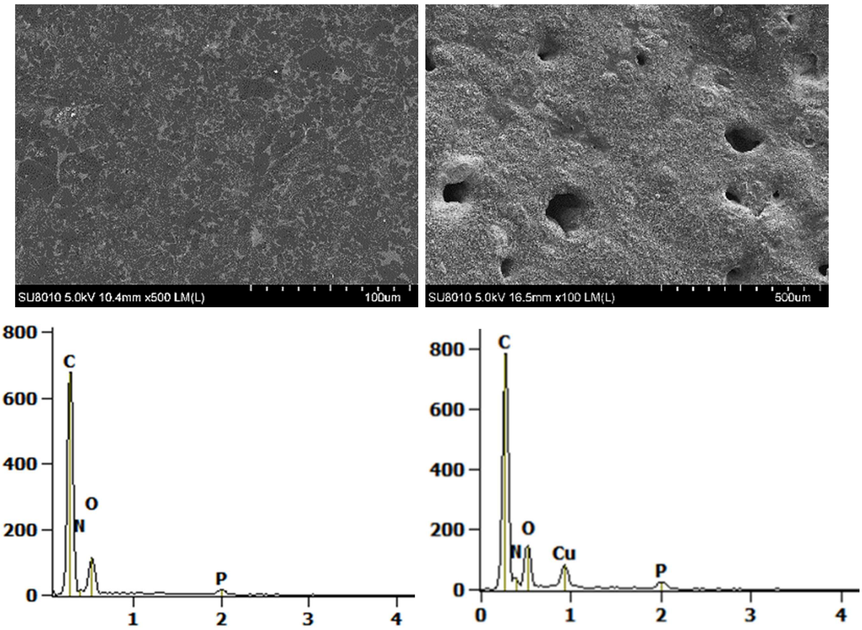

Element	Wt.%
C K	52.64
O K	30.08
N K	8.27
P K	9.02

Element	Wt.%
C K	38.89
O K	20.87
N K	9.05
P K	9.47
Cu K	21.73

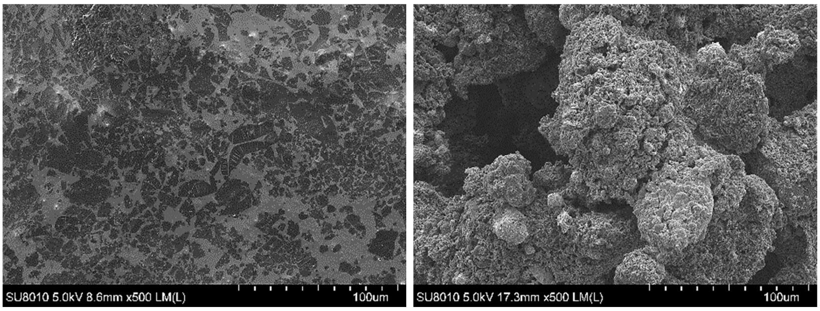

(a) (b)

Fig. 7. SEM photographs of cone calorimetry residues of PE/APP (a, outer and inner) and PE/CUMP (b, outer and inner), mag. 500.

The obtained data indicated that char layers comprised C, O, N and P elements as well as Cu in the case of CUMP. The results suggested that CUMP could decompose to CuO, melam (according to Fig. 8) and P_2O_7 [17].

Those compounds actively participate in formation of crosslink network in the char, resulting in a more compact char layer with better mechanical properties, and in consequence thicker, stronger char layer that enhances the flame retardant properties and increase higher thermal stability of materials.

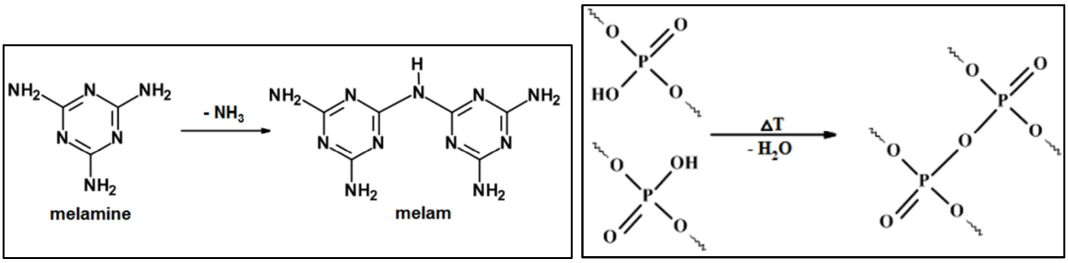

(a) (b)

Fig. 8. Thermal decomposition of melamine (a) and phosphoric acid (b).

Parameters characterising density of smoke generated during non-flammable test with use of smoke density chamber are presented in Table 5.

Table 5. Smoke emission of all examined materials[a]

Sample designation	MSOD	VOF4	Mass Loss (%)
PE	679.2 (31.4)	12.3 (1.4)	20.0 (2.1)
PE/APP	21.6 (3.6)	13.1 (2.5)	0.7 (0.1)
PE/CUMP	315.2 (30.6)	76.7 (4.1)	5.2 (0.5)

[a] The values in parentheses are the standard deviations.

The highest value of maximum specific optical density (MSOD) of smoke was obtained by unmodified PE sample. PE/APP show very good smoke suppressing properties during non-flammable test with MSOD and VOF4 values several times lower than those of PE/CUMP. Presence of copper can catalyze decomposition process which can be an advantage under pyrolysis conditions (accelerates char formation) and a disadvantage considering smoke density. Mass loss corresponds with the MSOD values although PE/CUMP generates very large amount of smoke while losing only ~5% mass.

CONCLUSIONS

It can be concluded that copper complex CUMP can be a good substitute of commercial flame retardant especially when it comes to suppressing heat release rate. PE/CUMP shows good thermal stability although presence of copper may catalyze the decomposition process which can have beneficial impact on char formation while showing some disadvantages when it comes to smoke development. Nonetheless, PE/CUMP generated much more firm and porous char layer on the surface of the sample that showed good impact on its flammability.

ACKNOWLEDGEMENT

This paper has been based on the results of a research task carried out within the scope of the fourth stage of the National Programme “Improvement of safety and working conditions” partly supported in 2017–2019 — within the scope of research and development — by the Ministry of Science and Higher Education/National Centre for Research and Development. The Central Institute for Labour Protection – National Research Institute is the Programme's main coordinator.

REFERENCES

[1] R. Geyer, J.R. Jambeck, K. Lavender, Law, Production, Use, and Fate of All Plastics Ever Made, Sci. Adv. 3 (2017) 1-5.

[2] L. Bisby, Grenfell Tower Inquiry – Phase 1 Expert Report, University of Edinburgh, 2018.

[3] A. Dasari, Z.Z. Yu, Y.W. Mai, G.P. Cai, H.H. Song, Roles of graphite oxide, clay and POSS during the combustion of polyamide 6, Polymer 50 (2009) 1577-87.

[4] M. Barczewski, D. Chmielewska, M. Dobrzyńska-Mizera, B. Dudziec, T. Sterzyński, Thermal stability and flammability of polypropylene-silsesquioxane nanocomposites, Int. J. Polym. Anal. Charact. 19 (2014) 500–9.

[5] G. Camino, N. Grassie, I.C. McNeill, Influence of the fire retardant, ammonium polyphosphate on the thermal degradation of poly(methyl methacrylate), J. Polymer Sci. Polymer Chem. Ed. 16 (1978) 95-106.

[6] P. Lv, Z.Z. Wang, K.L. Hu, W.C. Fan, Flammability and thermal degradation of flame retarded polypropylene composites containing. melamine phosphate and pentaerythritol derivatives, Polym. Degrad. Stab. 90 (2005) 523-534.

[7] J.D. Zuo, S.M. Liu, Q. Sheng, Synthesis and application in polypropylene of a novel of phosphorus-containing intumescent flame retardant, Molecules 15 (2010) 7593-7602.

[8] X. Lai, S. Tang, H. Li, X. Zeng, Flame-retardant mechanism of a novel polymericintumescent flame retardant containing caged bicyclic phosphate for poly-propylene, Polym. Degrad. Stab. 113 (2015) 22-31.

[9] P.Y. Wen, X.F. Wang, W.Y. Xing, X.M. Peng, B. Yu, Y.Q. Shi, et al., Synthesis of anovel triazine-based hyperbranched char foaming agent and the study of itsenhancement on flame retardancy and thermal stability of polypropylene, Ind. Eng. Chem. Res. 52 (2013) 17015-17022.

[10] N. Tian, X. Wen, Z. Jiang, J. Gong, Y. Wang, J. Xue, et al., Synergistic effect between a novel char forming agent and ammonium polyphosphate on flame retardancy and thermal properties of polypropylene, Ind. Eng. Chem. Res. 52 (2013) 10905-10915.

[11] Y. Huang, M. Song, J. Ma, Z. Lu, J. Yang, K. Cao, Synthesis of a phosphorus/silicon hybrid and its synergistic effect with melamine polyphosphates on flame retardant polypropylene system, J. Appl. Polym. Sci. 129 (2013) 316-323.

[12] S. Li, B. Long, Z. Wang, Y. Tian, Y. Zheng, Q. Zhang, Synthesis of hydrophobic zinc borate nanoflakes and its effect on flame retardant properties of polyethylene, J Solid State Chem. 183 (2010) 957-962.

[13] P. Müller, M. Morys, A. Sut, C. Jäger, B. Illerhaus, B. Schartel, Melamine poly(zinc phosphate) as flame retardant in epoxy resin: Decomposition pathways, molecular mechanisms and morphology of fire residues, Polymer Degrad. Stab. 130 (2016) 307-319.

[14] C. Manzi-Nshuti, J. M. Hossenlopp, C. A. Wilkie, Comparative study on the flammability of polyethylene modified with commercial fire retardants and a zinc aluminum oleate layered double hydroxide, Polym. Degrad. Stab. 94 (2009) 782-788.

[15] K-S. Lim, S-T. Bee, L.T. Sin, T-T Tee, C.T. Ratnam, D. Hui, A.R.Rahmat, A review of application of ammonium polyphosphate as intumescent flame retardant in thermoplastic composites, Composites Part B: Engineering, 84 (2016)155-174.

[16] X. Wanga, Y. Hua, L. Songa, H. Yanga, B. Yua, B. Kandolac, D. Delic, Comparative study on the synergistic effect of POSS and graphene with melamine phosphate on the flame retardance of poly(butylene succinate), Thermochim. Acta 543 (2012) 156– 164.

[17] C. Feng, Y. Zhang, D. Liang, S. Liu, Z. Chi, J. Xu, Influence of zinc borate on the flame retardancy and thermal stability of intumescent flame retardant polypropylene composites, J. Anal. Appl. Pyrolysis 115 (2015) 224-232.

Artificial Sweeteners or High Risk Sugar Alcohols

Celiński M., Salasińska K.*, Borucka M., Gajek A.

Central Institute for Labour Protection – National Research Institute,
Department of Chemical, Biological and Aerosol Hazards, Warsaw, Mazovia, Poland
**Corresponding author's email: macel@ciop.pl*

ABSTRACT

Growing popularity of artificial sweeteners commonly used as a sucrose substitute causes a rapid increase in their production which is close to 2 million metric tons annual. Large quantities both produces, transported and stored organic materials naturally pose a threat of a major industrial accident which can be prove only by a series of breakdowns related to the explosion of sugar dust. The purpose of this work was to determine and compare parameters describing thermal stability and characteristics of burning process of six compounds of the sugar alcohols: xylitol, D-mannitol, D-sorbitol, maltitol, myo-inositol, meso-erythritol; with sucrose. We also investigated gaseous products generated during thermal decomposition of tested polyalcohols. The tests were conducted using following devices: cone calorimeter, smoke density chamber, purser furnace, differential scanning calorimeter, gas chromatography in accordance with appropriate standards. Almost all of tested sugar alcohols generate more heat during combustion than sucrose. Under higher values of applied heat flux, maltitol shows the highest maximum heat release rate although its ignition time is almost twice the time of sucrose. The only compound that did not ignite during smoke density measurements was meso-erythritol. Sucrose did ignite before the VOF4 parameter could be measured. Based on gained results it can be concluded that under specific conditions sugar alcohols can be equally or even more dangerous than sucrose.

KEYWORDS: sucrose, sugar alcohols, cone calorimeter, smoke density chamber, heat release rate

INTRODUCTION

Sucrose is the most popular disaccharide used as a sweetener in food industry. It's annual global production ranks at 170 million metric tons [1]. Such large production quantity of organic compound in natural way poses a threat of the possibility of a major industrial accident. Chemical Safety Board in the report on fires and explosions of sugar dust stated that first reported combustion of sugar dust took place in 1925. Almost 100 years later, despite broad knowledge and security measures, accidents still occur i.e. sugar dust explosion; silo tower (Cantley, England, 2003), sugar mill (Baltimore, USA, 2007), silo tunnel (Georgia, USA, 2008); sugar fire: sugar warehouse (Santos, Brazil, 2013). [2, 3].

In the meantime group of artificial sweeteners appeared on the market. Those new and often unexamined in case of fire scenarios compounds from the group of sugar alcohols (polyols) may have similar or even stronger fire and explosion characteristics than sucrose. According to literature [4] global annual production scale of sugar alcohols i.e. sorbitol, xylitol, mannitol, maltitol and isomalt is 1.6 million metric tons and increases rapidly. It is assumed that it will reach value of 2 million metric tons by the end of year 2022. Such large production scale of organic compounds, despite the current lack of incidents reports, poses a threat of a major industrial accident. Sugar alcohols dust qualifies as a potentially flammable or explosive due to their chemical structure. Short carbon chains combined with several hydroxyl groups significantly increases molecular oxygen

Proceedings of the Ninth International Seminar on Fire and Explosion Hazards (ISFEH9), pp. 1029-1039
Edited by Snegirev A., Liu N.A., Tamanini F., Bradley D., Molkov V., and Chaumeix N.
Published by Saint-Petersburg Polytechnic University Press
ISBN: 978-5-7422-6498-9 DOI: 10.18720/spbpu/2/k19-108

balance in those compounds which makes them good fuel even in low oxygen conditions. Due to those properties sugar alcohols found application in pyrotechnics and explosives. Combined with nitrating mixture polyols form unstable and very strong explosive materials i.e. pentaerythritol tetranitrate (PETN) also known as penthrite, one of the most powerful modern secondary explosive, which is a derivative of pentaerythritol, polyol commonly used as an artificial sweetener [5]. Based on those information we decided that there is an urgent need to conduct studies of compounds so widely used and processed in large quantities for their flammability and explosive properties.

In this study we focused on the recognition of parameters describing the combustion process of six sugar alcohols: xylitol, D-mannitol, D-sorbitol, maltitol, myo-inositol, meso-erythritol and compared them to the values obtained for sucrose. Fire parameters were measured using two devices: cone calorimeter and smoke density chamber, in accordance with standards: ISO 5659 and ISO 5660. The thermal stability of selected materials was evaluated by thermogravimetric analysis (TG). Moreover, the steady state tube furnace (Purser furnace) has been used specifically to generate toxic products from real fires. The released species have been identified using gas chromatography with mass selective detector (GC-MS).

MATERIALS AND METHODS

Materials

All tested sugar alcohols are commercially available products delivered by Acros Organics and Alfa Aesar. The purity of tested compounds was 98-99%, except for Maltitol which purity was 95%. To create more comparable conditions all compounds were minced by a grinding mill and gained powder was subjected to a sieve analysis. Materials of equal grain size range (75-125 μm) were further used to determine calorimetric parameters.

Cone calorimeter flammability testing

Fire safety characteristics require the determination of the basic behavioral parameters under fire conditions. Parameters characterizing behavior of analyzed compounds in the presence of flame were studied using Dual Cone Calorimeter (FTT Limited, West Sussex) according to standard ISO 5660-1 [6]. Three samples of equal mass (20 grams) for each compound, were covered with aluminum foil (100 mm x 100 mm x 25 mm) and treated with external Heat Flux (HF) in range of 25-75 kW/m^2 simulating the thermal exposure during the first phase of fire. Based on gained results following parameters were estimated: Heat Release Rate – *HRR* (kW/m^2), peak of Heat Release Rate – *pHRR* (kW/m^2) time to peak of Heat Release Rate – *t-pHRR* (s), Total Heat Release – *THR* (MJ/m^2), Ignition Time – *TTI* (s), Total Smoke Release – *TSR* (m^2), Fire Growth Rate – *FIGRA* (kW/m^2s), Thermal Response Parameter – *TRP* ($kW\cdot s^{1/2}/m^2$).

NBS smoke density testing

The smoke density characteristics in a closed room can be described by two main parameters: Optical Density of Smoke (*Ds*) and *VOF4*. *Ds* parameter determines visibility reduction and is the determinant of an amount of smoke produced during the first ten minutes of thermal degradation of tested material. *VOF4* describes increasing rate of smoke density during the first four minutes, which are crucial during evacuation process. *VOF4* parameter is calculated according to the Eq. (1):

$$VOF4 = \frac{1}{2}(1Ds1 + 2Ds2 + 2Ds3 + Ds4)\ , \qquad (1)$$

where *Ds1, Ds2, Ds3, Ds4* – optical densities of smoke during four consecutive minutes of the test.

All parameters were measured using Smoke Density Chamber (FTT Limited, West Sussex) according to standard ISO 5659-2 [7]. Three samples of equal mass for each tested compound, were covered with aluminum foil (75 mm x 75 mm x 10 mm) and treated with external HF of 25 kW/m^2. Due to the high flammability of the test compounds, even in the absence of the ignition source (electric spark), two relevant comparative parameters were added: Time to Maximum Smoke Density (*TMDS*) and Ignition Time (*TTI'*).

Thermal analysis

The thermal degradation characteristics of polyalcohols were analyzed by the methods of TG-DTG and DSC using a simultaneous thermal analyzer (STA 449F3 Jupiter, Netzsch, Germany). The mass of the investigated materials was 10 mg. The heating rate was 10 K/min. The measurements were carried out in the air and nitrogen atmosphere.

Fire effluent analysis

Samples of materials (15 g) in test boats were delivered into the steady state tube furnace (ISO 19700) set at 350°C. The collection of fire effluent from mixing chamber of tube furnace was performed with the use of the solid phase microextraction manual holder supplied with carboxen/polydimethylsiloxane 75 µm fiber acquired from Supelco (USA). The sorption and desorption time was 5 min and 30 min accordingly. The chromatographic separation was achieved with an HP-5 MS fused silica capillary column (30mm×250µm×0.25µm film thickness) from Agilent Technologies (USA). The oven temperature was initially maintained at 40°C for 5 min, and then increased to 250 °C at the heating rate of 4 °C/min. Helium at the constant flow rate of 1 ml/min was used as the carrier gas and the split ratio was 10:1. The separated compounds were then analyzed by the mass spectrometer, which was operated in electron ionization (70 eV). The mass spectra were obtained from m/z 15 to 350. Chromatographic peaks were identified with NIST MS Library.

RESULTS AND DISCUSSION

Cone calorimeter parameters

The thermal response parameter (TRP) allows to estimate material resistance to generation of combustible gas mixture [8, 9]. The higher the TRP value, the longer it takes for the material to heat up, evaporate, ignite, and initiate a fire. TRP depends on the series of parameters ignition temperature (T_{ig}), ambient temperature (T_∞), thermal conductivity (λ), specific heat (C_p) and density (ρ) and can be calculated according to the Eqs. (2) and (3):

$$TRP = \left(T_{ig} - T_\infty\right)\sqrt{(\pi/4)\lambda\rho C_p}\ , \tag{2}$$

$$t_{ig} = (\pi/4)\lambda\rho C_p\left(\left(T_{ig} - T_\infty\right)/q''_e\right)^2 \tag{3}$$

By the combination of Eq. (2) with Eq. (3), *TRP* can be presented as a function of external heat flux, q''_e , and t_{ig} :

$$t_{ig}^{-1/2} = q''_e/TRP \tag{4}$$

The plot of the square root of the ignition time inverse versus the external heat flux allows to interpret the *TRP* form the curve slopes according by Eq. (5):

$$TRP = 1/slope\,. \tag{5}$$

All TRP values are presented in Table 1. Average values of parameters characterizing the behavior of sugar alcohols under the influence of intense radiant heat gained during cone calorimeter measurements were summarized in Table 2.

Table 1. *TRP* values calculated for tested sugar alcohols

Sample	*TRP*
	kW·s$^{1/2}$/m^2
D-mannitol	500
D-sorbitol	476
xylitol	500
maltitol	476
meso-erythritol	526
myo-inositol	400
sucrose	270

Sucrose

Based on the gained results it can be concluded that in a range of lower HF (25-50 kW/m^2) sucrose gain the highest values of *pHRR* and second only to maltitol at 75 kW/m^2. The *HRR* curves presented in Fig. 1, suggest that sucrose does not reach its fully grown steady flaming phase under any HF. Twenty gram samples simply burn to fast to reach maximum potential of this compound even under such low HF as 25 kW/m^2.

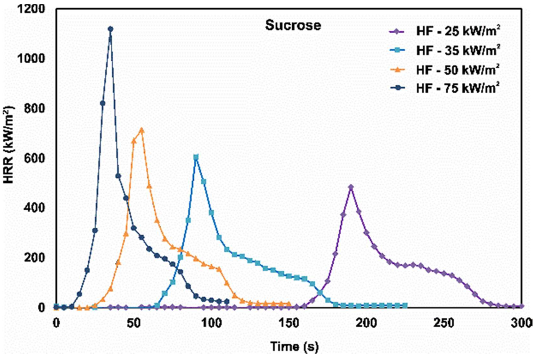

Fig. 1. HRR development for sucrose under different HF.

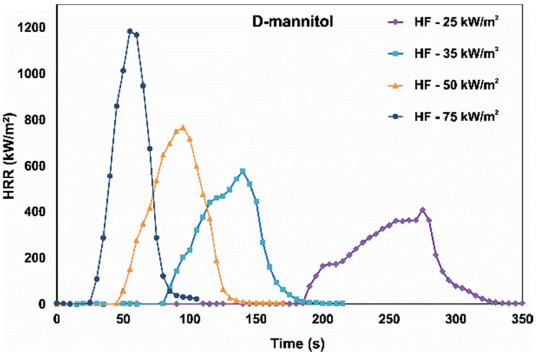

Fig. 2. Comparison of maltitol HRR development under different HF.

After the first peak one can observe (especially at 25 and 35 kW/m^2), the flaming phase with *HRR* at the level of 200 kW/m^2, but it is mostly due to the decomposition of weak char created during pyrolysis and the lack of pure organic material. Although sucrose is one of the largest tested compounds (only 2g/mol lighter than maltitol), it reaches lowest *THR* values. Probable explanation of this behaviour is associated with the chemical structure and chemical reactions in condensed phase. When heated above 140°C sucrose starts to decompose (caramelize) generating furans (i.e. furfuryl alcohol) with very low flashpoint temperature (*Fp*) (60-80°C) which is also the cause of short *TTI* under higher *HF* and in consequence very low *TRP* [10].

Table 2. Calorimetric values of fire parameters for sugar alcohols and sucrose

Sample	*TTI*	*FIGRA*	*HRR*	*pHRR*	*t-pHRR*	*THR*	*TSR*
	s	kW/m^{2}s	kW/m^2	kW/m^2	s	MJ/m^2	m^2/m^2
HF – 25 kW/m^2							
D-mannitol	224	0.87	170	256	293	31.9	43.8
D-sorbitol	197	0.88	152	228	260	31.7	42.1
xylitol	144	0.96	130	232	242	33.6	52.6
maltitol	209	1.51	196	415	285	29.0	60.7
meso-erythritol	110	1.25	164	247	197	31.7	35.6
myo-inositol	116	1.77	139	228	128	28.4	37.8
sucrose	165	2.59	150	484	187	20.7	5.22
HF – 35 kW/m^2							
D-mannitol	108	2.33	183	362	155	31.7	72.9
D-sorbitol	104	2.22	170	344	155	31.3	72.9
xylitol	77	2.26	138	301	133	31.5	79.5
maltitol	88	3.9	237	580	148	29.8	98.7
meso-erythritol	72	2.7	185	371	138	32.1	63.1
myo-inositol	60	4.46	126	305	68	28.0	65.1
sucrose	70	6.57	161	614	93	22.4	61.5
HF – 50 kW/m^2							
D-mannitol	65	4.46	263	491	110	34.9	207
D-sorbitol	63	6.32	241	558	88	35.2	206
xylitol	56	4.30	224	466	108	36.0	214
maltitol	65	7.78	297	764	98	35.5	219
meso-erythritol	48	4.50	262	472	105	36.6	202
myo-inositol	36	10.4	231	467	45	32.6	165
sucrose	29	14.0	197	771	55	23.8	47.2
HF – 75 kW/m^2							
D-mannitol	34	14.0	281	840	60	33.1	105
D-sorbitol	33	10.7	346	787	73	34.7	183
xylitol	29	8.03	272	616	77	34.1	162
maltitol	31	20.2	503	1144	57	36.2	230
meso-erythritol	29	7.88	300	578	73	35.7	211
myo-inositol	24	20.4	281	647	32	32.9	184
sucrose	17	29.8	250	1119	35	25.7	50.7

Maltitol

Main difference between maltitol and sucrose is the presence of the oxolane (tetrahydrofuran) ring instead of d-glucitol chain, so the combination of two cyclic ethers can explain reduction of molecule energy and t_{ig}. Secondly, maltitol does not undergo caramelization process and because cone calorimeter parameters are based on oxygen level in flaming phase, it is possible that decomposition of sucrose in the condensed phase is responsible for its low *THR*. As a result of analysis of maltitol's *HRR* curve under the HF = 25 kW/m^2, it can be concluded that the initial increase of the *HRR* is being followed by a slow growth up to the maximum value, see Fig. 2.

The initial raise is related to the ignition of flammable pyrolysis products whose concentration in the gas phase was sufficient to initiate a self-sustaining combustion process while the second stage is limited by the rate of decomposition and the emission of combustible products into the combustion zone. Similar behaviour can be observed under the *HF* =35 kW/m^2 , but in that case time of the growing phase is much shorter and the angle is higher. This characteristic changes under the influence of heat source in temperature range 750-900^{o}C (*HF* = 50-75 kW/m^2). In both cases it is hard to separate ignition phase from the growing phase. Decomposition process is fast enough, to provide sufficient amount of flammable gaseous to the flaming zone, to keep the stable growth of *HRR*. Due to the high molecular weight and contribution of functional groups, maltitol shows the highest *HRR*, *THR* and *TSR* values. Maltitol, like the other sugar alcohols, does not caramelize, therefore vaporized macromolecules generates large amount of soot in burning phase as a result of incomplete combustion.

D-sorbitol and D-mannitol

Two of tested sugar alcohols: d-mannitol and d-sorbitol, shows good thermal stability in low range of *HF*, without reaching characteristic *HRR* peak. Development of burning process in both cases leads to a maximum *HRR* after 2,5-3 minutes after the ignition and last until most of the organic material has been burned, see Fig. 3.

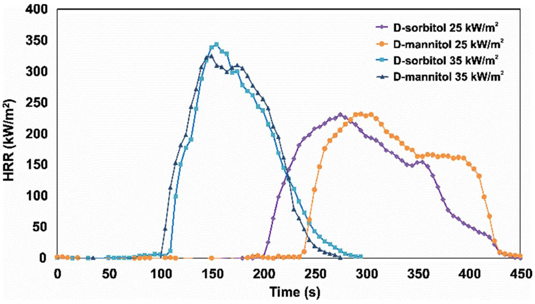

Fig. 3. D-sorbitol and d-mannitol HRR curved under HF = 25,35 kW/m^2.

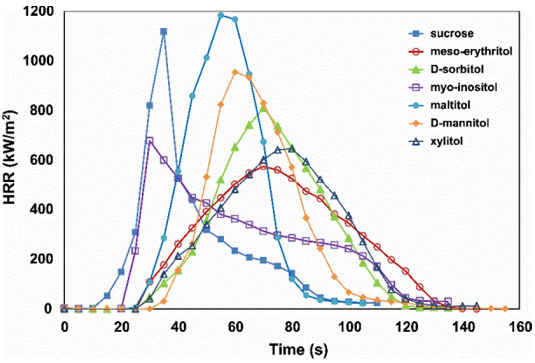

Fig. 4. Comparison of HRR development during burning stage for tested compounds (HF = 75 kW/m^2).

Similar characteristic of burning process of those two compounds is related to their identical chemical composition. Both compounds are isomers, and differ only in spatial orientation of hydroxyl group at second carbon atom. Even such subtle structural difference has an impact on compounds behaviour under fire conditions. As can be seen from the Table 1 data, D-mannitol is characterized by higher thermal stability (longer t_{ig}) than D-sorbitol.

Myo-inositol

Myo-inositol is one of the most interesting tested sugar alcohols. It is characterized by short tig and relatively high FIGRA values. On the other hand myo-inositol shows low *HRR*, and its flaming phase is statistically longer then for the rest of the tested compounds (Fig. 4.). Such characteristic is typical for compounds with the ability to generate a layer of swollen char on the surface of the sample under pyrolysis conditions. Similar phenomenon can by observed in plastics with an addition of intumescent flame retardants, where specific additives are responsible for generation and swelling process of formed char that protects polymer against the influence of external heat and oxygen [11,12]. Probable reason for the char formation is the presence of cyclohexane ring. Dehydration of hydroxyl groups leads to the formation of double bonds and aromatic structures being the foundation of char. It's worth noticing that rapid development of burning process and short *TTI* are important parameters for the evaluation of combustion characteristics of dust-air mixtures.

In such conditions myo-inositol will not be able to generate the char layer and will burn with the highest possible rate which can lead to very high explosion characteristics, similar or even stronger than sucrose. This lead will be further investigated and described in another paper.

Meso-erythritol and xylitol

Erythritol like the most of sugar alcohols does not have aldehyde or ether groups, therefore it does not undergo a Maillard reaction or caramelization and is relatively stable to heat (*Fp* = 209°). This means that erythritol rather vaporize than decompose during first stage of fire and its *Fp* is much higher than *Fp* of sucrose's decomposition products, like furfuryl alcohol (77°C) [13,14]. It was observed that compounds without structural rings show higher *TRP* values. For example, *TRP* of meso-erythritol is much higher than of any other tested sugar alcohol while sucrose, compound with two structural rings, shows the lowest *TRP* value. Although *TRP* is not the most accurate parameter, it allows defining general rules of behavior. Meso-erythritol is characterized by short *TTI* at *HF* = 25 kW/m^2 , but increase of HF to 75 kW/m^2 does not cause such drastic change in t_{ig} as in case of sucrose or maltitol and is a reason for smaller experimental line slope. This deduction coincides with the results gained from the smoke density chamber. For typical sugar alcohol, *pHRR* value doubles with the change of *HF* from 35 to 75 kW/m^2 and for meso-erythritol it rises by about 56% see Fig. 5.

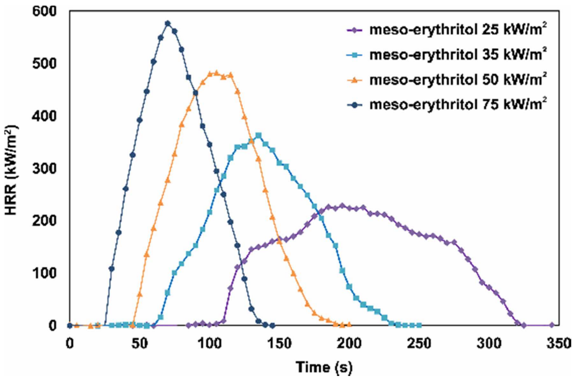

Fig. 5. Meso-erythritol HRR curves under different HF.

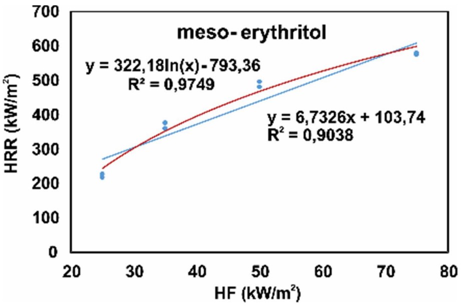

Fig. 6. Meso-erythritol's *pHRR* dependency on HF value.

Probably meso-erythritol is much closer to its maximum combustion rate and in this range HRR ceases to be linearly dependent on the power of the heat source and changes to a logarithmic dependency, see Fig. 6.

Xylitol is a compound most similar to the meso-erythritol based on the chemical structure. Additional carbon atom and hydroxyl group does not make significant changes in calorimetric parameters although show noticeable impact on smoke density and *TTI* during smoke chamber tests.

Smoke density chamber parameters

The results gained from the smoke density chamber tests indicate that the meso-erythritol, compound with the shortest *TTI* during cone calorimeter test, under same heat flux (25 kW/m^2), was the only one that did not ignite, see Table 3. This can be explained by the small mass of meso-erythritol. Four-hydroxyl butanoic chain probably evaporates from the sample before reaching the decomposition temperature, which is high enough to keep it from ignition in contact with a heat source of about 600°C without the presence of an electric spark.

Longest *TTI'* was observed for xylitol, compound most similar to meso-erythritol, than for isomers: d-mannitol and d-mannitol, maltitol and sucrose. Those results strongly agree with the conclusions drawn from the analysis of *TRP* values. Myo-inositol, due to its ability to form swollen char layer, did not ignite during the first test, resulting in a *VOF4* value of 204. Unfortunately, formed char is not always dense enough to effectively protect the sample from external heat, especially in case of compound with such a short tig and high *FIGRA* values like myo-inositol which ended in very short tig' during second test. Sucrose tig' was too short to determine *VOF4* parameter. Maximum value of smoke density obtained after ignition cannot be a comparative criterion for individual substances since the presence of a flame source interferes with the readings of the analyzer, making it impossible to determine the actual degree of smoke inside the chamber, hence further comparability of smoke density is unfounded. Lowest *VOF4* parameter was recorded for D-sorbitol with a self-ignition temperature of 420°C [15]. This compound ignited 6-7 minutes after the test began, allowing estimation of *VOF4* parameter on the level of 48,3. In turn, the highest value was obtained for mesoerythritol.

Table 3. Summary of smoke density chamber parameters for tested compounds

Sample	*Ds (TMDS)*	*VOF4*	*TTI'*
	- (s)	-	s
D-mannitol	497 (418)	51.6	410
D-sorbitol	391 (395)	48.3	395
xylitol	673 (433)	109	452
maltitol	281 (256)	148	251
meso-erythritol	890	238	-
myo-inositol	147 (530) / 507	- / 204	131 / -
sucrose	175 (202)	-	143

Table 4. Thermogravimetric characteristics of the selected polyalcohols

Chemical	Atmosphere	Mass losses (%)	Melting point (°C)	Beginning of degradation process (°C)	End of degradation process(°C)
D-Mannitol	Air	99.98	166	345.9	390.4
	Nitrogen	99.73	167.6	334.6	393.7
D-Sorbitol	Air	100	99.8	346.4	396.1
	Nitrogen	100	99.9	341	395.2
Xylitol	Air	99.75	94.2	309	368.1
	Nitrogen	100	95.2	309	367.3

Maltitol	Air	99.36	149.6	293	593
	Nitrogen	94.16	149	280	406
Meso-Erythritol	Air	100	119.6	268.9	323.9
	Nitrogen	99.86	120.8	277.9	352.4
Myo-Inositol	Air	99.69	-	148	586.4
	Nitrogen	93.19	-	148.9	394.8
Sucrose	Air	100	189.7	225.6	634.8
	Nitrogen	81.08	191.8	227.7	456.1

Thermal degradation studies

The TG, TDG and DSC curves for polyalcohols showed that thermal degradation in air atmosphere for all tested substances except meso-erythritol occurred in multi stage. When the testes were carried out in the nitrogen atmosphere, all substances except myo-inositol undergo one-stage degradation. The mass losses depended on the gaseous atmosphere used during the test and type of polyalcohol (Table 4).

The lowest temperature of the beginning of degradation process was observed for myo-inositol. That chemical was of xylitol in the air atmosphere, the sudden increase in temperature was observed, which may suggest that the tested substance ignited during the measurement. This phenomenon additionally decomposed in a complex way in both studied atmospheres. Interestingly, during the thermal decomposition of xylitol carrying out in nitrogen that situation was not observed.

Fire toxicity

The type of products formed during the measurements depends on the composition of the test material. However, some products such as ethenyl ester formic acid and hydroxy-acetaldehyde were presented in all gaseous samples. The largest number of thermal degradation products were created during the decomposition of the maltitol, myo-inositol and sucrose. Following chemicals were identified in samples of emitted gasses during the thermal degradation of those materials: furfural, 3-furaldehyde, 2-acetylfuran, 5-methyl-2-furancarboxaldehyde and furyl hydroxymethyl ketone. During thermal degradation of hydrogenated monosaccharides (d-mannitol, d-sorbitol and xylitol) in fire effluents furfural was also presented. All these substances are present in many food items as the natural products or as the contaminants. For example 2-acetylfuran is found in alcoholic beverages. 2- Acetylfuran as well as furfural, 3-furaldehyde, 5-methyl-2(5H)-furanone, 5-methyl-2-furancarboxaldehyde are used in flavored products. The 5-methyl-2-furancarboxaldehyde is a secondary produced from saccharides. Therefore, it can be assumed that the presence of these products in the emitted gas mixture can be caused both by the thermal degradation of polyalcohols and their presence in the tested materials. Table 5 presents the concentrations of released compounds during thermal degradation of selected materials using Purser furnace.

CONCLUSION

The characteristic parameters for the thermal decomposition during fire of sugar alcohols were quantitatively investigated with the use of cone calorimeter under a series of *HF* settings and smoke density chamber. Correlation analysis between the *HF* and the characteristic parameters was performed and properly described. Based on gained results in can be concluded that sucrose is the most flammable compound with most rapid fire growth, especially under higher *HF*. Yet it is important to notice that almost all tested sugar alcohols show higher average *HRR* and *THR* value, three of which under lower *HF* shows shorter *TTI*. Under the influence of 75 kW/m^2 *HF*, maltitol's *pHRR* was noticeable higher than sucrose's wherein the other parameters where significantly higher.

Myo-inositol shows very short t_{ig} and high *FIGRA*, but the fire growth is being inhibited by char layer forming on the surface of the sample. The thermal degradation characteristics of polyalcohols were analyzed by the methods of TG-DTG and DSC, and the results showed that most of the tested materials were decomposed as a result of a multi-stage process. In samples of gases and fumes, emitted during the thermal degradation and combustion of polyalkohols many chemicals were identified. The detected decomposition products depended on the type of substance that was degraded.

Table 5. Products formed during thermal degradation and combustion of tested polyalcohols

Compound	Emission yields (peak area x 10^6)						
	D-Mannitol	D-Sorbitol	Xylitol	Meso-Erythritol	Maltitol	Myo-Inositol	Sucrose
CO. CO_2	78.7	97.0	102.4	98.2	84.7	80.5	127.1
Formic acid. ethenyl ester	18.4	34.0	41.7	28.6	34.3	20.5	41.9
Acetaldehyde. hydroxy-	4.12	7.74	14.4	13.8	10.3	6.87	26.0
2(5H)-Furanone. 5-methyl-	-	-	28.1	-	-	-	-
Furfural	3.46	14.8	33.4	-	64.40	62.15	300.1
2-Furanmethanol	-	1.72	27.7	-	-	-	-
3-Furaldehyde	-	-	-	-	22.05	11.9	12.2
2-acetylfuran	7.17	9.60	-	-	25.0	12.4	14.6
2-Cyclopenten-1-one. 2-hydroxy-	-	-	-	-	7.34	8.12	21.7
2(5H)-Furanone. 5-methyl-	-	-	-	-	39.3	15.3	13.5
2-Furancarboxaldehyde. 5-methyl-	-	-	-	-	15.0	25.9	140.3
Phenol	-	-	-	-	6.66	18.16	7.03
Hydroquinon	6.59	7.23	-	-	28.9	2.16	3.87
2-Cyclopenten-1-one. 2-hydroxy-3-methyl-	6.63	1.01	-	-	20.1	5.69	17.5
3.4-Furandiol. tetrahydro-. trans-	-	-	201.8	196.0	-	-	9.68
2.5-Furandicarboxaldehyde	-	2.84	-	-	-	2.00	54.6
Furyl hydroxymethyl ketone	2.41	-	-	-	22.9	41.8	106.8
5-Acetoxymethyl-2-furaldehyde	-	-	-	-	-	-	65.7
5-Methyl-2-(5-methyl-2-furfuryl)furan	-	-	-	-	9.74	3.26	65.2
5-Hydroxymethylfurfural	-	-	-	-	-	-	138.0

ACKNOWLEDGMENTS

This paper has been based on the results of a research task carried out within the scope of the fourth stage of the National Programme —Improvement of safety and working conditions‖ partly supported in 2017–2019 — within the scope of research and development — by the Ministry of Science and Higher Education/National Centre for Research and Development. The Central Institute for Labour Protection – National Research Institute is the Programme‘s main coordinator.

REFERENCES

[1] Sugar production worldwide from 2009/2010 to 2017/18 (in million metric tons) https://www.statista.com/statistics/249679/total-production-of-sugar-worldwide/ (accessed 12 September 2018).

[2] CSB (2009) Sugar Dust Explosion And Fire – Investigation Report No. 2008-05-I-GA, http://www.csb.gov/assets/1/19/imperial_sugar_report_final_updated.pdf (accessed 12 September 2018).

[3] M. Westran, F. Sykes, S. Hawksworth, G. Eaton, Dust Explosion in Sugar Silo Tower: Investigation and Lessons Learnt, In: IChemE. Hazards XX – Process Safety & Environmental Protection – Harnessing Knowledge. Challenging Complacency, Crown Copyright, Rugby, 2008, pp. 1097-1111.

[4] Industry Experts (2017) Alternative sweeteners: Polyols (Sugar Alcohols) – A Global Market Overview, http://industry-experts.com/verticals/food-and-beverage/alternative-sweeteners-a-globalmarket-overview (accessed 12 September 2018).

[5] J. Boileau, C. Fauquignon, B Hueber, H.H. Meyer, Explosives. Ullmann's Encyclopedia of Industrial Chemistry, Weinheim Wiley-VCH, 2005.

[6] ISO 5660-1(2002) Reaction-to-fire tests – Heat release. smoke production and mass loss rate – Part 1: Heat release rate (cone calorimeter method).

[7] ISO 5659-2 (2006) Determination of optical density by a single-chamber test.

[8] A. Tewarson. Flammability parameters of materials: ignition. combustion. and fire propagation. J. Fire Sci. 10 (1994) 188-241.

[9] D. Quang Dao, J. Luche, F. Richard, T. Rogaume, C. Bourhy-Weber, S. Ruban, Determination of characteristic parameters for the thermal decomposition of epoxy resin/carbon fiber composites in cone calorimeter. Int. J. Hydrogen Energy 38 (2013) 8167-8178.

[10] S.E. Fayle, J.A. Gerrard, The Maillard Reaction. Cambridge. Royal Society of Chemistry. 2002.

[11] H. Horacek, S. Pieh, Importance of intumescent systems for fire protection of plastic materials, Polym. Int. 49 (2000) 1106-1114.

[12] S. Bourbigot, M. Le Bras, D. Sophie, R. Maryline, Recent Advances for Intumescent Polymers. Macromol. Mater. Eng. 289 (2004) 499-511.

[13] P. de Cock, Erythritol, In: L. O'Brien-Nabors, Alternative sweeteners, 4th Ed, CRC Press, Boca Raton, 2012, pp. 249-262.

[14] K.J. Zeitsch, The chemistry and technology of furfural and its many by-products, Sugar Series 13 (2000) 240.

[15] C. Roth, D-sorbit, Material Safety Data Sheet, 2015.

Pyrolysis

Experimental Study on the Flammability and Burning Behaviour of Live and Dead *Eucalyptus Saligna* Foliage

Ramadhan M.L.*, Zarate-Orrego S.A., Carrascal J., Osorio A.F., Hidalgo J.P.

[1] *School of Civil Engineering, The University of Queensland, St Lucia, QLD, Australia*
**Corresponding author's email: m.ramadhan@uq.edu.au*

ABSTRACT

Wildland fires are frequent catastrophic events that lead to the loss of life and economic devastation. Wildfires can involve dead and live fuels; however, only limited research has studied the combustion characteristics of those fuel conditions. This paper studies the burning behaviour of live and dead *Eucalyptus saligna* leaves using the Mass Loss Calorimeter. Tests were carried out using different indicent radiant heat flux and wide range of fuel moisture content (4-120% on dry weight for live leaves and 3-14% on dry weight for dead leaves). This study includes the proximate analysis and thermogravimetric analysis to observe the impact of chemical composition. Flammability parameters (i.e. ignition delay time, time to peak mass loss rate, burnout time, peak mass loss rate, and residual mass fraction) were analysed to identify the differences between live and dead leaves. The results show that ignition delay time of dead leaves are eight times faster than live leaves, thus the regression model derived from dead leaves cannot be used well to predict the ignition delay time of live leaves, and vice versa. From all parameters, it is concluded that live and dead leaves will not behave the same in fire condition; dead leaves are shown to be more flammable than live leaves, even though the leaves are in the same oven-dried condition. This confirms that the live fuels can no longer be assumed as wet dead fuels, and should be considered explicitly in assessing wildland fire risk.

KEYWORDS: Eucalyptus saligna, flammability, ignition, wildland fires.

INTRODUCTION

Wildland fires are the largest natural disaster in Australia that lead to the loss of life and economic devastation. However, there is still a lack of knowledge regarding the key factors that affect the flammability and burning behaviour of vegetation. Due to the climatological and seasonal conditions, as well as human interaction, water cycle plays a critical role in defining the vegetation, and eventually the intrinsic wildland fire risk. Previous research in the field of fire safety engineering has demonstrated a strong influence of moisture content on the flammability of solid fuels. In wildland fires, the fuel flammability term refers to the capability of a certain fuel to ignite and sustain fire. According to Anderson [1], the flammability can be characterised into four criteria, namely ignitability, combustibility, consumability, and sustainability. Therefore, the understanding of all parameters affecting the flammability and fire behaviour is crucial to predict future fire events and quantify the potential risks [2,3].

Wildland fires do not only spread through dead fuels, but also through a combination of dead and live (with relatively higher moisture content) fuels [4]. Wildland fires are classified as ground fire (which occurs in the decomposed organic materials), surface fire (that consumes dead fuel litters), and crown fire (that spreads through the live fuel canopies of trees) [5]. The fuel condition is an important factor for any of these type of fires. To date, there is limited work on the fire behaviour differences between dead and live fuels. This is why previous research in the area has generally

Proceedings of the Ninth International Seminar on Fire and Explosion Hazards (ISFEH9), pp. 1041-1052
Edited by Snegirev A., Liu N.A., Tamanini F., Bradley D., Molkov V., and Chaumeix N.
Published by Saint-Petersburg Polytechnic University Press
ISBN: 978-5-7422-6498-9 DOI: 10.18720/spbpu/2/k19-74

assumed that live fuels behave as wet dead fuels. Pickett et al. [4] summarized that the common models of wildland fire spread are developed from dead fuels correlations. Nonetheless, Jervis and Rein [6], through small-scale experiments using the Fire Propagation Apparatus on live, aged, and dead pine needles, demonstrated that moisture content is not the only factor governing the burning behaviour. There must be other physical and chemical properties which could influence the fire dynamics of live, aged, and dead pine needles [6]. However, further types and conditions of vegetation should also be explored in detail to get a clear observation particularly on thousand species of Australian vegetation.

Previous studies [7-10] indicate that fuel moisture content has a dominant role in determining the flammability and burning behaviour. In the preheating process, water vapour will be produced and increase the ignition delay time by diluting the flammable volatile in the reaction zone [3]. Dimitrikopoulous and Papaioannou [7] established the flammability classification of Mediterranean vegetation by correlating the ignition delay time and fuel moisture content. The ignition studies conducted by McAllister et al. [11] indicated that a linear regression between moisture content and ignition time only provides a 74-80% fit. Further observation also showed that the trend of ignition time is not captured properly with moisture content in the ignition of live fuels [11]. This finding also confirms that there is a difference between live and dead vegetation response under fire conditions.

In this paper, we examine the combustion characteristics of live and dead *Eucalyptus saligna* (Blue Gum) leaves, which is a common vegetation in Australia's south-eastern states [12]. The species Eucalypt genus was chosen as it forms three-quarters of the total native Australian forests [13] and woodlands. Flammability analyses were performed using the bench-scale Mass Loss Calorimeter device. Investigation on the influence of fuel moisture content to the burning behaviour was determined for each fuel condition (live and dead). This approach allowed us to fill the gaps from previous wildland fire studies on this area. The results provide robust data focusing on how one specific type of fuel under different conditions behave during the combustion process.

MATERIAL AND METHODS

Experimental procedure

Flammability and burning behaviour studies were carried out using thermal analysis and calorimetry. Thermogravimetric Analyses (TGA) were conducted to observe the impact of fuel properties and composition on thermal decomposition. Compared to the other thermal analysis techniques, TGA has a very accurate control of the heating rate for small samples, thus allowing to investigate the thermal decomposition at a kinetic regime [14]. A Perkin Elmer Simultaneous Thermal Analyzer (STA) 6000 was used for Thermogravimetric Analyses at a heating rate of 20°C/min between 20°C and 900°C. The selected temperature range covers the complete thermal decomposition of lignocellulosic materials. In order to get a clear observation of the pyrolysis and oxidation of leaves, two different carrier gases were used: (i) nitrogen to avoid solid-phase oxidation and obtain the volatile (or organic) compounds, and (ii) air to represent the actual oxidative conditions in wildfires and obtaining the inorganic content in the material.

An FTT Mass Loss Calorimeter (MLC) was used for the combustion tests in accordance to ISO 17554:2014. The MLC was utilized to measure the mass loss of the leaf samples in severe conditions of heat exposure without any additional instruments such as chimney or thermopile to measure heat release rate as conducted by previous studies [3,15-17]. The standard MLC closed sample holder (10 x 10 x 5 cm^3) was used to minimize the convective heat transfer coefficient and focus on the influence of the fuel properties. Tests were carried out using piloted ignition with various incident radiant heat fluxes (25, 35, and 50 kW/m^2) produced by the conical heater. The conical heater provided a constant heat flux until the fuel was totally consumed. The flammability criteria used for this study corresponds to the ignition delay time (the time from the beginning of heating until the piloted ignition occurs) and burnout time (the time from ignition until flame out) were noted visually. The mass loss rate (burning rate) was recorded at 1 Hz using a load cell with a data acquisition system. Before each test, the fuel moisture content was measured using a KERN DBS 60-3 Moisture Analyser. This device uses the mass loss method to measure the moisture content of the leaves. The temperature was set to 120°C to minimize the amount of volatile matter lost in the measurement. The instrument was programmed to stop when the sample reached a constant weight within ±0.05% accuracy of moisture content. The calibration of this method has previously carried out by Madrigal et al. [16] with a set point temperature of 175 °C. All of the tests were repeated at least three times to achieve consistent data for analysis.

Sample preparation

Eucalyptus saligna foliages were used in this study. The samples were collected from five different tree locations in a park located in The University of Queensland, St Lucia Campus. In order to investigate the influence of fuel condition, live leaves (above the fibre saturation point) were collected from alive trees; dead leaves (cells contracted below the fibre saturation point) were gathered from the litterfall. Examples of the fuel condition studied are shown in Fig. 1. At the time of collection, the moisture content of the fresh leaves were measured, resulting approximately 114±6% in dry base for live leaves and 14.2±2% in dry base for dead leaves. Proximate analysis was conducted for both fresh samples to obtain the properties (e.g. volatile matter, fixed carbon, and gross calorific value), which affects the burning behaviour as can be seen in Table 1.

(a) (b)

Fig. 1. Conditions of *E. saligna* leaves used in the experiment. (a) live leaves; (b) dead leaves.

For TGA testing, both leaf samples were dried using an oven at 60°C for 48 h. The final moisture content achieved for live and dead leaves was 4.39±0.21% and 3.48±0.19% respectively. After that, the oven-dried samples were crushed and grinded into powdered form to get uniform sample size and avoid problems related to heat and mass transfer [18]. In this study, no chemical treatment was undertaken to maintain the characteristic properties of the sample. The powdered leaves were weighed into 10 mg to be used on the test as suggested by Bilbao et al. [19]. Hence, there was no influence from sample mass differences to the pyrolysis and combustion characteristics on TGA.

To get a wide range analysis result in the flammability test using MLC, the leaves were conditioned to acquire different fuel moisture content. The first condition was 'fresh sample', where the leaves were analysed and tested immediately right after the collection. In the second condition, the leaves were exposed to ambient air and humidity in the laboratory up to seven days before being tested, therefore covering an extensive range in moisture content. The moisture content degradation was measured everyday using a moisture analyser. The last condition was 'oven-dried' (OD), where the samples were dried using an oven with a similar procedure as in the TGA. From those different conditioning processes, the variation of moisture content was obtained approximately 4-120% on dry weight for live leaves and 3-14% on dry weight for dead leaves. It is not possible to obtain zero percent of moisture content on oven-dried leaves because the leaves reach the equilibrium state immediately after exposure to the ambient humidity [20].

In order to reduce the disturbance of the experimental result due to dry mass variation, the initial sample mass was fixed to 5 g on dry weight for all tests. The sample was put into the sample holder until it covered the top surface of the holder and reproduce about 0.01 g/cm^3 (~10 kg/m^3) bulk density. Even though the sample has different wet mass, it still has a similar amount and thickness of individual leaves inside the sample holder. Thus, the fuel bed thickness could be maintained visually at 5 cm. By maintaining the initial dry mass and bulk density of the leaf samples, the effect of fuel condition and fuel moisture content on the burning behaviour could be evaluated.

Table 1. Proximate analysis of *E. saligna* leaves

Components	Live Leaves	Dead Leaves
Moisture Content (% adb[a])	114.21	14.22
Volatile Matter (% adb[a])	77.94	78.86
Fixed Carbon (% adb[a])	18.20	18.30
Ash Content (% adb[a])	3.86	2.84
Gross Calorific Value (MJ/kg adb[a])	20.90	22.89

[a] As dried basis.

Data analysis

For TGA results, pyrolytic variables classified by Dimitrakopoulos [21] such as total mass loss (TML), mean volatilization rate (MVR), and peak mass loss rate (pMLR) were determined for each sample. To analyze the influence of fuel conditions on the flammability criteria, a one-way analysis of variance (ANOVA) has been widely used for previous flammability studies [2,10,15-17]. The LSD-fitted ANOVA test was used to determine if the burning characteristics measured by Mass Loss Calorimeter such as ignition delay time (t_{ig}), time to peak mass loss rate (t_{pMLR}), burnout time (t_{flame}), peak mass loss rate (pMLR), and residual mass fraction (RMF) varied significantly for the live and dead leaves under every incident radiant heat flux (25, 35, and 50 kW/m^2). A linear regression method was used to assess the correlation of time to ignition with both leaf conditions and fuel moisture content. From the linear regression results, the flammability tendency was predicted using the slope [7]. All variables related to the flammability were compared with the average values and errors (standard deviations).

RESULTS AND DISCUSSION

Thermogravimetric analysis (TGA)

The Thermogravimetric (TG) and Derivative Thermogravimetric (DTG) curves for live and dead leaves are shown in Fig. 2 and 3. There is a weight loss difference between the test conducted with air and nitrogen environment. The residual mass of samples on the nitrogen environment are higher than in the air environment due to the absence of oxidation processes. Table 2 shows that the total mass loss in air condition for live and dead leaves are 96.0 ± 0.2% and 96.5 ± 0.3%, respectively. These results provide the total ash content (inorganic matter) provided in the proximate analysis on

Table 1. The total mass loss of both live and dead *E. saligna* leaves are similar with the results of mass loss on Mediterranean plant species with the maximum TGA temperature of 700°C [21]. On the nitrogen condition, the amount of organic compounds remaining are 22.4 ± 0.04% for live leaves and 20.9 ± 1.12% for dead leaves. The higher total mass loss of dead leaves in both air and nitrogen conditions indicates that the dead leaves have more volatile matter compared to the live ones.

Table 2. Pyrolytic variables of live and dead leaves from thermogravimetric analysis

Fuel Conditions	TML (% db)		MVR (%/°C)		pMLR (%/°C)	
	Air	Nitrogen	Air	Nitrogen	Air	Nitrogen
Live Leaves	96.002	77.632	0.137	0.086	0.372	0.383
Dead Leaves	96.516	79.119	0.138	0.088	0.378	0.376

As dried basis.

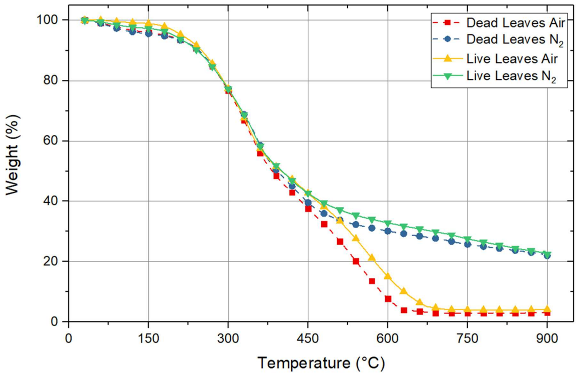

Fig. 2. TG-curves for the pyrolysis of live and dead leaves in air and nitrogen environment.

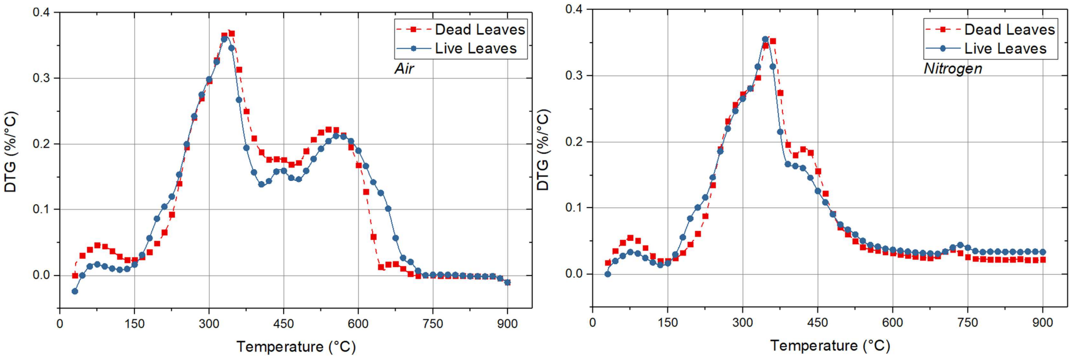

(a) (b)

Fig. 3. DTG-curves for the pyrolysis of live and dead leaves. (a) air environment; (b) nitrogen environment.

As a lignocellulosic material, a leaf is mainly composed of hemicellulose, cellulose, and lignin [22]. Overall, the live and dead leaves produce similar shapes in all DTG-curves. Figure 3a represents the DTG-curve in air environment and it shows four main processes: (i) moisture and light volatile compounds release (<120 °C); (ii) hemicellulose degradation at 220-315 °C; (iii) cellulose and lignin decomposition at 315-400 °C; and (iv) degradation of lignin (>450 °C) [22]. The decomposition of hemicellulose and cellulose occurred almost at the same time, showed by the appearance of small "shoulder" (Grønli et al. [23]) before the first peak at 330-350 °C for cellulose decomposition. In air, there is the second peak as the result of lignin degradation and oxidation when the temperature reaches about 550-560 °C.

In air, thermal decomposition is completed at 700°C, whereas in nitrogen there is an additional decrease just before 900°C as can be seen in Fig. 2. Compared to the Mediterranean species with mean volatilization rates varying from 0.215 to 0.242%/°C, the MVR values for *E. saligna* shown in Table 2 are lower [21]. The pyrolytic variables results are quite similar for the live and dead leaves. Therefore, it may concluded that the thermal decomposition and chemical kinetics of live and dead *E. saligna* leaves essentially behave the same. Even though the TGA results did not obtain a great distinction, the variability might be very critical if it is extrapolated to the actual wildfire phenomena.

The influence of moisture content of live and dead leaves

The effect of fuel moisture content on flammability parameters has been largely investigated in previous studies [7-10]. The impact of the moisture content on the different leaf conditions (live and dead) was analysed to get a clear comparison on its role on the burning behaviour. Ranges of fuel moisture content in both sample conditions are distinct because the leaves have different initial state. Figure 4 depicts the scatter plot of the ignition delay time (t_{ig}) versus moisture content for each condition. A linear regression is found in all measurements, similar with the results observed by Dimitrakopoulos and Papaioannou [7]; Xanthopoulos and Wakimoto [24]. Overall, the trends obtained indicate that, as expected, the increase of moisture content will extend the ignition delay time. This confirms that the production of water vapor dilutes the flammable pyrolizates and the endothermic reaction may affect the thermal balance in the ignition process [25]. External radiant heat flux was also shown to affect the ignition delay time; the higher the heat flux, the lower the ignition delay time is. This could be governed by the thermal behaviour of the leaf samples (i.e. thermally thick and thin behaviour). However, McAllister et al. [11] observed that the vegetation fuel could be assumed to have a thermally-intermediate behaviour. At the low heat flux (25 kW/m^2), large internal temperature gradients were formed and delayed the water evaporation process. On the contrary, no significant evaporation occurred at 35 and 50 kW/m^2 [11].

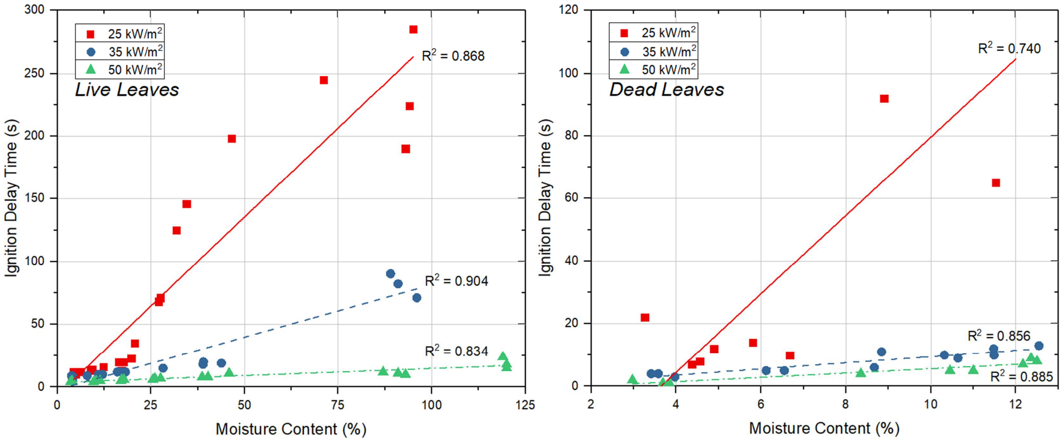

(a) (b)

Fig. 4. Effect of dry-weight moisture content on the ignition delay time (t_{ig}). (a) live leaves; (b) dead leaves.

Table 3 shows the linear regression models between moisture content and ignition delay time obtained from Fig. 4. In order to observe the correlation between live and dead leaves, the ignition delay time was calculated using linear fit models of the opposite fuel condition (models created from dead leaves were used to predict the ignition delay time of live leaves, and vice versa). Similar method was previously conducted by McAllister et al. [11] and Jolly et al. [26] to compare the observed ignition time on their experiment with the predicted value using different models. Figure 5 represents the comparison between the measured and estimated ignition delay time for both leaf conditions in all heat fluxes. From the plots, poor correlations are observed for each leaf condition. As seen in Fig. 5b, the prediction of the ignition delay times of dead leaves using the live leaves models denote adequate results since the live leaves models cover a wide range of moisture content. However, the predicted ignition delay time for dead leaves tends to underestimate the measured values. On the other hand, the dead leaves models can only predict the t_{ig} of live leaves on the relatively low moisture content (≤ 25% on dry weight). The linear fit model of dead leaves at 25 kW/m^2 was fixed by eliminating the peculiar values shown in Fig. 4b to produce a better estimation. The extended prediction for higher moisture content of live leaves would be difficult since the dead leaves only have limited range of moisture content. Different properties and water storage systems between live and dead leaves could be one of the possible influences on the ignition delay time [11].

Table 3. Linear regression models between fuel moisture content and ignition delay time

Heat Flux (kW/m^2)	Live Leaves		Dead Leaves	
	Regression Model	R^2	Regression Model	R^2
25	$y = -6.34+2.84x$	0.868	$y = -45.56+12.52x$	0.740
35	$y = -1.91+0.83x$	0.904	$y = -0.34+0.98x$	0.856
50	$y = 3.64+0.11x$	0.834	$y = -1.27+0.69x$	0.885

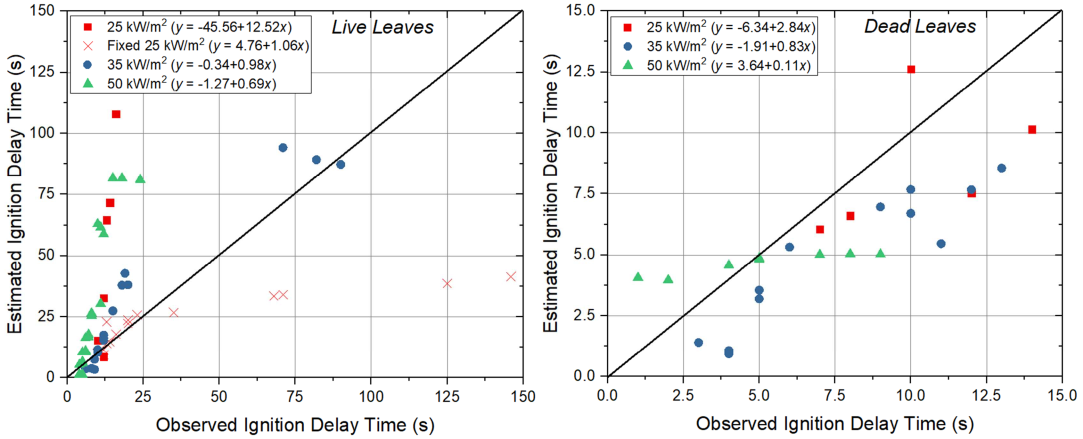

(a) (b)

Fig. 5. Comparison of observed and estimated ignition delay time (t_{ig}). (a) observed t_{ig} of live leaves and estimated t_{ig} by dead leaves models; (b) observed t_{ig} of dead leaves and estimated t_{ig} by live leaves models.

In general, peak mass loss rate (pMLR) tends to increase with the decrease of MC and increase of heat flux. For dead *E. saligna* leaves (3-14% MC), the peak mass loss rate ranged from 4.9 - 12.4 g/m^2.s at 25 kW/m^2; 12.9-17.8 g/m^2.s at 35 kW/m^2; and 16.1 – 20.6 g/m^2.s at 50 kW/m^2 heat flux. Meanwhile, for live leaves (4-120% MC), the peak mass loss rate increased from 3.8-12.4 g/m^2.s at 25 kW/m^2; 7.4 – 15.6 g/m^2.s at 35 kW/m^2; and 11.4 – 18.7 g/m^2.s at 50 kW/m^2 radiant heat flux. Almost all of the peak mass loss rate curves have linear fit correlation with fuel moisture content (R^2

≥ 0.6) as can be seen in Fig. 6. However, the exponential fit is only found on live leaves with 25 kW/m^2 heat flux condition generating $y = 11.268 \times \exp(-0.012x)$ ($R^2 = 0.732$; $P \leq 0.01$; data not shown). This exponential fit is in accordance with the peak heat release rate (pHRR) results conducted by Possell and Bell [3] for *Eucalyptus* species on 25 kW/m^2 heat flux; also Dahanayake and Chow [9] for ornamental plants at heat flux of 50 kW/m^2. Peak mass loss rate comparison between live and dead leaves could be observed in the relatively low moisture content (< 20%), with the pMLR values for live leaves are slightly lower than dead leaves, similar with the pHRR results obtained by Madrigal et al. [15]. These results indicate that the pMLR values are essentially controlled by fuel moisture content (changes the burning process [27]) and leaf conditions (different heat of combustion).

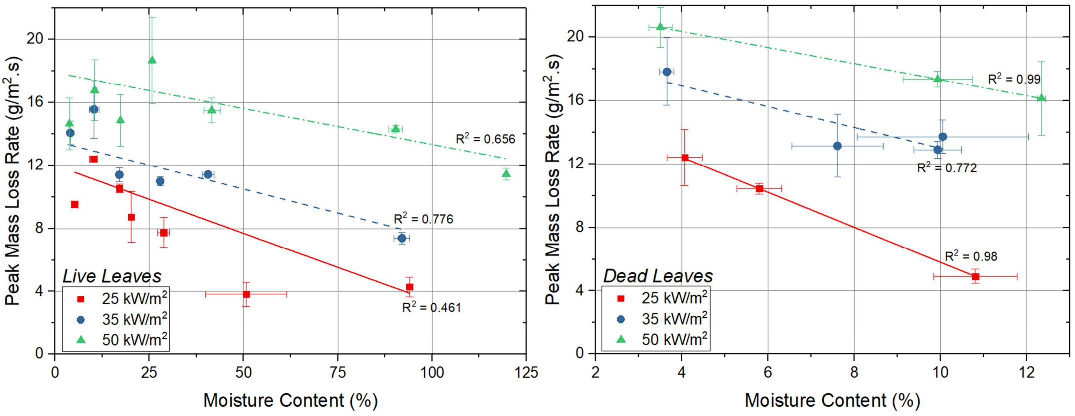

(a) (b)

Fig. 6. Effect of dry-weight moisture content on peak mass loss rate (pMLR). (a) live leaves; (b) dead leaves.

Comparison of flammability parameters between live and dead leaves

The results of the transient measurement of mass loss rate for live and dead leaves at 50 kW/m^2 heat flux condition can be found in Fig. 7. After the ignition occurs, the mass loss rate increases until it reaches the peak value and then declines along with the fuel consumption. At the time of peak mass loss rate, the flaming combustion dominates the burning process until it self-extinguishes, leading to a smouldering combustion of the char and left ash residues. As seen in Fig. 8, the differences between the ignition delay time and time to reach peak mass loss rate in every leaf condition and heat flux are very small. The linearity explains that at the time of ignition, the mass loss rate will immediately reach the peak. Thus, from the transient measurement, flaming duration for both leaves fluctuate and the quantitative results could be seen in the analysis of variance.

Figure 9 shows the normalised mass loss for oven-dried leaves on pre-ignition, also during flaming and smouldering combustion. According to Jervis and Rein [6], the mass loss occurred before ignition is mostly caused by water evaporation process. This process would be dependent on how much water is contained (moisture content) in the leaves, which tends to be higher in live leaves. Even though the oven-dried samples have similar moisture content (4.39±0.21% for live leaves and 3.48±0.19% for dead leaves), the measured pre-ignition mass loss in 50 kW/m^2 heat flux is approximately 0.14±0.04 (~14%) for live leaves and 0.02±0.01 (~2.3%) for dead leaves. This finding indicates that in the same level of moisture content, dead leaves could be ignited before all of the moisture is evaporated, while live leaves need more time to achieve enough volatile compound to be ignited. The amount of mass loss during flaming combustion indicates the quantity of volatile and carbon content, which results in dead leaves have higher amount than live leaves. On the contrary, live leaves have more char residue from flaming combustion that used for smouldering combustion, shown by the total mass consumed on smouldering combustion as seen in Fig. 9c.

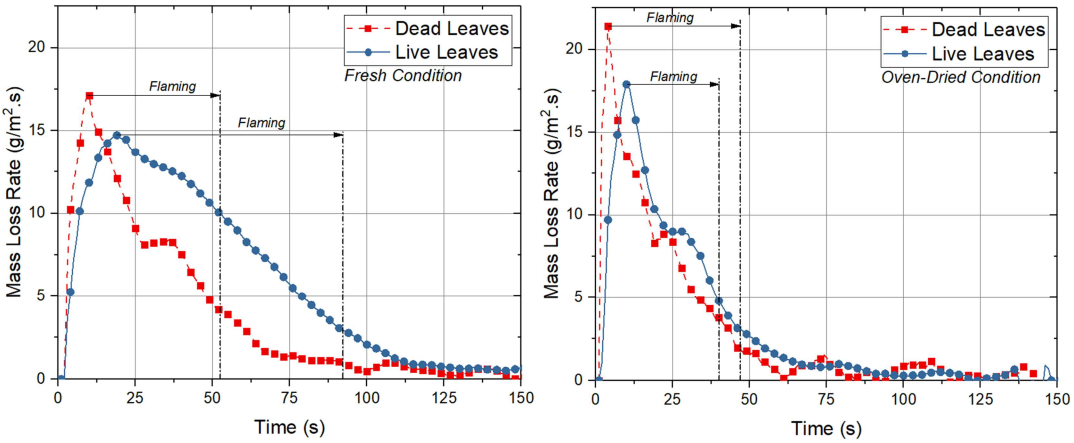

(a) (b)

Fig. 7. Mass loss rate per unit area in 50 kW/m^2 heat flux. (a) fresh samples; (b) oven-dried samples.

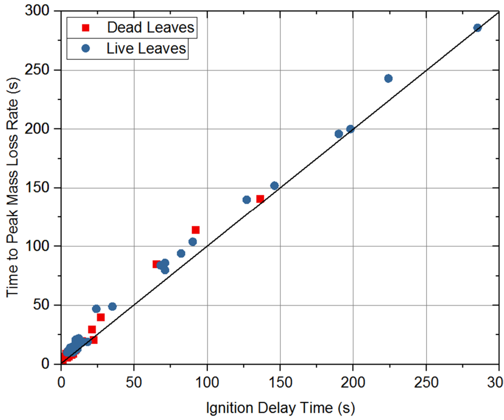

Fig. 8. Ignition delay time (t_{ig}) compared to the time to reaches peak mass loss rate (t_{pMLR}).

Analysis of variance (ANOVA) of live and dead leaves in all heat flux can be observed for some flammability parameters in Table 4. Overall, the analysis indicates that the leaf conditions that are strongly affected are t_{ig}, t_{pMLR}, and residual mass fraction (RMF); t_{flame} and pMLR are also affected under certain conditions. The ignition delay time (t_{ig}) and time to peak mass loss rate (t_{pMLR}) generate high significance level ($P \leq 0.01$) between live and dead leaves on 35 kW/m^2 and 50 kW/m^2 heat fluxes. As explained before, the ignition delay time for live leaves will always be longer than dead leaves, even in the oven-dried condition. Dead leaves could ignite up to eight times faster in fresh condition, and three times faster in oven-dried condition compared to the live leaves, consistent with the results of *Pinus contorta* (lodgepole pine) [26]. This understanding is also applied to t_{pMLR} because the peak mass loss rate would be reached no long after the fuel is ignited.

Burnout time or duration of flame occurrence (t_{flame}) for live and dead leaves have the least significance value. Four out of six analyses indicate that there is no influence of leaf conditions to burnout time. However, the average and standard deviation of oven-dried samples show that the dead leaves burnt longer than live leaves. Incident radiant heat flux of 35 kW/m^2 and 50 kW/m^2 conditions can significantly affect peak mass loss rate values, with the pMLR of live leaves being always lower than dead leaves in fresh and oven-dried situations. This is because the live leaves are less lignified which is affecting the amount of gross calorific value (commonly known as gross heat of combustion) from the proximate analysis in Table 1 [15]. The residual mass fraction (RMF) shown in Table 4 is strongly influenced by the organic content (volatile matter and carbon content), which can be seen in Table 1 and TGA results in Fig. 3. Dead leaves have a larger amount of organic content compared to the live ones, resulting in the smaller residual mass fraction.

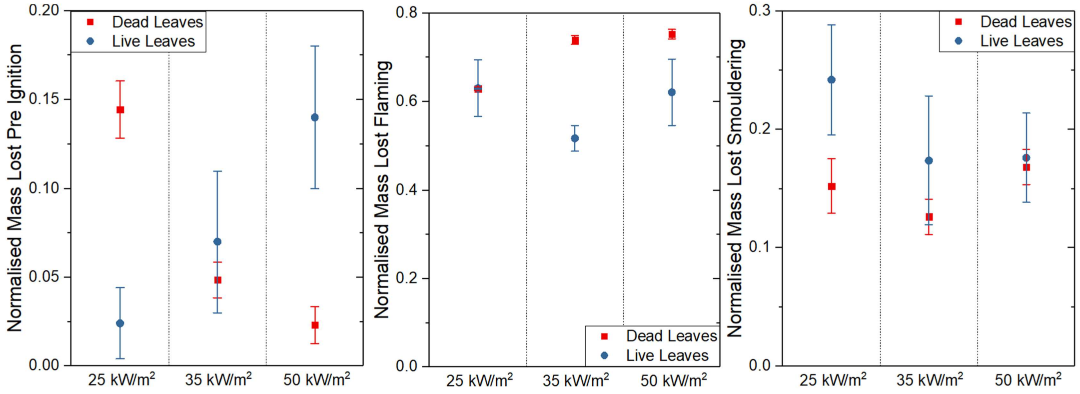

(a) (b) (c)

Fig. 9. Mass loss for oven-dried samples. (a) pre-ignition; (b) during flaming combustion; (c) during smouldering combustion.

Table 4. Summary of flammability parameters in every heat fluxes for fresh and oven-dried samples

Heat Flux (kW/m^2)	**Sample State**	**Sample Condition**	**t_{ig} (s)**	**t_{pMLR} (s)**	**t_{flame} (s)**	**pMLR (g/m^2.s)**	**RMF (%)**
25	Fresh	Live	233±48	241±45	30±8^a	4.29±1.08^a	14.81±0.03
		Dead	97±35	113±28	41±27^a	4.92±0.77^a	4.40±3
	Oven-Dried	Live	11±1^a	21±0.6^a	52±14^a	9.52±0.37^a	10.52±3.44^a
		Dead	12±8^a	12±7^a	51±5^a	12.42±3.07^a	11.26±5.46^a
35	Fresh	Live	81±9	94±9	48±23^a	7.39±0.66	8.72±1.92
		Dead	10±1	14±3	50±16^a	12.91±0.93	3.51±2.06
	Oven-Dried	Live	7±1	12±1	35±3	14.07±1.33^a	20.89±1.51
		Dead	3±0.6	8±1	48±3	17.84±3.68^a	6.02±1.54
50	Fresh	Live	11±1	18±1	79±3	14.31±0.41	13.21±0.53
		Dead	4±0.6	9±1	48±6	17.37±0.85	0.91±0.15
	Oven-Dried	Live	4±0.6	10±1	32±6^a	14.65±2.87	5.80±5.22
		Dead	1±0.6	6±1	46±7^a	20.62±2.18	7.57±0.58

^{a}Not significant ($P > 0.05$).

CONCLUSION

A series of bench-scale experiments on the burning behaviour and flammability of *Eucalyptus saligna* leaves have been conducted. Different fuel conditions (live and dead leaves) were tested in wide range of moisture content and heat fluxes. Proximate and thermogravimetric analysis were conducted to observe the micro-scale influence of fuel properties and composition on the burning behaviour. A Mass Loss Calorimeter was used to measure flammability parameters. The calorimetry results demonstrate that the combustion characteristics of live and dead *E. saligna* leaves are significantly different due to the chemical compounds.

Overall, live and dead leaves produce similar shapes in all DTG-curves. In the air, both live and dead leaves have an almost identical total mass loss of 96.0 ± 0.2% and 96.5 ± 0.3% respectively. On the nitrogen, live leaves have a slightly larger amount of remaining organic compounds compared to dead leaves, 22.368 ± 0.04% versus 20.881 ± 1.12% respectively. The higher total mass loss of dead leaves can be used to show that the dead leaves contain more flammable matter compared to the live leaves. Additional pyrolytic variables results are quite similar for both leaves, which suggests that there is only small differences on the thermal degradation process. However, these differences could lead to a critical issue if it is extrapolated to the actual wildfire phenomena.

The effect of fuel moisture content on the flammability parameters has been investigated by several authors [7-10], but only few studied the moisture content of different fuel conditions. The ignition delay time analyses of leaf conditions are separated in order to observe the correlation of the linear-regression model derived from dead leaves as a prediction on ignition delay time of live leaves, and vice versa. The results obtained for each leaf condition could not be used well to predict the ignition delay time of the opposite fuel condition. The peak mass loss rate of live and dead leaves could only be compared in the low moisture contents. Peak mass loss rate values for live leaves are slightly lower than dead leaves, similar with the peak heat release rate (pHRR) results obtained by Madrigal et al. [15]. These results indicate that the peak mass loss rate values are essentially controlled by fuel moisture content and leaf conditions.

In the transient studies of mass loss rate, the correlation between the ignition delay time and time to reach peak mass loss rate is almost linear. This proves that once the fuel ignited, the peak value of mass loss rate will be immediately reached. The measured mass loss before ignition for oven-dried samples is 14% for live leaves and 2.3% for dead leaves. This indicates that even in the same moisture content, dead leaves would ignite easier since the ignition could occur before all of the moisture evaporated. The ANOVA results determined that leaf conditions are strongly affecting all flammability parameters with the dead leaves tending to be more flammable, even though the leaves are in the same oven-dried treatment.

The results of this work justify the need to treat live and dead fuels separately, and not assume that live fuels are dead fuels with a higher moisture content. Therefore, further studies still need to be carried out for more types of vegetation. Leaf conditions are an additional fuel characteristic that needs to be considered as part of further development of wildland fire spread models and in assessing wildland fire risk.

ACKNOWLEDGEMENTS

The authors would like to thank Property and Facilities Division of The University of Queensland for their assistance in collecting samples, and to all members of Fire Safety Engineering Research Group (UQ Fire) for the constructive inputs and help with laboratory works.

REFERENCES

[1] H.E. Anderson, Forest Fuel Ignitability, Fire Technol. 6 (1970) 312–319.

[2] C.F. Schemel, A. Simeoni, H. Biteau, J.D. Rivera, J.L. Torero, A calorimetric study of wildland fuels, Exp. Thermal Fluid Sci. 32 (2008) 1381–1389.

[3] M. Possell, T.L. Bell, The influence of fuel moisture content on the combustion of Eucalyptus foliage, Int. J. Wildland Fire 22 (2013) 343–352.

[4] B.M. Pickett, C. Isackson, R. Wunder, T.H. Fletcher, B.W. Butler, D.R. Weise, Experimental measurements during combustion of moist individual foliage samples, Int. J. Wildland Fire 19 (2010) 153–162.

[5] J.S. Lozano, An Investigation of Surface and Crown Fire Dynamics in Shrub Fuels, PhD thesis, University of California Riverside, California, U.S., 2011.

[6] F.X. Jervis, G. Rein, Experimental study on the burning behaviour of Pinus halepensis needles using small-scale fire calorimetry of live, aged and dead samples, Fire and Mater. 40 (2016) 385–395.

[7] A.P. Dimitrakopoulos, K.K. Papaioannou, Flammability assessment of Mediterranean forest fuels, Fire Technol. 37 (2001) 143–152.

[8] M.E. Alexander, M.G. Cruz, Assessing the effect of foliar moisture on the spread rate of crown fires, Int. J. Wildland Fire 22 (2013) 415-427.

[9] K.C. Dahanayake, C.L. Chow, Moisture conten, ignitability, and fire risk of vegetation in vertical greenery systems, Fire Ecol. 14 (2018) 125-142.

[10] D.R. Weise, R.H. White, F.C. Beall, M. Etlinger, Use of the cone calorimeter to detect seasonal differences in selected combustion characteristics of ornamental vegetation, Int. J. Wildland Fire 14 (2005) 321-338.

[11] S. McAllister, I. Grenfell, A. Hadlow, W.M. Jolly, M. Finney, J. Cohen, Piloted ignition of live forest fuels, Fire Saf. J. 51 (2012) 133-142.

[12] Australian National Botanic Gardens, Eucalyptus saligna. https://www.anbg.gov.au, 2016 (accessed 31 July 2018).

[13] ABARES, Australian forest profiles: Australia's forests, Australian Bureau of Agricultural and Resource Economics and Sciences, Canberra, 2016.

[14] M.E. Brown, Introduction to Thermal analysis: Techniques and Applications, Chapman & Hall, London, 1996.

[15] J. Madrigal, C. Hernando, M. Guijarro, C. Diez, E. Marino, A.J. De Castro, Evaluation of Forest Fuel Flammability and Combustion Properties with an Adapted Mass Loss Calorimeter Device, J. Fire Sci. 27 (2009) 323-342.

[16] J. Madrigal, C. Hernando, M. Guijarro, A new bench-scale methodology for evaluating the flammability of live forest fuels, J. Fire Sci. 31 (2012) 131-142.

[17] B. Dehane, C. Hernando, M. Guijarro, J. Madrigal, Flammability of some companion species in cork oak (*Quercus suber* L.) forests, Annals Forest Sci. 74 (2017) 60.

[18] S.G. Krigstin, B.M. Wong, D.N. Roy, The contribution of the chemical components in juvenile hybrid *Salix* spp. to its total energy output, Wood Sci. Technol. 27 (1993) 309-320.

[19] R. Bilbao, J.F. Mastral, M.E. Aldea, J. Ceamanos, Kinetic study for the thermal decomposition of cellulose and pine sawdust in an air atmosphere, J. Anal. Appl. Pyrolysis 39 (1997) 53–64.

[20] T. Marcelli, P.A. Santoni, A. Simeoni, E. Leoni, B. Porterie, Fire spread across pine needle fuel beds: Characterization of temperature and velocity distributions within the fire plume, Int. J. Wildland Fire 13 (2004) 37-48.

[21] A.P. Dimitrakopoulos, Thermogravimetric analysis of Mediterranean plant species, J. Anal. Appl. Pyrolysis 60 (2001) 123-130.

[22] H. Yang, R. Yan, H. Chen, D.H. Lee, C. Zheng, Characteristics of hemicellulose, cellulose and lignin pyrolysis, Fuel 68 (2007) 1781-1788.

[23] M.G. Grønli, G. Varhegyi, C.D. Blasi, Thermogravimetric Analysis and Devolatilization Kinetics of Wood, Ind. Eng. Chem. Res. 41 (2002) 4201-4208.

[24] G. Xanthopoulos, R.H. Wakimoto, A time to ignition–temperature–moisture relationship for branches of three western conifers, Canadian J. Forest Res. 23 (1993) 253–258.

[25] S.C. Ferguson, A. Dahale, B. Shotorban, S. Mahalingam, D.R. Weise, The role of moisture on combustion of pyrolysis gases in wildland fires, Combust. Sci. Technol. 185 (2013) 435-453.

[26] W.M. Jolly, R.A. Parsons, A.M. Hadlow, G.M. Cohn, S.S. McAllister, J.B. Popp, R.M. Hubbard, J.F. Negron, Relationships between moisture, chemistry, and ignition of *Pinus contorta* needles during the early stages of mountain pine beetle attack, Forest Ecology Manag. 269 (2012) 52–59.

[27] V. Babrauskas, Effective Heat of Combustion for Flaming Combustion of Conifers, Canadian J. Forest Res. 36 (2006) 659–663.

Validation of a Pyrolysis Model of Wood Thermal Decomposition under Cone Calorimeter

Colombiano J.[1,2,*], **Dréan V.**[1], **Rogaume T.**[2], **Richard F.**[2], **Batiot B.**[2], **Fateh T.**[3], **Nadjai A.**[4], **Guillaume E.**[1]

[1] *Efectis France, France*
[2] *Instit Pprime/UPR3346 CNRS, Université de Poitiers, ISAE-ENSMA, France*
[3] *Efectis UK, Nothern Ireland*
[4] *Fire SERT, Ulster University, Northern Ireland*
**Corresponding author's email:* jeremy.colombiano@efectis.com

ABSTRACT

In this paper, the thermal decomposition of wood is investigated. The multi-scale approach followed here allows first to establish, at a small scale, the kinetic mechanism during the solid thermal decomposition and then validate it at a larger scale. At small scale, experiments were conducted by using Thermo-gravimetric analysis (TGA). Thermo-gravimetric results were also used to propose a kinetic mechanism for the thermal decomposition of the sample. The kinetic parameters of the different identified reactions were estimated by using an optimization technique, namely the Particle Swarms Optimization (PSO) method. The mass loss and mass loss rate model predictions show a good agreement with the experimental data. In addition, heat capacity, as well as heat of reaction, is determined using a TGA-DSC (Differential scanning calorimetry) apparatus.

At a larger scale, experiments were carried out in a cone calorimeter under air atmosphere. The sample is placed in an insulated sample holder (calcium silicate). The pyrolysis model developed at the TGA scale and the measured thermal parameters were used in numerical simulations of cone calorimeter experiments taking into account the modelling of heat transfer into the sample.

The comparison between experimental and numerical results under cone calorimeter is made on the mass loss, the mass loss rate, the temperatures and the pyrolysis front. The numerical results can predict the thermal behavior. The noted differences are mainly due to a lack of control of the experimental boundary condition, and are also partly attributable to the evaporation of water present in the sample holder which is not taken into account.

KEYWORDS: Thermal degradation, cone calorimeter, TGA, Fire Dynamics Simulator.

NOMENCLATURE

A	pre exponential factor (s^{-1})
E	Activation energy (kJ/kmol)
c_P	constant pressure specific heat (J/(kg·K))
q''	heat flux (W/m^2)
q'''	heat release rate (W/m^3)
n	reaction order
R	ideal gas constant value (kJ/(kmol·K))
T	temperature (K)
λ	thermal conductivity (W/(K·m))
ρ	density (kg/m^3)
ω	reaction rate (s^{-1})

Subscripts

0	initial
c	chemical
r	radiative
s	solid phase

Proceedings of the Ninth International Seminar on Fire and Explosion Hazards (ISFEH9), pp. 1053-1065
Edited by Snegirev A., Liu N.A., Tamanini F., Bradley D., Molkov V., and Chaumeix N.
Published by Saint-Petersburg Polytechnic University Press
ISBN: 978-5-7422-6498-9 DOI: 10.18720/spbpu/2/k19-87

t	time (s)

Greek

ε	emissivity (-)

g	gas phase
i	reaction number

INTRODUCTION

The equations of motion describing the gas phase in Computational Fluid Dynamics (CFD) are relatively well known and the approximations in the various gas phase sub-models have been extensively studied. However, the coupling between the gas phase and the condensed phase in order to describe flame spread over a burning solid has proven difficult to model. Due to lack of knowledge on the underlying phenomena during the decomposition of the solid, the poor characterization of the fundamental material properties that controls the burning process and the large assumption of wall submodels, fire ignition and propagation cannot be accurately predicted, taking into account a mechanism of decomposition [1, 2]. Some studies have been focused on fire ignition and propagation at large scales, but empirical laws are used, such as the definition of an ignition temperature and the prescription of a mass flow of pyrolysis versus time [3]. Other models avoided the use of an ignition temperature and described the ignition by a critical mass loss rate [4]. However, a detailed analysis of thermal decomposition was still avoided. Describing the material behavior for fire prediction is a key challenge for the fire community.

Therefore, it is of the first importance to determinate material parameters and to identify the physical and chemical phenomena involved in order to numerically predict the material behavior for prediction of fire dynamics. The goal of this study is to improve the capability of the fire model (e.g. Fire Dynamics Simulator [5]) to predict flame spread over materials that burn in a scale like compartment fire, by taking material behavior into account. This report is only focused on the TGA and cone calorimeter scale results.

There is a substantial volume of work in the literature regarding the material behavior and the transition between the TGA scales to the cone calorimeter. Bustamante studied the thermal decomposition of polyether polyurethane foam [6] and used for the first time the multi-scale approach. Since then, studies using this approach are mainly focused on the mass loss, mass loss rate and heat release rate prediction [7, 8]. Others studies attempted to numerically predict the temperature of the sample. But, as it is shown by Fateh [9], the prediction of the mass loss, the mass loss rate and the temperatures does not mean that the pyrolysis front is correctly predicted. Fateh [9] studied a multi-scale approach for plywood. The thermal decomposition model proposed in his study is composed of five reactions, taking into account oxygen effect. The thermal parameters are estimated based on the mass loss rate of the cone calorimeter experimental result. The numerical prediction for the mass loss, mass loss rate and temperatures (at the surface and bottom of the sample) are in good agreement with the experimental results, but the pyrolysis front is not correctly tracked.

This paper is focused on the prediction of the material behavior of fir wood under cone calorimeter. Wood constitutes a substantial fraction of the fuel load in building fires. For this reason, understanding of its behavior under high temperature conditions is important. Wood is a charring fuel and undergoes a variety of complex physical and chemical processes of momentum, heat and mass transfer, property variations, structural changes, char oxidation and secondary chemical reactions within the solid [10]. Oxygen concentration, irradiance, moisture content and the orientation of the solid fuel with respect to the external heat source affect the pyrolysis process (e.g. flames). TGA, TGA-DSC are used to determinate a model of thermal decomposition, heat capacity and heat of reaction. These parameters serve as input data for the prediction of the material behavior under cone calorimeter for different heat fluxes. Comparisons of numerical and experimental mass loss, mass loss rate, temperatures and pyrolysis front are presented.

THERMOGRAVIMETRIC ANALYSIS

The first part of this work intends to develop a pyrolysis model. An experimental investigation has then been conducted at matter scale in order to define the mechanism of thermal decomposition. The kinetic parameters associated have been calculated.

A Mettler TGA-DSC apparatus was used to study the decomposition kinetics of the sample. The furnace was heated at a constant heating rate (5 K/min) and experiments were performed under nitrogen and air, in order to separate the thermolysis and oxidative reactions. Using a small heating rate allow us to avoid temperature gradient and mass diffusion in the sample. For the same reason, the polymers were cut into thin samples of 0.3 mm high and 5 mm diameter, for a mass of 6 ± 2 mg. Thus, the temperature in the sample was assumed to be same as that of the sample compartment. The furnace was continuously purged with $5 \cdot 10^{-7}$ m^3/s of ultra-high purity nitrogen or air. Figure 1 presents the TGA experimental results as a function of temperature in inert and air atmosphere.

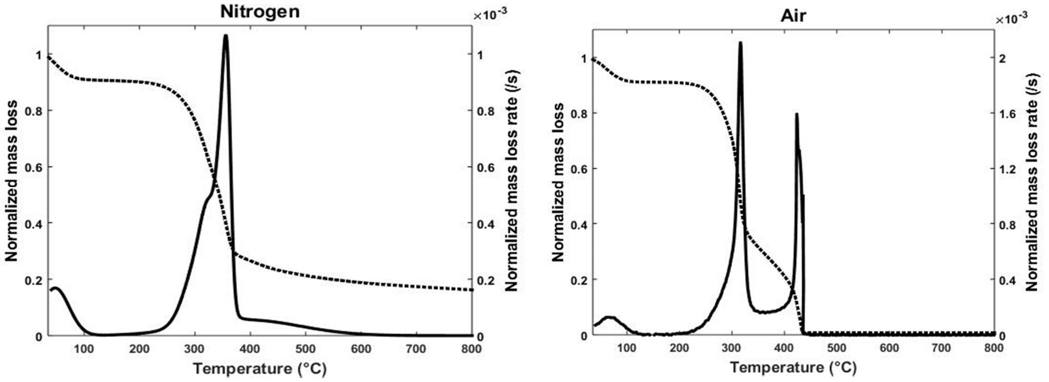

(a) (b)

Fig. 1. TGA experimental results of wood decomposition under nitrogen (a) and air (b) at 5 K/min.

After the water evaporation (up to 100°C), independently of the heating rate, the wood thermal degradation begins at 200°C up to around 600°C and leads to a residue of around 0.18 for nitrogen atmosphere. The results obtained are in accordance with the literature [10]. Indeed, several studies have been focused on the kinetic mechanism of the thermal decomposition of the wood and show that it begins to degrade with the hemicellulose, from 200 and 325°C. Then cellulose starts its degradation from 240 to 375°C, and lignin from 250 to 600°C [10]. In air atmosphere, wood degrades at around 300°C, and char oxidation takes places at 430°C, leading to no residue.

The thermal decomposition mechanism proposed here represents these degradations (hemicellulose, cellulose and lignin) by one reaction only. The decomposition mechanism is obtained from the coupled analysis of the curves of mass loss and mass loss rate, using a Lumped parameter approach (LPA). The model is composed of three reactions including the water evaporation:

$$\begin{aligned} &Wet\ wood \xrightarrow{N2} Dry\ wood + Water\ vapor \\ &Dry\ wood \xrightarrow{N2} Char\ wood + Gas \qquad . \\ &Char\ wood \xrightarrow{Air} Residue + Carbon\ dioxide \end{aligned} \qquad (1)$$

Oxygen effect is taken into account by the third reaction. In fact, it is assumed that there is no oxidation reaction in the sample at the cone calorimeter. Indeed, at the cone calorimeter scale, it is assumed that the pyrolysis flow avoids oxygen diffusion in the sample. In addition, at the surface of the sample, oxygen is practically consumed by oxidation reactions. This assumption is particularly true for high incident heat fluxes [10, 11]. Therefore, char oxidation is taken into account only for the surface of the sample.

Each reaction *i* is characterized by its reaction rate, defined as:

$$\dot{\omega}_i = A_i \exp\left(-\frac{E_i}{RT}\right) Y_{S,i}^{n} Y_{O_2,i}^{n_{O_2}}, \tag{2}$$

where A_i is the pre-exponential factor of the reaction *i*, E_i is the activation energy, $Y_{S,i}$ and $Y_{O_2,i}$ are, respectively, the mass fraction of the combustible and air, n and n_{O_2} expressing the order of each reagent.

The set of kinetic parameters of each reaction is determined using the heating rate of 5 K.min^{-1} to keep the assumption of no gradient of mass and temperature. The parameters are estimated using an inverse optimization method based on a modelistic approach (the parameters are constant for each reaction), here the particle swarm algorithm is used and its performance has already been demonstrated [12]. For more information about this algorithm, see [13]. Only the mass fractions of the generated species are estimated experimentally (with the mass loss curves). The set of kinetic parameters are presented in the Table 1. Figure 2 presents the mass loss rate for nitrogen and air obtain by the model, in comparison with the experimental results.

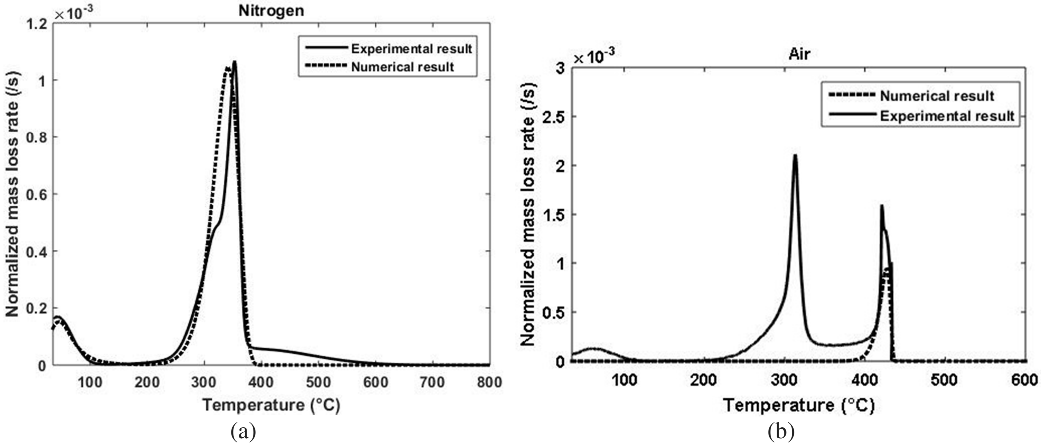

(a) (b)

Fig. 2. Experimental and numerical TGA results at 5K/min under nitrogen (a) and air (b).

It can be seen from Fig. 2(b) that the mass loss rate of the char oxidation is not correctly represented. This is due to the inability of the model to predict brutal reactions as char. Once the reactions and associated parameters of the condensed phase are identified, the pyrolysis model can be used to predict the thermal decomposition under cone calorimeter scale. Therefore, the thermal properties of the wood have to be determined. The Differential Scanning Calorimetric (DSC) apparatus is used for the characterization of the heat capacity of the wood and the char. No distinction between hemicellulose, cellulose and lignin is made, as the thermal mechanism used a LPA approach. The heat of reaction is also determined for each reaction, according to [14, 15]. The thermal conductivity of the wet wood is evaluated from measurements at room temperature with a

Modified Transient Plane Source (MTPS) Technique. Thermal conductivities of dry wood and char are chosen from the reference [16]. The density of the wet wood is directly measured, and the densities of dry wood and char are estimated according to [16]. Table 1 shows the parameters used in the simulation, the heat capacity is given here at room temperature, and the emissivity is equal to 1 for all materials [17].

Table 1. Kinetic parameters for the LPA model of decomposition

	A, s^{-1}	E, kJ/kmol	υ	n	n_{O2}	ρ, kg/m^3	λ, W/(m·K)	C_p, kJ/(kg·K)
Wet wood	4.06E8	6.7E4	0.9	2.8	0	447	0.13	1.39
Dry wood	1.59E9	1.37E5	0.2	1.36	0	410 [16]	[16]	1.39
Char	1.86E24	3.5E5	0	0.5	1	130 [16]	[16]	1.04

CONE CALORIMETER EXPERIMENTAL RESULTS

In order to validate the model of pyrolysis and the thermal parameters, tests using the cone calorimeter apparatus are performed. Then, comparisons of experimental and numerical mass loss, mass loss rate, temperatures and pyrolysis front are presented.

The sample is placed in the horizontal position in an insulated sample holder limiting the thermal transfer at the side and back of the sample. Heat and mass transfers are then assumed to be in one dimension (perpendicular to the surface exposed). A flame development appears at this scale.

The experiments are conducted under air atmosphere, with well-ventilated conditions and with a piloted ignition. The heat fluxes studied are 20, 30, and 50 kW/m^2. The size of the sample is 100×100×18 mm^3 and its mass is about 78g (± 6g). Figure 3 summarizes the evolution of the normalized mass loss and the normalized mass loss rate. The mass loss rate curves are obtained by first applying a Savitzky Golay filter, and then by fitting with Gaussian curves.

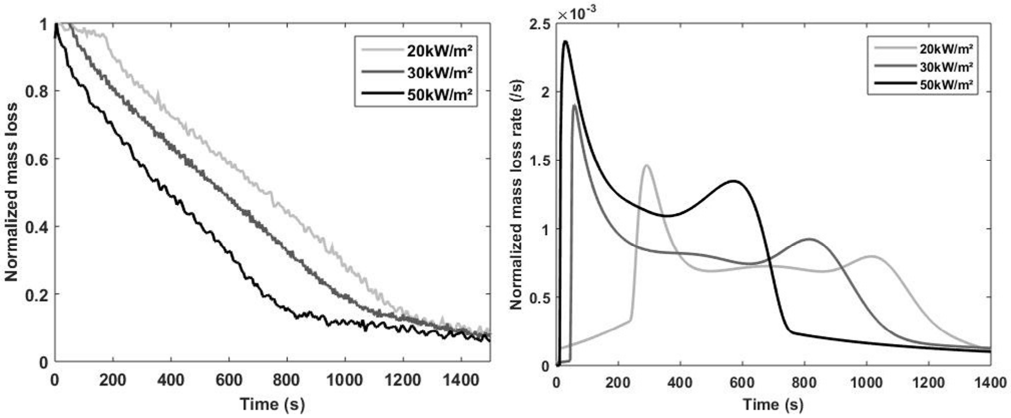

(a) (b)

Fig. 3. Experimental cone calorimeter results under air at different heat fluxes: (a) mass loss; (b) mass loss rate.

Similar shapes of the normalized mass loss rate (MLR) are observed for all heat fluxes. Wood is a charring material, therefore a char layer appears above the virgin layer. It explains the decreasing of the MLR after the first peak: the char layer acts as a thermal barrier. The last peak of the mass loss rate is attributed to the heat feedback. This increase of MLR is due to a thermal behavior, the boundary experimental condition causes a thermal feedback when the thermal wave reaches the back of the sample [18]. From the curves of mass loss, it can be seen a difference of slope when the flame is extinguished. After flame extinguishing, oxygen diffused into the material and oxidized the char residue.

In addition, experimental measurement of the pyrolysis front is made by stopping the test at different times (100, 150, 200, 400, 600 and 700s after the beginning of the experiment), cutting the sample, and measuring the distance between the pyrolysis zone and the bottom of the sample. The pyrolysis front is measured close to the middle of the sample, based on [19]:

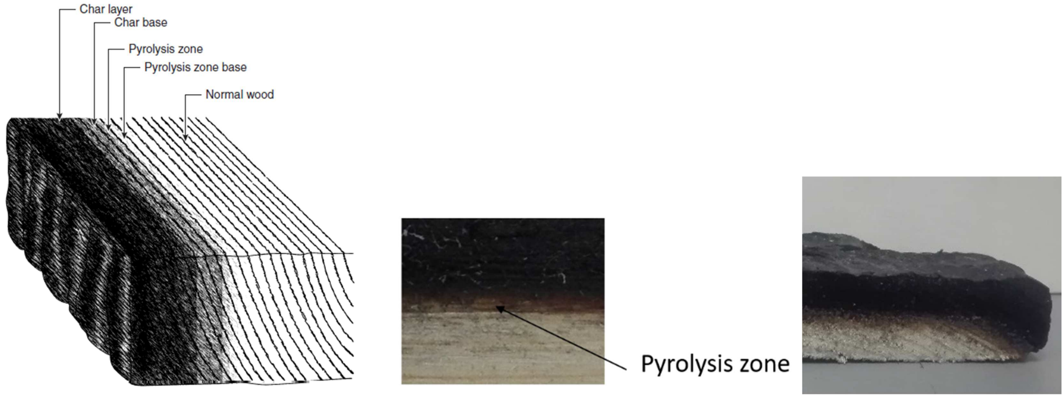

(a) (b) (c)

Fig. 4. Pyrolysis zone in a wood section: (a) from [19]; (b) current study; (c) pyrolysis front inhomogeneity (30 kW/m² at 600 s);

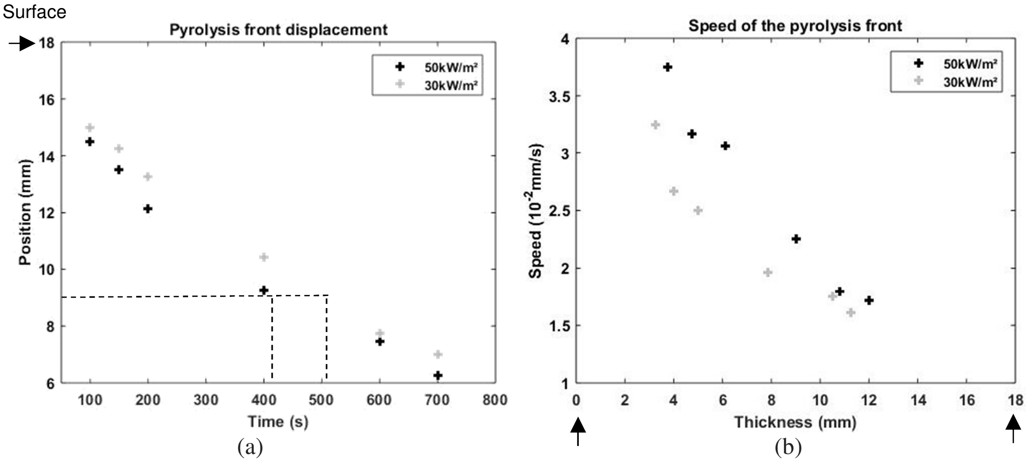

(a) (b)

Fig. 5. Experimental result for the pyrolysis front: (a) position of the pyrolysis front; (b) speed of the pyrolysis front along the thickness.

The thickness between the char layer and the virgin layer is very thin (Fig. 4(b)), leading to an accurate measurement of the pyrolysis front. However, it can be seen from the Fig. 4(c) that the pyrolysis front is not linear close to the side. This is due to a slight contraction of the material during the experiment, allowing the incident heat flux to pass through the sides. From the value obtained, the position of pyrolysis front versus time is tracked, as well as the speed of this front along the thickness of the material.

The pyrolysis front reaches the middle of the thickness at 415 s for 50 kW/m² and 510 s for 30 kW/m² (values obtained by polynomial interpolation). Knowing this time, the pyrolysis temperature can be estimated based on the temperature measurement at the middle of the thickness. From Fig. 5(b), the speed of the pyrolysis front decreases, as the char plays a heat barrier.

To finish, experimental investigations for the measurement of the temperature are made for two heat fluxes: 30 and 50 kW/m². The temperatures at 3 mm below the surface exposed, at the middle of the thickness, at the bottom of the sample and 1 cm below the back face (in the sample holder) are recorded using thermocouples of 0.5 mm diameter and of type K. The thermocouples are placed perpendicular to the surface exposed, and closed to the middle. At least seven experiments are performed per heat flux (only one for the 3 mm below the surface at 50 kW/m²). Figure 4 presents the results.

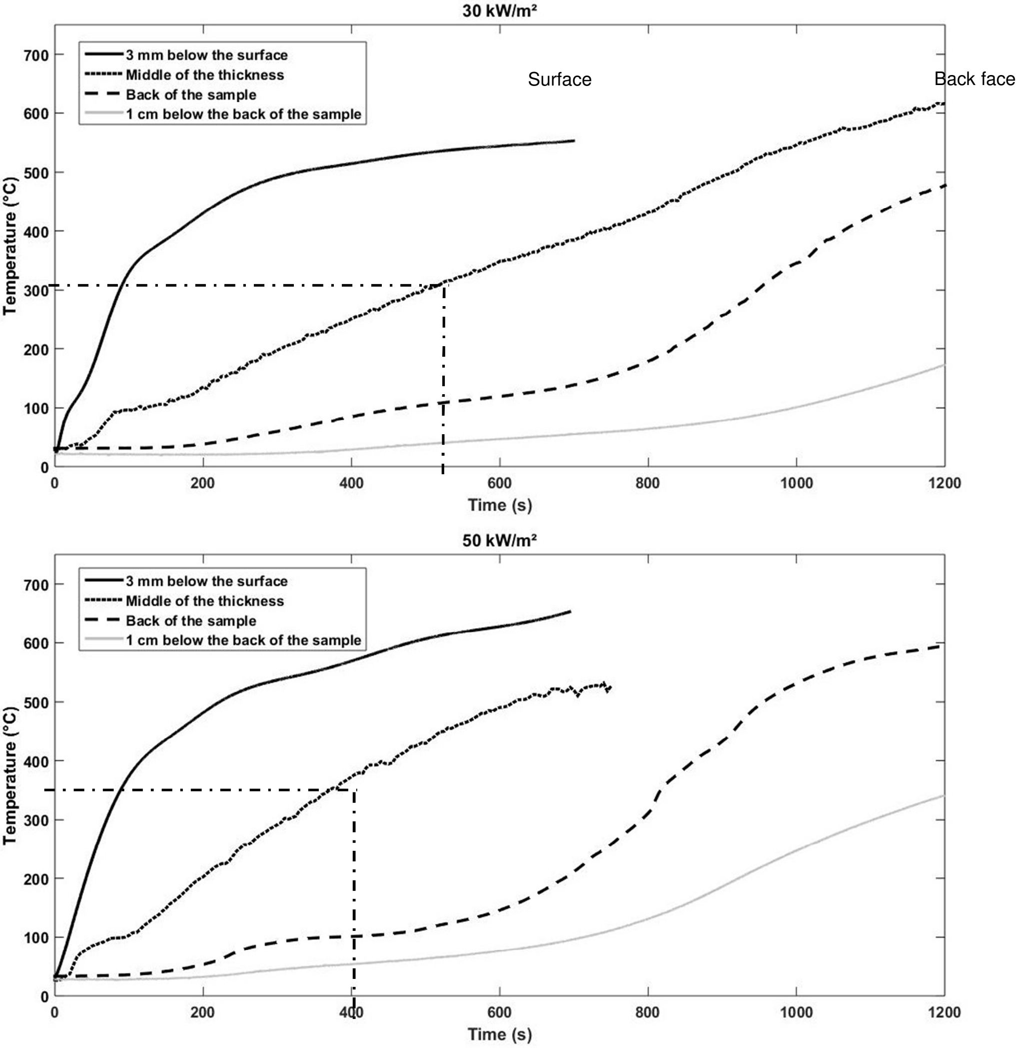

Fig. 6. Experimental temperature for 30 kW/m² and 50 kW/m².

For the 3 mm below to the surface temperature, and for the middle of the sample temperature at 50 kW/m², the results are presented up to 700 s, beyond this value, experimental discrepancies appear due to the physical change of the wood. The middle of the thickness temperature is used in order to estimate the pyrolysis temperature (dash-dot lines in the middle of the thickness temperature curves). For 50 kW/m², at 415 s, it is found that the temperature is 365 °C, and for 30 kW/m², at 510 s, the temperature is 310 °C. The discrepancy between the two pyrolysis temperatures can be due to the difference in the heating rate when the pyrolysis front reaches the middle of the sample. It can also be due to the discrepancy during the temperature measurement (maximum of 60 °C of standard deviation on the tests). From Fig. 6, the effect of the water evaporation is visible (constant evolution of temperature at around 100 °C). This is more visible in depth of the material. The fact that the water evaporation is more visible at the back of the sample is not due to a slowing down of the thermal wave (as the slopes of the curve of the middle of the thickness and of the back of the sample temperature are quite similar after water evaporation). It can be explained by the presence of water in the sample holder.

Knowing the pyrolysis temperature for each heat flux, the position (and the speed) of the pyrolysis front at 3 mm below the surface and at the back of the sample can be estimated. Figure 7 combines the measured (by cutting the sample) and estimated (by the temperature) position of the pyrolysis front.

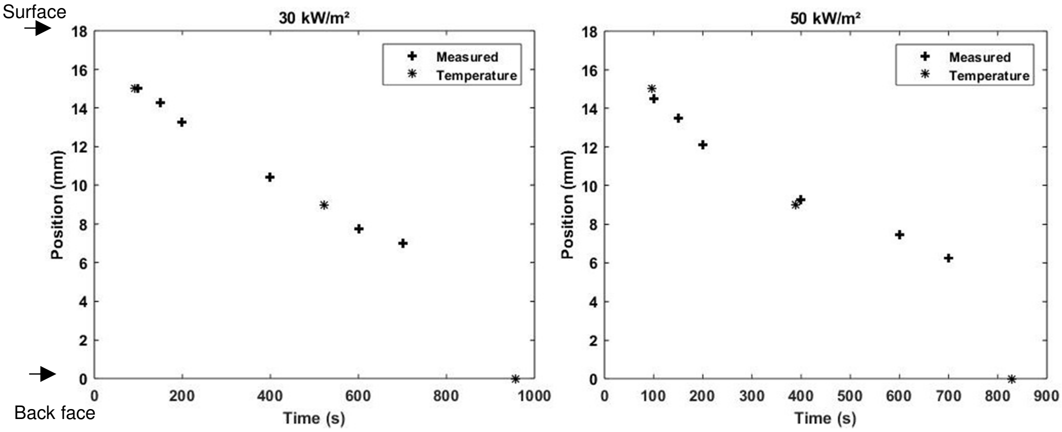

(a) (b)

Fig. 7. Experimental position of the pyrolysis front (measured and estimated) for 30kW/m² (a) and 50 kW/m² (b).

The measured and the estimated (with temperature) position of the pyrolysis front appears to be in quite good agreement. The pyrolysis front seems to accelerate close to the back of the sample; this is explained by the thermal feedback caused by the insulated sample holder.

CONE CALORIMETER NUMERICAL RESULTS

Numerical investigations are performed using Fire Dynamic Simulator in order to validate thermochemical properties. Heat transfer is treated in one dimension, and the equation solved is as follows, based on the component-averaged thermal properties:

$$\rho_s c_{P,s} \frac{\partial T_s}{\partial t} = \frac{\partial}{\partial x}\left(\lambda_s \frac{\partial T_s}{\partial x}\right) + \dot{q}'''_{s,c} , \tag{3}$$

where $\dot{q}'''_{s,c}$ is the chemical source term. More information can be found in [6]. The overall domain is 30 x 30 x 40 cm^3, with a uniform gas phase mesh of size 1 cm. During the simulations, the lateral faces are insulated (adiabatic conditions) and an insulated material is placed at the bottom of the sample, which thermal conductivity, heat capacity and density are 0.08 W/(m·K), 1.04 kJ/(kg·K) and 240 kg/m^3, respectively. A uniform mesh is generated for the solid phase (0.5 mm), in order to represent accurately the thermal wave. The Eddy Dissipation Concept is used as a combustion model, the fuel is assumed to be the elementary formula of wood $C_{3.4}H_{6.2}O_{2.5}$, with an effective heat of combustion of 14 MJ/kg, a soot fraction of 0.004 kg/kg and a CO fraction of 0.01 kg/kg. Oxygen diffusion in the sample is taken into account with

$$X_{O_2}(x) = X_{O_2,g}\exp(-x/L), \tag{4}$$

where $X_{O_2,g}$ and $X_{O_2}(x)$ are, respectively, the first gas phase cell oxygen concentration (above the solid), and the in depth oxygen concentration into the sample, L is the maximum length of oxygen penetration in the sample, assumed to be 1 mm. Only the shrinkage of the char reaction is represented.

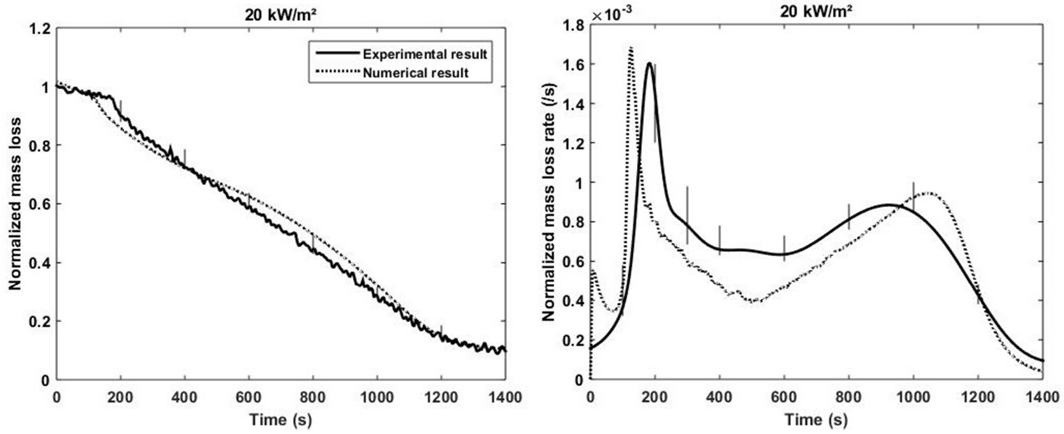

(a) (b)

Fig. 8. Experimental and numerical results at 20 kW/m²: (a) mass loss; (b) mass loss rate.

Mass loss and mass loss rate are presented in the Figs. 8, 9 and 10. Numerical results present a quite good agreement with experimental results, especially since the heat flux is high. However the second peak corresponding to the thermal feedback is over estimated and the steady phase (between the two peaks) is underestimated. This can be explained by the lack of control at the side boundary conditions. As shown in Fig. 4. c, the pyrolysis front reaches the back of the sample first by the side of the sample, which is not taken into account in the simulation. Therefore, between the two peaks, the numerical mass loss rate is slightly underestimated, and the second peak is overestimated. Despite these observations, the simple pyrolysis model can represent the mass loss and the mass loss rate for the three heat fluxes tested.

In addition, the thermal feedback from the insulated condition at the back of the sample is numerically predicated earlier.

Figures 11 and 12 present the comparison between experimental and numerical temperatures. The numerical results can predict correctly the temperature at 3 mm below the surface and at the middle of the thickness (for 50 kW/m², repeatability tests need to be performed). However, the simulations do not predict the temperature at the back of the sample and 1 cm below it, especially around 100 ° C, which can be explained by the presence of water in the sample holder, which is not taken into account in the simulations. The overestimations of the temperature at the back of the face and in the sample holder explain the fact that the thermal feedback is predicted earlier in the curves of MLR (Figs. 8, 9 and 10).

The final comparison is the pyrolysis front position versus time. Numerically, the pyrolysis front is composed of 50% of wet wood, and 50% of dry wood (270 kg/m^3). Figure 13 compares the numerical and experimental position of the front. For both 30 and 50 kW/m², the pyrolysis front is accurately represented in the simulation. However, when the thermal feedback appears, the front is not correctly estimated, as the temperature at the back of the sample is numerically overestimated.

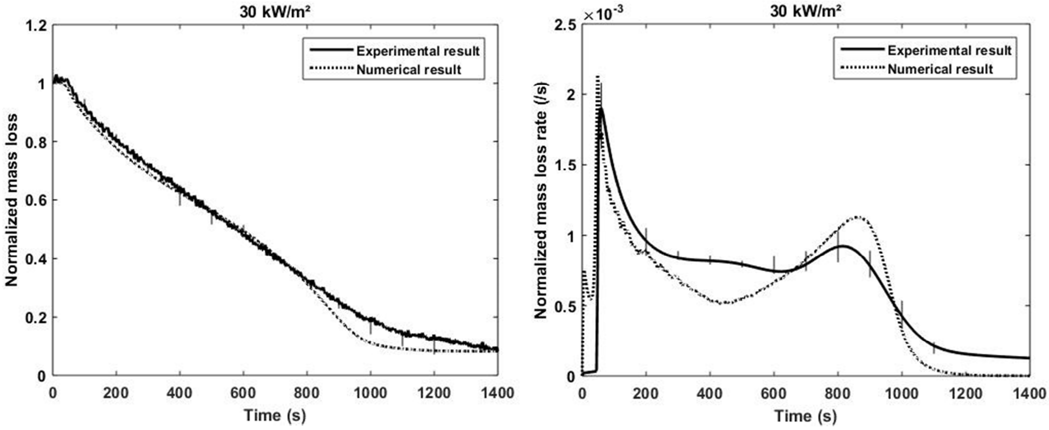

(a) (b)

Fig. 9. Experimental and numerical results at 30 kW/m²: (a) mass loss; (b) mass loss rate.

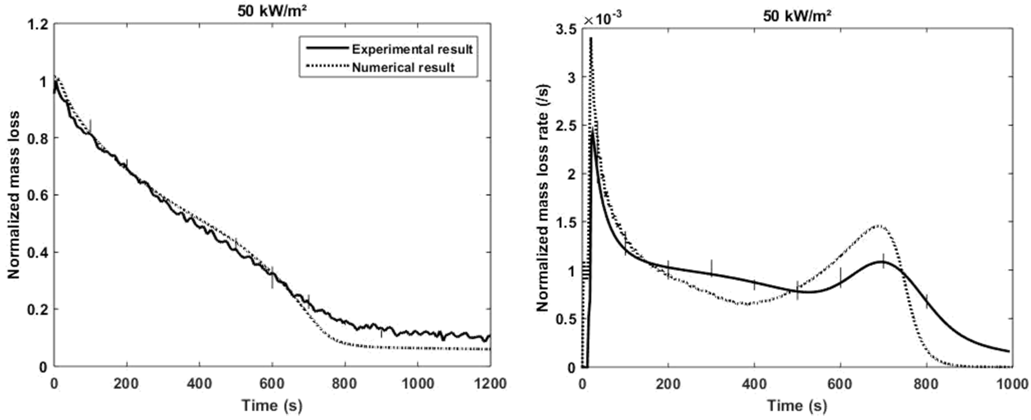

(a) (b)

Fig. 10. Experimental and numerical results at 50 kW/m²: (a) mass loss; (b) mass loss rate.

CONCLUSION

TGA experiments were performed under air and nitrogen at 5 K/min in order to define a model of thermal decomposition. A simple model was defined and kinetic parameters were obtained with a particle swarms optimization. In addition, heat capacity and heat of reaction were determined using the TGA-DSC apparatus. Thermal conductivity of the virgin wood was measured at room temperature with a Modified Transient Plane Source technique (MTPS). Other values of thermal conductivities are taken from the literature, as well as the densities. These parameters serve as input data for numerical models at cone calorimeter scale. Cone calorimeter experiments were performed with mass loss, mass loss rate, temperature, and pyrolysis front being recorded. The experimental and numerical results are in good agreement. The observed discrepancies are mainly explained by the lack of control of the side boundary conditions: the sides are not insulated, leading to an advanced thermal decomposition at this location. In addition, the presence of water in the sample holder can explain the discrepancies concerning the temperature at the back of the sample and 1 cm below it, as the water evaporation is not simulated in the sample holder. The overestimation of these temperatures leads to the earlier prediction of the thermal feedback and explains the fact that the numerical pyrolysis front reaches the rear face before the experiment.

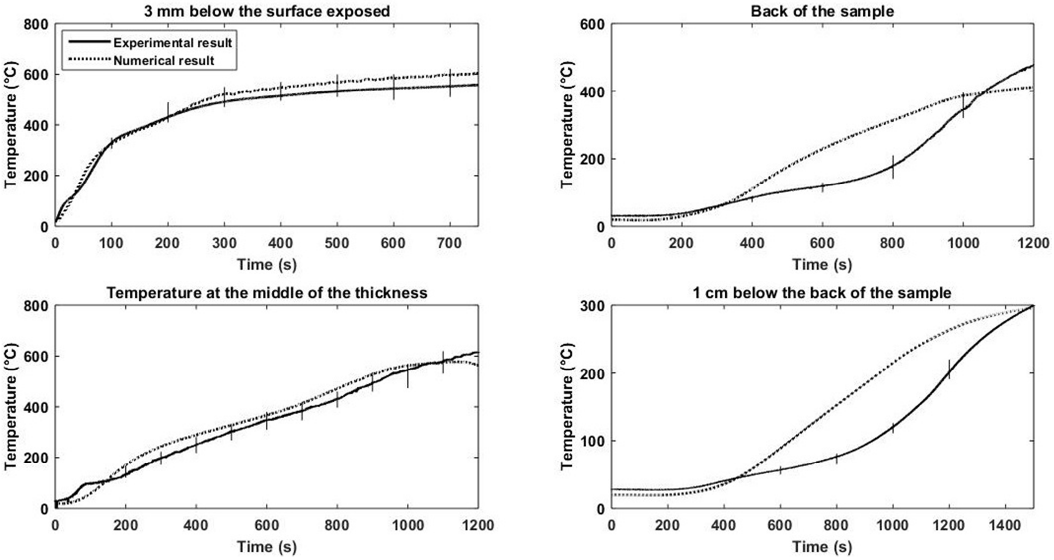

Fig. 11. Experimental and numerical results for temperatures at 30 kW/m²

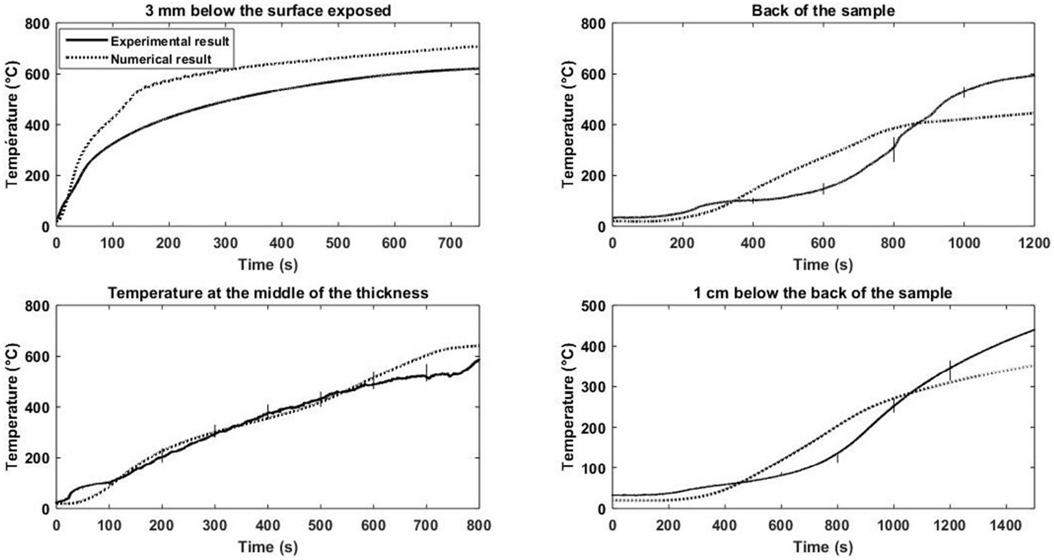

Fig. 12. Experimental and numerical results for temperatures at 50 kW/m².

The thermochemical parameters can represent the thermal behavior of the material. These input parameters can be extrapolated to the next scale of the study: LIFT apparatus for one dimensional lateral flame propagation and radiant panel for one dimensional vertical flame propagation.

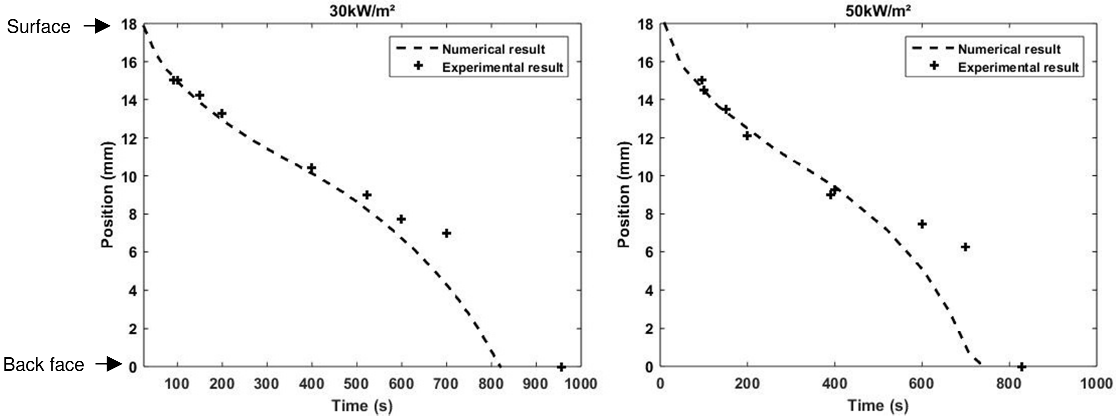

Fig. 13. Experimental and numerical comparison of the pyrolysis front at 30 kW/ (a), and 50 kW /m² (b).

REFERENCES

[1] A. Meunders et al. Parmeter optimization and sensitivity analysis for fire spread modelling with FDS, University of Canterbury, 2014

[2] K. Prasad et al. Numerical simulation of fire spread on polyurethane foam slabs, Proceedings of the Fire and Materials conference, San Francisco, 2009.

[3] J.G. Quintiere, D.W.I. Rouson. Application of CFD Modelling to room fire growth on walls, NIST GCR 03-849, April 2003.

[4] E. Markus, A. Snegirev, E. Kuznetsov, L. Tanklevskiy. Application of the thermal pyrolysis model to predict flame spread over continuous and discrete fire load, Fire Saf. J. (2019).

[5] NIST, Fire Dynamics Simulator User's Guide Sixth Edition – Version 6.6.0

[6] T. Rogaume, et al. Developement of the thermal decomposition mechanism of the polyether polyurethane foam using both condensed and gas phase release data. Combust. Sci. Technol. 627-644 (2011).

[7] D. Marquis, M. Pavageau, E. Guillaume. Multi-scale simulations of fire growth on a sandwich composite structure, J. Fire Sci. 31 (2013) 3-34.

[8] E. Guillaume, A. Camillo, T. Rogaume, Application and limitations of a method based on pyrolysis models to simulate railway rolling stock fire scenarios, Fire Technol. 50 (2014) 317–348.

[9] T. Fateh, F. Richard, T. Rogaume. Modeling of the Pyrolysis of Plywood Exposed to Heat Fluxes under Cone Calorimeter In: D. Nilsson, P. van Hees, R. Jansson. (Ed.), Fire Safety Science–Proceedings of the Eleventh International Symposium, pp, 208-221, 2017.

[10] C. Di Blasi, Modelling chemical and physical processes of wood and biomass pyrolysis, Progr. Energy Combust. Sci. 34 (2008) 47-90.

[11] M. A. Kanury, Thermal decomposition kinetics of wood pyrolysis, Combust. Flame 18 (1972) 75-83.

[12] E. Elbeltagi, T. Hegazy, D. Grierson, Comparison among five evolutionary-based optimization algorithms, Advanced Eng. Inf. 19 (2005) 43-53.

[13] Clerc M. Particle Swarm Optimization. ISTE Ltd, UK, 2006.

[14] S.I. Stoliarov, R.N. Walters, Determination of the heats of gasification of polymers using differential scanning calorimetry, Polymer Degrad. Stab. 93 (2008) 422-427.

[15] J. Li, S.I. Stoliarov, Measurement of kinetics and thermodynamics of the thermal degradation for non-charring polymers, Combust. Flame 160 (2013) 1287-1297.

[16] M. Janssens, Thermo-physical properties of wood for pyrolysis models, Australia, 1994.

[17] M.J. Spearpoint, J.G. Quintiere, Predicting the piloted ignition of wood in the cone calorimeter using an integral model, Combust. Flame 123 (2000) 308-324.

[18] B. Shartel, M. Bartholdi, U. Knoll, Some comments on the use of cone calorimeter data, Polymer Degrad. Stab. 88 (2005) 540–547.

[19] R.H. White, Analytical Methods for determining fire resistance of timber members, In: SFPE Handbook of Fire Protection Engineering, Third Ed., pp. 4-257 – 4-273, NFPA, 2002.

Development of the Controlled Atmosphere Cone Calorimeter to Simulate Compartment Fires

Irshad A.[1], **Andrews G.E.**[2,]***, Phylaktou H.N.**[2], **Gibbs B.M.**[2]

[1] *University of Engineering & Technology, Lahore, Pakistan*
[2] *University of Leeds, School of Chemical and Process Engineering, Leeds, West Yorkshire, UK*
**Corresponding author's email:* profgeandrews@hotmail.com

ABSTRACT

The cone calorimeter with the controlled atmosphere compartment was used to control the fire air ventilation and to simulate the behaviour of materials in compartment fires, with rich burning under post flashover conditions. The standard cone calorimeter with controlled atmosphere design has to be improved, by compartment wall insulation, to reduce heat losses which reduced the fire temperature. Heat losses from the test section to the water cooled load cell were shown to be significant and the test specimen was insultated from the support. A chimney was added to the cone outlet to enable the measurement of the mean composition of the raw discharge gases. A method was developed for determining the mean gas sample and to prevent back flow of external air. This improved design was used to create under ventilated fires with pine wood where the equivalence ratio was controlled by the air flow into the compartment. These modified procedures for the cone calorimeter greatly extend its usefulness in material testing to conditions close to those encountered in post flashover compartment fires.

KEYWORDS: Compartment fire, cone calorimeter, ventilation, toxicity.

INTRODUCTION

The testing of fire materials for heat release rate (HRR) and visible smoke production has used the freely ventilated cone calorimeter for many years [1, 2]. The development of the cone calorimeter to simulate a compartment fire is detailed in this paper, using the controlled atmosphere version of the cone calorimeter [2, 3], coupled with direct sampling of the exit gases from the fire to determine fire raw gas toxic gas emissions. The controlled atmosphere modification to the cone calorimeter involves enclosing the fire test section in an air sealed box with the air for combustion controlled so that the fire equivalence ratio can be controlled. Originally, the controlled atmosphere calorimeter was developed for combustion testing in the vitiated atmosphere that occurs in the later stages of fires [3]. However, the equipment can equally well be used to simulate ventilation controlled fires by metering the air flow to the fire compartment and this equipment as used in the present work is shown in Fig. 1. This paper follows the development of the equipment for the primary HRR (PHRR) measurement and toxic gas emissions. Three major problems have to be solved:

1. Heat losses to the compartment walls that reduced the fire temperature;
2. Heat losses from the sample holder downward to the water cooled load cell;
3. Oxygen back flow down the chimney so that the raw mixture appeared to be lean when a metered rich burning condition had been set up with the air flow control;
4. Obtaining a mean gas sample at the chimney outlet, as the chimney gases were not well mixed.

Proceedings of the Ninth International Seminar on Fire and Explosion Hazards (ISFEH9), pp. 1066-1077
Edited by Snegirev A., Liu N.A., Tamanini F., Bradley D., Molkov V., and Chaumeix N.
Published by Saint-Petersburg Polytechnic University Press
ISBN: 978-5-7422-6498-9 DOI: 10.18720/spbpu/2/k19-90

Stec and Hull [3] have claimed that the cone calorimeter is an unrealistic test method for toxic gas analysis as it uses diluted samples where post fire oxidation of the primary fire products from the cone could occur. However, there is a criticism that could be made of all current fire behaviour material testing techniques, all of which dilute the sample with entrained air to avoid water condensation of the fire product gases if cold gas sampling is used. This includes the furnace test method for toxic gas measurements that Stec and Hull favour [3]. Dilution of the fire products gases can be avoided if heated gas sampling systems are used and heating toxic gas analysers are used so that no dilution is necessary as the water vapour is kept in the gas phase in the hot sample and no post fire oxidation of the fire products can occur [4]. To achieve direct raw gas analysis of the products of the cone calorimeter test specimen fire a chimney was fitted to the cone heater outlet and the hot discharge gases from the primary combustion was sampled directly [4] with heated sample lines, filters and pumps.

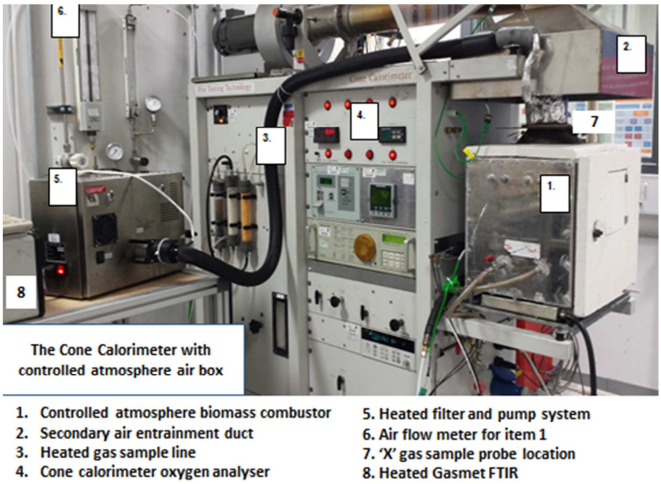

Fig. 1. Cone calorimeter with the controlled atmosphere campartment around the test section.

The controlled atmosphere fire compartment with oxygen analysis in the discharge gases can be used to determine the PHRR with the main cone calorimeter determining the total HRR (THRR). This enables any secondary oxidation outside the compartment fire to be determined, so that the concerns of Stec and Hull [3] in regard to post primary fire oxidation can be quantified. The key problem areas that have to be solved were: how to obtain a mean gas sample, with no external air dilution, at the exit from the cone heater; how to minimise the heat losses so that the temperature of the fire was not unrealistically low; how to determine the PHRR from the raw undiluted hot gases from the cone and how to keep the load cell from overheating.

EXPERIMENTAL EQUIPMENT

The cone calorimeter that was used is shown in Fig. 1. It had a sealed enclosure box around the test specimen. This was a 38 cm deep, 30 cm wide and 33 cm high air sealed box. This enclosure box had a opening sealed door with a glass window for observation of the fire flame throughout the test. This box had a metered air flow, using a variable area flowmeter, so that the equivalence ratio, Ø, of the fire could be controlled. The test fire load was supported on a load cell that determined the mass burning rate. The load cell was calibrated using reference weights before and after each test and was stable. The load cell was water cooled using a water cooled insert plate that was not fully effective.

There was a consistent problem of overheating the load cell during tests and the load cell ceased to operate if overheated. This load cell problem was caused by conduction of heat from the test fire down the support stem to the load cell and this showed that the fire temperature was lowered by this downward heat loss from the base of the material being tested.

The fire load was five sticks of pine construction wood with 20mm side square cross section, 100mm long placed in the 100mm square test section of the cone calorimeter, Only the top surface of the specimen was exposed to the cone radiation and air was only available at that surface. Type K mineral insulated thermocouples 2 mm below the wood surface were used to determine the temperature of the wood. Primary air was supplied to the compartment from two pipes in the bottom of the compartment. The air flow has been expressed in the results as flow per surface area of the test specimen, g/(m^2s). The sample was exposed to the conical heating of the cone calorimeter at 50 and 70 kW/m^2. It was found that 70 kW/m^2 resulted in the load cell overheating and this indicates that there were significant heat losses through the supporting metal rod to the water cooled load cell enclosure. At 50 kW/m^2 there were reduced problems with load cell overheating.

To determine the heat release and toxic gases from the restricted ventilation cone calorimeter a 75 mm internal diameter chimney 210 mm high was added to the discharge from the central 80 mm hole in the cone heater outlet. Obtaining a mean gas sample from the chimney was problematic and the development of a reliable method is discussed in this paper. The hot raw gas sample from the chimney was pumped via a PTFE tube inside a heated sample line to a heated filter and pump assembly and then via a further heated line to a heated Gasmet CR-series FTIR spectrometer. The temperature of the heated filter, pump, and heated line to and from the pump was maintained at 180 ^oC to keep the volatiles in the gas phase, so that the composition of the gas was determined correctly with no sample system losses of hydrocarbons [4].

The Gasmet CR 2000 FTIR was a purpose built portable multicomponent gas analyser that has UK Environmental Agency MCERT approval for legislated flue gas composition measurements. It was calibrated by the manufacturer for 60 gaseous species. This FTIR has been used for in vehicle real world exhaust gas measurement as well as in large scale compartment fires [4-6]. This analyzer uses a liquid nitrogen cooled MCT (mercury-cadmium telluride) spectrometer detector that enables the resolution of 8 or 4 cm^{-1} and gives 0.3 – 2 ppm minimum detection limits, depending on the gas. As it is fully heated it measures the total water vapour present in the sample and this is used to convert the dry oxygen measurement in the chimney gases to a wet concentration prior to the oxygen consumption calorimetry calculation of HRR. The oxygen analyser was a Servomex paramagnetic oxygen analyser and this was placed in the outlet of the hot FTIR with an ice bath water condenser followed by a silica gel water vapour absorber to dry the sample prior to oxygen analysis. The recorded FTIR sample spectra were analysed using Gasmet Calcmet software. Calcmet can analyse the sample for more than 50 components. However, it is not recommended to analyse more than 50 components at one time for the best accuracy of analysis. The analysis was based on detemining the most important gases present and then optimising the calibration for these gases. H_2 is not absorbed by infrared and cannot be detected by FTIR. It was calculated from the water gas shift reaction, as in equilibrium with the CO measurements.

RESULTS AND DISCUSSION

The initial fire tests showed a number of problems, as summarised in the Introduction. Firstly, the heat losses from the metal compartment walls were significant and if a small scale test was to be representative of a compartment fire it should not have excessive heat losses so that the fire temperature was too low. The conditions inside the compartment should be as adiabatic as possible. Modifications to the base equipment were applied step by step, by identifying the possible reasons for the problems and then developing solutions. Tests were performed in the following development order.

Configuration 1: the compartment in its original baseline state with the chimney on the top of the cone heater outlet from the compartment for raw hot gas sampling using a single-hole probe.

Configuration 2: insulation of the enclosure box walls and door using 20mm thick ceramic fibre board.

Configuration 3 used 20mm thick ceramic fibre insulating board below the fire test material to reduce conduction heat losses down the metal support rod to the water cooled load cell. A thicker wood sample (40mm) was also shown to achieve the same effect, as the extra wood thickness acted as an insulation for the surface fire above it.

Configuration 4 used a grid plate type restrictor to prevent backflow of air into the chimney.

Configuration 5 added a mean multi-hole gas sampler to achieve a reliable mean composition from the primary compartment fire. Several designs were investigated relative to the base line single hole.

The final design with all the above changes incorporated was used to investigate the toxic emissions from rich combustion for pine wood fires.

Configuration 1: initial setup results

The original configuration had metal compartment walls and a single point gas sample probe in the chimney. The maximum possible HRR based on the air flow was the air flow in g/(m^2s) times the heat release per mass of air, which is 3.05 MJ/$kg_{air,}$ or 13 MJ/kg of oxygen. The metered air to fuel flow ratio by mass, A/F, for the pine wood samples were determined from the measured constant air flow and the measured rate of mass consumption of the biomass. This was then converted to a metered equivalence ratio, $Ø_m$, using the stoichiometric A/F for the pine wood of 5.7 on a dry ash free basis (daf). This metered equivalence ratio, $Ø_m$, is shown as a function of time in Fig. 2a & b for a range of air flows and for 20mm thick pine wood (a) and 40mm (b). Fig. 2 shows that the aim of this work, to create controlled rich burning conditions, was achieved. Fig. 2a also shows that changing the air flow for pine at 50 kW/m^2 radiant heat flux decreased the $Ø_m$ from about 2.5 at the lowest air flow to 1.3 at the highest air flow. Fig. 2a also shows for 9 g/m^2s and 70kW/m^2 that $Ø_m$ was richer for Ash than for pine and this was due to the different stoichiometric A/F for Ash (6.0 daf) and its lower volatile content. All the results in Fig.2 show that there was an initial fast mass burn rate followed by a steady state burner phase between about 200 – 600s and the average mass burn rate, HRR and toxic emissions over this period were used in the later plots as a function of $Ø_m$. In the later stage of the fire there was a char burn out phase that had a much lower mass loss rate.

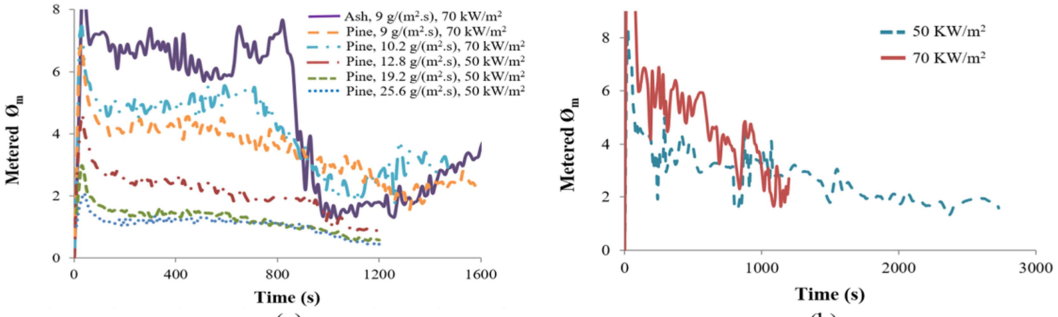

(a) (b)

Fig. 2. Metered equivalence ratio ($Ø_m$) for tests with (a) 20 mm thick wood load (5 sticks) (b) 40 mm thick wood load (10 sticks, 2 layers of 5 sticks) at 12.8 g/(m^2·s).

Figure 2b shows that for the 40 mm thick pine the influence of the radiant heating (50 to 70 kW/m^2) was significant at constant air flow, with richer mixtures due to more volatile release at the higher temperatures associated with high radiant flux. Comparison of the influence of the pine wood thickness in Fig. 2a shows that, for 40 and 20 mm wood thickness at 50 kW, with the same air flow of 12.8 g/(m^2·s), the steady state portion of the fire between 500 and 1000s $Ø_m$ was 3 for 40 mm pine wood and Ø = 2 for 20 mm thick pinewood. This shows more volatiles were released for the thicker wall giving richer overall mixtures. The thicker wood self insulates the top surface so that there are lower heat losses with the 40 mm wood thickness. This was why ceramic fibre board was used as an insulation to reduce downward heat transfer to the water cooled the load cell and the effect was the same as using thicker pine.

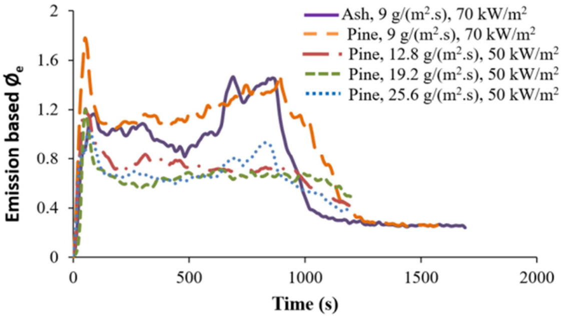

Fig. 3. Equivalence ratio $Ø_e$ by carbon balance for tests with 20 mm thick wood load.

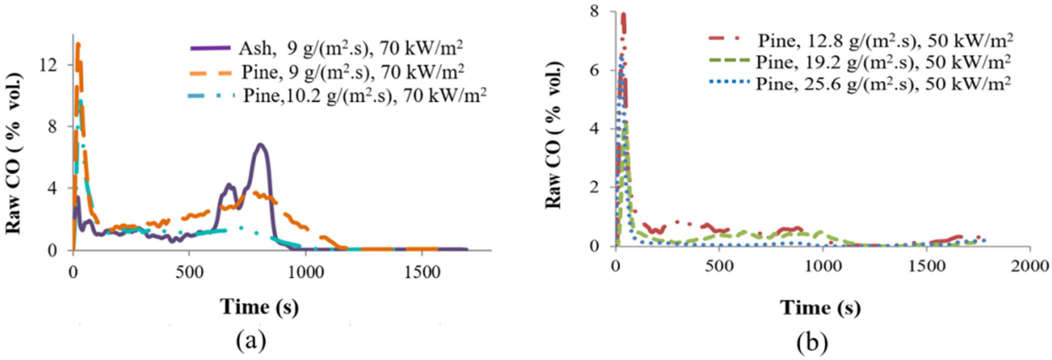

(a) (b)

Fig. 4. % CO from primary burning zone for 20 mm thick wood load (a) 70 kW/m^2 (b) 50 kW/m^2.

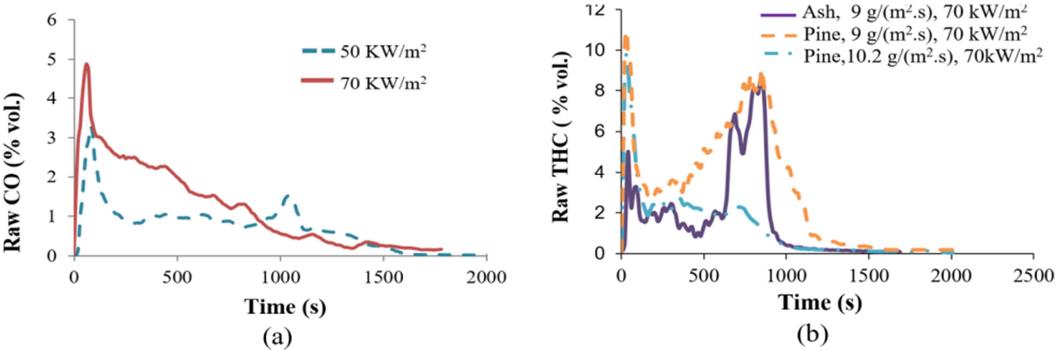

(a) (b)

Fig. 5. (a) % CO from primary burning zone for 40 mm thick wood load at air flow 12.8 g/(m^2·s);
(b) THC emissions during gasification of 5 wood sticks at heat flux 70 kW/m^2.

Figure 3 shows the single tube chimney emissions based (carbon balance) equivalence ratio, $Ø_e$, for the tests with 20 mm thick wood load. This shows that all the tests were lean in the steady state flame combustion phase, except for pine wood after 600 s at 70 kW/m^2. So it was concluded that in spite of the fact that box was provided with the limited air flow that should have provided rich combustion, as shown in Fig. 3, actual conditions appeared to be lean inside the compartment. However, this could be due to the single point gas sampling probe not giving a mean gas sample and this problem is addressed later. However, the very large difference between Fig. 2 and Fig. 3 shows that the task of getting a mean gas sample was essential in the development of this method.

The CO concentration, in the raw single point sample from the outlet from the rich burning zone, is shown in Fig 4. It can be seen in Fig. 4a that in all tests with a heat flux of 70 kW/m^2, the peak CO emissions occurred during the first stage of combustion, when the mixture was richer, as shown in Fig. 2a. In the 500 – 1000 s steady state combustion period the CO was higher (1%) for the 70 kW/m^2 radiant heating than the 50 kW/m^2 heating (0.5%), because the mixture was richer. In the 70 kW/m^2 tests with an air flow of 9 g/(m^2·s) CO increased due to the richer mixtures, as shown in Fig. 2. In tests with a heat flux of 50 kW/m^2 Fig. 4b shows that CO was reduced to less than 1% for the steady state fire, with almost 0% with an airflow 25.6 g/(m^2·s). This was due to the leaner mixtures shown in Fig. 2a as the air flow was increased. For 40 mm thick wood the CO was higher in the test with heat flux 70 kW/m^2, as shown in Fig 5a due to the richer mixture shown in Fig. 2b. The very high hydrocarbon emissions in Fig. 5b indicate conditions were far from adiabatic equilibrium as THC should be zero at equilibrium.

Configuration 2: Tests with insulation of the box and test sample of cone calorimeter

The top surface and the door of the compartment was insulated from the outside, while the rest of the compartment was insulated from the inside. The compartment wall insulation was 25 mm thick superwool insulation board. After insulation, the internal dimensions of the compartment were 330 mm long, 275 mm wide and 305 mm high. Tests were conducted at 50 kW/m^2 with an air flow of 12.8 g/m^{2}s to compare with previous test without insulation. It was found that the average value of mass loss rate was increased from 0.05 to 0.075 g/s, and the average metered $Ø_m$ from 2.5 to 3.5 after the insulation of the box.

Figure 6a shows that the oxygen levels were reduced with wall insulation as a result of the richer combustion, which was also found for $Ø_e$ as shown in Fig. 6b. The leaner $Ø_e$ after 1000s and the related increase in oxygen was due to the end of flaming combustion and the onset of char combustion at a much lower HRR. The residual O_2 with rich combustion was due to the combustion inefficiency. However, it was considered that the main problem was that the single hole gas sample tube was not obtaining a mean gas sample.

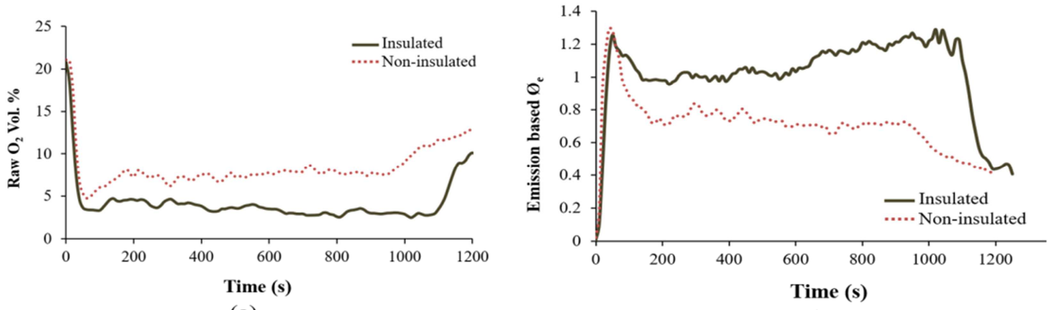

(a) (b)

Fig. 6 Heat flux 50 kW/m^2, air flow 12.8 g/(m^2·s): (a) O_2 % vol. vs time; (b) $Ø_e$ vs time.

The impact of insulating the controlled atmosphere volume walls was to increase the CO and THC emissions due to the richer mixtures, as shown in Fig. 7.

The reduction of heat losses by insulating the compartment should have increased the temperature of combustion. This was investigated using thermocouples inserted 2mm from top and bottom surfaces in the 40mm thick wood load with air flow 12.8 g/(m^2.s) at 70 kWm^2. Comparison was made for wood temperatures with and without the insulated compartment. Fig 8a shows that the compartment insulation increased the top thermocouple temperature by about 50^{o}C. The emissions of CO are shown in Fig 8b which shows that the CO was higher with insulation of the compartment due to the richer mixtures. At 600s only the top wood layer was partly burned and the bottom layer was not touched by the fire and acted as an insulating layer to the top 20mm wood.

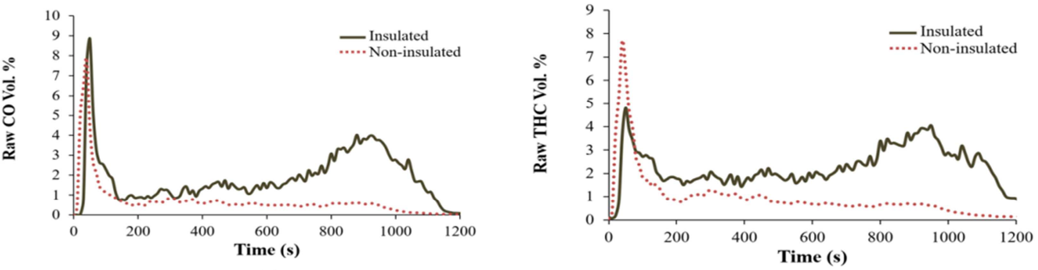

(a) (b)

Fig. 7. Heat flux 50 kW/m^2, air flow 12.8 g/(m^2·s): (a) CO % vol. vs time; (b) THC % vol. vs time.

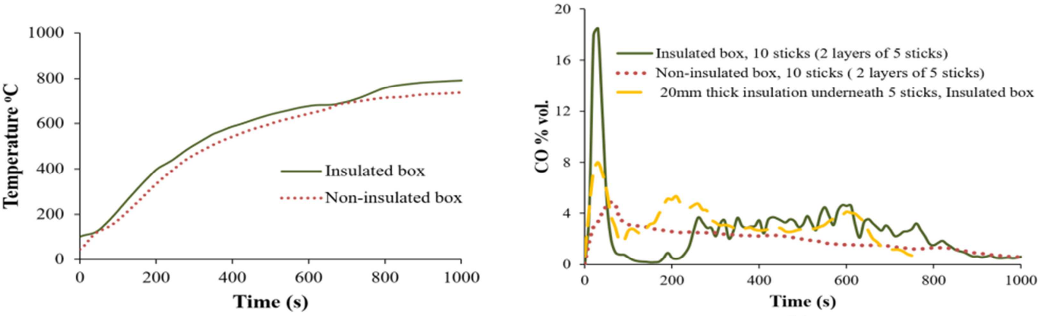

(a) (b)

Fig. 8. (a) Comparison of temperature vs time for 40 mm thick pine wood (2 layers of 5 sticks) 5mm from top surface with and without insulation at 70 kW/m^2 airflow 12.8 g/(m^2.s) (b) Comparison of % CO with different testing configurations including insulation of box and 20mm thick insulation under pine layer.

Configuration 3: Insulation of the fire load to reduce heat losses to the load cell support

In order to check this explanation another experiment was performed at same conditions of heat flux and air flow (insulated box, 70 kW/m^2, 12.8 g/ (m^2.s) with 5 pine wood sticks with an insulation of superwool board 20mm thick under the 20mm thick wood so that the total bed thickness was 40mm. The CO emissions are shown in Fig 8b and in the steady burning phase were higher than the test of 10 pine sticks (2 layers of 5 sticks, insulated box). This indicated richer mixtures due to the reduced heat losses from the test specimen to the load cell. This shows that test specimens should be insulated underneath in the cone calorimeter.

Configuration 4: Variation of gas sampling techniques to obtain better mixed products

The gas sampling for all the above tests used a single hole probe inserted into the centreline of the chimney 60 mm above the chimney inlet. Initial work with this simple gas sampling system had two problems: the carbon balance did not give the same Ø as that metered and was much leaner, as shown above by comparing Figs. 2a and 3. Part of this problem was that oxygen was present in the sample when rich mixture combustion was used and the combustion efficiency (CO and THC emissions energy content) was relatively low, whereas it should have been high for rich mixtures. The analysis assumed that the fire product gases were mixed after flowing through the cone heater and into the chimney. It also assumed that no air from outside the chimney could be entrained back into the chimney to dilute the product gases and oxidise some of them. Both of these assumptions were incorrect. Part of the oxygen entrainment problem was that the FTIR sample flow rate was 4 lpm which was significant relative to the compartment air flow, which at its lowest was only 6 lpm.

The problems were inter-related: there was significant oxygen in the gas sample and the sample was not mixed, as moving the one tube sample probe changed the sample composition. The solution to these problems was separate and the first to be dealt with was the issue of getting a better mean gas sample. This was done first as the oxygen problem could have been contributed to by unmixedness. All the initial tests were to improve the gas sample as a measure of the mean composition and the problem of the oxygen dilution by reverse suction by the gas sample probe was investigated last. In retrospect it would have been better to investigate the entrainment of air from the chimney exit first as this was found to be the dominant problem.

The following tests were carried out in addition to the tests performed with the original single hole probe .

1. Traverse of a single hole sample tube.
2. Traverse of the single hole sample tube with a grid plate mixer at the entry to the chimney.
3. Four hole sample probe with grid plate mixer at the entry to the chimney.
4. 76mm diameter 20 hole ‘X’ probe at the bottom of the chimney and no inlet grid plate. The 20 hole gas sampler was mounted in its own supporting wall and flanges to connected to the chimney and this added 48mm to the total chimney length which increased to 258mm.
5. A chimney exit backpressure grid plate was added with 90% blockage and the 20 hole ‘X’ gas sample probe was located at the bottom of the chimney. This immediately cured the problem and sensible gas analysis results were achieved.

All the above tests were performed with the insulated compartment and 20mm insulation below the test fuel at an air flow 9 g/(m^2.s) and a heat flux of 70 kW/m^2.

An attempt to improve the mixing in the chimney was made by placing a four hole grid plate at the base of the chimney, to generate flow turbulence and mixing. Radial single point traverses were carried out with this configuration. A single hole gas sampling probe was traversed across the chimney starting from the wall of the chimney. The traverses were carried out during the near steady state combustion period between 300 and 800s, as shown in Figs. 1-3. The probe was held for 45-50 s at each location. The % CO and the emission based equivalence ratio $\O_e$ by carbon balance is shown as a function of radial distance for single hole probe in Fig 9. This shows that the chimney was not well mixed and was rich in the centre and lean at the chimney wall.

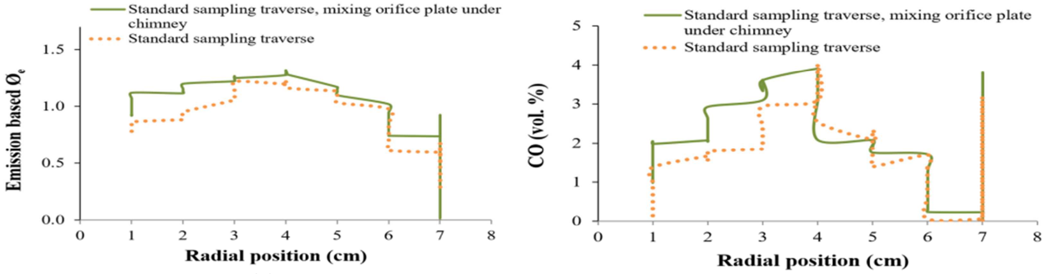

(a) (b)

Fig. 9. Traverse with single hole orifice plate with and without mixing orifice plate (a) Emission based $\O_e$ vs distance (b) % CO vs distance.

All the methods to achieve a better mixed sample are compared in Figs. 10 and 11. They will not be discussed in detail as only configuration 5 achieved better mixing. The four hole sample probe was also equally ineffective. All this was because the main problem was air being drawn from the chimney exit into the chimney and promoting oxidation of the gases from the rich fire combustion, which was why the CO and THC emissions were lower than expected for rich mixtures and why the equivalence ratio based on carbon balance was so much lower than that metered in Figs. 2 and 3. Using a 20 hole mean gas sampler on its own at the base of the chimney was also equally ineffective, with very high oxygen levels. This was due to the static pressure drop across the X probe causing the static pressure in the chimney to fall and more air to be entrained into the chimney.

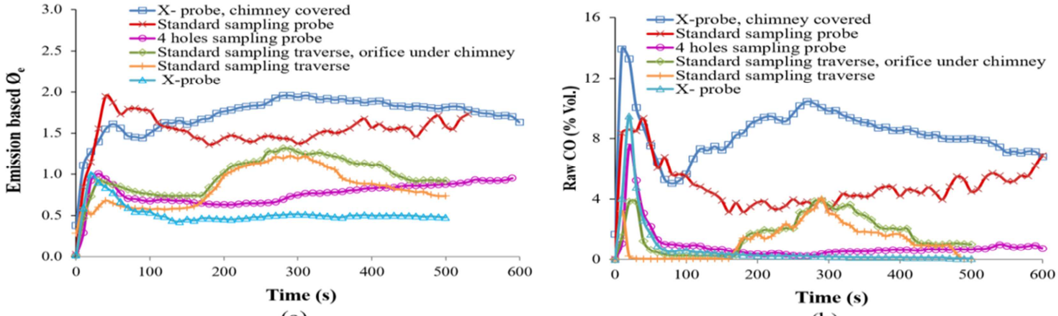

(a) (b)

Fig. 10. Tests with different gas sampling methods at heat flux 70 kW/m^2, air flow 9 g/(m^2·s): (a) emission based $Ø_e$ vs time; (b) CO % vol. vs time.

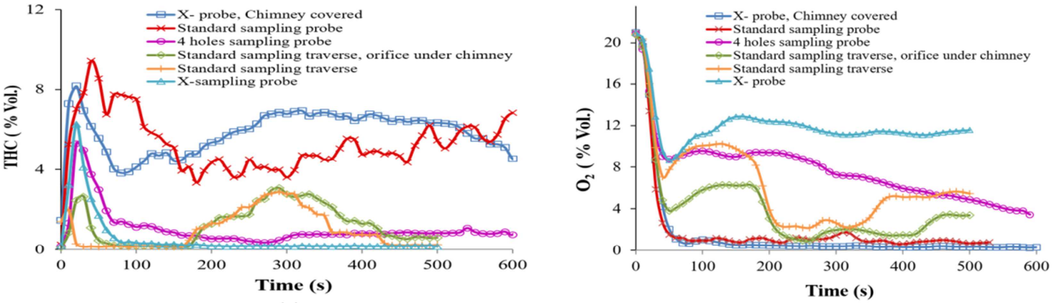

(a) (b)

Fig. 11. Tests with different gas sampling methods at heat flux 70 kW/m^2, air flow 9 g/(m^2·s): (a) THC vs time; (b) O_2 % vol. vs time.

To prove that air entrainment from the exhaust chimney was the problem, tests were carried out with N_2 at the same flow rate as the air. The standard single hole gas sample probe was used. It was found that even at high flow rates of nitrogen, the O_2 analyser downstream of FTIR was reading 10% O_2. This showed that air was entering the sampling system from the exit of the chimney. To prevent this, a grid plate with 90% restriction of the total chimney exit area was placed at the chimney exit. This 90% chimney exit blockage was found as the minimum required to achieve 0% oxygen when the metered equivalence ratio was very rich. This ensured that the static pressure in the chimney was always greater than atmospheric pressure, so that back flow of air into the chimney was prevented. The O_2 analyser read zero with nitrogen as the compartment flow and was zero after the initial fire at 150 s in Fig. 11b. The results in Figs. 10 and 11 show that the next best gas sampling system was the original single hole probe 60 mm above the cone outlet. Essentially the other gas sample probes had been located further up the chimney and so encountered more external air entrained into the chimney.

Fig 10a shows that the impact of the chimney exit grid plate was to make the mean mixture much richer, as there was now no backflow of air. By co-incidence the mean mixture was close to that for the central single hole sampling probe without an exit plane orifice. The CO and THC were high and the oxygen near zero after 150 s, all as expected for rich mixtures. However, there was still a big difference between the metered equivalence ratio in Fig. 2 and that by carbon balance in Fig. 10a. For example in Fig 10a at 9 g/(m^2·s) and 70 kW/m^2 Ø was 1.9 at 300 s using the developed 20 hole gas sampler with 90% blockage grid plate at the end of the chimney. In Fig. 2a at the same test conditions Ø was 4.5, much richer that that based on carbon balance. The problem was due to the use of the stoichiometric A/F of pine for the equivalence ratio definition. However, there is no such gas with the composition of wood and the equivalence ratio should be based on the stoichiometry of the gases evolved at a particular time in the fire. In related work nitrogen flows have been used instead of air with the radiant heater on, to determine the composition of the volatiles as a function of time. This will enable the actual gas equivalence ratio to be determined.

Performance of the developed system for compartment fires using the cone calorimeter

The developed experimental methodology included insulation of the walls and door of the compartment around the cone calorimeter test section, insulation between the test sample and the support, 210mm long 76mm diameter cone exit chimney with a 90% blockage grid plate on the top of the chimney and a 20 hole 'X' gas sample probe at the bottom of the chimney (which added 48mm to the chimney height). Pine wood tests were performed at various air flows to generate a range of HRR and equivalence ratios, $Ø_m$. The $Ø_m$, CO, THC were averaged over the steady state rich burning period from 300-500s in the fire, this omitted the initial fire growth period and the final char burn out period.

The variation of the average steady state CO with average $Ø_m$ is shown in Fig. 12a and compared with the predicted equilibrium CO. The maximum measured concentration of CO was 15% and was achieved with an air flow of 19.2 g/(m^2.s) with an equivalence ratio of 2.8. The trend of the experimental CO follows the same shape as equilibrium CO from $Ø_m$ 1.6 to 4.5, at $Ø_m$ = 6, another peak value of % CO was observed and was not following the equilibrium trend. The experiments were repeated 3 times at these conditions, but the same results CO were obtained.

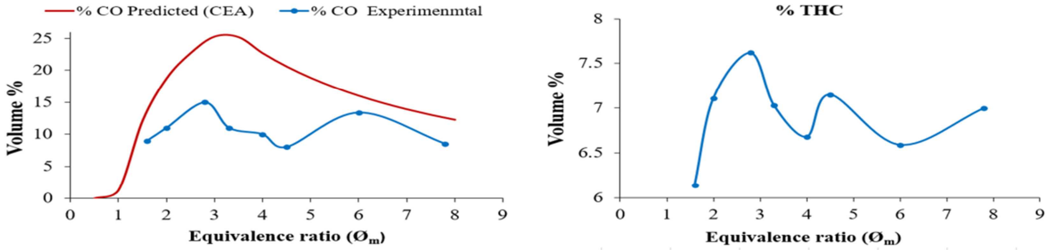

(a) (b)

Fig. 12. (a)Variation of experimental and predicted (equilibrium) CO concentration with $Ø_m$; (b) Variation of experimental % THC with $Ø_m$.

The difference in the adiabatic equilibrium CO and experimental CO shows that equilibrium was not achieved, due to remaining heat losses that had not been eliminated. This produced rich burning conditions well away from adiabatic equilibrium. This resulted in high hydrocarbons, as shown in Fig. 12b, when there should be no hydrocarbons at equilibrium. These hydrocarbons represent a loss of energy conversion efficiency. The CO and THC would burn in the second stage combustion on discharge from the chimney. This is equivalent to the flames seen exiting open windows from compartment fires.

An equilibrium gas that was not measured was hydrogen and this was calculated from the measured CO using the water gas shift equilibrium method. If the enthalpy of the gases is calculated from the composition and the CV of each individual gas and the sensible heat in the temperature of the gases in the chimney is added, then the hot gas efficiency (HGE) of the compartment combustion can be calculated. This is shown in Fig. 13a as a function of $Ø_m$. The average maximum high heating value was 14.95 MJ/kg at $Ø_m = 2.8$. However, the thermal efficiency was high over the range $Ø_m$ 1.5 – 2.8. Figure 13a was based on the steady state from 300 to 500 s. The primary heat release as a % of the total is shown in Fig. 13b as a function of $Ø_m$. This shows a decreasing primary heat release proportion as $Ø_m$ increases. The rich Ø are backdraft conditions in compartment fires, as this secondary combustion would occur if the door was opened to the primary rich fire and the fire combustion would propagate quickly in the air outside the door.

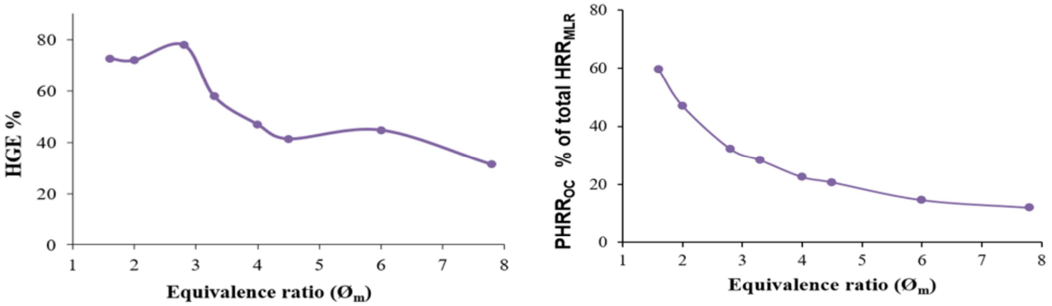

Fig. 13. (a) HGE as a function of $Ø_m$ (b) Primary compartment % of the total heat release as a function of $Ø_m$.

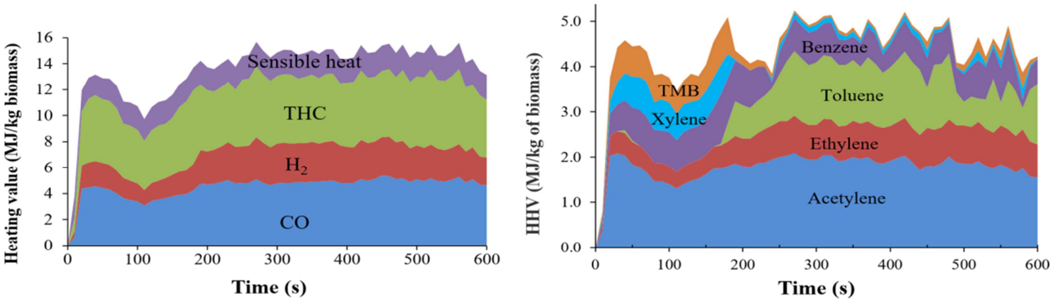

(a) (b)

Fig. 14. (a) Heating value as function of time for air flow 19.2 g/(m^2.s), $Ø_m = 2.8$ (b) Heating value proportion of hydrocarbon gases.

Fig. 14 a. shows the contribution of CO, H_2, hydrocarbons and sensible heat to the higher heating value of the products of combustion. The peak energy gives a thermal efficiency of 80%. The total hydrocarbons account for over 35% of the heating value of the gas as shown in Fig. 14 b. The major components of the hydrocarbon gases from an energy content viewpoint were acetylene, ethylene, toluene, benzene, xylene (sum of o-, m- and p-xylene) and trimethyl benzene (TMB) (sum of 1,2,3-, 1,2,4- and 1,3,5-TMB). These would all burn efficiently outside the compartment.

CONCLUSIONS

The cone calorimeter with the controlled atmosphere compartment was developed to reliably simulate the behaviour of materials in compartment fires with rich burning, under post flashover conditions. However, the baseline equipment had to be improved to enable the measurement of the composition of the raw discharge gases from the compartment outlet through the 76mm exit to the cone. This was done by adding a major chimney so that a mean gas sample could be made. Air entrainment into the chimney was a problem and this was controlled by placing a 90% blockage grid plate at the exit from the chimney. Various ways of obtaining a mean gas sample was investigated and a 20 hole 'X' probe was the best, located at the bottom of the chimney. The original compartment had excessive heat losses and these were reduced by wall thermal insulation. Also heat losses from the test section to the water cooled load cell were significant and the test specimen was insulated from the support. This system was shown to give rich burning, with the equivalence ratio controlled by the air flow into the compartment. The gases emerging from the chimney were shown to contain up to 80% of the energy in the fuel, depending on the equivalence ratio. For very rich mixtures only 20% of the energy in the fuel was release in the primary compartment fire and the rest was released in the secondary fire. This is the energy that forms backdraft or in compartment fires with a window open is the energy in the visible external flame. This shows that the modified procedures for the cone calorimeter greatly extend its usefulness in material testing to conditions close to those encountered in post flashover compartment fires.

REFERENCES

[1] BS ISO 5660-1:2015: Reaction-to-fire tests. Heat release, smoke production and mass loss rate. Heat release rate (cone calorimeter method) and smoke production rate (dynamic measurement). British Standards Institute.

[2] V. Babrauskas, R.H. Harris, E. Braun, B. Levin, M. Paabo, R.G. Gann, The Role of Bench Scale Test Data in Assessing Real-Scale Fire Toxicity, NIST Technical Note 1284, 1991.

[3] A.A. Stec, T.R. Hull, Eds., Fire Toxicity, Woodhead Publishing Ltd, Cambridge, 2010.

[4] A.A. Alarifi, H.N. Phylaktou, and G.E. Andrews. Heated Raw Gas Sampling with Heated FTIR Analysis of Toxic Effluents from Small and Large Scale Fire Tests, In: 10th Asia-Oceania Symposium on Fire Science and Technology, 2015, Tsukuba, Japan, IAFSS.

[5] H. Li, K. Ropkins, G.E. Andrews, B. Daham, M. Bell, J. Tate, G. Hawley, Evaluation of a FTIR Emission Measurement System for Legislated Emissions Using a SI Car, In: SAE International, 2006.

[6] B. Daham, G.E. Andrews, H. Li, R. Ballesteros, M.C. Bell, J. Tate, K. Ropkins, Application of a Portable FTIR for Measuring On-road Emissions, In: SAE International, 2005.

[7] E.M. Fitzpatrick, A.B. Ross, J. Bates, G. Andrews, J.M. Jones, H. Phylaktou, M. Pourkashanian, A. Williams, Emission of Oxygenated Species from the Combustion of Pine Wood and its Relation to Soot Formation, Proc. Saf. Environ. Prot. 85 (2007) 430-440.

[8] Z.A. Zainal, R. Ali, C.H. Lean, K.N. Seetharamu, Prediction of performance of a downdraft gasifier using equilibrium modeling for different biomass materials, Energy Convers. Manage. 42 (2001) 1499-1515.

Limitations of Ignition Theory for Transient Exposure. Ignition of Solids Exposed to Radiation from a Compartment Fire

Santamaria S.*, Hadden R.M.[1]

The University of Edinburgh, School of Engineering, Edinburgh, UK
**Corresponding author's email: S.Santamaria-Garcia@ed.ac.uk*

ABSTRACT

The piloted ignition of thermoplastic polymers exposed to transient irradiation is investigated. Previous research measured the radiation emitted through a full-scale, post-flashover compartment fire using Thin-Skin Calorimeters. This data is used in the present study to define the Incident Heat Flux time series to which the samples are exposed. Polymethyl-methacrylate and Polyamide 6 were used. A total of 20 experiments were performed in the Fire Propagation Apparatus. The temperature was recorded at depths of 4, 8, 12 and 16 mm from the surface. A regression analysis is used to estimate the temperature profile at each time step. The Net Heat Flux absorbed by the sample at the surface was calculated using Fourier's law. Conductive losses through the back face are also calculated. Assessing the evolution of the Net Heat Flux and the conductive losses, we found that under transient irradiation, there is a large uncertainty in the time to ignition of Polyamide samples as the surface phenomena introduces a non-negligible uncertainty which cannot be evaluated in current formulations. It was shown that surface phenomena affect mass transfer considerably, but has a lesser impact on the heat transfer process. An approach to study ignition based on controlling the absorbed energy is proposed for samples in which surface phenomena are significant.

KEYWORDS: Ignition, net heat flux, flammability.

INTRODUCTION

As the practice of fire safety engineering progresses towards a performance based design philosophy [1], it becomes ever more important to assess the definitions which underpin current design criteria. One such concept is the minimum separation between structures, which can be considered an extension of compartmentation. It is paramount to contain the fire to its room of origin and prevent any spread within the building or to nearby structures.

The current methodology used in the UK to assess the separation of buildings [2] establishes a minimum distance to the boundary of the property, as a function of the dimensions of the opening and the design fuel load. This is based on work conducted by Law [3]. The methodology allows an estimation of the Incident Heat Flux (IHF) as a function of distance. A key assumption behind the commonly used minimum distance tables found in standards is that the maximum irradiation permitted on a surface should not exceed 12.5 kW/m^2, considered as the critical IHF for the piloted ignition of wood. This is based on ignition studies where timber samples were exposed to constant irradiation.

The testing framework for analysing the flammability properties of a material [4-6], as well as the classical formulation of ignition theory [7], are built on the understanding that exposing materials to a constant IHF simplifies the experimental set-up and the mathematical expressions. However, what truly drives the ignition phenomenon is the net absorbed energy, which is a function of the boundary conditions (including the IHF) as well as the properties of the material.

Proceedings of the Ninth International Seminar on Fire and Explosion Hazards (ISFEH9), pp. 1078-1087
Edited by Snegirev A., Liu N.A., Tamanini F., Bradley D., Molkov V., and Chaumeix N.
Published by Saint-Petersburg Polytechnic University Press
ISBN: 978-5-7422-6498-9 DOI: 10.18720/spbpu/2/k19-123

The net flux of absorbed energy or Net Heat Flux (NHF) is not constant in a transient heating process. Even if the solid is exposed to a constant IHF, the NHF will decrease with time as the surface temperature and hence, the surface losses, increase. Different materials exposed to the same IHF will absorb different amounts of energy and this creates a fundamental difference in the way their flammability properties are assessed.

This paper studies the ignition of two different solids exposed to transient and constant IHF curves. The objective is to analyse the impact of a transient exposure by studying the NHF and assess the suitability of ignition theory, which is based on a constant exposure. The bench-scale experiments are informed by IHF curves measured from full-scale compartment fires. By looking at the evolution of the NHF, we aim at advancing our current framework for evaluating the fire risk associated to a material.

PRIOR RESEARCH

A set of five, full-scale compartment fires was carried out to study the impact of exposed combustible (timber) linings on compartment fire behaviour. The specific aim was to analyse if self-extinguishment of the exposed timber could be observed once the imposed fuel load had burnt out. The different experiments considered different configurations of exposed timber linings. Full details of this study can be found in [8, 9]. Approximately cubic compartments of dimensions 2.72 x 2.72 x 2.77 m^3 were used, with one opening of dimensions 1.84 x 0.76 m^2. Data from three experiments presented by Hadden et al. [8] are used here. These relate to the following configurations of exposed timber: back wall and sidewall (Alpha 2), ceiling and back wall (Beta 2) and ceiling, side wall and back wall (Gamma). All other surfaces are considered to be inert.

The radiation emitted from the opening and the plume was measured using Thin Skin Calorimeter (TSC) [10] towers. TSCs consist of an Inconel disc (ϕ = 10 mm and thickness = 2 mm) embedded into the surface of a vermiculite board (100 x 100 mm^2 x 25 mm). The temperature evolution of the Inconel disc is recorded. By solving the energy balance at the control volume of the metallic disc it is possible to calculate the Incident Heat Flux. A second thermocouple measures the gas phase temperature evolution close to the disc's surface. Surface convective losses are calculated assuming free convection from a vertical hot plate. The calibration factor is calculated as a function of the disc's temperature. TSCs are calibrated using a radiant panel against results obtained with a Schmidt-Boelter gauge.

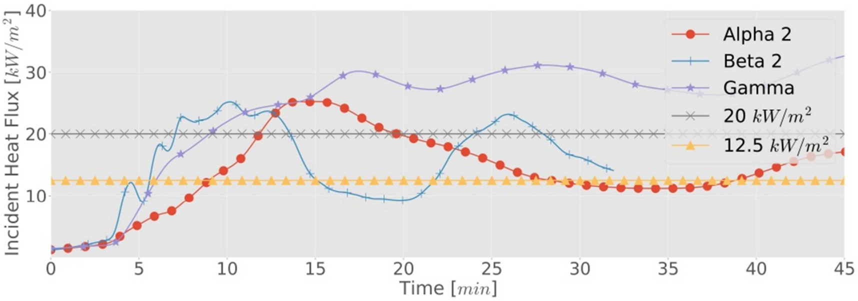

Fig. 1. Incident Heat Flux vs time for all experiments.

For this paper, we use IHF curves measured at 2 meters from the opening at a height of 1.6 meters, shown for Alpha 2, Beta 2 and Gamma in Fig. 1. The main difference between these curves is the oscillation defined by the growth/decay characteristic period of each test. All tests were terminated after 60 minutes. Figure 1 shows the IHF evolution for the first 45 minutes, as ignition testing is limited to 30 minutes. Beta 2 presents the smallest characteristic time period, where the time between peaks is 18 minutes. Alpha 2 shows a longer period of oscillation, with a slightly lower rate of increase in the IHF after flashover. Gamma shows a similar rate of increase to Beta 2 but no oscillations are observed, as an approximate steady value of 30 kW/m^2 is maintained until end of testing.

After flashover (~ 5 min for all tests), all curves show a continuous increase in the IHF perceived by the TSCs. If we assume a linear increase (constant rate of change) between flashover and the maximum IHF, the rate of change of the irradiation perceived by the TSCs is approximately 28 – 42 W/m^{2}s. This is in agreement with the values used by Santamaria et al [11] when studying the ignition of PA6 samples exposed to linearly increasing IHF.

In addition to these, constant IHFs of 20 and 12.5 kW/m^2 were used for comparison. 12.5 kW/m^2 is the commonly used critical IHF for piloted ignition of timber. 20 kW/m^2 is above PA6's and PMMA's critical IHF (CHF). The critical IHF for PMMA is 10 kW/m2 and for PA6 is 15 kW/m^2 [12]. The CHF is only defined for constant irradiation.

EXPERIMENTAL METHODOLOGY

Ignition experiments were undertaken using the Fire Propagation Apparatus [5]. This allows the heat flux incident on a sample be rapidly changed according to the values described above which cannot be achieved with other apparatus.

Samples of Polymethyl-methacrylate (PMMA) and polyamide 6 (PA6) are exposed to the five different IHF time series. Both PMMA and PA6 are thermoplastic polymers and their ignition behaviour has been studied extensively under constant IHF [13, 14]. A reduced number of studies have investigated their ignition behaviour under transient irradiation [11, 15].Samples were of dimensions 85 x 85 x 25 mm and 85 x 85 x 20 mm for PMMA and PA6 respectively. Each combination of IHF time series and material were repeated once.

Aluminium foil and two layers of ceramic paper insulation wrap the side of the samples to limit heat and mass transfer in the direction perpendicular to the IHF. Four K-type thermocouples (ϕ = 1 mm) record in-depth temperature at intervals of 4, 8, 12 and 16 mm from the surface. The samples rests on an aluminium block, measuring 90x90x20 mm, where the additional dimensions ensure that the total sample plus the insulation rest on the block. A thermal conductive paste improves heat conduction between the sample's back face and the aluminium block, and so the thermal conductive resistance is neglected. The temperature increase in the Al block is also recorded with the same type of thermocouple. Table 1 shows the material properties used for PMMA, PA6 and the aluminium block. A similar diffusion of heat process is expected for both samples, given their similar thermal diffusivities, which permits an assessment on the impact of surface phenomena on ignition.

Table 1. Material properties

Material	Thermal conductivity: *k*, W/(m·K)	Density: ρ, kg/m^3	Specific heat capacity: *c*, J/(kg·K)	Thermal diffusivity: α, m^2/s
PMMA	0.27 [12]	1190*	2090 [12]	$1.09 \cdot 10^{-7}$
PA6	0.29*	1183*	1900 [12]	$1.29 \cdot 10^{-7}$
Aluminium	205*	2707 [12]	896 [12]	-

* Data provided by the manufacturer.

A pilot flame is used, located 10 mm from the edge of the sample and at a height of 10 mm from the surface. The IHF is calibrated at the start of each experimental period using a Schmidt-Boelter gauge and a quadratic regression is used to calculate the IHF as a function of the infrared lamp supply voltage, as shown in Equation 1.

$$IHF = c_0 + c_1 V + c_2 V^2 \tag{1}$$

It is assumed that:

- the heat transfer process is one dimensional,
- the solid behaves as inert until ignition,
- all material properties are invariant with temperature,
- the temperature at the back face of the sample (x = 25 mm for PMMA or x = 20 mm for PA6) is equal to the temperature of the aluminium block,
- the aluminium block behaves as a thermally thin solid and heat losses from it to the environment are negligible.

A regression analysis is used at each time step to evaluate the temperature distribution within the solid. This allows the evolution of the absorbed energy in the solid to be calculated. In order to do this an assessment of the surface temperature is required. This is calculated from fitting a function that describes the temperature as a function of distance from the heated surface. For an inert solid exposed to a constant IHF, this function is described by Eq. (2) [7]. Where, T_0 is the initial temperature, q the IHF, h_t the total heat transfer coefficient, x the distance from the surface, α the thermal diffusivity, k the thermal conductivity, ρ the density, c the specific heat capacity and t the time. The total heat transfer coefficient (h_t) is obtained by linearizing the radiative heat losses and adding the convective losses [7].

$$T(x,t) = T_0 + \frac{q}{h_t}\left[erfc\left(\frac{x}{\sqrt{4\alpha t}}\right) - e^{\frac{h_t x}{\sqrt{\alpha}\sqrt{k\rho c}}+\frac{h_t^2 t}{k\rho c}} \cdot erfc\left(\frac{h_t\sqrt{t}}{\sqrt{k\rho c}} + \frac{x}{\sqrt{4\alpha t}}\right)\right] \tag{2}$$

Figure 2 shows a graphical representation of Eq. (2). These curves are obtained for a PMMA sample, 20 mm thick, using the properties shown in Table 1. The figure on the left shows the penetration of the thermal wave into the solid as time progresses. The figure on the right shows the effect of the linearized heat transfer coefficient on the temperature profile at t = 200 s (~ t_{ig} for PMMA when exposed to 20 kW/m^2). The total heat transfer coefficient has a considerable effect on the surface temperature but not on the thermal wave penetration (as this is determined by the thermal diffusivity).

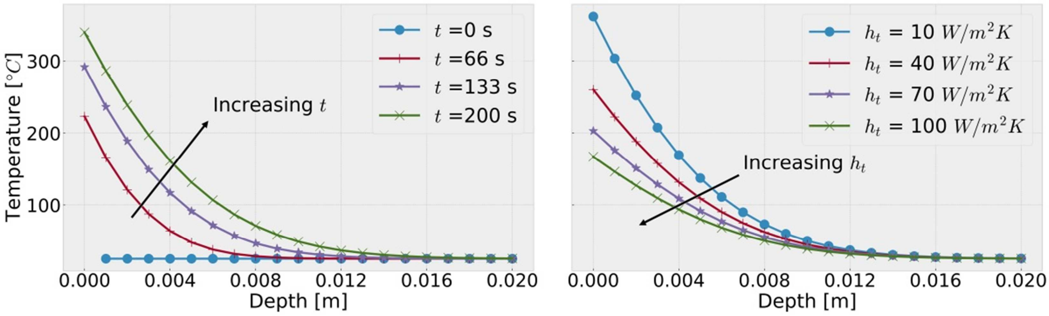

Fig. 2. Equation 2. Left: Temperature profile at different times (constant h_t). Right: Temperature profile at t = 200 s for different h_t. IHF = 20 kW/m^2 (constant).

The experimentally measured temperatures are fitted with an optimization process to determine the value of h_T by assessing the goodness of fit of Eq. (2) for all tests. The algorithm uses non-linear least squares to fit the Eq. (2) to the experimental data. The value of the heat transfer coefficient is constrained by the interval 0-60 W/(m^2·K). The initial guess at every time step was h_T = 20 W/(m^2·K). It is important to highlight that the heat transfer coefficient h_t is used as a fitting parameter. Therefore, it lumps uncertainties associated to the fitting of Eq. (2) to the experimental data and its value is chosen to minimize the fitting error. Therefore, this methodology is not expected to provide an accurate assessment of the heat transfer coefficient, but rather use h_t as the optimization parameter to ensure an adequate regression.

Equation (2) was derived for a solid exposed to constant irradiation. Hence, it does not completely capture thermal penetration for transient irradiation. This is addressed in the optimization for the heat transfer coefficient which indirectly accounts for the uncertainty introduced by the transient irradiation. At every time step a heat transfer coefficient is calculated which results in the best fit.

Figure 3 shows the results of the regression analysis at t = t_{ig} for all tests on PMMA (only one of each repeated tests is shown for clarity). As expected, the regression provides a better fit for a constant irradiation. Although there is a systematic over prediction in the temperatures for the transient exposure scenarios, the trend is captured qualitatively and is used as a basis for the analysis that follows.

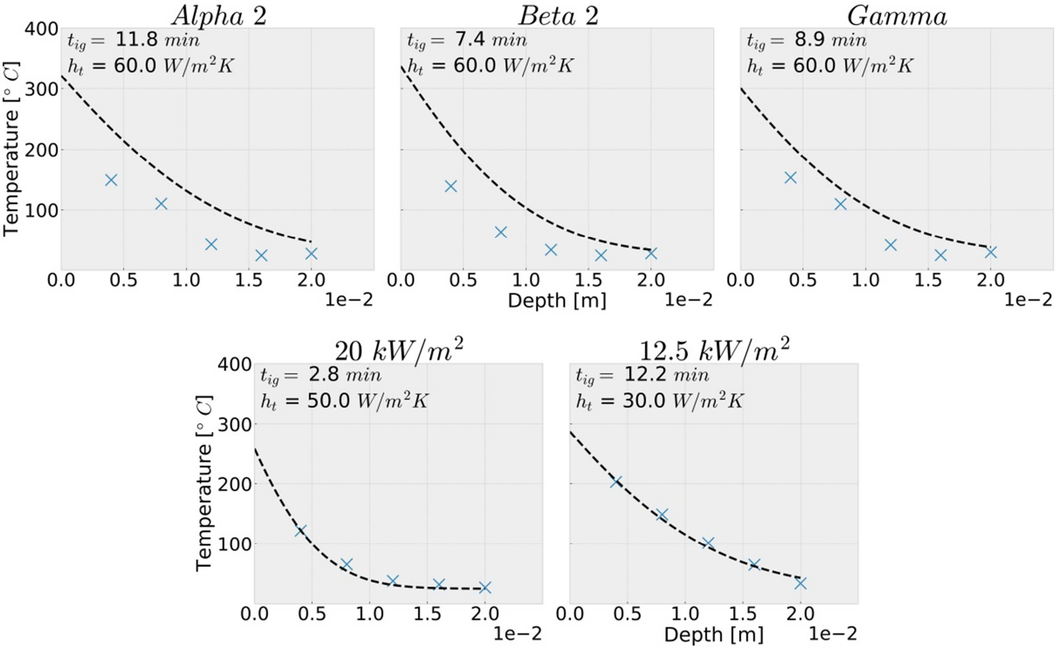

Fig. 3. Regression at t = t_{ig}. Fit was optimized for the heat transfer coefficient. Results shown for PMMA.

To obtain the NHF, Fourier's law is used with numerical differentiation for the rate of change of the temperature with depth, using a cell width of 0.5 mm, as shown in Eq. (4).

$$NHF = -k\frac{dT}{dx} \sim k\frac{T_{surf} - T_{0.5mm}}{0.0005} \tag{4}$$

A visual camera recorded all experiments and time to ignition is defined as the delay time between beginning of the exposure and the onset of flaming. Flashing before ignition did not occur in most experiments, with the exception of Alpha 2 and Beta 2 exposures for PA6. The conductive losses to the aluminium block are calculated using Eq. (5), assuming negligible heat losses from the aluminium to the environment. A smoothing algorithm is used to reduce the noise given by the numerical differentiation of dT/dt.

$$Losses_{conductive} = mc_p \frac{dT}{dt} \sim mc_p \frac{\Delta T}{\Delta t} \tag{5}$$

RESULTS AND DISCUSSION

Table 2 shows a summary of the time to ignition and surface temperature (calculated) at ignition for all experiments. For the time to ignition, PMMA presents a small range of values whereas the scatter for PA6 results is considerable for transient and constant IHF. Furthermore, ignition was not attained when the samples were exposed to Alpha 2 or 12.5 kW/m^2. The latter was expected as the CHF for PA6 is 15 kW/m^2. For a constant IHF, the ignition temperature of PA6 is 432 – 497 ˚C and for PMMA 378 – 383 ˚C [12].

Table 2. Average time to ignition and surface temperature (calculated) at ignition. Values between brackets show maximum and minimum. NI refers to No Ignition. [max - min]

Material	Exposure	t_{ig}, min	T_{surf} , ˚C
	Alpha 2	11.9 [12.0–11.9]	327 [323–331]
	Beta 2	7.5 [7.5–7.5]	342 [339–344]
	Gamma	9.0 [9.0–8.9]	296 [301–291]
	20 kW/m^2	2.95 [2.8–3.1]	264 [260–268]
	12.5 kW/m^2	12.7 [12.6–12.8]	279 [289–269]
PA6	Alpha 2	- [NI–NI]	-
	Beta 2	[12.6–25.8]	355 [344–366]
	Gamma	15.3 [15–15.5]	453 [466–439]
	20 kW/m^2	13.5 [11.1–15.8]	342 [324–360]
	12.5 kW/m^2	> 25 [–]	-

Constant IHF

Figure 4 shows the NHF absorbed at the surface for samples exposed to constant IHF. The NHF is calculated from Eq. (4). This depends on the accuracy of the regression analysis used to define the temperature profile and, in particular the surface temperature. It is worth noting that the NHF, as calculated in this study, does not depend on the optical properties of PMMA or PA6. The temperature increase that is measured in the solid already reflects the effective absorbed energy by the sample. This is also valid for transient IHF. This assumes negligible in-depth absorption of radiation, observed for low, constant IHFs (< 60 kW/m^2) [16]. To the knowledge of the authors', in-depth absorption of radiation has not been studied under transient irradiation.

The trends of NHF are similar for both materials and characterised by an initial peak followed by a sharp decline and a long tail of low heat flux. Despite the similarity in shape, there is a considerable difference between the NHF and ignition times for the two materials. The absorbed energy will depend on the thermo-physical and optical properties of the tested material. The changes in material properties, affect the Biot and Fourier numbers which dominate the heat transfer processes. Surface phenomena can also impact energy absorption, as shown by Fig. 4, where the absorbed energy prior to ignition varies between materials, and, for the two samples of PA6 exposed to 20 kW/m^2. This is due to changes to the geometry of the system and bubbling of molten PA6. These changes do not affect the NHF reported in Fig. 4 since the NHF is calculated from the curve fit.

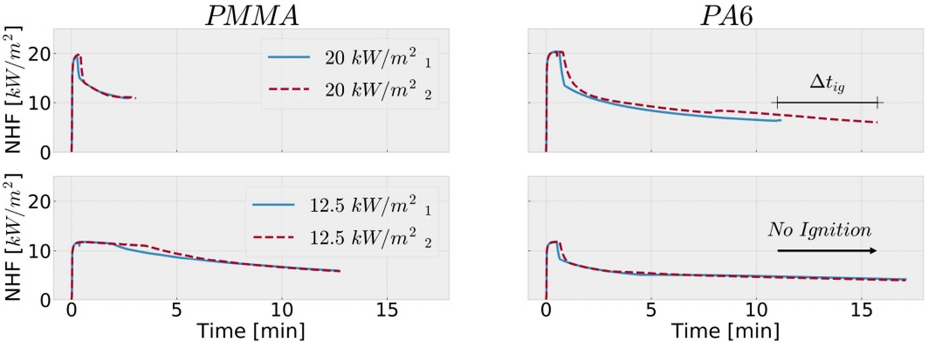

Fig. 4. Net Heat Flux for PMMA (left) and PA6 (right) exposed to constant IHF of 20 kW/m^2 (top row) and 12.5 kW/m^2 (bottom row).

Figure 5 shows the conductive losses through the back face as calculated by Eq. (5). For PMMA, the conductive losses remain lower than 10% of the IHF whereas, for PA6, this value increases to approximately 15%. This is due to the longer time to ignition allowing penetration of the thermal wave, indicating that the semi-infinite solution may no longer be a good approximation. Both in Fig. 4 (NHF) and Fig. 5 (Conductive Losses), the data seems to show the attainment of a quasi-steady situation where the rate of change with time becomes negligible. Since the temperature gradient in the sample at ignition is not negligible (Fig. 3), the constant NHF for a non-inert solid can be explained by the pyrolysis process as highlighted by Torero [17]. Surface temperature does not increase and the absorbed energy is used for pyrolysis. This suggests that this methodology is appropriate to study the energy balance leading to ignition.

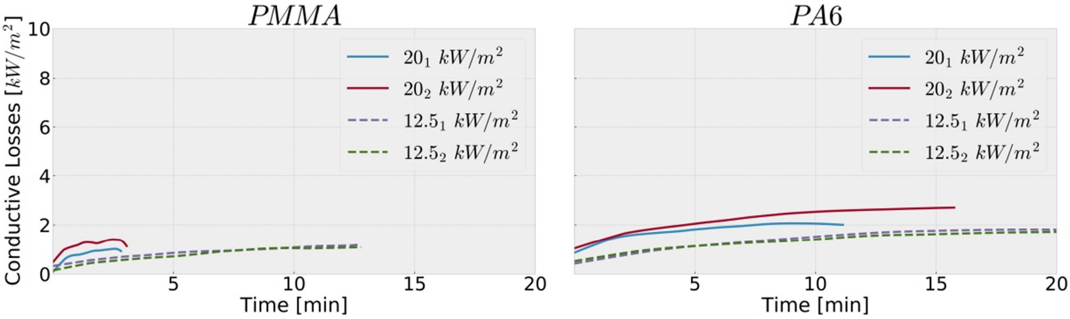

Fig. 5. Conductive losses to the aluminium block for constant exposures. Left: PMMA. Right: PA6. Solid lines show losses 20 kW/m^2 and dashed lines for 12.5 kW/m^2.

Transient IHF

Figure 6 shows the NHF absorbed at the surface by PMMA (solid lines) and PA6 (dashed lines). PMMA ignites at lower values of NHF for Alpha and Gamma exposures, compared to PA6. This agrees with PMMA having a lower CHF and ignition temperature. For Alpha 2 (left), ignition was not attained by PA6, even though the NHF is higher and the thermal properties of both materials are similar (Table 1). This difference can be explained by surface phenomena.

Figure 7 shows the pre-ignition behaviour of PA6 when exposed to Alpha 2. At 13 minutes, a maximum value of approximately 25 kW/m^2 for the IHF is reached, after which a slow decay follows. 20 minutes after the start of the exposure, the IHF has an approximate value of 20 kW/m^2, but a bubble has formed on the surface of the material, which prevents the free flow of pyrolyzates. If compared with Beta 2 and Gamma, the maximum NHF reached for Alpha 2 is lower. This phenomenon is not captured under constant heating rates and shows the importance of heating rate on the pyrolysis pathways.

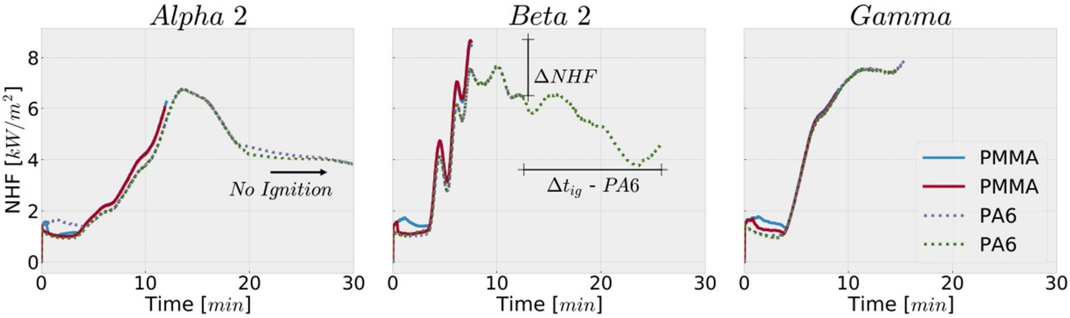

Fig. 6. Net Heat Flux for PMMA (solid lines) and PA6 (dashed lines) exposed to transient IHF.

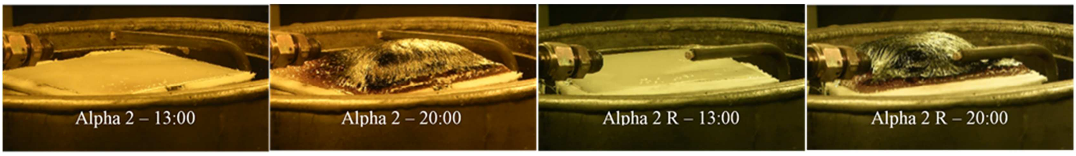

Fig. 7. Samples of PA6 exposed to Alpha 2. At 13:00, still shots show behaviour during the maximum IHF reached by the exposure. At 20:00, bubbling is shown, preventing ignition.

For PA6 samples exposed to Beta 2, there is a variability of approximately 100% in the time to ignition measured. Figure 8 shows images of both tests completed under this IHF curve. It is clear that surface phenomena taking place during the ignition of each sample (Fig. 8 left and right) differ. These differences can be explained by effects of the bubbling phenomena on the mass transfer process. This assessment implies that under the same exposure, small differences in boundary or initial conditions (mainly flow conditions) and material composition could result in considerable limitations when assessing the ignition behaviour of solids. Contrary to the other cases, PMMA ignites at a higher value of NHF, but at a lower total absorbed energy, since the time to ignition for PA6 is much longer.

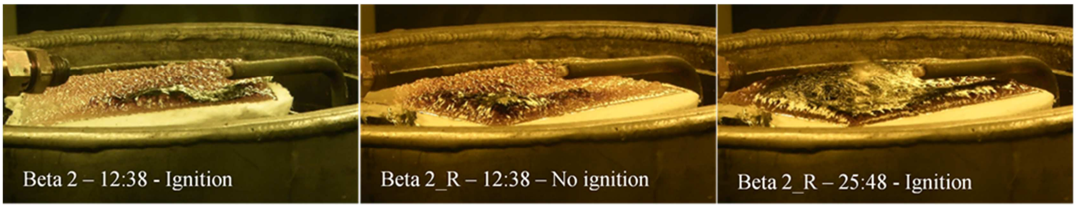

Fig. 8. Samples of PA6 exposed to Beta 2. Left: first experiment. Centre and right: repeat experiment.

Figure 9 shows the calculated conductive losses for both materials when exposed to transient IHF. The conductive losses remain approximately constant for all tests and between materials. Since the only difference between these experiments is the formation of the bubble, it can be inferred that the bubble has a small effect on the heat transfer and the energy absorbed by the sample (and hence pyrolysis rate) and delays ignition simply be preventing mass transfer and the formation of a flammable mixture. Previous studies using linearly increasing IHF [11] have shown that the bubble effect will be reduced as the rate of change of the IHF increases.

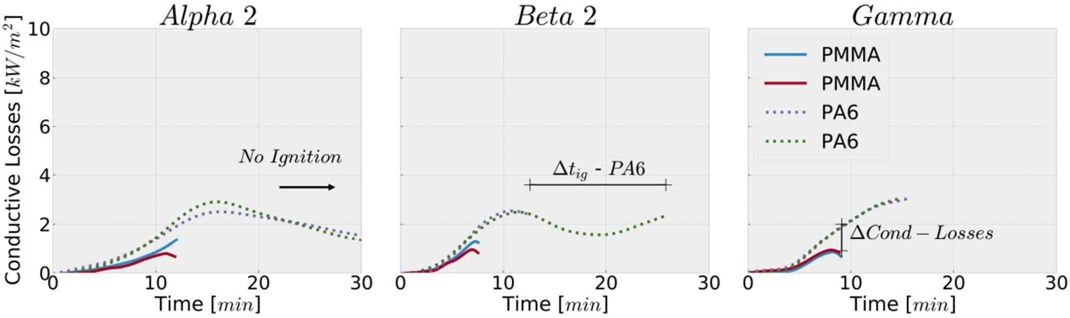

Fig. 9. Conductive losses for transient exposure for PMMA (solid lines) and PA6 (dashed lines).

CONCLUSIONS

This paper has investigated the effect of exposing samples of two different thermoplastic polymers to transient IHFs. The IHF curves were defined following measurements made from the radiation emitted by post-flashover compartment fires. The experiments analysed in this paper were completed using the Fire Propagation Apparatus. This study assessed the current ability for predicting ignition of these materials using ignition theory, traditionally derived for constant IHF.

The NHF's evolution was calculated for all tests. Even though PA6 and PMMA present similar thermos-physical properties, samples of the former reached ignition at higher values of the NHF, or even failed to ignite. This cannot be predicted using current ignition theory. Together with an assessment of the visual recordings, the processes driving ignition were investigated.

For samples exposed to a constant IHF, the NHF decreases with time, as the surface temperature and hence, the surface heat losses, increase. However, for samples exposed to increasing IHF, the NHF increases over time and so the ignition process differs as pyrolysis is driven by the NHF absorbed by the sample.

For transient exposures surface phenomena play a dominant and uncharacterized role. For PA6 samples, variations of up to 100% were measured in the ignition delay time. It is not currently possible to accurately manipulate surface phenomena during testing. This hinders our ability to understand their effects on ignition of materials exposed to transient irradiation.

Surface phenomenon was shown to have a considerable impact on ignition delay times through an effect on the mass transfer processes. The effect on heat transfer was shown to be small. This was evaluated through a comparison on the thermal diffusivities and an assessment of the conductive losses.

This study has shown that by exposing samples to transient IHF, different phenomena may dominate the ignition process. To accommodate for this complexities, it is proposed that new experimental frameworks are developed that seek to compare the ignition of materials by manipulating the flux of absorbed energy as opposed to the exposure.

ACKNOWLEDGEMENTS

Simon Santamaria is funded by the BRE Trust. Their support is gratefully acknowledged.

REFERENCES

[1] B.J. Meacham , R.L.P. Custer, Performance-Based Fire Safety Engineering: an Introduction of Basic Concepts, J. Fire Prot. Eng. 7(2) (1995) 35-53.

[2] 2010, T.B.R., Approved Document B, in Volume 2 - Buildings other than dwelling houses. 2007, HM Government: London.

[3] M. Law, Heat Radiation from Fires and Building Separation, D.o.S.a.I.R.a.F.O.C.J.F.R. Her Majesty's Stationery Office, London, p. 31, 1963.

[4] ISO 5660-1:2002, Reaction-to-fire tests – Heat release, smoke production and mass loss rate – Part 1: Heat release rate (cone calorimeter method), 2002.

[5] ASTM E2058–03, Standard Test Methods for Measurement of Material Flammability Using a Fire Propagation Apparatus (FPA), West Conshohocken, PA, 2013.

[6] ASTM E1321-13, Standard Test Method for Determining Material Ignition and Flame Spread Properties, ASTM International, West Conshohocken, 2013.

[7] J. Torero, Flaming ignition of solid fuels. SFPE Handbook of Fire Protection Engineering, 5th Ed., 2016 pp. 631-661.

[8] R.M. Hadden, A.I. Bartlett, J.P. Hidalgo, S. Santamaria, F. Wiesner, L.A. Bisby, S. Deeny, B. Lane, Effects of exposed cross laminated timber on compartment fire dynamics, Fire Saf. J. 91 (2017) 480-489.

[9] A.I. Bartlett, R.M. Hadden, J.P. Hidalgo, S. Santamaria, F. Wiesner, L.A. Bisby, S. Deeny, B. Lane, Auto-extinction of engineered timber: Application to compartment fires with exposed timber surfaces, Fire Saf. J. 91 (2017) 407-413.

[10] J.P. Hidalgo, C. Maluk, A. Cowlard, C. Abecassis-Empis, M. Krajcovica, J.L. Torero, A Thin Skin Calorimeter (TSC) for quantifying irradiation during large-scale fire testing, Int. J. Therm. Sci. 112 (2017) 383-394.

[11] S. Santamaria, R.M. Hadden, Experimental analysis of the pyrolysis of solids exposed to transient irradiaiton. Applications to ignition criteria, Proc. Combust. Inst. 37 (2018) 4221-4229.

[12] SFPE handbook of fire protection engineering, 2002, Quincy MA, NFPA.

[13] R.T. Long, J.L. Torero, J. Quintiere, A.C. Fernandez-Pello., Scale and Transport Considerations on Piloted Ignition of PMMA, In: Curtat, M. (Ed.), Fire Safety Science–Proceedings of the Sixth International Symposium, pp. 567-578, 2000.

[14] R. Carvel, et al., Determination of the flammability properties of polymeric materials: A novel method, Polym. Degrad. Stab. 96 (2011) 314-319.

[15] I. Vermesi, N. Roennera, P. Pironi, R.M. Hadden, G. Rein, Pyrolysis and ignition of a polymer by transient irradiation, Combust. Flame 163 (2016) 31-41.

[16] F. Jiang, J.L. de Ris, M.M. Khan, Absorption of thermal energy in PMMA by in-depth radiation, Fire Saf. J. 44 (2009) 106-112.

[17] J.L. Torero, Material properties that control ignition and spread of fire in micro-gravity environments, In: Proceedings of NHTC'00, ASME, Editor. 2000, ASME Heat Transfer Conference: Pittsburgh, Pennsylvania.

Numerical Study of Cross-Laminated Timber Under Fire

Wong B.V.Y.[1], *, Tee K.F.[2], Yau T.M.[1]

[1] Ramboll Fire, London, UK
[2]Department of Engineering Science, University of Greenwich, Kent, UK
**Corresponding author's email: bernice.wong@ramboll.co.uk*

ABSTRACT

This paper presents the fire performance of unprotected Cross-laminated timber (CLT) floor panel by comparing available experimental results against numerical and analytical analysis. A numerical model of multi-layered CLT panel has been developed using Finite Element (FE) Method. Temperature distribution within the cross-section of CLT panels was investigated. The charring rates for CLT panels obtained from the numerical model were compared with experimental results and those provided by Eurocode simplified approach. The falling off of the charred layer of the CLT panel has also been investigated using the FE modelling. The results show that assuming the immediate falling off of charred layer would happen when the interface between the layers has reached 300°C could lead to consevative prediction.

KEYWORDS: Timber structure, cross laminated timber, charring rate, fire resistance, numerical analysis.

INTRODUCTION

The fire behaviour of structural timber elements is an important research topic to ensure the attainment of the required safety level in timber buildings. Cross-laminated timber (CLT) is increasingly being used in the construction of high-rise buildings due to its simple manufacturing system. In terms of fire resistance, CLT panels are promoted as having excellent fire resistance, comparable to that of non-combustible materials and to heavy timber construction, due to the ability of thick wood assemblies to char slowly at a predictable rate while maintaining most of their strength during the fire exposure.

The investigation of the performance of timber product exposed to fire has increased over the past decades. Several experimental investigations have been carried out on different wood products, such as laminated veneer lumber [1, 2], glued laminated timber [3] and cross-laminated timber (CLT) [2, 4, 5]. Small- and large-scale tests were performed on loaded and unloaded specimens subjected to one- or two-dimensional heat fluxes in furnaces of different sizes. Design of timber structures has been outlined in Eurocode 5 [6], notional charring rate for softwood and hardwood timber is given. For timber member subjected to one-dimensional charring, a constant value of charring rate 0.65 mm/min is recommended for softwood. For the performance of the CLT panels in fire, only little information on charring is available and whether the fire behaviour of CLT panels is similar to homogenous timber panels has not yet been systematically analysed.

The fire behaviour of cross-laminated solid timber panels has been experimentally and numerically investigated [2, 4, 7-10] in the past decades. Experimental investigations on small and large scale tests of unloaded and loaded cross-laminated timber specimens manufactured by various producers with different characteristics were carried out [2, 4, 7-8], the outcome of the tests revealed that the fire behaviour of cross-laminated timber elements was mostly linked to the thickness of the layers

Proceedings of the Ninth International Seminar on Fire and Explosion Hazards (ISFEH9), pp. 1088-1096
Edited by Snegirev A., Liu N.A., Tamanini F., Bradley D., Molkov V., and Chaumeix N.
Published by Saint-Petersburg Polytechnic University Press
ISBN: 978-5-7422-6498-9 DOI: 10.18720/spbpu/2/k19-101

and the type of adhesive used to produce the timber panels [4]. A simplified charring model to determine the residual cross-section for CLT panel has been introduced [11, 12] based on the available fire tests. To develop a better understanding of CLT panels fire performance, applying analytical and numerical methods as a more effective way to study the mechanical and thermal performance of CLT elements exposed to fire. It can be done without performing experimental tests which are hazardous and expensive. At the same time, experimentation at different scales is required to provide the fundamental data for model development. The fire resistance of timber structures can be assessed by standardised fire tests, such as ISO 834 [13], and can be calculated by methods such as those suggested in the Eurocodes [6]. Design standards [6] allow the use of advanced calculation methods, which eliminate the cost of expensive fire testing by using validated numerical finite element (FE) computer models to determine the thermal and structural performance of timber members exposed to fire.

This paper presents the main results of the numerical analyses. Particular attention is given to the comparison of the fire behaviour of cross-laminated solid timber panels obtained from the numerical findings with the experimental results [2, 8].

NUMERICAL ANALYSIS

For the numerical analyses presented in this paper full versions of the programs SAFIR 2016 were used. SAFIR is a special purpose finite element program developed at the University of Liege, Belgium, for analysing the behaviour of building structures under ambient temperatures and subjected to fire. It consists of an integrated thermal and structural analysis program for carrying out two-dimensional (2D) and three-dimensional (3D) analyses of steel, concrete, timber and composite structures in fire conditions. The structure can be made of a 3D skeleton of linear elements such as beams and columns, in conjunction with planar elements such as slabs and walls. Complex model such as connections can be analyses using volumetric elements. The thermal and mechanical properties of steel, concrete and timber, following the Eurocodes, are incorporated into the program, but one can also use user-defined materials for the thermal or structural analysis [14-15]. The influence of temperature on the thermal properties is automatically implemented in the SAFIR finite element (FE) software. Alternatively, user-specified material thermal properties can also be defined through its thermo-physical parameters which govern the heat conduction process.

1D HEAT TRANSFER EXAMINATION

A simple solid timber member model has been set up using SAFIR to simulate an one-dimensional (1D) heating test on unprotected spruced timber members exposed to ISO-fire [13] on one side for 90 minutes, presented by König and Walleij [16]. The modelled section was discretized into 48 numbers of 2D SOLID elements to be representative of a 24mm by 96mm strip of solid timber specimen. The test specimen had an initial moisture content of 12% with a bulk density of 480 kg/m³. One side of the model was exposed to the ISO 834 fire curve. the emissivity of timber surface and convection factor assumed to be 0.8 and 25 W/m^{2}K, respectively, which the experimental data has not been made available the recommendations from the EN1995-1-2 [6] have been used. No heat and mass flux on the top side of cross section is considered, a convective coefficient of 9 W/m²K (which accounts for both radiative and convective losses) and an initial ambient temperature of 20°C were applied to the surface. The sides of the model were assumed adiabatic. Temperatures across the cross-sectional were measured in a depth of 6, 18, 30, 42 and 54 mm from the surface exposed to fire and compared to the experimental data [17]. Figure 1 illustrates the 2D SAFIR model and the temperature profile across the cross-sectional of the timber specimen at 3600 seconds. The charred material is represented by maroon red, whereas red colour corresponds to 300°C temperature, as is typical in the literature [6], where char depth was assumed as the location of the 300 °C isotherm.

The numerical variation of heat flux led to temperature increases close to the thermocouple records as displayed in Fig. 2. Note that the grey lines indicated were temperature measurements taken at various depths into the wood for a series of test [16], with the black line being the average of those measurements. The thermal analysis across the cross section of the timber strip has been predicted with good accuracy despite a coarse mesh was used in the FE model.

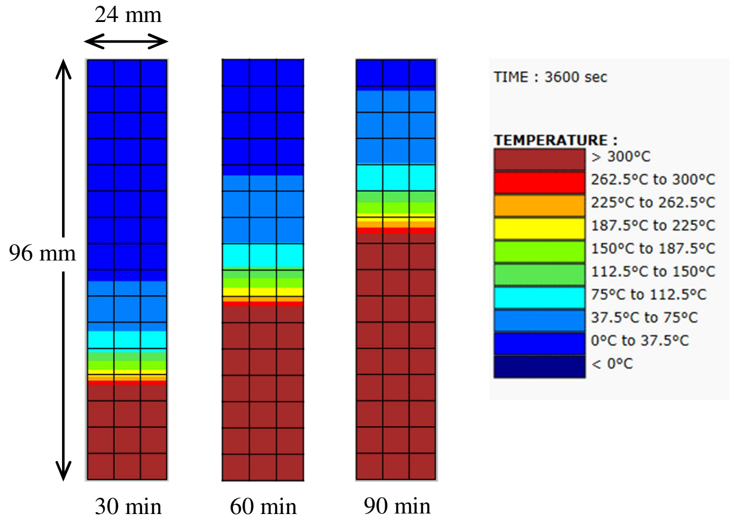

Fig. 1. Temperature distributions within the cross-section of solid timber after 60 minutes of fire exposure.

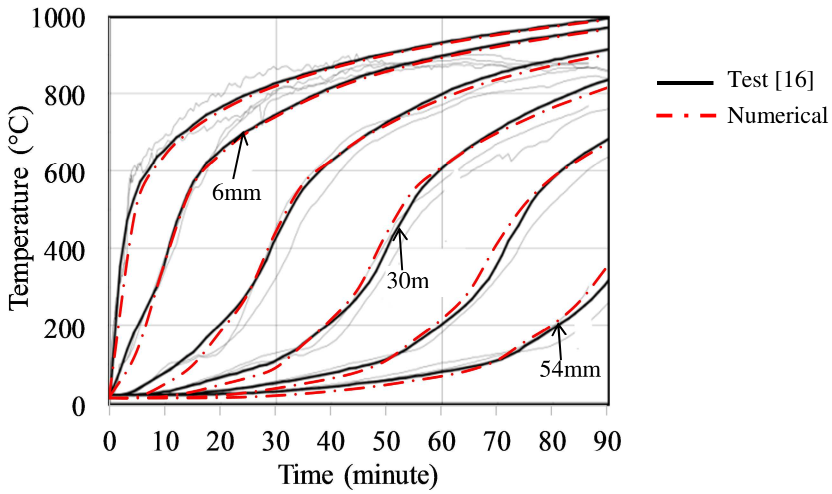

Fig. 2. Experimental [16] and numerical temperature distributions at various depth across the cross section of solid timber.

NUMERICAL-EXPERIMENTAL COMPARISONS FOR CROSS-LAMINATED TIMBER PANEL

Fire tests were conducted on CLT panel specimen as reported in [2]. The geometrical characteristics of the CLT panel are 600 mm thick, 150 mm width and 5600 mm long. The specimen was built using five bonded layers of 42, 19, 28, 19 and 42 mm. Polyurethane (PU) adhesive was used to manufacture the tested panels. The bottom side of the specimen was exposed to heat in the furnace, exposed to the standard ISO 834 fire [13].

A 2D finite element model has been built using 36 SOLID elements in SAFIR, was used to simulate the temperature distributions in the panel. The thermocouples considered in the numerical simulations were placed at coincident nodes corresponding to depths of 21 mm and 52 mm from the exposed surfaces (Fig. 3). In the finite element modelling, the moisture content of the CLT sample was assumed as 12%, and the corresponding initial density was 460 kg/m^3. From the collected experimental data [2], there was no evidence to suggest that any quick temperature increases indicating the falling-off of charred layers. Thus, the CLT cross section was modelled as solid wood, the delamination behaviour of the charred layer has not be considered in the numerical modelling. The adhesive layer between the CLT layers is relatively small (less than 0.2 mm) and it was neglected in the conduction process during the FE analysis of the CLT element. Nonetheless investigation [8, 17] on shear behavior of different adhesives at high temperatures has revealed that the fire behavior of CLT panels is strongly influenced by the behavior of the adhesive that used for the CLT panels bonding system. Degradation of adhesive between individual CLT layers can lead to charred layer fall-off which in turn leads to exposure of the directly underlying layer.

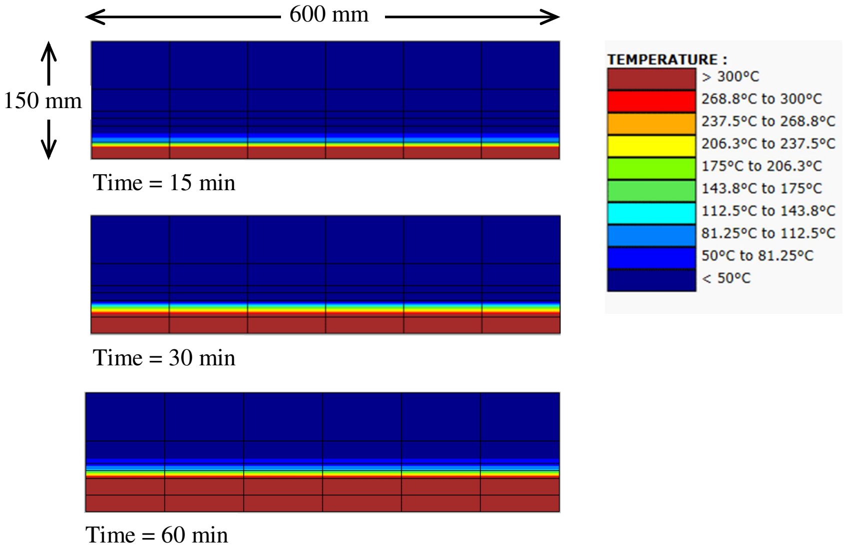

Fig. 3. Numerical temperature profiles across the cross section of CLT and the formation of charring layer at different fire-exposure times.

Figure 3 illustrates the predicted temperature profiles of the CLT sample as a function of fire-exposure time, and shows the formation of char layer increases as fire exposure time increases. Figure 4 compares the temperature distribution recorded during the fire test [2] at depth 21 and 52 mm from the bottom surface that exposed to fire, with the numerical thermal prediction. It can be seen that, the temperature-time curve for the depth at 21 mm obtained from the numerical and experimental data were almost corresponding, the slight differences could be due to the mesh size and time steps used in the model. The curves recorded at 52 mm depth indicate an acceptable approximation. The numerical and experimental data were in good agreement from the beginning till after 60 minutes fire exposure, the numerical prediction has the temperatures gradually increasing while the experiment data showed more rapid increase of temperature after 87 minutes at which time the recorded temperature was 300°C.

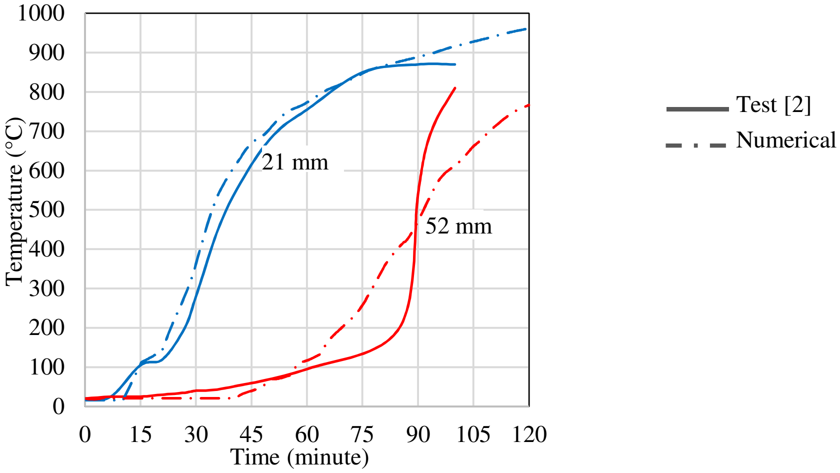

Fig. 4. Comparison between predicted and measured temperatures for CLT panel in fire.

NUMERICAL- EXPERIMENTAL COMPARISONS FOR THE DELAMINATION OF CLT PANEL

One of the main concern when comes to the fire resistance properties of CLT is the delamination of CLT layers due to fire exposure. The investigation on the influence of the temperature-dependent material properties of the adhesive on the resistance of CLT beams exposed to fire have been carried out [7], it was demonstrated that the fire behavior of cross-laminated timber panels is strongly influenced by the behavior of the adhesive that used for the CLT panels bonding system. CLT panels manufactured with a less temperature-sensitive adhesive the charred layers almost remained in place throughout the fire tests and the panels behave just similar to homogenous timber panels exposed to ISO 834 [13] on one side.

In this section, the numerical simulation aims to model the delamination of CLT and the rapid increase in temperature of the layer direct above the charred layer. Test specimens [8] consisted of cross-laminated timber panels made of spruce boards with the dimensions of 1.15 m by 0.95 m had the thickness of 60 mm. The specimens were exposed on one side to the standard fire curve according to ISO 834 [13]. It was observed during the fire tests [8], falling off of the charred layers was occurred for all specimens manufactured with the polyurethane (PU) adhesives, where temperatures measured between the layers starting at about 300°C increased very rapidly and reached the furnace temperature. It was suggested that the thermocouples placed between the CLT layers exposed directly to fire as the charred layers fell off during the fire tests.

In the numerical modelling, the finite element mesh consisted of 30 SOLID elements. The moisture content of the specimens was assumed to be 12%. The thermocouples considered in the numerical simulations were placed at coincident nodes corresponding to depths of 10, 20, 30 and 40mm from the exposed surface. To simulate the delamination behaviour of the CLT panel, two assumptions have been considered on the falling off of the charred timber layer, first when the interface between the layers has reached 300°C, the immediate falling off of charred layer is occurred, this has been based on the experimental observation [8] as mentioned above. The simulations result is shown in Fig. 5. The second assumption made is that the falling off of the charred layer occurs when the temperature of the subsequent layer at depth 10mm from the exposed surface has reached 300°C. Figure 6 illustrates the numerical prediction adopted the second assumption.

Figures 5 and 6 illustrate the result corresponding to the two assumptions made. The experimental test data are shown in black and red curves correspond to numerical predictions. It can be seen that the first assumption gives conservative predictions, the falling off of each timber layer formed the CLT panel occurs earlier than experimental observation [8]. The numerical simulation and experimental data were shown to be in good agreement with the second assumption (see Fig. 6).

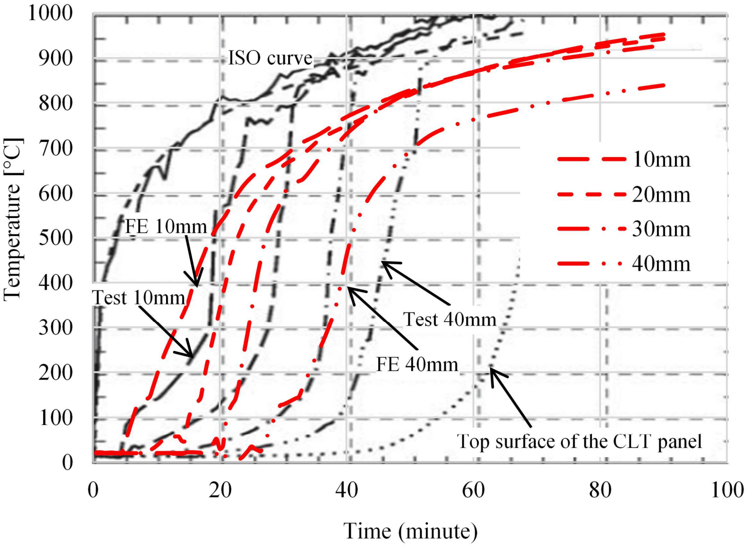

Fig. 5. Comparison between measured temperatures for the fire tests V2 [8] and numerical simulation with the assumption that charred layers immediately fall off after charring.

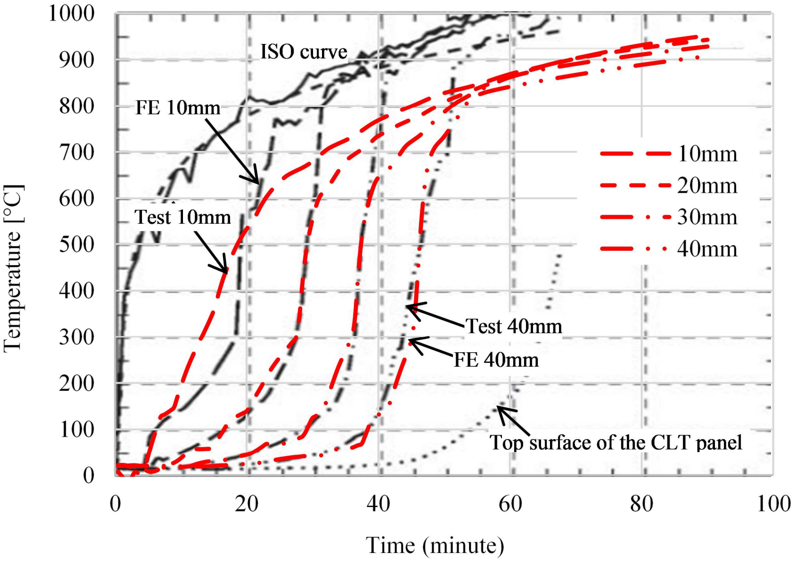

Fig.6. Temperature distributions across the cross-section of cross-laminated timber panels - experimental and numerical.

The delamination behaviour of the CLT panel where significant increase in temperature has been observed after the layer is completely charred, the time when the protective charcoal has fallen off have been well predicted by the numerical simulation, suggested that the polyurethane adhesives between individual layers was still holding the fire exposed charred panel and the subsequent layer, until which the formation of a new 10mm thick char layer on the subsequent layer, the adhesive bonding function lost, fire exposed charred layer is then fall-off. As mentioned above, the thermocouples has exposed to fire as the charred layers fell off, therefore the temperature profile after the falling off of the charred layer could be neglected.

Table 1. Charring depth (d_{char}) and charring rates calculated for cross-laminated timber panel under fire test [8] and numerical analysis of the 2nd assumption made

d_{char} (mm)	Time reached 300°C (min)		Charring rates (layer) (mm/min)		Charring rates (panel) (mm/min)	
	Test	FE	Test	FE	Test	FE
10	18	13	0.56	0.77	0.56	0.77
20	27	27.5	1.11	0.69	0.74	0.73
30	36	36	1.11	1.18	0.83	0.83
40	43	45	1.43	1.11	0.93	0.89

Simplified approach suggested by current codes of practice [6], the charring rate of timber is defined as the rate of movement of the 300ºC. The 300°C isotherm is assumed as the border between charred and heated wood as suggested by Eurocode 5, Part 1-2 [6]. Table 1 reports the time when the 300°C was measured at the interface between layers, for both obtained from experiments [8] and numerical modelling. The calculated charring rates for the single layers and for the whole cross-sections of the CLT panel are also shown in Table 1. For the calculation of the charring rate of the single layers it was assumed that a layer started charring when the temperature measured at its exposed bottom side reached 300°C and then it was completely charred when the temperature of 300°C was measured on the unexposed top side of that layer. The predicted charring rate of the first layer is 0.77 mm/min which showed a higher charring rate in comparison to the one-dimensional charring of 0.65 mm/min [6] as well as the test result 0.56 mm/min (see Table 1). The resulting average charring rate of the 5-layered timber panels was 0.76 mm/min (fire test [8]) and 0.80 mm/min (numerical model).

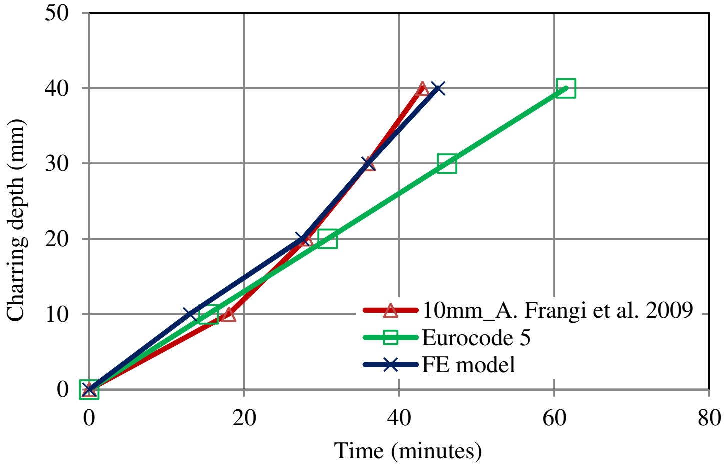

Fig.7. Charring depth for CLT panel measured from test [8] and compared with EN 1995-1-2 [6] and numerical model.

Figure 7 compares the charring depth as a function of time for the test result [8] and the numerical model. The charring depth corresponds to the Eurocode [6] recommended 0.65 mm/min one-dimensional charring rate for homogeneous timber was also shown for comparison. The measured charring depth agrees well with the numerical prediction. The effect of the increase of the charring rate can be seen from the test and numerical model, the differences between predicted and measured charring depth are very small. The measured [8] and predicted charring depth of the CLT panel is higher than for the solid homogeneous timber according to Eurocodes [6].

CONCLUSION

The paper presents a 2D finite element modelling with 1D heating implemented in SAFIR software package to simulate the thermal behaviour of unprotected cross-laminated timber panel with and without falling off of the charred layers subjected to the exposure to standard fire on the bottom side.

The numerical model validated by experimental results was compared with analytical approach by means of simplified design methods, proposed by EN 1995-1-2. Good agreement between numerical simulations and experimental data was found despite a coarse mesh was used in the FE model, it is however the presented model needs to be performed with mesh refinement analysis to investigate the influence of meshing in the simulation. The simplified approach was found given lower value charring rate among those.

When timber is exposed to elevated temperatures, the simulation of the pyrolysis is a key task for accurate prediction of the realistic temperature distributions, as the different chemical components in wood undergo thermal degradation that would affect the performance of timber in fire. The numerical investigation was found to agree well with the experimental approach if assuming that the falling off of the charred layer occurred when the temperature of the next layer at depth 10 mm from the exposed surface has reached 300°C. Although further numerical investigation is recommended to be performed on CLT panels that formed by various layer thicknesses to provide further verification on the assumptions made on the simulations of the phenomenon of delamination of a CLT-elements. The fire behaviour of timber panels subjected to a standard fire could be differ significantly to a real fire, which requires considerable additional research to be performed to investigate the heat transfer beneath the charred layer under a range of possible heating conditions cases.

REFERENCES

[1] W.H. Tsai, Charring rates for different cross sections of laminated veneer lumber (LVL). Master thesis, University of Canterbury, Christchurch, New Zealand, 2010.

[2] A. Menis, Fire resistance of Laminated Veneer Lumber (LVL) and Cross-Laminated Timber (XLAM) Elements, PhD thesis, Universita Degli Studi Di Cagliari, Italy, 2012.

[3] T.H. Yang, S.Y. Wang, M.J. Tsai and C.Y. Lin, Temperature distribution within glued laminated timber during a standard fire exposure test. Materials and Design 30(3) (2009) 518-525.

[4] A. Frangi, G. Bochicchio, A. Ceccotti, Natural full-scale fire test on a 3 storey xlam timber building, Proc. of 10th World Conference on Timber Engineering, Japan, 2008.

[5] P. Wilinder, Fire resistance in cross-laminated timber. Bachelor Thesis, Jönköping University, Jönköping, Sweden, 2010.

[6] EN 1995-1-2:2004, Eurocode 5: Design of timber structures - Part 1-2: General - Structural fire design. BSI, 2004.

[7] A. Frangi, M. Fontana, M. Knobloch, G. Bochicchio, Fire Behaviour of Cross-Laminated Solid Timber Panels, Fire Saf. Sci. 9 (2009) 1279-1290.

[8] A. Frangi, M. Fontana, E. Hugi, R. Jöbstl, Experimental analysis of cross-laminated timber panels in fire, Fire Saf. J. 44 (2009) 1078–1087.

[9] V.D. Thi, M. Khelifa, M. Oudjene, M. El Ganaoui, Y. Rogaume, Finite element analysis of heat transfer through timber elements exposed to fire, Eng. Struct. 143 (2017) 11-21.

[10] A. Menis, M. Fragiacomo, I. Clemente, Fire resistance of unprotected cross-laminated timber floor panels: Parametric study and simplified design, Fire Saf. J. (2018), in press.

[11] B.V.Y.Wong, K.F.Tee, The Fire Performance of Exposed Timber Panels, Int. J. Civil, Env., Struct., Construct. Architect. Eng. 8(10) (2014) 1045-1051.

[12] B.V.Y.Wong, K.F.Tee, Charring Rate for Fire Exposed X-Lam, IOP Conference Series: Materials Science and Engineering, 216 (2017) 012061.

[13] ISO-834, Fire-Resistance Test-Elements of Building Construction: Part 1.General Requirements, ISO 834-1, International Organization for Standardization, Geneva, Switzerland, 1999.

[14] J.M. Franssen, SAFIR: A thermal-structural program for modelling structures under fire, Engineering Journal-American Institute of Steel Construction Inc, 42(3) (2005) 143-158.

[15] J.M. Franssen, T. Gernay, Modeling structures in fire with SAFIR®: Theoretical background and capabilities, J. Struct. Fire Eng. 8(3) (2017) 300-323. https://doi.org/10.1108/JSFE-07-2016-0010.

[16] J. König, L. Walleij, One-dimensional charring of timber exposed to standard and parametric fires in initially unprotected and post-protected situations. Report No. 9908029, Swedish Institute for Wood Technology Research, Stockholm, Sweden, 1999.

[17] A. Frangi, M. Fontana, A. Mischler, Shear behaviour of bond lines in glued laminated timber beams at high temperatures, Wood Sci. Technol. 38 (2004) 119–126.

Thermal Decomposition of Flexible Polyurethane Foams in Air

Pau D.S.W.[1, *], Fleischmann C.M.[1], Delichatsios M.A.[2]

[1] University of Canterbury, Christchurch, Canterbury, New Zealand
[2] Northeastern University, Boston, Massachusetts, USA
**Corresponding author's email: dennis.pau@canterbury.ac.nz*

ABSTRACT

The oxidative thermal decomposition of a non-fire retardant and a fire retardant polyurethane foam is investigated over 1 – 60 °C/min of heating rate. From the thermogravimetry results under the oxidative environment of air, additional oxidative reactions which are heating rate dependent compete with the pyrolysis reactions over similar temperature range. The decomposition behaviour differs for the foams and the heating rates investigated. Due to the presence of fire retardant additives, the oxidative thermal decomposition from heating rates of 1 – 20 °C/min occurs at a higher rate and over a narrower temperature range for the fire retardant foam. However, at 60 °C/min, the fire retardant foam shows a reduced decomposition rate spreading over a wider temperature range. This shows the fire retardant foam can decompose rapidly at low heating rate, under the condition of low temperature with ample of oxygen. This is similar to the incipient phase of a fire, and ignition inhibition is possible when coupled with the gas phase fire retardant mechanisms of the fire retardant foam. The char residue formed by the solid phase fire retardant mechanism slows the decomposition rate, and as the heating rate increases, the decomposition extends over a greater temperature range due to improved thermal stability. For both foams, the increase in heating rate shows a gradual reduction to the influence from oxidative reaction of foam, shifting towards the pyrolysis reaction of polyol. Kinetic properties of Arrhenius equation governing the decomposition rate are estimated graphically using the Inflection Point Methods and the model shows reasonable agreement with the experimental results. From the heat flow results, the heat of reaction for the oxidative thermal decomposition of foams is calculated and is found to be exothermic.

KEYWORDS: Kinetic properties, oxidative thermal decomposition, polyurethane foam, DSC, TGA.

INTRODUCTION

During smouldering combustion, condensed solid undergoes decomposition which is chemically more complex when compared to flaming combustion. This is caused by the presence of oxygen which results in additional oxidative reactions that compete with the pyrolysis reactions in smouldering combustion. A number of researchers have presented the science and physical phenomena in great details relating to smouldering combustion [1-5]. In flaming combustion, the oxygen is mostly consumed in the gas phase, producing flame which is an oxidative reaction zone [6]. While this assumption is valid for most condensed solid, the porous nature of flexible polyurethane (PU) foam allows oxygen to permeate the material by means of convection and diffusion hence the influence of oxidative reactions in flaming combustion could be significant [7].

A number of researchers have demonstrated that the thermal decomposition behaviour of flexible PU foam in air is more complex than under an inert environment [7-13]. These researchers have estimated the kinetic properties governing the decomposition via graphical method or genetic algorithm; however, the information is scarce as the studies mainly involved flexible foam without fire retardant additives, and at relatively low heating rates, below 20 °C/min in comparison with heating rate achieved in flaming combustion, 200 – 400 °C/min. Based on the thermogravimetry

Proceedings of the Ninth International Seminar on Fire and Explosion Hazards (ISFEH9), pp. 1097-1108
Edited by Snegirev A., Liu N.A., Tamanini F., Bradley D., Molkov V., and Chaumeix N.
Published by Saint-Petersburg Polytechnic University Press
ISBN: 978-5-7422-6498-9   DOI: 10.18720/spbpu/2/k19-31

(TG) results [9], Rein et al. [10] proposed a 2-step pyrolysis mechanism to describe the thermal decomposition of flexible foam under inert nitrogen environment, and included 3 additional oxidative reactions for the decomposition under oxidative air environment. The proposed 5-step oxidative decomposition mechanism was further validated by Valencia et al. [11, 12] and Rogaume et al. [13] via detailed experimental studies involving Thermogravimetric Analysis (TGA), Differential Scanning Calorimetry (DSC), tubular furnace and Fourier Transform Infra-Red (FTIR) spectroscopy, leading to an improved understanding of the competition between pyrolysis and oxidative reactions and the characterisation of the gaseous products released during each macro-scale decomposition step. Krämer et al. [7] demonstrated that the oxidative decomposition behavior changes with heating rate, and for heating rate experienced in flaming combustion, the 2-step mechanism was found to dominate under both nitrogen and air environments.

This paper aims to supplement the current knowledge on oxidative thermal decomposition of PU foam by presenting the experimental study on a non-fire retardant (NFR) and a fire retardant (FR) foam using Simultaneous Differential Scanning Calorimetry and Thermogravimetry Analysis (SDT), at four different heating rates, 1, 5, 20 and 60 °C/min, under inert nitrogen environment and oxidative air environment. The kinetic properties consisting of reaction order (n), pre-exponential factor (A) and activation energy (E), relating to the oxidative and pyrolysis reactions are established using the Inflection Point Methods [14] from the temperature varying TG results. The heat of reaction (Δh_r) relating to the oxidative thermal decomposition is established from the heat flow measurements attained from DSC.

EXPERIMENTAL TECHNIQUE AND POLYURETHANE FOAM SELECTION

The instrument used is SDT 600, a product of TA Instruments which simultaneously acquires both DSC and TGA measurements from the same sample. The experiments were conducted in dynamic mode where the foam sample was subjected to a constant heating rate within a purged furnace from room temperature (~20 °C) up to a maximum of 600 °C for inert nitrogen environment and 900 °C for oxidative air environment. The sample mass ranged between 3 and 4 mg, comprising shredded flexible foam fragments within a half-filled 90 μL alumina cup. The sample was tested in open configuration without the presence of a lid to allow the release of volatiles from decomposition. The relatively small sample size ensures negligible thermal gradient spatially through the specimen during the transient heating process thus satisfying the assumption of a lumped capacitance system. The TGA measurements are the changes in sample mass during decomposition, registered based on the current signal required to correct a taut-band meter movement. The DSC measurements are the changes in enthalpy, registered based on the heat flux concept where the heat flow is determined from the changes in sample temperature according to the thermal equivalence of Ohm's Law. The heating rates investigated were 1, 5, 20 and 60 °C/min, and for each heating rate, three replicates were tested. The selected heating rates were limited by the allowable maximum of the instrument at 100 °C/min.

The flexible PU foams investigated are referred to as NFR-SB-31 for the non-fire retardant foam with a density of 31 kg/m^3 and FR-Y-36 for the fire retardant foam with a density of 36 kg/m^3. The polyurethane foams are manufactured from the polycondensation of toluene diisocyanate, water and polyalkoxy polyether polyol. The polyol also contains styrene and acrylonitrile polymer. In smaller quantity, other ingredients include inorganic fillers, plasticisers, extenders, antimicrobial agents and pigments. The fire retardant additives within FR-Y-36 comprise melamine and halophosphate which have solid and gas phase fire retardant capability. In the gas phase, chlorine from the breakdown of halophosphate neutralises the reactive radicals produced by foam decomposition [15] while the breakdown of melamine also releases ammonia and nitrogen gas which dilute the concentration of combustible gas to inhibit combustion [16]. Melamine and phosphate structure are also reactive towards the gaseous isocyanates released, forming residue hence reducing the quantity of isocyanates available for gas phase combustion [17, 18]. In the solid phase, melamine reacts with phosphoric acid from halophosphate breakdown to form thermally stable cross-linked residue or char at varying temperatures, melam at 350 °C, melem at 450 °C and melon at 600 °C [19]. Further details relating to the experimental technique, calibrations and selection of flexible PU foams have been documented in a few publications for reference [20-22].

PYROLYSIS AND OXIDATIVE REACTIONS OF POLYURETHANE FOAM THERMAL DECOMPOSITION

Thermal decomposition of PU foam is described by the plot of decomposition rate, *dα/dT* versus reaction temperature, *T* where a peak over a defined temperature range signifies the occurrence of a solid phase reaction. *α* is defined as the fraction decomposed and the decomposition rate is normalised by dividing *dα/dt* by the heating rate *β*. The decomposition behaviour of NFR-SB-31 is shown in Fig. 1 a – d for the different heating rates while the different line types on each plot denote the different environments, solid line represents air, dashed line represents nitrogen and dotted line represents the derived oxidative reactions. Decomposition under nitrogen environment shows a consistent 2-step pyrolysis mechanism at all heating rates as follow [13].

(1) PU Foam → Regenerated Polyol + Gaseous Isocyanates

(2) Regenerated Polyol → Char + OH Species, H_2CO, CH_4 and H_2O

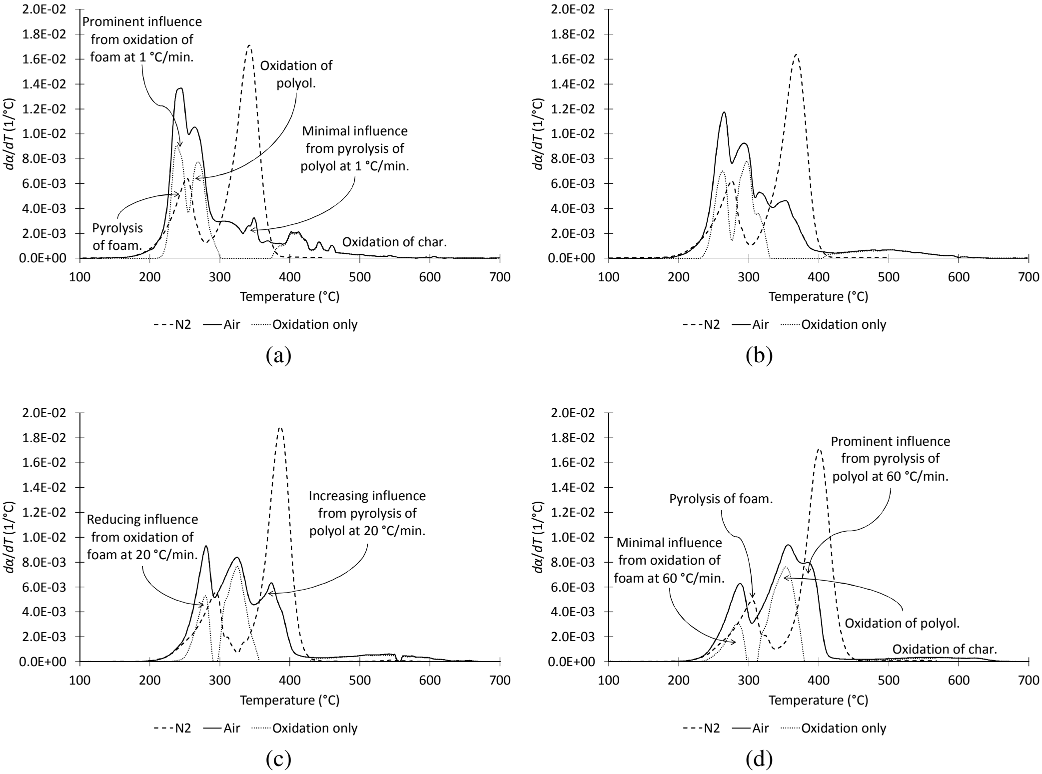

(a) (b)

(c) (d)

Fig. 1. Decomposition rate versus temperature of NFR-SB-31 in air and nitrogen, and the derived oxidative reactions. (a) 1 °C/min; (b) 5 °C/min; (c) 20 °C/min; (d) 60 °C/min.

The decomposition under air environment shows the outcome of a series of reactions overlapping closely across similar temperature range. The decomposition behaviour is also heating rate dependent where the peak of the curve shifts towards higher temperature as the heating rate increases. Assuming that the 2 pyrolysis reactions proceed and remain unaffected by the additional oxidative reactions under air, subtracting the decomposition under nitrogen (dashed line) from that of air (solid line) and setting all negative values to zero, yields the derived oxidative reactions (dotted line). These derived results illustrate the presence of 3 additional oxidative reactions as follow [13] which produce final and secondary products similar to the pyrolysis reactions, and also the common products of combustion such as carbon monoxide and carbon dioxide.

(1) PU Foam + O_2 → Regenerated Polyol + OH Species, CO_2 and H_2O

(2) Regenerated Polyol + O_2 → Char + OH Species, H_2CO, CH_4, CO, CO_2 and H_2O

(3) Char + O_2 → OH Species, H_2CO, CH_4, CO, CO_2 and H_2O

The pyrolysis and oxidation of foam overlap over a similar temperature range, competing for the same reactant. The oxidative thermal decomposition initiates with the pyrolysis of foam but the competing oxidative reaction is able to accelerate and reach its peak first. With increasing heating rate, the reduction of the influence from oxidative reaction of foam (dotted line) is noted where the peak value reduces from $\sim 9.1 \times 10^{-3}$ to 3.1×10^{-3} 1/°C. The competing reactions for foam are followed by the oxidation of foam decomposition product, polyol which shows a fairly consistent influence at all heating rates, $\sim 7.7 \times 10^{-3}$ 1/°C. Similar to foam, there is also a competing pyrolysis reaction for polyol but this is sufficiently separated over a higher temperature range. As heating rate increases, the influence from the pyrolysis of polyol (solid line) becomes more prominent where the peak value increases from $\sim 2.3 \times 10^{-3}$ to 8.0×10^{-3} 1/°C. Lastly, the char from pyrolysis and oxidation of polyol undergoes oxidation, and its magnitude is relatively small compared to the other main reactions. Nonetheless, a reduction in the influence of char oxidation is noted as the heating rate increases. The sequence of pyrolysis and oxidative reactions for the oxidative thermal decomposition of NFR-SB-31 is found to be consistent with the literature [11-13].

The decomposition behaviour of FR-Y-36 for the different heating rates is shown in Fig. 2 a – d based on the same legends of NFR-SB-31 for the different environments. Note that the vertical axis of (a) and (b) have greater magnitude than (c) and (d). Similar to NFR-SB-31, the decomposition under nitrogen of FR-Y-36 shows the consistent 2-step pyrolysis mechanism at all heating rates. The decomposition under air also shows overlapping and heating rate dependent reactions but the 3 oxidative reactions are not always apparent, different from NFR-SB-31. At 1 and 5 °C/min, following the initial pyrolysis reaction of foam, a single peak is noted from the derived oxidative reactions suggesting that the oxidation of foam and polyol overlap each other closely. This is possibly due to the fire retardant additives within the foam, where the acidic condition generated by the breakdown of halophosphate and the reactivity of melamine towards the products of foam decomposition might have catalysed the oxidation of foam and polyol, allowing these to proceed at lower temperature under such heating rates [17, 18]. This lowers the ignitability of the gaseous products released and also allows the gas phase fire retardant mechanisms via means of neutralisation and dilution to be more effective. At 20 and 60 °C/min, separated peaks are noted for the oxidation of foam and polyol, and the influence of these oxidative reactions has diminished with increasing heating rate, from $\sim 2.7 \times 10^{-2}$ at 1 °C/min to 4.6×10^{-3} 1/°C at 60 °C/min.

While the influence from pyrolysis of polyol is negligible at 1 and 5 °C/min, this has increased at higher heating rates but compared to NFR-SB-31, the peak of the reaction is not as apparent. The char oxidation shows a similar trend to NFR-SB-31 in relation to heating rate but with greater magnitude due to char formation from melamine. According to Chao et al. [4], oxidative reaction is believed to be favored by slow heating and comparing Fig. 1 and Fig. 2, the results support this, showing the oxidative reactions having greater influence than the pyrolysis reactions at low heating rate. The temperature range where the main reactions occurs is ~200 °C for NFR-SB-31, consistently between 200 and 400 °C but for FR-Y-36, this range can vary from ~100 – 250 °C. The main reactions occur between 200 and 300 °C below 5 °C/min, between 200 and 400 °C at 20 °C/min, and increasing to between 200 and 450 °C at 60 °C/min. The extended temperature range of FR-Y-36 at high heating is due to the char formation from the breakdown of melamine which improves the thermal stability of the decomposing sample.

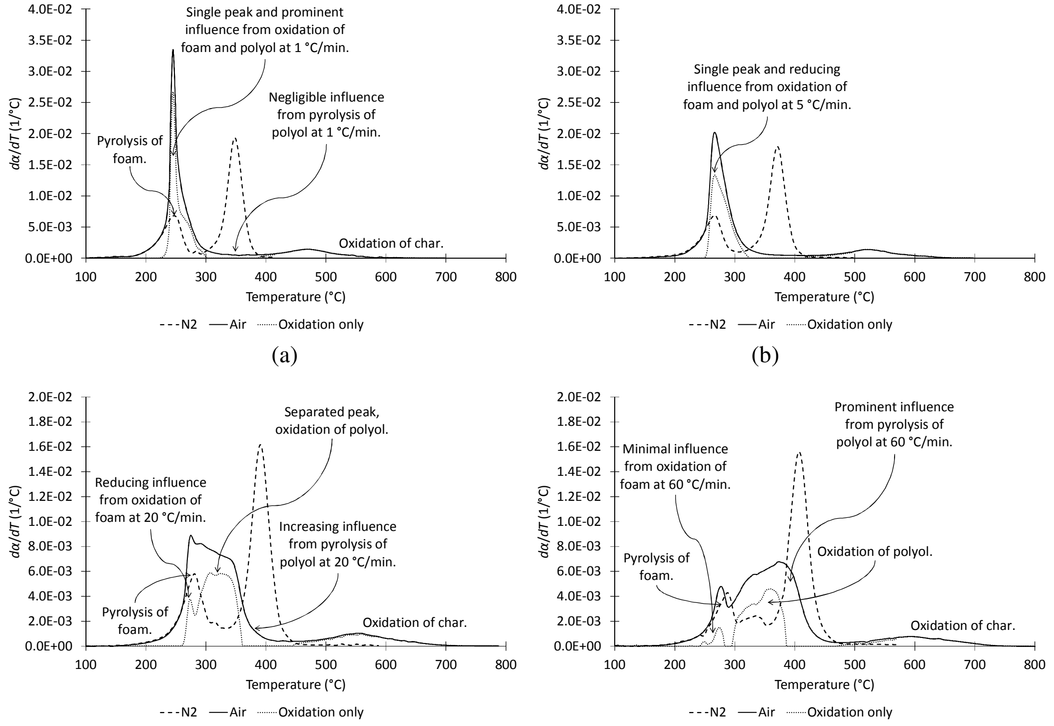

(a) (b)

(c) (d)

Fig. 2. Decomposition rate versus temperature of FR-Y-36 in air and nitrogen, and the derived oxidative reactions. (a) 1 °C/min; (b) 5 °C/min; (c) 20 °C/min; (d) 60 °C/min.

APPLICATION OF INFLECTION POINT METHODS

Based on the decomposition behaviour noted in Fig. 1 and Fig. 2, the kinetic properties, n, A and E for the 2 pyrolysis reactions and 3 oxidative reactions for the oxidative thermal decomposition of NFR-SB-31 and FR-Y-36 are determined using the Inflection Point Methods [14]. This graphical approach has previously been applied to determine the kinetic properties for the thermal decomposition of NFR-SB-31 and FR-Y-36 in nitrogen environment [21]. These references have presented the assumptions and derivation of the graphical technique and the description of the TG results analysed, from the start of a reaction to its peak. In Eq. (1), the temperature dependent rate constant, k is presented as the decomposition rate, $d\alpha/dT$ divided by the nth order kinetic model, $(1 - \alpha)^n$. On the right hand side, the remainder of the Arrhenius equation is in temperature basis by dividing A with the heating rate, β and R is the universal gas constant, 8.314 J/mol·K. At the peak of a reaction or the maximum inflection point, $n = (E/RT^2)(1 - \alpha)/(d\alpha/dT)$ and rearranging Eq. (1) yields Eq. (2) where $\Phi = T^2(d\alpha/dT)/(1 - \alpha)$, and all inputs for n and Φ are inflection point values.

$$\ln(k) = \ln\frac{d\alpha/dT}{(1-\alpha)^n} = -\frac{E}{RT} + \ln\left(\frac{A}{\beta}\right), \tag{1}$$

$$\ln\left(\frac{d\alpha}{dT}\right) = \frac{E}{R}\left(\frac{\ln(1-\alpha)}{\Phi} - \frac{1}{T}\right) + \ln\left(\frac{A}{\beta}\right), \tag{2}$$

The determination of the kinetic properties for the derived oxidative reactions of NFR-SB-31 at 60 °C/min is presented in Fig. 3 a – b as an example calculation. From the plot of ln(*dα*/*dT*) versus [ln(1 – α)/Φ] – 1/*T* in Fig. 3 a, as per Eq. (2), the value of *E*/*R* is determined from the slope for the 1st, 2nd and 3rd reactions which correspond to the oxidation of foam, polyol and char, respectively. Applying *E*/*R* determined into *n* yield 37.71, 10.38 and 31.27, respectively for these reactions. Applying *n* found into Eq. (1), from the plot of ln(*k*) versus 1/*T* in Fig. 3 b, *E* is determined from the slope and *A* is determined from intercept. The pair of values are 315 kJ/mol and 1.36×10^{28} 1/s for the 1st reaction, 352 kJ/mol and 6.23×10^{28} 1/s for the 2nd reaction, and 109 kJ/mol and 5.98×10^{10} 1/s for the 3rd reaction.

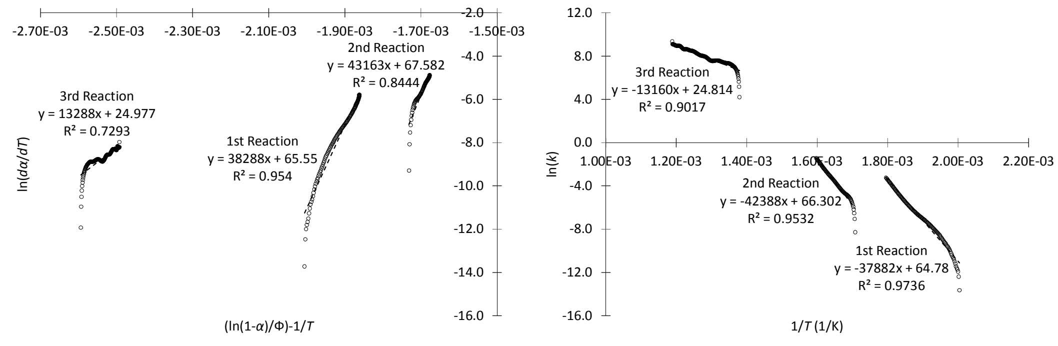

(a) (b)

Fig. 3. Application of Inflection Point Methods on derived oxidative reactions of NFR-SB-31 at 60 °C/min. (a) ln(*dα*/*dT*) versus [ln(1 – α)/Φ] – 1/*T*; (b) ln(*k*) versus 1/*T*.

KINETIC PROPERTIES AND HEAT OF REACTION

Wang et al. [23] described a multiple-component decomposition scheme where the overall decomposition rate, *dα*/*dt* is the summation of the decomposition rate of each component, $(d\alpha/dt)_i$ based on the respective mass fraction, c_i as per Eq. (3). This decomposition scheme is adopted as a simplified approach to model the competing pyrolysis and oxidative reactions of the heating rate dependent oxidative thermal decomposition of PU foam. Treating each reaction as a separate component, the model also contains a number of simplified assumptions, including (1) the 2 pyrolysis reactions can proceed, unaffected by the additional oxidative reactions, (2) the c_i for each component can be reasonably estimated from the area under the curve of *dα*/*dT* for each reaction, and (3) the residue generated from each reaction is considered negligible. The last assumption is the least pertinent as pyrolysis and oxidation of foam is known to generate polyol; however, given there are negligible amount of residue formed following the final oxidation of char, the overall impact of this assumption is perhaps lessened.

$$\frac{d\alpha}{dt} = \sum_i \left(\frac{d\alpha}{dt}\right)_i = \sum_i c_i A_i \exp\left(-\frac{E_i}{RT}\right)(1-\alpha)^{n_i}, \tag{3}$$

The refinement of kinetic properties introduced by Wang et al. [23] is also applied to refine n and c_i to achieve a reasonable comparison between the model and experimental $d\alpha/dT$. The refinement is qualitatively based on matching the peak values of each reaction, between the model and the experiment. Table 1 and Table 2 present the refined kinetic properties for each reaction implemented in the model where the subscript represents the different reactions, (1) oxidation of foam, (2) pyrolysis of foam, (3) oxidation of polyol, (4) pyrolysis of polyol and (5) oxidation of char. Also included in the tables is Δh_r calculated from the DSC heat flow measurements, the details of this analysis are presented later in this manuscript. A few reactions with low magnitude over an extended temperature range, such as the final char oxidation, the negligible polyol pyrolysis of FR-Y-36 from 1 – 20 °C/min, and the negligible foam oxidation of FR-Y-36 at 60 °C/min, have been excluded due to difficulty in calculating the kinetic properties and modelling the reaction with reasonable accuracy. Based on the single peak observed in Fig. 2 a – b, the oxidation of foam and polyol for FR-Y-36 are not differentiable at 1 and 5 °C/min so these merged reactions are simply denoted by subscript (1).

Table 1. Refined kinetic properties and heat of reaction for NFR-SB-31 at all heating rates

Reaction	Parameter	1 °C/min	5 °C/min	20 °C/min	60 °C/min
Foam oxidation	n_1	18.50	20.80	13.00	22.00
	A_1 (1/s)	3.96×10^{62}	3.04×10^{56}	1.45×10^{31}	1.36×10^{28}
	E_1 (kJ/mol)	639	597	350	315
	c_1	0.206	0.186	0.143	0.107
Foam pyrolysis	n_2	3.50	4.50	6.58	9.50
	A_2 (1/s)	8.27×10^{9}	5.68×10^{8}	7.73×10^{8}	5.41×10^{9}
	E_2 (kJ/mol)	134	121	121	127
	c_2	0.279	0.314	0.298	0.298
Polyol oxidation	n_3	9.50	10.30	13.30	6.70
	A_3 (1/s)	1.08×10^{51}	3.78×10^{52}	4.59×10^{61}	6.23×10^{28}
	E_3 (kJ/mol)	539	579	700	352
	c_3	0.206	0.267	0.297	0.298
Polyol pyrolysis	n_4	1.04	0.96	1.20	1.36
	A_4 (1/s)	1.07×10^{13}	2.22×10^{12}	1.95×10^{18}	2.47×10^{19}
	E_4 (kJ/mol)	189	181	251	265
	c_4	0.175	0.233	0.262	0.297
Char oxidation	n_5	4.70	excluded[a]	excluded[a]	excluded[a]
	A_5 (1/s)	2.34×10^{44}	excluded[a]	excluded[a]	excluded[a]
	E_5 (kJ/mol)	511	excluded[a]	excluded[a]	excluded[a]
	c_5	0.134	excluded[a]	excluded[a]	excluded[a]
Overall	Δh_r (J/g)	5499	4900	5252	5315

[a] Reaction has been excluded from the model.

From Table 1 and Table 2, the heating rate dependency of the oxidative reactions have resulted in greater variation in the kinetic properties across the heating rates investigated when compared with the pyrolysis reactions. From the trend of c_i, there is a notable reduction to the influence of foam oxidation as the heating rate increases while the influence of foam pyrolysis remains relatively constant. The reduction is compensated by the increase to the influence from oxidation and pyrolysis of polyol, particularly the latter showing notable increase at 60 °C/min. Figure 4 shows examples of the modelled decomposition rate for NFR-SB-31 and FR-Y-36 at specific heating rate, including the individual reactions that constitute the overall oxidative thermal decomposition.

Table 2. Refined kinetic properties and heat of reaction for FR-Y-36 at all heating rates

Reaction	Parameter	1 °C/min	5 °C/min	20 °C/min	60 °C/min
Foam oxidation	n_1	6.10	22.00	51.00	excluded[a]
	A_1 (1/s)	1.02×10^{73}	2.57×10^{121}	7.03×10^{136}	excluded[a]
	E_1 (kJ/mol)	753	1266	1446	excluded[a]
	c_1	0.582	0.454	0.053	excluded[a]
Foam pyrolysis	n_2	2.00	3.10	4.80	6.70
	A_2 (1/s)	5.46×10^{9}	4.27×10^{10}	1.20×10^{11}	1.12×10^{9}
	E_2 (kJ/mol)	130	137	141	118
	c_2	0.418	0.333	0.340	0.385
Polyol oxidation	n_3	excluded[a]	excluded[a]	3.10	2.90
	A_3 (1/s)	excluded[a]	excluded[a]	3.80×10^{14}	7.37×10^{10}
	E_3 (kJ/mol)	excluded[a]	excluded[a]	185	149
	c_3	excluded[a]	excluded[a]	0.394	0.372
Polyol pyrolysis	n_4	excluded[a]	excluded[a]	excluded[a]	1.91
	A_4 (1/s)	excluded[a]	excluded[a]	excluded[a]	3.07×10^{24}
	E_4 (kJ/mol)	excluded[a]	excluded[a]	excluded[a]	331
	c_4	excluded[a]	excluded[a]	excluded[a]	0.243
Char oxidation	n_5	excluded[a]	1.10	1.70	excluded[a]
	A_5 (1/s)	excluded[a]	2.46×10^{9}	2.56×10^{10}	excluded[a]
	E_5 (kJ/mol)	excluded[a]	156	155	excluded[a]
	c_5	excluded[a]	0.213	0.213	excluded[a]
Overall	Δh_r (J/g)	8362	5657	6045	6786

[a] Reaction has been excluded from the model.

Based on the sequence of the individual reactions, the modelled oxidative thermal decomposition initiates with the pyrolysis of foam, followed closely by the oxidation of foam which forms the first peak of the decomposition illustrated in Fig. 4. FR-Y-36 at 60 °C/min is an exception where the oxidation of foam is excluded from the model due to minimal influence on decomposition as noted in Fig. 2 d. The modelled decomposition continues with the oxidation of polyol which forms the second peak of the decomposition for NFR-SB-31 in Fig. 4 a and the plateau for FR-Y-36 in Fig. 4 b. FR-Y-36 at 1 and 5 °C/min are exception where the oxidation of polyol is not modelled because this reaction merges with the oxidation of foam to form a single peak. Unlike the pyrolysis and oxidative reactions of foam which closely overlap, the pyrolysis of polyol occurs over higher temperature and is relatively distanced from the oxidation of polyol as seen in Fig. 4 a for NFR-SB-31. FR-Y-36 from 1 – 20 °C/min are exception where pyrolysis of polyol is not modelled due to its negligible influence on decomposition as seen in Fig. 2 a – c. The pyrolysis of polyol captures the third and final peak of the main reactions. Lastly, the oxidation of char captures the extended decomposition at high temperature but this reaction is mostly excluded due to its minor contribution to the overall decomposition and the difficulty in accurately estimating its kinetic properties.

The comparison between model and experimental decomposition rate are illustrated in Fig. 5 and Fig. 6 for NFR-SB-31 and FR-Y-36, respectively at all the heating rates investigated. The solid line represents the experimental results while the dotted line represents the model results.

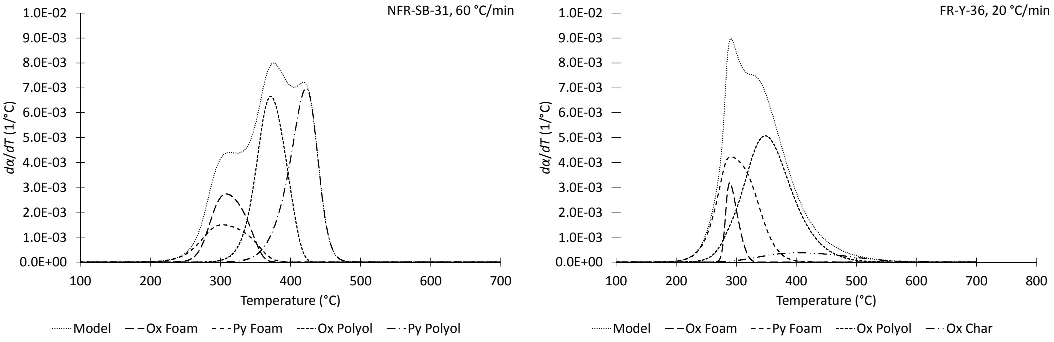

(a) (b)

Fig. 4. Modelled decomposition rate versus temperature for oxidative thermal decomposition of PU foams. (a) NFR-SB-31 at 60 °C/min; (b) FR-Y-36 at 20 °C/min.

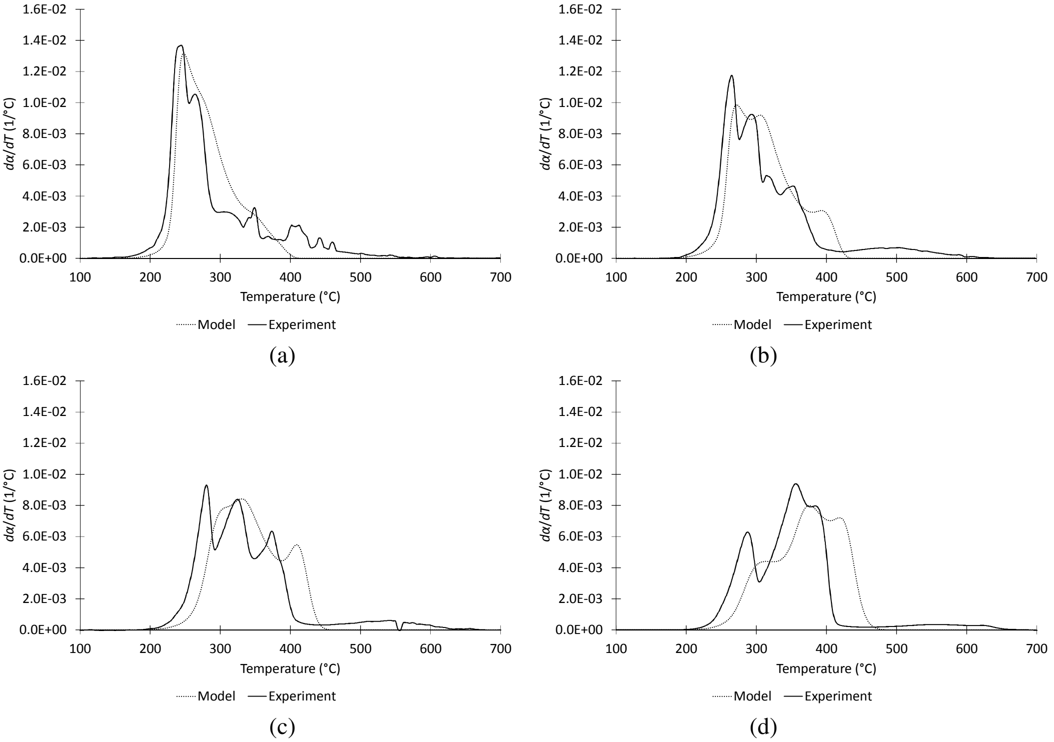

(a) (b)

(c) (d)

Fig. 5. Decomposition rate versus temperature between model and experiment for NFR-SB-31 in air. (a) 1 °C/min; (b) 5 °C/min; (c) 20 °C/min; (d) 60 °C/min.

The simplified model is able to capture the general trend observed experimentally for oxidative thermal decomposition of foams where the maximum *dα/dT* shifts from an initial lower temperature region towards a final higher temperature region with increasing heating rate. This is due to the reduction in the influence of foam oxidation and the increase in the influence of polyol pyrolysis. Three peaks for the oxidative thermal decomposition of NFR-SB-31 are evidenced from 5 – 60

°C/min, and these are captured by the overlapping individual reactions modelled. FR-Y-36 exhibits more variation in decomposition behaviour with a single peak at 1 – 5 °C/min which transitions into a plateau at 20 °C/min, and these features are captured by the model with reasonable accuracy. Note that the vertical scale utilised in Fig. 6 a – b is different to the others. Due to the simplified assumptions and the difficulty in accurately determining the kinetic properties of extended, low magnitude reaction, the model has not been able to capture the final stage of decomposition involving char oxidation. The model also consistently shows oxidative thermal decomposition initiating and occurring over slightly higher temperature range compared to the experiment, and such inherent mismatch is not uncommon [24]. The likely causes of mismatch include the selection of data points analysed and the adopted graphical technique to determine the kinetic properties, the assumptions made to establish the derived oxidative reactions, and the exponential nature of Arrhenius equation where minor change of inputs translate into relatively greater change of outputs.

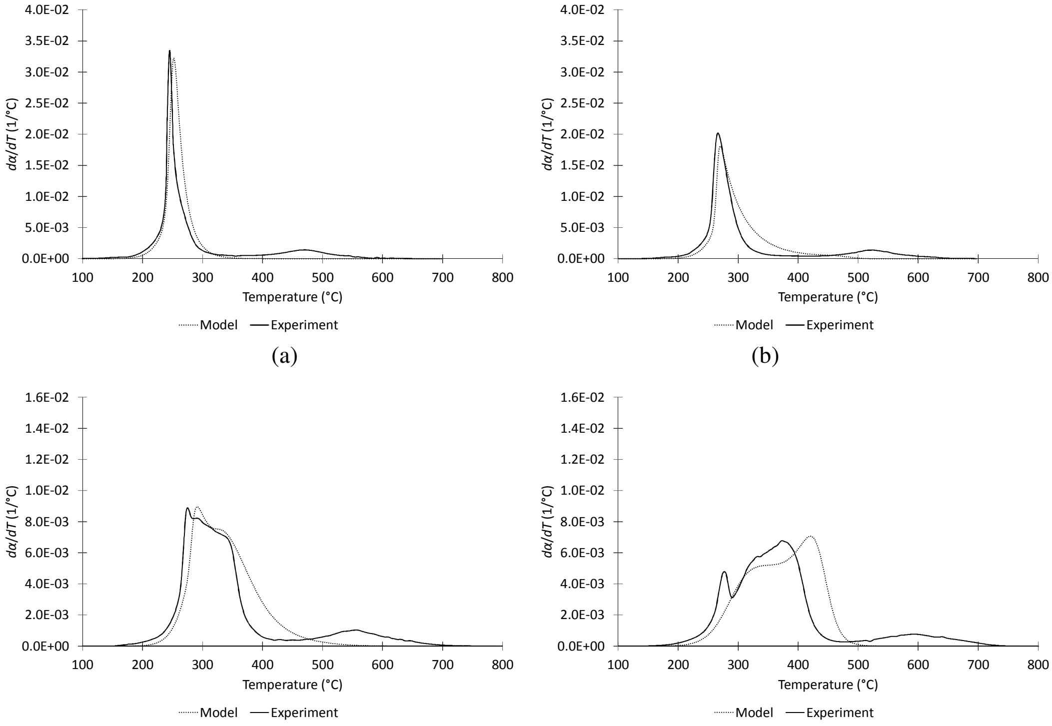

(a) (b)

(c) (d)

Fig. 6. Decomposition rate versus temperature between model and experiment for FR-Y-36 in air.
(a) 1 °C/min; (b) 5 °C/min; (c) 20 °C/min; (d) 60 °C/min.

Table 1 and Table 2 also presents the heat of reaction for the oxidative thermal decomposition of foams, determined from the DSC heat flow results. The method of analysis adopted has previously been applied to determine the heat of reaction for foam and polyol decomposition under inert nitrogen environment [22]. In oxidative air environment, the decomposition is exothermic in nature, releasing energy to its surrounding in lieu of endothermic where energy is absorbed for the thermal decomposition as noted under nitrogen environment. For NFR-SB-31, the exothermic heat of reaction ranges from 4900 – 5499 J/g while for FR-Y-36, this has a higher magnitude from 5657 – 8362 J/g due to the oxidation of additional char from the fire retardant additives [4]. This amounts to approximately 19 % for NFR-SB-31 and 26 % for FR-Y-36, in terms of energy released during complete combustion while the remaining 81 % and 74 % are released in the gas phase upon ignition, similar to the findings in [13]. The breakdown of fire retardants within FR-Y-36 probably amount to the higher heat of reaction measured and the reduction in the amount of energy released in gas phase. The heat of reaction measured for the 2 pyrolysis reactions of foam and polyol ranges from endothermic 610 – 1023 J/g and 164 – 295 J/g, respectively and it is evident that significantly more energy would be released than absorbed over the oxidative thermal decomposition of foam.

CONCLUSIONS

The oxidative thermal decomposition of PU foams is represented by a total of 5 reactions, 2 pyrolysis and 3 oxidative. From TG experiments, the 2 pyrolysis reactions demonstrated consistent trend with increasing heating rate while the additional 3 oxidative reactions are noted to be heating rate dependent. A simplified model is developed and applied to simulate the experimental behaviour. The model captures the essential heating rate dependent trend where the influence of foam oxidation reduces and the influence of polyol pyrolysis increases towards higher heating rate. The fire retardant additives of the FR foam, halophosphate and melamine appear to show characteristics which potentially improve the foam's fire performance. These include the notable decomposition over lower temperature region at low heating rate where the gaseous fuel released could be neutralised or diluted by the gas phase fire retardant mechanisms, and at high heating rate, the decomposition occurs over greater temperature range with lower magnitude due to char formation. However, the literature has also showed that FR foams can be prone to smouldering combustion due to the complex char formation and oxidation. The toxicity of smouldering combustion and its likelihood of transitioning into flaming combustion can diminish the fire performance of FR foams. Going forward, the research can benefit from better understanding on the impact of varying local oxygen concentration has on the oxidative thermal decomposition.

ACKNOWLEDGEMENTS

The authors would like to acknowledge the Chemistry Department for offering the experimental equipment; the lab technicians, Mr. Mike Van der Colk and Mr. Grant Dunlop for their technical support; Dr. Kai-Yuan Li for the intellectual discussions on the topic of material decomposition.

REFERENCES

[1] T.J. Ohlemiller, J. Bellan, F. Rogers, A Model of Smoldering Combustion Applied to Flexible Polyurethane Foams, Combust. Flame 36 (1979) 197–215.

[2] J.L. Torero, A.C. Fernandez-Pello, M. Kitano, Opposed Forced Flow Smoldering of Polyurethane Foam, Combust. Sci. Technol. 91 (1993) 95–117.

[3] D.C. Walther, A.C. Fernandez-Pello, D.L. Urban, Space Shuttle Based Microgravity Smoldering Combustion Experiments, Combust. Flame 116 (1999) 398–414.

[4] C.Y.H. Chao, J.H. Wang, Transition from Smoldering to Flaming Combustion of Horizontally Oriented Flexible Polyurethane Foam with Natural Convection, Combust. Flame 127 (2001) 2252–2264.

[5] G. Rein, Smouldering Combustion Phenomena in Science and Technology, Int. Rev. Chem. Eng. 1 (2009) 3–18.

[6] K. Prasad, R. Krämer, N. Marsh, M. Nyden, T. Ohlemiller, M. Zammarano, Numerical Simulation of Fire Spread on Polyurethane Foam Slabs, Proc. Fire Mater. 11 (2009) 697–708.

[7] R.H. Krämer, M. Zammarano, G.T. Linteris, U.W. Gedde, J.W. Gilman, Heat Release and Structural Collapse of Flexible Polyurethane Foam, Polym. Degrad. Stab. 95 (2010) 1115–1122.

[8] R. Bilbao, J.F. Mastral, J. Ceamanos, M.E. Aldea, Kinetics of the Thermal Decomposition of Polyurethane Foams in Nitrogen and Air Atmospheres, J. Anal. Appl. Pyrolysis 37 (1996) 69–82.

[9] C.Y.H. Chao, J.H. Wang, Comparison of the Thermal Decomposition Behavior of a Non-Fire Retarded and a Fire Retarded Flexible Polyurethane Foam with Phosphorus and Brominated Additives, J. Fire Sci. 19 (2001) 137–156.

[10] G. Rein, C. Lautenberger, A.C. Fernandez-Pello, J.L. Torero, D.L. Urban, Application of Genetic Algorithms and Thermogravimetry to Determine the Kinetics of Polyurethane Foam in Smoldering Combustion, Combust. Flame 146 (2006) 95–108.

[11] L.B. Valencia, Experimental and Numerical Investigation of the Thermal Decomposition of Materials at Three Scales: Application to Polyether Polyurethane Foam Used in Upholstered Furniture, PhD thesis, École Nationale Supérieure de Mécanique et d'Aérotechnique, Poitiers, France, 2009.

[12] L.B. Valencia, T. Rogaume, E. Guillaume, New Method for Simulating the Kinetic of Toxic Gases Production of Upholstered Furniture Fire, Proc. Fire Mater. 11 (2009) 685–695.

[13] T. Rogaume, L.B. Valencia, E. Guillaume, F. Richard, J. Luche, G. Rein, J.L. Torero, Development of the Thermal Decomposition Mechanism of Polyether Polyurethane Foam Using Both Condensed and Gas-Phase Release Data, Combust. Sci. Technol. 183 (2011) 627–644.

[14] S.G. Viswanath, M.C. Gupta, Estimation of Nonisothermal Kinetic Parameters from a TG Curve by the Methods of Overdetermined System and Inflection Point, Thermochim. Acta 285 (1996) 259–267.

[15] H.C. Ashton, Fire Retardants, in: M. Xanthos (Ed.), Functional Fillers for Plastics, Wiley-VCH, Weinheim, 2010, pp. 309–350.

[16] S.V. Levchik, Introduction to Flame Retardancy and Polymer Flammability, in: A.B. Morgan, C.A. Wilkie (Eds.), Flame Retardant Polymer Nanocomposites, John Wiley & Sons Inc., New Jersey, 2007, pp. 1–30.

[17] N. Grassie, G.A.P. Mendoza, Thermal Degradation of Polyether-Urethanes: Part 4 – Effect of Ammonium Polyphosphate on the Thermal Degradation of Polyether-Urethanes Prepared from Methylene Bis(4-Phenylisocyanate) and Low Molecular Weight Poly(Ethylene Gylcols), Polym. Degrad. Stab. 11 (1985) 145–166.

[18] D. Price, Y. Liu, G.J. Milnes, R. Hull, B.K. Kandola, A.R. Horrocks, An Investigation into the Mechanism of Flame Retardancy and Smoke Suppression by Melamine in Flexible Polyurethane Foam, Fire Mater. 26 (2002) 201–206.

[19] C. Denecker, J.J. Liggat, C.E. Snape, Relationship between the Thermal Degradation Chemistry and Flammability of Commercial Flexible Polyurethane Foams, J. Appl. Polym. Sci. 100 (2006) 3024–3033.

[20] D.S.W. Pau, A Comparative Study on Combustion Behaviours of Polyurethane Foams with Numerical Simulations using Pyrolysis Models, PhD thesis, University of Canterbury, Christchurch, New Zealand, 2013.

[21] D.S.W. Pau, C.M. Fleischmann, M.J. Spearpoint, K.Y. Li, Determination of Kinetic Properties of Polyurethane Foam Decomposition for Pyrolysis Modelling, J. Fire Sci. 31 (2013) 356–384.

[22] D. Pau, C. Fleischmann, M. Spearpoint, K.Y. Li, Sensitivity of Heat of Reaction for Polyurethane Foams, In: Nilsson, D., van Hees, P., Jansson, R. (Eds.), Fire Safety Science–Proceedings of the Eleventh International Symposium, pp, 179–192, 2014.

[23] X. Wang, C.M. Fleischmann, M.J. Spearpoint, Parameterising Study of Tunnel Experiment Materials for Application to the Fire Dynamics Simulator Pyrolysis Model, J. Fire Sci. 34 (2016) 490–514.

[24] F. Hache, M. Delichatsios, T. Fateh, J. Zhang, Comparison of Methods for Thermal Analysis: Application to PEEK and a Composite PEEK + CF, J. Fire Sci. 33 (2015) 232–246.

Comparison of Pyrolysis and Combustion Properties of Rigid and Plasticized Poly(vinyl chloride)

Swann J.*, Ding Y., Stoliarov S.

University of Maryland, Department of Fire Protection Engineering, College Park, MD, USA
**Corresponding author's email: jswann91@umd.edu*

ABSTRACT

A methodology to fully parameterize a comprehensive pyrolysis model is demonstrated on specimens of plasticized and rigid poly(vinyl chloride). Thermogravimetric analysis, differential scanning calorimetry and microscale combustion calorimetry were employed to characterize the kinetics and thermodynamics of thermal decomposition and heats of complete combustion of gaseous decomposition products. Controlled Atmosphere Pyrolysis Apparatus II gasification experiments were utilized to determine the thermal transport parameters within the undecomposed material and developing char layer. A recently expanded, fully verified and validated numerical framework, ThermaKin2Ds, was employed to simulate the axisymmetric gasification experiments and analyze all experimental results. The model was shown to reproduce the experimental results with a high degree of detail. Idealistic, one-dimensional simulations of burning of solid materials in the presence of external radiant heat flux, subsequently conducted using the fully parameterized comprehensive pyrolysis models, indicated that plasticized and rigid poly(vinyl chloride) have similar mass loss rate histories. However, significant differences become apparent when the mass loss rates of gaseous decomposition products are converted to heat release rate.

KEYWORDS: Intumescence, material flammability, pyrolysis modeling, ThermaKin.

INTRODUCTION

Poly(vinyl chloride) (PVC) is a commonly used material in the built environment, which possesses desirable flammability properties. Hirschler [1] found that PVC was more difficult to ignite, easier to extinguish, more resistant to flame spread and had a lower heat release rate per unit initial mass than the majority of natural and synthetic polymers studied. The introduction of plasticizers to PVC produces flexible PVC (FPVC) to widen its range of applications, such as electrical cable [2]. The introduction of additional combustible plasticizers can alter the materials reaction to fire, which is a distinction that is often neglected in fire modeling efforts of PVC materials. Comprehensive pyrolysis modeling is important for many fire safety considerations; however, the reliability of modeling results is proportional to the accuracy of the parameters representing the materials of interest.

Our group has developed a methodology employing novel experimental tools coupled with an advanced numerical model to characterize many common materials for pyrolysis modeling [3, 4]; this methodology has recently been expanded to charring and intumescent materials [5, 6]. Thermogravimetric analysis (TGA) and differential scanning calorimetry (DSC) techniques were coupled with a comprehensive pyrolysis solver, ThermaKin, to characterize the kinetics and thermodynamics of thermal decomposition through inverse analysis. Microscale combustion calorimetry (MCC) was employed to parameterize the heats of complete combustion of pyrolyzate gases. Newly developed gasification experiments [5] were conducted to determine thermal transport parameters within the pyrolyzing samples, also analyzed through inverse analyses. This

Proceedings of the Ninth International Seminar on Fire and Explosion Hazards (ISFEH9), pp. 1109-1121
Edited by Snegirev A., Liu N.A., Tamanini F., Bradley D., Molkov V., and Chaumeix N.
Published by Saint-Petersburg Polytechnic University Press
ISBN: 978-5-7422-6498-9 DOI: 10.18720/spbpu/2/k19-50

methodology permits a comprehensive characterization of charring and intumescent materials and their associated reaction to fire. The objective of this study was to demonstrate this methodology to characterize FPVC for comprehensive pyrolysis modeling as well as provide a meaningful comparison between the fire behavior of FPVC and a rigid PVC studied previously [6].

EXPERIMENTAL AND NUMERICAL METHODS

Materials

A transparent FPVC was studied in this work. The FPVC samples were obtained from TMI Vinyl Solutions in $5.45 \cdot 10^{-3}$ m thick sheets and had a density computed at room temperature of 1226 kg/m^3. The milligram-scale test samples were carefully cut into very small flat pieces approximately 4–7 mg in mass. The samples for the gasification tests were cut to 0.07 m diameter disks using a computer numerical control (CNC) milling machine. Samples for the absorption coefficient measurements (discussed in a later section) were manufactured by machining the 0.07 m diameter disks to a thickness of $1 \cdot 10^{-3}$ m in the center (0.02 m diameter) portion of the specimen. All samples were stored in a desiccator for a minimum of 48 h prior to testing. The pyrolytic behavior of this FPVC material was compared to a pure rigid PVC studied previously [6].

Milligram-scale experiments

TGA and DSC tests were conducted simultaneously using a Netzsch 449 F3 Jupiter Simultaneous Thermal Analyzer (STA) to characterize the kinetics and thermodynamics of thermal decomposition. The temperature program for all STA tests consisted of a conditioning period, with the sample maintained at 313 K for 25 min, followed by a linear heating to 973 K. The STA tests of FPVC used in the reaction model development (see Table 1) were conducted at 10 K/min and repeated 10 times to accumulate the necessary statistics. Additional TGA tests were performed in triplicate at 5 and 20 K/min to verify that the developed reaction model correctly extrapolates the material's behavior to alternate thermal conditions. All the tests were performed in a nitrogen environment. Platinum-rhodium crucibles with lids containing a small opening were used for all STA tests to maximize temperature uniformity and heat flow sensitivity. The sample mass and heat flow data were collected as a function of time and pyrolyzing sample temperature. A detailed description of the instrument calibration and testing protocol can be found in an earlier publication [7].

MCC is a standardized test method employed to measure the heat release rate (HRR) associated with a complete combustion of gaseous products generated by a thermally decomposing solid as a function of time and solid sample temperature [8]. All MCC tests were conducted using a nominal heating rate of 10 K/min in the pyrolyzer to facilitate direct comparison with STA data. The samples were heated within the pyrolyzer in an open ceramic crucible within a fully anaerobic environment. The gaseous pyrolyzate was then mixed with excess oxygen and oxidized in the combustor. The temperature of the combustor was set at 1173 K to ensure completeness of the oxidation process. The heat released during oxidation was measured using the oxygen consumption principle [9]. The MCC apparatus was carefully calibrated on a weekly basis following recommended procedures [9]. All MCC tests on FPVC were conducted in triplicate due to a high degree of reproducibility.

Gram-scale experiments

The radiation absorption coefficient measurement was based on a methodology described by Linteris et al. [10]. A well-defined radiant heat flux from an electric conical heater was transmitted through the FPVC sample, positioned 0.07 m below the base of the heater housing, and subsequently measured with a water-cooled Schmidt-Boelter heat flux transducer. The incoming radiation was collimated by Kaowool PM insulation board to direct it through a thin ($\approx 1 \cdot 10^{-3}$ m) portion of the specimen. All measurements were performed at a heater temperature of 940 K, which corresponded to an incident radiant heat flux of 45 kW/m^2 at a distance of 0.04 m below the heater housing. The transmitted heat flux was averaged for the first 3 s of sample exposure. Absorption coefficient tests were conducted in duplicate. The emissivity required to compute the absorption coefficient was obtained from literature. Details of the absorption coefficient measurement methodology can be found elsewhere [4, 11].

Gasification tests were conducted using the newly developed Controlled Atmosphere Pyrolysis Apparatus II (CAPA II), which enables carefully controlled pyrolysis utilizing water-cooled chamber walls. The disk-shaped samples were subjected to a nominal radiative heat flux of 30 and 60 kW/m^2. The radiative heat flux was carefully characterized to account for changes in this heat flux incident to the top sample surface due to the evolving shape and position of the sample surface associated with intumescence. All tests were conducted in duplicate in a nitrogen environment (O_2 volumetric fraction < 1%) until no mass loss was observed. The samples mass, spatially resolved bottom surface temperature and sample profile evolution were collected as a function of time. Additional information on the instrument characterization and application can be found elsewhere [5, 6].

Numerical modeling

A comprehensive pyrolysis solver, ThermaKin [12, 13], was employed to inversely analyze all experimental data and make predictions. The solver, a new version of which was named ThermaKin2Ds, was recently expanded to include a new 2Dax module capable of simulating two-dimensional axisymmetric objects [6]. ThermaKin2Ds solves for the transient rate of gaseous fuel production using fundamental physical and chemical properties of constituents of a pyrolyzing object exposed to external heat. An arbitrary reaction mechanism, consisting of first- and second-order chemical reactions, can be defined using the Arrhenius expression for the reaction rate constants.

In the modeling of the milligram-scale experiments, all samples were treated as thermally thin and simulated using a single element. The element temperature was forced to follow the experimental temperature profile by defining a sufficiently high convection coefficient, $1\cdot10^5$ W/(m$^2\cdot$K), at the boundary. The experimental temperature profile was prescribed by expressing the heating rate via an exponentially decaying sinusoidal function to account for the variation in the instantaneous experimental heating rate with time, as explained in detail elsewhere [4, 14]. The mass flow boundary conditions were defined such that the gaseous pyrolyzate instantaneously escaped the element.

The modeling of the bench-scale (CAPA II) experiments was carried out using the 2Dax module of ThermaKin2Ds. The 2Dax module was employed by defining a single computational element in the radial direction to represent a one-dimensional (1D) simulation or by defining 10 elements in the radial direction to represent a two-dimensional (2D) simulation, which took into account non-uniform swelling of the CAPA II sample. The elements were characterized by size Δx for 1D, and Δx (axial) and Δz (radial) for 2D simulations. Each element was characterized by the component masses and temperature, which were calculated for each time step. A detailed description of this integration procedure can be found in earlier publications [12, 13].

All calculations were conducted using $\Delta x = 5\cdot10^{-5}$ m and $\Delta z = 3.5\cdot10^{-3}$ m (2D model only) spatial discretization and 0.01 s time step. Increasing or decreasing these integration parameters by a factor of 2 did not produce any significant changes in the results of the simulations, indicating convergence of the numerical solutions. The gaseous products were assumed not to contribute to the volume of the sample in all simulations conducted in this work. The prescribed density of each decomposition product was decreased systematically to model the expansion of the intumescent sample. The external thermal boundary conditions were implemented to emulate those in the CAPA II experimental setup. Additional information on the modeling methodology can be found elsewhere [6].

RESULTS AND DISCUSSION

Overall methodology

The following methodology, consisting of three consecutive steps, was employed to characterize FPVC pyrolysis. The first step included milligram-scale experiments, which decoupled thermal decomposition from thermal transport to enable the determination of the kinetics and thermodynamics of thermal decomposition and the heats of complete combustion of gaseous decomposition products through manually iterative inverse analyses. The second step employed gram-scale gasification experimental results to characterize the density and thermal conductivity of each condensed-phase component through a manually iterative inverse analysis procedure. Throughout the parameterization process, an attempt was made to minimize the number of independent parameters and thus create the simplest model that captures the experimental data with the accuracy comparable to their uncertainty. The third step utilized CAPA II MLR histories obtained at a range of external heating intensities to validate the parameterized pyrolysis model. This methodology is a hierarchical process which relies on the results of previous steps to enable a well-posed mathematical problem ensuring a single solution at each step. The resulting FPVC pyrolysis model and the rigid PVC model from an earlier work [6] were compared to determine the impact of plasticizers on the material’s reaction to fire.

Inverse analysis of milligram-scale experiments

The mean experimental TGA and DSC data are presented as symbols in Fig. 1. The instantaneous mass, m, and associated mass loss rate, MLR, normalized by the initial mass, m_0, as a function of temperature, T, are shown in Fig. 1(a). The heat flow to the sample and integral heat flow, both normalized by the initial mass, are presented as a function of temperature in Fig. 1(b). Here, all positive values of heat flow represent endothermic processes. The error was calculated from the scatter of the data as two standard deviations of the mean (some error bars are difficult to discern because they are comparable in size to the data symbols). The experimental MLR profile contains two prominent peaks, the first at 586 K and the second at 740 K, corresponding to the thermal decomposition process. The decomposition produced 6.4 wt.% of final condensed-phase residue. The heat flow curve contains two distinct maxima that closely correspond to the MLR profile.

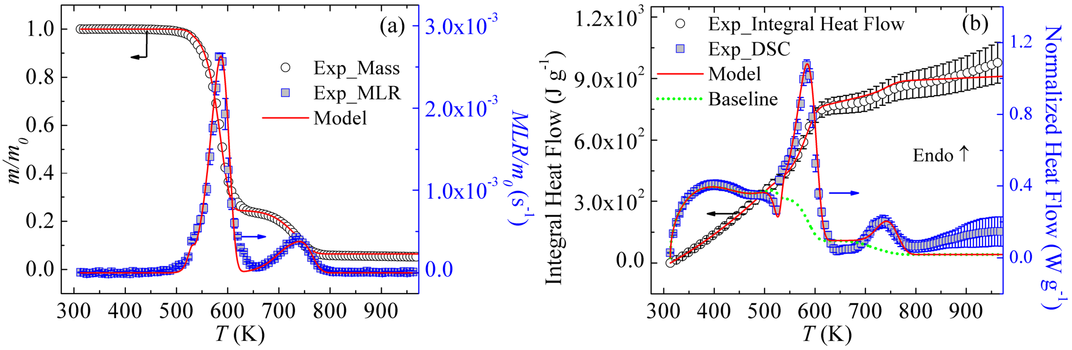

Fig. 1. Averaged experimental and simulated (a) TGA and (b) DSC data obtained for FPVC at a nominal heating rate of 10 K/min.

Inverse modeling of the STA data was performed using the approach described in detail in earlier publications [7, 14-17]. The stoichiometric coefficients and Arrhenius parameters of a single first-order reaction was initially employed to model the TGA data. The parameters were refined through a manually iterative process using ThermaKin2Ds until the modeling results were found to be in agreement with the experimental data. The agreement was declared satisfactory when the differences between the average experimental and modeled final mass residues, and temperatures and magnitudes of MLR maxima were found to be within 3%, 5 K and 8%, respectively. If it was impossible to achieve such agreement, an additional reaction was added to the reaction scheme and its parameters were adjusted iteratively to achieve further improvement. In the case of FPVC, four consecutive reactions, Reactions 1 to 4, were required to capture the intricacies of the initial rise, multiple maxima and final decay of the MLR within the accuracy of the experimental data. This series of first-order reactions are provided in Table 1 and the resulting model is shown in Fig. 1 as solid lines. The resulting reaction scheme was validated by predicting the temperatures and magnitudes of the MLR maxima within 10 K and 13%, respectively, of the average TGA experimental data collected at 5 and 20 K/min.

Table 1. Reaction scheme and kinetic parameters for the thermal decomposition of FPVC. A negative value for heats of decomposition (*h*) represents endothermic processes

#	Reaction	A, s^{-1}	E, J/mol	H, J/kg
1	FPVC → 0.98 FPVC_Res1 + 0.02 FPVC_Gas1	$1.5{\cdot}10^{32}$	$3.41{\cdot}10^{5}$	$1.8{\cdot}10^{4}$
2	FPVC_Res1 → 0.25 FPVC_Res2 + 0.75 FPVC_Gas2	$7.0{\cdot}10^{11}$	$1.56{\cdot}10^{5}$	$-2.5{\cdot}10^{5}$
3	FPVC_Res2 → 0.75 FPVC_Res3 + 0.25 FPVC_Gas3	$3.0{\cdot}10^{10}$	$1.70{\cdot}10^{5}$	$-1.0{\cdot}10^{4}$
4	FPVC_Res3 → 0.35 FPVC_ Res4 + 0.65 FPVC_Gas4	$3.0{\cdot}10^{10}$	$1.80{\cdot}10^{5}$	$-3.0{\cdot}10^{5}$

The heat flow data were analyzed by first focusing on the regions not associated with melting or decomposition. The data corresponding to these regions were divided by the instantaneous heating rate and fitted with linear functions representing heat capacities, c, of the corresponding condensed-phase components. The heat flow data between 313 and 500 K were used to determine the heat capacity of undecomposed FPVC. Due to the small residual char yield, the heat capacity of FPVC_Res4 was prescribed to be the average heat capacity of chars generated by several representative charring polymers [15]. It was assumed that the heat capacity of FPVC_Res3 was identical to FPVC_Res4 due to the reaction occurring at a similar temperature range. The heat capacity of the remaining intermediate condensed-phase products (FPVC_Res1 and FPVC_Res2) were assumed identical and equal to the average heat capacity of FPVC and FPVC_ Res4 to reduce the number of independently adjustable parameters. All heat capacity values are listed in Table 2. The heat capacity of all gaseous decomposition products were assumed equal to 2100 J/(kg·K), which was the mean heat capacity of a collection of C1 to C8 hydrocarbons at a temperature of 600 K [18]. The value of this heat capacity had negligible impact on the presented modeling results.

Table 2. Heat capacities of condensed-phase components for FPVC decomposition

Component	c, J/(kg·K)	Component	c, J/(kg·K)
FPVC	$-221 + 5.10T$	FPVC_Res3	1700
FPVC_Res1	$739.5 + 2.55T$	FPVC_Res4	1700
FPVC_Res2	$739.5 + 2.55T$		

The sensible heat flow baseline was subsequently calculated as a product of the mass fractions of condensed-phase components (whose temporal evolution was computed by ThermaKin2Ds), corresponding heat capacities and instantaneous heating rate. The baseline obtained for FPVC is shown as a dotted line in Fig. 1(b). Subtraction of this baseline from the normalized experimental heat flow and subsequent integration of the differences yielded the values of the heats of decomposition, h. The heats of decomposition were subsequently refined until the simulated heat flow maxima were within 10%, temperatures of the maxima were within 8 K and the final integral heat flow value was within 5% of the corresponding experimental data. The results of this exercise are shown as solid lines in Fig. 1(b). The heats of decomposition are listed in Table 1.

The mean experimental MCC HRR and total heat release (THR) data, both normalized by the initial FPVC sample mass, are presented as a function of temperature in Fig. 2. The heats of combustion, h_c, of gaseous components defined in the reaction mechanism (see Table 1) were determined through simulating the HRR curves. Initial comparisons between the experimental HRR and modeled MLR profiles generated using the heating rate history specific to the MCC revealed some discrepancies. These discrepancies were identified through a recognition that any significant heat release should require a concurrent mass loss. These discrepancies were attributed to sample temperature deviations from that measured by the MCC sensor and were corrected by shifting the experimental curves to a slightly higher temperature, as shown in Fig. 2.

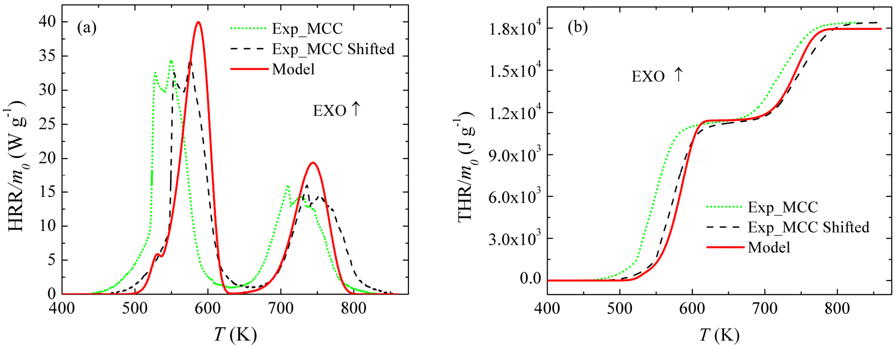

Fig. 2. Mean experimental and simulated normalized (a) heat release rate and (b) total heat release from MCC tests on FPVC at a nominal heating rate of 10 K/min.

The heats of combustion were first estimated by dividing the shifted experimental HRR data by the rate of production of gaseous components computed by ThermaKin2Ds. A simulated HRR curve was subsequently generated using the estimated h_c values. The values of h_c were further refined until the simulated and experimental HRR and THR data agreed within established MCC criteria. The criteria were defined as differences of less than 8% between the height of the experimental and modeled HRR maxima, less than 10 K between the temperatures of the maxima, and less than 8% between the final integral HRR values. The resulting heats of combustion are shown in Table 3. The simulated MCC data, using these h_c values, is shown as solid lines in Fig. 2.

Table 3. Heats of complete combustion of FPVC gaseous decomposition products (positive values represent exothermic processes)

Component	h_c, J/kg	Component	h_c, J/kg
FPVC_Gas1	$2.70 \cdot 10^7$	FPVC_Gas3	$1.20 \cdot 10^7$
FPVC_Gas2	$1.39 \cdot 10^7$	FPVC_Gas4	$4.90 \cdot 10^7$

Analysis of gram-scale experiments

Analysis of the gram-scale tests requires knowledge of the emissivity and absorption coefficients *a priori*. The initial emissivity of FPVC (0.90) was assumed to be equal to rigid PVC and was obtained from literature [19]. The emissivity of FPVC_Res4 (0.94), and thus FPVC_Res3, was estimated based on independent tests described elsewhere [6]. The remaining reactants, FPVC_Res1 and FPVC_Res2, were prescribed to have the average emissivity of FPVC and FPVC_Res4. The absorption coefficient of virgin FPVC, normalized by its density at ambient temperature, was estimated to be 1.1 ± 0.2 m^2/kg based on measurements performed in the current study. The upper char layer was observed to appear very optically dark and graphitic in nature. Therefore, the absorption coefficient of FPVC_Res4 was defined sufficiently high (100 m^2/kg) such that all the radiation was absorbed at the top surface. The absorption coefficient of FPVC_Res1 and FPVC_Res2 were defined to be the average of FPVC and FPVC_Res4.

The experimental CAPA II dataset for FPVC pyrolysis, at a nominal heat flux of 30 and 60 kW/m^2, are shown in Fig. 3 and Fig. 4. Representative shape profiles are provided in Fig. 3 as a function of time, t. The bottom surface temperature histories of the center ($r_z/R = 0$) and edge ($r_z/R = 0.86$) of the sample are presented as symbols in Fig. 4(a)(c), where r_z is the instantaneous sample radius and R is the initial total sample radius. The mean experimental MLR is shown in Fig. 4(b)(d). The uncertainty was computed from the scatter of the data as two standard deviations of the mean. The modeling results, also presented in Fig.3 and Fig. 4, are discussed in a later portion of the manuscript.

The sample's swelling process includes simultaneous increase in thickness and reduction in diameter at later stages of decomposition. At all heat fluxes, the increase in thickness is monotonic. The bottom surface temperature is spatially uniform in the early stages of pyrolysis. In later stages, the temperature becomes non-uniform with the edge of the surface being systematically cooler than the center. The MLR data at 30 kW/m^2 exhibit a single prominent peak, while the 60 kW/m^2 MLR data exhibit multiple peaks during pyrolysis.

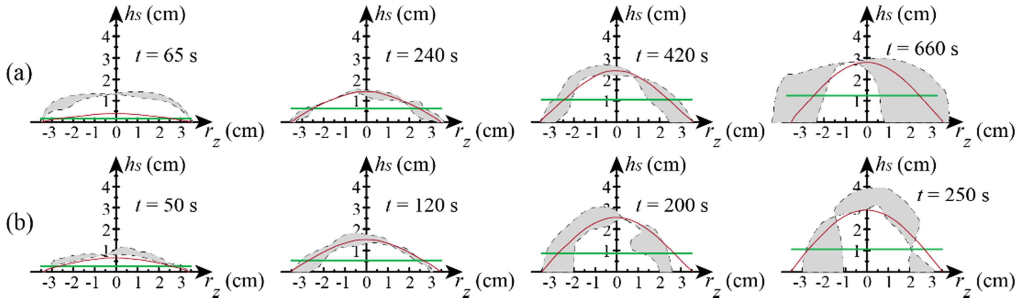

Fig. 3. The black dashed lines are experimental data from duplicate FPVC tests at (a) 30 kW/m^2 and (b) 60 kW/m^2. The vertical axis (h_S) begins at the initial position of the top sample surface. The shaded area indicates the profiles uncertainty. The straight and curved solid lines represent 1D and 2D model results, respectively.

In the following gram-scale model characterization, the 30 kW/m^2 shape profile and temperature dataset is employed as fitting targets; therefore, the 60 kW/m^2 dataset is strictly used as validation for the resulting model. The intumescent behavior of the FPVC pyrolysis was captured numerically in ThermaKin2Ds by prescribing decreasing component densities to account for increased sample thicknesses. In the 1D simulation, the sample thickness expanded uniformly across the entire radius; therefore, the average experimental sample thickness was employed as a target value for the density parametrization. The densities were decreased through a manually iterative procedure such that the fitted sample thickness (solid straight line) captured the critical shape changes in the 30 kW/m^2 dataset, shown in Fig. 3(a). The densities also factored in reductions in mass associated with the individual reaction steps (listed in Table 1). The densities of each reactant of 1D FPVC pyrolysis are provided in Table 4. The density parameterization was dependent upon the thermal transport parameters; therefore, the density and thermal conductivity parameters were iteratively adjusted simultaneously until satisfactory results were obtained

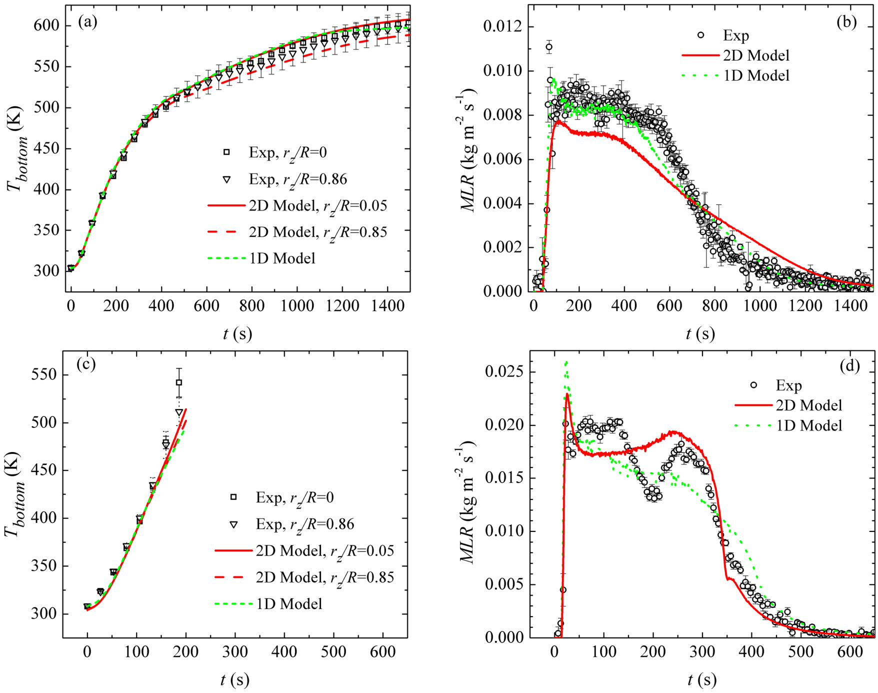

Fig. 4. Averaged experimental and modeled bottom surface temperatures and MLR data obtained at (a)(b) 30 kW/m^2 and (c)(d) 60 kW/m^2. The 60 kW/m^2 temperature data was truncated during later stages of pyrolysis due to the sample decoupling from the copper foil, resulting in poor thermal contact and unreliable data.

The average bottom surface temperature of the 30 kW/m^2 dataset was employed as target data for the inverse analysis of the thermal transport parameterization of the 1D model. The thermal conductivity of each component was first defined as a constant value, to maintain the simplest model possible. However, it was identified that a constant thermal conductivity was unable to capture the temperature history of the sample. Therefore, additional complexity was added through the introduction of a constant term multiplied by the third power of temperature; this term was only introduced to FPVC_Res3 and FPVC_Res4. The third power of temperature is an approximation to capture the thermal transport within porous media through radiation diffusion [20]; therefore, it was only physically meaningful to apply to components that experience a high temperature and porous structure. The resulting fitted bottom surface temperature is shown as the dotted line in Fig. 4(a). The final thermal conductivities are provided in Table 4. The predicted bottom surface temperature for the 60 kW/m^2 dataset is shown in Fig. 4(c). The average error between the experimental and simulated bottom surface temperatures for 30 and 60 kW/m^2 was found to be 1.1 and 2.8%, respectively.

The 30 kW/m^2 MLR data, shown in Fig. 4(b), were not utilized in the inverse analysis model calibration; therefore, this dataset serves as a model validation. The 1D model predicted the

30 kW/m^2 MLR data with excellent agreement. The overall error between the experimental and modeled MLR was found to be 8.7%. The MLR prediction for the higher flux, shown in Fig. 4(d), notably underestimated the experimental MLR data. The overall error between the experimental and modeled MLR for the 60 kW/m^2 dataset was found to be 11.9%. The 1D FPVC pyrolysis model was capable of simulating the MLR with reasonable accuracy for both the 30 and 60 kW/m^2 datasets.

Table 4. Densities and thermal conductivities of condensed phase components for 1D pyrolysis model

Component	ρ, kg/m^3	k, W/(m·K)
FPVC	1226	0.12
FPVC_Res1	391	0.41
FPVC_Res2	98	0.41
FPVC_Res3	62	$0.70 + (5.0\cdot10^{-10})T^3$
FPVC_Res4	22	$0.70 + (5.0\cdot10^{-10})T^3$

2D modeling was subsequently performed to account for variation in the heating conditions along the sample radius and top surface non-uniformity (see Fig. 3). Similar to the 1D model parameterization, the 30 kW/m^2 experiments were employed as the target data because these experiments produced the maximum reliable data with minimal radial sample reduction during pyrolysis. In the 2D model, the radial dependence of the intumescent behavior of FPVC pyrolysis was captured more accurately by effectively defining the densities as a function of radius. To simplify the parametrization, the radial dependence was prescribed as a combination of the center and edge densities. Independent knowledge of the center and edge char expansion dynamics enabled individual parameterization of the respective densities. Two separate initial FPVC components, FPVC$_c$ (center) and FPVC$_e$ (edge), were created with identical properties. FPVC$_c$ and FPVC$_e$ were defined to follow an identical decomposition reaction scheme; however, the densities and thermal conductivities of their products of decomposition were different. Distinguishing between the center and edge enabled parameterization of the radially dependent sample shape profiles.

To capture the intumescence at the center axis, the densities were prescribed following an identical process to the 1D model development; however, the center char thicknesses were employed as fitting targets instead of the average. While fitting the center densities, the sample diameter in the model was reduced from 0.035 m to 0.02 m to ensure that the heat flux to the sample was representative of the heat flux incident to the center portion of the sample. The densities were manually adjusted until the center experimental thicknesses, shown in Fig. 3(a), were well represented. The densities for the edge components were defined such that the thickness of the sample remained constant to emulate negligible swelling, as experimentally observed, which was achieved by multiplying the density by the corresponding stoichiometric mass coefficient of each reaction. The resulting densities of all reactants are provided in Table 5 denoted by the respective subscript.

To couple the densities between the center and edge components, a profile describing the mass fraction of the center component ($mf_{\mathrm{FPVC,c}}$) was computed; details on this methodology can be found elsewhere [6]. The center component mass fraction is given as a function of sample radius, r_z (m), in Eq. (1). The summation of the center and edge mass fractions must equal unity. The radially dependent mass fraction of the center components was computed to emulate the FPVC sample shape profile at 240 s of the 30 kW/m^2 dataset, a representative shape profile. It was observed that the center of the sample was comprised entirely of the center component. As the radius increased, the center mass fraction decreased, which resulted in the edge mass fraction increasing. The resulting sample shape profiles computed with the 2D axisymmetric model are shown in Fig. 3 as the solid curved lines. With the exception of under-estimating the initial rapid expansion in the 30 kW/m^2 dataset, it was observed that the model captured the overall dynamics of swelling with excellent accuracy.

$$mf_{\mathrm{FPVC,c}} = 1.24 \cdot 10^5 r_z^{\ 4} - 9.52 \cdot 10^2 r_z^{\ 2} + 1 \tag{1}$$

The thermal conductivities of the center components were parameterized following the same methodology discussed for the 1D model; however, the values were modified to capture the center experimental temperature profile instead of the average. The thermal conductivities of the edge components were scaled based on the density ratio between the center (FPVC$_c$) and edge (FPVC$_e$) components. The thermal conductivity was assumed inversely proportional to the density; therefore, the solid that expanded more upon decomposition was assumed to have proportionally larger thermal conductivity. This scaling was based on a physical argument provided in an earlier publication [21]. Consequently, the edge thermal conductivities were not fitting parameters; instead, they were directly coupled to the center parameters. The resulting temperature predictions at the center and edge of the sample are shown as the solid and dashed lines in Fig. 4(a)(c). An average error between the experimental and simulated results of the 30 and 60 kW/m^2 data was found to be 0.4 and 2.8%, respectively. The thermal conductivities of all center and edge components are shown in Table 5.

Table 5. Densities and thermal conductivities of the center (denoted by subscript c) and edge (denoted by subscript e) condensed phase components of 2D FPVC pyrolysis

Component	ρ, kg/m^3	*k*, W/(m·K)	Component	ρ, kg/m^3	*k*, W/(m·K)
FPVC$_c$	1226	0.12	FPVC$_e$	1226	0.12
FPVC$_c$_Res1	219	0.62	FPVC$_e$_Res1	1202	0.11
FPVC$_c$_Res2	55	0.62	FPVC$_e$_Res2	300	0.11
FPVC$_c$_Res3	35	$1.1 + (8.0 \cdot 10^{-9})\,T^3$	FPVC$_e$_Res3	225	$0.17 + (1.2 \cdot 10^{-9})\,T^3$
FPVC$_c$_Res4	12	$1.1 + (8.0 \cdot 10^{-9})\,T^3$	FPVC$_e$_Res4	79	$0.17 + (1.2 \cdot 10^{-9})\,T^3$

The MLR data, shown in Fig. 4(b)(d), were not utilized in the model development. The predicted MLR for the 30 kW/m^2 data was under estimated during the first 700 s and was subsequently over predicted during later stages of pyrolysis. The simulated MLR for the 60 kW/m^2 tests was found to capture the data well. The overall agreement between the experimental and 2D modeled MLR for the 30 and 60 kW/m^2 datasets were found to have a mean error of 18.7 and 14.1%, respectively.

Additionally, Fig. 4 provides a comparison between the 1D and 2D model predictions. The dotted lines represent the 1D model and the solid and dashed lines represent the 2D model. The bottom temperatures, shown in Fig. 4(a)(c), demonstrate minimal discrepancies between the two models. The MLR, however, reveals differences that are more noticeable. These differences are likely attributed to the 1D and 2D model's ability to capture the evolution of the top sample surface and its associated interactions with the radiation field. The 2D model better captures these surface interactions resulting in excellent predictions for the 60 kW/m^2 dataset. However, the 2D model under predicts the MLR at 30 kW/m^2 due to its inability to capture the rapid sample swelling during initial stages of pyrolysis.

COMPARISON BETWEEN LARGE-SCALE PLASTICIZED AND RIGID PVC MODELS

A simulation of a large burning surface exposed to radiant heat flux, emulating a large-scale fire, was conducted to compare the FPVC characterized in this work and rigid PVC studied elsewhere [6]. The simulation enabled a quantitative comparison between the predicted area-normalized large-scale mass loss rate (MLR_{LS}) and heat release rate (HRR_{LS}) of FPVC and PVC exposed to identical conditions. A $6.15 \cdot 10^{-3}$ m thick sample was subjected to a constant radiant heat flux of 40 and 70 kW/m^2 to provide a direct comparison. The convective losses from the top sample surface were neglected and the bottom sample surface employed adiabatic boundary conditions. The simulations neglected the potential impact of sample surface oxidation prior to ignition, because the condensed-phase model was parameterized based on anaerobic measurements. Moreover, the additional heat flux provided by a flame that forms on the sample surface upon ignition was also ignored in these simulations. The calculations were terminated when no additional mass loss was observed.

The large surface burning model employed the thermal transport parameters of the center components of the 2D model (see Table 5) to factor out the edge effects observed in the CAPA II [6]. The simulated HRR_{LS} was constructed as the product of the simulated MLR_{LS} of individual gaseous decomposition products from the reaction scheme (see Table 1) and the corresponding heats of combustion of each independent decomposition product derived from MCC measurements (see Table 3). It is especially critical to characterize independent heats of combustion for the decomposition products of materials like rigid PVC, where the heats of combustion of individual products differ substantially [6].

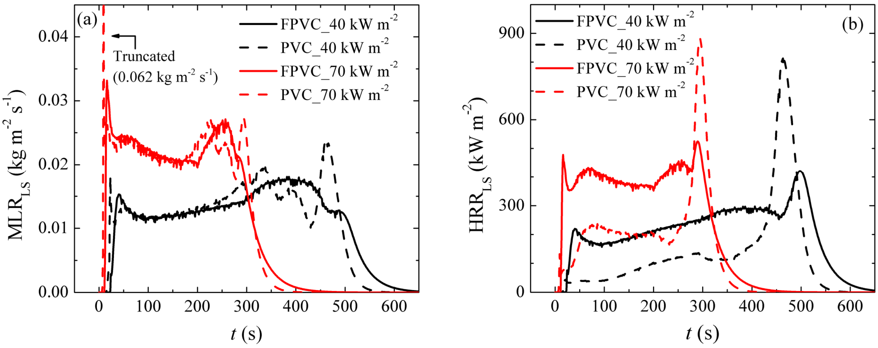

Fig. 5. Simulated (a) MLR_{LS} and (b) HRR_{LS} of FPVC and PVC, employing the center parameters from the 2D model parameterization, under a nominal heat flux of 40 and 70 kW/m^2.

A comparison between the simulated MLR_{LS} and subsequently computed HRR_{LS} of both FPVC and PVC large-scale burning is portrayed in Fig. 5. It is shown that there are negligible differences in the MLR_{LS} profiles between the two materials under both 40 and 70 kW/m^2. The HRR_{LS}, however, displays substantial differences between FPVC and PVC at both incident heat fluxes. In the early stages of burning, the HRR_{LS} of PVC is lower than that of the FPVC by a factor of two. However, during the final stages of burning, the HRR_{LS} estimated for PVC has a maximum peak that is a factor of two greater in magnitude than FPVC. Although PVC produces a greater HRR_{LS} during the final stages of burning in idealistic conditions, this peak is unlikely to contribute significantly to fire growth because it does not occur until very late stages of pyrolysis (requiring high heat flux exposure) and the extensive deformation of the burning material is expected to mitigate its reaction to fire. Therefore, the larger HRR_{LS} of FPVC during the early stages of burning will likely result in a greater flame spread rate during an actual fire event, consequently, making FPVC a greater fire hazard. Unlike rigid PVC which produces a small HRR in the first step of decomposition [6], FPVC produces a large amount of heat (see Fig. 2) which is believed to be originated from the organic plasticizers that are added to these materials. As a result, it is imperative that these differences between FPVC and PVC are included in all modeling efforts to capture the material's unique reaction to fire.

CONCLUSIONS

This manuscript presents a systematic methodology to fully parameterize a comprehensive pyrolysis model of FPVC. The complete set of parameters was derived from a combination of milligram-scale (TGA, DSC and MCC) tests and gram-scale (CAPA II) gasification experiments, which were coupled with inverse numerical modeling using ThermaKin2Ds, a newly expanded axial symmetric modeling framework. TGA and DSC experimental data were employed to parameterize a numerical reaction model, comprised of sequential first-order reactions, capable of predicting the kinetics and thermodynamics of thermal decomposition within the accuracy of the instrumentation. The heats of complete combustion of volatile gases produced in each reaction were determined by inversely analyzing the MCC datasets. A comprehensive pyrolysis model was derived by coupling the previously determined reaction parameters with the thermal transport properties estimated from CAPA II data. The model was subsequently validated against several experimental datasets collected from outside the model calibration thermal exposure. Finally, a comparison between the developed FPVC pyrolysis model and a rigid PVC pyrolysis model developed elsewhere [6] yielded similar burning rates but substantially different heat release rates between the materials. The combustion of gaseous products originated from the organic plasticizers during the first step of FPVC decomposition is largely responsible for the significant increase in the heat release rate exhibited by FPVC, with respect to rigid PVC, early in the burning process. It should be noted that the results presented in this manuscript cannot necessarily be generalized to all commercially available flexible PVC materials as their compositions may differ significantly.

ACKNOWLEDGEMENTS

The authors would like to acknowledge this research was supported by the U.S. National Science Foundation CAREER Award #1347196 under the grant monitor Dr. Song-Charng Kong.

REFERENCES

[1] M.M. Hirschler, Poly(vinyl chloride) and its Fire Properties, Fire Mater. 41 (2017) 993–1006.

[2] T. Gong, Q. Xie, X. Huang, Fire Behaviors of Flame-Retardant Cables Part I: Decomposition, Swelling and Spontaneous Ignition, Fire Saf. J. 95 (2018) 113–121.

[3] S.I. Stoliarov, J. Li, Parameterization and Validation of Pyrolysis Models for Polymeric Materials, Fire Technol. 52 (2016) 79–91.

[4] M.B. McKinnon, S.I. Stoliarov, Pyrolysis Model Development for a Multilayer Floor Covering, Materials. 8 (2015) 6117–6153.

[5] J.D. Swann, Y. Ding, M.B. McKinnon, S.I. Stoliarov, Controlled Atmosphere Pyrolysis Apparatus II (CAPA II): A New Tool for Analysis of Pyrolysis of Charring and Intumescent Polymers, Fire Saf. J. 91 (2017) 130–139.

[6] J.D. Swann, Y. Ding, S.I. Stoliarov, Characterization of Pyrolysis and Combustion of Rigid Poly(vinyl chloride) using Two-Dimensional Modeling, Int. J. Heat Mass Transf. 132 (2019) 347-361.

[7] J. Li, S.I. Stoliarov, Measurement of Kinetics and Thermodynamics of the Thermal Degradation for Non-Charring Polymers, Combust. Flame 160 (2013) 1287–1297.

[8] ASTM International, D7309-11 Standard Test Method for Determining Flammability Characteristics of Plastics and Other Solid Materials Using Microscale Combustion Calorimetry, West Conshohocken, 2011. doi:10.1520/D7309-11.

[9] R.E. Lyon, R.N. Walters, S.I. Stoliarov, N. Safronava, Principles and Practice of Microscale Combustion Calorimetry, Fed. Aviat. Adm. Atl. City Airport, NJ 8405. (2013). doi:DOT/FAA/TC-12/53, R1.

[10] G. Linteris, M. Zammarano, B. Wilthan, L. Hanssen, Absorption and Reflection of Infrared Radiation by Polymers in Fire-like Environments, Fire Mater. 36 (2012) 537–553.

[11] J. Li, J. Gong, S.I. Stoliarov, Gasification Experiments for Pyrolysis Model Parameterization and Validation, Int. J. Heat Mass Transf. 77 (2014) 738–744.

[12] S.I. Stoliarov, R.E. Lyon, Thermo-Kinetic Model of Burning for Pyrolyzing Materials, in: Fire Saf. Sci. - Proc. 9th Int. Symp., 2008: pp. 1141–1152.

[13] S.I. Stoliarov, I.T. Leventon, R.E. Lyon, Two-Dimensional Model of Burning for Pyrolyzable Solids, Fire Mater. 38 (2014) 391–408.

[14] Y. Ding, M.B. McKinnon, S.I. Stoliarov, G. Fontaine, S. Bourbigot, Determination of Kinetics and Thermodynamics of Thermal Decomposition for Polymers Containing Reactive Flame Retardants: Application to Poly(lactic acid) Blended with Melamine and Ammonium Polyphosphate, Polym. Degrad. Stab. 129 (2016) 347–362.

[15] J. Li, S.I. Stoliarov, Measurement of Kinetics and Thermodynamics of the Thermal Degradation for Charring Polymers, Polym. Degrad. Stab. 106 (2014) 2–15.

[16] M.B. McKinnon, S.I. Stoliarov, A. Witkowski, Development of a Pyrolysis Model for Corrugated Cardboard, Combust. Flame 160 (2013) 2595–2607.

[17] Y. Ding, K. Kwon, S.I. Stoliarov, R.H. Kraemer, Development of a Semi-global Reaction Mechanism for Thermal Decomposition of a Polymer Containing Reactive Flame Retardant, Proc. Combust. Inst. 37 (2019) 4247-4255.

[18] P.J. Linstrom, W.G. Mallard, NIST Chemistry WebBook, NIST Standard Reference Database Number 69, (2018). doi:10.18434/T4D303.

[19] M. Försth, A. Roos, Absorptivity and its Dependence on Heat Source Temperature and Degree of Thermal Breakdown, Fire Mater. 35 (2011) 285–301.

[20] R. Siegel, J. Howell, Thermal Radiation Heat Transfer, Fourth, Taylor & Francis, New York, 2002.

[21] S.I. Stoliarov, S. Crowley, R.N. Walters, R.E. Lyon, Prediction of the Burning Rates of Charring Polymers, Combust. Flame 157 (2010) 2024–2034.

Pyrolysis and Combustion of Polymer Mixtures. Is the Heat Release Rate an Additive Quantity?

Handawy M.K., Snegirev A.*, Stepanov V., Talalov V.

Peter the Great St-Petersburg Polytechnic University, Saint-Petersburg, Russia
**Corresponding author's email: a.snegirev@phmf.spbstu.ru*

ABSTRACT

The microscale combustion calorimetry study of polymer mixture pyrolysis is presented. Binary mixtures of HDPE with a number of massively produced polymers (LDPE, PET, PS, PC, PVC, PMMA), binary PMMA-PVC mixtures, and the ternary mixture composed of HDPE, PC, and PS are considered. The extent of interaction between the mixture components in pyrolysis is assessed by comparing the shapes of the measured temperature dependencies of the heat release rate in volatile oxidation with those for the curves obtained by the mass-weighted summation of the individual contributions of the pure polymers constituting the mixture. The strongest interaction is observed in HDPE-PET, HDPE-PS, HDPE-PS-PC, and in PMMA-PVC mixtures. A destabilizing interaction occurs in mixtures containing polyethylene and polystyrene, while the presence of polyvinylchloride has a stabilizing effect.

Except for PMMA-PVC mixtures, in all binary mixtures considered in this work the heat of volatile combustion and the char yield were found to be additive quantities and varied almost linearly with the variation of the component mass fractions. Dissimilar to that, the PMMA-PVC mixtures produced a higher amount of charring residue and a lower heat of combustion of volatiles compared to the component-based predictions assuming additivity.

KEYWORDS: Pyrolysis, microscale combustion calorimetry, polymer, flammability.

INTRODUCTION

Predicting the heat release rate generated by a multi-component fire load as well as in the design of equipment for incineration of municipal solid wastes justifies the need to consider pyrolysis of plastic mixtures. Although both the fire load and the plastic wastes normally consist of the mixture of combustible materials, a majority of the previous studies of material pyrolysis have been mainly focused on individual polymers. Additivity of the heat release rates in burning the volatiles generated by the individual mixture components is a common assumption used in the engineering simulations. This assumption implies that no chemical interaction occurs neither in the solid phase nor in the gas volatiles.

Current literature offers rather controversial conclusions on the importance of the interaction effects in polymer mixture pyrolysis. Indeed, the interaction between the components of the plastic mixture in the pyrolysis was found (or assumed) to be insignificant in some of the previous studies [1, 2], while a more thorough investigation may demonstrate such an interaction to occur in certain mixtures [3, 4]. Furthermore, a demonstration of the synergetic effect (even though it is claimed in a number of papers) is not always convincing since the experimental errors and repeatability are rarely assessed and reported.

The interaction mechanism in a polymer mixture is essentially attributed to the formation of active radicals in thermal decomposition of an individual polymer, radical migration across the component

Proceedings of the Ninth International Seminar on Fire and Explosion Hazards (ISFEH9), pp. 1122-1133
Edited by Snegirev A., Liu N.A., Tamanini F., Bradley D., Molkov V., and Chaumeix N.
Published by Saint-Petersburg Polytechnic University Press
ISBN: 978-5-7422-6498-9   DOI: 10.18720/spbpu/2/k19-106

interfaces, and the subsequent reactions of such radicals with the polymers in the mixture and with other radicals [4]. In its turn, radical consumption by a particular mixture component proceeds along with the radical production, and the outcome of this competition determines whether the synergy has a stabilizing or destabilizing effect.

A possible reason of the controversial conclusions is that the pyrolysis and combustion of polymer mixtures might be affected not only by the polymer type, but also by the heating rate, proportion of the components in the mixture, and the degree of mixture homogeneity. Depending on how the components are combined, we will distinguish the blends and the mixtures. The polymer blends are prepared as an (almost) homogeneous sample, normally by melting and molding [4, 3]. Alternatively, a combination of materials that is heterogeneous on the macroscopic level shall be termed as a mixture.

In the two practical cases listed above, the polymers are never perfectly mixed, and the degree of heterogeneity may vary. Spatial separation of and the interface between the mixture components crucially affects the intensity of potential interaction. Quality of mixing is difficult to control, and it might be a possible reason for controversial conclusions on the interaction effects observed in the mixtures with the same polymers.

In this work, we consider the mg-scale samples and mix the powder components at the inter-particle level, i.e. more thoroughly than they are mixed in practice. Therefore, if additivity (absence of interaction) is confirmed here, it will work even more so in practice. At the same time, mechanical mixing is not as fine as that in polymer blends, and the interaction effects in the blends should be more pronounced than those in the relatively coarse mixtures.

One of the most convincing studies of the effect of the mixing quality on polymer interaction in pyrolysis is the study undertaken by Faravelli *et al.* in Ref. [5]. The experimental (TGA) and modeling results obtained in this study for PE-PS mixtures confirm that in poor mixing the decomposition of each polymer behaves independently. However, when the polymers are finely mixed, a co-pyrolysis and interaction occur. As such, the measurement data (either TGA or MCC) depend on mixing quality, and a possible interaction should be taken into account in data interpretation.

As shown, for example, in Ref. [7], the interaction between two components can be approximately quantified by a single adjustable parameter. However, the interaction complexity rapidly increases with the number of interacting components, and it motivates the authors of Refs. [6, 7, 8] to neglect any interaction between the molecular groups and to assume additivity of the group contributions in evaluating flammability properties of the polymers.

With the component interaction taken into account, the degradation behavior of either blends or mixtures cannot be theoretically predicted, both due to the incomplete knowledge of chemical degradation roots and the interactions at the interfaces controlled by morphology. This highlights the importance of getting new experimental evidence of the effects of mixing on polymer thermochemical stability and flammability. An example of *a posteriori* formulation of the interactive kinetic model of mixture pyrolysis is Ref. [10], in which both binary and ternary mixtures of PE, PP, and PET plastics are investigated by TGA. The interaction effects have been observed (although not systematically investigated) and then included in the kinetic model using the quadratic expressions with the cross-product terms.

Previous studies of the blend and mixture pyrolysis have mainly been undertaken by using thermogravimetric analysis (TGA) or, more rarely, using the isothermal methods. In this work, we apply an alternative experimental methodology, microscale combustion calorimetry (MCC) [11]. Rare examples of previous MCC studies considering a combination of distinct polymers are Refs. [7] and [9], where no visible interaction was observed in pyrolysis of the PC-ABS blend. At the same time, analysis of molecular group contribution to the flammability properties undertaken in Refs. [6, 7, 8] focuses on the individual polymers, not on mixtures or blends. To the current knowledge by the authors, this work as well as Ref. [12] represent the first systematic study of commingled plastics pyrolysis undertaken by MCC. Similar to the TGA, a mg-scale sample is exposed to the constant heating rate, while, dissimilar to the TGA, additional information on the heat of combustion of pyrolysis volatiles is also produced in MCC. Collection of the new MCC measurement data for the mixtures composed of most widely used plastics (LDPE, PET, PS, PC, PVC, PMMA) and evaluation of the interaction effects is the objective of this work. Based on these measurement data, the quantitative indicators of mixture thermochemical stability and flammability (heat of combustion of pyrolysis volatiles, char yield in anaerobic pyrolysis, heat release capacity, and characteristic pyrolysis temperature) are evaluated, and the additivity of these quantities is assessed.

MCC STUDY OF POLYMER MIXTURES

Methodology

Commercially available flammable polymers (Scientific Polymer Products Inc.) listed in Table 1 have been studied in this work. In the MCC apparatus, the mg-scale samples were exposed to the constant rate heating (from 0.25 to 1 K/s) in the nitrogen flow of 80 cc/min. Oxygen flow of 20 cc/min is added to the volatile-nitrogen flow to replicate the oxygen-to-nitrogen ratio characteristic of air. Pyrolysis volatiles are then completely oxidized in the combustion chamber at the temperature of 900 °C, and the oxygen consumption rate, $\dot{m}_{O_2}$, is measured. Based on the assumption of the constant heat of combustion per unit mass of oxygen consumed (taken equal to Δq_{O_2} = 13.1 kJ/g O_2), the specific heat release rate, $\dot{q}$, is recorded as a function of time, t, and of the sample temperature, $T = T_0 + \beta t$, where T_0 is the initial temperature, and β is the heating rate.

Table 1. Material properties provided by the manufacturer

Designation	Name	Molecular weight, kg/mol	Appearance	Density, kg/m^3	Melting/ softening point, °C
LDPE	Low density polyethylene	50	Pellets	920	107-135
HDPE	High density polyethylene	125	Pellets	950	121
PET	Poly(ethylene terephthalate)	N/A	Pellets	1385	252
PS1.2	Polystyrene	1.2	Granular	1060	74
PC	Polycarbonate	45	Pellets	1200	151
PMMA	Poly(methyl methacrylate)	35	Beads	1200	N/A
PVC	Poly(vinyl chloride)	350	Powder	1400	285

The individual polymers in Table 1 have already been studied by MCC in Refs. [13, 14, 15], and the measurement data for the heating rates of 0.25, 0.5, 1, and 1.5 K/s are summarized in Ref. [13], where the kinetic models of the polymer decomposition are also provided as well as the comparisons with the published data. Two types of polyethylene (HDPE and LDPE) are considered here. As shown in Ref. [13], thermal decomposition of HDPE and LDPE proceeds quite similarly, and its quantitative characteristics are also similar. Note, that the low molecular mass polystyrene PS1.2 (1.2 kg/mol) is rather different from the high molecular mass polystyrenes, considered, for example, in Refs. [14, 15]. Thermal decomposition of PS1.2 produces much lower peak heat release rate, wider pyrolysis temperature range, and higher peak temperature value [13]. As a result, PS1.2 has a lower heat release capacity.

The pellets and beads were crunched and the small pieces of the polymers were manually mixed in the sample cup as uniformly as possible. Each small particle had the mass of 0.3-0.4 mg and the size of about 0.6 mm. Additional measurements with very large particles (5 mg, 2-3 mm) produced very similar results. The weak effect of the initial particle size is due to melting and mixing the components before the pyrolysis starts (see the melting points in Table 1). To repeat identical runs, sufficiently large amounts of the mixtures were prepared. In binary mixtures (except PMMA-PVC), the following initial component mass fractions are considered: 20, 40, 50, 60, and 80%. In ternary mixtures, equal masses of all three components were taken.

To ensure the prescribed proportions of the mixture components in a sample, the samples with the sufficiently large mass (normally about $m_0 \approx 10$ mg) were used in the MCC measurements for the mixtures. It is worthy of note that, for the given initial sample mass, the maximum heating rate exists (about 0.5 K/s for the mixtures with prevalence of PE) beyond which the oxygen flow becomes insufficient to completely oxidize all the volatiles.

Alternatively, several single runs were performed with the PMMA-PVC mixture having various component proportions, which were not exactly prescribed in advance. This enabled using of a smaller sample mass and a higher heating rate, albeit at the expense of impossibility to repeat identical tests with the same mixture composition.

The measurement procedure for each heating rate follows that described in ASTM D7309-07a [16] with the exception of multiple heating rates. The detailed description of the measurement procedure and data processing is provided in Refs. [13, 14]. Each measurement was performed 2–5 times to ensure repeatability of heat release rate-temperature curves and to assess the average value and standard deviation. The measured dependencies of heat release rate (per unit sample mass) on sample temperature, $\dot{q}(T)$, were pre-processed by applying the following operations: (i) interpolation to the sample temperature values aliquot 1°C; (ii) subtracting the baseline (straight line between the sample temperature before the onset and after completion of the process); (iii) averaging over identical runs and evaluating standard deviation. Pre-processing of the MCC measurement data included evaluating transient (conversion, reaction rate), integral (total heat release, effective heat release capacity) and other (peak temperature, 10%, 50%, and 90% conversion temperatures) characteristics of material decomposition.

If volatile oxidation proceeds in an excess of oxygen (this is controlled by limiting the sample mass and the heating rate), then the heat release rate per unit sample mass is

$$\dot{q} = -\Delta q_{O_2} \frac{\dot{m}_{O_2}}{m_0} = -\Delta q_{O_2} \sigma_{O_2} \frac{\dot{m}}{m_0} = -\Delta q \frac{\dot{m}}{m_0}, \tag{1}$$

where m_0 is the initial sample mass, σ_{O_2} is the stoichiometric oxygen to fuel mass ratio, $\dot{m}$ is the sample mass loss rate, and $\Delta q_{O_2} \sigma_{O_2} = \Delta q$ is the heat of combustion per unit mass of volatiles. In the MCC apparatus, oxygen consumption and sample temperature are synchronized by allowing for the residence time of the gas reactants in the combustor. Due to complete volatile oxidation and synchronization of oxygen consumption rate with the sample temperature, the dependence $\dot{q}(T)$ measured in MCC characterizes the rate of sample decomposition, similar to the mass loss rate $\dot{m}(T)$ measured in TGA.

Let the relation (1) holds for the i-th mixture component: $\dot{q}_i = -\Delta q_i \left(\dot{m}_i / m_{0,i} \right)$. In case of independent pyrolysis of and oxidation of volatiles produced by each component (no interaction neither in condensed nor in gas phase), the additivity principle holds for the multicomponent mixture:

$$\dot{q} = \frac{1}{m_0} \sum_i \dot{m}_i \Delta q_i = \frac{1}{m_0} \sum_i m_{0,i} \dot{q}_i = \sum_i y_{0,i} \dot{q}_i \ , \tag{2}$$

where $y_{0,i} = m_{0,i} / m_0$ is the initial mass fraction of the i-th component, and $m_0 = \sum_i m_{0,i}$ is the initial mass of the mixture. Thus, the heat release rate produced by the mixture of independently reacting (non-interacting) components can be evaluated as the mass-weighted sum of the individual component contributions. Deviation from the additivity principle is an indication of the component interaction in pyrolysis. An interaction in the gas phase is also possible but is not expected to be important due to complete volatile oxidation.

In processing the MCC measurement data, we use the heat release-based global conversion,

$$\alpha = \frac{1}{\overline{\Delta q'}} \int_{T_0}^{T} \dot{q}(T) \, dT \ , \tag{3}$$

where T is the current sample temperature, $T_{\max}$ = 800 °C is the final temperature at which pyrolysis is complete. By definition, $0 \leq \alpha \leq 1$.

The heat of combustion per unit sample mass, $\overline{\Delta q'}$, is evaluated by integrating the heat release rate over the entire process:

$$\overline{\Delta q'} = \int_0^{t_{\max}} \dot{q} dt = \frac{1}{\beta} \int_{T_0}^{T_{\max}} \dot{q} dT \ . \tag{4}$$

Note, that $\overline{\Delta q'} = (1 - \nu_r) \overline{\Delta q}$, where $\nu_r = m_\infty / m_0$ is the solid residual mass fraction. If additivity holds, then according to Eq. (2) the heat of combustion is also an additive quantity:

$$\overline{\Delta q'} = \sum_i y_{0,i} \overline{\Delta q'_i} \ . \tag{5}$$

The integral in Eq. (4) can be represented as a product $\int_{T_0}^{T_{\max}} \dot{q} dT = \langle \dot{q} \rangle \Delta T_{pyr}$, where ΔT_{pyr} is the pyrolysis temperature interval, and $\langle \dot{q} \rangle$ is the characteristic heat release rate in this interval. Substituting this product in Eq. (4) yields:

$$\overline{\Delta q'} / \Delta T_{pyr} = \langle \dot{q} \rangle / \beta \ . \tag{6}$$

The ratio on the left-hand side of Eq. (6) is called the heat release capacity and is used as an indicator of the material thermochemical stability and flammability [11, 16]: $\eta = \overline{\Delta q'} / \Delta T_{pyr}$.

The heat release capacity is often evaluated as $\eta_p = \dot{q}_p / \beta$, where $\dot{q}_p$ is the peak heat release rate [11]. This definition (which is formally derived for the special case of a single-step reaction) is not suitable in case of multi-peak dependencies $\dot{q}(T)$, particularly when a lower (and wider) peak contains more heat release. Following Refs. [13, 14], we, therefore, define the effective heat release capacity as $\eta_{10-90\%} = \overline{\Delta q'}/\Delta T_{10-90\%}$, where $\Delta T_{10-90\%}$ is the temperature interval between 10% and 90% conversion.

Thermochemical stability of a material is also quantified by the characteristic temperature at which pyrolysis reaction attains its maximum rate (the peak temperature, T_p). In addition to the peak temperature, we use in this work the temperature corresponding to 50% conversion (the median temperature, $T_{50\%}$), which is less sensitive to the experimental errors and can be used in multi-reaction scenarios represented by multiple peaks. For the polymers decomposing in a single step (for example PE, PP, PS980 etc.), the dependencies $\dot{q}(T)$ are nearly symmetric, and the peak and median temperatures are close to each other (the difference is few degrees only).

Thus, three quantities, $\overline{\Delta q'}$, $\eta_{10-90\%}$, and $T_{50\%}$, along with the shape of the $\dot{q}(T)$ curve, will be used in this work to characterize material thermochemical stability and flammability. A material is regarded as more stable and less flammable in case of lower heat of combustion and heat release capacity ($\overline{\Delta q'}$ and $\eta_{10-90\%}$) and higher pyrolysis temperatures ($T_{50\%}$ and T_p). If components in the mixture react independently, then the heat of combustion, $\overline{\Delta q'}$, (as well as the solid residual mass fraction, ν_r) is the additive quantity, while the heat release capacity and the median temperature, $\eta_{10-90\%}$, and $T_{50\%}$, are not. Indeed, according to the definition

$$\eta = \frac{\overline{\Delta q'}}{\Delta T_{pyr}} = \frac{\sum_i y_{0,i}\overline{\Delta q'_i}}{\Delta T_{pyr}} = \sum_i \frac{\Delta T_{pyr,i}}{\Delta T_{pyr}} y_{0,i}\eta_i \ , \tag{7}$$

where $\Delta T_{pyr,i}$ and $\eta_i = \overline{\Delta q'_i}/\Delta T_{pyr,i}$ are the pyrolysis temperature interval and the heat release capacity of the i-th component. Since $\Delta T_{pyr} > \Delta T_{pyr,i}$ (the pyrolysis temperature interval of a mixture is wider than that for an either of the components), the heat release capacity of the mixture (defined by Eq. (7)) is lower than the weighted sum of the heat release capacities of the components: $\eta < \sum_i y_{0,i}\eta_i$. Note, that this conclusion is dissimilar to the additivity assumption used for the heat release capacity in Ref. [7].

For a binary mixture with $y_{0,1} + y_{0,2} = 1$, the simplest approximation of a non-additive quantity is (see Eq. (4) in Ref. [7]):

$$\psi = y_{0,1}\psi_1 + \left(1 - y_{0,1}\right)\psi_2 + \lambda\left(y_{0,1}\left(1 - y_{0,1}\right)\right)^{1/2}\left(\psi_1 + \psi_2\right), \tag{8}$$

where the first two terms represent the additive part, and the last term approximates the deviation from additivity, which is quantified by parameter λ . This parameter can be regarded as the degree of interaction only if Eq. (8) is applied to $\overline{\Delta q'}$ or ν_r but not to $\eta_{10-90\%}$ or $T_{50\%}$. In the latter case, parameter λ is non-zero even in case of independently reacting components.

RESULTS AND DISCUSSION

The individual polymers were investigated first, and the results are summarized in Table 2. As established in Ref. [12], thermal decomposition of most of the polymers presented in Table 2 is of an autocatalytic type.

The binary compositions considered in this work include the mixtures of HDPE with PC, PS1.2, PET, PVC as well as the mixture of PMMA with PVC. As expected and in agreement with Ref. [17], no interaction effects were observed in HDPE-LDPE mixtures. The absence of a visible interaction between HDPE and LDPE supports the assumption that the presence of other polymers should have a similar effect in the mixture with either HDPE or LDPE.

Table 2. MCC measurement data for pure polymers[a]. Pyrolysis in a nitrogen flow at 0.5 K/s

Polymer	$\overline{\Delta q'}$, MJ/kg	ν_r, –	$\eta_{10-90\%}$, kJ/(kg K)	$T_{50\%}$, °C	E_a, kJ/mol[b]
Non-charring					
HDPE	41.3±0.1	0	1245	494	229±7
LDPE	41.5±0.6	0	1012	486	227±7
PS1.2	33.9±0.3	0	237	429	167±10
PMMA	24.9±0.2	0	433	393	212±18
Charring					
PC	20.0±0.2	0.234±0.005	417	533	233±13
PET	14.3±0.6	0.09±0.03	168	453	217±23
PVC	13.8±0.2	0.057±0.001	73.9	464	268±50c

a Average values and standard deviations obtained in several tests

b Conversion-averaged apparent activation energy evaluated by the iso-conversional method of Friedman (see Ref. [12] for details) using three heating rates 0.25, 0.5, and 1.0 K/s. Standard deviation is also given

c Strong variation with conversion in the multi-step pyrolysis

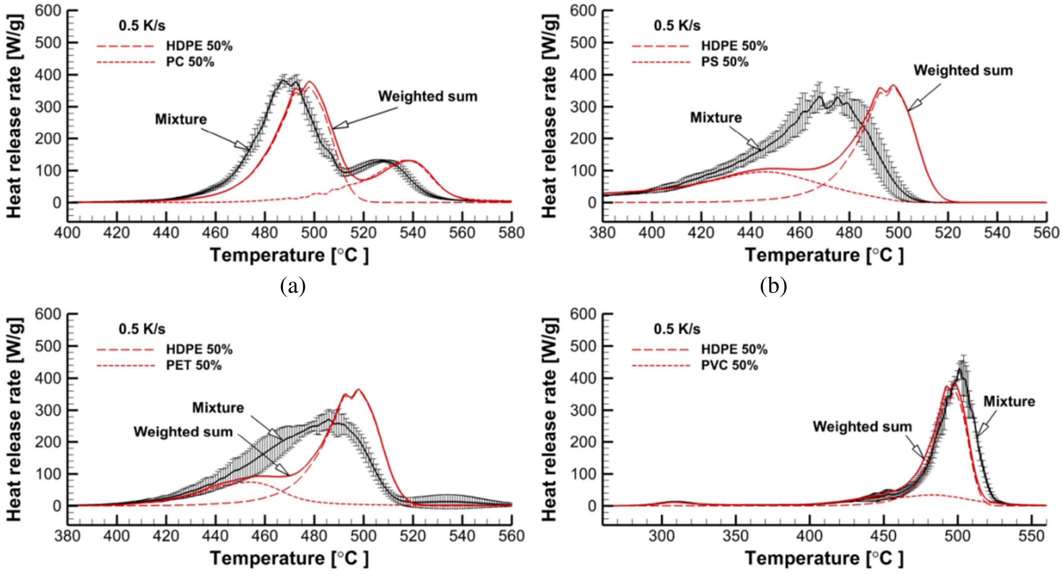

(a) (b)

(c) (d)

Fig. 1. MCC measurements $\dot{q}(T)$ for the binary mixtures (solid lines with vertical bars), contributions of the individual polymers $y_{0,i}\dot{q}_i(T)$ (dashed lines) and the weighted sum $\sum_i y_{0,i}\dot{q}_i$ (solid line, no bars) at the heating rates of 0.5 K/s. Vertical bars show the standard deviation in multiple measurements. a) – HDPE-PC; b) – HDPE-PS1.2; c) – HDPE-PET; d) – HDPE-PVC

Thermal decomposition of binary mixtures with equal initial mass fractions of the components is further represented by the MCC measurement data in Fig. 1 (various component proportions have also been investigated). For the HDPE-PC binary mixture (see Fig. 1, a), the maximum deviation from the mass-weighted average is observed at $y_{0,i}$ = 0.5. In the mixture measurement, the HDPE peak is shifted to lower temperatures compared to that in the mass-weighted average at any mixture composition, which implies destabilization of HDPE in presence of a sufficiently large amount of PC. The PC peak exhibits the same trend at $y_{0,i}$ = 0.5. When either component dominates, the heat release rate recorded for the mixture is quite close to that predicted by the mass-weighted average. For the HDPE-PS1.2 binary mixture (Fig. 1, b), a very strong deviation from the mass-weighted average is observed at any mixture composition, and the HDPE peak of the mixture occurs at remarkably lower temperatures compared to those in the mass-weighted average. This implies that decomposition of HDPE is strongly facilitated by the presence of PS regardless of its amount. This observation is in agreement with the results of Ref. [17]. A similarly strong destabilizing interaction effects are also observed in Fig. 1, c, for the HDPE-PET binary mixtures.

The interaction effects in the joint decomposition of HDPE and PVC are not crucial and hardly exceed the experimental uncertainty (see Fig. 1, d), although HDPE decomposition is slightly delayed in presence of PVC. In spite of the weak interaction in HDPE-PVC mixture, the presence of PVC causes a much more pronounced delay of PMMA decomposition. This is clearly visible in Fig. 2, which shows that the reaction peak is shifted significantly towards higher temperatures. Thus, the stabilizing effect of PVC, albeit of different strength, can be concluded for the binary mixtures with PE and PMMA.

Such a stabilizing effect, demonstrated here by MCC, has already been observed in earlier non-isothermal (TGA) and isothermal studies (see Ref. [18] and the review in Ref. [4]). In these studies, it has been concluded that combination of the radicals produces by both PMMA and PVC may produce some cross-linked structures, which are more difficult to destroy. A possible mechanism of the stabilizing effect introduced by PVC is also discussed in Ref. [17].

Consistent with the above observations, decomposition of the ternary mixture considered in Fig. 3 is strongly affected and destabilized by the presence of polystyrene.

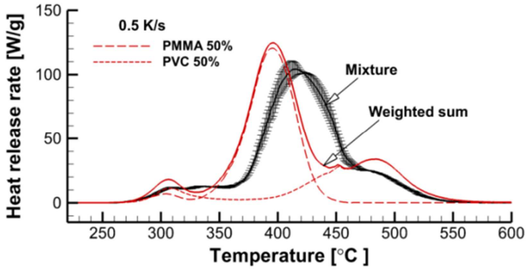

Fig. 2. MCC measurements $\dot{q}(T)$ for the 50%PMMA+50%PVC binary mixture (see the caption in Fig. 1).

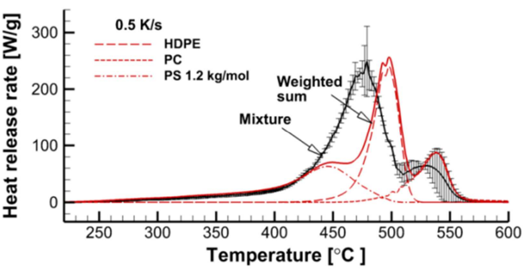

Fig. 3. MCC measurements for the HDPE-PS1.2-PC ternary mixture, $y_{0,i}$ = 1/3 (see the caption in Fig. 1).

To formally quantify the degree of deviation from the additivity rule, we evaluate the following non-additivity indicator:

$$\zeta = \frac{1}{\langle \Delta q \rangle} \int_{T_0}^{T_{\max}} \left| \dot{q}_{add} - \dot{q}_{mixt} \right| dT \, , \qquad (9)$$

where $\dot{q}_{add}$ is the heat release rate evaluated as the weighted sum of the measured component contributions, $\dot{q}_{mixt}$ is the heat release rate measured in the mixture, and $\langle \Delta q \rangle$ = $\left(\int_{T_0}^{T_{\max}} (\dot{q}_{add} + \dot{q}_{mixt}) dT \right) \Big/ 2$. The value of ζ was found to be weakly sensitive to the heating rate.

The above analysis and evaluation of the non-additivity indicator, ζ, indicates a various degree of component interaction in mixture decomposition:

1. Strong interaction in HDPE-PS1.2 (ζ = 0.69), HDPE-PS1.2-PC (ζ = 0.51), HDPE-PET (ζ = 0.5) and PMMA-PVC (ζ = 0.52) mixtures. The shape of the MCC curves is very different, and the peak temperatures differ greatly compared to those predicted by the weighted sum of the individual component contributions. Decomposition of the most flammable component (HDPE or PMMA) is destabilized in HDPE-PS1.2, HDPE-PS1.2-PC, and HDPE-PET mixtures, and, in contrast, stabilized in the PMMA-PVC mixture. Destabilization of the HDPE-PS1.2 mixture observed in this work is qualitatively consistent with the conclusions of Ref. [5], where the increased reactivity of PE-PS mixture is explained by the attack of radicals coming from the PS.
2. Moderate interaction is observed in HDPE-PC (ζ = 0.42), HDPE-PP (ζ = 0.3) mixtures. The shape of the MCC curves is qualitatively similar to that predicted by the weighted sum of the individual component contributions, albeit some shift of the peaks to lower temperature occurs.
3. The interaction is weak and is of the order of the experimental uncertainty in HDPE-PVC (ζ = 0.27) and PC-PS1.2 (ζ = 0.26) mixtures. No interaction in HDPE-LDPE mixtures (ζ = 0.08).

Note, that the statistical variation of multiple identical measurements (repeatability error) causes the value of ζ to be below 0.1. Weak, moderate, and strong interactions correspond to ζ in the ranges 0.1–0.3, 0.3–0.4, and 0.5–0.7, respectively. The interaction effect can be either stabilizing or destabilizing, and it can also be quantified by comparing the median temperatures evaluated for both $\dot{q}_{add}$ and $\dot{q}_{mixt}$. This comparison is presented in Table 3.

As shown in Fig. 4, a, the integral heat of combustion (which is evaluated as the total oxygen consumption in the combustor multiplied by 13.1 MJ/kg O_2, see Eqs. (4) and (1)) remains to be the additive quantity regardless of the extent of the interaction during the process. Indeed, the MCC measurements for the mixtures presented in Fig. 4, a, correspond to the mass-weighted sum of the component HOCs, to within the experimental uncertainty. The same conclusion applies to the char yield demonstrated in Fig. 4, b. As discussed above, the heat release capacity is the non-additive quantity, and the measurement data for the mixtures are well below the mass-weighted values (Fig. 4, c), as expected. The measurement data can be approximated by Eq. (8), and the best fit is achieved with λ = 0.25 for HDPE-PVC and λ = 0.35 for the binary mixtures of HDPE with PET, PS1.2, and PC. Data shown in Fig. 4, d, indicate that the deviation from (or agreement with) the mass-weighted values of the median temperature is different in the considered mixtures. The interaction parameter corresponding to the best fit with Eq. (8) is λ = -0.03 for HDPE-PC, λ = 0.035 for HDPE-PVC, and λ = 0 for HPDE-PS1.2 and HDPE-PET.

Alternatively, for the PMMA-PVC mixture, it can be concluded that the solid residual mass fraction in mixture pyrolysis is observably greater than the mass-weighted value, and this deviation exceeds the experimental uncertainty (see Fig. 5, b). This observation correlates with the measured HOCs in the mixture being lower than the mass-weighted values (see Fig. 5, a). Therefore, the chemical interaction between PMMA and PVC, which is quite pronounced in this mixture (see also Fig. 2), also facilitates excessive char formation and suppresses volatile production.

Table 3. Overview of the interaction effects

Mixture	Interaction	ζ	$T_{50\%}$, °C, mixture	$T_{50\%}$, °C, weighted sum	$\Delta T_{50\%}$, K
			0.5 K/s		
Strong interaction					
HDPE-PS1.2	Destabilizing	0.69	461	477	–16
HDPE-PS1.2-PC	Destabilizing	0.51	473	488	–15
HDPE-PET	Destabilizing	0.5	477	490	–13
PMMA-PVC	Stabilizing	0.52	419	403	16
Moderate interaction					
HDPE-PC	Destabilizing	0.42	493	500	–7
HDPE-PP	Destabilizing	0.3	477	482	–5
Weak interaction					
HDPE-PVC	Stabilizing	0.27	496	491	5
PC-PS1.2	Stabilizing	0.26	464	454	10
HDPE-LDPE	Non	0.08	489	489	0

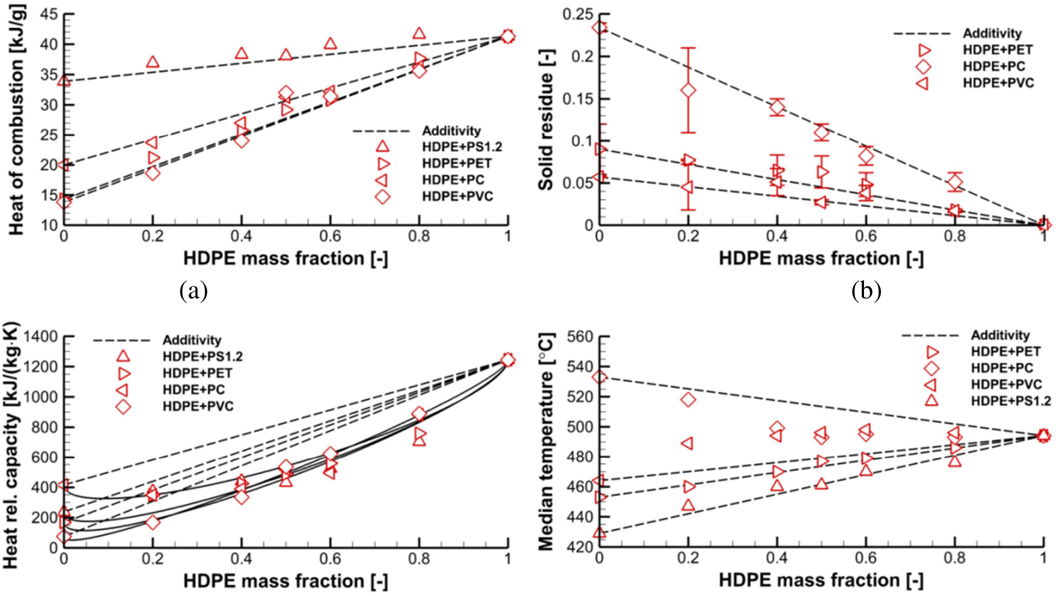

(a) (b)

(c) (d)

Fig. 4. The effect of HDPE mass fraction on flammability properties of the binary mixtures: a) – heat of combustion; b) – solid residue mass fraction; c) – heat release capacity (solid lines correspond to Eq. (8) with λ = -0.35 for all the mixtures except HDPE+PVC for which λ = -0.25); d) – median temperature.

CONCLUSIONS

Binary mixtures of HDPE with a number of most widely produced polymers (LDPE, PET, PS, PC, PVC, PMMA), binary mixture of PMMA with PVC, and the ternary mixture composed of HDPE, PC, and PS have been studied by means of microscale combustion calorimetry.

These mixtures are shown to exhibit a various degree of component interaction in mixture pyrolysis. The interaction degree was assessed by comparing the shapes of the measured temperature dependencies of the heat release rate in volatile oxidation with those for the curves obtained by the mass-weighted summation of the individual contributions of the pure polymers constituting the mixture.

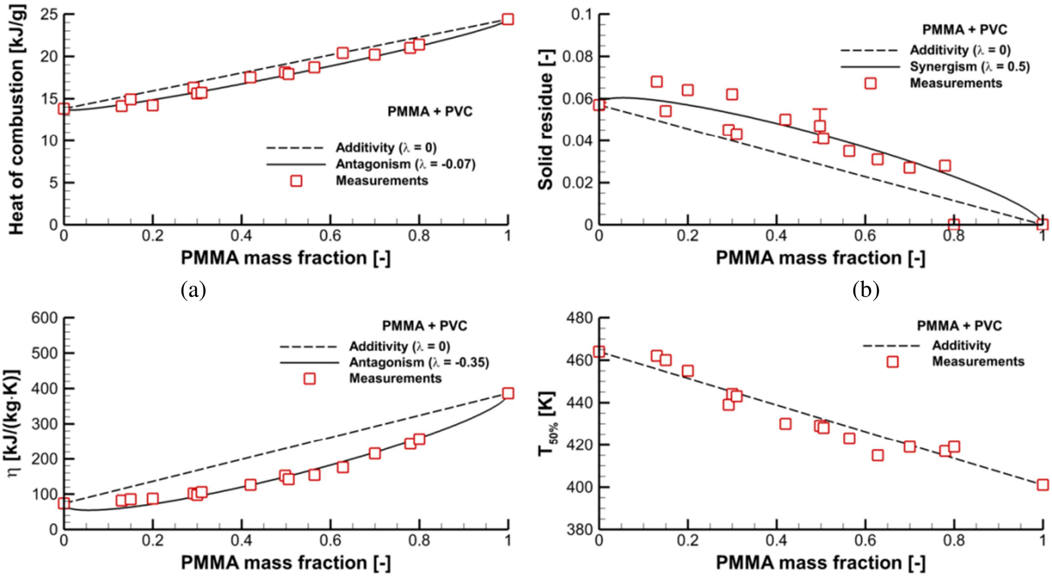

(a) (b)

(c) (d)

Fig. 5. The effect of PMMA-PVC mixture composition on flammability properties: a) – heat of combustion; b) – solid residue mass fraction; c) – heat release capacity; d) – median temperature.

The strongest interaction was observed in HDPE-PET, HDPE-PS1.2, HDPE-PS1.2-PC and in PMMA-PVC mixtures. Decomposition of the most flammable component (HDPE or PMMA) is destabilized in HDPE-PS1.2, HDPE-PS1.2-PC, and HDPE-PET mixtures, and, in contrast, stabilized in the PMMA-PVC mixture as determined by the shift of the reaction peaks to the lower and higher temperatures, respectively. The interaction observed in HDPE-PC mixture is moderate albeit it, nevertheless, exceeds the experimental uncertainty. In this interaction HDPE-PC mixture is destabilized, while the HDPE-PVC mixture is weakly stabilized. No interaction effects exceeding the experimental uncertainty were observed in HDPE-LDPE and PC-PS1.2 mixtures. It can, therefore, be concluded that the destabilizing interaction occurs between PE and PS, while the presence of PVC has the stabilizing effect.

Except for PMMA-PVC mixtures, in all binary mixtures considered in this work the heat of volatile combustion and the char yield were found to be additive quantities and varied almost linearly with the variation of the component mass fractions. Dissimilar to that, the PMMA-PVC mixtures produced a higher amount of charring residue and a lower heat of combustion of volatiles compared to the component-based predictions assuming additivity.

ACKNOWLEDGMENT

This work is supported by the RSF grant 16-49-02017. Support by the Supercomputer center "Polytechnic" (SPbPU) is gratefully acknowledged.

REFERENCES

[1] R.W.J. Westerhout, J. Waanders, J.A.M. Kuipers, W.P.M. van Swaaij, Kinetics of the Low-Temperature Pyrolysis of Polyethene, Polypropene, and Polystyrene Modeling, Experimental Determination, and Comparison with Literature Models and Data, Ind. Eng. Chem. Res. 36 (1997) 1955–1964.

[2] C.-H. Wu, C.-Y. Chang, J.-L. Hor, S.-M. Shih, L.-W. Chen, F.-W. Chang, On the thermal treatment of plastic mixtures of MSW: Pyrolysis kinetics, Waste Manage., 13 (1993) 221–235.

[3] F.P. La Mantia, M. Morreale, L. Botta, M.C. Mistretta, M. Ceraulo, R. Scaffaro, Degradation of polymer blends: A brief review, Polym. Degrad. Stab. 145 (2017) 79–92.

[4] Z. Matusinovic, C.A. Wilkie, Degradation, stabilization, and flammability of polymer blends, in: L.A. Utracki, C.A. Wilkie (Eds.), Polym. Blends Handb., Springer, 2014, pp. 1395–1430.

[5] T. Faravelli, G. Bozzano, M. Colombo, E. Ranzi, M. Dente, Kinetic modeling of the thermal degradation of polyethylene and polystyrene mixtures, J. Anal. Appl. Pyrolysis 70 (2003) 761–777.

[6] R.N. Walters, R.E. Lyon, Molar Group Contributions to Polymer Flammability, J. Appl. Polym. Sci. 87 (2003) 548–563.

[7] R.E. Lyon, M.T. Takemori, N. Safronava, S.I. Stoliarov, R.N. Walters, A molecular basis for polymer flammability, Polymer 50 (2009) 2608–2617.

[8] R. Sonnier, B. Otazaghine, L. Dumazert, R. Ménard, A. Viretto, L. Dumas, L. Bonnaud, P. Dubois, N. Safronava, R. Walters, R. Lyon, Prediction of thermosets flammability using a model based on group contributions, Polymer 127 (2017) 203-213.

[9] B. Schartel, K.H. Pawlowski, R.E. Lyon, Pyrolysis combustion flow calorimeter: A tool to assess flame retarded PC/ABS materials? Thermochim. Acta 462 (2007) 1–14.

[10] U. Hujuri, A.K. Ghoshal, S. Gumma, Modeling pyrolysis kinetics of plastic mixtures, Polym. Degrad. Stab. 93 (2008) 1832–1837.

[11] R.E. Lyon, R.N. Walters, S.I. Stoliarov, N. Safronava, Principles and Practice of Microscale Combustion Calorimetry. Technical Report DOT/FAA/TC-12/53(R1), Federal Aviation Administration, 2014, 95 P.

[12] A.Yu. Snegirev, M. Koraiem, V.V. Stepanov, V.A. Talalov, Pyrolysis and combustion of polymer mixtures: exploring additivity of the heat release rate, Polym. Degrad. Stab. 161 (2019) 245-259.

[13] A.Yu. Snegirev, V.A. Talalov, V.V. Stepanov, O.P. Korobeinichev, I.E. Gerasimov, A.G. Shmakov, Autocatalysis in thermal decomposition of polymers, Polym. Degrad. Stab. 137 (2017) 151–161.

[14] A.Yu. Snegirev, Generalized approach to model pyrolysis of flammable materials, Thermochim. Acta 590 (2014) 242–250.

[15] A.Yu. Snegirev, V.V. Talalov, V.V. Stepanov, J.N. Harris, Formal kinetics of polystyrene pyrolysis in non-oxidizing atmosphere, Thermochim. Acta 548 (2012) 17–26.

[16] ASTM D7309-07a, Standard Test Method for Determining Flammability Characteristics of Plastics and Other Solid Materials Using Microscale Combustion Calorimetry, ASTM Int., 2007, pp. 1–8.

[17] R. Miranda, J. Yang, C. Roy, C. Vasile, Vacuum pyrolysis of commingled plastics containing PVC. I. Kinetic study, Polym. Degrad. Stab. 72 (2001) 469–491.

[18] Z. Ahmad, N.A. Al-Awadi, F. Al-Sagheer, Thermal degradation studies in poly(vinyl chloride)/poly(methyl methacrylate) blends, Polym. Degrad. Stab. 93 (2008) 456–465.

Thermal Decomposition of Wildland Material: Interactions among Biomass and Shallow Soil under Nitrogen and Air Atmospheres

Zhu H., Liu N.*

State Key Laboratory of Fire Science, University of Science and Technology of China,
Hefei, Anhui, China
**Corresponding author's email: liunai@ustc.edu.cn*

ABSTRACT

In a wildland fire, the thermal decomposition of biomass supports the burning of wildland material, while the pyrolysis of shallow soil has a considerable impact on the underground smoldering. So far, the interaction between biomass and shallow soil has been scarcely studied. This work presents an effort on this problem. The thermal behaviors of pine needle, pine bark, pine branch, shallow soil and their mixtures are investigated using a thermogravimetric analyzer under nitrogen and air atmospheres. The calculated TG curves of the forest combustible mixtures, obtained with the mixing ratios and experimental data of individual materials, agree well with the experimental data. This indicates that the interaction among biomass and shallow soil mixture is negligible under nitrogen and air atmospheres. The deviation parameter and the deviation of residue yield between the calculated and experimental curves are used to evaluate the influence of interactions on the organic and inorganic components, respectively. The calculated lower values of these parameters (<3%) confirm insignificant effect of interaction between biomass and shallow soil on pyrolysis and combustion. In addition, results further indicate that the effect of interactions on the thermal decomposition of the organic component is closely associated with the atmosphere and mixing ratio, while the effect on inorganic component has no perceptible relationship with these two factors. A kinetic model, involving *n*th-order independent parallel reactions, is applied to verify the reliability of the evaluation result. The pyrolysis rate of biomass is considered as the sum of the three pseudo-components, namely cellulose, hemicellulose, and lignin. While in the pyrolysis of shallow soil, the three pseudo-components are composed of labile, intermediate, and stable organic materials. The major mass loss of single material in combustion is interpreted as the sum of the parallel reactions of the above three pseudo-components as well as char. The theoretical TG curves of the mixtures, based on mixing ratio and kinetic parameters of individual materials, are in good agreement with experimental data, which also suggests an insignificant interaction effect on pyrolysis and combustion.

KEYWORDS: Thermal decomposition, wildland material, interaction, kinetic analysis.

NOMENCLATURE

A	frequency factor (1/min)
E	activation energy (kJ/mol)
$f(\alpha)$	reaction function
m	sample mass (mg)
n	reaction order
r	fraction of component
R	gas constant (8.314 J/(mol·K))
T	temperature (K)
t	time (min)

Greek

α	conversion
β	heating rate (K/min)

Subscripts

0	initial value
∞	final value
i	number of components
j	number of experimental runs

Proceedings of the Ninth International Seminar on Fire and Explosion Hazards (ISFEH9), pp. 1134-1143
Edited by Snegirev A., Liu N.A., Tamanini F., Bradley D., Molkov V., and Chaumeix N.
Published by Saint-Petersburg Polytechnic University Press
ISBN: 978-5-7422-6498-9 DOI: 10.18720/spbpu/2/k19-77

k number of data points in each run

INTRODUCTION

In a wildland fire, the thermal decomposition of biomass supports the burning of wildland material, while the pyrolysis of shallow soil has a considerable impact on the underground smoldering. So far, there have been numerous reports on the thermal decomposition of biomass or soil separately [1-4]. Niu and Liu [2] established a consistent kinetic scheme with the same proportions of three pseudo-components to simulate the pyrolytic reactions in pyrolysis and combustion of pine branch. Chen et al. [3] simulated peat pyrolysis using stages of moisture evaporation and organic matter pyrolysis (which consists of pyrolysis of hemicellulose, cellulose, and lignin), and also simulated combustion processes with a scheme containing moisture evaporation and two consecutive reactions. Kučeríka et al. [4] divided the soil organic material thermal stability into three categories: labile, intermediate, and stable, linking with contents of clay, bound water, organic carbon and nitrogen.

The major organic components of biomass include cellulose, hemicellulose, and lignin. The fraction of the inorganic ash varies from less than 1% in softwoods to 15% in herbaceous biomass and agricultural residues [5]. Soil organic matter contains carbohydrates, proteins, lipids, phenol-aromatics, protein-derived and cyclic nitrogenous compounds, and some still unknown compounds [6]. The inorganic content of duff and soil below forest ground surface increases with the increment of depth [7]. The organic composition of shallow soil is different with that of plants. At the same time, shallow soil generally contains more inorganic proportion than biomass. Shallow soil and plants are in close contact under natural conditions, which may cause interactions among them when suffering from a wildland fire. Among the limited studies, Giudicianni et al. [8] reported that the presence of inorganic elements significantly affects the pyrolysis behaviours of A. donax canes, in terms of characteristic temperatures and products yields. Yang et al. [9] detected an obvious catalytic effect of K_2CO_3 on the pyrolysis of palm oil wastes by analyzing the peak value of mass loss rate, while most of the other mineral additives have a negligible influence. Nevertheless, the interactions between biomass and shallow soil have been scarcely studied.

The objective of this work is to evaluate the interactions between biomass and shallow soil under nitrogen and air atmospheres by analyses of organic and inorganic components. The reliability of the evaluation method is verified by kinetic calculations and experimental data.

EXPERIMENTAL

Sample

The materials used in this work include pine needle (pn), pine bark (pb), pine branch (pbr), shallow soil (ss) and their equal-proportion mixtures consisting of two or three components (pn-ss, pb-ss, pbr-ss, pn-pb-ss, pn-pbr-ss, and pb-pbr-ss). The forest combustible materials were collected in the Great Khingan, northeast of China. The biomass samples (pn, pb, pbr) were obtained from living Pinus Sylvestris to prevent from being polluted or mixed with impurities. The shallow soil (ss) containing humus and black soil was collected at a depth of 0~5 cm from the ground surface. Before formal sampling, the litter above the shallow soil was removed. The raw samples were dried at 75 °C for 24 h in an electric oven. Prior to thermogravimetric tests, samples were milled to powder (less than 125 μm in size).

Ultimate analysis

The ultimate analysis of four single samples was performed by an Elementar vario EL cube, and the results are shown in Table 1. Before oxygen analysis of shallow soil, demineralization of shallow soil was conducted by stirring the flour in 1M HCl at room temperature for 24 h. After filtration, the sample was washed with distilled water repeatedly until the pH of the supernatant became neutral. This procedure was repeated twice, and the processed sample was dried at 75 °C for 24 h.

Table 1. Ultimate analysis results of samples

Material	N (%)	C (%)	H (%)	O (%)
Pine needle (pn)	1.33	51.30	7.01	37.51
Pine bark (pb)	0.35	52.44	6.37	38.13
Pine branch (pbr)	0.43	47.64	6.85	40.15
Shallow soil (ss)	1.30	28.82	3.84	26.12[a]

[a]Demineralized.

Pyrolysis and combustion experiments

A Netzsch thermobalance model STA 449F3 was employed for thermogravimetric (TG) experiments. The samples were evenly distributed over the crucible with the initial mass of 7.5~8.5 mg and 2~3 mg under nitrogen and air atmospheres, respectively. Dynamic experiments were carried out at heating rates of 5, 10, 15, 20 and 30 K/min, from room temperature up to 800 °C. The flow rate of sweeping gas was 100 ml/min. Some runs were repeated to check the repeatability of the tests under the same conditions.

Kinetic analysis

In the present work, a multi-component model is used to simulate the thermal decomposition of the forest combustible materials. If a pseudo-component i goes through an n-order reaction, the decomposition rate (DTG) can be expressed by

$$d\alpha_i/dT = (A_i/\beta)\exp(-E_i/RT)(1-\alpha_i)^{n_i}, \tag{1}$$

where A is the pre-exponential factor, E is the activation energy, n is the reaction order, $\beta = dT/dt$ is the heating rate and R is the gas constant. The conversion fraction α_i is expressed as

$$\alpha_i = (m_{i0} - m_i)/(m_{i0} - m_{i\infty}), \tag{2}$$

where the subscripts "0" and "∞" respectively denote the initial and final masses of the sample.

The total conversion is thus formulated as

$$\alpha = \sum_i r_i \alpha_i, \tag{3}$$

where r_i represents the fraction of component i ($\sum r_i = 1$).

By using the experimental data, the genetic algorithm (GA) is applied for kinetic analysis of individual fuels. The objective function is defined as Eq. (4) to minimize the differences between experimental and theoretical mass loss rate curves.

$$Dev = 100\% \cdot \sum_{j} \sqrt{S_j \big/ \left(Z_j - N_j\right)} \Big/ \max\left[-\left(d\alpha/dT\right)^{Exp}\right] \Big/ j\,. \tag{4}$$

Here, j is the number of experimental runs, Z_j is the number of data points on the j-th experimental curve, N_j is the number of independent parameters to be determined, and S_j is expressed by

$$S_j = \sum_{k} \left[\left(\left(d\alpha/dT\right)^{Exp}\right)_{j,k} - \left(\left(d\alpha/dT\right)^{Cal}\right)_{j,k}\right]^2, \tag{5}$$

where k is the number of data points in each run. The superscripts Exp and Cal denote the experimental and simulated values, respectively. Experimental data at heating rates of 5, 10, 15, 20 and 30 K/min are simultaneously applied to the optimization calculations in order to overcome the kinetic compensation effects. The GA codes in MATLAB are used to perform the search.

RESULTS AND DISCUSSION

Thermogravimetric analysis of individual materials

Pyrolysis and combustion experiments: The normalized DTG curves for individual fuel obtained at different heating rates follow similar trends under nitrogen and air atmospheres. The DTG curves at the constant heating rate of 10 K/min are shown in Fig. 1. At temperatures lower than about 373.15 K, the small mass loss of the samples is attributed to moisture evaporation. As indicated in Fig. 1(a), the pine needle starts to decompose earlier at a temperature slightly below 400 K, followed by pine bark, pine branch and shallow soil. Comparing the DTG peaks of the different samples shows that the shallow soil has the widest peak temperature range. As shown in Fig. 1(b), under oxidative atmosphere, two stages are distinguished in the DTG curves for biomass fuels. The first stage in the range of 400~650 K is caused by the combination of total decomposition of hemicellulose and cellulose and partial decomposition of lignin, and the second one in the range of 650~800 K corresponds to the decomposition of the remaining lignin and char oxidation, leaving behind only ash [14]. The mass loss rate of the shallow soil increases sharply from about 450 K, and then reaches the maximum at around 590 K. This peak temperature is close to the first peak temperature of biomass fuels. After that, the mass loss rate drops to a platform and then decreases again. As shown in Table 2, the residual proportions of biomass fuels are lower than that of shallow soil in pyrolysis and combustion.

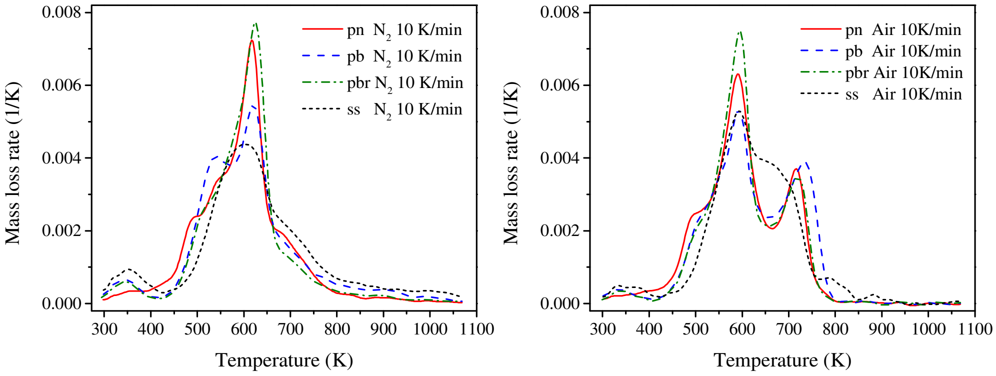

(a) (b)

Fig. 1. Experimental DTG curves of single materials in (a) pyrolysis and (b) combustion at the heating rate of 10 K/min.

Table 2. Residual fraction of TG experiment under nitrogen and air atmospheres

Residual fraction (%)	pn	pb	pbr	ss
N_2	18.72±0.29	25.35±0.56	19.63 ±0.10	57.93±0.63
Air	2.63±0.73	3.58±0.13	2.88±0.29	42.56±1.00

Multi-step devolatilization mechanism of single materials: The three-step devolatilization mechanism for the volatile fractions of the pseudo-components, hemicellulose, cellulose, and lignin, is applied to describe the dynamic thermogravimetric curves of the biomass fuels under nitrogen atmosphere. For shallow soil pyrolysis, the three-step kinetic model is interpreted as the reactions of labile, intermediate and stable organic materials. The char oxidation is simulated as the fourth reaction in combustion of biomass fuels and shallow soil. The calculated kinetic parameters of the individual materials under nitrogen and air atmospheres are listed in Tables 3 and 4. Here, the char fraction under air atmosphere is expressed as

$$r_{char} = \left(residue_{nitrogen} - residue_{air}\right) / \left(100 - residue_{air}\right) \tag{6}$$

while the other parameters are determined by the GA method. The Dev values lie within the range of 2.30~3.24%, suggesting good fit between the theoretical and experimental DTG data. The simulated curves of shallow soil at the heating rate of 10 K/min are presented in Fig. 2, for which the data of dehydration stage have been removed since the focus of this work is on the thermal decomposition reaction. As shown, the theoretical DTG curves are in good agreement with the experimental ones. For the figures in this work, the sub-reactions 1~4 are defined as the thermal decomposition of hemicellulose, cellulose, lignin, and char for biomass materials. While for shallow soil, the four corresponding pseudo-components are labile, intermediate, stable organic materials and char, respectively.

Table 3. Optimal solutions of kinetic parameters in pyrolysis

Material	Component	E (kJ/mol)	$\lg A$ [lg (min-1)]	n	r (%)	Dev (%)
pn	Hemicellulose	68.40	6.21	2.30	44.94	2.93
	Cellulose	163.33	13.58	1.19	32.35	
	Lignin	195.75	14.77	4.85	22.71	
pb	Hemicellulose	94.46	8.75	2.22	42.71	2.76
	Cellulose	187.47	15.51	2.79	35.88	
	Lignin	184.17	12.63	9.77	21.41	
pbr	Hemicellulose	92.29	8.40	2.80	44.99	2.78
	Cellulose	179.87	14.83	1.47	36.18	
	Lignin	191.25	14.16	9.82	18.83	
ss	Labile organic materials	96.09	8.82	3.48	33.94	2.93
	Intermediate organic materials	207.04	18.41	3.46	16.59	

	Stable organic materials	192.13	15.42	9.65	49.47

Table 4. Optimal solutions of kinetic parameters in combustion

Sample	Component	E (kJ/mol)	lg A [lg (min-1)]	n	r (%)	Dev (%)
pn	Hemicellulose	86.09	8.40	2.55	29.95	2.46
	Cellulose	147.63	12.77	1.55	36.13	
	Lignin	158.85	12.27	2.96	17.40	
	Char	196.18	13.90	1.00	16.52	
pb	Hemicellulose	92.32	8.82	2.79	30.38	2.46
	Cellulose	160.34	13.85	2.67	35.73	
	Lignin	178.74	13.09	2.23	11.32	
	Char	152.74	10.32	0.90	22.57	
pbr	Hemicellulose	85.24	7.96	2.56	30.13	2.30
	Cellulose	147.42	12.67	1.23	36.71	
	Lignin	161.71	12.32	2.97	15.92	
	Char	174.08	12.29	1.08	17.24	
ss	Labile organic materials	109.25	10.23	2.51	22.82	3.24
	Intermediate organic materials	162.35	14.04	2.74	35.01	
	Stable organic materials	165.43	12.85	2.96	15.41	
	Char	158.26	11.47	2.58	26.76	

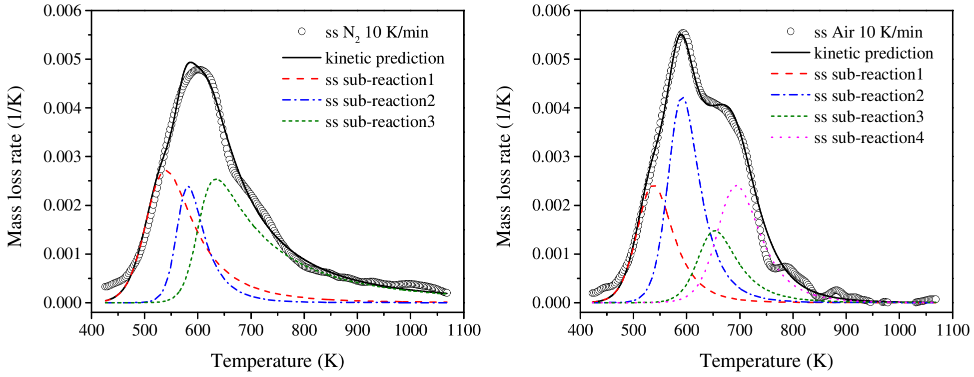

(a) (b)

Fig. 2. Theoretical and experimental DTG curves of shallow soil in (a) pyrolysis and (b) combustion at the heating rate of 10 K/min.

Thermogravimetric analysis of mixtures

Calculated and experimental curves: We calculate TG curves of mixtures by a weighted sum of experimental curves of individual materials and then compare the calculated curves with the experimental data in Fig. 3. The results suggest that there is no obvious interaction between biomass and shallow soil during pyrolysis and combustion. As shown in Table 5, the residual fractions of blends are in range of 32.47 ~ 41.44% for pyrolysis, and 15.67 ~ 23.94% for combustion. As indicated, under a certain atmosphere, the residue mass fractions for two-component mixtures are higher than those for three-component mixtures. In other words, the residual mass fractions increase with the decrease of biomass proportion.

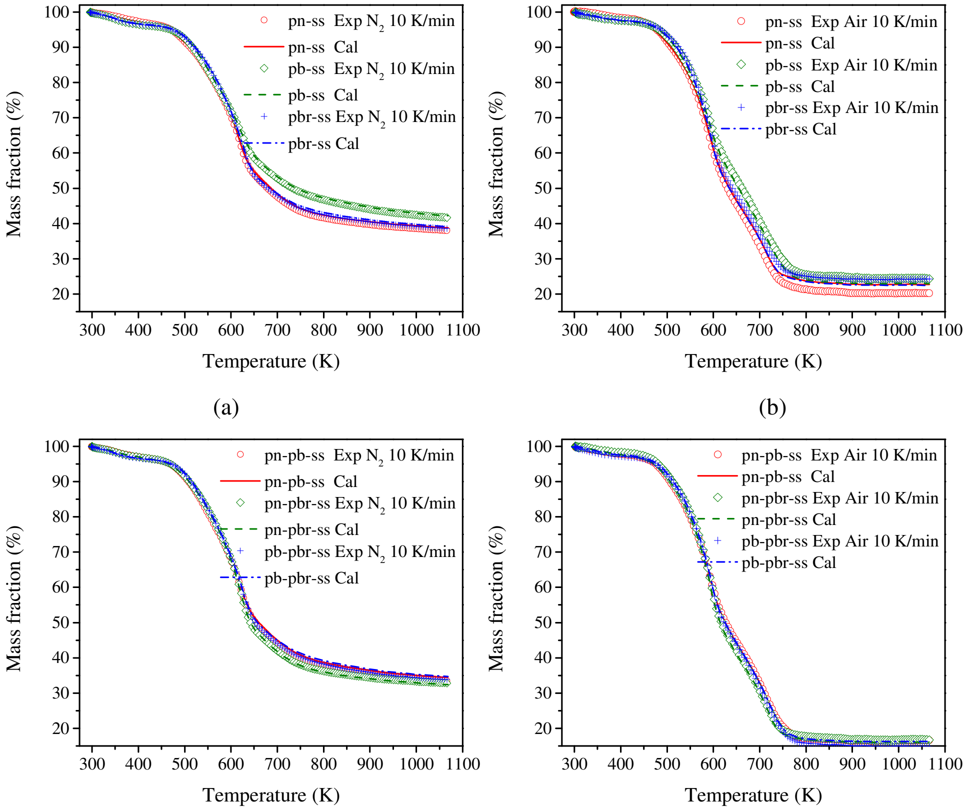

(a) (b)

(c) (d)

Fig. 3. Comparison between calculated and experimental TG curves for mixtures heated at 10 K/min in pyrolysis and combustion.

Table 5. Residual fraction of mixtures under nitrogen and air atmospheres

Residual fraction (%)	pn-ss	pb-ss	pbr-ss	pn-pb-ss	pn-pbr-ss	pb-pbr-ss
N_2	37.88±0.23	41.44±0.92	37.78±0.77	33.76±0.43	32.47±0.57	33.83±0.19
Air	21.78±1.19	23.30±2.84	23.94±0.77	16.13±1.07	16.16±1.80	15.67±1.70

Quantitative method of interaction assessment: Usually, single-point values of TG or DTG curves (such as peak mass loss rate, peak temperatures, and product yield) were used to evaluate the influence of interactions on the thermal decomposition of mixtures [8-12]. A more reasonable quantitative method is by using a quantity that reflects the overall feature of the curves. For example, by using the root mean square (RMS) value of relative error in prediction of fractional residue, Sadhukhan et al. [13] revealed that there were no synergistic effects between coal and biomass. In this work, a similar quantitative approach is used to assess the interaction effect among mixtures. The parameter Dev (Eq. (4)) and the deviation of unreacted mass between the calculated and experimental curves are used to evaluate the influence of interactions on organic and inorganic components, respectively. As shown in Fig. 4, among all the tests, a maximum Dev of 2.63% is reached for pb-ss under air atmosphere. For this mixture, all the calculated and experimental results are in good agreements (see Fig. 5). Besides, a maximum $\left|\Delta residue\right|$ of 1.17% is reached for pbr-ss under air atmosphere.

The calculated low parameters of Dev and $\left|\Delta residue\right|$ (<3%) also indicate insignificant effect of interaction between biomass and shallow soil on pyrolysis and combustion. In addition, the effect of interactions on the thermal decomposition of organic component is closely associated with the atmosphere and mixing ratio: interaction under air is more significant than that under nitrogen, and the interaction is generally enhanced with higher shallow soil content. However, there is no obvious relationship between these two factors and the effect on the inorganic component.

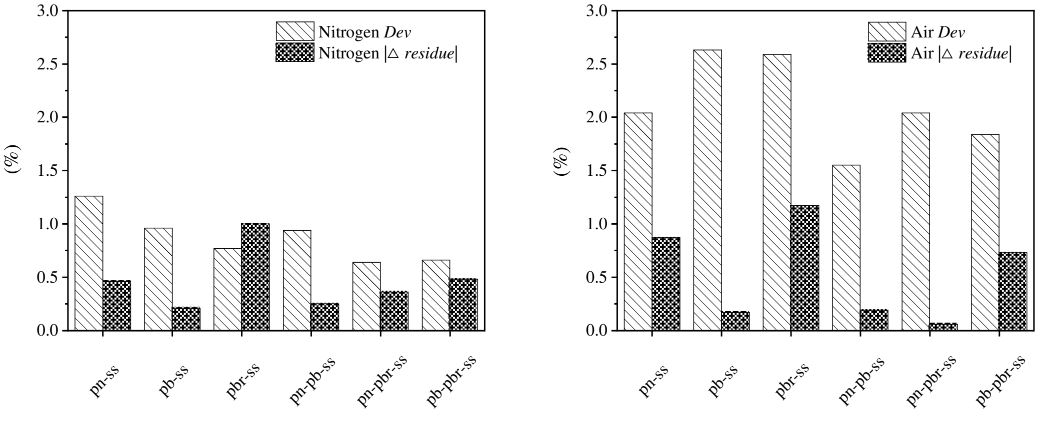

(a) (b)

Fig. 4. Quantitative evaluation of interaction effect among mixtures under (a) nitrogen and (b) air atmospheres.

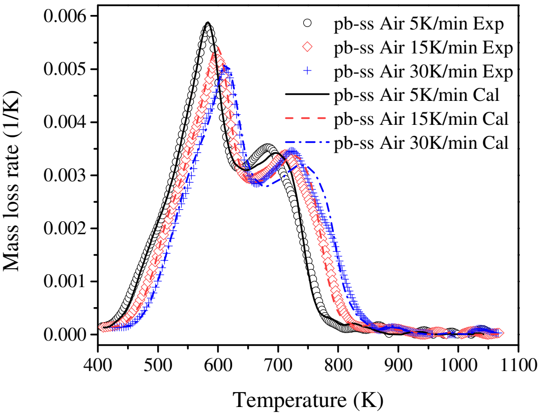

Fig. 5. Comparison between calculated and experimental DTG curves for pb-ss in combustion.

Theoretical and experimental curves: In the previous section, the multi-step devolatilization mechanism is used to obtain the kinetic parameters of single materials. Here, the theoretical curves of individual materials are summed, based on the mixing ratio, to predict the DTG curves of the mixtures. The Dev values of biomass-shallow soil mixture vary in the range of 2.53~3.92%, which implies that the theoretical and experimental DTG curves have good agreement, and the materials undergo thermal decomposition independent of each other. This verifies the applicability of the model for predicting the pyrolysis and combustion behavior of the biomass-shallow soil mixture without losing any generality [13, 14].

The maximum Dev of 3.92% corresponds to the combustion processes of pb-ss, for which the theoretical and experimental DTG curves of this mixture are indicated in Fig. 6. The curves for the sub-reactions of pine bark and shallow soil are also plotted. The good comparison between theoretical and experimental DTG curves also suggests an insignificant effect of the interactions on pyrolysis and combustion.

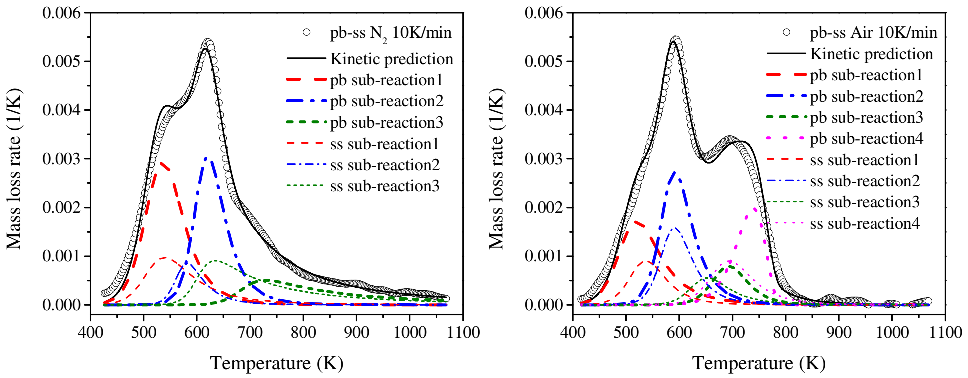

(a) (b)

Fig. 6. Comparison of theoretical and experimental curves of pb-ss at the heating rate of 10 K/min under (a) nitrogen and (b) air atmospheres.

CONCLUSIONS

In this work, the interactions between biomass and shallow soil are studied to promote the understanding of thermal decomposition of forest combustible mixtures when suffering from a wildland fire. A quantitative method is applied to compare the calculated and experimental curves, in which the parameters Dev and $|\Delta residue|$ are used to evaluate the influence of mixing on organic and inorganic components, respectively. A kinetic method is used to check the reliability of this assessment method. The interaction under different conditions can be examined by using this quantitative method. The results show that the interaction between biomass and shallow soil has an insignificant effect on pyrolysis and combustion. In addition, the effect of interactions on thermal decomposition of the organic component is closely associated with the atmosphere and mixing ratio: interactions under air are stronger than that under nitrogen, and the interaction is generally enhanced with higher shallow soil content. However, the effect on thermal decomposition of the inorganic component is hardly related to these two factors. The residual fractions of blends increase with the increase of the shallow soil proportion of blend under a certain atmosphere.

ACKNOWLEDGEMENTS

This research is funded by the National Key R&D Program (No. 2016YFC0800100) and the National Natural Science Foundation of China (No. 51625602). This work is also supported by the Fundamental Research Funds for the Central Universities under Grants No. WK2320000038 and No. WK2320000036.

REFERENCES

[1] C. Di Blasi, Modeling chemical and physical processes of wood and biomass pyrolysis, Prog. Energy Combust. Sci. 34 (2008) 47-90.

[2] H. Niu, N. Liu, Thermal decomposition of pine branch: Unified kinetic model on pyrolytic reactions in pyrolysis and combustion, Fuel 160 (2015) 339-345.

[3] H. Chen, W. Zhao, N. Liu, Thermal analysis and decomposition kinetics of Chinese wildland peat under nitrogen and air atmospheres, Energy Fuels 25 (2011) 797-803.

[4] J. Kučerík, D. Tokarski, M. S. Demyan, I. Merbach, C. Siewert, Linking soil organic matter thermal stability with contents of clay, bound water, organic carbon and nitrogen, Geoderma. 316 (2018) 38-46.

[5] S. Yaman, Pyrolysis of biomass to produce fuels and chemical feedstocks, Energy Convers. Manage. 45 (2004) 651-671.

[6] E. A. Paul, The nature and dynamics of soil organic matter: plant inputs, microbial transformations, and organic matter stabilization, Soil Biol. Biochem. 98 (2016) 109-126.

[7] H. Chen, W. Zhao, N. Liu, J. Zhou, Thermal decomposition extent of duff due to surface wildland fire, Procedia Eng. 62 (2013) 1000-1006.

[8] P. Giudicianni, G. Cardone, G. Sorrentino, R. Ragucci, Hemicellulose, cellulose and lignin interactions on Arundo donax steam assisted pyrolysis, J. Anal. Appl. Pyrolysis 110 (2014) 138-146.

[9] H. Yang, R. Yan, H. Chen, C. Zheng, D. H. Lee, D. T. Liang, Influence of mineral matter on pyrolysis of palm oil wastes, Combust. Flame 146 (2006) 605-611.

[10] N. Nishioka, S. Hamabe, T. Murakami, T. Kitagawa, Thermal decomposition behavior of miscible cellulose/synthetic polymer blends, J. Appl. Polym. Sci. 69 (1998) 2133-2137.

[11] V. I. Sharypov, N. Marin, N. G. Beregovtsova, S. V. Baryshnikov, B. N. Kuznetsov, V. L. Cebolla, J. V. Weber, Co-pyrolysis of wood biomass and synthetic polymer mixtures. Part I: influence of experimental conditions on the evolution of solids, liquids and gases, J. Anal. Appl. Pyrolysis 64 (2002) 15-28.

[12] L. Xu, Y. Jiang, R. Qiu, Parametric study and global sensitivity analysis for co-pyrolysis of rape straw and waste tire via variance-based decomposition, Bioresour. Technol. 247 (2018) 545-552.

[13] A. K. Sadhukhan, P. Gupta, T. Goyal, R. K. Saha, Modelling of pyrolysis of coal-biomass blends using thermogravimetric analysis, Bioresour. Technol. 99 (2008) 8022-8026.

[14] A. Skreiberg, Ø. Skreiberg, J. Sandquist, L. Sørum, TGA and macro-TGA characterisation of biomass fuels and fuel mixtures, Fuel 90(2011) 2182-2197.

Apparent Activation Energy of Coal Oxidation with Different Particle Sizes based on Temperature-programmed Approach

Zhao J.Y.[1,2,3,] *, Zhang Y.X.[1,2], Deng J.[1,2], Shu C.M.[4,] *, Cheng Y.C.[4], Yi X.[1,2]

[1] Xi'an University of Science and Technology, Xi'an, China
[2] Shaanxi Key Laboratory of Prevention and Control of Coal Fire, Xi'an, China
[3] Institute for Arid Ecology and Environment, Urumqi, China
[4] National Yunlin University of Science and Technology, Yunlin, Taiwan, ROC
**Corresponding author's email: zhaojingyu2014@126.com*

ABSTRACT

To study the effect of coal particle size on the activation energy of coal oxidation reaction in different oxidation stages, the experimental equipment of temperature-programmed tests was adopted. To determine the relationship between oxygen consumption rate and gas products, the temperature was explored in the low-temperature oxidation stage of coal samples with different particle sizes. The critical temperature point for coal samples of different particle sizes was obtained by analyzing the change rule of gas product and oxygen consumption rate with temperature, and dynamic analysis was carried out on this basis. Establishing an Arrhenius formula between the oxygen consumption rate and the coal temperature, the apparent activation energy equation was obtained from the logarithmic treatment method. The linear regression on straight line gradient of the equation was analyzed and the apparent activation energy for the low temperature oxidized coal sample was calculated. The results showed that the particle sizes affected the apparent activation energy, and the larger the particle size was, the larger the activation energy was. However, the coal samples with a particle size of 5–7 mm had the maximum apparent activation energy before the critical temperature. Compared with other particle sizes, the coal sample of this particle size did spontaneously combust easily.

KEYWORDS: Coal oxidation, oxygen consumption, critical temperature, dynamic analysis, spontaneous combustion.

NOMENCLATURE

A	Pre-exponential factor s^{-1}	Q	Air supply volumetric flow rate mL/s
A_{ad}	Ash content air-dried basis %	R	Universal gas constant 8.314 J mol^{-1} K^{-1}
E	Apparent activation energy kJ mol^{-1}	S	Test tube sectional area cm^2
FC_{ad}	Fixed carbon content air-dried basis %	T	Temperature °C
L	Height of coal sample cm	V_{ad}	Volatile matter content air-dried basis %
M_{ad}	Moisture content air-dried basis %	V_m	Volume of the experimental coal sample cm^3
n	Reaction order dimensionless		

INTRODUCTION

As an economical and low-cost energy source, coal accounts for the largest share of global electricity production. However, spontaneous combustion of coal has been, and continues to be, a major threat associated with the extraction and storage of coal. Once this happens, it can cause

Proceedings of the Ninth International Seminar on Fire and Explosion Hazards (ISFEH9), pp. 1144-1153
Edited by Snegirev A., Liu N.A., Tamanini F., Bradley D., Molkov V., and Chaumeix N.
Published by Saint-Petersburg Polytechnic University Press
ISBN: 978-5-7422-6498-9 DOI: 10.18720/spbpu/2/k19-62

major problems, such as huge losses of coal resources, environmental damage, and death [1-3]. In underground coal mining, spontaneous combustion usually occurs in concealed areas, such as inaccessible gobs. Research on the characteristics of spontaneous combustion is useful for monitoring and assessing the severity of coal fires, as well as preventing and controlling them.

The low-temperature oxidation reaction is complex and varies with the temperature [4-6]. The spontaneous combustion tendency of coal reflects the easy degree of coal spontaneous combustion and the low-temperature oxidation characteristics [7, 8]. Coal oxidation is an irreversible exothermic process, and the reaction rate increases with increasing temperature [9-12]. To predict this critical temperature, numerous methods have been established, such as adiabatic oxidation, temperature programmed and exponential gas growth rates. In recent years, the influence of particle size on combustion reactions has received increasing attention. Some scholars have studied this effect in the study of coal spontaneous combustion. The effects of coal particle size on kinetic parameters (apparent activation energy, reaction rate), exothermic intensity and oxygen consumption rate in coal oxidation and pyrolysis have been studied [13-16].

At present, many scholars are carrying out kinetic analysis of coal samples with different degrees of metamorphism by using thermal analysis experiments, and testing the effects of various influencing factors such as oxygen concentration, particle size and heating rate on activation energy [17-23]. Gao conducted a simultaneous thermal analyzer (STA) experiment to explore the relationship between the apparent activation energy of coal and heating rate and oxygen concentration. The bituminous coal samples were analyzed using a simultaneous thermal analyzer [24]. Wang studied the mass gain of coal oxidation observed by thermogravimetric analysis. Thermogravimetric infrared and thermogravimetric in-situ infrared experiments were carried out on a typical Jurassic coal in western China, and the kinetics and mechanism of coal oxidation were determined [25, 26]. The scholars mentioned that the above used fewer coal samples, and the critical temperature was used as a key temperature point for coal in the low-temperature oxidation stage; there were few macroscopic experiments near this temperature point. Therefore, it is meaningful to perform a segmentation calculation of the activation energy of the low-temperature oxidation process of coal with the critical temperature as the segmentation point.

In this paper, the critical temperature of coal spontaneous combustion was measured by the temperature-programmed experimental system. The gas products of different particle sizes were obtained, and the apparent activation energy was calculated. The relationship between particle size and coal spontaneous combustion tendency was obtained, and the spontaneous combustion tendency of coal in different coal seams was studied.

EXPERIMENTAL

Coal sample preparation

The coal samples of the 2^{-2mid} and 3^{-1} coal seams in Wantugou coal mine were selected as long-flame coal samples. The samples were divided into two groups. Each group was pulverized in the air, and the coal was screened according to the five particle sizes of 0–0.9, 0.9–3, 3–5, 5–7, 7–10 mm. Each of the five particle sizes was screened at 1.2 kg, and each particle size was used to complete the experiment with 1.0 kg; the remaining 200 g was composed of the mixed coal sample. Coal quality was established by proximate and ultimate analyses, the results (Table 1) are presented on an air-dried basis.

Experimental apparatus

A self-designed temperature-programmed experimental system was employed to investigate the characteristics of coal spontaneous combustion during the decaying process. The experimental system consisted of three parts: gas supply system, temperature-programmed system, and gas sample analysis system. The gas supply system can provide a variety of oxygen content of the carrier gas for the oxidation of coal. The temperature-programmed system consists of an oven, a sample reactor and a thermocouple sensor inserted into the center of the reactor. The inner surface of the oven is insulated with asbestos and stainless material. The sample reactor is a cylindrical body with a diameter of 9.5 cm and a length of 25 cm. Before entering the sample reactor, the carrier is preheated by a long curved copper tube. Gas sample analysis systems include gas chromatograph and computer. Figures 1 (a) and (b) show the schematic of the reactor.

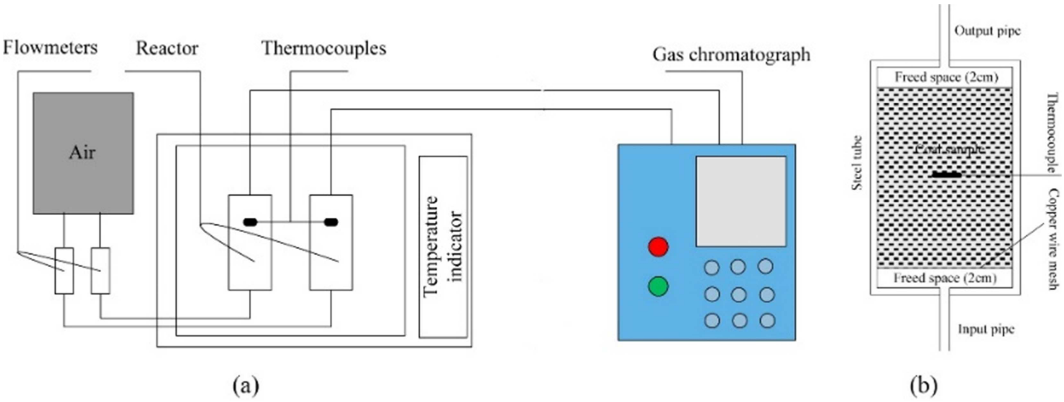

Fig. 1. Temperature-programmed experimental system: (a) overall picture and (b) reactor enlargement.

At the beginning of the experiment, the coal sample was first put into the reactor, and then into the heating box to connect the gas path which was open to the air pump, the flow rate to 120 mL/min, ventilation started to pick up an hour later, the heating rate 0.3 °C/min. Since 30 °C, using gas chromatograph analysis of gas composition, every 10 °C temperature interval of half an hour to receive gas analysis, the end of the experiment temperature was 170 °C. A total of 15.0 gas extraction analyses were conducted. Then the heating was stopped. Finally, the gas source was closed, and the experiment was finished.

Table 1. Analysis of coal quality of experimental coal samples

Sample	M_{ad} (%)	A_{ad} (%)	V_{ad} (%)	FC_{ad} (%)
2^{-2mid}	6.44	6.45	29.60	57.51
3^{-1}	8.73	7.23	47.43	42.61

RESULTS AND DISCUSSION

CO gas analysis

CO gas was selected as the index gas for different stages of the low-temperature oxidation process of coal. It can be seen from Fig. 2(a) that the CO emission of coal samples with different particle sizes in the 2^{-2mid} coal seam at normal temperature was almost the same. With the increase in temperature, the release amount of CO gas had a large change, and the gas release amount was measured at 170 °C. The gap was exceptionally obvious, and the law was that as the particle size increased, the amount of CO gas released decreased, while the amount of CO gas released from the sample was moderate. The CO gas generated by different particle sizes on coal samples showed two mutations during the heating process. The first abrupt temperature changed with the particle size, 0–0.9 mm particle size, 0.9–3 mm particle size. The temperature point of the mixed sample was 60 °C, the temperature point of the particle diameter of 3–5 mm was 70 °C, and the temperature point of the particle diameter of 5 to 7 mm and 7–10 mm was 80 °C, which indicated that the larger the particle size, the first abrupt temperature. The later the hysteresis, the temperature of the abrupt was the critical temperature of the coal sample. After the critical temperature, the growth rate of CO gas was significantly higher than the critical temperature, and the second abrupt temperature occurred. 120 °C, which indicated that the temperature was the dry cracking temperature of the coal sample; the gas growth rate was close to exponential growth after this temperature point.

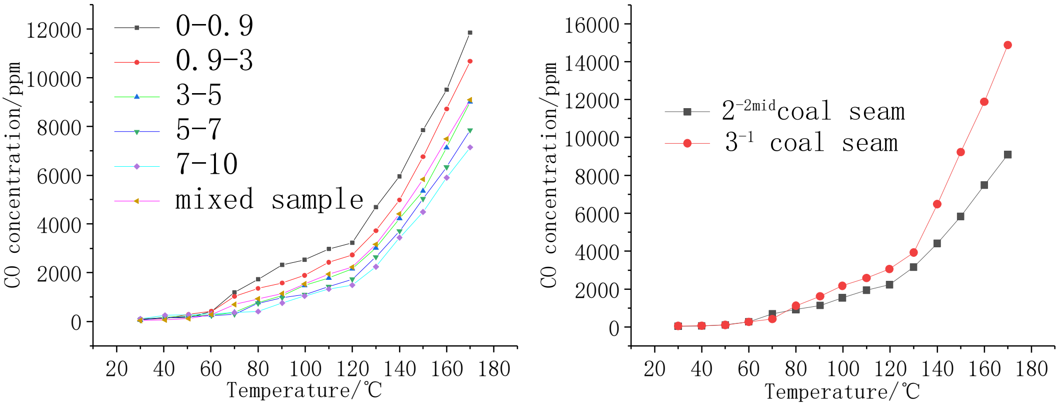

(a) (b)

Fig. 2. CO gas and temperature curve of coal sample: (a) different particle sizes and (b) different coal seams.

C_2H_4 gas analysis

C_2H_4 gas was selected as the index gas to assist in the different stages of low-temperature oxidation of coal. It can be seen from Fig. 3(a) that the C_2H_4 gas produced by the coal samples with different particle sizes of the same coal seam increased with the increase of temperature. At the same temperature point, as the particle size increased, the amount of gas released was less, and the mixture was mixed. The amount of gas released was at a moderate level. The gas appears at a temperature point of 80 to 100 °C; the law is that the temperature point lags with the increase of the particle size, while the mixed sample is in the centered position. Moreover, the growth rate of the gas before the cracking temperature was relatively slow; the cracking temperature shows an exponential growth.

It can be seen from Fig. 3(b) that under the condition that the particle size is the same as the mixed sample, the amount of C_2H_4 gas released by the 3^{-1} coal sample was larger than that of the coal sample of 2^{-2mid}, and the temperature at which the gas was generated was also earlier than that of the coal in 2^{-2mid}. Similarly, the temperature point at which the gas amount was abrupt was also delayed by 10 °C in the 2^{-2mid} coal sample.

Analysis of the oxygen consumption rate

The gas source used in this experiment was air, so the oxygen concentration at the inlet of the coal sample tank was 21 vol.%, and the oxygen concentration at the outlet could be measured by gas chromatography, so that the oxygen consumption rate of the coal sample can be calculated and the temperature was obtained by law of change.

The oxygen consumption rate of the coal sample in the sample reactor is expressed by Eq. (1):

$$v_{O_2}^0 = \frac{Qc_{O_2}^0}{SL}\cdot ln\frac{c_{O_2}^1}{c_{O_2}^2} = \frac{Qc_{O_2}^0}{V_m}\cdot ln\frac{c_{O_2}^0}{c_{O_2}^2} \tag{1}$$

where $v_{O_2}^0(T)$ is the average rate of oxygen consumption per unit volume of coal sample in fresh air current, mol/(cm^3·s) ; $C_{O_2}^0$ is the oxygen concentration in fresh airflow, $C_{O_2}^0$ = 9.375×10^{-6} mol/mL; Q is the air supply volume, mL/s; S is the test tube sectional area, cm^2; L is the height of coal sample, cm; $C_{O_2}^1$, $C_{O_2}^2$ is the oxygen concentration at the inlet and outlet of the coal sample, $C_{O_2}^1$ = $C_{O_2}^2$ = 9.375×10^{-6} mol/mL; V_m indicates the volume of the experimental coal sample, cm^3.

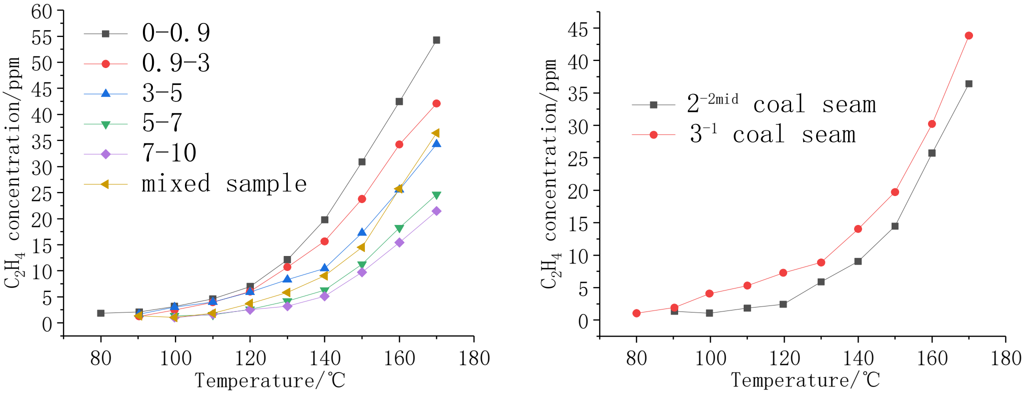

(a) (b)

Fig. 3. C_2H_4 gas and temperature curve of coal sample: (a) different particle sizes (b) different coal seams.

According to Eq. (1), curves of oxygen consumption rates with different particle sizes and coal types can be obtained.

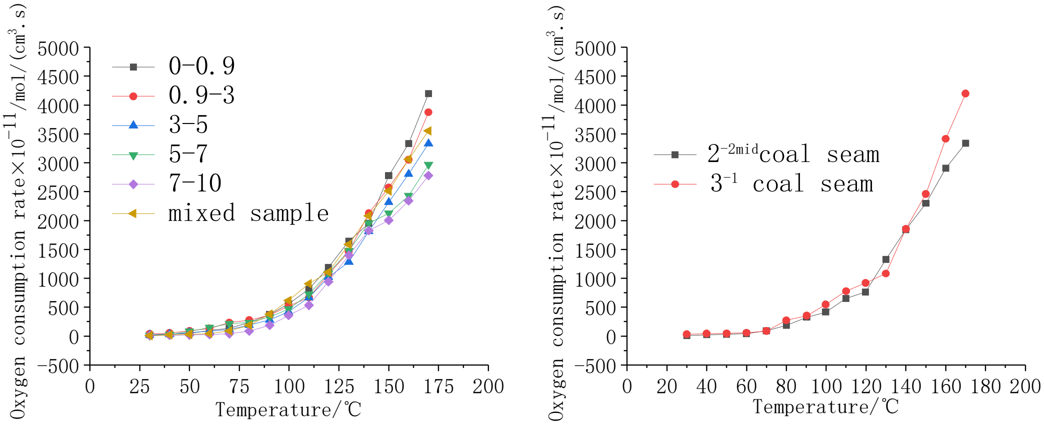

(a) (b)

Fig. 4. Oxygen consumption rate and temperature curve of coal sample: (a) different particle sizes and (b) different coal seams.

It can be seen from Fig. 4(a) that the oxygen consumption rate of coal samples with different particle sizes of the same coal seam increased with the increase of temperature. When at the same temperature point, the law showed that the oxygen consumption rate was lower as the particle size increased, and the oxygen consumption rate of the mixed sample was at a higher level. Before the critical temperature, the oxygen consumption rates of different particle sizes were not much different. At the critical temperature, the oxygen consumption rate demonstrated the first mutation, and after the critical temperature, its growth rate increased significantly. At the cracking temperature, the second abrupt temperature occurred, and then the rate of oxygen consumption showed exponential growth.

It can be seen from Fig. 4(b) that when the particle size was mixed, the oxygen consumption rate of the 3^{-1} coal seam was substantially larger than that of the $2^{-2\text{mid}}$ coal seam, because the dry cracking temperature of the 3^{-1} coal seam was greater than the coal seam of $2^{-2\text{mid}}$, so at 130 and 140 °C, the oxygen consumption rate of the 3^{-1} coal seam was less than $2^{-2\text{mid}}$ coal seam.

By analyzing the change law of CO and C_2H_4 gas and oxygen consumption rate with temperature, the critical temperature point was obtained, and the dynamic analysis was carried out by dividing the stage.

Oxidation kinetics analysis

During the spontaneous combustion of coal, the surface of the coal body is chemically adsorbed and oxidized by oxygen molecules, releasing many gases and a large amount of heat.

Coal + $O_2 \rightarrow$ mCO + gCO_2 + other products

According to the reaction rate calculation method and the Arrhenius equation, the reaction rate obeys the first-order Arrhenius equation, and Eq. (2) is obtained as follows:

$$v_{o_2}(T) = AC_{o_2}^{n} exp\left(-\frac{E_\text{a}}{RT_i}\right) \tag{2}$$

where $v_{o_2}(T)$ is the actual oxygen consumption rate, mol/(cm^3·s); A is the pre-exponential factor; E_a is the activation energy; and R is the gas constant, R=8.314 J/(mol·K), n is the reaction order, taking $n = 1$; C_{O_2} indicates the oxygen content in the reaction gas, mol/cm^3.

Combining Eqs. (1) and (2), the formula for calculating the oxygen consumption rate and activation energy can be determined:

$$v_{o_2}^{0}(T) = AC_{o_2}^{0} exp\left(-\frac{E_\text{a}}{RT_i}\right) \tag{3}$$

Further, simplifying the formula in Eq. (3), that is, taking the logarithm on both sides:

$$\text{Ln}\, v_{o_2}^{0} = \ln A + \ln C_{o_2}^{0} - \frac{E_\text{a}}{RT_i} \tag{4}$$

Finishing up:

$$\ln\frac{v_{o_2}^{0}}{C_{o_2}^{0}} = -\frac{E_\text{a}}{RT_i} + \ln A \tag{5}$$

It can be seen from the formula that in the Cartesian coordinate system, $\ln(v_{o_2}^{0}/C_{o_2}^{0})$ is the ordinate and $1/T$ is the abscissa, and the data can be fitted to a straight line. The slope of the line can be used to calculate the apparent activation energy. By taking the different particle sizes of the same coal seam and the oxygen consumption rate of different coal seam samples into the above formula, the apparent activation energy of the coal sample can be obtained. Since the apparent activation energy of coal samples before and after the critical temperature was quite different, the Arrhenius curves of different coal seams and different particle sizes before and after the critical temperature are, respectively, fitted, as shown in Figs. 5 and 6.

According to the above fitting curve, the activation energies corresponding to the critical temperatures of different coal samples are summarized as given in Table 2.

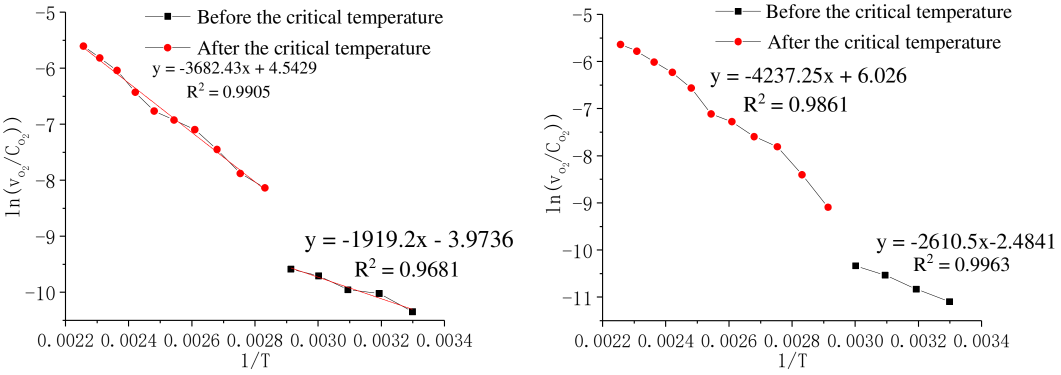

(c) (d)

Fig. 5. $\ln(v^0_{O_2}/C^0_{O_2})$ and 1/T relative curves of mixed coal seams: (a) 2-2mid coal sample mixed sample and (b) 3-1 coal sample mixed sample.

Table 2 Apparent activation energy of different coal samples

Coal sample number	Critical temperature, °C	E_1, kJ/mol	E_2, kJ/mol
0–0.9	60.0	17.06	29.57
0.9–3	60.0	23.25	37.46
3–5	70.0	27.40	41.28
5–7	80.0	34.97	41.75
7–10	80	33.44	44.63
2^{-2mid} mixed sample	60	21.70	35.22
3^{-1} mixed sample	70	15.95	30.61

It can be seen from Table 2 that with the increase of the particle size of the coal sample, the apparent activation energy before the critical temperature basically shows an increasing situation, which is because the smaller the particle size of the coal sample, the specific surface area of its reaction with oxygen. The larger, the more active coal molecules were exposed at the same time, so the easier it was to react with oxygen, which, in turn, generated more heat and accelerated the reaction. The apparent activation energy after the critical temperature also showed that the apparent activation energy increased as the particle size increased. That mentioned above was because, after the critical temperature, the macromolecular structure in the coal body accelerated the fracture, increasing the number of active groups. In addition, the larger the particle size, the smaller the specific surface area, and the less likely it was to react with oxygen. The apparent activation energy after the critical temperature was much larger than before the critical temperature, because the reaction before the critical temperature consumed a large amount of unstable reactive functional groups in the coal molecules, and the critical temperature requires a more stable functional group structure. Therefore, the reaction was more difficult than before. The apparent activation energy required for the mixed reaction was less because the mixed sample contained all the particle diameters, and its specific surface area was relatively large, and its reaction with oxygen was relatively easy to occur. At the same time, under the same coal quality conditions, the particle size of 5–7 mm in the early stage of the reaction showed a difference: it was the critical particle size. Accordingly, the apparent activation energy required was the largest.

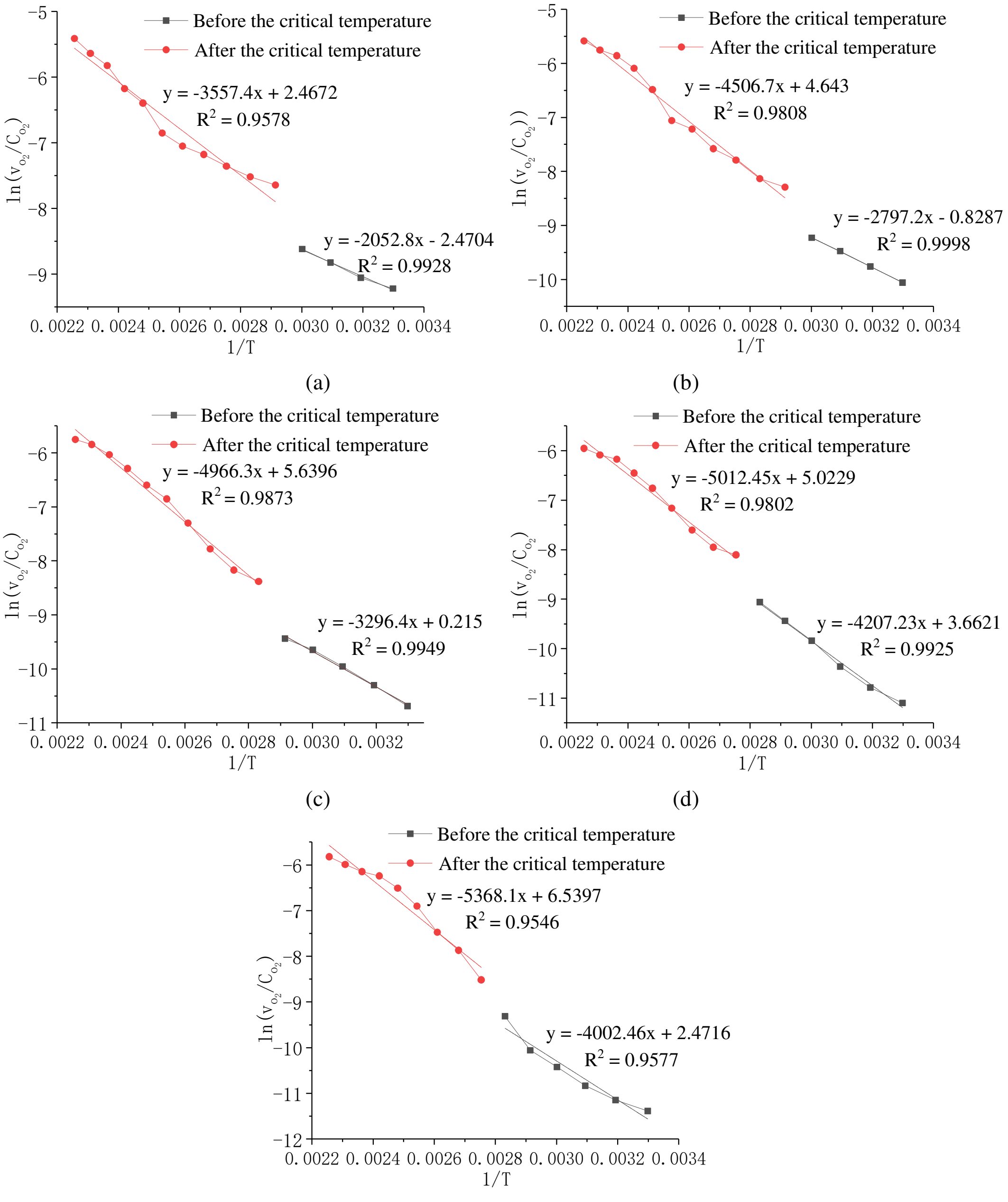

(a) (b) (c) (d) (e)

Fig. 6. ln($v_{O_2}^0/C_{O_2}^0$) and 1/T relative curves of different particle sizes: (a) 0–0.9 mm, (b) 0.9–3 mm, (c) 3–5 mm, (d) 5–7 mm, (e) 7–10 mm.

CONCLUSIONS

(1) From analyzing the release law of the index gas, the law of CO gas release and the growth rate of oxygen consumption rate were basically consistent. The critical temperature of different coal samples was received as the basis for dividing the activation energy.

(2) After the division stage, the equation for the dynamic analysis fit better, and the equation can better reflect the relationship between $\ln(v_{o_2}^0/C_{o_2}^0)$ and $1/T$. Before the critical temperature, the apparent activation energy increased with the increase of the particle size. Since the particle size of 5–7 mm was the critical particle size, the apparent activation energy required for the particle size reaction was the most. After the critical temperature, as the particle size increased, the apparent activation energy also increased. The apparent activation energy differed greatly before and after the critical temperature. The apparent activation energy of the mixed particle size was small, as between 0–0.9 and 0.9–3 mm particle sizes.

(3) The apparent activation energy of the low-temperature oxidation reaction of 3^{-1} coal seam was less than that of the coal seam in $2^{-2\mathrm{mid}}$, indicating that the coal spontaneous combustion tendency of this coal seam was greater than that of the coal seam in $2^{-2\mathrm{mid}}$. Attention should be paid to the actual production process of the mine, to avoid harm to personnel and loss of property.

ACKNOWLEDGMENTS

Financial support for this study was kindly provided by National Natural Science Foundation Project of China (Nos. 5180-4246 and 5170-4226), and Doctor Start-up Project of Xi’an University of Science and Technology (No. 2017QDJ057), Xi’an, China.

REFERENCES

[1] G.B. Stracher, T.P. Taylor, Coal fires burning out of control around the world: thermodynamic recipe for environmental catastrophe, Int. J. Coal Geol. 59 (2004) 7–17.

[2] J.N. Carras, S.J. Day, A. Saghafi, D.J. Williams, Greenhouse gas emissions from low-temperature oxidation and spontaneous combustion at open-cut coal mines in Australia, Int. J. Coal Geol. 78 (2009) 161–168.

[3] S.T. Ide, F.M. Orr, Comparison of methods to estimate the rate of CO2 emissions and coal consumption from a coal fire near Durango, CO, Int. J. Coal Geol. 86 (2011) 95–107.

[4] A. Sarwar, M.N. Khan, K.F. Azhar, Kinetic studies of pyrolysis and combustion of Thar coal by thermogravimetry and chemometric data analysis, J. Therm. Anal. Calorim. 109 (2011) 97–103.

[5] J.A. MacPhee, J.P. Charland, L. Giroux, Application of TG–FTIR to the determination of organic oxygen and its speciation in the Argonne premium coal samples, Fuel Process Technol. 87 (2006) 335–341.

[6] L.I. Ali, A. Amin, A.M. Ibrahim, Thermal behavior and effect of compaction on phase changes and catalytic properties of some solid acid catalysts, Hung. J. Ind. Chem. 25 (1997) 1–6.

[7] A. Williams, M. Pourkashanian, J.M. Jones, The combustion of coal and some other solid fuels, Proc. Combust. Inst. 28 (2000) 2141–2162.

[8] M.E. Brown, M. Maciejewski, S. Vyazovkin, R. Nomen, J. Sempere, A. Burnham, et al., Computational aspects of kinetic analysis: part A: the ICTAC kinetics project-data, methods and results, Thermochim. Acta 355 (2000) 125–143.

[9] P. Budrugeac, The Kissinger law and the IKP method for evaluating the non-isothermal kinetic parameters, J. Therm. Anal. Calorim. 89 (2007) 143–151.

[10] D. Chen, D. Liu, H. Zhang, Y. Chen, Q. Li, Bamboo pyrolysis using TG–FTIR and a lab-scale reactor: analysis of pyrolysis behavior, product properties, and carbon and energy yields, Fuel 148 (2015) 79–86.

[11] R. Comesaña, J. Porteiro, E. Granada, J.A. Vilán, M.A. Álvarez Feijoo, P. Eguía, CFD analysis of the modification of the furnace of a TG–FTIR facility to improve the correspondence between the emission and detection of gaseous species, Appl. Energy 89 (2012) 262–272.

[12] J.L. Goldfarb, S. Ceylan, Second-generation sustainability: application of the distributed activation energy model to the pyrolysis of locally sourced biomass-coal blends for use in co-firing scenarios, Fuel 160 (2015) 297–308.

[13] Y.S. Nugroho, A.C. Mcintosh, B.M. Gibbs, Low-temperature oxidation of single and blended coals, Fuel 79 (2000) 1951–1961.

[14] B. Coda, L. Tognotti, The prediction of char combustion kinetics at high temperature, Exp. Therm. Fluid Sci. 21 (2000) 79–86.

[15] M. Duz, Y. Tonbul, A. Baysal, et al., Pyrolysis kinetics and chemical composition of Hazro coal according to the particle size, J. Therm. Anal. Calorim. 81 (2005) 395–398.

[16] D. Yu, M. Xu, J. Sui, et al. Effect of coal particle size on the proximate composition and combustion properties, Thermochim. Acta 439 (2005) 103–109.

[17] Y. Zhang, Y. Li, Y. Huang, et al., Characteristics of mass, heat and gaseous products during coal spontaneous combustion using TG/DSC–FTIR technology, J. Therm. Anal. Calorim. 131 (2018) 2963–2974.

[18] J. Deng, J.Y. Zhao, Y. Xiao, et al., Thermal analysis of the pyrolysis and oxidation behaviour of 1/3 coking coal, J. Therm. Anal. Calorim. 129 (2017) 1779–1786.

[19] C. Herce, B. de Caprariis, S. Stendardo, et al., Comparison of global models of sub-bituminous coal devolatilization by means of thermogravimetric analysis, J. Therm. Anal. Calorim. 117 (2014) 507–516.

[20] J. Wu, B. Wang, F. Cheng, Thermal and kinetic characteristics of combustion of coal sludge, J. Therm. Anal. Calorim. 129 (2017) 1899–1909.

[21] X. Cui, X. Li, Y. Li, et al., Evolution mechanism of oxygen functional groups during pyrolysis of Datong coal, J. Therm. Anal. Calorim. 129 (2017) 1169–1180.

[22] D. Wu, M. Schmidt, X. Huang, et al., Self-ignition and smoldering characteristics of coal dust accumulations in O_2/N_2 and O_2/CO_2 atmospheres, Proc. Combust. Inst. 36 (2017) 3195–202.

[23] Y. Xu, Y. Zhang, G. Zhang, et al., Pyrolysis characteristics and kinetics of two Chinese low-rank coals, J. Therm. Anal. Calorim. 122 (2015) 975–984.

[24] J. Gao, M. Chang, J. Shen, Comparison of bituminous coal apparent activation energy in different heating rates and oxygen concentrations based on thermogravimetric analysis, J. Therm. Anal. Calorim. 130 (2017) 1181–1189.

[25] K. Wang, J. Deng, Y. Zhang, et al., Kinetics and mechanisms of coal oxidation mass gain phenomenon by TG–FTIR and in situ IR analysis, J. Therm. Anal. Calorim. 132 (2018) 591–598.

[26] Z. Song, X. Huang, M. Luo, et al., Experimental study on the diffusion–kinetics interaction in heterogeneous reaction of coal, J. Therm. Anal. Calorim. 129 (2017) 1–13.

The Effect of Imidazolium-based Ionic Liquid on Oxidation Kinetics of Coal

Deng J.[1,2], **Bai Z.J.**[1,] *, **Wang C.P.**[1,2], **Luo Z.M.**[1,2], **Wang Y.C.**[1,2]

[1] *School of Safety Science and Engineering,*
Xi'an University of Science and Technology, Xi'an, Shaanxi, China
[2] *Shaanxi Key Laboratory of Prevention and Control of Coal Fire,*
Xi'an University of Science and Technology, Xi'an, Shaanxi, China
**Corresponding author's email: 1693058198@qq.com*

ABSTRACT

To investigate the effects of ionic liquids (ILs) on the oxidative combustion characteristics of coal, four types of imidazole ([EMIm][BF_4], [BMIm][BF_4], [BMIm][NO_3], [BMIm][I]) were selected to treat coal samples; pr-[BMIm][BF_4] was processed one month ago. The thermogravimetry (TG) experiments and oxidation kinetics analysis methods were employed to study the oxidation characteristics of ILs on coal, such as characteristic temperature, thermal mass loss rate, and oxidation kinetics characteristic parameters. The results showed that the characteristic temperatures of the treated coal samples increased. Among them, the [BMIm][I]-treated coal samples increased cracking temperature (T_1), maximum oxidization mass gain (T_2), ignition temperature (T_3), burnout temperature (T_4), minimum thermal rate (T_a), maximum thermal energy (T_b), and maximum thermal rate (T_c) by 33.2, 29.3, 20.7, 42.8, 11.4, 23.0, and 27.9°C, respectively. The increase mass ratio of coal samples treated with ILs increased and decreased at the water evaporation and thermal decomposition stages. The apparent activation energy (E_a) of coal samples treated with ILs increased, and the mechanism function also changed accordingly. These showed that the ILs improved the thermal stability of the coal samples in the stages of absorbing oxygen and increased mass, and the loss of combustion. The ILs caused damage to the molecular structure of the coal, and ultimately effected changes in the combustion performance. In addition, the combustion properties of the coal sample treated before one month were the same, indicating that the [BMIm][BF_4] did not weaken the inhibitory effectiveness of the coal sample over time, coal spontaneous combustion could be effectively suppressed.

KEYWORDS: Oxidation, thermal stability, inhibition

NOMENCLATURE

A	pre-exponential factor (1/min)
E_a	apparent activation energy (J/mol)
R	universal gas constant 8.3143 J/(K·mol)
T_1	cracking temperature (°C)
T_2	maximum oxidization mass gain (°C)
T_3	ignition temperature (°C)
T_4	burnout temperature (°C)
T_a	temperature of minimum thermal rate (°C)
T_b	temperature of maximum thermal energy (°C)
T_c	temperature of maximum thermal rate (°C)
r	correlation coefficient

Greek

α	conversion
β	heating rate (°C/min)

INTRODUCTION

Coal resources are mainly bituminous coal and lignite, and more than 90% of coal seams have a

Proceedings of the Ninth International Seminar on Fire and Explosion Hazards (ISFEH9), pp. 1154-1163
Edited by Snegirev A., Liu N.A., Tamanini F., Bradley D., Molkov V., and Chaumeix N.
Published by Saint-Petersburg Polytechnic University Press
ISBN: 978-5-7422-6498-9 DOI: 10.18720/spbpu/2/k19-12

tendency for spontaneous combustion in classes I and II. Coal spontaneous combustion is extremely serious, not only causing major property damage, but also resulting in significant personal injury and death [1, 2]. Therefore, the inhibition of coal spontaneous combustion has become the main direction for mine fire prevention.

To scientifically, effectively, and fundamentally inhibit coal spontaneous combustion, numerous mine fire inhibition technologies have been developed which include resistance, inerting, and cooling [3, 4]. Among them, physical inhibitors are the most popular, altering physical effects of the coal body and the surrounding environment. As time goes on, the inhibiting capacity gradually declines until it disappears completely [5–8]. Therefore, the development of chemical inhibitors can effectively destroy coal microscopic active groups and inhibit the active structure on the surface of coal molecules to forestall coal spontaneous combustion [9, 10]. The current research showed that in coal spontaneous combustion the functional groups in the coal molecules react with oxygen continuously to release heat and accumulate, which, in turn, causes the coal body to heat [11, 12]. ILs are environmentally friendly green solvents with low volatilization, low distillation, odorless, non-combustible, easy to handle, and have high applicability [13]. The results showed that different ILs could reduce the oxidation characteristics and dissolve and destroy the microscopic active structure on the surface of coal molecules, which could fundamentally destroy the microscopic active groups of coal or inhibit the active structure of coal to prevent spontaneous combustion [14]. Studies of liquefaction, extraction, and desulfurization consistently concluded that ILs could break hydrogen bonds, covalent bonds, and carbonyl groups in the side chains of coal molecules. Due to the electrical covalent bond balance of the coal molecule, it was destroyed by the π bond contained in the anion and cation in ILs [15–23]. In the oxidative heating process of treating coal with ILs, studies have pointed out that ILs could reduce the oxidation characteristics of coal, of the released index gases, and of the mass loss rate [24–27]. Above studies were summarized to show that the inhibiting of coal by ILs mainly destroyed and dissolved the active groups of coal, including hydrogen bonds, aromatic structures, aliphatic chain hydrocarbons, and oxygenates, such as hydrocarbon groups, carbonyl groups, and ether bonds, methyl, methylene aliphatic side chain group. The aromatic ring structure of coal molecules was relatively stable and could not be destroyed. The main reason for hindering the oxidation process of coal is that the oxygen-removing ability of coal molecules is weakened. The formation of stable carbonyl groups is increased, and the quantity of active carbonyl groups is reduced. The low-temperature oxidation activity of coal is closely related to hydrogen bonding, and the reduction of hydrogen bonding causes the oxidation activity of coal to be weakened to varying degrees.

In this paper, the oxidation kinetics method was used to study the kinetic characteristics of coal samples treated with ILs in the process of spontaneous combustion, such as characteristic temperature, E_a, and ln$A$. To investigate that the inhibiting effect does not decrease with time, the inhibition ability of the coal sample treated before one month was studied. This paper provides an in-depth understanding of the spontaneous combustion process of coal oxidation and provides scientific and effective indicators and theoretical basis for the oxidative coal spontaneous combustion in different inhibitory stages. Therefore, it opens up new scientific and technological techniques for inhibiting coal spontaneous combustion.

EXPERIMENTAL

Materials

Coal sample preparation

The fresh lignite sample used in this study was obtained from Wangwa, Ningxia, China. It was ground and pulverized to a size of approximately 200–280 μm. The coal sample was vacuum dried at room temperature for 24 h, sealed and stored in the dark, Table 1 lists the coal quality indicators.

Table 1. Coal quality indicators of the coal samples

Sample	M_{ad}/%	A_{ad}/%	V_{ad}/%	FC_{ad}/%	H/%	C/%	N/%	S/%
lignite	10.31	9.71	35.54	44.44	3.391	64.15	1.338	1.641

IL preparation

Four ILs, considering the sound dissolution and destruction properties, namely 1-ethyl-3-methylimidazolium tetrafluoroborate ([EMIm][BF_4]), 1-butyl-3-methylimidazolium iodide ([BMIm]I), 1-butyl-3-methylimidazolium tetrafluoroborate ([BMIm][BF_4]), 1-butyl-3-methylimidazolium nitrate ([BMIm][NO_3]), were from the Lanzhou Institute of Physical Chemistry of the Chinese Academy of Sciences, with a purity of over 99 mass% [28].

IL treatment of coal subsamples

The coal sample and the four ILs were thoroughly mixed in a ratio of 1:2 (g:mL), and stirred eight hours. Taking into account the interference of the IL on the experimental process, the mixture was rinsed by a centrifuge, and the distilled water was repeatedly washed. By measuring the pH of the solution, until the acidity and alkalinity of the coal samples no longer changed. The rinse was placed in a specific bottle for recycling to avoid contamination of the environment. Then, it was vacuum dried at 27 °C for 48 hours until the mass did not change, and the treated sample was obtained, which was sealed and stored. To study whether the IL inhibit to coal samples would degrade over time, [BMIm][BF_4] treated coal samples were produced before 30 days and termed Pr-[BMIm][BF_4]. To avoid the influence of distilled water on the error of the results, the same process was used to prepare distilled water to wash the coal sample as a comparative coal sample. The coal samples treated with [EMIm][BF_4], [BMIm][BF_4], [BMIm][NO_3], [BMIm][I], Pr-[BMIm][BF_4] and H_2O were defined as EBTC, BBTC, BNTC, BITC, PBBTC, and HTC, respectively.

Experimental procedure

Six coal samples were conducted by the German NETZSCH STA409PC DSC-TGA synchronous thermal analyzer. The procedure was strictly followed by an operating procedure with a mass of ca. 10.0 mg per sample. The sample was heated in an air atmosphere at a temperature ranging from 30.0 to 800.0 °C at a heating rate of 10 °C/min.

RESULTS AND DISCUSSION

Characteristics of coal oxidation pyrolysis curve

Characteristic temperature

Figure 1 shows the pyrolysis curve of the EBTC sample during oxidation. Experiments showed that the trend of TG-DTG curves for treating coal samples was different. It is generally considered that T_1 is the maximum evaporation of water and desorption of gases and called “dry cracking temperature”; T_2 represents the maximum oxidization mass gain. T_3 is the ignition point; T_4 is the temperature burnout point corresponding to the complete combustion. Therefore, the entire process of oxidizing coal from oxygen to combustion is divided into five stages. Stage Ⅰ is called the water evaporation mass loss stage (starting temperature T_0–T_1; oxygen absorption mass increase stage (T_1–T_2) is stage Ⅱ; coal thermal decomposition stage (T_2–T_3) is classified into stage Ⅲ; stages Ⅳ and Ⅴ are the combustion stage (T_3–T_4) and the complete burnout stage (T>T_4), respectively. TG and DTG curves of the BBTC, BNTC, BITC, PBBTC, and HTC subsamples are illustrated in

Fig. 2. Figure 3 describes the DSC and DDSC curves for the BBTC, BNTC, BITC, PBBTC, and HTC subsamples. Considering that oxygen absorption mass increase stage and thermal decomposition stage play an important role in oxidative spontaneous combustion [29–31], therefore, the stages Ⅱ and Ⅲ were considered to investigate the kinetic parameters in this paper. According to the above division principles, the characteristic temperatures corresponding to the respective stages of the six coal samples are summarized in Table 2.

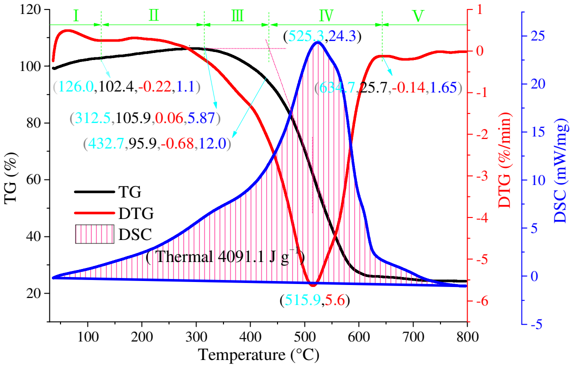

Fig. 1. The pyrolysis curve of the EBTC.

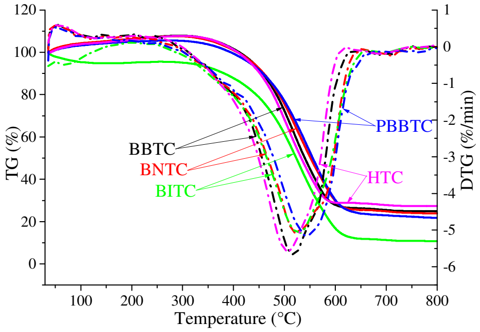

Fig. 2. TG and DTG curves of subsamples.

Table 2. Characteristic temperature points of coal samples

Sample	T_1, °C	T_2, °C	T_3, °C	T_4, °C	T_a, °C	T_b, °C	T_c, °C
EBTC	128.0	312.4	432.7	648.2	483.5	525.3	583.6
BBTC	126.5	287.1	443.8	653.0	487.8	526.9	586.3
BNTC	126.6	290.3	446.2	655.4	491.6	538.7	605.9
BITC	145.2	297.1	438.9	665.2	486.6	539.3	610.2
PBBTC	126.3	278.4	445.3	650.6	490.7	550.3	607.8
HTC	111.0	267.8	418.2	622.4	475.2	516.3	582.3

T_2 is the temperature at which the coal sample mass ratio is at a maximum point. In the oxygen absorption and mass gain stage of the low temperature oxidation process, the mass change of coal sample was mainly affected by the combined effect of coal oxygen composite mass gain and reaction consumption mass loss. With the increase of temperature, the oxidation process of coal samples accelerated, and the active groups in the coal molecular structure accumulated to a certain extent. The reaction consumption began to increase drastically. After T_2, the active groups began to participate in large-scale reactions. Then the rate of mass gain of the coal sample began to decrease. Table 2 shows that the T_2 temperature value of the treated coal sample increased; the coal sample was treated with [EMIm][BF$_4$] which reaches the maximum value: 44.6 °C higher than the HTC. The T_2 values of the BBTC and PBBTC did not change much, indicating the inhibition effectiveness had not diminished. The above situations might occur because the ILs destroyed the reactive functional groups, and it was more difficult to carry out the reaction when the coal molecule contained fewer functional groups. Therefore, more energy was required and the corresponding temperature point rose.

When the temperature of the coal sample exceeded T_3, the molecular structure of the coal began to decompose drastically, and a large amount of CO, CO_2, and small molecular organic gases were generated, releasing a large amount of thermal, and the mass of the coal began to drop drastically and started to burn. In the six coal samples, the HTC started to ignite at the lowest temperature, indicating that the ILs can inhibit the combustion ability of the coal sample. The ignition temperature was related to the number of reactive functional groups in the coal molecules, which meant that the active functional groups of the coal were subjected to the ILs damage. The T_3 of the sample was arranged in order of BNTC>PBBTC>BBTC>BITC>EBTC>HTC. Among them, the BNTC reached the highest ignition point, indicating that the BNTC was the most difficult to combust. The coal samples had different ignition temperatures, indicating that the damage to the active structure of coal molecules was also different.

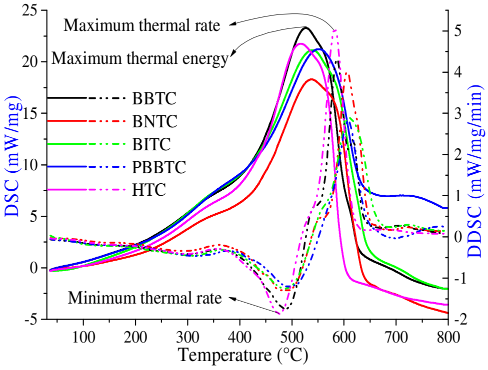

Fig. 3. DSC and DDSC curves for subsamples.

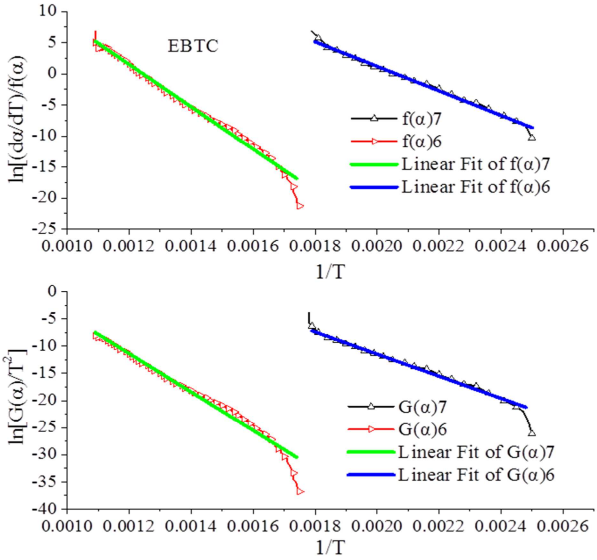

Fig.4. Fitting curves of EBTC at stages Ⅱ and Ⅲ.

At T_4 the coal sample was almost completely burned out with residual ash. The T_4 of HTC had the lowest temperature because the HTC had more active molecular structures on the surface of the molecule, so it can be burned out at a lower temperature. In addition, this further illustrated that the IL had caused damage to the coal molecular structure. In other coal samples treated with ILs, coal molecules contained fewer reactive functional groups. Therefore, it required higher temperature and more energies to completely burn out.

The heat flow curves of six coal samples were observed and analyzed during the oxidation, in which appeared the same exothermic trend. T_a was the minimum enthalpy rate, T_b represented the maximum enthalpy, T_c was maximum enthalpy rate. The T_a, T_b, and T_c of the six samples are summarized in Table 2. The values of the treated sample increased. BNTC, PBBTC, and BITC contained the highest T_a, T_b, and T_c, which were 16.4, 34.0, and 27.9 °C higher than HTC sample, respectively. This revealed that the inhibited samples required more energy to be completely burned because some of the reactive functional groups were destroyed by the ILs. The remaining molecules in the surface of the coal sample were reactive functional groups that were hardly to oxidize, so more energy was required to react.

Characterization of coal sample mass loss

From the oxygen absorption mass gain of the coal sample to the mass loss of combustion, the TG curve reflected the change of the mass of the coal sample at each temperature point. Therefore, compared with the HTC, the dissolution and destruction of the surface functional group of the coal by the IL could be analyzed. On the TG curve, each coal sample showed different trends of mass loss and mass gain at different temperature points caused by physical adsorption and chemical reaction of coal oxygen [32]. The solvency of the ILs to each activated functional group in the coal could be reflected in the TG curve according to the ratio of the mass loss. As the temperature increased, the active oxygen-absorbing active molecules in the coal first showed a strong reaction to oxygen molecules, which was manifested by an increase in oxygen uptake, at which the mass of the coal increased. The mass increase ratio and the mass loss ratio at each stage for coal samples are summarized in Table 3.

Table 3. The mass increase ratio and the mass loss ratio at each stage for coal samples

Sample	Stage Ⅰ	Stage Ⅱ		Stage Ⅲ and stage Ⅳ	
	TR^a, °C	TR^a, °C	Mass increase ratio, %	TR^a, °C	Mass loss ratio, %
EBTC	<128.0	128.0–312.4	0.82	312.4–648.2	7.06
BBTC	<126.5	126.5–287.1	0.30	287.1–653.1	8.01
BNTC	<126.6	126.6–290.3	0.07	290.3–655.4	7.72
BITC	<145.2	145.2–297.1	0.04	297.1–665.2	6.68
PBBTC	<126.3	126.3–278.4	0.04	278.4–680.6	5.68
HTC	<111.0	111.0–267.8	0.32	267.8–622.4	8.10

TR^a is temperature range

At the water evaporation stage, the treated coal sample required a higher temperature than the HTC, indicating that adsorption of water in the molecular structure of the coal samples treated with ILs required a higher temperature to evaporate completely. The mass gain ratio of HTC was relatively larger than other coal samples, indicating that there were more functional groups in coal molecules that are more likely to absorb oxygen. At the stage of thermal decomposition and loss of combustion, the mass loss ratio of HTC was the largest, indicating that the coal sample treated by ILs was more difficult to decompose during the thermal decomposition process.

Characteristics of oxidation kinetics of coal sample

The reaction of pulverized coal during thermo-gravimetric analysis was a heterogeneous solid-state reaction and it could be described by Eqs 1and 2 [33]:

Achar differential method:

$$\ln\frac{d\alpha/dT}{f(\alpha)}=\ln\frac{A}{\beta}-\frac{E_a}{RT} \tag{1}$$

Coast-Redfern integration method:

$$\ln\frac{G(\alpha)}{T^2}=\ln\left(\frac{AR}{\beta E_\mathrm{a}}\right)-\frac{E_\mathrm{a}}{RT} \tag{2}$$

where α is the degree of conversion, $f(\alpha)$ and $G(\alpha)$ are functions called the “reaction model” that describes the dependence of the reaction rate on the reaction’s extent, A represents the pre-exponential Arrhenius factor, E_a is the apparent activation energy, T is the temperature , R is the gas constants and β is heating rate.

Many methods exist for kinetics analysis and 18 general solid reaction mechanism functions were selected in this paper [34,35]. At a constant heating rate, $\ln[(d\alpha/dT)/f(\alpha)]$ and $\ln[G(\alpha)/T^2]$ are linear with $1/T$. The E_a is determined from the slope of a plot of $\ln[(d\alpha/dT)/f(\alpha)]$ and $[G(\alpha)/T^2]$ against $1/T$. The corresponding pre-exponential factors (A) and correlation coefficients are derived from the intercept of the fitted curve. If the E_a and A (or $\ln A$) values obtained by the integral and differential methods are supposed to be similar, a straight line with excellent linear relationship is necessarily obtained (represented by the correlation coefficient R). Then, the selected $G(\alpha)$ and $f(\alpha)$ are also the most suitable mechanism function for this reaction. The integral and differential curves of coal samples are achieved by plotting $\ln[(d\alpha/dT)/f(\alpha)]$ and $\ln[G(\alpha)/T^2]$ with 1/T, and fitting to obtain relevant parameters. Figure 4 shows the fitting curves of the coal samples at the stage of oxygen absorption mass increase stage and mass loss. Tables 4 and 5 summarize the kinetic parameters determined by integration and differentiation in the stages of oxygen absorption mass increase stage and mass loss.

Table 4. Kinetic parameters of integral and differential of coal samples at stage Ⅱ

Sample	Integral				Differential			
	function	r	E_{a2g}, J/mol	$\ln A_{2g}$, $\ln(\min^{-1})$	function	r	E_{a2f}, J/mol	$\ln A_{2f}$, $\ln(\min^{-1})$
EBTC	7	0.988	173.5	42.6	7	0.957	179.3	46.7
BBTC	7	0.961	175.8	43.3	7	0.955	171.8	44.9
BNTC	7	0.977	177.1	44.2	7	0.981	168.7	44.7
BITC	7	0.97	309.7	75.7	7	0.969	289.5	72.9
PBBTC	6	0.947	128.8	32.4	6	0.966	115.4	19.4
HTC	5	0.954	96.9	22.6	5	0.977	85.6	22.4

Table 5. Kinetic parameters of integral and differential of coal samples at stage Ⅲ

Sample	Integral				Differential			
	function	r	E_{a3g}, J/mol	$\ln A_{3g}$, $\ln(\min^{-1})$	function	r	E_{a3f}, J/mol	$\ln A_{3f}$, $\ln(\min^{-1})$
EBTC	6	0.973	301.2	44.9	6	0.986	289.5	45.6
BBTC	7	0.98	400.9	60.3	7	0.984	393.4	61.5
BNTC	6	0.984	269.3	39.6	6	0.985	268.1	41.9
BITC	6	0.987	254.4	37.4	6	0.989	251.9	39.5
PBBTC	6	0.998	256.9	38.2	6	0.977	264.3	40.8
HTC	13	0.955	86.9	10.1	13	0.988	74.22	10.6

The curve fitting results of the six coal types were screened and analyzed. It shows that the coal sample has different reaction mechanism functions in the stages of oxygen absorption mass increase and mass loss. The mechanism functions of the coal sample treated by the ILs were also different. It illustrates that the active structure of the coal molecule was swollen and destroyed in the process of ILs treatment. The active groups that caused the coal to participate in the reaction during combustion appear at different characteristic temperature points. It was consistent with the performance of coal samples at characteristic temperatures. The amount of some reactive groups was reduced or disappeared, so the combustion mechanism changed when the coal underwent a composite reaction. The oxidation kinetic parameters of the coal samples are listed in Table 6, and ΔE_a is the difference in apparent activation energy (E_a) between the treated coal sample and the treated water treated with distilled water.

The structural activity of coal molecules was determined by the E_a. The larger the value is, the smaller the reactivity was. The rate of the chemical reaction was determined by the A. The larger the value is, the greater the rate of chemical reaction is. As coal and oxygen reacted completely, thermal energy was concentrated, and the degree of reaction was severer. The E_a was gradually increased. The magnitude of the increase of the six types of coal samples was also different, which further explained the difference in molecular structure and the reaction mechanism. Therefore, the combustion mass loss had a higher E_a than the oxygen absorption mass increased. Table 6 displays that the E_a values of the coal samples treated with ILs increased, indicating that the ILs had an inhibitory effect on the coal samples, and the inhibiting ability was different. In the stage of oxygen absorption mass increase, the E_a was in the order of BITC>BBTC>BNTC>EBTC>PBBTC>HTC, revealing that the inhibitory ability of the IL was [BMIm][I]>[BMIm][BF_4]>[BMIm][NO_3]>[EMIm][BF_4]. Among the six samples, the value of E_a for the [BMIm][I] sample was 299.6 J/mol, which may have been due to the active structure in the molecule being the least compared to the other three ILs, resulting in a decrease in activation energy. It is concluded that [BMIm][I] had the strongest inhibiting effect. The order of inhibition was ranked as follows: [BMIm][BF_4]>[EMIm][BF_4]>[BMIm][NO_3]>[BMIm][I] in the stage of combustion mass loss; [BMIm][BF_4] had the strongest inhibitory. The combustion properties exhibited in the two oxidation stages were different, indicating that the IL's inhibition to coal was different at each stage.

Table 6. Oxidation kinetic parameters of coal samples

Sample	Stage Ⅱ				Stage Ⅲ			
	E_{a2}, J/mol	ΔE_{a2}, J/mol	$\ln A_2$, $\ln(\min^{-1})$	r	E_{a3}, J/mol	ΔE_{a3}, J/mol	$\ln A_3$, $\ln(\min^{-1})$	r
EBTC	161.4	70.2	44.6	0.968	295.4	214.9	45.3	0.979
BBTC	173.8	85.5	44.1	0.958	397.2	316.7	60.9	0.98
BNTC	172.9	81.6	44.4	0.979	268.7	188.3	40.7	0.984
BITC	299.6	208.3	74.3	0.969	253.2	172.7	38.5	0.988
PBBTC	122.1	30.9	25.9	0.956	260.6	180.1	39.5	0.983
HTC	91.3	0	22.5	0.965	80.5	0	10.4	0.971

CONCLUSIONS

The T_1, T_2, T_3, T_4, T_a, T_b, and T_c of the coal samples treated with the IL increased, and the characteristic temperature of the coal sample treated by the [BMIm][I] increased the mos,t which increased 34.2, 29.3, 20.7, 42.8, 11.4, 23.0, and 27.9 °C, respectively. Coal samples treated with ILs required higher temperatures for water evaporation and oxygen gain, and the mass gain ratios increased and decreased during the evaporation and thermal decomposition stages, indicating that the IL treated coal samples were much harder to decompose.

The E_a of the coal sample treated by ILs increased, and the mechanism function also changed accordingly, indicating that the ILs could improve the thermal stability of the coal sample in the oxygen absorption and mass gain stage and the combustion mass loss stage. In the oxygen absorption and mass increase stage, the inhibitory properties of the four ILs were as follows: [BMIm][I]>[BMIm][BF_4]>[BMIm][NO_3]>[EMIm][BF_4]. In the stage of combustion mass loss, the inhibition effectiveness was ranked as: [BMIm][BF_4]>[EMIm][BF_4]>[BMIm][NO_3]>[BMIm][I]. Moreover, the ILs inhibited the combustion reaction of coal was carried out in stages, and exhibited different properties at various stages.

Samples treated with the same IL one month earlier and one month later exhibited essentially the same properties during combustion. Compared with the comparative sample, it also showed an increase in characteristic temperature, an increase in E_a, and a change in the mechanism function. This indicated that the inhibition effectiveness of the IL on the coal sample hardly decreased with time.

ACKNOWLEDGMENTS

This work was sponsored by the International Science and Technology Cooperation and Exchange of Shaanxi Province (Grant no. 2016KW-070), the Shaanxi Province Innovative Talent Promotion Plan-Youth Science and Technology New Star Project (No. S2019-ZC-XXXM-0037), and and National Key Research and Development Plan of China (No. 2018-YFC-0807900).

REFERENCES

[1] C. Kuenzer, G.B. Stracher, Geomorphology of coal seam fires, Geomorphology 138 (2012) 209–222.

[2] Z.Y. Song, C. Kuenzer, Coal fires in China over the last decade: A comprehensive review, Int. J. Coal Geol. 133 (2014) 72–99.

[3] D.M. Wang, G.L. Dou, X.X. Zhong, H.H. Xin, B.T. Qin, An experimental approach to selecting chemical inhibitors to retard the spontaneous combustion of coal, Fuel 117 (2014) 218–223.

[4] J.H. Li, Z.H. Li, Y.L. Yang, B. Kong, C.J. Wang, Laboratory study on the inhibitory effect of free radical scavenger on coal spontaneous combustion, Fuel Process. Technol. 171 (2018) 350–360.

[5] J.H. Li, Z.H. Li, C.J. Wang, X.Y. Zhang, Experimental study on the inhibitory effect of ethylenediaminetetraacetic acid (EDTA) on coal spontaneous combustion, Fuel Process. Technol. 2018, 178.

[6] C.Y. Hao, Y.L. Chen, J.R. Wang, C.B. Deng, G. Xu, F.W. Dai, R. Si, H.F. Wang, H.Y. Wang, Study on the effect of iron-based deoxidizing inhibitors for coal spontaneous combustion prevention, Energies 11 (2018) 789.

[7] J.H. Li, Z.H. Li, Y.L. Yang, X.Y. Zhang, D.C. Yan, L.W. Liu, Inhibitive effects of antioxidants on coal spontaneous combustion, Energy Fuels 31 (2017) 14180–14190.

[8] W.M. Cheng, X.M. Hu, J. Xie, Y.Y. Zhao, An intelligent gel designed to control the spontaneous combustion of coal: Fire prevention and extinguishing properties, Fuel 210 (2017) 826–835.

[9] Y. Yang, Y.T. Tsai, Y.N. Zhang, C.M. Shu, J. Deng, Inhibition of spontaneous combustion for different metamorphic degrees of coal by Zn/Mg/Al-CO3-layered double hydroxide, Process Saf. Env. Prot. 113 (2017) 401–412.

[10] J. Deng, Y. Yang, Y.N. Zhang, B. Liu, C.M. Shu, Inhibiting effects of three commercial inhibitors in spontaneous coal combustion, Energy 160 (2018) 1174–1185.

[11] D.M. Wang, H.H. Xin, X.Y. Qi, G.L. Dou, G.S. Qi, L.Y. Ma, Reaction pathway of coal oxidation at low temperatures: a model of cyclic chain reactions and kinetic characteristics, Combust. Flame 163 (2016) 447–460.

[12] B. Li, G. Chen, H. Zhang, C.D. Sheng, Development of non-isothermal TGA–DSC for kinetics analysis of low temperature coal oxidation prior to ignition, Fuel 118 (2014) 385–391.

[13] P.V. Kortunov, L.S. Baugh, M. Siskin, Pathways of the chemical reaction of carbon dioxide with Ionic Liquids and amines in ionic liquid solution, Energy Fuels 29 (2015) 5990–6007.

[14] W.Q. Zhang, S.G. Jiang, Z.Y. Wu, K. Wang, H. Shao, T. Qin, X. Xi, H.b. Tian, Influence of imidazolium-based ionic liquids on coal oxidation, Fuel 217 (2018) 529–535.

[15] J. Cummings, S. Kundu, P. Tremain, B. Moghtaderi, R. Atkin, K. Shah, Investigations into physicochemical changes in thermal coals during low-temperature ionic liquid Treatment, Energy Fuels 29 (2015) 7080–7088.

[16] J. Cummings, P. Tremain, K. Shah, E. Heldt, B. Moghtaderi, R. Atkin, S. Kundu, H. Vuthaluru, Modification of lignites via low temperature ionic liquid treatment, Fuel Process. Technol. 155 (2017) 51–58.

[17] Z.P. Lei, Y.Q. Zhang, L. Wu, H.F. Shui, Z.C. Wang, S.B. Ren, The dissolution of lignite in ionic liquids, RSC Adv. 3 (2013) 2385–2389.

[18] Z.P. Lei, L.L. Cheng, S.F. Zhang, Y.Q. Zhang, H.F. Shui, S.B. Ren, Z.C. Wang, Dissolution performance of coals in ionic liquid 1-butyl-3-methyl-imidazolium chloride, Fuel Process. Technol. 129 (2015) 222–226.

[19] K. Shah, R. Atkin, R. Stanger, T. Wal, B. Moghtaderi, Interactions between vitrinite and inertinite-rich coals and the ionic liquid – [bmim][Cl], Fuel 119 (2014) 214–218.

[20] P. Painter, N. Pulati, R. Cetiner, M. Sobkowiak, G. Mitchell, J. Mathews, Dissolution and dispersion of coal in ionic liquids, Energy Fuels 24 (2010) 1848–1853.

[21] P. Painter, R. Cetiner, N. Pulati, M. Sobkowiak, J. Mathews, Dispersion of liquefaction catalysts in coal using ionic liquids, Energy Fuels 24 (2010) 3086–3092.

[22] Y. Li, X.P. Zhang, S.Y. Lai, H.F. Dong, X.L. Chen, X.L. Wang, Y. Nie, Y. Sheng, S.J. Zhang, Ionic liquids to extract valuable components from direct coal liquefaction residues, Fuel 94 (2012) 617–619.

[23] Z.P. Lei, L.L. Wu, Y.Q. Zhang, H.F. Shui, Z.C. Wang, C.X. Pan, H.P. Li, S.B. Ren, S.G. Kang. Microwave-assisted extraction of Xianfeng lignite in 1-butyl-3-methyl-imidazolium chloride, Fuel 95 (2012) 630–633.

[24] L.Y. Wang, Y.L. Xu, S.G. Jiang, M.G. Yu, T.X. Chu, W.Q. Zhang, Z.Y. Wu, L.W. Kou, Imidazolium based ionic liquids affecting functional groups and oxidation properties of bituminous coal, Saf. Sci. 50 (2012) 1528–1534.

[25] W.Q. Zhang, S.G. Jiang, C. Hardacre, P.Goodrich, K.Wang, Z.Y. Wu, H. Shao, Inhibitory effect of phosphonium-based ionic liquids on coal oxidation, Energy Fuels 28 (2014) 4333–4441.

[26] W.Q. Zhang, S.G. Jiang, Z.Y. Wu, K. Wang, H. Shao, T. Qin, X. Xi, H.B. Tian, Influence of imidazolium-based ionic liquids on coal oxidation, Fuel 217 (2018) 529–535.

[27] F.S. Cui, B. Laiwang, C.M. Shu, J.C. Jiang, Inhibiting effect of imidazolium-based ionic liquids on the spontaneous combustion characteristics of lignite, Fuel 217 (2018) 508–514.

[28] R.L. Vekariya, A review of ionic liquids: Applications towards catalytic organic transformations, J. Mol. Liq. 227 (2017) 44–60.

[29] J. Deng, Z.J. Bai, Y. Xiao, Effects on the activities of coal microstructure and oxidation treated by imidazolium-based ionic liquids, J. Therm. Anal. Calorim. 133 (2018) 453–463.

[30] J. Deng, B. Li, Y. Xiao, L. Ma, C.P. Wang, B. Laiwang, C.M. Shu, Combustion properties of coal gangue using thermogravimetry–Fouriertransform infrared spectroscopy, Appl. Therm. Eng. 116 (2017) 244–252.

[31] J. Deng, Q.W. Li, Y. Xiao, H. Wen, The effect of oxygen concentration on the non-isothermal combustion of coal, Thermochim. Acta 653 (2017) 106–115.

[32] B. Li, G. Chen, H. Zhang, C.D. Sheng, Development of non-isothermal TGA–DSC for kinetics analysis of low temperature coal oxidation prior to ignition, Fuel 118 (2014) 385–391.

[33] X.Y. Qi, Q.Z. Li, H.H. Zhang, H.H. Xin, Thermodynamic characteristics of coal reaction under low oxygen concentration conditions, J. Energy Inst. 90 (2017) 544–555.

[34] S. Vyazovkin, A. K. Burnham, J. M. Criado, L. A. Pérez-Maqueda, C. Popescu, N. Sbirrazzuoli, ICTAC Kinetics Committee recommendations for performing kineticcomputations on thermal analysis data, Thermochim. Acta 520 (2011) 1–19.

[35] G. Chen, X.Q. Ma, M.S. Lin, Y.Z. Lin, Z.S. Yu, Study on thermochemical kinetic characteristics and interaction during low temperature oxidation of blended coals, J. Energy Inst. 88 (2015) 221–228.

Toxicity

Characterization of Toxic Gases and Particulates in Wood Smoke using a Standard Chamber

Matsuyama Y., Takahashi F.*

Case Western Reserve University, Department of Mechanical and Aerospace Engingeering,
Cleveland, Ohio, USA
**Corresponding author's email: fxt13@case.edu*

ABSTRACT

Smoke inhalation is a major cause of civilian and firefighter deaths during a fire incident. To characterize effluents from burning or pyrolyzing wood, real-time measurements of the smoke obscurity (the specific optical density), the concentrations of particulates, and toxic gases in a standard smoke density chamber have been made with a tapered element oscillating microbalance (TEOM) dust monitor and a Fourier transform infrared (FTIR) gas analyzer. The FTIR analyzes a total of 21 gases, including both asphyxiants and irritants. In addition to the smoke characteristics, the temperature in the interior of the specimen under selected conditions are measured by thermocouples to study the heat transfer and pyrolysis processes. Common building materials, i.e., selected woods at various moisture contents, are used. A specimen, placed in a vertical or horizontal orientation, is exposed to an incident radiant flux of 25 kW/m^2 for a flaming or non-flaming case. The effluent concentrations depend significantly on whether or not the flame exists and the specimen orientation as they influence the gas-phase reactions and the convection around the specimen. The non-flaming case in the horizontal configuration produces the highest smoke and toxicants (CO, formaldehyde, and acrolein) concentrations due to partial oxidation, while the flaming and horizontal case generates the lowest because of high-temperature oxidation (to form CO_2 and H_2O) in a flame with a longer residence time.

KEYWORDS: Fire toxicity, smoke obscurity, wood pyrolysis, moisture content, carbon monoxide, acrolein, formaldehyde

INTRODUCTION

Between 2011 and 2015, the U.S. fire departments responded to an average of 358,500 home structure fires per year, which, caused an average of 2,510 civilian deaths annually [1]. Many of these deaths were caused by smoke inhalation, where hot smoke injured or burned the respiratory system [1] or toxic gases exceed the exposure limits. Certain gases only require small concentrations for them to be lethal to the victims [2, 3].

Fire responders are often at a greater risk of inhaling toxic gases during the cleanup phase after a fire when they remove the self-contained breathing apparatus (SCBA) or replace with lesser personal protection equipment (PPE). Table 1 shows a limited list of occupational exposure limit standards of selected toxicants, which have been detected in excess concentrations during the post-fire (overhaul) period. Firefighters' safety officer often uses a detector of a major asphyxiant gas, i.e., carbon monoxide (CO), to make sure the environment is safe for them to enter, as gas masks can only filter out some particulates and toxic gases [4]. For example, when they are in open area zone with no visible fire (but possibly smoldering), they can use CO detectors to ensure that the concentration is not lethal [4, 5], e.g., less than 35 ppm. This value corresponds to the National Institute for Occupational Safety and Health (NIOSH) recommended exposure limit (REL) and

Proceedings of the Ninth International Seminar on Fire and Explosion Hazards (ISFEH9), pp. 1165-1175
Edited by Snegirev A., Liu N.A., Tamanini F., Bradley D., Molkov V., and Chaumeix N.
Published by Saint-Petersburg Polytechnic University Press
ISBN: 978-5-7422-6498-9 DOI: 10.18720/spbpu/2/k19-84

much lower than the immediately dangerous to life or health (IDLH) concentration. However, it would be possible that other toxicants, e.g., hydrogen cyanide (HCN), and ultrafine particles (< 100 nm) exist in significant concentrations. Nevertheless, there are no commercially available hand-held devices that can detect both particulates and traces of toxic gases, and development of such device is currently underway [7].

Hence, irritants (e.g., formaldehyde and acrolein) are particularly important as they often incapacitate so quickly that people cannot make it to an exit. Due to their highly toxic nature, NIOSH REl and IDLH concentrations of formaldehyde (CH_2O) or acrolein (C_3H_4O) are very low [6, 7].

Table 1. Exposure standards of selected toxicants

Chemical	Formula	NIOSH REL[a]	IDLH[b]
Carbon Monoxide	CO	35 ppm	1200 ppm
Hydrogen Cyanide	HCN	4.7 ppm	50 ppm
Formaldehyde	CH_2O	0.016 ppm	20 ppm
Acrolein	C_3H_4O	0.1 ppm	2 ppm
Benzene	C_6H_6	0.1 ppm	500 ppm

[a] National Institute for Occupational Safety and Health, recommended exposure limit.

[b] Immediately dangerous to life or health.

Formaldehyde is a highly reactive aldehyde gas formed by oxidation or incomplete combustion of hydrocarbons [6]. Direct skin contact to formaldehyde at 100 ppm causes a severe reaction. It can be readily absorbed when inhaled and can cause headaches and respiratory issues from 0.5 ppm [8, 9]. Acrolein is a strong irritant to skin and mucous membranes. It is also extremely toxic if inhaled or ingested, and still dangerous with skin contact [7]. The occupational exposure limits in the short-term exposure limit (STEL) is 0.1 ppm [10, 11]. In addition to these acute effects, chronic effects (e.g., cancer) can result from accumulated damage from multiple exposures for firefighters. Formaldehyde and benzene are known carcinogens.

The objectives of this study are: (1) to determine the types and concentrations of various toxicants in fire smoke from common building materials; (2) to gain a greater understanding of smoke toxicant generation processes, including pyrolysis, off-gassing, and burning; and (3) to assist in the development of particulates and toxic gas detectors for fire responders.

EXPERIMENTAL METHODS

Apparatus

A standard smoke density chamber (SDC, Fire Testing Technology [FTT]) is used with the capability of a Fourier transform infrared (FTIR) gas analyzer (Protea atmosFIR AFS-A-15) and a tapered element oscillating microbalance (TEOM) personal dust monitor (Thermo Environmental Instruments, PDM 3700).

The SDC provides a safe isolated environment (0.914 m width × 0.610 m depth × 0.914 m height) and consists of a radiant cone heater, a specimen holder, and a smoke obscurity measurement system, including a vertically upward light source and a photo detector. The radiant heat flux can be directed horizontally with a vertical fuel surface (ASTM E266) or vertically with a horizontal surface (ISO 5659). The specific optical density (SOD or Ds), i.e., a measurement characteristic of the concentration of smoke, is calculated, while the light beam is obscured by the smoke generated by the fuel, as follows:

$$Ds = V/(AL) \times \log(100/T), \qquad (1)$$

where V = chamber volume (0.510 m^3), A = exposed specimen area (0.0043 m^2), and L = light path length (0.914 m), and T = actual light transmission (relative intensity, %).

The FTIR gas analyzer and the TEOM dust monitor are connected to gas-sampling tubes (stainless steel, 5 mm i.d., 30 cm length) installed inside the SDC through the sampling ports near the center of the top wall. Gases are extracted at fixed sampling rates from each sampling port (FTIR: 1.5 lpm, TEOM: 2.2 lpm), and once analyzed, are returned to the chamber through another port near the sampling ports to prevent a vacuum pressure. The sampling line between the SDC and FTIR is maintained at 180 °C to prevent species condensation.

The FTIR has a multi-pass gas cell operating at 180 °C with the path length set as 4.2 m and the spectral resolution of the interferometer set to 4 cm^{-1}. The FTIR gas analyzer distinguishes 21 unique compounds from a library, including gases of interest in the present study: combustion products (H_2O, and CO_2) asphyxiant gases (CO and HCN), sensory irritant gases (formaldehyde and acrolein). The FTIR is calibrated for each species in the following ranges: H_2O (0-30.14%), CO_2 (0-2.47 %), CO (0-98.72 ppm), HCN (0-606 ppm), HCHO (0-16.5 ppm), and C_3H_4O (0-431 ppm). To prevent contamination from previous test runs, the FTIR is purged with N_2 (99.999 %) and checked daily with a standard gas mixture (0.85 % CO and 8.5 % CO_2). The data acquisition rate is typically 1/4 Hz.

The TEOM dust monitor is typically used by coal miners to take direct measurements of particulate mass concentration. Particulates are collected on a filter and their mass is measured by a tapered element oscillating microbalance in real time. The data acquisition rate is 1/60 Hz.

All experiments (except for the specimen temperature measurement to be described) are run in accordance to ASTM E662 (with a horizontal incident heat flux, q, of 25 kW/m^2 on a vertical specimen surface) or ISO 5659 (vertically downward heat flux on a horizontal specimen). For the ASTM flaming test, a pilot flamelet burner is placed between the horizontal heating furnace and the specimen to introduce pilot flames. Multiple pilot flames are set to have contact with the sample as soon as the test begins. To achieve the proper flame length, the average propane and air flow rates are around 70 ccm and 550 ccm, respectively. For the ISO vertical cone flaming test, a single pilot flame, about 30 mm in length, is oriented from the side, such that the tip of the flame is approximately in the center of the sample. To achieve proper flame length, the average propane and air flow rates are around 50 ccm and 300 ccm, respectively. It is possible that CO and CO2 from the pilot flame could affect the total readings from the chamber. Thus, the apparatus has been tested without a specimen for gas emissions of the pilot flame. The concentrations of CO and CO2 produced from said pilot flame is near negligible in comparison to those produced from the burning specimen.

The standards used are made to test for building materials and textiles on a bench scale. There are limitations of any bench-scale testing of materials when applying findings to a large-scale testing or a real fire where the imposed incident heat flux may vary with time. The present approach does not attempt to simulate the larger-scale standard fire resistance test or compartment fire conditions. Unlike some other tests such as the cone calorimeter with a vitiation chamber, in which incoming air flow rate is controlled, there is no such combustion condition like the fuel:air equivalence ratio exists in the overventilated smoke density chamber test. The toxic product yields have been determined but not reported here as the results depend on the location where the gases are sampled.

Specimen preparation

Each specimen is cut to 75 ± 1 mm by 75 ± 1 mm and planed to the thickness L = 12.7 ± 0.2 mm, and prepared by drying them in a forced-convection oven at 103 ± 2 ºC for at least 24 hours to get a base mass. Then, they are submerged in distilled water under a controlled environment for an extended period until the desired moisture content is achieved.

The moisture content of the wood is calculated by the following [12]:

$$\mathrm{MC} = (A - B)/B \times 100\ \%, \tag{2}$$

where A = original mass (g) and B = oven-dry mass (g). For selected wood specimens for the ISO 5659 setup, interior temperatures are measured by five K-type thermocouples (TCs) at incremented depths from the initial top surface of the specimens. The thermocouples (labeled by numbers in Figure 1) are placed at the following coordinates, depth (y) and radius (r) in mm; No. 1: (0, 0), Nos. 2 and 4: (6.35, 10), No. 3: (9.53, 10), No. 5: (12.7, 10). In addition to the five TCs in the specimen, two TCs are placed nearby the inlet of the sampling tube and the chamber floor.

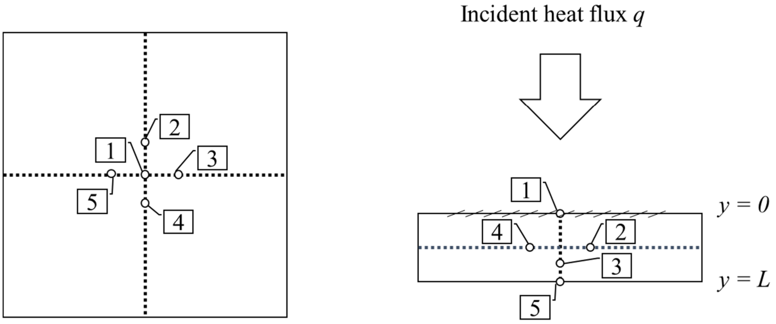

(a) (b)

Fig. 1. Thermocouple set up in a specimen oriented horizontally (with a vertical radiant flux from the cone heater. (a) top view; (b) cross-section view.

RESULTS AND DISCUSSION

Vertical specimen configuration

Under the vertical specimen configuration (ASTM E662), the effects of the type of wood (species including softwood—pine and cedar, and hardwood—oak) and the moisture content are studied in the flaming and non-flaming cases. Tables 2 and 3 summarize the results for the flaming and non-flaming cases, respectively. For each sample, the mass loss (%), the maximum specific optical density (Ds), the ignition time, and the concentrations of selected species, i.e., H_2O, CO_2, CO, formaldehyde, and acrolein, are listed.

For both flaming and non-flaming cases, the mass loss at the end of experiment (the elapse time: between 10-15min for flaming and around 18-20min for non-flaming) generally decreases with the moisture content. It is expected that there is a decrease in the mass loss, i.e., an increase in the residual wood material (and moisture), because more heat is required to raise the temperature of the material with increased total heat capacity from water and to vaporize the water, i.e., the heat of vaporization.

This is also reflected in the ignition times for the flaming tests; that is, the more moisture a sample contains the longer it takes to ignite. Oak also experiences less mass loss and much longer ignition time since it is denser and has larger heat capacities than the other two types of wood.

For the flaming test, all the specimens ignite, leading to vigorous burning, and produce less smoke (lower max. Ds), compared to the non-flaming tests. There is less consistency in the flaming test for Ds and MC correlation. It is known that for a complete combustion, CO_2 and H_2O are formed, whereas for an incomplete combustion or pyrolysis, more CO is produced. Thus, Tables 2 and 3 show that the concentrations of CO_2 and H_2O are generally higher and that of CO is generally lower in the flaming test compared to the non-flaming. When the wood is ignited, a charring process will occur and continue to propagate within the wood. Wood with higher MC require more energy due to the heat of vaporization and higher specific heat, leading to a delay in the charring process. The efficiency of the combustion is reduced, thus increasing by-products of incomplete combustion such as CO and smoke. If there is no ignition, it is probable that the moisture is protecting the interior of sample from pyrolysis. Therefore, less MC wood is more likely to produce complete combustion products, leading to less smoke and aerosol (steam).

Table 2. Characteristics of smoke from flaming vertical woods at various moisture contents

Wood Type	MC (%)	Mass loss (%)	Max Ds[a]	Ignition (s)	H_2O (%)	CO_2 (%)	CO (ppm)	Formaldehyde (ppm)	Acrolein (ppm)
Pine	0	39.8	105	2	2.74	1.61	711	37.3	3.9
Pine	20	38.7	61	3	2.95	1.41	670	28.3	3.1
Pine	40	36.3	142	7	2.99	1.09	853	42.5	6.1
Cedar	0	51.3	131	3	3.58	2.18	1600	95.3	5.9
Cedar	20	44.7	153	5	3.33	1.21	1020	73.6	7.6
Cedar	40	36.7	21	9	3.04	1.05	825	39.2	2.5
Oak	0	40.8	70	19	3.06	2.18	286	43.0	9.5
Oak	20	34.2	142	23	4.67	1.97	911	52.1	10.5
Oak	40	31.9	250	29	4.66	1.32	858	51.9	8.4

[a] Ds values after 10 minutes of exposure – for flaming tests, there is no “peak”, and Ds increases until end of test

Table 3. Characteristics of smoke from non-flaming vertical woods at various moisture contents

Wood Type	MC (%)	Mass loss (%)	Max Ds	Density (g/cm^3)[a]	H_2O (%)	CO_2 (%)	CO (ppm)	Formaldehyde (ppm)	Acrolein (ppm)
Pine	0	47.0	413	0.33	1.56	0.72	4300	95.9	8.2
Pine	20	43.4	337	0.38	2.32	0.35	2213	75.9	3.7
Pine	40	42.2	351	0.44	2.55	0.32	1965	66.8	3.3
Cedar	0	45.8	452	0.34	1.59	0.64	2766	116.2	1.4
Cedar	20	45.2	296	0.40	3.02	0.48	2167	94.1	0.8
Cedar	40	36.4	227	0.47	2.91	0.27	907	63.0	0.8
Oak	0	25.6	530	0.71	1.86	0.33	1614	68.2	7.3
Oak	20	21.6	118	0.87	3.15	0.12	162	35.3	1.3
Oak	40	22.9	74.6	0.99	3.59	0.10	108	27.8	3.5

[a] Average between same wood type and MC – same values for flaming condition.

The concentrations of formaldehyde and acrolein exhibit, to some extent, opposite trend between flaming and non-flaming cases. The concentration of formaldehyde is generally lower (except oak, MC: 20 and 40 %) and that of acrolein (except pine, MC: 0 and 20 %) is generally higher in flaming than non-flaming. As these species are intermediates in the high-temperature gas-phase oxidation processes, the higher temperature in the flaming case may be a factor affecting the differences.

In the non-flaming case, smoke would contain aerosols of condensed water vapor and/or thermally degraded fuel pyrolyzates. Both formaldehyde and acrolein are water soluble. As such, both species can be dissolved in aerosol particles and conveyed as vaporized gases through the heated line to the FTIR gas analyzer. This may also hold for the flaming test for higher moisture contents, in which less fully burned fuel is observed.

Effects of specimen orientation

Because of the Earth gravity, the orientation of the specimen surface; i.e., vertical (ASTM E662) and horizontal (ISO 5659), affects the results significantly. In the vertical orientation, the pilot flame is directly facing the specimen, and the convective forces and buoyancy from the flame runs parallelly with the surface of the specimen. In the horizontal orientation, the pilot flame is parallel to the specimen surface, and the convective forces and buoyancy is perpendicular to the specimen surface. Therefore, the heat transfer throughout the sample is influenced. This situation relates to a difference between a wall burning and the floor burning.

Table 4 shows a summary of the effects of the specimen orientation for pine with 0 % MC in the flaming and non-flaming cases. The measurement data for the first 20 min are recorded. No auto-ignition occurs without a pilot flame, while the piloted ignition takes place within the first few seconds for both orientations. The experiment is repeated three times for consistency with results. As is already described for the vertical orientation in the preceding section, for the horizontal as well, there is more CO_2 and H_2O, while there is less smoke and CO in the flaming case. The non-flaming case, particularly in the horizontal configuration, produces the highest smoke and toxicants (CO, formaldehyde, and acrolein) concentrations due to partial oxidation, while the flaming and horizontal case generates the lowest because of high-temperature oxidation (to form CO_2 and H_2O) in a flame with a longer residence time.

Table 4. Effects of specimen orientation for dry pine under the flaming and non-flameing conditions

Specimen Orientation	Flaming Condition[a]	Mass Loss (%)[b]	Max. Ds	H_2O (%)[b]	CO_2 (%)[b]	CO (ppm)[b]	Formaldehyde (ppm)[b]	Acrolein (ppm)[b]
Vertical	NF	53.13	413	1.56	0.72	4300	95.9	8.2
Vertical	F	54.04	208	3.81	2.32	2326	56.3	11.0
Horizontal	NF	56.76	570	2.82	0.84	4757	164.4	13.2
Horizontal	F	64.18	90	4.01	3.64	638	21.7	4.1

[a] NF: non-flaming, F: flaming [b] After 20 minutes of heat exposure

Figure 2 shows the temporal variations of the specific optical density and the particulate mass concentration. In Fig. 2a, note that for both vertical and horizontal orientations, the smoke density is much less with the flaming condition. For the flaming case, the vertical orientation produces much more smoke in comparison to the horizontal orientation. There is more than double the Ds value of horizontal observed in the vertical orientation by the end of the 20 minutes.

For the non-flaming condition, the horizontal orientation has more smoke than vertical orientation. The Ds for non-flaming tapers off after reaching a maximum value, which results in the Ds' to have a greater difference at the end of test. The vertical Ds does not taper off as much horizontal orientation, and appears to plateau.

Figure 2b shows a striking difference; the mass concentration of particulates in the non-flaming case has large peaks, whereas that in the flaming case is very low. Unlike Ds, which is a line-of-sight measurement, the the mass concentration is measured for the gas sampled at fixed location in the chamber (≈30 cm below, i.e., ≈1/3 of the chamber height, near the center of the top wall surface). Thus, measured mass concentration becomes zero if particles do not enter the sampling tube inlet. Mass loss rate for the flaming and non-flaming is different in horizontal orientation, but not too different in vertical orientation. It is likely that the convection from the pilot flame in the vertical orientation in flaming facilitated the mass loss in a similar fashion for non-flaming case.

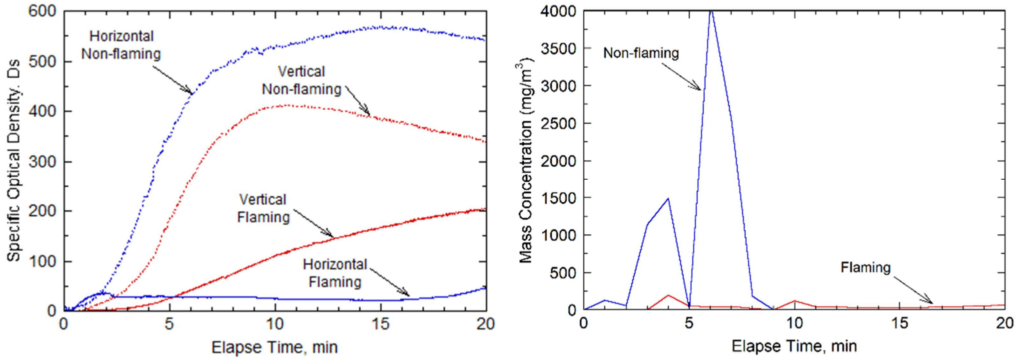

(a) (b)

Fig. 2. Temporal variations of (a) the specific optical density (vertical and horizontal specimen) and (b) the particulate mass concentration (horizontal specimen).

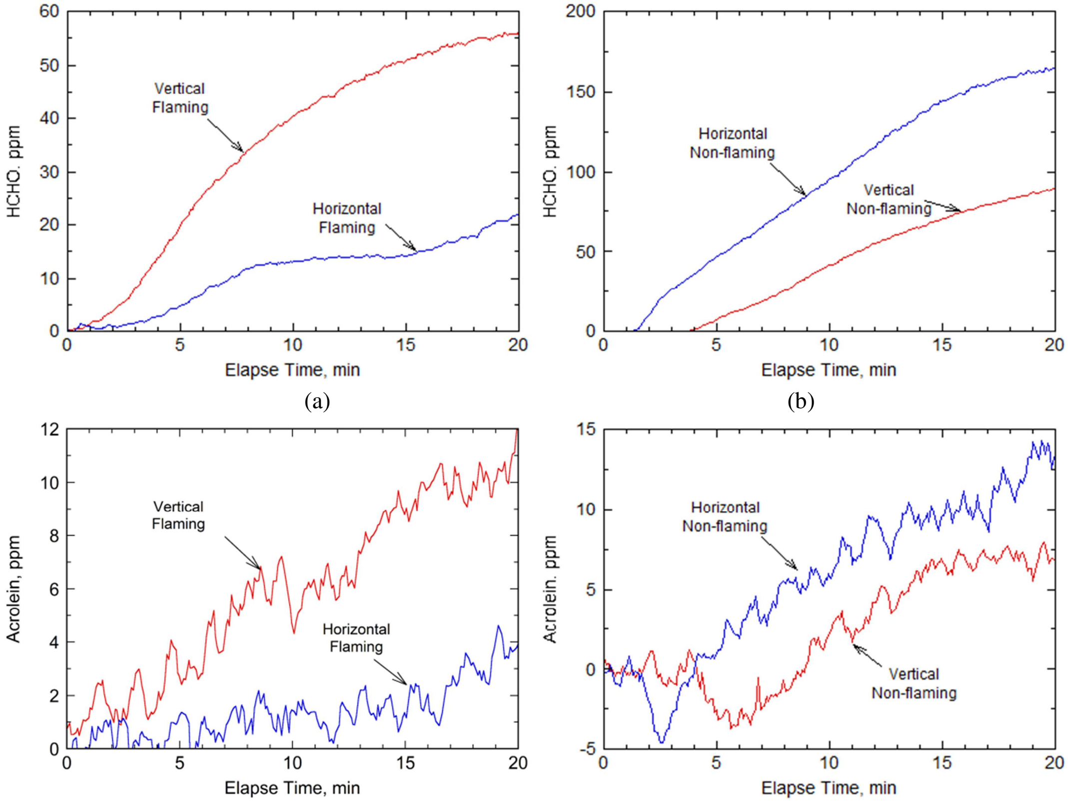

(a) (b)

(c) (d)

Fig. 3. Temporal variations of (a, b) formaldehyde and (c, d) acrolein concentrations. (a, c) Flaming and (b, d) non-flaming cases. Negative values indicate concentrations are too low for FTIR to read accurately.

Figure 3 shows the temporal variations of (a, b) formaldehyde and (c, d) acrolein concentrations in (a, c) flaming and (b, d) non-flaming cases . For both vertical and horizontal specimen orientation, the concentrations of both formaldehyde and acrolein are generally higher in the non-flaming case than in the flaming case. However, the measured concentration of formaldehyde largely exceeds its maximum calibration range (16.5 ppm) and that of acrolein is small (< 3.5 % of full scale). As a result, quantitative values of these measurements less reliable than a stated accuracy of 2% with respect to the actual values. Nevertheless, the differences between the flaming and non-flaming as well as the vertical and horizontal specimen surface seem to be significant.

For the flaming cases (Fig. 3a and 3c), the concentration of both formaldehyde and acrolein are much higher in the vertical specimen orientation than the horizontal. This correlates with the max Ds for vertical orientation being much higher than the horizontal orientation. As described for Table 4, the flaming and horizontal case generates the lowest because of high-temperature oxidation (to form CO_2 and H_2O) in a flame with a longer residence time, whereas the vertical case induces natural convection along the specimen and reduce the residence time.

For non-flaming cases (Fig. 3b and 3d), the trend is opposite; the concentration of both formaldehyde and acrolein are higher in the horizontal specimen orientation than the vertical. Here, the maximum Ds for horizontal orientation is higher, indicating more irritants are produced in the wood smoke.

Specimen temperature

Figures 4 shows the temporal variations in the measured temperature in the interior of the horizontally orientated specimen (pine at 0% MC, 12.7 mm thickness) in (a) flaming and (b) non-flaming. For both flaming and non-flaming cases, the temperatures in the depth of 6.35-12.7 mm (TC2 – TC5) exhibit a consistent decreases in their slopes to a steady, almost linear slope at ≈12 min, The slopes appear to be quite similar, indicating that the specimen is experiencing the similar processes. For the flaming case (Fig. 4a), at 15 min, the thermocouple at the depth of 0 mm (TC1), which is exposed as the surface regresses, exhibit a sudden decrease, most likely reflecting a change in the flame condition. For the non-flaming case (Fig. 4a), the temperature at 0 mm reaches its maximum (≈600 ºC) at 17 min more gradually.

The back of the specimen is ceramic wool with lots of air in void spaces, so it is intended to be insultated. Since the temperature gradient in the direction parallel to the specimen surface must be negligible, compared to that in the perpendicular direction (as shown in Fig. 4), the heat loss to the stainless steel sample holder in the periphery of the specimen must be negligible.

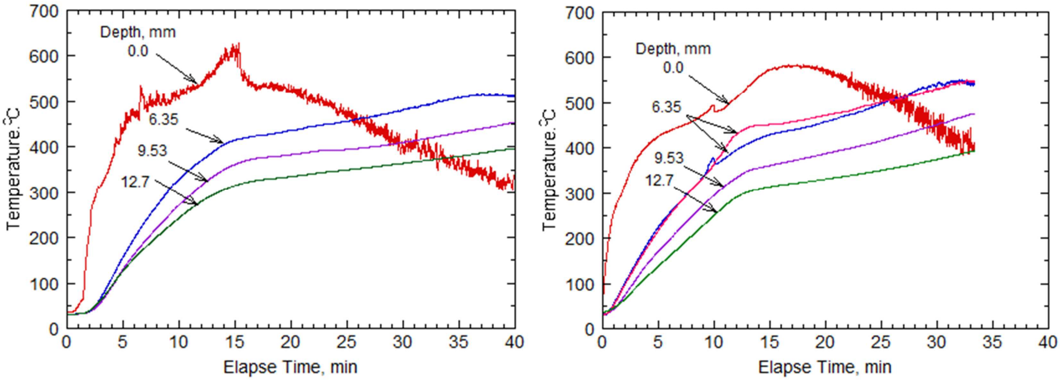

(a) (b)

Fig. 4. Temporal variations of the temperature in the interior of the horizontally orientated specimen. (a) Flaming and (b) Non-flaming.

Figure 5 shows spacial variations in the measured temperature in the interior of the horizontally orientated specimen in (a) flaming and (b) non-flaming. For both flaming and non-flaming cases, by absorbing the incident heat, the surface temperature increases first, and resulting temperature gradient causes heat conduction to the specimen interior, thereby increasing the internal temperature. At ≈ 12 min, the thermocouple at the bottom of the specimen at the depth of 12.7 mm (TC5) reaches ≈290 ºC.

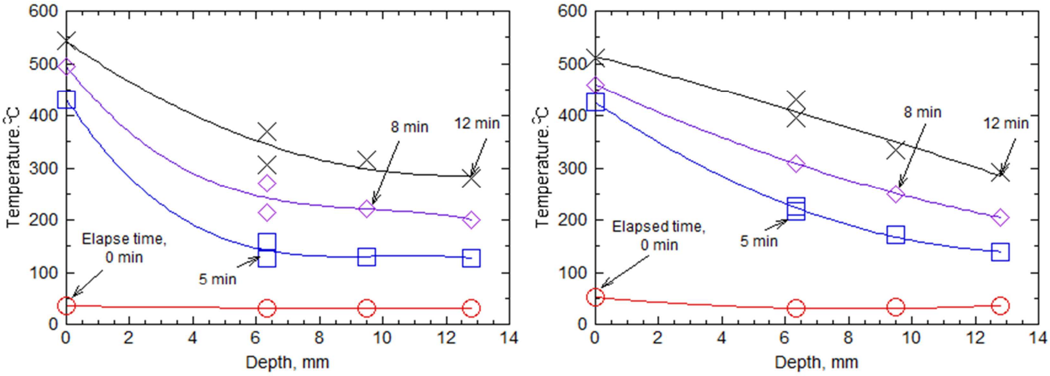

(a) (b)

Fig. 5. Temperature in the interior of the horizontally orientated specimen. (a) Flaming and (b) Non-flaming.

The thermal degradation processes of wood are well understood [12]. Wood dehydrates and generates water vapor, CO_2, formic acid, acetic acid, and H_2O between 100 and 200 ºC . Between 200 and 300 ºC , significant amounts of CO are produced as a result of significant pyrolysis within some parts of the wood. Around 300 to 350 ºC, cellulose begins to show significant depolymerization, Once the temperature reaches around 450 ºC, which is the peak at which lignin degrades, the wood sample will cease volatile emissions.

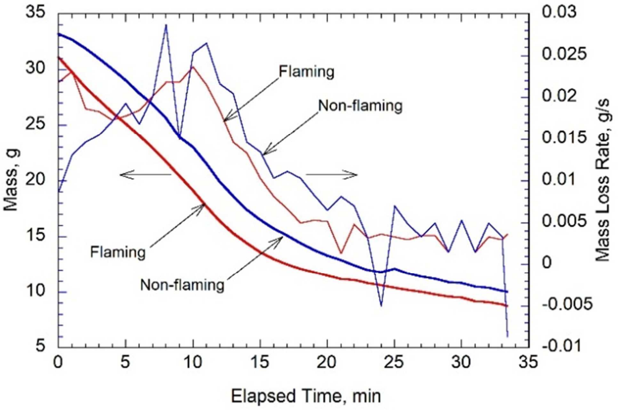

Fig. 6. Specimen mass and mass loss rate for flaming and non-flaming cases. The mass is presented at 1Hz, and mass loss rate is shown at 1/60Hz due to load cell sensitivity.

Since temporal variations of the temperature are similar for flaming and non-flaming cases (Fig. 4), thermal degradation processes must be similar as well. In the first 5 min, the specimen temperature becomes > 100 ºC in every depth (Figs. 5a and 5b). At 8 min, the temperature increases to 200 – 300 ºC. At 12 min, > ≈300 ºC and thus, the charring front reaches the back side of the specimen.. At slightly before 15 minutes, around 300 to 350 ºC in the back side of the specimen, Afterwards, the sample is simply being heated up at a constant rate (Fig. 4). Anything above 450 ºC is mostly char, and as observed during the test, there is a thin layer of ashes covering the charred sample. Thus, the charring front must reaches the back side of the specimen.

The advantages of using ISO 5659 (horizontal orientation) is that it provides mass loss data. Figure 6 shows the specimen mass and mass loss rate for flaming and non-flaming cases. The mass is presented at 1Hz, and mass loss rate is shown at 1/60Hz due to the sensitivity of the load cell.

The mass loss rate does not appear to be significantly different between flaming and non-flaming cases at first glance, except for the initial flaring (< 4 min) for the flaming case. This is specifically for 0% MC pine, and data shown is representative of the all flaming and non-flaming tests conducted with the same conditioned specimen.

CONCLUSION

Fire toxicity of wood smoke has been studied under flaming and non-flaming heating conditions using selected woods with various moisture contents, placed vertically or horizontally in the standard smoke density chamber with analytical instruments: a FTIR gas analyzer and a TEOM dust monitor. The conclusion can be summarized as follows.

1. The type of wood and the moisture content affect the pyrolysis, burning processes, and in turn, the toxic effluent emission through the variations in the fuel density and specific heat. A hardwood (oak) has a density about twice as large as soft woods (pine and cedar) and, in turn, a larger specific heat. As a result, oak takes a longer ignition delay time and generates less CO. Higher moisture content results in larger density and specific heat due to increase in mass and water within the specimen, thus requiring more energy to heat up the wood and leading to delay in charring. This reduces the efficiency of combustion, which leads to more smoke (higher Ds), and more toxic incomplete combustion products (CO, formaldehyde).
2. The effuluent concentrations depend significantly on whether or not the flame exists and the specimen orientation as they influence the gas-phase reactions and the natural convection due to buoyancy around the specimen. The non-flaming case, particularly in the horizontal configuration, produces the highest smoke and toxicants (Ds, CO, formaldehyde, and acrolein) concentrations due to partial oxidation, while the flaming and horizontal case generates the lowest because of high-temperature oxidation (to form CO_2 and H_2O) in a flame with a longer residence time.
3. For both flaming and non-flaming cases, the heat exposure increases the specimen interior temperature rapidly until the pyrolysis and charring front reaches the back side of the specimen and the mass loss rate (or the fuel consumption rate) peaks out (around the elapse time of 12-15 min), As a result of charring of the entire specimen, the increasing rate of the specimen temperature decreased to a steady condition.

ACKNOWLEDGEMENTS

This work was supported by the U.S. Department of Homeland Security, Federal Emergency Management Agency, Assistance to Firefighters Grant Program, Fire Prevention and Safety grant (No. EMW-2014-FP-00688). Assistance in conducting the experiment by senior students: Aaron Aguilar, Jeffrie Brown, and Ian Finlay is acknowledged.

REFERENCES

[1] M. Ahrens, Home Structure Fires, National Fire Protection Association, Quincy, MA, Sept. 2017.

[2] V. Babrauskas, et al., Toxic Potency Measurement for Fire Hazard Analysis (Special Publication 827). National Institute of Standards and Technology, 1991.

[3] Lowery, et al., Studies of Toxic Gas Production During Actual Structural Fires in the Dallas Area, Journal of Forensic Sciences, JFSSCA, Vol. 30, No 1, Jan. 1985

[4] B. Lake, Firefighter Safety Depends on Gas Detector Accuracy, Fire Engineering, vol. 1, issue 11, 2012.

[5] R.J. Crewe, Experimental Results of a Residential House Fire Test on Tenability: Temperature, Smoke, and Gas Analyses, J. Forensic Sci. 59 (2014) 139–154.

[6] Anon, NIOSH Pocket Guide to Chemical Hazards, National Institute for Occupational Safety and Health, DHHS (NIOSH) Publication No. 2005-149, September 2007.

[7] F. Takahashi, P.S. Greenberg, G.W. Hunter, Firefighter Particulate and Gas Sensor Technology, Fire Safety (FS)-World, Fall edition, 2014, pp. 32-38.

[8] Compound Summary for Formaldehyde, PubChem, Open Chemistry Database, 2004, Updated April 2018.

[9] Medical Management Guidelines for Formaldehyde, Agency for Toxic Substances and Disease Registry, Published 2014.

[10] D. Arntz, Acrolein and Methoacrolein, Ullmann’s Encyclopedia of Industrial Chemistry (2012), vol. 1, 329 – 346. DOI: 10.1002/14356007.a01_149.pub2

[11] ACGIH, American Conference of Governmental Industrial Hygienists, Threshold Limit Values and Biological Exposure Indices, 2006.

[12] Forest Products Laboratory, Wood Handbook - Wood as an Engineering Material,General Technical Report FPL-GTR-190, Madison, WI., U.S. Forest Service, 2010.

PVC Sheathed Electrical Cable Fire Smoke Toxicity

Mat Kiah M.H.[1,2,] *, Mustafa B.G.[1], Andrews G.E.[1,] *, Phylaktou H.N.[1], Li H.[1]

[1] *University of Leeds, School of Chemical and Process Engineering, Leeds, UK*
[2] *Universiti Teknologi Malaysia, Faculty of Chemical and Energy Engineering,*
Skudai, Johor, Malaysia
**Corresponding author emails: profgeandrews@hotmail.com; misshasimawaty@yahoo.com*

ABSTRACT

The cone calorimeter, under free and restricted ventilation conditions, was used to investigate the toxic emissions from PVC cable fires. Toxic gases were measured using direct high temperature gas sampling from the exit of the cone calorimeter with a short chimney attached to the exit from the electrical cone. Toxic species CO and HCl were identified as a function of time using a heated Gasmet FTIR. The particle number was determined using the Cambustion DMS500 fast response particle sizer with a diluted sample taken from the diluted cone calorimeter exhaust flow at the same location as the optical obscuration smoke meter. The HCl concentrations from the Chlorine in the PVC sheath demonstrated HCl levels well above the LC_{50} concentration for HCl. The restricted ventilation reduced the peak fire heat release rate and the peak toxicity and HCl occurred later than for free ventilation. The equivalence ratio in the gases from the combustion zone, were both rich at 1.5 for free ventilation and 1.3-1.4 for restricted ventilation. The toxicity results showed the classic phases of compartment fires: growth, steady state burning and then fire decay. After flaming combustion was extinguished, slow char combustion continued with high CO emissions. The particle size distribution showed peak particle number, PN, nuclei mode particles at 10 nm and an accumulation mode at 100 nm. The number of particles at 10 nm for free and restricted ventilation were extremely high and showed that the freely ventilated fires had the highest PN, but later in the fire the restricted ventilation PN were higher. Nano-particle emissions < 50 nm from PVC fires are a health hazard that is currently unrecognized and unregulated.

KEYWORDS: Fire toxicity, compartment fires, electrical cable fires, PVC, particle.

INTRODUCTION

Deaths in fires are mainly due to toxic gases breathed in during exposure to fire smoke [1], yet there is no requirement to measure the toxic gases (other than smoke obscuration) from materials as part of their approval for use in buildings [2]. The Grenfell Tower fire in London in 2017 had toxic smoke emissions as a major cause of death and many survivors had to have their lungs flushed out to remove black carbon deposits [3]. To reach the lungs particles have to be < 100 nm diameter and yet there is hardly any information on the particle size distribution of particulate material generated in fires. The medical effects of ultra-fine particles that cause lung and heart related problems within days of exposure [4-8] are well known in atmospheric pollution, but the exposure to very high levels of fine particles in fires can be much greater in a short time than exposure to fine particles in the a poor quality atmospheric exposure in roadside air pollution, where concentrations are around 50µg/m^3 compared with over 2000 times this concentration in fires [9]. This means that a one minute exposure to fire particulates during escape is equivalent to a full day exposure to roadside air pollution, with most fires giving a higher exposure than this. Escape times are at least 10 minutes, often walking through significant smoke concentrations. This work presents data on particle number

Proceedings of the Ninth International Seminar on Fire and Explosion Hazards (ISFEH9), pp. 1176-1186
Edited by Snegirev A., Liu N.A., Tamanini F., Bradley D., Molkov V., and Chaumeix N.
Published by Saint-Petersburg Polytechnic University Press
ISBN: 978-5-7422-6498-9 DOI: 10.18720/spbpu/2/k19-89

in PVC cable fires as well as toxic gas emissions. Fine particulates are shown to be a significant contribution to smoke in building fires and could be formed as HCl droplets.

Polyvinyl Chloride (PVC) is the second most important fire load after wood [10] and PVC sheathed electrical cables are the most common source of PVC in fires. It has been estimated that there are 250m of electrical cable per house (50m per room) and 140 fires/million km cable/year [10]. Electrical cable fires may occur as part of a fire load for a fire that has started elsewhere and spread to ignite the cables externally. This is simulated in the present work using the cone calorimeter to represent radiant heating from a fire that engulfs the cables. There is no requirement in material approval tests for electrical cables to have any toxicity measurements, other than the visible obscuration that smoke generates [2].

One of major applications of PVC in buildings is in electrical cables, as the electrical insulation sheath. However, in building products PVC is widely used, for example clear sheets, skirting boards and roofs. PVC is also used in other electrical components such as computers, electrical cords or cables, component housing and phone system [11]. About 8% PVC, about 40 million tons of worldwide production capacities each year was used for cable production between 2006 and 2017 [12, 13]. Chlorine based material with a high chlorine content (>56%) are classified as fire retardant and widely used in many applications because it can prevent or slow down the burning process [14]. However, it can produce toxic gases, mainly hydrogen chloride (HCl), when burnt, which is an irritant depending to the concentration level. Irritancy effects due to exposure to HCl can impair or reduce the escape ability of occupants during the fire. Fire-retarded substances can increase smoke toxicity more than they reduce fire growth rate [15].

Sundstrom [2] has reviewed methods of testing of cables for their fire resistance and concluded that current tests concentrate on fire propagation rates and not on toxicity. However, he concludes that the future must address the toxicity issue and the measurement requirements, as reliable test methods are lacking. Hirschler [16, 17] has compared the large scale cable tray fire tests of ASTM D921 and IEC 332-3 with the cone calorimeter [18] and concluded that the heat release rate, HRR and smoke production measured in the cone calorimeter can be used to predict the results of the larger scale tests. This was the reason for the use of the cone calorimeter in the present work. A very small number of studies of toxic gases and particulate emissions in fires have involved electrical cables and polymer fires and particle size measurement [19-22].

Al-Sayegh et al. [21] have used the cone calorimeter with PVC cables with free ventilation, with heated gas sampling and analysis, using the Gasmet FTIR, of the toxic gases from the diluted products of the fire at the same location as the smoke meter. Their work showed that at 40 kW/m^2 radiant heat the toxic yields peaked at the time of peak HRR and were 0.18 for CO, 0.4 – 0.5 for HCl, 0.04 – 0.05 for Acrolein and 0.02 – 0.03 for Formaldehyde. The relative toxicity on an LC_{50} basis showed that of the total toxicity 20% was from HCl, 41% from Acrolein and 33% from Formaldehyde. On a $COSHH_{15min}$ basis, which is important for no impairment of escape, HCl was 33% of the total toxicity, Acrolein was 53% and Formaldehyde was 12%. In both cases the contribution of CO to the toxicity was small, but this could be due to the diluted combustion and post flame oxidation. The present work sampled directly from the hot gases at the exit from the cone calorimeter and so post flame oxidation of toxic gases was avoided. However, the conclusion from the work of Al-Sayegh et al. [21] was that the main toxic gases on an LC_{50} or $COSHH_{15min}$ basis were Aldehydes and that the toxicity of HCl was only 20% (LC_{50}) or 33% ($COSHH_{15min}$) of the toxic gas problem. The HCl yields were shown by Al-Sayegh et al. [21] to be higher than most previous work, especially in small scale tests such as the Purser furnace test [23, 24]. However, the agreement was very good with the previous cone calorimeter work of Babrauskas et al. [25] for PVC sheet samples. However, the HCl yields were significantly lower than the 100% conversion of Chlorine to HCl, which gives a yield of 0.58. The reason for this was shown by Al-Sayegh et al.

[21] to be due to Chlorine remaining in the char at the end of flaming combustion. Al-Sayegh et al. [22] have also burnt PVC cables with a pine wood crib fire in a 1.6m^3 compartment fire. They showed that the yield of HCl was 0.3 – 0.35 which is a little lower than the 0.4 – 0.5 yield for the cone calorimeter [15], but still higher than most values for HCl yield in the literature [21].

EXPERIMENTAL EQUIPMENT

The cone calorimeter (ISO 5660) [18] is a standard bench scale piece of equipment designed to measure the heat release rate and flammability properties of materials. The authors have adapted the standard cone calorimeter [18] for raw gas toxicity and particle size measurements from the cone heater outlet, for both the free and restricted ventilation. The modified calorimeter and associated instrumentation is shown in Fig. 1. The restricted ventilation version of the cone calorimeter uses an airtight stainless-steel box set up to create restricted ventilation combustion conditions. It was operated with a controlled air supply design to create rich combustion conditions that occur in air starved compartment fires. The load cell, sample holder and cone heater were enclosed in the steel box, which had a metered air supply through the bottom of the air tight box. The airtight box was 38 cm long, 30 cm wide and 33 cm high, with a volume of 0.0376 m^3. In the process of developing this experimental method it was observed that there was excessive heat loss from the metal box, which influenced the temperature of the test specimen and hence influenced the HRR. The airtight box design was improved by insulating the inside walls and the door was insulated from the outside. An insulation board 25mm thick was used to avoid heat loss. The combustion process was observed through a glass window on the cone calorimeter enclosure which was also insulated, when not being used for viewing the flame. An insulation board was also placed in the sample holder underneath the test specimen to prevent heat losses to the supporting metal cylinder leading to the load cell heating.

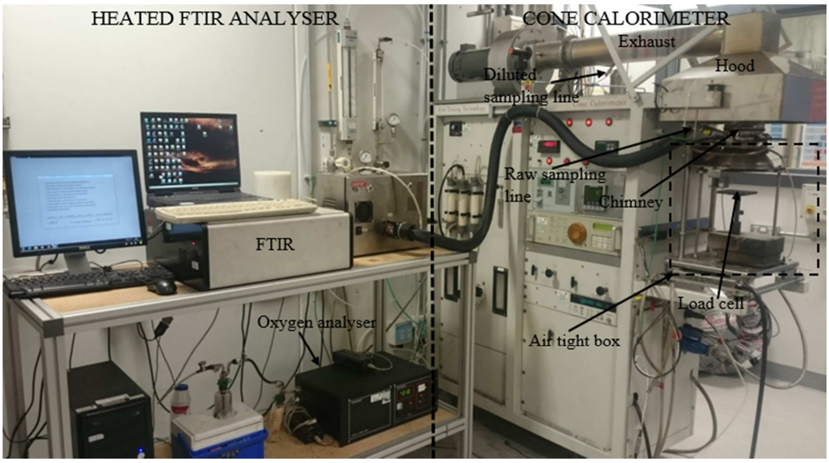

Fig. 1. Configuration of the cone calorimeter and FTIR analyser.

The airflow introduced to the combustion chamber was from a compressed air supply and was measured using a variable air flow meter with the air flow varying from 6 – 28 L/min. This variable airflow translates to 0.12 – 0.56 g/s air mass flow. A more general parameter is considered to be the air mass flow per exposed surface area of the test specimen (0.01m^2) and this converts to 12 – 56 g/sm^2 in these terms. The simple assumption that for all fuels there are 3.05 MJ of heat release per kg of air is another way of representing the ventilation conditions. This translates the air mass flow range into fire HRR in kW as 0.37 – 1.71 kW fires and in terms of the exposed surface area of the wood is 37 – 171 kW/m^2. In the present work a single air flow was used of 19.2 g/sm^2 or 59 kW/m^2

for the restricted ventilation condition. This is the maximum possible heat release rate (HRR) in the primary fire in the enclosed compartment.

A radiant heat level of 35 kW/m^2 was used for both the free and restricted ventilation tests. This is the recommended standard heat flux by British Standards [18] for use in material evaluation for performance in fires using the standard cone calorimeter [18]. Also, 35 kW/m^2 was recommended by Flecknoe-Brown et al. [26]. Herzberg and Blomqvist, [19] noted that 35 kW/m^2 was a "trade-off between a lower value, which possibly would have caused material pyrolysis only, and a higher value which might have provoked an unrealistically clean burning behaviour". This radiant flux was a little lower than the 40 kW/m^2 used in the work of Al-Sayegh et al. [21] where 40 kW/m^2 was used. However, they investigated 20, 30 and 40 kW/m^2 and 20 and 30 were too low to lead to ignition of the PVC, but the 35 kW/m^2 was not tested and this did give ignition of PVC in the present work. The temperature of the cone was about 700^{o}C for the 35 kW/m^2 irradiation level.

Test sample preparation

BS 6004 6242Y Prysmian A electrical cable with PVC insulation and sheath [27] were cut into 100mm strips and a single layer of 7 pieces filled the 100mm square test section of the cone calorimeter, as shown in Fig. 2. Only one side of the cable was exposed to the cone heater during the burning test. The initial mass of cables were weighed, as a check on the value measured by the cone calorimeter load cell.

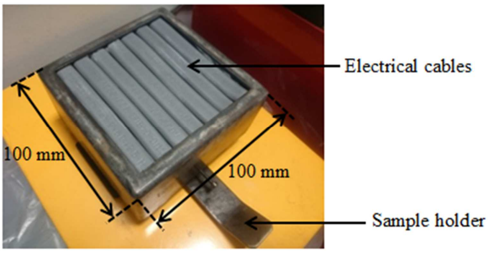

Fig. 2. PVC electrical cables in sample holder.

Heated Fourier-Transform Infrared Spectroscopy

The heated Gasmet FTIR analyser was calibrated by the manufacturer for 60 species, including all major toxic species in fires. Also a diluted gas sample was sent from the cone calorimeter collection duct for particle size analysis using the Cambustion DMS500 [28]. The overall experimental rig of the cone calorimeter and portable analysers used is shown in Fig. 1.

Cambustion DMS500 particle size analyser

For particle size analysis a diluted sample is required for two reasons. Firstly, the dilution lowers the dew point by cooling and reducing the concentration and this prevents water vapour from the combustion products appearing as droplets and being counted as particles. However, higher molecular weight unburned hydrocarbons from the fire can form liquid aerosols in the dilution process and these are part of the particles that may be a health hazard. If the fire forms acidic gases then with the water vapour present acid droplets can form, for example Hydrocholric acid droplets will form in the present work. For total particle size analysis it is not known whether particles in any size range are liquid or solid or a mixture of both. The second reason for particle number size distribution needing to be measured in a diluted sample is that for low dilution particles agglomerate in the sampling system and the size distribution changes and the number of particles is reduced. Usually a dilution ratio of around 100/1 or more is advocated [29, 30]. The cone calorimeter dilutes the products of combustion from the cone heater outlet (chimney outlet in the present case) with ambient air. Thus a diluted gas sample for particle size analysis taken from the cone calorimeter dilution tunnel is the obvious choice of gas sample location. The sample point was close to where the smoke production was measured in the cone calorimeter using the standard obscuration meter, so that particle number and smoke obscuration can be directly compared. It was shown above that at the present test conditions the dilution ratio was 112/1 and hence meets Kittleson's [29, 30] recommended dilution ratio of >100/1.

The Cambustion DMS500 (Differential Mobility Spectrometer) [28] particle size measurement equipment was used to measure real time particle sizes in the size range 5 – 1000 nm. The DMS500 size separates particles on the basis of their electrical mobility and the size may be different from an aerodynamic mobility analyser. Electrical mobility is the dominant mode of particle size measurement for nano-particles. It is a transient instrument and can take several size distributions per second. In the present work the size distribution as a function of the fire time duration was measured.

Initial analysis of PVC Prysmian A electrical cable

Shimadzu TGA-50, CHNS Thermo AE2000 and PARR 6200 Bomb Calorimeter were used to determine its chemical composition, energy content, volatiles, moisture, fixed Carbon and ash contents. Table 1 shows the results for the PVC cable composition. The stoichiometric A/F was computed by carbon balance from the elemental composition. Chlorine was not determined, but was assumed to be the missing mass from the elemental analysis. The chemical formula in Table 1 was close to that of PVC but the Hydrogen was significantly lower, indicating that this was not a pure PVC cable sheath but had some other hydrocarbons mixed in. As the CH_y had y too low, this indicates the use of low H/C ratio polymers in the electrical sheath material.

Table 1. Pre-analysis results for PVC Prysmian A electrical cable (BS6004)

Analyser	Parameter	Data/Value
Thermogravimetric analyser	Proximate analysis (wt.%)(daf)	
	Volatile matter	96.36
	Fixed Carbon	3.64
	Moisture (as received)	0.40
	Ash (as received)	28.91
CHNS analyser	Ultimate analysis (wt.%)(daf)	
	Carbon	35.63
	Hydrogen	3.84
	Chlorine	60.53
Bomb calorimeter	GCV (MJ/kg)	17.95
Other information		
	Stoichiometric A/F	4.85
	Chemical formula (daf)	$CH_{1.29}Cl_{0.57}$
	Pure PVC	$CH_{1.5}Cl_{0.5}$

For TGA analysis, the test sample was heated to 920°C in Nitrogen. The process removes fixed Carbon. At 920°C Nitrogen was change to air to burn the fixed Carbon. The balance from the total of 100% mass after deduction of moisture, volatiles and fixed Carbon was ash. The TGA mass loss in Nitrogen is shown as a function of temperature in Fig. 3 and compared with that of Al-Sayegh et al. [21], where there is good agreement. The release of HCl occurs between 250 and 300°C.

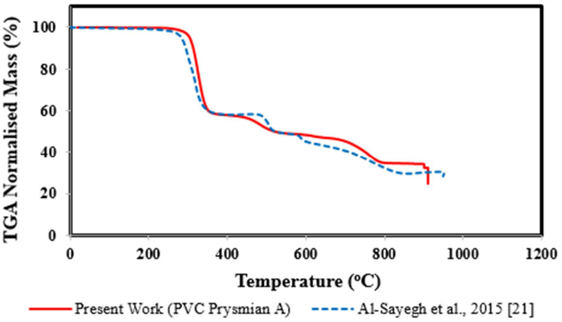

Fig. 3. Normalised mass loss as a function of temperature from TGA analysis.

The elemental analysis gave 60% of the PVC mass as Chlorine; this would produce a yield of HCl of 62%. Fig. 3 shows there was a 42% weight loss due to HCl loss in the temperature range 250 – 300°C. However, there is evidence of another volatile loss at 400-500°C and assuming that this is also HCl. The total weight loss due to release of HCl is 52% close to the expected total yield of HCl. Bowes [31] commented that 70% of the expected HCl yield (41%) occurs rapidly at 272°C and this was also found in Fig. 3.

An SEM model of Carl Zeiss EVO MA15 was used to perform a full elemental analysis. The SEM analysis showed that other than Chlorine there were the flame retardant minerals Aluminum and Calcium. Mineral type flame retardants are added to polymers, including the modern cables, to inhibit combustion and smoke production [32]. It is likely in this case that Calcium carbonate was added as a thermal inert that would decompose to release CO_2 in a fire. This was the cause of the long ignition delay in the tests.

RESULTS

Heat release rate, fire equivalence ratio and combustion efficiency

The heat release rate by oxygen consumption and the fire equivalence ratio from carbon balance are shown in Fig. 4 and Fig. 5 respectively. These show that the ignition delay at 35 kw/m^2 radiant heat was about the same for free and restricted air ventilation at 22s.This compares with about 50s in the work of Al-Sayegh et al. [21]. These relatively short ignition delay indicate little effect of any fire retardant for the PVC cables.

Fig. 4 shows the primary heat release by Oxygen consumption for the cone calorimeter chimney gas sample. The primary HRR with restricted ventilation was higher than that for free ventilation and at its peak was close to that for the theoretical HRR if all the Oxygen in the air was consumed, 59 kW/m^2. The reason for the higher primary HRR was the higher temperature of the confined restricted ventilation fire which gives higher combustion efficiency. The total primary and secondary combustion HRR is also shown in Fig. 4, based on the standard cone calorimeter Oxygen consumption method. The difference from the primary HRR is the secondary combustion HRR, which occurs as the gases from the chimney on top of the cone heater are discharged and entrain air when secondary combustion can occur. The secondary HRR is small but significant and equal for free and restricted ventilation. This is the main reason that the cone calorimeter with toxic gases measured at the same location as the smoke meter is not deemed [33] to be a good experimental device for toxic gas emissions, as the secondary oxidation may reduce the toxic emissions or generate other emissions such as the partial oxidation Aldehyde gases. The free ventilation total

HRR is still lower than that for restricted ventilation, although at the highest HRR there was very little difference. These Oxygen based overall HRRs are shown in Fig. 4 to be substantially lower than the HRR based on the PVC cable mass loss, particularly at the start of combustion. The reason is that HCl mass loss has no heat release and the poor efficiency of secondary combustion.

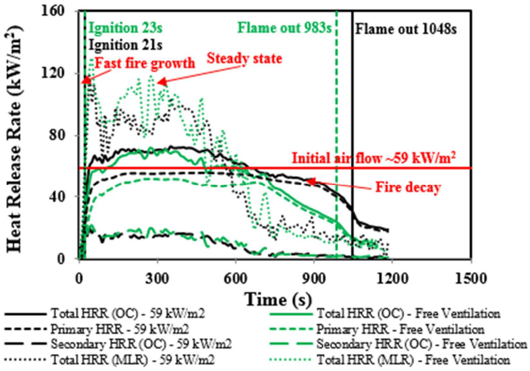

Fig. 4. Heat release rate against time.

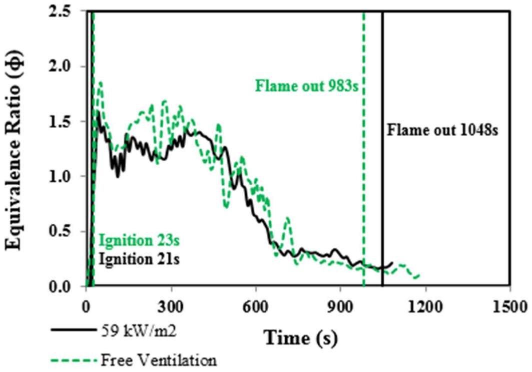

Fig. 5. Equivalence ratio against time.

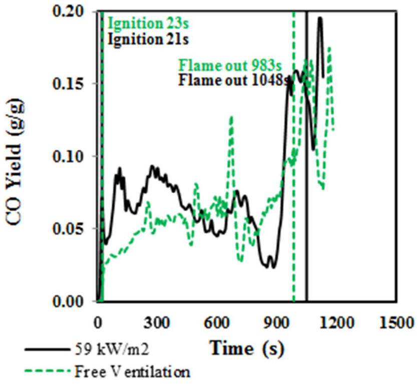

Fig. 6. CO yield as a function of time.

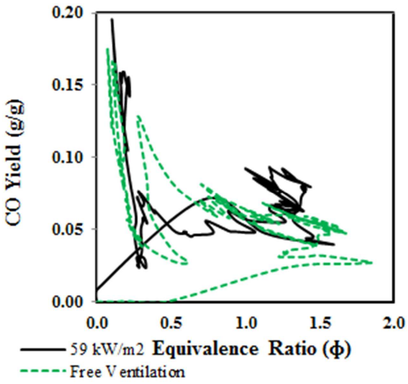

Fig. 7. CO yield as a function of ϕ.

Figure 5 shows that in the region of the highest HRR in Fig. 4, the primary equivalence ratio, ϕ, was rich for both free and restricted ventilation. Surprisingly ϕ was richer for the free ventilation case due to the higher oxygen availability which enabled more fuel to burn which created richer mixtures. However, the lower HRR was due to the richer mixture and the associated lower temperatures. For both free and restricted ventilation the HRR reduced after 450s and the equivalence ratio became lean after 550s. The high HRR up to 450s is associated with the rapid release of flammable volatiles from the PVC cables and the slower later HRR is char combustion of the residual material. This later burning lean phase was the source of the highest yields of CO and THC, as shown in Figs. 6 and 8, which gave a poor combustion efficiency as shown in Fig. 9. The CO yield as a function of ϕ in Fig. 7 shows that the lean mixtures were the greatest region of high CO yield. This was not expected as rich mixtures normally have high CO due to equilibrium chemistry. However, in this case the poor combustion efficiency dominated the production of CO. Aljumaiah et al. [34] have shown for pool fires that CO yields were high for lean low temperature pool fires in restricted ventilation enclosures, due to poor combustion efficiency.

Figure 10 shows the HCl yield as a function of time for free and restricted ventilation fires. Fig. 11 shows the HCl yield as a function of ϕ and there was no correlation for both ventilations. The yield peaked for both ventilations at 0.1, which is well below the theoretical yield of 0.58 and lower than the 0.2 – 0.3 peak yield found by Al-Sayegh et al. [21] for a different PVC cable. Their work sampled the toxic gases after dilution for free ventilation fires. Fig. 10 shows that the peak HCl yield occurred at different times for the two ventilations. It peaked at 300s for the restricted ventilation case and at 700s for the free ventilation case. Other toxic gases also had the same features of later generation with free ventilation. The reason for this difference is not known as there was no significant difference in the HRR or the equivalence ratio at these times. Al-Sayegh et al. [21] had the peak HCl yield 100-200s after ignition, which was much sooner than that in Fig. 10 for both ventilations. It is possible that the fire retardant in the cables delayed the release of HCl, but this would not explain the different times for the release of HCl for the two ventilations.

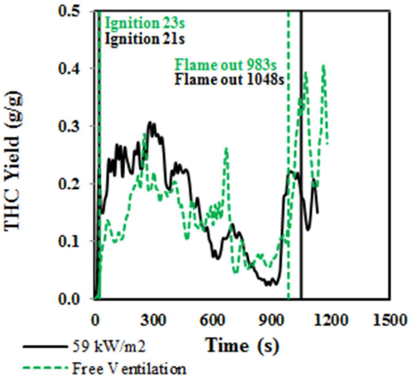

Fig. 8. THC as a function of time.

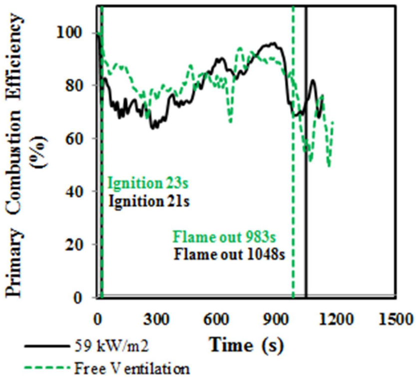

Fig. 9. Primary Combustion Efficiency against time.

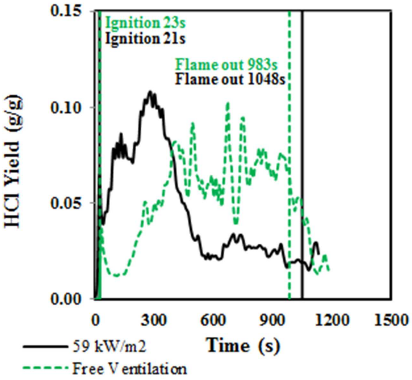

Fig. 10. HCl yield for free and restricted ventilation.

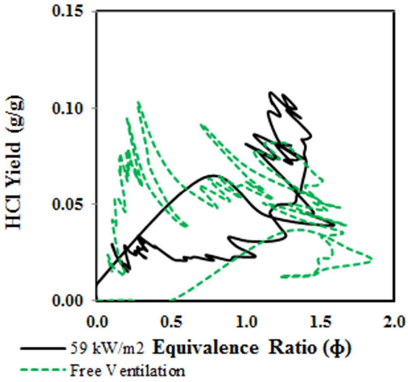

Fig. 11. HCl yield as a function of ϕ.

Al-Sayegh et al. [21] reviewed the published yields for CO and HCl in the literature for PVC fires, most of which were not PVC cable fires. Babrauskas et al. [25] for the standard cone calorimeter found the HCl yield to be 0.3 with the CO yield at 0.07 which is three times the HCl yield in the present work. However, the present yields for CO and HCl were similar to some in the literature such as the 0.09 HCl yield of Bowes [31] and the 0.045 – 0.13 yield for HCl of Blomqvist et al. [35], who also had a CO yield of 0.04 –0.13 which is similar to the present range in Fig. 6. Hull et al. [24] used the Purser furnace with HCl yields of 0.11-0.15 and CO yields of 0.025 – 0.12, both of which are similar to the present results.

Particle size distributions

Figure 12 shows the particle size distribution as a function of time for the free and restricted ventilation PVC cable fires. For free ventilation there was a nuclei mode peak number at 20 nm and an accumulation mode peak number at 500 nm. The size distribution was more varied for restricted ventilation and there were three size peaks at 20, 200 and 500 nm. After the flame went out the 500 nm peak did not occur but the 20nm nuclei mode was still present at the highest values. For restricted ventilation there was a large variation in the 20 nm nuclei peak particle number, whereas for free ventilation the 20 nm number had a much smaller variation. The 20nm size range is that with the worst health effects [4-8], but all the particles below 50 nm have a health effect [4-8]. It is likely that the 20 nm particle size was contributed to by HCl aerosols from the large concentration of HCl. Fig. 10 shows that HCl peaks later in the fire for free ventilation and this is where the peak accumulation mode particle number occurred. HCl peaked early with restricted ventilation and the 20 nm particles occurred earlier.

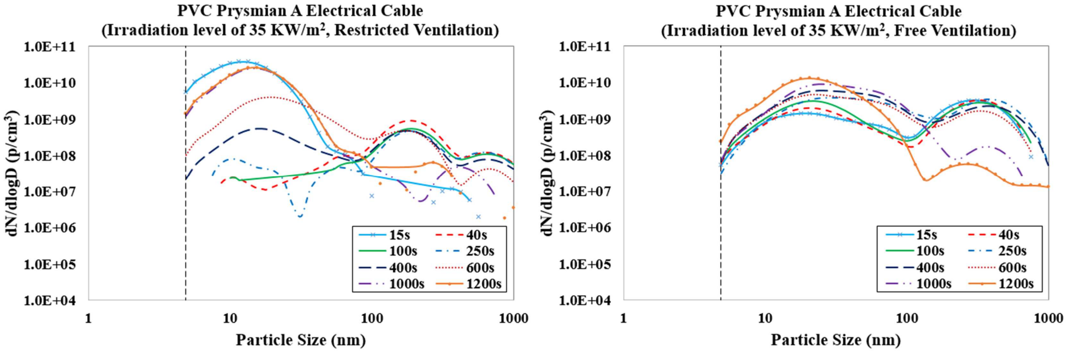

Fig. 12. Particle number distributions for free and restricted ventilation for various times.

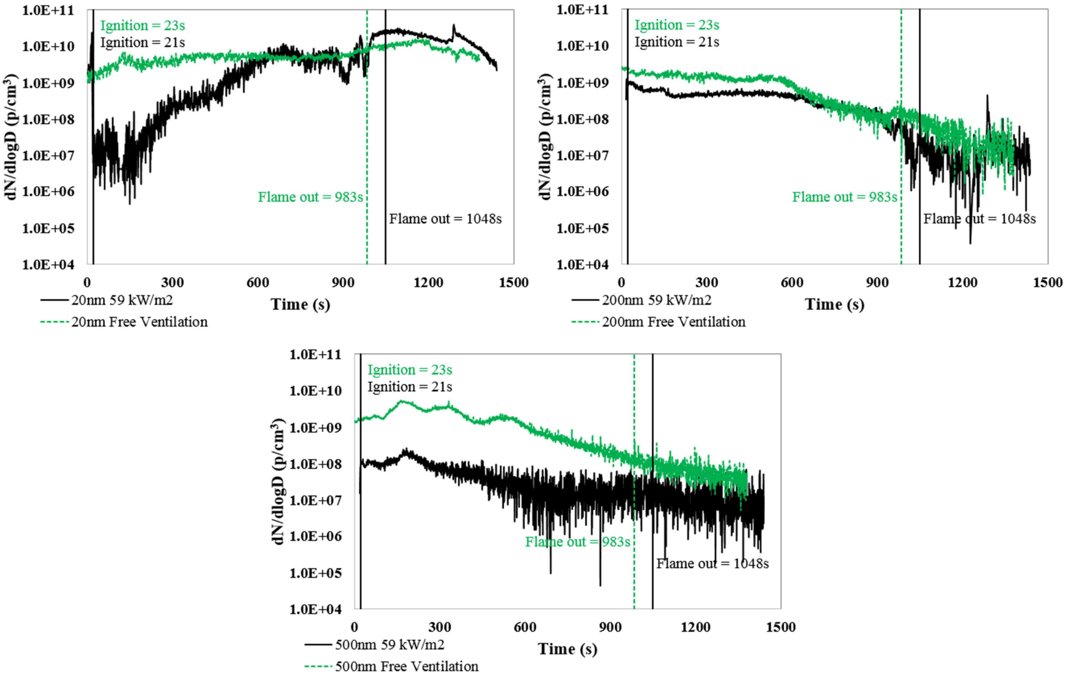

Fig. 13. 20, 200, and 500 nm particle numbers against time for free and restricted ventilation.

Figure 5 shows that up to 500 s the fire was rich for both ventilations and this would lead to high soot formation, so that the 20 nm particles could be Carbon from rich combustion. The free ventilation results in Fig. 5 were richer for the first 400 s and this would produce higher Carbon nuclei particles. In the same period the primary HRR was lower for the free ventilation case and this would produce lower temperatures and lower soot oxidation rates. A feature of the free ventilation results in Fig. 12, which is unusual in combustion size distributions, was the very high number of coarse particles with a peak at 500 nm. This indicates high mass emissions would occur. However, it is the high number of 20 nm particles that would cause the most harm to those exposed to this smoke.

The number of particles at the three size peaks in Fig. 12, 20, 200 and 500 nm, are shown as a function of time in Fig. 13 for free and restricted ventilation. This shows that for all size ranges the free ventilation fire was much higher in particle number for the first 600 s of the fire, where the HRR was highest and the combustion was rich. The 500 nm number was much higher for free ventilation and this may have been due to the late generation of HCl, shown in Fig. 10. Coagulation may have been faster in the absence of HCl vapour condensation, which would occur earlier in the restricted ventilation fire.

CONCLUSIONS

The cone calorimeter, with restricted ventilation and raw gas cone exit toxic gas measurements, is a good test method to access fire materials for gaseous toxicity and particulate emissions. For gaseous species, primary heat release rate and equivalence ratio the difference between free and restricted ventilation was small. However, the release of HCl was quite different with this occurring later after the main HRR period for free ventilation. There were major differences in the particle size distribution and the peak numbers. The free ventilation fire had much high coagulation particle number as well as high 20 nm particle number. The high number of coagulation particles may have been due to the low HCl in the high HRR period of the fire.

REFERENCES

[1] Fire Statistics United Kingdom; Department for Communities and Local Government: London, 2016. http://www.communities.gov.uk/fire/researchandstatistics/firestatistics/firestatisticsuk/, 2018 (accessed 08 Sepember 2018).

[2] B. Sundstrom, Flammability Tests for Cables, in: V.B. Apte (Ed.), Flammability Testing of Materials used in Construction, Transport and Mining, Woodhead Publishing Ltd., Camridge, 2006, pp. 187-199.

[3] R.G. Watt, Grenfell Tower fire - a tragic case study in health inequalities, British Dental J. 223 (2017) 478–480.

[4] A. Violi, Effects of Combustion-Generated Nanoparticles on Cellular Membranes, Combust. Sci. Technol. 188 (2016) 769-775.

[5] C.A. Pope, R.L.Verrier, E.G. Lovett, A.C. Larson, M.E. Raizenne, R.E. Kanner, J. Schwartz, G.M. Villegas, D.R.Gold, D.W. Dockery, Heart rate variability associated with particulate air pollution, Amer. Heart J. 138 (1999) 890-899.

[6] J.S. Lighty, J.M. Veranth, A.F. Sarofim, Combustion Aerosols: Factors Governing Their Size and Composition and Implications to Human Health, J. Air Waste Management Assoc. 50 (2000) 1565-1618.

[7] A. Seaton, D. Godden, W. MacNee, K. Donaldson, Particulate air pollution and acute health effects, The Lancet 345 (1995) 176-178.

[8] A. Peters, H.E. Wichmann, T. Tuch, J. Heinrich, J. Heyder, Respiratory effects are associated with the number of ultrafine particles. Amer. J. Respirat. Crit. Care Med. 155 (1997) 1376-1383.

[9] G.E. Andrews, J. Ledger, H.N. Phylaktou, The Gravimetric Determination of Soot Yields in Enclosed Pool Fires, In: 3rd International Colloquia on Explosions in Reactive Systems, Windermere, 2000.

[10] B. Persson, M. Simonson, Fire Emissions into the Atmosphere, Fire Technol. 34 (1998) 266-279.

[11] P. Andersson, M. Simonson, L. Rosell, P. Blomqvist, H. Stripple, Fire Safety of Up holstered Furniture, SP Report 2003:22, SP Swedish National Testing and Research Institute, 2003.

[12] J. Yu, L. Sun, C. Ma, Y. Qiao, H. Yao, Thermal degradation of PVC: A review, Waste Management 48 (2016) 300–314.

[13] K.-M. Schellerer, T. Kufner, P. Attenberger, F. Riedmiller, M. Bahls, O. Mieden, Polyvinyl Chloride (PVC), Kunststoffe International. 10 (2017) 8–13.

[14] A.W. Coaker, Fire and flame retardants for PVC, J. Vinyl Additive Technol. 2 (2003) 108–115.

[15] S.T. McKennaa, R. Birtles, K. Dickens, R.G. Walker, M.J. Spearpoint, A.A. Stec, T.R. Hull, Flame retardants in UK furniture increase smoke toxicity more than they reduce fire growth rate, Chemosphere. 196 (2018) 429–439.

[16] M.M. Hirschler, Comparison of large and small-scale heat release tests with electrical cables, Fire and Mater. 18 (1994) 61-76.

[17] M.M. Hirschler, Can the Cone Calorimeter be Used to Predict Full Scale Heat and Smoke Release Cable Tray Results from a Full Scale Test Protocol, In: Proc. Interflam, Interscience Comm., London, 2001.

[18] BS ISO 5660-1:2015: Reaction-to-fire tests. Heat release, smoke production and mass loss rate. Heat release rate (cone calorimeter method) and smoke production rate (dynamic measurement). British Standards Institute.

[19] T. Hertzberg, P. Blomqvist, Particle from fires-a screening of common materials found in buildings, Fire and Mater. 27 (2003) 295–314.

[20] J. Goo, Development of the size distribution of smoke particles in a compartment fire, Fire Saf. J. 27 (2012) 46–53.

[21] W.A. Al-Sayegh, O. Aljumaiah, G.E. Andrews, H.N. Phylaktou, PVC Cable Fire Toxicity using the Cone Calorimeter, In: Harada, K. Matsuyama, K. Himoto, K. Nakamura, Y. Wakatsuki, K. (Eds.), Fire Science and Technology– 10th Asia-Oceania Symposium on Fire Science and Technology, pp, 175–182, 2015.

[22] W.A. Al-Sayegh, O. Aljumaiah, G.E. Andrews, H.N. Phylaktou, Wood Crib with PVC Cables: Compartment Fire Toxicity, In: Proceedings of the Eighth International Seminar on Fire & Explosion Hazards (ISFEH8), Eighth International Seminar on Fire & Explosion Hazards (ISFEH8), 2016.

[23] T.R. Hull, K. Lebek, K.T. Paul, Correlation of toxic product yields from tube furnace tests and Large Scale tests, Fire Saf. Sci. 8 (2005) 1059-1070.

[24] T.R. Hull, K. Lebek, M. Pezzani, S. Messa, Comparison of toxic product yields of burning cables in bench and large-scale experiments, Fire Saf. J. 43 (2008) 140-150.

[25] V. Babrauskas, R.H. Harris, E. Braun, B. Levin, M. Paabo, R.G. Gann, The Role of Bench Scale Test Data in Assessing Real-Scale Fire Toxicity, NIST Technical Note 1284, National Institute of Standards and Technology, 1991.

[26] K.W. Flecknoe-Brown, K. Livkiss, P. Van Hees, Experimental and Numerical Investigation on Fire Behaviour of Foam/Fabric Composites, in: Proc. 15th International Conference on Fire and Materials, Interscience Communications Ltd., San Francisco, USA, 2017, pp. 240-253.

[27] PVC Flat Wiring Cables with Bare CPC. https://www.whyprysmian.co.uk/6241Y-_6242Y-_6243Y.pdf, 2018 (accessed 08 Sepember 2018).

[28] Cambustion, DMS500 Fast Particulate Spectrometer with Heated Sample Line High Ratio Diluter User Manual 2011: Cambridge.

[29] D.B. Kittelson, W. F. Watts, J. P. Johnson, On-road and Laboratory Evaluation of Combustion Aerosols Part 1: Summary of Diesel Engine Results, J. Aerosol Sci. 37 (2006) 913– 930.

[30] I. Abdul-Khalek, D.B. Kittelson, F. Brear, The Influence of Dilution Conditions on Diesel Exhaust Particle Size Distribution Measurements, SAE Paper No. 1999-01-1142, SAE International, 1999.

[31] P.C. Bowes, Smoke and Toxicity Hazards of Plastics in Fires", Annals Occupat. Hyg. 17 (1974) 143-156.

[32] F. Laoutid, M. Lorgouilloux, D. Lesueur, L. Bonnaud, P. Dubois, Calcium-based hydrated minerals: Promising halogen-free flame retardant and fire resistant additives for polyethylene and ethylene vinyl acetate copolymers, Polymer Degrad. Stab. 98 (2013) 1617–1625

[33] A.A. Stec, T.R. Hull, Fire Toxicity, 2010 ed., Woodhead Publishing Ltd, Cambridge, 2010.

[34] O. Aljumaiah, G.E. Andrews, A. Jimenez, N.R. Duhoon, H.N. Phylaktou, Fuel volatility effects on pool fires in compartments with low ventilation, In: Fire Safety Science–Proceedings of the Eleventh International Symposium, pp, 331-345, 2014.

[35] P. Blomqvist, Emissions from Fires: Consequences for Human Safety and the Environment, PhD thesis, University of Lund, Sweden, 2005.

Thermal Degradation and Combustion of Plant Protection Products

Borucka M.*, Celiński M., Sałasińska K., Gajek A.

Central Institute for Labour Protection – National Research Institute,
Department of Chemical, Biological and Aerosol Hazards, Warsaw, Poland
**Corresponding author's email: monika.borucka@ciop.pl*

ABSTRACT

In a fire, the plant protection products can produce large amounts of toxic effluents in the smoke. Since most fire deaths and injuries result from inhalation of toxic effluents, knowledge of the amount and type of generated substances is important for fire hazard assessment and investigation. In this study, thermal degradation and combustion of three plant protection products, which are based on: quinoclamine (Product 1); spiroxamine, tebuconazole and triadimenol (Product 2); and tebuconazole (Product 3) were investigated. Cone calorimeter (ISO 5660) was used to measure ignitability and heat release rate. Thermal decomposition of the materials was studied using thermal analysis coupled with the Fourier transform infrared spectroscopy. The steady-state tube furnace (ISO 19700) was used to generate gaseous combustion products. The emitted thermal degradation products were identified by gas chromatography with mass spectrometry.

Among all tested compounds, Product 2 was found to be the most flammable plant protection product. The mechanism of thermal degradation depends on the product type. In fire effluents, different kinds of chemicals were identified, including volatile and semi-volatile compounds including substituted benzenes, aldehydes, aliphatic hydrocarbons and polycyclic hydrocarbons. Most of detected substances are carcinogenic and mutagenic with biological accumulation.

KEYWORDS: Pesticide, cone calorimeter, fire toxicity, gas analysis.

INTRODUCTION

Thermal decomposition and combustion of pesticide as well as plant protection products can occur in different situations. Large amounts of these hazardous substances are handled and stored every day in chemical plants and warehouses as a consequence of their massive use in the agricultural field [1, 2]. It has been reported in the past that fire occurred in a certain number of both of these installations involving large quantities of chemicals [3]. Toxicity, thermal instability and reactivity of pesticides caused several accidents also during the production and transport of these chemicals [4-6]. Another possibility of release the toxic species is the incorrect method of disposal of agricultural waste, for example burning of empty pesticide containers in open fires [7]. Additionally even during the processing of vegetables and foods poisoned by traces of pesticides the thermal degradation products of pesticides can be released [2, 8-10].

Most fire deaths are due to toxic gases, oxygen deprivation and other effects that have been widely referred to as smoke inhalation instead of burns [11]. That's why the smoke toxicity is very important factor and has been considered in the evaluation of fire safety in new fire safety regulation. Moreover the products released during thermal degradation and combustion of pesticide and plant protection products can cause serious airborne pollution, harmful not only to firefighters but also to people living in the surrounding areas [12]. Furthermore, water used by fire fighting,

Proceedings of the Ninth International Seminar on Fire and Explosion Hazards (ISFEH9), pp. 1187-1196
Edited by Snegirev A., Liu N.A., Tamanini F., Bradley D., Molkov V., and Chaumeix N.
Published by Saint-Petersburg Polytechnic University Press
ISBN: 978-5-7422-6498-9 DOI: 10.18720/spbpu/2/k19-107

mixed with these toxic products can contaminate the surface and ground water and cause major environmental pollution affecting the ecosystems [13].

To enable a realistic assessment of the toxicity and environmental impact of compounds, it is clearly important to understand the range and concentrations of chemical species likely to be produced in fires. Currently, the main species of interest for acute effects from exposure to fire effluents are: carbon dioxide (CO_2), carbon monoxide (CO), reduced oxygen (O_2), hydrogen chloride (HCl), hydrogen bromide (HBr), hydrogen cyanide (HCN), hydrogen fluoride (HF), nitrogen oxide (NO), nitrogen dioxide (NO_2), sulphur dioxide (SO_2), formaldehyde (HCHO) and acrolein (C_3H_4O). However this list is not exhaustive. Fire effluents also contain a number of carcinogenic and other chronic toxicants (persistent organic pollutants and polycyclic aromatic hydrocarbons) [14].

While burning behavior is dependent on physical aspects of fire scenario, such as shape and orientation of the fuel, effluent toxicity is most dependent on material composition temperature and oxygen concentration. The generalised development of the fire has been recognised, and used to classify fire growth into stages, from smoudering combustion and early well-ventilated flaming, through to fully-developed under-ventilated flaming [15].

This work presents information on the thermal degradation and combustion processes occurring upon heating of the three plant protection products under air atmosphere. Experimental work consists of thermogravimetric (TG) experiments coupled with differential scanning calorimetry (DSC). Application of the simultaneous thermal analysis (STA) coupled on-line with Fourier transform infrared spectrometry (FT-IR) allows to analyze the released gaseous products. Moreover the steady state tube furnace (Purser furnace, ISO 19700 [16]) has been used specifically to generate toxic products from real fires under different temperature conditions. The emitted species have been identified using gas chromatography with mass spectrometry (GC-MS). To achieve this goal the solid phase microextraction (SPME) was used as a technique which combines sampling and concentrating analyses as well as introducing them to the chromatographic system [17]. Moreover evaluation of flammability of the composites was performed by using the cone colorimeter [18].

MATERIALS AND METHODS

Materials

For the studies, plant protection products commonly used in Poland have been selected. The compositions of materials are shown in Table 1.

Table 1. Information on ingredients of plant protection products

Name	Active Ingredients	Composition
Product 1	Quinoclamine 25-30 %	Quartz (SiO2) 25-30 % Kaolin 10-20 %, Silica amorphous 1-2 %
Product 2	Spiroxamine 250 g/L Tebuconazole 167 g/L Triadimenol 43 g/L	N,N-Dimethyl decanamide >20 % Alkylarylpolyglycol ether >1 and < 25 % gamma-Butyrolactone >1 and< 15 %
Product 3	Tebuconazole 430 g/L	1-octyl-2-pyrrolidone 20-60 % Hydrocarbons, C10-C13, aromatics, <1% naphthalene 5-15 %

Methods

To characterize the fire behaviour, the plant protection products were investigated in the cone calorimeter (Fire Testing Technology Ltd., FTT, West Sussex), which simulated forced-flaming combustion according to ISO 5660 [18]. The specimens, 100 mm x 100 mm in size and placed in an aluminium tray, were tested at a heat flux of 35 kW/m^2. Based on gained results following parameters were estimated: Heat Release Rate – HRR (kW/m^2), peak of Heat Release Rate – pHRR (kW/m^2) time to peak of Heat Release Rate – t-pHRR (s), Maximum Average Rate of Heat Emission – MARHE, Total Heat Release – THR (MJ/m^2), Ignition Time – t_{ig} (s), Total Smoke Release – TSR (m^2), Fire Growth Rate – FIGRA (kW/(m^2·s)).

The Fire Growth Rate (FIGRA) is a very useful parameter that allows to evaluate reaction of tested material to the fire properties. FIGRA is defined as the p-HRR, divided by time during which the maximum value was reached according to the equation:

$$\mathrm{FIGRA} = \frac{\mathrm{pHRR}}{\mathrm{t{-}pHRR}}\,.$$

The thermal decomposition under air were monitored via thermogravimetric analysis and differential scanning calorimetry using a simultaneous thermal analysis (STA 449F3 Jupiter, Netzsch, Germany). The mass of the investigated materials was 10 mg. The heating rate was 10 K/min. Gas analysis was conducted by coupling the STA with a Fourier transform infrared spectroscope (FTIR Tensor 27, Bruker, Germany) via a heated transfer tube. The transfer line tube and the gas cell of FTIR were heated to 250 °C.

Because the different fire conditions can have a significant effect on the effluent produced, the Purser furnace was used to generate gaseous products from real fires. The samples of plant protection products (15 g) in special test specimen boats were delivered into the steady state tube furnace set at 350, 650 or 825 °C. The samples of effluent were taken from the mixing chamber of tube furnace by introducing the SPME device with the fiber to sampling port. The chromatographic separation was achieved with an HP-5 MS fused silica capillary column (30 m × 250 μm × 0.25 μm film thickness) from Agilent Technologies (USA). The oven temperature was initially maintained at 40 °C for 10 min, and then increased to 250 °C at a heating rate of 10 °C/min. Helium at a constant flow rate of 1 ml/min was used as the carrier gas and the split ratio was 10:1. The separated compounds were then analyzed by the mass spectrometer, which was operated in electron ionization (EI) mode at the ionization energy of 70 eV. The mass spectra were obtained from m/z 15 to 350. Chromatographic peaks were identified through comparing the mass ions of each peak with NIST MS Library. On the basis of the NIST library, the highest possibility of product identification was chosen. The chromatographic peak area of a specific compound is correlated linearly with its quantity, and its concentration can be reflected by the peak area ratio. The summed identified peak areas were normalized to 100% and the relative abundance of specific compound can be reflected by its peak area ratio.

RESULTS AND DISSCUSION

Average values of parameters characterizing the behavior of tested plant protection products under the influence of intense radiant heat gained during cone calorimeter measurements were summarized in Table 2.

Based on the date acquired from the flammability test in cone calorimeter it can be deduced that Product 2 was the most flammable plant protection product among all tested compounds. High amount of flammable solvents (~60 % wt.) such as N,N-dimethyldecanamide, gamma-butyrolactone and alkyl/aryl-glycol ethers is responsible for shot t_{ig} and in combination with active agents creates a mixture which exceeds 1000 kW/m^2 during CC test. Such high value of HRR is relatively rare even for highly flammable plastics like polyethylene or epoxy resin with similar size and mass of a sample.

Table 2. Average heat release rate (HRR) and other fire parameters results from cone calorimeter tests for tested plant protection products

Sample	*It*	F_{out}	MARHE	HRR	pHRR	t-pHRR	FIGRA	THR	TSR
	s	s	kW/m^2	kW/m^2	kW/m^2	s	kW/(m^2·s)	MJ/m^2	m^2/m^2
Product 1	43	247	56.5	44.5	126	77	1.65	8.9	312
Product 2	12	163	574	447	1019	68	14.9	66.3	769
Product 3	128	220	98.8	232	493	177	2.79	19.8	658

Presence of spiroxamine with the flashpoint ~140 °C [19], and load of 25 % wt. has also a large impact on flaming process and on the FIGRA value which is almost ten times higher than that reported for Product 1. Based on the composition of Product 1 it is reasonable to assume that all heat emitted during CC test comes from quinclamine, although some parameters like t_{ig}, FIGRA and even HRR are decreased by the overwhelming amount of non-organic compounds (over 70 %) and it's thermal capacity. On the other hand quinoclamine contains chlorine and amine groups. During fire generated ammonium acts as the oxygen diluting agent, and chlorine participates in free radical recombination process in gas phase according to presented mechanism:

- release of chlorine radicals (Cl•):

$R – Cl \rightarrow R\bullet + Cl\bullet$

- generation of hydrogen chloride (HCl):

$RH + Cl\bullet \rightarrow HCl + R\bullet$

- neutralization of energy-reach radicals:

$HCl + H\bullet \rightarrow H_2 + Cl\bullet$,

$HCl + OH\bullet \rightarrow H_2O + Cl\bullet$.

Those properties combined with a high amount of non-flammable compounds are reflected in very low HRR value, although for a mixture containing only 25 % of organic compound Product 1 shows rather high amount of released smoke, Fig. 1.

Product 3 shows the longest t_{ig} from all tested plant protection products and rather low value of HRR. Flashpoint of tebuconazole exceeds 240 °C and has great impact on flammability of tested product. Maximum value of HRR is below 500 kW/m^{2,} THR is three times lower than for Product 2 and it's important to notice that both of this pesticides burn out completely, under testing conditions, leaving no residue.

Analysis of TSR values shows that Product 2 and Product 3 produce similar amount of smoke during CC test. Lower CO production rate for Product 3 corresponds with the HRR values, yet production of CO for Product 3 clearly exceeds Product 2. Lower flame temperature and higher concentration of chloride can, possibly, be explained by these results, although it correlates with production of CO and CO_2 by Product 1.

The thermogravimetric analysis (TGA) and differential thermogravimetric analysis (DTG) of thermal degradation of the plant protection products are shown in Fig. 2.

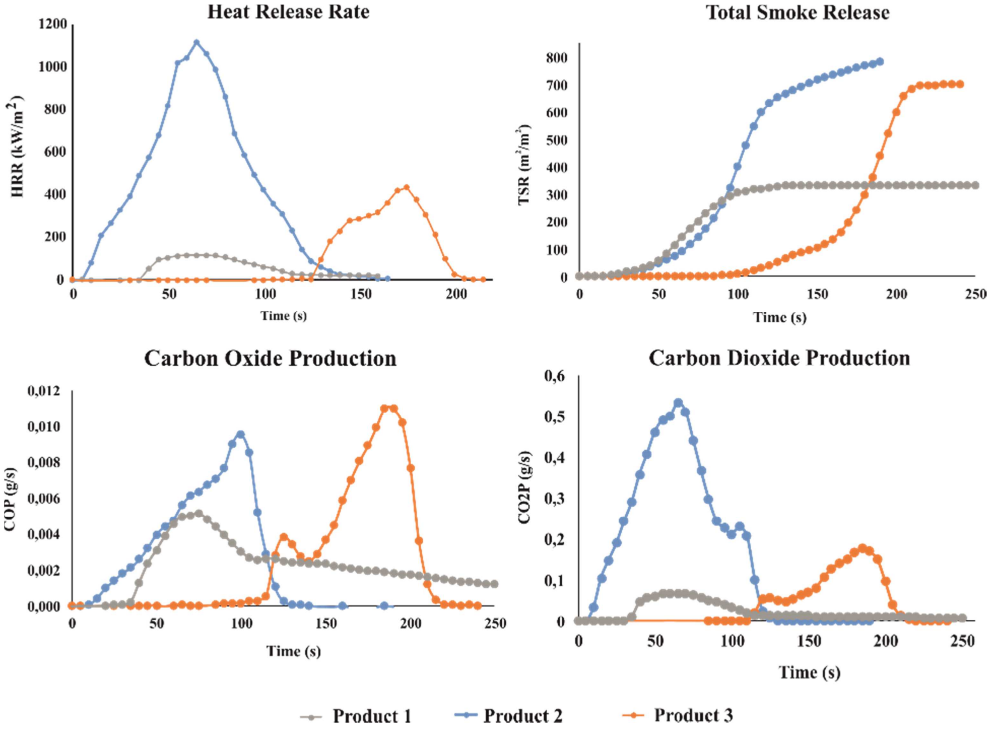

Fig. 1. Graphic representation of HRR, TSR, CO and CO_2 production for tested plant protection products.

The multi-stage degradation process was observed for all tested material. It suggests that the samples exposed to heat in air undergo both thermal degradation and oxidation. The Product 2 and Product 3 began to degrade in lower temperature then Product 1. The mass loss was about ~ 34 % for Product 1, ~47 % for Product 3 and ~ 100 % for Product 2. In case of Product 2 in the first degradation stage to the temperature about 171 °C, the substances present in the plant protection product, such as: spiroxamine, N,N-dimethyl decanamide, triadimenol and tebuconazole, were melted and evaporated. Subsequently, the individual substances were decomposed in several steps, up to the temperature of 590 °C, to form gaseous products. All tested substances were degraded to 600 °C.

Figure 2 presents also IR spectra corresponding to decomposition of the materials. The main product found during thermal degradation of Product 2 was gamma-butyrolactone. This is confirmed by the bands occurring at 1822, 1146, and 1048 cm^{-1}. The same component was also identified in the emitted products during the entire measurement. The IR spectra imply that carbon oxides also present in the volatiles evolved in thermal degradation of Product 2. The main degradation products of Product 3 and Product 1 were carbon oxides (bands at 2360 cm^{-1} associated with asymmetric tensile vibrations of the R branch). Additionally, peaks recorded at temperature 510 °C, may suggest that aliphatic compounds were also present in the gas mixture.

Based on the results obtained using Purser furnace and GC-MS, it was found that the quantity and type of products detected in the fire effluents emitted during thermal degradation and combustion of selected materials strongly depends on experiment conditions (temperature) and composition of the material, Fig. 3. The largest number of species were detected in the samples emitted in conditions representative post-flashover fire (temperature = 825 °C, primary air flow = 2 L/min) for Product 1 and in conditions representative small flaming vitiated fire (temperature = 650 °C, primary air flow = 2 L/min) for Product 2 and Product 3. Unfortunately not all detected compounds have been identified.

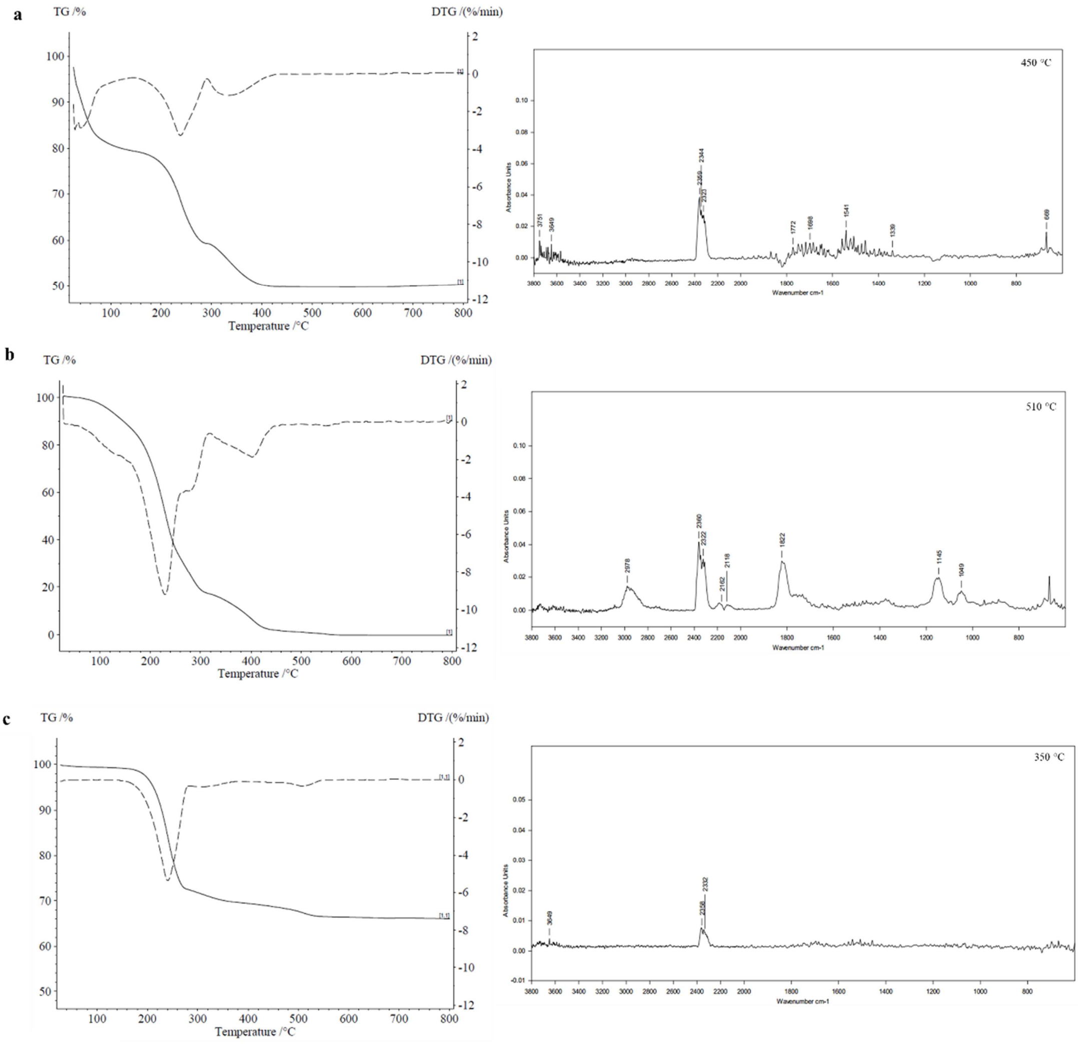

Fig. 2. TG-FTIR results: TG and DTG with corresponding IR spectra for the decomposition steps of (a) Product 3, (b) Product 2 and (c) Product 1.

When Product 1 was tested, the largest number of gaseous products was emitted when the thermal degradation occurred at 825 °C, under-ventilated flaming post flashover. In the emitted gases in the largest amount, substances such as: phthalic anhydride, 4,9-dihydro-1H-naphtho[2,3-d]triazole-4,9-dione, 6-chloro-2,3dihydrofuro-(2,3-b)-quonoline, 1H-inden-1,3(2H)-dione, benzonitrile and m-chloroamine were presented.

In contrast, in the mixture of fumes and gases emitted during decomposition of the Product 2 at 350 °C were present ingredients such as butyrolactone, N,N-dimethyldecanamide and spiroxamine.

The presence of 4-(1,1-dimethylethyl)cyclohexanone means that some of the spiroxamine has already decomposed under the test conditions. However, the main substances present in the gases samples were: 4-chlorobenzaldehyde, 1-chloro-4-ethenylbenzene, naphthalene, 1-chloronaphthalene, acenaphthylene and 2-chlorohydrocinnonitrile. When the degradation took place in 650 °C, many polycyclic aromatic hydrocarbons (naphthalene, biphenyl, acenaphthylene) and chlorine derivatives of aromatic compounds (1-chloronaphthalene, 1-(chloromethyl)-naphthalene) were identified. In gases emitted the post-flashover fire mainly polycyclic aromatic hydrocarbons were detected. However, butyrolactone and N,N-dimethyldecanamide proved to be very stable components and were still present in analyzed gases and fumes.

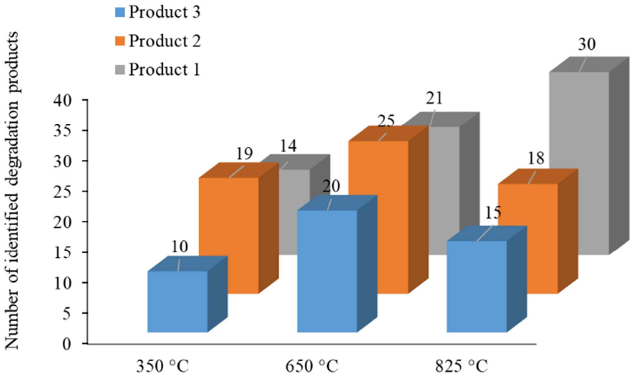

Fig. 3. The number of thermal degradation products identified in fire effluents when the decomposition occurred at 350 °C, 650 °C and 825 °C.

Decomposition of Product 3 resulted in the formation of 1-chloronaphthalene – the main thermal decomposition product of tebuconazole. In considerable amounts, 1,2-propanediol and 4-(1,1-dimethylethyl)-cyclohexanone were detected in emitted gases and smoke. In smaller amounts, substances such as 1-chloro-4-ethenylbenzene, 4-chlorobenzonitrile, naphthalene, 1-(4-chlorophenyl)-ethanone, acenaphthylene and 2-chloro-hydroxyammonitrile were present in the smoke emitted during thermal degradation of Product 3. These compounds were also detected in gas and fume samples emitted during decomposition of the active substance present in this preparation (-tebuconazole).

Based on the obtained results, it can be stated that during the combustion and thermal degradation of plant protection products, significant quantities of hazardous substances are released. At the same time in the United States, the Emergency Management Issues Special Interest Group (EMI SIG) state that "Protective Action Criteria (PACs) are the essential components for planning and response to uncontrolled releases of hazardous chemicals. These criteria, combined with estimates of exposure, provide the information necessary to evaluate chemical release events for the purpose of taking appropriate protective actions. During an emergency response, these criteria may be used to evaluate the severity of the event, to identify potential outcomes, and to decide what protective actions should be taken"[20]. PAC values are based on the following exposure limit values:

- Acute Exposure Guideline Levels (AEGL) values published by the U.S. Environmental Protection Agency (EPA),
- Emergency Response Planning Guideline (ERPG) values produced by the American Industrial Hygiene Association (AIHA),
- Temporary Emergency Exposure Limit (TEEL) values developed by SCAPA.

AEGL, ERPG and TEEL benchmark values are not available for all chemicals as the clinical effects are still an active research area. Consequently, when defining PAC values the following procedure is followed. Use AEGLs (including final or interim values) if they are available. If AEGLs are not available, use ERPGs. If neither AEGLs or ERPGs are available, use TEELs.

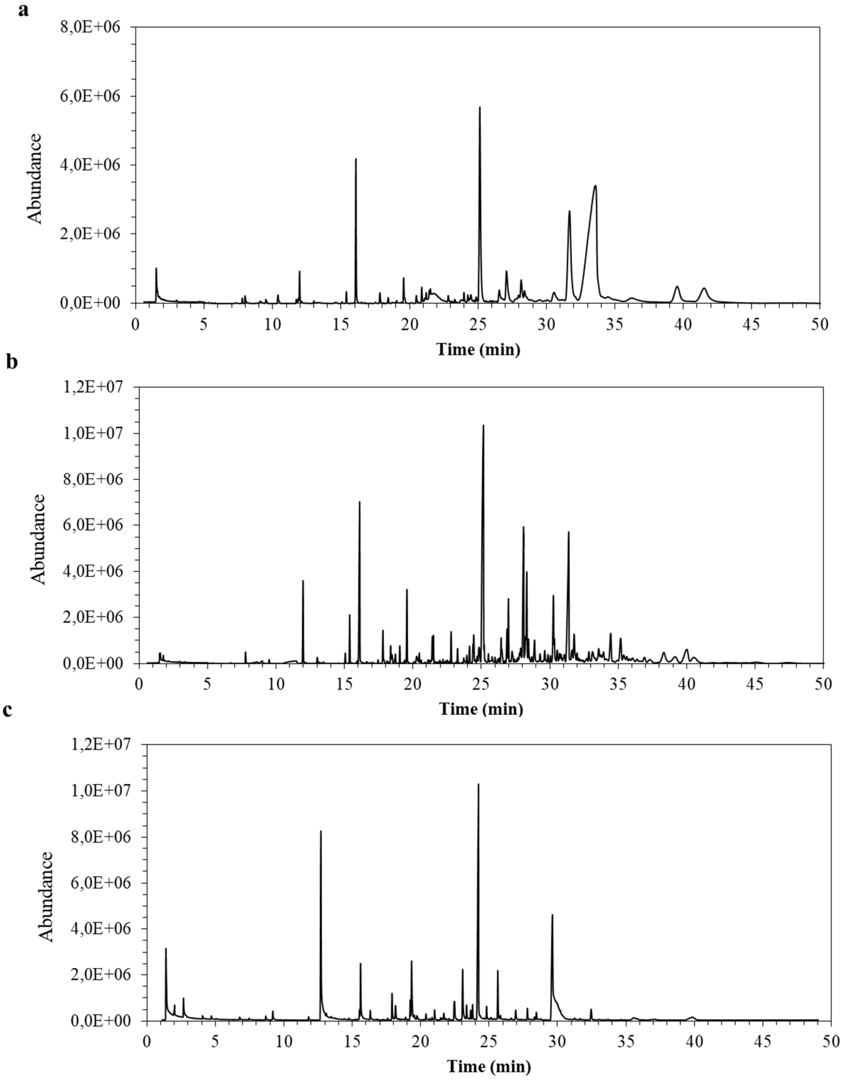

Fig. 4. Chromatograms of products emitted during thermal degradation of Product 1 (a), Product 2 (b) and Product 3 (c). The decomposition of Product 1 occurred at 850 °C, of Product 2 and Product 3 at 650 °C.

There are three levels of PAC value (1 to 3) where each successive value is associated with an increasingly severe effect from a higher level of exposure. Each level is defined as follows:

PAC-1: Mild, transient health effects.
PAC-2: Irreversible or other serious health effects that could impair the ability to take protective action.
PAC-3: Life-threatening health effects [20].

In Table 3, there are presented the value of PAC for the main organic substances that have been detected and identified in mixtures of gases and fumes emitted during the thermal decomposition and combustion of selected plant protection products. Unfortunately, the values of these parameters are not available for all detected chemicals, because clinical effects are still an active area of research.

Table 3. PAC-1, PAC-2, PAC-3 values for the main organic substances detected in mixtures of gases and fumes emitted during the thermal decomposition and combustion of plant [21]

Identificated substance	CAS	PAC-1 (mg/m^3)	PAC-2 (mg/m^3)	PAC-3 (mg/m^3)
1-chloronaphthalene	90-13-1	4,6	51	310
1,2-propanediol	57-55-6	30	1300	7900
acenaphthylene	208-96-8	10	110	660
benzonitrile	100-47-0	2.4	26_A	80_A
biphenyl	92-52-4	5.5	61_A	1900
butyrolactone	96-48-0	3.6	39	310
naphthalene	91-20-3	79	430	2600
phthalic anhydride	85-44-9	18	56	10000

PAC values marked with a subscript "A" correspond to 60-minute AEGL values.

CONCLUSIONS

It was found that Product 2 is the most flammable plant protection product. This is probably due to the presence of large amount of flammable solvents such as N,N-dimethyldecanamide, gamma-butyrolactone and alkyl/aryl-glycol ethers. All the tested plant protection products emit significant amounts of gases and fumes during combustion and thermal decomposition. Different chemicals, including volatile and semi-volatile compounds, were identified in the volatiles which appear to be very toxic and hazardous. It is worthy of note, that real fires may yield even more toxic products than the amount generated in the small-scale laboratory fire testing equipment.

ACKNOWLEDGEMENT

This paper has been based on the results of a research task carried out within the scope of the fourth stage of the National Programme “Improvement of safety and working conditions” partly supported in 2017–2019 — within the scope of research and development — by the Ministry of Science and Higher Education/National Centre for Research and Development. The Central Institute for Labour Protection – National Research Institute is the Programme’s main coordinator.

REFERENCES

[1] R. Andreozzi, G. Ialongo, R. Marotta, R. Sanchirico, The thermal decomposition of dimethoate, J. Hazard. Mater. B:64 (1999) 283–294.

[2] O. Senneca, F. Scherillo, A. Nunziata, Thermal degradation of pesticides under oxidative conditions, J. Anal. Appl. Pyrolysis 80 (2007) 61–76.

[3] V. Christiansen, Combustion of some pesticides and evaluation of the environmental impact, J. Loss. Prevent. Process Ind. 71 (1994) 39–48.

[4] V. Cozzani, M. Smeder, S. Zanelli, Formation of hazardous compounds by unwanted reactions in industrial accidents, J. Hazard. Mater. 63 (1998) 131–142.

[5] G. Koller, U. Fischer, K. Hungerbühler, Assessing safety, health, and environmental impact early during process development, Ind. Eng. Chem. Res. 39 (2000) 960–972.

[6] R. Sanchirico, G. Pinto, A. Pollio, M. Cordella, V. Cozzani, Thermal degradation of Fenitrothion: Identification and eco-toxicity of decomposition products, J. Hazard. Mater. 199–200 (2012) 390–400.

[7] C.A. Damalas, G.K. Telidis, S.D. Thanos, Assessing Farmers' Practices on Disposal of Pesticide Waste after Use, Sci. Total. Environ. 390 (2008) 341–345.

[8] A.J. Holden, L. Chen, I.C. Shaw, Thermal Stability of Ogranophosphorus Pesticide Triazophos and Its Relevance in the Assessment of Risk to the Consumer of Triazophos Residues in Food, J. Agric. Food Chem. 49 (2001) 103–106.

[9] R.K. Juhler, Supercritical fluid extraction of pesticides from meat: a systematic approach for optimization, Analyst 123 (1998) 1551–1556.

[10] M. Sankowska, A. Gajek, M. Celiński, K. Sałasińska, Determination of gaseous products of thermal degradation of thiram, J. Therm. Anal. Calorim. 128 (2017) 1639-1647.

[11] C.M. Jiao, C.J. Zhang, J. Dong, X.L. Chen,, Y. Qian, S.X. Li, Combustion behavior and thermal pyrolysis kinetics of flameretardant epoxy composites based on organic-inorganic intumescent flame retardant, J. Therm. Anal. Calorim. 119 (2015) 1759-1767.

[12] L. Smith-Hansen, K.H. Jogensen, Characterisation of fire products from organophosphorus pesticide using the DIN 53436 method, J. Loss. Prevent. Process Ind. 6 (1993) 227-232.

[13] G.T. Atkinson, S.F. Jagger, Exposufe of organophosphorus pesticides to turbulent diffusion flames, J. Loss. Prevent. Process Ind. 5 (1992) 271-277.

[14] R. Fardell, E. Guillaume, Sampling and measurement of toxic fire effluent, in: A.A. Stec, T. R. Hull (Eds.), Fire Toxicity, Woodhead Publishing Limited, 2010, pp. 385-422.

[15] A.A. Stec, T.R. Hull, D.A. Purser, J.A. Purser, Fire toxicity assessment: Comparison of asphyxiant yields from laboratory and large scale flaming fires, Fire Saf. Sci. 11 (2014) 404-418.

[16] ISO/TS 19700:2007, Controlled equivalence ratio method for the determination of hazardous components of fire effluents, International Organization for Standardization, Geneva, Switzerland.

[17] P. Mark, L. Sandercock, Fire investigation and ignitable liquid residue analysis-a review: 2001-2007, Forensic Sci. Int. 176 (2008) 93-110.

[18] ISO 5660-1: 2000, Reaction-to-fire tests - Heat release, smoke production and mass loss rate -- Part 1: Heat release rate (cone calorimeter method), International Organization for Standardization, Geneva, Switzerland.

[19] http://www.molbase.com/en/msds_118134-30-8-moldata-475923.html

[20] Protective Action Criteria for Chemicals - Including AEGLs, ERPGs, & TEELs. Emergency Preparedness. The Emergency Management Issues Special Interest Group (EMI SIG), Retrieved 3 February 2012.

[21] U.S. Department of Energy, https://sp.eota.energy.gov/pac/Search

Part 7. Fire Safety Engineering

Detection. Suppression

Addressing the Problem of Poor Gas Leak Detection Rates on UK Offshore Platforms

Hilditch R.[1,*], **McNay J.**[2]

[1]WSP, Fire Engineering, Brisbane, Queensland, Australia
[2]Micropack (Engineering) Ltd., Aberdeen, Scotland, UK
**Corresponding author's email: ryan.hilditch@wsp.com*

ABSTRACT

On offshore installations the successful detection of an uncontrolled release of flammable gas is one of the last lines of defence against fire and explosion events. A brief analysis of UK continental shelf (UKCS) offshore hydrocarbon release (OHR) statistics during 1992-2015 shows that an appreciation of performance of *currently installed* gas detection arrangements is of paramount importance, since almost half (48.5%) of the recorded accidental gas releases were apparently not detected by the fixed gas detection systems in place. Detection results for experimental, simulated gas leaks are compared with the offshore statistics finding that the experiments demonstrate ~97% successful detection rate, highlighting the disparity between research and real offshore experience. The experimental simulations are conducted for the traditionally recommended target gas cloud (TGC) detector arrangement at 5 m spacing. We have reasoned that such experimental work is of limited benefit if the same detector approach is not applied offshore. No research has investigated this issue or considered the impact of actual detector layouts upon the detection performance statistics. We have evaluated 27 real offshore gas detector layouts from 18 facilities and found that the TGC approach is present in less than 50% of cases and less than 50% of those achieve typical coverage targets. This is a simple yet important finding previously unaddressed in industry or in literature. In addition, a preliminary review of the statistics demonstrates little or no evidence to corroborate prevailing industry anecdote that low overall detection is due to the high number of small leaks which are not the true target of the detection system. We recommend that detector layouts be submitted by operators during hydrocarbon release reporting so that this missing link in the analysis of the performance of offshore detection can be fundamentally understood, and the issue of detection performance can finally be addressed.

KEYWORDS: Gas detection, hydrocarbon release, target gas cloud, offshore statistics.

INTRODUCTION

On offshore installations the successful detection of an uncontrolled release of flammable gas is one of the last lines of defence against fire and explosion events. Early detection can mitigate a fire or explosion event before it occurs and control actions, initiated automatically or manually following confirmed detection, can be used to trigger emergency shutdown (ESD) before the loss of inventory reaches a critical volume presenting a significant potential for escalation. A range of location, propagation, pressure, orifice size and wind conditions may be modelled and evaluated using appropriate computational models (utilising CFD), however analysis of probable gas dispersion scenarios is not a matured process and essentially no guidance exists for the purpose of defining a standardised, repeatable and industry-wide procedure.

The traditionally adopted *target gas cloud* (TGC) approach has been to limit the undetected gas cloud size of any theoretical leak to a volume which should not create a damaging overpressure if ignited. Knowledge of the performance of this approach with regard to real gas leak events is

Proceedings of the Ninth International Seminar on Fire and Explosion Hazards (ISFEH9), pp. 1198-1209
Edited by Snegirev A., Liu N.A., Tamanini F., Bradley D., Molkov V., and Chaumeix N.
Published by Saint-Petersburg Polytechnic University Press
ISBN: 978-5-7422-6498-9 DOI: 10.18720/spbpu/2/k19-26

extremely limited. A small body of literature evaluating the performance of a 5 m-TGC arrangement in a simulated offshore module exists [1, 2], however in order to relate the results of those studies to real world performance, the assumption is required that all installations in the UK North Sea have a 5 m-TGC arrangement in place, as per the traditionally adopted guidance. The primary goal of this paper is to evaluate the validity of this critical assumption.

A brief analysis of UK continental shelf (UKCS) offshore hydrocarbon release (OHR) statistics [3, 4] during 1992-2015 shows that the question of performance of *currently installed* gas detection arrangements is essential, since almost half (48.5%) of the recorded accidental gas releases were apparently not detected by the fixed gas detection system. While leaks (minor/significant/major) have decreased over the 22-year period, the detection rate by fixed gas detection has also decreased with time. Significant leaks in 1993 were detected at a rate of ~70% but have averaged ~50% over the last 15 years. Minor leaks have dropped from ~60% in 1993, averaging ~38% over the last 10 years. The number of major leaks is arguably too few to be statistically significant in this sense, yet is still numerous enough to cause concern. The Health & Safety Executive (HSE) in the UK recently publicised their concerns [5] over what was described as “perilous” gas leak trends in recent years. It is common for practitioners to reference a 50-60% gas leak detection rate, [6] for example, however we can find no concerted efforts to explain this low detection success rate in the published literature. Within industry we have consistently witnessed the propagation of typical, anecdotal explanations with no apparent evidence. A common example is that the whole OHR data is skewed by many undetected small leaks which are not in fact the target of a fixed detection system. We have documented a preliminary review of some of the OHR data which possibly could support these claims to see if corresponding evidence can be uncovered.

An evaluation of 27 actual offshore gas detector layouts has been undertaken to determine if the traditional TGC approach is commonly applied offshore as generally assumed. This is critical for two reasons: (1) efforts to address the poor offshore gas detection rate by improving the TGC approach detection rate [2] are only of benefit if this methodology is commonly applied offshore, and (2) any attempt to explain the poor offshore gas detection rate without knowledge of the gas detector layout in each leak case provides no context and an incomplete analysis. These issues have not been addressed in industry or in the literature and are critical to understanding and improving the apparently poor detection rate.

The authors have visited over 40 UK offshore platforms and reviewed detection strategies for over 150 facilities globally. This study was conceived out of the evident disconnect we observed between industry dialogue and gas detection as applied offshore. We aim to shed light on fundamental issues previously unaddressed, provide direction for further critical analysis and conclude with a simple solution for acquiring a large set of actual detector arrangement data to allow the problem of poor gas leak detection in the UKCS to be seriously addressed for the first time.

BACKGROUND: INDUSTRY AND SCIENTIFIC LITERATURE

Origins of the target gas cloud methodology

In 1993 the UK Health & Safety Executive published a report [7] reviewing the results of the available gas explosion behaviour studies of the time, which were mainly conducted throughout the 1980s. The review concluded that a 6-m diameter methane or propane cloud, when ignited by a point source did not achieve flame speeds greater than 100 m/sec (methane) and 125 m/sec (propane). To allow for realistic compromises during design and construction, oil and gas operators who would use this approach opted to specify a ‘design’ detector spacing of 5 m thus adding a factor of safety such that if practitioners slightly relaxed the positioning rule, the 6 m parameter from the experimental work should still be met. The approach of targeting a specific volumetric gas cloud by installing detectors at a particular spacing was subsequently adopted into several major-operator guidance documents globally. Commonly 5 m is the target, but variations have been adopted depending on the operator and the location across the facility.

Locating gas detectors: industry guidance

Standards and guidance documents provide relatively little information regarding the number and placement locations of gas detectors for offshore facilities affording the engineer a great deal of latitude but simultaneously requiring suitable justification and verification of the final approach. Instead, guidance on calibration and testing and technology type / installation is prominent. A non-exhaustive list of examples includes API 2001 [8], CSA 2001 [9], ISA 2003 [10], ISO 1999 [11], UKOOA 1995 [12], UKOOA 2003 [13] and more generally in PFEER 1995 [14]. The stipulation that detector layout design should be someway justified with reference to dispersion/hazard analyses is evident in HSE 2001 [15], IEC 2007 [16] and NORSOK 2008 [17] as well as in some oil operator group practices and company-wide fire and gas philosophy/guidance documents. A cautionary note on boundary condition considerations for dispersion modelling based on real events has been presented [18]. Subsequently, ISA TR84.00.07 [19] describes to an extent, an approach incorporating dispersion analysis data into the gas detector placement study. It is important to understand that the guidance detail provided in operator/oil company philosophies regarding fire and gas detection ranges from specific spacing requirements directly or loosely based upon the findings from [7], to the generic requirement that detector layout should be designed in reference to the relevant project fire/hazard analysis. Overall, the level of design detail provided is inconsistent from company to company. The risk here is that the use of rules of thumb and prescriptive targets is retained whilst a fundamental understanding of the original intent of the selection is not.

It is commonly discussed within industry that, historically, gas detectors were placed based on the experience or intuition of the relevant project engineers. Fire and Gas (F&G) mapping is a study which is used to demonstrate the theoretical performance of a gas (or flame) detection arrangement based against a set of pre-defined performance targets and has become increasingly prominent within the industry. F&G Modelling software programs have remained proprietary in-house tools, however. To this end a few authors [20-24] have published in the scientific literature alternative and theoretical approaches to designing and justifying gas detector layouts for offshore process/production modules generally based on data from a set of dispersion scenarios analysed for each case, which may not be reflective of what standard practice in the industry consisted of.

Risk-based detector layouts using dispersion modelling

Within industry at present, the concept approach for risk-based gas detection derived from analysis of a set of credible gas leak simulations is burgeoning. The detector layout is optimised based upon the presence-probability of detectable gas concentrations following a large number (10^2-10^4) of computational leak simulations. Benavides-Serrano et al. [25] represents a rare published work directly comparing the detector requirement of a TGC layout with that of various optimisation approaches to detector placement using a dataset of computational fluid dynamics (CFD) gas leak simulations [26, 27]. The results are compared with a TGC layout of point gas detectors (PGDs). It is clearly demonstrated that the performance of such an arrangement is a function of the number and type of leak scenarios modelled. A decrease in performance was demonstrated when an optimised arrangement based upon a randomly selected 75% of total leak scenarios was then tested against the remaining 25% of simulated leak scenarios. This confidence factor is critical for procedural validation as the notion of designing detector layouts based upon a finite number of leak scenarios becomes more common.

Of great concern, however, is the study's conclusion that the TGC approach performed poorly and in some cases was the worst of all trialed approaches. This can be traced to the use of only PGDs and the elevation of implementation (12.5 m) of the detector grid. Of great further interest, therefore, would be the repetition of this analysis with a TGC layout positioned at a reasonable elevation within the context of the module and local structures, and in relation to specific hazards. The inclusion of open-path gas detectors (OPGD) in the TGC approach would also be of great interest for practical purposes since (based on major operator guidance) one OPGD *could* replace up to 13 PGDs in an offshore module, potentially providing greater detection coverage while significantly reducing the detector count, unit and cabling requirements as well as installation and long-term maintenance burden.

Literature on TGC performance

Where the 1993 HSE report [7] set a baseline guide, further work [1, 2] was conducted performing a sensitivity analysis of the 5 m-TGC approach to a range of simulated leak scenarios for offshore modules. These papers are of great relevance since they represent rare published literature attempting to evaluate the theoretical performance of the traditionally recommended approach to flammable gas detection. Importantly, the detector layout is in-line with how a TGC layout might typically be designed for a congested offshore module and the results are strongly juxtaposed with those reported by [25].

In Kelsey et al. [1] previous data from a joint-industry-project (JIP) on gas dispersion/concentration in a simulated offshore module was overlaid with a detection arrangement based on 5 m-target within the module, utilising infra-red (IR) PGDs, catalytic PGDs and IR OPGDs. From a range of leak scenarios time to detection was evaluated for each case. The results are discussed in detail in the following section.

Comparison with offshore statistics

The Health & Safety Executive (HSE) in the UK publishes an Offshore Hydrocarbon Releases (OHR) database [3-4] covering approximately the last 22 years (Oct 1992-Dec 2015) of release statistics from UK Continental Shelf (UKCS) facilities. Updated statistics for 2015-2016 have more recently been published [28], however, some of the data-capture categories relating to detection have been amended since the previous data were published so we will focus on the 1992-2015 results [4]. Statistics from 2001-2008 have previously been reviewed [3] using partial and full datasets with general focus on leak frequency for significant and major releases, and to review the use of the dataset to inform quantitative risk assessments (QRAs). Difficulties with linking offshore leak statistics to actual experience of operators is discussed in detail elsewhere [29]. Kelsey et al. [1] produced results which may be compared with the offshore hydrocarbon release statistics [4]. The JIP release data (that [1] is based upon) are biased toward larger release rates (commonly 10 kg/s, to align with the lower-bounding definition of a “major” leak) [3,4], however, the vast majority of releases were detected when the leak size corresponded with the significant category. This makes comparison for individual categories difficult since an offshore leak might be categorised at time of detection or considering total release quantity. Table 1 presents those data for the OHR database [4] and the study by Kelsey et al. [1]. It was demonstrated by Kelsey et al. [1] that the 5 m-TGC layout had an excellent detection rate, detecting on average 97% (of 64 cases) for major and significant releases (all leaks detected by the first detector when the leak size corresponded to significant, with 70% growing to major) compared to 53.8% (of 1409 significant cases) successfully detected from the offshore statistics [4]. 3% of simulated releases were not detected due to (1) a lack of buoyancy following horizontal releases which did not rise to the elevation of the lowest detectors at 3.9 m and (2) smaller releases which did not result in gas clouds of detectable concentrations. This information supports the premise that the TGC results appeared poorer in [25] because of the inappropriate detector placement. Sufficient data to allow direct comparison are not provided in [25]. It is notable from the offshore statistics that detection success rates appear to improve with increasing severity. It seems credible, therefore, that actual detection performance offshore is *to some extent* a function of the leak mass. However, there are several boundary conditions that have some level of influence, and this is clear since even the largest leaks (major approximately 10^3 - 10^6 kg) are only detected in ~ 64% of cases. It is critical to note that direct comparison of the simulated data with the offshore statistics also requires the assumption that all offshore installations have utilised a 5 m-TGC detector layout as per the simulations.

Table 1. Gas leak distribution and detection – Offshore statistics [4] vs. simulated [1]

Leak Category Distribution			**Leaks Detected**		
Type	Offshore stats [4]	Simulated [1] (final release size)	Type	Offshore stats [4]	Simulated [1] (at detection)
Major	5.8% (n = 152)	70% (n = 45)	Major	63.8% (n = 97)	N/A
Significant	53.8% (n = 1409)	30% (n = 19)	Significant	54.6% (n = 770)	97% (62 of 64)
Minor	40.4% (n = 1058)	N/A	Minor	45.5% (n = 482)	N/A
Total	2619	64	Weight Avg	51.5% (n=1349)	97%

This is underlined by Kelsey et al. [2] where the results from [1] are built upon and the potential for improvement of the 5 m-TGC performance is investigated. One possibility attributing to the offshore detection results is that the environmental conditions offshore are typically more severe than in the simulated tests thus reducing detection performance of the offshore systems. It is noted, however, that when gas leaks are quickly diluted and dispersed by weather a reduction in potential for escalation is typically also true. Regardless, an average detection rate of 51.5% by dedicated, fixed gas detection systems in high hazard/high consequence sites is concerning, and a better understanding of causal factors is imperative. It is noted that these low detection rates are often cited in industry literature without any further explanation, and no work appears to have been undertaken to provide context for such statements.

INVESTIGATION OF COMMON INDUSTRY HYPOTHESIS

The following section presents an introductory evaluation on the validity of a common industry hypothesis as to why detection rates are so low. There appears to be no precise evidence of validation of the hypothesis in industry literature or scientific literature. A detailed review is required, however this is outside the main scope of this paper and will be completed in future work. It would be preferable if this hypothesis were true as it would conclude that offshore gas detection is in fact more effective than current statistics suggest. If it cannot, however, clearly be demonstrated to be true, then simply assuming its validity is irresponsible and dangerous and prevents the pursuit of a fundamental understanding of the causes of poor detection performance.

Evaluation of hypothesis

The smaller the leak, in theory, the more difficult it is to detect with fixed detection, and based on this principle it is often cited that the reason the detection statistics are poor is because the data are skewed by many undetected small leaks which are not in fact the target of a fixed detection system. It is true that the philosophy of the TGC approach is to target gas clouds once they reach critical volume (and concentration) and that smaller leaks are not the target. Actual detection data describe a more complex landscape, however. It is true that failure to detect increases as the leak category diminishes, that is to say major, significant and minor leaks go undetected in 36.2%, 45.4% and 54.4% of cases, respectively. Note that there is only a 10 point difference in detection success for significant and minor leaks. Detection rates between categories are relatively comparable and do not appear, in principle, significant enough to support the skewed data theory. Each gas leak category occurrence accounted for the percentage of gas leaks as follows - sig (53.8%), minor (40.4%) and major (5.8%). Furthermore, undetected significant gas leaks accounted for 50.3% of all undetected gas leaks, where undetected minor gas leaks account for 45.4% of all undetected. Even if we take the minor detection category out of the equation altogether, there still remains an average detection rate for significant and major leaks of 55.5%. This is a small improvement on the 51.5% detection rate for all categories combined. Based on this simple observation, it is clear that the minor detection rate is comparable with the significant detection rate and no evidence of skewing is yet apparent. An in-depth multi-variable analysis of all detection rate causal factors is out with the scope of this paper but we would like to lay the ground work here briefly.

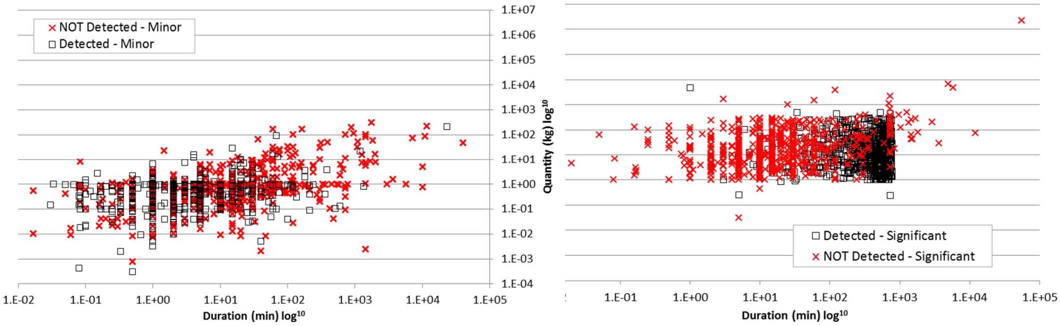

(a) (b)

Fig. 1. (Estimated) leak quantity (kg) vs. leak duration (min) for (a) minor leaks and (b) significant leaks.

Exploring the actual data further, Fig. 1 shows the *detected* and *not detected* minor and significant leak data when the (estimated) leak quantity is compared with leak duration. Figure 1(a) demonstrates the general trend, as might be expected, that leak quantity and leak duration are positively correlated. Perhaps counter-intuitively, however, the detected minor cases tend to occupy the lower end of the quantity/duration data (<10 min) meaning that in general the smaller minor leaks tended to be more commonly detected by the gas detection system. By contrast, Fig. 1(b) shows that those detected significant leaks corresponded almost exclusively to leak durations greater than 90 minutes and the vast majority of undetected leaks ranged from 1 to 90 minutes. It is therefore true that smaller significant leaks were overwhelmingly not detected despite commonly lasting for significant periods of time. We note that leak quantity vs. leak pressure and hole diameter data have also been reviewed (but are not presented here) and are oriented more similarly to Fig. 1(b) and do not demonstrate intuitive correlations as seen in Fig. 1(a). Detected and undetected leaks are equally distributed across the range of leak pressures for both minor and significant leaks. Similarly, detected and undetected leaks are also roughly equally distributed across the range of leak orifice diameters for minor leaks. However, for significant leaks larger hole diameter leaks are almost exclusively not detected and smaller hole diameter leaks are almost exclusively detected. The data appear unnatural when plotted. Major leak data are more evenly distributed for all categories described so we suggest that the reporting practices across each category may need to be reviewed for evidence of impact upon global results. The data tell a complex story, which is nuanced by the many variables including human decision-making when reporting on leak event details - the inherent variability of which is unaccounted for in the statistics. Nevertheless, a preliminary review of the broad statistics does not show recognisable evidence in support of the hypothesis. We have also found no evidence to support the hypothesis that *the majority of* *undetected leaks occurs during manned operations and are therefore detected manually before the gas detection system is triggered*. This evaluation will be included in a future publication.

ANALYSIS OF ACTUAL OFFSHORE DETECTOR LAYOUT DATA

An analysis of 27 actual offshore gas detector layouts is presented with the intent of determining if the TGC approach is commonly applied offshore as generally assumed, and determine if it is reasonable to consider generally the detector layout to be a constant across facilities or whether significant variation is apparent. The latter implies that the impact of detector layout upon detection rates represents an unknown variable that presents a problem for the analysis of offshore gas leak detection rates.

When undetected gas leaks do occur offshore, rarely are the results of a detailed investigation shared in order that industry knowledge can be improved. Therefore, research that seeks to evaluate a TGC layout with the goal of improving offshore gas detection performance, actually has very little basis in this context. A more fundamental line of questioning might be: What form do typical offshore gas detection arrangements take? What was the basis for their design? And, how do they perform when subjected to real boundary conditions?

Investigation parameters and assumptions

An evaluation of typical gas detector layouts in hydrocarbon processing areas on 18 fixed platforms in the UKCS was carried out in order to attain a sample of real detector layouts. The sample size represents approximately 7.5% of operational UKCS assets, which is statistically small. However, as far as can be discerned no other study with the same goal has been published so far. On that basis alone, the results presented here should be of interest, at the very least, as a starting point for further discussion and research. The parameters and assumptions of the study were as follows:

- Layouts were chosen at random from the available information. A range of major and minor operators were included. F&G detection drawings were typically dated 2008-2014.
- Site information and operator and platform details cannot be disclosed. We feel that the critical lack of knowledge and absence of any similar study far outweighs this limitation to transparency.
- Process / wellbay areas with significant physical congestion (>0.3) were targeted since in such locations the (5 m) TGC approach is recommended by numerous operators.
- *Coverage factor* is a quantified output that states what fraction of the module total area is provided gas detection coverage based on a 5 m-TGC requirement.
- Module total heights were unavailable, and detector elevations were often unavailable, therefore in each case it was assumed that all detectors are located at the same elevation.
- The coverage factor is applicable only to one theoretical 2D plane at any supposed elevation. Had each coverage factor result been based on 3 dimensions, the density figure would most likely always have been lower (less favourable) since process modules and wellbays are normally greater than 5 m in height (deck-to-deck). The results may therefore generally be considered to be on the optimistic side.
- The analysis does not investigate the capacity for the detector layout to achieve voted alarm (two or more detectors simultaneously alarming to the same theoretical gas accumulation, written as *2ooN*), as would be required in an industry mapping analysis.
- Since the coverage factor calculation assumes 1 PGD per 25 m^2 area, when OPGDs have been utilised, beam length divided by 5 was used to give the PGD equivalency. Where a PGD or OPGD is located at the perimeter of a fire zone, the coverage provided was discounted based on what proportion of the detector theoretical coverage area fell outside the fire zone/ area of

concern. Similarly, the coverage of a PGD located within the 5 m of another PGD was proportionally discounted (i.e., each detector would then not contribute a full 25 m^2 coverage).

- Coverage factor is given simply by: Number of PGDs Equiv/(Total area / 25).

The overarching purpose of the analysis is to surmise whether a TGC or leak detection approach had been taken when placing detectors in each case. This was possible to achieve because the leak approach typically sees detectors being placed *at the location* of potential leak sources only, leaving gaps in coverage between equipment. The coverage factor is important because this is what operators use to judge the *theoretical performance* of a detector layout based on prescriptive TGC rules. A figure of 1.0 means that 100% of the area is covered by the number of detectors present; given the specific location of each detector (based in each case here on a 5 m-target cloud).

Results and discussion

Results are presented in Table 2. Due to size constraints, data for only 14 of the 27 areas are presented for reference. For each of the 18 platforms assessed, layout data for different modules or areas were included where available (27 areas in total) in order to minimise bias for choosing particularly high or low detector density cases. This proved particularly interesting where different process modules of the same platform demonstrated significantly different coverage results (asset 3 for example). This approach highlighted the potential for inconsistency in detector layout across one platform. This variation is explainable since whole-platform F&G detection reviews are not necessarily that common once the platform comes on-line, and quite often one module or a number of targeted areas will be reviewed as new equipment/tie-ins are installed on the platform. Detectors may be added/removed/relocated at such times, requiring that the engineer/designer be aware of the original intent of the existing detector locations.

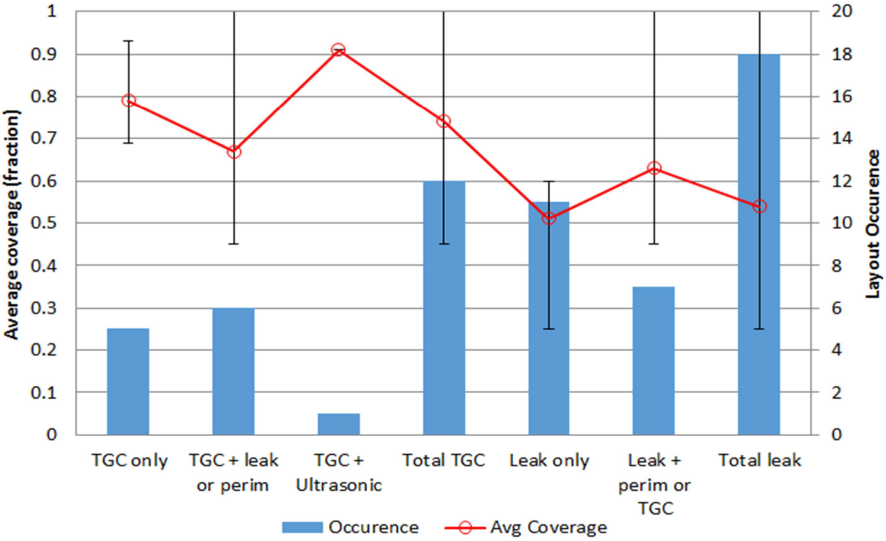

Fig. 2. Breakdown of detection approach occurrence and detection fraction.

Figure 2 demonstrates the frequency of occurrence of each approach considering specifically TGC and leak arrangements, as well as cases where a combination of approaches was identified. A TGC arrangement occurred in 12 of the 27 cases assessed (44.4%) while a leak detection approach was present in 18 cases (66.7%). There was an overlap in 5 cases where TGC and leak approaches are both applied. The average coverage and the range of coverage (error bars) are noted for each detection philosophy combination.

Table 2. Gas detection approach and coverage factors for 1-8 of 18 offshore platforms reviewed

Asset	Area Description	TGC applied?	No. of detectors			PGD Equiv	Area (m^2)	Coverage factor	Distribution	EL. (m)	Description
			PGD	OPGD	US						
1	Process: vessels, pipework	No	10				450	0.56	Leak	6.4 / 8.1	Detectors located near some equipment and pipework
2	Process: vessels, pipework	Yes		6	5	24	660	0.91	TGC / US	2.8	Significant TGC coverage, US detection for additional redundancy
3	Process: vessels, pipework	No	3	2		7	375	0.47	Leak / Perim	unknown	Leak in selected locations, OPGDs to north end as perimeter, some PGDs at HVAC inlets
	Pumps, gas handling	No	2				200	0.25	Leak	unknown	2 x PGD leak outside crane cabin, further 4 PGDs at 4 HVAC inlets
	Process: vessels, pipework	Yes		4		8.4	280	0.75	TGC / Perim	unknown	Consistent vol between equipment
	Process: vessels	No		4		7	380	0.46	Perim	unknown	2x OPGD used as perimeter to segregate area and 1 vessel boxed in by 2 further OPGD
4	Process: pumps, pipework	Yes		2		12	660	0.45	TGC / leak	3.0	Significant PGD distribution at machine/enclosure air intakes at low elevation in addition (approx 31)
	Process: pumps, pipework	Yes		7		26	1200	0.54	TGC / leak	3.0	Some PGD distribution at equipment air intakes at low elevation in addition (approx 9)
5	Process / pipework	No	5				240	0.52	Leak	Various	PGD's located at selected flanged connections
	Wellbays	Yes	36				1150	0.78	TGC	3.0	Generally consistent vol layout
6	Process: vessels, pipework	No	6				300	0.50	Leak	unknown	1 PGD per vessel and 3 in open space
7	Process, vessels, wellbay	Yes		5		29	900	0.81	TGC	4	Significant volumetric coverage
8	Process: pumps, pipework	No	13				625	0.52	Leak	3	PGDs located at equipment/pumps
	Process pipework, wellbay	No		4		9	500	0.45	Perim	2.5 / 5.0	Perimeter to segregate areas, on average 12m apart

PGD = point gas detector, OPGD = open-path gas detector, US = ultrasonic, EL = elevation, TGC = target gas cloud, perim = perimeter, heavy = low elevation

For the TGC cases only one provided ~100% spatial coverage (appearing in four separate categories). Typically, major operators give a performance target for percentage coverage (for single alarm) of 80-95%, depending upon operator guidance (for *confirmed alarm* the target may be similar or slightly lower). In only five TGC cases was an 80% coverage achieved. Subsequently, it should be remembered that the analyses here assumed all detectors to be located on a single elevation plane and so the coverage factor assessment is for a 2D slice (imagine a plan view).

Oil operators require an assessment in 3 dimensions – taking account of the entire *volume* of each area. For any asset reviewed here, where the deck-to-deck height was greater than 5 m (which is of course quite common), a 3-dimensional analysis would automatically result in poorer coverage factor. Thus, the five cases exceeding the 80% coverage figure here may well fall short of the 80% target in an official, technical 3D mapping review. Coverage factors provided for the leak approaches are purely for context since spatial coverage percentage is not a performance indicator in these instances.

Since the full complexity and nuance of each of the gas detection layouts cannot be fully described in a quantitative manner, a qualitative outline of the results would be beneficial. Certain attributes could be noticed during the analysis, for example, in leak detection cases PGDs were overwhelmingly located *at* potential leak sources (equipment/vessel/pipework-flanged area) and in only one clear case in a large, open space adjacent to the potential source. The number of PGDs placed at equipment in leak cases generally ranged from 1 to 3, and did not particularly correlate with equipment size. When multiple PGDs were located at a piece of equipment, the detectors were typically within ~5 m of each other, suggesting that maximum area coverage based on a target gas cloud size, was not a driving factor when placing detectors to target gas leaks. Furthermore, equipment of several metres in length with only a single gas detector was relatively common, appearing in most leak-approach cases. This suggests that *a PGD-per-item* (checklist style) approach is common when placing detectors rather than an engineering analysis of a range of credible leak scenarios. Subsequently most leak-PGDs were located within approximately one metre of equipment (if *within* the equipment footprint (above) was not possible). This suggests that inventory pressure is not factored into the decision on detector location, since high pressure gas leaks may result in a very thin jet with high initial velocity where dispersion may not occur until leak fluid momentum has diminished sufficiently, some distance from the source.

Only 46% of the TGC cases (5 of 12) provided the coverage factor required by the major operator prescriptive guidance (again, based only on a 2-dimensional analysis). There are of course many factors that contribute to the final detector layout design from an operational point of view, which go beyond the scope of "design philosophy". There is often a fundamental disconnect between the intent of operator guidance and the extent of what can practically be implemented in terms of detector count - often limited by CAPEX constraints. This arises commonly on brownfield and tie-in projects when a small number of new pieces of equipment are installed into an existing area, which it is later found out not to meet the required performance in terms of coverage factor (where a TGC approach is required by the operator guidance). It is then impossible for the additional hazards introduced by the new equipment to be met with coverage compliance without addressing the existing area as a whole. In our experience, on greenfield projects often when the F&G budget is allocated, long before detailed design is undertaken, the costs required to achieve full F&G compliance with the operator's own guidance is consistently underestimated. It can be argued that the results found here may reflect such practice.

CONCLUSIONS

The UKCS gas detection layout study showed that strict adherence to the generally-accepted, current, industry best-practice of the 5 m-target gas cloud approach first suggested in 1993 is not that common across the sample of UK North Sea platforms. The approach was adopted in less than 50% of the cases investigated, and less than half of those met the typical operator performance target for area coverage. Therefore, while theoretical investigations into the performance of the 5 m-spacing detection approach are of worth, they do not address the issue of the poor historical and current detection performance statistics. The first step toward improving offshore gas detection performance is in understanding *why* the current detection rates are so poor. Our introductory analysis of the offshore statistics and UKCS detector arrangement study demonstrate that knowledge of the detector arrangement is a necessary component in truly understanding the leak detection performance. The analysis sheds light upon this critical lack of knowledge within industry, and we hope it will start an important and necessary conversation.

Further, we have found that the offshore statistics reviewed do not appear to support the anecdotal industry hypothesis that the poor detection statistics are skewed by the number of small leaks. Further work is required to evaluate this more thoroughly. Given the potential hazards following uncontrolled offshore gas release, such claims must shoulder the burden of proof. An additional industry hypothesis: *detection appears so low because the majority of undetected leaks occur during manned operations and so the alarm is raised manually before the gas detection system is triggered* has also been given preliminary review and we find it to be unsupported by the data contained in the HSE database. This evaluation will be included in a future publication.

The primary recommendation here is that, when leaks are reported to the HSE, a current F&G detection layout for the area where the leak occurred should be submitted along with the hydrocarbon release data already provided when reporting. All company names should be removed and layouts should be made public along with the HSE OHR statistics report so that, in a short time, a large data set can be acquired, providing dozens and soon, hundreds of real-life case studies. These studies may then be analysed with the goal of identifying and understanding the common failure modes of current industry gas detection arrangements. This understanding is critical for improving life, environment and asset safety offshore given the poor performance of actual gas detection systems over the last 22 years.

REFERENCES

[1] A. Kelsey, M. Hemingway, P. Walsh, S. Connolly, Evaluation of flammable gas detector networks based on experimental simulations of offshore, high pressure gas releases, Proc. Saf. Environ. Prot. 80 (2002) 78–86.

[2] A. Kelsey, M. Ivings, M. Hemingway, P. Walsh, S. Connolly, Sensitivity studies of offshore gas detector networks based on experimental simulations of high pressure gas releases, Proc. Saf. Environ. Prot. 83 (2005) 262–269.

[3] McGillivray, A. & Hare, J., Research Report 672 - Offshore Hydrocarbon Releases 2001-2008. Prepared by the Health and Safety Laboratory for the Health and Safety Executive 2008.

[4] Offshore hydrocarbon releases 1992 – 2015, HSE, 2015, available at http://www.hse.gov.uk/offshore/statistics.htm. (Last accessed 04-JUN-2016).

[5] BBC News. https://www.bbc.com/news/uk-scotland-north-east-orkney-shetland-43910845, 2018 (accessed 23 June 2018).

[6] B. Gordon, Mapping fixed gas detectors and flame detectors. https://www.Det-tronics.com, (accessed 08 September 2018)

[7] Offshore detector siting criterion investigation of detector spacing by LLoyds Register. In Offshore Technology Report OTO 93002, HSE, 1993.

[8] Recommended Practice 14C. Recommended practice for analysis, design, installation, and testing of basic surface safety systems for offshore production platforms, Seventh ed., API, 2001.

[9] Combustible Gas Detection Instruments Canadian Electrical Code Part 2. Industrial Products, Standard CSA-C22.2 No 152-M1984 (R2006), Canadian Standards Association, 2001.

[10] ANSI/ISA-RP12.13.02 (IEC 61779-6 Mod) Recommended Practice for the Installation, Operation, and Maintenance of Combustible Gas Detection Instruments, ISA, 2003.

[11] ISO 13702-Petroleum and Natural Gas Industries e Control and Mitigation of Fires and Explosions on Offshore Production Installations e Requirements and Guidelines, ISO, 1999.

[12] Guidelines for Fire and Explosion Hazard Management (Technical Report), UKOOA, 1995.

[13] Fire and Explosion Guidance. Part 0. Fire and Explosion Hazard Management, UKOOA, 2003.

[14] Prevention of fire and explosion, and emergency response on offshore installations, Offshore Installations (Prevention of Fire and Explosion, and Emergency Response) Regulations 1995. Approved Code of Practice and guidance, HSE, 1995.

[15] Framework for HSE Guidance on Gas Detectors (On-line Checking of Flammability Monitoring Equipment - Final Report), HSE, 2001.

[16] IEC 60079, Explosive Atmospheres – Part 29-2: Gas Detectors e Selection, Installation, Use and Maintenance of Detectors for Flammable Gases and Oxygen, IEC, 2007.

[17] Standard S-001: Technical Safety. Norway, Fourth ed, NORSOK, 2008.

[18] Atkinson, G., Cowpe1, E., Halliday, J. and Painter, D., A Review of Very Large Vapor Cloud Explosions. Texas A&M 19th International Symposium, October 25-27 2016, College Station, Texas.

[19] ISA-TR84.00.07-2018: Technical Report Guidance on the Evaluation of Fire, Combustible Gas and Toxic Gas System Effectiveness, ISA, 2018.

[20] S. DeFriend, M. Dejmek, L. Porter, B. Deshotels, B. Natvig, A risk-based approach to flammable gas detector spacing, J. Hazard. Mater. 159 (2008) 142–151.

[21] E. Mariotti, A. Di Padova, T. Barbaresi, F. Tallone, A. Tugnoli, G. Spadoni, V. Cozzani, Development of improved strategies for the lay-out of fire and gas detectors, Chem. Eng. Trans. 36 (2014) 283-288.

[22] J.K. Seo, D.C. Kim, Y.C. Ha, B.J. Kim, J.K. Paik, A methodology for determining efficient gas detector locations on offshore installations, Ships Offshore Struc. 8 (2013) 524-535.

[23] Ø. Strøm, J. Bakke, Gas detector location. Safety on offshore installations (pp.3.3.1–3.3.12). ERA Technology Ltd, 1999, London.

[24] R. Lee, J. Kulesz, A risk-based sensor placement methodology, J. Hazard. Mater. 158 (2008) 417–429.

[25] AJ. Benavides-Serrano, M.S. Mannan, C.D. Laird, A quantitative assessment on the placement practices of gas detectors in the process industries, J. Loss Prev. Process Ind. 35 (2015) 339-351.

[26] S.W. Legg, A.J. Benavides-Serrano, J. Siirola, J. Watson, S. Davis, A. Bratteteig, C.D. Laird, A stochastic programming approach for gas detector placement using cfd-based dispersion simulations. Comput. Chem. Eng. 47 (2012) 194-201.

[27] S.W. Legg, C. Wang, A.J. Benavides-Serrano, C.D. Laird, Optimal gas detector placement under uncertainty considering conditional-value-at-risk, J. Loss Prev. Process Ind. 26 (2013) 410-417.

[28] Offshore hydrocarbon releases 2015 – 2016, HSE, 2015, available at http://www.hse.gov.uk/offshore/statistics.htm. (Last accessed 04-SEPT-2018).

[29] J. Spouge, Leak frequencies from the hydrocarbon release database, Symposium series no. 151, IChemE 2006.

Using Odors to Detect Fire in a Study with Rooms Reduced to 75%Size

Kamiya K.[1,] *, Sugawa O.[1], Watanabe N.[2]

[1] Suwa University of Science, Department of Mechanical and Electrical Engineering,
Chino, Nagano, Japan
[2] Graduate School of Suwa University of Science, Engineering and Management,
Chino, Nagano, Japan
**Corresponding author's email: kamiya@rs.sus.ac.jp*

ABSTRACT

Odors related to scorching are emitted by substances undergoing oxidative pyrolysis during combustion. In this study, changes in odor quality were investigated and used to detect fire. Selecting a fire detector that would operate because of an odor change required appropriate gases for recognizing fire to be selected. Odor gases created during the oxidative pyrolysis of wood and synthetic polymers were used as standard gases to allow appropriate gases to be selected. The standard gases were then used in combustion experiments in model rooms in which heat was generated rapidly using a combustible fluid or slowly from smoldering material. Precursor oxidative pyrolysis odors were identified for various test materials. The odors that were generated depended on the type of combustible material present, so wood and plastics were both used to generate standard gases. Already available fire detectors and the measured odor changes were compared, and it was found that odor changes were detected at the same time as or after the fire was detected by the fire detectors when the fire was spreading rapidly or when the detectors and odor sensor were close to the fire source. However, detecting odor changes was faster than using the fire detectors for smoldering fire with little flame.

KEYWORDS: Fire detection, electronic nose, reduced-sized rooms, odor index.

INTRODUCTION

Fire detectors are installed in buildings to allow fires to be detected quickly and to alert the residents to allow them to fight the fire and/or escape. Installing fire detectors in homes became mandatory in Japan in 2004, and this led to deaths caused by fires decreasing every year. There were > 27% fewer deaths caused by fire in 2016 than in 2005 [1]. This proved that fire detectors save lives. Smoke, heat, and flame sensors are widely used in fire detectors, but it has been found that CO sensors are also effective at detecting fire [2]. Multi-criteria fire detectors in which CO, temperature, and smoke sensors are combined are currently being studied [3–5]. Fires emit odors in addition to heat, smoke, and toxic gases such as CO [6]. Odor is often the first sign of fire to be noticed by the people in the building affected. The size of the molecules that make up odor is approximately 10^{-10} m, while smoke particles are 10^{-8} to 10^{-7} m. Therefore, odor molecules are diffused by thermal air currents from fire more quickly than smoke particles, and it may be possible to detect a fire more quickly using odor than using smoke. We have performed tests using odor identification sensors to detect odor changes during the oxidative pyrolysis of wood and plastic [7–8]. We found that oxidative pyrolysis caused dramatic odor changes and increased odor strength [9-10]. Mixtures of chemicals are responsible for the odors produced, so determining the concentrations of specific substances was not helpful. Here, odors related to fire are therefore selected experimentally and then used as

Proceedings of the Ninth International Seminar on Fire and Explosion Hazards (ISFEH9), pp. 1210-1220
Edited by Snegirev A., Liu N.A., Tamanini F., Bradley D., Molkov V., and Chaumeix N.
Published by Saint-Petersburg Polytechnic University Press
ISBN: 978-5-7422-6498-9   DOI: 10.18720/spbpu/2/k19-57

reference odors to allow a fire to be detected from odor changes. The results obtained using the system in full-sized and reduced-size fire experiments are compared with the results obtained using other fire detection systems.

EXPERIMENTAL

Odor analysis

An FF-2A electronic nose (Shimadzu, Kyoto, Japan) with ten oxide semiconductor sensors (to imitate receptor proteins in the nose) was used. The data obtained were subjected to multiple classification analysis to characterize the sensor signal patterns. The electronic nose detected the overall odor molecule balance rather than individual chemicals (which would be the case using analytical methods such as gas chromatography mass spectrometry). The electronic nose was exposed to standard gases and produced indices that were used to determine the degrees to which the standard gas odor components were similar. A calibration curve was produced for each index using the sensor responses at different standard gas concentrations [11]. Studies were performed to develop similarity indices to represent odor quality. The methods used to analyze the indices are described below. The similarity indices indicated the degree to which the sensor response patterns represented the nine standard gas odor types. Calculations were performed using angle θ between the standard gas vector and sample gas vector in the 10-dimensional space created by the responses of the 10 sensors. The similarity index was 100% (i.e., the sample gas was the same as the standard gas) at $\theta = 0°$ and 0% at $\theta >$ the acceptable angle β (~5°).

Selection of fire type and recognized odors

The gas generated when a test material was heated in a TG-8120 thermogravimetry–differential thermal analysis system (Rigaku, Tokyo, Japan) was collected in an odor bag attached to the exhaust port of the system. A sample (~5 mg) was placed in an aluminum pan. The reference material was alumina, the atmosphere was purified air (G3), the flow rate was 300 mL/min, the temperature was increased at 10 °C/min, and the final temperature was 550 °C. A new odor bag was attached every 5 min, and 1.5 L of gas was collected in each bag. Odor gases released from the sample before thermal decomposition started to occur were collected by passing purified air through the instrument with the sample in place immediately after heating started. Each gas sample was diluted by a factor of 5–20 (depending on the odor intensity) with pure N_2, then the odor was assessed using the electronic nose. Wood and plastic test samples were analyzed. Four of the wood samples were from coniferous trees (hemlock, Japanese cedar, Japanese cypress, and pine), three from broad-leaved trees (Japanese oak, kihada, and white birch), and one from bamboo. Each wood sample was ground using a WB-1 Wonder Blender (Osaka Chemical, Osaka, Japan), and only particles that passed through a 200-mesh screen were tested. The effects of water in the wood samples were minimized by keeping the samples in a desiccator containing silica gel at room temperature for at least 15 days before the tests were performed. Nine types of pure plastic were used. These were low-density polyethylene, high-density polyethylene, polypropylene, polystyrene, acrylonitrile butadiene styrene, poly methyl methacrylate, polyvinyl alcohol, Nylon 66, and polycarbonate. Each plastic sample was cut into small pieces before being used in a test.

Reduced-sized fire experiments

Fire experiments were performed using actual-sized rooms to allow the abilities of the odor detection system and existing fire detection systems to be compared. The comparison allowed a system for identifying the status of a fire from the odor emitted to be developed. The results indicated that the system reliably detected fire from the odor emitted.

One-room model fire experiment

A mock-up of one room (floor surface area 5.4 m^2) in a regular house was used as a model space for a fire experiment. The layout of the room is shown in Fig. 1. The room was 2.4 m × 2.4 m × 2.4 m. The room had a suspended ceiling with 0.3 m space above (making the actual ceiling 2.7 m high). The walls were covered with 12.5 mm gypsum board, and the ceiling was covered with 9 mm gypsum board. The floor was covered with 12 mm plywood, and that was covered with 3 mm finishing plywood. The room had a sliding glass window with an air vent on one side and an entrance door on the other. The window was closed and the door was partly opened, leaving a 19 cm gap. The room contained a polyester sofa (1.2 m × 0.43 m × 0.7 m), a bookcase containing comic books, and a wooden television stand with a 20-inch display set on top. A wooden structure measuring 30 mm × 40 mm × 300 mm was the fire source. Kerosene (400 g) was sprinkled on the structure and the floor around, then a fire was started at the base of the structure. The weight of the wooden structure, room temperature, concentrations of gases of interest in the room, and odors emitted were measured during the experiment. Temperature measurements were made at 39 points, which were mainly inside the room (e.g., the wall behind the sofa). Gas concentrations were measured at four points (including inside the room and by the door) using CGT-7000 gas analyzers (Shimadzu). Odor gases were collected at five points. Three points were in the center of the room, at 1.6 and 2.4 m above the floor and 2.55 m above the floor (i.e., above the suspended ceiling) One point was above the entrance door 1.8 m above the floor, and the other point was on the wall behind the sofa 2.4 m above the floor. The odor samples were collected using MV-6500VP pumps (Enomoto Micro Pump, Tokyo, Japan). Each odor sample was collected into an odor bag, and a new odor bag was fitted at each sampling point every minute throughout the experiment. Each collected odor sample was diluted by a factor of 5–50 with pure N_2 and then analyzed using the odor analysis system. The nine standard gases stipulated by the Japanese Offensive Odor Control Law were used, and 11 commercially available types of gasoline and kerosene were used.

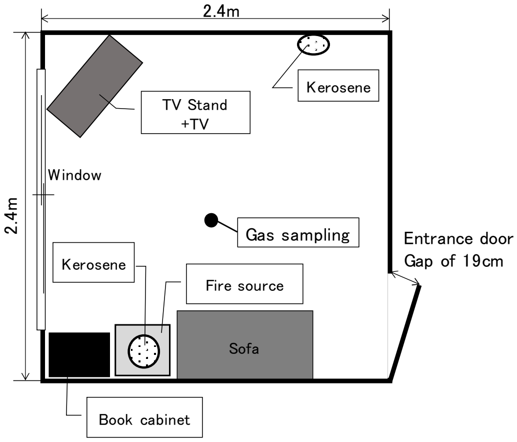

Fig. 1. Layout of the model room used in the one-room experiment.

Two-room model fire experiment

A mock-up of two rooms, each 2.4 m × 2.4 m × 2.4 m, connected by a 0.9 m × 2 m opening was used in another fire experiment. The room layouts are shown in Fig. 2. The walls and ceiling were covered with two-ply gypsum board and the floor was covered with two-ply plywood, which was then covered with poly (vinyl chloride) cushioned flooring. Each room had a double-glazed sliding glass door, each with an air vent. Each room contained a foam sofa (1.2 m × 0.6 m × 0.9 m) with a polypropylene cover, a wooden bookcase containing comic books, and a wooden television stand with a display set on top. Two tatami mats were placed in the center of each room. Tatami mats are flooring materials used only in Japan. Each tatami mat was made of polystyrene foam between insulating boards sandwiched between wooden boards. The sliding glass doors were both closed. The fire source was 1 L of kerosene sprinkled on the tatami mats in Room A. The fire was started using a lighter. The weights of the tatami mats, room temperatures, concentrations of gases of interest in the rooms, and odors emitted were measured during the experiment. Temperature measurements were made at 46 points, mostly inside the rooms (e.g., by the sofas). Gas concentrations were measured at seven points (including 0.4 and 2.35 m above the floor in the center of each room) and at the air vents using CGT-7000 and PG-330 (Horiba, Kyoto, Japan) meters. Odor gas samples were collected at three points (2.35 m above the floor in the center of each room and in the center of the upper part of the door frame). Each odor gas sample was collected using a pump connected to an odor bag. The odor bag at each sampling point was replaced every minute. A type 2 photoelectric spot sensor and a type 2 differential sensor (Nittan, Tokyo, Japan) were attached to the ceiling in each room, and the response time for each sensor was compared with the time taken for an odor change to be detected. Each odor gas sample was diluted with pure N_2 by a factor of 5–50 and then analyzed using the odor analysis system. Gas emitted during oxidative pyrolysis was used as the reference gas.

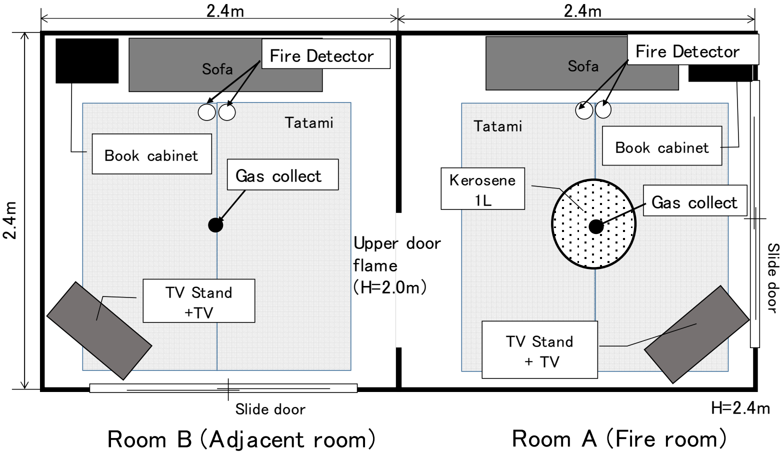

Fig. 2. Layouts of the model rooms used in the two-room experiment.

Reduced-sized experiment in part of a two-story house

Another experiment was performed in a mock-up of three rooms at 75% of the actual size. Each room was 1.8 m × 1.8 m × 1.8 m. Two rooms were on the ground floor and one on the upper floor. The room layouts are shown in Fig. 3. The two ground-floor rooms were connected by a 30 cm hanging partition wall. There was a 0.36 m^2 opening, representing a staircase, in the center of the floor of the upper-floor room. The upper-floor room had two sliding glass doors, which were each left with a 10 mm opening. The rooms were constructed to allow smoke and gases generated in the fire-outbreak room (on the ground floor) to pass around the hanging partition wall and spread into the adjoining room and through the opening in the center of that room to the upper floor, meaning the smoke and gas could flow and diffuse throughout both floors. The walls and ceilings were covered with 12.5 mm thick single-ply gypsum board, but one wall was made of 4 mm thick polycarbonate sheet, to allow the fire and smoke flow to be observed. No furniture or other items were placed in the rooms. Temperature measurements were made at 28 points, including at the point the combustible material was placed, in front of the hanging partition in the room in which the fire was started, and along the vertical axis of the center of the rooms on each floor. Odor and gas concentrations were measured at eight points, including directly above the fire source, in the center of the room in which the fire was started, in front of the hanging partition in the room in which the fire was started, and on the surface of the upper-floor ceiling. Odor gas samples were collected into bags using MF-1 pumps (IBS, Osaka, Japan), and the odor bag at each sampling point was replaced every 30 s during the experiment. A type 2 photoelectric spot sensor and a type 2 differential sensor (Nittan) were attached to the center of the room in which the fire was started and in the upper-floor room, and the response time for each sensor was compared with the time taken for an odor change to be detected. Each odor gas sample was diluted by a factor of 5–50 with pure N_2 and then analyzed using the odor analysis system. Gas emitted during oxidative pyrolysis was used as the reference gas. Odor from an experiment lingered within each room during subsequent experiments. The odor gas from the previous experiment was used as the baseline for each experiment to remove the effects of the odor remaining from the previous experiment. Tests were performed using three types of combustible material to identify odors emitted by different combustible materials. In the first experiment, three 100% cotton towels were placed on top of an electric heater. In the second experiment, three polyethylene bags each containing 5–10 sheets of A4 paper were placed in a plastic garbage box and ignited using an electric heater. These experiments did not involve flammable liquid.

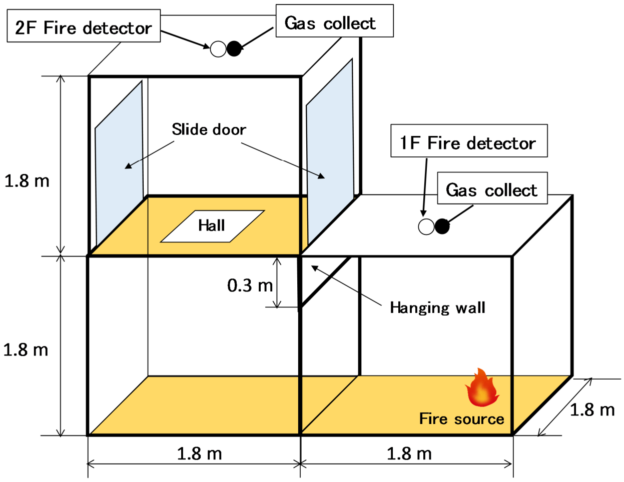

Fig. 3. Layout of the rooms used in the experiment using part of a two-story building.

RESULTS AND DISCUSSION

Selection of odors for recognizing fire

The odor measurement results for the gas collected during the oxidative pyrolysis of Japanese cedar wood are shown in Fig. 4. The results for four of the nine sensors are shown. The odor sensor outputs reached maxima at between 220 and 270 °C, indicating that the Japanese cedar wood was actively emitting odorous gases in this temperature range. The gas emitted between 220 and 270°C (in the section marked (1) in Fig. 4) and the gases emitted between 170 and 220 °C (in the section marked (2) in Fig. 4) were used as standard gases for detecting fire in subsequent experiments. For the other 15 materials, the gases emitted when the maximum sensor output was found and in the step before were used as standard gases (1) and (2), respectively.

Reduced-sized fire experiments

One-room model fire experiment

The fire in the one-room model experiment caused the sofa-side sliding window to crack 110 s after the fire was ignited and the other side to crack approximately 180 s after the fire was ignited. The heat generation rate was calculated from the weight loss rate and the unit heating value for the material. The heat generation rate increased immediately after the fire was ignited, and the equation $Q = \alpha t^2$ gave an α value of 0.38, indicating that the fire spread extremely quickly [12]. The heat generation rate decreased ~180 s after ignition, and the fire was extinguished by spraying it with water 660 s after ignition. The odor and gas concentration results are shown in Fig. 5. The gas concentrations 2.4 m above the floor in the center of the room are shown in Fig. 5(a). The similarity indices for the reference odors for kerosene and hydrocarbons are shown in Fig. 5(b) and 5(c), respectively.

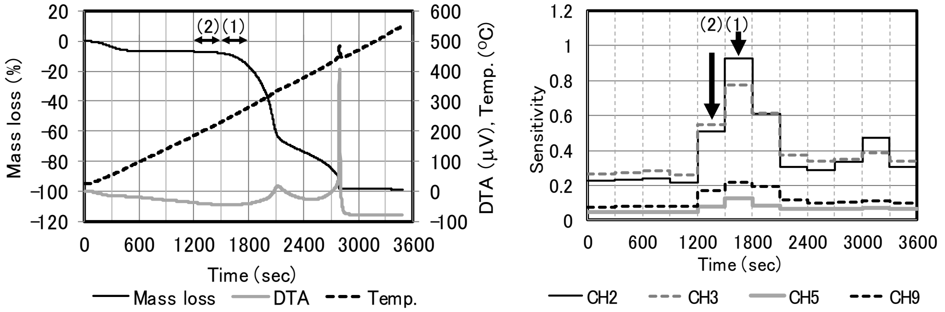

Fig. 4. Thermogravimetry–differential thermal analysis results and electronic nose sensor responses for Japanese cedar wood.

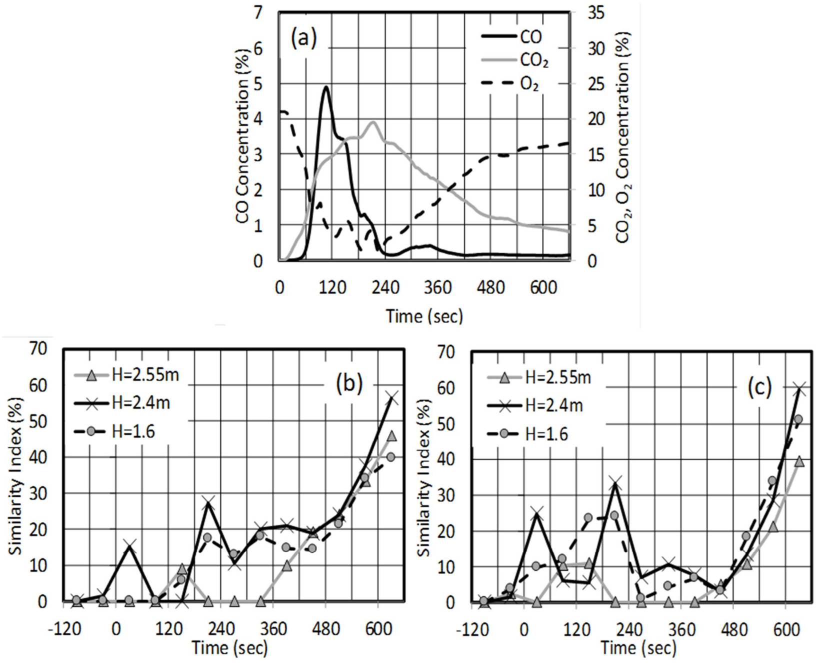

Fig. 5. Gas concentration and odor measurement results for the full-sized one-room experiment. (a) Gas concentrations 2.4 m above the floor in the center of the room, (b) kerosene similarity index for the odor, and (c) hydrocarbons similarity index for the odor.

Each odor measurement was plotted in the middle of the time period in which the measurement was made (i.e., at 30 s for a 1 min sample). It should be noted that kerosene was sprinkled from −60 to 0 s and the fire ignited at 0 s. It can be seen from Fig. 5(a) that CO and CO_2 reached the ceiling 30 s after ignition. Oxygen deficiency occurred at 110 s before the window glass cracked, and this caused the CO concentration to reach a maximum immediately before the window glass cracked, after which the fresh air that entered the room allowed the fire to continue burning. The maximum CO_2 generation rate occurred ~180 s after ignition, when the fire approached its maximum intensity. It can be seen from Fig. 5(b) that the kerosene similarity index increased between −30 and 30 s at all measurement points except for the point 2.55 m above the center of the room (above the suspended ceiling), indicating that the kerosene that had been sprinkled on the floor could be detected. It can be seen from Fig. 5(c) that the hydrocarbons similarity index increased as the fire spread for 60 s after ignition at all measurement points except the point above the suspended ceiling. This may have been because of the effects of the fire itself and of the kerosene sprinkled in the room. The aldehydes similarity index increased during the oxidative pyrolysis of wood and plastics in a previous study but not in this study. In this experiment, aldehydes were generated during the pyrolysis of the wood samples, but they were probably pyrolyzed and oxidized shortly after being generated because the fire intensity increased extremely quickly.

Two-room full-sized experiment

The odor measurement results for room A (the room in which the fire was started) and room B (the adjacent room) for the Japanese cedar and PS standard gases are shown in Fig. 6.

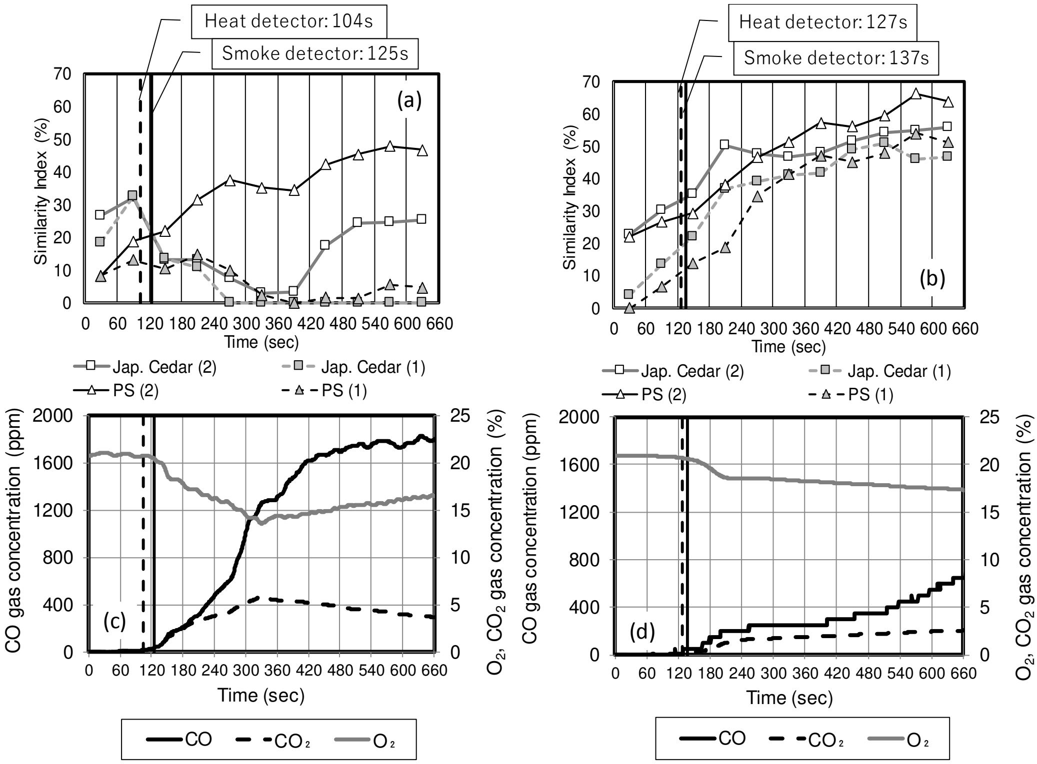

Fig. 6. Gas concentration and odor measurement results for the full-sized two-room experiment. (a) Odor results for room A (the room in which the fire was started), (b) odor results for room B (the room adjacent to the room in which the fire was started), (c) gas concentrations in room A, and (d) gas concentrations in room B.

Each measurement was plotted in the middle of the collection period (i.e., at 30 s for a sample collected for 60 s). The heat and smoke sensors in room A reacted 104 and 125 s after ignition, respectively, and the heat and smoke sensors in room B reacted 127 and 137 s after ignition, respectively. The Japanese cedar and PS similarity indices for rooms A and B increased for 60 s after ignition, then the sensors reacted, indicating that the odors generated by the wood and PS had changed. The Japanese cedar and PS similarity indices for reference gas (2) were high in room A, but the similarity indices were low in room B. The increase in the PS similarity index suggested that burning and pyrolysis in room A transferred from the wood in the tatami mats to plastic in the first 120 s after ignition. We concluded that the odor gases generated in room A entered and accumulated in room B (which was a confined space with no outlet), causing the Japanese cedar and PS similarity indices in room B to increase over time. The CO and CO_2 concentrations in room A 120 s after ignition were ~50 ppm and 0.5%, respectively, and the concentrations in room B were ~0 ppm and 0.25%, respectively. This indicated that fire could be detected earlier by monitoring odor changes than by measuring gas concentration changes.

Reduced-sized model of part of a two-story house

In the test using towels as the fire source, the towels emitted a little smoke 230 s after starting the electric heater. The fire did not develop to the flaming combustion stage during the 600 s of measurements. The smoke sensors in the room in which the fire was started on the ground floor reacted at 316 s, but the other sensors did not react. The odor and gas concentration measurement results for the test using towels as the fire source are shown in Fig. 7.

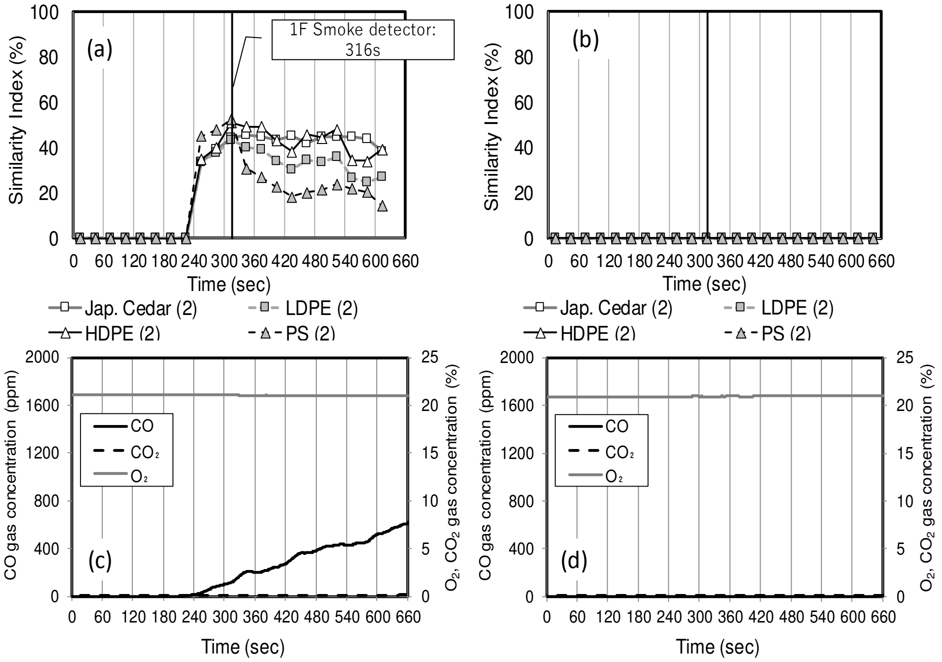

Fig. 7. Odor and gas concentration measurement results for the two-floor house model when towels were used as the fire source. (a) Odor results for the center of the ground-floor room in which the fire was started, (b) gas concentration results for the center of the ground-floor room. (c) Odor results for the center of the upper-floor room, (d) gas concentration results for the center of the upper-floor room.

It can be seen from Fig. 7(a) that the odor in the center of the room in which the fire started changed between 240 and 270 s. The PS (2) similarity index was slightly lower than the Japanese cedar (2) similarity index, low-density polyethylene (2) similarity index, and high-density polyethylene (2) similarity index. Wood and polyethylene emit materials containing aldehyde groups during oxidative pyrolysis. Emissions of large amounts of materials containing aldehyde groups during the slow oxidative pyrolysis of the cotton towels could therefore explain the high similarity indices for Japanese cedar and polyethylene. It can be seen from Fig. 7(b) that the gas concentrations on the ground floor started to increase 240 s after ignition and that the odor changed and CO was emitted at almost the same time but that the CO_2 concentration did not change. Odor change was detected >30 s before the smoke and fire sensors reacted. The odor and gas concentration measurement results for the upper floor are shown in Fig. 7(c) and 7(d). The short duration of this experiment meant that not enough heat was produced to provide the buoyancy required for the odor gases to reach the upper floor, so the fire sensors did not react and no odor or gas concentration changes were observed.

When the garbage box was used as the fire source, smoke was emitted 14 s after ignition and flames were observed at 26 s. The heat and smoke sensors on the ground floor operated after 53 and 154 s, respectively, and the smoke detectors on the upper floor operated after 262 s. The fire transitioned to the flaming combustion stage immediately after the electric heater was switched on, and this caused heat and smoke generated by combustible plastic to be observed at an early stage.

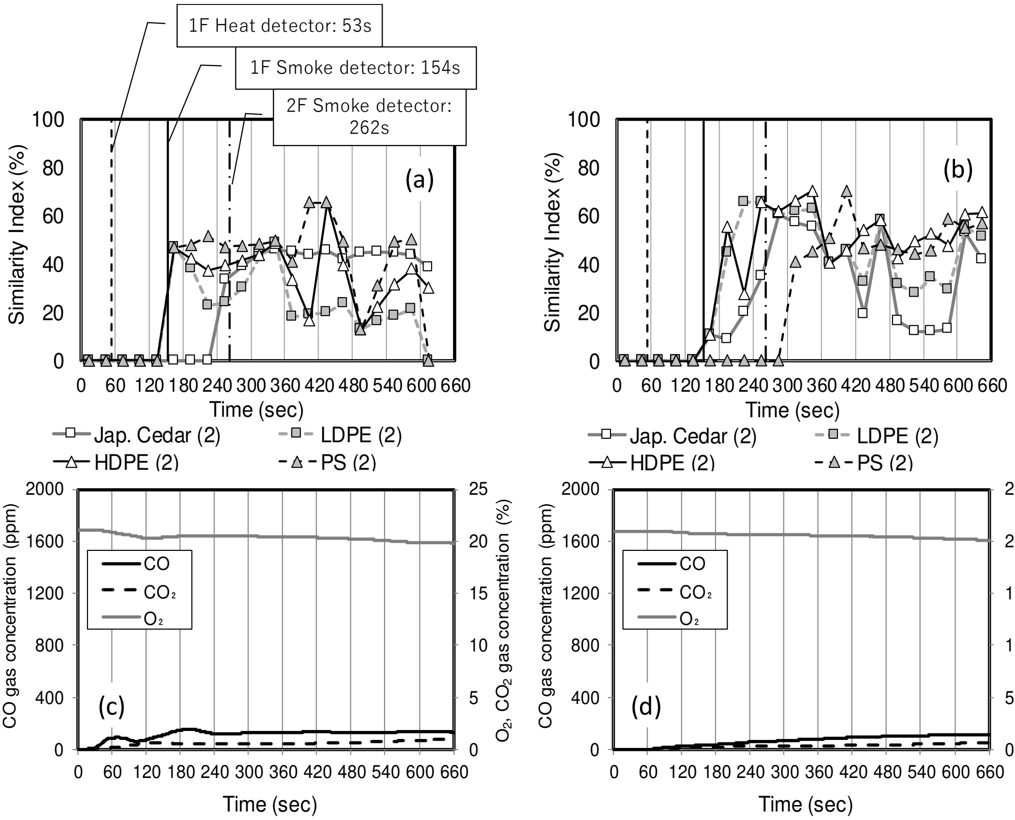

Fig. 8. Odor and gas concentration measurement results for the two-floor house model test when a garbage box was used as the fire source. (a) Odor results for the center of the ground-floor room in which the fire was started, (b) gas concentration results for the center of the ground-floor room. (c) Odor results for the center of the upper-floor room, (d) gas concentration results for the center of the upper-floor room.

The results of the experiment performed using combustible material in the garbage box are shown in Fig. 8. The odor before the experiment was performed the first time (i.e., with no smoke odor present) was used as the baseline odor, and the similarity indices for all the standard gases increased relative to the indices before ignition. Odor changes were only found in the test using a garbage box to start the fire because the odor from the previous experiment was used as the baseline. The odor on the ground floor changed from 150 s. This was around 100 and 25 s later than the ground-floor heat and smoke sensors, respectively, reacted. The CO concentration increased by ~50 ppm 30 s after ignition and to 100 ppm later, but the large increase found in the experiment using towels to start the fire was not observed. The odor similarity indices increased after 150 s, indicating that the odors became stronger. Odor change on the upper floor was observed at 180 s, which was ~80 s before the upper-floor smoke sensors reacted. The standard sensor systems reacted quickly near to the fire source, but odor change was observed sooner than the smoke sensors reacted on the upper floor because of the degree to which flow and dispersion affected the upper floor. The plastic similarity indices increased more rapidly than the Japanese cedar similarity index for both the ground and upper floors, indicating that different combustible materials emitted different odors.

CONCLUSIONS

Appropriate reference gases need to be selected to allow fire detectors based on odor changes to recognize a fire. Odor gases created during the oxidative pyrolysis of wood and synthetic polymers were therefore used as standard gases. These standard gases were used in combustion experiments in which heat was generated rapidly by sprinkling a combustible fluid in a model and also in model fire experiments involving smoldering combustion. The precursor odors of oxidative pyrolysis for each material could be detected because these standard gases were used. Different odors were generated by different types of combustible material, so we concluded that one of the best options was to use both wood and plastic materials to provide standard gases.

The results obtained using already available fire detectors and the odor change system were compared, and odor change was detected at the same time or later than the other fire detectors reacted when the fire was spreading rapidly or the sensors were close to the fire source. However, odor changes were detected more quickly than the other fire detectors reacted when the fire was smoldering and had only small flames. Various odors (such as those produced during normal activities) will be emitted in a room, but the results of this study indicate that misdetection of fire by the odor sensor system can be prevented by using odorous gases from the room as the baseline for the measurement period.

ACKNOWLEDGMENTS

This study was partly supported through a grant-in-aid for scientific research (Basic Research B, grant No. 15H02982) for the financial years 2015–2017.

REFERENCES

[1] Japanese Fire and Disaster Management Agency, Overview of the 2017 White Paper on the Fire Service, No. 2018, 2018, pp. 68–71 (in Japanese).

[2] M.A. Jackson, I. Robins, Gas Sensing for Fire Detection: Measurements of CO, CO2, H2, O2, and Smoke Density in European Standard Fire Tests, Fire Saf. J. 22 (1994) 181–205.

[3] N.L. Ryder, Multicriteria Detection: Leveraging Building Control and Comfort Sensors for Fire State Determination, Proc. 16th Int. Conf. Autom. Fire Detect. I (2017) 349–355.

[4] A. Mensch, T. Cleary, A Comparison of Carbon Monoxide Gas Sensing to Particle Smoke Detection in Residential Fire Scenarios, Proc. 16th Int. Conf. Autom. Fire Detect. I (2017) 363–370.

[5] G. Arndt, S. Suchy, D. Vialkowitsch, Multi-criteria/Multi-sensor Early Fire Detection in the Engine Compartment of Road Vehicles: Evaluation Process of Gas Sensors, Proc. 16th Int. Conf. Autom. Fire Detect. II (2017) 47–54.

[6] D. Kohla, A. Eberheim, P. Schieberle, Detection Mechanisms of Smoke Compounds on Homogenous Semiconductor Sensor Films, Thin Solid Films 290 (2005) 1–6.

[7] O. Sugawa, K. Kamiya, Y. Oka, Evaluation on Odor Intensity and Quality from Plastic and Wood Materials in Pre-combustion Condition, Proc. 15th Int. Conf. Autom. Fire Detect. II (2014) 21–28.

[8] K. Kamiya, O. Sugawa, T. Imamura, Y. Oka, Experimental Study of Odor Intensity and Quality for Wood Materials Undergoing Oxidative Pyrolysis, Bull. Jpn. Assoc. Fire Sci. Eng. 63 (2013) 25–35 (in Japanese).

[9] K. Kamiya, O. Sugawa, H. Kanai, T. Imamura, Y. Oka, Evaluation on Odor Intensity and Quality from Wood in Pre-combustion Condition, Proc. Asia Pac. Symp. Saf. (2011) 344–347.

[10] O. Sugawa, K. Kamiya, Experimental Study on FT-IR Analysis of Chemical Species from Wooden Materials in Pre-combustion Condition, Proc. 16th Int. Conf. Autom. Fire Detect. I (2017) 371–378.

[11] J. Kita, Y. Aoyama, M. Kinoshita, H. Nakano, H. Akamaru, Technical Digest of the 17th Sensor Symposium (2000) 301–305.

[12] R.L. Alpert, Ceiling Jet Flows, in: M.J. Hurley et al. (Eds.), SFPE Handbook of Fire Protection Engineering, third ed., Springer, New York, 2002, pp. 429–454.

A New Multi-level Gradual Coverage Location Model for Optimizing Fire Station Locations Based on Fire Risk

Ming J.K.[1]**, Song C.**[2]**, Zhu J.P.**[1,]*****

[1] *University of Science and Technology of China, Hefei, Anhui, China*
[2] *China Academy of Electronics and Information Technology, Beijing, China*
**Corresponding author's email: jpzhu@ustc.edu.cn*

ABSTRACT

Research on the locations of facilities has been very popular in many fields especially for emergency facilities. This study addresses the location of new fire stations based on dynamic fire risks. In order to give consideration to both fairness (well-performed coverage of demand points) and efficiency (rapid response and dealing with each demand point on its own weight) during the process of locating fire stations, a Multi-Level Gradual Coverage Location Model (MLGCLM), based on Maximal Covering Location Problem in the presence of Partial coverage (MCLP-P), is proposed to optimize fire station locations. A computational experiment tested on the data set used in MCLP-P validates that the proposed model has a better performance and demonstrates that the Genetic Algorithm (GA) procedure with adaptive operator designed on Matlab platform is able to effectively solve the problem. Then, this paper uses fire data of Hefei city to estimate the performance of the MLGCLM under different selected fire stations and compares the MLGCLM with the other two classic facility location models: p-median model and maximal covering location model. The results suggest that MLGCLM takes into account both p-median and maximal covering objectives and can be useful in guiding the future optimization scheme of new fire stations in a city.

KEYWORDS: Fire station, fire risk, genetic algorithm, multi-level gradual coverage, location model.

NOMENCLATURE

d_{ij}	Euclidean distance between demand point i and facility j (km)
D	maximum coverage distance of demand points (km)
$f_{ij}\left(d_{ij}\right)$	coverage decay function
I	set of demand points
J	set of candidate facilities
R_i	ideal coverage radius of demand, point i (km)
x_{ij}	binary variable
y_i	binary variable
z_i	binary variable

Subscripts

i	index of a demand point
j	index of a potential facility point

INTRODUCTION

The optimized selection of locations of public facilities has been very popular in many fields particularly for emergency facilities. A particular problem having attracted considerable attention from researchers is to locate optimally fire stations [1-3] that, like any other emergency service, should also consider a limited budget, universal coverage and rapid response among other factors.

Proceedings of the Ninth International Seminar on Fire and Explosion Hazards (ISFEH9), pp. 1221-1232
Edited by Snegirev A., Liu N.A., Tamanini F., Bradley D., Molkov V., and Chaumeix N.
Published by Saint-Petersburg Polytechnic University Press
ISBN: 978-5-7422-6498-9 DOI: 10.18720/spbpu/2/k19-65

Naturally, there have been many location-allocation models for research during the past few decades.

Classical location theories divide traditional facility location problems into three main categories: covering problem, P-center problem and P-medial problem. One of the most popular among facility location models is the covering problem due to its applicability in practice, especially for emergency facilities. Schilling, Jayaraman and Barkhi [4] classified coverage models into two categories: (1) Set Covering Problem (SCP) where full coverage is required and (2) Maximal Covering Location Problem (MCLP) where coverage is optimized. Since then, an increasing number of publications has dealt with the covering problems. Farahani R. Z. et al. [5] wrote a good review of covering problems in facility location in 2011, which presents a trend of those covering studies over time (since 1992 till 2011) and divides the development of covering models into three kinds: the development of SCP, the development of MCLP and other extended models related to the nature of covering problems. Specifically, the SCP includes a series of direct extensions of the model, such as Location set covering problem (LSCP) Implicit and Explicit presented by Murray, Tong and Kim [6], Probabilistic SCP [7] and Stochastic SCP [8], etc. In addition, the main extensions of the MCLP are as follows: Generalized MCLP [9], Gradual Coverage Location Problem [10, 11], etc. Lastly, several extended models mainly include Anti-covering [12] and Spatial covering location problem [13], etc.

Despite the numerous location models mentioned above, there are few models incorporating equity factor which includes two different equity concepts referred to as horizontal equity and vertical equity. Horizontal equity suggests that all demand points are considered in an equal manner. It means that every demand point is treated without discrimination. Vertical equity is concerned with the distribution of the demand weight among demand points. Horizontal equity and vertical equity have been studied extensively in emergency facility locations separately [14]. Moreover, studying how to incorporate the equity concept from both a horizontal and vertical point of view is still an urgent need given the lack of a unitary measure of horizontal and vertical equity [15]. Besides, this paper adopts the future fire risk spatial distribution of the study area as the weights of demand points, which is a new trend in fire station locations [3].

Motivated by the lack of research in this area, this paper proposes the Multi-Level Gradual Coverage Location Model (MLGCLM) which is an expansion of the gradual coverage decay model. The objective function is to maximize the overall match degree. The match degree is a function of distance and demand weight, which indicates the satisfaction level of a demand point with its serving facilities. And this evaluation metric combines the horizontal equity with the vertical equity. In other words, the goal in this model considers both fairness (corresponding to the meaning of horizontal equity) and efficiency (equal to the definition of vertical equity). The details will be shown in the next section.

To solve the MLGCLM, this paper improves a Genetic Algorithm (GA) with adaptive crossover and mutation operators to find optimal solutions. In the remainder of this paper, the proposed model is first introduced. Then, the principles as well as the relative performance of the MCLP-P model and MLGCLM are compared and analyzed under simulated data. Data preparation and initial selection of the candidate sites in Hefei city are presented next. The following section outlines the implementation procedure for the model and discusses the results obtained. Finally, the section on conclusions and recommendations includes a discussion of practical application and conceptual limitations of the method along with ideas for further research.

MODEL FORMULATION

Karasakal and Karasakal [10] developed a model named MCLP-P, which relaxes the “all or nothing” assumption. In this model, service decays with the increasing distance from a “fully covered” level to a “partially covered” level and drops to a no-service level beyond the maximal coverage range. But it only involves the horizontal equity. In order to incorporate both kinds of equity concepts, this paper modifies the MCLP-P model. Consider the coverage decay function $f_i\left(d_{ij}\right)$ as follows:

$$f_{ij}\left(d_{ij}\right)=\begin{cases} 1, & d_{ij}\le R_i \\ 1\big/\left(1+\exp\left(A\left(d_{ij}-\left(R_i+D\right)/2\right)\right)\right), & R_i\le d_{ij}\le D,\ A=5. \\ 0, & d_{ij}>D \end{cases} \tag{1}$$

The function $f_i\left(d_{ij}\right)$ depends on the distance between demand points and facilities, as well as the demand weights of demand points. On the one hand, $f_i\left(d_{ij}\right)$ sets a maximum coverage distance D to cover as many as possible demand points and this corresponds to horizontal equity; on the other hand, vertical equity can be integrated by applying R_i to the proposed model, which is the ideal coverage radius of demand point i inversely proportional to its own demand weight. It means that demand point i with a larger weight should be served by one facility within a smaller distance R_i, A sample depicting the coverage decay function $f_i\left(d_{ij}\right)$ is followed.

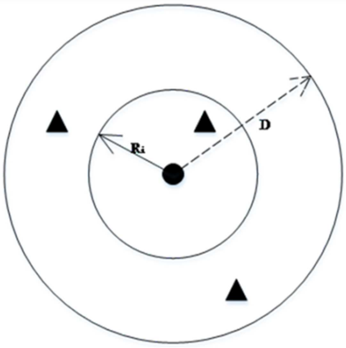

Fig. 1. Solid circle – demand point *i*, solid triangles – facility points

The example in Fig. 1 assumes that there is one demand point i, one candidate facility location within the ideal coverage radius R_i and two candidate facility locations within the maximum coverage distance D. Now the match degree of demand point i provided by the three facilities can be calculated based on the coverage decay function $f_i\left(d_{ij}\right)$.

Eventually, the model is formulated as follows:

$$z=\max\sum_{i\in I}\sum_{j\in J}f_{ij}(d_{ij})z_i\ , \tag{2}$$

Subject to

$$\textstyle\sum_{j=1}^{n}y_j=p\ , \tag{3}$$

$$\sum_{j=1}^{n} x_{ij} \le 1 \ \forall i \in I \ , \tag{4}$$

$$x_{ij} \le \mathrm{y}_j \ \ \forall i \in I, \forall j \in J \ , \tag{5}$$

$$x_{ij} = \begin{cases} 1 & \text{if the demand at point } i \text{ is covered by a facility at } j \text{ within } \mathrm{R}_i, \\ 0 & \text{otherwise} \end{cases} , \tag{6}$$

$$y_j = \begin{cases} 1 & \text{if a facility is sited at } j \\ 0 & \text{otherwise} \end{cases} , \tag{7}$$

$$z_i = \begin{cases} 1 & \text{if the demand at point } i \text{ is covered within } D \\ 0 & \text{otherwise} \end{cases} , \tag{8}$$

Objective function (2) maximizes overall match degree that is the sum of match degree of all demand points. Constraint (3) imposes the selected number of facilities. Constraint (4) expresses that demand point i will be covered by at most one facility within R_i. Constraint (5) guarantees that demand point i is only covered by selected facilities. Constraints (6), (7) and (8) impose binary restrictions on the decision variables.

COMPUTATIONAL EXPERIMENTS ON SIMULATED DATA

A similar simulated data set derived from the literature [10], is generated to compare the performance between MLGCLM and MCLP-P. Data pairs representing the demand points are provided from a uniform distribution within the ranges [0, 50] and [0, 100]. Data for the candidate facility sites are drawn from the same distribution within the ranges [5, 45] and [10, 90] for the respective sides of the rectangle. The coverage levels can be obtained by the decay function using the Euclidean distances between demand points and candidate facility sites.

Additionally, this paper presets some parameters for the two models. For one thing, the R_i in the MLGCLM is determined by the weights of demand points selected from a uniform distribution within the ranges [0, 1]. More concretely, the demand weight needs to be divided into 3 levels, namely 0-0.333, 0.333-0.667 and finally greater than 0.667, and then the ideal covering radius of demand points in first level (the highest demand weight) is 10; the second level is 15; the third level is 20. The reason why the ideal covering radius is set as the above values is that the higher the demand weight of each demand point, the shorter the ideal covering radius (equal to response time). Furthermore, the coverage radius D is deemed to be the maximum coverage distance of demand points. For another, the MCLP-P deals with the coverage problem from the point of view of facilities, which supposes that the facility sites are likely to fully cover the demand points within the range of R_i (the constant should be equal to 20). A 10% increase in the coverage range is assumed in the presence of partial coverage ($D = 22$).

Figure 2 shows an example of the randomly generated sample with 200 demand points and 10 candidate facility sites. It also depicts the optimal solutions of two different models for selecting 3 facilities. Table 1 presents a significant evidence that all kinds of measurement metrics in MLGCLM are larger than those in MCLP-P. Intuitively, the larger the first two measurement metrics, the shorter the response time of demand point. Besides, the larger the overall coverage rate, the greater the responsibility area of selected facilities. So, MLGCLM has a better performance than MCLP-P. With regard to the reasons, firstly, the former formulates its own ideal coverage radius based on the demand weights, which possibly provides a corresponding response time for demand points in different levels. This point is extremely significant for emergency service. Secondly, the latter fails to consider the demand weights and requires that demand points should only be either partially covered or fully covered by at most one of the selected facilities, causing some of them (demand points under first and second level) to be ill served by located facilities.

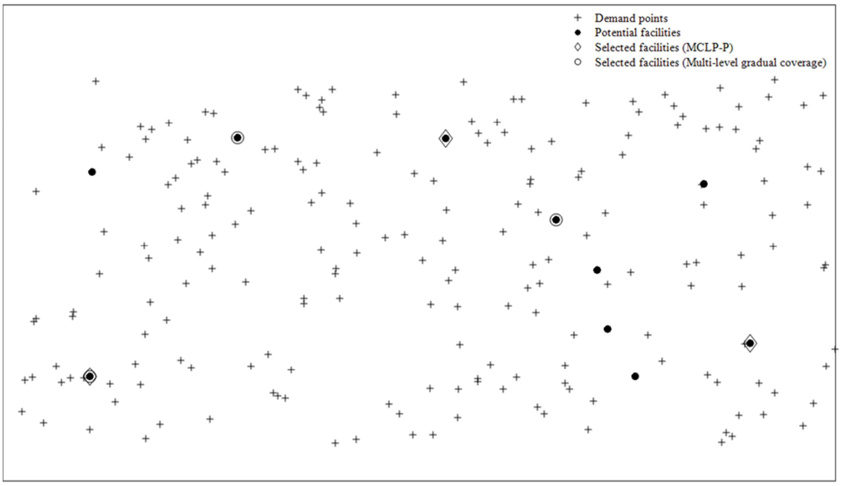

Fig. 2. Example of a random problem and its solutions.

Table 1. Results of MCLP-P and multi-level gradual coverage model

Location models	Overall match degree	Effective match rate	Overall coverage rate
MCLP-P	93.9	0.34	0.595
MLGCLM	109.1	0.425	0.685

[a] Overall match degree is the sum of match degree of all demand points.

[b] Effective match rate means the percentage of demand points whose match degree provided by selected facilities is over 1 among all demand points, indicating these demand points can be well served.

[c] Overall coverage rate refers to the percentage of demand points covered by selected facilities at least once.

DATA PREPARATION

The study area is located in Hefei city that is the provincial capital of Anhui. Along with the acceleration of urbanization, the increasing numbers of people migrating to urban centers has resulted in more security problems and the enlargement of original urban centers has led to the fire risk changing in the spatio-temporal scale. Therefore, it is necessary to reallocate the fire resources in Hefei city. On the basis of the future development mode and fire risk in the city of Hefei, this paper is aimed at guiding the fire protection planning from “catch-up planning” to “planning ahead”.

Determination of the distribution of demand points

In this paper, the layout optimization of new fire stations is guided by the future fire risk spatial distribution in Hefei. Consequently, the discrete distribution of the future fire risk is used to replace the distribution of demand points.

Fire risk is determined by fire probability and fire consequence. The fire probability can be briefly expressed by annual average fire density (number of fires per square kilometer every year). Due to the lack of related historical fire loss data, the direct fire property loss density (amount of property loss per square kilometer) in 2011, which is generated through the kernel density analysis tool in GIS, is simply applied to represent the future distribution of annual average fire consequence from 2011 to 2020 across Hefei. When using the kernel density to express its distribution, this paper uses a 5 km fixed window width to obtain the result as shown in Fig. 3. The resolution is 1 km by 1 km and the study area has been subdivided into a total of 1317 grids. The pixel value in each grid represents the fire consequence of its centroid, which can be obtained from the kernel density surface using the "extract to points" tool in GIS.

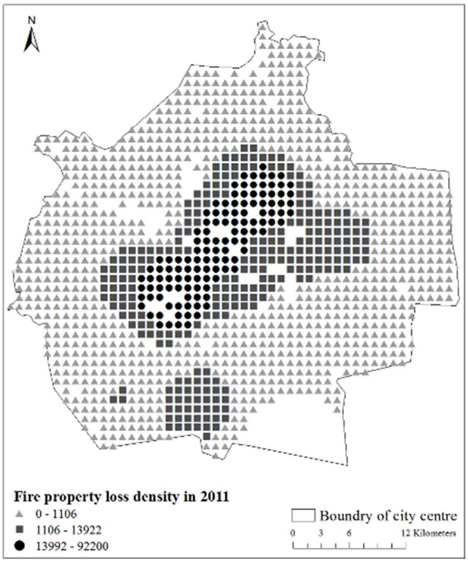

Fig. 3. Fire property loss density in 2011.

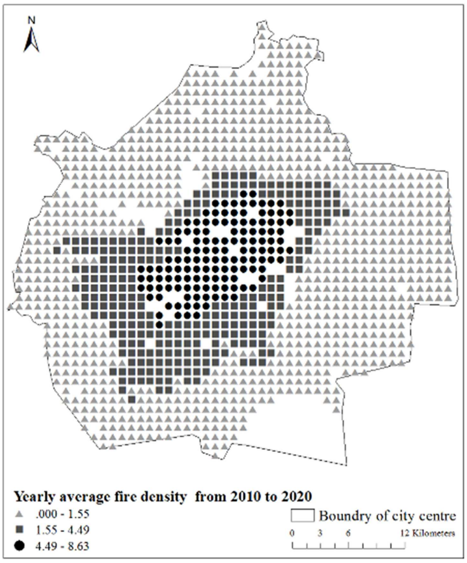

Fig. 4. Annual average fire density.

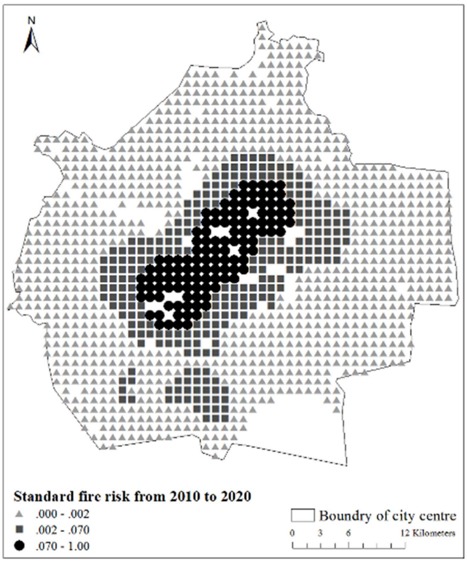

Fig. 5. Distribution of annual average fire risk.

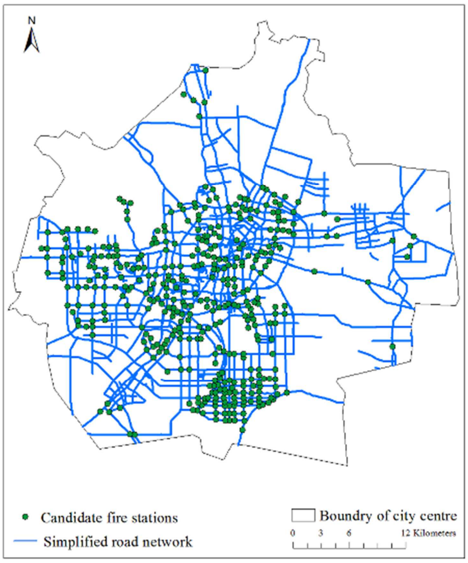

Fig. 6. Candidate fire stations.

In Fig. 4, the annual average fire density distribution from 2011 to 2020 is referenced from "A Comparison between Spatial Econometric Models and Random Forest for Modeling Fire Occurrence [16]" and it has been predicted by the Random Forest (RF) algorithm based on historical fire data from 2002 to 2005. Next, fire probabilities for centroids of abovementioned 1317 grids can also be extracted.

Eventually, combined with GIS technology, the standard spatial distribution of fire risk from 2011 to 2020 can be obtained by the product of fire density and the kernel density of fire property loss, which means that the fire risk in the center of each grid is the product of its fire probability and fire consequence. Consequently, every demand point shown in Fig. 5 has its own fire risk. Furthermore, different demand points should correspond to different ideal coverage radiuses based on the fire risk to reflect actual fire "rank corresponding" thought (different levels of fire risk should be consistent with the level of fire resources). To be specific, the higher the fire risk of each demand point, the shorter the ideal coverage radius (equal to response time). In light of the fire risk of demand point, this paper divides it into three levels, namely 0-0.002 (about 70 percent of demand points), 0.002-0.07 (about 20 percent) and finally greater than 0.07 (the remaining 10 percent). Fire fighting code of Hefei has estimated the speed of fire engines is approximately from 40 to 60 kilometers per hour on trunk roads and secondary trunk roads and the response time of high fire risk areas is around 2 minutes. So, this paper sets the ideal covering radius of demand points in first level (the highest fire risk) as 1 km; the second level is 1.5 km; the third level is 2 km. The ideal coverage radius interval between two levels is set as 0.5 km due to the linear distance approximately equal to two-minute driving distance. Moreover, the coverage radius of demand points called D is set as 5 km because of the speed of fire engines and the response time of fire areas within 5 minutes.

Determination of the candidate fire stations

The selection of candidate fire stations relies on fire passage simplified by main road network. Firstly, through use of GIS functions as well as network analysis tools, the fire passage is applicable for construction of the network dataset. Then, the initial candidate sites of fire stations are selected according to the nodes in the road network dataset. After that, the analysis function of "buffer calculation" and "attribute selection" make it feasible to remove the sites that are quite close to POI as well as the existing fire stations. Lastly, 396 potential fire stations are selected in Fig. 6.

The "City Fire Planning Manual" established by Hefei city planning bureau in 2008 determined to build 21 standard ordinary fire stations, 5 small ordinary fire stations, 1 fire station involving air duty and 1 fire station on the water on the basis of the existing 34 fire stations. Taking into account the cost of fire investment and the study area restricted to the central area of Hefei, the number of new fire stations will be set as 20 for the discussion in the last section.

RESULTS AND DISCUSSION

This paper uses GA to solve the MLGCLM and find the optimal locations. The key of using GA is to construct a fitness function, which is the objective function of the model. For each individual solution, it is encoded as a real number string of N bits, and the population size is 50. Note that the string is random and without repetition, in the range of 1 to 396 candidate sites. To improve the diversity of the solutions found, the GA function implemented in the Matlab platform utilizes two mechanism called elitism and adaptive evolution, which dynamically maintains the best solution in each iteration and contributes to exploring the solution space sufficiently. For more details about the use of GA, the readers can refer to the relevant literature [17]. Now the results for the location model are presented in the following section.

Sensitivity analysis for the MLGCLM

In Fig. 7 a, each point represents an optimal solution. The overall match degree (defined on Table 1) linearly increases with the number of stations. It has concluded that the number of fire locations has a positive relationship with the qualities of fire service. The trend of diminishing gain of effective match rate (defined on Table 1) has been displayed. For example, a gain of 17 percent in effective match rate can be achieved when the number of fire stations increases from 10 to 20, while a mere 3 percent increase is reached when the number of fire stations increases from 40 to 50. The most probable reason is that it requires further stations to provide fire resources for any other demand points. In Fig. 7 b, the coverage distance D is set as 5 km to calculate overall coverage rate (defined in Table 1), multiple coverage rate (the percentage of demand points covered by multi fire stations) and fire risk coverage rate (the percentage of demand points at the first or second level covered by fire stations among those points). And then a similar trend can be observed between the number of stations and the three kinds of coverage rates, for which the curves gradually flatten out. Intuitively, a high rate of overall coverage, multiple coverage and fire risk coverage may be possible by increasing the number of fire stations, but may be at a higher cost per unit.

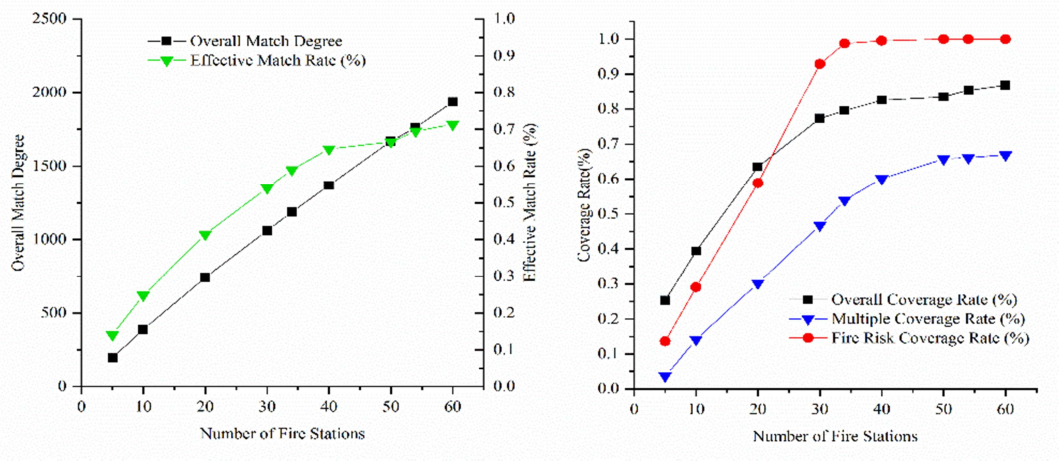

(a) (b)

Fig. 7. Relationship between the number of fire stations and all kinds of evaluation metrics.
(a) followed by overall match degree and effective match rate;
(b) ordered by overall coverage rate, multiple coverage rate and fire risk coverage rate.

Additionally, notice that the solutions take an abrupt turn when the number of fire stations is around 40 in Fig. 7 a and 35 in Fig. 7 b. The most probable cause is that 35 stations are just sufficient to provide coverage service but inadequate to offer strong fire service for high fire risk areas, which need more fire resources. For simplicity, this paper sets 30 fire stations to test the performance of the three kinds of location models during the discussion of the next section.

Evaluation and comparison of the three location models

As was mentioned earlier, the number of selected fire stations is set as 30. Then the optimal location solutions to the three models are presented in Table 2. When the measurement metric is overall match degree, the sorted results are successively p-median, maximum coverage, multi-level gradual coverage which means MLGCLM has the best performance. When it comes to the other two metrics including area coverage (fairness) and fire risk coverage (efficiency), the result in our model has a median performance between p-median model (fire risk coverage) and maximal coverage model (area coverage), which validates the model’s ability to simultaneously consider horizontal equity and vertical equity. Note that the demand weights in high fire risk area are far greater than those in median and low fire risk areas, leading to extensive fire resources used. Therefore, the fire risk coverage rate in p-median model is at the minimum level.

Moreover, for the purpose of further exploring how the results of the three kinds of location models influence the overall coverage, multi ring buffer analysis from 1 km to 5 km is depicted in Fig. 8. The outcomes imply that the optimal solution in the p-median model concentrates excessively in the central region, thus leading to a significant overlap of coverage and waste of fire resources, and the optimal solution in the maximum coverage model is too discrete resulting in many new fire stations built in areas with low fire risk and high fire risk areas with inadequate fire resources. While the optimal solution in the multi-level gradual coverage model combines the advantages of the other two models, coordinating area coverage and fire risk coverage. So, it makes use of fire resources effectively and reasonably. Meanwhile, the locations of new fire stations from MLGCLM mainly expand to the southwest which is consistent with the overall direction of Hefei city planning in the future.

Table 2. Results of three location models with selected fire stations

Location models	Overall match degree	Overall coverage rate	Fire risk coverage rate
P-median	980.1	0.3759	0.9596
MCLP	1147.2	0.8876	1
MLGCLM	1223.0	0.8246	0.9950

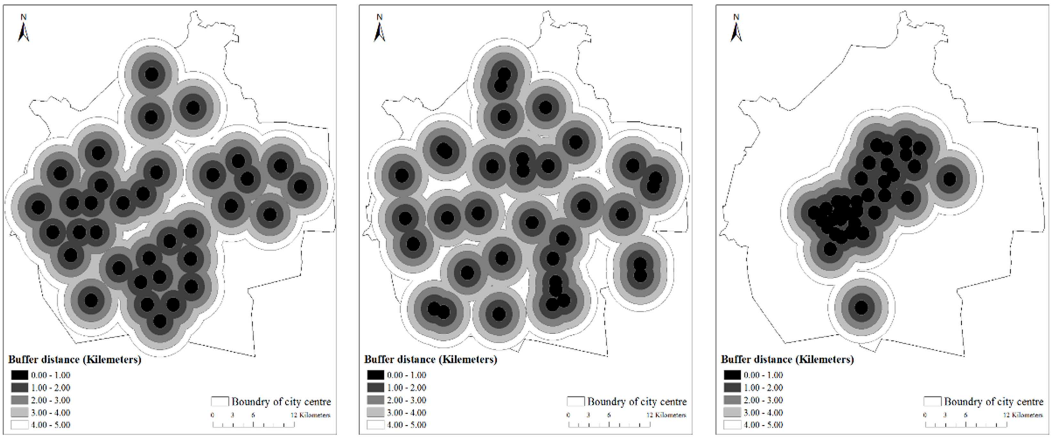

(a) (b) (c)

Fig. 8. Multi ring buffer analysis of the three models' optimal results: (a) the solution in multi-level gradual coverage combines the advantages of the other two models, including area coverage and fire risk rank coverage which means that the higher fire risk areas correspond to the shorter response time; (b) the solution in maximal coverage is too discrete resulting in many new fire stations built in areas with low fire risk and high fire risk areas with inadequate fire resources; (c) the solution in p-median concentrates excessively in the central region leading to a significant overlap of coverage and waste of fire resources.

Relaxing fixed existing fire stations

In order to examine the impact of existing fire stations, this section relaxes the fixed existing fire stations. In other words, assuming they can be relocated. In this case, all the 396 candidate locations with the existing 34 locations are able to be considered. As mentioned in the section discussing the selection of the candidate sites, two scenarios are tested: reconstructing 34 fire stations compared with the performance of the existing stations, reconstructing 54 fire stations compared with the performance of constructing 20 new fire stations on the basis of the existing fire stations. Table 3 summarizes the results. Under the condition of 34 existing fire stations built in Hefei city, solution A1 is known without calculation, and solution A2 is calculated by assuming the existing locations can be relocated. In comparison with solution A1, solution A2 probably covers more demand points by including those that are not served under solution A1 and by reducing those that are included by multi fire stations. Moreover, the effective match rate in solution A2 is greater than that in solution A1, which means more demand points can be served well by the selected fire stations. The relationship of fire risk coverage rate between A1 and A2 is the same as above. Under the condition of 54 fire stations built in Hefei city, solutions B1 (fixed existing fire stations) and B2 (existing fire stations can move) are calculated. The results demonstrate that the latter has a larger effective match rate and overall coverage rate, which makes it possible to reduce the total number of fire stations and reach the same objective if the existing fire stations could have been built at different locations.

Table 3. Results of multi-level gradual coverage model

Location models	Effective match rate	Overall coverage rate	Fire risk coverage rate
A1	0.5163	0.6993	0.9848
A2	0.59	0.795	0.9874
B1	0.6651	0.8413	1
B2	0.6948	0.8542	1

[a] A1 means the existing 34 fire stations as a solution.

[b] A2 means reconstructing 34 fire stations with existing fire stations relocated as a solution.

[c] B1 means constructing 20 new fire stations with existing fire stations fixed as a solution.

[d] B2 means reconstructing 54 fire stations with existing fire stations relocated as a solution.

CONCLUSIONS AND RECOMMENDATIONS

This paper illuminates the MLGCLM for the purpose of simultaneously considering two goals: well-performed coverage and hierarchical rapid response based on the fire risk. GA is used to solve the problem for locating fire stations. The main contents in this paper are divided into three parts: (i) a simple computational experiment validating that the model has a better performance than MCLP-P; (ii) data preparation including the determination of demand points and candidate location sites by using GIS; (iii) the results of the model demonstrated from three aspects, as previously mentioned, to reveal how the model affects the two goals (fairness and efficiency) with only one objective, namely, overall match degree. Even though this paper mainly focuses on the location of fire stations, the model developed can be applied in a broader context including all kinds of emergency facility location problems (ambulance, hospital and fire brigade, etc.). The key to applying the model in different situations is to determine the ideal covering radius of demand points. In this research, the speed of fire engine and the response time of high-risk areas are used to predefine them. Eventually, according to the fire risk of Hefei in the future, an optimized location solution on the basis of the existing fire stations is developed so that it is able to guide the future strategic planning and layout of fire stations in Hefei.

In this research, there are certainly many aspects to be further studied. Firstly, the Euclidean distance between the demand points and the candidate location sites proves to be the basis of the optimization. Nevertheless, like many other distance related problems, the usage of network distance has been more convincing. On the one hand, it can provide travel distance under real traffic flow between accident points and fire stations; on the other hand, it also offers a favourable condition for the incorporation of multi-period into the model because the traffic statuses at different times of the day are obviously different. Secondly, the initial candidate sites, which are important and critical for the establishment of fire stations, are just selected by using the nodes of the main road network with several constraints in relation to distance and spatial distribution. However, it is essential to select the candidate sites by combining more details relevant to the fire stations. Thirdly, simultaneous use of different quantities and types of vehicles, limited to the capacity of fire stations and the demand for fire service in real-world fire emergency rescue process, is one of most important requirements which should also be incorporated into the location model. If so, the optimal solutions to the model not only determine where to establish new fire stations but also define how many quantities and types of fire vehicles in each station, which would be more useful for fire service personnel. Fourthly, in this thesis, it seems somewhat simple for the approach to determining the future spatial distribution of fire risk described as the product of future fire density (shown as fire probability) and kernel density of future direct fire property loss (indicated as fire consequence). Particularly, the determination of future fire consequence appears to be oversimplified because it consists of not only economic losses but also casualties. So, it might be necessary to study how to forecast fire consequence with a unified metric. Other areas of future work may be extended to cost-benefit analysis of adding additional stations for which a limit budget should be integrated into the model and priority sequence for the selected new fire stations that can be achieved by the inclusion of extra constraints. To summarize, a more comprehensive location model might be a realistic and appropriate method in future research.

ACKNOWLEDGEMENTS

This work was sponsored by the National Key Research and Development Plan of China (Grant No. 2016YFC0800104, 2016YFC0800601) and the Fundamental Research Funds for the Central Universities of China (Grant No. WK2320000033, WK2320000036). The authors are also grateful to the Fire Bureau of Anhui Province, China, from whom researchers could obtain the historical fire records.

REFERENCES

[1] P. Chevalier, I. Thomas, D. Gerates, Locating Fire Stations: An Integrated Approach for Belgium, Socio-Econ. Planning Sci. 46 (2012) 173-182.

[2] A.T. Murray, Optimising the Spatial Location of Urban Fire Stations, Fire Saf. J. 62 (2013) 64-71.

[3] J. Perez, S. Maldonado, V. Marianov, A Reconfiguration of Fire Station and Fleet Locations for the Santiago Fire Department, Int. J. Product. Res. 54 (2016) 3170-3186.

[4] D.A. Schilling, V. Jayaraman, R. Barkhi, A Review of Covering Problems in Facility Location, Comput. Operations Res. 1(1993) 25-55.

[5] R.Z. Farahani, N. Asgari, N. Heidari, et al, Covering Problems in Facility Location: A Review, Comput. Ind. Eng. 62(2012) 368-407.

[6] A.T. Murray, D. Tong, K. Kim, Enhancing Classic Coverage Location Models, Int. Regional Sci. Rev. 33 (2010) 115-133.

[7] P. Beraldi, A. Ruszczynski, The Probabilistic Set-Covering Problem, Operations Res. 50 (2002) 956-967.

[8] O. Baron, O. Berman, S. Kim, et al,. Ensuring Feasibility in Location Problems with Stochastic Demands and Congestion, IIE Trans. 41 (2009) 467-481.

[9] G. Alexandris, I. Giannikos, A New Model for Maximal Coverage Exploiting GIS Capabilities, European J. Operational Res. 202 (2010) 328-338.

[10] O. Karasakal, E.K. Karasakal, A Maximal Covering Location Model in the Presence of Partial Coverage, Comput. Operations Res. 31 (2004) 1515-1526.

[11] O. Berman, J. Wang, The Minmax Regret Gradual Covering Location Problem on a Network with Incomplete Information of Demand Weights, Europ. J. Operational Res. 208 (2011) 233-238.

[12] I.D. Moon, S.S. Chaudhry, An Analysis of Network Location-Problems with Distance Constraints, Management Sci. 30 (1984) 290-307.

[13] A.T. Murray, D. Tong, Coverage Optimization in Continuous Space Facility Siting, Int. J. Geogr. Inform. Sci. 21 (2007) 757-776.

[14] S. Khodaparasti, H.R. Maleki, M.E. Bruni, S. Jahedi, P. Beraldi, D. Conforti, Balancing Efficiency and Equity in Location-Allocation models with an Application to Strategic EMS Design, Optimizat. Letters 10 (2016) 1053-1070.

[15] R. Aringhieri, M.E. Bruni, S. Khodaparasti, J.T. van Essen, Emergency Medical Services and Beyond: Addressing New Challenges Through a Wide Literature Review, Comput. Operations Res. 78 (2017) 349-368.

[16] C. Song, M.P. Kwan, W. Song, J. Zhu, A Comparison between Spatial Econometric Models and Random Forest for Modeling Fire Occurrence, Sustainability. 9 (2017) 819-837.

[17] B. Saeidian, M.S. Mesgari, M. Ghodousi, Evaluation and Comparison of Genetic Algorithm and Bees Algorithm for Location-Allocation of Earthquake Relief Centers, Int. J. Disaster Risk Reduction 15 (2016) 94-107.

Industrial fires and explosions

On the Usefulness of Phenomenological Approach to Model Explosions in Complex Industrial Systems

Grégoire Y.[1,]***, Leprette E.**[1]**, Proust C.**[1,2]

[1] *INERIS, PHDS Department, Parc Technologique ALATA, Verneuil-en-Halatte, France*
[2] *UTC, TIMR laboratory (EA4297), Compiègne, France*
**Corresponding author's email: yann.gregoire@ineris.fr*

ABSTRACT

Explosion protection is the object of various national and international documents, which are focused on the functions, the intended uses or the dimensioning rules for specific systems. However, despite a few application examples are described in the usual guidelines, they are limited to the description of a protection that can be added on a single piece of equipment while it is not the case in industrial processes. Furthermore, in an ATEX explosion there is a strong coupling between the explosion and its environment. Because of this the guidelines recommendations cannot be transposed on an industrial site without due consideration. In this paper, a way to consider the real explosion conditions is given allowing a choice and dimensioning of a set of safety systems. An example is shown based on the example of a model of a real installation. The functional properties of the safety system are extracted from the certification tests whereas the explosion characteristics are extracted both from the standard combustion properties of the dust and from the latest knowledge about flame propagation. A specific focus is made on two fundamental aspects: on the one hand, the critical importance to understand how the flame propagates in a given complex system. On the other hand, the behaviour of the protection systems that can be used with caution as they quite systematically influence the explosion driven flow

KEYWORDS: Dust explosions, explosion mitigation, phenomenological modelling.

INTRODUCTION

ATEX directives introduce everywhere in Europe the obligation to take dispositions to protect the workers in industry from the explosion risk. In many situations, and especially when dust explosions are identified, prevention measures are insufficient, and protection should be ensured. Explosion protection is the object of various national and international documents that are focused on the functions, the intended uses or the dimensioning rules for specific systems: NFPA68:2012 [1], EN14797:2007 (testing) [2] and EN14991:2014 (dimensioning) [3] for dust explosion venting techniques. Despite a few application examples are described in the usual guidelines, they are limited to the description of a protection that can be added on a single piece of equipment in which an explosion may occur, in quite an ideal configuration with fully known turbulence conditions, combustible reactivity, repartition or concentration. Such observation is general to most of the safety barrier used in the industry. However, in real installations, the device to be protected is rarely isolated but often connected to various ducts and vessels in which the explosion may propagate. This is a critical point as in an ATEX explosion there is a strong coupling between the explosion and its environment. A direct consequence of this is that the guidelines recommendations cannot be transposed on an industrial site without due consideration. In such occurrence modelling of the explosion phenomenon at stake can be helpful firstly to understand the possible course of events, then to dimension a protection strategy accordingly. When a complex system at an industrial scale is

Proceedings of the Ninth International Seminar on Fire and Explosion Hazards (ISFEH9), pp. 1234-1245
Edited by Snegirev A., Liu N.A., Tamanini F., Bradley D., Molkov V., and Chaumeix N.
Published by Saint-Petersburg Polytechnic University Press
ISBN: 978-5-7422-6498-9 DOI: 10.18720/spbpu/2/k19-35

considered, the most evolved tools such as CFD models can be used but their use can be associated with prohibitive costs. They most often require, in addition to engineering skills, large computing power as well as significant post-processing works to ensure the consistency of the results. In this paper a phenomenological approach is suggested in view of grasping the physics at stake. An example is show based on a real installation. The example of coal grinding installation is considered and is schematized in Fig. 1. It consists of a mill, a cyclone and a dust collecting filter, connected by pipes. The supply and product circuits are excluded from the present study. After passing through the mill, the grinded coal-gas mixture is sucked into the cyclone, where the coarsest particles are isolated, then resent towards the mill. Alternatively, the thinner particles travel towards the filter after which they are collected. The major objective is to protect the installation from the explosion effects as well as to limit the explosion effects in the medium range.

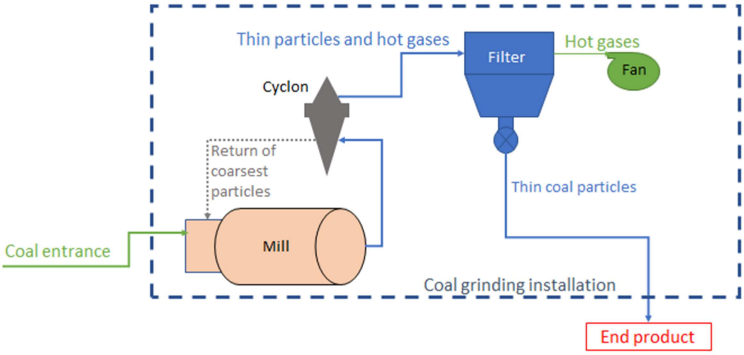

Fig. 1. Schematized coal grinding installation.

However, the very first step is to identify the explosion risk. Filters are prime causes of powder explosion but the same can be said on the mills. In fact, not only there is a large multiplicity and complexity of industrial installations, but also, once the choice is made on a setup, the process itself can vary. For example, some coal installations may also operate occasionally with petcoke. Different phases of the process (starting, usual operation, maintenance) imply different risks. At last the explosion may be triggered at various stages of the installation then propagate to the totality of it. This illustrates the needs behind the use of comprehensive phenomenological tools such as the one described here.

PHENOMENOLOGICAL MODELLING OF THE EXPLOSION IN A PROCESS

To model such explosion phenomena and keep a satisfying understanding on the course of the events, INERIS developed the EFFEX code [4], phenomenological software consisting of interlinked models each dedicated to a single aspect such as flame propagation in a volume, turbulence characteristics prediction, combustion rates, mechanical resistance, pressure effects… Most of the physics is derived from fundamental research. Each model is qualified separately, and the overall consistency can be compared to realistic full-scale experimentation or actual accidents.

The typical situation is that of a flammable cloud of suspended particles in a confined or semi-confined space. A reactive fuel-air mixture is formed. The size, composition and internal level of agitation ("turbulence") depend on the type of leakage and the geometric characteristics of the containment. If an adequate source of ignition is present inside the flammable area of the cloud, it will ignite, and a flame will propagate step by step from the ignition point. Figure 2 illustrates the development of the flame in the containment.

The flame develops spherically around the source of ignition. On its way, it almost instantaneously transforms cold reactants into hot combustion products (typically from 1000 to 2000 ° C). Hot gases being less dense than cold ones, it results in a high-volume expansion of the gases. This process is directly responsible for increasing the pressure in the enclosure.

The pressure rise due to the dust explosion is directly linked to the quantity of gases produced by the combustion minus the gases lost by the various openings on the filter (ducts, opened vents). Thus, the pressure rise curve as function of time can be estimated with a model such as that of Lewis and Von Elbe [5]:

$$\frac{1}{P}\frac{dP}{dt} = \gamma \frac{Q_{produced} - Q_{lost}}{V} \tag{1}$$

where P, V and γ are the enclosure pressure, its volume and the specific heat ratio of the gaseous species. $Q_{produced}$ and Q_{lost} are respectively the volumetric fluxes produced by the combustion and lost through the vent.

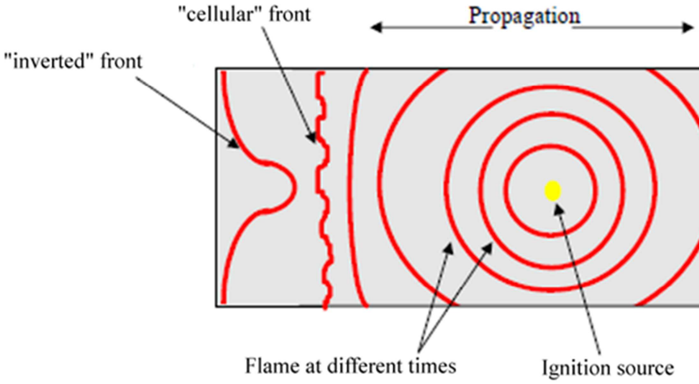

Fig. 2. Flame front evolution as a function of time.

Such model clearly indicates that the effect of the explosion will be directly linked to the reacting products, which will determine the rate of the gases production and the environment through the action of the vents in the Q_{lost} parameter. Q_{lost} can be estimated through some various models derived from the generalized Bernoulli's laws. In practice whether the flow is subsonic or supersonic it is possible to estimate the Q_{lost} term through equation (2) or (3) respectively for the subsonic and supersonic cases:

$$Q_{lost} = C_d S \left(\frac{P_2}{P_1}\right)^{1/\gamma} \sqrt{\frac{2\cdot\gamma}{\gamma-1}\cdot\frac{P_1}{\rho_1}\cdot\left(1-\left(\frac{P_2}{P_1}\right)^{\frac{\gamma-1}{\gamma}}\right)}\ , \tag{2}$$

$$Q_{lost} = C_d S \sqrt{\gamma \frac{P_1}{\rho_1}\left(\frac{2}{\gamma+1}\right)^{\frac{\gamma+1}{\gamma-1}}}\ . \tag{3}$$

However, the problem of the estimation of the produced gases flux $Q_{produced}$ is more challenging as it depends both on the products that are reacting but also on their environment which will influence the flame surface or impose concentration or turbulence gradients. The excess volume produced per unit of time, is proportional: on the surface of the flame, the burn rate of reactant consumed per unit of flame surface (this parameter has the dimension of a speed and is often called "burning rate"), and the volume expansion ratio (which is linked to the temperature of the products: the hotter the more volume is produced). Gas production through combustion can be approximated as follows in our model: the fresh combustible mixture is instantaneously transformed in hot burnt products through the passage of the flame whose thickness is zero. Thus, it is a function of the area of the reacting surface *Af*, its velocity *St* and an expansion ratio α:

$$Q_{produced} = St \cdot Af(\alpha - 1) \tag{4}$$

Firstly, the expansion ratio α is a thermodynamic data which depends only on the heat released by the combustion and can be expressed through the first principle of thermodynamics:

$$\alpha = \frac{\rho_{fresh}}{\rho_{burnt}} \approx \frac{T_{burnt}}{T_{fresh}} = \frac{\Delta H_{Comb}}{C_P T_{fresh}} + 1\ , \tag{5}$$

where ΔH_{Comb} is the reaction enthalpy, T_{fresh} and T_{burnt} are the temperatures of the reactants and the burnt products, ρ_{fresh} and ρ_{burnt} are the densities of the reactants and the burnt gases, and C_P is the specific heat of the burnt products. The expansion ratio α is a fundamental parameter which depends strongly on the combustible mixture composition and is poorly influenced by the propagation. For most common mixtures found in the process industries it is comprised between 6 and 8 [6]. Alternatively, the shape of the confined structure suffering the explosion can have an influence on the flame surface *Af* and so is the case for the local flow velocities, or when obstacles are present. Even in a medium initially at rest, the flame grows spherically until the spherical front reaches the closest wall. When contacting the wall, the flame front is stopped then reversed. During this phase the flame front surface can become cellular or be curved toward the combustion products most likely because of local perturbations such as Landeau-Darrieus instabilities [7]. In all case the maximal flame area is linked to the dimensions of the volume and its cross section. Extensive comparisons of EFFEX calculations with experiments indicate that a decent agreement can be achieved when the flame surface is roughly equivalent to the largest inscribed sphere in the enclosure [8].

Finally, the flame velocity in a mixture attached referential is also expected to be a property intrinsic of the mixture. The fundamental combustion velocity S_{lad} obeys to the laws of thermokinetics (thermodynamic equilibrium, Arrhenius law) and can be described as the volume of reactants consumed by a square meter of the flame surface. However, this definition corresponds to a configuration in which the reactive mixture is at rest in which case the effect of an explosion would be limited to the maximum. For a more realistic approach, it is necessary to consider a turbulent flame velocity St that can be determined for industrial applications based on the empirical definition of K_{st}:

$$K_{St} = \left(\frac{dP}{dt}\right)_{max} V^{1/3} \tag{6}$$

Replacing this in equation (1) (and assuming no openings on the vessel), we obtain:

$$\frac{1}{P_{max}} K_{St} = \gamma \frac{St \cdot Af_{max} \cdot (\alpha - 1)}{V^{2/3}} \Rightarrow \quad St \approx \frac{K_{st}}{\gamma P_{max}(\alpha - 1)} \tag{7}$$

Even in the isolated enclosure the effects of the dust explosion are strongly dependent not only on the nature of the reactants but also on the specificities of their environment such as the geometry or local turbulence effect. The model described in the previous paragraphs is only applicable if the flame propagation velocity is sufficiently low (typically < 30 m/s) for the internal pressure to remain “uniform”. This condition is very generally satisfied when the ratio between the largest and the smallest dimension of the apparatus is less than 5 [4], which is not the case for pipes for example. In practice, there would be an explosion at one end, for example in a mill and the atmospheric pressure at the other end. For ST1 class dusts (which is the case here), the contribution of the duct combustion to the overpressure in the installation studied is low and the flow is largely dominated by the pressure differences between the upstream and downstream sides of the pipes [9]. A direct consequence of this is that the flame velocity in such situation quickly reaches hundreds of meters per second. Empirical data show that the flame velocity in a duct downstream an enclosure is well correlated with the square-root of the overpressure P_{red} (stands for "reduced explosion pressure" a term often used to design the maximal overpressure in a vented vessel) in the enclosure (analogy to a Bernoulli model):

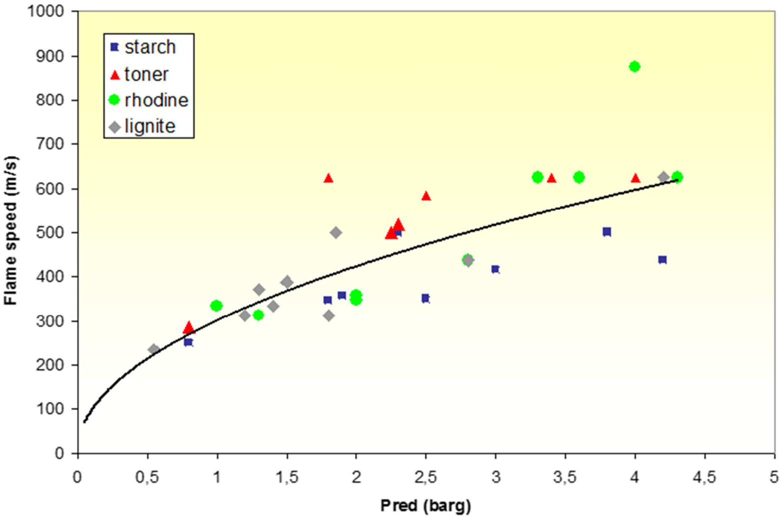

Fig. 3. Correlation between vessel overpressure and maximal flame velocity in a connected in a duct [10].

In this last situation, the velocity flow is driven by the pressure difference between both ends of the pipe, and so is the flame. It is also noted that in such case, until the flame has reached the other end of the pipe, the pressure in the upstream equipment (the mill) continues to increase as if the duct was closed [10]. The pressure rise is then less related to thermal expansion than to the inherent dynamics of the flame (speed and acceleration). There is therefore a piston effect and the main problem of the propagation of the explosion in a pipeline is to determine the speed of the flame, because ducts usually show large overpressure resistance and it is this same fast flame that is transmitted in equipment downstream. Moreover, the presence of singularities on the pipe such as bends is likely to modify the flame surface and accelerate it. In EFFEX, a relatively simple model of the compressible Bernoulli equation type has been implemented to estimate this velocity. The basic assumption is that the flame propagates at a speed St^* which depends, as for non-elongated enclosures, on the turbulence and reactivity of the dust (thus on the usual turbulent flame velocity St) but also on "Ve", the forced flow by the pressure difference between the upstream and downstream of the pipeline. Singularities such as elbows are therefore ignored. The cases of subsonic and shocked flows are differentiated. Noting P_1 and P_2 the pressures at each sides of the duct, and with $P_2 > P_1$. If the condition $\frac{P_2}{P_1} > \left(\frac{\gamma+1}{2}\right)^{\frac{\gamma}{\gamma-1}}$ is fullfield then the flow is chocked, and the Mach number M is 1. In the other case, M can be computed as follows:

$$M = \sqrt{\frac{2}{\gamma-1}\left(\frac{P_2}{P_1}\right)^{\frac{\gamma-1}{\gamma}}}\,. \tag{8}$$

From the temperature T and the molar mass M, we obtain the flow velocity by computing the speed of sound which depends on the temperature T. In the chocked and subsonic case, we obtain respectively these 2 equations for the flow velocity:

$$Ve = \sqrt{\frac{8.314}{M}\frac{2\cdot\gamma}{\gamma+1}T} \quad \text{and} \quad Ve = M\sqrt{\frac{8.314}{M}\frac{2\cdot\gamma}{\gamma+1}\frac{T}{\frac{\gamma-1}{2}\cdot M^2+1}}\,. \tag{9}$$

Although they remain approximate, the results provided by this model give satisfactory orders of magnitude, they have been successfully confronted with experiments carried out at INERIS as well as with published data. Again, the major objective here is to be able to estimate the characteristic times of the explosion propagation rather than the pressure built up in the pipes. When an explosion occurs in a structure made of interconnected enclosures the explosion can be transmitted from one vessel to its neighbours and the flame propagation can become of an extreme complexity [11]. In such case. A schematic of a possible course of events is presented in Fig. 4: the dust ignition in the primary enclosure induces a first explosion (4a) and generates a significant turbulence and flow velocity in the connected pipe (4b). Then large quantities of the combustible mixture will be pushed in the downstream enclosure and pressurize it. After its significant acceleration in the duct, the flame will enter the pressurized and highly turbulent combustible mixture in the secondary volume. A secondary explosion, of much greater violence can then happen (4c). It can also reverse the flow completely and push the reactive front back in the primary vessel where the combustion is not terminated (4d).

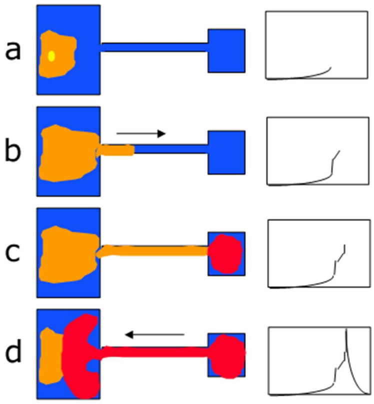

Fig. 4. Schematic representation of explosion development in interconnected enclosures [11].

Because in a wide range of situation the decoupling of 2 enclosures in only partial or impossible, it is of a great importance to account for this phenomenon. In other words, it is necessary to estimate the turbulence in the model structure and adapt the turbulent flame velocity *St* in the downstream equipment accordingly. Phenomenological semi-empirical models are available to estimate the pressure effects due to the flame arrival in the turbulent mixture of the secondary volume. In most situations, the turbulent flow will be induced by jets which characteristics are relatively well known (see [12] for further details on jet theory). A prediction tool was elaborated from this knowledge database. Analytic models can be to estimate the local turbulence velocity u' and the characteristic sizes of the turbulent structures *Lt* were proposed by Hinze [13]. The two flow turbulence parameters *u'* and *Lt* can then be used to estimate the turbulent flame velocity with a Gülder empirical model [14]. Further details on the application of this model have been published more recently by Proust [4]. The main interest here is the order of magnitude to the flame velocities enhancement due to the turbulence effect that can be on the order of 5 to 20 times that observed in the same mixture at rest. Empirical estimations can be made on the turbulence parameters *Lt* and *u'*.

Tamanini [15] proposed an integral version of the well-established k-epsilon model for turbulence. For the present illustration, we retain the steady state version of k-epsilon equation where the production rate (P_k) is equal to the dissipation rate (ε). Proust [16] assumed that *Lt* might be chosen constant and proportional to a linear dimension of the volume since this parameter can be seen as a measure of the mean velocity gradients so that:

$$Lt = C_L V^{\frac{1}{3}} \quad k = \frac{3}{2} u'^2 \quad P_k = \frac{1}{2} q_m U_{inj} \quad \varepsilon = \frac{P_k}{M} \quad Lt = C_\mu^{\frac{3}{4}} \frac{k^{\frac{3}{2}}}{\varepsilon}\,. \tag{8}$$

where q_m is the injected mass flowrate with the velocity U_{inj} in the volume *V* of mass *M*. C_μ and C_L are constants of the order of 0.05 and 0.09 [15]. Proust compared the model results with experimental results and published data and showed a satisfying compatibility in both cases [16].

THE EXPLOSION SCENARIO

Because of the specific phenomenology of flame development in the complex structure made of interconnected enclosures it is necessary to define first an explosion scenario which is the baseline for the comprehensive analysis of the explosion effects in the structure. In face of the multiplicity of the possible explosion scenario at stake in the current example, we will consider the example of an ignition in the mill during normal operation, that is then transmitted to the cyclone and to the filter. In the present case, the explosible dust is coal powder which is known to have a K_{St} value close to 150 bar.m/s and a $P_{\max}$ on the order of 8 bar (data from the Staubex database). Depending on the technology, mills and cyclones can resist to explosion pressures up to 3 bar. The filter is however of a lesser resistance, 500 mbar in this example. For this reason, let's assume it is sold to the industrial already equipped with 5 m^2 of vent panels. In this case we consider a volume of and 60, 20 and 300 m^3 respectively for the mill, cyclone and filter. They are connected by DN800 ducts of length 15 m.

The explosion is initiated in the mill and is transmitted to the first duct. The flame propagates to the cyclone, pushed by the overpressure in the mill at a speed of 200 m/s. Under these conditions, when the flame arrives in the cyclone, the mixture is highly turbulent as not only the flame has a very high velocity but also it is pushing large amounts of the reactive dust (as much as 70 to 90 % of the reactants in the duct [9], [11]) inside the cyclone. The combustion occurs at a quasi-constant volume inside the cyclone will occur (despite the exhaust ducts). An overpressure of the order of the dust $P_{\max}$, 8 bars seems possible but again a complete failure of the cyclone happen before reaching this value (we assume a resistance of the cyclone of 3 bar in this case study). Such scenario was simulated with the EFFEX code and the results support this summary of events:

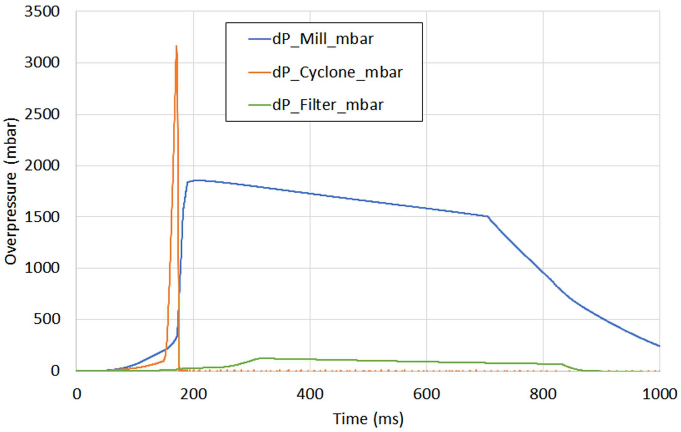

Fig. 5. Overpressure calculated in the mill, cyclone and duct; explosion ignition in the mill.

The flame should continue to the filter at speeds more than 400 m/s at the beginning of its propagation but is eventually slowed down to less than 100 m/s before reaching the filter, because of the sudden bursting of the cyclone. Note that while the vents in the filter strongly limited the overpressure, in the mill the reversal of the flow lead to a significant increase of turbulence and an intensification of the combustion. It appears that in the current example, the filter and the mill withstood the internal explosion, but the consequences of such scenario are not acceptable because of the bursting of the cyclone. It implies the projection of fragments up to several tens of meters and the emission of a pressure wave corresponding to a bursting energy of 20 MJ, that is roughly equivalent to the detonation of 5 kg of TNT, the effects of which are known to be dangerous for humans from 20 to 40 m in open field.

IMPLEMENTING THE EXPLOSION PROTECTION STRATEGY

The potential effects of an explosion within such installation are not acceptable and make it absolutely essential to equip it with explosion protection devices. As the most fundamental principle is the safety of people. As a result, the cyclone protection is a requirement here. Different techniques may be used such as deflagration venting which consists in discharging the explosion through an orifice. The vent area must be calculated so that the maximum pressure reached in the protected vessel, P_{red} remains significantly lower than the mechanical pressure resistance of the enclosure. A mistake would be to consider the cyclone separately: knowing the dust reactivity parameters (K_{St} = 150 bar.m/s, $P_{\max}$ = 8 bar) in this “independent” volume, one would estimate vent areas on the order of 0,5 m^2 to limit the P_{red} to 1 bar in the cyclone (calculations based on EN14991:2014 [3]). However, proceeding such way completely occults the flow and flame acceleration effects in the pipes (supported by the upstream exploding enclosure) and the significantly enhanced combustion effects downstream the pipes, thus rendering the protective equipment completely inefficient. A simulation of this scenario in EFFEX shows that despite the vent, the cyclone burst because of the large flame velocity transmitted from the pipe. Thus, a much larger vent area is needed, 3 m^2 are computed with EFFEX. However, protecting the cyclone alone is not sufficient:

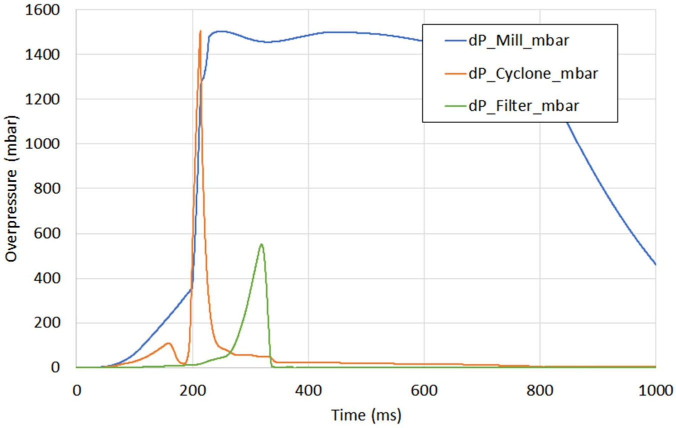

Fig. 6. Overpressure calculated in the mill, cyclon and duct; with 3 m^3 vents protection on the cyclone.

Now that the mill-cyclone system is protected, there is still a large overpressure responsible for significant flame acceleration in the second duct section, between the cyclon and the filter. The flame reaches the filter at a velocity close to 300 m/s, and the vent area installed on the filter becomes clearly insufficient.

A critical aspect in this example scenario is the coupling between the three enclosures, that need to be accounted for when choosing and dimensioning an explosion mitigation technique. Several options exist, a few are presented in the subsequent paragraphs:

- vents protection of the cyclone and the filter,
- vents protection in addition to decoupling system on the ducts,
- isolation of the duct and vent protection of the enclosures,
- explosion suppression,
- mixed systems protection.

Vents protection of the cyclone and filter

In the normative document EN14491:2014 [3], a dimensioning method is proposed to limit the violence of the explosion in an assembly “enclosure 1 – duct – enclosure 2”. The vent areas to install are often much wider as those predicted by the usual method in the same document. In such situation, the purpose of the vents is not only to unload the explosion but also to reduce the flame acceleration in the duct. The EN14491:2014 [3] document indicates an order of magnitudes for these vent areas, which imply typically a coefficient ($Av/V^{0,753}$) of 0,4. It can be highlighted that inconsistencies exist between such recommendations and the calculations that can be made with the formulas concerning the vents connected to ducts. Nonetheless the use of such technique is theoretically feasible in the present case with some additional calculations. Knowing the available vent area on the cyclone and the acceptable reduced explosion pressure P_{red}, one can estimate a maximal flame velocity acceptable in the duct. Then the vent area to install on the filter will selected in view of unloading the explosion but also limiting the flame velocity in the duct to the maximal acceptable value. In practice, this is barely achievable on the scale considered: according to Fig. 3, one would need to limit the overpressure in each enclosure to 0.5 bar, so that the flame speed remains low enough to allow a vent protection. This implies the use of much larger vent areas. Consequently, this is not a practical solution for the current example.

It is also important to point out that these vents only solution relies on the hypothesis of an ignition in the mill. When the explosion starts in the filter it is be necessary to perform new, yet similar, calculations. Also note that the environment around the enclosures (a road, workers, a wall, etc.) may impose to have vent ducts, deflectors or flame arrestors at the exhaust of the vents. All these systems impede the explosion discharge and induce a lower vent efficiency, thus the necessity again to install larger vent areas.

Vents protection in addition to decoupling system on the ducts

The previous mitigation solution imposes to have large vent areas on each device, which may not be feasible for practical reasons such as the bulk around the structure. The smallest possible vent areas Av, for each equipment, can be estimated separately form the EN14491:2014 [3] formulas. For instance, for the cyclone we computed earlier 0.5 m^2, and for the furnisher of the filter sold it with 5 m^2 of vent area. In the case of isolated enclosures, this is expected a conservative approach as the $P_{\max}$ and K_{St} terms are measured in more penalizing conditions (dust concentration, turbulence) than they are supposed to exist in the industrial process. However, for this model to be valid for connected enclosures, the violence of the explosion must correspond to the limitations defined in the standard, which implies that the turbulence level must remain in the range of the test that were performed to establish this formula. A direct consequence of this is that these lower venting areas may be used provided the duct effect can be neglected, which can be done when the explosion is either decoupled or isolated. Firstly, we will consider the option of the explosion decoupling.

Explosion decoupling devices are designed to limit the flame velocity in a duct. It can be realized by adding vents on the duct that are designed to open before the flame arrival and slow down the flow in the event of an explosion. Such systems may also be constructed in view of forcing the flame to change directions, to prevent excessive accelerations. Those decoupling systems can be dimensioned so that the turbulence induced in the downstream enclosure remain at an acceptable level, however they will not stop the flame but only slow it down. Experiments performed at INERIS confirmed that an explosion generating a 2 bar overpressure in an enclosure can induce a flame velocity on the order of 400 m/s in the connected duct without any protection while having vents on the duct close to the exploding vessel can limit significantly the pressure effects and reduce the flame velocity by a factor 2 to 4 [17]. In the present case this would not be sufficient but reducing the flame velocity level between the two enclosures can make it possible to use smaller vent areas than those presented in the earlier paragraph, in fact one can use the vent area calculated earlier with EN14491:2014 [3] for the isolated cyclone. A calculation was performed with two explosion decouplers located at the middle of each duct, and with the 0.5 m^2 vent on the cyclone (in addition to the already installed 5 m^2 vents on the filter). The measured overpressure are presented in Fig. 7.

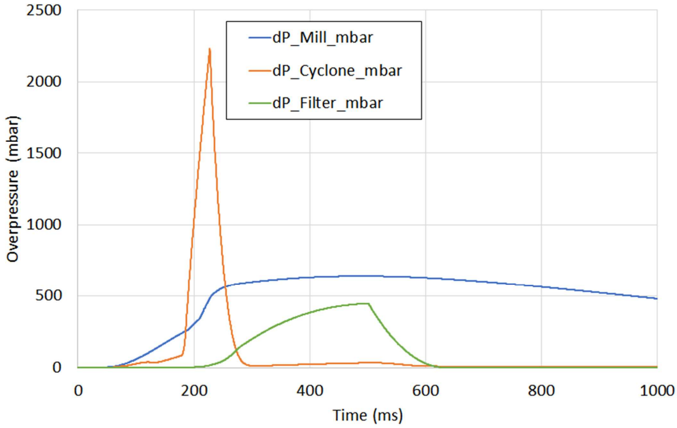

Fig. 7. Overpressure calculated in the mill, cyclone and duct; with 0.5 m^3 vents protection on the cyclone and an explosion decoupler on each duct.

In this case the installation is protected. Thanks to the decouplers, the flame velocity is sufficiently limited in the ducts, also leading to a lesser turbulence level in the cyclone and the filter, thus allowing the vents to fulfil their role efficiently.

Isolation of the duct and vent protection of each volume

If an isolation system is present on the duct, the flame will not propagate from one enclosure to the other one and then standard venting protection rules for isolated enclosures may be applied. These isolating devices can be of several types and based on very different technologies, for example: active (electronic detection of the explosion) or passive (purely inertial) flap valves, gate valves, pinch valves or chemical flame extinguishers. However, as any explosion mitigation device, they have their own limits that need to be accounted for. Firstly, some of those, such as the flap valves can only function in one direction, to stop a flame traveling in a direction opposed to the usual flow observed during the functioning of the process. Secondly some of these systems rely on the mechanical closing of the duct, which imply there are not efficient before a certain amount of time. From past experience on systems tested at INERIS, sometimes in the scope of ATEX certification, this delay is typically ranging around a few ms for active devices (with actual explosion detection and non-passive closing system such as in the case of gate valves or pinch valves) to a several dozens of ms when the device is fully passive and actuated by the explosion generated flow. Depending on the flame velocity (which can hardly be lower than 150 m/s in the present configuration) and the duct length (15 m here) it is necessary to ensure that the chosen system is really able to stop the flame. Also, quite regularly singularities, such as bends or a restriction generating a Venturi effect, are present on the ducts of industrial processes; they may alter the flow significantly. This needs to be considered when installing the isolation devices. Finally, there is also an upper limit in time (chemical isolation) or installation distance (mechanical isolation) after which the extinguishing cloud has settled down or the duct pressure has become too high and the isolating system will fail mechanically.

Explosion suppression in the mill and the cyclone

Alternatively, it is possible to use explosion suppressors on the mill and the cyclone. Those are based on the active and early detection of explosions coupled with a chemical agent that is injected at a sufficient rate so that the explosion can be quenched before it becomes too damaging for the structure. Typical delays for flame quenching are on the order of a few dozens of ms. As it is intended to extinguish the flame in each of the capacities, there should not be significant acceleration effect through the pipe between the cyclone and the filter, so that it is not necessary to install an isolation device. However, this is only true in the specific case of this installation and because a ST1 dust is chosen. Under these conditions, the risk of dust explosion in the filter persists. It is therefore a fundamental requirement to have vents on the filter. Methods for modelling the suppression devices have been implemented in EFFEX but they will not be described at this stage. Further details on this specific aspect may be found in [18].

Mixed systems protection

The solutions presented in the previous paragraphs can be combined, but again without losing the perspective that the enclosures are connected by a duct. For example, if the filter is outside of the building and the cyclone is located inside, the former can be protected by a vent while the later cannot (it is assumed that people are working in the same building). It would be possible in such case to protect the cyclone with explosion suppressor. Again, it cannot be done without a due consideration of flame velocity / acceleration in the duct. Explosion suppressors are certified within limits in terms of dust reactivity (among other limits such as the throw of the extinguishing cloud or the activation delay) that are applicable to the case of isolated enclosures. This is not the case if the flame has been significantly accelerated in a duct before reaching an enclosure in which the turbulence has been significantly increased compared to the standard process conditions. Consequently, for the suppression technique to remain effective in this situation a decoupling device or an isolation valve might be needed between the mill and the cyclone. The limitations referred to in the preceding paragraphs for the different explosion mitigation devices apply.

CONCLUSION

A strategy to implement an explosion mitigation solution has been presented around the example of a simplified industrial coal grinding process made of a mill, a cyclone, and a filter. A phenomenological analysis of explosion development and propagation in dual enclosure-duct systems was presented. The scenario of an explosion starting from the mill was selected as a reference to highlight the critical mechanisms involved when explosions propagate between interconnected enclosures. In the fourth part a way to account for the real explosion conditions is given, allowing a choice and dimensioning of a set of safety systems. Vent area calculations were presented together with the order of magnitudes of the characteristic functioning parameters of the other safety systems that may be implemented. Beyond that an important focus is given on the actual strategy of protection to implement, which aims at protecting firstly the people working close by then the structure and must always rely on a physical understanding of the dust flame propagation (in enclosures and in ducts) as well as its interaction with its environment (turbulence generation, pressure effects). A specific focus can thus be made on two fundamental aspects: on the one hand, it is of critical importance to understand how the flame propagates in a given complex system. On the other hand, the behaviour of the protection systems that might be used must also be carefully studied as it cannot be dissociated form the previous analysis, those systems will indeed systematically have an effect on the explosion driven flow.

REFERENCES

[1] NFPA68:2012 Standard on Explosion Protection by Deflagration Venting.

[2] EN14797:2007 Explosion venting devices.

[3] EN14991:2014 Dust explosion venting protective systems.

[4] C. Proust, The usefulness of phenomenological tools to simulate the consequences of dust explosions: the experience of EFFEX, International ESMG symposium, Nürnberg, Germany, 2005.

[5] B. Lewis, G. Von Elbe, Combustion, flames and explosions of gases: 3rd edition, Academic Press, London, 1987, ISBN 0-12-446751-2.

[6] R.K. Eckhoff, Dust explosions in the process industries, 3rd ed., 2003, ISBN 0-7506-7602-7.

[7] G. Darrieus, Propagation d'un front de flamme. Essais de théorie anormales de déflagration par développement spontané de la turbulence, 6th International Congress of applied mechanics, Paris, 1944.

[8] C. Proust, Prévoir les effets des explosions de poussières sur l'environnement, EFFEX, un outil de simulation, Rapport produit pour le compte du MATE, available at www.ineris.com, 1999.

[9] C. Proust, Dust explosion in pipes: a review, J. Loss Prevent. Process Ind. 9 (1996) 267-277.

[10] Y. Grégoire, C. Proust, E. Leprette, Dust explosion development in a vessel-duct arrangement, 10th International Symposium on Hazards, Prevention, and Mitigation of Industrial Explosions, Bergen, Norway, 2014.

[11] H.N. Phylaktou, G.E. Andrews, Explosion development in pipeline systems and linked vessels UKELG 25th meeting, Industrial Combustion Hazards, Joint Meeting with the Combustion Institute (British Section), 1999.

[12] E. Ruffin, Etude des jets turbulents à densité variable à l'aide de modèles de transport au second ordre, thèse de doctorat de l'université d'Aix-Marseille II, n° 207-94-59, 1994.

[13] J.O. Hinze, Turbulence, 2nd edition, Mc Graw-Hill company, New-York, 1975, ISBN 0-07-029037-7.

[14] Ö.L. Gülder, Turbulent premixed flame propagation models for different combustion regimes, Proc. Combust. Inst. 23 (1990) 743-750.

[15] F. Tamanini, The role of turbulence in dust explosions, J. Loss Prevent. Process Ind. 11 (1998) 1–10.

[16] C. Proust, J. Daubech, E. Leprette, Differentiated routes for the simulation of the consequences of explosions, J. Loss Prevent. Process Ind. 22 (2009) 288–294.

[17] P. Roux, C. Proust, Méthode de protection contre les explosions: évents – explosions de poussières, rapport INERIS-DRA-PRo-CPr-02-25313, 2003.

[18] K. Chatrathi, J. Going, Dust deflagration extinction. Proc. Saf. Progr. 19 (2000) 146–153.

The Use of CFD to Support ALARP Designs for Energy Centres

Giacopinelli P.*, Coffey C., Morrison G., Price D.

Gexcon, Birchwood, Warrington, UK
**Corresponding author's email: pablo.giacopinelli@gexcon.com*

ABSTRACT

Due to the increasing demand for energy in the UK both for housing and industrial needs in recent years, the government has incentivised 'distributed' energy generation in order to reduce the strain on central generation capacity and increase energy efficiency. Since these Energy Centres use natural gas, the installation must comply with the Dangerous Substances and Explosive Atmospheres Regulations (DSEAR). Due to space constraints, many new developments are unable to house the energy centre in a totally separate building. The basement location for an energy centre is not ideal for reducing the risk from explosion to members of the public and workers; industry standards and guidance recommend against this location. However, it can still be considered for building design, provided that the risks have been suitably assessed and can be shown to be As Low As Reasonably Practicable (ALARP). Standards provide high level design guidance, but no information is given on "how to" or "need to" properly assess this design concept. By means of detailed consequence analysis based on CFD simulations, this paper presents Gexcon's methodology to help review mitigation barriers and allow the design to be optimised with respect to them, and so assisting to demonstrate compliance with regulations and reduction of risk in line with the ALARP principle. The impact of ventilation, dispersion and gas detection on the explosion risks are discussed in detail.

KEYWORDS: CFD, ALARP, risk assessment, mitigation barriers.

INTRODUCTION

Due to the increasing demand for energy in the UK both for housing and industrial needs in recent years, the government has incentivised "distributed grid" energy generation in order to reduce the strain on central generation capacity and increase energy efficiency. This approach considers localised centres generating energy by means of Combined Heat and Power (CHP) systems and highly efficient boilers. CHP plants use waste heat to achieve efficiencies in excess of 80%, while traditional gas power stations range around 50% and coal 40%.

As a result of large urban building developments, combined with a desire to maximise the use of limited space within the construction area, the number of designs incorporating energy centres within multi-use occupied buildings (e.g. basements) have increased dramatically. These centres, which are normally unmanned, usually combine large amounts of congestion (due to a wide variety of piping and equipment sizes) within very confined areas. This could lead to significant explosion consequences following the ignition of an accidental gas release.

Gexcon have seen a rise in requests for assistance in these type of facilities over the past few years, in order to provide advice concerning explosion safety related to the use of natural gas. Ultimately our support was to ensure that the schemes are designed and built in compliance with standards to demonstrate:

1. That the risks have been suitably assessed and to assist with demonstrating that the risks are As Low As Reasonably Practicable (ALARP) [1], in line with UK law, and

Proceedings of the Ninth International Seminar on Fire and Explosion Hazards (ISFEH9), pp. 1246-1258
Edited by Snegirev A., Liu N.A., Tamanini F., Bradley D., Molkov V., and Chaumeix N.
Published by Saint-Petersburg Polytechnic University Press
ISBN: 978-5-7422-6498-9 DOI: 10.18720/spbpu/2/k19-118

2. That the facility complies with the requirements of the Dangerous Substances and Explosive Atmospheres Regulations (DSEAR) [2]

Due to space constraints, many new developments are unable to house the energy centre in a separate building. The basement location for an energy centre is not ideal for reducing the risk from explosion to members of the public and workers whose place of work is located within the multi-use building, and certain standards (e.g. IGEM/G/5 [3]) recommend against this location. However, basements can still be considered for building design, provided that the risks have been suitably assessed and can be shown to be ALARP [1], in line with the general duties under the Health and Safety at Work Act 1974 [4] and reinforced in Regulation 6 of DSEAR [2] which calls for the elimination or reduction of risks due to hazardous substances. Standards provide high-level design guidance, but no detailed information is available within accepted good practice and literature to properly assess this design concept and demonstrate that risks are ALARP [1].

By means of detailed consequence analysis based on Computational Fluid Dynamics (CFD) simulations using FLACS [5], a methodology is presented to help review mitigation barriers and allow the design to be optimised with respect to them, and so assisting to demonstrate compliance with the regulations.

FLACS CFD SOFTWARE

The simulations in the present study were conducted by means of FLACS [5], a specialised CFD tool for safety applications developed by Gexcon AS. One of the key features that distinguishes FLACS [5] from most commercial CFD codes is the use of the porosity / distributed resistance (PDR) concept for representing complex geometries on relatively coarse computational meshes. Simulations were setup in a manner consistent with specific user guidelines. The User's Manual provides comprehensive information on how to set up simulations, the modelling and theory underlying the code, its experimental validations and its limitations.

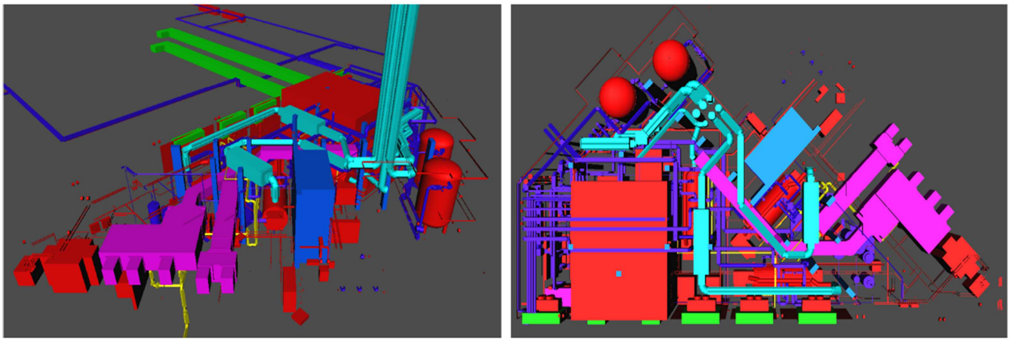

Fig. 1. Geometrical model created for the simulations of the energy centre (left, side view; right, top view).

GEOMETRICAL MODEL

The first step in a simulation study is the construction of a geometry model. Gexcon has many years of experience in analysing onshore and offshore installations, at all stages of the project life cycle, from concept phase to decommissioning. An incomplete geometry model can be a significant source of uncertainty in the CFD analyses. For this reason, our studies tend to focus on building a representative model of the installation, paying close attention to congested regions, which contribute towards enhancing turbulence levels and mixing. This could result in higher overpressures in explosion scenarios or less effective ventilation and dispersion of gas clouds.

Figure 1 shows the geometrical model created for the study, where boilers, pipelines of different diameters, water tanks and even ventilation and flue extraction ducts (among others) were considered.

VENTILATION ANALYSIS

An internal ventilation study was first conducted to provide the basis for the subsequent analysis. A detailed prediction of the internal flow patterns helps determine the effectiveness of the ventilation system and allows any potential dead spots to be identified. Ventilation patterns also provide valuable information to predict the potential behaviour of (low momentum) gas dispersion scenarios.

The energy centre accounted for several supply and extraction units distributed across the room and at different levels. Figure 2 provides an example of the flow velocity (UVW_3D) contour map at ground level. Good ventilation was observed in the room at different heights, particularly in the region in between boilers A and B and in front of boiler C, where there are gas lines and connections (i.e. flanges, valves, etc). Some areas of lower ventilation were observed around the water tanks and the lower right corner of the energy centre. This should not be a major issue, with respect to DSEAR [2], given that no gas lines were present in those regions.

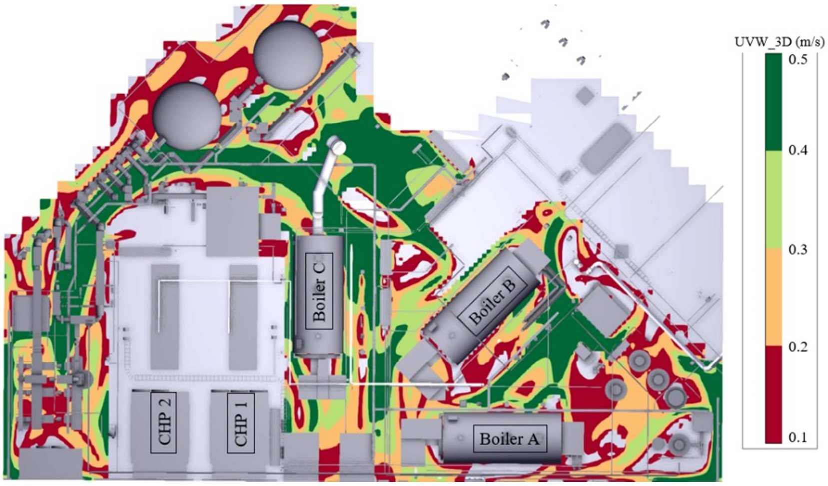

Fig. 2. Velocity contour map at ground level.

DISPERSION ANALYSIS

The objective of the dispersion studies was to simulate a number of unintended gas releases that would provide realistic and accurate data on how gas might disperse and accumulate in different areas of the energy centre. Based on the gas line P&ID, a combination of leak locations, leak directions and leak rates were modelled so that the simulated gas clouds cover a representative number of realistic loss of containment scenarios. Leak scenarios were chosen based on those most likely to develop large clouds and those most likely to be challenging for the gas detection system. The flow patterns determined in the ventilation study were used to make this assessment. Figure 3 shows some of the leak locations and directions defined for the dispersion analysis at ground level. Releases were directed towards areas of ‘reduced’ ventilation, where dilution could be less effective.

Table 1 provides further details of the jet release pressures and hole sizes considered, which will directly affect the mass flow rate of the releases. A combination of full bore rupture (i.e. line diameter) and small hole size (30 mm) leak scenarios were considered.

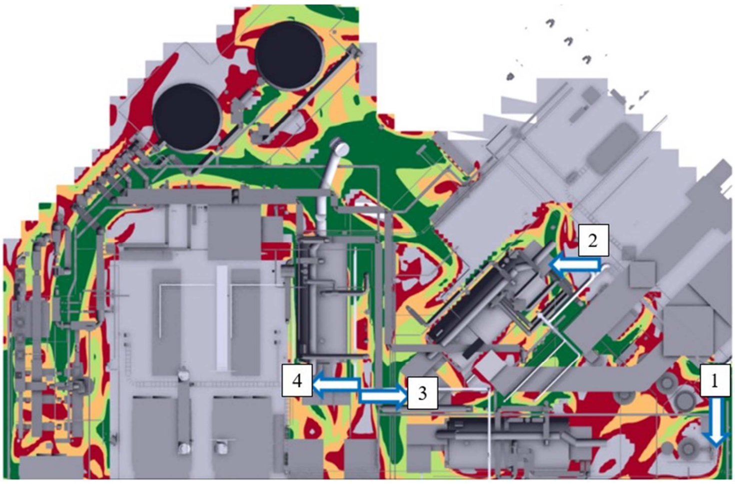

Fig. 3. Location and direction of leaks at ground level.

Table 1. Combinations of release pressure and hole sizes considered for the study

Jet location	Release pressure (mbar)	Hole size (mm)
1, 2, 5, 6	250	30 and 250
3, 4	250	30 and 100
7	150	30 and 125

The small hole sizes which statistically represent a typical installation are very demanding in terms of computational resources, hence a trade-off was made between the size of hole modelled and the time and resource required to model the scenario. Some design standards [3] consider hole sizes of 0.5 to 2.5 mm^2 depending on the type of installation when assessing the extent of hazardous areas for these types of facilities. This therefore results in the dispersion scenarios modelled being conservative when assessing small hole size releases. Item “FR 1.3 Pipework” [6] quantifies the frequencies for the small and large ruptures considered as 1x10^{-6} and 5x10^{-7} (per m per yr.) respectively for pipework diameter up to 149 mm, and 7x10^{-7} and 2x10^{-7} (per m per yr.) respectively for pipework diameter up to 299 mm.

Figure 4 and Fig. 5 show the evolution of the flammable gas cloud (i.e. between the Lower and Upper Flammability limits, LFL and UFL, respectively) based on the equivalence ratio as %LFL (ERLFL) for one of the release locations and different hole sizes. For a full bore rupture scenario, the upper half of the room is filled within a minute and a half following the release (see Fig. 4). But for a small hole size release, the extent of the flammable gas cloud remains within a 3 m radius of the release source (see Fig. 5). For a constant line pressure, the hole size plays a key role as the mass flow rate is significantly increased with a larger hole size. For this case, the mass flow rate achieved for a full bore rupture was 7.3 kg/s, while for a small hole size release this was just 0.1 kg/s (i.e. 73 times smaller).

Further information on the flammable gas cloud size for the different release scenarios simulated is shown in Fig. 6 (full bore rupture) for the release time modelled. To evaluate the hazard of a given gas cloud, Gexcon has developed methods for natural gas that aim at estimating an equivalent stoichiometric gas cloud (Q9) with comparable explosion consequences [7]. The resulting cloud is a scaling of the non-homogeneous gas cloud to a smaller stoichiometric gas cloud that is expected to give similar explosion loads as the original cloud (provided the shape and position of the cloud are chosen conservatively, as is the ignition point).

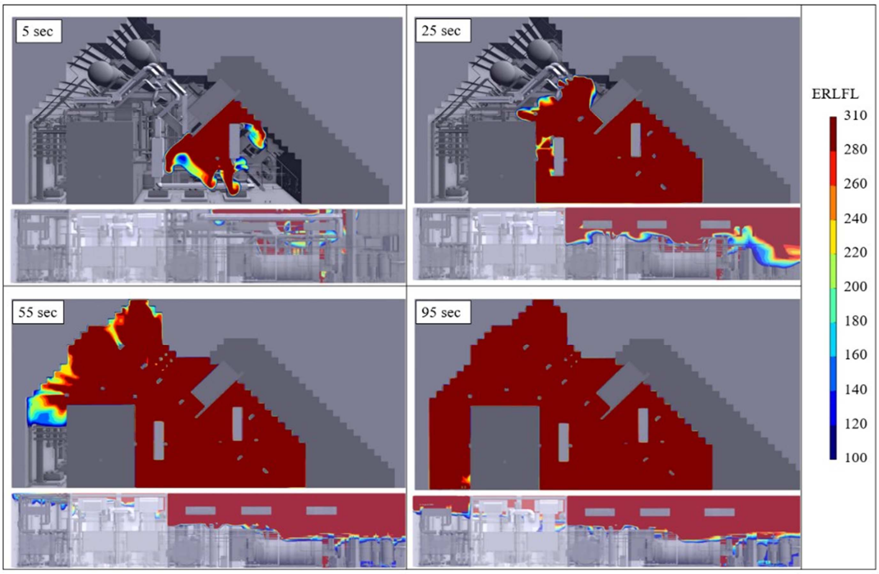

Fig. 4. Flammable gas cloud evolution from a 'full bore rupture' release at location #2 (LFL blue, UFL red).

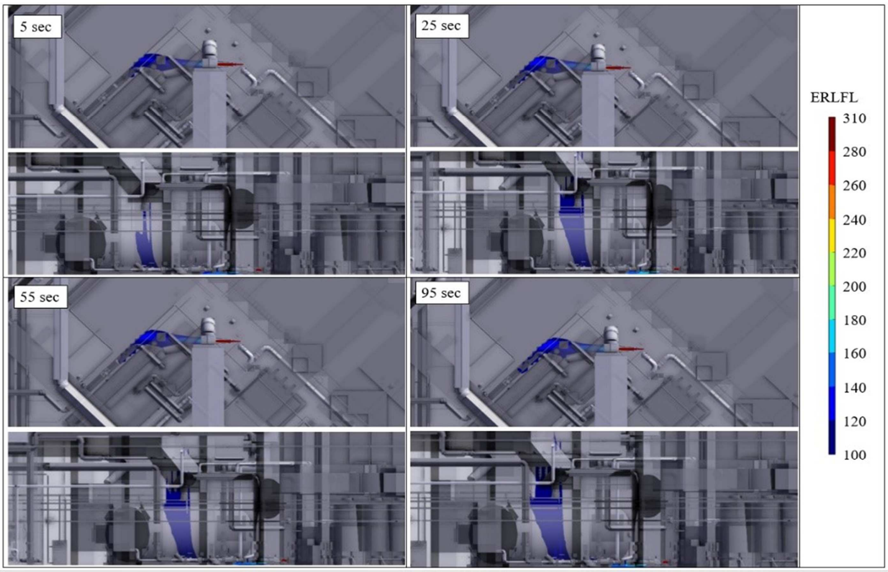

Fig. 5. Flammable gas cloud evolution from a 'small hole size' release at location #2 (LFL blue, UFL red).

A wide range of cloud sizes was obtained for full bore rupture scenarios as shown in Fig. 6, ranging from 175 m^3 up to almost 1200 m^3. These low frequency catastrophic scenarios are very unlikely to occur except in certain specific circumstances, such as physical impact or long-term vibration fatigue [6]. A good inspection and maintenance program coupled with control of activities in the area will substantially reduce the likelihood of these scenarios.

On the other hand, for the smaller hole size with higher event frequency, representing releases at flanges and other connections, the cloud sizes were several orders of magnitude smaller than those for catastrophic full bore rupture scenarios. Here, the maximum gas cloud was approximately 0.33 m^3 for the scenarios considered. It is thus deemed that the ventilation system was effective at preventing the build-up of a dangerous flammable gas cloud within the room for these situations.

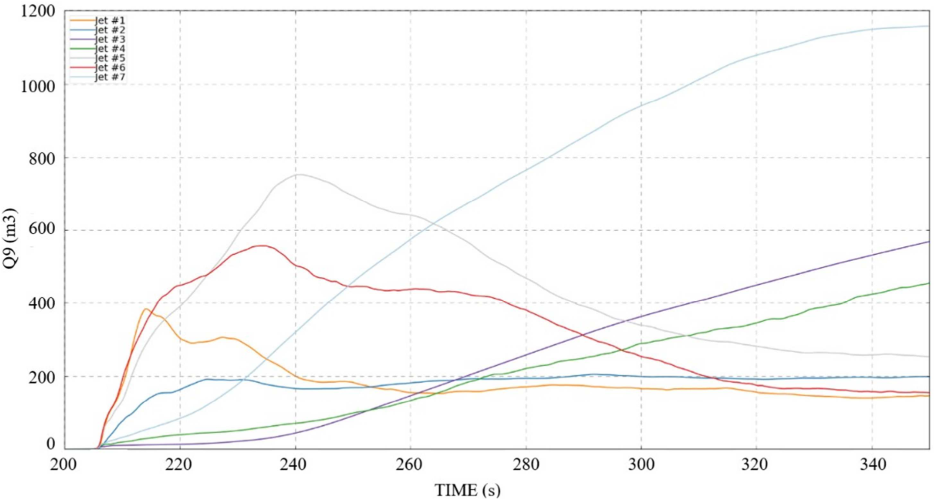

Fig. 6. Equivalent gas cloud sizes (Q9) obtained from full bore rupture release scenarios.

GAS DETECTION ANALYSIS

From the dispersion scenarios modelled it was possible to observe that small hole size leaks created small clouds which remain localised to the leak source. However, catastrophic full bore rupture scenarios created a wider range of flammable gas clouds that could fill the entire room.

A gas detection study was conducted to analyse the most effective means to mitigate the formation of large gas clouds in the event of a release. Different gas detector layouts with a varying number of detectors and locations were considered as shown in Fig. 7.

The performance of the detectors was evaluated based on an actuation set point relative to the LFL (i.e. 20%). A 1ooN (i.e. 1 out of N detectors) voting criteria was considered, meaning that detection arising from a single detector is needed to trigger an action (e.g. emergency automatic isolation of the gas solenoid valve). The different gas detector layouts proposed and analysed were tested against the results obtained from the dispersion study. Table 2 summarises the performance for each layout in terms of isolation time, were a shut-off valve response time of 1 second was considered for this exercise and so added to the detection time.

While all the scenarios simulated were detected, some differences between layouts were observed with respect to isolation time. For the full bore rupture scenarios, detection times between the layouts did not change considerably, consistent with the formation of large gas clouds within a short period of time resulted in consistent and short time to detection. For small hole size releases, differences in detection time were observed in most of the dispersion scenarios. While the performance between a system with 4 detectors (i.e. Layout 1) and 8 detectors (i.e. Layout 2) was very similar, 5 out of 7 scenarios were detected earlier with a larger number of detectors (i.e. 10 for Layout 3 and 12 for Layout 4). In the scenarios considered, Layout 4 appears to detect faster than Layout 3 for most of the releases, and so it was the recommended layout based on the analysis.

It should be noted, however, that testing a larger number of and different leak locations/directions other than those considered here could provide a different outcome and hence these results are indicative only, although they have been selected based on reasonable assumptions on the likely leak locations. Detection performance will also ultimately rely on selecting the correct detector type, proper system design and installation, coupled with ongoing inspection and maintenance of the system.

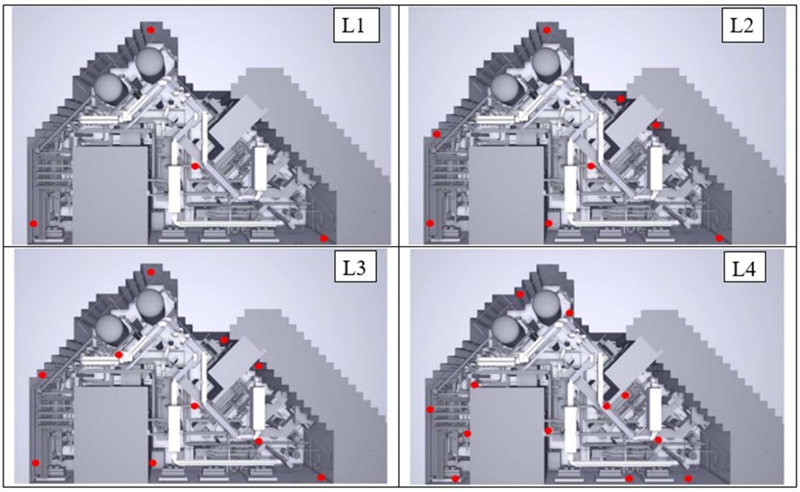

Fig. 7. Proposed point gas detector layouts. Red dots indicate the location of the gas sensors at ceiling height.

Table 2. Gas detector layouts performance for different releases conditions

Jet location	Isolation time (s) – Full bore rupture release				Isolation time (s) – Small hole size release			
	L1	L2	L3	L4	L1	L2	L3	L4
1	2.5	2.5	2.5	3.0	7.5	7.5	7.5	26.0
2	6.0	4.0	3.0	2.0	117.5	21.0	13.0	7.5
3	6.0	6.0	6.0	6.0	52.5	52.5	52.5	38.0
4	6.0	6.0	5.0	6.0	46.0	46.0	37.5	20.0
5	3.5	3.5	3.5	2.5	23.5	23.5	23.5	11.5
6	3.0	3.0	3.0	3.0	57.5	57.5	57.5	53.0
7	2.5	2.5	2.5	3.0	5.0	5.0	5.0	5.0

EXPLOSION ANALYSIS

Gas explosion simulations were conducted to ascertain the magnitude of the internal overpressures that could be generated if the cloud size (at the time of isolation) was ignited by a potential ignition source.

Table 3 summarises the gas cloud sizes obtained for full bore rupture and small hole size releases respectively for the different gas detection layouts. Clouds up to 110 m^3 were observed for full bore rupture scenarios, showing a significant decrease in the achievable maximum gas cloud compared to the values shown in Fig. 6. On the other hand, gas clouds from small hole size releases remained very small (maximum 0.33 m^3).

Figure 8 shows a comparison of the gas clouds for a full bore rupture and a small hole size release for dispersion scenario #2. The size of the clouds corresponds to the maximum value obtained for each corresponding scenario upon isolation (i.e. 91 m^3 for full bore rupture and 0.33 m^3 for small hole size release). The locations of the clouds were selected based on the dispersion patterns observed for the different release scenarios. The orange dot in the figures represents the ignition location, a combination of corner and centre-based positions were considered for the different dispersion scenarios studied.

Table 3. Gas cloud size upon isolation for the different dispersion scenarios and detection layouts

Jet location	Full bore rupture release					Small hole size release				
	L1	L2	L3	L4	**MAX**	L1	L2	L3	L4	**MAX**
1	90.0	90.0	90.0	106.0	**106.0**	0.06	0.06	0.06	0.06	**0.06**
2	91.0	58.0	38.0	19.0	**91.0**	0.33	0.22	0.21	0.16	**0.33**
3	11.0	11.0	11.0	11.0	**11.0**	0.09	0.09	0.09	0.09	**0.09**
4	21.0	21.0	19.0	21.0	**21.0**	0.09	0.09	0.09	0.08	**0.09**
5	98.0	98.0	98.0	75.0	**98.0**	0.08	0.08	0.08	0.08	**0.08**
6	109.0	109.0	109.0	109.0	**109.0**	0.07	0.07	0.07	0.07	**0.07**
7	20.0	20.0	20.0	23.0	**23.0**	0.11	0.11	0.11	0.11	**0.11**

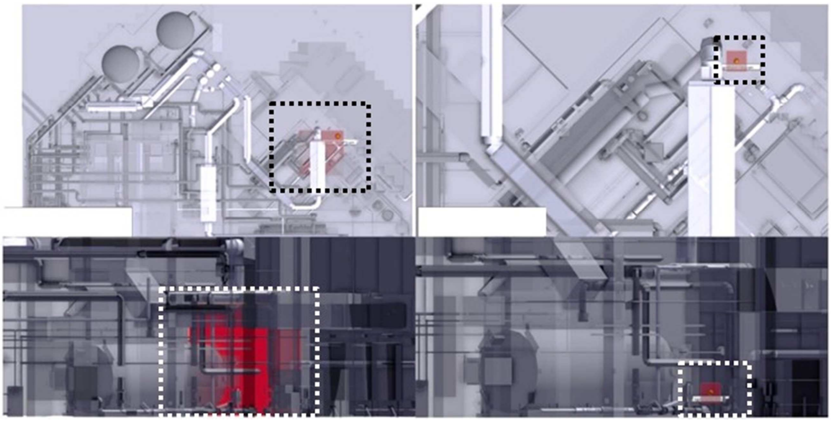

Fig. 8. Clouds (in red) defined for dispersion scenario #2 (left, full bore rupture; right: small hole size).

Figure 9 shows the approximate internal pressures reached following ignition of the different maximum gas cloud sizes (upon isolation) from full bore rupture scenarios. Pressure magnitudes (P) ranged from 0.02 barg for the smallest cloud considered (~11 m^3) up to 0.23 barg for the largest clouds (~109 m^3), remaining below the building slab resistance (~0.35 barg). No heat transfer through the walls was considered for the explosion analysis, hence the reason why the pressure does not decay in time after reaching a peak value. On the other hand, and for small hole size releases, very low internal pressures in the room were obtained for all the scenarios analysed and did not exceed 0.002 barg (i.e. typical pressure required to shatter a large glass window [8]).

A closer look at the internal pressure distribution inside the energy centre is shown in Fig. 10, where it is possible to observe that this peak pressure was only seen around the lower left corner area.

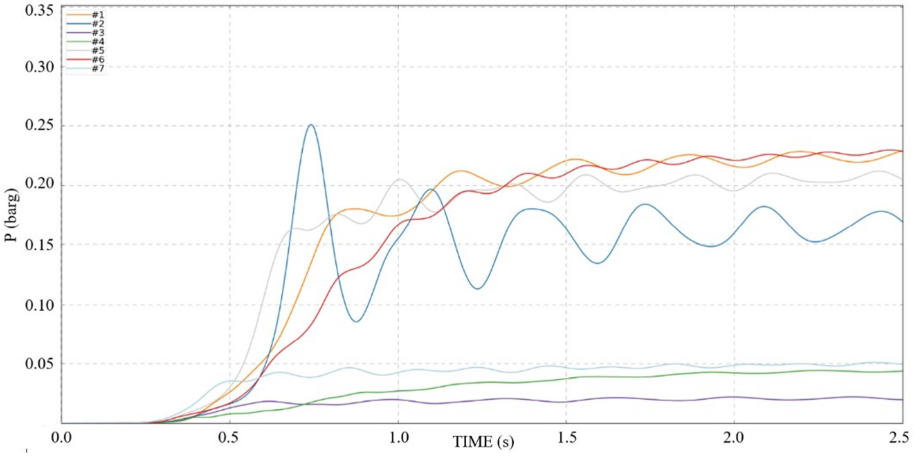

Fig. 9. Internal overpressures inside the energy centre following a gas explosion after full bore rupture.

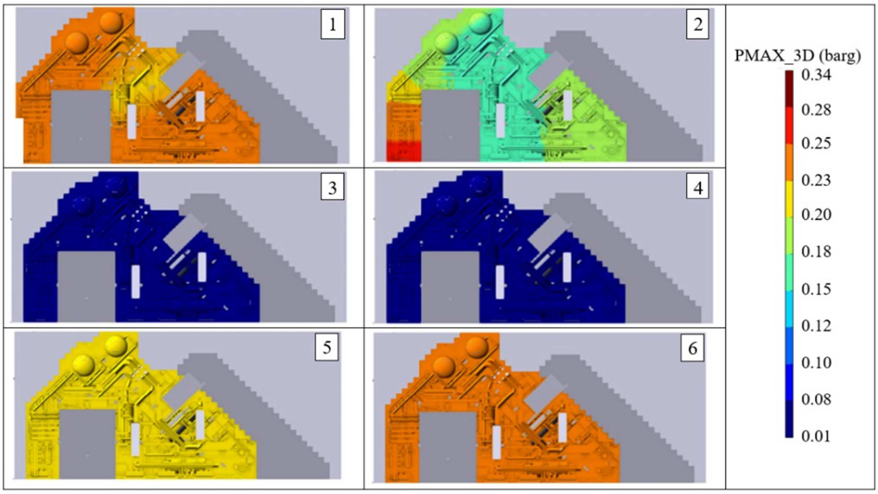

Fig. 10. Maximum pressure distribution (PMAX_3D) following a gas cloud explosion - full bore rupture.

DSEAR COMPLIANCE AND RISK ASSESSMENT

Since the facility (multi-use building) incorporates workers and uses natural gas, which has the potential to create a flammable or explosive atmosphere, the installation must comply with the DSEAR regulations [2]. These require amongst other things to conduct a Hazardous Area Classification (Regulation 5) and a suitable and sufficient Risk Assessment (Regulation 7). While catastrophic releases should be considered as part of the Risk Assessment, the Hazardous Area Classification focuses on “reasonably foreseeable” releases, which may occur during normal operation.

Hazardous Area Classification

Regulation 7 of DSEAR [2] requires that all employers shall classify places at the workplace where an explosive atmosphere may occur into hazardous or non-hazardous places. Detailed ventilation, dispersion and gas explosion simulations were conducted with FLACS [5] to determine the magnitude of the internal overpressures that could be generated if the cloud size (at the time of isolation) arising from a small hole size release was ignited by a potential ignition source.

Table 3 above shows the gas cloud size upon isolation for the different dispersion scenarios and detection layouts modelled using a leak orifice diameter of 30 mm. This is a very conservative leak orifice diameter, since generally 0.56 mm (calculated from a 0.25 mm^2 cross sectional orifice area) is used in IGEM standards [3], which is already considered to provide conservative results. The modelling results showed that the maximum gas cloud which could be formed is 0.33 m^3, which would have a diameter of 0.85 m assuming a spherical cloud. As the leak orifice diameter used for modelling is so conservative, the volume of gas cloud formed from a typical secondary grade of release (e.g. a flange leak) would typically be significantly smaller than this in reality.

The ventilation study concluded that good ventilation was present in the room at different heights, particularly in the region around the boilers, and around connections (i.e. flanges, valves, etc) on the gas lines. The degree of ventilation can then be considered as high relative to the potential gas cloud volume with fair availability for this installation, therefore the installation can be classified and maintained as Zone 2 NE (i.e. a hazardous zone in theory which would have negligible effect if ignited) in line with European Standard EN 60079-10-1 [9].

Evaluation of the Guidance from IGEM/G/5 Edition 2

An evaluation has been made in respect to the industry guidance document IGEM/G/5 [3]. The standard makes use of the terms ‘must’, ‘shall’ and ‘should’, when prescribing requirements according to the law. Several sections of the standard, that advise against the location of an Energy Centre in the basement, could be challenged based on the information provided by the simulations:

- Section 8.1.3 Note 2 deals with the response of the building structure to a range of releases. It has been demonstrated that even large leaks (i.e. 30 mm diameter hole size, which at 707 mm^2 are much greater than the typical size of 0.25 mm^2 recommended by IGEM guidance [3]) do not form a gas cloud which would compromise the structure of the energy centre.
- Section 8.2.1 deals with the location of the EC in the building. Leak detection, emergency isolation and robust ventilation systems are considered to reduce the risk to ALARP for the chosen location. FLACS [5] modelling shows that if an explosion occurs, then the structure will be protected as the peak overpressure is below the maximum allowable slab resistance.

Risk Assessment

In order to demonstrate ALARP, risks must be assessed, and additional risk reduction measures should be put in place to reduce the risks, where it is reasonably practicable to do so. An explosion following a catastrophic full bore rupture or a small hole size release is a credible worst-case consequence. Various barriers exist to either prevent or mitigate against this, including ventilation (to disperse gas clouds) and detection (to identify leaks and isolate the gas supply).

Barrier Assessment by means of bowtie diagrams

A 'bowtie' is a diagram that visualizes the risk in one easy to communicate picture. The diagram is shaped like a bowtie, where the ‘hazard’ sits on top, followed by the ‘top event’ (moment when control is lost over the hazard). Described on the left are the ‘threats’ (whatever will cause the top event), while on the right are the ‘consequences’ (results from the top event). Finally, in between, the ‘barriers’ controlling (on the left) and mitigating (on the right) unwanted scenarios.

The bowtie diagram in Fig. 11 [10] shows the relationship between the potential causes and consequences of a gas leak in the pipework of the energy centre, together with the barriers identified and required under European Standard EN 60079-10-1 [9] and the IGEM/G/5 [3]. While an explosion was identified as a credible worst-case consequence, the assessment shows that maintenance and inspection are of critical importance in preventing the degradation of the facility over time. It was assumed that the pipework and gas and fire detection systems are inspected and maintained periodically, and that the equipment will be commissioned by a competent person so that, where appropriate, the gas supply will be promptly and safely isolated upon an alarm being triggered.

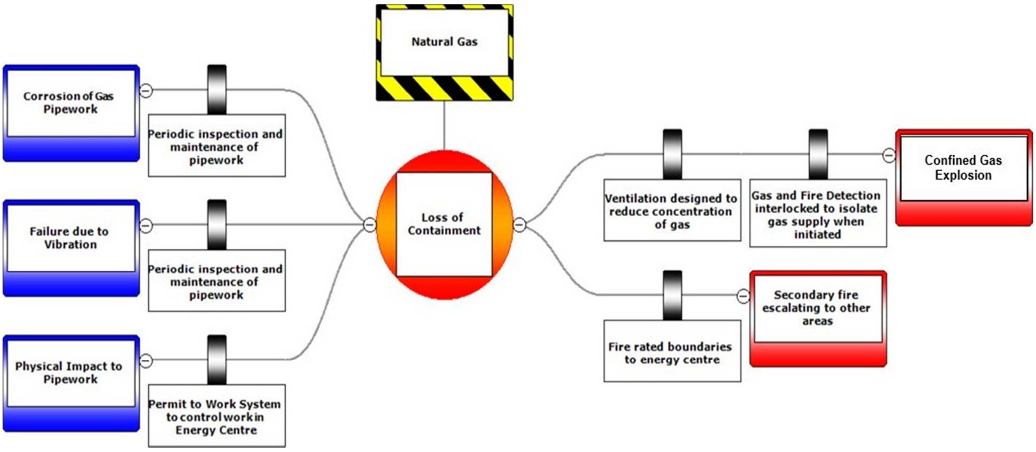

Fig. 11. Bowtie diagram for natural gas leak in the energy centre pipework.

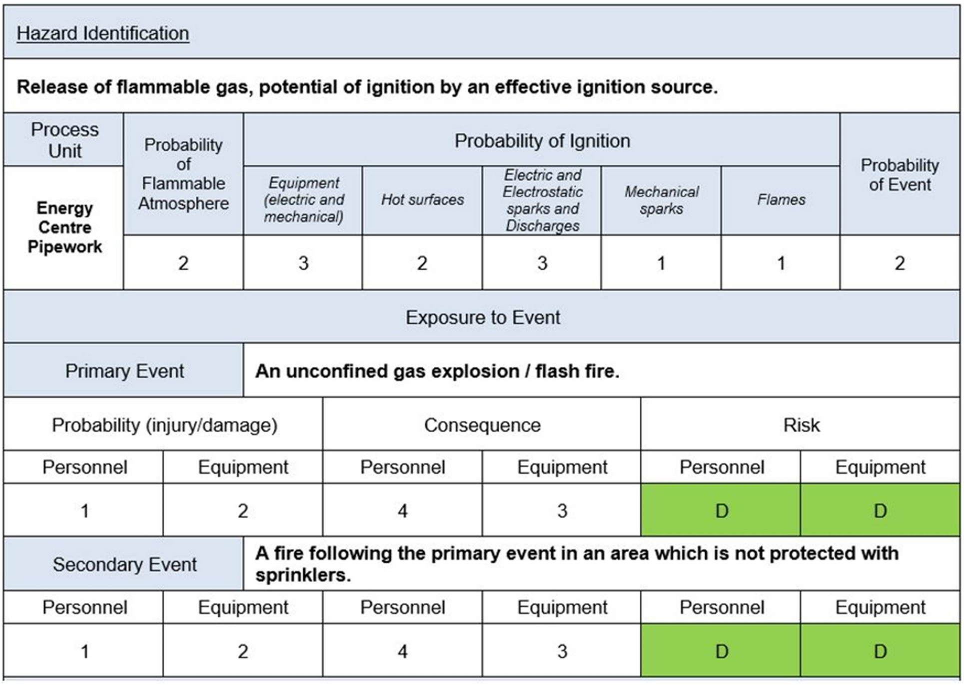

<table>
<tr><td colspan="8"><u>Hazard Identification</u></td></tr>
<tr><td colspan="8">Release of flammable gas, potential of ignition by an effective ignition source.</td></tr>
<tr><td>Process Unit</td><td rowspan="2">Probability of Flammable Atmosphere</td><td colspan="5">Probability of Ignition</td><td rowspan="2">Probability of Event</td></tr>
<tr><td rowspan="2">Energy Centre Pipework</td><td><i>Equipment (electric and mechanical)</i></td><td><i>Hot surfaces</i></td><td><i>Electric and Electrostatic sparks and Discharges</i></td><td><i>Mechanical sparks</i></td><td><i>Flames</i></td></tr>
<tr><td>2</td><td>3</td><td>2</td><td>3</td><td>1</td><td>1</td><td>2</td></tr>
<tr><td colspan="8">Exposure to Event</td></tr>
<tr><td colspan="2">Primary Event</td><td colspan="6">An unconfined gas explosion / flash fire.</td></tr>
<tr><td colspan="2">Probability (injury/damage)</td><td colspan="2">Consequence</td><td colspan="2">Risk</td></tr>
<tr><td>Personnel</td><td>Equipment</td><td>Personnel</td><td>Equipment</td><td>Personnel</td><td>Equipment</td></tr>
<tr><td>1</td><td>2</td><td>4</td><td>3</td><td>D</td><td>D</td></tr>
<tr><td colspan="2">Secondary Event</td><td colspan="6">A fire following the primary event in an area which is not protected with sprinklers.</td></tr>
<tr><td>Personnel</td><td>Equipment</td><td>Personnel</td><td>Equipment</td><td>Personnel</td><td>Equipment</td></tr>
<tr><td>1</td><td>2</td><td>4</td><td>3</td><td>D</td><td>D</td></tr>
</table>

Fig. 12. Risk assessment for a natural gas release inside the energy centre.

Summary Risk Assessment

The risk assessment presented in Fig. 12 summarises the estimated explosion risks for this installation, taking into account the barriers and risk reduction measures that were identified based on the Zone 2 NE classification (supported by the CFD results). Gexcon's risk assessment uses a semi-quantitative approach [11] designed to meet the requirements of DSEAR [2]. The risk assessment not only considers risks to people as required by health and safety law but also the risks to the business (plant and equipment).

Generally speaking, both the probability of formation of a flammable atmosphere and of an effective ignition source are ranked between 1 (very unlikely) to 5 (very likely), resulting in a probability (or the frequency) of an event occurring with a similar scale. Finally, different risk levels are assessed, ranging from E (very low and acceptable) to A (very high and unacceptable).

CONCLUSIONS

This paper presented a methodology following detailed consequence analysis based on CFD simulations to help review mitigation barriers and allow the design to be optimised with respect to them, and so assisting to demonstrate compliance with regulations.

An Energy Centre has undergone a significant technical safety assessment in order to determine a suitable level of safety for the installation and to support in demonstrating that the risks are reduced to a level which can be considered ALARP [1], in line with UK law and industry guidance in IGEM/G/5 [3]. Although this study considered a specific building design, it is straightforward to extend the proposed methodology to other configurations.

Hazardous area classification was supported by a comprehensive CFD study including ventilation, dispersion, gas detection and gas explosion analysis, in order to demonstrates that a Zone 2 NE classification was appropriate in line with the relevant European Standards [9].

The risk assessment indicated that the risk is tolerable, considering the implemented measures for risk reduction. Based on CFD analysis, it is believed that the basis of safety analysed (i.e. ventilation plus gas detection) was adequate in that the more likely (yet still very conservative) releases generate very small flammable clouds resulting in low internal overpressures in the event of ignition.

Finally, the barrier assessments showed that maintenance and inspection is of critical importance in preventing the degradation of the facility over time. It is then essential that the facility operator has rigorous inspection and maintenance procedures and that these are followed.

By means of CFD simulations, it was possible not only to assess the impact of ventilation and gas detection upon realistic dispersion scenarios, but also to determine the impact of explosion consequences from both likely (small) and unlikely (catastrophic) releases, in order to properly quantify risks to personnel and equipment and help to select appropriate mitigation barriers. This approach to risk analysis and management provides valuable information to the engineer or operator, helping to better represent the risk picture, and so assisting to improve the design of the installation and potentially reducing its CAPEX and OPEX.

ACKNOWLEDGMENTS

We are grateful to our colleagues Dr. Trygve Skjold, Dr. Kees van Wingerden and Mr. Djurre Siccama from Gexcon AS for their contribution to the final manuscript.

REFERENCES

[1] ALARP "at a glance", http://www.hse.gov.uk/risk/theory/alarpglance.htm (accessed 10 December 2018).

[2] Dangerous Substances and Explosive Atmospheres Regulations 2002, http://www.hse.gov.uk/fireandexplosion/dsear-regulations.htm, 2002 (accessed 10 December 2018).

[3] IGEM/G/5 Gas in Multi-occupancy Buildings, http://www.igem.org.uk/technical-standards/igem-standards/new/igemg5.aspx, 2012 (accessed 10 December 2018).

[4] Health and Safety at Work etc Act 1974, http://www.hse.gov.uk/legislation/hswa.htm, 1974 (accessed 10 December 2018).

[5] FLACS Software, https://www.gexcon.com/products-services/FLACS-Software/22/en (accessed 10 December 2018).

[6] HSE. Failure Rate and Event Data for Use within Risk Assessments, 2012.

[7] O.R. Hansen, F. Gavelli, S. G. Davis, P. Middha, Equivalent cloud methods used for explosion risk and consequence studies, J. Loss Prev. Process Ind. 26 (2013) 511-527.

[8] R. Eckhoff, Explosion Hazards in the Process Industries, second ed., Gulf Professional Publishing, 2016.

[9] BS EN 60079-10-1:2015 Explosive Atmospheres. Classification of Areas. Explosive Gas Atmospheres.

[10] BowTieXP Software, www.bowtiexp.com/uk (accessed 10 December 2018).

[11] K. van Wingerden, G. Pedersen, S. Davis, Application of a Short Cut Risk Analysis Methodology for Analyzing Dust Explosion Hazards, In: Am. Inst. Chem. Eng. 2010 Spring Meeting, 2010.

Hydrogen Safety in Design of the Nuclear Power Plant

Kotov V.*, Bezlepkin V., Kapitsa D.

JSC "Atomproekt", Research Engineering department, Saint-Petersburg, Russia
**Corresponding author's email: VVKotov@atomproekt.com*

ABSTRACT

In Russian project AES-2006 (NPP-2006), the overall safety concept for the nuclear power plant (NPP) is based on the in-depth defense principle, which implies the system of multiple barriers preventing the spread of ionizing radiation and radioactive substances into the environment. The last barrier preventing the release of fission products into the environment is the nuclear reactor building containment. During a severe accident like LOCA (Lost Of Coolant Accident), a large amount of hydrogen is produced in core reflooding and in oxidation of Zr fuel cladding by steam. When hydrogen appears inside the containment compartments, it mixes with steam and air thereby producing combustible mixture prone to detonation. In this paper, we present 3D simulation results of hydrogen-air-steam combustion in the NPP containment compartments using specialized 3D code FIRECON 1.0, with the complex geometry and a wide range of combustion regimes (from slow combustion to detonation) taken into account. Three scenarios are considered: (i) severe accident with break of pressurizer surge line accompanied by failure of active Emergency Core Cooling System (Large Break, LB LOCA); (ii) small leakage (Small Break, SB LOCA) from the cold loop thread with pressurizer failure, and (iii) uncontrolled severe accident (UnSA). The software is validated, and the dynamic loads imposed on the containment walls and inner structures are analyzed.

KEYWORDS: Hydrogen combustion, nuclear safety, CFD.

NOMENCLATURE

C_{H_2}, C_{O_2}, C_{H_2O}	volume fractions of H_2, O_2, H_2O (steam) (-)
E	internal energy (J)
e	specific internal energy (J/kg)
K	momentum ((kg·m)/s)
L	characteristic linear size (m)
Le	Lewis number (-)
M	mass (kg)
P	pressure (Pa)
S	surface area (m2)
T	temperature (K)
t	time (s)
V	volume (m^3)

u, v, w	velocity vector components (m/s)

Greek

α	molar fraction of combustion products (-)
δ	laminar flame thickness (m)
η	H_2/O_2 molar ratio (-)
λ	detonation cell size (m)
ρ	density (kg/m^3)
σ	reactant/product density ratio (-)
σ^*	critical density ratio (-)

Subscripts

i	gas mixture component
x, y, z	Cartesian coordinates

Proceedings of the Ninth International Seminar on Fire and Explosion Hazards (ISFEH9), pp. 1259-1268
Edited by Snegirev A., Liu N.A., Tamanini F., Bradley D., Molkov V., and Chaumeix N.
Published by Saint-Petersburg Polytechnic University Press
ISBN: 978-5-7422-6498-9 DOI: 10.18720/spbpu/2/k19-118

INTRODUCTION

Investigations of severe accidents made in recent years for pressurized water reactors show that in case of meltdown accidents, ignition and subsequent detonation of hydrogen-containing mixtures may cause the integrity violation of Nuclear Power Plant (NPP) containment, followed by the radionuclide release into the atmosphere and radioactive contamination of the environment.

During severe accident such as LOCA (Lost Of Coolant Accident), that is, loss of the coolant, as a result of dehumidification of the reactor core and vapor oxidation of the zirconium fuel cell shells, a large amount of hydrogen is produced. In the course of further development of the accident, hydrogen can penetrate into the containment compartments and form combustible mixtures with air and steam. From the point of view of severe accidents analysis, the most dangerous case is the detonation of such mixtures, since in this case the building structures inside the containment are subjected to the greatest dynamic load.

According to the requirements of national supervisory authorities, the rationale for hydrogen explosion protection must be fulfilled in the design of the nuclear power plant and presented in the safety justification report. At present, numerical modeling is one of the effective methods for such a justification. During the analysis of hydrogen safety, all possible scenarios of emergencies are modeled, and a technical solution is chosen that contributes to reducing the threat of possible combustion and detonation.

There are many different computer codes that are used to analyze severe accidents for different types of nuclear power plants. The application of these codes includes research and development, safety analysis regarding the introduction of hydrogen suppression systems, licensing or periodic safety assessment.

Depending on the mathematical models embedded in the codes, some codes are used to model all aspects of hydrogen safety (hydrogen generation, propagation, combustion, suppression), some codes are used only to calculate the formation of hydrogen inside the reactor facility, thus giving the boundary conditions for the codes, which simulate the spread, combustion and removal of hydrogen.

There are codes specifically designed for modeling combustion and in particular hydrogen detonation, which require as input data information on the distribution of hydrogen inside the nuclear power plant containment [1].

One of the first numerical approaches to simulate combustion processes in large scale facilities was provided by Efimenko and Dorofeev [2]. They combined a system of criteria and combustion models into a computer code CREBCOM for conservative estimates of possible pressure loads resulting from combustion of fuel-air mixtures. These models were validated on experimental data and then successfully employed in several industrial CFD (Computational Fluid Dynamics) codes, such as TONUS [3] and COM3D [4].

Interesting results according flame acceleration and deflagration to detonation (DDT) phenomena in APR1400 containment were obtained in [5]. As calculation tool the open-source CFD package OpenFOAM was chosen.

ACCIDENT SCENARIO

According to the dynamics of the coolant and hydrogen outlet inside the containment, the heavy accidents considered can be divided into two main groups:

- Accidents with a small leakage of the coolant and an accident with a complete blackout of the station;

- Accidents with a large leakage of the coolant.

Accidents with small leakage and accidents with complete blackout are characterized by a continuous release of the coolant into the leak with a low emission intensity and the greatest integral yields of hydrogen. Accidents with a large leakage of the coolant, on the contrary, are characterized by a high emission intensity at individual time intervals and smaller integral hydrogen outputs to the interior of the containment compartments. That was proved in many simulation tests, carried out for Nuclear Power Plant design solutions justification.

The choice of scenarios for the calculation of severe accidents is determined by the objectives of the deterministic analyzes being performed. The safety analysis should focus on quantifying station safety stocks and demonstrating that a certain degree of defense in depth is provided for this class of accidents.

As calculation scenarios, severe accidents with break of pressurizer surge line accompanied by failure of active Emergency Core Cooling System (Large Break, LB LOCA) and the small leakage (Small Break, SB LOCA) from the cold loop thread with pressurizer failure with the failure of the active part of the emergency cooling system active zone of the reactor were chosen. A characteristic feature of these accidents is the high hydrogen content in the steam generator room, where the leak from the pipeline rupture is directly modeled and the complexity of managing these accidents.

In addition to the calculations for the above scenarios, an uncontrolled severe accident (UnSA) calculation was performed that did not take into account the work of severe accident management systems such as the hydrogen removal system and the passive heat removal system from the containment. This calculation was interesting from the point of view of the possibility of the software used to simulate the combustion of hydrogen-containing gas mixtures under such conditions.

The initial parameters for combustion calculating are the results of a calculation analysis of the propagation, accumulation of hydrogen, and changes in the parameters of the environment in the containment compartments during the development of the emergency scenario in question, performed using the Russian code in the lumped parameters KUPOL-M [6] (not presented here because of paper volume limitation). Then, for each time point, an analysis was made of the possible burning regimes in the containment compartments and a time cut was selected in which combustion or detonation of the gas mixture is possible. For this time cut three-dimensional modeling of combustion in the containment compartments was carried out.

The resulting dynamic loads on the walls of the containment compartments can be used in the subsequent strength analysis, which shows the level of effect of combustion of the hydrogen-containing steam-air mixture on the integrity of the nuclear power plant containment.

SIMULATION METHODOLOGY

To simulate the combustion of hydrogen-containing gas mixtures in closed volumes of complex geometry in a wide range of combustion regimes (from slow combustion to detonation) and subsequent analysis of dynamic loads on the walls of a nuclear power plant, 3D computer code FIRECON 1.0 was developed by Russian Federal Nuclear Center in Sarov city with the participation of Joint Stock Company “Atomproekt” specialists [7].

As basic equations describing non-steady-state 3D multi-material gas flows relations expressing the laws of conservation for a motionless volume were taken:

$$\frac{d\vec{K}}{dt}+\int_S \rho\left(\vec{u},\vec{u}\right)d\vec{s}=-\int_S Pd\vec{s}\ , \qquad (1)$$

$$\frac{dM_i}{dt}+\int_{S_i}\rho_i\vec{u}_i d\vec{s}=0, \tag{2}$$

$$\frac{dV_i}{dt}+\int_{S_i}\vec{u}_i d\vec{s}=0, \tag{3}$$

$$\frac{dE_i}{dt}+\int_{S_i}\rho_i e_i\vec{u}_i d\vec{s}=-\int_{V_i}P_i div\left(\vec{u}_i\right)dV, \tag{4}$$

The system (1-4) is closed by the equation of materials state:

$$P_i=P_i\left(\rho_i,T_i,\alpha_i\right). \tag{5}$$

Differential equations describing the propagation of turbulent deflagration and detonation in gas mixtures are approximated using the method of decomposition to several steps logically related to certain physical processes. The values of quantities calculated at a certain step are used as initial data for the subsequent step.

The basic system of Eq. (1) – (4) calculated at first step is equivalent to the following system:

$$\frac{d\vec{u}}{dt}=-\frac{1}{\rho}grad\left(P\right), \tag{6}$$

$$\frac{d\rho_i}{dt}=-\rho_i div\left(\vec{u}_i\right), \tag{7}$$

$$\frac{d\beta_i}{dt}=\beta_i\left(div\left(\vec{u}_i\right)-div\left(\vec{u}\right)\right), \tag{8}$$

$$\frac{de_i}{dt}=-\frac{P_i}{\rho_i}div\left(\vec{u}_i\right). \tag{9}$$

The combustion model of hydrogen-containing mixtures in the code FIRECON 1.0 is based on a criterial approach similar to that used in [8-10] and is intended for practical use in calculations of hydrogen combustion in a nuclear power plant containment for the purpose of safety analysis.

There are three possible combustion regimes:

- Slow combustion;
- Fast combustion;
- Detonation.

To determine the limits of flammability at various temperatures and pressures, the experimental dependences of the lower and upper limits of hydrogen-air mixture flammability on the temperature and pressure of the surrounding medium are used.

The criterion for the flame acceleration is the fulfillment of the following inequality:

$$\sigma>\sigma^{*}.$$

Deflagration to detonation transition (DDT) is possible under fulfillment of the inequality:

$$L>7\lambda.$$

The flame front in this model is treated as a hydrodynamic discontinuity. It propagates through the parent mixture with velocity S_t (turbulent flame velocity) relative to the matter before flame front, and this velocity depends on the parameters of the parent mixture immediately before flame front.

The flame front moves perpendicular to its surface. The initial flame front location is specified in simulations.

In two regions (strong and weak turbulence), the flame velocity is defined in different ways.

For the S_t/S_u ratio, we use the relationships from [9].

In the strong turbulence region, where $L/\delta > 500$:

$$\frac{S_t}{S_u} = 0.5(\sigma - 1)\left(\frac{L}{\delta}\right)^{1/3} \mathrm{Le}^{-2/3}. \tag{10}$$

In the weak turbulence region, where $L/\delta < 500$:

$$\frac{S_t}{S_u} = \begin{cases} 8 \cdot 10^{-4} (\sigma - 1)^3 \left(\frac{L}{\delta}\right), & \eta > 1 \\ 1, \quad \eta \le 1 \end{cases}, \tag{11}$$

where S_u is the laminar flame velocity.

The code FIRECON was specially developed for the architecture of cluster computing systems with mass parallelism and distributed random access memory, so all calculations were performed using a supercomputer.

The calculation scheme of containment compartments should generally simulate all characteristics of a real object with sufficient accuracy (free room volumes, space between buildings, building structures and large equipment located in containment compartments).

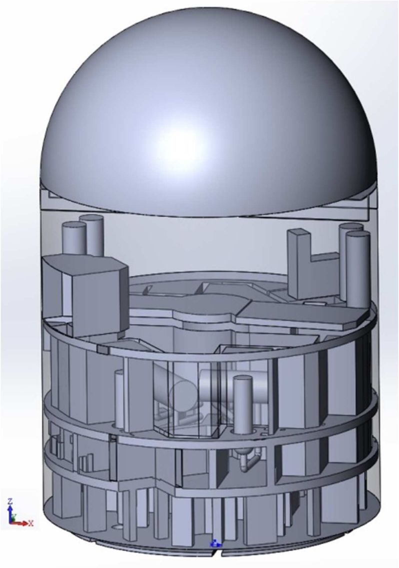

Fig. 1. NPP containment 3D CAD model.

Figure 1 shows the Russian project AES-2006 (NPP-2006) NPP containment 3D CAD (Computer Aided Design) model, which was used for simulation. To decrease calculation time costs we used rough computational grid of containment, but preliminary tests and convergence analysis proved, that its accuracy is enough to get relatively good results. The number of nodes in the computational grid was ~ $1.3 \cdot 10^6$.

The ignition point can be set in any room. In this case, the initiation of combustion can occur both in one counting cell and in a certain volume specified earlier. At the external boundary of the system, the condition of non-flow (a rigid wall) is used as the boundary condition, that is, the normal velocity component equals to zero. The leakage condition can also be specified inside the region along certain faces of the grid, which are the boundaries of the fictitious incompressible components.

SIMULATION RESULTS

On the basis of the hydrogen distribution inside NPP containment compartments analysis results, the room with the highest concentration of hydrogen in mixture was chosen, in which combustion was initiated (i.e., the ignition point was set). According to hydrogen distribution analysis in most cases the highest amount of hydrogen is accumulated in steam generator room. The mixture parameters (component concentrations and initial pressure) in chosen room for each severe accident are given in Table 1.

Table 1. Mixture parameters (obtained from hydrogen distribution calculations)

Accident scenario	C_{H2}, % vol.	C_{O2}, % vol.	C_{steam},% vol.	P_0, MPa
SB_1	12.5	10.9	34.6	0.16
SB_2	15.3	8.95	37.2	0.22
LB_1	13.0	7.2	52.9	0.24
LB_2	19.0	7.9	43.4	0.23
LB_3	10.1	7.4	53.3	0.22
UnSA	21.5	10.0	25.5	0.15

The general views of the burning pattern in a containment at different times for a different scenario are shown in Fig. 2-7, which show the boundary (concentration iso-surface - highlighted in red) of the burned mixture. According to the iso-surface of the formation of combustion products, one can judge the flame front propagation. The most intensive flame propagation within the containment compartments can be seen in the case of UnSA (Fig. 7).

To estimate the dynamic load during the combustion of the mixture in different containment areas, the pressure values at the preselected control points were calculated. Figure 8 shows the maximum pressure values in steam generator room and pressure drops on the outer containment wall for different variants of severe accidents. The results of the calculations showed that the maximum inner pressure within containment from hydrogenous mixture fast deflagration is about 0.36 MPa (LB_1 case) and the maximum pressure at the outer containment wall differs from the atmospheric by 0.29 MPa (SB_2 case) and does not exceed the design allowable value (0.6 MPa).

In the case of UnSA absence of severe accident management systems led to sharp pressure spike at the beginning of the accident, which is characteristic to detonation regime. Pressure drop value on the outer containment wall exceeds the overpressure value (0.6 MPa), laid in the station design (Fig. 9).

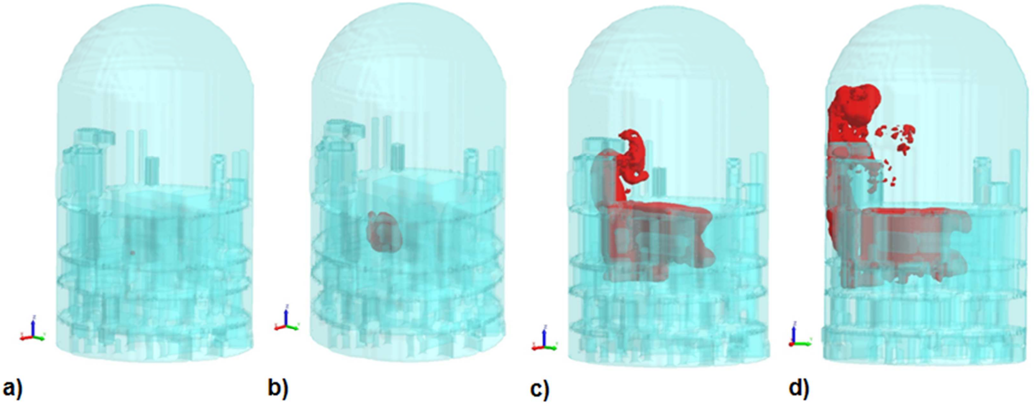

Fig. 2. The iso-surfaces of the burnt mixture concentration for different time instants: a) 0.0 s; b) 0.1 s; c) 0.5 s; d) 1.0 s (SB1).

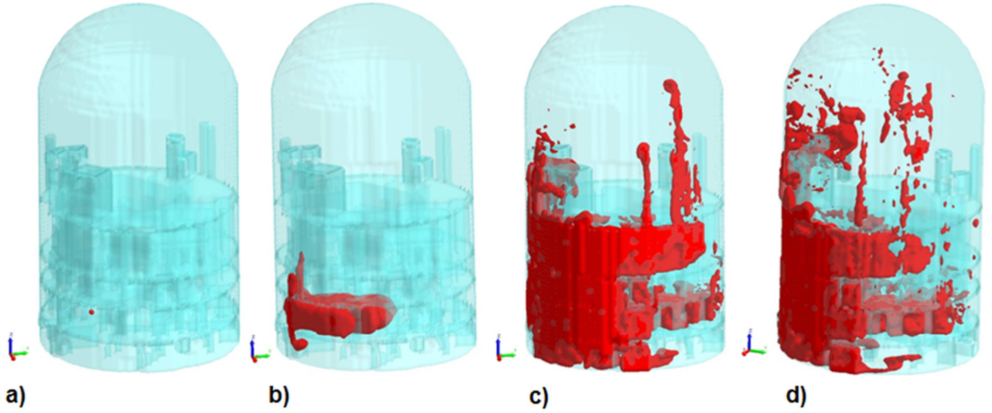

Fig. 3. The iso-surfaces of the burnt mixture concentration for different time instants: a) 0.0 s; b) 0.1 s; c) 0.5 s; d) 1.0 s (SB2).

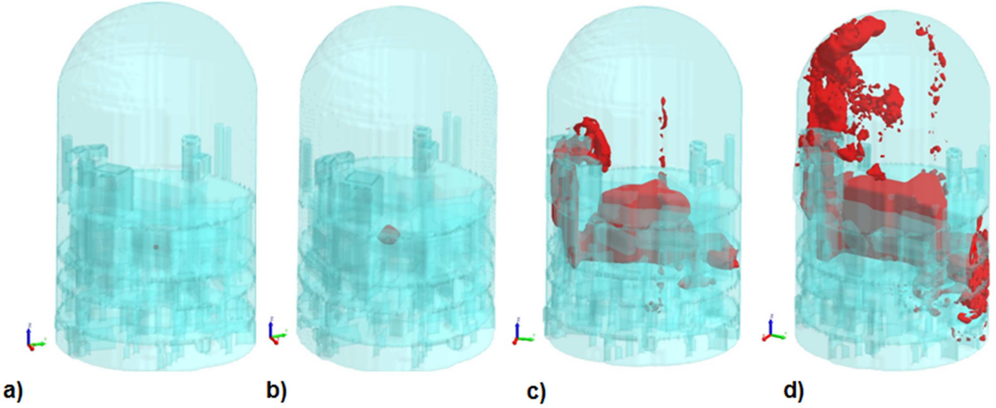

Fig. 4. The iso-surfaces of the burnt mixture concentration for different time instants: a) 0.0 s; b) 0.1 s; c) 0.5 s; d) 1.0 s (LB1).

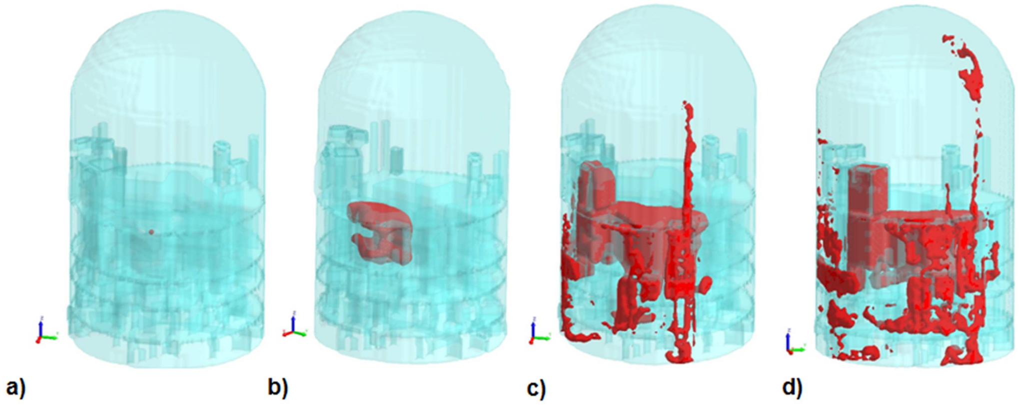

Fig. 5. The iso-surfaces of the burnt mixture concentration for different time instants: a) 0.0 s; b) 0.1 s; c) 0.5 s; d) 1.0 s (LB2).

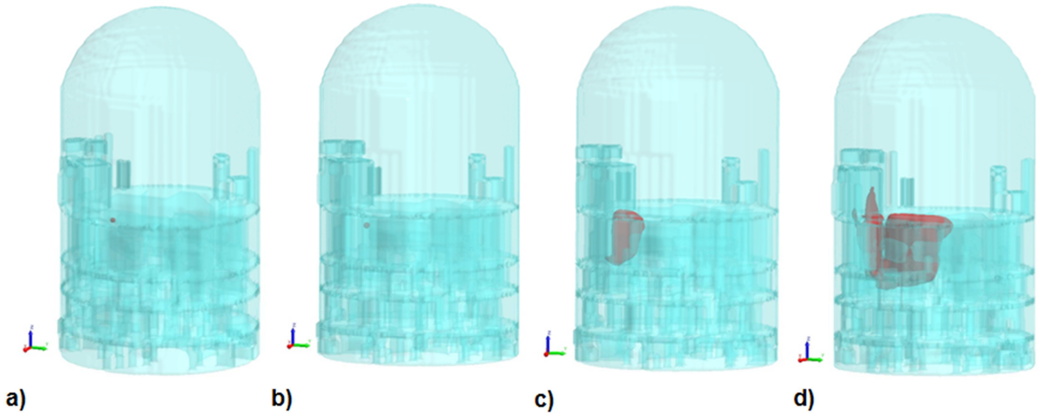

Fig. 6. The iso-surfaces of the burnt mixture concentration for different time instants: a) 0.0 s; b) 0.1 s; c) 0.5 s; d) 1.0 s (LB3).

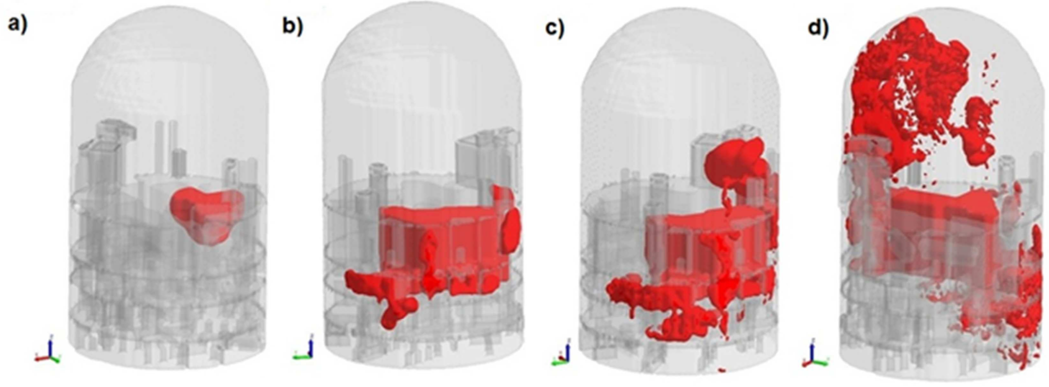

Fig. 7. The iso-surfaces of the burnt mixture concentration for different time instants: a) 0.0 s; b) 0.1 s; c) 0.5 s; d) 1.0 s (UnSA).

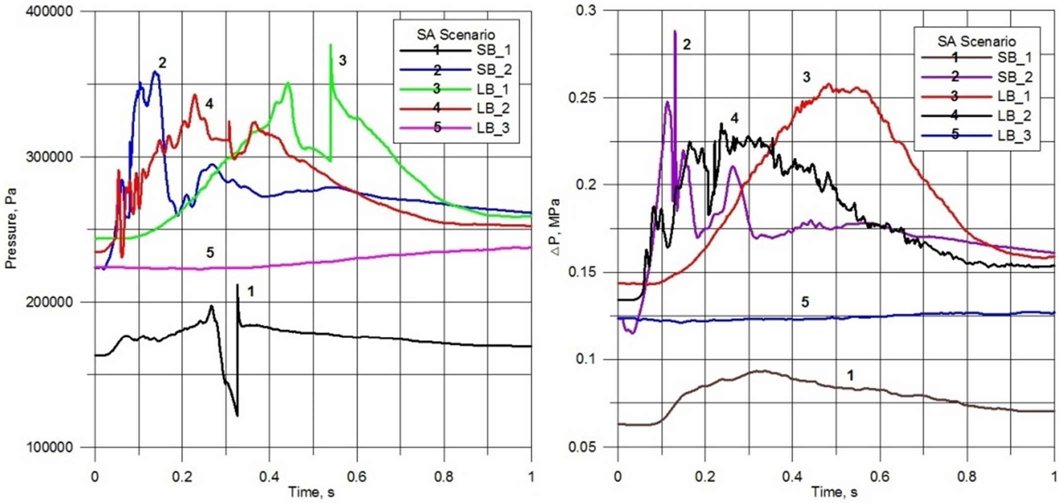

Fig. 8. Maximum pressures in steam generator room (left) and pressure drops on the outer containment wall (right) for different scenarios.

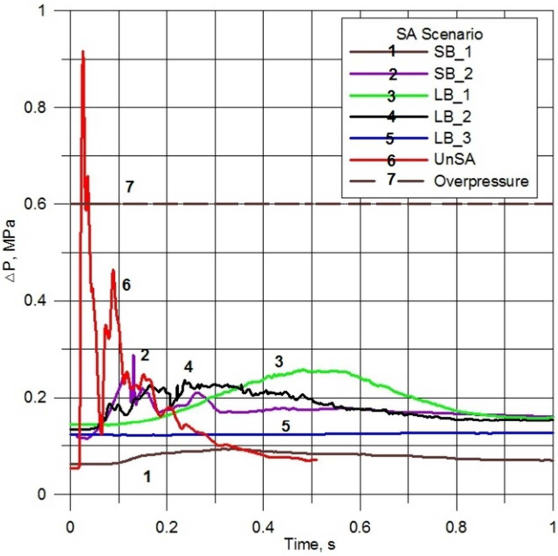

Fig. 9. Pressure drops on the outer containment wall for different scenarios (with UnSA and overpressure value).

CONCLUSION

Within the framework of the NPP safety, a three-dimensional modeling of the hydrogen-air-steam mixture combustion in the containment compartments was carried out. For the calculation, five scenarios of severe accidents (two with small collant leak and three with large leak) were considered, as well as an example of a hypothetical accident in which work of severe accidents control systems was not deliberately taken into account.

The results of the calculation showed that the operation of severe accident management systems incorporated in the plant design makes it possible to avoid formation of explosive hydrogen-containing gas mixtures. The magnitude of the pressure drop on the external wall of the containment for accidents with large and small leaks does not exceed the excess value required by the plant design.

REFERENCES

[1] OECD/NEA report, “Status Report on Hydrogen Management and Related Computer Codes”, Report No. NEA/CSNI/R(2014)8, 2014.

[2] A.A. Efimenko, S.B. Dorofeev, CREBCOM code system for description of gaseous combustion, J. Numer. Methods Fluids 76 (2001) 662-696.

[3] S. Kudriakov, F. Dabenne, E. Studer, A. Beccantini, J.P. Magnaud, H. Paillre, A. Bentaib, A. Bleyer, J. Malet, E. Procheron, C. Caroli, The TONUS-CFD code for hydrogen risk analysis, numerical schemes and validation matrix, Nucl. Eng. Design 238 (2008) 551-565.

[4] U. Bielert, W. Breitung, A. Kotchourko, P. Royl, W. Scholtyssek, A. Veser, A. Beccantini, F. Dabbene, H. Paillre, E. Studer, T. Huld, H. Wilkening, B. Edlinger, C. Poruba, M. Mohaved, Multi-dimensional simulation of hydrogen distribution and turbulent combustion in severe accidents, Nucl. Eng. Design 209 (2001) 165-172.

[5] J. Hasslberger, H.K. Kim, B.J. Kim, I.C.Ryu, T. Sattelmayer, Three-dimensional CFD analysis of hydrogen-air-steam explosions in APR1400 containment, Nucl. Eng. Design 320 (2017) 386–399.

[6] A. Epifanov, A. Luckyanov, N. Shan’gin, A. Zaitsev, C. Solov’ev, L. Zaichik, Containment code KUPOL-M development for the NPP with VVER projects safety justification, Atomic Energy (2003).

[7] Yanilkin Yu.V., Statsenko V.P., Tarasov V.I., Stadnik A.L., Eliseev G.M., Sinkova O.G., Solovyov V.P., Shemyakin V.Yu., Tsykin S.V., Zharova G.V. The FIRECON Code for Numerical Simulations of 3D NPP Hydrogen Mitigation Problems. Meeting on the ISTC Project #436-97. Physical Model and Code Development for Deflagration to Detonation Transition and Detonation of Hydrogen Containing Mixtures. Cologne, May 17-19, 2000.

[8] S.B. Dorofeev, V.P. Sidorov, A.E. Droinishnikov, W. Breitung, Deflagration to Detonation Transition in Large Confined Volume of Lean Hydrogen-Air Mixtures, Combust. Flame 104 (1996) 95-110.

[9] G.W. Koroll, R.K. Kumar, E.M. Bowles, Burning Velocities of Hydrogen-Air Mixtures, Combust. Flame 94 (1993) 330-340.

[10] R.K. Kumar, Flammability Limits of Hydrogen-Oxygen-Diluent Mixtures, J. Fire Sci. 4 (1985) 245-262.

Evacuation modeling

On the Validation of Pedestrian Movement Models under Transition and Steady-state Conditions

Kirik E.[1,2,]*, **Vitova T.**[1], **Malyshev A.**[1], **Popel E.**[1]

[1] *Institute of Computational Modelling, Krasnoyarsk Scientific Center,*
Russian Academy of Sciences, Siberian Branch, Krasnoyarsk, Russia.
[2] *Siberian Federal University, Petroleum and Gas Engineering Department, Krasnoyarsk, Russia.*
**Corresponding author's email: kirik@icm.krasn.ru*

ABSTRACT

Validation of computer modules simulating pedestrian movement is discussed. Albeit not new, this subject is studied here for transition and steady-state regimes to show different manifestations of people dynamics. The goals of the validation, explanations of the simulation experiments, and interpretation of the simulation results are discussed. The velocity-density dependence under transition and steady-state conditions of people flow in a straight corridor has been investigated. The simulation results are compared with experimental data using specific and full flow rates as quantitative measures.

KEYWORDS: Pedestrian dynamics, evacuation modelling.

INTRODUCTION

Simulation of pedestrian dynamics is used in many applications including entertainment (e.g. cinema and computer games) and fire safety precautions in buildings, ships, and aircrafts. Different approaches, including the social force model based on differential equations and stochastic CA models have been developed [1]. The most attractive for application is the use of individual approaches, when each person is considered separately and the model can determine the coordinates of each person. In such a model, every person can have individual properties, including free movement velocity, evacuation delay time, size of projection, and direction of movement. These give wider opportunities to state a simulation task and reproduce real phenomena compared to a macroscopic approach.

When we speak about people's safety, the main goal of the simulation is to estimate the inflow and outflow travel times in different scenarios to check and/or provide safe conditions for visitors or passengers in normal and emergency situations. Validation of pedestrian movement simulation modules is not a new subject in the literature. The commonly used test is to check the velocity-density dependence under periodic boundary conditions as a main feature of people movement. The aim of this study was to present and discuss some issues related to the validation of this feature. We would like to explore more deeply the process and present a more complex set of tests for identifying different manifestations of the velocity-density dependence in different movement regimes. The tests were undertaken using the SigmaEva module [2-4].

The next section presents the main concept of the validation approach. Then we describe the tests, simulation experiments, expected results, and results obtained using the SigmaEva module.

Proceedings of the Ninth International Seminar on Fire and Explosion Hazards (ISFEH9), pp. 1270-1280
Edited by Snegirev A., Liu N.A., Tamanini F., Bradley D., Molkov V., and Chaumeix N.
Published by Saint-Petersburg Polytechnic University Press
ISBN: 978-5-7422-6498-9 DOI: 10.18720/spbpu/2/k19-67

WHAT IS THE SUBJECT TO VALIDATE? WHAT FOR? HOW?

The purpose of this paper is not to discuss the pros and cons of the mathematics of the pedestrian movement models. A mathematical model, as well as its numerical presentation and program implementation, are considered as a whole. Thus, the objective of this study is testing computer simulation modules (hereinafter, the model is a computer module implementing it) and analyzing the simulation results.

People movement is a complex process, which can be divided into the movement (i.e., physical displacement which is mainly driven by a desire to reach a destination point) and behavioral contribution (e.g., decision-making aspects) [1, 5, 6]. To succeed in the validation, it is important to establish the range of the investigations. Here, we estimate the travel time under the so-called normal movement conditions, when only the movement component determines the process (no decision-making contribution). People are aiming to reach a destination point and they are aware of the environment (modeling area). In this study, the behavioral aspects are ignored. Thus, our goal is to discuss a way of testing a model to make sure that the model estimates correctly the "pure" travel time. It means that the movement dynamic reproduced by a model should be investigated. (It should be noted that, in contrast to [7-9], the aim here is not to consider the verification of the modules for program bugs, for instance, when people should not cross the modeling area boundary or should choose a certain exit, or if the pre-evacuation time should have a certain distribution. The behavioral aspects, including group behavior, social influence on choosing an exit, a decrease in the walking velocity with visibility degradation, and incapacitation, are not discussed.)

The next question is about the cases to be studied. We consider a set of basic geometrical situations, when certain people movement phenomena were observed repeatedly in real experiments, and compare the real-life data with the simulation data. The total path traversed by people (until reaching a destination) consists of several parts. We assume the correct simulation of people movement for each pattern to give the correct simulation for the entire path. The main geometrical patterns are a straight corridor, a corridor with a corner (90 and 180 degrees), bottlenecks, and up and down staircases.

People movement dynamics depends on the type of conditions (transition or steady). Here, a key factor is the existing velocity-density relationship [1, 10-12], which is different for the conditions of different types. Thus, we have to study the combination of geometrical patterns, density, and movement conditions.

We focus on the dynamics of people movement in a straight corridor at different densities and consider the following cases:

- flow spreading;
- speed independent of the local density up to a certain critical value (free movement speed invariable up to a certain density value);
- dynamics of people flow under steady conditions.

These cases allow us to capture if a model reproduces the velocity-density dependence under the transition and steady conditions.

The next important, yet still unanswered question concerns a measure of the quality [13]. The "yes-no" approach can be used when the test only results in detecting the presence or absence of a phenomenon. Such an approach is applied when a phenomenon takes place in real-life, but there is a lack of a quantitative method for measuring it. Here, we consider a test revealing the flow spreading.

If experimental data are available, then simulation results should be obtained under conditions similar to the experimental ones. In this case, the data can be directly compared. Obviously, strict coincidence between the simulation and real data is improbable and an acceptable deviation range should be established. Both cases are presented in the next section.

DESCRIPTION OF THE TESTS

General conditions

The specific and total flow rates were used as a quantitative measure for comparing the simulation results with the experimental data. To obtain flow rates, the travel times are measured. To present the results, we will use values that can be calculated exactly and only in one way, for example, the number of people in a modelling area, square of a modelling area, or travel times (total, between control points).

Since the people movement process is stochastic, many mathematical models contain stochastic components; for instance, the free movement speed is considered as a random variable for each pedestrian. For such models, a set of simulation experiments is conducted under the same conditions and the travel time is averaged over all the experiments. Certainly, stable results are obtained when a model is characterized by the low dispersion; then, the result of even one run is reliable. To ensure a convergence of results over repeated runs one can use a method proposed in [5,7].

Test 1: flow spreading

The flow spreading is caused by the fact that people tend to move under comfortable local density conditions. If there is an opportunity to keep distant from others, people will do so. This effect is especially pronounced when a dense body of people starts moving. In this case, the front line has a place to move and is characterized by the highest speed. Those people who are behind gradually start moving when there is a sufficient space for a step and their speed is controlled by the local density in front of them. This is a qualitative description of the phenomenon. Unfortunately, there is a lack of real-life data to make the quantitative comparison. Here, the problems to be solved are to design the simulation experiment conditions that would ensure the pronounced flow spreading and develop a method that would allow us not only to visualize it but also numerically estimate it.

To capture this phenomenon, we conducted the following simulation experiment. The nature of the phenomenon suggested that it could be carried out in the transition regime under so-called open boundary conditions: people leave two corridors 50 × 2 m and 100 × 2 m in size. Initially, people occupy the first 50 m of the corridor, Fig. 1. People are assumed to be uniformly distributed over the grey area and have identical individual characteristics. The person that crosses the control line is no longer involved in the simulation. A set of initial numbers of people (densities) is considered.

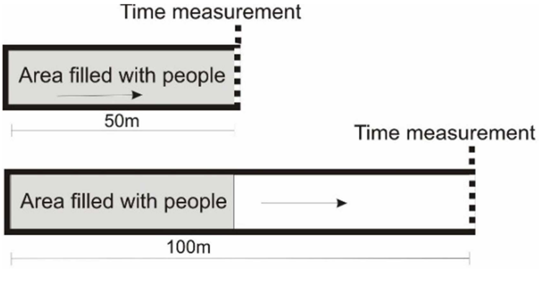

Fig. 1. Test 1. Geometry set up. Two corridors 50 × 2 m and 100 × 2 m in size, respectively, initial positions of people, and control lines.

Time T (s) in which the initial number of people N (persons) should cross the control line at the end of each corridor is a quantity to be measured. (In the stochastic model, the time is averaged over a series of experiments conducted under the same initial conditions.)

To estimate the flow rate for each initial number of people N, the following formulas are used: $J^{50} = N/\tilde{T}^{50}$, $J^{100} = N/\tilde{T}^{100}$, (person/s), where $\tilde{T}^{50} = T^{50}_{tot}$ is the (average) time of evacuation from the 50-m corridor, $\tilde{T}^{100} = T^{100}_{tot} - t^{50}$ is the (average) time of evacuation from the 100-m corridor without the time $t^{50} = 50/v^0$ for which the front line reaches the control line when moving with free movement speed v^0 (m/s) (thus, it is correct to assume the time $t^{50} = 50/v^0$ to be the same for all N values). The respective specific flows are $J^{50}_s = N/\tilde{T}^{50}/2$, and $J^{100}_s = N/\tilde{T}^{100}/2$ (person/(m × s)).

The flow in the 100-m corridor should be calculated using the above-mentioned approach, so the results for both corridors could be compared from one position; $\tilde{T}^{50}$ and $\tilde{T}^{100}$ are the periods of crossing the control line. Hence, the difference between flow rates at the same initial density (number of people in the starting area) is indicative of a difference in dynamics.

This is a conventional way to relate the flow rate and density. The question arises as to what the density is. In this test, the density is the initial density given by $\rho = N/S_{inpos}$ (person/m^2), where S_{inpos} = 100 m^2, is the square of initial positions (grey area in Fig. 1).

It is worth noting that only exact values are used to calculate ρ. These are the initial number of people, N, and the square of the initially occupied area. In fact, when we say that the "initial density" is equal to ρ, we only assume people to be initially uniformly distributed over the gray area in Fig. 1 and assign our qualitative description of the initial conditions with the quantitative characteristic ρ.

If the model reproduces the flow spreading, the following qualitative behavior of the flow rates under initial density variation for both corridors should be observed. The specific flow J^{50}_s for the 50- m corridor has two typical phases; it should increase until a certain initial density and then reach a constant value. This indicates that the maximum capacity is attained and a growth the initial density does not lead to a corresponding increase in the flow. Such a behavior is consistent with the data from [12].

The flow J^{100}_s should increase to the highest density, but not attain the highest value of J^{50}_s. Such a behaviour shows that with increasing initial density people tend to use the available space to reach a comfortable density around them (in the 100-m corridor, there are such places, in contrast to the 50-m corridor), the flow spreading is implemented, and the maximum capacity is not attained.

Figure 2 presents the test results obtained with the SigmaEva evacuation module. The specific flows $J^{50}_s = N/\tilde{T}^{50}/2$ and $J^{100}_s = N/\tilde{T}^{100}/2$ as functions of the initial density $\rho = N/S_{inpos}$ are shown.

We considered a set of initial numbers of people $N_i, i = \overline{1,k}$. The corresponding initial densities were $\rho_i = N_i/100, i = \overline{1,k}$, (person/m^2). Each person was assigned a free movement speed of $v^0_1 = 1.75$ m/s in one series of experiments and $v^0_2 = 1.3$ m/s in the other series of experiments. All persons were assigned the same square of projection 0.125 m^2. For each pair $N_i, i=\overline{1,k}$, v_j^0, $j=\overline{1,2}$, a set of 500 runs was made and the average evacuation times were calculated:

$$T_{tot}^{100}(\rho_i)=\frac{1}{500}\sum_{j=1}^{500}T_j^{50}\ ,\ T_{tot}^{100}(\rho_i)=\frac{1}{500}\left(\sum_{j=1}^{500}T_j^{100}-t^{50}\right),\ i=\overline{1,k}\ .$$

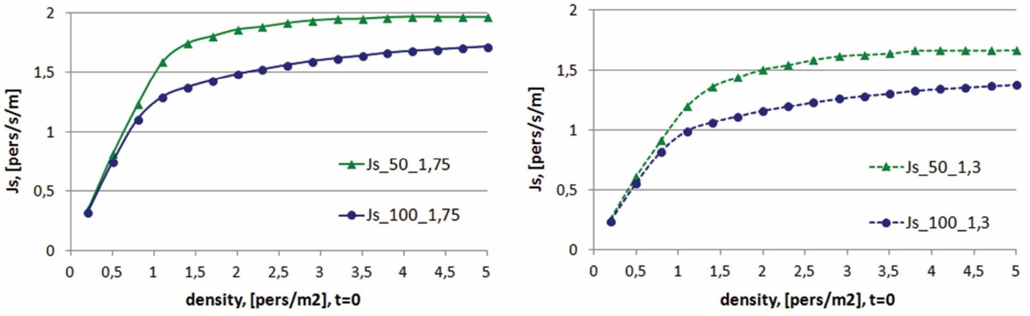

(a) (b)

Fig. 2. Test 1. The SigmaEva module results: the specific flows for the 50-m corridor (Js_{50}) and 100-m corridor (Js_{100}) (on the left $v_1^0=1.75$ m/s and on the right $v_2^0=1.3$ m/s).

Let us interpret the results obtained. At both velocities, the flow J_s^{50} increases until the initial density takes a value of ≈ 3 person/m^2 and then reaches constant values of 1.8-1.9 person/(m × s) at $v_1^0=1.75$ m/s and ≈ 1.6-1.7 person/(m × s) at $v_2^0=1.3$ m/s. This indicates that the maximum capacity is attained and the initial density growth does not lead to a corresponding increase in the flow. Flows J_s^{100} (at both v_j^0 values) permanently grow to the highest initial density and do not reach the value of J_s^{50}. As the initial density increases, people start using the available free space to reduce the local density down to the possible comfortable conditions; as a result, flow spreading is implemented and the maximum capacity is not attained up to the highest N value. Thus, we may conclude that the model tested reproduces the expected behaviour of the specific flows as a function of the initial density and implements flow spreading.

Test 2: the velocity is independent of the local density up to the critical value

The experimental data reported in [1,10-12] show that the people moving in a flow maintain a free (unimpeded) movement speed under comfortable density conditions in the nearest neighborhood. It means that the nearest people do not influence each other and have enough space to keep their free movement speed unchanged. In other words, we can say that, all other conditions being equal, if there is an additional space, people will not fill it. The critical local density is $\rho^0 \approx 0.5$ person/m^2, which corresponds to the data from [10-12].

This phenomenon is observed both under transition and steady-state conditions. One of the ways to capture this phenomenon is to use the conditions of Test 1 in the transition regime. The manifestation is as follows. Up to the critical initial density, conditions are comfortable and all persons should start moving simultaneously in both corridors. If the phenomenon is reproduced by the model, it results in the fact that, if people in the 100-m corridor do not use the available space (there is no flow spreading), the periods which people need to cross the control lines should be equal or very similar for both corridors ($T_{tot}^{50} \approx T_{tot}^{100} - t^{50}$). Thus, the flow rates J_s^{50} and J_s^{100} should be equal or very similar.

Let us now interpret the results of Test 1 in connection with this phenomenon. The SigmaEva module yields the following results. The flows coincide perfectly ((a) and (b) pictures in Fig. 2) for initial densities of up to 0.5-0.6 person/m^2. Therefore, in the two corridors the times that people need to cross the control lines are equal or very similar. It means that the density is comfortable and persons (in the 100-m corridor) do not take the opportunity to reduce the local density at the expense of the available space. Thus, the initial density remains invariant for the entire experiment.

Test 3: steady conditions of the people flow movement

Another manifestation of the density dependence of the velocity is implemented in the steady-state regime, when (in contrast to the previous case) the time-spatial density is assumed to be constant and there are no conditions for transformations of the flow. People are assumed to be uniformly distributed over the entire area (e.g., in an extended corridor without narrowing) and move in one direction. Under these limitations, the speed decreases with increasing density. This is the basic dependence called the fundamental diagram. In terms of the specific flow, the fundamental diagram looks as follows. As the density increases, the specific flow increases, attains its maximum, and then decreases.

There exist various fundamental diagrams determined by many factors, including demographics [15]; however, all have the same basic feature. For example, the velocity-density dependence can be presented in analytical form [8, 9]:

$$v^{KhS}(\rho) = v^0 \begin{cases} 1 - a_l \ln\left(\rho/\rho^0\right), & \rho > \rho^0 \\ 1, & \rho \le \rho^0 \end{cases} \tag{1}$$

where ρ^0 is the limit people density up to which people can move with a free movement speed (it means that the local density does not influence people's speed); a_l is the parameter of adaptation of people to the current density during their movement in different ways: $\rho^0 = 0.5$ person/m^2 and $a_1 = 0.295$ for the horizontal way, $\rho^0 = 0.8$ person/m^2 and $a_2 = 0.4$ for movement downstairs and $\rho^0 = 0.64$ person/m^2 and $a_3 = 0.305$ for movement upstairs; v^0 is the unimpeded (free movement) speed of a person; and ρ is the local density for a person.

In [14] and [15] speed versus density are given in the following ways correspondingly:

$$v^{WM}(\rho) = v^0 \begin{cases} 1, & \rho = 0 \\ 1 - \exp\left(-1.913\left(1/\rho - 1/\rho_{\max}\right)\right), & \rho < \rho_{\max} \\ 0, & \rho \ge \rho_{\max} \end{cases} \tag{2}$$

$$v^{SFPE}(\rho) = v^0 \begin{cases} 1 - \rho/\rho_{\max}, & 0 \le \rho < \rho_{\max} \\ 0, & \rho \ge \rho_{\max} \end{cases} \tag{3}$$

In Eq. (2) and Eq. (3), ρ_{max} is the acceptable maximum density. The original forms of the velocity-density dependences from [16] and [17] were transformed in the formulas to the explicit input ρ_{max} value, which was made a parameter. It was assumed that $\rho_{max} = 5.4$ person/m^2 in Eq. (2) and $\rho_{max} = 3.8$ person/m^2 in Eq. (3). Note that, in Eq. (1), $\rho_{\max}$ is not a parameter and cannot be varied.

However, Eq. (1) contains ρ^0 as a limit people density up to which people can move with a free speed.

Figure 3 shows the specific flows $\hat{J}_s = \rho v(\rho)$, (person/(m × s)), for Eq. (1)-(3) (curves KhS, WM, and SFPE, respectively; $v^0 = 1.66$ m/s).

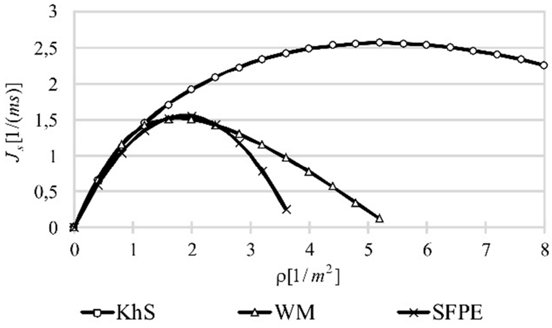

Fig. 3. Test 3. Specific flows for Eq. (1)-(3), $v^0 = 1.66$ m/s.

To see if the model reproduces this phenomenon, we consider the simulation experiment under the so-called periodic boundary conditions. A straight corridor 50 × 2 m in size with the control line in the right-hand side is the modeling area, Fig. 4. People uniformly fill the entire area.

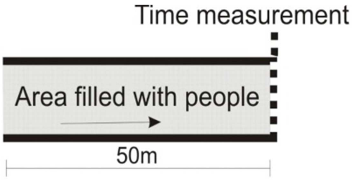

Fig. 4. Test 3. Geometry set up. Corridor 50 × 2 m in size, initial position of people (modelling area), and control line.

To reproduce the steady regime (periodic boundary conditions), the initial number of people N should be maintained. It means that when a person reaches the control line (leaves the modeling area from the right-hand side), another person with the same parameters appears from the left (i.e., the inflow should tend to the outflow value).

Time T required for M people (for example, $M = 1000$) to cross the control line at the end of the corridor at given N is a quantity to be measured. In the stochastic model, the time should be averaged over a set of K runs under the same initial conditions.

To estimate the flow rate, the formula $J = M / T$, (person/s) for each density $\rho = N/100$ is used, where $T = \sum_{j=1}^{K} T_j / K$ is the average time over K runs required for M people to cross the control line. The corresponding specific flow is $J_s = M / T / 2$, person/(m × s).

In this test, the density $\rho = N/100$ is used to estimate the distribution of people over the modeling area (grey area in Fig. 4) in the simulation experiment.

When comparing the simulation and reference data and interpreting the results, it is very important to pay attention to the acceptable ρ_{max} value in the mathematical model and reference data. For example, if a square of the person's projection in the model is assumed to be 0.125 m^2, the projection has the form of a circle with a radius of 0.2 m; then, we can put closed circles with $\rho_{max} = 6.25$ person/m^2. Thus, it is the most accurate to compare the simulation and reference data with similar ρ_{max} values.

As an example, let us now discuss the results obtained with the SigmaEva evacuation module. We considered a set of numbers of people $N_i, i = \overline{1,m}$ involved in the simulation. The corresponding densities are estimated as $\rho_i = N_i / 100, i = \overline{1,m}$, (person/m^2). Each person was assigned a free movement speed of $v^0 = 1.66$ m/s. All persons were assigned the same square of projection, specifically, 0.125 m^2.

Since the shape of a person's projection is a solid disc, the maximum number that can be placed in an area of 100 m^2 is 625 and the maximum density is $\rho_{max} = 6.25$ person/m^2. In accordance with the reference data, it was reduced (see below).

The SigmaEva evacuation module implements a stochastic discrete-continuous model [2-4], so a set of 500 runs for each $N_i, i = \overline{1,m}$ was performed and the average times were calculated: $T(\rho_i) = \sum_{j=1}^{500} T_j(\rho_i) / 500, i = \overline{1,m}$, where $T_j(\rho_i)$ is the time required for $M = 1000$ people to cross the control line in one run at given ρ_i.

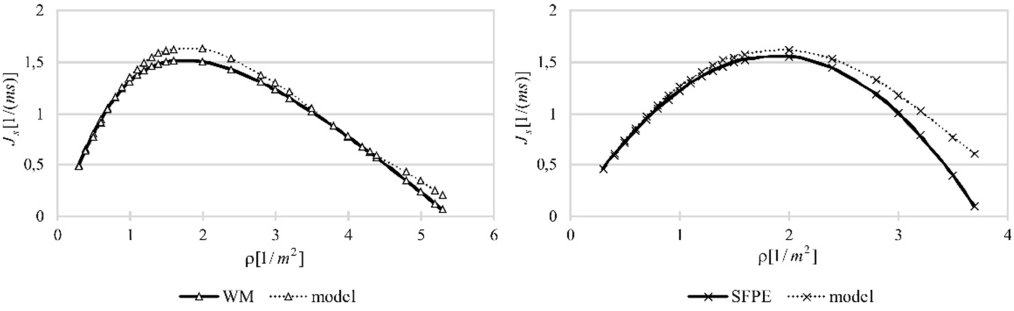

(a) (b)

Fig. 5. Test 3. (a) Original Weidmann data ("WM") with $\rho_{max} = 5.4$ person/m^2 and simulation data ("model") with Eq. (2) as an input model data, $N_{max} = 540$ persons; (b) Original SFPE data with $\rho_{max} = 3.8$ person/m^2 and simulation data ("model") with Eq. (3) as an input model data and $N_{max} = 340$ persons.

Figures 5-6 show the specific flows as a function of density $\rho = N_i / 100, i = \overline{1,m}$. The simulation data are compared with the Weidmann, SFPE, and Kholshevnikov and Samoshin diagrams [10]. The Kholshevnikov and Samoshin data were obtained under similar real-life conditions and the same movement regime (the densities for these curves are given in the literature).

It can be seen that the data in the two figures are very similar. In both cases, $\rho_{max}^{model} > \rho_{max}^{data}$: 6.25 person/m^2 versus 5.4 person/m^2 in Fig. 5 a, 6.25 person/m^2 versus 3.8 person/m^2 in Fig. 5 b.

The other important factor is that the conditions of real experiments ensure the same body size at all densities. This is consistent with the model statement that the projections of persons are solid discs with a constant radius.

The Kholshevnikov and Samoshin data give a considerably higher flow at the middle and higher densities. Equation $v^{KhS}(\rho)=0$ gives $\rho_{max}=15$ person/m^2. This density can be obtained at smaller body sizes (square of projection) only. However, there is a lack of data on the impact of body size reduction.

In Fig. 6, the model reproduces the expected behavior of the specific flow under density variation: the flow J_s increases until a density of ≈ 2.5-3 person/m^2, attains a value of 1.7-1.8 person/(m × s), and then decreases.

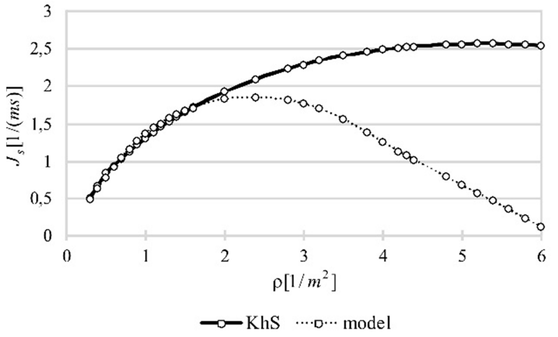

Fig. 6. Test 3. Kholshevnikov and Samoshin data (“KhS”) and simulation data (“model”) with Eq. (1) as an input model data; $N_{\max}=600$ persons.

At the low and middle densities, the model flows agree very well with the real data. At the high densities, the model flow is much slower than the Kholshevnikov and Samoshin flow. This is apparently related to the strong impact of the constant square of a person’s projection.

Table 1. Quantitative measures for results presented in Figs. 5-6

	Relative difference	Cosine	Projection coefficient
KhS	0.570195	0.852454	1.364238
WM	0.067695	0.998818	0.954949
SFPE	0.142952	0.992588	0.929509

To compare curves quantitatively one can use a method from [18]. There are three measures: Relative difference, Cosine, and Projection coefficient (Table 1). The first norm provides a measure of the difference in the overall magnitude for the two curves normalized to the experimental data. The norm approaches zero when the two curves are identical in magnitude. In the second, Cosine, the angle between the two vectors represents a measure of how well the shape of the two vectors match. As the cosine of the angle approaches unity, the two curves represented by the two vectors differ only by a constant multiplier. The third, Projection coefficient, provides a measure of the best possible fit of the two curves. When the projection coefficient approaches unity, remaining differences between the two curves are either due to random noise in the experimental measurements or physical effects not included in the model.

Figure 7 shows the velocity field for one simulation step at different densities. The length of each vector is the length of the person's shift in this time step. One can see a strong decrease in the step length (and, correspondingly, in the velocity) with increasing density. The directions of the vectors show that the model provides the expected movement direction.

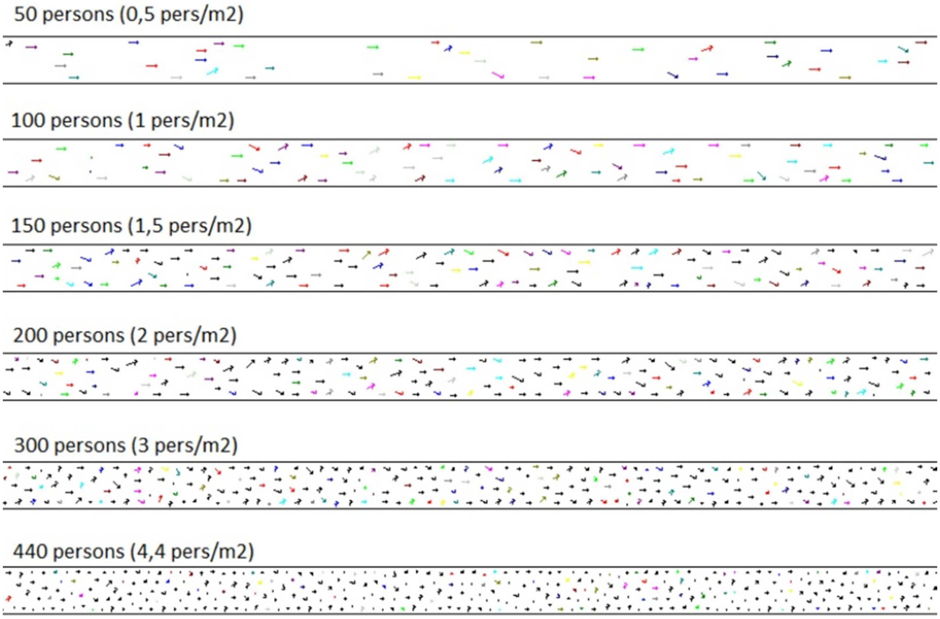

Fig. 7. Test 3. Screenshots of velocity fields in one time step for different densities.

CONCLUSIONS

The approach to validation of the pedestrian movement simulation modules was considered. The focus of the study was the velocity-density dependence as a self-organized phenomenon without influence of the simulation space geometry. Transition and steady-state conditions were considered.

The transition condition implies a flow transformation (spreading), which is pronounced stronger or weaker, depending on the initial density and available space, due to the interrelation between the velocity and local density. The tests for flow spreading and maintaining a free (unimpeded) movement velocity were considered for the first time.

The steady-state condition implies a constant density in the movement area, no flow transformations, and the speeds of individuals and flow controlled by the current density. In this regime, the velocities of individuals and flow coincide.

While people move from their initial positions to a destination, both conditions can be implemented and should be correctly reproduced by a model.

Another series of obligatory tests for checking the ability of a model to reproduce the movement component should be focused on the effect of geometry (bottleneck flows, movement around the corner, stairway case, etc.) on the model dynamics.

The correct simulation of people movement for each part separately is assumed to give the correct simulation for the entire path.

REFERENCES

[1] A. Schadschneider, W. Klingsch, H. Kluepfel, T. Kretz, C. Rogsch, A. Seyfried, Evacuation Dynamics: Empirical Results, Modeling and Applications, In: Encyclopedia of Complexity and System Science, Vol. 3, Springer, 2009, pp. 3142-3192.

[2] E. Kirik, A. Malyshev, E. Popel, Fundamental diagram as a model input – direct movement equation of pedestrian dynamics, Proceedings of the International conference "Pedestrian and Evacuation Dynamics'2012", In: U. Weidmann, U. Kirsch, M. Schreckenberg (Ed.). Springer, 2014, pp. 691-703.

[3] E. Kirik, A. Malyshev, A discrete-continuous agent model for fire evacuation modelling from multistory buildings. Civil Engineering and Urban Planning III, CRC Press, 2014, pp. 5-9.

[4] E. Kirik, A. Malyshev, M. Senashova, On the evacuation module SigmaEva based on a discrete-continuous pedestrian dynamics model, Lecture Notes in Computer Science, Proc. 11th Int. Conf. Parallel Processing and Applied Mathematics, Vol. 9574, 2016, pp. 539-549.

[5] R. Lovreglio, E. Ronchi, D. Borri, The validation of evacuation simulation models through the analysis of behavioural uncertainty, Reliab. Eng. System Saf. 131 (2014) 166-174.

[6] R. Lovreglio, Modelling Decision-Making in Fire Evacuation based on Random Utility Theory, PhD thesis, Politecnico of Bari, Milan and Turin, 2016.

[7] E. Ronchi, E. Kuligowski, P. Reneck, R. Peacock, D. Nilsson, The process of verification and validation of building fire evacuation models, NIST Technical Note, 2013.

[8] International Maritime Organization/MSC.1/Circ 1533 - Revised Guidelines on Evacuation Analysis for New and Existing Passenger Ships. https://www.traffgo-ht.com, 2016 (accessed 07 December 2018).

[9] Guideline for Microscopic Evacuation Analysis. Version: 3.0.0 2016. https://rimea.de/, 2016 (accessed 07 December 2018).

[10] V. Kholshevnikov, D. Samoshin, Evacuation and human behavior in fire, Moscow. Academy of State Fire Service, EMERCOM of Russia, 2009 (in Russian).

[11] V. Kholshevnikov, Forecast of human behavior during fire evacuation, Proc. Int. Conf. Emergency Evacuation of People from Buildings – EMEVAC, Warsaw, Belstudio, 2011, pp. 139-153.

[12] V.M. Predtechenskii, A.I. Milinskii, Planning for foot traffic flow in buildings, American Publishing, New Dehli, 1978.

[13] C. Rogsch, Vergleichende Untersuchungen zur dynamischen Simulation von Personenstroumen, Diploma thesis of the University of Wuppertal and the Research Center Julich, 2005.

[14] J. Zhang, A. Seyfried, Experimental studies of pedestrian flows under different boundary conditions. Proc. 17th Int. IEEE Conf. Intelligent Transportation Systems, 2014, pp. 542-547.

[15] U. Chattaraj, A. Seyfried, P. Chakroborty, Comparison of pedestrian fundamental diagram across cultures, Advances Complex Syst. 12 (2009) 393-405.

[16] U. Weidmann, Transporttechnik der Fussganger. Transporttechnische Eigenschaften des Fussgangerverkehrs (Literaturauswertung). Zurich: IVT, Institut fur Verkehrsplanung, Transporttechnik, Strassen- und Eisenbahnbau, 1992.

[17] H.E. Nelson, F.W. Mowrer, Emergency Movement, In: The SFPE Handbook of Fire Protection Engineering, National Fire Protection Association, 2002, 3-367–3-380.

[18] R.D. Peacock, P.A. Reneke, W.D. Davis, W.W. Jones, Quantifying fire model evaluation using functional analysis, Fire Saf. J. 33 (1991) 167–184.

Simulations of Fire Evacuations in “Sigma FS” Software as a Fire Safety Training Instrument

Kirik E.[2,3,] *, Litvintsev K.[1], Dekterev A.[1,3], Khasanov I.[4], Gavrilov A.[1], Malyshev A.[2], Harlamov E.[1], Popel E.[2]

[1] *S.S. Kutateladze Institute of Thermophysics, SB RAS, Novosibirsk, Russia*
[2] *Institute of Computational Modeling SB RAS, Krasnoyarsk, Russia*
[3] *Siberian Federal University, Krasnoyarsk, Russia*
[4] *VNIIPO of EMERCOM of Russia*
**Corresponding author's email: kirik@icm.krasn.ru*

ABSTRACT

This paper deals with an up-to-date fire evacuation simulation technique and explores the possibilities which a simulation gives to solve fire safety training tasks in buildings. To model evacuation an individual discrete-continuous model is used. To model fire spread a CFD approach is realized in program code. Both modules work with one initial building file that provides the opportunity to make integrated simulations of both processes and make a time-spatial analysis automatically. Some case studies of fire evacuation simulation are presented.

KEYWORDS: Evacuation modeling, numerical simulation, fire safety training.

INTRODUCTION

Fire evacuation simulations are used in many fields from organization of mass events to fire safety of buildings, ships, and aircrafts. The main task of applying such simulations is to estimate the total evacuation time in different scenarios, duration of congestions, compare this time with time available for safe evacuation from a building and provide/find safe conditions for visitors, passengers in emergency situations. In a regime of every day operation of the building, a number of different scenarios may be used for virtual training systems to instruct staff on means of supporting evacuation. Under construction/reconstruction, simulations of fire spread and evacuation are applied for design of fire safety equipment (alarm systems, ventilation, smoke removing systems, fire extinguish systems), geometrical sizes of evacuation routes and the whole construction, safe delay of the evacuation start, people initial position, etc.

The software tools are based on different mathematical models. For instance, the dense flow model cannot consider bi-directional flow, assign individual projection areas and free movement speed with each person. Functionality of the software may or may not allow for the individual properties for the persons, and CFD prediction of smoke movement. The current trend is to simulate fire dynamics and people evacuation using the same software and the single building file. Temporal and spatial superposition of both fire dynamics and people evacuation provides more accurate prediction results represented in a user-friendly format, with joint visualization of fire products dynamics (distributions of smoke, toxic gases, heat fluxes, and temperatures) and evacuation dynamics.

The other main contribution in modern fire evacuation simulations are mathematical models. They determine the range of application and variety of conditions and characteristics which may be taken

Proceedings of the Ninth International Seminar on Fire and Explosion Hazards (ISFEH9), pp. 1281-1291
Edited by Snegirev A., Liu N.A., Tamanini F., Bradley D., Molkov V., and Chaumeix N.
Published by Saint-Petersburg Polytechnic University Press
ISBN: 978-5-7422-6498-9 DOI: 10.18720/spbpu/2/k19-120

into account. As a result, using a mathematical model provides the opportunity to reproduce some conditions which are a matter of concern and which would not otherwise be investigated.

The accuracy of the model and numerical presentation of the model are important to allow a reliance on simulation under given conditions. Nevertheless, one should remember that a simulation not always estimate reality. When we deal with fire safety simulations, we should keep in mind the following specifics concerning interpretation of the whole fire evacuation scenario(s). Simulation does not give us an answer to the question "Which will an emergency situation be?" It is wrong to try to predict (estimate) by simulation real pre-evacuation time, for example. If we input some pre-evacuation time T_{start} in seconds it means that people will start to move to exits T_{start} seconds later then a fire started. Simulation gives an estimate of evacuation duration from rooms, floors, building and provides information on people exposure by dangerous fire factors if they started at T_{start}. And that is all. However, simulation helps us to answer another question: "What should pre-evacuation time be to provide safe evacuation conditions?" A collection of scenarios with different T_{start} and other conditions are a source of information to produce instructions for staff to manage evacuation depending on their location.

This paper is organized as follows. In the next section, mathematical models are presented. This is followed by the software section and then a case study section, where some fire evacuation examples are considered under different initial conditions. The paper ends with conclusions.

MATHEMATICAL MODELS

Evacuation

Different approaches from the social force model based on differential equations to stochastic CA models are developed; see [1] and references therein. They reproduce many collective properties including lane formation, oscillations of the direction at bottlenecks, the so-called "faster-is-slower" effect.

The most popular for practical applications is the agent-based approach when each person is considered as individual agent, and a model gives coordinates of each person in each time step. Each person may be assigned with individual properties: free movement velocity, pre-evacuation time, projection size, evacuation way. This approach enables solving a variety of pedestrian movement tasks, including fire evacuation tasks, and makes this model a powerful simulation tool.

At the present time there are two main approaches to simulate individual people movement: continuous and discrete. Combining the advantages of the continuity of a modeling space (as in continuous models) with the intuitive clarity of update rules (in discrete models) a discrete-continuous model Sigma.DC was developed [2, 3]. In this model, the agents move in a continuous space (in this sense the model is continuous), but the number of directions where agents may move is limited and predetermined by the user (in this sense the model is discrete). Real sizes are considered, which is very important to allow for narrow places such as doors. At the same time, the model is quite simple. The main concept is worth explaining here.

A discrete-continuous evacuation model - Sigma.DC

The following assumptions and restrictions are considered in the model: people movement is a stochastic process; while moving people do not exceed their free movement velocity, every person maintains his/her velocity in accordance with local time-spatial density conditions (the tighter the crowd and the more urgency, the smaller this distance); the main driving force is approaching a destination point; people follow one of two strategies: the shortest path and the shortest time.

A continuous modeling space $\Omega \in R^2$ and including the infrastructure (obstacles) and the free space are prescribed in the unified coordinate system. Obstacles include walls and furniture. People are modeled as discrete agents, which move in free space. To navigate in the space, the agents use the static floor field S [4]. Each agent is assigned a certain target point (exit).

The shape of each agent is a hard disk with diameter d_i, $i = \overline{1, N}$, N – number of agents, $\vec{x}_i(0) = \left(x_i^1(0),\ x_i^2(0)\right)$, $i = \overline{1, N}$ – initial positions of each agent which are the coordinates of the disk's centers (it is supposed that they are the coordinates of body's mass center projection). Each agent is assigned with a free movement speed v_i^0, $i = \overline{1, N}$, and with the projection area. We assume that free movement speed is a random normally distributed value with a certain mathematical expectation and dispersion. It is supposed that, while moving, people do not exceed the maximum speed (free movement speed), and they control the speed according to the local density.

Each time step t particle i may move in one of predetermined directions $\vec{e}_i(t) \in \left\{\vec{e}_i^{\,\alpha}(t),\ \alpha = \overline{1, q}\right\}$, q is number of directions, a model parameter (here a set of directions uniformly distributed around the circle is considered). Agents which cross the target line leave the modeling space. For each time t, the coordinates of each particle i are:

$$\vec{x}_i(t) = \vec{x}_i(t - \Delta t) + v_i(t)\,\vec{e}_i(t)\,\Delta t, \quad i = \overline{1, N}, \tag{1}$$

where $\vec{x}_i(t - \Delta t)$ is the coordinates in the previous time step; $v_i(t)$, [m/s] is the agent's speed; $\vec{e}_i(t)$ is unit direction vector. The constant time step of Δt = 0.25 s is used.

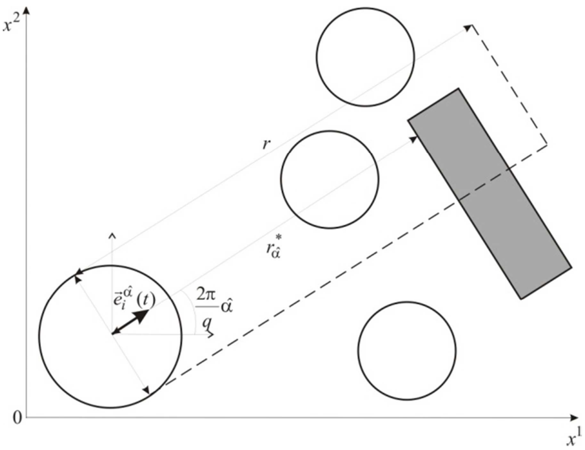

Fig. 1. Scheme of a visibility area of the particle in the direction $\vec{e}_i^{\,\alpha}(t)$.

The direction of the next step $\vec{e}_i(t)$ is proposed to be stochastic with probability distribution calculated from the discrete CA approach and inspired by the previously presented stochastic CA FF model [6, 7]. All predetermined directions for every agent to move at each time step are assigned with some probabilities, and a target direction is determined according to the probability distribution obtained. To reproduce directed movement, a static floor field S is used as a "map" that stores the information on the shortest distance to the nearest exit [4]. This field increases radially from the exit and it is zero in the exit(s) line(s) [6]. It does not change with time and is independent of the presence of the particles.

Personal probabilities to move in every direction at each time step are not static but vary dynamically and are affected by: (a) the main driving force (given by destination point), (b) interaction with other pedestrians, (c) interaction with the infrastructure (non-movable obstacles). The highest probability (mainly with a value > 0.9) is given to the direction that has the most preferable conditions for movement considering other particles and obstacles and the strategy of the peoples' movement (the shortest path and/or the shortest time).

We omit here exact formulas to calculate probabilities for particle i to move from present position to directions $\vec{e}_i(t) \in \left\{\vec{e}_i^{\,\alpha}(t), \alpha = \overline{1,q}\right\}$, decision rules to choose direction $\vec{e}_i^{\,\hat{\alpha}}(t)$, and the final conflict resolution procedure. All this information has been provided previously in [2]. The speed $v_i(t)$ of each agent is determined from the experimental data (the fundamental diagram, for example, see [5]), taking into account the local density $F(r_{\hat{\alpha}}^{*})$ in the direction chosen $\vec{e}_i(t) = \vec{e}_i^{\,\hat{\alpha}}(t)$:

$$v_i(t) = v_i^{\hat{\alpha}}(t) = v_i^0 \begin{cases} 1 - a_l \ln\left(F\left(r_{\hat{\alpha}}^{*}\right)/F^0\right), & F\left(r_{\hat{\alpha}}^{*}\right) > F^0 \\ 1, & F\left(r_{\hat{\alpha}}^{*}\right) \le F^0 \end{cases} \tag{2}$$

where F^0 – limit on people density up to which free people movement is possible (density does not influence the speed of people movement); $a_1 = 0.295$ is for horizontal travel; $a_2 = 0.4$, for stair descent; $a_3 = 0.305$, for stair ascent.

Numerical procedures that are used to estimate the local density are presented in [2]. The density is only determined in the region consistent with the direction of movement and visibility, see Fig. 1.

In this discrete-continuous model, in contrast with pure continuous force-based models [8, 9], the task of finding the velocity vector is divided in two parts. Firstly, the direction is determined; secondly, the speed is calculated according to local density in the direction chosen. Using this strategy we omit the step of describing any forces that act on persons, thereby avoiding the numerical solution of N differential equations. As a result, the computational cost of the model is reduced compared to the force-based models, and the relaxation parameter Δt is allowed to be at least 10 times larger. At the same time, the modeling space is considered to be continuous, which is valuable in terms of practical applications.

Validation of the discrete-continuous evacuation model

The model presented here was realized in the computer program module SigmaEva©. A validation of the module was performed under basic conditions which take place in a normal evacuation process and which are provided with empirical data. The following tests were considered: movement in a straight corridor under open and periodic boundary conditions; movement in bottlenecks. A specific flow versus the density was investigated.

The investigation showed good dynamic properties, i.e., maintaining the speed in accordance with the local density under periodic and open boundary conditions. An initial density and a free movement speed were unchanged until the density of about 0.5 [persons/m^2] (in open boundary conditions), [5]; a flow diffusion realizes if it is possible (open boundary conditions for an experiment with 50 m and 100 m corridor); the model total flow increases as the bottleneck width increases, specific flow is approximately constant, except for small widths when an arch effect is often pronounced [2, 3, 10]. A comparison with corresponding data ([1], [5], [11] and others) suggests that the model works within the context of empirical data on speed versus density.

Fire simulation

Modern computers allow everyday use of powerful simulation tools such as CFD (computational fluid dynamics) for fire simulations. CFD provides an approximate three-dimensional solution to the equations governing fluid motion. The modeling area is spanned by a very large number of grid cells. Complex geometries, and time-dependent flows, are readily handled. The solution provides distributions of velocity, pressure and gas concentrations, calculated at each grid cell. It provides a three-dimensional, time-dependent picture of complex fluid flows.

The use of CFD modeling techniques is widespread and well investigated already. There are many available sources related to it, for example [12], and a good guideline is provided in [13] and the references therein. Here we only mention algorithms that are used in our CFD code and implemented in the SigmaFire© fire simulation computer module: numerical method - finite-volume methods; calculation of cell-center gradient - least-squares method; convective terms – UDS (Upwind Differencing Scheme [14]), QUICK [15], UMIST (The Upstream Monotonic Interpolation for Scalar Transport [16]), TVD (Total variation diminishing [17]), Superbee TVD; pressure-velocity coupling - SIMPLE-like (Semi-Implicit Method for Pressure Linked Equations [14]) algorithm with Rhie-Chow interpolation (collocated grid arrangement) [18]; solution of algebraic equation systems - conjugate-gradient method, conjugate-residuals method, Algebraic Multigrid (AMG) Method [19]; approximation of unsteady terms - implicit 2nd order method; parallelization - domain decomposition, MPI.

To model turbulence, the shear-stress transport k-ω model (Reynolds-Averaged Approach - RANS) is used [20]. To resolve near-wall regions, blending of the viscous sublayer formulation and logarithmic layer formulation is implemented. For highly unsteady flow, unsteady RANS is used.

An iterative procedure is used to obtain a solution which stops if a satisfying solution is reached. There are two criteria: number of iterations and value of residuals.

To model fire the following combustion model for solid fuels is used: $\Psi = \psi_s \pi v^2 t^2$, where Ψ is rate of burning, kg/s; ψ_s is specific rate burning, kg/(s·m^2); v is speed of fire spread, m/s; t is time, s. The speed of volatile is $\phi_{volatile} = \alpha\Psi$, kg/s.

Validation procedures, which showed appropriate convergence with real and experimental data [23, 24, 25], were made.

In Table 1, some features of SigmaFire© versus the well-known CFD code FDS are presented.

Table 1. SigmaFire© components compared to those in FDS

Feature	SigmaFire	FDS
Turbulence	URANS	LES
Grid	Unstructured nonorthogonal	Orthogonal
Pyrolysis reaction rate	Constant	Arrhenius
Radiation	P_1-aproximation [21]	Finite-volume method [22]
Liquid spray	No	Yes

Fire and evacuation integrated simulations

There are at least two levels of integration of fire and evacuation models. The first one means that the software provides an opportunity to work with one building file for both fire spread and evacuation modules. In this case, time and spatial superposition of both results is more accurate and comfortable for the user, the 3D-visualization of fire products dynamic (smoke, toxic gases, heat flow, temperature) and evacuation dynamics gives a more illustrative understanding of processes (for example, total and/or detailed time-spatial distributed information on that the time during which individuals were affected by extreme fire conditions, corresponding concentrations (life compatible/incompatible) of toxic gases and other).

The next level of integration means that fire products (smoke, toxic gases, heat flow, etc.) may have an influence on people and/or people can influence fire spread. Such an approach may be used to improve the reliability of the simulation, extend information about a simulated scenario, or extend the application area.

From a computational point of view, such a statement of the simulation problem implies several subpoints including a formalization of people's reaction to fire, a formalization and implementation of a calculation scheme and influence of people on fire spread, time and spatial compatibility of calculation schemes for evacuation and fire spread models and 3D-visualization.

The simplest part is to realize the influence of people on fire dynamics, for example when people may open and close doors while moving. From a CFD computational point of view, it means that a modeling area is changing at certain moments. To remain stable in computing terms, these changes should be smoothed in time. This task is rather technical and needs accurate numerical realization. Note that there is also a time factor. The CFD simulation is very slow compared to the evacuation simulation. To overcome this, an iterative procedure is proposed. First, we calculate evacuation under a given scenario and estimate intervals when flow (or individuals) passes doors. Then we input this information into the CFD module and the simulation is made. Such an algorithm is already realized in the software SigmaFS©.

Another way that people may influence the fire development is when using a hand-held fire extinguisher. The simplest way to model this is to reduce the area of the fire in accordance with the extinguisher characteristics.

Simulation of people's reaction to fire products requires a new task that is a (mathematical) formalization of people's reaction to fire and influence of fire products on movement activity. An agent-based approach to simulate people movement is very convenient in this case, since each person is considered individually, and the model can give the coordinates of every person.

There are some data in the literature on the psychological reaction to fire (smoke, smell) and there are also data on the physiological reaction of the human body to toxic gases, heat, temperature, lack of oxygen, for example [5, 26-30]. Almost all sources contain descriptive information on people's reaction to fire and fire products. Among the variety of human responses, it seems reasonable to extract the most common behavioral features which are: human velocity decreasing due to smoke and the influence of toxic gases; individuals may not change their evacuation route if smoke concentration is low; however, a human may change an evacuation path if the nearest way is blocked by fire factors. Note that we do not consider the impact of the fire/smoke on the pre-evacuation period.

Decision-making is based on sensitivity and visibility of dangerous fire factors. Smoke is visible at a distance. Temperature and heat flow may be sensed by touch. High concentrations of some gases (CO_2, CO) cannot be sensed by humans but they influence activity with time. Smoke spreads faster than other fire factors. We rely on literature data which indicate that the front region can be defined by the threshold values of smoke density 0.0001-0.0006 kg/m^3, visibility 6-12 m, O_2 concentration 16%.

We formalize smoke recognition as follows:

- max r^{fire} (model parameter) is a distance from a person when smoke zone may be sensed,
- a person recognizes a fire (fire attributes) in the direction chosen in the distance, max r^{fire} if optical density μ is greater than 0.238 ($\mu > 0.238$ means that visibility is less than 10 m);
- γ_0 (model parameter) is the initial probability to move in the smoke region;
- a person decides to maintain the chosen direction with the probability of $0.16\gamma_0 / \mu$ ($1 - 0.16\gamma_0 / \mu$ is the probability of changing the direction).

We assume that a person may take another way because of fire only one time per scenario. A decision to move towards a smoke zone could not be reconsidered.

In reality, when people move along a corridor, and a changing of the route takes place because of fire detection, an inertia effect takes place. Some people (from the front line) decide to change the direction, whilst others still move in the same direction. Such an inertia effect is to be implemented as follows. Once the direction is changed, there are M steps when the fire recognition procedure is applied, then it is stopped and all people are redirected to another exit. Computationally, the redirection means changing the static field, S.

Information from the literature allows an estimation of intervals for concentration of dangerous fire factors and range them according to reaction on the human body.

Simulation case studies by "Sigma FS" software

Simulation computer modules SigmaEva© and SigmaFire© are parts of the Russian software "Sigma FS" ©. One can create a 3D-model of a building using the 3D-building editor, input initial and boundary conditions, simulate fire dynamics by CFD code (that is pure Russian code), simulate evacuation by the Sigma.DC model, visualize results in 3D and get automatically the super-positioned and analyzed outcome on the contact of people with dangerous fire conditions, evacuation and blocking times for the evacuation paths.

The first level of integrated simulations is already realized in the software. The influence of people on fire spread is also possible, albeit only the influence of fire on people is considered here.

"Sigma FS" is a tool for simulations that may be used in many fields from organization of mass events to fire safety of buildings, ships, aircrafts under operation and construction conditions. One may vary construction of a building, a combustible material and its mass, place of fire, systems of smoke removal, pressurization systems, using hand extinguisher, doors' conditions, number of people, their initial positions, individual properties (free movement speed, pre-evacuation time, projection size, evacuation way), and furniture location.

The main task of applying such simulations is to estimate evacuation time (including duration of congestions) in different scenarios in order to provide safe conditions for visitors in emergency situations.

Let us consider and compare fire *evacuation scenarios 1 and 2* from a school under fire conditions. According to both scenarios, people evacuate from a 3-storey building using the nearest stairways (Stw) numbers 1 and 2 and exits 4 and 2 respectively. A fire started in a marked room, Fig. 2.

During the simulation it was assumed that doors in the corridors were open (one may interpret this condition as doors' closers are missing or non-operational). The regions of interest are denoted by circles in the figure.

In this analysis, two scenarios were considered – one where the pre-evacuation time of the occupants was 30 s and the other where the pre-evacuation time was 120 s from ignition. Here the pre-evacuation time is not modelled explicitly but rather is assumed to be a constant value. This is because the primary goal is to investigate differences in evacuation results. One can interpret the 30 s delay as an example of a fast reaction to an alarm system. The delay of 120 s may be interpreted as representing low discipline or an alarm system fault.

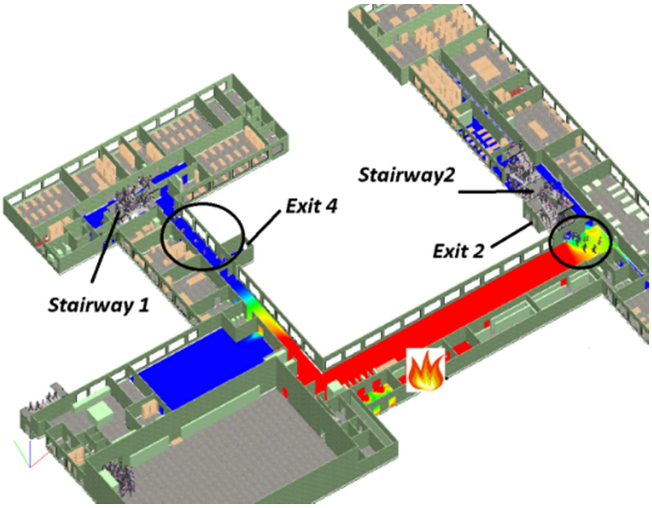

Fig. 2. Location of fire, exits and stairways in 3-storey buildings.

Fire conditions in the picture are presented as a 2D-slice at a height of 1.7 m above the floor. This slice is extracted from the 3D-fire-simulation results. In the figure, the blue color smoke slice is for safe areas for people health, red color is for dangerous areas (boundary values are from the Russian fire safety legislation).

Integrated simulation of the evacuation and the fire spread helps to show and estimate potentially dangerous consequences of some initial conditions. Here the evacuation start delay is considered. The most important areas are marked in Figs. 3 and 4.

For the case of a 120 s pre-evacuation delay (scenario 1) one can see that people moving in a corridor to Exit 2 are in a risk area at 142 s, Fig. 3a (right circled area). Combustion products need more time to reach Exit 4. Nevertheless, the pre-evacuation time was very long, and people moving to Exit 4 are in a dangerous area at 215 s, Fig. 3b. In both cases, evacuation is not finished by these times. The analysis suggests that over 100 people evacuate in unsafe conditions if they start moving with a 120 s delay after ignition. Exposure time was calculated to be greater than 60 s, and this information may be used to estimate possible health damage.

If the pre-evacuation period is 30 seconds only (scenario 2), people evacuate in comfortable conditions, Fig. 4 (remember that we changed only the duration of the pre-evacuation period and consider the same fire scenario). One can see in Fig. 4a that evacuation is already finishing; only some people are on Stairway 2, and conditions at that time (142 s from ignition) are still comfortable in that region. Figure 4b shows that only some people have to leave the building using

Exit 4 but smoke is only coming to the corridor. In Table 1 evacuation result data for both scenarios are presented.

To understand the influence of using door closers, let us consider another scenario (*scenario 3*) when the doors that are marked in Fig. 5 worked with a door closer during the simulation: pre-evacuation time is 30 s; fire position and all other conditions are as in scenarios 1, 2. Note that, from a computational point of view, the valid closer means that 10% of the doorway cross-section is open. Figure 6 presents the same point of interest in a building as in the previous scenarios. It was estimated that door closers postponed dangerous smoke conditions by up to 360 s.

Table 1. Evacuation result data for scenarios 1, 2

Pre-evacuation delay, s	Number of people in risk zone	Exposure time, s
120 (Scenario 1)	~100	>60
30 (Scenario 2)	~5-10	1-5

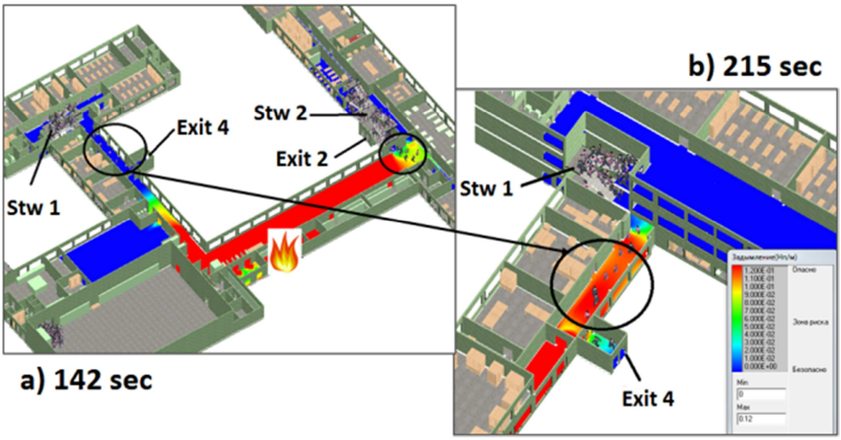

Fig 3. Evacuation from the building under fire conditions, evacuation started 120 s after ignition.

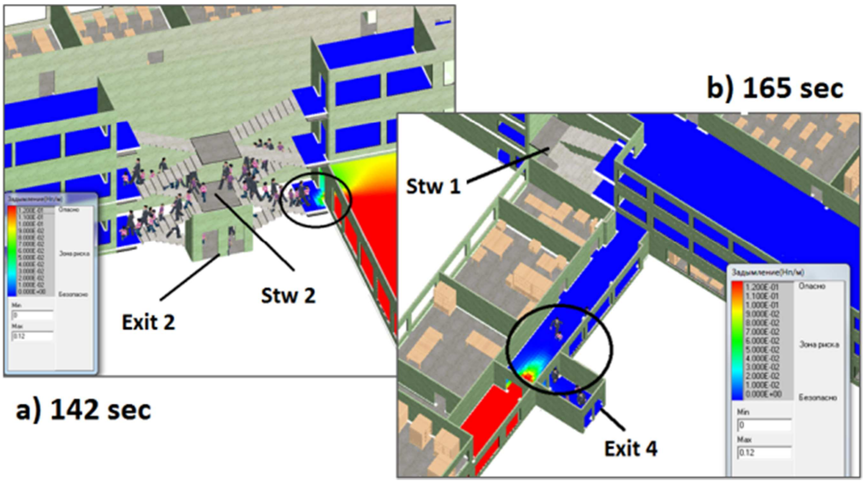

Fig 4. Evacuation from the building under fire conditions, evacuation started 30 s after ignition.

CONCLUSIONS

The paper has demonstrated how real conditions could be taken into account in modern fire evacuation simulations. The scenarios considered show the influence of different initial conditions on evacuation results. This information could be used to estimate possible time gaps to react on fire alarm, start evacuation, available routes and form the basis for instructing staff on how to manage the evacuation process.

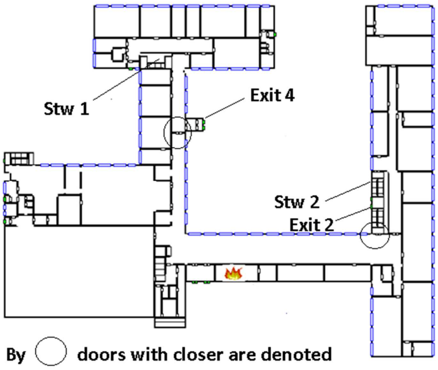

Fig. 5. Doors which were considered with closers while simulation in scenario 3.

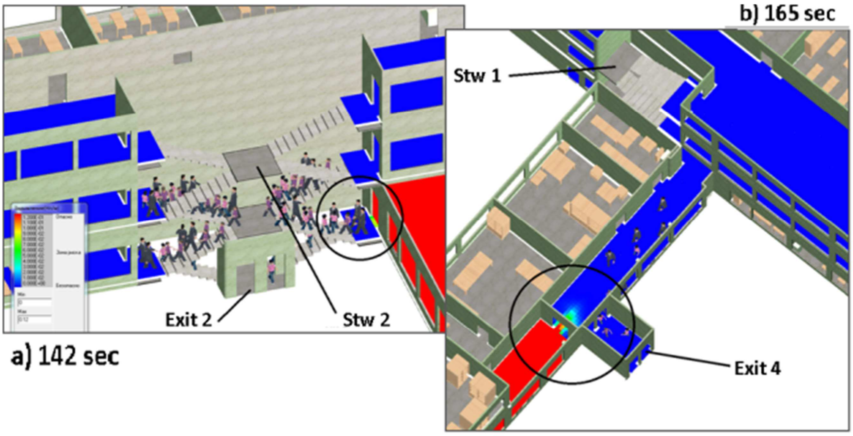

Fig. 6. Evacuation from the building under fire conditions, an evacuation started 30 s after ignition, doors closers are valid.

REFERENCES

[1] A. Schadschneider, W. Klingsch, W. Kluepfel, T. Kretz, C. Rogsch, A. Seyfried, Evacuation Dynamics: Empirical Results, Modeling and Applications, In: Encyclopedia of Complexity and System Science. Springer, Berlin, Vol. 3, 2009, pp. 142–3192.

[2] E. Kirik, A. Malyshev, E. Popel, Fundamental diagram as a model input – direct movement equation of pedestrian dynamics, In U. Weidmann, U. Kirsch, M. Schreckenberg (Eds.), In: Proc. of the Int. Conf. "Pedestrian and Evacuation Dynamics'2012". Springer, Hiedelberg, 2014, pp. 691-703.

[3] E. Kirik, A, Malyshev, On validation of SigmaEva pedestrian evacuation computer simulation module with bottleneck flow, J. Comput. Sci. 5 (2014) 847-850.

[4] A. Schadschneider, A. Seyfried, Validation of CA models of pedestrian dynamics with fundamental diagrams, Cybernetics and Systems 40(5) (2009) 367-389.

[5] V.V. Kholshevnikov, D.A. Samoshin, Evacuation and human behavior in fire, Moscow: Academy of State Fire Service, EMERCOM of Russia. 2009 (in Russian).

[6] E. Kirik , T. Yurgel'yan, D. Krouglov, On realizing the shortest time strategy in a CA FF pedestrian dynamics model, Cybernetics and Systems 42(1) (2011) 1-15.

[7] E. Kirik, T. Vitova, On Formal Presentation of Update Rules, Density Estimate and Using Floor Fields in CA FF Pedestrian Dynamics Model SIgMA.CA, In: El Yacoubi S., Was J., Bandini S. (Eds) Cellular Automata, ACRI 2016, LNCS. Springer, Vol. 9863, 2016, pp. 435-445.

[8] M. Chraibi, A. Seyfried, A. Schadschneider, Generalized centrifugal-force model for pedestrian dynamics, Phys. Revew E 82 (2010) 046111.

[9] D. Helbing, D. Farkas, T. Vicsek, Simulating dynamical features of escape panic, Nature 407 (2000) 487–490.

[10] E. Kirik, A. Malyshev, M.Yu. Senashova, On the evacuation module SigmaEva based on a discrete-continuous pedestrian dynamics model, LNCS, In: Proceedings of the 11th International Conference “Parallel processing and applied mathematics”, Springer, Vol. 9574, 2016, pp. 539-549.

[11] U. Weidmann, Transporttechnik der Fussgaenger. Transporttechnische Eigenschaften des Fussgaengerverkehrs (Literaturauswertung). Zuerich: IVT, Institut fuer Verkehrsplanung, Transporttechnik, Strassen-und Eisenbahnbau, 1992.

[12] J.H. Ferziger, M. Peric, Computational methods for fluid dynamics, Third Ed., Berlin, Springer, 2002.

[13] M.J. Ivings, C.J. Lea, H.S. Ledin, Outstanding safety questions concerning the analysis of ventilation and gas dispersion in gas turbine enclosures: Best Practice Guidelines for CFD, Health Safety Laboratory report CM/03/12, 2003.

[14] S.V. Patankar, Numerical Heat Transfer and Fluid Flow, Hemisphere, Washington DC, 1980.

[15] B.P. Leonard, A stable and accurate convective modelling procedure based on quadratic upstream interpolation, Comput. Meth. Appl. Mech. Eng. 19 (1979) 59-98.

[16] F.S. Lien, M.A. Leschziner, Upstream monotonic interpolation for scalar transport with application to complex turbulent flows, Int. J. Num. Meth. Fluids 19 (1994) 527-548.

[17] A. Harten, High resolution schemes for hyperbolic conservation laws, J. Comput. Phys. 49 (1983) 357-393.

[18] C.M. Rhie, W.L. Chow, Numerical study of the turbulent flow past an airfoil with trailing edge separation, AIAA J. 21 (1983) 1525-1532.

[19] U. Trottenberg, C. Oosterlee, A. Schüller, Multigrid, Academic Press, 2001.

[20] F.R. Menter, Two-Equation Eddy-Viscosity Turbulence Models for Engineering Applications, AIAA J. 32 (1994) 1598–1605.

[21] M.F. Modest, Radiative Heat Transfer, Academic Press, New York, 2nd Ed., 2003.

[22] J.C. Chai, S.V. Patankar, Finite-Volume Method for Radiation Heat Transfer. Advances in Numerical Heat Tiansfer, Vol. 2, Ch. 4, Taylor & Francis, pp. 109-138, 2000.

[23] A.A. Gavrilov, A.A. Dekterev, A.V. Sentyabov, Modeling of swirling flows with coherent structures using the unsteady Reynolds stress transport model, Fluid Dyn. 50 (2015) 471-482.

[24] K.Yu. Litvintsev, A.A. Dekterev, Comparison of the Finite-Volume and Discrete-Ordinate Methods and Diffusion Approximation for the Radiative Heat Transfer Equation, Heat Trans. Res. 39 (2008) 653-655.

[25] A.A. Dekteryev, K.Yu. Litvintsev, A.A. Gavrilov, E.B. Kharlamov, The development of free engineering software package for numerical simulation of hydrodynamics, heat transfer, and chemical reaction processes, Bulletin of the South Ural State University, Series: Mathematical Modelling, Programming and Computer Software. 10 (4) (2017) 105-112.

[26] D. Drysdale, An Introduction Fire Dynamics, Second Ed., Willey, 1998.

[27] H. Frantzich, D. Nilsson, Evacuation Experiments in a Smoke Filled Tunnel, In: Proc. of the Third International Symposium “Human Behaviour in Fire”, Belfast, UK, 2004, pp. 229-238.

[28] T. Jin, Studies on Human Behavior and Tenability, In: Fire Safety Science - Proceedings of the Fifth International Symposium, pp. 3-21, 1997.

[29] D. Purser, Toxicity Assessment of Combustion Products, SFPE handbook, Quincy, 1995.

[30] E. Ronchi, E. Kuligowski, P. Reneck, R. Peacock, D. Nilsson, The process of verification and validation of building fire evacuation models, NIST Technical Note, 2013.

Part 8. Hydrogen Safety

Stratified Hydrogen Combustion and Water Spray Mitigation Tests in a Containment of 220 m^3

Kuznetsov M.[1,] *****, **Xiao J.**[1], **Hu P.**[2]

[1] *Karlsruhe Institute of Technology (KIT), Karlsruhe, Germany.*
[2] *Shanghai Jiao Tong University (SJTU), Shanghai, China.*
**Corresponding author's email:* kuznetsov@kit.edu

ABSTRACT

A series of 11 large scale experiments was performed at the HYKA test site in order to experimentally simulate different flame propagation regimes in a stratified hydrogen-air atmosphere. The total volume of the facility is equal to 220 m^3 with an aspect ratio H/D=1.5. Hydrogen concentration was kept constant (7% vol. in air) for all the experiments. Combustion of a stratified hydrogen-air mixture with different steepness of hydrogen concentration gradient (I: 10=>7=>4% H_2; II: 12=>7=>2% H_2; III: 14=>7=>0% H_2) was investigated and then compared to uniform (7% H_2) mixture combustion using Background Oriented Schlieren (BOS) method combined with high speed camera, pressure and temperature measurements. The mixture was ignited in the center. Ambient initial conditions were 293 K and 1 bar in the tests. Two tests with water spray suppression system demonstrated not a mitigation efficiency but even promote the combustion process due to the generation of highly turbulent flow. The experimental results demonstrate that the highest hydrogen concentration at the top of the containment plays a governing role in combustion process leading to much higher combustion pressure and temperature compared to the combustion of uniform mixture of the same amount of hydrogen in the volume (equal to 7% H_2).

KEYWORDS: Hydrogen, combustion, stratified mixture, water spray mitigation.

INTRODUCTION

Hydrogen release due to the Loss of Cooling Accident (LOCA) and then Molten Corium-Concrete Interaction (MCCI) accidents may lead to formation of a stratified layer of hydrogen-air mixture at the top of the reactor building. Its immediate ignition due to operating ignitors or catalytic recombiners results in fame propagation through a gradient of reactivity and establishing of high pressure and temperature in a containment or reactor building. Such a scenario can be the cause of loss of integrity or damage of the structure. Thus, hydrogen explosion following an accidental hydrogen release in a containment is one of the important safety issues in the case of LOCA and MCCI accident as discovered due to the post-accident analysis of Fukushima-Daiichi accident in Unit 1 and Unit 3 [1-3].

A number of CFD modelling have considered different scenarios of hydrogen distribution in a containment of nuclear reactor [4-7]. Depending on hydrogen inventory, geometry of the containment and exposure time for hydrogen distribution, it might initially be a vertical column (t = 300 s) or, later on, a stratified layer of hydrogen-air mixture (t = 1200 s) (Fig. 1). Similar hydrogen distribution profiles were obtained in [5] for t = 9290 s and t = 9358 s (Fig. 2).

There is no possibility to experimentally reproduce such calculations in real scale in order to validate the CFD codes. The only LACOMECO project proposed to European organizations an

Proceedings of the Ninth International Seminar on Fire and Explosion Hazards (ISFEH9), pp. 1293-1304
Edited by Snegirev A., Liu N.A., Tamanini F., Bradley D., Molkov V., and Chaumeix N.
Published by Saint-Petersburg Polytechnic University Press
ISBN: 978-5-7422-6498-9 DOI: 10.18720/spbpu/2/k19-129

access to large scale experimental facilities at Karlsruhe Institute of Technology (KIT) to study severe accident safety issues, including the coolability of a degraded core, corium coolability in Reactor Pressure Vessel (RPV), melt dispersion to the reactor cavity, and hydrogen mixing and combustion in the containment [8-9]. Among all facilities the HYKA test site with a number of large and medium scale experimental vessels from 9 to 220 m^3 was chosen to investigate hydrogen behavior in a containment geometry under well controlled conditions. Several experiments have been performed using HYKA facilities to investigate the hydrogen-related phenomena in severe accidents, including hydrogen distribution, hydrogen combustion and hydrogen mitigation measures.

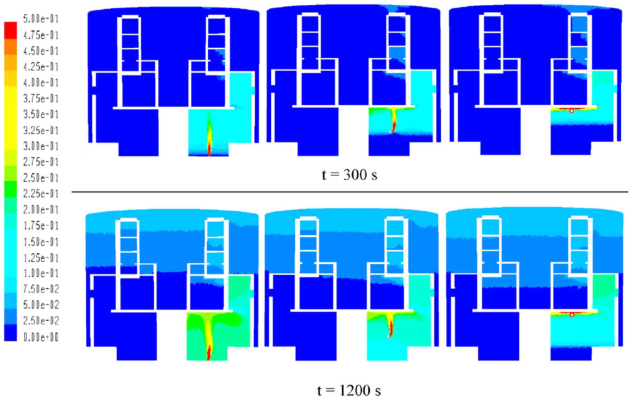

Fig. 1. Distribution of hydrogen for different injection time [4].

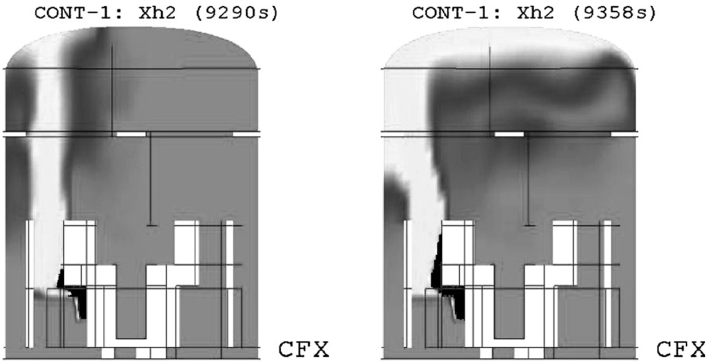

Fig. 2. Hydrogen distribution at a vertical plane through the break room of the PWR Westinghouse case [5].

A set of experiments performed in the framework of LACOMECO project is devoted to flame propagation in an obstructed large scale facility A3 (V = 33 m^3) with initially vertical hydrogen concentration gradients. Positive and negative concentration gradients with respect to gravity are created prior to ignition in the range from 4% to 13%, and the process of flame acceleration is investigated depending on hydrogen concentration gradient and ignition positions [10-11]. Especially, a combustion model was implemented in Europlexus code. This model was successfully applied and validated for some of the tests, and the numerical data for overpressure and flame times of arrival are compared with experimental results.

Very specific problem of local or global flame extinction during the flame propagation through the longitudinal concentration gradient should also be investigated for the complex 3D geometry. For instance, the global flame quenching occurred at the distance of 8 m from ignition point (Fig. 3) in the case of flame propagation in a non-uniform mixture with a gradient of hydrogen concentration from 14% to 6% H_2 in a DRIVER shock tube of ID=174 mm and L = 12 m [12]. It happens independent of reaching the speed of sound for the flame. It was found that the quenching issue in a tube geometry was reached at relatively high local hydrogen concentration of 8% H_2 (two times higher than the lower flammability limit) due to the turbulent flow produced by the obstructions with high blockage ratio in presence of descending mixture reactivity.

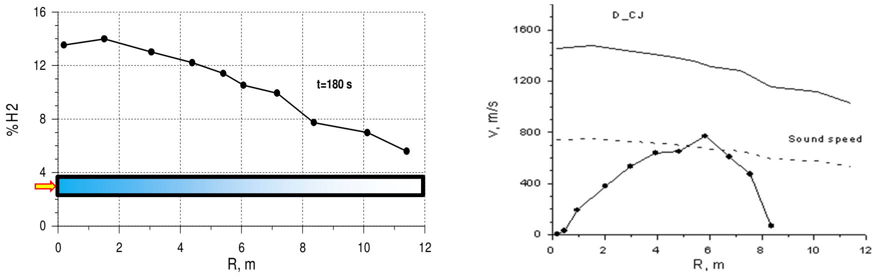

Fig. 3. Hydrogen concentration profile (left) and dynamics of flame propagation velocity with a concentration gradient 14→6% H_2 (right) [12]. A sub-image of DRIVER shock tube with ignition position is shown (left).

During a hypothetical severe accident in a nuclear reactor and reactor core degradation hydrogen can be produced and then accumulated as a stratified layer of hydrogen-air mixture at the top of reactor building [4-5]. Different flame propagation regimes of such a mixture may occur. Water spay as a combustion suppression system can be used.

In the present ALISA project, we choose the HYKA-A2 facility and analyze the experimental data obtained during the project. The HYKA-A2 facility was chosen as the most representative for the scaling analysis. The advantage is that the real objects as EPR or APWR reactor containments and HYKA-A2 facility are related as 8.3:1.5 in terms of the scale. They also have almost the same aspect ratios (H/D ratio): 1.3(EPR):1.5(A2). This might be a very important issue for the experimental scaling of combustion processes in a containment of nuclear reactor.

OBJECTIVES

The main purpose of the experiment is to investigate the influence of hydrogen stratification and water spray mitigation system on combustion characteristics in a large scale of the combustion vessel HYKA A2. The experimental data are also required to be used as benchmark experiments for CFD codes and lamped-parameter models validation of large scale hydrogen deflagrations.

To do that a series of experiments on flame propagation in a stratified hydrogen-air mixture in a large scale facility HYKA-A2 (220 m^3) has been performed. Three different vertical linear hydrogen concentration gradients of 14→0, 12→2 and 10→4% H_2 with the same amount of hydrogen equal to 7% of the average concentration are investigated. Experiments with central ignition point with uniform and non-uniform hydrogen concentration are performed. A mitigation test with water spray on flame suppression is also conducted.

Dynamics of the combustion process is registered by measuring of temperature, pressure, acoustic effects and use of optical observation by Background Oriented Schlieren Method (BOS).

EXPERIMENTAL DETAILS

Experimental facility

The largest safety vessel A2 of the KIT HYKA test site with main dimensions of 6 m id and 9 m height provides an empty test volume of about 220 m^3 (Fig. 4). It is designed for fire and explosion tests with an operating overpressure from -1 to 10 bar. Depending on the purpose, large samples or structures can be tested inside, or the whole vessel can be used as a test volume. The vessel can be evacuated or filled with inert atmosphere of nitrogen or steam and be heated up to 150 °C. The vessel is equipped with many vents and ports for experiment and measurement set-ups as well as with windows for visual observations. It has 3 vents of 2000 mm id, 4 vents of 700 mm id, 5 vents of 400 mm id and about 40 vents of smaller inner diameters (50-250 mm). The measuring system consists of thermocouples array (gas temperature, flame arrival time); piezoelectric and piezoresistive gauges (initial pressure, explosion pressure); gas analyzer and mass spectrometer (to control mixture composition); sonic hydrogen sensors, photodiodes and ion probes (flame arrival time, flame speed), strain gauges (deformations). The data acquisition system is based on multi-channel (64) ADC with a sampling rate of 1 MHz. The vessel was successfully tested within LACOMECO Project using 2 large scale combustion experiments of hydrogen-steam-air mixture (10:25:75 = H_2:H_2O:air) at 1.5 bar of initial pressure and 90 °C temperature [8-9].

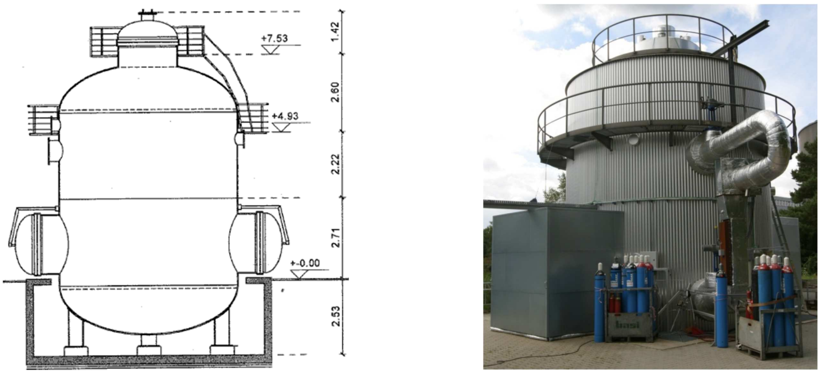

Fig. 4. HYKA-A2 facility: main dimensions and a side view.

Test matrix and experimental technique. Measurements

Full arrangement of the measuring system is schematically shown in Fig. 5. The measurement system consists of 7 pressure sensors, 24 thermoelements, 7 H_2-sampling probes, 3 Stemmer high speed cameras (70 fps), 2 Canon cameras (30 fps), 2 finger cameras (25 fps) and 2 microphones. The facility is also equipped with a gas filling system, sampling probes and concentration measurements and ignition device. Two ventilators and a system of pneumatic valves also belong to the gas filling system. Safety alarm sensors were installed inside the A2-vessel to control a flammable hydrogen concentration and minimum oxygen concentration for personal in between the experiments to be able to work for test preparation inside the vessel A2. A detailed scheme of gauges location inside the test vessel is shown in Fig. 5.

Three different types of pressure sensors were used in order to test their availability for such combustion processes. The location of all three types at the same position H = 3.27 m allows to compare the pressure signals with respect to thermal sensitivity of pressure sensors. All the sensors were mounted flush to the internal wall surface to measure the level of combustion pressure and dynamics of combustion. Initial part of the pressure records was used to evaluate an initial quasi-laminar flame speed using so called pressure method in an assumption of spherical flame shape.

To eliminate the effect of mechanical vibrations all the gauges were sitting inside the massive led brick mounted directly to the side wall. It was four layers of pressure measurements at the altitude H = 1.77, 3.27, 6.07 and 9.80 m above the floor. The temperature compensation is operating in the range 27–232 °C, with a thermal drift of ±5% of full scale output for the Kulite transducers, for instance. The compensated operating high temperature range for Kistler type was 70–140 °C. The

PCB pressure transducers had no thermal compensation. The total record time was about 10 and 20 seconds with a time response of 1 microsecond.

An array of 24 thermoelements type K was installed to cover 4 radial positions and 8 positions at the centerline ($R = 0$). The positioning of thermoelements is also shown in Fig. 5. Thermocouples (Type K [NiCr/Ni] 0.36 mm, open tip) allow to measure local temperature and also flame arrival time in order to measure flame shape and flame propagation velocity. The data processing is based on the data of arrival time against thermocouple co-ordinate (x, H). The procedure allows to interpolate all positioned arrival time points to build isochrones, the lines of equal flame arrival time which correspond to flame shape at different moments.

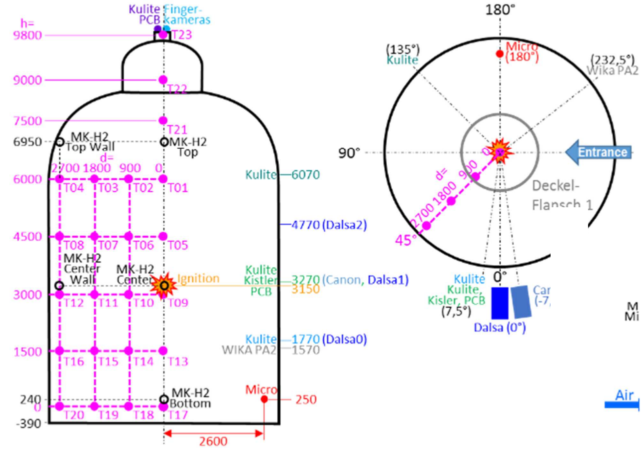

Fig. 5. Positions and orientation of sensors: thermocouples (T); gas analyzer (MK-H2); microphone (Micro). A center ignition position (CI) is shown.

Gas filling system

Three different vertical linear hydrogen concentration gradients of 14→0, 12→2 and 10→4%H_2 with the same amount of hydrogen equal to 7% of the average hydrogen concentration have been created using a gas filling system. Required amount of hydrogen equal to 7% H_2 in average was injected with or without mixing by fans. Mixing option was only used for uniform compositions. To create a gradient of concentration, hydrogen-air mixtures of required concentrations (14, 12, 10, 7, 4, 2% H_2) were injected at different altitude and then equilibrated due to a turbulent diffusion. Local hydrogen concentration was measured by 5 to 7 sampling probes. Then, a thermo-conductivity gas-analyzer Fisher-Rosemount was used to measure hydrogen concentration in air. The accuracy of measured concentrations was within the limit ±0.15%. 5 measuring points were located at the centerline and two at the side wall. The level of 7% H_2 was always kept at the ignition point in the center. Required hydrogen concentrations at the top (14, 12, 10% H_2) and bottom (4, 2, 0% H_2) have also been well established and controlled.

Experimental conditions and main experimental results are shown in Table 1. It includes a series of experiments with stratified compositions of 3 different gradients, two tests with uniform mixture of 6.5 and 7% H_2, one test with upper ignition position (UI) and two experiments with water spray (SPRAY). Table 1 mentions maximum combustion over-pressure and temperature and characteristic combustion time, $t_{1/2}$, as integral characteristics of combustion process. Characteristic combustion velocity can roughly be evaluated as a ratio $U_f = R/ t_{1/2}$.

Since the mixtures to be tested have so called Lewis number $Le = 0.33$ ($Le < 1$), the flame for such compositions might be characterized as unstable due to thermal diffusion instability, with a trend to produce highly wrinkled cellular flames. Such an unstable flame will be very sensitive to acoustic instability as well [4, 5]. The expansion ratio σ is not only a factor of visible flame speed amplification but also a criterion for the capability of the flame to accelerate to speed of sound. According to paper [6], the threshold between subsonic and sonic flames for hydrogen-air at ambient pressure and temperature is $\sigma^* = 3.75$. This means that in presence of obstructions in a proper geometry the test mixtures with local hydrogen concentration above 11% have a potential to efficiently accelerate to speed of sound and then even to detonate.

Table 1. HYKA-A2 test conditions and main results (T_0 = 300 K, P_0 =1 bar)

Test#	Mixture % [H_2]	Spray	Ignition	Time $t_{1/2}$ [s]	Over-pressure [bar]			Temperature
					KU*	KI*	PCB*	T_{max} [^oC]
Test1	**6.5**	**DRY**	**CI***	**12.66**	**0.096**	**0.095**	**0.023**	**261**
Test2	**7**	**DRY**	**CI**	**4.67**	**0.161**	**0.162**	**0.048**	**371**
Test3	10-7-1	DRY	CI	4.46	1.456	1.441	0.864	823
Test4	10-7-4	DRY	CI	4.59	1.393	1.378	0.504	809
Test5	12-7-2	DRY	CI	2.53	1.701	1.693	0.807	1338
Test6	12-7-2	DRY	CI	3.34	1.594	1.579	1.443	991
Test7	14-7-0	DRY	CI	3.05	(-)	1.632	1.809	1025
Test8	14-7-0	DRY	CI	3.24	1.559	1.544	1.766	1680
Test9	**14-7-0**	**SPRAY**	**CI**	**2.72**	**1.689**	**1.66**	**1.829**	**1138**
Test10	**14-7-0**	**SPRAY**	**CI**	**2.72**	**1.793**	**1.711**	**1.403**	**1419**
Test11	14-7-0	DRY	UI*	0.71	1.712	1.708	1.554	988

Note: CI – center ignition; UI – upper ignition; KU – Kulite pressure sensors; KI – Kistler pressure sensors; PCB – PCB pressure sensors

Ignition

A hot wire provided an ignition of the test mixtures in 2-3 minutes after the mixing procedure to suppress a turbulence generated by mixing fans. A center ignition (CI) position at the centerline H = 3.15 m from floor level was used in the tests where the concentration kept constant 7% H_2. The only one test with upper ignition (UI) position (H = 6.95 m) at highest hydrogen concentration was used (Table 1). Pressure, temperature records simultaneously with video observations of combustion process were performed in the tests. Total record time was about 10.5-21.0 seconds for fast controllers and about 1400 seconds for slow controllers. All the pressure and temperature records and video cameras were synchronized with an ignition moment with a pre-record time of about 0.5 s.

Mitigation system. Water spray

A water dispersion system has built on top of the A2 vessel at H = 8.14m. It was based on the WhirlJet Spray Nozzles type 1CX-SS15, full cone spray, with a capacity of 100 liter/min. The water spray provides a 120^o of opening angle (Fig. 6).

The spray is initiated by overpressure up to 8 bar. In order to investigate the efficiency of water spray mitigation, the spray was actuated with 100 and 60 ms of time delay after an ignition moment. The time delay has provided to allow a well-developed flame kernel. The flame dimension with such a delay was about 1 m radius.

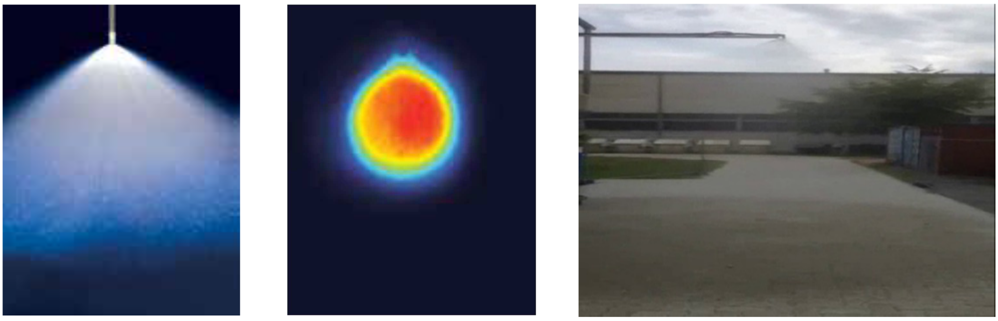

Fig. 6. Structure of water spray: declared by manufacturer (left); actual (right).

EXPERIMENTAL RESULTS AND DISCUSSION

Strong influence of hydrogen stratification and ignition position was found in the tests (Fig. 7). The most representative and reliable pressure sensor KU3 (Kulite) at the middle position H = 3.27 m was chosen for the analysis. The maximum combustion pressure of 1.7 bar increases 10 times for stratified hydrogen mixtures as compared with uniform mixture of the same amount of hydrogen equal to 7% H_2 (0.16 bar). The time for maximum pressure roughly corresponds to complete combustion time equal to ~$2 \cdot t_{1/2}$, which is inversely proportional to the average flame speed (Table 1). Assuming a spherical shape of combustion zone after ignition, a visible flame speed can be calculated according to papers [13-14]. Figure 7 (right) shows that combustion velocity for a stratified mixture (1.5-3.5 m/s) is about 2.5-6 times higher than that (0.6 m/s) for uniform mixture of the same amount of hydrogen (7% H_2). An additional confirmation of the importance of maximum hydrogen concentration on combustion process is done by upper ignition position (UI). The ignition at highest hydrogen concentration of 14% H_2 leads to maximum combustion pressure increase up to 1.7 bar and two times higher average combustion velocity (~6 m/s) compared to center ignition at 7% H_2 for the same stratified mixture 14→7→0% H_2. Upper ignition position at 14% H_2 also leads to tenfold velocity increase compared to that for uniform composition of the same amount of hydrogen (7% in average).

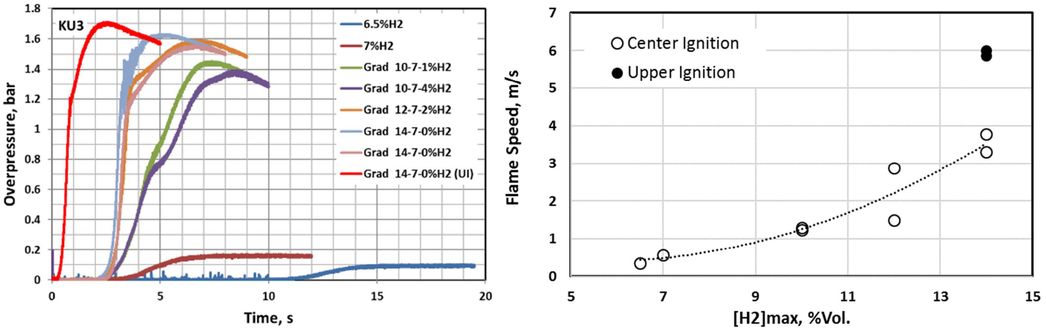

Fig. 7. Combustion pressure records (left) and visible flame velocity as function of maximum hydrogen concentration (right) for stratified and uniform hydrogen-air mixtures.

Maximum combustion temperature behaves almost the same way as the pressure. Namely, the maximum combustion temperature of 1300-1600 °C for stratified combustion is much higher than for uniform combustion (260 °C for 6.5% H_2 and 380 °C for 7% H_2). Figures 7-8 confirm that for stratified compositions the combustion rate governs by highest hydrogen concentration at the sealing rather than an average hydrogen concentration of the mixture. The changing of highest hydrogen concentration from 10 to 14% H_2 leads to maximum combustion pressure increase from 1.4 bar to 1.7 bar and combustion temperature increase from 800 ^oC to 1300 ^oC.

The temperature grows very quick until the mixture completely or partially burns. At least until the flame reaches the top of the volume. Since the downward flame propagation limit for hydrogen-air mixtures is 8% H_2, the flame at 6.5 and 7% H_2 is able to propagate only upward after center ignition. This means that only a part of the mixture burns completely. Bottom part of the volume up to H = 3.0 m remains unburned. The maximum temperature within unburned part does not exceed 30-35 ^oC. The difference between stratified and uniform compositions is that for uniform compositions 6.5% and 7% H_2 more than half of the mixture remains unburned in comparison with stratified mixture with much higher completeness of combustion.

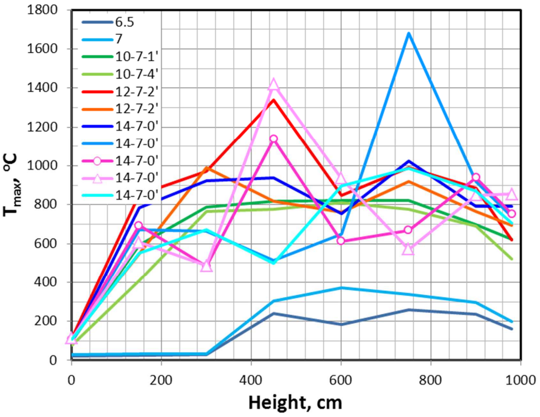

Fig. 8. Distribution of maximum combustion temperature for stratified and uniform hydrogen-air mixtures.

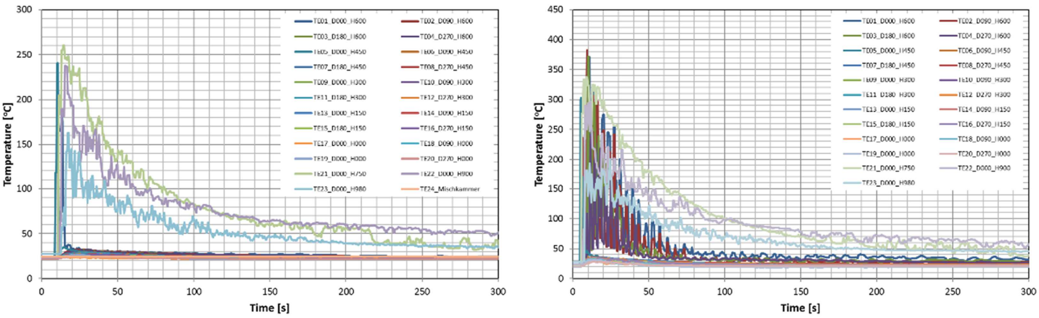

Fig. 9. Maximum combustion temperature for uniform compositions of hydrogen – air mixtures with 6.5% (left) and 7% H_2 (right).

Figure 9 shows temperature records for uniform compositions with 6.5% and 7% H_2. Thermoelements at the centerline positions H = 4.5 m and H = 6 m showed very short heating time corresponding to passing a fireball through the thermocouple. It takes only 3 sec for 4.5 m and 4 sec for 6 m positions. Then, the combustible zone is localized at upper center part of the volume (H > 7.5 m), without horizontal expansion of the flame. The maximum combustion temperature (260 ^oC for 6.5% H_2 and 380 ^oC for 7% H_2) is reached in 6 sec (6.5% H_2) or 3.5 sec (7% H_2) after ignition then the temperature of combustion products slowly decays to 30-50 ^oC within 150 sec. The difference of flame arrival time for gauges positions 4.5 m and 6 m takes about 2 sec for 6.5% H_2 in air. It corresponds to flame propagation velocity of about 0.75 m/s. The same procedure for 7% H_2

gave the local flame propagation velocity of about 2 m/s. Such slow flame propagation velocity is almost equal to characteristic velocity of hot buoyant gas lifting up due to the convection.

An influence of hydrogen concentration gradient on maximum temperature was found in the tests for stratified compositions. Stronger hydrogen concentration gradient from 10=>7=>4 to 12=>7=>2% H_2 leads to the increase of maximum combustion temperature from 810 ^oC to 1330 ^oC (Fig. 10). The completeness of combustion for stratified compositions is much higher than for uniform compositions. The highest combustion temperature >700 ^oC is kept at H = 3 m, even below the ignition point. The temperature of about 400 °C occurs at H = 1.5 m probably due to turbulent mixing of combustion products and reactants. At ground level the temperature does not exceed 80 °C. As follows from Fig. 8, the maximum combustion temperature for stratified compositions is localized at the upper part of the system H = 7.5 m with highest hydrogen concentration.

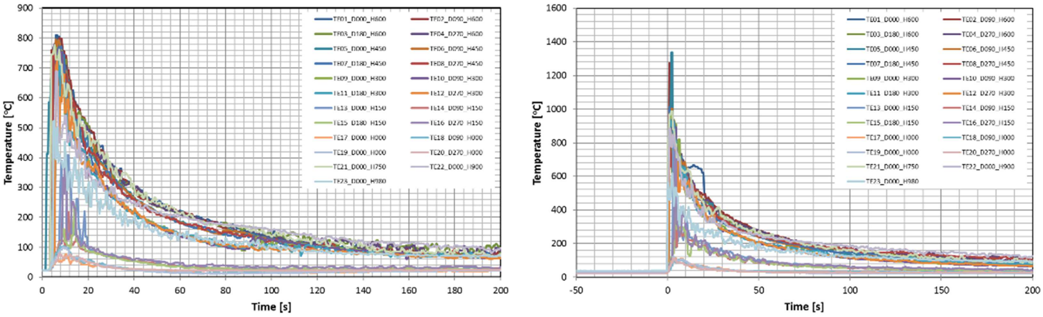

Fig. 10. Maximum combustion temperature for stratified compositions of hydrogen-air mixtures with two gradients from 10=>7=>4% H_2 (left) to 12=>7=>2% H_2 (right).

A weak influence or even promoting effect of water spray on combustion process has been found. The spray was initiated 60 ms after ignition of the mixture when the flame develops quite well (about 1 m radius). Higher combustion pressure (1.6-1.7 bar) and faster combustion time ($t_{1/2}$ = 2.72 s) were registered due to an additional turbulence in the presence of water spray (Fig. 11, left). It corresponds to 1.5-2 times of the flame velocity increase according to Fig. 11, right. The velocities also were calculated from pressure measurements using a procedure described in papers [13-14]. Combustion temperature has also increased by 100-200 ^oC compared to dry mixtures of the same concentration profile (Fig. 8). The highest combustion temperature is localized at H = 4.5 m, exactly at the interacting interface of water spray and combustion zone. The reason could be a turbulent transport of hydrogen enriched mixture to the combustion zone by water spray injection from the upper position.

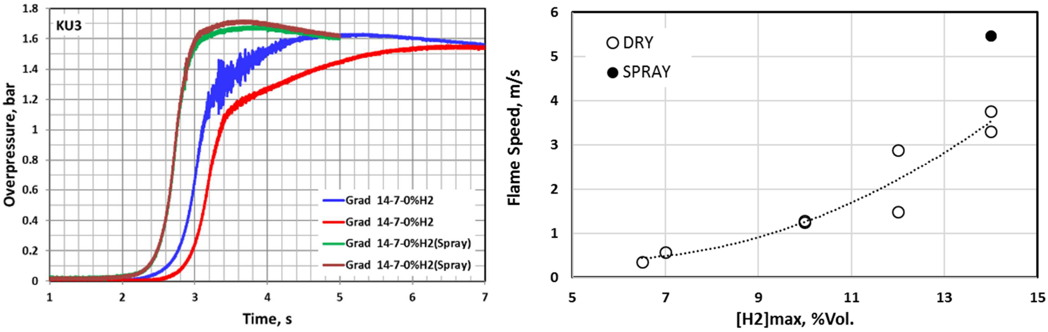

Fig. 11. Maximum combustion pressure (left) and visible flame velocity as function of maximum hydrogen concentration (right) for dry mixture and wet composition in presence of water spray.

Acoustic oscillations due to the flame instability have also been measured by microphone in the tests. For instance, two resonance frequencies 86 and 366 Hz in the test with a gradient 12-7-2% H_2 were distinguished (Fig. 12). It might be an evidence of acoustic and parametric flame instabilities. Characteristic frequencies of acoustic oscillations in presence of water spray can be shifted to 150 Hz and 450 Hz for two first resonant bands.

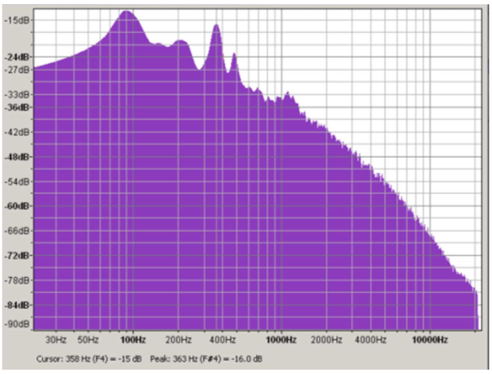

Fig. 12. Spectrum of sound record for stratified combustion of the mixture with a gradient 12-7-2% H_2.

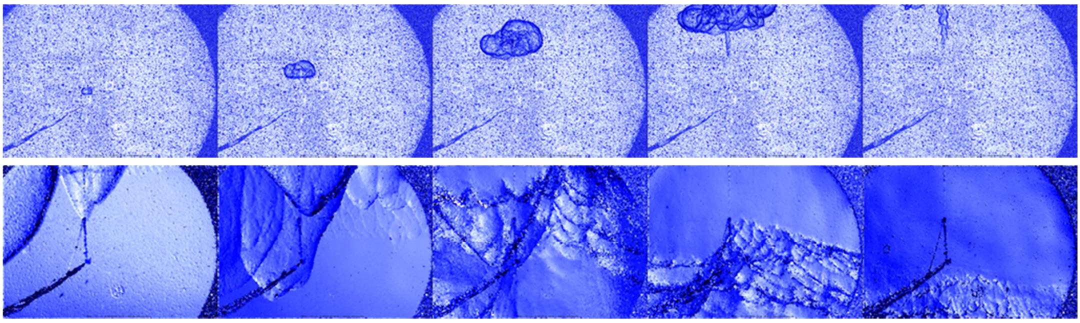

Fig. 13. A sequence of BOS images for non-uniform combustion with a gradient 10-7-4% H_2.

An example of BOS images for non-uniform combustion with a gradient 10-7-4% H_2 and a center ignition is shown in Fig. 13. Initially, the flame ball develops with a velocity 0.16-0.52 m/s. It lifts up due to the buoyancy in the direction of more reactive mixture. Then, the turbulent wrinkled flame propagates downward with a velocity 1.11-2.83 m/s. This is very close to calculations by pressure.

CONCLUSIONS

(1) Hydrogen distribution experiments in HYKA-A2 vessel were performed in order to create a relatively stable vertical hydrogen concentration gradients.

(2) Flame propagation experiments with uniform hydrogen concentration of 6.5% and 7% H_2 for center ignition (CI) point have been carried out as reference tests.

(3) Flame propagation tests with center ignition point for three different hydrogen concentration gradients 14→0, 12→2 and 10→4% H_2 with the same amount of hydrogen equal to 7% of average concentration in the whole vessel volume have been performed. Strong influence of hydrogen stratification was found. The combustion maximum pressure (1.7 bar) was increased by 10 times for stratified mixture compared to uniform mixture with the same amount of hydrogen equal to 7% H_2

(0.16 bar). The same factor of 10 was found to be applicable to the flame velocity increase (from 0.6 to 6 m/s). The temperature is increased from 370 ^oC (7%) to 1300-1700 ^oC (14→7→0% H_2).

(4) The governing role of highest hydrogen concentration on combustion process for stratified mixture was experimentally shown. There is no effect of average hydrogen concentration.

(5) One test with upper ignition (UI) position and vertical hydrogen concentration gradient of 14→7→0% H_2 was performed. It leads to the highest combustion over-pressure (1.7 bar) due to two times higher combustion velocity as compared to stratified composition with a center ignition (CI) point. It confirms a dominating role of highest hydrogen concentration on combustion process.

(6) An effect of water spray on flame propagation was studied in two tests with center ignition and vertical hydrogen concentration gradient of 14→7→0% H_2. No suppression effect of water spray (100 l/min) was found on combustion. Maximum combustion temperature increases from 1020 ^oC to 1400 ^oC due to an additional turbulence in the presence of water spray.

ACKNOWLEDGMENT

The authors are very grateful to ALISA community (EU and Chinese authorities) for very helpful comments and discussions.

REFERENCES

[1] J. Yanez, M. Kuznetsov, A. Souto-Iglesias, An analysis of the hydrogen explosion in the Fukushima-Daiichi accident, Int. J. Hydrogen Energy 40 (2015) 8261-8280.

[2] M. Kuznetsov, J. Yanez, J. Grune, A. Friedrich, T. Jordan, Hydrogen Combustion in a Flat Semi-Confined Layer with Respect to the Fukushima Daiichi Accident, Nucl. Eng. Des. 286 (2015) 36-48.

[3] J. Xiao, W. Breitung, M. Kuznetsov, H. Zhang, J. R. Travis, R. Redlinger, T. Jordan, GASFLOW-MPI: A new 3-D parallel all-speed CFD code for turbulent dispersion and combustion simulations Part II: First analysis of the hydrogen explosion in Fukushima Daiichi Unit 1, Int. J. Hydrogen Energy 42 (2017) 8369-8381.

[4] D.M. Prabhudharwadkar, K. N. Iyer, N. Mohan, S. S. Bajaj, S. G. Markandeya, Simulation of hydrogen distribution in an Indian Nuclear Reactor Containment, Nuc. Eng. Des. 241 (2011) 832-842.

[5] J.M. Martín-Valdepeñas, M.A. Jiménez, F. Martín-Fuertes, J.A. Fernández, Improvements in a CFD code for analysis of hydrogen behaviour within containments, Nuc. Eng. Des. 237 (2007) 627-647.

[6] W. Breitung, et al., Integral large scale experiments on hydrogen combustion for severe accident code validation-HYCOM, Nuc. Eng. Des. 235 (2005) 253-270.

[7] N. Agrawal, A. Prabhakar, S.K. Das, Hydrogen Distribution in Nuclear Reactor Containment During Accidents and Associated Heat and Mass Transfer Issues—A Review, Heat Transfer Engineering, 36, Heat Trans. Eng. 36 (2015) 859–879.

[8] I. Kljenak, M. Kuznetsov, P. Kostka, L. Kubišova, M. Maltsev, G. Manzini, M. Povilaitis, Simulation of hydrogen deflagration experiment – Benchmark exercise with lumped-parameter codes, Nucl. Eng. Des. 283 (2015) 51-59.

[9] M. Kuznetsov, G. Stern, I. Kljenak, M. Matkovič, B. Mavko, Upward flame propagation experiments on hydrogen combustion in a 220 cub. m vessel, In: Proc. of the 22nd International Conference on Nuclear Engineering (ICONE22), ICONE22-30160, pp. 1-11, 2014.

[10] S. Kudriakov, E. Studer, M. Kuznetsov, J. Grune, Experimental and numerical investigation of hydrogen-air deflagration in the presence of concentration gradients, In: Proc. of the 21st International Conference on Nuclear Engineering, ICONE21, ICONE21-16910, pp. 1-10, 2013.

[11] S. Kudriakov, E. Studer, M. Kuznetsov, J. Grune, Hydrogen-air deflagration in the presence of longitudinal concentration gradients, In: Proc. of the ASME 2013 International Mechanical Engineering Congress and Exposition (IMECE2013), IMECE2013-66619, pp. 1-9, 2013.

[12] M.S. Kuznetsov, V.I. Alekseev, S.B. Dorofeev, I.D. Matsukov. Propagation and Quenching of Turbulent Flames in Nonuniform Mixtures, In: Proc. 16th ICDERS, p. 617, 1997.

[13] G E Andrews, D. Bradley, The burning velocity of methane-air mixtures, Combust. Flame, 19 (1972) 275-288.

[14] M. Kuznetsov, R. Redlinger, W. Breitung, J. Grune, A. Friedrich, N. Ichikawa, Laminar burning velocities of hydrogen-oxygen-steam mixtures at elevated temperatures and pressures, Proc. Comb. Inst. 33 (2011) 895-903.

Scientific Principles of e-Laboratory of Hydrogen Safety

Shentsov V.*, Makarov D., Molkov V.

Hydrogen Safety Engineering and Research Centre (HySAFER),
Ulster University, Shore Road, Newtownabbey, BT37 0QB, UK
**Corresponding author's email: v.shentsov@ulster.ac.uk*

ABSTRACT

Education and training are crucial for provision of safety of fuel cell and hydrogen (FCH) systems and infrastructure. The European project "Novel Education and Training Tools based on digital Applications related to Hydrogen and Fuel Cell Technology" (NET-Tools) is developing digital platform and providing online contemporary tools and information services for education and training within FCH sector. The project is delivering an innovative platform, influencing robust and effective learning while offering a unique blend of novel digital tools. The platform has two main pillars, i.e. e-Education and e-Laboratory. The essential part of e-Laboratory is a suit of hydrogen safety tools. The aim of this paper is to present scientific principles behind the hydrogen safety engineering tools of the e-Laboratory. The principles describe or predict a range of natural phenomena in unignited releases, jet-fires, deflagrations, blast-waves and fireball etc. They summarize and explain a large collection of facts determined by experiments and supported by physics and mathematics. Principles are tested based on their ability to predict the results of future experiments and possible safety related scenarios to calculate flame lengths, concentrations, overpressures, hazard distances, etc., and supported by peer-reviewed publications.

KEYWORDS: Deflagration, ventilation, jet fire, blast wave, fireball.

INTRODUCTION

Education and training for emerging fuel cell and hydrogen (FCH) sector is critical for professional development of current and future workforce. This underpins the leadership and competitiveness of European FCH products. The European project "Novel Education and Training Tools based on digital Applications related to Hydrogen and Fuel Cell Technology" (NET-Tools) is developing digital infrastructure and providing contemporary online tools and information services for education and training within FCH technologies sector.

The NET-Tools project is delivering a technology platform, influencing robust and effective open source and free access learning management system while offering a unique blend of novel digital tools encompassing generic information, education and research. The digital platform includes two main pillars i.e. e-Education and e-Laboratory. The platform addresses educational interests of various groups of stakeholders with different levels of education from higher schools and universities, both undergraduate and graduate students, to professionals and engineers from industry, offering both e-learning modules and on-line design tools. The aim of this paper is to give an overview of the scientific principles that lay behind the engineering tools developed within Safety Engineering Toolbox of e-Laboratory.

Performance-based calculation of hazard distances, the term introduced recently by ISO TC197 Hydrogen Technologies, is a key element of hydrogen safety engineering of FCH systems and infrastructure, e.g. refuelling stations. The principles behind the e-Laboratory of Hydrogen Safety allow assessing hazard distances for unignited releases (flammable envelope size); ignited releases

Proceedings of the Ninth International Seminar on Fire and Explosion Hazards (ISFEH9), pp. 1305-1313
Edited by Snegirev A., Liu N.A., Tamanini F., Bradley D., Molkov V., and Chaumeix N.
Published by Saint-Petersburg Polytechnic University Press
ISBN: 978-5-7422-6498-9   DOI: 10.18720/spbpu/2/k19-82

(jet fires); blast wave decay from deflagrations, detonations and high-pressure hydrogen storage tank rupture in a fire, fireballs, etc. This long expected by hydrogen industry toolbox provides determination of hazard distances for unignited releases and jet fires in interactive regime, e.g. by varying system parameters like pressure and pipe (leak) diameter. The state-of-the-art safety tools of the e-Laboratory of Hydrogen Safety is a free-access expanded European analogy of the HyRAM (Hydrogen Risk Assessment Methods) tool, which has been developed by Sandia National Laboratories (SNL) during last decade under funding of the US Department of Energy. The e-Laboratory demonstrates European leadership in hydrogen safety engineering, e.g. by capability to calculate hazard distances determined by thermal and pressure effects from a fireball and blast wave after tank rupture in a fire, which are absent in the HyRAM tool and similar Canadian (UTRQ) framework is implemented using Smalltalk Seaside web development environment.

SCIENTIFIC PRINCIPLES

This section describes scientific principles behind the engineering tools of the e-Laboratory of Hydrogen Safety. The tools are gathered in groups by similarity in applications.

Unignited releases

The under-expanded jet theory [1], [2] is behind the “Jet parameters” and other tools related to under-expanded jets. It allows calculation of hydrogen flow parameters in real and notional nozzles. Density in the real nozzle is needed for the use in the similarity law for concentration decay in hydrogen jet [2], [3] and parameters at the notional nozzle, which are widely used as boundary conditions for computational fluid dynamics (CFD) simulations. The tool allows calculation of mass flow rate of high-pressure hydrogen release through both a hole in a storage vessel and a narrow channel with losses. The tool for prediction of axial concentration decay of a leaking hydrogen for sub-sonic, sonic, and super-sonic jets employs the similarity law, which is validated in a wide range of conditions from expanded to highly under-expanded jets [2]. This tool calculates hazard distance, i.e. length of the flammable envelope, for momentum-dominated jets, which represent practically all realistic releases from high-pressure hydrogen equipment and storage.

The under-expanded jet theory is used to build and validate described in the next section the universal similarity law, which is valid for both expanded and under-expanded jets in the momentum-controlled regime. The theory is applied to derive: the universal correlation for hydrogen jet flame length, the tool for calculation of blow down time of hydrogen release from the storage vessel, etc. The theory is essential to carry out hydrogen safety engineering for different applications.

The similarity law

It must be noted that thermal effects of jet fires, pressure effects of deflagration or detonation, and pressure and thermal effects of high-pressure storage rupture in a fire (blast wave and fireball) could override the hazard distance determined by the size of flammable envelope or hazard distances of a jet fire. Thus, knowledge of laws describing hydrogen dispersion and flammable cloud formation, including axial concentration decay for arbitrary jets is essential for hydrogen safety engineering.

Figure 1 shows the similarity law for prediction of axial concentration decay of a leaking gas for sub-sonic, sonic, and super-sonic jets is derived and presented in [2], [3]. It is valid in a wide range of conditions from expanded to highly under-expanded jets. It can be applied for calculation of hazard distances informed by the size of the flammable envelope. The non-ideal behaviour of hydrogen at high pressures and the under-expansion of flow in a nozzle exit are considered by employing the Abel-Noble equation of state (EoS) for real gas.

It can be seen that all experimental points are on or below the similarity law line. This is thought due to friction and minor losses in experimental equipment, which were not accounted for when the under-expanded jet theory without losses was applied. Indeed, from the similarity law equation it follows that if losses decrease pressure at the nozzle exit, and then they reduce hydrogen density and therefore the concentration in the jet for a fixed distance from the nozzle. This is equivalent to shifting experimental points down on the graph. If the spouting pressure (actual nozzle exit pressure) is applied instead of the pressure in a storage tank the difference between the similarity law curve and experimental data would reduce to zero in the limit. The universal character of the similarity law for both expanded and under-expanded jets makes it an efficient tool for hydrogen safety engineering.

For hydrogen jets into stagnant air for a fixed concentration expressed in percent by mass C_{ax}, the ratio of a distance, x, to the nozzle diameter is a constant, i.e. x/D=const. This means that the distance to the lower flammability limit (hazard distance) is directly proportional to the leak diameter. Thus, the design of hydrogen and fuel cell systems has to be carried out bearing in mind the requirement to minimise the internal diameter of piping, i.e. leak size for conservative full bore rupture scenario, yet keeping technological requirements to mass flow rate.

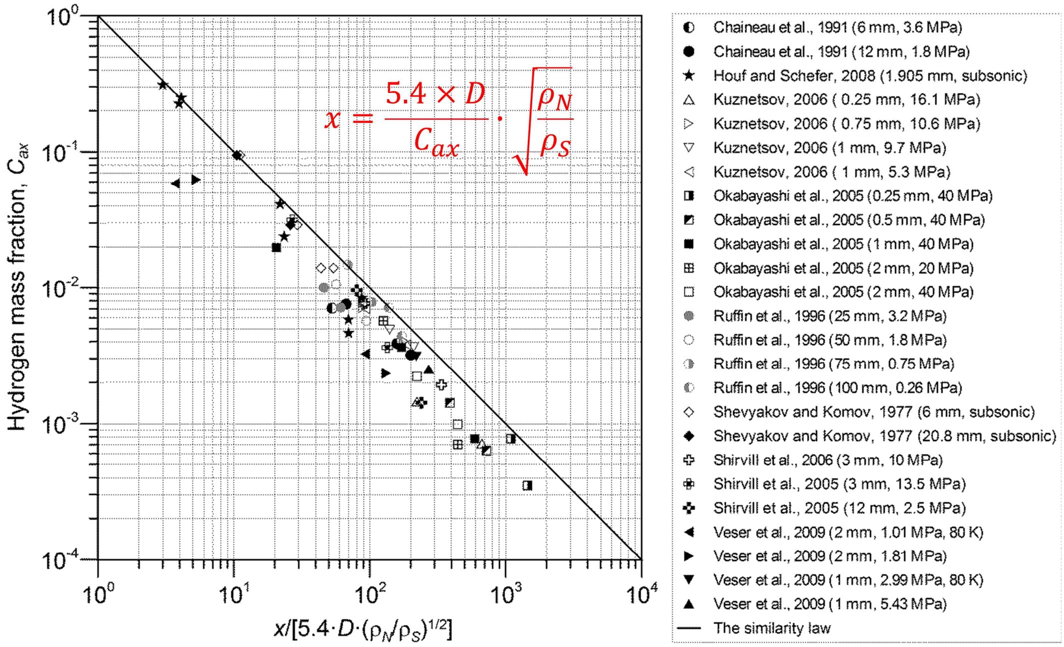

Fig. 1. Similarity law [2].

Effect of buoyancy

The "Effect of buoyancy" tool allows to calculate the decrease of hazard distance for initially momentum-dominated hydrogen jets when it transforms to buoyancy-controlled jet. It is based on validated against experiments the theory of Shevyakov which can be found elsewhere [2]. The engineering technique [2] qualifies which part of hydrogen jet (both expanded and under-expanded) is momentum-controlled with the rest of the jet downstream being buoyancy-controlled.

There are three types of jets depending on the role of buoyancy Fig. 2 (left): fully momentum-controlled jets are not affected by buoyancy; fully buoyancy-controlled jets are quickly diverted from the horizontal to vertical flow direction; the third type of jets is transitional with momentum-dominated part closer to the nozzle and buoyancy-controlled flow further downstream when the jet velocity drops and diameter increases. For hydrogen safety engineering it is important to know when this transition takes place. This has direct implication on hazard distance and thus the infrastructure cost.

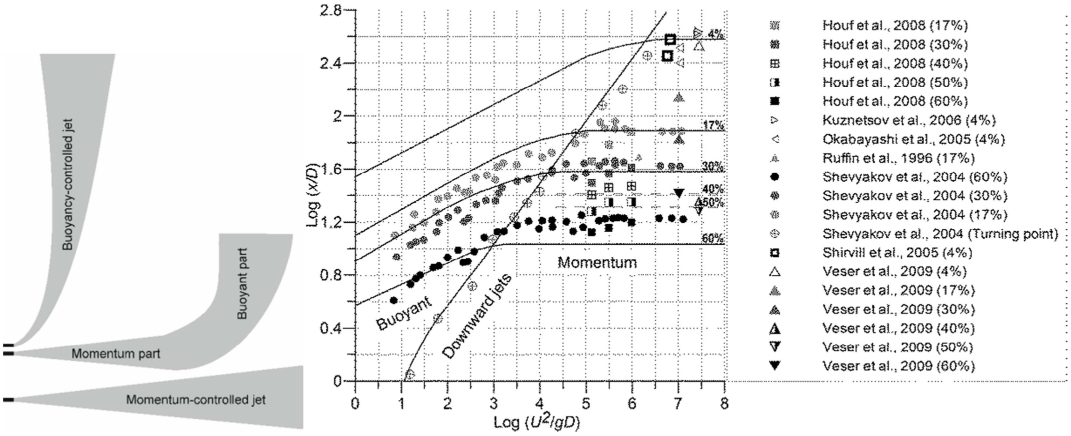

Fig. 2. Types of jets depending on the role of buoyancy (left), dependence of the distance to the nozzle diameter ratio *x/D,* for particular hydrogen concentration in air, on the Froude number (right).

Five theoretical curves (solid lines) and experimental data for expanded jets, and data of other researchers for under-expanded jets are shown in Fig. 2 (right). Practically all under-expanded jets in hydrogen incidents/accidents will be in the momentum-controlled regime as follows from available tests applied to validate the correlation. Four of five theoretical curves in the graph are related to hydrogen concentrations of 4%, 17%, 30%, and 60% by volume respectively. Each of these four curves has an ascending buoyant part and a momentum "plateau" part. The fifth curve "Downward jets" is of special interest. It gives for a jet directed vertically downward a dimensionless distance from the nozzle to the turning point, where the jet changes direction of flow from downward to upward. The fifth curve intersects each of the four other curves in the graph in the region of transition from momentum-dominated to buoyancy-controlled flow as expected.

The following sequence is applied in use of the correlation in Fig. 2. Firstly, the nozzle exit Froude number is calculated and its logarithm. The under-expanded theory is applied to calculate the notional nozzle exit diameter and the velocity in the notional nozzle exit when applicable. Then, a vertical line is drawn upward from a point on the abscissa axis equal to the calculated Froude number logarithm. The intersection of this vertical line with the line marked "Downward jets" on the graph indicates the concentration above which the jet is momentum-dominated and below which the jet is buoyancy-controlled and logarithm of the distance to the nozzle diameter. Further intersection with theoretical curves gives the distance to concentration of interest where the jet is buoyant by potentiation of *log(x/D)*. The idea behind the engineering tool lays in representation of the curves by the set of polynomial functions of the curves and the sequence of logical expressions to solve the problem.

The easy to apply technique Fig. 2 (right) can be very useful to develop cost-effective hydrogen safety engineering solutions. For instance, hazard distance for a horizontal jet release can be essentially reduced as only the length of the momentum-dominated part of the jet can be taken as an indication of the separation rather than the aggregated distance, i.e. both momentum- and buoyancy-controlled parts of the jet to the lower flammability limit (LFL) of 4% by volume of hydrogen.

Blowdown

The "Blowdown of storage tank" tool calculates pressure dynamics inside the tank during release for adiabatic and isothermal conditions, which can be combined to reproduce blowdown dynamics closer to reality. Both models give close pressure dynamics but different temperature dynamics of the released hydrogen.

The adiabatic blowdown model is based on the assumption of a quick release from a high-pressure reservoir and negligible heat transfer effects to the released hydrogen temperature. The adiabatic model gives lower temperature of released hydrogen at the end of the process. While, the isothermal blowdown of a storage tank assumes of a relatively long release from a high-pressure reservoir, so that heat transfer significantly changes the temperature of the outflowing hydrogen. The combination of adiabatic at the beginning and then isothermal model afterwards gives a good approximation for dynamics of temperature of released hydrogen observed in experiments.

Both models are built on the model for expanded and under-expanded jet parameters, which describes parameters in an expanded and under-expanded jet through the characteristic stages of its development – in the storage reservoir, the orifice, and the notional (effective) nozzle exit and utilises Abel-Noble EoS and the conservation equations for mass and energy.

The tool can be used to formulate mitigating measures and safety strategies based on fire resistance rating of onboard hydrogen storage tank. The fire resistance rating should be greater than the sum of time for a thermally activated pressure relief devices (TPRD) initiation and blowdown time of the storage tank to exclude its catastrophic failure in the case of fire. Obviously, the use of a TPRD with a larger diameter would create a larger flammable cloud or a jet flame. It would generate higher overpressure during "delayed ignition" or deflagration of turbulent flammable cloud. By this reasoning the TPRD diameter should be reduced as much as possible provided the fire resistance rating is increased consequently.

Passive ventilation

The "Passive ventilation" tool allows to calculate hydrogen concentration in an enclosure with known vent size for the given release rate or solve inverse problem method (calculate vent size to keep concentration below desirable level for known hydrogen release rate).

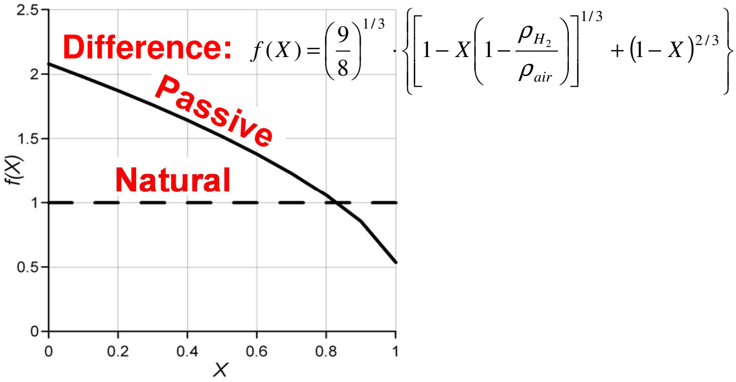

Fig. 3. Difference between passive and natural ventilation.

The model is developed in the assumption of perfect mixing and equations for passive (release of flammable or toxic gas) and natural (air quality problems) ventilation were compared [4] to show the essential difference between two approaches. The natural ventilation equations are usually derived in the assumption that the neutral plane is located at the half of the vent height, however for the passive ventilation of accidental release in an enclosure the neutral plane can be located anywhere below the half of the vent height. The development of passive ventilation model has demonstrated that the accurate analytical solution for passive ventilation differs from the approximate solution for natural ventilation by more than 2 times for lean and rich mixtures as shown in Fig. 3, where X is hydrogen mole fraction.

This could have serious safety implications and should be dealt with care while performing safety engineering involving hydrogen releases. The passive ventilation theory states that, vertical vent is more efficient compared to horizontal vent of the same area and this should be taken into account during the design of passive ventilation systems.

Forced ventilation

The "Forced ventilation" tool calculates parameters of the mechanical ventilation system to keep hydrogen concentration below required level. The parameters include the volume flow rate of air required for the given mass flow rate of hydrogen to be lower that specified limit in the assumption of perfect mixing. The model is based on the principles of passive ventilation and its calculation of ventilation flow rate to provide hydrogen concentration in an enclosure below required level. Application of forced ventilation in numerical experiments proved calculations and demonstrated a decreased gas concentration to the required level. This confirms that the proposed methodology can be applied to calculate the ventilation rate for fuel cell and hydrogen systems and can be used as a tool for hydrogen safety engineering.

Pressure peaking phenomenon

The revealed in 2010 at Ulster the pressure peaking phenomenon (PPP) [5] is another unique of the e-Laboratory of Hydrogen Safety not available in other similar hazard and risk assessment software. It allows calculation of pressure dynamics in an enclosure like garage in case of unscheduled release of hydrogen. Both hydrogen blowdown release and constant mass flow rate release options are available. The tool is applicable for both ignited (fire from TPRD) and unignited (TPRD failure) releases.

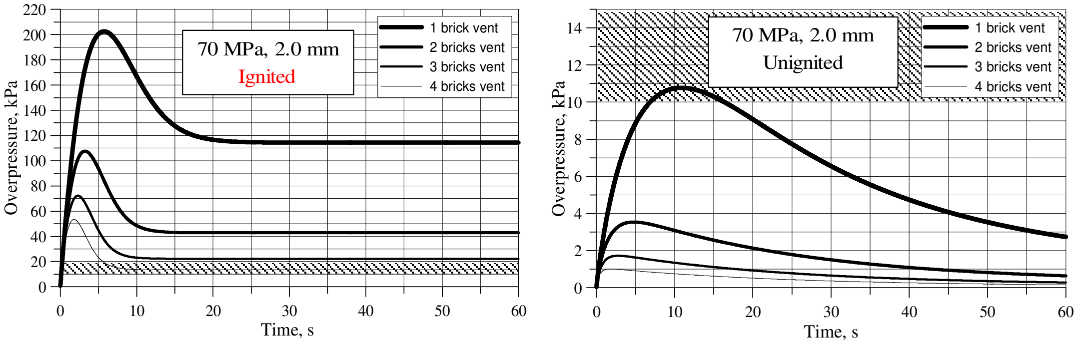

Fig. 4. Overpressure dynamics of hydrogen jet fire in the garage: TPRD diameter 2 mm and storage pressure 70 MPa (release rate 107 g/s) Ignited (left) vs unignited (right) [6].

The pressure peaking phenomenon is characteristic only for gases lighter than air when they are released into an enclosure with limited area of vents. The PPP is more pronounced for ignited release compared to unignited release from the same source [6], see Fig. 4. ISO standard requires the PPP to be taken into account when performing hydrogen safety engineering for indoor use of hydrogen and fuel cell systems.

The prevention and mitigation of the PPP can be achieved only through the decrease of mass flow rate from TPRD, i.e. its nozzle diameter. This is turn will require higher fire resistance rating of on-board storage tanks.

JET FIRE HAZARD DISTANCES

The "Jet fire" tool uses the dimensionless hydrogen flame length correlation [3] to calculate three hazard distances, i.e. "no harm" distance to T=70°C, which is 3.5 times of flame length; "pain limit" (115°C, 5 min), which is 3 times of flame length; and "fatality limit" (309°C, 20 s), which is 2 times of flame length. The universal flame length correlation includes laminar and turbulent flames, buoyancy- and momentum-controlled fires, expanded (subsonic and sonic) and under-expanded (sonic and supersonic) jet fires, thereby covering the entire spectrum of hydrogen reacting leaks [3]. Theoretical and experimental results indicate that the flame length has to be a function of not only the Froude number (*Fr*) but also the Reynolds (*Re*) number and the Mach (*M*) number and in this correlation, all are taken into account. One of its advantages is the absence of parameters at the notional nozzle exit, which are derived in the limited validity range assumption of sonic flow at the notional nozzle. The parameters needed to predict the flame length are those at the actual nozzle exit only: diameter, hydrogen density and flow velocity, the speed of sound at pressure and temperature at the real nozzle exit. The dimensionless correlation for hydrogen jet flame length in still air is L_F/D–$(\rho_N/\rho_S)\cdot(U_N/C_N)^3$ and shown in Fig. 5. Here L_F is the flame length, D is the nozzle diameter, ρ_N and ρ_S are release densities at the nozzle and surrounding air respectively, while U_N and C_N are velocity at the nozzle and speed of sound in the released gas in the nozzle.

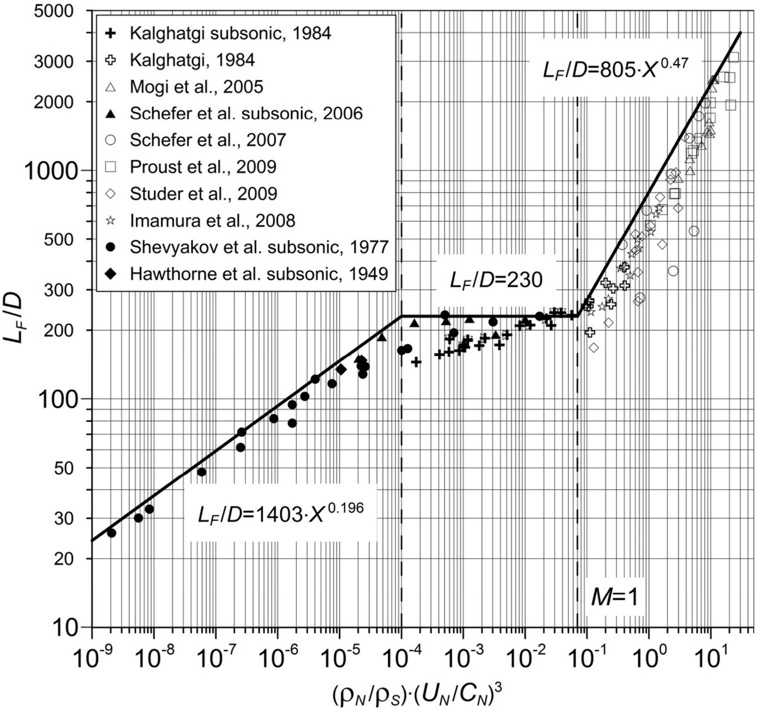

Fig. 5. Dimensionless flame length correlation [3].

The use of the correlation requires application of an under-expanded jet theory to calculate these parameters. There is lesser uncertainty in calculation of flow parameters in the actual nozzle exit compared to uncertainties at the notional nozzle. Indeed, there is a strong non-uniformity of velocity downstream of the Mach disk that deviates from the common for all under-expanded jet theories assumption of uniform velocity at the notional nozzle exit.

Mitigation of deflagrations

There are three deflagration mitigation tools in e-Laboratory of Hydrogen Safety: vent sizing of enclosure with uniform hydrogen-air mixture [7], vent sizing of enclosure with localised non-uniform mixture [8], calculation of upper limit of hydrogen inventory that can be allowed in a closed space like warehouse [8].

The vent sizing correlation for the uniform hydrogen-air mixture in vented enclosure [7] is based on recent advancements in understanding and modelling of combustion phenomena relevant to hydrogen–air vented deflagrations and unique large-scale tests carried out by different research groups. The combustion phenomena accounted for by the correlation include: turbulence generated by the flame front itself; leading point mechanism stemming from the preferential diffusion of hydrogen in air in stretched flames; growth of the fractal area of the turbulent flame surface; initial turbulence in the flammable mixture; as well as effects of enclosure aspect ratio and presence of obstacles. The tool allows to calculate the vent area to reduce the deflagration pressure to the desired limit and estimate the overpressure inside vented enclosure for the vent of given size.

The model for localised non-uniform mixture [8] describes deflagrations of hydrogen-air mixtures and defines safety requirements for vented deflagrations of localised mixtures in an enclosure. Examples of localised mixtures include ‘pockets’ of gas within an enclosure as well as stratified gas distributions which are especially relevant to hydrogen releases. It allows to estimate the maximum overpressure inside vented enclosure as well as calculating the vent size in order not to exceed the required safety limit.

Thermodynamic model to predict maximum mass of hydrogen, which may be allowed to be released in an enclosure of particular volume without causing destructive deflagration overpressure was developed [8] and realised as a tool in e-Laboratory. The model presumes that an enclosure is partially filled with air and hydrogen-air mixture. If this hydrogen-air mixture is burnt in a sealed enclosure, the model solution for resulting absolute pressure may be found. The tool allows to calculate the inventory mass for the given overpressure and enclosure volume for the given overpressure and inventory mass.

Blast wave and fireball after tank rupture in a fire

The “Blast wave” overpressure decay tool is available for stand-alone and under-vehicle storage tank scenarios. The model developed accounts for the real gas effects and combustion of the flammable gas released into the air (chemical energy) as a contribution into the blast wave strength [9]. The chemical energy of combustion is dynamically added to the mechanical energy and is accounted for in the energy-scaled non-dimensional distance. The model can be applied as a safety engineering tool for typical hydrogen storage applications, including on-board vehicle storage tanks and a stand-alone refuelling station storage tanks. The predictive model is required for calculation of hazard distances defined by the parameters of a blast wave, which is generated by a high-pressure gas storage tank rupture in a fire.

The tool for calculation of “Fireball” diameter after hydrogen tank rupture in a fire is based on the assumption of complete combustion of released hydrogen in air [9], [10]. It is based on limited amount of experimental data and thus requires further validation.

CONCLUSIONS

The scientific principles behind engineering tools of the e-Laboratory of Hydrogen Safety are overviewed. They predict a wide range of realistic phenomena related to hydrogen safety engineering not limited to assessment of overpressures caused by pressure peaking, deflagration and tank explosion, concentration of hydrogen in the jet and indoors, temperature along the jet fire, parameters of the jet and others. The developed engineering tools are being implemented for the stakeholders' free access in the e-Laboratory of the NET-Tools project. All principles behind the implemented online tools of e-Laboratory are based on peer-review publications and their ability to reproduce the results of future experiments is tested and widely validated in order to predict most of accidents related to hydrogen storage, production and distribution and help to develop safety solutions. The e-Laboratory of Hydrogen Safety has the largest number of tools for calculation of hydrogen hazards compared to other similar tools being developed in North America, including but not limited to unignited and ignited released in the open and confined spaces, mitigation of deflagrations, assessment of blast wave and fireball after high-pressure hydrogen tank storage in a fire, etc.

ACKNOWLEDGEMENTS

This project has received funding from the Fuel Cells and Hydrogen 2 Joint Undertaking under grant agreement No (736648). This Joint Undertaking receives support from the European Union’s Horizon 2020 research and innovation programme, Hydrogen Europe and Hydrogen Europe research.

REFERENCES

[1] V. Molkov, M. Bragin, High-Pressure Hydrogen Leak Through a Narrow Channel, In: Nonequilibrium Phenomena: Plasma, Combustion, Atmosphere, pp. 332–338, 2009.

[2] V. Molkov, Fundamentals of Hydrogen Safety Engineering, bookboon.com, free download online book, 2012.

[3] V. Molkov, J.-B. Saffers, Hydrogen Jet Flames, Int. J. Hydrogen Energy 38 (2013) 8141–8158.

[4] V. Molkov, V. Shentsov, J. Quintiere, Passive Ventilation of a Sustained Gaseous Release in an Enclosure With One Vent, Int. J. Hydrogen Energy 39 (2014) 8158–8168.

[5] S. Brennan, V. Molkov, Safety Assessment of Unignited Hydrogen Discharge From Onboard Storage in Garages With Low Levels of Natural Ventilation, Int. J. Hydrogen Energy 38 (2013) 8159–8166.

[6] D. Makarov, V. Shentsov, M. Kuznetsov, V. Molkov, Pressure Peaking Phenomenon: Model Validation Against Unignited Release and Jet Fire Experiments, Int. J. Hydrogen Energy 43 (2018) 9454–9469.

[7] V. Molkov, M. Bragin, Hydrogen–Air Deflagrations: Vent Sizing Correlation For Low-Strength Equipment and Buildings, Int. J. Hydrogen Energy 40 (2015) 1256–1266.

[8] D. Makarov, P. Hooker, M. Kuznetsov, V. Molkov, Deflagrations of Localised Homogeneous and Inhomogeneous Hydrogen-Air Mixtures in Enclosures, Int. J. Hydrogen Energy 43 (2018) 9848–9869.

[9] V. Molkov, S. Kashkarov, Blast Wave from a High-Pressure Gas Tank Rupture in a Fire: Stand-Alone and Under-Vehicle Hydrogen Tanks, Int. J. Hydrogen Energy 40 (2015) 12581–12603.

[10] M. Dadashzadeh, S. Kashkarov, D. Makarov, V. Molkov, Socio-Economic Analysis and Quantitative Risk Assessment Methodology for Safety Design of Onboard Storage Systems, In: International Conference on Hydrogen Safety, Hamburg, Germany, Vol. 184, 2017.

Stand-Alone Hemisphere-Tank Rupture in Tunnel Fire: Effect of Hydrogen Inventory on Blast Wave Strength in Far Field

Shentsov V.*, Makarov D., Dery W.

Hydrogen Safety Engineering and Research Centre (HySAFER),
Ulster University, Shore Road, Newtownabbey, BT37 0QB, UK
**Corresponding author's email: v.shentsov@ulster.ac.uk*

ABSTRACT

High-pressure hydrogen onboard storage rupture in a fire generates blast wave and fireball. These hazards are not yet investigated enough, especially in a tunnel. Consequences of such event, e.g. a blast wave, could be devastating depending on amount of stored hydrogen and tunnel dimensions. This raises the question about the dependence of blast wave overpressure on hydrogen inventory in the tank. The problem is studied here numerically. Large eddy simulation (LES) turbulence model with the eddy dissipation concept (EDC) for combustion were employed in series of numerical simulations in three different tunnel cross-sections with four hemispherical tank volumes at pressures of 94.5 MPa. The dependence of blast wave overpressure on hydrogen inventory is defined. The results are conservative and require experimental validation in tunnel tests.

KEYWORDS: Tunnel, blast wave, tank rupture, inventory.

INTRODUCTION

As the worlds demand for global energy increases for each day, uncertainty regarding fossil and hydrocarbon energy supply sources and long-term effects on the environment are of major concern. An industry-led effort in aims to steer away from fossil-fuelled energy carrier dependencies are therefore gaining vast interest. A growing attitude towards a more environmentally friendly and sustainable energy, hydrogen is specifically targeted in the energy evolution with it representing a clean fuel with high energy content. Presently, utilisation of hydrogen as a commercial energy carrier is being veered onto private and public automotive domains, such as in the transportation sector (e.g. cars and buses). Major car companies such as Honda, Mercedes Benz, Hyundai and Toyota etc. all have cars available for the public in select markets, with hydrogen stations growing steadily (additional 15 000 new hydrogen filling stations are slated for year 2030 globally) [1].

Even though tunnels are an obligated part of everyday vehicular transportation, there are a number of safety concerns not extensively researched upon. The potential hazards associated with hydrogen vehicles in road tunnels was internally identified and investigated by a project called HyTunnel [2]. Mainly non-instantaneous hydrogen releases (i.e. through vents) were illustrated through reviewing current hydrogen designs, tunnel design practice and a programme of experiments and computational fluid dynamics (CFD) modelling performed for selected scenarios. Despite specifying a simultaneous release of a large mass of hydrogen found to be more hazardous compared to when the same mass being released through a single vent, a study extended to examine this issue was left unattended. One of the main knowledge gaps is of a blast wave that can be generated by catastrophic onboard tank rupture in a tunnel caused by fire. The regulation requires that each onboard storage tank is equipped by thermally-activated pressure relief device (TPRD) to

Proceedings of the Ninth International Seminar on Fire and Explosion Hazards (ISFEH9), pp. 1314-1323
Edited by Snegirev A., Liu N.A., Tamanini F., Bradley D., Molkov V., and Chaumeix N.
Published by Saint-Petersburg Polytechnic University Press
ISBN: 978-5-7422-6498-9   DOI: 10.18720/spbpu/2/k19-72

prevent tank rupture in a fire by releasing stored hydrogen. However, a TPRD can fail to function, be blocked from a fire during accident, or be not affected in case of localised fire [3].

Tunnels represents a structure strong enough to withstand tremendous pressure from all sides, as the close-in and reflection effects of the tunnel distinguishes characteristics known from an unconfined space [4]. It was found that the blast wave generated in a tunnel will propagate along the tunnel practically without decay independent of the tunnel length [5]. This could have serious safety implications. A significant incident involving a hydrogen project could negatively impact the public's perception and clean alternatives to conventional energy systems may never experience commercial deployment successfully [6]. This involves covering different aspects of vehicle conduct within day-to-day activities, anticipating accidents and accounting for unforeseen consequences. This information is of primary interest for public and especially for first responders.

There is a paucity of data in experimental work conducted in tunnels of natural provenance and original size involving pressurised tank bursts. Of those available, experimental and numerical studies have been performed to understand the phenomena and develop engineering tools for blast wave propagation in confined spaces (i.e. garages and tunnels) using explosive charges such as TNT [7], [8], [9]. Early understanding of a blast wave from a high explosive source within a structure was claimed to undergo reflections with the inner surface, with decay after each reflection, "eventually, the pressure settles to a slowly decaying level, which is a function of the volume and vent area of the structure and the nature and energy release of the explosion" [10].

Experiments in full-scale tunnels are unaffordably too expensive. The use of CFD eliminates this restriction and allows the ability to use realistic scenarios. Following experimental studies by Zalosh and Weyandt [11], Kim et al. [12] simulated the blast wave and fireball in their test numerically. The realizable k-ε turbulence model was applied and combustion was simulated by the eddy dissipation model, which reproduced the experimental trends. Weyandt [13] performed a bonfire test with Type 4 tank of 72.4 L volume and storage pressure of 34.3 MPa without TPRD to estimate the blast wave and fireball parameters. In 2015, an original theoretical model was developed that allows to calculate parameters of a blast wave from a tank rupture in a fire at different distances in the open atmosphere [14]. In this paper, it was concluded that about 5% of chemical energy of released hydrogen contributes to the blast wave strength through its combustion for a stand-alone tank, and 9% of chemical energy for an under-vehicle tank. In addition, the harm to people and damage to buildings from a blast wave was used to assess hazard distances.

This overall research seeks the ability to explore, pin down and mitigate hazards associated with the current understanding of onboard hydrogen storage applications. With a non-zero probability of a high-pressure hydrogen storage tank rupturing catastrophically, this phenomenon is pivotal to have gained a complete overview over, prior to an incident and its aftermath. The hazards following such an event are found significant, not only in the near vicinity of the blast source, but also in the far field for both humans and structures. Methods of predicting effects of the blast wave and fireball from a pressurised vessel is found in the literature not straightforward – especially the former catering for intricate rupture dynamics and volumetric effects of various tank sizes.

Our previous study of tank rupture inside the tunnel [15] was based on the conservative scenario of a road tunnel with smallest cross-section area and a storage tank with the highest amount of hydrogen for passenger cars (70 MPa, 140 L). The established quasi-steady blast wave in the tunnel was 25 kPa for the case of rupture without combustion (observed at 40 m from the tank location) and 37 kPa for the tank rupture with combustion (blast wave stabilised at 30 m), i.e. 50% higher for a tunnel scenario. This result confirmed our previous conclusion that hydrogen combustion at the contact surface between air and hydrogen behind the shock increases the blast wave strength. Both values of blast wave overpressure are above of the serious injury threshold of 16.5 kPa [16].

The previous RANS model has been changed in this study to more advanced LES for turbulence, and the EDC for combustion. In addition, the further increase of pressure and temperature in the tank before rupture observed has been taken into account in these simulations, measured in experiments [17]. Two fire tests were carried with both tanks pressurised up to 70 MPa. Test 1 was conducted with Type 4 tank of 35 L volume in which the pressure at the moment of rupture was 94.54 MPa, i.e. 35% higher than nominal working pressure. In Test 2, a Type 3 tank of 36 L volume was used, the pressure before burst increasing to 99.47 MPa, i.e. 42% higher than before the test.

NUMERICAL MODEL

Simulations are performed using ANSYS Fluent. The pressure-based solver coupled with PISO pressure-velocity algorithm is applied. The numerical model used in this study included the use of LES for turbulence with the Smagorinsky-Lilly model for simulation of sub-grid scale turbulence and the EDC combustion employing one-step reaction. The comparison with 37 reactions scheme did not show any difference in pressure but provided essential speedup in calculation. The governing equations are based on the filtered conservation equations for mass, momentum, and energy in their compressible form. The tunnel walls and floor are specified as non-adiabatic to allow heat transfer from the combustion no-slip wall conditions applied. The external non-reflecting boundary is defined as pressure outlet with zero-gauge pressure. The second order upwind discretization scheme is used for pressure to improve simulation accuracy for compressible flows, the second order upwind scheme is used for convective terms. The first order is employed for time advancement. To conserve the mechanical energy of compressed hydrogen the tank volume with "ideal gas" in simulations was reduced compared to real tank volume (the pressure was kept as in experiment to get the same starting shock pressure) using the following equation $V_{ideal} = V_{real} - mb$. Were V is volume (m^3), m is mass (kg) and b = 7.69·10^{-3} is the co-volume constant (m^3/kg). The original time step adapting technique was employed to maintain a constant Courant-Friedrichs-Lewy (CFL) number at value of 0.2 in all simulations based on sensitivity study. All calculations are carried out with 20 iterations per time step.

MODEL VALIDATION

This model has been validated against experiments with stand-alone tank rupture in fire in the open atmosphere at storage pressures of 35 MPa [13] and 70 MPa [17]. Good agreement between the simulations and experimental data for the blast wave and fireball dynamics has been achieved (see Fig. 1 for the 35 MPa test) [10]. Figure 1 shows the comparison of experimental (solid) and simulated (dashed) pressure transients at three different locations. The model reproduces the experimental maximum peaks and dynamics results very well. The first peak at distance 1.9 m from the tank (achieved at 1.4 ms) is overestimated in simulations by approximately 50 kPa. This is thought due to neglecting the energy loss to propel tank fragments, destroy the burner structure and to crater the ground.

Figure 2 shows the comparison of fireball size in the test and simulations at 45 ms after the tank rupture. Both the size and the shape of fireball, including the area of bridging shock, are well reproduced. The validated model in the open space model for stand-alone tank is then applied for a series of simulations inside the tunnel to first and foremost assess the effect of inventory on the blast strength.

TUNNEL GEOMETRY

For determination of the tunnel geometry, the minimum standard solution for cross-section areas in road tunnel following the guidelines for the equipment and operation, with regards to road design and alignment was considered. Without requirements accommodating passage for an eventual broken-down vehicle, the width of the road necessary is standardised as 3.5 m including a verge area of a meter added on each side referring to the area outside the marked driving lane [18]. These minimum cross-sectional dimensions for the lane width of the tunnel were kept unaltered for all three tunnels considered in this study. The chosen number of lanes (1, 2 and 5) for each tunnel were due to several reasons. The first tunnel chosen, a single lane with cross-section area of 24.1 m^2 enclosure mostly found on country roads, was considered to treat the worst-case scenario; the blast wave would expand and dissipate less through the close-in effects of the tunnel wall. The second tunnel encapsulating the other end of the worst-case scenario scale accommodating the largest cross-sectional area currently built, the Yerba Buena tunnel as part of the San Francisco–Oakland Bay Bridge [19]. It features a double-decked design each with five lanes, and the larger upper deck with a total cross-section area of 139.1 m^2 was chosen for this study. Road traffic is mostly constructed using two lanes, and in some countries (e.g. Germany) constitute up until 90% of all rural roads including tunnels [20]. Therefore, the third tunnel used in this study contained two lanes as the median with cross-section area of 39.5 m^2. The one and two lane tunnels both has an inner tunnel height of 4.5 m, the minimum required headroom for road traffic [21]. The inner height of the five-lane tunnel was set at 7.2 m.

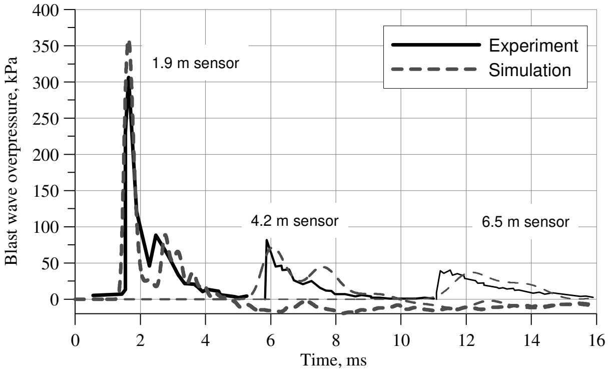

Fig. 1. Pressure dynamics experimental (solid) vs simulated (dashed).

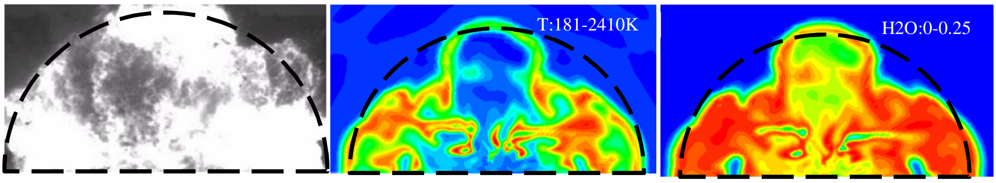

Fig. 2. Fireball size at 45 ms: experiment (left), simulated temperature (centre) and water mole fraction (right).

COMPUTATIONAL DOMAIN

A total volume of the domain ($LxHxW$ = 300x100x75 m) being 2.25E+06 m^3, a considerable size of domain was used to place the tunnel within, limiting the boundary conditions altering any pressure dynamics in and around the tunnel. Each tunnel employed was placed on the midpoint of the outer boundary domain, with a fixed length of 200 m. The rupture location of the high-pressure hydrogen enclosure was set 50 m from one exit, 150 m from the other exit. This was done mostly to ensure a stabilized and undisturbed pressure propagation and stabilisation throughout the long end of the tunnel without influence from the other exit. The control volumes (CV) of the boundary zone, outside the tunnel, were tetrahedral shaped and varied in size relative to its position away from the tunnel. This was carried out with a scale factor of 2 and a max CV size of 10, allowing the actual maximum CV size used for meshing to get as big as 2x10=20 m in size. However, this would be dependent on the need of accuracy required in its position. CVs close to the tunnels exits would be smaller in size, set to be 0.1 m. One of the advantages using ANSYS Fluent is the ability to convert mesh, with one option being combining tetrahedral cells into polyhedral ones and executed for the boundary zone across all three tunnels. A summary of the tunnel dimensions and total number of CVs for each tunnel are listed in Table 1.

Table 1. Tunnel dimensions and control volumes

Tunnel	Cross-section, m^2	Control volumes
Single lane	24.1	201 156
Double lane	39.5	175 596
Five lanes	139.1	450 226

CVs inside the tunnel domain were of hexahedral shape, enclosing not only the entire tunnel boundary, but also the high-pressure hydrogen tank area. A hexahedral mesh was used to ensure a better approximation of the initial high gradient pressure and velocity values. The mesh size ranged from 0.02-0.03 m from the hydrogen surface and using a BiGeometric meshing law, would grow ranging from 0.05 to 0.75 m uniformly. This refined area around each respective tank sizes were kept unchanged across all three tunnels for consistency and stability. The entire domain containing sub-zones of tunnel and tank geometry are illustrated in Fig. 3.

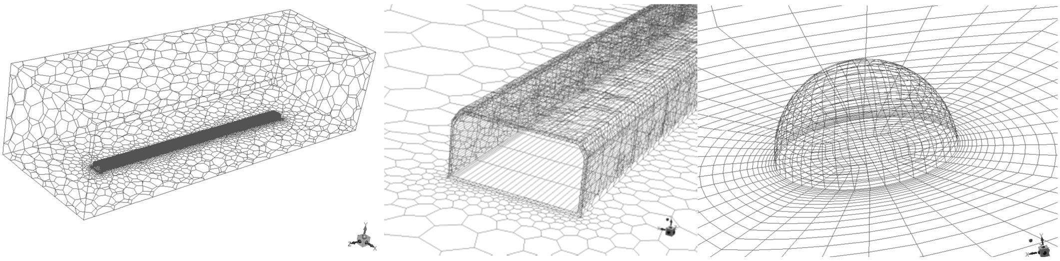

Fig. 3. Mesh of the entire domain (left), cut out of the tunnel exit (middle) and hydrogen hemispherical tank (right).

The quality of the mesh was measured and assured in Fluent by the maximum orthogonal quality and aspect ratio and the minimum orthogonal skewness. The quality ranges from 0 to 1, where values close to 0 correspond to low quality in the case of the minimum orthogonal quality and reversed for the case of the maximum orthogonal skewness. A value of 0.4 and 0.7 were obtained respectively for each ran case with a corresponding maximum aspect of 28.4. The bottleneck for improved mesh arose from the coarseness of the large CVs at the boundary outside the tunnel, whereby the ambient conditions does not require a sophisticated mesh. Nonetheless, these quality values were all above the recommended quality threshold given by Fluent.

INITIAL CONDITIONS

Atmospheric pressure i.e. 101325 Pa, and air i.e. 23% O_2 and 77% N_2 with quiescent conditions, $ui=uj=uk=0$, was set for the entire domain as initial conditions. It is to be noted that for simplification, the part of the gasses with minor concentration, H_2, CH_4, CO_2, were discounted and given to the concentration of oxygen explaining its higher value originally being 20.1% [22]. To adhere to the notion that the increase of internal pressure in hydrogen prior to ignition due to the tank's engulfment in a bonfire, the near vicinity of the tank was set to envisage only combustion products. The circumference of the patch around the tank had a width double the radius of the tank, and diameter of the tank as the added height of the tank, the patch contains mass fraction 0.1 of H_2O and 0.9 of N_2.

The tank was then set to contain only H_2 with a pressure of 94.5 MPa and a temperature of 395 K. This was to reflect the conditions of the tank measured right before it catastrophic ruptured in the earlier mentioned experiment [17]. Reproducing the tank rupturing in the simulations was done by setting the tank wall condition as interior, with the volume thereby modelled directly as an instantaneous release of high-pressure hydrogen. The properties of the different size of tanks simulated are listed in Table 2, covering tank sizes currently available for hydrogen-powered vehicles.

Table 2. Parameters of hydrogen tanks used in rupture simulation in all three different tunnels

Volume, L	Real gas tank volume, L	Hemisphere diameter, m	Mass, kg
10	14.5	0.25	0.58
30	43.1	0.45	1.73
60	86.0	0.61	3.45
120	173.5	0.77	6.96

Inside the tunnel, the walls were set to being stationary, impermeable and opaque with diffuse fraction equal to 1 with no-slip conditions omitting any wall roughness. Thermal heat flux was set with a concrete density of 2300 kg/m^3, with a wall temperature equal to that of the atmospheric conditions of 280 K. Outside the tunnel, non-reflective properties were applied to ensure any parameter such as energy, mass, momentum etc. not influence the properties inside the tunnel in any way.

CFL CONVERGENCE

To enforce numerical stability and accurate description of the resolved scales of motion, the time advancement scheme is a meticulous choice to make. The Courant-Friedrichs-Lewy (CFL) number was applied, defined as: $CFL = U\Delta t/\Delta x$, where Δt is the time step, Δx is the cell size and U is the flow velocity. In compressible flows, the flow velocity is often replaced with the highest velocity of acoustic waves, $|U| + c$ in each cell to make it more applicable. This is useful in terms of limiting the time step, as the isolated convective flow velocity might not be sufficient to capture all the prevailing acoustic wave-speeds. By using a constant CFL number, it in turn reflects not only the time step that would best optimize the solution on a particular grid at particular time step, it also provides an indication of the complexity of a problem, type of flow and model chosen to carry out simulations.

A user defined function (UDF) first developed in house was used to superimpose the CFL number during transient simulations. There was no definite way of predicting the upper bound CFL number, and therefore conducted by trial and error until the convergence is obtained between different CFL numbers. A way of authenticating the applied CFL number is done by conducting a sensitivity test, reducing the value until convergence in the results is found ensuring CFL number independence. As seen in Fig. 4, $CFL \leq 0.2$ was found to give convergence in burned hydrogen, with a corresponding numerical “loss” in hydrogen mass of close to 0%. Onwards, all simulations were carried out with $CFL = 0.2$.

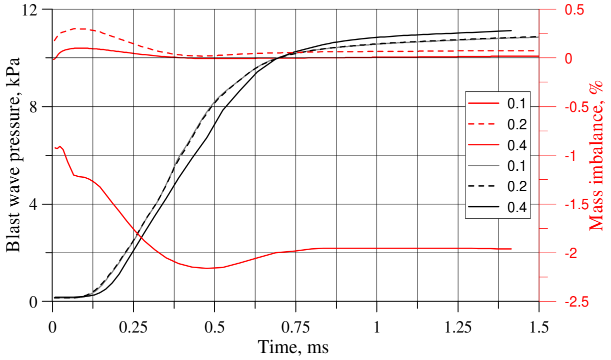

Fig. 4. Percentage of hydrogen burned mass (black curves) and imbalance (red curves) for various CFL numbers as a function of time.

MESH SENSITIVITY

The balance between a fine enough mesh to capture calculations of minor turbulent and diffusive mechanism, but still coarse enough to ensure a practical computational time is always tricky to get just right. The former more crucial, this would ensure that results obtained are not mesh dependent, removing that accuracy-bias from results obtained. A sensitivity test was carried out using two meshes; one coarse with a total control volume number of 176 K, and the other with 486 K denoted as fine mesh. The fine mesh was created by subdividing the cells widths in every direction, which resulted in 8 times (2x2x2) more cells for three-dimensional cells. It is to be noted that the mesh outside the tunnel was kept the same during the mesh sensitivity test. Modelling both meshes gave close convergence in the peak pressure during early stages of simulation when the pressure is most abrupt, with slight under prediction for the coarse grid as can be seen in Fig. 5. The measurements were obtained from 25 cm above the ground where the pressure is maximum, and within 5 CVs which forms the shock front in CFD. Since the case itself is already conservative and things like energy loss on car deformation, cratering, presence of obstacles etc. not taken into account, the coarse grid is therefore utilized in all simulations in order to retain an effective computational time.

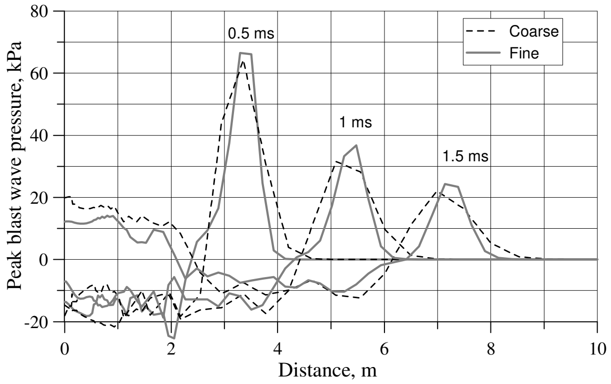

Fig. 5. Blast wave pressure along the tunnel for coarse (black dashed) and fine (grey solid) mesh, measured at a height 0.25 m above the ground at 0.5, 1, and 1.5 ms after tank rupture.

RESULTS AND DISSCUSSION

The results of simulations presented in Fig. 6, where maximum overpressure along the tunnel is plotted as a function of the distance. Also depicted are three horizontal lines representing the three hazard distances thresholds i.e. “no-harm” (green, 1.34 kPa), “injury” (orange, 16.5 kPa) and “fatality” (purple, 100 kPa) [23]. These harm criteria for people thresholds are for each case described as temporal loss of hearing, 1% eardrum rupture probability and 1% fatality probability respectively. The “injury” threshold separates slight and serious injury, such as eardrum rupture and lung haemorrhage as direct effects due to blast wave.

Observed up to 40 m for all tunnels is the dominant oscillating nature of pressure dynamics due to the series of blast reflections. From here onwards, the general trend of all the curves are very similar, the level difference in overpressure originating of the different cross-section areas and mass of hydrogen initially stored in the tank. As this quasi-steady pressure front is established, the pressure attenuation rate is significantly reduced with more than half the pressure retained until the tunnel exit for nearly all cases. In the far field (i.e. after 40 m), all cases of tunnel area and mass combinations fall below the “fatality” zone threshold into the “injury” zone. However, most cases with tank mass above 0.58 kg regardless of the tunnel cross-section are above “injury” threshold during the whole length of the tunnel. The average time blast wave took to reach the exit was 0.45 s.

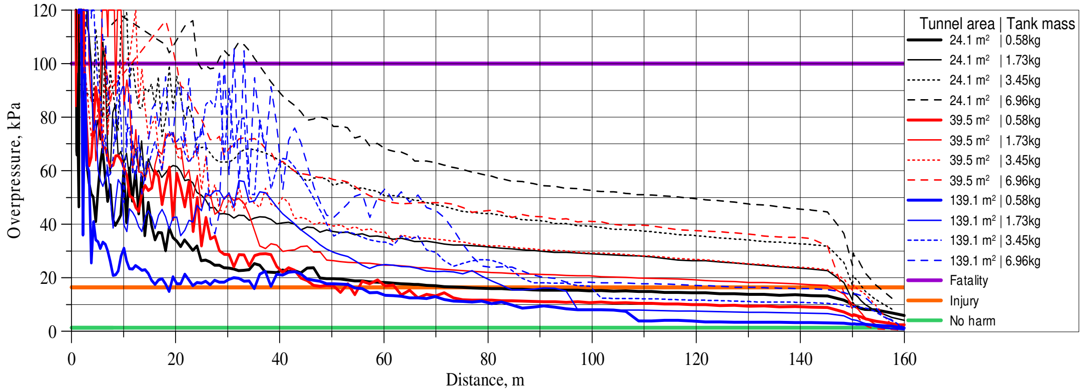

Fig. 6. Maximum blast wave pressure as a function of distance from centre of the tank for different tank sizes and tunnel cross-sections.

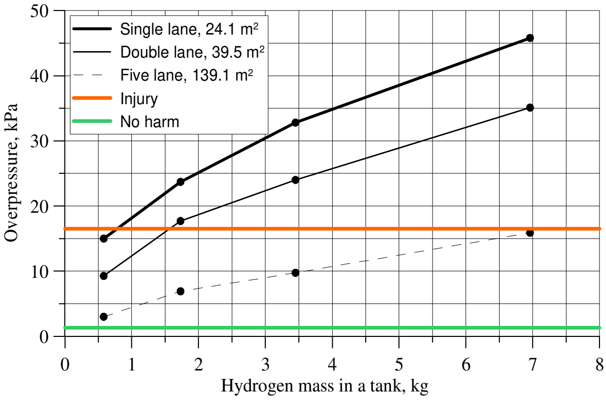

Fig. 7. Maximum blast wave pressure recorded at 140 m from the tank as a function of tank mass for three tunnel cross-sections.

Figure 7 shows dependence of the maximum blast overpressure recorded at 140 m i.e. 10 m before the tunnel exit for all three tunnels and various tank inventories. Symbols represent the exact tank inventory for each simulation. Connecting lines give approximate estimation of the overpressure for certain tunnel cross-sections with different amounts of hydrogen inventory. For the singe-lane tunnel hydrogen inventory above 0.75 kg would create overpressure above "injury" limit. For the two-lane tunnel, this minimum inventory mass value is doubled to around 1.6 kg. For the five-lane tunnel, all cases are below the "injury" limit up until 7 kg of hydrogen inventory, the enlarged confinement of the tunnel facilitating a more pronounced pressure decay. The "no-harm" limit is however not obtained at 140 m in any tunnel for hydrogen mass inventories down to 0.58 kg. All cases are well below the "fatality" threshold of 100 kPa.

CONCLUSIONS

The CFD model for simulation of blast wave and fireball created by high-pressure hydrogen tank rupture in a fire is developed and validated against bonfire test with tank rupture in open atmosphere. The validated model is further applied to simulate blast wave generated in a tunnel, analysing its propagation in such a confined space. Within a 150 m tunnel, results allow graphical estimation of the overpressure at any distance for cross sections ranging between 24-139 m^2 and inventory mass of hydrogen from 0.58-6.96 kg at pressure before burst of 94.5 MPa, the worst-case scenario of tank pressure before rupture.

The consequences analysis based on the comparison of harm criteria with pressure generated at distances from the tank rupture along the tunnel has shown that there is no "no-harm" zone. People in the tunnel would encounter fatality in the near field or injury in the far field by the generated blast, an unacceptable consequence. It is worth mentioning that blast damping effects either wise dedicated to propulsion of tank wall and other fragments (i.e. vehicle) are not accounted for in this study.

This is a preliminary study of mainly academic interest rather than a source of safety guidelines for storage tank and hydrogen-powered vehicle developers. However, more research should be done in order exclude injuries and/or fatalities and develop innovative safety technologies to exclude tank rupture in a fire at all. One of such technologies called leak-no-burst is currently under development at Ulster.

ACKNOWLEDGEMENTS

The authors are grateful to EPSRC for funding through SUPERGEN H2FC Hub (extension) project (EP/P024807/1).

This project has received funding from the Fuel Cells and Hydrogen 2 Joint Undertaking under grant agreement No (736648). This Joint Undertaking receives support from the European Union's Horizon 2020 research and innovation programme, Hydrogen Europe and Hydrogen Europe research.

REFERENCES

[1] H. T. Hwang, A. Varma, Hydrogen Storage for Fuel Cell Vehicles, Current Opinion Chem. Eng. 5, Suppl. C (2014) 42–48.

[2] S. Kumar *et al.*, HyTunnel Project to Investigate the Use of Hydrogen Vehicles in Road Tunnels, In: International Conference on Hydrogen Safety, 241, Ajaccio, 2009.

[3] M. Dadashzadeh, S. Kashkarov, D. Makarov, V. Molkov, Risk assessment methodology for onboard hydrogen storage, Int. J. Hydrogen Energy 43 (2018) 6462–6475.

[4] A. M. Benselama, M. J.-P. William-Louis, F. Monnoyer, C. Proust, A Numerical Study of the Evolution of the Blast Wave Shape in Tunnels, J. Hazard. Mater. 181 (2010) 609–616.

[5] V. Molkov, F. Verbecke, D. Makarov, LES of Hydrogen-Air Deflagrations in a 78.5 m Tunnel, Combust. Sci. Technol. 180 (2008) 796–808.

[6] S. W. Jorgensen, Hydrogen Storage Tanks for Vehicles: Recent Progress and Current Status, Current Opinion Solid State Mater. Sci. 15(2) (2011) 39–43.

[7] W. J. Taylor, Blast Wave Behavior in Confined Regions, Annals of the New York Academy of Sciences, 152 (1968) 339–356.

[8] B. W. Skews and W. R. Law, The Propagation of Shock Waves in a Complex Tunnel System, J. of South Africa Inst. Min. Metallurgy 91(4) (1991) 137–144.

[9] D. Uystepruyst and F. Monnoyer, A Numerical Study of the Evolution of the Blast Wave Shape in Rectangular Tunnels, J. Loss Prevent. Process Ind. 34 Suppl. C (2015) 225–231.

[10] W. E. Baker, P. A. Cox, P. S. Westine, J. J. Kulesz, and R. A. Strehlow, Explosion Hazards and Evaluation, Elsevier Scientific Publishing Company, 1983.

[11] R. Zalosh , N. Weyandt, Hydrogen Fuel Tank Fire Exposure Burst Test, SAE Paper, vol. 2005-01–1886, (2005).

[12] W. Kim, V. Shentsov, D. Makarov, V. Molkov, High Pressure Hydrogen Tank Rupture: Blast Wave and Fireball, Intentional Conference on Hydrogen Safety, Yokohama, Japan, 2015, Vol. 243.

[13] N. Weyandt, Analysis of Induced Catastrophic Failure of a 5000 psig Type IV Hydrogen Cylinder, Southwest Research Institute Report for the Motor Vehicle Fire Research Institute, 01.06939.01.001, 2005.

[14] V. Molkov and S. Kashkarov, Blast Wave From a High-Pressure Gas Tank Rupture in a Fire: Stand-Alone and Under-Vehicle Hydrogen Tanks, Int. J. Hydrogen Energy 40 (2015) 12581–12603.

[15] V. Shentsov, D. Makarov, and V. Molkov, Blast Wave After Hydrogen Storage Tank Rupture in a Tunnel Fire, International Symposium on Tunnel Safety and Security 2018, Borås, Sweden, 2018.

[16] S. Mannan, Lees' Loss Prevention in the Process Industries, 3rd ed., vol. 1. Elsevier Butterworth-Heinemann, 2005.

[17] Y. Tamura, M. Takahashi, Y. Maeda, H. Mitsuishi, J. Suzuki, S. Watanabe, Fire Exposure Burst Test of 70MPa Automobile High-pressure Hydrogen Cylinders, Society of Automotive Engineers of Japan Annual Autum Congress, 2006.

[18] B. Maidl, M. Thewes, U. Maidl, General Principles for the Design of the Cross-Section, Handbook of Tunnel Engineering *II*, D-69451 Weinheim, Germany: Wiley-VCH Verlag GmbH, pp. 1–20, 2014.

[19] M. Vickers, Northern California Coastal Bridges: Picturesque and Distinctive Spans, Marquis Publishing, 2017.

[20] W. Brilon and F. Weiser, Two-Lane Rural Highways: The German Experience, Transportation Research Record, J. Transport. Res. Board, 1988, (2006) 38–47.

[21] Norwegian Public Roads Administration, Road Tunnels, Statens vegvesen, 21, 2004.

[22] ANSYS FLUENT 12.0 User's Guide, Available: http://users.ugent.be/~mvbelleg/flug-12-0.pdf, 2009 (accessed: 30 September 2018).

[23] S. Kashkarov, Z. Y. Li, V. Molkov, Hazard Distance Nomograms for a Blast Wave From a Compressed Hydrogen Tank Rupture in a Fire, International Conference on Hydrogen Safety, Hamburg, 2017, Vol. 126.

Influence of Chemical Kinetics on Detonation Initiation by Temperature Gradients in H_2/air and CH_4/air Explosions

Wang C.[1, *], **Qian C.**[1], **Liu J.**[1], **Liberman M.**[2, *]

[1] *State Key Laboratory of Explosion Science and Technology, Beijing Institute of Technology, Beijing, China*
[2] *Nordic Institute for Theoretical Physics, Stockholm University, Stockholm, Sweden*
**Corresponding author emails: mliber@nordita.org; wangbit666@163.com*

ABSTRACT

Understanding the mechanisms of explosions is essential for the development of safety measured and for minimizing devastating hazards. Due to the complexity of real chemistry, a one-step reaction model has been often used for theoretical and numerical studies. In this paper we compare conditions for the detonation development from the spontaneous wave in a hot spot for a one-step model with that obtained for detailed chemical models. It is shown that for detailed chemical models conditions required for the detonation development from the spontaneous wave in a hot spot are more limited than that for the use of simplified chemical models. In particular, the minimum hot spot size capable of producing a detonation calculated with the detailed chemical model is at least an order of magnitude larger than that predicted by a one-step model even at high initial pressures. The impact of a detailed chemical model is particularly pronounced for the methane/air mixture, where not only is the hot spot size much greater than that predicted by a one-step model, but the initiation of detonation by the hot spot with a temperature gradient is possible only if the ambient temperature outside the gradient is above 1100 K.

KEYWORDS: detailed chemistry, spontaneous wave, detonation, explosion.

INTRODUCTION

Understanding the causes and mechanisms of explosions is essential for the development of safety measured and for minimizing devastating hazards in many industrial processes, such as coal mines, natural gas pipelines, hydrogen energy, nuclear, chemical and other industries [1-3]. Much experimental, theoretical and numerical work has been undertaken in an attempt to identify mechanism of the flame acceleration and the deflagration-to-detonation transition (DDT) [1, 4, 5]. Until recently a common approach to study DDT has been to use simulations based on a one-step chemical model [4, 5, 6] because complexity of real chemical kinetics. It was argued that the accelerating flame creates conditions in nearby unreacted material that ignite involving the Zel'dovich gradient mechanism and spontaneous reaction wave, and this is the mechanism of DDT. However, it was shown experimentally [7, 8] that for hydrogen/oxygen and ethylene-air mixtures the temperature in the vicinity of the flame prior to DDT does not exceed 550 K, which is too low for spontaneous ignition. Experimental studies and numerical simulations of DDT [8, 9, 10, 11] based on detailed chemical models for H_2/O_2 and H_2/air have shown that the DDT mechanism is different from the gradient mechanism. In this paper we consider the conditions for which the hot spots where the spontaneous reaction wave can undergo a transition to detonation through the Zel'dovich gradient mechanism for a one-step and for detailed chemical models in highly reactive H_2/air and in slow reactive CH_4/air. This may probably help in future (if this is possible in principle)

Proceedings of the Ninth International Seminar on Fire and Explosion Hazards (ISFEH9), pp. 1324-1334
Edited by Snegirev A., Liu N.A., Tamanini F., Bradley D., Molkov V., and Chaumeix N.
Published by Saint-Petersburg Polytechnic University Press
ISBN: 978-5-7422-6498-9 DOI: 10.18720/spbpu/2/k19-5

to try to optimize simplified models (e.g. ignition delay time as a parameter) to make them more reliable for simulations DDT.

INDUCTION TIMES: ONE-STEP AND DETAILED CHEMICAL MODELS

For H_2/air we consider the one-step Arrhenius model used in [12] for 2D simulations of the hydrogen/air flame acceleration and DDT in channel with obstacles.

$$W = A\rho Y \exp\left(-E_a/RT\right), \tag{1}$$

where all the parameters, the pre-exponential factor $A = 6.86 \cdot 10^{12}$ cm^3/(g·s), the gas density and the unburned mass fraction, ρ and Y, the activation energy of the reaction, $E_a = 46.37\,RT_0$, $\gamma = 1.17$ is the ratio of specific heats, etc. are the same as in [12]. The detailed mechanism for hydrogen/air chemistry is the mechanism developed by Kéromnès et al. [13], which consists of 19 reactions and 9 species. This mechanism was extensively validated over a large number of experimental conditions, especially focused on high pressures and it shows an excellent agreement between the modeling and experimental measurements.

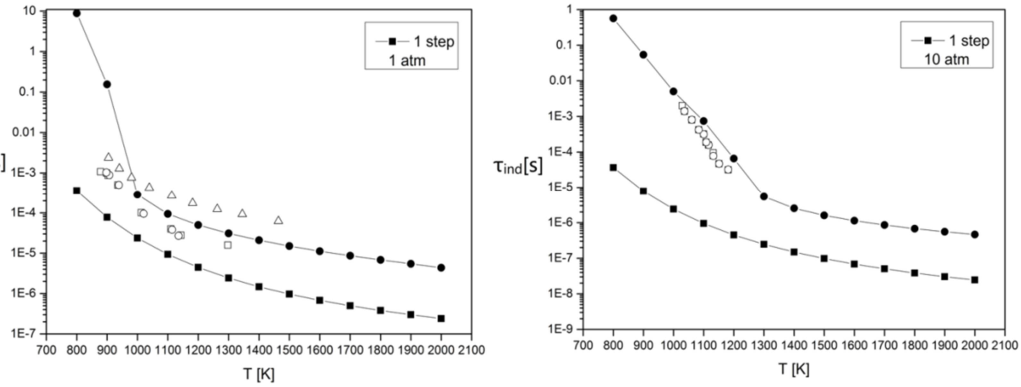

(a) (b)

Fig. 1. Induction times for H_2/air calculated for the one-step and detailed models. (a) 1atm; (b) 10 atm. Empty symbols are experimental measurements. (a) □ – [15]; ○ – [16]; Δ – [17]; (b) □ – [15], ○ – [18].

The one-step model for methane/air involves the same Eq.(1) used by Kessler et al. [6] for 2D simulations of the methane/air flame acceleration and DDT in a channel with obstacles. The same parameters as in [6] were used: $E_a = 67.55\,RT_0$, $A = 1.64 \cdot 10^{13}$ cm^3/(g·s), $\gamma = 1.197$, etc. The detailed model for CH_4/air is the detailed reaction mechanism DRM-19 developed by Kazakov and Frenklach [14], which consists of 19 species and 84 reactions. The DRM-19 mechanism was extensively validated by many researchers for combustion characteristics related to ignition delay times and laminar flame velocities over a wide range of pressures, temperatures, and equivalence ratios.

The ignition delay times were calculated for different chemical reaction schemes using the standard constant volume adiabatic model. The ignition delay time can be defined as the time during which the maximum rate of temperature rise, $\max\left(dT/dt\right)$, is achieved, which is close to the time of the exothermic reactions activation. Figures 1 (a, b) show the induction times for H_2/air versus temperature computed using the one-step model [12] and the detailed chemical model [13] at initial pressures $P_0 = 1$ atm and 10 atm. Open symbols indicate experimental measurements.

Figures 2 (a, b) show the induction times for methane/air at 1atm and 10atm computed for the one-step model [6], GRI 3.0 Mech, the detailed chemical model DRM-19 [14] and the experimental measurements (open symbols).

It is seen that the induction times predicted by the detailed chemical model are in a good agreement with the experimental results, but differ by up to three orders of magnitude from that predicted by the one-step model for H_2/air. Another feature of the "real" induction time is an abrupt change of $d\tau_{ind}/dT$ at the crossover temperatures, which correspond to the transition from the endothermal induction stage to the exothermal stage. The difference between the induction time given by the one-step model and the induction time calculated with the detailed chemical models for methane/air is about 10 times larger than it is for hydrogen/air.

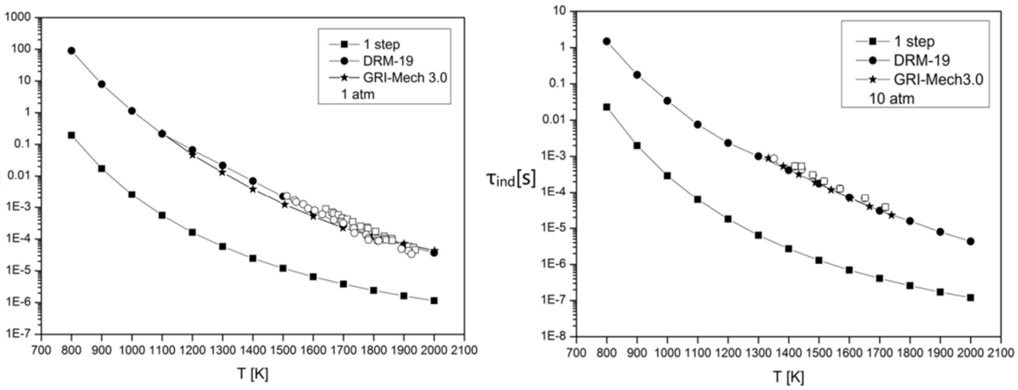

(a) (b)

Fig. 2. Induction times for CH_4/air calculated for the one-step and detailed models. (a) 1 atm; (b) 10 atm. Experiments: ○ – [19], □ – [20].

THE GRADIENT MECHANISM; SPONTANEOUS WAVES

We will use the conventional term a "hot spot", which is an area within a reactive mixture, where the temperature is higher than in the surrounding mixture. The scale of the temperature gradient in the hot spot $L = T/(dT/dx)$ is considered as the size of the hot spot.

The Zeldovich gradient mechanism

The ignition of a flammable mixtures is one of the most important and fundamental problems in combustion physics. In practical cases ignition begins in a small area of combustible mixture, which is locally heated by means of an electric spark, hot wire, and such like. Such local energy release results in the formation of an initially nonuniform distribution of temperature (or reactivity), which depending on the mixture reactivity and the initial pressure determines the evolution of the reaction wave. One needs to know how the initial conditions in such "hot spots" influence the regime of the reaction wave, which is ignited and propagates out from the ignition location. The question of how a hot spot can give rise to different combustion modes remained open until the Zel'dovich's concept [21] of the spontaneous reaction wave propagating along a spatial gradient of reactivity opened an avenue to study ignition of different regimes of the reaction wave that is initiated by the initial non-uniformity in temperature or reactivity caused by the local energy release [22]. In a region with nonuniform distribution of temperature the reaction begins at the point of minimum ignition delay time $\tau_{ind}(T(x)$ and, correspondingly, the maximum temperature, and then it spreads along the temperature gradient by spontaneous autoignition at neighboring locations where τ_{ind} is longer. In the case of a one-step chemical model the induction time is defined by the time-scale of the maximum reaction rate. For a detailed chemistry this is the time scale of the stage when endothermic chain initiation completed and branching reactions begin. In the case of a one dimensional problem the spontaneous autoignition wave propagates relative to the unburned mixture in the direction of temperature gradient with the velocity:

$$U_{sp} = \left|\left(d\tau_{ind} / dx\right)\right|^{-1} = \left|\left(\partial\tau_{ind} / \partial T\right)^{-1} \left(\partial T / \partial x\right)^{-1}\right|, \tag{1}$$

Since there is no causal link between successive autoignitions, there is no restriction on the value of U_{sp}, which depends only on the steepness of temperature gradient and $\partial\tau_{ind} / \partial T$. It is obvious, that a very steep gradient (hot wall) ignites a flame, while a zero gradient corresponds to thermal explosion, which occurs within the induction time. The velocity of the spontaneous wave initiated by the temperature gradient decreases while the autoignition wave propagates along the gradient, and reaches the minimum value at the point close to the cross-over temperature [23], where it can be caught-up and coupled with the pressure wave, which was generated behind the high-speed spontaneous wave front due to the chemical energy release. As a result, the pressure peak is formed at the reaction front, which grows at the expense of energy released in the reaction. After the intersection of the spontaneous wave front and the pressure wave, the spontaneous wave transforms into a combustion wave and the pressure wave steepens into the shock wave. After the pressure peak becomes large enough, it steepens into a shock wave, forming an overdriven detonation wave. Classification of combustion regimes initiated by a temperature gradient has been studied in [21] for a one-step model, and for detailed chemical kinetics of hydrogen-oxygen and hydrogen-air in [23].

SPONTANEOUS WAVES AND TRIGGERING DETONATIONS

Problem setup

We consider uniform initial conditions apart from a linear temperature gradient within a hot spot. The model of the linear temperature gradient is convenient for analysis and it has been widely used in many previous studies. The initial conditions at $t = 0$, prior to ignition are constant pressure and zero velocity of the unburned mixture. At the left boundary $x = 0$ the conditions are for a solid reflecting wall, where $u(x,0) = 0$ and the initial temperature, $T = T^*$ exceeds the ignition threshold value. Thus, the initial conditions are quiescent and uniform, except for a linear gradient in temperature (and hence density):

$$T(x,0) = T^* - (T^* - T_0)(x / L)\,,\ 0 \le x \le L\,, \tag{2}$$

$$P(x,0) = P_0,\ u(x,0) = 0 \tag{3}$$

The temperature gradient is characterized by the temperature $T(0,0) = T^*$ at $x = 0$, by the mixture temperature outside the hot spot, $T(x \ge L, 0) = T_0$ and by the gradient steepness, $(T^* - T_0) / L$. The "length" L, which characterizes the gradient steepness can be viewed as the size of the hot spot, at which the initial temperature gradient was formed.

The 1D direct numerical simulations are performed to solve the set of the one-dimensional time-dependent, fully compressible reactive Navier-Stokes equations and chemical kinetics. The equations of state for the reactive mixture and for the combustion products were taken with the temperature dependence of the specific heats and enthalpies of each species borrowed from the JANAF tables (Joint Army Navy NASA Air Force Thermochemical Tables) and interpolated by the fifth-order polynomials. In the case of a one-step model the ideal gas equation of state was used. The viscosity and thermal conductivity coefficients of the mixture were calculated from the gas kinetic theory using the Lennard-Jones potential. Coefficients of the heat conduction of i-th species $\kappa_i = \mu_i c_{pi} / \mathrm{Pr}$ are expressed via the viscosity μ_i and the Prandtl number, $\mathrm{Pr} = 0.75$. Simulations of the time evolution of spontaneous wave and the detonation initiation were performed using fifth order conservative finite difference scheme (WENO). Thorough resolution (up to 5 μm) and convergence tests were performed to ensure that the resolution is adequate to capture details of the problem and to avoid computational artifacts. Because of limited space, we refer readers to Refs. [24, 25] for fuller details of the hydrodynamic solver and resolution tests.

Detonation initiation by temperature gradient in H_2/air

Figures 3(a, b) show the time evolution of a spontaneous wave and the detonation initiation by the steepest temperature gradient in H_2/air (the minimum hot spot size) at the initial P_0 = 1 atm computed for a one-step (3a) detailed (3b) models.

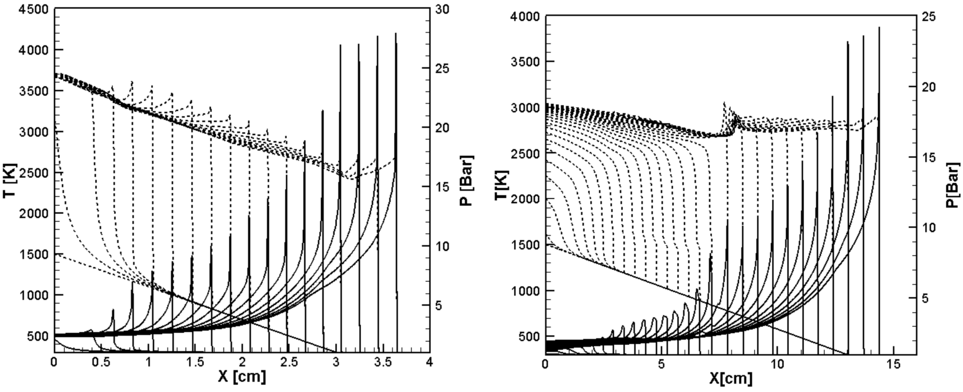

(a) (b)

Fig. 3. Time evolution of the temperature (dashed lines) and pressure (solid lines) profiles during detonation initiation in H_2/air, at P_0 = 1 atm. (a) one-step model [11]; (b) detailed model [13].

The velocity at which the spontaneous reaction wave decreases, starts below the upper point of the gradient. If the gradient is sufficiently shallow, such that the minimum speed of the spontaneous wave is close to the sound speed $a_s(T_{cr}^*)$ at this point, the spontaneous reaction wave can couple with the pressure pulse produced by the energy released in the reaction. As a result, a pressure peak will grow at the expense of the energy released in the reaction. After the pressure peak has become large enough, it steepens into a shock wave, forming an overdriven detonation wave. For a steeper temperature gradient (larger size of the hot spot) the velocity of the spontaneous wave at the minimum point is not sufficient to sustain synchronous feedback amplification between the reaction and the pressure pulse. In this case, the pressure waves run ahead of the reaction wave, out of the gradient, and the result will be a deflagration, or fast deflagration, with weak shocks running away ahead of the flame.

The velocity of the spontaneous wave reaches its minimum value at the point close to the crossover temperature T_{cr}^*, which corresponds to the transition from the endothermal induction to the exothermal stage. Therefore, the necessary condition for initiating detonation by the spontaneous reaction wave is that the spontaneous wave initiated by the initial temperature gradient can be caught up and coupled with the pressure wave generated behind the high-speed spontaneous wave:

$$U_{sp}\left(T_{cr}^{*}\right)=\left(\frac{\partial\tau}{\partial T}\left(T_{cr}^{*}\right)\right)^{-1}\left(\frac{\partial T}{\partial x}\left(T_{cr}^{*}\right)\right)^{-1}=\left(\frac{\partial\tau}{\partial T}\left(T_{cr}^{*}\right)\right)^{-1}\frac{L}{T^{*}-T_{0}}\geq a_{s}\left(T_{cr}^{*}\right), \tag{4}$$

where T_{cr}^{*} at the point corresponding to $\min\{U_{sp}\}$ is slightly above the crossover temperature T_{cr}. Using this condition we can estimate the minimum size of the hot spot for the successful triggering detonation. Figures 4 (a, b) show velocities of spontaneous wave at the point $\min\{U_{sp}\}$ as a function of the hot spot size L calculated for the one-step (Fig. 4 a) and detailed (Fig. 4 b) models at P_0 = 1, 5, and 10 atm. At high pressures, when triple collisions dominate, the crossover temperature corresponding to the equilibrium of the induction and termination stages shifts to higher temperatures. Therefore, the minimum steepness of gradients for detonation initiation increases, but the corresponding minimum size of the hot spot ($L=L_{cr}$) required for triggering the detonation predicted by the one-step model remains much smaller than that predicted by detailed model.

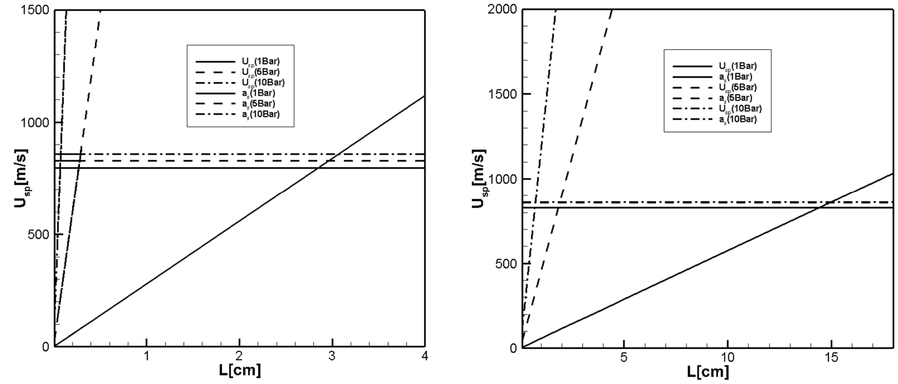

(a) (b)

Fig. 4. $L=L_{cr}$ for H$_2$/air at P_0 = 1, 5, 10atm. (a): detailed model, T_{cr}^{*} (1 atm) = 1300 K, T_{cr}^{*} (5 atm) = 1400 K, T_{cr}^{*} (10 atm) = 1410 K. (b): one-step model T_{cr}^{*} (1 atm) = 1200 K, T_{cr}^{*} (5 atm) = 1300 K, T_{cr}^{*} (10 atm) = 1400 K.

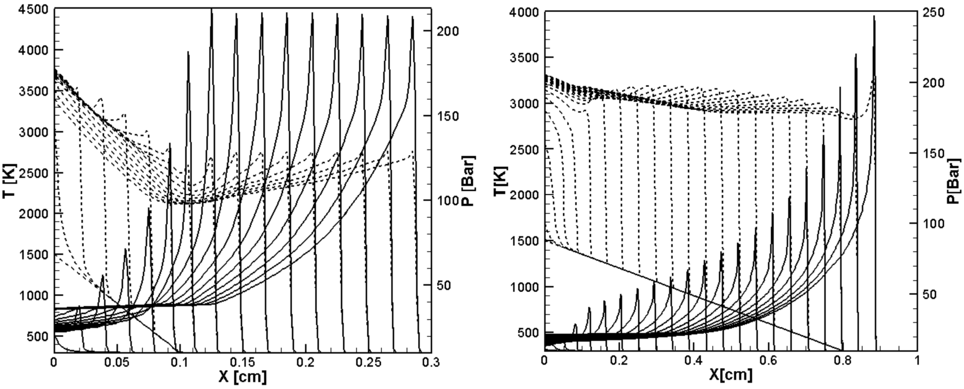

(a) (b)

Fig. 5. Time evolution of the temperature (dashed lines) and pressure (solid lines) profiles during detonation initiation in H$_2$/air at P_0 = 10 atm. (a) one-step model; (b) detailed model.

Figures 5 (a, b) show the time evolution of temperature and pressure profiles during the initiation of detonation in H_2/air computed for one-step and detailed models at initial pressures 10 atm.

The hot spot sizes L_{cr} , at which the temperature gradient can produce a steady detonation for the one-step and for detailed models differ because of large difference in $\partial\tau_{ind}/\partial T$ for these models, which determines the speed of the spontaneous wave. The ratio of critical sizes of for detailed and one-step models is defined by large difference in $\partial\tau_{ind}/\partial T$ for the models

$$L_{cr_{det}} / L_{cr_{1-step}} \approx \left(\partial\tau_{ind}/\partial T\right)_{det} / \left(\partial\tau_{ind}/\partial T\right)_{1-step} . \qquad (5)$$

Detonation initiation by temperature gradient in CH4/air

The induction times for methane/air are much longer for all temperatures compared to the hydrogen/air mixture. Therefore, the spontaneous wave velocity in methane/air is smaller for the same temperature gradients. Since the values of sound speeds and the Chapman-Jouguet velocities for H_2/air and CH_4/air are fairly close, one can expect that the minimum size of the hot spot, which can produce detonation in CH_4/air, will be about ten times greater than it is for H_2/air. Fig. 6 (a) shows the minimum size of the hot spot, which can produce detonation for the one-step model, but simulations with the detailed chemistry (Fig. 6 (b)) show that only a deflagration can be produced even for the hot spots, which was checked in simulations up to x > 50 cm..

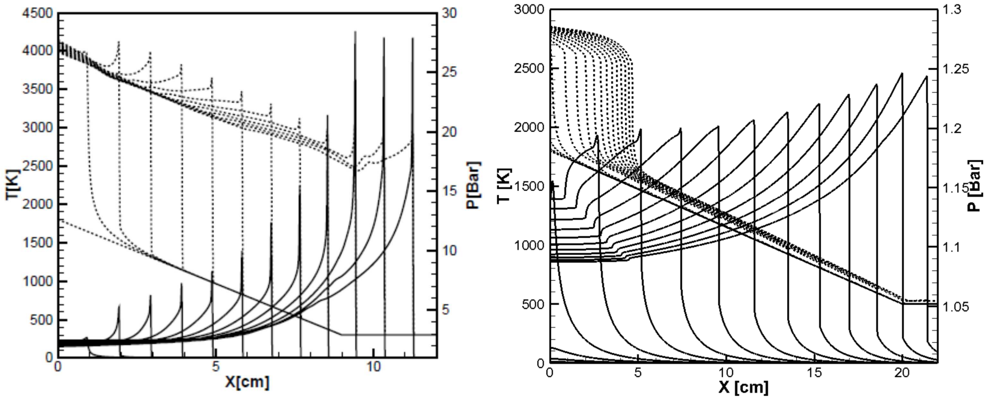

(a) (b)

Fig. 6. Time evolution of the temperature (dashed lines) and pressure (solid lines) profiles for CH_4/air (P_0 = 1 atm, T_0 = 300 K, T^* = 1800 K). (a) one-step model [6]; (b) detailed model [14].

As the initial pressure increases, the induction time decreases, and the spontaneous wave speed increases rapidly. Therefore, at high pressures the minimum size of the hot spot capable of triggering detonation decreases. The minimum hot spot size, which can trigger detonation in CH_4/air at P_0 = 10 atm, T^* = 1800 K, T_0 =300 K, according to Eq. (4) could be L = 12 cm for the detailed DRM19 model. But in contrast to the scenario in Fig. 7 (a) calculated for the one-step model, the developing detonation in Fig.7 (b) quenches at x = 10 cm, even for a shallower temperature gradient, L = 20 cm. The reactive wave starts to move slowly away from the leading shock wave. The rarefaction wave propagates into the reaction zone and the separation between the heat release zone and the leading shock increases. As a result, the shock weakens and the detonation quenches. The phenomenon of spontaneous quenching of the developing detonation has been studied by He and Clavin [26, 27], who also pointed out that, for the same temperature gradient, for which a detonation is quenching, a steady detonation can be ignited for a higher temperature T_0 outside the hot spot.

It was found that at the initial pressure 10 atm a steady detonation can be produced by the temperature gradient only if ambient temperature T_0 = 1100 K. Fig. 8 shows the evolution of temperature and pressure profiles during the development of a steady CJ-detonation from the temperature gradient L = 6 cm, T_0 = 1100 K. In a sense, high temperature outside the gradient is equivalent, but not completely, to a shallower gradient. The induction stage, which is distinctive for real chemical reactions can be "skipped" at sufficiently high ambient temperatures. The reaction front propagates at smoother ambient density, so that hydrodynamic resistance at the end and outside the gradient is smaller and the transition to detonation may occur for a steeper gradient [23].

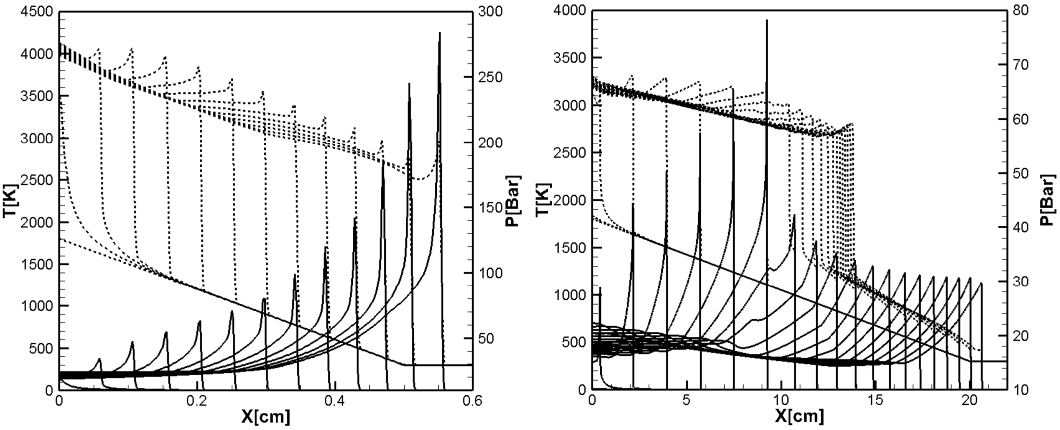

(a) (b)

Fig. 7. Evolution of the temperature (dashed lines) and pressure (solid lines) profiles; P_0 = 10 atm, T_0 = 300 K, T^* = 1800 K. CH$_4$/air: (a) one-step model [6]; (b) detailed model [14].

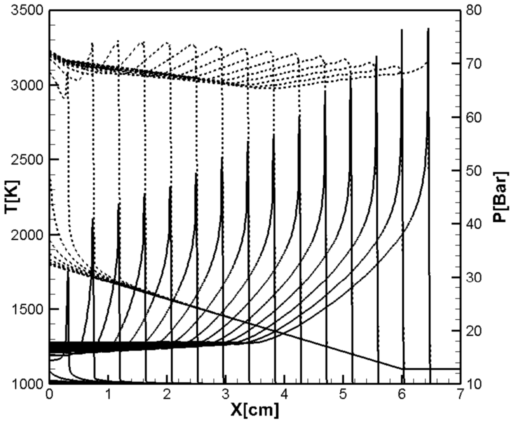

Fig. 8. Time evolution of the temperature (dashed lines) and pressure (solid lines) profiles during development of a steady detonation in CH$_4$/air for DRM19 model.

To verify the validity of the temperature of detonation, obtained in simulations we use the conservation laws. The value of reaction energy (q) obtained from conservation of energy for deflagration: $C_{p2}T_b = C_{p1}T_1 + q$. Using this value of q and conservation of mass, momentum and energy, we obtain formulas for velocity and temperature of CJ detonation: $C_{v2}T_{CJ} = u_{CJ}^2 / \gamma_2(\gamma_2 - 1)$,

$$u_{CJ} = \left\{ \frac{\gamma_2 - 1}{2} \left((\gamma_2 + 1)q + (\gamma_1 + \gamma_2) C_{v1} T_1 \right) \right\}^{1/2} + \frac{\gamma_2 - 1}{\gamma_2 + 1} \left\{ \frac{\gamma_2 + 1}{2} \left((\gamma_2 - 1)q + (\gamma_1 - \gamma_2) C_{v1} T_1 \right) \right\}^{1/2} .$$

It should be noted that the temperature of detonation for a one-step model in Figs. 6 (a) and 7 (a), $T_{CJ} \approx 2820$ K is slightly above $T_{CJ} \approx 2700$ K for H_2/air. Since a steady detonation can be triggered by the temperature gradient only at high ambient temperatures (T_0 = 1100 K), the temperature of detonation shown in Fig. 8 calculated for detailed chemical model is $T_{CJ} \approx 3300$ K, in agreement with theoretical formulas for T_{CJ}.

CONCLUSIONS

The purpose of this study is to look more deeply into the influence of chemistry on the detonation initiation by a spontaneous wave developed by a temperature gradient for the highly reactive and low reactive mixtures. Although significant insights have been obtained through many experimental, theoretical and numerical studies, an identification of the basic mechanisms controlling deflagration-to-detonation transition remains one of the major challenges of combustion physics. Since interpretation of the multidimensional simulations, which used a one-step model, suggested that in most of the cases a spontaneous wave produced by the temperature gradient initiates detonation, it is important to know the real conditions when it is possible, and can be viewed as the mechanism of DDT. The results of high resolution simulations performed for one-step models were compared with simulations for detailed chemical models. The calculated values of induction times for H_2/air and for CH_4/air were validated against experimental measurements for a wide range of temperatures and pressures. It was found that the requirements, in terms of temperature and size of the hot spots, which produce a spontaneous wave, which in turn can initiate the detonation, are quantitatively and qualitatively different for one-step models compared to the detailed chemical models. The induction time and its temperature derivative of the induction time, which determines the speed of the spontaneous wave, are by orders of magnitude smaller for the one-step models, in comparison with the real values calculated for the detailed models and measured in experiments. As a consequence, for the one-step models the hot spots are much smaller and the temperature gradients initiating a detonation are much steeper than those calculated using detailed chemical models. The difference between the one-step and the detailed chemical model is more pronounced for low reactive CH4/air mixture. In this case, even at a high pressure of 10 atm, the minimum size of the hot spot, for which the spontaneous wave can initiate detonation, exceeds 6 cm and a steady detonation can be produced only for high ambient temperatures outside the hot spot exceeding 1100 K. Such a temperature can trigger a thermal explosion and is unlikely to be achieved during the flame acceleration prior to DDT. One of the conclusions is that the gradient mechanism of DDT, which was previously proposed on the basis of two-dimensional simulations using a one-step model, is unlikely at least in the case of methane/air. The results presented here may be used to improve the calibration of the simplified chemical-diffusive approach developed by Kaplan et al. [28], see also [6]. However, according to Fomin et al. [29] it seems to be impossible to calibrate simplified models so that they give a correct ignition delay times and even, more or less, correct burning velocities. The authors [29] used a 2-step model calibrated to reproduce induction times according to that measured in experiments, and they obtained excellent results for the cellular structure of detonation. But such a calibrated model does not describe correctly deflagration. For modelling DDT an accurate modelling of burning velocities and ignition delay times are required to predict correct run-up distances and mechanism of DDT. Therefore, an accurate modelling of burning velocities and ignition delay times are an absolute requirement.

REFERENCES

[1] S. Kundu, J. Zanganeh, B. Moghtaderi, A review on understanding explosions from methane–air mixture, J. Loss Prevent. Process Ind. 40 (2016) 507-23.

[2] G.Atkinson, E. Cowpe, J. Halliday, D. Painter. A review of very large vapour cloud explosions: Cloud formation and explosion severity. J. Loss Prevent. Process Ind. 48 (2017) 367-375.

[3] H.J. Pasman, Challenges to improve confidence level of risk assessment of hydrogen technologies. Int. J. Hydrogen Energy 36 (2011) 2407–2413.

[4] E. S. Oran, V. N. Gamezo, Origins of the deflagration-to-detonation transition in gas-phase combustion, Combust. Flame 148 (2007) 4–47.

[5] G. Ciccarelli, S. Dorofeev, Flame acceleration and transition to detonation in ducts, Prog. Energy Combust. Sci. 34 (2008) 499–550.

[6] D.A. Kessler, V.N. Gamezo, E.S. Oran, Simulations of flame acceleration and deflagration-to-detonation transitions in methane–air systems, Combust. Flame 157 (2010) 2063–2077.

[7] M. Kuznetsov, M. Liberman, I. Matsukov, Experimental study of the preheat zone formation and deflagration to detonation transition, Combust. Sci. Technol. 182 (2010) 1628–1644.

[8] M. Liberman, M. Ivanov, A. Kiverin, M. Kuznetsov, A. Chukalovsky, T. Rakhimova, Deflagration-to-detonation transition in highly reactive combustible mixtures, Acta Astronaut. 67 (2010) 688–701.

[9] M. Ivanov, A. Kiverin, M. Liberman, Flame acceleration and DDT of hydrogen-oxygen gaseous mixtures in channels with no-slip walls, Int. J. Hydrogen Energy 36 (2011) 7714–7727.

[10] M.F. Ivanov, A.D. Kiverin, M.A. Liberman, Hydrogen-oxygen flame acceleration and transition to detonation in channels with no-slip walls for a detailed chemical reaction model, Phys. Rev. E 83 (2011) 056313.

[11] O. Dounia O. Vermorel, A. Misdariis, T. Poinsot, Influence of kinetics on DDT simulations, Combust. Flame 200 (2019) 1-14.

[12] V.N. Gamezo, T. Ogawa, E.S. Oran, Flame acceleration and DDT in channels with obstacles: Effect of obstacle spacing, Combust. Flame 155 (2008) 302–315.

[13] A. Kéromnès, W.K. Metcalfe, K.A. Heufer, N. Donohoe, A.K. Das, C.-J. Sung, J. Herzler, C. Naumann, P. Griebel, O. Mathieu, M.C. Krejci, E.L. Petersen, W.J. Pitz, H.J. Curran, Combust. Flame 160 (2013) 995–1011.

[14] A. Kazakov, M. Frenklach, Reduced Reaction Sets based on GRI–Mech 1.2: 19–species reaction set; http://www.me.berkeley.edu/drm/

[15] A.D. Snyder, J. Robertson, D.L. Zanders, G.B. Skinner, Technical Report AFAPL-TR-65-93(1965).

[16] M. Slack, A. Grillo, Investigation of hydrogen-air ignition sensitized by nitric oxide and by nitrogen dioxide, Tech. Rep. RE-537, Grumman Research Department (1977).

[17] E. Hu, L. Pan, Z. Gao, Shock tube study on ignition delay of hydrogen and evaluation of various kinetic models, Int. J. Hydrogen Energy 41 (2016) 13261-13280.

[18] L. Pan, E. Hu, F. Deng, Z. Zhang, Z. Huang, Effect of pressure and equivalence ratio on the ignition characteristics of dimethyl ether-hydrogen mixtures, Int. J. Hydrogen Energy 39 (2014) 19212–19223.

[19] W. Zeng, H. Ma, Y. Liang, E. Hu, Experimental and modeling study on effects of N2 and CO2 on ignition characteristics of methane/air mixture. J. Advanced Research 6 (2015) 189-201.

[20] E. Hu, X. Li, X. Meng, Y. Chen, Y. Cheng, Y. Xie, Z. Huang, Laminar flame speeds and ignition delay times of methane–air mixtures at elevated temperatures and pressures, Fuel 158 (2015) 1-10.

[21] Ya.B. Zel'dovich, Regime classification of an exothermic reaction with nonuniform initial conditions, Combust. Flame 39 (1980) 211-214.

[22] A.D. Kiverin, D.R. Kassoy, M.F. Ivanov and M.A. Liberman, Mechanisms of Ignition by Transient Energy Deposition: Regimes of Combustion Waves Propagation, Phys. Rev. E87 (2013) 033015.

[23] M.A. Liberman, A.D. Kiverin, M.F. Ivanov, Regimes of chemical reaction waves initiated by nonuniform initial conditions for detailed chemical reaction models, Phys. Rev. E 85 (2012) 056312.

[24] C.Wang, C. Qian, J. Liu, and M. A. Liberman, Influence of chemical kinetics on detonation initiating by temperature gradients in methane/air, Combustion and Flame 197 (2018) 400–415.

[25] M. Liberman, C.Wang, C. Qian, J. Liu, Influence of chemical kinetics on spontaneous waves and detonation initiation in highly reactive and low reactive mixtures, Combust. Theor. Modelling, (2018) https://doi.org/10.1080/13647830.2018.1551578.

[26] L. He and P. Clavin, Critical conditions for detonation initiation in cold gaseous mixtures by nonuniform hot pockets of reactive gases, Proc. Combust. Inst. 24 (1992) 1861-1867.

[27] L. He and P. Clavin, Theoretical and numerical analysis of the photochemical initiation of detonations in Hydrogen-Oxygen mixtures, Proc. Combust. Inst. 25 (1994) 45–51.

[28] R.C.Kaplan, Alp. Özgen, E.S. Oran, Chemical-diffusive models for flame acceleration and transition-to-detonation: genetic algorithm and optimisation procedure, Combust. Theor. Modelling, (2018) https://doi.org/10.1080/13647830.2018.1481228.

[29] P.A. Fomin, A.V. Trotsyuk, A.A. Vasil’ev, Approximate Model of Chemical Reaction Kinetics for Detonation Processes in Mixture of CH4 with Air, Combust. Sci. Techn. 186 (2014) 1716–1735.

Analysis of the Interaction between Jet and Plume Flows of a Light Gas with an Extended Ceiling Based on the Results of Experimental Studies

Denisenko V.P.[1], Kirillov I.A.[1], Korobtsev S.V.[1], Nikolaev I.I.[1],*, Bystrov P.A.[2]

[1] *NRC "Kurchatov Institute", Russian Federation*
[2] *IPCE RAS, Russian Federation*
**Corresponding author's email:* hitcliff68@mail.ru

ABSTRACT

The study is devoted to the generalization of the experimental results obtained by means of investigation of the quantitative characteristics of the modeled flammable hydrogen-air cloud which can occur in case of emergency leaks of hydrogen in underground or multi-story parking lots of hydrogen transport. Data are presented on 28 runs of light helium gas (hydrogen substitute) during its vertical propagation and interaction with an extended ceiling in case of two main types of outflow - jet and plume. The analysis of the experimental data by varying the parameters of helium release revealed different types of asymptotic decline of helium concentration in the under-ceiling layer along the radius of spreading, as well as different behavior of the under-ceiling layer thickness. The consequence of this difference was that, in the case of plume outflow, much larger volumes of the simulated fire-hazardous mixture were observed in the under-ceiling layer than in case of jet outflows. Some qualitative analytical explanation of the observed phenomena was proposed, that could be used to establish quantitative theoretical dependencies useful for development of the engineering guidelines on safety of the semi-confined and confined parking areas for hydrogen-fueled vehicles.

KEYWORDS: Hydrogen leak, plume and jet flow, flammable volume, under-ceiling layer.

INTRODUCTION

The main features of the distribution of hydrogen-air mixtures in confined spaces (ventilated and unventilated rooms of nuclear power plants, individual garages or repair shops) where the vertical and horizontal dimensions of the premises are commensurate with each other have been intensively studied recently [1-6]. Specific features and engineering relations for the case of formation of flammable hydrogen-air volumes in non-ventilated, semi-confined spaces are currently in the stage of preliminary studies. A typical example of a semi-confined space is the underground parking of vehicles using light combustible gas (hydrogen, methane), where the ceiling height is much less than the width and length of the parking hall.

This experimental study is devoted to the modeling of vertical leakage of light gas-helium (as hydrogen surrogate) under conditions simulating the outflow of hydrogen under an extended ceiling. A detailed study of the main features of the interaction of light floating gas with the horizontal surface of the ceiling in a semi–confined room in two main modes of vertical outflow - jet and plume - was carried out using a specially developed multipoint system for measuring helium concentrations in real time.

Proceedings of the Ninth International Seminar on Fire and Explosion Hazards (ISFEH9), pp. 1335-1347
Edited by Snegirev A., Liu N.A., Tamanini F., Bradley D., Molkov V., and Chaumeix N.
Published by Saint-Petersburg Polytechnic University Press
ISBN: 978-5-7422-6498-9 DOI: 10.18720/spbpu/2/k19-116

EXPERIMENTS

Description of the diagnostic system

The data acquisition system from sensors of helium concentration is a matrix of sensor boards connected in a line with a serial interface. The sensor boards are composed of a microprocessor module based on the Atmega48 microcontroller, through which they communicate with a personal computer by the standard digital serial interface RS485 on one or two parallel twisted pair wires with a wave resistance of 120 Ohms. The interface baud-rate was selected as 57600. The information from the whole matrix of sensors was updated every 0.5 s. The communication protocol was MODBUS or special. The sensing element in the sensors is a gas thermal conductivity detector of TCG-3880 type pre-calibrated for helium individually for each sensor. The long-term calibration accuracy is 0.1 volume percent. This diagnostic system is described in more detail in [7].

Description of the experimental setup

The basis of the experimental setup was a rectangular frame made of metal beams, in the upper part of which a suspended ceiling of thick polyethylene membrane was stretched. The suspended ceiling had a height of 2.07 m and was placed in a wide closed room with ceiling height of 3 m. The length and width of the frame was 4.04 m. Helium was released vertically upwards in the exact center of the installation. After contacting the suspended ceiling, the flow spreads radially from the release axis forming an under-ceiling layer. After reaching the edges of the suspended ceiling, helium flowed up to the ceiling of the experimental room.

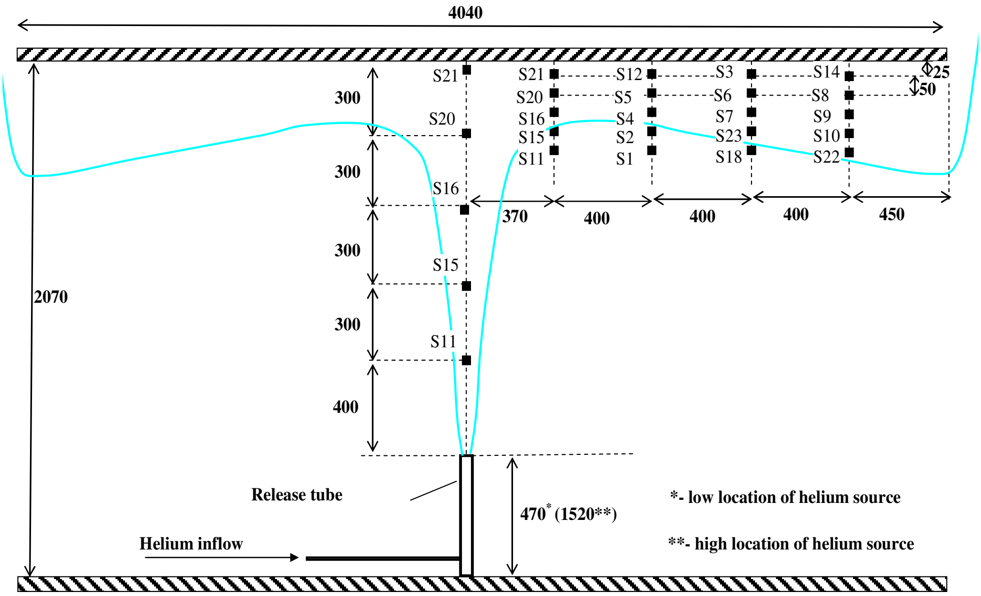

Fig. 1. Location of helium sensors relative to the up-flow axis and suspended ceiling.

The electronic sensor boards were fixed on a wooden plane along one of the spreading radiuses away from the axis and 1.5 m below the suspended ceiling. The helium sensor heads, which have a typical size of about 10 mm, were placed at certain distances from the boards on the shielded cables and fixed on four vertical threaded studs with a diameter of 8 mm by means of pairs of nuts with clamps moving along the studs. The scheme of their locations relative to the axis of the helium flow and the suspended ceiling is shown in Fig. 1 with the coordinates of all sensors. All dimensions are in millimeters. Sensors № 11, 15, 16, 20, 21 were used twice. Once in the general scheme when all sensor heads were located away from the axis. For the second time they were used to measure helium concentrations on the axis of the up-flow.

The difference between the jet and plume regimes of subsonic gas up-flow is the difference between the initial conditions of the gas release. If the initial momentum of the up-flow is large enough, then for the description of dynamics of a light gas one can neglect its buoyancy within some distance from the release point. However, it is clear that any vertical jet of light gas upon reaching some distance from the release point due to the action of buoyancy forces acquires an additional momentum which eventually surpasses the initial one, and the jet passes into the plume where the influence of the initial impulse is, as it were, forgotten. The length at which this occurs is called the plume formation distance. It is calculated for hydrogen by the formula [2, 8, 9]:

$$L_j = 0.32 v_0 \sqrt{D_0}\ , \tag{1}$$

In this formula D_0 is the initial diameter of the outflow, v_0 is the initial velocity of the outflow. For helium the numerical coefficient in this formula changes to 0.33. If the distance from the release point to the ceiling $H >> L_j$, the up-flow is plume type. If, on the contrary, the considered distances $H << L_j$, then the up-flow is jet type.

For realization of two main regimes of flowing – jet and plume – two different output pipes for vertical helium release were used. Both of them had a height of 470 mm, but the nozzle for jet flow was a narrow steel tube with inner diameter of 8 mm, and the nozzle for plume flow was a wide plastic pipe with an inner diameter of 98 mm. In the second case a metal mesh sponge was laid inside the wide pipe to equalize the gas flow in the cross section, and a disk of highly porous sponge metal was installed in the output section. The flowrates of helium in the experiments were from 5 to 16 l/s (i.e., from 0.89 to 2.85 g/s), and so the plume formation distance for jet modes were lying in the range 3 - 9 m, i.e., obviously greater than the height of the suspended ceiling, while for plume modes, in the range of 0.07 - 0.22 m, that is, certainly less than this height. These flowrates were chosen also to generate concentrations under the ceiling that would be reliably measurable with good accuracy and in accordance with the adopted level of hydrogen risk of the order of 4% and above. In eight experiments the injection pipes were lifted so that their outlets were at a height of 1520 mm above the floor to change the aspect ratio.

Experiments

Table 1 shows all the experimental runs carried out indicating the conditions of their realization and according to the sequence numbers.

The first two experiments were trials. All other experiments can be divided into two groups – experiments under the ceiling and experiments with the free up-flow of helium with the dismantled suspended ceiling and five sensors on the release axis – as shown in Fig. 1. The latter group includes four of the tests, №. 25-28. These experiments are connected with the two tests under the suspended ceiling, № 7 and 8, which also involved five sensors on the axis. These experiments were carried out to understand the effect of the ceiling on the change in helium concentration along the flow axis.

The main experiments under the ceiling differ in the type of up-flow (plume, jet), flowrate (5 and 16 l/s) and the height of the release point above the floor (470 and 1520 mm). All experiments with the same parameters were repeated two or three times.

RESULTS

The main experimental results are drawn out from the measurements of helium concentration dependencies in the periphery of the up-flow at distances from 25 to 225 mm from the suspended ceiling surface and from 370 to 1570 mm from the release axis. However, in tests №. 7, 8 and 25-28, measurements were made of the concentrations on the release axis by means of the five sensors placed 300 mm apart from each other (see Fig. 1). In these experiments the free up-flow was compared with the up-flow under the ceiling.

Table 1. Description of all experimental tests

№ test	Type of release	Release diameter, mm	Helium flowrate, l/s	Height of helium source, mm	Comment
3	jet	8	16	470	no sensors on axis
4	plume	98	16	470	no sensors on axis
5	plume	98	16	470	no sensors on axis
6	plume	98	16	470	no sensors on axis
7	jet	8	16	470	5 sensors on axis
8	plume	98	16	470	5 sensors on axis
9	plume	98	5	470	1 sensor on axis in top point
10	plume	98	5	1520	1 sensor on axis in top point
11	plume	98	5	1520	1 sensor on axis in top point
12	plume	98	16	1520	1 sensor on axis in top point
13	plume	98	16	1520	1 sensor on axis in top point
14	jet	8	5	1520	1 sensor on axis in top point
15	jet	8	5	1520	1 sensor on axis in top point
16	jet	8	16	1520	1 sensor on axis in top point
17	jet	8	16	1520	1 sensor on axis in top point
18	jet	8	5	470	1 sensor on axis in top point
19	jet	8	5	470	1 sensor on axis in top point
20	jet	8	16	470	1 sensor on axis in top point
21	jet	8	16	470	1 sensor on axis in top point
22	plume	98	5	470	1 sensor on axis in top point
23	plume	98	5	470	1 sensor on axis in top point
24	plume	98	16	470	1 sensor on axis in top point
25	plume	98	16	470	without ceiling, 5 sensors on axis
26	jet	8	16	470	without ceiling, 5 sensors on axis
27	jet	8	5	470	without ceiling, 5 sensors on axis
28	plume	98	5	470	without ceiling, 5 sensors on axis

In each experiment the reducer on the gas cylinder was used to set a constant flowrate on the calibrated differential pressure gauge which was maintained for 25-30 seconds. At this time there was an automatic recording of the readings of all sensors with the help of the described above digital data collection system directly to a personal computer, where the data for each experiment were stored as a file.

On the basis of these stationary readings, two main experimental values were calculated – the thickness of the under-ceiling layer and the decay in the under-ceiling concentration along the radius from the release axis. The thickness of the under-ceiling layer was calculated on each of the four vertical sensor lines, which were 370, 770, 1170, and 1570 mm away from the flow axis (see

Fig. 1). The sensors on each of these vertical lines were spaced from the ceiling by 25, 75, 125, 175, and 225 mm. The concentration values at these points of the experimental dependences can be approximated by the Gauss curve $A\exp\left(-z^2/h^2\right)$ by regression method with two parameters for the smallest sum of squared deviations. In this case z characterizes the distance from the ceiling, A is the first regression parameter characterizing the maximum value of the concentration directly under the ceiling, while h can be interpreted as the characteristic thickness of the under-ceiling layer of helium spreading along the ceiling at a given radius from the release axis of the up-flow. This is a calculated value and it will be used further as an estimate of the characteristic thickness of the under-ceiling layer.

In Fig. 2 the data from five near-ceiling sensors collected in the experiments, № 3, 12, 14, 16 and 21, are shown including sensor № 21 directly on the release axis. According to these data, an average value was calculated for the signal of each sensor at the time of reaching the stationary readings by all sensors.

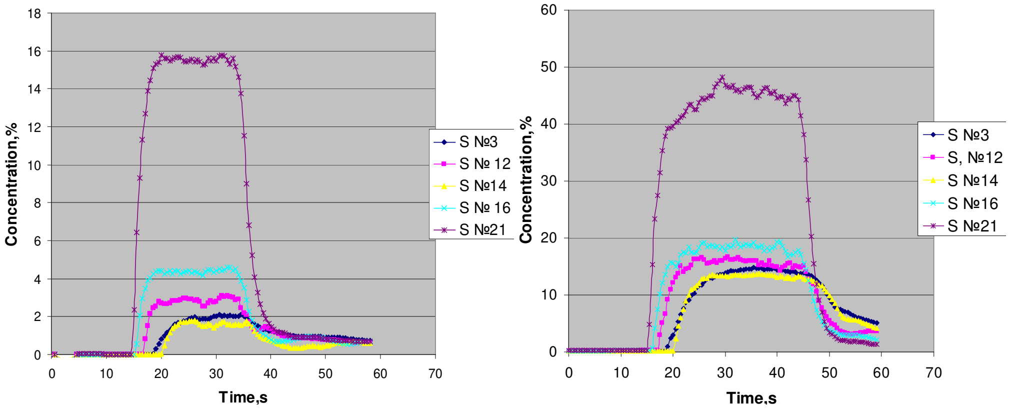

(a) (b)

Fig. 2. Concentration versus time on the near-ceiling sensors № 21, 16, 12, 3, and 14: (a) – experiment №16, jet; (b) – experiment №12, plume.

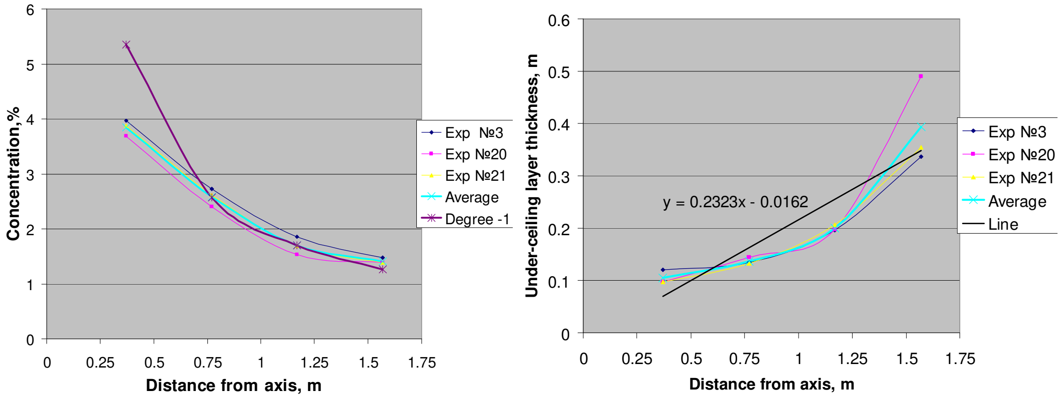

(a) (b)

Fig. 3. Experimental dependences of under-ceiling concentration and layer thickness at the distance r from the flow axis. Jet regime, helium flowrate 16 l/s, release point is 470 mm above the floor. (a) – Concentration decline ~ r^{-1}; (b) – Linear approximation of the layer thickness growth has a slope of 0.2323.

In Fig. 3 the specified dependences of the decrease in the under-ceiling concentration and the thickness of the under-ceiling layer for the experiments in the jet regime at helium flowrate of 16 l/s and the height of the release point above the floor of 470 mm are presented. The results of three similar experiments of № 3, 20 and 21 are presented as well as the average value. For all the experiments with the same parameters, the average value at each point was determined and a corresponding average curve was constructed.

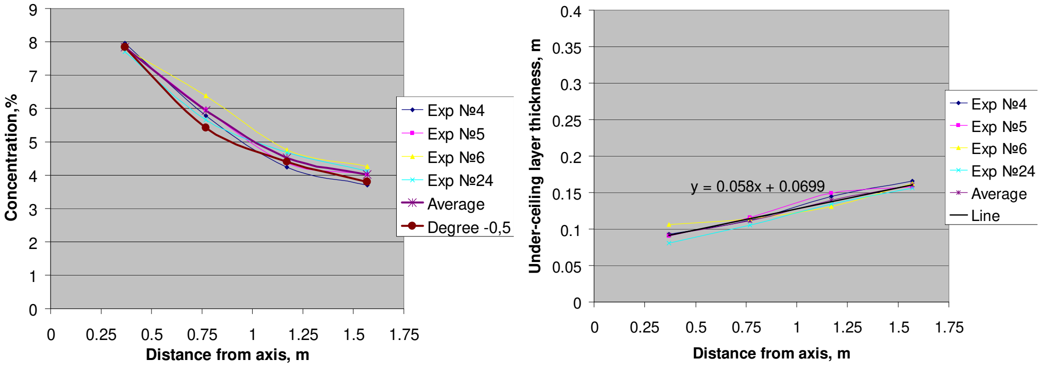

(a) (b)

Fig. 4. Experimental dependences of under-ceiling concentration and layer thickness at the distance r from the flow axis. Plume regime, helium flowrate 16 l/s, release point is 470 mm above the floor. (a) – Concentration decline ~ $r^{-0.5}$; (b) – Linear approximation of the layer thickness growth has a slope of 0.058.

For the approximation of the decrease rate of the under-ceiling concentration with distance from the release axis the power-law dependences of the type $r^{-\alpha}$ were chosen, where r is the distance from the release axis. This approximation was made for average values of the dependences obtained in three similar experiments. In this case, the approximation was carried out in such a way that the concentration values in it and in the experiment at a distance of 770 mm from the flow axis coincide. From Fig. 3a one can see that, for the given parameters of the experiment, the last three most remote points from the flow axis, which characterize the decline of the concentration on the radius r, fit very well to the dependence r^{-1}.

The thickness of the under-ceiling layer grows quite rapidly with distance from the release axis. If it is approximated by a linear approximation, the slope coefficient is quite large and is equal to 0.2323 (Fig. 3b).

Figure 4 shows the dependences of the under-ceiling concentration and layer thickness on the distance from the release axis for the same flowrate of 16 1 / s and the same height of the release point as in Fig. 3, but for the plume regime. The decline in the near-ceiling concentration on the upper sensors is significantly slower than in Fig. 3 and is well approximated by the dependence $r^{-0.5}$. The thickness of the layer also grows significantly slower than in the jet regime with the same flowrate.

In Fig. 5, data similar to those in Fig. 4 for the jet regime with the height of the release point above the floor of 470 mm are shown, but for the smaller flowrate of 5 l/s. It can be seen that the rate of decay of the concentration with a decrease in the flowrate slowed to $r^{-0.75}$ and, at the same time, the growth of the layer thickness with distance from the release axis also became slower. It should be noted that a significant (3.2 times) decrease in helium flowrate did not lead to any significant decrease in the concentration on the near-ceiling sensors in comparison with the data in Fig. 3.

In Fig. 6 the dependences of the concentration and under-ceiling layer thickness are depicted for the same flowrate of 5 l/s and the same height of the release point of 470 mm as for Fig. 5, but for the plume regime. The dependencies are almost the same as for the plume data in Fig. 4 with a flowrate of 16 l/s: the same degree $r^{-0.5}$ reflecting the rate of decay of the under-ceiling concentration and almost the same slope angle of the linear approximation. The total concentration level at each point is about two times lower than in Fig. 4 for a flowrate of 16 l/s. Thus, in contrast to the jet regime, a decrease in the volume flowrate at the release point by 3.2 times in case of the plume regime led to a decrease in the near-ceiling concentrations by about a factor of two.

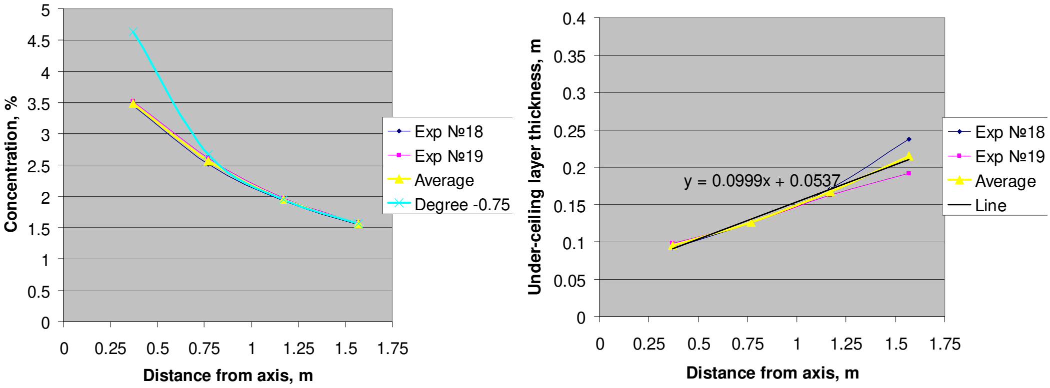

(a) (b)

Fig. 5. Experimental dependences of under-ceiling concentration and layer thickness at the distance r from the flow axis. Jet regime, helium flowrate 5 l/s, release point is 470 mm above the floor. (a) – Concentration decline ~ $r^{-0.75}$; (b) – Linear approximation of the layer thickness growth has a slope of 0.1.

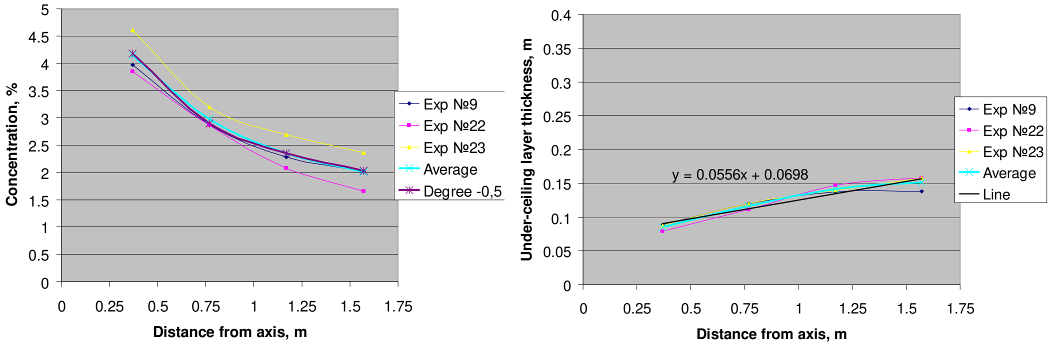

(a) (b)

Fig. 6. Experimental dependences of under-ceiling concentration and layer thickness at the distance r from the flow axis. Plume regime, helium flowrate 5 l/s, release point is 470 mm above the floor. (a) – Concentration decline ~ $r^{-0.5}$; (b) – Linear approximation of the layer thickness growth has a slope of 0.056.

The experiments where the release point was raised to a height of 1520 mm above the floor are presented starting from Fig. 7. This mode is particularly interesting because it increases the aspect ratio of the available length of the ceiling from the edge to the release axis (2 m) with respect to the distance from the ceiling to the release point (0.55 m) up to almost 4.

In Fig. 7 the data on the jet up-flow under the ceiling from the height of 1520 mm above the floor at the flowrate of 16 l/s in two experiments are presented. The difference with the experimental conditions shown in Fig. 3 is only in the height of the release point. As it can be seen from Fig. 7, the raising of the release point introduced no significant difference. There is the same rate of decline in the under-ceiling concentration ~ r^{-1}. The growth rate of the under-ceiling layer thickness is about the same, with a slope coefficient of 0.21. Also, the initial value of the thickness of the under–ceiling layer on the nearest to the axis vertical line of sensors is almost 2 times less – only 0.06 m.

Figure 8 presents the experiments in the plume regime of up-flow with the same experimental conditions shown in Fig. 4 except for raising the release point to 1520 mm above the floor. This mode is characterized by a significant difference in the rate of decline of the near-ceiling concentration – it significantly slows down and its asymptotic is well described by the dependence ~ $r^{-0.25}$.

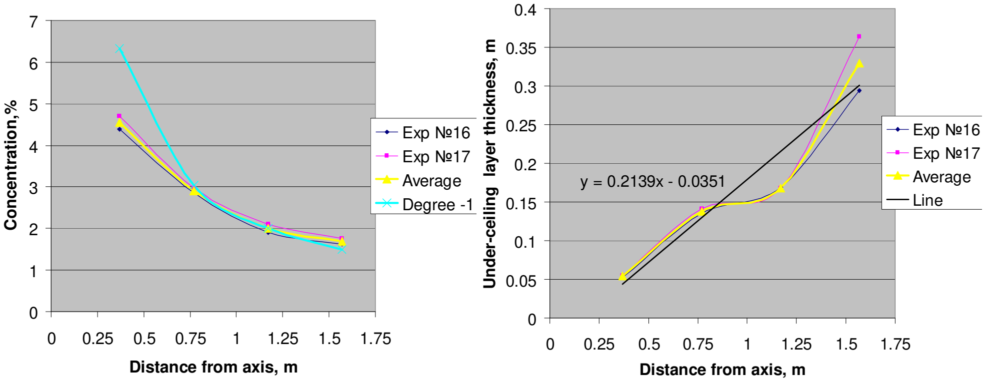

(a) (b)

Fig. 7. Experimental dependences of under-ceiling concentration and layer thickness at the distance r from the flow axis. Jet regime, helium flowrate 16 l/s, release point is 1520 mm above the floor. (a) – Concentration decline ~ r^{-1}; (b) – Linear approximation of the layer thickness growth has a slope of 0.21.

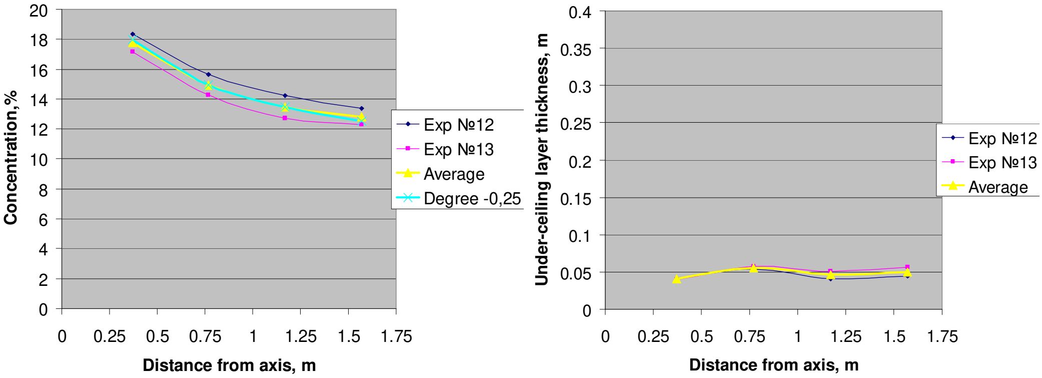

(a) (b)

Fig. 8. Experimental dependences of under-ceiling concentration and layer thickness at the distance r from the flow axis. Plume regime, helium flowrate 16 l/s, release point is 1520 mm above the floor. (a) – Concentration decline ~ $r^{-0.25}$; (b) – Thickness of the layer practically does not increase with distance from release axis.

At the same time this is accompanied by the fact that the thickness of the under-ceiling layer practically ceases to grow with distance from the release axis, its value is 0.05 m at any available radius of the experiments, while at the release from the position of 470 mm above the floor (Fig. 4b) this thickness began to grow with a value of 0.1 m with a slope of 0.058. The total values of the near-ceiling concentrations significantly increase in comparison with Fig. 4. It is obvious that this experimentally detected feature of the plume flow regimes should directly lead to a sharp increase in the volume of the flammable hydrogen-air mixture in the under-ceiling spreading layer in comparison with the jet regime with the same flowrate in Fig. 7.

The experiments, carried out with the sensors on the release axis in case of the suspended ceiling and without it, showed that the concentration at the upper under-ceiling sensor in the plume regime exceeds that in the jet regime with the same flowrate 16 l/s by 2.4 times in case of the ceiling and by 1.9 times in its absence. So, the much slower decrease in the concentration in the plume regime in the under-ceiling layer along the radius from a larger initial concentration leads to the formation of an extended area of flammable volume (where the concentration exceeds 4%) in the form of a flat pancake directly under the ceiling. In the jet regime, with a rapid decline of under-ceiling concentration along the radius from a smaller initial value, the area of flammable concentration occupies an insignificant volume mostly near the release axis.

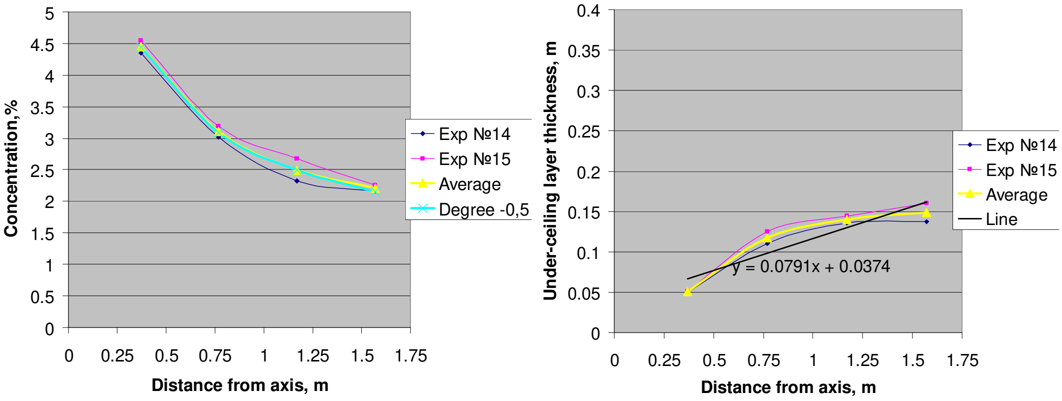

(a) (b)

Fig. 9. Experimental dependences of under-ceiling concentration and layer thickness on the distance r from the flow axis. Jet regime, helium flowrate 5 l/s, release point is 1520 mm above the floor. (a) – Concentration decline ~ $r^{-0.5}$; (b) – Linear approximation of the layer thickness growth has a slope of 0.08.

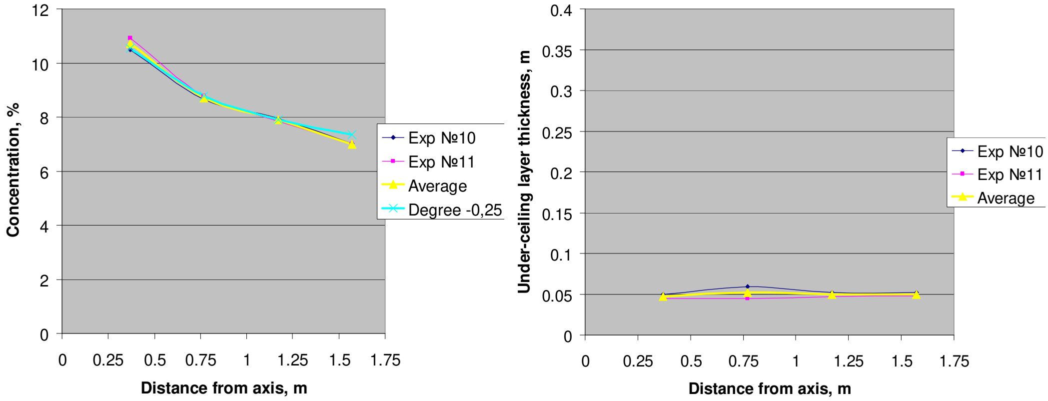

(a) (b)

Fig. 10. Experimental dependences of under-ceiling concentration and layer thickness at the distance r from the flow axis. Plume regime, helium flowrate 5 l/s, release point is 1520 mm above the floor.

(a) – Concentration decline ~ $r^{-0.25}$; (b) – Thickness of the layer practically does not increase with distance from release axis.

In Fig. 9 one can see the dependences of the concentration and the under-ceiling layer thickness on the distance from the release axis in the experiments in the jet regime at helium flowrate of 5 l/s and the height of the release point of 1520 mm above the floor. The decline in the near-ceiling concentration here is the slowest for all the considered jet flow regimes and is characterized by a rate ~ $r^{-0.5}$ – just like for plume regimes with the release point height of 470 mm. Also, the average slope of the linear approximation of the layer thickness growth is sufficiently small.

Figure 10 presents the experiments in the plume regime similar by conditions to those shown in Fig. 8 but with the small flowrate of 5 l/s. The type of dependence has the same remarkable characteristics from the point of view of fire risk as in Fig. 8: slow rate of concentration decline ~ $r^{-0.25}$ and constant thickness of the under-ceiling layer at any distance from the flow axis within the sensor locations. The lower flowrate leads to smaller levels of concentration but did not affect the thickness of the under-ceiling layer which remained equal to 0.05 m.

ANALYSIS

Figure 11 shows the relative boundaries of the jet and plume up-flows at the interaction with the ceiling. The boundaries of the jet and the plume at the vertical up-flow from the corresponding nozzle are constructed on the basis of the standard opening angle of the turbulent jet α, lying in the range 12-14° and determined by the coefficient of turbulent entrainment of ambient air. The relative boundaries of the layer lying under the ceiling in both cases are shown on the assumption of above-described features of the change in the thickness of the under-ceiling layer revealed in the experiments. The main feature of the jet outflow at the high flowrate of 16 l/s is that the angle formed by the boundary of the spreading under-ceiling layer at the interaction with the ceiling and the ceiling plane (angle β in Fig. 11) is sufficiently large and numerically approximately equal to the opening angle of the turbulent jet α ($\tan\beta \approx 0.23$ – see Fig. 3 and 7). In case of the smaller flowrate of 5 l/s, the tangent of the angle β decreases to 0.1, and there is a tendency to slow the growth rate of the thickness of the ceiling layer with distance from the axis (dotted line in Fig. 11) in case of approach to the ceiling of the release point of the jet up-flow.

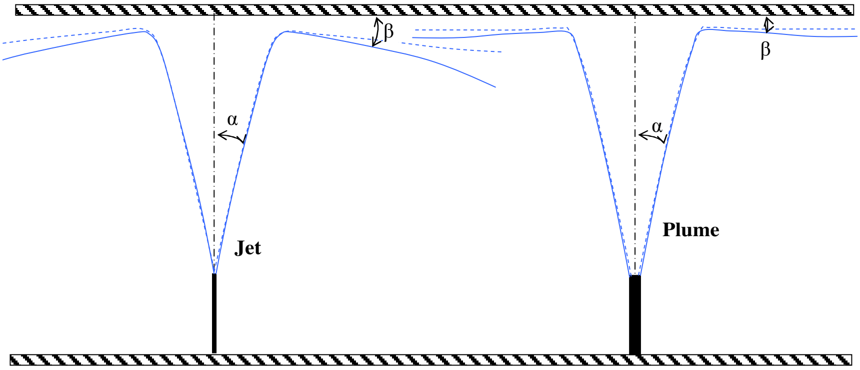

Fig. 11. The characteristic shape of the jet and plume at interaction with the ceiling**.**

In the jet regimes, the under-ceiling concentration falls quite rapidly with distance from the release axis: in case of a large flowrate the asymptotic decline behaves as ~ r^{-1} at any height of the release point, while a reduction in the volumetric flowrate in the jet leads to a slower rate of decline in the under-ceiling concentration from ~ $r^{-0.75}$ (at a lower position of the release point) to ~ $r^{-0.5}$ when approaching the release point to the ceiling. This results in a very small volume of flammable hydrogen-air mixture concentrated mainly near the release axis.

The plume regimes are characterized by a small angle of reflection from the ceiling β at the spreading of the under-ceiling layer in case of a lower position of the release point both at a large and small flowrate (tan β ≈ 0.05-0.06). In this case the approximation of decay in the near-ceiling concentration is fitted well by the slow dependence ~ $r^{-0.5}$. In the case where the release point is moved closer to the ceiling, the plume regimes both with small and large volume flowrates produce a layer under the ceiling whose thickness practically does not change as it moves away from the axis of the plume. In this case, the asymptotic decay in the near-ceiling concentration is well described by a very slow dependence ~ $r^{-0.25}$. This leads to the formation of an extended flat area under the ceiling in the form of a pancake, in which flammable concentrations of hydrogen are present at large distances from the release axis.

There is a clear correlation between the angle of reflection of the gas flow from the ceiling β and the rate of decrease of the near-ceiling concentration along the radius. It looks like a decrease in the rate of decay of the near-ceiling concentration as the angle of reflection β decreases in all regimes - jet and plume.

We can try to apply the conservation equations to the stationary state of gas motion in the under-ceiling layer to analyze the experimental results. To do this, we assume that within its characteristic thickness h the layer moves with the same average velocity v, and outside h there is no movement. The real profile of the volume concentration of light gas in the layer C is also replaced by a rectangular one with the same thickness h. At any radius r remote from the release axis by a sufficient distance for a vertical flow to pass into the creeping under-ceiling layer, the same number of light gas particles must pass through the ring vertical cross-section of the layer with an area of $2\pi rh$ per time unit. This enforces conservation of mass of injected material. Hence, we have the first integral of stationary motion of the buoyant under-ceiling layer:

$$Cvrh = const\ . \tag{2}$$

The second integral can be obtained under the assumption that the friction of the moving layer on the ceiling can be neglected. In the case of its applicability there is a law of conservation of the radial momentum in the layer. Neglecting the slow change in the density of the gas mixture in the layer as it spreads over the radius, we obtain the second integral of motion:

$$rhv^2 = const\ . \tag{3}$$

Combining Eqs. (2) and (3) we get:

$$v(r) = const \cdot C(r)\ , \tag{4}$$

and

$$C^2(r)\, r\, h(r) = const\ . \tag{5}$$

For jet release regimes, as was found above, the growth of the under-ceiling layer thickness is according to the law $h(r) = r\,\mathrm{tg}\beta$ (see Fig. 11). Substituting this expression in Eq. (5) we obtain that the concentration in the layer should fall according to the law $C = const \cdot r^{-1}$, which in general was observed in the experiments for jet regimes of up-flow. Besides, it follows from Eq. (4) that the average radial velocity in the under-ceiling layer is subject to the same dependence. This result is in good agreement with the data of reference [10], where a turbulent radial wall jet formed by an impinging circular jet on a smooth flat plate was investigated. For plume release regimes characterized by a small increase in the thickness of the under-ceiling layer with radius or no such growth, substituting $h = const$ in Eq. (5), we obtain $C = const \cdot r^{-0.5}$, while for plumes with a constant thickness of the under-ceiling layer a slower dependence $C = const \cdot r^{-0.25}$ is observed experimentally. This means that for jet flow regimes characterized by a large initial momentum friction against the ceiling can be neglected at least at some distance from the jet axis (in experiments up to the edge of the suspended ceiling), because the application of conservation of momentum (Eq. (3)) gave a rate of concentration decay in the layer consistent with the experiment. While for plume flow regimes characterized by a low initial momentum it is obvious that the application of Eq. (3) is too strong an assumption, and therefore the friction against the ceiling cannot be neglected.

Thus, while deriving the theoretical dependences of the parameters of the flowing under-ceiling layer at the interaction of a vertical jet and plume with the ceiling, we can now conclude that for jets the friction on the ceiling (at least up to a certain distance from release axis) can be neglected, while for plumes it cannot be. Weak jets (with a small initial flowrate) while interacting with the ceiling behave similar to the plumes with a lower point of release, according to the characteristic dependencies of their under-ceiling layers. This leads to the conclusion that the key parameters characterizing the interaction of the vertical flow of a light gas with the ceiling are the value of the initial momentum and the distance to the ceiling from the release point of the gas.

CONCLUSION

The results of the experiments and their analyses clearly demonstrate that the two modes of hydrogen release – plume and jet – can produce at the same flowrate radically (perhaps by orders of magnitude) different flammable volumes in case of a sufficiently long release of hydrogen under an extended ceiling.

The experiments were carried out at moderately high flowrates of helium (hydrogen substitute) > 1 g/s, which can be considered as a conservative estimate for hydrogen outflows from the fuel tanks of hydrogen cars in garages and closed parking lots with an extended ceiling. It was found that the most dangerous leakages are those that generate plume (not jet) release regimes of formation of flammable hydrogen-air clouds. At the same flowrate of hydrogen leakage, the volumes and masses of flammable hydrogen-air mixtures can increase manifold due to a principally different character of interaction with extended ceilings in plume regimes compared with jet regimes. Thus, the influence of the release momentum of hydrogen leakage, as well as the distance from the leakage point to the ceiling are fundamental for hydrogen safety.

The correlations of concentration fields of light gas under the extended ceiling depending on the different release regimes obtained in conditions of a direct experiment modeling of real hydrogen leaks can be used to specify rules of hydrogen safety for parking of hydrogen cars, as well as for industrial and infrastructure facilities where hydrogen is used.

REFERENCES

[1] M.R. Swain, P. Filoso, E.S. Grilliot, M.N. Swain, Hydrogen Leakage into Simple Geometric Enclosures, Int. J. Hydrogen Energy 28 (2003) 229-248.

[2] R. Zalosh, Hydrogen Mixing in Large Enclosures, HYSAFE Lecture, University of Ulster, 2006.

[3] S. Benteboula, A. Bengaouer, B. Cariteau, Comparison of Two Simplified Models Predictions with Experimental Measurements for Gas Release within an Enclosure, In: ICHS2009, Ajaccio – Corsica, 2009, ID 226.

[4] V.P. Denisenko, I.A. Kirillov, S.V. Korobtsev, I.I. Nikolaev, Hydrogen-Air Explosive Envelope Behaviour in Confined Space at Different Leak Velocities, In: ICHS2009, Ajaccio – Corsica, 2009, ID 194.

[5] V.P. Denisenko, I.A. Kirillov, S.V. Korobtsev, I.I. Nikolaev, Hydrogen Distribution in Enclosures: on Distinction Criterion between Quasi-Homogeneous Mixing and Stratification Modes, In: ICHS2013, Brussels, 2013, ID 170.

[6] S. Jallais, Build-up in Unventilated Rooms and Enclosures with One and Two Vents: Engineering Point of View, In: Hyindoor Research WorkShop, Brussels, 2013.

[7] V.P. Denisenko, I.A. Kirillov, S.V. Korobtsev, I.I. Nikolaev, A.V. Kuznetsov, V.A. FeldStein, V.V. Ustinov, Experiments on Subsonic Release and Propagation of Hydrogen in Closed Cylindrical Volume. Empirical Analysis, J. Fire Saf. 2 (2011) 38-46 (in Russian).

[8] B.R. Morton, Forced Plumes, J. Fluid Mech. 5 (1959) 151-163.

[9] W.D. Baines, J.S. Turner, Turbulent Buoyant Convection from a Source in a Confined Region, J. Fluid Mech. 37 (1969) 51-80.

[10] M. Poreh, Y.G. Tsuei, J. E. Cermak, Investigation of a Turbulent Radial Wall Jet, Trans. ASME, J. Appl. Mech. 34 (1967) 457–463.

Experimental Study on Shock Waves, Spontaneous Ignition and Flame Propagation Produced by Hydrogen Release through Tubes with Varying Obstacle Location

Li P., Duan Q.*, Zeng Q., Gong L., Jin K., Qi K., Sun J.*

State Key Laboratory of Fire Science, University of Science and Technology of China,
Hefei 230026, China
**Corresponding author's email: duanql@mail.ustc.edu.cn, sunjh@ustc.edu.cn*

ABSTRACT

Experimental investigations were performed to evaluate the effects of obstacles inside tube on the pressure dynamics evolution, spontaneous ignition and flame propagation during pressurized hydrogen release. The obstacles region was consisted of seven metal obstacles and six metal spacers. Pressure transducers and light detectors were installed along the tube to measure pressure variation and hydrogen flame inside tube. The influence of obstacles was examined for three different locations inside tube. The results show that the strength of shock wave is weaken by flow divergence, and then gradually recovers as it travelling along the tube. The light signal analysis shows that the presence of obstacles in different locations has almost no influence on the minimum burst pressure for spontaneous ignition in our tests. However, the presence of obstacles plays an important role in the hydrogen combustion inside tube. Once the spontaneous ignition occurring inside tube, the reflected shock wave promotes combustion before obstacles. And the probability of the flame intensity enhancement increases with increasing distance between burst disk and obstacle location. In addition, the combustion inside tube is only temporarily intensified after obstacles.

KEYWORDS: High-pressure hydrogen, spontaneous ignition, obstacle locations, shock wave, flame propagation.

INTRODUCTION

As a renewable clean energy, hydrogen presents excellent characteristic such as high efficiency and no-emissions. The application of hydrogen fuel cell vehicles (HFCVs) is gaining an increasing attention worldwide. However, there are some technical problems impeding the development of HFCVs, one of which is the onboard high-pressure hydrogen storage safety. Severe fires and explosions maybe caused when hydrogen sudden leaks from high-pressure container or a pipe without the presence of ignition sources. It is necessary to understand the kinetic characteristic of spontaneous ignition and subsequent flame evolution during pressurized hydrogen release.

The diffusion ignition mechanism for spontaneous ignition was first proposed by Wolanski and Wojcicji [1], and it has been extensively studied since then. Wolanski and Wojcicji [1] demonstrated that ignition may occur inside the tube when the temperature of hydrogen-air mixture behind the leading shock wave is flammable and the temperature is high enough. Dryer et al. [2] suggested the multi-dimensional transient flow plays an important role in spontaneous ignition, which can facilitate mixing of shock-heated air and expanding hydrogen behind the shock wave. Shock-induced vortices and turbulence generated at the hydrogen-air contact surface promote molecular diffusion and provide more combustible mixtures for spontaneous ignition [3-5]. Except for high temperature hydrogen-air mixture in contact surface, another key factor for spontaneous

Proceedings of the Ninth International Seminar on Fire and Explosion Hazards (ISFEH9), pp. 1348-1359
Edited by Snegirev A., Liu N.A., Tamanini F., Bradley D., Molkov V., and Chaumeix N.
Published by Saint-Petersburg Polytechnic University Press
ISBN: 978-5-7422-6498-9 DOI: 10.18720/spbpu/2/k19-16

ignition is that the mixture maintains for a long enough time until inflammation [6, 7]. Several flow visualization studies [8-11] were conducted to investigate the ignition process and the flame propagation inside tube by the shadowgraph and high-speed direct photography. The duration period of mixing increases as the leading shock wave travels along the tube, and the ignition takes place after a certain induction time elapsing from the start of mixing [9]. There were two possible locations where initial ignition was captured: one was in the boundary layer along the wall and another one was on the tube axis at the contact region [9-11]. The hydrogen flame produced by spontaneous ignition inside the tube may be quenched or developed into a hydrogen jet flame after it exits the tube. It was suggested that the formation of a complete flame across the tube is important for a sustained hydrogen jet flame outside the tube [12]. The hydrogen flame propagation dynamics outside tubes was also studied in [13-16]. It was found that the flame grows gradually after jetting into air, then vortex induces the flame splitting into upstream and downstream region, and the upstream flame region sustains near the tube exit finally [15, 16].

The majority of previous studies have focused on the spontaneous ignition of high-pressure hydrogen sudden release through a tube without obstacles. In practice, there is often the presence of obstacles either inside or outside tube during pressurized hydrogen release. Xu et al. [17] found that the presence of obstacle may quench the flame when a direct pressurized hydrogen release into air by numerical simulation. However, Kim et al. [18] pointed out that the existence of an obstacle outside the tube could not change the type of ignition patterns but may promote flame stabilization outside the tube. Morii et al. [19] reported that small obstacles inside a tube drastically changed the spontaneous ignition mechanisms when pressurized hydrogen sudden discharged through the tube. When the leading shock wave passed through the lateral orifice [20] or bottom orifice [21] along release tubes, it was suggested the reflected shock wave was produced and was necessary for spontaneous ignition. Nevertheless, the experimental investigation is necessary to deep understand the effects of obstacles inside tube on hydrogen spontaneous ignition. In this paper, an experimental study is carried out to investigate the effect of obstacle locations inside the tube on the shock wave, spontaneous ignition and flame propagation of high-pressure hydrogen.

EXPERIMENTAL APPARATUS

Figure 1 shows the schematic of experimental apparatus which is based on a shock tube system. The drive section is a 0.44 l high-pressure hydrogen tank and the driven section is a downstream release tube with ambient pressure air. A circular nickel burst disk with cross scores (Dalian Ligong Safety Equipment Co., Ltd) is used as diaphragm to separate the high-pressure tank and release tube. The burst pressure (P_b) is measured by a strain gauge pressure sensor (Kulite, ETM-375M-20MPa) mounted in the high-pressure tank. Cylindrical release tubes with three obstacle locations are considered and the schematic of obstacle locations inside tube is shown in Fig 2 (a). The experimental results of the tube with obstacles in location 3 have been reported in our recent publication [22]. Figure 2 (b) presents the detailed composition of obstacle region, which is composed of 7 metal obstacles (2 mm width) and 6 metal spacers (4 mm width) alternately. The burst disk, downstream release tube, metal obstacle and metal intervals have the same internal diameters of 15 mm. Four pressure transducers P_n (PCB Piezotronics, 113B22) and four light detectors L_n (Thorlabs, Si photodiode, FDS010) are symmetrically installed along the release tube for measuring the pressure dynamics and flame signals. The burst pressure (P_b) is varied from 2 MPa to 7 MPa in this study.

The experimental procedure is as follows. First, air is evacuated from high-pressure tank and supply gas pipeline. High-pressure hydrogen is then gradually supplied to the tank until the diaphragm ruptures, resulting in the sudden release of hydrogen into the semi-confined exhaust chamber through the downstream release tube with obstacle. The exhaust chamber is a rectangular cavity of

1200 mm × 470 mm × 500 mm, which is connected with release tube on the left and open to atmosphere on the right. There is a pressure transducer (PCB Piezotronics, 113B22) installed on the top wall of the chamber to measure the overpressure (P_{out}) variation in the exhaust chamber. A high-speed video camera (Phantom, v700) is used to record the flame propagation phenomena outside tube from two viewports (230 mm × 230 mm) on the two exhaust chamber sides. The images are obtained at the recording speed of 79069 fps and resolution of 256×256 pixels. The time when P_1 detects a sudden pressure increase is set to trigger the high-speed video camera and the data recording system (HIOKI, 8860-50).

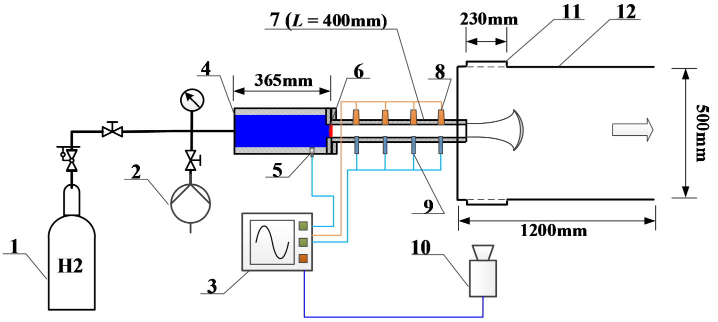

Fig. 1. Schematic of experimental apparatus:(1) compressed gas cylinder, (2) vacuum pump, (3) data recorder, (4) high-pressure tank, (5) strain gauge pressure sensor, (6) burst disk, (7) release tube, (8) light detector, (9) piezoelectric pressure transducer, (10) high-speed video camera, (11) viewport, (12) exhaust chamber.

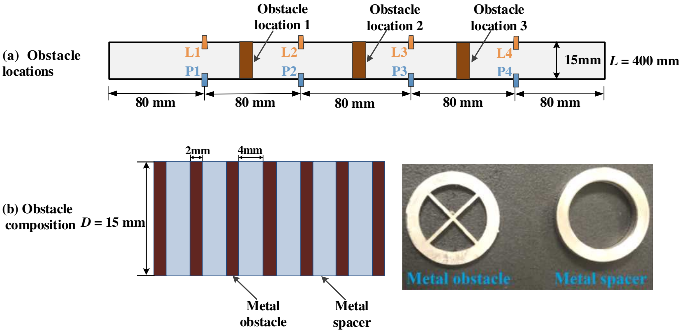

Fig. 2. (a) Schematic of obstacle locations inside tube, L – tube length, P_n – pressure transducer, L_n – light detector; (b) Schematic of obstacles arrangement and photos, D – diameter.

RESULTS AND DISCUSSION

The sudden release of high-pressure hydrogen into the tube can generate a shock wave which impacts on the piezoelectric pressure transducers (P_n). When spontaneous ignition occurs inside the tube, light signal can be detected by the light detectors (L_n). In total, 71 tests are conducted with different release tubes, in which 18 tests are carried out in a tube without obstacles for comparison. Here, the effects of obstacles inside tube on shock wave propagation are first discussed. Then, the spontaneous ignition inside the tube with and without obstacles is analyzed. Finally, the influence of obstacles on hydrogen flame propagation inside tube is studied.

Effect of obstacles on shock wave propagation inside the tube

Figure 3 shows the typical time history of pressure and light signals at different positions inside tube with varying obstacle locations. A shock wave is formed and propagates inside tube with the fact that a sharp pressure rise is sequentially detected by pressure transducers P_1, P_2, P_3 and P_4. When the shock wave impacts on the obstacles, a reflected shock wave is formed and propagates to upstream in the tube. As the reflected shock wave passing the pressure transducers in upstream, a second pressure rise is detected by transducer P_1 in Fig. 3(a), P_2, P_1 in Fig. 3(b) and P_3, P_2, P_1 in Fig. 3(c). However, there is no reflected shock wave in the tube without obstacles.

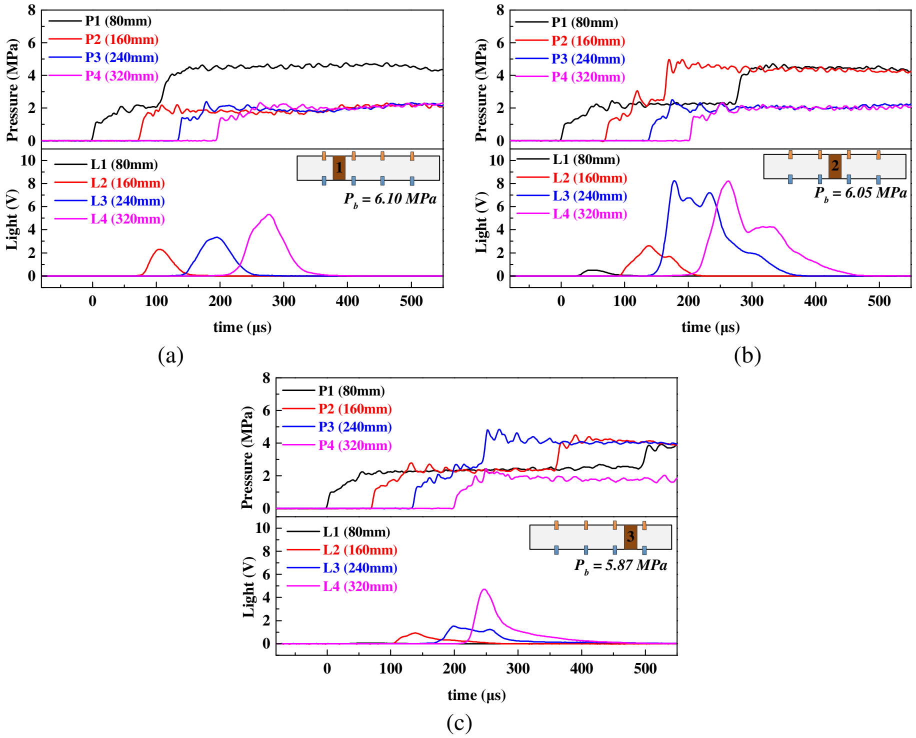

(a)

(b)

(c)

Fig. 3. Time history of pressure and light signals at different positions inside tube with varying obstacle location. (a) Obstacles in location 1, (b) obstacles in location 2, (c) obstacles in location 3.

Figure 4 shows relationships of the shock Mach number in tube with and without obstacles versus burst pressure for varying obstacle locations. The shock Mach number inside tube is obtained from the mean shock speed calculated between two adjacent pressure transducers. It is found that the shock Mach number increases with increasing the burst pressure in tube either with obstacles or without obstacles. In addition, the shock Mach number in tube with obstacles is always less than that without obstacles under the same burst pressure as shown in Fig. 4. This indicates that the shock strength undergoes a reduction when the shock wave passes through obstacles, which may be caused by the flow divergence.

In order to further understand the effect of obstacles on the shock wave propagation inside tube, Fig. 5 plots the shock Mach number versus propagation distance for some typical tests with different release tubes. It is shown in Fig. 5(a) that the shock Mach number almost keeps at a constant value as the shock wave propagates in the tube without obstacles. However, the appearance of obstacles in tube would weaken the strength of the shock wave. Experimental results show that the shock Mach number in the obstacles region, such as at 120 mm in Fig. 5(b), 200 mm in Fig. 5(c) and 280 mm in Fig. 5(d), is less than that at the same location in the tube without obstacles in Fig. 5(a). After the shock wave passes through obstacles, the strength of the shock wave increases gradually due to shock focusing, shock-shock and shock-wall interactions [23, 24]. The stronger initial shock wave increases more quickly than weaker ones after passing through obstacles. As shown in Fig. 5(b), when placing the obstacle at the location 1, the shock Mach number decreases at the position 120 mm compared with that in the tube without obstacles. And it increases at the position 200 mm for burst pressure P_b = 4.32/5.72/7.13 MPa (in red colors), while the shock Mach number begins to increase until the shock wave propagating to the position 280 mm for relatively low burst pressure P_b = 2.04/2.95 MPa (in blue colors). When the obstacles are arranged at the location 2 in Fig. 5(c), the shock Mach number decreases at the position 200 mm due to obstacles, and it increases immediately at the position 280 mm for burst pressure P_b = 5.27/6.39/7.60 MPa (in red colors). It can be inferred that for the relative low burst pressure P_b = 2.00/2.86 MPa (in blue colors), the shock Mach number would increase as the shock wave propagating to the downstream of the tube.

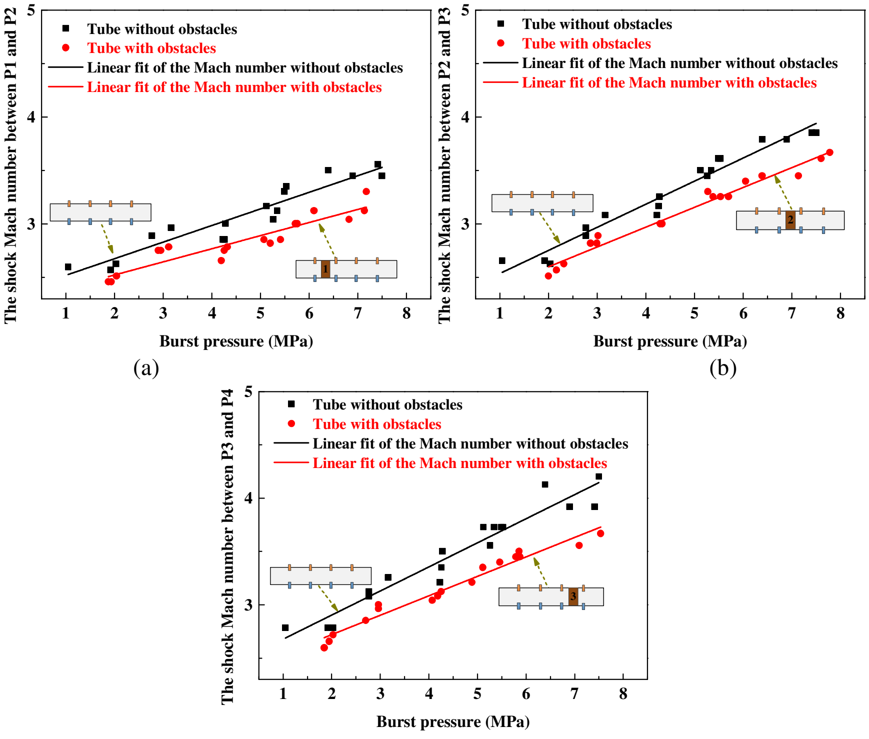

(a) (b)

(c)

Fig. 4. Relationships of the shock Mach number in tube with and without obstacles versus burst pressure for varying obstacle locations: (a) Obstacles in location 1, (b) obstacles in location 2, (c) obstacles in location 3.

In order to further understand the effect of obstacles on the shock wave propagation inside tube, Fig. 5 plots the shock Mach number versus propagation distance for some typical tests with different release tubes. It is shown in Fig. 5(a) that the shock Mach number almost keeps at a constant value as the shock wave propagates in the tube without obstacles. However, the appearance of obstacles in tube would weaken the strength of the shock wave. Experimental results show that the shock Mach number in the obstacles region, such as at 120 mm in Fig. 5(b), 200 mm in Fig. 5(c) and 280 mm in Fig. 5(d), is less than that at the same location in the tube without obstacles in Fig. 5(a). After the shock wave passes through obstacles, the strength of the shock wave increases gradually due to shock focusing, shock-shock and shock-wall interactions [23, 24]. The stronger initial shock wave increases more quickly than weaker ones after passing through obstacles. As shown in Fig. 5(b), when placing the obstacle at the location 1, the shock Mach number decreases at the position 120 mm compared with that in the tube without obstacles. And it increases at the position 200 mm for burst pressure P_b = 4.32/5.72/7.13 MPa (in red colors), while the shock Mach number begins to increase until the shock wave propagating to the position 280 mm for relatively low burst pressure P_b = 2.04/2.95 MPa (in blue colors). When the obstacles are arranged at the location 2 in Fig. 5(c), the shock Mach number decreases at the position 200 mm due to obstacles, and it increases immediately at the position 280 mm for burst pressure P_b = 5.27/6.39/7.60 MPa (in red colors). It can be inferred that for the relative low burst pressure P_b = 2.00/2.86 MPa (in blue colors), the shock Mach number would increase as the shock wave propagating to the downstream of the tube.

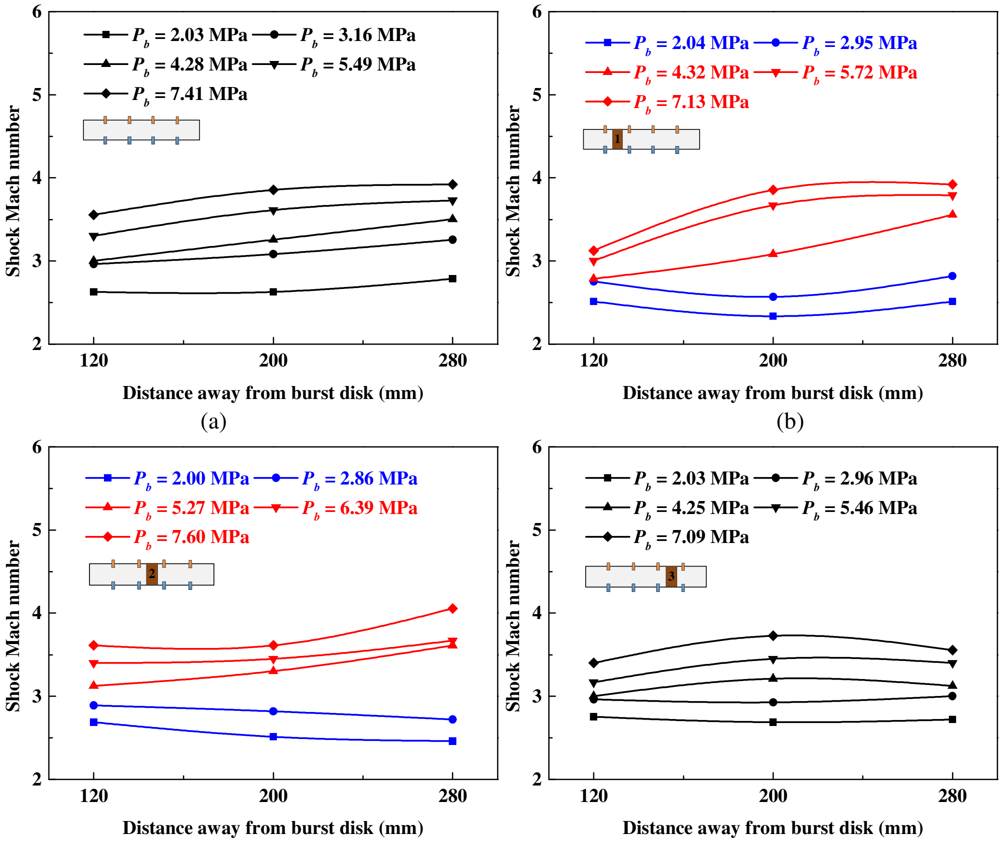

(a)

(b)

(c)

(d)

Fig. 5. Shock Mach number versus propagation distance in different tubes. (a) Tube without obstacles, (b) tube with obstacles in location 1, (c) tube with obstacles in location 2, (d) tube with obstacles in location 3.

When the shock wave propagates into the exhaust chamber and strikes the pressure transducer P_{out}, a rapid increase in pressure can be detected in either the self-ignition case or the non-ignition case. Figure 6 shows the typical overpressure variation in exhaust chamber as a function of time in the tube with obstacles in location 2. The initial increase in pressure is caused by the shock wave originating from the tube, and the shock wave overpressure are 0.044 MPa and 0.018 MPa for the self-ignition case and non-ignition case in Fig. 6, respectively. The shock wave overpressure refers to the peak pressure of the shock wave striking the pressure transducer. Furthermore, Fig. 7 plots the relationships of shock wave overpressure with burst pressure from tubes without obstacles and with varying obstacle locations. It is found that the shock wave overpressure increases with the burst pressure in all tubes, and the presence of obstacles in tube has no significant effects on the shock wave overpressure in the exhaust chamber, as shown in Fig. 7. For example, under the same burst pressure, the shock wave overpressure in the exhaust chamber shows almost the same in the four tubes. That is, the strength of the shock wave decreases when passing through the obstacles inside tube first, and then gradually increases and finally recovers to a similar value to the shock intensity in the tube without obstacles as propagating to downstream the tube.

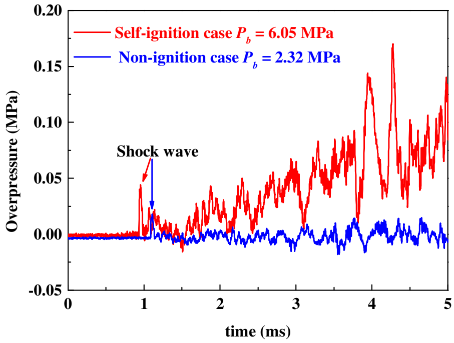

Fig. 6. Typical overpressure variation in exhaust chamber as a function of time (with obstacles in location 2).

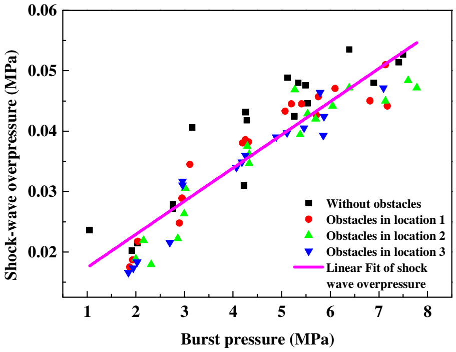

Fig. 7. Relationships of shock wave overpressure with burst pressure from different tubes.

EFFECT OF OBSTACLES ON SPONTANEOUS IGNITION INSIDE TUBE

To investigate the effect of obstacles on the spontaneous ignition, the relationship between ignition and burst pressure for different tubes are plotted in Fig. 8. There are two experimental phenomena observed according to the measurement of light signal inside tube, which are non-ignition and self-ignition. Regardless of whether obstacles are placed in the tube, the likelihood of spontaneous ignition increases with increasing the burst pressure. A higher burst pressure leads to a stronger shock wave, which produces higher temperature of air and promotes the occurrence of ignition. The minimum burst pressure which induces spontaneous ignition in tubes with varying obstacle locations are listed in Table 1. It is found that the minimum burst pressure for the four tubes are about 3 MPa and the appearance of obstacles inside tube has no significant influence on minimum burst pressure in our tests. This is not consistent with the result of Baev et al. [21, 25], which suggested that the reflected shock wave from obstacle is necessary for spontaneous ignition and a larger distance between burst disk and obstacle leads to a smaller minimum burst pressure for spontaneous ignition.

Figure 9 shows the pressure profiles (left axis) and light signals (right axis) at different positions under minimum burst pressure of self-ignition inside tubes with varying obstacle locations. When obstacles are placed in the location 2 (Fig. 9(c)) and location 3 (Fig. 9(d)), the light signal are first detected by L_1 as the case in the tube without obstacles (Fig. 9(a)), which means that the initial ignition occurs before obstacles. Thus it is reasonable that the occurrence of obstacles has no significant effect on the minimum burst pressure in our tests. The reflected shock wave is formed inside tube when the shock wave passes through obstacles as discussed in section 1. When the reflected shock wave propagates upstream and strikes the nearest pressure transducer, such as P_1 in Fig. 9(b), P_2 in Fig. 9(c), and P_3 in Fig. 9(d), the H_2-air mixture is heated and the mixing of H_2-air is promoted. However, the temperature and the amount of the hydrogen-air mixture maybe not enough to induce ignition [2, 21], so there is no light signal detected by the light sensors.

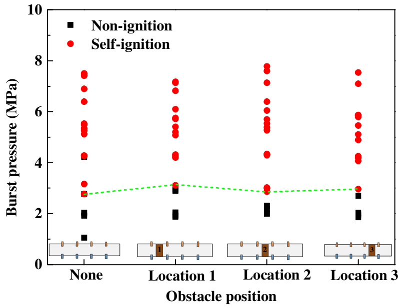

Fig. 8. Ignition occurrence associated with burst pressure for tubes with varying obstacle location.

Table 1. Minimum pressures of hydrogen spontaneous ignition in tubes with varying obstacle locations

Obstacle location	Minimum burst pressure of spontaneous ignition (MPa)
Without obstacles [22]	2.77
Location 1	3.11
Location 2	2.86
Location 3 [22]	2.96

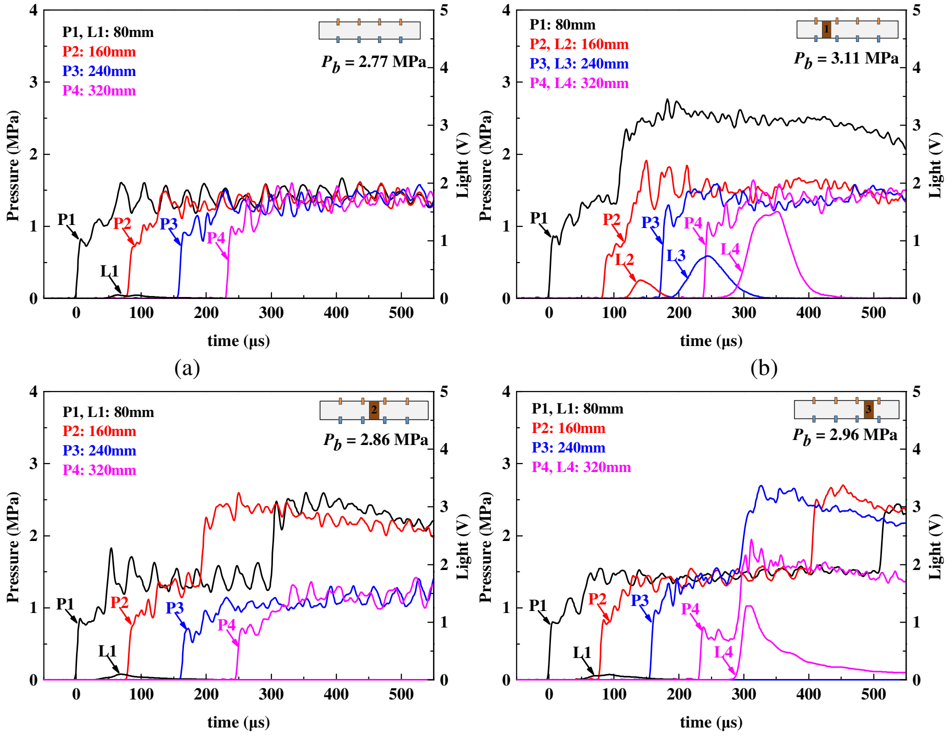

(a) (b)

(c) (d)

Fig. 9. Time history of pressure (left axis) and light signals (right axis) at different positions under minimum burst pressure of self-ignition inside tubes with varying obstacle locations. (a) Tube without obstacles [22], (b) tube with obstacles in location 1, (c) tube with obstacles in location 2, (d) tube with obstacles in location 3 [22].

EFFECT OF OBSTACLES ON FLAME PROPAGATION

Detected light signal is relative to flame intensity, which is one of indicators to describe hydrogen combustion intensity inside tube. It is worth mentioning that two light peak values are detected by light detector L_2 in Fig. 3(b) and L_3 in Fig. 3(c). And the second peak value is observed after the reflected shock wave passing through the position. When spontaneous ignition has induced inside tube, the reflected shock wave may further increase the temperature of hydrogen-air and promote the mixing of combustible mixture, which enhances combustion inside tube. Table 2 lists the probability of the flame intensity enhancement by the reflected shock wave when obstacles places in varying locations. It is found that the probability of the combustion enhancement by the reflected shock wave increases as the increasing distance between burst disk and obstacle location.

Table 2. Probability of the flame intensity enhancement by the reflected shock wave

Obstacle location	The light signal been enhanced by reflected wave
Location 1	0
Location 2	77%
Location 3	85%

Figure 10 shows the schematic of affected distance (*L*) by reflected shock wave. According to the shock tube theory, the speed of the hydrogen jet front can be obtained as [26]

$$\frac{V_2}{a_1} = \frac{2}{\gamma_1 + 1}\left(M_s - \frac{1}{M_s}\right), \tag{1}$$

where V_2 is the speed of hydrogen jet front and a_1 is the speed of sound, M_s is the shock Mach number, γ_1 is the heat capacity ratio of air. Reflected shock wave is formed when shock wave impacting on the obstacles, so the affected distance by reflected shock wave can be estimated by Eq. (2)

$$L = x_{SW} - x_{Hydrogen\ jet\ front} = M_s a_1 t - \frac{2a_1}{\gamma_1 + 1}\left(M_s - \frac{1}{M_s}\right)t, \tag{2}$$

where *L* is the affected distance by reflected shock wave, x_{sw} is the distance between burst disk and shock wave, $x_{hydrogen\ jet\ front}$ is the distance between burst disk and hydrogen jet front, *t* is time required for shock wave travelling to obstacles. Shock Mach number (M_s) is related to burst pressure (P_b). When the obstacles region is placed more far away from burst disk, such as location 3, a longer time (*t*) is required for shock wave travelling to the obstacles under a same burst pressure, which leads to the increase of the reflected shock wave affected distance (*L*). Meanwhile, the amount of hydrogen-air mixture increases as the shock wave travelling along tube [9]. As a result, the probability of combustion enhancement by reflected shock wave increases as the increasing distance between burst disk and obstacle location.

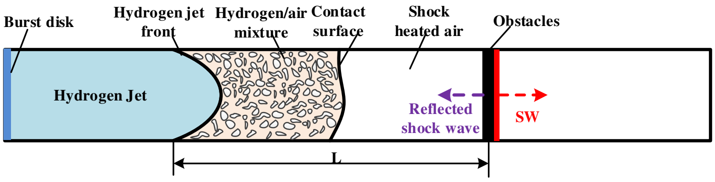

Fig. 10. Schematic of affected distance by reflected shock wave in the tube.

In order to further understand the effect of obstacles on flame propagation inside tube, the mean flame velocity relative to tube wall is chosen to represent the flame intensity, which is determined from the peak light arrival time between two light detectors. Figure 11 plots the mean flame velocity as a function of distance between the release tube and the burst disk in different tubes. The flame in the tube without obstacles is relative stable with the fact that the mean flame velocity almost keeps at a constant value, as shown in Fig. 11(a). An obvious flame acceleration is observed when flame travels across obstacles. For example, the flame velocity increases at 120 mm in Fig. 11(b), at 200 mm in Fig. 11(c), and at 280 mm in Fig. 11(d). The reasons may be as follows: (1) the presence of circular obstacle leads to the faster flow velocity in contraction structure; (2) the turbulent flow produced by obstacles, as shown in previous numerical study [23, 24], results in an increase of the amount of hydrogen-air mixture between hydrogen and shock-heated air, which enhances the combustion inside the tube. The flame velocity drops back at 200 mm in Fig. 11(b) and 280 mm in Fig. 11(c), which means that the flame intensity return to normal level once flow velocity drop back after obstacles and the extra amount of hydrogen-air is consumed.

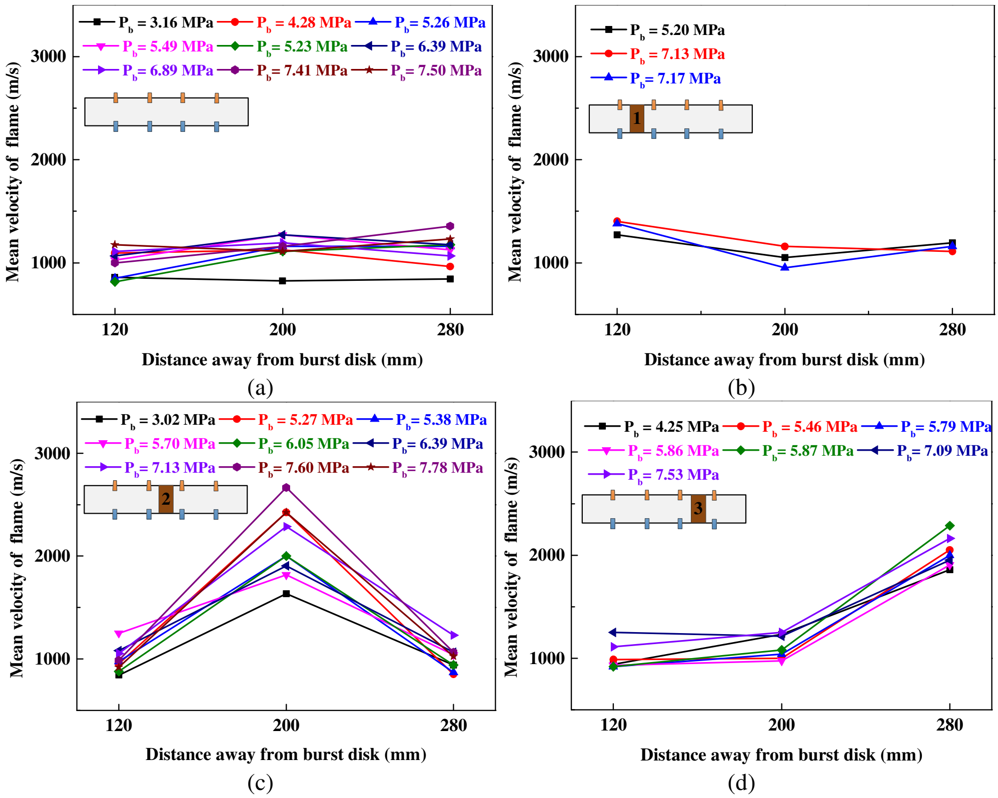

(a) (b)

(c) (d)

Fig. 11. The mean flame velocity relatives to the tube wall as a function of distance between the release tube and the burst disk in different tubes. (a) Tube without obstacles [22], (b) tube with obstacles in location 1, (c) tube with obstacles in location 2, (d) tube with obstacles in location 3 [22].

After the flame produced by spontaneous ignition jets out of the tube with obstacles, it propagates forward along with hydrogen flow and eventually develops into a jet flame in the atmosphere. The flame propagation characteristics outside the tube between release tubes with and without obstacles have no significant difference. A detailed discussion about the hydrogen flame propagation outside the tube has been reported in our previous work [7, 16], so no more discussion here.

CONCLUSIONS

Experimental investigation of pressurized hydrogen release in tubes with obstacles have been conducted to measure pressure variation and hydrogen spontaneous ignition inside tubes. Three kind of tubes with varying obstacle location were considered here to show the effect of obstacle location on the pressure dynamics evolution, spontaneous ignition and flame propagation.

When the obstacle is placed inside tube, the shock Mach number always decrease when the shock wave travels through obstacles. This might be due to flow divergence when the shock wave passes through obstacles. Subsequently, the strength of the shock wave gradually recovers under the effect of multi-dimensional shock wave interactions.

In tubes with varying obstacle locations, the reflected shock wave is generated when the shock wave encounters obstacles. The appearance of reflected shock wave leads to more intensive flame ahead of obstacles in the evidence of initial spontaneous ignition has been occurred inside tube. And more far away from burst disk that obstacles are placed, more likely that the reflected shock wave enhances flame before obstacles. However, the presence of obstacles has no significant influence on the minimum burst pressure which induces spontaneous ignition in the tests.

For tubes with obstacles, a faster flow velocity and a turbulent flow may be generated after obstacles, which induces an extra amount of hydrogen-air mixture formed in the obstacles region. Thus, the mean flame velocity inside the tube is always increases when the flame propagates through obstacles. After that, the velocity drops. In brief, it is suggested that the presence of obstacle inside the tube would only temporarily promote combustion inside the tube.

ACKNOWLEDGMENTS

This work was supported by National Natural Science Foundation of China (grant number 51706220) and National Key Research and Development Program of China (grant number 2016YFC0800100).

REFERENCES

[1] W.S. Wolanski P, Investigation into the mechanism of the diffusion ignition of a combustible gas flowing into an oxidizing atmosphere, Proc. Combust. Inst. 14 (1972) 1217-1223.

[2] F.L. Dryer, M. Chaos, Z. Zhao, J.N. Stein, J.Y. Alpert, C.J. Homer, Spontaneous ignition of pressurized releases of hydrogen and natural gas into air, Combust. Sci. Techn. 179 (2007) 663-694.

[3] B. Xu, L. El Hima, J. Wen, S. Dembele, V. Tam, T. Donchev, Numerical study on the spontaneous ignition of pressurized hydrogen release through a tube into air, J. Loss Prevent. Proc. Ind. 21 (2008) 205-213.

[4] B. Xu, L.E. Hima, J. Wen, V. Tam, Numerical study of spontaneous ignition of pressurized hydrogen release into air, Int. J. Hydrog. Energy 34 (2009) 5954-5960.

[5] E. Yamada, N. Kitabayashi, A.K. Hayashi, N. Tsuboi, Mechanism of high-pressure hydrogen auto-ignition when spouting into air, Int. J. Hydrog. Energy 36 (2011) 2560-2566.

[6] V. Golub, D. Baklanov, T. Bazhenova, S. Golovastov, M. Ivanov, I. Laskin, N. Semin, V. Volodin, Experimental and numerical investigation of hydrogen gas auto-ignition, Int. J. Hydrog. Energy 34 (2009) 5946-5953.

[7] Q. Duan, H. Xiao, W. Gao, L. Gong, Q. Wang, J. Sun, Experimental study on spontaneous ignition and flame propagation of high-pressure hydrogen release via a tube into air, Fuel 181 (2016) 811-819.

[8] J. Grune, K. Sempert, M. Kuznetsov, T. Jordan, Experimental investigation of flame and pressure dynamics after spontaneous ignition in tube geometry, Int. J. Hydrog. Energy 39 (2014) 20396-20403.

[9] Y.R. Kim, H.J. Lee, S. Kim, I.-S. Jeung, A flow visualization study on self-ignition of high pressure hydrogen gas released into a tube, Proc. Combust. Inst. 34 (2013) 2057-2064.

[10] K. Yamashita, T. Saburi, Y. Wada, M. Asahara, T. Mogi, A. Hayashi, Visualization of spontaneous ignition under controlled burst pressure, Int. J. Hydrog. Energy 42 (2017) 7755-7760.

[11] W. Kaneko, K. Ishii, An experimental study on the mechanism of self-ignition of high-pressure hydrogen, Int. J. Hydrog. Energy 42 (2017) 7374-7379.

[12] H.J. Lee, Y.R. Kim, S.-H. Kim, I.-S. Jeung, Experimental investigation on the self-ignition of pressurized hydrogen released by the failure of a rupture disk through tubes, Proc. Combust. Inst. 33 (2011) 2351-2358.

[13] T. Mogi, D. Kim, H. Shiina, S. Horiguchi, Self-ignition and explosion during discharge of high-pressure hydrogen, J. Loss Prevent. Proc. Ind., 21 (2008) 199-204.

[14] J. Grune, K. Sempert, M. Kuznetsov, W. Breitung, Experimental study of ignited unsteady hydrogen jets into air, Int. J. Hydrog. Energy 36 (2011) 2497-2504.

[15] M.V. Bragin, V.V. Molkov, Physics of spontaneous ignition of high-pressure hydrogen release and transition to jet fire, Int. J. Hydrog. Energy 36 (2011) 2589-2596.

[16] Q. Duan, H. Xiao, L. Gong, K. Jin, W. Gao, H. Chai, J. Sun, Experimental study on spontaneous ignition and subsequent flame development caused by high-pressure hydrogen release: Coupled effects of tube dimensions and burst pressure, Fire Saf. J. 97 (2018) 44-53.

[17] B. Xu, J. Wen, V. Tam, The effect of an obstacle plate on the spontaneous ignition in pressurized hydrogen release: A numerical study, Int. J. Hydrog. Energy 36 (2011) 2637-2644.

[18] S. Kim, H.J. Lee, J.H. Park, I.-S. Jeung, Effects of a wall on the self-ignition patterns and flame propagation of high-pressure hydrogen release through a tube, Proc. Combust. Inst. 34 (2013) 2049-2056.

[19] Y. Morii, H. Terashima, M. Koshi, T. Shimizu, Numerical study of the effect of obstacles on the spontaneous ignition of high-pressure hydrogen, J. Loss Prevent. Proc. Ind., 34 (2015) 92-99.

[20] S.V. Golovastov, O. Terekhova, Self-ignition of hydrogen jet discharged under high pressure into a perforated channel, J. Loss Prevent. Proc. Ind., 43 (2016) 198-202.

[21] V. Baev, V. Shumskii, M. Yaroslavtsev, Self-ignition of a fuel gas escaping into an oxidizing medium, Combust., Explos. Shock Waves 19 (1983) 600-605.

[22] P. Li, Q. Duan, L. Gong, K. Jin, J. Chen, J. Sun, Effects of obstacles inside the tube on the shock wave propagation and spontaneous ignition of high-pressure hydrogen, Fuel 236 (2019) 1586-1594.

[23] B. Xu, J. Wen, Numerical study of spontaneous ignition in pressurized hydrogen release through a length of tube with local contraction, Int. J. Hydrog. Energy 37 (2012) 17571-17579.

[24] B. Xu, J. Wen, The effect of tube internal geometry on the propensity to spontaneous ignition in pressurized hydrogen release, Int. J. Hydrog. Energy 39 (2014) 20503-20508.

[25] V. Baev, A. Buzukov, V. Shumskii, Conditions of self-ignition upon pulsed high-pressure injection of combustible gases into a bounded space, Combust. Explos. Shock Waves 36 (2000) 283-290.

[26] A.G. Gaydon, I.R. Hurle, The shock tube in high-temperature chemical physics, Chapman and Hall, 1963.

Near Field Thermal Dose of Cryogenic Hydrogen Jet Fires

Cirrone D.*, Makarov D., Molkov V.

Hydrogen Safety Engineering and Research Centre (HySAFER),
Ulster University, Shore Road, Newtownabbey, BT37 0QB, UK
**Corresponding author's email: cirrone-dmc@ulster.ac.uk*

ABSTRACT

A competitive technique to store large quantities of hydrogen is the cryo-compression of the gas. A deeper understanding of the thermal hazards associated to ignited under-expanded cryogenic releases is fundamental to protect life and prevent property loss. The present study aims at the CFD modelling of thermal hazards beside jet fires with release temperature in the cryogenic range 48-78 K and pressure up to 4 bar abs. The harm level is assessed in terms of thermal dose. The CFD model employs realizable k-ε for turbulence modelling, along with Eddy Dissipation Concept for combustion and Discrete Ordinates model for radiation. The model has been previously validated against experiments by Sandia National Laboratories (SNL) on cryogenic hydrogen fires with release pressure up to 5 bar abs and temperature up to 82 K. Simulations were performed for three experimental tests conducted at SNL. The thermal dose was calculated for several exposure times in the near field to the jet fire. The harm criteria for people were defined according to the thermal dose thresholds for infrared radiation. The maximum exposure time to not be "harmed" at 0.5 m from the flame axis resulted to be lower than 30 s for all the 3 tests. In test 3 (T = 78 K, P = 4 bar abs, m = 0.56 g/s), 60 s exposure resulted in second degree burns within 0.5 m from the jet flame axis. At the same distance, 4 minutes is the maximum exposure time before third degree burns occurrence.

KEYWORDS: Thermal dose, cryogenic jet fires, hydrogen safety.

NOMENCLATURE

I	incident radiative heat flux (W/m^2)
L	length (m)
k	turbulent kinetic energy (m^2/s^2)
$\dot{m}$	mass flow rate (kg/s)
T	temperature (K)
t	time (s)
TD	thermal dose ((kW/m^2)$^{4/3}$s)
v	velocity (m/s)
x	distance (m)

Greek

ε	turbulence dissipation rate (m^2/s^3)
ρ	density (kg/m^3)

Subscripts

not	notional nozzle
f	flame

INTRODUCTION

A competitive technique to store and transport large quantities of hydrogen is the cryo-compression of the gas [1]. In case of an unintended release or Thermally activated Pressure Relief Device (TPRD) opening, hydrogen is likely to ignite, producing a jet fire. The development of engineering tools capable of predicting thermal hazards from cryogenic jet fires and associated harm levels is needed to support a safer deployment of the hydrogen infrastructure. A predictive engineering tool has been developed in [2] to calculate hazard distances along the jet flame axis based on the

Proceedings of the Ninth International Seminar on Fire and Explosion Hazards (ISFEH9), pp. 1360-1366
Edited by Snegirev A., Liu N.A., Tamanini F., Bradley D., Molkov V., and Chaumeix N.
Published by Saint-Petersburg Polytechnic University Press
ISBN: 978-5-7422-6498-9 DOI: 10.18720/spbpu/2/k19-117

temperature distribution and hot air currents in its surroundings. The "fatality" limit condition is achieved at a distance (x) equal to twice the flame length (L_f), the "pain" limit at $x = 3L_f$ and the "no harm" limit at $3.5L_f$. However, engineering tools able to predict the harm level on the sides of the jet fires are currently missing. This information may be of utmost importance to define first responders' intervention strategy in the case of a fire involving a hydrogen-powered vehicle. The thermal dose is a comprehensive parameter to define such harm levels, as it considers the exposure duration in addition to the radiative heat flux from a source. Previous works calculated the safety distances for jet fires from a 60 l/min liquified hydrogen (LH_2) spillage [3]. It was found that a distance greater than 8.7 m from the flame extent (~5 m) should be maintained to avoid a harmful thermal dose for an exposure time up to 200 s. A distance equal to 7.6 m was found to be sufficient to reach the pain limit after 28 s exposure in high wind conditions (2.15 m/s), whereas a longer exposure time of 44 s was needed in low wind conditions (0.59 m/s). However, calculations are based on experimental measurements of radiative heat flux at 8.7 and 7.6 m along the jet axis, without provision of a tool to calculate thermal dose in arbitrary conditions. The present study aims at the development of a Computational Fluid Dynamics (CFD) model to predict distances beside the jet fire to harmful levels of thermal dose for humans. The CFD model is applied to jet fires with release temperature in the range 48-78 K, pressure up to 4 bar abs and orifice diameter equal to 1.25 mm. Only the near field to the jet fire is considered for the analysis in this study to assess the time available for first responders to act on an accident scene.

CASES OF STUDY

Simulations were performed for three experimental tests conducted at Sandia National Laboratories (SNL) on cryogenic hydrogen fires [4]. The analysed scenarios involve hydrogen releases with temperature in the range 48-78 K and pressure 2-4 bar abs. The release temperature and pressure were maintained constant during each test and monitored upstream of the orifice, with a diameter equal to 1.25 mm. Operating conditions for each of the 3 tests are described in Table 1. The cases of study are part of the set of experimental tests selected for validation of the CFD model in [5], as described in the following section.

Table 1. Operating conditions at the release

Test No.	T, K	P, bar abs	$\dot{m}$, g/s
1	64	2	0.33
2	48	2	0.38
3	78	4	0.56

CFD MODEL AND NUMERICAL DETAILS

The CFD model employed in the present study has been previously validated against experiments by SNL on cryogenic hydrogen fires from storage with pressure up to 5 bar abs and temperature in the range 48-82 K [4]. For all the five tests, experimental radiative heat flux at 5 sensors along the jet flame was predicted within ±15% accuracy, with few exceptions [5]. The CFD approach is based on the Reynolds-Averaged Navier Stokes (RANS) conservation equations for mass, momentum, energy and species. The transport equations for turbulent kinetic energy, k, and turbulence dissipation rate, ε, are solved through the realizable k-ε model [6]. The Eddy Dissipation Concept [7] is employed to model hydrogen combustion in air, considering a subset of Peters and Rogg's mechanisms with 18 elementary reactions and 9 species [8]. The Discrete Ordinates model is used to solve the Radiative Transfer Equation (RTE) [9]. Water vapour is the only emitting/absorbing species considered in the study, and it is treated as a grey gas. The absorption coefficient is defined as a function of a control volume temperature and water vapour concentration according to Hubbard and Tien's data [10]. Scattering is neglected, given that soot is not involved in hydrogen-air combustion. 10x10 angular divisions are employed to discretise the RTE, following the results of the parametric study performed in [5], along with 3x3 pixels. ANSYS Fluent is used as the platform for calculations.

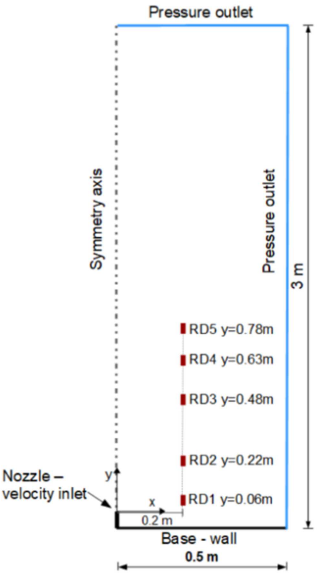

Fig. 1. Scheme of the release, sensors and domain set-up (domain height not in scale).

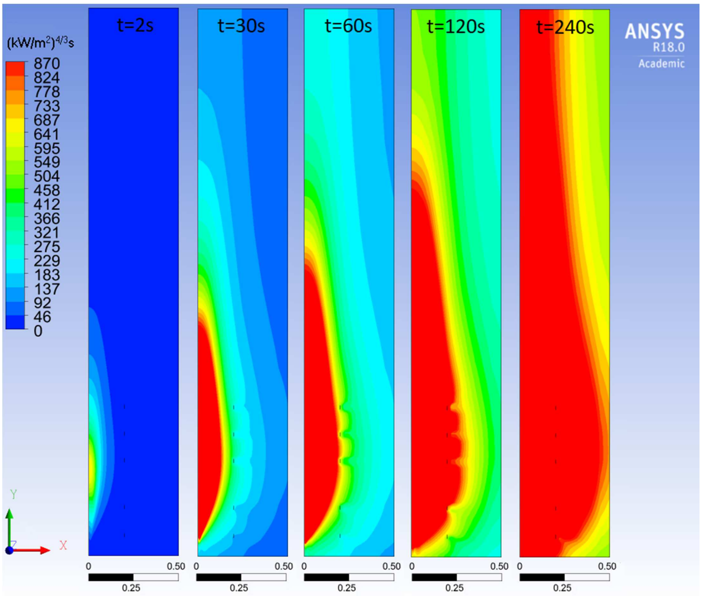

Fig. 2. Calculated thermal dose distribution for Test 3.

Table 2. Calculated notional nozzle conditions for the simulated tests

Test No.	T, K	v, m/s	ρ, kg/m^3	d_{not}, mm	$\dot{m}$, g/s	Variation $\dot{m}$ from experiment, %
1	53	554.9	0.461	1.27	0.326	-1.26
2	40	480.6	0.614	1.27	0.376	-1.10
3	65	612.6	0.378	1.80	0.589	4.93

The Ulster's notional nozzle theory [11] is used to model the release source, as it was validated also for the investigated cryogenic jets with release pressure up to 4 bar abs [5]. The conditions calculated at the notional nozzle are reported in Table 2 and they are imposed as inlet conditions in simulations, along with turbulent intensity and turbulent length scale equal to 25% and $0.07D_{eff}$ respectively, according to the LES study on hydrogen under-expanded jet fire [12]. The releases are assumed to be steady-state, given that the experimental set-up was arranged to maintain constant release parameters. A quarter of the domain is considered, and it has dimensions L x W x H=0.5 m x 0.5 m x 3 m. Figure 1 shows the scheme of the release and the computational domain with specification of the imposed boundary conditions. The scheme includes the 5 sensors (rd) measuring the radiative heat flux in the experiments used for validation of the CFD model in [5]. The domain is initialised with temperature and pressure equal to 288 K and 1 atm respectively. Moist air with 74% relative humidity is considered, according to the average meteorological data for SNL location

[13]. However, relative humidity may be lower in environments where controlled air ventilation systems are present, such as combustion or chemical laboratories. The effect of relative humidity was assessed in [5], considering as limiting case dry air. The absence of water vapour in air caused up to 13% increase of radiative heat flux at the sensors. The boundaries are modelled as pressure outlets with gauge pressure equal to 0. A second order upwind scheme is employed to discretise convective terms, and SIMPLE procedure for velocity-pressure coupling.

THERMAL DOSE AND HARMFUL EFFECTS ON HUMANS

Jet flames originated by pressurised hydrogen ignited releases can cause life threatening conditions in their surroundings, i.e. injury or death of the exposed subject. It could be conservatively assumed that the direct contact with the flame can result in fatality, whereas exposure to the radiative heat flux of the flame can have as consequent injury harm levels: first, second or third degree burns. The potential damage depends on the vulnerability of the target, which is determined by age, health conditions, etc. The resulting level of harm is a function of the exposure duration in addition to the incident thermal flux. Therefore, it is usually expressed in terms of thermal dose (TD):

$$TD = \int_0^t I^{4/3}(t)\,dt\,, \tag{1}$$

where I is the incident radiative heat flux (kW/m^2) and t is the exposure time (s). The thermal dose unit (TDU) is equal to 1 (kW/m^2)$^{4/3}$s. Thermal dose harm levels are different depending on whether emitted radiation is included in the ultraviolet or infrared range of the spectrum. Table 3 reports the thresholds provided by [14] for both spectrum ranges. Exposure to infrared radiation results to be more dangerous, as shown by the lower and more conservative TD limits. Furthermore, water vapour is the dominant emitting species in hydrogen combustion in air and the emitted thermal radiation is mainly included in the infrared range [15]. Therefore, the associated TD thresholds are selected for calculation of hazard distances. The range 86-103 (kW/m^2)$^{4/3}$s was employed in [3] to identify the pain limit for infrared radiation. Given that the thresholds are within the range reported for first degree burns (see Table 3), only the latter will be considered in the study as it is valid also for the pain limit.

Table 3. Thermal dose thresholds for people

Burn Severity	Threshold Dose, (kW/m^2)$^{4/3}$s	
	Ultraviolet	Infrared
First degree	260-440	80-130
Second degree	670-1100	240-730
Third degree	1220-3100	870-2640

RESULTS AND DISCUSSION

A first analysis involves the calculation of distances along the jet fire axis to the harmful effects for exposure of people to hot air currents according to [2]. The average of the calculation for temperature 1300 K and 1500 K was considered, as this is the region on the jet axis where the flame tip is generally located [16]. Results for the 3 tests are presented in Table 4. It is shown that the distance from the release point indicated for “no harm” of people can vary from 2.43 m for test 1 to 3.08 m for test 3.

A second analysis addresses the calculation of separation distances on the sides of the jet fire through evaluation of the thermal dose. Figure 2 shows the thermal dose distribution at several times of exposure for Test 3, including representation of the five 2x2 cm sensors where radiative heat flux was measured for validation of the CFD model in [5]. Maximum thermal dose was recorded inside the flame and it varied from 684 to $8.2 \cdot 10^4$ $(kW/m^2)^{4/3}s$ in the range of time 2-240 s. The graph legend is limited to a maximum value 870 $(kW/m^2)^{4/3}s$, to represent distinctively the range of values characterising the thresholds reported in Table 3. Higher thermal doses are represented in red as for 870 $(kW/m^2)^{4/3}s$. It is noticeable that 60 s exposure would result in first degree burns within 0.5 m from the jet flame axis.

Table 4. Distances to harm levels for people considering the jet fire flame length

Test No.	1	2	3
Average calculated flame length, m	0.70	0.75	0.88
"no harm" limit, m *70°C for any exposure duration*	2.43	2.63	3.08
"pain" limit, m *115°C for 5 minutes exposure*	2.09	2.25	2.64
"fatality" limit, m *309°C, third degree burns for 20 s exposure*	1.39	1.50	1.76
Maximum calculated flame width, m	0.09	0.09	0.11

Figure 3 provides the thermal dose classified by the associated harm criteria, as function of distance and exposure time for Tests 1, 2 and 3. As shown in Fig. 2, the thermal dose is not uniformly distributed around the jet fire due to the changing properties and width along the flame axis, and its radial distribution depends on the distance from the release point. The values of thermal dose presented in Fig. 3 are maximum thermal dose at a particular radial distance recorded among all distances along flame axis. The maximum exposure time to not reach the pain limit and to not incur in first degree burns at 0.5 m from the flame axis was found to be lower than 30 s for all the 3 Tests. In Test 3, an exposure longer than 60 s resulted in second degree burns within 0.5 m from the jet flame axis, whereas 4 minutes is the maximum exposure time before third degree burns occurrence. The same harm level is reached in only 20 s of exposure at 0.7 m from the flame tip along the jet axis. However, it must be considered that this study does not include convective heat flux and deals with comparatively small-scale vertical jet fires, whereas conclusions may be different for horizontal fires due to the effect of buoyancy on combustion products and for releases from larger orifices and higher pressures. Furthermore, one radiation level in the surroundings of the jet is affected by the presence of water vapour in the atmosphere, which corresponds to a mass fraction equal to 0.008 in the present case of SNL location.

The considerations above are for people not wearing protecting clothes. The same conclusions on hazard distances can be withdrawn for operators wearing standard workwear, as they are characterised by similar tolerance to radiative heat flux [17]. In case of an accident involving hydrogen ignited releases, fire fighters responding to the scene will wear thermal protective clothing, increasing significantly the tolerable levels of radiative heat flux for short term activities (~2 minutes) in the near field of the jet fire, such as opening or closing valves [17]. Emergency operations can be performed for a maximum duration of 3 minutes when exposed to heat fluxes up to 4.6 kW/m^2, which agrees with the intensity indicated as tolerable for emergency personnel in [18]. Simulation results have shown that for Test 3 fire fighters can stay as close as 0.27 m from the jet axis for up to 3 min, receiving a thermal dose of approximately 1380 $(kW/m^2)^{4/3}s$. A limit of 6.3 kW/m^2 is given for an operating time of 5 minutes if fire fighters are wearing aluminised clothing (TD ≈ 3490 $(kW/m^2)^{4/3}s$), reducing further the distance from the jet axis to about 0.20 m. A radiation level of approximately 3.8 kW/m^2 is recorded 5 cm upstream the release point, allowing fire fighters to act to open or close valves at this distance behind the release, whereas first responders not wearing protecting clothes can be exposed less than 13 s to prevent first degree burns occurrence.

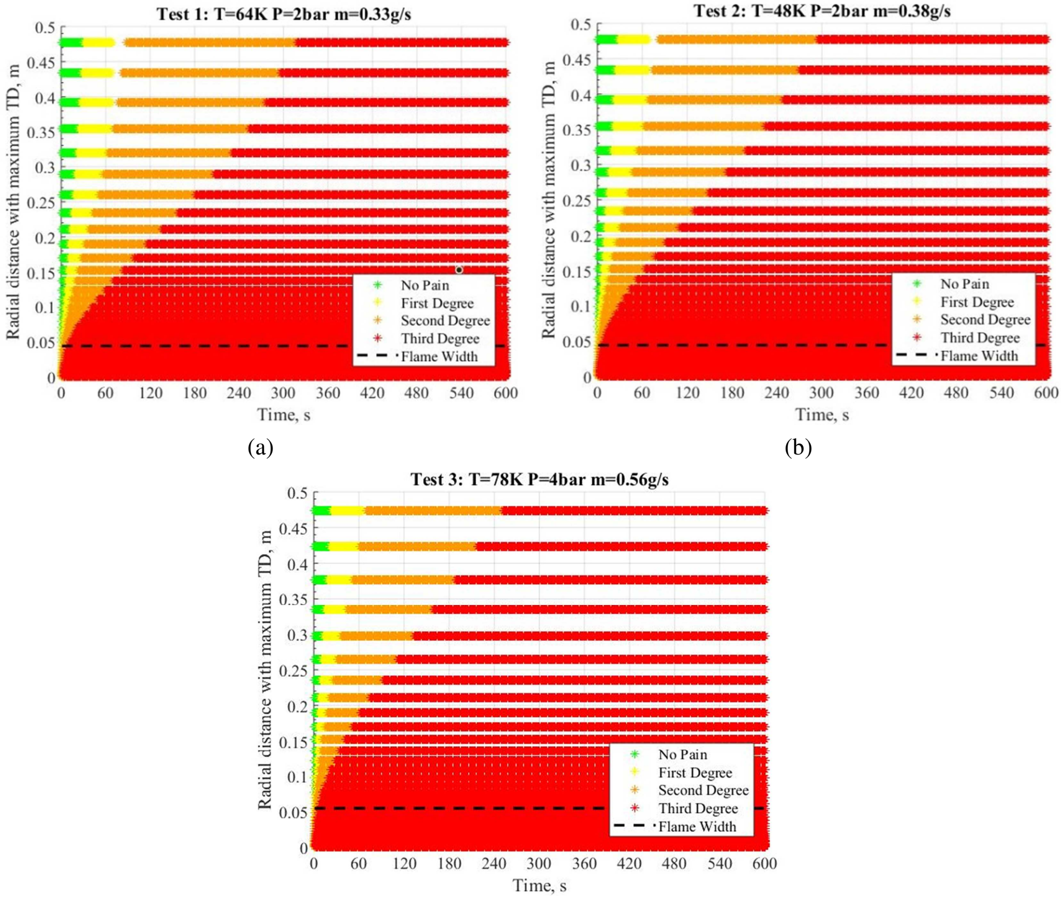

(a) (b)

(c)

Fig. 3. Thermal dose harm levels: time versus radial distance with maximum TD for Test 1 (a), Test 2 (b) and Test 3 (c).

CONCLUSIONS

The present study aimed at the CFD modelling of thermal dose in the near surroundings of cryogenic jet fires with release temperature in the range 48-78 K and pressure 2-4 bar abs from 1.25 mm orifice. The engineering tool for prediction of harmful thermal effects on the sides of the jet fires was developed. It can be integrated to the existing tool for calculation of hazard distances along the jet axis provided in [2]. The employed CFD model had been previously validated [5] against experiments by SNL on cryogenic hydrogen fires [4]. For example, it was found that at 0.5 m distance from the flame axis, the time of exposure should be lower than 30 s to not incur first degree burns for all the Tests. For a release with $\dot{m}$ = 0.56 g/s (Test 3), an exposure time longer than 60 s resulted in second degree burns within 0.5 m from the jet flame axis, whereas 4 minutes led to the occurrence of third degree burns.

ACKNOWLEDGMENTS

The authors are grateful to Dr. P.P. Panda for providing experimental data indispensable to conduct this numerical study. This study has received funding from EPSRC SUPERGEN H2FC Hub project (EP/J016454/1) and the Fuel Cell and Hydrogen 2 Joint Undertaking under grant agreements No.736648 (NET-Tools project) and No.779613 (PRESLHY). This Joint Undertaking received support from the European Union's Horizon 2020 research and innovation programme and Hydrogen Europe and Hydrogen Europe Research.

REFERENCES

[1] DOE, Technical Assessment: Cryo-Compressed Hydrogen Storage for Vehicular Applications, 2006.

[2] V. Molkov, Fundamentals of Hydrogen Safety Engineering I, www.bookboon.com, 2012.

[3] J.E. Hall, P. Hooker, D. Willoughby, Ignited Releases of Liquid Hydrogen: Safety Considerations of Thermal and Overpressure Effects, Int. J. Hydrogen Energy 39 (2014) 20547–20553.

[4] P.P. Panda, E.S. Hecht, Ignition and Flame Characteristics of Cryogenic Hydrogen Releases, Int. J. Hydrogen Energy 42 (2016) 775–785.

[5] D.M.C. Cirrone, D. Makarov, V. Molkov, Thermal Radiation from Cryogenic Hydrogen Jet Fires, Int. J. Hydrogen Energy (2018) in press.

[6] T.H. Shih, W.W. Liou, A. Shabbir, Z. Yang, J. Zhu, A New Eddy-Viscosity Model for High Reynolds Number Turbulent Flows – Model Development and Validation, Comput. Fluids 24 (1995) 227–238.

[7] B. Magnussen, On the Structure of Turbulence and a Generalized Eddy Dissipation Concept for Chemical Reaction in Turbulent Flow, In: 19th Aerospace Sciences Meeting, 1981, doi:10.2514/6.1981-42.

[8] R.B. Peters N, Reduced Kinetic Mechanisms for Applications in Combustion Systems, Berlin, 1993.

[9] J.Y. Murthy, S.R. Mathur, A Finite Volume Method for Radiative Heat Transfer Using Unstructured Meshes, J. Quant. Spectrosc. Radiat. Transf. 12 (1998) 313–321.

[10] C. Hubbard, G.L. Tien, Infrared Mean Absorption Coefficients of Luminous Flames and Smoke, J. Heat Transfer 100 (1978) 235–239.

[11] V. Molkov, V. Makarov, M.V. Bragin, Physics and Modelling of Underexpanded Jets and Hydrogen Dispersion in Atmosphere, In: Physis of Extreme States of Matter, Institute of Problems of Chemical Physics, Russian Academy of Sciences, Chernogolovka, 2009, pp. 146–149.

[12] S. L. Brennan, D. V. Makarov, V. Molkov, LES of High Pressure Hydrogen Jet Fire, J. Loss Prev. Process Ind. 22 (2009) 353–359.

[13] Current Results Weather and Science Facts, California Average Relative Humidity, available from www.currentresults.com/Weather/California/humidity-annual.php.

[14] J. Lachance, A. Tchouvelev, A. Engebo, Development of Uniform Harm Criteria for Use in Quantitative Risk Analysis of the Hydrogen Infrastructure, Int. J. Hydrogen Energy 36 (2010) 2381–2388.

[15] J.R. Howell, Mengüc M.P., Siegel R., Thermal Radiation Heat Transfer, 6th Ed., Taylor and Francis Group, 2016.

[16] R. Schefer, B. Houf, B. Bourne, and J. Colton, Experimental Measurements to Characterize the Thermal and Radiation Properties of an Open-flame Hydrogen Plume, In: Proceedings of the 15th annual hydrogen conference and hydrogen expo, 2004.

[17] R. Heus, Maximum Allowable Exposure to Different Heat Radiation Levels, Instituut Fysieke Veiligheid, 2016, 29 p.

[18] S. Tretsiakova-McNally, D. Makarov, Lecture – Harm Criteria for People and Environment, Damage Criteria for Structures and Equipment, 2015.

Theoretical Physics-based Definition and Accurate Characterization of Lower Concentration Limit for Hydrogen-Air Mixtures

Kirillov I.A.

National Research Centre "Kurchatov Institute", Moscow, Russia
kirillov_ia@nrcki.ru

ABSTRACT

Understanding of nature and knowledge of the specific numerical values of the concentration limits for explosions in hydrogen-containing mixtures is important for existing nuclear power plants, future thermonuclear installations, multiple industrial applications in petrochemical and chemical industry, coming generation of the hydrogen-fueled vehicles and hydrogen energy infrastructure. In this paper a theoretical physics-based definition for the concentration limits of hydrogen-air gas explosions. Gas explosions have been and are attributed to the self-spreading frontal deflagration flames, whose evolution through flammable gas cloud after ignition results in the substantial baric effects. Specifically in the hydrogen-air mixtures within flammability limits two generic flames can propagate – self-propagating frontal deflagration flames (described by Zeldovich-Frank-Kamenetskii model) and confined in space the buoyant flame-balls (aka Zeldovich model). Fundamental concentration limit difference between these two generic types of flames could be regarded as a critical value for severity of hydrogen-air explosions. Within a Deflagration-to-Flame Ball Transition (DFBT) concentration range (7-12 vol% H_2) three traceable candidates exist – two empirical and one theoretical concentration limits. Relations between these candidates and their specific physico-chemical features are described. Targets for three future studies are proposed – one for direct (empirical or computational) evidence in support of a fundamental character of concentration limits under consideration and two studies for accurate quantitative characterization of the ultimate lower concentration limit for hydrogen-air explosions.

KEYWORDS: Hydrogen safety, explosion, concentration limits, deflagration flames, flame balls, deflagration-to-detonation-transition, deflagration-to-flame ball-transition.

INTRODUCTION

Understanding of nature and knowledge of the specific numerical values of the concentration limits for explosions in hydrogen-containing gaseous mixtures is important for existing nuclear power plants, future thermonuclear installations, multiple industrial applications in petrochemical and chemical industry, coming generation of the hydrogen-fueled vehicles and hydrogen energy infrastructure. Today an ample knowledge exists on the different modes of hydrogen-air explosions, encountered in industrial practice. The associated phenomena (deflagrations, detonations, fast flames, DDT, etc.) are described and characterized in traceable and verifiable manner in multiple research and engineering publications [1].

However, unambiguous and generally agreed definition of the concept of gas explosion is still absent. In pre-normative study [2] it was attempted to provide a consistent and non-contradictory definition of term "explosion" from three perspectives – a societal, regulatory and scientific ones. Focus of work [2] was on the inconsistencies in the prior art definitions of term "explosion" from viewpoint of the experts involved in developing Regulations, Codes and Standards (RCS).

Proceedings of the Ninth International Seminar on Fire and Explosion Hazards (ISFEH9), pp. 1367-1374
Edited by Snegirev A., Liu N.A., Tamanini F., Bradley D., Molkov V., and Chaumeix N.
Published by Saint-Petersburg Polytechnic University Press
ISBN: 978-5-7422-6498-9 DOI: 10.18720/spbpu/2/k19-115

Empirical-based approach [3-10] to hazardous hydrogen-air gas explosions definition and characterization is based on the “Slow-to-Fast Flame Transition” (SFFT) framework and/or “Deflagration-to-Detonation-Transition” (DDT) framework. In both cases the key physical process under consideration is a deflagration flame (laminar, turbulent or accelerated). Accelerated flames can result in the high baric loads, which are the inherent attributes of the explosions. Results of the experiments on the fast flame concentration limits are well documented and are used now in the multiple hydrogen safety applications. However, mentioned empirical approach has its own limits, restrictions and inconsistencies, which cannot be overcome without appropriate theoretical interpretation and refinement.

In order to reduce the uncertainties in the empirical-based estimations of the flame acceleration concentration limits, an alternative, model-based framework was proposed in [11]. The proposed theoretical approach to definition of the concentration limits for hydrogen-air explosions is based on “Deflagration-to-Flame-Ball-Transition” (DFBT) framework. It was hypothesized, that the fundamental concentration limits for deflagration flames are the ultimate edges (envelopes) for the empirical concentration limits for flame acceleration and for downward flame propagation. The quantitative estimations of the fundamental concentration limits for the plane hydrogen-air deflagration flames have been made using a non-empiric, kinetic-thermodynamic method, developed in [12]. It was revealed in [11] that the theoretical estimations for the fundamental concentration limits provide more conservative approximations of the lower concentration limits then the empirical ones.

From practical viewpoint (in the hydrogen-air gas explosion protection applications) it will be reasonable to clarify – what kind of the new studies (physical or computational ones) does it necessary to prepare and to perform for accurate characterization of the lower concentration limits for hydrogen-air explosions? This is the main goal of this paper.

The paper structure is as follows. For readers’ convenience the key concepts of the proposed theoretical approach are briefly described in Section 2 and 3 by citing previous works [11, 12]. The following questions are discussed accordingly - what are the fundamental concentration limits for plane deflagration flames? What are the relations between the empirical and fundamental concentration limits for deflagration flames propagation? In Section 4 three targets for the future physical (real) or computational (virtual) experiments are proposed. All proposed in Section 4 studies are focused on understanding of physico-chemical nature and further quantitative refining of the lower concentration limit for “Deflagration-to-Flame-Fall-Transition”.

FUNDAMENTAL CONCENTRATION LIMITS FOR PLANE DEFLAGRATION

In the non-empirical theoretical estimations [11, 13, 14] (see Table 1 below), term “fundamental concentration limit” means - an inherent physico-chemical property of a combustible mixture, independent of external influences, associated with or defined by specific experimental setup, particular measurement procedure or empirical observation criterion for a given combustion regime (flame ball, deflagration, detonation, etc.).

In [11] it was assumed that, fundamental lower concentration limit for deflagration flame propagation (see Fig. 1 below) is a natural border between two generic types of flames – the baric frontal deflagration flames, described by Zeldovich-Frank-Kamenetskii model, and the quasi-isobaric spherical flame balls, described by Zeldovich model.

Table 1. Fundamental concentration limits for the plane deflagration flames in premixed, quiescent, dry hydrogen-air mixtures under normal initial conditions (T_u = 298 K, P=1 atm), calculated "from-the-first-principles"

Lower limit, equivalence ratio (vol.% H_2)	Upper limit, equivalence ratio (vol.% H_2)	Criterion	Source
-	10.1 (80,9)	Kinetic: flammability exponent $\alpha = 1$	[13]
0.251 (9.5)	-	Kinetic-thermodynamic: $T_b = T_c$	[14]
0.247 (9.4)	8.697 (78.5)	Kinetic-thermodynamic: $T_b = T_c$	[11]

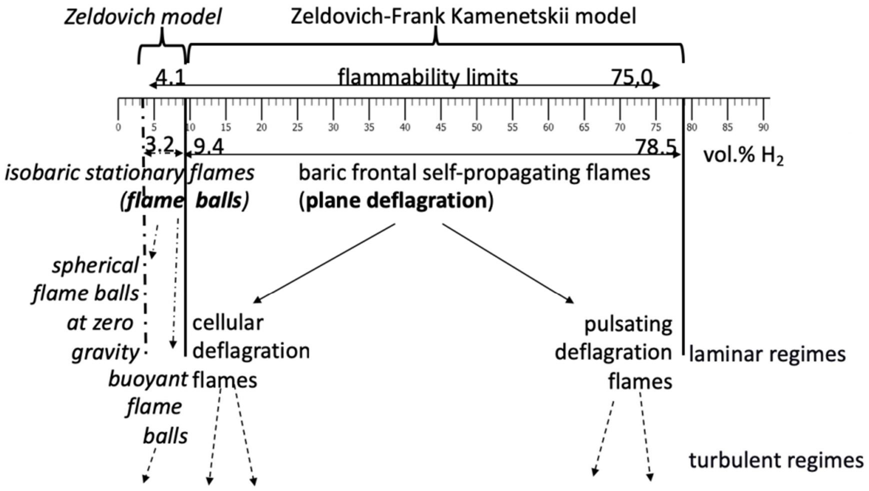

Fig. 1. Theoretical taxonomy of the concentration limits for the basic laminar combustion regimes in premixed, quiescent, dry hydrogen-air gas mixtures under normal conditions (1 atm, 298 K) [11].

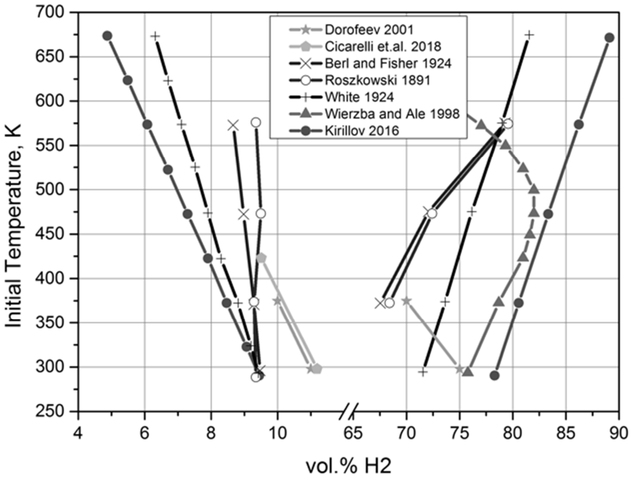

Fig. 2. Fundamental concentration limit for plane deflagration propagation model (black circles) as an ultimate limit for the different empirical data sets [11].

Comparison of the temperature dependencies of the empirical and theoretical concentration limits (shown in Fig. 2) for the different combustion regimes/models gives a rational basis for considering of the fundamental concentration limit for plane ZFK deflagration flame propagation as an ultimate (or edge) value for lower concentration limit of the hydrogen-air explosions. In Fig. 2, the theoretical envelope (shown by black circles) represents an envelope for the empirical concentration limits for

- the fast flames, shown by stars (Dorofeev 2001) and by white circles (Cicarelli 2018),
- downward flame propagation, shown by crests (+) (White 1924), by sign (x) (Berl 1924), by triangles (Wierzba 1998)).

RELATIONS BETWEEN EMPIRICAL AND FUNDAMENTAL CONCENTRATION LIMITS

Within a transient concentration range (namely 7-12 vol% H_2), which in fact is a "Deflagration-to-Flame-Ball-Transition" concentration range, the potential candidates on lower concentration limit for hydrogen-air explosions (i.e. the flames with baric effect) are listed in Table 2 below.

Table 2. Candidates for a lower concentration limit of the hydrogen-air flames with baric effect

Assessment method	Lower Concentration Limit, (vol.% H2)	Content of water vapor for normal initial conditions (1 atm, 298K) under the normal gravity	Combustion phenomenon / model	Ref.
empirical	7.7	dried	downward deflagration flame propagation	[15]
empirical	9.0	dried	downward deflagration flame propagation	[16]
empirical	9.45	partly dried	downward deflagration flame propagation	[17]
empirical	7.5 ∓ 0.5	dry	downward deflagration flame propagation	[18]
empirical	10.0	not explicitly reported	flame acceleration in horizontal tube	[4]
empirical	11.0	not explicitly reported	flame acceleration in horizontal tube	[8]
theoretical	9.4	dry	plane deflagration flame propagation	[11]
theoretical	9.5	dry	plane deflagration flame propagation	[14]

In Table 2, three families of the numerical values of concentration limits for combustion phenomena/models are listed:

- empirical limits for flame acceleration,
- empirical limits for downward flame propagation,
- theoretical limits for plane ZFK deflagration flame propagation.

All families of the concentration limit values have their own uncertainties (aleatoric and/or epistemic). For example, now

- experiments on downward flame propagation [15-18] have large variability in the boundary (closed or open at firing end, radius of test tube) and initial (dry or wet gas mixture) conditions;

- experiments on flame acceleration [4, 8] have been performed in horizontal tubes only. Information on influence of buoyancy on flame acceleration phenomenon in vertical tubes is absent now;
- non-empiric calculations [14, 11] of ZFK flame propagation have been made for plane fronts only. They do not take into account cellular structure of deflagration flames in ultra-lean (< 12 vol% H2) hydrogen-air gas mixtures and the associated effects of preferential diffusion and Soret on internal structure of the deflagration reaction front.

Due to mentioned uncertainties in the available now numerical values of concentration limits for combustion regimes/models, which can be regarded as lower concentration limit for hydrogen-air explosions, it is necessary to refine their accuracy in a new studies.

TARGETS FOR FUTURE ACCURATE CHARACTERIZATION OF LOWER CONCENTRATION LIMIT FOR HYDROGEN-AIR EXPLOSIONS

Determination of the ultimate lower concentration limit for hydrogen-air explosions with higher (then now) accuracy can be made either in future empirical experiments or in 3-dimensional high fidelity computations.

In both cases it will be necessary to perform a set of tests (real or virtual), which shall be in compliance with the following requirements

- increment 0.05 vol% H_2 in variation of hydrogen concentration at least,
- control of humidity level in hydrogen-air gas mixtures. A high sensitivity of fundamental concentration limits upon initial steam concentration in hydrogen-air mixture is a well-established fact [19].

Direct experimental evidence on existence of two generic combustion flames in premixed hydrogen-air gas mixtures under zero gravity conditions

For direct experimental evidence, that deflagration flames and flame ball-like flames have principally different macroscopic behavior the following experiment under zero gravity conditions is required.

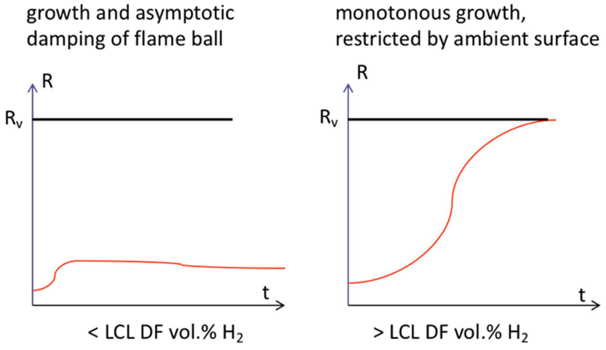

(a) (b)

Fig. 3. Critical behavior of flame front during variation of chemical composition in Deflagration-to-Flame Ball-Transition concentration range (7 -12 vol% H_2) under zero gravity conditions.

In closed vessel with characteristic size R_v ignition of flammable (within concentration range 4.1-75 vol% H_2) hydrogen-air gas mixtures will results in one of the two possible types of combustion front behavior. In cases of the hydrogen-air mixtures, which are leaner (see Fig. 3a) then Lower

Concertation Limit for Deflagration propagation (LCL DF), an initial ignition kernel will grow up into spherical flame ball with limited (in comparison with vessel size) radius, defined by chemical composition, temperature and pressure of mixture. In case of the hydrogen-air mixtures, which are richer (see Fig. 3b) then Lower Concertation Limit for Deflagration propagation, an initial ignition kernel converts into self-expanding flame front, which will occupy all available space with combustible mixture and will be extinguished at border of test vessel.

Two targets for future experiments under zero gravity conditions are:

- determination of the numerical value of the Lower Concentration Limit for Deflagration propagation and its comparison with candidates from Table 2,
- determination of possible stochastic nature of Deflagration-to-Flame Ball-Transition.

Principally different dependence of maximal flame temperature upon hydrogen concentration in the deflagration flames and in the flame balls

On the base of theoretical analysis of the fundamental concentration limits in [11], it is possible to formulate a goal for the future physical or computational experiments, aimed at exploring a second direct evidence, that deflagration flames and flame ball-like flames have the different physical natures and, hence, exhibit different macroscopic behavior during gradual variation of the hydrogen concentration in initial gas mixture under the Earth gravity conditions.

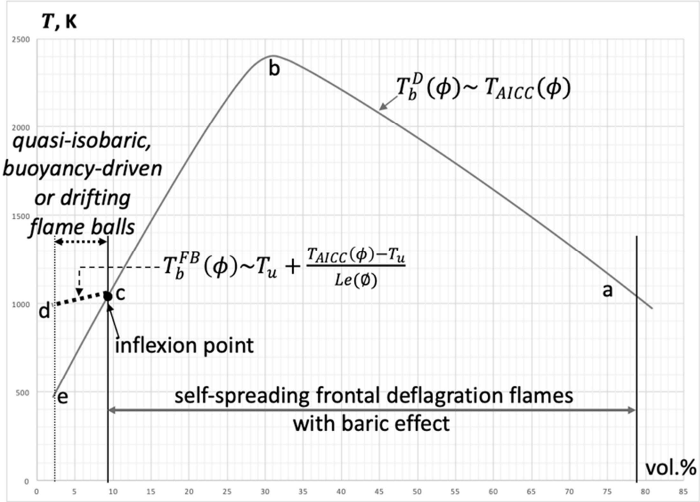

Fig. 2. Two different types of maximal flame temperature dependence upon hydrogen concentration in hydrogen-air mixtures.

During a gradual decrement of hydrogen concentration in the hydrogen-air mixtures (it can be named as a Deflagration-to-Flame Ball-Transition, DFBT) maximum flame temperature T_b will follow (will be symbatic to) two different asymptotic curves (see Fig. 4):

1) path "a-b-c" on Fig. 4, where $T_b^D(\phi)\sim T_{AICC}(\phi)$ in concentration range [9.4 – 78.5] vol.% H_2 and $T_{AICC}(\phi)$ is a dependence of the adiabatic isobaric complete combustion temperature upon hydrogen concentration for given initial conditions (temperature T_u and pressure p_u). Function $T_{AICC}(\phi)$ is shown by continuous line "a-b-c-e";

2) path "c-d" on Fig. 4, where $T_b^{FB}(\phi)\sim T_u+\frac{T_{AICC}(\phi)-T_u}{Le(\emptyset)}$ in concentration range [3.35 – 9.4]

vol.%H_2. Here $Le(\phi)$ is a dependence of the effective Lewis number [20] for hydrogen-air mixture upon stoichiometric ratio for a given initial pressure p_u. Function $T_b^{FB}(\phi)$ is shown below by dotted line "c-d". Due to impact of the Lewis number, it is dependence upon ϕ is less steep than for the deflagration case.

Dependence of the lower concentration limit for hydrogen-air flame acceleration upon propagation direction with respect to the Earth gravity

All currently available empirical data on the concentration limits for deflagration flame acceleration have been obtained in medium (10^0 m) [8] or in large (10^1-10^2 m) scale [3, 4] experimental tubes, allocated in horizontal direction (perpendicular to the Earth gravity direction).

However, in the near-limit deflagration flames (for 7–12 vol% H_2) role of buoyancy is substantial [21]. It will be reasonable to expect, that in the experimental tubes, allocated in vertical direction (collinear to the Earth gravity direction), the concentration limits for deflagration flame acceleration will be dependent upon propagation direction – one quantitative value for flame acceleration in upward direction, and the other ones for flame acceleration in downward direction.

ACKNOWLEDGMENTS

Author is grateful to the anonymous reviewers for their careful reading of paper draft, critical comments and insightful suggestions. This work has been partially supported by the Russian Ministry of Science and Education.

CONCLUSIONS

1. In spite of a long term tradition in experimental and theoretical studies of the hydrogen-air combustion a clear understanding – that frontal self-propagating deflagration flames and confined flame balls are the two principally different combustion regimes existing within known flammability limits – is still absent in hydrogen safety and industrial safety professional communities.
2. Empirical evidences and theoretical arguments are described in support of the author's hypothesis, that fundamental lower concentration limit for deflagration flame propagation is a natural border between these two generic types of flames – baric frontal deflagration flames, described by ZFK-like models, and quasi-isobaric buoyant flame balls, simulated on the base of ZFB-like models.
3. In the first time, a theoretical taxonomy of the concentration limits for the basic laminar combustion regimes in premixed, quiescent hydrogen-air gas mixtures is proposed on the base of "Deflagration-to-Flame-Ball-Transition" (DFBT) framework.
4. Uncertainties for accurate definition of the three families of concentration limits for laminar combustion are described for the Deflagration-to-Flame Ball-Transition (DFBT) range (7-12 vol.% H_2) in hydrogen-air gas mixtures.
5. Targets for three future studies are proposed. These studies can test the predictive capability of the proposed theoretical instruments – "Deflagration-to-Flame-Ball-Transition" (DFBT) framework, concept of "fundamental concentration limits" and kinetic-thermodynamic model for their quantitative estimation. One study is aimed at the exploration of the direct evidence in support of a fundamental character of concentration limits under consideration. Two other studies are focused on accurate quantitative characterization of the ultimate lower concentration limit for the hydrogen-air explosions.

REFERENCES

[1] A. Koutchourko , et al., State-of-Art and Research Priorities in Hydrogen Safety, ICHS 2013, paper 229.

[2] J.O. Keller, et al., What is an explosion? Int. J. Hydrogen Energy 39 (2014) 20426-29343.

[3] O. Peraldi, R. Knystautas, J.H. Lee, Criteria for transition to detonation in tubes, Proc. Combust. Inst. 21 (1986) 1629-1637.

[4] Dorofeev. S.V., et al, Effect of Scale and Mixture Properties on Behaviour of Turbulent Flames in Obstructed Areas, IAE-6137/3 or FZKA-6268, 1999.

[5] M. Kuznetsov, et al., Effect of Obstacle Geometry on Behavior of Turbulent Flames, IAE-6137/3 or FZKA-6328, 1999.

[6] S. Dorofeev, et al., Evaluation of limits for Effective Flame Acceleration in Hydrogen Mixtures, IAE-6150/3 or FZKA-6349, 1999.

[7] S.B. Dorofeev, M.S. Kuznetsov, V.I. Alekseev, A.A. Efimenko, W. Breitung, Evaluation of limits for effective flame acceleration in hydrogen mixtures, J. Loss Prev. Process Ind. 14 (2001) 583-589.

[8] G. Ciccarelli, N. Chaumeix, A.Z. Mendiburu, K.N. Guessan, A. Comandini, Fast-flame limit for hydrogen/methane-air mixtures, Proc. Combust. Inst. 37 (2019) 3661-3668.

[9] G. Cicarelli, S.B. Dorofeev, Flame acceleration and transition to detonation in ducts, Progr. Energy Combust. Sci. 34 (2008) 499-5508.

[10] R. Scarpa, E. Studer, S. Kudriakov, B. Cariteau, N. Chaumeix, Influence of initial pressure on hydrogen/air flame acceleration during severe accident in NPP, Int. J. Hydrogen Energy (2018), in press, https://doi.org/10.1016/j.ijhydene.2018.06.160

[11] I.A. Kirillov, Physics-based Approach for Reduction Uncertainties in Concentration Limits of “Slow-to-Fast” Flame Transtion in Hydrogen-Air Gas Mixtures, Hydrogen Management in Severe Accidents, Technical Meeting EVT1701911, 25-28 September 2018, Vienna, TECDOC, IAEA, in press.

[12] I.A. Kirillov, On fundamental concentration limits for basic regimes of combustion in premixed hydrogen-air gas mixtures, In: Research Seminar “Physico-chemical kinetics in gas dynamics”, Institute of Mechanics, Moscow State University, 7th April, 2016, Moscow, Russia, http://www.imec.msu.ru/content/education/seminars/chemphys/2016-04-07.pdf (in Russian).

[13] C.K. Law, F.N. Egolfopoulos, A Unified Chain-Thermal Theory of Fundamental Flammability Limits, Proc. Combust. Inst. 24 (1992) 137-144.

[14] D. Fernandez-Galisteo, Numerical and Asymptotic Analyses of Lean Hydrogen-air Deflagrations, PhD thesis, Universidad Carlos III De Madrid, 2009.

[15] A. La Fleur, Ternary and Quaternary Explosion Regions and Le Chatelier’s Formula, Rec. Travaux. Chim. Pays. Bas. 56 (1937) 442-473.

[16] A.G. White, Limits for the Propagation of Flames in Inflammable Gas-Air Mixtures. I. Mixtures of Air and One Gas at the Ordinary Temperature and Pressure, J. Chem. Soc. 125 (1924) 2387-2396.

[17] H.W. Thompson, Ztschr. Physikal. Chem, v.B18 (1932) 219-240.

[18] H. Cheikhravat, N. Chaumeix, A. Bentaib, C.-E. Paillard, Flammability limits of hydrogen-air mixtures, Nuclear Technology 178 (2012) 5-16.

[19] H.F. Coward, G.W. Jones, Limits of Flammability of Gases and Vapors, Bulletin 503, Bureau of Mines, 1952.

[20] F.A. Williams, Combustion Theory, Benjamin/Cummings, 1985.

[21] V.N. Krivulin, L.A. Lovachev E.A. Kudryavtsev, A.N. Baratov, Combust. Explos. Shock Waves 11 (1975) 759-764.

Development of CNAFT Model for Lower Flammability Limits of Hydrogen Mixtures for Severe Accident Analysis Code in Nuclear Power Plant

Jeon J.[1], **Jung H.**[1], **Kim S.J.**[1,2,] *

[1] *Department of Nuclear Engineering, Hanyang University, Seoul, Republic of Korea*
[2] *Institute of Nano Science & Technology, Hanyang University, Seoul, Republic of Korea*
**Corresponding author's email: sungjkim@hanyang.ac.kr*

ABSTRACT

After Fukushima-Daiichi accident, predicting lower flammability limits (LFL) of hydrogen has became an ever-important task for safety of nuclear industry. Experimental identification of LFL for all mixtures in accident conditions is considerably difficult due to wide variety of mixture types. For this reason, we have been developed a calculated non-adiabatic flame temperature (CNAFT) model to facilitate prediction of LFL. The uniqueness of this model is its ability to incorporate heat loss due to radiative heat transfer from flame during propagation using the CNAFT coefficient. The CNAFT model is more consistent with the experimental results for various mixtures compared with the previous model, which relied on the calculated adiabatic flame temperature (CAFT) to predict the LFL. However, the current model does not make a reasonable prediction of LFL under mixtures containing steam. Because steam is classified as radiating species, the presence of steam in the initial condition results more radiant heat loss. Therefore, we developed the extended CNAFT model through simulation of a seven-step combustion mechanism to consider steam effect on radiant heat loss. The extended model shows the maximum relative error with experimental results for various mixture types about 13 % even for containing steam. This study suggests that extended CNAFT model can be effectively utilized for flammability prediction in severe accident analysis code.

KEYWORDS: Hydrogen, lower flammability limit, radiative heat transfer, CAFT, CNAFT.

INTRODUCTION

After Fukushima-Daiichi accident, Korea Hydro & Nuclear Power (KHNP) classified hydrogen combustion phenomena as a major threat to containment integrity [1]. The lower flammability limit (LFL) is the minimum fuel concentration, at which a flame can propagate. If the mole fraction of the released hydrogen exceeds the LFL, a more detailed risk analysis of the NPP should be performed to verify the potential risk of flame acceleration (FA) and detonation. Because hydrogen explosions diverting to FA or detonation may add significant dynamic pressure and temperature loads that can affect containment integrity [2]. In severe accident analysis, it is of obvious importance to clarify the LFL of hydrogen mixtures under different mixture conditions. The flammability limits of various mixtures have been determined through many experimental studies [3-7]. Nevertheless, experimental identification of LFL for all mixtures during severe accident is considerably difficult due to wide variety of mixture types. Evaporation of the coolant in reactor coolant system (RCS) can cause a high concentration of steam and various gases including carbon dioxide can be released by the molten corium-concrete reaction (MCCI) in reactor cavity [8, 9]. The elevated temperature and pressure also contribute to the variety of mixture conditions. However, even the MELCOR code, which is the regulatory code of severe accident analysis developed by the US Nuclear

Proceedings of the Ninth International Seminar on Fire and Explosion Hazards (ISFEH9), pp. 1375-1385
Edited by Snegirev A., Liu N.A., Tamanini F., Bradley D., Molkov V., and Chaumeix N.
Published by Saint-Petersburg Polytechnic University Press
ISBN: 978-5-7422-6498-9 DOI: 10.18720/spbpu/2/k19-75

Regulatory Committee, adopts a rather simple logic for predicting the LFL. For example, in case of upward flame propagation, the code uses a constant LFL of 4.1 vol% regardless of the mixture conditions [10]. Such simplified LFLs can increase the uncertainty of the results on the hydrogen risk of NPPs.

Therefore, it has been considered mandatory to develop a theoretical model to reasonably predict the LFL in contingency with mixture conditions. Recently, Vidal et al. pointed out that calculated adiabatic flame temperature (CAFT) is a powerful model for estimating the LFL of gaseous mixtures [11]. The model has the advantage that it does not involve the complex algorithms considering peculiarities of the chemical kinetics of gaseous organic substances in air. It concluded that the threshold peak temperature for flame propagation was proportional to the CAFT. However, researchers have found that relying on the CAFT concept tends to result in inconsistent accuracy depending on the mixture conditions as shown Fig. 1. The mixture conditions for this model validation is shown in Table 1. This is especially true when the initial temperature of mixture is high or the diluent gas is helium or steam. The limitations of the CAFT model came from its reliance on an adiabatic value whereas actual flame propagation involves heat loss mechanisms. Many thermal theories of the flammability limits attributed the existence of the LFL to heat loss from the reaction zone [12-14]. The amount of heat loss substantially affects the peak flame temperature and hence determines the intrinsic LFL value of the mixture.

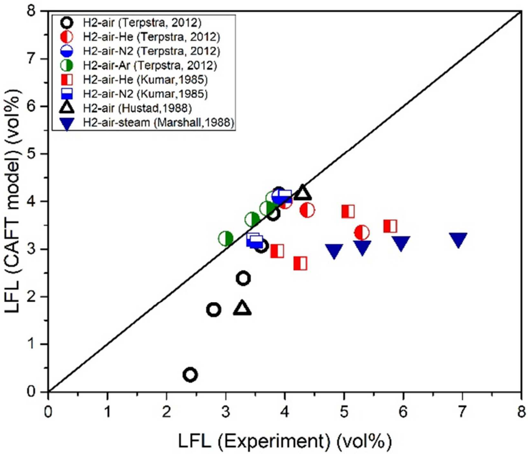

Fig. 1. Validation of CAFT model in various mixture conditions

For this reason, Jeon et al. proposed a calculated non-adiabatic flame temperature (CNAFT) model to predict the LFL considering heat loss mechanism together with the concept of the CAFT model [15]. The proposed model analysed the physics of flame propagation in a non-adiabatic condition that focused on heat loss mechanisms during upward propagation. It confirmed that radiative heat loss dominantly determines the total amount of the heat loss from the reaction zone to the ambient environment. However, the current CNAFT model does not make a reasonable prediction of LFL under mixture conditions with steam. Because steam is classified as radiating species, the presence of steam in the initial condition results more radiant heat loss. Since most mixtures during nuclear reactor accident contains steam, the current model has limitation on the hydrogen risk of NPPs.

Therefore, the objective of this study is to extend the CNAFT model to predict mixtures with steam. The amount of radiant heat loss was estimated based on the optically thin radiation model that can be used for lean hydrogen mixture conditions. Also seven-step chemical kinetics was solved for prediction of steam concentration in burned gas. As it becomes able to predict the increased amount of heat loss by higher steam concentration, the range of model reliability was extended to H_2-Air-Steam. The validation was also carried out for mixture conditions in Table 1.

MODELLING

Concept of calculated adiabatic flame temperature

According to Arrhenius theory [16], the peak temperature occurring at the flame front determines the chemical reaction rate because the number of molecules participating in the reaction increases by the temperature. The threshold peak temperature is the temperature that can produce the minimum reaction rate to sustain propagation [17]. Previous studies concluded that the threshold peak temperature being determined by fuel type was proportional to the CAFT of the limiting mixtures. Because direct prediction of the peak temperature is almost impossible, representing the peak temperature using the CAFT was frequently done for LFL predictions in the previous studies [11]. The CAFT can be calculated from the energy balance of the reaction at equilibrium as shown in Eq. (1), where $\Delta H_{f,i}^{0}$ is the formation enthalpy of species i and T_{ref} is the reference temperature. The average heat capacity $\bar{c}_{p,i}^{0}$ was calculated for each compound using the corresponding adiabatic flame temperature,

$$\sum n_i \left[\Delta H_{f,i}^{0}\right]_{reactants} - \sum n_i \left[\Delta H_{f,i}^{0} + \bar{c}_{p,i}^{0}\left(T_{CAFT} - T_{ref}\right)\right]_{products} = 0 \,. \tag{1}$$

However, the limitation of this concept was confirmed through experimental results in Table 1. These experiments identified the LFL near atmospheric pressure according to initial conditions such as the diluent concentration or initial temperature of the mixture. The H_2-Air-Steam flammability data was fit with the empirical equation based on results of Marshall's experiment Based on the conditions of the limiting mixtures, the value of CAFT was determined by Eq. (1). It should be noted that, although the temperature remains nearly constant for some mixtures at approximately 600 K, other mixtures show significant differences. This is especially true when the initial temperature is high or the diluent gas is steam and helium. As a result, it was confirmed that the model showed inconsistent accuracy depending on the mixture conditions as shown Fig. 1. These inconsistent with experimental results was also identified by Terpstra [7]. The reason was due to the simplified assumption of adiabatic flame expansion. In reality, however, flames do not propagate under adiabatic conditions, and heat loss processes play a part. This implies that the effects of heat loss depending on the mixture conditions cannot be ignored when predicting the LFL. In other words, the CAFT model can be applied in limited cases because it cannot account for heat transfer from the reaction zone to the environment. For this reason, Jeon et al. proposed a CNAFT model to predict the LFL considering heat loss mechanism together with the concept of the CAFT model.

Table 1. Various experimental results used in model validation

Reference	Mixture	T_i (°C)	Diluent (vol%)	CAFT (K)
Kumar [3]	H_2-O_2-He	20-100	0-40	670-800
	H_2-O_2-N_2	20-100	0-40	590-630
Hustad [4]	H_2-Air	20-200	0	610-720
Marshall [5]	H_2-Air-Steam	100-120	0-40	730-850
Terpstra [7]	H_2-Air	20-300	0	580-750
	H_2-Air-He	20	0-50	580-780
	H_2-Air-Ar	20	0-60	~580
	H_2-Air-N_2	20	0-20	~590

Non-adiabatic flame temperature model

As many theories have concluded, the effects of the heat loss from the reaction zone to the post-reaction zone play an important role in determining the peak temperature. That is to say, the heat loss mechanism ultimately affects the flammability limit of mixtures [12-14]. The essential heat loss mechanisms for laminar flame are the convective and radiative heat transfer from the flame to the environment [18]. However, convective transfer can be ignored if the tube diameter is larger than a certain value. Fernandez-Galisteo explained that it is because the burnt temperature is close to crossover value for lean flames close to the flammability limit [19]. This approach can be applied for a standard apparatus for determining the flammability limits, as done by Coward and Jones. Such apparatus consisted of a vertical tube 51 mm in diameter and 1.8 m long, closed at the upper end and open to the atmosphere at the bottom [20]. Therefore, the effect of radiative heat loss has been dominantly adopted as the explanation of the flammability limit [21].

The effects of radiative heat loss from the flame to the ambient environment can be classified as conduction of heat into the post-reaction zone, which is cooled via radiative heat loss $q_{rad,1}$ and radiative heat loss from the reaction zone itself, $q_{rad,2}$ [18]. First, the heat conduction into the post-reaction zone is caused by the temperature gradient near the end of the reaction zone. In steady-state one-dimensional flame propagation, the energy balance in the post-reaction zone can be defined as in Eq. (2), where R is the radiative volumetric heat loss and depends on the mixture properties and the local temperature distribution in the post-reaction zone, and k is the thermal conductivity. In this study, the effect of a specific flame structure depending on mixture conditions was not considered. Because the combustion regime of the observed cap-like flames at the ultrelean H_2-Air mixture is not fully understood [22]. Although the approach with the one-dimensional energy equation is difficult to depict local heat transfer phenomena, it makes possible to estimate sum of heat loss in the reaction zone. Mayer noted that the diffusion term on the left is much smaller than the convection term in the region of peak flame temperature over the range of mass flow rates in typical flame propagation [18]. It means that the $q_{rad,1}$ can be calculated with peak temperature gradient under the influence of radiative heat loss as shown in Eq. (3). The equation consists of several variables determined by the mixture properties. The thermal conductivity value is based on flame front temperature, while the density and specific heat are based on the unburned gas temperature,

$$\rho_u c_p S_u \frac{dT}{dx} - \frac{d}{dx} k \frac{dT}{dx} = -R(T) \,, \tag{2}$$

$$\left(\frac{dT}{dx}\right)_{x=x_f} = -\frac{R(T_f)}{\rho_u c_p S_u(T_f)} \rightarrow q_{rad,1} = -k_f \left(\frac{dT}{dx}\right)_{x=x_f} = k_f \frac{R(T_f)}{\rho_u c_p S_u(T_f)} \,. \tag{3}$$

Second, the radiative heat loss rate from the reaction zone itself can be calculated via integration of the space-averaged radiative volumetric heat loss. However, Lakshmisha et al. proved that the fraction of $q_{rad,2}$ was very small compared to heat release rate for CH_4-Air. They numerically solved the equations for premixed flames near lean flammability limits, considering detailed chemistry and variable properties [23]. Recently, Liaw et al. confirmed that the effect of $q_{rad,2}$ is non-sizable on the H_2-Air mixtures as well as the CH_4-Air mixture by comparison between their model and experimental results [24]. These conclusion are also consistent with the experimental observations of Shoshin et al. that limit flame extinction behavior is connected with the formation of the stagnation zone of combustion products. They pointed out that the reaction zone is effectively cooled by heat conduction to the stagnation zone, which rises upward together with flame and cooled due to radiation heat loss [25]. As a result, most of the heat loss needed for calculating the peak temperature can be estimated only by considering $q_{rad,1}$.

As shown in Eq. (4), the magnitude of the radiative heat loss rate can be determined using the thermal diffusivity, flame speed, and volumetric heat loss rate. In ultralean H_2-Air flames, the laminar flame speed is severely affected by cellular instabilities as the stretch rate approaches zero. This is the profound characteristic for unstretched flames that the Lewis number is much smaller than one [26]. The flame speed of the limiting mixtures is independent of the mixture properties and its finite value can be calculated from the results presented by Davies and Taylor. Their observations were derived from experimental results, which proved that an upward propagating flame at the limit of flammability has properties in common with a rising Taylor bubble of hot gas [27]. On the other hand, according to a previously proposed optically thin radiation model, volumetric heat loss rate is determined by the threshold peak temperature and the presence of radiating species [28]. Because the threshold peak temperatures of the limiting mixtures were assumed to be invariable, the volumetric heat loss rate was considered to be constant with the exception of mixtures containing the radiating species. Consequently, the radiative heat loss rate $q_{rad,1}$ can be estimated using a linear function of thermal diffusivity through experimental and theoretical evidence. In conclusion, Jeon et al. proposed a parameter of calculated non-adiabatic flame temperature (CNAFT) through Eq. (5) to predict the LFL for each mixture condition [15]. He expected that the limiting hydrogen mixtures have similar value of CNAFT as similar with concept of CAFT. Thermal diffusivity is divided by the molar concentration C to predict heat loss in mole units. This coefficient was defined as a CNAFT coefficient, π, which can be calculated as the mean value of the physical properties of each gas component of the mixture,

$$q_{rad,1} = k_f \frac{R\left(T_f\right)}{\rho_u c_p S_u\left(T_f\right)} = \alpha \frac{R\left(T_f\right)}{S_u\left(T_f\right)} \sim \alpha \,, \tag{4}$$

$$\sum n_i \left[\Delta H^0_{f,i}\right]_{reac\tan ts} - \sum n_i \left[\Delta H^0_{f,i} + \bar{c}^0_{p,i}\left(T_{CNAFT} - T_{ref}\right)\right]_{products} = Q_{rad,1} \sim \alpha/C \,. \tag{5}$$

The mechanistically derived Eq. (5), which considers that radiative heat loss and the linearly proportional CNAFT coefficient, was validated using the experimental results of Terpstra and Marshall presented in Table 1. To validate this linear relationship, a reference mixture was required, and this condition was selected to be the H_2-Air mixture at 20 °C. It is because the heat loss effects on LFL is noticeable from the CNAFT coefficient on the ambient air condition. The LFL prediction in the adiabatic condition does not make noticeable error until the coefficient value at the reference mixture. Thus, the difference in heat loss was inversely estimated using Eq. (11) based on 581 K which is value of CAFT at the reference mixture. The difference in CNAFT coefficient was also calculated based on the reference mixture. The thermal conductivity used for calculating the coefficient was substituted with a corresponding value at this temperature. Figure 2 shows the difference in volumetric heat loss for each mixture based on their initial mole number before the reaction. As a result, a proportional relationship between the two variables was confirmed and Eq. (6) was determined by a least-squares analysis with R-square value of R^2-0.98. It implies that they show a strong linear relationship except for H_2-Air-Steam. Also, it should be noted that the elevated initial temperature mixtures or helium mixtures have higher CNAFT coefficient than other mixtures. Because these two types of mixtures are representative mixtures, predicting the LFL is difficult with the CAFT model, we concluded that there is a direct relationship between the overestimated CAFT and the high CNAFT coefficient of these limiting mixtures. In other words, a mixture having a high coefficient requires more combustion heat to compensate for its higher radiative heat loss than other mixtures

$$Q_{rad,1}(\pi) = 0.246\left(\pi - \pi_{air,20^\circ C}\right),\ \pi = \alpha/C\ \ 10^3\ \mathrm{cm^5/(mol\cdot s)}. \tag{6}$$

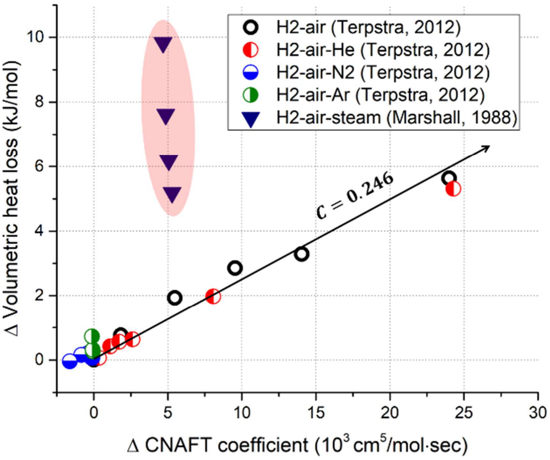

Fig. 2. Linear relationship between the CNAFT coefficient and radiative heat loss.

THE ROLE OF STEAM IN RADIANT HEAT LOSS

The reason why the linear relation between the CNAFT coefficient and radiative heat loss was not identified only for the H_2-Air-Steam mixtures can be explained by the optically thin approximation. Since the flame thickness at the flammability limits was very small, the assumption of optically thin conditions is justified by referring to the Hottel's charts. Therefore, the volumetric radiative heat loss can be calculated by Eq. (7) [20], where σ is the Stefan-Boltzmann constant, T_0 is the ambient temperature, p_{steam} is the partial pressure of steam and a_{steam} is the Planck's mean absorption coefficient of steam. The independence of the peak flame temperature and mixture conditions remains as before. It should be noted that, in the case of a mixture containing steam, the volumetric rate increases proportionally as the partial pressure of steam increases. In other words, the volumetric rate cannot be assumed to be constant as in a mixture without steam. Therefore, the total amount of radiative heat loss during flame propagation of a mixture with steam under isobaric condition can be estimated by Eq. (8). The reference value $X_{steam,ref}$ is the steam mole fraction at the flame front during flame propagation in mixtures without steam. Even if there is no steam in the initial mixture, steam can be produced through the combustion process. However, it was deduced that the variation of the steam concentration was negligible in other diluent types through confirmation of the proportional relationship between the CNAFT coefficient and the amount of heat loss. It is because the difference of initial hydrogen concentration between the limiting mixtures is sufficiently small. Therefore, the amount of heat loss in a mixture containing steam can be estimated if the value of steam mole fraction at the flame front during propagation $X_{steam,flame\ front}$ can be predicted,

$$R = 4\sigma\left(T_f^4 - T_0^4\right) p_{steam} a_{steam}\ , \tag{7}$$

$$Q_{rad,1}\left(\pi\right) = 0.246\left(\pi - \pi_{air,20°C}\right)\left(X_{steam,\,flame\ front} / X_{steam,ref}\right). \tag{8}$$

Fernandez-Gasliteo showed, for hydrogen-air mixtures that are very fuel lean, the seven-step mechanism including three reversible shuffle reactions 1-3 and the irreversible recombination 4f suffices to describe accurately progress of combustion as shown Table 2. Therefore, in this study, the mechanism was solved to predict the variation of the steam mole fraction during combustion process [29]. Because the rate coefficient in the Arrhenius form $\mathrm{k} = AT^n\exp(-T_a/T)$ constants for all reactions, the reaction rate is calculated solely as a function of temperature. The backward rate of reactions 1-3 are approximate fits calculated from the forward parameter using the thermodynamic data. In calculating the pressure dependence of the reaction rate constant, the value of falloff factor F_c was determined by the previous computation by Troe [30].

Table 2. The 7-step mechanism with rate coefficient in the Arrhenius form [24]

Reaction		A	n	$T_a[K]$
$\mathbf{1. H + O_2 \leftrightarrow OH + O}$		3.52E+16	-0.7	8590
$\mathbf{2. H_2 + O \leftrightarrow OH + H}$		5.06E+04	2.67	3166
$\mathbf{3. H_2 + OH \leftrightarrow H_2O + H}$		1.17E+09	1.3	1829
$\mathbf{4f. H + O_2 + M \rightarrow HO_2 + M *}$	k_0	5.75E+19	-1.4	0
	k_∞	4.65E+12	0.44	0
$\mathbf{5f. HO_2 + H \rightarrow OH + OH}$		7.08E+13	0	148
$\mathbf{6f. HO_2 + H \rightarrow H_2 + O_2}$		1.66E+13	0	414
$\mathbf{7f. HO_2 + OH \rightarrow HO_2 + O_2}$		2.89E+13	0	-250

In the case of combustion of limiting mixture with very low flame speed, the structure at the flame front can be predicted by computation of homogenous ignition above crossover temperature. Figure 3 shows the verification of our computation by a typical time history obtained ignition above crossover temperature for a stoichiometric H_2-Air mixture with San Diego mechanism obtained from Ref. [19]. It was identified that the seven-step chemistry provides a sufficiently accurate results in the temporal evolution of hydrogen mole fraction. Although the temperature change shows a slight difference, it is clear that this difference will be further reduced in lean conditions. It means that the steam mole fraction at flame front during propagation of hydrogen lean flame can be predicted by this simplified chemistry.

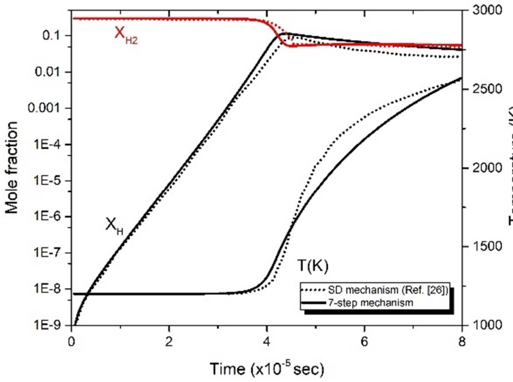

Fig. 3. Code validation for ignition of stochiometric H_2-Air mixture in a homogenous adiabatic reactor at constant atmospheric pressure and initial temperature $T = 1200$ K.

Figure 4 shows the temporal evolution of hydrogen and steam mole fraction for each limiting mixture during homogenous ignition above crossover temperature. When the steam concentration is zero, the LFL is 3.9% and it burns completely in a very short time. This aspect is equally founded in the other three cases with steam, and the steam mole fraction in burned gas is very close to the sum of initial hydrogen and steam mole fraction. This complete combustion in the hydrogen lean condition with steam was identified not only in this homogeneous ignition simulation, but also in a computation of steady planar deflagration obtained with COSILAB code [19]. However, as mentioned, the specific modes of flame propagation were observed such as cap-like flames in ultralieean H2-Air flames. These observed natures can affect the steam concentration near the end of the reaction zone. This is our further study.

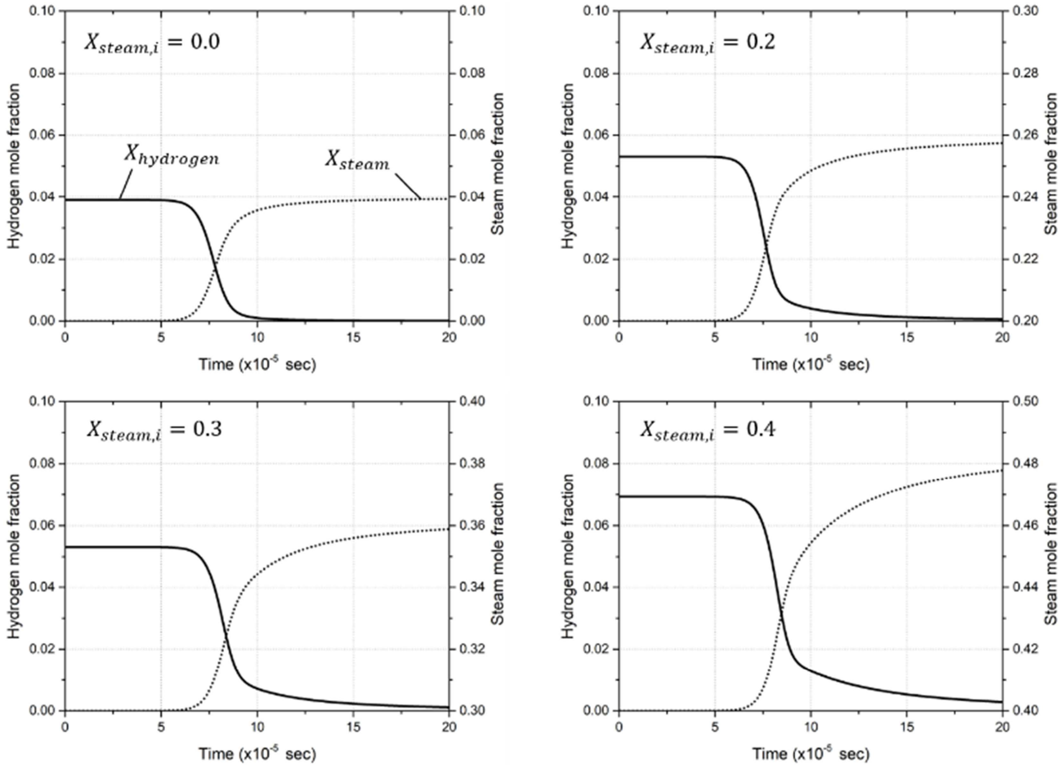

Fig. 4. Temporal evolution of $X_{hydrogen}, X_{steam}$ for each limiting H2-Air-Steam mixture as obtained from numerical integrations with 7-step mechanism of Table 1 ($X_{steam} = 0.0, 0.2, 0.3, 0.4$).

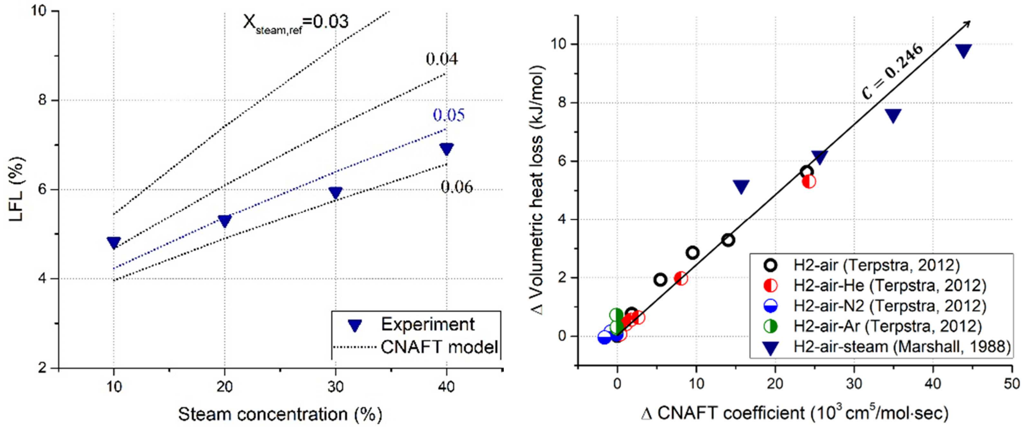

Fig. 5. Sensitivity analysis for determination of optimum reference steam mole fraction (left) and linear relationship between the extended CNAFT coefficient and radiative heat loss with $X_{steam,ref} = 0.05$ (right).

In conclusion, the calculation of steam concentration during flame propagation under each limiting mixture condition can be substituted by a complete combustion approach as shown Eq. (9). The amount which can be estimated by the initial condition including CNAFT coefficient and initial mole fraction increases proportionally as the sum of initial hydrogen and steam mole fraction increases. The reference steam mole fraction, which was neglected to predict the heat loss of mixtures without steam, was determined by sensitivity analysis. Because the mixtures without steam produce steam at flame front as hydrogen combustion proceeds, the reference mole fraction will be in the LFL range of 0.03-0.06. Therefore, the sensitivity analysis was performed to obtain the optimum value for estimation of radiant heat loss based on the range as shown Fig. 5. It was confirmed that the average prediction accuracy was the highest when the reference mole fraction was set to 0.05. Although this approach for averaged reference temperature may cause non-negligible errors, this empirical derivation was considered to essential for predicting the LFL in a H_2-Air-Steam mixture. The term of steam effect can be negligible when no steam is present in the initial mixture,

$$Q_{rad,1}(\pi) = 0.246\left(\pi - \pi_{air,20^\circ C}\right)\left(X_{H_2,initial} + X_{steam,initial}\right)\Big/X_{steam,ref} \ . \tag{9}$$

RESULTS AND DISCUSSION

The accuracy of the CNAFT model and extended CNAFT model was compared in Fig. 6 based on the experimental results in Table 1. For mixtures without steam, both models show reasonable accuracy because the radiant heat loss increases due to helium concentration or high temperature can be predicted by the CNAFT coefficient. However, in the case of the mixture containing steam, the current CNAFT model has a consistent tendency to predict higher LFL values than the experimental values. This is because the amount of radiant heat loss, which increases with the presence of steam in the initial condition, was underestimated. On the other hand, the extended CNAFT model shows high accuracy for all listing mixtures as consideration of steam effect on radiant heat loss except for a H_2-Air-He mixture. The reason was a significantly large thermal diffusivity value of the mixture compared to other mixtures because of both high temperature and helium concentration ($X_{He} = 40\ \%, T_i = 100\ ^\circ C$). The maximum relative error was 13 % except for the mixture. As as result, by knowing the initial condition of a mixture for which the LFL is not known experimentally, the amount of heat loss in the CNAFT model can be estimated. Then, the hydrogen concentration at which the CNAFT reaches 581 K according to Eq. (5) and (9) is the LFL value predicted by the CNAFT model.

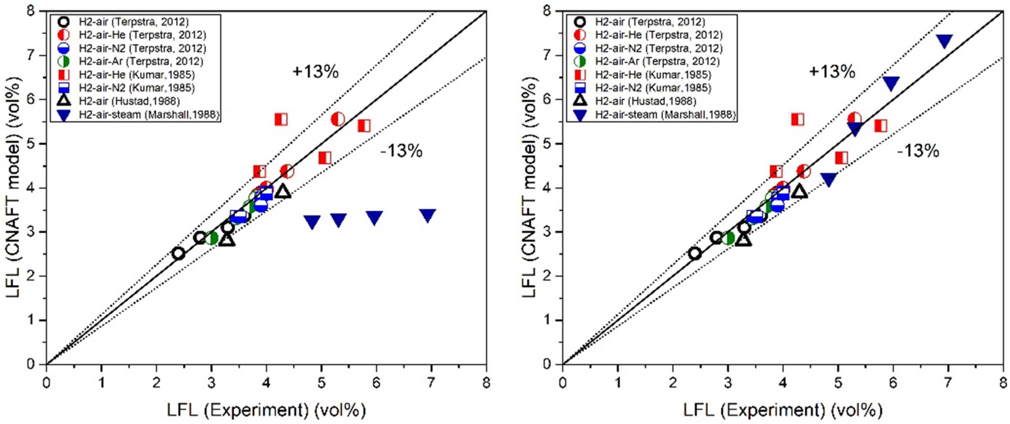

Fig. 6. Validation of CNAFT model in various mixture conditions (left: current, right: extended).

CONCLUSIONS

In this study, the extended CNAFT model was developed to predict the LFL of H_2-Air-Steam mixture based on the heat transfer mechanisms during flame propagation. The simulation of seven-step combustion mechanism provided a rationality for a complete combustion approach in terms of predicting the steam mole fraction at the flame front. Agreement with experimental LFL results on H_2-Air-Steam mixtures was improved significantly, for which the current CNAFT model showed technical limitations. We confirmed that considering radiative heat loss induced by steam mole fraction is essential for estimating the peak flame temperature for various mixture conditions. This study suggests that extended CNAFT model can be effectively utilized for flammability prediction in severe accident analysis code. Our major findings and future work can be summarized as follows.

- The reason why the current CNAFT coefficient cannot proportionally estimate the amount of radiant heat loss for H_2-Air-Steam mixtures can be explained by the optically thin approximation. In the case of a mixture containing steam, the radiant volumetric rate increases proportionally as the partial pressure of steam increases.
- The seven-step simulation for combustion process of liming H_2-Air-Steam mixtures identified that the steam mole fraction in flame front is very close to the sum of initial hydrogen and steam mole fraction regardless of the initial steam mole fraction.
- The amount of heat loss in a mixture containing steam can be estimated with the complete combustion approach. The amount which can be estimated by the initial condition including CNAFT coefficient and initial mole fraction increases proportionally as the sum of initial hydrogen and steam mole fraction increases.
- However, the specific modes of flame propagation were observed such as cap-like flames in ultraliean H2-Air flames. These observed natures can affect the steam concentration near the end of the reaction zone. This is our further study.

ACKNOWLEDGEMENT

This work was supported by Korea Hydro & Nuclear Porea Co., LTD (No. 2017-tech-9).

REFERENCES

[1] M.R. Seo, Status of Severe Accident Analysis for New Accident Management Plan, Trans. Korean. Nucl. Soci., Jeju, Korea, 2017.

[2] N.K. Kim, J. Jeon, W. Choi, S.J. Kim, Systematic Hydrogen Risk Analysis of OPR1000 Containment before RPV Failure Under Station Blackout Scenario, Ann. Nucl. Energy 116 (2018) 429–438.

[3] R. K. Kumar, Flammability Limits of Hydrogen-Oxygen-Diluent Mixtures, J. Fire Sci. 3 (1985) 245-262.

[4] J.E. Hustad, O.K. Sønju, Experimental Studies of Lower Flammability Limits of Gases and Mixtures of Gases at Elevated Temperatures, Combust. Flame 71 (1988) 283-294.

[5] B.W. Marshall, Hydrogen:Air:Steam Flammability Limits and Combustion Characteristics in the FITS Vessel, Report No. SAND84-0383, Sandia National Lab., 1986.

[6] Y.N. Shebeko, S.G. Tsarichenko, A.YA. Korolchenko et al., Burning Velocities and Flammability Limits of Gaseous Mixtures at Elevated Temperatures and Pressures, Combust. Flame 102 (1995) 427-437.

[7] M. Terpstra, Flammability Limits of Hydrogen-Diluent Mixtures in Air, MSc thesis, University of Calgary, Canada, 2012.

[8] W. Choi, S.O. Yu, S.J. Kim, Efficacy Analysis of Hydrogen Mitigation Measures of CANDU Containment under LOCA Scenario, Ann. Nucl. Energy 118 (2018) 122-130.

[9] T. Kim, W. Choi, J. Jeon, N.K. Kim, H. Jung, S.J. Kim, A Conceptual Approach to Eliminate Bypass Release of Fission Products by In-Containment Relief Valve under SGTR Accident, Sci. Technol. Nucl. Install. Vol. 2018, Article ID 5936214, 12 p.

[10] R.O. Gauntt et al., MELCOR Computer Code Manuals Version 1.8.6, Report No. SAND2001-0929P, Sandia National Lab., 2005.

[11] M. Vidal, W. Wong, W.J. Rogers, M.S. Mannan, Evaluation of Lower Flammability Limits of Fuel–Air–Diluent Mixtures using Calculated Adiabatic Flame Temperatures, J. Hazard. Mater. 130 (2006) 21–27.

[12] H.Y. Shih, Computed Extinction Limits and Flame Structures of H2/O2 Counterflow Diffusion Flames with CO_2 Dilution, Int. J. Hydrogen Energy 34 (2009) 4005-4013.

[13] J.S. Ha, C.W. Moon, J. Park et al., A Study on Flame Interaction between Methane/Air and Nitrogen-Diluted Hydrogen-Air Premixed Flames, Int. J. Hydrogen Energy 35 (2010) 6992-7001.

[14] P.G. Holborn, P. Battersby et al., Modelling the Effect of Water Fog on the Upper Flammability Limit of Hydrogen-Oxygen-Nitrogen Mixtures, Int. J. Hydrogen Energy 38 (2013) 6896-6903.

[15] J. Jeon, N. K. Kim, W. Choi, T. Kim, S. J. Kim, Investigation of Flammability of Hydrogen Gases with Diluent Gases under Severe Accident Conditions using CNFT Model, Int. Con. Nucl. Eng., London, England, 2018.

[16] I. Glassman, R.A. Yetter, N.G. Glumac, Combustion, Academic press, 2014.

[17] D.M. Himmelblau, J.B. Riggs, Basic Principles and Calculations in Chemical Engineering, FT press, 2012.

[18] E. Mayer, A theory of Flame Propagation Limits due to Heat Loss, Combust. Flame 1 (1957) 438–452.

[19] D. Fernandez-Galisteo, A.L. Sanchez, A. Linan, F.A. Williams, The Hydrogen-Air Burning Rate Near the Lean Flammability Limit, Combust. Theor. Model. 13 (2009) 741-761.

[20] H.F. Coward, G.W. Jones, Limits of Flammability of Gases and Vapors, US Bureau of Mines, Bulletin 627, Pittsburgh, Pennsylvania, USA, 1952.

[21] C.K. Law, F.N. Egolfopoulos, A Unified Chain-Thermal Theory of Fundamental Flammability Limits, Proc. Combust. Inst. 24 (1992) 137–144.

[22] Z. Zhou, Y. Shoshin, F.E. Hernandez-Perez, et al., Experimental and numerical study of cap-like lean limit flames in H_2-CH_4-air mixtures, Combust. Flame 189 (2018) 212-224.

[23] K.P. Lakshmisha, P. Paul, H. Mukunda, On the Flammability Limit and Heat Loss in Flames with Detailed Chemistry, Proc. Combust. Inst. 23 (1991) 433–440.

[24] H.J. Liaw, K.Y. Chen, A model for predicting temperature effect on flammability limits, Fuel 178 (2016) 179-187.

[25] Y. Shoshin, J. Jarosinski, On extinction mechanism of lean limit methane-air flame in a standatd flammability tube, Proc. Combust. Inst. 32 (2009) 1043–1050.

[26] Y. Dong, A.T. Holley, M.G. Andac, et al., Extinction of premixed H_2/air flames: chemical kinetics and molecular diffusion effect, Combust. Flame 142 (2005) 374-387.

[27] A. Levy, An Optical Study of Flammability Limits, Proc. R. Soc. Lond. A. 283 (1965) 134–145.

[28] Y. Ju, G. Masuya, P.D. Ronney, Effects of Radiative Emission and Absorption on the Propagation and Extinction of Premixed Gas Flames, Proc. Combust. Inst. 27 (1998) 2619–2626.

[29] D. Fernandez-Galisteo, A.L. Sanchez, A. Linan, F.A. Williams, One-Step Reduced Kinetics for Lean Hydrogen-Air Deflagration, Combust. Flame 156 (2009) 985-996.

[30] J. Troe, Detailed Modeling of the Temperature and Pressure Dependence of the Reaction H+ O2 (+ M)→ HO2 (+ M), Proc. Combust. Inst. 28 (2000) 1463–1469.

A Holistic Approach to Promote the Safe Development of Hydrogen As an Energy Vector

Gökalp I.

ICARE-CNRS, 1C, Avenue de la Recherche Scientifique 45071 Orléans cedex 2, France
iskender.gokalp@cnrs-orleans.fr

ABSTRACT

If generated using clean technologies (non CO2 emitting technologies), hydrogen may constitute a clean sustainable energy vector usable in the power sector, in the transportation sector, in various industrial sectors and in households. However, the physical and chemical properties of the hydrogen (its leakage, flammability and explosion propensities) call for extreme care for its generalized use, especially at the level of the general public. To make the general public use of hydrogen as safe as electricity will certainly take a long time and will necessitate huge investments. To open the way to the so-called hydrogen society may necessitate a different approach, that we call a holistic approach, meaning that the advent of hydrogen as a generalized energy vector should solve world energy and environmental problems without adding new ones. Among such approaches, the paper discusses the following ones: (i) in situ & on site hydrogen generation to avoid hydrogen transport and storage; (ii) use of renewable hydrogen for captured CO_2 hydrogenation and (iii) hydrogen generation from organic waste streams to contribute to the achievement of circular economy.

KEYWORDS: hydrogen safety, hydrogen generation, CO_2 hydrogenation, organic waste gasification.

INTRODUCTION

The world energy system is undergoing a large mutation today, the pace of which will certainly fasten in the coming decades. Sustainability issues of energy systems and policies are considered more seriously than before. Sustainability goes obviously hand in hand with long term energy sources availability and environmental considerations. Focusing on climate change risks triggered by greenhouse gas emissions, and namely CO2 emissions from burning fossil fuels, clearly shows the complexity of rapidly modifying an already established energy system. This is mainly because energy systems are large scale socio-technical systems impacting all the human activities but also impacted by the social sphere, from economy to geopolitics. Consequently they present an important resistance to any important changes so that energy transitions are usually characterized by long durations.

An energy system is composed of several sub systems, such as resource gathering and transporting (for example mining or building pipelines), resource conversion to useful energy vectors (for example refining or electricity generation), distribution of the energy vectors (for example electricity or gas networks). Changing an element of the energy system, for example the fuel or the useful energy vector, impacts the whole energy system. Each energy sub-system also carries specific hazards and environmental risks [1-3].

Hydrogen is a specific energy vector. If generated using clean technologies (non CO2 emitting technologies), it may constitute a clean sustainable energy vector usable in the power sector, in the transportation sector, in various industrial sectors and in households. However, the physical and

Proceedings of the Ninth International Seminar on Fire and Explosion Hazards (ISFEH9), pp. 1386-1394
Edited by Snegirev A., Liu N.A., Tamanini F., Bradley D., Molkov V., and Chaumeix N.
Published by Saint-Petersburg Polytechnic University Press
ISBN: 978-5-7422-6498-9 DOI: 10.18720/spbpu/2/k19-127

chemical properties of the hydrogen (its leakage, flammability and explosion propensities) call for extreme care for its generalized use, especially at the level of the general public. To make the general public use of hydrogen as safe as electricity will certainly take a long time and will necessitate huge investments.

To open the way to the so-called hydrogen society may necessitate a different approach, that we call a holistic approach, meaning that it should solve world energy and environmental problems without adding new ones. This paper will discuss some aspects of this approach. In the first section of the paper we outline what we mean by the 'holistic' approach. In the continuing sections, we briefly present three developments within this approach. We finish the paper by some recommendations.

THE HOLISTIC APPROACH

The energy transition strategies should not add new problems but solve simultaneously several existing ones. The transition to a more sustainable energy system needs decarbonized energy resources, de-nuclearized electricity systems, increased renewables based electricity generation and advances in the circular economy.

In this context, hydrogen as an energy vector opens-up several opportunities. Indeed, hydrogen conversion to useful energy by thermo-chemical or electro-chemical processes only generates water and no greenhouse gases. But hydrogen generation should also use clean processes (without emitting GHGs). On the other hand, because of its leakage propensity, including metal fragilization, low density and high reactivity, the transport and storage of hydrogen pose serious threats.

The approach we call 'holistic' aims to use some characteristics of hydrogen and of its use to promote energy transition without introducing new risks or threats. Several strategies to ease the introduction of hydrogen in the energy scenery within the holistic approach can be imagined. In this paper, we develop three of them. They are the following:

- In order to minimize hydrogen leakage, fire and explosion risks in the case of hydrogen use generalization, the most rational strategy is to avoid hydrogen transport and storage, by developing *in situ and on demand* hydrogen generation technologies
- Instead of using hydrogen as a final energy vector, another rational strategy would be to use it as an intermediary one to generate conventional fuels (for which optimized conversion technologies exist such as internal combustion engines, gas turbines, fuel cells) by the hydrogenation of the CO2 emitted from carbon intensive sectors.
- Another rational strategy would be to generate hydrogen from various solid materials including organic waste streams by gasification technologies.

The paper argues that rational uses of hydrogen such as these three strategies suggest may accelerate the generalized use of hydrogen with minimal risks and contribute to the development of a low carbon circular economy. The following sections briefly develop these strategies, based on the worldwide knowledge accumulation in the concerned areas, including the authors' own work.

IN SITU AND ON DEMAND HYDROGEN GENERATION

In order to diminish the leakage, fire and explosion risks of a generalized use of hydrogen, one rational approach is to shorten the duration and the distance between its generation and energy conversion steps and locations. This also means generating hydrogen and using it without storing, which is a "in situ & on demand" hydrogen generation approach. A promising way within this approach is using low temperature reactions between water and Aluminum for water splitting. Several studies exist in this domain, including at ICARE-CNRS [4, 5].

Metal particles such as Ni, Fe, V, Mn, Ti, Ag, Ca, Zn, Zr, Al, and their corresponding alloys can be potentially used to produce hydrogen through catalyst (water-soluble inorganic salts) assisted reactions in water. For example, some theoretical hydrogen production rates are: 1 g of sodium borohydride gives 2.4 l of hydrogen; 1 g of aluminum gives 1.244 l with bayerite/boehmite formation; 1 g of magnesium gives 0.95 l, and Al and Mg hydrides give respectively 2.24 l and 1.88 l of hydrogen. Compared to other systems, aluminum has several favorable features, such as cost-effectiveness, non-reactivity at normal conditions, easy storability, safety during transportation, and non-toxicity.

As aluminum is covered by its natural oxide, several researchers have investigated various aluminum activation processes, such as treatment with iodine vapor, reaction at supercritical conditions, treatment of the metal surface with NaOH or KOH solutions, surface contact with activator metals (mercury, gallium, indium) and metal-alloys (gallium-indium eutectics). For example, Kravchenko et al. [6] investigated the reaction of water with aluminum-based metal composites doped with gallium (Ga), indium (In), zinc (Zn), or tin (Sn). Parmuzina and Kravchenko [7] demonstrated the method of aluminum activation by liquid eutectics Ga–In (70:30) and Ga–In–Sn–Zn (60:25:10:5) (galinstan) leading to reactions with water and hydrogen production. Activator metals remove the alumina layer and generate fractures on the aluminum core which is a potential way to enhance the reactivity of the aluminum. For safety and environmental reasons, the gallium-indium eutectics seem to be the best choice to activate aluminum particle reactions with water.

At ICARE we have chosen the galinstan (Ga–In–Sn–Zn -60:25:10:5) eutectic, which gives optimized performances over Ga-In eutectics [4] and we have addressed some of the associated problems in this aluminum activation method, and mainly the dependency of hydrogen production rate and yield on aluminum particle sizes, aluminum and galinstan eutectic content, and reaction temperature. In addition we have examined the effects of Al particles specific surface area and galinstan eutectic content on hydrogen production rate and yield. We have examined three compositions of mixtures: 85% Al -15% galinstan eutectics, 90% Al-10% galinstan eutectics and 95% Al – 5% galinstan eutectics by mass. The galinstan eutectic composition is fixed as Ga-In-Sn-Zn (60:25:10:5). Figure 1 shows cracks initiation and propagation under the effect of the galinstan eutectics. Figure 2 displays the hydrogen evolution rate for various aluminum particle sizes and water temperatures, showing the effects of both parameters.

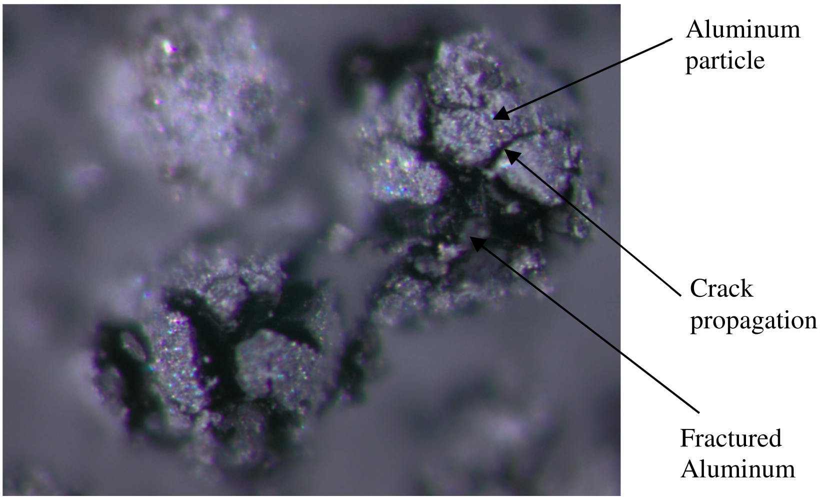

Fig. 1. Crack formation on the activated aluminum particles at ~30 °C.

These preliminary studies indicate that low temperature reactions between water and aluminum constitute a promising way for water splitting and in situ and on site hydrogen generation. Once optimized this approach may considerably reduce the hydrogen storage necessity and the associated risks for on-board and portable systems applications using fuel cells.

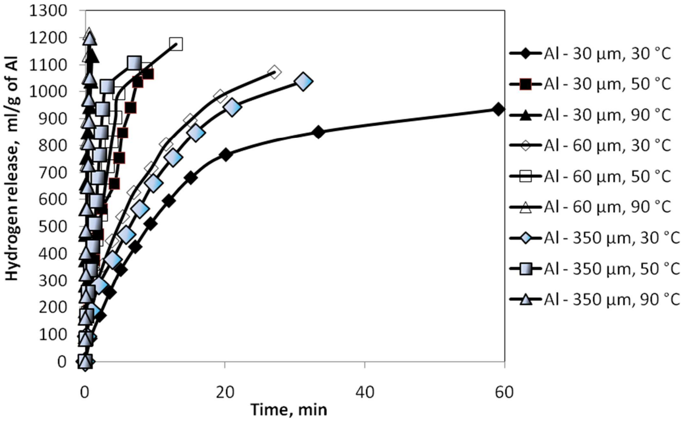

Fig. 2. Hydrogen evolution rate of the activated aluminum mixtures with water, Al-85% and Galinstan eutectics 15% by mass (Ga-In-Sn-Zn = 60-25-10-5).

HYDROGEN GENERATION USING RENEWABLE ELECTRICITY AND CO_2 HYDROGENERATION TO GASEOUS AND LIQUID FUELS

Wind energy and solar power are clean, sustainable but intermittent electricity generation technologies. Given the difficulties to store electricity, hydrogen generation by water electrolysis using renewable electricity is a way of storing PV electricity during day time and the excess wind electricity during lower electricity consumption periods such as nights. The generated renewable electricity can be used to electrolyze water for hydrogen generation and for CO_2 hydrogenation to gaseous (methane) or liquid (methanol, DME) fuels. This approach may permit to continue to use well optimized energy conversion technologies such as gas turbines and internal combustion engines, but also fuel cells. It might then provide a nice solution for the valorization of captured CO_2 especially from CO_2 intensive industries such as cement, glass, steel and refineries by creating a carbon circulation or transfer process between sectors [8-11].

Carbon dioxide is one of the major greenhouse gases. The need to control the emission of CO_2 into the atmosphere has encouraged its capture from flue gases generated by power plants and carbon intensive industrial processes. Several methods for capturing CO_2 in the atmosphere have been investigated. Separation techniques are today mature and can be implemented on a large scale. CO_2 capture using membranes is a less energy consuming capture technology especially suited for CO_2 concentrations nearing 15 % and higher. This is for example appropriate for calcination kilns in the cement industry where CO_2 concentrations are high. For power plants CO_2 concentrations in the flue gases can be increased using combustion in oxygen enriched air. Figure 3 shows the efficiency of this technology for a swirling turbulent methane – oxygen enriched air flame [12].

The utilization of the captured carbon dioxide has an economic value as a waste is converted into useful, added value products. The availability of large amounts of recovered CO_2 may sustain the development of new synthetic fuel technologies based on its hydrogenation. The free energy of formation of CO_2 (ΔG = -96.5 kcal/mol) suggests that its conversion may require a large energy input.

The conversion processes such as

$CO_2 + 3H_2 \rightarrow CH_3OH + H_2O$ ($\Delta H = -49.5$ KJ/mol),

$CO_2 + 4H_2 \rightarrow CH_4 + 2H_2O$ ($\Delta H = -164.9$ KJ/mol),

are likely to be a catalytic or thermal treatment processes. In both processes, the fundamental mechanism involves creation and stabilization of active species, which initiate the necessary reactions under kinetic and thermodynamic limitations. Incorporation of catalysts to this conversion process is already studied extensively to promote these conversions. One of the elementary mechanisms is to produce the reactive species which helps dissociating the molecules. Once the species are generated, it should have enough energy to propagate the desired reactions. One of the approach to generate the reactive environment is by means of gas discharges.

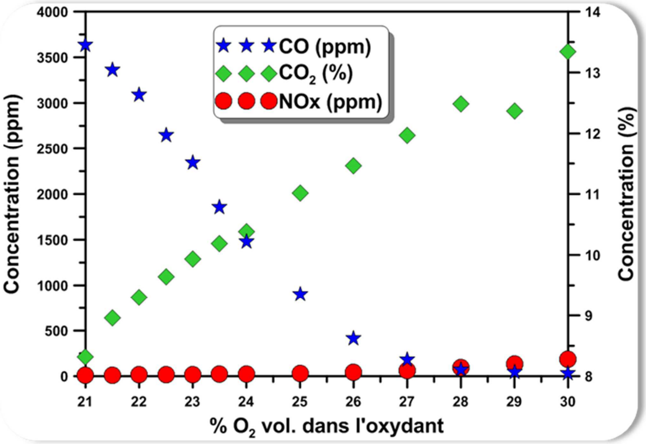

Fig. 3. Effect of the oxygen enrichment rate on the CO2 concentration in the burnt gases of a swirled turbulent methane – air flame.

Atmospheric non-thermal plasmas (ANTPs) or atmospheric pressure gas discharges have received a great deal of attention in the recent years [13,14]. ANTPs are generated by a diversity of electrical discharges such as corona discharges, dielectric barrier discharges (DBD), atmospheric pressure plasma jet (APPJ) and micro hollow cathode discharges (MHCD), all having their own characteristic properties and applications. The important characteristics of non-thermal plasmas is their high electron temperature (~10^5 K) while the bulk gas temperature remains as low as room temperature and its generation of high energy electrons (6 ~10eV) which dissociates the molecules and hence creates the necessary reactive environment. Therefore, this conversion process can be performed independently of the gas temperature, an inherent advantage being to perform the chemical conversion at low temperatures as demonstrated by bench scale investigations involving batch experiments and column reactors.

Once optimized, the integration of hydrogen generation from renewable electricity through water electrolysis and of the captured CO_2 hydrogenation to liquid or gaseous fuels will become a viable sustainable CO_2 valorization technology. The rationale behind this approach is to circulate the carbon between various sectors without using additional carbon containing fuels, for example using the CO_2 generated in the process industry as a carbon containing fuel source for the transport sector.

HYDROGEN GENERATION BY GASIFICATION OF SOLID FUELS INCLUDING ORGANIC WASTE

An important environmental and sustainability issue of today's societies is the waste management problem. Humanity is generating on a daily basis huge amounts of various kinds of organic waste streams which pose disposal and resource management problems. Good examples are end-of-life tires, organic fractions of municipal waste, sewage sludge from water purification facilities, agriculture and food industry waste. Gasification technologies are appropriate ways to produce a synthetic gas (composed mainly of H_2 and CO) from such organic waste. Depending on the moisture content of the waste material, conventional thermal gasification (for example for scrap tires) or hydrothermal gasification (for example for sewage sludge) technologies can be mobilized. In addition, several countries do not possess natural gas or oil reserves but have large reserves of lignite type coal. The generation of synthetic gas by gasification from lignite is a viable technology for natural gas import substitution in such countries. The produced gas can be used as a natural gas substitute for various uses, can be further processed to produce various chemicals and liquid fuels or for pure H_2 generation after a water gas shift process. H_2 can be used to enrich natural gas and the separated CO_2 may enter the carbon circulation approach as outlined above. Several studies are conducted worldwide and also at ICARE-CNRS to optimize syngas generation technologies from solid fuels and to solve both the organic waste disposal and natural gas import substitution problems [15-18].

Figure 4 shows the 1 MW circulating fluidized bed solid fuel gasification facility developed during the FP7 OPTIMASH project (2011-2016) in order to optimize the gasification of high ash content lignites from India and Turkey. The gasification cold gas efficiencies of 70% were obtained with this facility and the design of upscaled versions of the facility in under progress to approach commercial scales [17].

Fig. 4. 1 MW circulating fluidized bed gasification facility developed within the EU OPTIMASH project.

Based on the knowledge gained on circulating fluidized bed gasification technologies, a scrap tire granules gasification facility has been designed. In order to feed this design, scrap tires gasification kinetics has been first determined at ICARE-CNRS using a high heating rate thermogravimetric analysis apparatus coupled to a mass-spectrometer and to a gas chromatography [15]. Figure 5 displays typical mass loss curves showing that scrap tires can be efficiently gasified.

Based both on the basic knowledge on scrap tire gasification kinetics and on the technological expertise gained on circulating fluidized bed gasification technologies a 5 MW electricity generation facility has been designed [19]. The main features of this facility are shown on Fig. 6.

For very humid organic waste such as sewage sludge or several other agricultural and food industry waste streams, conventional thermo-chemical gasification techniques are not appropriate as the waste needs to undergo a pre-drying process. This of course considerably diminishes the waste to energy potential. Instead, hydrothermal processes can be used. Figure 7 shows a major result from ICARE-CNRS on the hydrothermal carbonization of olive pomace, a 70 % humid waste issuing from olive oil industry. It is observed that once optimized hydrothermal carbonization process is able to generate a solid fuel having chemical composition and thermo-physical properties very close to a lignite type coal [20]. This solid fuel can be therefore readily gasified or co-gasified to generate a syngas.

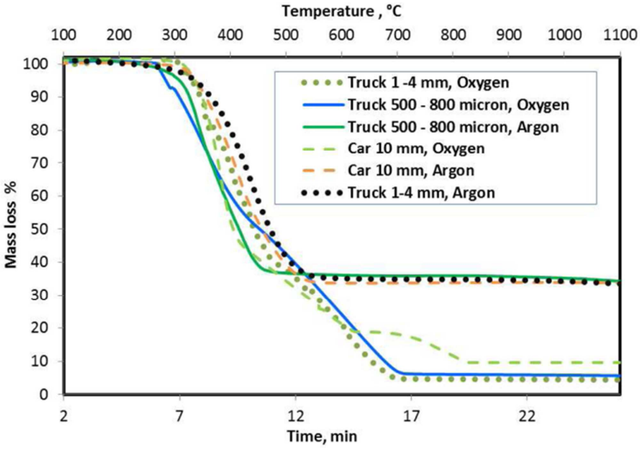

Fig. 5. TGA studies of scrap tires.

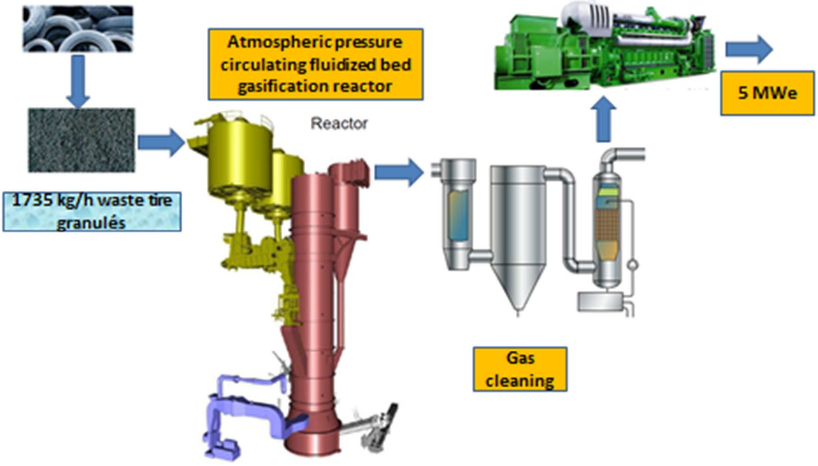

Fig. 6. Gasification of used tire granules: a project for 5 MW electricity generation.

CONCLUSIONS

This paper argued that in order to generalize the use of hydrogen as an important element in the energy transition, a holistic approach is necessary. The approach we call 'holistic' aims to use some characteristics of the hydrogen and of its use to facilitate energy transition without introducing new risks or threats. In this paper, we briefly developed three technological paths that may contribute to this approach. They are the following.

- In order to minimize hydrogen leakage, fire and explosion risks in the case of hydrogen use generalization, it is proposed to avoid hydrogen transport and storage, by developing *in situ and on demand* hydrogen generation technologies.
- Instead of using hydrogen as a final energy vector, it is proposed to use it as an intermediary one to synthetize conventional gaseous or liquid fuels (for which optimized conversion technologies exist such as internal combustion engines, gas turbines, fuel cells) by the hydrogenation of the CO_2 emitted from carbon intensive sectors. For this purpose it is proposed to generate hydrogen by water electrolysis using renewable electricity.
- Finally, it is proposed to develop hydrogen or syngas generation technologies from various solid fuels including organic waste streams by optimized gasification technologies

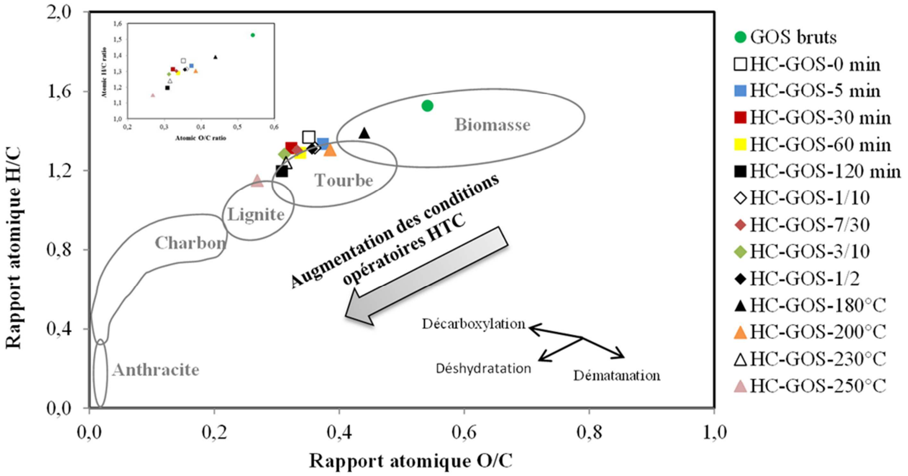

Fig. 7. Van Krevelen diagram for olive pomace.

The main argument of the paper is that hydrogen related technologies here outlined may help developing sustainable energy policies to accelerate the generalization of hydrogen use by reducing the associated risks, and at the same time, constitute solutions for renewable electricity storage, captured CO2 valorization, organic waste management, natural gas import substitution for some countries and therefore facilitate the transition to a low carbon circular economy.

ACKNOWLEDGMENTS

The author greatly acknowledges the contributions of his colleagues, from ICARE-CNRS mainly, to the studies used in this paper and also the support of the CNRS, the University of Orléans, the Conseil Régional Centre and the European Commission.

REFERENCES

[1] B.K. Sovacool, R. Andersen, S. Sorensen, K. Sorensen, V. Tienda, A. Vainorius, O. M. Schirach, F. Bjørn-Thygesen, Balancing safety with sustainability: assessing the risk of accidents for modern low-carbon energy systems, J. Cleaner Production 112 (2016) 3952-3965.

[2] N. Boccard, Safety along the energy chain, Energy 150 (2018) 1018-1030.

[3] M. Spada, F. Paraschiv, P. Burgherr, A comparison of risk measures for accidents in the energy sector and their implications on decision-making strategies, Energy 154 (2018) 277-288.

[4] K. Jayaraman, C. Chauveau, I. Gökalp, Effects of Aluminum Particle Size, Galinstan Content and Reaction Temperature on Hydrogen Generation Rate Using Activated Aluminum and Water. Energy Power Eng. 7 (2015) 426-432.

[5] J. Petrovic, G. Thomas, Reaction of Aluminum with Water to Produce Hydrogen, DOE Report, 2008

[6] O.V. Kravchenko, K.N. Semenenko, B.M. Bulychev, K.B. Kalmykov, Activation of aluminum metal and its reaction with water, J. Alloys Compounds 397 (2005) 58-62.

[7] A.V. Parmuzina, O.V. Kravchenko, Activation of aluminium metal to evolve hydrogen from water, Int. J. Hydrogen Energy 33 (2008) 3073-3076.

[8] A. Behr, R. Kuhlmann, Chemical Conversion of Carbon Dioxide, Chemie Ingenieur Technik 90 (2018) 593-601.

[9] W. Li, H. Wang, X. Jiang, J. Zhu, Z. Liu, X. Guo, C. Song, A short review of recent advances in CO2 hydrogenation to hydrocarbons over heterogeneous catalysts, RSC Advances 8 (2018) 7651-7669.

[10] E. Catizzone, G. Bonura, M. Migliori, F. Frusteri, G. Giordano, CO2 Recycling to Dimethyl Ether: State-of-the-Art and Perspectives, Molecules 23 (2017) 31.

[11] S. Kar, J. Kothandaraman, A. Goeppert, G.K.S. Prakash, Advances in catalytic homogeneous hydrogenation of carbon dioxide to methanol, J. CO2 Utilization 23 (2018) 212-218.

[12] T. Boushaki, N. Merlo, C. Chauveau , I. Gökalp, Study of pollutant emissions and dynamics of non-premixed turbulent oxygen enriched flames from a swirl burner, Proc. Combust. Inst. 36 (2017) 3959–3968.

[13] J. Luche, Q. Falcoz, T. Bastien, J.P. Leininger, K. Arabi, O. Aubry, A. Khacef, J.M. Cormier, J. Lédé, Plasma Treatments and Biomass Gasification, IOP Conf. Ser.: Mater. Sci. Eng. 29 (2012) 012011.

[14] A. Khacef, K. Arabi, O. Aubry, J.M. Cormier, Atmospheric Pressure Low-Current Plasma for Syngas Production From Alcohol, IEEE Trans. Plasma Sci. 11 (2011) 39

[15] Jayaraman, Kandasamy and Gökalp, Iskender, Pyrolysis, Combustion, and Steam Gasification of Various Types of Scrap Tires for Energy Recovery, Energy & Fuels 29 (2015) 346-354

[16] K. Jayaraman, I. Gökalp, Pyrolysis, combustion and gasification characteristics of miscanthus and sewage sludge, Energy Conserv. Managment 89 (2015) 83-91.

[17] K. Jayaraman, I. Gokalp, E. Bonifaci, N. Merlo, Kinetics of steam and CO2 gasification of high ash coal–char produced under various heating rates, Fuel 154 (2015) 370–379.

[18] F.H.C. Chauveau, N. Chaumeix, I. Gökalp, Characterization of the effects of pressure and hydrogen concentration on laminar burning velocities of methane-hydrogen-air mixtures, Proc. Combust. Inst. 30 (2005) 201-208.

[19] I. Gökalp, O. Kaya, S. Keçecioglu, D. Boden, A techno-economic feasibility analysis of the gasification of used tires for energy generation in Turkey, VENICE2018 7^{Th} International Symposium on Energy from Biomass and Waste, Venice 15-18 October 2018.

[20] A. Missaoui, S. Bostyn, V. Belandria, B. Cagnon, B. Sarh, I. Gökalp, Hydrothermal carbonization of dried olive pomace: Energy potential and process performances, J. Analyt. Appl. Pyrolysis 128 (2017) 281–290.

Modelling of Hydrogen Tank Fuelling

Dadashzadeh M.*, Makarov D., Molkov V.

HySAFER, Ulster University, Belfast School of Architecture and the Built Environment,
Newtownabbey, Co. Antrim, UK
**Corresponding author's email: s.dadashzadeh@ulster.ac.uk*

ABSTRACT

A model to simulate thermal behaviour of an onboard storage tank and parameters of hydrogen inside the tank during fuelling is presented. The energy conservation equation, Abel-Noble real gas equation of state, and the entrainment theory are applied in the model to reproduce the experimentally recorded dynamics of hydrogen temperature inside the tank and distribution of temperature through the wall. Convective heat transfer between hydrogen, tank wall and the atmosphere are modelled using Nusselt number correlations. An original methodology, based on the entrainment theory, is devised to calculate changing velocity of the gas inside the tank during the fuelling. Conductive heat transfer through the tank wall, composed of load-bearing carbon fibre reinforced polymer and a layer of liner, is modelled by employing one-dimensional unsteady heat transfer equation. The model is validated against experiments on fuelling of Type III and IV composite tanks for onboard hydrogen storage. Hydrogen temperature inside a tank is predicted by the model within the experimental non-uniformity of 5^0C.

KEYWORDS: Hydrogen fuelling, model, validation, fuelling protocol.

NOMENCLATURE

A_{int}	Internal tank surface (m^2)
b	Co-volume constant for hydrogen in Abel-Noble equation (m^3/kg)
$c_{p,\,air}$	Specific heat capacity of air at constant pressure (J/kg/K)
$c_{p,g}$	Specific heat capacity of the inside gas at constant pressure (J/kg/K)
$c_{p,wall}$	Specific heat capacity of the tank wall (CFRP: $c_{p\ wall\ (CFRP)}$; liner: $c_{p\ wall\ (liner)}$) (J/kg/ K)
Dext	External tank diameter (m)
D_{inlet}	Nozzle diameter (m)
D_{int}	Internal tank diameter (m)
f	Friction factor (-)
Gr_{tank}	Grashof number (-)
g	Gravity acceleration (m/s^2)
h_{in}	Enthalpy of gas entering the tank (J/kg)
k_{ext}	Convective heat transfer coefficient at external surface of tank wall ($W/m^2/K$)
$k_{int\ forced}$	Convective heat transfer coefficient
Pr	Prandtl number of gas inside tank (-)
Q	Heat into tank from surrounding (J)
R_{H_2}	Hydrogen gas constant ($m^2\ s^2$/K)
Re_{tank}	Effective Reynolds number inside tank (-)
T_{amb}	Ambient temperature (K)
T_{tank}	Temperature of gas inside tank (K)
$T_{wall\ (ext)}$	Temperature of tank external surface (K)
$T_{wall(int)}$	Temperature of tank internal surface (K)
T_{del}	Delivery temperature of gas during fuelling (K)
T^0_{tank}	Initial temperature of gas inside tank (K)
$T_{wall\ (n)}$	Temperature of tank wall at the grid-point "n" (K)
T^0_{wall}	Initial temperature of tank wall (K)
t	Time (s)

Proceedings of the Ninth International Seminar on Fire and Explosion Hazards (ISFEH9), pp. 1395-1406
Edited by Snegirev A., Liu N.A., Tamanini F., Bradley D., Molkov V., and Chaumeix N.
Published by Saint-Petersburg Polytechnic University Press
ISBN: 978-5-7422-6498-9 DOI: 10.18720/spbpu/2/k19-20

	at external surface of tank wall (forced convection) (W/ m2/K)
$k_{int\ natural}$	Convective heat transfer coefficient at internal surface of tank wall (natural convection) (W/m2/K)
k_{int}	Convective heat transfer coefficient at internal surface of tank wall (W/m^2/K)
L	Internal tank length (m)
$\dot{m}_{ent}$	Entrainment mass flow rate (kg/s)
$\dot{m}_{inlet}$	Inlet mass flow rate (kg/s)
$\dot{m}^0_{inlet}$	Initial inlet mass flow rate (kg/s)
M_0	Momentum flux (m/kg/s2)
m_{ent}	Mass of gas at entrainment
m_{inlet}	Mass of gas at inlet (in considerations of kinetic energy) (kg)
m_{tank}	Mass of gas in tank (kg)
m^0_{tank}	Initial mass of gas in tank (kg)
$Nu_{int\ natural}$	Nusselt number for natural convection (-)
$Nu_{int\ forced}$	Nusselt number for forced convection (-)
P_{tank}	Pressure of gas inside tank (Pa)
P^0_{tank}	Initial pressure of gas inside tank (Pa)
u_{ent}	Gas velocity due to entrainment (m/s)
u_{inlet}	Inlet gas velocity (m/s)
u_{tank}	Tank gas velocity (m/s)
U	Total internal energy in tank (J)
V	Tank volume (m3)
Z	Hydrogen compressibility factor (-)
Greek	
β	Thermal expansion coefficient of gas (1/K)
γ	Specific heats ratio (-)
λ_g	Thermal conductivity of gas (W/m/K)
μ_g	Dynamic viscosity of gas (Pa s)
μ_{air}	Viscosity of air (Pa s)
λ_{air}	Thermal conductivity of air (W/m/K)
ρ_{air}	Density of air (kg/m3)
λ_{wall}	Thermal conductivity of tank wall (CFRP: $\lambda_{wall\ (CFRP)}$; liner: $\lambda_{wall\ (liner)}$) (W/m/K)
ρ^0_{tank}	Initial gas density inside tank (kg/m3)
ρ_{inlet}	Gas density at inlet (kg/m3)
ρ_{tank}	Gas density inside tank (kg/m3)
ρ_{wall}	Tank wall density (CFRP: $\rho_{wall\ (CFRP)}$; liner: $\rho_{wall\ (liner)}$) (kg/m3)

INTRODUCTION

The inherently safer fuelling of onboard hydrogen composite storage container is a challenging problem. Independent on tank design and materials used for load bearing wall and liner, tank's volume, its initial and nominal working pressure (NWP), temperature of hydrogen supplied to tank, the regulation and standards [1–4] require that the temperature inside the tank does not exceed 85^{0}C and pressure does not exceed 1.25×NWP, i.e. 87.5 MPa for 70 MPa onboard storage tanks. The consumer expectations include the fuelling time of hydrogen-powered passenger car within 3 min. Longer fuelling time is acceptable for busses. The problem of fuelling control is complicated by changing pressure and temperature inside the tank and at the inlet, changing diameter of fuelling nozzle to keep a required pressure ramp profile, requirements to the fuelling time, conjugate heat transfer from/to hydrogen through a tank wall to/from the ambience, use of wall and liner materials of different thermal conductivity, thermal capacity, etc.

Experimental investigation of hydrogen fuelling for arbitrary conditions is expensive. Up to now experimental studies did not yet end up by clear and transparent fuelling protocol. Computational fluid dynamics (CFD) is a contemporary research method to get insights into underlying physical phenomena. It helps as well to avoid carrying out hazardous and expensive experiments. CFD studies on hydrogen fuelling are extensive [5–14]. However, CFD simulations are not always time efficient [15] and hardly could be used as a part of automated fuelling system with a short response time.

Hydrogen fuelling models and their applications can be found elsewhere [7,15–21]. A major drawback in these studies is a lack of universal approach for estimation of heat transfer coefficient.

The convective heat transfer on a tank walls depends on the heat transfer coefficient [22,23]. The universal modelling approach to estimate this coefficient is vital [21].

The aim of this study is to develop and validate a model to better understand and reproduce the underlying phenomena of onboard hydrogen tank fuelling. The model can be used as a basis for creation of a predictive tool for the thermal behaviour of the system dispenser-hydrogen-tank-atmosphere during fuelling.

MODEL

The schematic diagram of the hydrogen storage tank during the fuelling and phenomena on its boundaries are presented in Fig. 1.

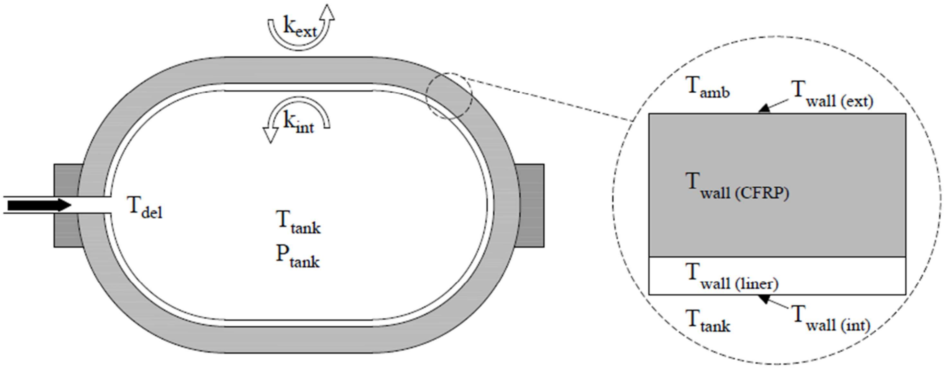

Fig. 1. Scheme of a tank and related phenomena during fuelling.

Hydrogen thermodynamic parameters during fuelling are related through Abel-Noble real gas equation of state (EOS) [24]

$$P_{tank} = Z\rho_{tank}R_{H_2}T_{tank}, \tag{1}$$

where $Z = 1/(1 - b\rho_{tank})$ is the compressibility factor.

The first law of thermodynamic is used in the model to bring together the rate of change of internal energy of hydrogen in the tank, rate of heat transfer to/from hydrogen through the tank wall, composed of a composite polymer and a liner with different thermodynamic parameters, and the rate of enthalpy brought into the tank by hydrogen inflow

$$\frac{dU}{dt} = \frac{dQ}{dt} + h_{in}\frac{dm_{tank}}{dt}, \tag{2}$$

where the enthalpy of the gas entering (delivered into) the tank is realised as $h_{in} = c_{p,g}T_{del}$.

The internal energy of real gas is calculated similar to [25] as

$$U = \frac{P_{tank}(V - m_{tank}b)}{\gamma - 1}. \tag{3}$$

The rate of heat transfer can be modelled as elsewhere, e.g. [19],

$$\frac{dQ}{dt} = k_{int}A_{int}\left(T_{wall(int)} - T_{tank}\right), \tag{4}$$

where T_{tank} is the gas temperature inside the tank in the assumption of its uniformity. The criteria to define the regime of convective heat transfer (natural convection, forced convection, or combined regime) is defined as [26]

$$\begin{cases} If\ \dfrac{Gr_{tank}}{(Re_{tank})^2} < 0.1,\ \ k_{int} = k_{int\,forced}, & (5) \\ If\ 0.1 \leq \dfrac{Gr_{tank}}{(Re_{tank})^2} \leq 10,\ \ k_{int} = \left({k_{int\,natural}}^4 + {k_{int\,forced}}^4\right)^{\frac{1}{4}}, & (6) \\ If\ \dfrac{Gr_{tank}}{(Re_{tank})^2} > 10,\ \ k_{int} = k_{int\,natural}, & (7) \end{cases}$$

where Grashof number, Gr_{tank}, is calculated as

$$Gr_{tank} = \frac{g\beta\left|T_{tank} - T_{wall(int)}\right|\rho_{tank}^2 D_{int}^3}{{\mu_g}^2}. \tag{8}$$

Gas thermal properties, i.e. thermal conductivity (λ_g); specific heat capacity ($c_{p,g}$); viscosity (μ_g), extracted for different pressure and temperature were interpolated based on gas pressure and temperature from [27].

The values of heat transfer coefficients $k_{int\,forced}$ and $k_{int\,natural}$ are calculated as a function of Nusselt number, internal tank diameter, and gas thermal conductivity which is interpolated for different pressure and temperature from [27], respectively as

$$k_{int\,natural} = \frac{\lambda_g \times Nu_{int\,natural}}{D_{int}}, \tag{9}$$

$$k_{int\,forced} = \frac{\lambda_g \times Nu_{int\,forced}}{D_{int}}. \tag{10}$$

Natural convection Nusselt number, $Nu_{int\,natural}$, is calculated by the empirical equation [18]

$$Nu_{int\,natural} = 0.104 \times \left(\frac{g\beta\left|T_{tank} - T_{wall(int)}\right|c_{p,g}(\rho_{tank})^2 D_{int}^3}{\mu_g\lambda_g}\right)^{0.352}. \tag{11}$$

Forced convection Nusselt number, $Nu_{int\,forced}$, is calculated using the correlation [26]

$$Nu_{int\,forced} = \frac{(f/8)(Re_{tank} - 1000)Pr}{1 + 12.7(f/8)^{0.5}\left(Pr^{2/3} - 1\right)}, \tag{12}$$

where the friction factor, f, and Prandtl number, Pr, inside the tank are calculated by the following correlation [26] and definition respectively

$$f = (0.790 \cdot \ln Re_{tank} - 1.64)^{-2}, \tag{13}$$

$$Pr = \frac{\mu_g \cdot c_{p,g}}{\lambda_g}. \tag{14}$$

Reynolds number inside the tank for calculation of the friction factor and Nusselt number for forced convection is

$$Re_{tank} = \frac{\rho_{tank} u_{tank} D_{int}}{\mu_g}. \tag{15}$$

The original modelling approach is applied in this study to calculate characteristic velocity of hydrogen in a tank. It is based on the entrainment theory [28]. The procedure is as follows. The density of hydrogen at inlet is calculated using Abel-Noble EOS

$$\rho_{inlet} = \frac{P_{tank}}{P_{tank} b + R_{H_2} T_{del}}. \tag{16}$$

The inlet velocity is calculated by the mass flow rate

$$u_{inlet} = \frac{4\dot{m}_{inlet}}{\rho_{inlet} (D_{inlet})^2 \pi}. \tag{17}$$

Using the inlet density, ρ_{inlet}, and inlet velocity, u_{inlet}, the momentum flux, M_0, and the entrainment mass flow rate inside the tank, $\dot{m}_{ent}$, are calculated respectively as [28]

$$M_0 = \frac{1}{4} \pi (D_{inlet})^2 \rho_{inlet} (u_{inlet})^2, \tag{18}$$

$$\dot{m}_{ent} = 0.282 (M_0)^{0.5} (\rho_{tank})^{0.5} L. \tag{19}$$

Then, the velocity of hydrogen in the tank due to the process of entrainment can be calculated as

$$u_{ent} = \frac{4\dot{m}_{ent}}{\rho_{tank} (D_{int})^2 \pi}. \tag{20}$$

To calculate a characteristic velocity inside the tank, u_{tank}, the kinetic energy of hydrogen entering the tank and the kinetic energy of hydrogen moving inside the tank due to entrainment, are added

$$\frac{m_{tank} (u_{tank})^2}{2} = \frac{m_{ent} (u_{ent})^2}{2} + \frac{m_{inlet} (u_{inlet})^2}{2}. \tag{21}$$

Considering that all hydrogen inside the tank is involved in the movement due to the entrainment phenomenon, i.e. $m_{ent} = m_{tank}$, and using the definition $m_{inlet} = \dot{m}_{inlet} \Delta t$, this equation can be solved for the characteristic velocity for use in the calculation of Reynolds number as

$$u_{tank} = \left[\frac{m_{tank} (u_{ent})^2 + m_{inlet} (u_{inlet})^2}{m_{tank}} \right]^{1/2}. \tag{22}$$

Differentiating Eq. (3) and considering the rate of heat transfer, defined by Eq. (4), the differencial equation for calculation of hydrogen mass in the tank (m_{tank}) is obtained from Eq. (2)

$$\frac{dm_{tank}}{dt} = \frac{\frac{dP_{tank}}{dt} \cdot \frac{(V - m_{tank} \cdot b)}{\gamma - 1} - k_{int} A_{int} \left(T_{wall(int)} - T_{tank} \right)}{\frac{P_{tank}}{\gamma - 1} \cdot b + c_{p,g} \cdot T_{del}}. \tag{23}$$

The density is calculated as $\rho_{tank} = \frac{m_{tank}}{V}$ and it is followed by using Eq. (24) [24] to calculate the temperature of the hydrogen inside the tank in the assumption of uniformity of hydrogen parameters throughout the tank (T_{tank})

$$T_{tank} = \frac{P_{tank} (1 - b \rho_{tank})}{\rho_{tank} R_{H_2}}. \tag{24}$$

Conservation of energy requires the equality of the convective heat flux between gas and the wall to the conductive heat flux at the wall boundary. Thus, boundary conditions at internal and external surfaces of the tank are defined by Eq. (25) and Eq. (26) respectively

$$q''_{conduction}\ (internal) = q''_{convection} \Rightarrow -\lambda_{wall}\frac{dT_{wall\,(n)}}{dx}\bigg|_{n=int} = k_{int}\big(T_{tank} - T_{wall\,(int)}\big), \quad (25)$$

$$q''_{conduction}\ (external) = q''_{convection} \Rightarrow -\lambda_{wall}\frac{dT_{wall\,(n)}}{dx}\bigg|_{n=ext} = k_{ext}\big(T_{wall\,(ext)} - T_{amb}\big). \quad (26)$$

It was concluded in [9,19,29] that in the case of fuelling, the external heat transfer coefficient (k_{ext}) does not have a significant effect. The value of k_{ext} is then accepted to be 6 W/m^2/K in our study following [9].

The model implies the unsteady heat conduction inside the cylinder wall. The equation per each control volume (CV) of the wall can be found elsewhere [30]

$$\rho_{wall}c_{p\,wall}\frac{dT_{wall}}{dt} = \frac{d}{dx}\left(\lambda_{wall}\frac{dT_{wall}}{dx}\right). \quad (27)$$

The model input parameters are defined as the following categories:

- Tank properties: volume, internal surface, diameter & length, external diameter, load-bearing wall and liner thickness and their thermal properties (thermal conductivity, specific heat capacity, density), external heat transfer coefficient; nozzle diameter, initial temperature,
- Hydrogen properties: co-volume constant, specific heat capacity, thermal conductivity, specific gas constant, dynamic viscosity, initial pressure and temperature, pressure ramp, delivery temperature, thermal expansion coefficient, specific heat capacities ratio,
- Other input parameters: ambient temperature, air specific heat capacity, air viscosity, air thermal conductivity, air density, fuelling time, acceleration due to gravity.

The model can predict the dynamics of gas temperature inside the tank, the temperature profile within the load bearing wall and the liner, the gas density or State of Charge (SOC), etc.

Input parameters, order of equations which are solved at each time step, and expected output of calculation at each stage are summarised in Table 1. It must be noted that $\frac{dP_{tank}}{dt}$ is the pressure ramp which is defined as an input.

Two hydrogen tank fuelling experiments [8,29] were selected for the validation of the physical model of fuelling developed in this study. Table 2 presents the characteristics of the tanks in these experiments. The details of experiments were out of scope of the current study and they are available in [8] for the 29 L, Type IV tank and in [29] for the 74 L, Type III tank. According to [8], for 29 L, Type IV tank, the measurement for the gas temperature inside the tank was facilitated by 8 thermocouples. It was concluded in [8,10] that five out of 8 thermocouples, i.e. in the middle of the tank from top to bottom, were assigned to be used for the averaging the temperature due to having same temperature trend with the maximum temperature difference of 3^{0}C. Sixteen thermocouples were used to measure the gas temperature inside the 74 L, Type III tank of [29] experiment. Unfortunately, there was no argument in [29] that how the temperatures were averaged and it was only mentioned that the maximum difference of gas temperature measured by different thermocouples was 5^{0}C.

Table 1. Input parameters, calculation procedure and output parameters

Input parameters

$V, b, \gamma, T_{amb}, T_{del}, \frac{dP_{tank}}{dt}, T_{tank}^{0}, T_{wall}^{0}, A_{int}, \Delta x, \Delta t, R_{H_2}, \rho_{wall(n)}, c_{p\,wall(n)}, \lambda_{wall}, k_{ext}, D_{int}, L, g, \beta,$
$T_{wall}^{0}, k_{int}^{0}, c_{p,g}, \mu_g, \lambda_g, \rho_{tank}^{0}, m_{tank}^{0}$

Calculation procedures

Step No.	Output parameters
1	Hydrogen pressure in the tank, ($P_{tank}^{i} = P_{tank}^{i-1} + \left(\frac{dP_{tank}}{dt}\right)\Delta t$)
2	Hydrogen mass flow rate in tank ($\dot{m}_{inlet}^{i} = \frac{dm_{tank}}{dt}$), Eq. (23)
3	Hydrogen mass in tank ($m_{tank}^{i} = m_{tank}^{i-1} + dm_{tank}$)
4	Hydrogen density in tank ($\rho_{tank} = \frac{m_{tank}}{V}$)
5	Hydrogen temperature in tank (T_{tank}), Eq. (24)
6	Temperature of wall control volumes ($T_{wall\,(n)}$), Eq. (27)
7	Temperature of wall internal surface ($T_{wall\,(int)}$), Eq. (25)
8	Temperature of wall external surface ($T_{wall\,(ext)}$), Eq. (26)
9	Hydrogen density at inlet (ρ_{inlet}), Eq. (16)
10	Hydrogen velocity at inlet (u_{inlet}), Eq. (17)
11	Momentum flux at inlet (M_0), Eq. (18)
12	Entrained mass flow rate ($\dot{m}_{ent}$), Eq. (19)
13	Velocity of entrained gas (u_{ent}), Eq. (20)
14	Hydrogen mass passing inlet during time step Δt ($m_{inlet} = \dot{m}_{inlet}\Delta t$)
15	Hydrogen mass participating in entrainment ($m_{ent} = m_{tank}$), used in Eq. (21)
16	Hydrogen velocity in tank (u_{tank}), Eq. (21)
17	Reynolds number of hydrogen flow in tank (Re_{tank}), Eq. (15)
18	Friction coefficient for flow in tank (f), Eq. (13)
19	Prandtl number in tank (Pr), Eq. (14)
20	Natural convection Nusselt number ($Nu_{int\,natural}$), Eq. (11)
21	Forced convection Nusselt number ($Nu_{int\,forced}$), Eq. (12)
22	Natural convection heat transfer coefficient ($k_{int\,natural}$), Eq. (9)
23	Forced convection heat transfer coefficient ($k_{int\,forced}$), Eq. (10)
24	Grashof number (Gr_{tank}), Eq. 8
25	Internal surface heat transfer coefficient (Eq. (5) or Eq. (6) or Eq. (7)),
26	Repeating steps 1 to 25 as long as $T_{tank} < 85^{0}C\ or\ P_{tank} < 1.25 \times$ NWP $or\ SOC \leq 100\%$.

VALIDATION EXPERIMENTS

Table 2. Characteristics of tanks used in validation experiments [8,14,29]

Characteristics	Type IV	Type III
Reference	[8]	[29]
Volume (L)	29	74
External length (mm)	827	1030
External diameter (mm)	279	427
Internal diameter (mm)	230	354
Liner material	HDPE*	AA*
$\lambda_{\text{wall (liner)}}$ (W/m/K)	0.385	238
$c_{\text{p wall (liner)}}$ (J/kg/K)	1580	902
$\rho_{\text{wall (liner)}}$ (kg/m^3)	945	2700
Composite shell material	CFRP	CFRP
$\lambda_{\text{wall (CFRP)}}$ (W/m/K)	0.74	0.612
$c_{\text{p wall (CFRP)}}$ (J/kg/K)	1120	840
$\rho_{\text{wall (CFRP)}}$ (kg/m^3)	1494	1570
Injector diameter (mm)	3	5
Ambient temperature (K)	293	303
Initial temperature (K)	293	288
Gas delivery temperature (K)	298	298
Initial pressure (MPa)	2	5.5
Target pressure (MPa)	77	70
Filling time (s)	250	640

* HDPE: High density polyethylene; AA: Aluminium alloy;
CFRP: Carbon fibre reinforced polymer.

RESULTS AND DISCUSSION

Figures 2 and 3 demonstrate the comparison of simulation results obtained by the developed physical model against the validation experiments for 29 L Type IV tank [8] and 74 L Type III tank [29]. The pressure ramp used in each experiment is also presented with small graph on the right bottom of each figure.

The temperature dynamics by the physical model is in good agreement with measured in the experiments temperature [8,29].

In the case of the smallest tank of volume 29 L (Fig. 2), the model slightly underpredicts the experimental temperature at the beginning of the process (0-60 s), and the calculations are more accurate to the end of the fuelling.

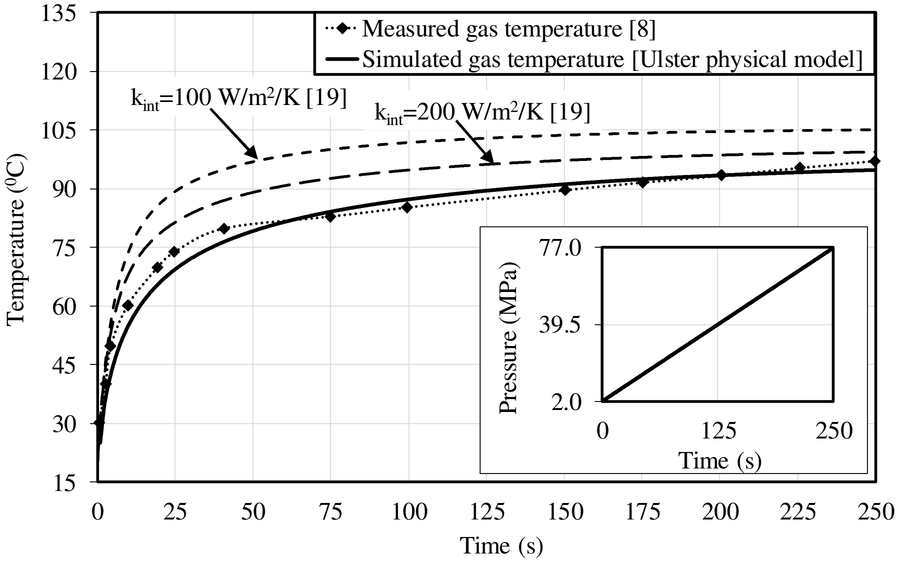

Fig. 2. Experimental and calculated temperature dynamics for the Type IV tank, 29 L [8].

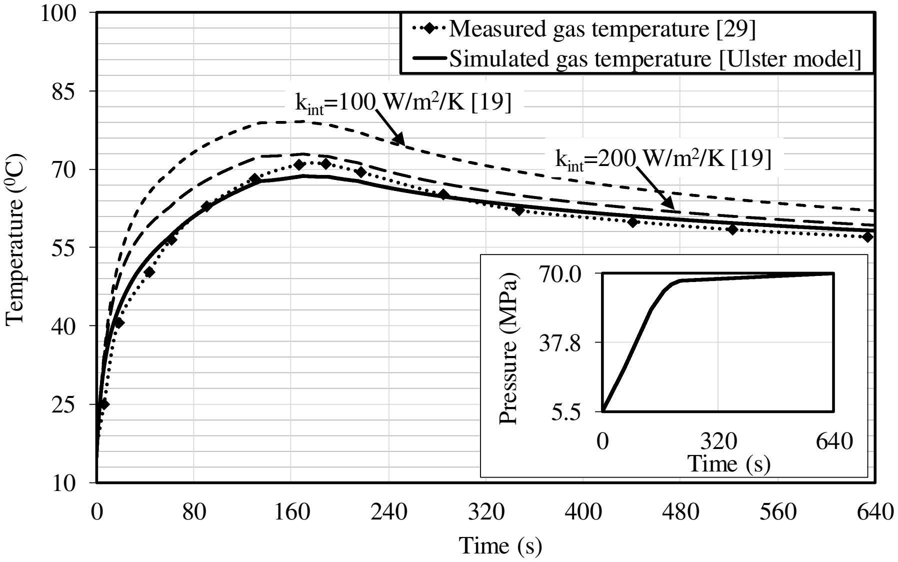

Fig. 3. Experimental and calculated temperature dynamics for the Type III tank, 74 L [29].

The relative deviation between the simulation and experimental results are observed in Fig. 2. The maximum deviation of the simulation results from the experiment is 5^0C. The maximum experimental temperature difference in the tank is 3^0C [10]. This proves that the simulation results are in a good agreement with the experimental data. Two more simulations were also performed with constant k_{int} of 100 W/m^2/K and 200 W/m^2/K following the study of [19]. As presented in Fig. 2, simulations with constant k_{int} of [19] overpredict the temperature of the gas inside the tank, i.e. 10^0C and 15^0C overprediction by using k_{int} of 100 W/m^2/K and 200 W/m^2/K respectively. The effect of employing entrainment theory in our modeling approach is obvious, i.e. dynamic calculation of the internal heat transfer coefficient (k_{int}) following by accurate prediction of the gas temperature inside the tank.

In the case of the largest 74 L volume Type III tank (Fig. 3), the model slightly overpredicts at the beginning, but then slightly underpredicts when the simulation continues until the end of fuelling. This third validation experiment has changing during fuelling pressure ramp compared to constant but different pressure ramps in the first and the second validation tests. The pressure ramp is significantly higher at the beginning of the fuelling and the pressure ramp slope reduces significantly after around 160-180 s. The result is the temperature peak in the temperature dynamics. One may observe the relative deviation between the simulation results and experiment in Fig. 3. The maximum deviation of the simulation in is again 3^0C. According to [29], the maximum experimental difference in the tank is 5^0C which makes an excellent agreement between the simulation results and those obtained by the experiment. It is worth noting that the model reproduced the temperature peak. The impact of Ulster approach in employing entrainment theory for the estimation of $k_{int}$is again obvious in Fig. 3. While using constant k_{int} of 100 W/m^2/K and 200 W/m^2/K, following the study of [19], overpredicts the inside temperature of the gas, our model simulates the gas temperature inside the tank within an acceptable level of accuracy.

CONCLUSIONS

The significance of this study is in the development of the model accounting for underlying phenomena during hydrogen fuelling of composite onboard high-pressure cylinders that can be used for development of automated hydrogen fuelling protocols for light- and heavy-duty vehicles. The model provides the parameters for the regulatory control of the thermal behaviour of the tank during the fuelling, including but not limited to gas temperature, gas density or state of charge (SOC), etc. The rigour of the study is in the model validation against experimental data on fuelling of hydrogen storage tanks of Type III and Type IV with the volumes of 29 L and 74 L, respectively up to pressure 77 MPa with constant and changing fuelling pressure ramp. The model reproduced experimental temperatures within acceptable maximum value of 5^0C characteristic for hydrogen temperature non-uniformity in fuelling tests. The originality of this study is based on integrating physics and thermodynamic methods and correlations in an engineering application to achieve the synergy through their complementarities. The cornerstone of the model is the use of the entrainment theory in combination with conservation of kinetic energy for calculation of gas velocity inside the tank to calculate Reynolds number used in estimation of the Nusselt number and thus the heat transfer coefficient for convective heat transfer between the tank wall and the gas.

ACKNOWLEDGEMENT

The authors are grateful to UK Engineering and Physical Sciences Research Council (EPSRC) for funding through EPSRC SUPERGEN H2FC Hub (EP/J016454/1 and EP/P024807/1) and EPSRC SUPERGEN Challenge “Integrated safety strategies for onboard hydrogen storage” (EP/K021109/1) projects. This study has received funding from the Fuel Cell and Hydrogen 2 Joint Undertaking under grant agreement No.736648 (NET-Tools project). This Joint Undertaking received support from the European Union’s Horizon 2020 research and innovation programme and Hydrogen Europe (HE) and Hydrogen Europe Research (HER). This research is supported by the Project “HYLANTIC”–EAPA_204/2016 which is co-financed by the European Regional Development Found in the framework of the Interreg Atlantic programme.

REFERENCES

[1] GTR ECE/TRANS/WP.29/2013/41, Global technical regulation (GTR) on hydrogen and fuel cell vehicles, (2013).

[2] Commission Regulation No 406/2010, Implementing Regulation (EC) No 79/2009 of the Parliament and of the Council on type-approval of hydrogen-powered vehicles, Off. J. Eur. Union. (2010).

[3] SAE J2601, Fueling protocols for light duty gaseous hydrogen surface vehicles, SAE Int. (2016).

[4] SAE J2579_201806, Standard for Fuel Systems in Fuel Cell and Other Hydrogen Vehicles, SAE Int. Detroit MI, U.S. (2018).

[5] T. Bourgeois, F. Ammouri, D. Baraldi, P. Moretto, The temperature evolution in compressed gas filling processes: A review, Int. J. Hydrogen Energy 43 (2018) 2268–2292.

[6] D. Melideo, D. Baraldi, N. De Miguel Echevarria, B. Acosta Iborra, Effects of the injector directions on the temperature distribution during filling of hydrogen tanks, in: 7th Int. Conf. Hydrog. Saf. (ICHS 2017), 2017.

[7] T. Bourgeois, T. Brachmann, F. Barth, F. Ammouri, D. Baraldi, D. Melideo, B. Acosta-Iborra, D. Zaepffel, D. Saury, D. Lemonnier, Optimization of hydrogen vehicle refuelling requirements, Int. J. Hydrogen Energy 42 (2017) 13789–13809.

[8] N. de Miguel, B. Acosta, D. Baraldi, R. Melido, R. Ortiz Cebolla, P. Moretto, The role of initial tank temperature on refuelling of on-board hydrogen tanks, Int. J. Hydrogen Energy 41 (2016) 8606–8615.

[9] I. Simonovski, D. Baraldi, D. Melideo, B. Acosta-Iborra, Thermal simulations of a hydrogen storage tank during fast filling, Int. J. Hydrogen Energy 40 (2015) 12560–12571.

[10] R. Ortiz Cebolla, B. Acosta, P. Moretto, N. Frischauf, F. Harskamp, C. Bonato, D. Baraldi, Hydrogen tank first filling experiments at the JRC-IET GasTeF facility, Int. J. Hydrogen Energy 39 (2014) 6261–6267.

[11] D. Melideo, D. Baraldi, M.C. Galassi, R. Ortiz Cebolla, B. Acosta Iborra, P. Moretto, CFD model performance benchmark of fast filling simulations of hydrogen tanks with pre-cooling, Int. J. Hydrogen Energy 39 (2014) 4389–4395.

[12] M. Heitsch, D. Baraldi, P. Moretto, Numerical investigations on the fast filling of hydrogen tanks, Int. J. Hydrogen Energy 36 (2011) 2606–2612.

[13] N. de Miguel, R. Ortiz Cebolla, B. Acosta, P. Moretto, F. Harskamp, C. Bonato, Compressed hydrogen tanks for on-board application: Thermal behaviour during cycling, Int. J. Hydrogen Energy 40 (2015) 6449–6458.

[14] B. Acosta, P. Moretto, N. de Miguel, R. Ortiz, F. Harskamp, C. Bonato, JRC reference data from experiments of on-board hydrogen tanks fast filling, Int. J. Hydrogen Energy 39 (2014) 20531–20537.

[15] T. Bourgeois, F. Ammouri, M. Weber, C. Knapik, Evaluating the temperature inside a tank during a filling with highly-pressurized gas, Int. J. Hydrogen Energy 40 (2015) 11748–11755.

[16] M. Monde, Y. Mitsutake, P. Woodfield, S. Maruyama, Characteristics of heat transfer and temperature rise of hydrogen during rapid hydrogen filling at high pressure, Heat Transf. Res. 36 (2006) 13–27.

[17] P.L. Woodfield, T. Takano, M. Monde, Characteristics of heat transfer for hydrogen and wall during filling hydrogen into actual tank at high pressure, in: Asme/Jsme Therm. Eng. Summer Heat Transf. Conf., 2007: pp. 1069–1076.

[18] P.L. Woodfield, M. Monde, T. Takano, Heat tranfer charateristics for practical hydrogen vessels being filled at high pressure, J. Therm. Sci. Technol. 3 (2008) 241–253.

[19] M. Monde, P. Woodfield, T. Takano, M. Kosaka, Estimation of temperature change in practical hydrogen pressure tanks being filled at high pressures of 35 and 70 MPa, Int. J. Hydrogen Energy 37 (2012) 5723–5734.

[20] M. Monde, M. Kosaka, Understanding of Thermal Characteristics of Fueling Hydrogen High Pressure Tanks and Governing Parameters, SAE Int. J. Altern. Powertrains. 2 (2013) 61–67.

[21] P.L. Woodfield, M. Monde, Y. Mitsutake, Measurement of average heat tranfer coefficients in high-pressure vessel during charging with hydrogen, nitrogen or argon gas, J. Therm. Sci. Eng. 2 (2007) 180–190.

[22] R.W. Schefer, W.G. Houf, T.C. Williams, B. Bourne, J. Colton, Characterization of high-pressure, underexpanded hydrogen-jet flames, Int. J. Hydrogen Energy 32 (2007) 2081–2093.

[23] M. Dadashzadeh, D. Makarov, V. Molkov, Non-adiabatic blowdown model: a complimentary tool for the safety design of tank-TPRD system, in: Int. Conf. Hydrog. Safety, Sept. 11-13, 2018, Hamburg, Ger., 2017.

[24] I. Johnson, The Noble-Abel equation of state: thermodynamic derivations for ballistics modelling, 2005.

[25] V. Molkov, S. Kashkarov, Blast wave from a high-pressure gas tank rupture in a fire: Stand-alone and under-vehicle hydrogen tanks, Int. J. Hydrogen Energy 40 (2015) 12581–12603.

[26] Y.A. Çengel, Heat and Mass Transfer: A Practical Approach, McGraw-Hill, 2007.

[27] NIST, Isothermal properties for hydrogen, 2017, http://webbook.nist.gov/cgi/inchi?ID=C1333740&Mask=1#Thermo-Gas.

[28] F.P. Ricou, D.B. Spalding, Measurements of entrainment by axisymmetrical turbulent jets, J. Fluid Mech. 11 (1961) 21–32.

[29] J. Zheng, J. Guo, J. Yang, Y. Zhao, L. Zhao, X. Pan, J. Ma, L. Zhang, Experimental and numerical study on temperature rise within a 70 MPa type III cylinder during fast refueling, Int. J. Hydrogen Energy 38 (2013) 10956–10962.

[30] S.V. Patankar, Numerical heat transfer and fluid flow (Series in computational methods in mechanics and thermal sciences), McGraw-Hill, New York, 1980.

Safety Considerations of an Unignited Hydrogen Release from Onboard Storage in a Naturally Ventilated Covered Car Park

Hussein H.G., Brennan S.*, Makarov D., Shentsov V., Molkov V.

[1] *Hydrogen Safety Engineering and Research Centre (HySAFER),*
Ulster University, Shore Road, Newtownabbey, BT37 0QB, UK
**Corresponding author's email: sl.brennan@ulster.ac.uk*

ABSTRACT

Unignited hydrogen release from 700 bar onboard storage in a naturally ventilated covered car park has been simulated and analysed. A typical car park with dimensions LxWxH=30x28.6x2.6 m was considered. The car park had two vents of equal area on opposing walls: front and back to facilitate cross-flow ventilation based on the British standard (BS 7346-7:2013). Each vent had an area equal to 2.5% of the car park floor area, in line with BS 7346-7:2013 and similar international standards. Releases through three different Thermally Activated Pressure Relief Devices (TPRD) diameters of 3.34, 2.00 and 0.50 mm were compared, to understand the gas dispersion, specifically the dynamics of the flammable envelope (4% vol H_2), and envelopes of 1% and 2% H_2 as these are relevant to sensor and ventilation system activation as required by NFPA 2 standard for enclosures. Concentrations in the vicinity of the vehicle and of the vents are of particular interest. A blowdown model developed in Ulster University was applied to simulate realistic scenarios, and a comparison between an idealistic constant flow rate release and blowdown through a 3.34 mm TPRD diameter highlighted the conservative nature of a constant flow rate release. However, even accounting for the blowdown demonstrated that a release through a TPRD diameter of 3.34 mm leads to the formation of a flammable cloud throughout the majority of the carpark space in less than 20 s. Such a flammable envelope is not observed to the same extent for a TPRD diameter of 2 mm and the flammable envelope is negligible for a 0.5 mm diameter TPRD. Based on ISO/DIS 19880-1, NFPA 2 and IEC (60079-10) standards for equipment with gaseous hydrogen, the ventilation system must work to maintain hydrogen concentration under 1% of hydrogen mole fraction in the air, above this there should be ventilation sensor activation. Whilst a release through a 2 mm TPRD diameter resulted in concentrations of 1% hydrogen along the length of the car park ceiling within 20 s, in contrast an upward release through a 0.5 mm diameter led to concentrations of 1% reaching a very limited area of the ceiling. The simulations comparing an upward and downward release through a 0.5 mm TPRD demonstrated the effect of release direction on hydrogen dispersion. However, this effect is not as pronounced as the effect of changing TPRD diameter. It can be concluded that onboard vehicle storage with a TPRD diameter of 0.5 mm appears to be inherently safer for the scenario considered, as opposed to "typical" larger diameter TPRDs which the study indicates should be carefully investigated to ensure safety in a naturally ventilated covered car park.

KEYWORDS: Unignited release, covered carpark, hydrogen safety, indoor dispersion, natural ventilation.

INTRODUCTION

The number of hydrogen-powered vehicles on the market is growing and it is important to ensure they are at least as safe as conventional vehicles. Onboard hydrogen is typically stored as a compressed gas under high pressure (35 MPa for buses and 70 MPa for cars) and storage tanks are fitted with Thermally Activated Pressure Relief Devices (TPRD) to release hydrogen, avoiding tank rupture when the surrounding temperature reaches 110°C or above. In the event of a TPRD

Proceedings of the Ninth International Seminar on Fire and Explosion Hazards (ISFEH9), pp. 1407-1421
Edited by Snegirev A., Liu N.A., Tamanini F., Bradley D., Molkov V., and Chaumeix N.
Published by Saint-Petersburg Polytechnic University Press
ISBN: 978-5-7422-6498-9 DOI: 10.18720/spbpu/2/k19-27

activation, the released hydrogen might not ignite, instead of forming a flammable atmosphere and an explosion may occur in the presence of an ignition source. The potential delayed ignition and explosion event will not be explored in this study which instead focuses on release and dispersion. Failure of a TPRD or a fire on the opposite side of the tank has potential to cause an unignited release, it is this potential unignited release from a TPRD, in a covered car park which is discussed here. By necessity, hydrogen vehicles will be parked indoors, in garages, underground car parks, and present in tunnels, etc. Unignited hydrogen releases in an enclosure have been covered in the literature to a certain extent. However, with the exception of the work by Houf et al. [1], who considered releases from forklifts in warehouses, to date, the emphasis of numerical studies has tended towards low release rates and/or smaller enclosures. For instance, Venetsanos et al. [2] undertook an inter-comparison of CFD models in 2009 to investigate the model capability to reproduce hydrogen dispersion in a garage for a 1 g/s release from a 20 mm leak diameter in a 78.38 m^3 enclosure with two 5 cm diameter vents on one wall. In 2010, Papanikolaou et al. [3] assessed numerically the ventilation requirements for a residential garage with onboard hydrogen storage. In 2013, Bernard-Michel et al. [4] performed an inter-comparison of CFD models for a 4 Nl/min helium release in a 1 m^3 enclosure with 1 cm circular vent at the base of one wall. Molkov and Shentsov [5] validated the CFD model for buoyant hydrogen releases against the experimental study of Cariteau and Tkatschenko [6] for a small laboratory scale enclosure. When considering unignited releases in an enclosure, both the concentration decay and overpressure may be of interest. Free jets have been previously studied at Ulster and a nomogram is presented in Molkov [7, 8] to calculate hydrogen concentration decay in a jet. Li et al. [9] numerically investigated unignited and ignited releases from a 4.2 mm diameter TPRD under the car in the open air and it was concluded that the hazard distance for the unignited releases was somewhat longer than those for the ignited release. Previous numerical and analytical work by the authors on unignited releases indoors have been focused on momentum-dominated releases in enclosures with minimum ventilation, leading to the pressure peaking phenomenon [10-13]. However, in order for pressure peaking phenomenon to occur the release and enclosure geometry must be such that no air ingress occurs into the enclosure. Whilst this is relevant to residential garages, pressure peaking will not be caused by releases from typical TPRD diameters in car parks with the minimal ventilation legally required. To date, little or no publications exist on hydrogen unignited releases in car parks.

Ventilation recommendations exist to minimise the potential formation of a flammable atmosphere within an enclosure. Ventilation systems should be able to keep hydrogen concentration below the lower flammability limit (LFL) of 4% vol in order to eliminate potential ignition and flame propagation with pressure build up. Indeed, standards typically recommend concentrations do not exceed fractions of the LFL. Standards ISO/DIS 19880-1 [14], NFPA 2 [15] and IEC (60079-10) [16] require that the ventilation rate should ensure a maximum hydrogen mole fraction at 25% of the LFL for enclosures and buildings containing hydrogen equipment, i.e. 1% vol in the case of hydrogen. As an increasing number of car parks are built the majority are constructed in the basement of residential and commercial buildings [17]. In the literature, both underground car parks and those with two or more sides and a roof are referred to as covered car parks. Previous studies have focused on car fires in a car park and the amount of heat released from such a fire [18]. For example, the smoke movement and fire spread were numerically investigated by Zhang et al. [19] for an underground car park containing three burning cars. Joyeux et al. [20] indicated that the majority of fires in covered car parks involve only one car with the exception of the Schiphol fire accident, where around 10 to 30 cars were engulfed with fire. The difference in ventilation approaches should also be noted, with only wind and buoyancy the influencing factors where natural ventilation is considered. There are no existing studies, either experimental or numerical investigating safety aspects of an unignited hydrogen release in a large confined space such as a naturally ventilated covered car park. The release of hydrogen through a TPRD, dispersion and potential accumulation should be investigated to understand the potential hazards, helping to address potential safety issues. Such an investigation is necessary and in the public interest and hence is the subject of this paper.

PROBLEM DESCRIPTION

This work focuses on an unignited hydrogen release in a naturally ventilated covered car park. CFD is used to provide insight into the flow process, including the prediction of flammable zone formation, temperature gradient, and flow patterns inside the covered car park. A typical covered car park has been simulated with dimensions of LxWxH=30x28.4x2.6 m as can be seen in Fig. 1 (ceiling is not shown). The car park has two ventilation openings: a back vent and front vent. They have an equal area but differ in shape. The front vent consists of a top to the bottom opening to drive through and two smaller connected side vents near the car park ceiling, representing an area typical of "door with two side vents". In contrast, the back vent is located on the top centre of the back-wall opposite to the front vent. The ventilation requirements were accounted for based on British Standard BS 7346-7:2013 [21] where it is recommended that a covered car park with natural ventilation should have an opening area equivalent to 5% of the floor area for each floor in a level. Similarly, the standard in the Netherlands NEN 2443 [22], requires vents area equivalent to 2.5% of the floor area on each opposite wall (5% in total). Thus, the two vents considered were of equal area (21.45 m^2) and located on opposite walls.

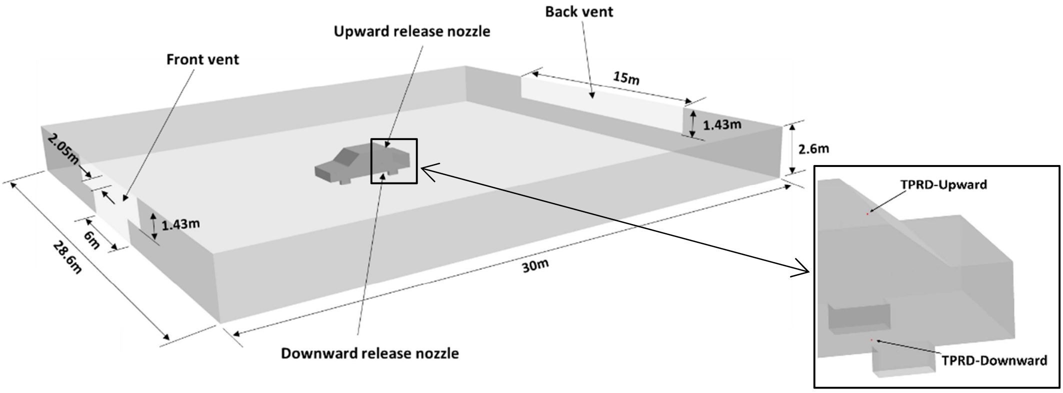

Fig. 1. Sketch of the naturally ventilated covered carpark with car geometry. Insert highlights TPRD location.

Six scenarios were considered by varying TPRD diameters and release type, these are listed in Table 1. The under-expanded jet theory developed at Ulster University [23] was used to calculate the equivalent diameter for the leak inlet (notional nozzle), thus avoiding the need to resolve the shock structure of the real jet at the TPRD exit. The car volume was not considered in 4 of the 6 cases. This allowed a safer diameter to be determined independent of car geometry. The release in these cases was located exactly at the centre of the car park at a position 0.5 m above the floor. However, a car geometry was considered for two scenarios with a release through a 0.5 mm TPRD diameter where release direction and position on the car was assessed. A typical saloon car with dimensions of 4.9 m length, 1.88 m width, and 1.47 m height was chosen. It was assumed that the car was stationary at the time of the leak and the onboard hydrogen tank was filled to capacity. This allows investigation of the worst case scenario. The hydrogen tank was assumed to have a volume of 117 litres and storage pressure of 70 MPa, with a capacity of approximately 5 kg. It was assumed that the car body is 0.25 m above the ground, with "square" wheels representing the actual equivalent circular diameter.

There are two possibilities for TPRD location: underneath the car close to the rear left the wheel or the upper rear of the car close to back windshield facing upwards. These two scenarios have been considered in this study and it was assumed that both were located to the left side of the car with the same horizontal coordinates but differing height, (1.47 and 0.25 m from the floor respectively). The centre of the leak was situated in the centre of the car park, meaning the car body was positioned slightly left of centre. The ambient temperature and pressure were taken as 293 K and 101325 Pa respectively, and the fully quiescent conditions were considered, i.e. no wind effects, replicating a car park located in an urban setting. It is noted that a TPRD release is likely to result in an ignited release when it is triggered by a high temperature, and this is the subject of ongoing studies by the authors. However, the malfunction of a TPRD or activation through impact, warrants investigation, particularly with standard ventilation requirements based on gas concentrations.

Table 1. Scenarios considered for unignited hydrogen release in a naturally ventilated covered car park

Case number	Real release diameter (Notional nozzle diameter) (mm)	Release direction	Car geometry	Blow-down model	Hydrogen mass flow rate (kg/s)
1	3.34 (56.4)	Upward	No	No	0.2993
2	3.34 (56.4)	Upward	No	Yes	0.2993
3	2 (33.8)	Upward	No	Yes	0.1072*
4	0.5 (8.44)	Upward	No	Yes	0.0067*
5	0.5 (8.44)	Upward	Yes	Yes	0.0067*
6	0.5 (8.44)	Downward	Yes	Yes	0.0067*

* Value at the initial stage, before blow down.

MODEL AND NUMERICAL APPROACH

Overview

The CFD package ANSYS Fluent [24] was the base software tool used to simulate this high-pressure hydrogen release scenario. Whilst this study is timely and needed to inform the development of RCS, no previous work exsists on hydrogen releases in carparks, and as such there is no experimental data. Indeed there is limited experimental data for high pressure impinging hydrogen jets at a large scale. Indeed it is hoped that this work can thus assist in addressing hydrogen safety issues regarding large size enclosures with vents. ICEM CFD was used to generate the geometries and hexahedral meshes, with ANSYS Fluent to solve the governing equations. A pressure-based solver has been used and PISO (Pressure Implicit with the Splitting of Operators) was applied in this study for transient flow calculations. The compressible flow was considered, and second-order upwind schemes have been used for all spatial discretisation, with the exception of the pressure gradient where the PRESTO! interpolation method was applied. A least-squares cell-based approach was used for interpolation methods (gradients). Heat transfer by conduction, convection, and radiation was accounted for as described in previous work by the authors [10, 25].

Governing equations

The Reynolds-Average Navier-Stokes (RANS) conservation equations were considered solving mass, momentum, energy, and species,

$$\frac{\partial \bar{\rho}}{\partial t} + \frac{\partial \bar{\rho}\tilde{u}_j}{\partial x_j} = S_{mass}, \tag{1}$$

$$\frac{\partial(\bar{\rho}\tilde{u}_i)}{\partial t}+\frac{\partial(\bar{\rho}\tilde{u}_i\tilde{u}_j)}{\partial x_j}=-\frac{\partial\bar{p}}{\partial x_i}+\frac{\partial}{\partial x_j}(\mu+\mu_t)\left(\frac{\partial\tilde{u}_i}{\partial x_j}+\frac{\partial\tilde{u}_j}{\partial x_i}-\frac{2}{3}\delta_{ij}\frac{\partial\tilde{u}_k}{\partial x_k}\right)+\bar{\rho}g_i, \tag{2}$$

$$\frac{\partial(\bar{\rho}\tilde{E})}{\partial t}+\frac{\partial}{\partial x_j}\left(\tilde{u}_j\left(\bar{\rho}\tilde{E}+\bar{p}\right)\right)=\frac{\partial}{\partial x_j}\left(\left(k+\frac{\mu_t c_p}{Pr_t}\right)\frac{\partial\tilde{T}}{\partial x_j}-\sum_m\tilde{h}_m\left(-\left(\rho D_m+\frac{\mu_t}{Sc_t}\right)\frac{\partial\tilde{Y}_m}{\partial x_j}\right)+\tilde{u}_i\,(\mu+\mu_t)\left(\frac{\partial\tilde{u}_i}{\partial x_j}+\frac{\partial\tilde{u}_j}{\partial x_i}-\frac{2}{3}\frac{\partial\tilde{u}_k}{\partial x_k}\,\delta_{ij}\right)\right)+S_E, \tag{3}$$

$$\frac{\partial(\bar{\rho}\,\tilde{Y}_m)}{\partial t}+\frac{\partial}{\partial x_j}\left(\bar{\rho}\tilde{u}_j\tilde{Y}_m\right)=\frac{\partial}{\partial x_i}\left[\left(\bar{\rho}D_m+\frac{\mu_t}{Sc_t}\right)\frac{\partial\tilde{Y}_m}{\partial x_j}\right]+R_m+S_m, \tag{4}$$

where t is the time, ρ is the density, k represents turbulence kinetic energy, μ_t is the turbulent dynamic viscosity, p is the pressure, S_{mass} is the source term which can be added by user define function (UDF), u represents the velocity components, E is the total energy, δ_{ij} is the Kronecker symbol, c_p is the specific heat at constant pressure, g_i is the gravitational acceleration, Sc_t and Pr_t are the turbulent Schmidt and energy turbulent Prandtl numbers, which are 0.7 and 0.85 respectively, Y_m is the mass fraction, D_m is the molecular diffusivity of the species m, S_E are the source terms in the energy equation, R_m and S_m are the net production/consumption rate by species m chemical reaction and the source term connected to any functions defined by the users for dispersed phase.

Turbulence model

The realizable k-ε turbulent model [25] was considered to solve the transport equation for turbulence kinetic energy (k) and turbulent dissipation rate (ε):

$$\frac{\partial(\rho k)}{\partial t}+\frac{\partial}{\partial x_i}(\rho k u_i)=\frac{\partial}{\partial x_i}\left[\left(\mu+\frac{\mu_t}{\sigma_k}\right)\frac{\partial k}{\partial x_i}\right]+G_k+G_b-\rho\,\varepsilon-Y_m+S_k, \tag{5}$$

$$\frac{\partial(\rho\,\varepsilon)}{\partial t}+\frac{\partial}{\partial x_i}(\rho\varepsilon u_i)=\frac{\partial}{\partial x_i}\left[\left(\mu+\frac{\mu_t}{\sigma_\varepsilon}\right)\frac{\partial\varepsilon}{\partial x_i}\right]+\rho C_1 S\varepsilon-\rho C_2\frac{\varepsilon^2}{k+\sqrt{\nu\varepsilon}}-C_{1\varepsilon}\frac{\varepsilon}{k}C_{3\varepsilon}\,G_b+S_\varepsilon, \tag{6}$$

where, Y_m is the contribution of the fluctuating dilatation in compressible turbulence to the overall dissipation rate, G_b and G_k are the buoyancy and the mean velocity gradient respectively, which presents the k generation, ν is the kinematic viscosity, σ_k and σ_ε are the Prandtl numbers of turbulence for k and ε, corresponding to 1 and 1.2. $C_{3\varepsilon}$ is calculated as a function of the flow velocity components with respect to the gravitational vector while C_2 and $C_{1\varepsilon}$ are constants 1.90 and 1.44 respectively. C_1 is evaluated as a function of the modulus of the mean rate of the strain sensor, S. S_k is a source term to be defined by User Define Function (UDF) for Turbulence Kinetic Energy while S_ε represents a UDF source term for turbulence dissipation rate, which was calculated from blowdown parameters via a UDF in this study. This model outperforms the standard κ-ε model especially for calculating spreading rate in axisymmetric jets [24,27].

Boundary and initial conditions

A domain with outer dimensions 170x 128.6 x 92.6 m (LxWxH) was used, which is axisymmetric lengthwise. A hexahedral mesh was generated throughout the domain, details of which are given later in this paper. The walls were not meshed in depth. The car park floor, walls, and the roof had a thickness of 0.15 m and were assumed to be constructed of concrete, and the release pipe or car body was considered to be made of aluminium. The material properties chosen are similar to concrete typically used for car parks in the UK. Two materials were used in this study: aluminium and concrete, and the details of the material properties can be found in a previous publication [25]. A box mesh technique with mesh interfaces was implemented to provide a refined mesh around the nozzle and inside the car park, making it possible to improve resolution without a significant increase in total number of control volumes. A no-slip condition was applied at the solid surfaces.

The domain was assumed to be initially 100% air at normal ambient pressure and temperature (101325 Pa and 293 K respectively).

Notional nozzle model and blowdown process

Hydrogen released from a 70 MPa tank through a TPRD forms an under-expanded jet, leading to a complex shock structure at the nozzle exit, which is computationally intensive to capture. It is not necessary to solve this shock structure in this work as it is not the focus of this study. Therefore, the notional nozzle theory developed by Molkov et al. [23] and described in detail in [8] has been applied. In addition, their blowdown model was implemented. Molkov et al. [23], found that the adiabatic blowdown model provided better agreement with experiment than an isothermal approach for the initial stage whilst the isothermal blowdown model provided better agreement compared to experimental data for high-pressure hydrogen storage (930 bar) in later stages in case of release temperature prediction as studied by Cirrone et al. [28] . Thus, an adiabatic model has been used in this study to reproduce the hydrogen tank blowdown since only the initial stage of the blowdown process was considered. Predicted pressure dynamics for blowdown through 3.34 mm, 2 mm and 0.5 mm diameters are shown in Fig. 2.

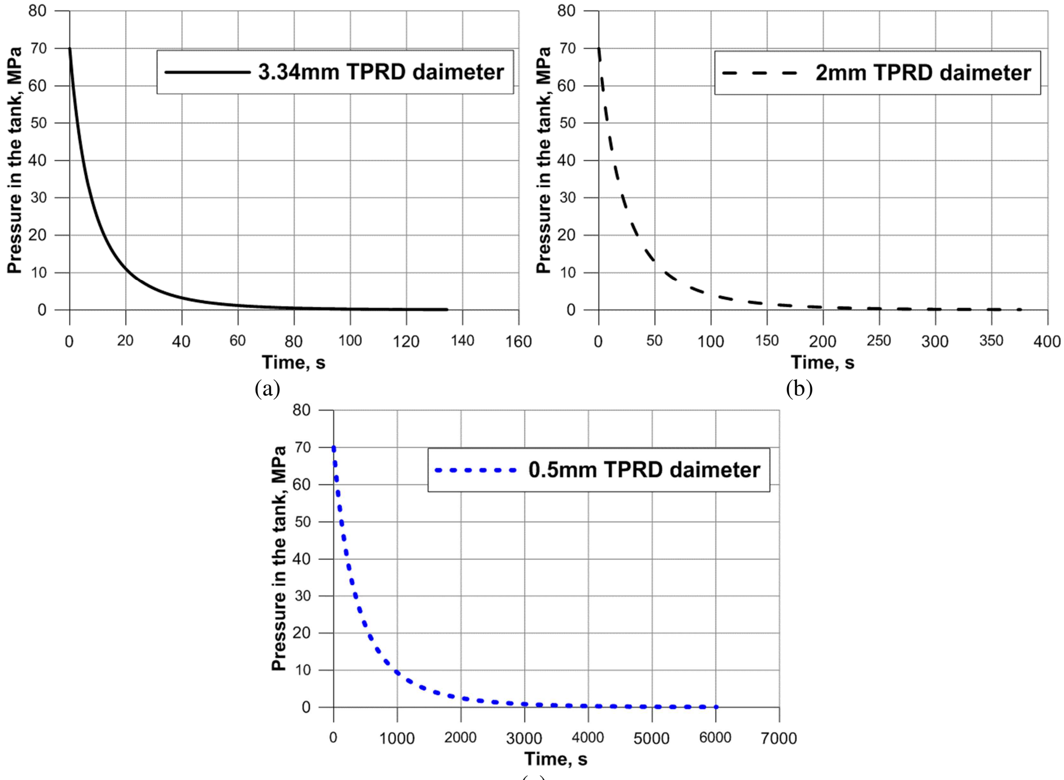

(a)

(b)

(c)

Fig. 2. Tank pressure for adiabatic blowdown from 70 MPa. (a) 3.34 mm diameter TPRD; (b) 2 mm diameter TPRD; (c) 0.5 mm diameter TPRD.

When the TPRD diameter is 3.34 mm for a 117 L tank at 70 MPa, the total blowdown takes over 138 s and the transition from under-expanded jet to expanded jet occurs at 106 s. In contrast, a 0.5 mm diameter TPRD requires 6000 s to fully blowdown and 4742 s to transit to an expanded jet. These differences have to be accounted for by hydrogen tank designers as they affect the required thermal resistance of tank to a fire. It is acknowledged that this presents a significant engineering challenge. Redesign of ventilation systems is also an option. However, this would not eliminate problems associated with ignited releases and vehicles would be restricted to use in enclosures that had been retrofitted or newly designed, rather than ensuring all uses are inherently safe.

Volumetric source model

Decreasing tank pressure during blowdown leads to a corresponding reduction in the notional nozzle diameter. In order to avoid constantly changing the release diameter in the CFD calculation, a volumetric source approach [23] was implemented in a single cell above the leak. This mimics the hydrogen mass inflow by taking mass, momentum, energy, turbulent kinetic energy and turbulent dissipation energy data from written for Fluent the User Defined Function (UDF). This approach enables changes in the notional nozzle parameters to be reflected in the volumetric sources without any change in the release shape and volume. This method was experimentally validated for hydrogen releases through a 3 mm diameter [29] and the results were presented in detail in [23]. It was demonstrated that a volumetric source equivalent to 4 times (or less) the notional nozzle diameter can accurately reproduce concentration decay in the under-expanded jets. All volumetric sources used in this study are either equal to or larger than the notional nozzle diameter.

Grid independency

In order to comply with the CFD model evaluation protocols [30], three different grids were considered (coarse, intermediate, and refined). In each grid refinement, the average length of the computational cells was halved inside the car park, particularly in areas where high gradients and complex phenomena were expected. Specifically, localised refinement was provided around the hydrogen inlet, the ceiling and regions of the enclosure volume for all grids as recommended by Baraldi et al. [30]. The study was conducted for case 1 and the mesh details are summarised in Table 2.

Table 2: Mesh details for grid independence study

Mesh size	No. of cells	No. of faces	No. of nodes
1. Coarse	479,977	1,639,600	532,532
2. Intermediate	691,759	2,302,631	745,416
3. Refine	1,222,412	3,978,771	1,296,276

It should be noted that only the mesh within the car park was changed in this grid independence study since the outer domain does not effect conditions in the initial stages of the release. The hydrogen mole fraction was measured at points along the jet axis at increasing height relative to the release, results from a flow time of 0.7 s are shown in Fig. 3a. In addition, concentrations were recorded for points 0.021 m under the car park ceiling at an increasing radius from the jet axis, these results at 0.7 s are shown in Fig. 3b.

As seen in Fig. 3b the hydrogen cloud has a radius of 4m at 0.7 s. The grid independence study showed no significant changes in the results when a coarser grid is used, yet significant savings were made in computational time. Therefore, an “intermediate grid”, as described in Table 2 was used in the study to achieve a balance between accuracy and computational time.

MODEL VALIDATION

As discussed, no exsisting experimental data exsists for a hydrogen release in a covered car park, and limited data exsists for impinging uignited jets. However, experimental data for impinging helium jets, produced by KIT-HYKA has been considered for comparison. The experiments were carried out within the H2FC European Infrastructure project (http://www.h2fc.eu/) and have not been published in their entirety, however, they are summarised in the work by Dadashzadah et al. [31]. The experiments involved blowdown from a 19 l tank at 70 MPa through a release diameter of 1 mm. The release occurred vertically and impinged on to a plate with dimensions 1.52 x 1.51 m. The plate was located 85 cm from the release point. Helium concentration was was measured at locations along the surface locations. Two sensors were considered for validation purposes, as shown in Fig. 4. Pos 1 was located at a distance of 100 mm distance from the jet axis, and Pos 2 was located 250 mm from the jet axis. on the exact axis as the first one. Two steps were taken in the validation process; blowdown parameters were compared with those predicted by the Ulster blowdown model, then these validated pressure dynamic curves were used as an input to the CFD simulation.

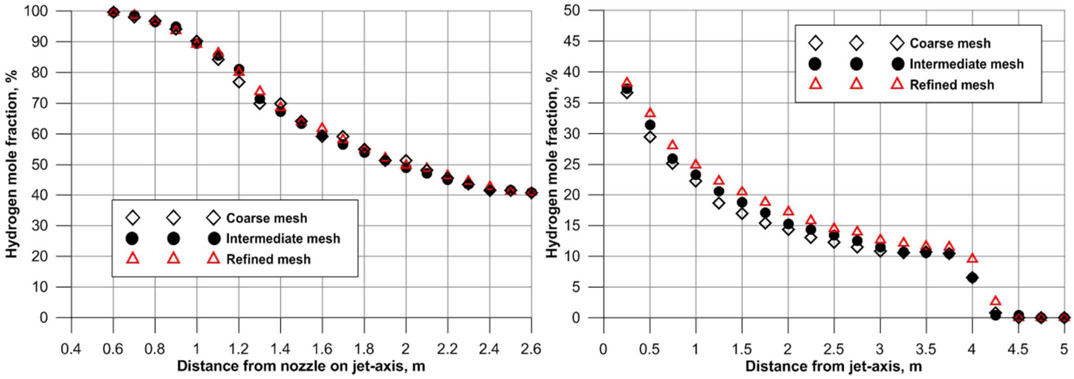

(a) (b)

Fig. 3. Grid independence study for 3.34 mm TPRD diameter with constant release (case 1) at a flow time of 0.7 s. (a) Hydrogen mole fraction at increasing vertical distance from the leak nozzle along jet axis; (b) Hydrogen mole fraction at increasing radial distance from the jet axis at a position 0.021 m under the car park ceiling.

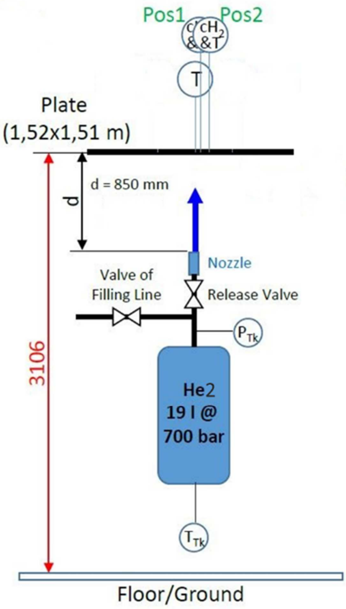

Fig. 4. Schematic diagram of KIT experiment for an impinging helium jet.

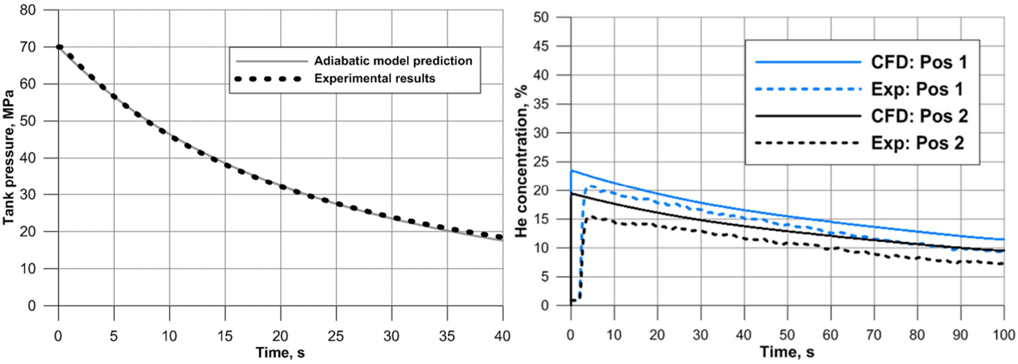

(a) (b)

Fig. 5. Experimental and numerical predictions. (a) Storage pressure dynamics ; (b) Helium concentration at plate surface sensors

Experimentally measured pressure dynamics at the release point were compared with those predicted using the Ulster adiabatic blowdown model with a Discharge Coefficient (C_D) of 0.8. Good agreement was found between the model predictions and experiment as shown in Fig. 5a.

A volumetric source model was employed for the helium release in the CFD simulations. A hexahedral grid was used with refinement in the region of the nozzle area and plate. An indoor environment was considered with dimensions of L x W x H of (25.32 x 7.87 x 10.42) m. A comparison of the concentraion measurements at Pos 1 and Pos 2 is given in Fig 5b. Differences are within allowable engineering limits, with differences observed of 10 to 12%. It should be noted that in the experiments, in order to measure concentration, helium gas was suctioned at the plate surface to a helium measuring device along an 80 cm tube, this may be a factor in the time delay observed between the experimental measurements at the beginning of the experiment. Differences between the numerical prediction and the experiment decreased with increasing time.

RESULTS

Previous studies by the authors have focused on unignited and ignited hydrogen release in small laboratory-scale enclosures and residential garages to evaluate TPRD diameters, vent position, and size, to avoid the safety risk due to the pressure peaking phenomena [10]. Whereas in this work the larger vents mean that overpressure is not the most significant hazard. Thus, the focus of this work is on the development of a flammable atmosphere for the six cases, with a specific emphasis on 1% vol as this represents the maximum allowable mole fraction of hydrogen in an enclosure containing hydrogen equipment in accordance to ISO/DIS 19880-1 [14], NFPA 2 [15] and IEC (60079-10) [16] standards and guidelines

Development of flammable atmosphere for constant hydrogen release

A constant hydrogen release of 0.299 kg/s through a 3.34 mm TPRD diameter as simulated in [24] was considered. Current TPRD diameters can range from 2 to 5 mm and 3.34 mm was taken as the largest diameter in this study. Whilst this facilitates tank blowdown in a shorter period of time and decreases the risk of tank rupture, the hazards for indoor release, where the gas may accumulate should be considered. This case represents the worst case scenario considered in this study as blowdown is not accounted for. However, accumulation is evident within the first seconds of the release before the pressure drop in a blowdown scenario would be significant. It is also indicative of what may occur in the event of leaks from other compressed hydrogen gas sources, where pipes and tanks may have a leak with a constant release of hydrogen flow for a longer period. Dispersion of hydrogen over the first 20 s of the release can be seen in Fig. 6, the iso-surfaces show the extent of the flammable atmosphere (4% vol), and of 25% the LFL (1% vol). Where 1% vol represents the maximum allowable mole fraction of hydrogen in an enclosure containing hydrogen equipment in accordance to ISO/DIS 19880-1 [14], NFPA 2 [15] and IEC (60079-10) [16] standards and guidelines.

It can be seen from Fig. 6 that within just 20 s hydrogen concentration is 1% vol or higher throughout the enclosure, demonstrating that for the particular release, the natural ventilation of the car park is incapable of maintaining a hydrogen mole fraction below 1%, any hydrogen sensors present would be activated. It can also be seen how a flammable atmosphere has been formed across almost the entire ceiling of the carpark and around the ventilation openings within just 20 s of release. Whilst this is a worst case scenario it does highlight potential safety concerns which should be taken into account by engineers.

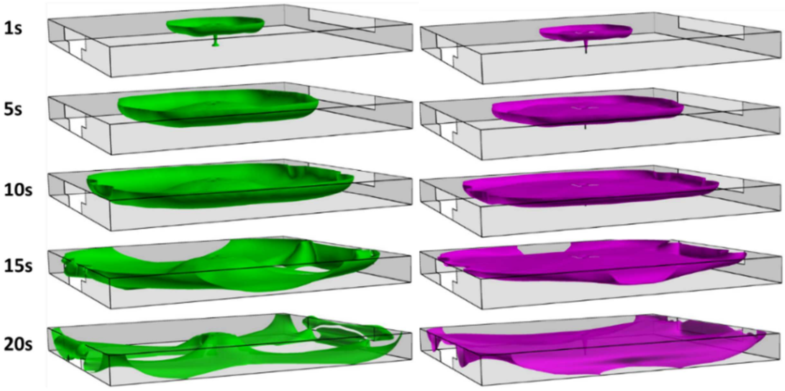

(a) (b)

Fig. 6. Hydrogen mole fraction for a constant release of 0.299 kg/s through a 3.34 mm diameter TPRD. (a) Iso-surface 1% vol; (b) Iso-surface 4% vol.

The effect of TPRD diameter on hydrogen dispersion in the car park

To reflect more realistic scenarios a blowdown model was implemented using the volumetric source as described in the previous sections. Three different (3.34 mm, 2 mm, 0.5 mm) TPRD diameters were considered and compared with the constant release from 3.34 mm TPRD diameter described previously. Iso-surfaces of 1% vol and 2% vol for the various TPRD diameters at 20 s can be seen in Fig. 7. In Fig. 8 Iso-surfaces of 4% vol for the various TPRD diameters at 20 s are shown representing the LFL. The effect of accounting for blowdown through the 3.34 mm TPRD can be clearly seen and is most evident in Fig. 8.

It can be seen that even when blowdown is accounted for a TPRD diameter of 3.34 mm can lead to safety concerns, with a flammable atmosphere being formed throughout the carpark. In contrast, it is shown how a release through a 2 mm diameter TPRD from 700 bar leads to a much smaller flammable hydrogen cloud around the release nozzle and under the ceiling. Concentrations of 1% vol, are predicted in the vicinity of the vents within 20 s. A 2 mm TPRD diameter led to a flammable cloud with a radius of approximately 5 m above the leak and underneath the ceiling.

A 0.5 mm TPRD diameter was also investigated and it can be seen from Fig. 9 how a flammable cloud is formed in a very limited area above the leak in contrast with the larger diameters considered. From Fig. 9 it can be seen how the extent of the flammable atmosphere remains almost constant over the initial 20 s of the of the release. Thus, a TPRD diameter of 0.5 mm could be considered as an inherently safer diameter for unignited hydrogen release from onboard storage in this case. In contrast, the extent of the hydrogen cloud at 1% continues to grow over 20 s, as shown in Fig. 9.

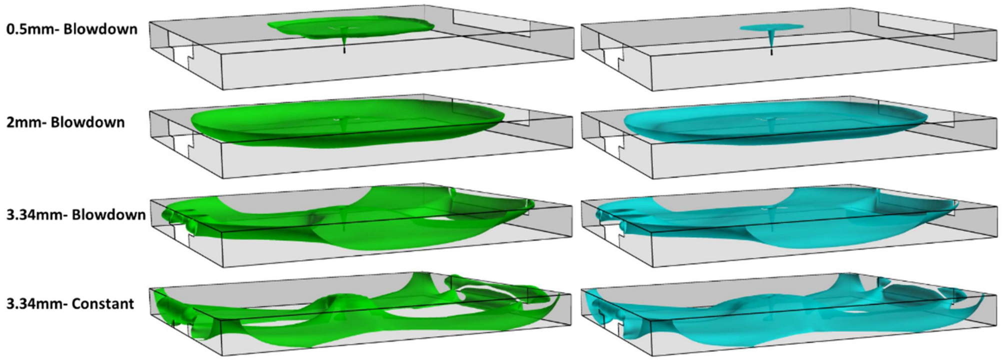

(a) (b)

Fig. 7 Hydrogen mole fraction after 20 s for releases from 700 bar through 0.5 mm, 2 mm and 3.34 mm TPRD diameters. (a) Iso-surface 1% vol; (b) Iso-surface 2% vol.

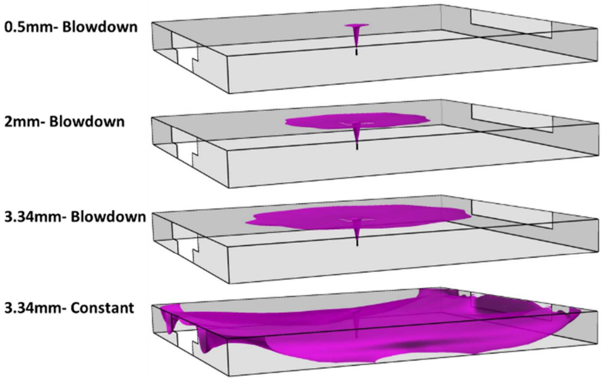

Fig. 8. Iso-surface showing 4% hydrogen mole fraction after 20 s for releases from 700 bar through 0.5 mm, 2 mm and 3.34 mm TPRD diameters.

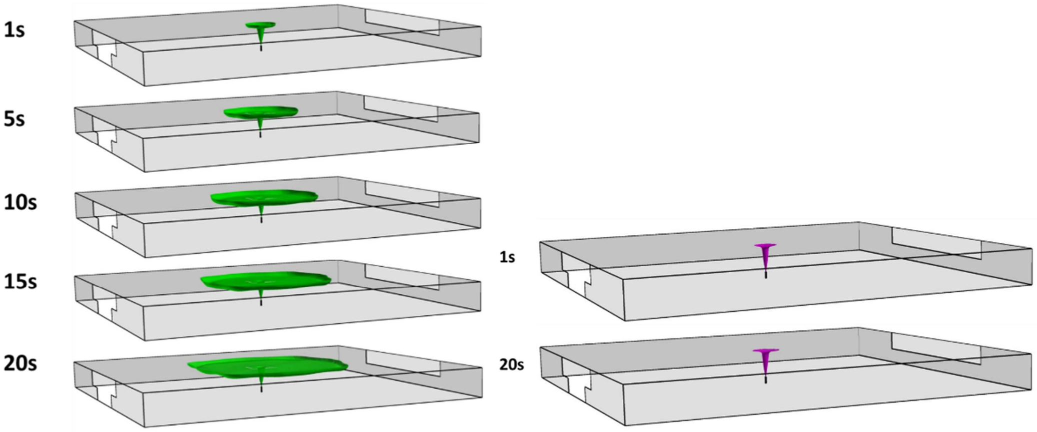

(a) (b)

Fig. 9. Hydrogen mole fraction for a blowdown release from 700 bar through a 0.5 mm TPRD. (a) Iso-surface 1% vol; (b) Iso-surface 4% vol.

Hydrogen release direction from onboard storage in a naturally ventilated covered car park

In addition to releasing hydrogen through a “pipe” 0.5 m pipe above the car park floor, a car body was also considered to represent a more realistic scenario. Two different release directions were considered using a 0.5 mm TPRD diameter in order to investigate the effect of release orientation and release location. Results for a downward release, from a location under the car beside the rear left wheel, are shown in Fig. 10 for 4% hydrogen mole fraction.

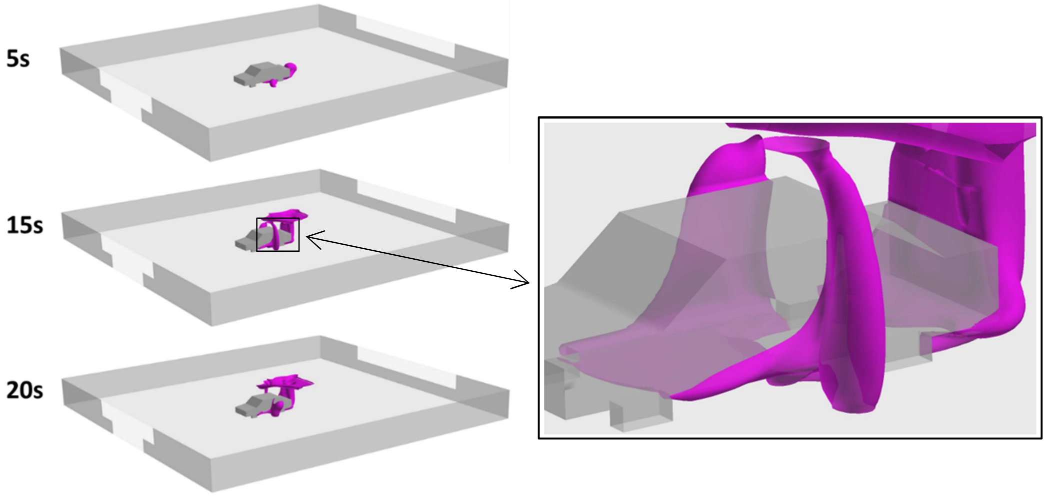

Fig. 10. Iso-surface showing 4% hydrogen mole fraction for a *downward* release from 700 bar through a 0.5 mm TPRD.

The maximum flammable envelope was reached at a release time of approximately 15 s, after which time the height of the jets at the sides and rear of the car began to reduce, this height reduction is observed by 20 s. Since the release was downwards, impinging on the floor, the car wheels obstructed some of the flow dispersion, leading to a non-uniform release pattern. H release. Within 15 s of the release, the flammable envelope covered the rear, left and right of the car in addition to regions of the ceiling. This presents a clear safety concern for any passengers in the car in the event ignition sources may be present. Nevertheless, the flammable cloud is relatively small and the hydrogen disperses quickly.

An upward release was also simulated at a height of 1.13 m from the ground, representing the top of the car and the results are shown in Fig. 11 for 4% hydrogen mole fraction.

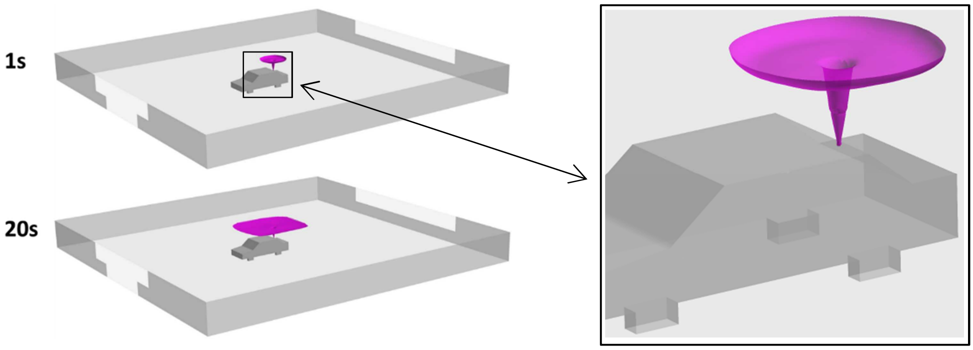

Fig. 11. Iso-surface showing 4% hydrogen mole fraction an *upward* release from 700 bar through a 0.5 mm TPRD.

For an upward release the maximum flammable envelope was formed at approximately 20 s, i.e. 5 s later than for the downward case. It can be seen from Fig. 11 how the flammable envelope covers a comparably larger area beneath the ceiling but is spread over a smaller region surrounding the car, and hence has a higher average hydrogen concentration.

A comparison of the gas envelope development for 1% hydrogen mole fraction for a downward and upward release through a 0.5 mm TPRD diameter is shown in Fig. 12. It is seen how for the downward release the envelope of 1% volume is considerably smaller in the region underneath the ceiling, however, the car itself is surrounded on three sides by the gas cloud at 1% hydrogen. In contrast, the upward release led to a relatively larger envelope of 1% hydrogen in the region beneath the ceiling, but a minimal envelope was seen in the vicinity of the car. It should be mentioned that both downward and upward releases could be classified as inherently safe if a 0.5 mm TPRD diameter is used because the flammable cloud produced is limited in a very small area, predominately near the ceiling, and it disperses quickly with continuing tank blowdown. However, TPRD diameters larger than 0.5 mm can lead to the more significant flammable cloud in the absence of additional ventilation. It should be emphasised that whilst the envelope at 1% vol has not reached a maximum at 1%, the flammable zone has already begun to reduce by this time, as discussed in the previous section.

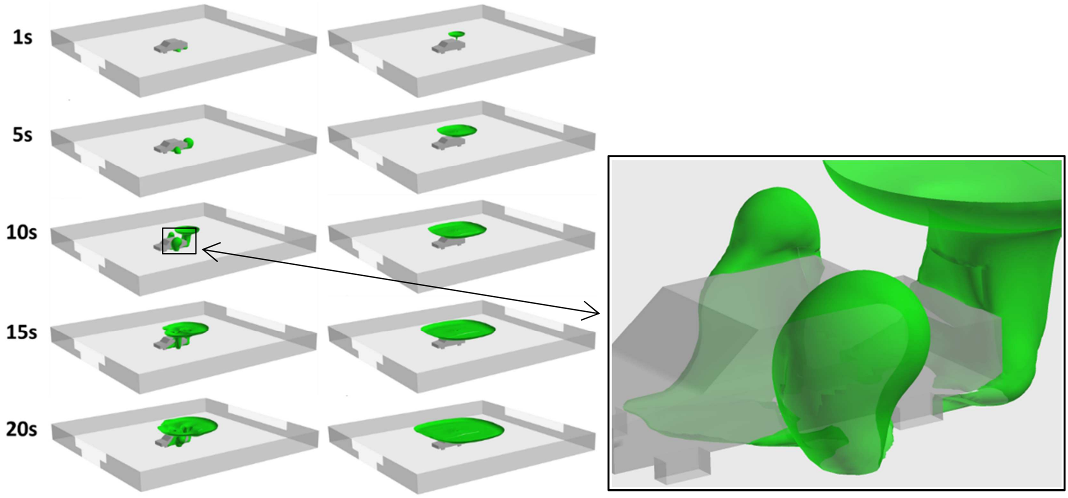

(a) (b)

Fig. 12. Hydrogen release from 700 bar through a 0.5 mm TPRD. (a) Downward release; (b) Upward release.

CONCLUSIONS

Unignited hydrogen release from onboard vehicle storage in a naturally ventilated covered car park has been considered numerically for the first time. Simulations were carried out for a car park with dimensions LxWxH=30x28.6x2.6 m, incorporating two vents which provided an opening equivalent in area to 5% of the floor area across two opposing walls in accordance with British Standard BS 7346-7:2013. Six release cases from 700 bar storage were considered; four upward releases from a pipe 0.5 m above the floor, and a downward and upward release where the car geometry was included. A blowdown model, developed at Ulster University [23], was applied for all but one constant release scenario. As expected, a constant mass flow rate release resulted in a larger flammable cloud compared for a blowdown release through the same TPRD diameter, demonstrating the importance of including blowdown for real scenarios. It was demonstrated how a

0.5 mm diameter TPRD resulted in a considerably smaller flammable cloud. Concerns have been highlighted for ”typical” TPRD diameters and it has been demonstrated how the diameter should be reduced as much as is reasonably practicable. In order to investigate a real case scenario, a car body geometry was modelled, and downward and upward releases from 700 bar storage through a 0.5 mm TPRD were compared. The downward release resulted in a larger flammable envelope in the vicinity of the car, particularly surrounding the doors and rear. However, the average hydrogen concentration within the flammable cloud was lower compared with the upward release. In contrast, an upward release let to a greater flammable envelope beneath the ceiling, but not surrounding the car. Both downward and upward releases from 700 bar through a 0.5 mm TPRD in a covered car park can be considered as inherently safe producing a limited flammable cloud which disperses quickly. However, the work does indicate that if larger diameter TPRDs are to be used, then safety considerations for an unignited release in a covered car park should be further investigated and addressed.

REFERENCES

[1] W.G. Houf, G.H. Evans, I.W. Ekoto, E.G. Merilo, M.A. Groethe, Hydrogen fuel-cell forklift vehicle releases in enclosed spaces, Int. J. Hydrogen Energy 38 (2013) 8179-8189. doi:10.1016/j.ijhydene.2012.05.115.

[2] A.G. Venetsanos, E. Papanikolaou, M. Delichatsios, J. Garcia, O.R. Hansen, M. Heitsch, A. Huser, W. Jahn, T. Jordan, J.M. Lacome, H.S. Ledin, D. Makarov, P. Middha, E. Studer, A. V. Tchouvelev, A. Teodorczyk, F. Verbecke, M.M. Van der Voort, An inter-comparison exercise on the capabilities of CFD models to predict the short and long term distribution and mixing of hydrogen in a garage, Int. J. Hydrogen Energy 34 (2009) 5912-5923. doi:10.1016/j.ijhydene.2009.01.055.

[3] E.A. Papanikolaou, A.G. Venetsanos, M. Heitsch, D. Baraldi, A. Huser, J. Pujol, J. Garcia, N. Markatos, HySafe SBEP-V20: Numerical studies of release experiments inside a naturally ventilated residential garage, Int. J. Hydrogen Energy 35 (2010) 4747-4757. doi:10.1016/j.ijhydene.2010.02.020.

[4] G. Bernard-Michel, B. Cariteau, J. Ni, S. Jallais, E. Vyazmina, D. Melideo, CFD Benchmark Based Exp. Helium Dispers. a 1 M3 Enclos. e Intercomparisons Plume, In: Proceedings of ICHS 2013, Brussels, Belgium, 2013: p. paper ID No. 145.

[5] V. Molkov, V. Shentsov, Numerical and physical requirements to simulation of gas release and dispersion in an enclosure with one vent, i Int. J. Hydrogen Energy 39 (2014) 13328-13345. doi:10.1016/j.ijhydene.2014.06.154.

[6] B. Cariteau, I. Tkatschenko, Experimental study of the effects of vent geometry on the dispersion of a buoyant gas in a small enclosure, Int. J. Hydrogen Energy 38 (2013) 8030-8038. doi:10.1016/j.ijhydene.2013.03.100.

[7] V. Molkov, Hydrogen non-reacting and reacting jets in stagnant air: overview and state of the art, Proceedings of the 10th International Conference on Fluid Control, Measurement, and Visualization (FLUCOM2009), 17-21 August 2009. Moscow, Russia.

[8] V. Molkov, Fundamentals of Hydrogen Safety Engineering I, www.bookboon.com, 2012.

[9] Z.Y. Li, D. Makarov, J. Keenan, V. Molkov, CFD study of the unignited and ignited hydrogen releases from TPRD under a fuel cell car, ICHS (2015), Paper No.322.

[10] S. Brennan, H. G. Hussein, D. Makarov, V. Shentsov, V. Molkov, Pressure effects of an ignited release from onboard storage in a garage with a single vent, Int. J. Hydrogen Energy (2018). https://doi.org/10.1016/j.ijhydene.2018.07.130.

[11] S. Brennan, V. Molkov, Safety assessment of unignited hydrogen discharge from onboard storage in garages with low levels of natural ventilation, Int. J. Hydrogen Energy 38 (2013) 8159-8166. doi:10.1016/j.ijhydene.2012.08.036.

[12] D. Makarov, V. Shentsov, M. Kuznetsov, V. Molkov, Pressure peaking phenomenon: model validation against unignited release and jet fire experiments, Int. J. Hydrog. Energy 43 (2018) 9454-9469.

[13] S. Brennan, D. Makarov, V. Molkov, Dynamics of Flammable Hydrogen-Air Mixture Formation in an Enclosure with a Single Vent, Sixth Int. Semin. Fire Explos. Hazards. (2011) 978–981. doi:10.3850/978-981-08-7724-8.

[14] International Electrochnical commission IEC 60079-10-1, Explosive atmospheres – Part 10-1: Classification of areas - Explosive gas atmospheres, 2015.

[15] National fire protection association NFPA 2, Hydrogen technologies code, 2011.

[16] The International organization for standardization ISO/DIS 19880-1, Gaseous hydrogen – fuelling stations, Part 1: General requirements, 2018.

[17] W.K. Chow, On safety systems for underground car parks, Tunn. Undergr. Sp. Technol. (1998). doi:10.1016/S0886-7798(98)00060-1.

[18] M.G.M. van der Heijden, M.G.L.C. Loomans, A.D. Lemaire, J.L.M. Hensen, Fire safety assessment of semi-open car parks based on validated CFD simulations, Build. Simul. 6 (2013) 385–394. doi:10.1007/s12273-013-0118-7.

[19] X.G. Zhang, Y.C. Guo, C.K. Chan, W.Y. Lin, Numerical simulations on fire spread and smoke movement in an underground car park, Build. Environ. 42 (2007) 3466-3475. doi:10.1016/j.buildenv.2006.11.002.

[20] D. Joyeux, J. Kruppa, L.-G. Cajot, J.-B. Schleich, P. Van de Leur, L. Twilt, Demonstration of real fire tests in car parks and high buildings, Report EUR 20466, 2002.

[21] British Standard institution BS 7346-7:2013, Components for smoke and heat control systems – Part 7: Code of practice on functional recommendations and calculation methods for smoke and heat control systems for covered car parks, 2013.

[22] Nederlands Normalisatie-Instituut NEN 2443. parkeren en stallen van personenauto's op terreinen en garages, ICS 91.040.99, 2000.

[23] V. Molkov, D. Makarov, M. Bragin, Physics and modelling of underexpanded jets and hydrogen dispersion in atmosphere, In: Physics of Extreme States of Matter, 2009, pp. 146-149.

[24] ANSYS Fluent R16.2 User Guide, (2016).

[25] H. G. Hussein, S. Brennan, D. Makarov, V. Shentsov, V. Molkov, Numerical validation of pressure peaking from an ignited hydrogen release in a laboratory-scale enclosure and application to a garage, Int. J. Hydrogen Energy 43 (2018) 17954-17968.

[26] T.-H. Shih, W.W. Liou, A. Shabbir, Z. Yang, J. Zhu, A new k-ϵ eddy viscosity model for high Reynolds number turbulent flows, Comput. Fluids 24 (1995) 227–238. doi:10.1016/0045-7930(94)00032-T.

[27] S.B. Pope, An explanation of the turbulent round-jet/plane-jet anomaly, AIAA J. 16 (1978) 279-281. doi:10.2514/3.7521.

[28] D.M.C. Cirrone, D. Makarov, V. Molkov, Simulation of thermal hazards from hydrogen under-expanded jet fire. Int. J. Hydrogen Energy (2018).

[29] P.T. Roberts, L.C. Shirvill, T.A. Roberts, C.J. Butler, M. Royle, Dispersion of hydrogen from high-pressure sources, in: Inst. Chem. Eng. Symp. Ser., 2006, p. 410.

[30] D. Baraldi, D. Melideo, A. Kotchourko, K. Ren, J. Yanez, O. Jedicke, S.G. Giannissi, I.C. Tolias, A.G. Venetsanos, J. Keenan, D. Makarov, V. Molkov, S. Slater, F. Verbecke, A. Duclos, The CFD Model Evaluation Protocol, 2016.

[31] M. Dadashzadeh, D. Makarov, V. Molkov, Non-adiabatic blowdown model: a complementary tool for the safety design of tank-TPRD system, In: Proceedings of ICHS 2017, Hamburg, Germany, 2017.

Flame Propagation through Ultra-Lean Hydrogen-Air Mixture under Terrestrial Gravity Conditions

Yakovenko I.[1, *], **Kiverin A.**[1], **Melnikova K.**[1]

[1] *Joint Institute for High Temperatures of Russian Academy of Sciences,*
Laboratory of Mathematical Modeling, Moscow, Russia
**Corresponding author's email: yakovenko.ivan@bk.ru*

ABSTRACT

The paper is devoted to the study of peculiarities of flame dynamics in ultra-lean hydrogen-air mixtures in terrestrial gravity conditions. By means of numerical methods, it is shown that gas-dynamical flows, which develop due to buoyancy force exerted on hot combustion products, play a crucial role on the overall ultra-lean flame dynamics from the earliest stage after ignition and up to large-scale motion of the developed flame. Immediately after ignition convective flows determine the flame kernel stability. It is shown that despite the superadiabatic temperature of the flame products that is considered as one of the main stability factors of the ultra-lean flames in microgravity conditions the influence of convective flows on the ultra-lean flames in terrestrial gravity conditions can alter flammability limits from that measured in microgravity. On the other hand, the propagation dynamics of the stable flame kernels is also mainly determined by the buoyancy forces. Rising velocity of the flame kernel in the ultra-lean mixture occurs to be much greater than burning velocity and correlates well with estimations obtained for the bubble rising in liquid. Apart from the upward rising, the developed flame is shown to be expanding laterally so the complex large-scale flame structure is observed which could be a possible hazard of explosion and fire for many industrial environments.

KEYWORDS: Ultra-lean flames, hydrogen safety, numerical modeling, flame ball.

INTRODUCTION

Abnormal leakage of flammable gases into the atmospheric air inside the confined chambers poses a serious threat of fire and explosion. The most dangerous conditions arise when the chamber volume is rather small so almost perfectly stirred stoichiometric composition of the combustible gas with the atmosphere is formed inside the chamber. In this case, accidental ignition can result in combustion wave propagating in such devastating regimes as fast deflagration or even detonation. However, in a real emergency situation stoichiometric composition of the combustible mixture is rarely observed. In case of low leakage rates of the flammable gas together with large room volume, formed combustible mixture could be of overall lean composition. Combustion of the lean mixtures, despite being less harmful compared to fast deflagration and detonation, can result in ignition of more chemically active substances or cause malfunction of equipment and have to be considered as a potential danger as well. Taking into account current developments aimed at deployment of hydrogen as a perspective environmentally friendly fuel and possible accidental scenarios on nuclear power plants involving hydrogen accumulation in the atmosphere under containment, it is of great importance to analyse details of flame propagation in lean hydrogen-air mixtures including ultra-lean compositions.

Lean combustion is a subject for extensive experimental and theoretical studies in the last decades. Usually, those studies were performed in microgravity conditions that allowed obtaining significant

Proceedings of the Ninth International Seminar on Fire and Explosion Hazards (ISFEH9), pp. 1422-1427
Edited by Snegirev A., Liu N.A., Tamanini F., Bradley D., Molkov V., and Chaumeix N.
Published by Saint-Petersburg Polytechnic University Press
ISBN: 978-5-7422-6498-9 DOI: 10.18720/spbpu/2/k19-139

results on flammability limits and stabilization mechanisms of those flames [1]. However, features of the lean flames subjected to terrestrial gravity conditions are still poorly investigated and understood, despite it is of crucial importance for practical fire safety applications. The aim of the present paper is to analyse by means of numerical modelling lean hydrogen-air flame structure and stability under terrestrial gravity conditions.

PROBLEM SETUP

To understand features of flame dynamics in ultra-lean gaseous mixtures we consider the following problem setup (see Fig. 1). Semi-unconfined space is filled with the ultra-lean hydrogen-air mixture with 5-9 vol% hydrogen content (corresponding equivalence ratios $\varphi = 0.125\text{-}0.235$) at normal initial conditions ($T = 300$ K, $p = 1$ atm). Hydrogen-air mixtures are considered firstly due to a large amount of accumulated data on hydrogen combustion and secondly due to perspectives of hydrogen use as a green fuel. The bottom wall is isothermal and its temperature is equal to the initial ambient temperature of the mixture ($T_{\text{wall}} = 300$ K). The numerical ignition of the mixture occurs near the bottom wall in the small region instantly “heated up” to 1500 K. Terrestrial gravity force is taken into account, gravity acceleration value $g = 9.8$ m/s^2. For reference cases from the hydrogen concentration range 5–6 vol% the cell size of the Cartesian numerical grid was taken equal to 0.2 mm, which is in convergence region for one-dimensional flame velocity tests carried out in advance. For the richer concentration region (8–9 vol%) a finer grid (0.1 mm) was used.

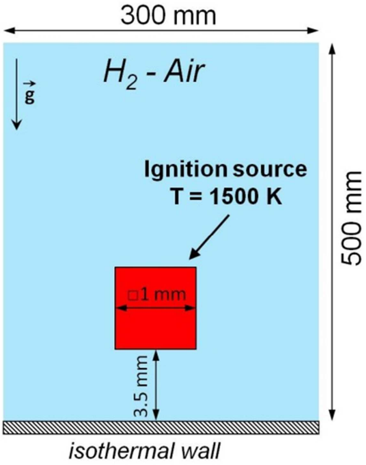

Fig. 1. Problem setup.

Governing equations represent a gas-dynamical model in the low-Mach number approximation. According to the considered low-Mach number approximation, the pressure is represented as a sum of thermodynamic pressure, which is assumed to be constant, and dynamic component of pressure fluctuations. To determine dynamic pressure a Poisson equation is solved at each time step. Herewith the value of velocity divergence is calculated from the equation for energy, taking into account both energy change due to heat release and heat transfer and the energy change according to the equation of state. To achieve detailed description of the simulated processes the thermal conductivity, multicomponent diffusion, natural convection and energy release due to chemical transformations were taken into account. Specific heat capacities and enthalpies of formation are calculated using the JANAF tables [2]. Diffusion model is based on the zeroth-order Hirshfelder-Curtiss approximation [3]. Mixture averaged transport coefficients were obtained from the first principles of the gas kinetics theory [4]. Diffusion velocities were calculated taking into account the correction velocity approach proposed in [5]. Thermal diffusion and Soret effects were not incorporated into the model. Chemical kinetics was calculated according to the contemporary kinetic scheme [6].

RESULTS AND DISCUSSION

Let us first analyze the stability of the flame ball subjected to the buoyancy force immediately after ignition. After the mixture is ignited near the isothermal wall the main mechanism of the combustion is the diffusion of the deficient reactant, which is hydrogen in our case, to the reaction zone. Stability of this diffusive flame is determined by the heat loss to the cold isothermal wall [7]. As combustion proceeds, hot combustion products become involved in upward motion by the buoyancy force. That motion determines the formation of gas-dynamical convective flow that consists of toroidal vortex located in the region related to the flame kernel (see Fig. 2). Gas-dynamical vortical motion determines flame surface stretch and lateral extension. In the case of 6 vol% (and richer) mixture, this surface stretch leads to the cap-shaped flame structure formation, whose further evolution will be discussed later. In less reactive 5 vol% hydrogen (and leaner) mixture flame stretch results in flame surface local breakup in the stagnation point near vicinity of the flame surface. Kinetic energy dissipation into heat within vortical structures defines local temperature increase in this area that supports flame kernels located near the center of vortical motion. However, spatial scales of these kernels are not enough to maintain stable combustion. So, the reaction quenches finally.

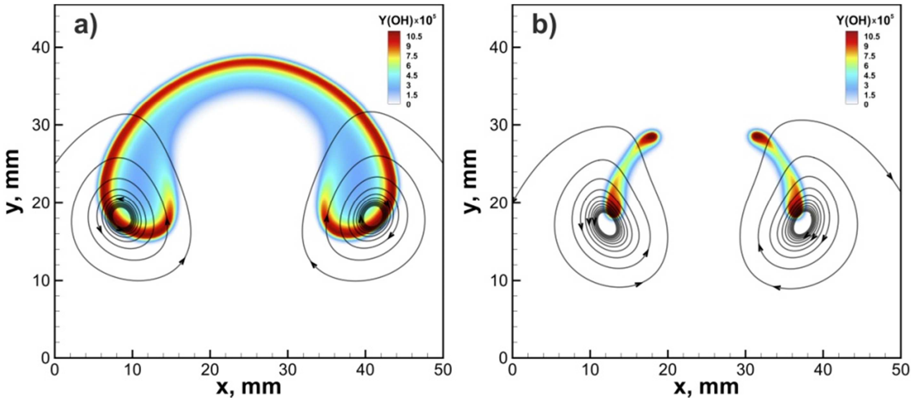

Fig. 2. Flame structure for time instant 180 ms after ignition. (a) mixture with hydrogen content 6 vol%; (b) mixture with hydrogen content 5 vol%. Background is colored by OH concentration.

One of the distinguishing features of the ultra-lean flame is the superadiabatic temperature of the hot combustion products which is due to the dominant diffusion mechanism of combustion. In microgravity conditions, the balance between the superadiabatic temperature of the flame on the one hand and heat losses, on the other hand, determines its stability. That defines lower lean flammability limit measured for ultra-lean flame balls than that predicted for planar adiabatic flames. The same mechanism is relevant for the flame in terrestrial gravity conditions where the temperature of ultra-lean flame combustion products is as well higher than adiabatic values. In terrestrial gravity conditions, an additional factor in the form of the flame stretch by the convective flows alters lower flammability limit, which however is still lower than that for the adiabatic flame (see Fig. 3). Thus flammability limit obtained for microgravity conditions in spherical symmetry is estimated as ~4 vol% H_2, which is in good agreement with the leanest composition for which flame balls were observed [1]. At the same time the flammability limit for the flame in terrestrial gravity is 5.25-5.50 vol% H_2 whereas adiabatic planar flame limit is 9 vol% H_2.

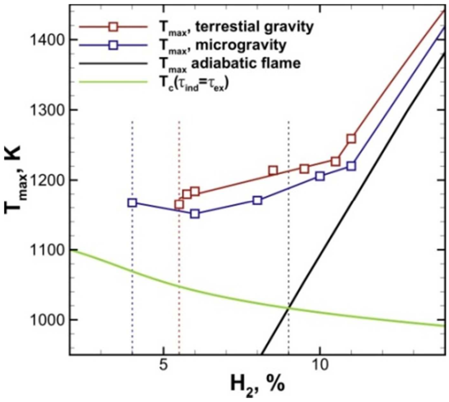

Fig. 3. Maximum temperature of the flame for various compositions of hydrogen-air mixture. Green line – T_c, crossover temperature; red line – T_{max} for terrestrial gravity conditions; blue line – T_{max} for microgravity conditions obtained from additional calculations in spherical symmetry; black line – T_{max} for adiabatic flame. Dashed lines represent stable combustion limits for ultra-lean flames in microgravity conditions (dashed blue line), terrestrial gravity conditions (dashed red line) and freely propagating planar flame (dashed black line).

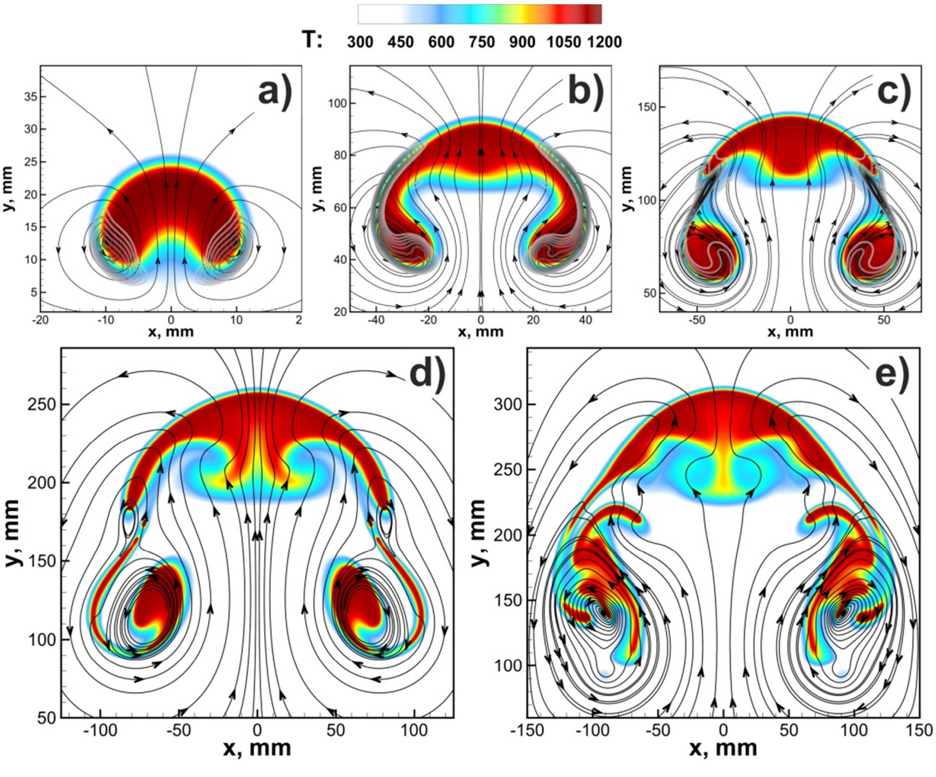

Fig. 4. Ultra-lean hydrogen flame evolution. (a) 100 ms, (b) 350 ms, (c) 500 ms, (d) 800 ms, (c) 950 ms. Background is colored by temperature. Streamlines are illustrated by the solid lines with arrows. On figures (a), (b), (c) vorticity contours colored by the vorticity are also presented.

After the initial stage, if the flame overcomes stretch induced by convection (e.g. in a mixture with hydrogen content 6 vol% and richer), the upward propagation caused by the buoyancy force continues. At the same time, the flame area becomes larger (see Fig. 4 a,b). Cap-shaped flame structure evolves and undergoes several breakup events due to the lateral flame surface detachment in recirculation area behind the main flame core (see Fig. 4 c,d). However, detached flame kernels do not quench and rise with the main core in its thermal wake. Due to a higher temperature in the wake, these kernels sometimes even reconnect with the main flame core. All these processes determine complex large-scale structure of the stable developed flame ball (see Fig. 4 e) which consists of the main flame core and several stable flame kernels moving behind it.

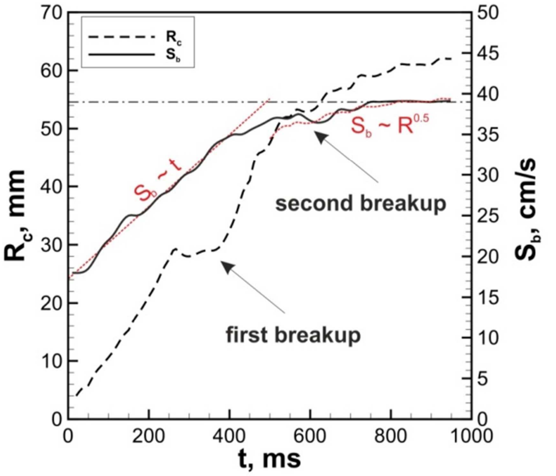

Fig. 5. Histories of the flame front leading point rising velocity (S_b) and curvature radius of the main flame core (R_c). Theoretically predicted terminal velocity for the closed bubble with curvature radius 62 mm shown by dash-dotted horizontal line. Dashed red lines represent approximations of the rising velocity on different stages of flame development.

Evolution of the flame in the ultra-lean hydrogen-air mixture is similar to that of the gas bubble rising in liquid [8]. Gas-dynamical flows induced by the upward motion of the flame are also in good agreement with those developing during the bubble rising [9] and similar to the bubble with small values of the surface tension. In such a case high enough strain rates lead to the peripheral breakup of the flame structure [10]. Taking into account qualitative correspondence between two phenomena one can use theoretical estimations obtained for the closed bubble to describe flame-ball rising in the ultra-lean mixture under terrestrial gravity conditions. In particular, it is known that bubble achieves terminal rising velocity that can be estimated as $S_b = 0.5\sqrt{gR}$, where R is the curvature radius of the bubble [11]. Figure 5 shows histories of the rising velocity and the curvature radius of the main flame core measured near the symmetry plane. From Fig. 5 it is evident that flame core achieves terminal velocity S_b~38.9 cm/s, that is in a good agreement with theoretical estimation for bubble terminal velocity. It should be noted that flame core terminal velocity is much higher than combustion velocity in the mixture of the considered compound.

CONCLUSIONS

Convective gas-dynamical flows accompanying the process of flame evolution in ultra-lean hydrogen-air mixtures in terrestrial gravity conditions play a crucial role on every stage of the flame development. Immediately after ignition convective flows determine stretch of the flame surface that in the case of the near limit flames can result in the local breakup of the flame and subsequent flame quenching despite the superadiabatic temperature of the combustion products. As a result, lean concentrations limit for the stable flame formation in terrestrial gravity occurs to be greater compared with that measured in microgravity conditions but still lower than the limit for the adiabatic planar flame. Further development of the flame is governed by the convective rise of the hot combustion products and lateral expansion due to vortical flows. Obtained structure of the ultra-lean hydrogen-air flame represents the stable cap-shaped main core followed by the widely spread in space multi-kernel combustion zone. Stable large-scale structure of the flame propagating with the terminal velocity much greater than burning velocity in ultra-lean mixtures pose a threat for fire and explosion safety that should be taken into account in the development of safety measures.

ACKNOWLEDGMENTS

The research was carried out using the equipment of the shared research facilities of HPC computing resources at Lomonosov Moscow State University and supercomputers at Joint Supercomputer Center of the Russian Academy of Sciences (JSCC RAS).

REFERENCES

[1] P.D. Ronney, M.S. Wu, G.H. Pearlman and J.W. Karen, Experimental Study of Flame Balls in Space: Preliminary Results from STS-83, AIAA J. 36 (1998) 1361–1368.

[2] M.W. Chase Jr, NIST-JANAF Thermochemical Tables, 4th Edition, Washington, DC, American Chemical Society & New York, American Institute of Physics for the National Institute of Standards and Thechnology, 1998.

[3] J.O. Hirschfelder, C.F. Curtiss, R. B. Bird, The molecular theory of gases and liquids, revised Edition, Wiley, New York, 1964

[4] R.J. Kee, M.E. Coltrin, P. Glarborg, Chemically Reacting Flow: Theory and Practice, 1st Edition, Wiley-Interscience, Hoboken, New Jersey, 2003.

[5] T. Coffee, J. Heimerl, Transport algorithms for premixed, laminar steady-state flames, Combust. Flame 43 (1981) 273-289.

[6] A. Keromnes, W.K. Metcalfe, K.A. Heufer, N. Donohoe, A.K. Das, C-J. Sung, et al. An experimental and detailed chemical kinetic modeling study of hydrogen and syngas mixture oxidation at elevated pressures, Combust. Flame 160 (2013) 995–1011.

[7] J.D. Buckmaster, G. Joulin, Influence of boundary-induced losses on the structure and dynamics of flame-balls, Combust. Sci. Technol. 89 (1993) 57–69.

[8] V.V. Bychkov, M.A. Liberman, Dynamics and stability of premixed flames, Phys Rep 325(4-5) (2000) 115–237.

[9] J. Hua, J.F. Stene, P. Lin, Numerical simulation of 3D bubbles rising in viscous liquids using a front tracking method, J. Comput. Phys. 227 (2008) 3358–82.

[10] M.K. Tripathi, K.C. Sahu, R. Govindarajan, Dynamics of an initially spherical bubble rising in quiescent liquid, Nat. Commun. 6 (2015) 62–8.

[11] R.M. Davies, G. Taylor, The mechanics of large bubbles rising through extended liquids and through liquids in tubes, Proc. R. Soc. Lond. Ser. A 200(1062) (1950) 375–90.

Author Index

Proceedings of the Ninth International Seminar
on Fire and Explosion Hazards

Vol. 2

Подписано в печать 01.04.2019. Формат 70x100/16. Печать офсетная.
Усл. печ. л. 58.0. Тираж 210. Заказ 44.

Отпечатано с готового оригинал-макета, предоставленного составителями,
в Издательско-типографском центре политехнического университета.
195251, Санкт-Петербург, Политехническая ул., 29.
Тел. (812) 552-77-17; 550-40-14.